19th INTERNATIONAL CONFERENCE ON MACHINE DESIGN AND PRODUCTION

CONFERENCE PROCEEDINGS

Editorial Board

Metin AKKÖK
Besim BARANOĞLU
Cemal ÇAKIR
S. Engin KILIÇ
E. İlhan KONUKSEVEN
Bahram LOTFİ
Ali ORAL
Ulvi ŞEKER
Hakkı Özgür ÜNVER
Volkan ESAT
Selcuk HIMMETOĞLU

umtik 2022

31 August - 03 September 2022

CAPPADOCIA- TURKIYE

MATIMAREN
DEPARTMENT OF MECHANICAL ENGINEERING
MIDDLE EAST TECHNICAL UNIVERSITY
ANKARA-TURKEY

Dedicated to the memory of

Memiş ACAR,
Tibor TÓTH,
Emmanuel O. EZUGWU,
Günter PRITSCHOW,

and of all other IPC members we have lost in previous years.

All rights of this book are reserved by the Middle East Technical University.
None of the papers printed in this book may be reproduced without the prior permission, in writing, from the Author(s) of the paper(s) and the editors of the book. The papers can however be cited by giving the source.

This book can be obtained from the following addresses:

UMTIK
Mechanical Engineering Department
Middle East Technical University
06800 Ankara- Turkey

Manufacturing Engineering Department
ATILIM University
06830 Ankara- Turkey

Cover Print:

METU- Ankara

Printing and Binding:

METU- Ankara

Printed by:

ODTÜ

ISBN

Organizing Committee

Metin AKKÖK	(METU, Dept. of Mechanical Eng.)	akkok@metu.edu.tr
Besim BARANOĞLU	(Novumek Technology Corp.)	Besim.baranoglu@novumek.com
Cemal ÇAKIR	(Uludağ, Dept. of Mechanical Eng.)	cemal@uludag.edu.tr
S. Engin KILIÇ	(Atılım, Dept. of Manufacturing Eng.)	engin.kilic@atilim.edu.tr
E. İlhan KONUKSEVEN	(METU, Dept. of Mechanical Eng.)	konuk@metu.edu.tr
Bahram LOTFI	(Atılım, Dept. of Mechanical Eng.)	Bahram.lotfisadigh@atilim.edu.tr
Ali ORAL	(Balıkesiri, Dept. of Mechanical Eng.)	alioral@balikesir.edu.tr
Ulvi ŞEKER	(Gazi, Dept. of Mechanical Eng.)	useker@gazi.edu.tr
Vesile ŞENOL	(Cappadocia, School of Health Sciences)	vesile.senol@kapadokya.edu.tr
Hakkı Özgür ÜNVER	(TOBB ETÜ, Dept. of Mechanical Eng.)	hounver@etu.edu.tr

Organizing Committee of "Commemoration of Professor Memiş ACAR Day"

Volkan ESAT	(METU NCC, Dept. of Mechanical Eng.)	evolkan@metu.edu.tr
Selcuk HIMMETOĞLU	(Hacettepe, Dept. of Mechanical Eng.)	s.himmetoglu@hacettepe.edu.tr

Contact: umtik@metu.edu.tr **Tel:** +90 312 586 8888

International Program Committee

Erdem	ACAR	TÜRKİYE
Serpil	ACAR	UNITED KINGDOM
Samet	AKAR	TÜRKİYE
Mehmet	AKÇAY	TÜRKİYE
M. Oktay	ALNIAK	TÜRKİYE
Ali M.	ALSAMHAN	SAUDI ARABIA
Yusuf	ALTINTAŞ	CANADA
Carla	ANFLOR	BRASIL
Ömer	ANLAĞAN	TÜRKİYE
Ahmet Hakan	ARGEŞO	TÜRKİYE
Özgür	ASLAN	TÜRKİYE
Paulo Jorge	BÁRTOLO	UNITED KINGDOM
Bekir	BEDİZ	TÜRKİYE
Erhan	BUDAK	TÜRKİYE
Barış	ÇETİN	TÜRKİYE
Ender	CİĞEROĞLU	TÜRKİYE
Leo	COURTY	FRANCE
Samad	DADVANDIPOUR	HUNGARY
László	DUDÁS	HUNGARY
Ferenc	ERDELYI	HUNGARY
Kaan	ERKORKMAZ	CANADA
Tahir	FİDAN	TÜRKİYE
Faby	FONG	TAIWAN R.O.C.
Necdet	GEREN	TÜRKİYE
Greg	GIBBONS	UNITED KINGDOM
Wen-Yuh	JYWE	TAIWAN R.O.C.
Bilgin	KAFTANOĞLU	TÜRKİYE
Hakan	KALKAN	TÜRKİYE
Yiğit	KARPAT	TÜRKİYE
Şükran	KATMER	TÜRKİYE
Yusuf	KAYNAK	TÜRKİYE
Zafer	KAZANCI	UNITED KINGDOM
Behzat Bahadır	KENTEL	TÜRKİYE
Z. Murat	KILIÇ	UNITED KINGDOM
İsmail	LAZOĞLU	TÜRKİYE
Yangmin	LI	HONG KONG
Ming-Chyuan	LU	TAIWAN R.O.C.
Tzuo Liang	LUO	TAIWAN R.O.C.
Yoshiyuki	MATSUOKA	JAPAN
Pınar	MENGÜÇ	TÜRKİYE
Tuğrul	ÖZEL	USA

Emre	ÖZLÜ	TÜRKİYE
Fahrettin	ÖZTÜRK	TÜRKİYE
K.G.Durga	PRASAD	INDIA
PVJ Mohan	RAO	INDIA
Ferit	SAİT	TÜRKİYE
İbrahim Etem	SAKLAKOĞLU	TÜRKİYE
Durmuş Tayyar	ŞEN	TÜRKİYE
Eiji	SHAMATO	JAPAN
Sergey	SHEVTSOV	RUSSIA
Vadim S.	SILBERSCHMIDT	UNITED KINGDOM
Uğur	ŞİMŞİR	TÜRKİYE
Cihan	TURHAN	TÜRKİYE
Ali	ÜNÜVAR	TÜRKİYE
Min	WAN	P.R.C.
Ulaş	YAMAN	TÜRKİYE
Hakan	YAVAŞ	TÜRKİYE
Wong Kuan	YEW	MALAYSIA
Ali Rıza	YILDIZ	TÜRKİYE
Bülent	YILMAZ	TÜRKİYE
Michael	ZAEH	GERMANY

SUPPORTING MUNICIPALITIES AND ASSOCIATIONS

CAPPADOCIA UNIVERSITY

ATILIM UNIVERSITY

TÜBİTAK

MAKİNA İHRACATÇILARI BİRLİĞİ

MATIMAREN
Makina Mühendisliği Bölümü
Orta Doğu Teknik Üniversitesi
Ankara-Türkiye

MATİMAREN

MAIN SPONSOR



ARMADA YAZILIM

SILVER SPONSORS

ASSYSTEM

MARRİN MAKİNE



HAIMER

BRONZE SPONSORS

VAN PRECISION ENGINEERING

USEL

GESBEY

PAKSAN

YEMTAR

ENGINSOFT

FNSS

BELGIN

Conference Secretariat

ORIGIN EMC
Çamlık Mahallesi, Dinç sok. Muyar Plaza No: 4 D: 25 P.O. Box: 34774 Ümraniye, İSTANBUL
TEL: +90 216 372 23 30

www.originemc.com.tr
info@originemc.com.tr

Contact Address

http://www.umtik.com
umtik@metu.edu.tr

PREFACE

It gives us great pleasure to welcome you to the 19th International Conference on Machine Design and Production which we could finally organize after a two-year delay due to the worldwide outbreak of the Covid 19 pandemic.

When we were about to start planning the UMTIK 2020 Conference after the UMTIK 2018 Conference in Eskişehir, we received the sad news: the death of Professor Memiş Acar due to an aggressive illness on the 8th of August 2018. Memiş was a devoted and active member of the International Program Committee (IPC) of the past UMTIK conferences. He and his wife, Professor Serpil Acar, participated in our conferences and organized numerous events such as special sessions, forums and panels. We then decided to dedicate UMTIK 2020 to the memory of Professor Memiş Acar and to name the first day of the conference "The Commemoration Day of Professor Memiş Acar". Cappadocia University was selected as the venue because Cappadocia was Memiş's hometown.

During the isolation days of the COVID 19 pandemic, we lost three more IPC members: Professor Tibor Toth of Miskolc University, Hungary, Professor Günter Pritschow of the University of Stuttgart, Germany and Professor Emmanuel O. Ezugwu of the Airforce Institute of Technology, Nigeria, whose valuable friendship and contributions to UMTIK conferences will always be remembered.
As the first-day program will start with an opening session which will be followed by the plenary session on the memory of Prof. Memiş Acar chaired by Memiş's two former students: Assoc. Prof. Dr. Volkan Esat of METU NCC and Asst. Prof. Dr. Selçuk Himmetoğlu of Hacettepe University. His family, his friends, and his colleagues will tell their memories about Memiş to share with the participants. The next session in the morning will be the Keynote Speech of Prof. Serpil B. Acar on "Automotive Safety and Development of Passive Prevention Systems". The special "4th Design for Transport Safety" organized and to be chaired by Prof. Serpil B. Acar will take place in the afternoon in two parts. The first-day program will be closed with the Wellcome Cocktail in the evening.

The second-day program starts with a plenary session of two Keynote presentations by Professor Yusuf Altıntaş of British Columbia University on mathematical modeling of machining, machine tool vibrations and control, and by Professor Charlie C.L. Wang of the University of Manchester on simulation, sensing and control of soft robots. Honorary chairmen of UMTIK 2022, presidents of 7 supporting universities, will be the panellists of the panel "The role and the responsibilities of the universities for regional development will be moderated by Mr Cengiz Ultav, Board Member of Vestel Ventures. In the afternoon, Professor Ismail Lazoğlu of Koç University will deliver his online Keynote speech and share his experience on the critical role of advanced manufacturing in society and on human life in the age of Industry 4.0. About 20 conference papers will be presented and discussed in the remaining time until 18:00 three parallel sessions. The Conference Dinner will be in the evening as a closing event.

The third-day program starts with a plenary session. The first speaker of this session is Assoc. Prof. Tanfer Yandayan of the National Metrology Institute of Turkiye. He will deliver a perspective on the European Metrology Network (EMN) for Advanced Manufacturing. The next speech will be given by Prof. Erhan Budak of Sabancı University on "High-performance machining through process modelling". Prof. Vadim V. Silberschimidt of Loughborough University is the third speaker to talk on "Hybrid machining of advanced materials". About ten papers somehow related to the keynotes will be presented in the three parallel sessions before lunch. The afternoon session will start with the keynote speech of Prof. Matsuoka on "Design science towards integration of design". Related Special Session on "Design science and time-axis design" and other sessions comprising about 20 papers will take place in three parallel sessions until 18:00.

The fourth-day program is mainly concentrated on the implementation of Industry 4.0 in three countries: Croatia, Taiwan and Turkiye. The program starts with a plenary session of 2 keynotes: Prof. Ivica Veza of the University of Split will talk about the lean factory concept implemented at the University of Split; Dr Tzou-Liang Luo of ITRI, Taiwan will give a talk on intelligent machinery technology. Taiwanese experience in the implementation of intelligent manufacturing will be presented, discussed and shared in 5 different presentations in the following special session before lunch. Papers on automotive engineering will be presented and discussed in a parallel session. There will be a panel on "Industry 4.0 practices and case studies" as the first event in the afternoon. The panel will be moderated by Dr Doğan Hasan, CEO of UNOPro of Turkiye to present, discuss and share Turkiye's experience in Industry 4.0 implementation. The last plenary session of the day and the conference will be "5-Axis New Generation CNC Controller". It will be presented by Prof. Onur Tuncer, CEO of Milteksan, Turkiye.

We would like to express our sincere thanks to the Presidency and all members of Cappadocia University for hosting UMTIK 2022 and providing its facilities for our use as the Golden Sponsor of UMTIK 2022. We hope all the participants will feel the warm and positive atmosphere at Cappadocia University.

We highly acknowledge the Honorary Chair Persons of the Conference: Presidents of the seven universities, Professor Hasan Ali Karasar of Cappadocia University, Professor Yıldırım Üçtuğ of Atılım University, Professor Turkay Dereli of Hasan Kalyoncu University, Professor Ihsan Sabuncuoğlu of TED University, Professor Can Çoğun of Çankaya University, Professor Semih Aktekin of Nevşehir Hacı Bektaş Veli University and Professor Babür Özçelk of Konya Teknik University for their kind support and participation in our conference as the panelists in the 2nd Day Panel. We would like to express our sincere appreciation to Mr Cengiz Ultav for his hard work in organizing and moderating the 2nd Day Panel. We would like to thank all the keynote speakers, Professor Yusuf Altıntaş, Professor Charlie C. L. Wang, Professor Serpil B. Acar, Professor İsmail Lazoğlu, Professor Tanfer Yandayan, Professor Erhan Budak, Professor Vadim V. Silberschmidt, Professor Yoshiyuki Matsuoka, Professor Ivica Veza and Professor Onur Tunçer. Fourth Day Panel Moderator Dr Doğan Hasan and the panellists, organizers of the special sessions, session chairpersons, authors and all the participants are highly acknowledged for their valuable contributions. Asst. Prof. Dr Bahram Lotfi is gratefully acknowledged for the tremendous time and effort he spent in every phase of the conference organization and in the editorial work of the Conference Proceedings and the Abstracts Book.

Last, but not least, we would also like to thank TUBITAK, "The Scientific and Technological Research Council of Turkey", Turkish Machinery Exporters Union, silver and bronze sponsors, the International Program Committee Members, our Conference Secretariat, ORIGINEMC, UMTIK Scientific Secretariat: Res. Asst. Yunus Emre Nehri, Ramazan Namlu, Furkan Özbey and all those who contributed to the success of UMTIK 2022.
We wish all the participants a highly memorable time during their stay in Cappadocia.

The Organizing Committee
UMTIK 2022, August 31st - September 3rd 2022
Cappadocia, Turkiye

PREFACE

in loving memory of Professor Memiş Acar

The first day of the UMTIK 2022 Conference is dedicated to the late Professor Memiş Acar, whom we lost in 2018. Professor Memiş Acar was a keen supporter of the UMTIK conferences; and a friend, a valued colleague, a father figure to many. It gives us utmost pleasure not only to celebrate his life and achievements, but also to remember and cherish all the qualities he brought to the lives of everyone around him on the first day of the UMTIK 2022 Conference.
Professor Memiş Acar was a prominent academic and a scholar who educated successful engineers over his many years in academia, and conducted socially responsible research that saved, improved, and touched many lives. After having been educated in Türkiye, he developed and flourished for the vast majority of his academic career in the UK, establishing ties to many academic environments mainly in EU countries, the USA, and Türkiye. His research interests ranged from vehicle occupant safety, crashworthiness, child restraint systems, biomechanical modelling and design to textile engineering, nonwoven materials and its processing. He was highly productive accomplishing various research projects, publishing a great deal of international technical research papers attracting many researchers across the globe, and receiving a record number of citations. It would not be an exaggeration to say that he was undoubtedly one of the leading academics of Loughborough University, consistently a top ten UK higher education institution, with his world-class research, the roles he assumed within the University, its Council, and the Senate, and the quality he poured into teaching. One of his most valuable contributions to academia as well as to society at large was the researchers he moulded into successful academics and professionals, who are enjoying their fruitful careers in various areas in several countries.

Maybe more importantly than his academic achievements, Professor Memiş Acar was one of the finest human beings that people around him had the chance to meet and know. He was extremely polite, exceptionally thoughtful and considerate. He had unique personal qualities that brought out the best in people. He never hesitated to support not only his students, but everyone around him on and off campus, academically or personally. He had a great sense of humour, which was one of the colourful sides of his character. He had kind eyes and a comforting smile on his face which never faded whatever the circumstance. He had an undeniable impact on the community that surrounded him. He is missed dearly and remembered as a beacon of light for everyone around him.

We would like to extend our gratitude to the UMTIK Organising Committee, and Professor S. Engin Kılıç in particular, for making this commemoration and celebration event possible. A special heartfelt thanks goes to Professor Serpil Acar, the beloved wife of Memiş Hoca, for helping out to achieve a commemoration / celebration event worthy of Memiş Hoca. Last but not least, we would like to thank everyone that attends the first day and contributes to it, making it ultimately meaningful.

Dr Volkan Esat & Dr Selçuk Himmetoğlu
Organizing Committee of “Commemoration of Professor Memiş ACAR Day”
UMTIK 2022, August 31st - September 3rd 2022
Cappadocia, Turkiye

CONTENTS page

Machine Design, Modelling and Manufcturing

Determination of Fiber Orientations and Stiffness Properties via Micro-CT Scan Images: Application to Composite Materials with Microvascular Channels 27
Barış SABUNCUOĞLU, Hamed TANABI, Jeroen SOETE, Stepan V. LOMOV

Design for Transport Safety

A Dynamic Characterisation of Full-Overlap Low-Speed Rear Impacts 41
Selçuk HİMMETOĞLU, Canberk BEYHAN, Elif Nur ZENGİN

Analysis of Seat Belt Use and Thorax Injuries Sustained by Female Occupants in Frontal Impacts 53
Volkan ESAT, B. Serpil ACAR

Improving the Safety of London Bus Users Through Design 73
Jo BARNES, Laurie BROWN, Andrew MORRIS

E-Scooter Safety Studies and A User Trial Study
Sally MAYNARD, Graham HANCOX, Andrew MORRIS, B. Serpil ACAR 83

Occupant Protection in Seats with Fixed Recliners in Rear-End Collisions
Selçuk HİMMETOĞLU 97

Impact of Energy Technologies and Smart Systems on Human's Life

Experimental Studies on Thermal Degradation, Ignition and Combustion of Low-Vulnerability Gun Propellants 111
Leo COURTY, Samuel DELBARRE

Re-Defining Temperature Set-Point of An HVAC System Based on Thermal Comfort Zone of Students in A University Study Hall 125
Cihan TURHAN, Mehmet Furkan ÖZBEY

Metal Cutting I

Design of An Active Magnetic Bearing Spindle for Micro-Milling Applications 137
Kazi Sher AHMED, Bekir BEDİZ

Investigation of Dimensionality Reduction Methods for Chatter Detection with SVM 153
Kerem Utku DEMİR, Batıhan ŞENER, Hakkı Özgür ÜNVER

Development of An Ontology Based Dynamic Process Planning and Scheduling Methodology for Discrete Manufacturing Systems 171
Elaf Riyadh RESEN, Bahram LOTFİ, Saman AMİNBAKHSH

On the Finite Element Modeling Best Practices for the Metal Cutting Simulations 191
Ersen HATİPOĞLU, Mustafa BAKKAL, Erhan BUDAK

Metal Cutting II

Determination Cutting Parameters for Aggressive-High Performance Chip Removal of The Beveling Machine with Automated Workpiece Determination and Tool Path Generation System 209
Can TUNCER, Sakıp TÜRKÖZ, Ali ORAL

Comparison of ANN and RSM in Prediction of The Tangential Force in Turning of AISI 4140 Hardened Steel Considering Flank Wear 221
Osman ÖZTÜRK, Ali ÜNÜVAR

A Method to Obtain the Cross-Sectional Profile of the Region Swept by A Toroidal Cutter During A Screw Motion 231
Ahmet DOĞRUSADIK

Metal Cutting III

Dynamometer Design to Measure 2- Directional Cutting Forces in Turning Process 241
Ayberk TÜRK, Kaan Songür, Suat BENGÜR, Samet AKAR

Recursive Defining of Force Coefficients in Milling Process with Accelerometer 259
Barış ALTUN, Hakan ÇALIŞKAN, Orkun ÖZŞAHİN

A Design Improvement and Structural Analysis in A Pre-Designed Hybrid Drilling Machine 275
Mustafa BAKKAL, Mahmut YILMAZ, Alper YETER, Hasan Aytuğ KURT

Materials Behavior I

Changes on Surface Properties of Metals Due to Boron Nitride Coatings 289
Tuğçe HACALOĞLU, Asude AYDOĞAN, Bilgin KAFTANOĞLU

Influence of Punch Properties on Contact Mechanics of Coated Substrates 301
Mehmet N. BALCI

Materials Behavior II

Numerical Determination of The Necking Phenomenon using Stress Wave Propagation Technique 317
Şehram DİZECİ, Bahman PAYGOZAR

Computational Fluid Mechanics

Analysis of Acoustically Actuated Sedimentation Prevention System for Syringe Pumps 325
Arda KAYA, Güven ÖNER, Ömer Faruk ERGÜVEN, Ender YILDIRIM, F. Ginaz ALMUS

Design of An Anti-Sedimentation Syringe Pump for Microfluidics Applications 339
Eminalp KOYUNCU, A. Tardu KOÇUM, Enes KOÇ, Cem KÜÇÜKGENÇ, Baturay KURTOĞLU, Oğuzhan KARAKAŞ, Ender KURUKAHVECI, Bülent ÖZCAN, Ender YILDIRIM, F. Ginaz ALMUS

Investigation of the Effect of Hub Curve on the Performance of Radial Compressor for High-Speed Turbomachinery 357
Okan Deniz YILMAZ

Computational Mechanics

An Experimental and Numerical Study of Multi-Stage Hot Forging Process of CW617N Brass Alloy 369
Hakan COŞKUN, Tayfun ORHAN, Sami KURAL, Yusuf KAYNAK

Engineering Design

Bulk Passive Sensorless Sorting of Complex Cylindrical Components with Internal Features and Symmetrical External Tapers 381
Toby WILLIAMS, Kaddour BOUAZZA-MAROUF

Optimum Design of An Airplane Bracket using Topology and Shape Optimization Methods 391
Betül Sultan YILDIZ

The Optimum Structural Design of Aircraft Components for Additive Manufacturing 399
Betül Sultan YILDIZ

Automotive Engineering I

Modeling and Simulation of Active Double-Acting Hydro-Pneumatic Suspension System Using Fuzzy Logic Controller for 6x6 Terrain Vehicle 409
Kaan Berke ULUSOY, Bensu DEĞİRMENCİ, Erkin FİLİZ, Derin TÜREDİ, Mustafa KARAMAN, Ahmet Hamdi ALKAN, Erhan ilhan KONUKSEVEN

Design of A Two-Speed Dual-Clutch Transmission for Electric Vehicles 423
Selahattin Can BECERİKLİ, Hatice ERDOĞAN, Mustafa Bahdır BAYRAM, Ozan TEKİN, Ramin BARZEGAR

An Investigation of The Crashworthiness of Multi-Cell Filled Battery Side Beams 433
İsmail YAY, Emre DEMİRCİ

Automotive Engineering II

Design and Analysis of A Lightweight Chassis for An Electric Vehicle 447
Özgür AKDENİZ, Mert ALPAR, İsmail Utku HOROZOĞLU, Ozan TEKİN, Ramin BARZEGAR

Development of An Image Processing System for The Automatic Quality Control of Vehicle Airbag Plastic Parts 457
Bilgin DALLI, Mustafa Cemal ÇAKIR

System Optimization of Battery Discharge State using Artificial Neural Network in an Electric Vehicle Powertrain 471
Mehmet Onur GENÇ, Necmettin KAYA

Design Of Modular Planetary Gearbox with Two-Stage Planet Gears For Use in Valve Actuators 485
Seher SEVEN, Muhammed Mahbub İBİŞ, Evren COŞKUNER, Besim BARANOĞLU

Design of Machines

Cancellation of Singularities of RRRRP Planar Parallel Robots 497
Mustafa ÖZDEMİR, Sinan Yalçın ÖNAL

Investigating Effects of Polarization and Dimensions of Magnetic Coupling on Transmitted Torque by Finite Element Analysis 511
Seyed Hamed POUR RAHMATI KHALEJAN

Investigation of Permanent Magnet Synchronous Motors with Three Different Slot-Pole Combinations for Scooter Application 523
Hayatullah NORY, Serhat AKŞUN, Cansu AKSOY, Salıh ÇELİK

TÜRKÇE BİLDİRİLER

Computational Fluid Mechanics

3-Denklemli Türbülans Geçiş Modelinin Jenerik Gövde Geometrisi ile Başarim Değerlendirmesi 543
Hediye ATİK

Talaşlı İmalat

Daire Testere Tezgahlarında, Kesici Takım Üzerinde Oluşan Titreşimin İş Parçasına Etkisinin İncelenmesi 557
M. Berkan ALİSİNOĞLU, Hasan Ali CİVELEK, Onur GÖKMEN, Kadir ÇAVDAR

Tavlama Benzetimi Yöntemi ve Yanıt Yüzey Metodu Kullanılarak Yüzey Pürüzlülüğü için İşleme Parametrelerinin Optimizasyonu 567
Yunus Emre NEHRİ, Enes EZME, Gülşen AYDIN KESKİN, Ali ORAL

Isil İşlem Uygulanan AISI 420 Paslanmaz Çeliğin Tornalama İşlemi Üzerinde CBN Uçlar İle Yüzey Pürüzlülüğü Araştirmasi 579
Hasan Safa ÇAVUŞOĞLU, Seher SEVEN, Besim BARANOĞLU

Eklemeli İmalat Teknolojisiyle Üretilmiş Inconel 718 ve Ti6Al4V 'Nin Mikro Frezelenmesinde Kesme Koşullarının Etkisinin Araştırılması 591
Ahmet HASÇELİK, kubilay ASLANTAŞ, Mohd DANISH

Üretim Süreçleri ve Tasarımı

AlCrN Esaslı PVD Kaplamanın Enjeksiyon Kalıp Yüzey Kalitesine Etkileri 603
Yusuf ASLAN, Şükran KATMER, Ulvi ŞEKER

Görsel Lazer Nokta Kaynağı Uygulamalarında Açısal Konumlandırma Hatalarının Kaynak Kalitesine Etkisinin İncelenmesi 613
Emre ŞERİFAĞAOĞLU, Murat Erkin AKYÜZ, Barış KOYAŞ, Murat REİS

Taşıtlarda Ağırlık Azaltımında Hafif Malzeme Olarak Alüminyum Kullanımı 627
Yahya IŞIK, Recep ÇAĞLAYAN

Tasarımda Yaratıcılık ve Yenileşim

BİR SİLAH NAMLUSUNDA KOVAN-ATIM YATAĞI ETKİLEŞİMİNİN İNCELENMESİ 641
Muhammet Mustafa YILMAZ, Sadettin ORHAN

Düzlemsel Beş Çubuk Mekanizmasının Optimizasyon Sonucunda Elde Edilen Parametrelerin Dizayn Edilebilirliğinin İncelenmesi 663
Deniz Kavala ŞEN, Osman KOPMAZ

İnsansı Yüz Mimiklerine Sahip Animatronik Robot Surat Tasarımı ve İmalatı 673
Furkan TÜTÜNCÜ, Mustafa Cemal ÇAKIR

Otomotiv Mühendisliği

İş Makineleri Tasarımında Düşük Emisyonlu Alternatif Yakıt Uygulamaları 689
Ceyhun GÜL, L. Furkan MUMCU, T. Yasin ALTINAY, M. Can KATMER, Fatma YALÇIN, Ferhan FIÇICI

Tüp Hidroşekillendirmede Yükleme Profillerinin Bulanık Mantık Kontrol Algoritması ile Belirlenmesi 705
Yusuf Furkan YAPAN, Mevlüt TÜRKÖZ, MURAT DİLMEÇ, Hüseyin Selçuk HALKACI

PA12 Malzemesinden İmal Edilmiş 3 Katmanlı Yakıt Borusunun Sıcaklık ile Şekillendirme Analizi ve Yapılan Analizin Doğrulanması 721
Metin ALİBAŞOĞLU, Mustafa Cemal ÇAKIR

PAPERS

DETERMINATION OF FIBER ORIENTATIONS AND STIFFNESS PROPERTIES VIA MICRO-CT SCAN IMAGES: APPLICATION TO COMPOSITE MATERIALS WITH MICROVASCULAR CHANNELS

Barış SABUNCUOĞLU, *barissabuncuoglu@hacettepe.edu.tr,* Hacettepe University, 06800, Ankara, Turkey

Hamed TANABI, *h.tanabi@thk.edu.tr,* University of Turkish Aeronautical Association, 06790 Ankara, Turkey

Jeroen SOETE, *jeroen.soete@kuleuven.be,* Catholic University of Leuven, B-3001, Leuven Belgium

Stepan V. LOMOV, *stepan.lomov@kuleuven.be,* Catholic University of Leuven, B-3001, Leuven Belgium

ABSTRACT

Previously, a method with an in-house software was developed in KU Leuven Composite materials department, for the determination of several mechanical properties of composites from the scanned Micro-CT images. In this study, this method was used to determine the effect of microvascular channels on the mechanical behavior of composites Initially, the fiber orientation disturbance due to the channels was evaluated. Then the channel's effect on the composite stiffness is determined. The results revealed orientation disturbance in the out-of-plane direction with a maximum of about 6°. The presence of micro-channel reduced local stiffness up to 19%. Expected change in the mechanical properties were successfully determined with the proposed method.

Keywords: Composites, Micro-CT, Micro-vascular channels, fiber orientation, mechanical properties

1. INTRODUCTION

Investigating the internal structure of composites under micro-CT scanning device has become very popular in recent years. Using the images obtained from these scans, a volumetric 3D view of a composite sample can be constructed revealing the detailed internal structures [Soete et al. 2017, Wevers et al. 2018]. Previously, a method with a software called VoxTEX

was developed in KULeuven to determine the mechanical properties of fiber –reinforced composites via this 3D constructed images obtained from Micro-CT. Applying some novel image analysis techniques, the software can detect the constituents of the composite and provide valueable information regarding the fiber orientation, porosity, stiffness and permeability of the combined structure. The software has successfully been utilized to analyze the internal structure of various types of composites [Barburski et al. 2015, Liu et al. 2017, Straumit et al. 2017, Baran et al. 2018].

Aiming to develop techniques for health monitoring and self-healing composites with micro-vascular channels have gained attention in the literature [Wu et al. 2012]. In spite of their advantages, these channels cause a physical change in the lamina morphology near the channel affecting the predicted deformation behavior of the material. In quite a number of papers in the literature the effect of these channels on the mechanical behavior of composites is experimentally studied regarding the tensile [Zhou et al. 2004, Kousourakis et al. 2008], compressive [Trask et al. 2007], bending [Williams et al. 2007] deformation and interlaminar shear [Walker. 2004, Kousourakis et al. 2006, Norris et al. 2011]. There also exist numerical studies discussing the adverse effect of the channels [Huang et al. 2010, Nguyen et al. 2012, Liu et al. 2015, Hartl et al. 2016, Al-Shawk et al. 2018]. However, most of them are performed using simplified assumptions of the reinforcement geometry near the channel rather than direct representation of the actual fibrous architecture. In this study, the effect of microvascular channels on the fiber orientation and local composite stiffness are evaluated by image processing of micro-CT images taken around the channel region using the mentioned method. This image based technique also provides accurate representation of the models for numerical methods such as finite element analysis

2. SPECIMENS AND THE TEST PREPARATION

The analyses were performed for cross-ply glass-fiber composites with two configurations, $[0/90]_{3s}$ and $[90/0]_{3s}$. For convenience, in the rest of the paper the “3S” indication will not be mentioned. 12 plies for both configurations are prepared with glass fabric of areal weight, 350 gr/m2. The thickness of each ply was 4.5 mm. Taking the density of glass as 2.5 gr/cm3, the fiber volume fraction was calculated as approximately 37%. The diameter of micro-channel to be manufactured was determined as 1 mm based on the maximum channel diameter with respect to the laminate thickness suggested due to the considerations in manufacturing issues in [Kousourakis et al. 2008, Al-Shawk et al. 2018]. The channels were generated via removable solid wires technique [Huang et al. 2010, Wu et al. 2012].

3. MICRO-CT SCANNING ACQUISITION and IMAGE ANALYSIS

Micro-CT image acquisition was performed with a Nanotom S X-ray computed tomography system. Tomographic projections were acquired for a 180° rotation angle, with a 0.2° rotation step. X-ray source voltage and current were fixed at 90 KV and 180 µA for all scans. The pixel resolution in all scans was set between (4 µm)³ and (5 µm)³, specifically chosen to be smaller than the diameter of the reinforcing continuous glass fibers, while still keeping the entire sample within the field of view of the detector. Datos|x software was used to reconstruct the micro-CT scans and to export cross-sectional images. The 3D rendering of the [90/0] and [0/90] layup samples are given in Figure 1. In this paper, only the results of [0/90] layup are shown as more disturbance was observed in this configuration.

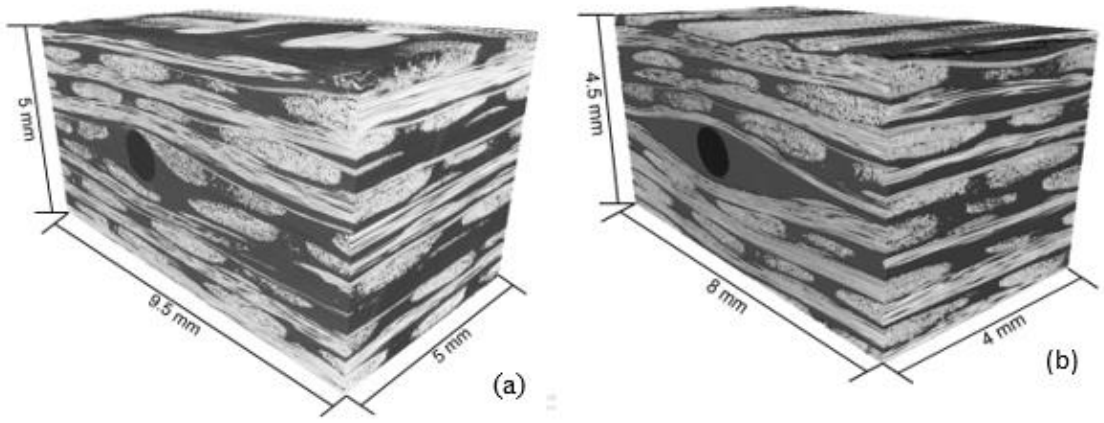


Figure 1. Micro-CT image of the samples: (a) [90/0]; (b) [0/90] configurations

Micro-CT images were imported into VoxTex in order to convert the datasets into voxel models, The structure tensor of the image was used to assign local fiber direction information to the elements in the voxel model. The procedure for generating voxel models is described in detail in [Straumit et al. 2015]. The voxel grey value and anisotropy were used in VoxTex to segment the voxel model into yarn and matrix elements, as described in [Straumit et al. 2015, Nguyen et al. 2018].

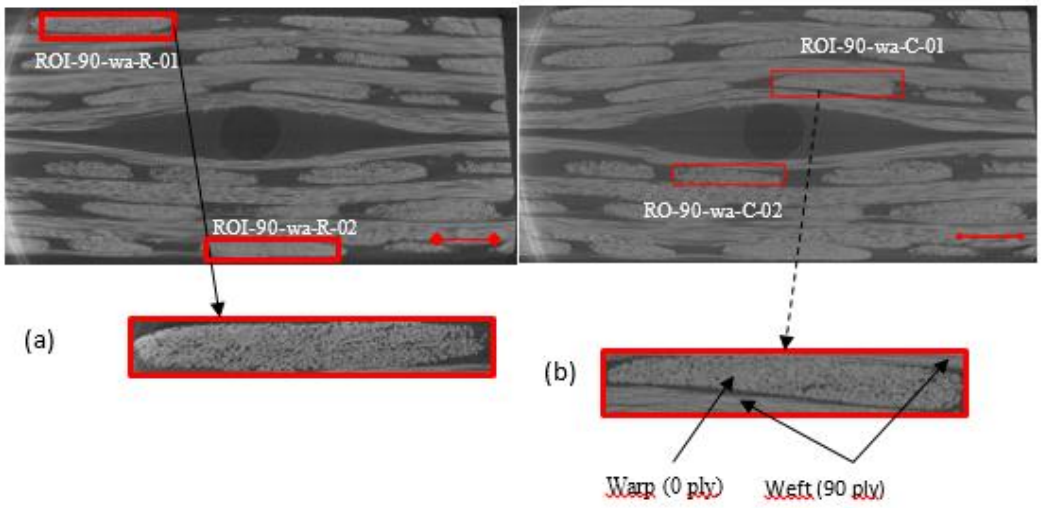
The disturbance of the warp and weft yarns were investigated separately. Here the warp yarns are the yarns that are oriented with the same direction with respect to the channel direction whereas the weft yarns are the transverse ones. The codes presented in Table 1 are used throughout the paper in order to separate the analyzed region of interest (ROI) for the orientation and grey scale histogram calculations. In some cases, two or more yarns are investigated with the same code. In such a case, the identification code is followed by two

more digits as 01, 02, etc. ROI images are presented in Figure 2. For each stacking condition and warp/weft fibers, the fibers away from the region and the fibers close to the region are studied.

The orientation vectors of the voxels were defined in a Cartesian coordinate system where xz-plane is the plane of the laminates and y-axis is the stacking direction. The vector orientation angles were defined in the spherical coordinate system as shown in Figure 3. Here the term "in plane angle (φ)" is used to define the angle in the plane of stacks and "out of plane angle (θ)" is used to define the angle in the image plane

Table 1. Codes used in the study and the definitions

ROI Code	**Definition**
ROI-90/0-W	**R**egion **o**f **I**nterest – Direction of the layer above the channel **(90/0)** - the entire image (**W**hole)
ROI-90/0-wa/we-R/C	**R**egion **o**f **I**nterest - Direction of the layer above the channel **(90/0)** – **wa**rp / **we**ft yarn – away from (**R**eference) / near (**C**hannel) the vascular channel



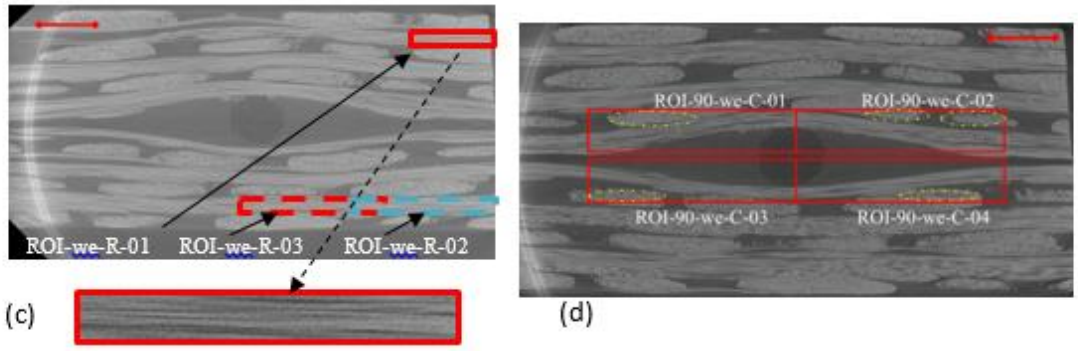


Figure 2. ROI images: (a) ROI-90-W; (b) ROI-90-wa-R; (c) ROI-90-wa-C; (d) ROI-90-we-R; (e) ROI-90-we-C;

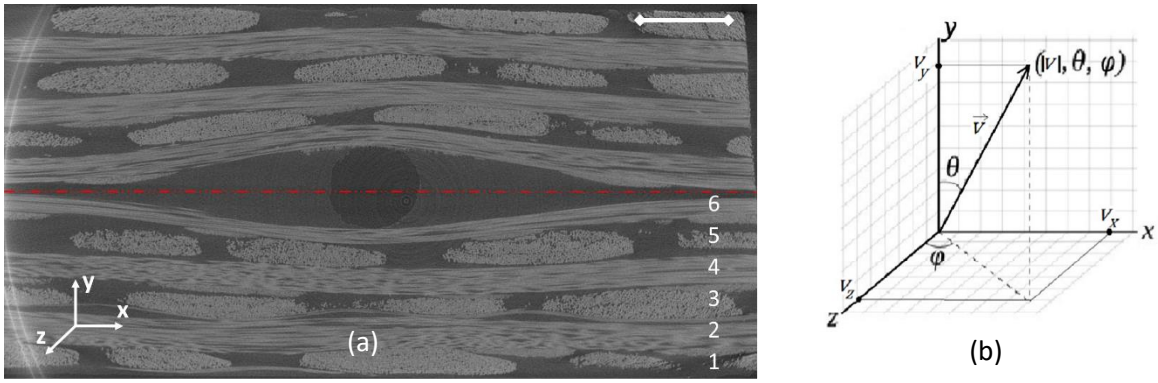


Figure 3. (a) Cross section of the vascularized glass fiber composite with [0,90]3s stacking configuration; (b) In plane (φ) and out of plane (θ) angles in spherical coordinate system.

4. FIBER ORIENTATION RESULTS

Figure 4 shows the anisotropy and density histogram of ROI-90-W. From the histograms, the presence of yarns, matrix and channel can clearly be observed. These are indicated in the respective locations on the histograms. To determine the orientations of the yarns solely, the density and anisotropy values of the channel and the matrix should be eliminated. This was provided by assigning threshold values while determining the orientations; 0.65 for anisotropy and 140 for the density threshold values were used. The orientation histograms of fibers are computed from the voxel model by considering the voxels with density and anisotropy values greater than these thresholds.

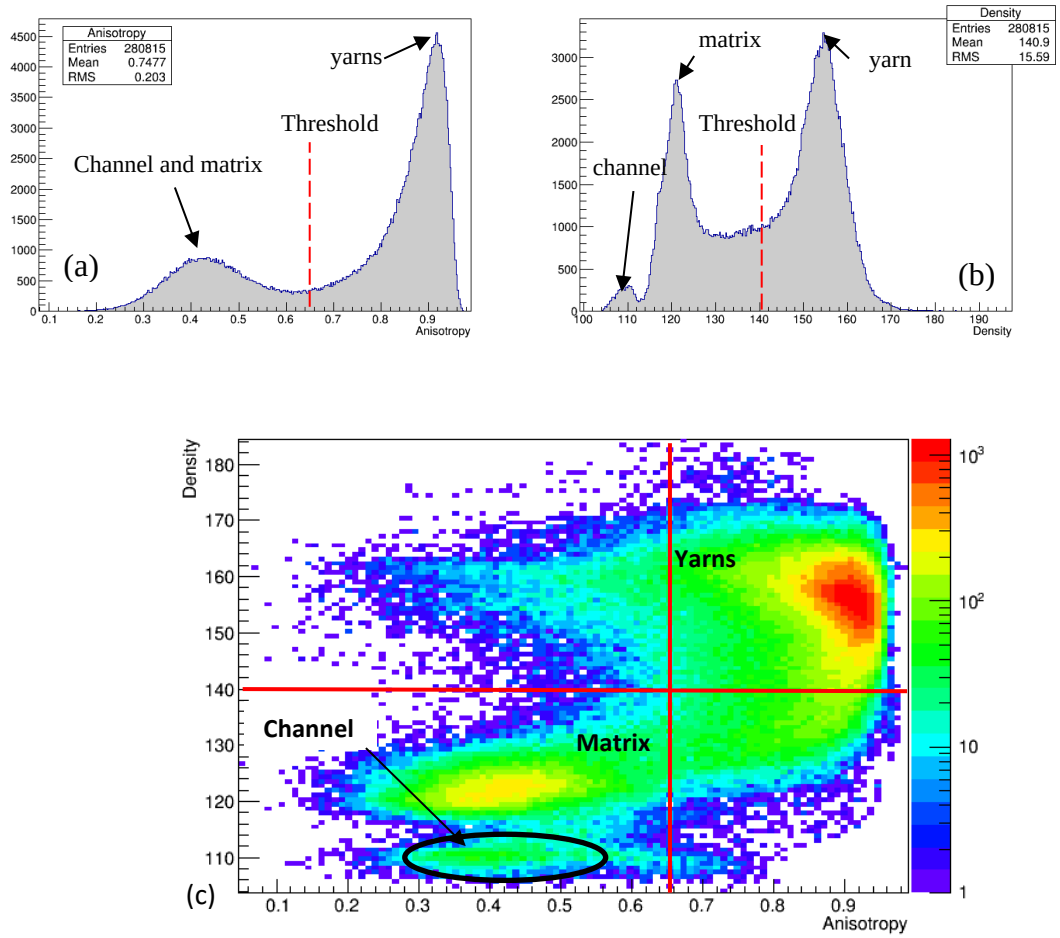


Figure 4. ROI_W results: (a) anisotropy; (b) density histogram; (c) anisotropy vs density (Thresholds are shown by red dashed lines in (a) and (b).

The orientation distribution of ROI-90-wa-R and ROI-90-wa-C reveal the effect of the channel on the warp yarns (Figure 5) Considering the presented histograms, the mean values of in-plane orientation for the warp yarns ROI-90-wa-R-01 and ROI-90-wa-R-02 were calculated as 1.5° and -1°, respectively. Note that the nominal value for the warp yarns' in-plane orientation angle is 0°. In Figure 5 c,d some voxels with in-plane orientation angle around 90° and -90° are present. They are due to the small portion of weft yarns, which cannot be avoided as a ROI has to be in a rectangular shape (see the zoomed image in Figure 2b). The out-of-plane (θ) orientation histograms show no significant difference in the channel region, so they are not presented here.

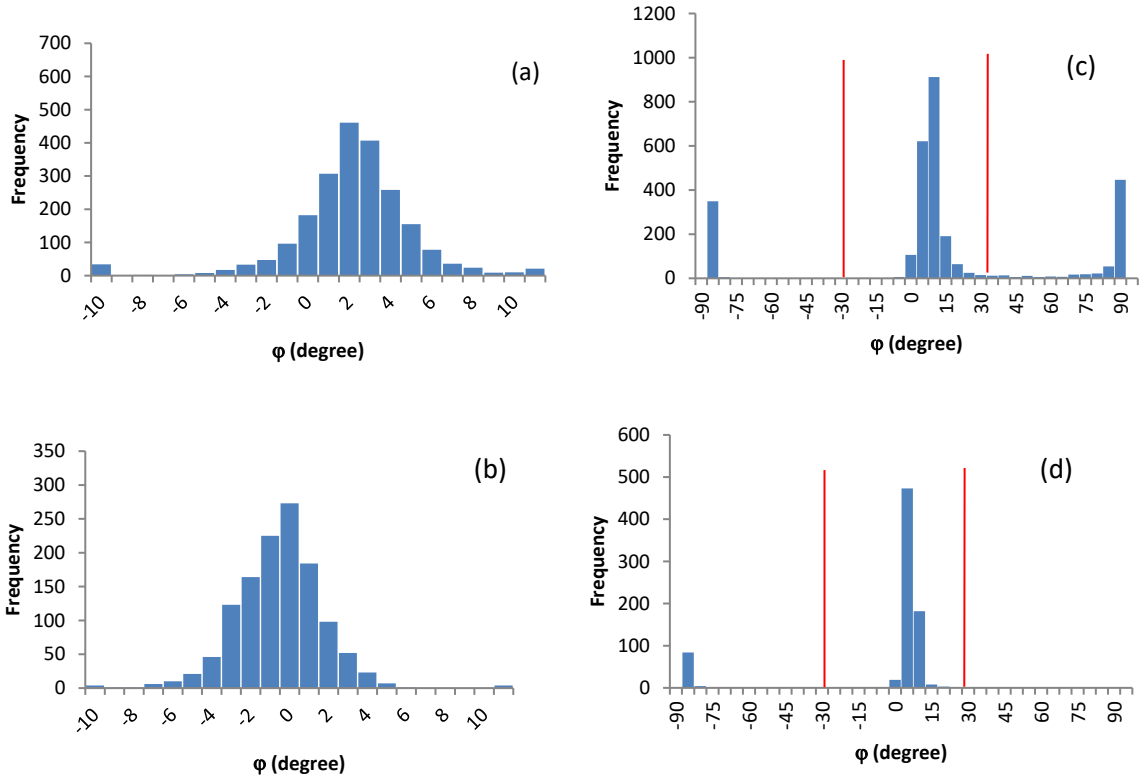


Figure 5. In-plane orientation histogram, (a)ROI-90-wa-R-01, (b)ROI-90-wa-R-02, (c)ROI-90-wa-C-01, (d) ROI-90-wa-C-02

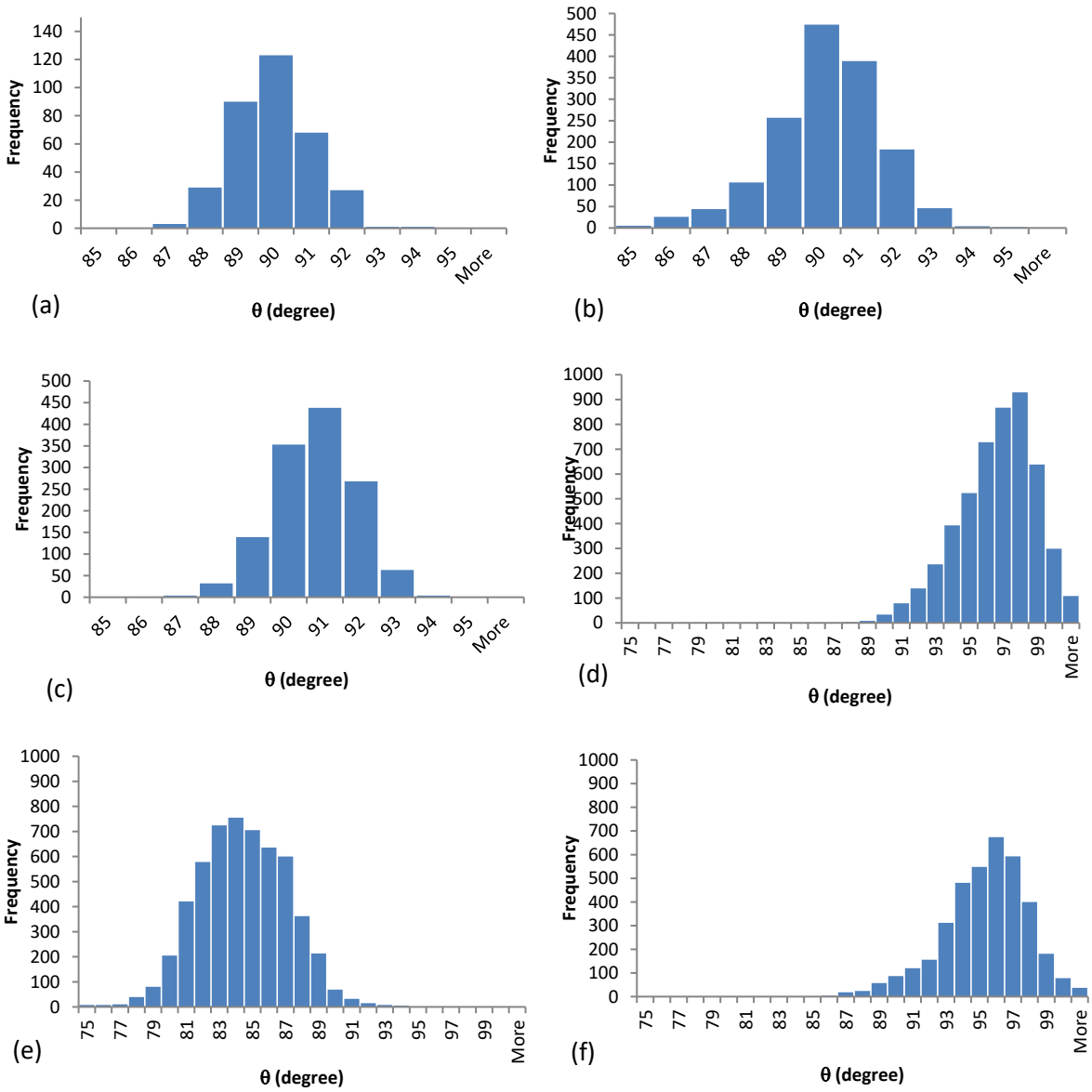
The mean value and standard deviation of the in-plane angle distribution of warp yarns near and away from channel are presented in Table 2. A larger deviation from nominal in-plane orientation were seen in yarns near channel, as expected.

Table 2 (a) In-plane orientation angle of warp yarns

ROI	φ_N (°)	$\bar{\varphi}$ (°)	$\bar{\varphi} - \varphi_N$ (°)	Stdv
ROI-90-wa-R-01	0	1.5	1.5	2.9
ROI-90-wa-R-02	0	-1	-1	2.3
ROI-90-wa-C-01	0	5.7	5.7	4
ROI-90-wa-C-02	0	3.9	3.9	2.3

φ_N : Nominal fiber orientation; $\bar{\varphi}$: Measured fiber orientation

Similar to warp yarns, weft yarns were also analyzed for the regions away and close to the channel. The histogram of only out of plane orientations for ROI-90-we-R and ROI-90-we-C are presented this time as no significant difference was observed in the in plane orientations For the weft yarns close to the channel, there is an apparent asymmetrical disturbance in the orientation of the yarns, which can be seen clearly even with the naked eye. Therefore, the left and right parts of the yarns, above and below the channel are investigated separately increasing the number of ROI's investigated in this configuration to four. The results are presented in Figure 6.



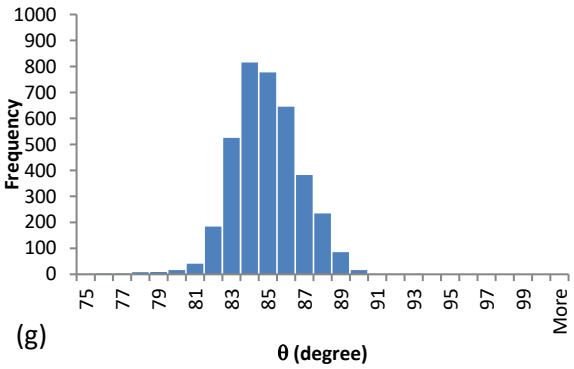


Figure 6. Out-of-plane orientation histogram, (a) ROI-90-we-R-01, (b) ROI-90-we-R-02, (c) ROI-90-we-R-03 (d) ROI-90-we-C-01, (e) ROI-90-we-C-02, (f) ROI-90-we-C-03, and (g) ROI-90-we-C-04.

The calculated mean and standard values for in-plane and out-of-plane angles are shown in Table 3 for all the weft yarns in this configuration. The mean values for the two ROIs in the left-hand side of the channel were determined as 84.4° and 83.9° whereas in the ones in the right-hand side, the mean values were 94.8° and 96.1°. Thus, the disturbance is calculated between 6.1° maximum near the channel. In addition to this change in the mean orientation, the standard deviation values of ROI-90-we-C-01 to 04 are relatively higher than the reference ones due to this disturbance.

Table 3. Out-of-plane orientation angle of weft yarns

ROI	φ_N (°)	$\bar{\varphi}$ (°)	$\bar{\varphi} - \varphi_N$ (°)	Stdv
ROI-90-we-R-01	90	89.4	-0.6	1.1
ROI-90-we-R-02	90	89.6	-0.4	1.4
ROI-90-we-R-03	90	90.2	0.2	1.1
ROI-90-we-C -01	90	96.1	6.1	2.4
ROI-90-we-C -02	90	83.9	-6.1	2.7
ROI-90-we-C -03	90	94.8	4.8	2.6
ROI-90-we-C -04	90	84.4	-5.6	1.9

φ_N : Nominal fiber orientation; $\bar{\varphi}$: Measured fiber orientation

5. STIFFNESS ANALYSIS

In this section, the effect of the channel on the local stiffness is investigated. VoxTex software uses an orientation averaging based homogenization scheme to calculate the stiffness of the region of interest. The calculations, also used in [Baran et al. 2018] proceed as follows:

First, the stiffness properties are assigned to all the voxels in the model. The stiffness matrices are defined in local coordinate systems of voxels, obtained from the structure tensor's anisotropy calculation using the Chamis model [Chamis. 1989]. The stiffness matrix of voxels, containing only matrix, is isotropic and is defined by the elastic properties of the matrix; the stiffness of the voxels, corresponding to voids, is zero. The local coordinate systems in the two latter cases are the same as the global system. Then the effective stiffness tensor $[C_{eff}]$ is approximated as:

$$[C_{eff}] = \sum_{i=1}^{N} w_i [T_i]^T [C_i][T_i] \quad (1)$$

where w_i is the volume fraction of the i-th voxel, N is the total number of voxels, C_i is the stiffness matrix of i-th voxel (zero for a voxel corresponding to a void) and $[T_i]$ is the transformation matrix which transforms the local coordinate system of i-th voxel to the global coordinate system.

The focused regions of interest are shown in Figure 7a. Initially, the stiffness components of ROI-Control-01 and ROI-Control-02 regions which are away from the channel are calculated as reference. Then the stiffness components of the entire image, referred as ROI-W, are calculated and compared with the results of control ROI's. Additionally, the stiffness values obtained from only a warp and weft yarn are presented to verify the results. They are indicated as ROI-warp and ROI-weft.

First, three ROIs were marked on the entire image as void, matrix and yarns (Figure 7a). Then VoxTex segments the control and vascularized regions, considering the anisotropy and gray scale density of the predefined void, matrix and yarn regions. The segmented volumes are shown in Figure 7b indicating that the channel, yarns and the matrix are segmented correctly. Finally, the mechanical properties of each constituent were assigned.

In order to determine the properties of yarns, the fiber volume ratio in each yarn should be determined. First, the mass for a unit length of a single yarn was calculated by measuring the weight of a yarn of a certain length. Then the cross-sectional area of yarns was measured using the open source software ImageJ. Finally, the fiber volume fraction of fibers inside the yarns (VoF) was calculated by equation (2):

$$VoF = \frac{m}{\rho . A . L} \quad (2)$$

Where m is the measure weight of the yarn (0.118∓0.002 gr), A is the cross-sectional area (610∓25 mm^2), ρ is the density of the glass fibers (2.5 gr/cm^3) and L is the length of the weighted yarn (10 cm). Using this equation, VoF was determined as 78 ∓ 4%

The properties of yarns are calculated by the software considering this ratio and the properties of matrix and the fibers. Young's modulus of 75 GPa and Poisson's ratio of 0.25 was used for the properties of glass fibers in micro-scale [Sabuncuoglu et al. 2014] whereas 2.5 GPa and 0.35 was used for the same properties of epoxy [Al-Shawk et al. 2018]. Finally, a very low Young's modulus value was assigned to the void region that would not affect the overall stiffness. The calculated stiffness for entire (ROI-W), control ROIs, yarns are presented in Table 4.

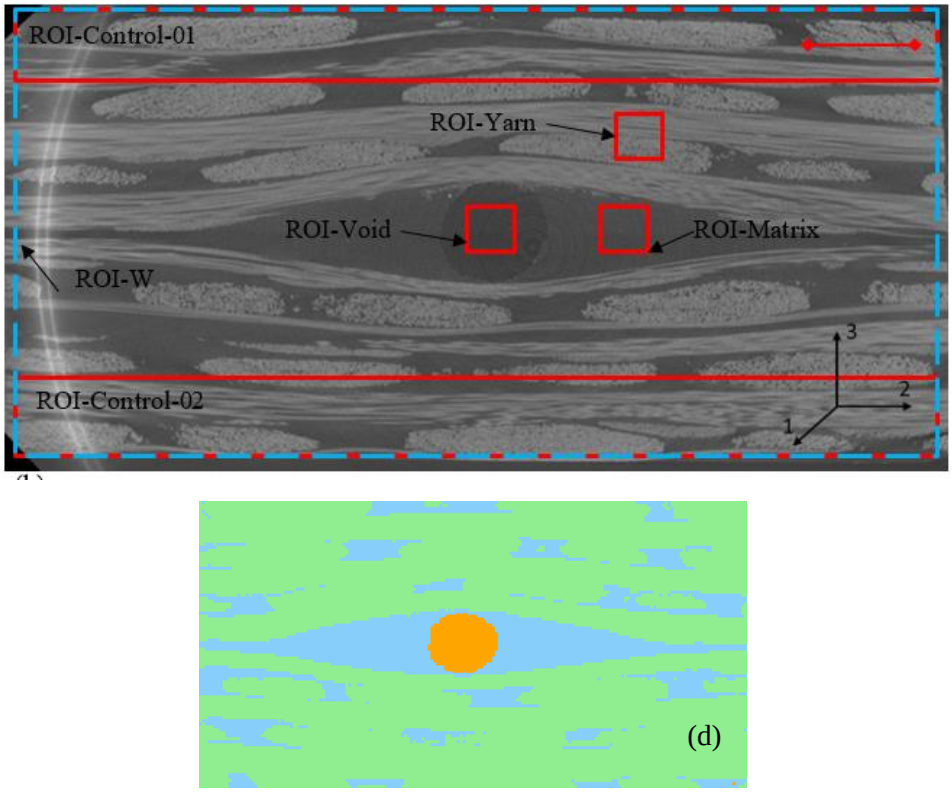


Figure 7. (a) Selected ROIs for stiffness analysis; (b) segmented regions

Table 4. Stiffness Calculation Results: (b)[0,90]3s

ROI-	Control-01	Control-02	W	Warp	Weft
E_1 (GPa)	30.2	27.0	23.6	58.5	17.1
E_2 (GPa)	32.0	31.7	27.1	17.1	58.7
E_3 (GPa)	15.1	14.7	12.6	17.1	17.1
ν_{12} (%)	0.14	0.18	0.15	0.08	0.33
ν_{13} (%)	0.16	0.15	0.18	0.08	0.27
ν_{23} (%)	0.32	0.32	0.33	0.33	0.27
G_{12} (GPa)	5.6	5.1	4.5	6.4	6.4
G_{13} (GPa)	5.4	5.4	4.7	5.5	6.4
G_{23} (GPa)	5.5	5.1	4.6	6.4	76.4

ROI-warp and ROI-weft results indicate that the ratio of the longitudinal and transverse moduli of the impregnated yarns is about 3:1. In the other configurations, Young's moduli lie between these two extremes. ROI-W results show that the calculated overall stiffness values for warp and weft yarns were very close to each other. This was expected since the laminate thickness and fiber volume fraction were kept same at both configurations. When ROI-W results are compared with ROI-Control-01 and 02, approximately 17% and 15% reduction was observed in E_1 and E_2 respectively. The disturbance of yarns near to channel and the presence of a large resin pocket caused this reduction.

6. CONCLUSIONS

The internal structure of a composite with a microvascular channel was investigated in this study. The micro-CT provided a very detailed image and revealed all the microstructure around the channel. VoxTex software is a very practical tool to analyze the fiber orientations and stiffness of a certain region. The fiber orientation results clearly reveal the adverse effect of channels especially in the out of plane direction. The stiffness calculations showed confidence in the identification of orientations. The asymmetry in the overall Young's moduli for warp and weft directions were clearly revealed. The results from different control volumes indicated a reduction in overall stiffness due to the presence of a channel. This is the largest suggested diameter channel to laminate thickness ratio considering the manufacturing issues thus a further reduction in stiffness was not expected. However, other material parameters such as different fiber volume ratio or the presence of multiple channels can significantly affect the stiffness.

REFERENCES

1. **Soete, J., et al. (2017)**. "Lattice Boltzmann Simulations of Fluid Flow in Continental Carbonate Reservoir Rocks and in Upscaled Rock Models Generated with Multiple-Point Geostatistics", Geofluids, Vol.2017, pp.

2. **Wevers, M., et al. (2018)**. Applications of CT for non-destructive testing and materials characterization. Industrial X-Ray Computed Tomography, Springer**:** 267-331.

3. **Barburski, M., et al. (2015)**. "Micro-CT analysis of internal structure of sheared textile composite reinforcement", Composites Part A: Applied Science and Manufacturing, Vol.73, pp 45-54.

4. **Liu, Y., et al. (2017)**. "Prediction of linear and non-linear behavior of 3D woven composite using mesoscopic voxel models reconstructed from X-ray micro-tomography", Composite Structures, Vol.179, pp 568-579.

5. **Straumit, I., et al. (2017)**. "Identification of the flax fibre modulus based on an impregnated quasi-unidirectional fibre bundle test and X-ray computed tomography", Composites Science and Technology, Vol.151, pp 124-130.

6. **Baran, I., et al. (2018)**. "X-ray computed tomography characterization of manufacturing induced defects in a glass/polyester pultruded profile", Composite Structures, Vol.195, pp 74-82.

7. **Wu, A. S., et al. (2012)**. "Sensing of damage and healing in three-dimensional braided composites with vascular channels", Composites Science and Technology, Vol.72, No.13, pp 1618-1626.

8. **Zhou, G., et al. (2004)**. "Through-the-thickness mechanical properties of smart quasi-isotropic carbon/epoxy laminates", Composites Part A: Applied Science and Manufacturing, Vol.35, No.7, pp 797-815.

9. **Kousourakis, A., et al. (2008)**. "Tensile and compressive properties of polymer laminates containing internal sensor cavities", Composites Part A: Applied Science and Manufacturing, Vol.39, No.9, pp 1394-1403.

10. **Trask, R. S., et al. (2007)**. "Bioinspired self-healing of advanced composite structures using hollow glass fibres", Journal of The Royal Society Interface, Vol.4, No.13, pp 363-371.

11. **Williams, G., et al. (2007)**. "A self-healing carbon fibre reinforced polymer for aerospace applications", Composites Part A - Applied Science and Manufacturing, Vol.38, No.6, pp 1525-1532.

12. **Walker, L. (2004)**. Real time structural health monitoring–is it really this simple. International SAMPE Technical Conference, SAMPLE.

13. **Kousourakis, A., et al. (2006)**. "Interlaminar properties of polymer laminates containing internal sensor cavities", Composite Structures, Vol.75, No.1, pp 610-618.

14. **Norris, C. J., et al. (2011)**. "Interactions between propagating cracks and bioinspired self-healing vascules embedded in glass fibre reinforced composites", Composites Science and Technology, Vol.71, No.6, pp 847-853.

15. **Huang, C.-Y., et al. (2010)**. "Characterization and analysis of carbon fibre-reinforced polymer composite laminates with embedded circular vasculature", Journal of The Royal Society Interface, pp.

16. **Nguyen, A. T. T. and A. C. Orifici (2012)**. "Structural assessment of microvascular self-healing laminates using progressive damage finite element analysis", Composites Part A: Applied Science and Manufacturing, Vol.43, No.11, pp 1886-1894.

17. **Liu, P. F., et al. (2015)**. "Finite Element Analysis of Progressive Failure and Strain Localization of Carbon Fiber/Epoxy Composite Laminates by ABAQUS", Applied Composite Materials, Vol.22, No.6, pp 711-731.

18. **Hartl, D. J., et al. (2016)**. "Effects of microchannels on the mechanical performance of multifunctional composite laminates with unidirectional laminae", Composite Structures, Vol.143, pp 242-254.

19. **Al-Shawk, A., et al. (2018)**. "Investigation of stress distributions in the resin rich region and failure behavior in glass fiber composites with microvascular channels under tensile loading", Composite Structures, Vol.192, pp 101-114.

20. **Straumit, I., et al. (2015)**. "Quantification of the internal structure and automatic generation of voxel models of textile composites from X-ray computed tomography data", Composites Part A: Applied Science and Manufacturing, Vol.69, No.Supplement C, pp 150-158.

21. **Nguyen, N. Q., et al. (2018)**. "Micro-CT measurement of fibre misalignment: Application to carbon/epoxy laminates manufactured in autoclave and by vacuum assisted resin transfer moulding", Composites Part A: Applied Science and Manufacturing, Vol.104, pp 14-23.

22. **Chamis, C. C. (1989)**. "Mechanics of composite materials: past, present, and future", Journal of Composites, Technology and Research, Vol.11, No.1, pp 3-14.

23. **Sabuncuoglu, B., et al. (2014)**. "Micro-scale finite element analysis of stress concentrations in steel fiber composites under transverse loading", Journal of Composite Materials, Vol.49, No.9, pp 1057-1069.

A DYNAMIC CHARACTERISATION OF FULL-OVERLAP LOW-SPEED REAR IMPACTS

Selçuk HİMMETOĞLU, *s.himmetoglu@hacettepe.edu.tr* Hacettepe University, Turkey

Canberk BEYHAN, *canberkbeyhan@hacettepe.edu.tr* Hacettepe University, Turkey

Elif Nur ZENGİN, *elifzengin@hacettepe.edu.tr* Hacettepe University, Turkey

ABSTRACT

This study presents a dynamic and statistical analysis of full-overlap low-speed staged rear impacts conducted by the AGU Research Group in Switzerland. A total of 101 staged two-vehicle rear impacts are analysed in which there are override/underride impacts or crashes with full engagement of the bumpers. A work-energy approach is applied to model dynamically two-vehicle full-overlap rear impacts. In the second stage of this study, regression analyses are performed to find correlations between closing speed versus coefficient of restitution, mutual crush, and the ratio of returned and absorbed energies. The presented analysis in this study can be a useful source for accident reconstruction and modelling low-speed rear impacts.

Keywords: Rear impact, Stiffness, Energy analysis

1. INTRODUCTION

Low-speed rear impacts are a common source of whiplash associated disorders whose injury mechanisms are still not completely understood [Nishimura et al., 2015]. In whiplash associated disorders, there occurs pain and discomfort in the head and neck system. Whiplash associated disorders (or simply whiplash) occur typically in low-speed rear impacts with delta-V less than 25 km/h [Eis et al., 2005]. Delta-V is the change in velocity of the struck car as a result of impact. Therefore, it is important to quantify the velocities, accelerations and the energies involved in low-speed rear impacts to assess whiplash risk. Moreover, modelling low-speed rear impacts is useful in accident reconstruction and simulation studies.

Staged rear-impact tests are valuable experiments to characterise dynamically the mechanics of crashes. The most recent staged low-speed rear impacts (with delta-V around 10 km/h) were performed by AGU Research Group (Arbeitsgruppe für Unfallmechanik) in Zürich, Switzerland [AGU, 2022] involving both braked and unbraked tests. Nishimura et al. (2015) analysed 45 unbraked rear-impact tests from the AGU database to model low-speed rear impacts by using lumped-mass modelling approach using a linear spring-mass model and linear acceleration time model; this modelling approach was coupled with regression analysis to find relationships between vehicle stiffness, mean and peak acceleration, impact speed, time to common velocity and maximum dynamic crush. Scott et al. (2010) conducted low-speed bumper-to-bumper rear impact tests (with delta-V up to 5.5 km/h) to extract force versus deformation curves of the bumpers at the contact interface to model low-speed rear impacts using lumped masses.

The effects of braking cannot be neglected in the modelling of low-speed rear impacts and it has been shown that as the braking force increases, coefficient of restitution decreases, the impact duration increases, the deformations of the vehicles increase and the velocities at the end of impact decrease. These conclusions were validated by staged rear-impact tests and lumped-mass modelling for delta-V's up to 14.7 km/h corresponding to closing speeds of up to 25 km/h [Han, 2007; Mastandrea and Vangi, 2005]. In another study, the relationship between closing speed and coefficient of restitution was analysed by conducting 30 unbraked low-speed collinear collisions; it was observed that the coefficient of restitution (ranging from 0.2 to 0.6) decreases as the closing speed (ranging from 1 km/h to 24 km/h) increases [Cipriani et al., 2002]. Regression curves were then fit to these data.

In this paper, 101 staged low-speed rear impacts from the AGU database with delta-V's around 10.5 km/h are analysed involving both braked and unbraked tests. These tests are modelled by using work-energy equations [Himmetoglu, 2016; Huang, 2002] and then regression analyses are performed. With the aid of this provided data, the modelling of the tests yields coefficient of restitution of the impact, maximum dynamic mutual crush, local stiffnesses of the interacting structures, total energy absorbed by both cars, total energy returned in the unloading phase, maximum dynamic deformations, elastic rebound of structures during the unloading phase and the elastic rebound of structures after separation of cars. This paper presents the modelling of braked tests in the AGU database which has not been performed before. The number of the tests in the AGU database is large and very suitable to perform statistical analyses. This experimental data provides useful information from which crash pulses and the energies involved in low-speed rear impacts can be derived.

2. STAGED LOW-SPEED REAR IMPACT TESTS

In order to characterise dynamically low-speed rear impacts, 101 staged impact tests from the AGU database are selected and analysed. In these tests, the struck vehicle (2) is stationary before impact whereas the striking vehicle (1), with an impact velocity V_1 between 12.4 km/h and 27.1 km/h, is braked in 89 tests and unbraked in 12 tests (see Figure 1). The resulting velocity change (ΔV_2) of the struck vehicles (2) ranges from 8.4 km/h to 16.3 km/h with corresponding standard deviations (std) shown in Table 1. In these tests, the masses of the cars (m_1, m_2) range from 880 kg to 2550 kg. The coefficients of restitutions (e) of the impacts vary between 0.07 and 0.478. The tests involve 100% overlap (full-overlap) override/underride impacts or collisions with full engagement of the bumpers. Overlap is the percentage of the total width of a vehicle covered by its collision partner.

The striking vehicles (1) were accelerated to the desired impact speed and then released just before the collision in the unbraked tests. A similar procedure was applied for the braked tests in which the striking vehicle was released before the braking point. Brake was applied only to the striking vehicle and no gear was engaged in both the striking and struck vehicles. In the braked tests, the braking force was applied to the striking car throughout the impact. SAE J211 standard is applied to filter and process the experimental data [AGU, 2022; SAE, 2007]. At the end of each collision, vehicle accelerations and static crush were measured. The staged tests involved vehicles mostly with model years between 1991 and 2018.

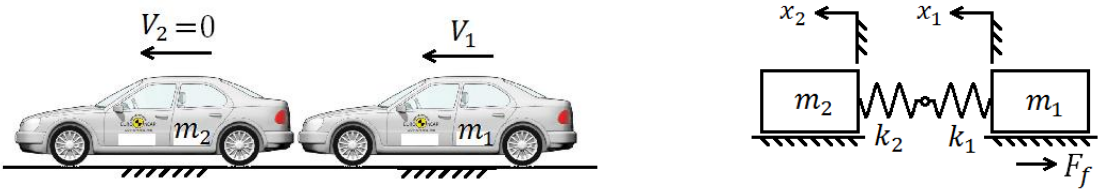


Figure 1. AGU low-speed rear impact tests (adapted from [EuroNCAP, 2014])

Table 1. AGU low-speed rear impact test data

	Unbraked					Braked			
	max	min	avg	std		max	min	avg	std
m_1 [kg]	1903	1028	1392.3	254.2		2550	880	1456.7	292.9
m_2 [kg]	1900	972.5	1326.5	259.2		2506	940.5	1500.9	335.3
V_1 [km/h]	27.1	12.4	16.9	4.07		26.6	14.2	19.56	2.98
ΔV_2 [km/h]	16.3	8.4	10.45	2.04		12.9	8.6	10.69	0.95
e	0.388	0.155	0.261	0.08		0.478	0.07	0.277	0.09

The results of an exemplar test are given in Figure 2, in which the striking vehicle (Car1) was braked and weighed 951.5 kg, the struck vehicle (Car2) weighed 1704.5 kg. Prior to impact, the striking vehicle had an impact speed of 26 km/h and the struck vehicle was stationary. As shown in Figure 2, braking produced an almost constant deceleration of 7.3 m/s^2 which was reported in the crash test data. The acceleration data are integrated numerically to calculate the velocities and displacements of the cars. Mutual crush is calculated by taking the difference of the displacements of the cars ($x_1 - x_2$) as shown in Figure 1 and it represents the total deformation of both cars until they separate from each other. Negative values of mutual crush indicate that cars have already separated from each other in the rebound phase of the collision.

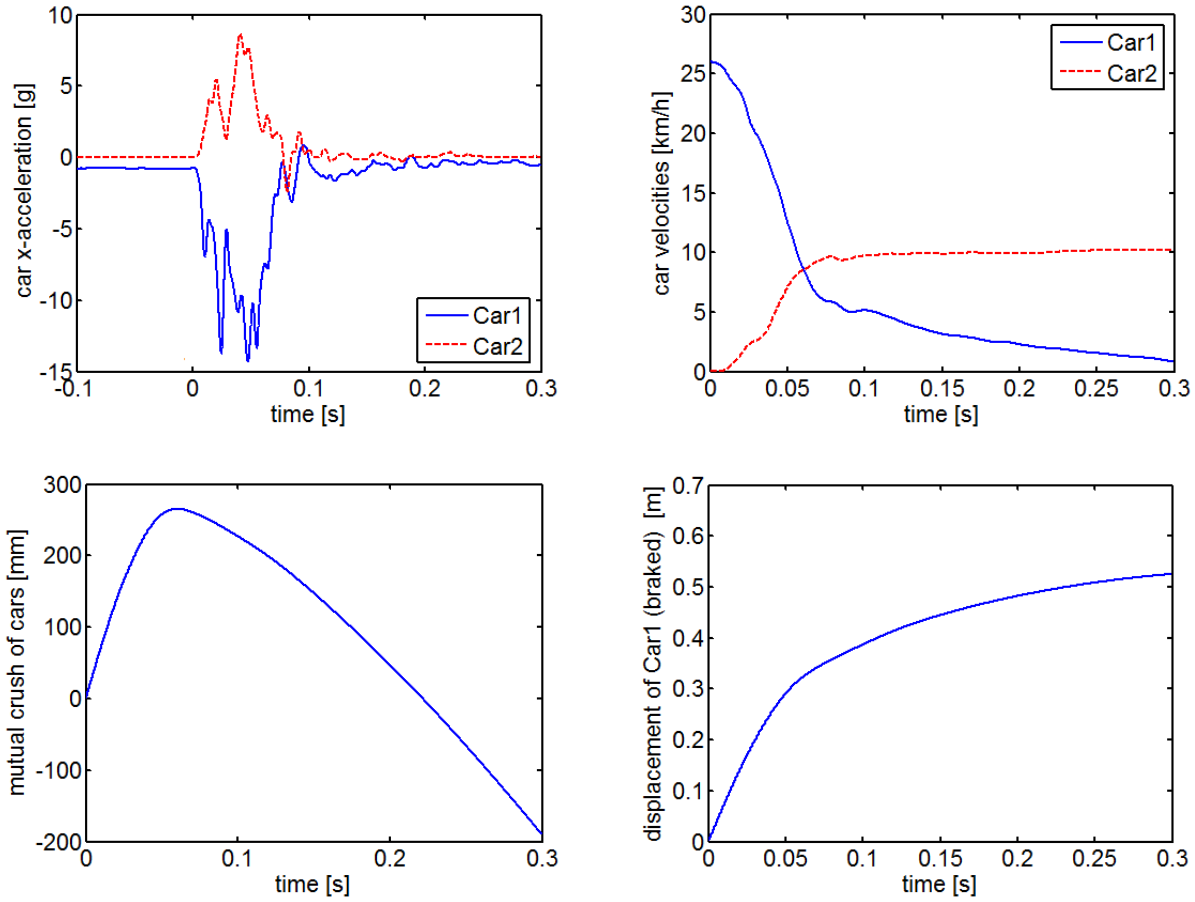


Figure 2. An exemplar braked test: accelerations, velocities, displacements

3. MODELLING OF FULL-OVERLAP LOW-SPEED REAR IMPACTS

Figure 1 shows the lumped-mass modelling of full-overlap low-speed rear impacts in which V_1 and V_2 are the pre-impact velocities of the cars, m_1 and m_2 are the masses of the cars, x_1 and x_2 are the displacements of the cars, k_1 and k_2 are the stiffnesses of the cars at the contact region and F_f is the braking force applied on Car1. The collected experimental data

comprises car accelerations, pre-impact velocities, delta-V of both cars, the amount of braking, the impact duration and the static crush after the impact. The following notation is used in the formulations given in Equations (1) to (9) whose derivations and the principles of crash mechanics can be found in the reference by Himmetoglu (2016).

$V_1 - V_2 = V$: closing speed

V_c : common velocity at the end of the loading phase of the impact

W_T : total crush energy absorbed by both cars in the loading phase of the impact

a_b : deceleration of the striking car due to braking alone

Δx_{1L} : displacement of the braked car in the loading phase of the impact (see Figure 2)

t_L : time when the loading phase ends and cars reach common velocity

k_{L1}, k_{L2} : local loading stiffnesses of the cars at the contact area

F_{max} : magnitude of the crush force acting on both cars at the end of the loading phase

s_{T1}, s_{T2} : maximum deformations (dynamic crush) of the cars at the end of the loading phase

s_T : total deformation (mutual crush) of both cars at the end of the loading phase

k_{eqL} : equivalent local loading stiffness of both cars

W_R : total elastic energy returned to the cars in the unloading (rebound) phase of the impact

V_1', V_2' : velocities of the cars when they separate from each other in the unloading phase

t_f : time when cars separate from each other in the rebound phase of the impact

Δx_{1U} : displacement of the braked car in the unloading phase of the impact (see Figure 2)

R : a ratio of returned over absorbed energies

r : ratio of the static crushes measured after the impact

s_{c1}, s_{c2} : maximum local static crushes of the cars measured at the end of the impact

s_p : mutual crush at the separation of cars when the unloading phase ends

s_{p1}, s_{p2} : individual crushes at the time of separation

s_{e1}, s_{e2} : elastic rebound displacement of car structures at the time of separation

s_{ef1}, s_{ef2} : elastic rebound displacement of car structures after separation of cars

e : coefficient of restitution

$$m_1 V_1^2/2 + m_2 V_2^2/2 = (m_1 + m_2) V_c^2/2 + W_T + F_f |\Delta x_{1L}| \quad (1)$$

$$\Delta x_{1L} = x_1(t_L) - x_1(0) \quad , \quad F_f = m_1 a_b \quad (2)$$

$$W_T = k_{L1} s_{T1}^2/2 + k_{L2} s_{T2}^2/2 = F_{max} s_{T1}/2 + F_{max} s_{T2}/2 = F_{max}(s_{T1} + s_{T2})/2 \quad (3)$$

$$W_T = {F_{max}}^2/(2k_{L1}) + {F_{max}}^2/(2k_{L2}) = {F_{max}}^2/(2k_{eqL}) \quad , \quad k_{eqL} = k_{L1} k_{L2}/(k_{L1} + k_{L2}) \quad (4)$$

$$W_R = m_1 (V_1')^2/2 + m_2 (V_2')^2/2 - (m_1 + m_2) V_c^2/2 + F_f |\Delta x_{1U}| \quad (5)$$

$$\Delta x_{1U} = x_1(t_f) - x_1(t_L) \quad , \quad R = \sqrt{W_R/W_T} \tag{6}$$

$$r = s_{c2}/s_{c1} = s_{T2}/s_{T1} = k_{L1}/k_{L2} = s_{p2}/s_{p1} \quad , \quad s_p = s_{p1} + s_{p2} \quad , \quad s_T = s_{T1} + s_{T2} \tag{7}$$

$$s_{e1} = s_{T1} - s_{p1} \quad , \quad s_{e2} = s_{T2} - s_{p2} \quad , \quad s_{ef1} = s_{p1} - s_{c1} \quad , \quad s_{ef2} = s_{p2} - s_{c2} \tag{8}$$

$$e = (V_2' - V_1')/(V_1 - V_2) \tag{9}$$

The loading stiffness as defined in Equation (3) is the slope of the straight line that is fitted to the crush force versus deformation graph of the structures in the loading phase. Approximating the crush force versus deformation behaviour of the structures by a best-fit straight line has been shown to be a reasonable estimation in work-energy analysis of collisions [Scott et al., 2010; Himmetoglu, 2016; Huang, 2002; Himmetoglu, 2021]. In the literature, the term stiffness is commonly used to indicate the resistance of car structures to impact, hence the term stiffness involves the overall effects of the stiffness and damping properties of the materials in car structure [Huang, 2002; Himmetoglu, 2021]. At the end of the impact, the deformations on both cars at the contact areas are measured and in this analysis, the maximum local deformations occurring on both cars are recorded and identified as the maximum local static crushes of the cars. Hence, the loading stiffnesses are actually local corresponding to the areas where maximum static crushes occur.

The ratio of static crushes is utilised to obtain estimations of the local loading stiffnesses by using Equations (4) and (7). It is also assumed that the ratio of static crushes is approximately equal to ratios of maximum deformations of the cars at the end of the loading phase and the ratio of crushes at the time of separation. This has been shown to be a viable approximation in other studies [AGU, 2022; Himmetoglu, 2021]. Once the mutual crush at the end of the loading phase (s_T) and the mutual crush at the time of separation (s_p) are found, Equation (7) is used to calculate the individual crushes.

In the unloading phase, there occurs elastic spring-back effect in which the car structures tend to return to their original dimensions due to the returned energy W_R. Hence, there is rebound of the structures but since the crash is not fully elastic, the structures usually do not return to their original shapes unless the closing speed is too low. It has been observed in several studies that the structures continue to rebound after separation of cars [AGU, 2022; Himmetoglu, 2021; Varat and Husher, 2000], hence this elastic rebound after separation is calculated as well in Equation (8).

4. DATA ANALYSIS AND RESULTS

The experimental data and the equations in the previous section are used together to obtain estimations for the local loading stiffnesses, maximum deformations of the cars, the parameter R indicating a ratio of returned over absorbed energies (see Equation (6)) and the ratios between maximum deformations and elastic rebound displacements. The results are shown in Table 2 for both unbraked and braked tests with maximum (max), minimum (min), average (avg) and standard deviation (std) values.

A regression analysis is also performed to find correlations between closing speed versus coefficient of restitution (e) and closing speed versus mutual crush (s_T) in mm which are shown in Figure 3. In the graphs involving closing speed and mutual crush (s_T), a least-squares regression line passing through the origin is fit to the data and the corresponding coefficient of determination r^2 and the equation for the regression line are reported. For the unbraked tests, an empirical curve [Mastandrea and Vangi, 2005; Cipriani et al., 2002] given in Equation (10) is fitted to closing speed versus coefficient of restitution graph. For the braked tests, no regression curve is fitted since no correlation was observed between closing speed and *e* because different amounts of braking are applied to the striking vehicles which affect the coefficient of restitution values significantly.

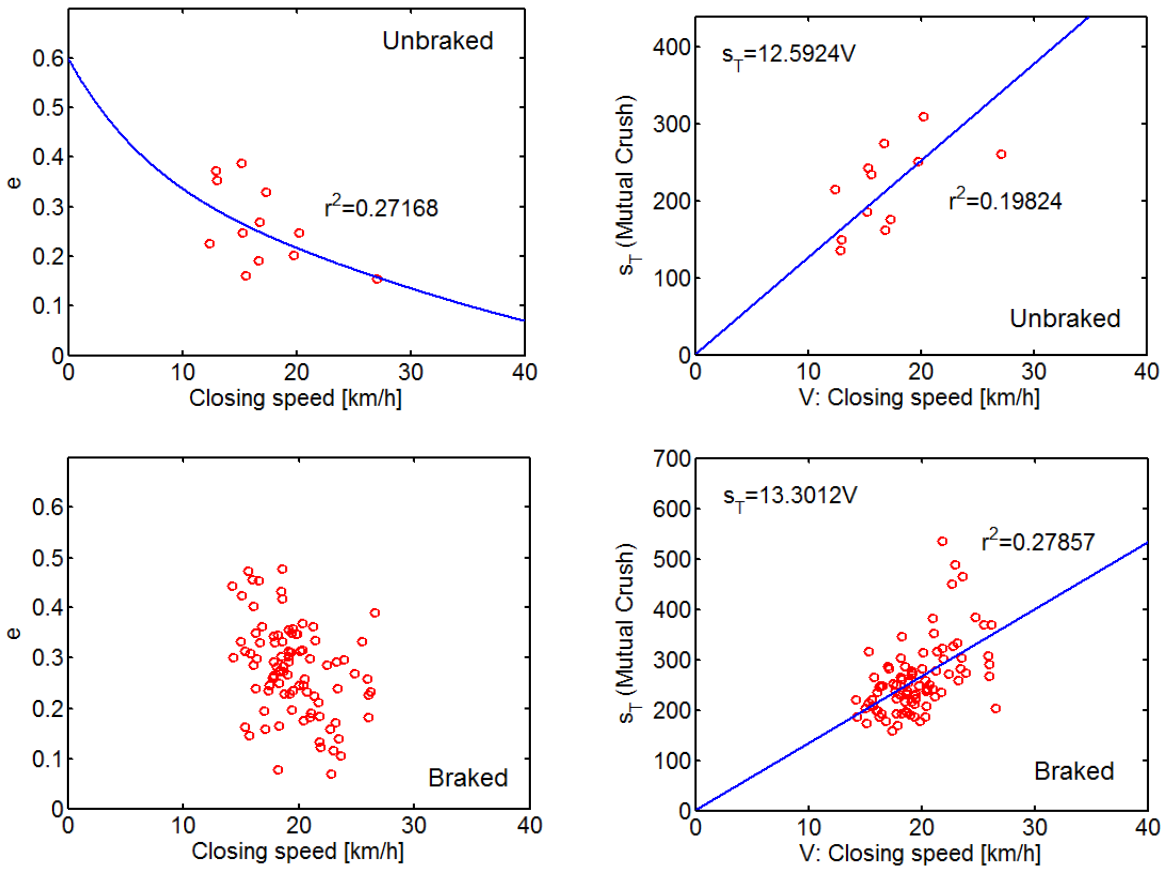


Figure 3. Relationships between closing speed, mutual crush and e

$$e = 0.5992 \cdot \exp\left(-0.2508V + 0.01934V^2 - 0.001279V^3\right) \quad (10)$$

Table 2. Calculated parameters

	Unbraked					Braked			
	max	min	avg	std		max	min	avg	std
k_{L1}*10^{-7} [N/m]	1.297	0.018	0.327	0.423		2.05	0.012	0.141	0.27
k_{L2}*10^{-7} [N/m]	0.371	0.0182	0.0988	0.124		2.86	0.0118	0.172	0.362
R	0.388	0.155	0.261	0.08		0.425	0.0259	0.248	0.10
s_{T1} [mm]	232.12	5.78	89.3	87.9		381.52	4.73	137.9	91.70
s_{T2} [mm]	215.4	11.19	127.3	62.5		305.37	3.98	122.6	76.0
s_{e1}/s_{T1}, s_{e2}/s_{T2}	0.402	0.069	0.161	0.10		0.476	0.007	0.154	0.10
s_{ef1}/s_{e1}, s_{ef2}/s_{e2}	12.82	0.132	4.780	4.65		125.8	0.266	8.192	15.31

5. DISCUSSION

In this study, 89 braked and 12 unbraked full-overlap low-speed rear impact tests are analysed with the aid of work-energy formulations. As seen in Table 2, there is a wide range of local loading stiffness and maximum deformation values since the stiffnesses of the interacting structures vary between tests especially due to override/underride impacts in which softer areas can come into contact with stiffer areas of the vehicles. A reasonable correlation is found between the closing speed and coefficient of restitution in the unbraked tests since the fitted curve given by Equation (10) is derived for unbraked collisions. On the other hand the varying amounts of braking in each braked test make it difficult to find clear correlations between closing speed, coefficient of restitution and the ratio of returned and absorbed energies given by R. It has been shown that [Mastandrea and Vangi, 2005; Cipriani et al., 2002] coefficient of restitution decreases with the increase in closing speed which is also obtained in the unbraked tests in this study. It has also been shown that coefficient of restitution decreases as the braking force is increased and this can lead to diverse values for the coefficient of restitution [Mastandrea and Vangi, 2005] which is also observed in this study for the braked tests as shown in Figure 3. Consequently, a wide range of coefficient of restitutions (between 0.07 and 0.478) is found. In the AGU database, there are no tests which involve the same two cars tested at the same closing speed with different levels of braking force hence deriving experimentally clear conclusions between braking force and coefficient of restitution is not possible.

The ratio R is equal to the coefficient of restitution for the unbraked tests which can also be shown mathematically [Himmetoglu, 2016]. For the braked tests, R is a useful parameter

which can be used to model the unloading characteristics of structures in the presence of braking. The ratios between elastic rebound displacements vary widely as shown in Table 2; this is due to the fact that during impact different materials with different stiffnesses and energy absorption properties interact at the contact areas. As expected, elastic rebound displacements at the end of the unloading phase (i.e. at the time of separation) are always smaller than the maximum deformations at the end of the loading phase. It has been observed in this study that the elastic rebound displacements after separation of cars can be either smaller or larger than those at the time of separation. Due to the approximation applied in Equation (7), s_{e1}/s_{T1} and s_{e2}/s_{T2} values are equal; the same applies for s_{ef1}/s_{e1} and s_{ef2}/s_{e2} values; this might have affected the elastic rebound displacements to some extent.

As expected, mutual crush (s_T) at the end of the loading phase increases as the closing speed increases as shown in Figure 3. It can be seen that the slope of the regression line for the braked tests is greater than that of the unbraked tests which can lead one to think that mutual crush (s_T) at the end of the loading phase, increases in the presence of braking. However, this can be misleading since the number of unbraked tests is quite low compared to braked tests. Therefore, one test from the AGU database is selected and the differential equations of motion of this test are derived with known values of car masses (m_1 being 1874 kg and m_2 being 1541 kg) and derived values of local loading stiffnesses (k_{L1} and k_{L2} being 224450 N/m and 386983 N/m, respectively). This approach helps to find out the influence of braking force on crash related parameters at different closing speeds in the absence of experimental data. It can be shown that the differential equation of motion of the two-car system shown in Figure 1 is given by Equation (11) for the loading phase of the impact where B is the deceleration of the striking car and m_{eq} is the equivalent mass of the system. The analytical solution of this differential equation is given in Equation (12) where t is the time, V is the closing speed and ω_n is the natural frequency of the system in the loading phase. The time t_L at which the loading phase ends is given in Equation (13). The common velocity V_c of the cars at the end of the loading phase is given by Equation (14) in which V_2 is the pre-impact velocity of the struck car. The mutual crush (s_T) is given by $-x_r(t_L)$.

$$m_{eq}\ddot{x}_r + k_{eqL}x_r = m_{eq}B \quad , \quad m_{eq} = m_1m_2/(m_1+m_2) \quad , \quad x_r = x_2 - x_1 \tag{11}$$

$$x_r(t) = \frac{B}{\omega_n^2} - \frac{BCos(\omega_n t)+V\omega_n Sin(\omega_n t)}{\omega_n^2} \quad , \quad \omega_n^2 = k_{eqL}/m_{eq} \tag{12}$$

$$t_L = (1/\omega_n)\cdot \text{atan}\,(V\omega_n/B) \tag{13}$$

$$V_c = V_2 - \beta_2 B t_L + \left(\frac{\beta_2 B}{\omega_n}\right) Sin(\omega_n t_L) - \beta_2 V(Cos(\omega_n t_L) - 1) \quad , \quad \beta_2 = \frac{m_1}{m_1+m_2} \tag{14}$$

Using Equations (11) to (14), mutual crush (s_T) and common velocity V_c at the end of loading phase are calculated together with t_L (duration of the loading phase) for different values of closing speed and deceleration of the striking car. The decelerations are 0.2, 2, 4, 6, 8 and 10 m/s^2. The results are shown in Figure 4 which indicate that mutual crush and common velocity of the cars at the end of loading phase, increases with closing speed. Higher levels of braking force decrease both mutual crush and common velocity. Increasing the deceleration from 0.2 m/s^2 to 10 m/s^2 reduces the mutual crush by 60 mm for closing speeds of 10 km/h and higher. The duration of loading phase decreases as the closing speed decreases and this effect is more pronounced for higher levels of braking (or decelaration). For the same closing speed, the duration of loading phase is shorter for higher levels of braking.

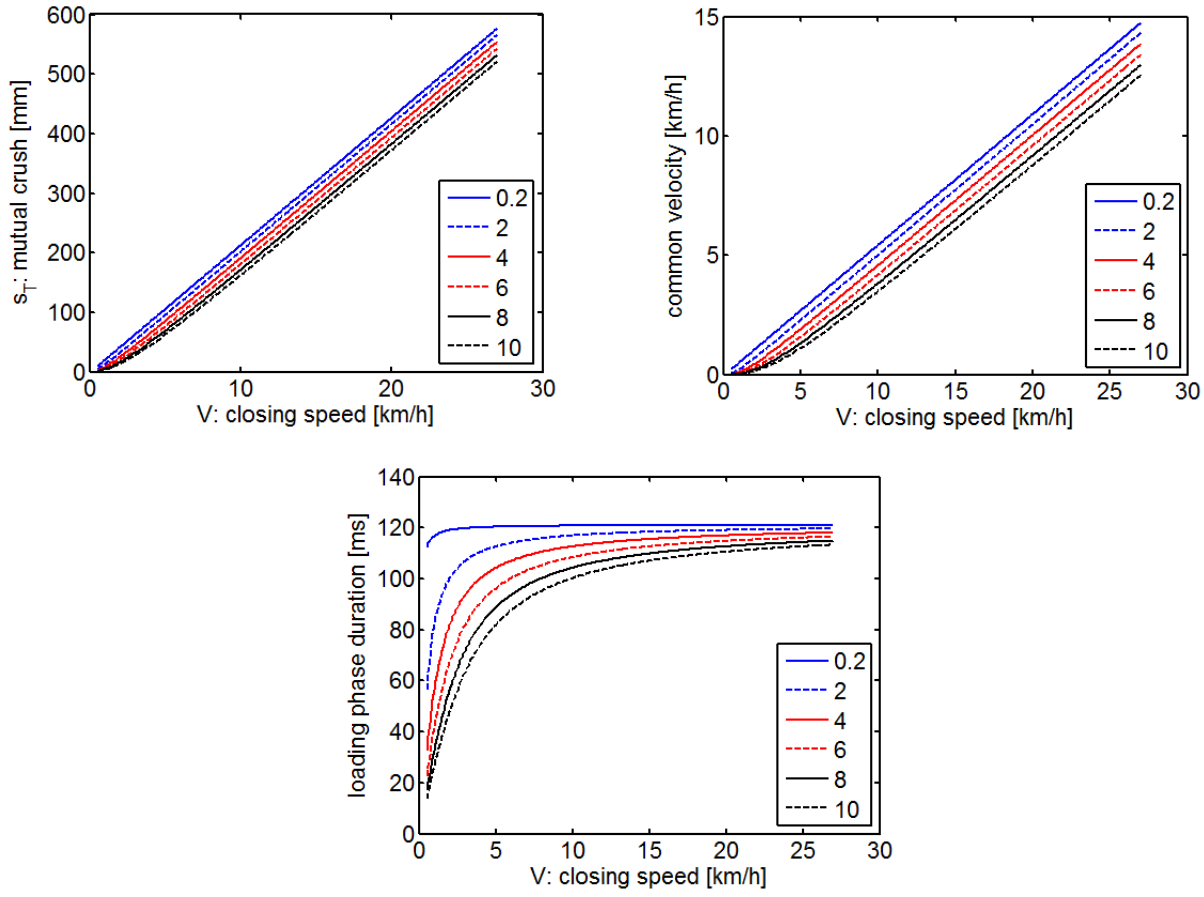


Figure 4. Effects of closing speed and braking (theoretical calculations)

6. CONCLUSIONS

This paper presents a statistical analysis of low-speed rear impacts documented in the AGU database coupled with lumped-mass modelling of the system. The analysed tests involve rear impacts performed with the most recent vehicle models available in the literature. The

crash pulses obtained from this experimental data can be used in rear-impact simulations. The dynamic modelling involving work-energy formulation, provides hand computation of the key parameters in vehicle crash mechanics, hence the presented approach is useful for accident reconstruction and modelling low-speed rear impacts in which whiplash can be a concern. Using the loading stiffnesses, amounts of crush and the parameter R, different scenarios involving various closing speeds and braking forces can be studied by doing simulations with the aid of the formulations presented in this study.

REFERENCES

1. **Nishimura, N., Simms, C.K., and Wood, D.P., (2015),** "Impact Characteristics of a Vehicle Population in Low Speed Front to Rear Collisions", Accident Analysis and Prevention, Vol.79, pp 1-12.

2. **Eis, V., Fay, P. and Sferco R., (2005),** "A Detailed Analysis of the Characteristics of European Rear Impacts", Proc. of 19th ESV Conference, Washington DC, USA, NHTSA, paper 05-0385-O.

3. **Arbeitsgruppe für Unfallmechanik (AGU), (2022),** Zürich, Switzerland, www.agu.ch.

4. **Scott, W.R., Bain, C., Manoogian, S.J., Cormier, J.M., and Funk, J.R., (2010),** "Simulation Model for Low-Speed Bumper-to-Bumper Crashes", SAE Paper 2010-01-0051.

5. **Han, I., (2007),** "Non-linear Continuous-contact-force Model for Low-speed Front-to-rear Vehicle Impact", Proc. IMechE Part-D J. of Automobile Engineering, Vol.221, pp 1197-1208.

6. **Mastandrea, M., and Vangi, D., (2005),** "Influence of Braking Force in Low-speed Vehicle Collisions", Proc. IMechE Part-D J. of Automobile Engineering, Vol.219, pp 151-164.

7. **Cipriani, A.L., Bayan, F.P., Woodhouse, M.L., Cornetto, A.D., Dalton, A.P., Tanner, C.B., Timbario, T.A., and Deyerl, E.S., (2002),** "Low Speed Collinear Impact Severity: A Comparison between Full Scale Testing and Analytical Prediction Tools with Restitution Analysis", SAE Paper 2002-01-0540.

8. **Himmetoglu, S., (2016)**, "An Analysis of Load Incompatibility in Central in-line Collisions of Vehicles Using Lumped-mass Modelling", Proc. of 17th UMTIK Conference, Bursa, Turkey.

9. **Huang, M., (2002),** Vehicle Crash Mechanics, CRC Press, Taylor & Francis Group, Boca Raton, Florida, USA.

10. **European New Car Assessment Programme (EuroNCAP), (2014),** Film & Photo Protocol, Version 1.1, www.euroncap.com.

11. **Society of Automotive Engineers (SAE), (2007),** SAE J211-1 (1995): Instrumentation for Impact Test, Part 1, Electronic Instrumentation.

12. **Himmetoglu, S., (2021),** "An Analysis of Head-on Frontal Collisions by Modelling Crash Tests", Proc. of the 25th International Scientific Conference Transport Means, Kaunas, Lithuania, pp 86-91.

13. **Varat, M.S. and Husher, S.E., (2000),** "Vehicle Impact Response Analysis Through the Use of Accelerometer Data", SAE Paper 2000-01-0850.

ANALYSIS OF SEAT BELT USE AND THORAX INJURIES SUSTAINED BY FEMALE OCCUPANTS IN FRONTAL IMPACTS

in loving memory of Prof. Dr. Memiş ACAR

Volkan ESAT, *evolkan@metu.edu.tr* Middle East Technical University – Northern Cyprus Campus, 99738, Kalkanli, Guzelyurt, Mersin 10, Turkey

B. Serpil ACAR, *B.S.Acar@lboro.ac.uk* Loughborough University, LE11 3TU, Leicestershire, UK

ABSTRACT

Accidents involving road motor vehicles not only cause thousands of fatalities and even more injuries worldwide every year, but also bring a huge burden on the global economy. This research investigates various factors that potentially affect thorax injury types and severities sustained by female occupants in frontal impacts with a particular focus on seat belt use. A database is formed using NHTSA's Crash Injury Research Engineering Network (CIREN) data. The generated database brings together selected information of 463 female occupants who are involved in frontal vehicle collisions in the US within the period of 2005 - 2014. Statistics regarding vehicles' seat belt condition, subjects' features and conditions, and types and levels of the injuries suffered are provided. Dependence of severities of injuries on seat belt use and seating position during the accidents is investigated through descriptive and inferential statistical analysis.

Keywords: Seat Belt, Thorax Injury, Female Occupants, CIREN, Frontal Impact

1. INTRODUCTION

Road vehicle collisions are a primary cause of fatalities worldwide [1, 2]. World Health Organization's most recent Global Status Report on Road Safety states that there were 1.35 million fatalities due to road traffic accidents globally in 2018, 93% of which turn out to be in low- and middle-income countries. The report recites that particularly younger individuals across the world, aged 5-29 years, are killed mostly due to road traffic injuries [2]. According to the statistics published by IIHS, 34,247 fatal motor vehicle crashes took place in the United States in 2017 which resulted in 37,133 deaths [3]. European Union (EU) data show that there were 25,250 fatalities on EU roads in 2017 [4]. Road casualties in Great Britain decreased by

39% in a decade, being 1,793 in 2017; however, 24,831 individuals were also reported to be seriously injured in those accidents [5]. Road motor vehicle crashes continue to bring an enormous burden on societies economically, psychologically, and socially, not only due to loss of lives but also through non-fatally injured people involved in such accidents.

The efforts for improving safety on the road worldwide, and minimizing fatalities and injuries due to road vehicle accidents evolve around developing safer vehicles and roads as well as improving road user behaviour. One of the main aspects of improving road user behaviour is properly wearing seat belts in all seating positions in a road motor vehicle. Majority of countries in the world aim to increase seat belt use as a countermeasure against the undesirable outcomes of road crashes. Although seat-belt legislation is in effect in many countries, a significant portion of them have exceptions or different views in their laws that might weaken seat belt use. As an example, it has been reported that although 161 countries enforce national seat-belt laws, only 105 countries among them, with a total population of 4.8 billion people, require rear-seat occupants to wear their seat belts as well as front-seat occupants [2]. However, a survey in 2015 revealed that, even in EU countries where seat belt laws and applications are some of the best practices, many Europeans did not take seat belt laws seriously by one third of the occupants admitting to not belting up in the rear seats, and a quarter of drivers not insisting rear seat passengers to wear seat belts [6].

Seat belts are passive safety systems which restrain occupants in the event of a crash mitigating, if not preventing from, the effects of secondary impacts with the vehicle interior and other occupants, distributing and controlling the restraining force, and averting possible ejection out of the vehicle. Various research work and accompanying statistical analyses show that proper use of seat belt in all seating positions for the whole spectrum of occupants significantly reduces fatalities and severe life-threatening injuries in road vehicle collisions. The general consensus worldwide is that seat belts must always be properly worn not only to avoid such traumatic and disastrous outcomes, but also to enable air bags to serve as supplementary restraint systems to further protect the occupants. National Highway Traffic Safety Administration (NHTSA) in the USA reports that seat belt use saved around an estimated 14,000 lives in 2015, whereas 48% of occupants who were not wearing seat belts ended up dead in the same year [7]. Several reports and research studies reveal that use of seat belt reduces fatalities of front-seat occupants in the band of 43% to 60% and serious injuries by 45% to 55% depending on the seating position of the occupant, size and class of the road vehicle, and speed and direction of impact [1, 2, 7, 8, 9].

Increasing use of seat belt appears to intensify the possibility of a different set of generally minor injuries, particularly occurring as a result of higher speed collisions and sometimes due to improper wearing of the belt. While protecting the occupants to a great extent, seat belt may

cause contusions and/or abrasions on the skin starting from the neck onto the thorax in line with the shoulder belt portion of the seat belt, and possibly onto the abdomen due to the lap portion of the seat belt, which is generally referred to as seat belt sign. If seat belt sign is accompanied by internal injury due to the restraining effect of the seat belt, the injury is called as seat belt syndrome [10, 11, 12]. Researchers in various disciplines investigated various types and combinations of seat belt related injuries comprised of seat belt sign and/or seat belt syndrome such as intra-abdominal trauma in general [10]; swelling, cleft deformity and haemorrhage of the breast [11]; lipid cyst formation and fat necrosis in the breast [11, 13, 14, 15, 16]; subclavian artery rupture [17, 18], and vein thrombosis [19]; crushing of the chest and fracture of ribs, sternum, and clavicles [20, 21]; renal injuries that required nephrectomy [9]; and peritonitis and intestinal injuries [12].

In the case of a road vehicle collision, female occupants are prone to sustain somewhat different injuries when compared to male occupants due to the anatomical differences between genders. The seat belt related injuries reported for female occupants are generally related to breast trauma. Several studies present and discuss breast trauma, which results in lipid cyst formation and fat necrosis in the breast [11, 13, 14, 15, 16, 22]. The investigations carried out in some studies are based on mammographic and/or sonographic findings, and discuss the possibility of developing carcinoma following fat necrosis due to the similarities in their features when visualised with the aforementioned techniques [11, 13, 16]. According to these studies, there appears to be no evidence relating fat necrosis with carcinoma, for which needle biopsy was recommended for precise identification of the lesions. Some breast traumas involve bisection and deformity of the breast due to seat belt loading after impact which require reconstructive procedures afterwards to correct the indentation of the breast [14, 15]. Different injuries that female occupants suffered due to seat belt loading are also reported in the literature such as milk-duct injury sustained by a pregnant woman [23], muscle tear and clavicular dislocation with sternal and costal fractures [21], isolated subclavian vein thrombosis [19], haemorrhage into and enlarging of the breast [22, 24, 25], and breast implant rupture [26].

2. PREVIOUS RESEARCH ON STATISTICAL ANALYSES OF THORAX INJURIES WITH A FOCUS ON SEAT BELT USE

Multiple research work involving seat belt related injuries are published in the literature that make use of descriptive and/or inferential statistical methods in analysing the actual crash data collected. Bansal et al. employed NHTSA's Crash Injury Research Engineering Network (CIREN) data to associate seat belt sign and severe intra-abdominal trauma employing statistical techniques such as multivariate analysis, adjusted odds ratios, chi-square test and

logistic regression [10]. The authors investigated cases of 1539 female and male occupants and concluded that front seat occupants experiencing seat belt signs were more than twice as likely to suffer from intraabdominal injury. Al-Ozaibi et al. approached seat belt syndrome from an intestinal injury perspective and claimed that presence of seat belt sign suggests abdominal injury [12]. Yoganandan et al. utilised NHTSA's National Automotive Sampling System - Crashworthiness Data System (NASS-CDS) to analyse crash characteristics and injury patterns for female and male front seat occupants in far side impacts [27]. They addressed whether vehicle-, occupant-, and crash-related factors predicted injury via employing multivariate analysis and odds ratios with confidence intervals. Their findings show that thoracic injuries are more common at the MAIS 3+ level and the presence of another front seat occupant contributes to MAIS 3+ trauma. In a study based on Germany data, Müller et al. analysed the vertebral fractures at cervical, thoracic, and lumbar levels for 33,015 injured female and male front seat occupants in motor vehicle accidents [28]. The authors used Student's t-test, Pearson's correlation, and multivariate analysis in their research and claimed that high speed and complex injury mechanisms due to multiple collisions or rollovers were associated with vertebral fractures. According to their findings, seat belt use plays a significant role in impeding vertebral fractures provided that the vehicle remains structurally intact during crash. In another European study based on Denmark crash data of two-vehicle two-driver impacts, Abay et al. looked into 5077 crashes with 10154 female and male drivers [1]. The authors investigated injury severity of drivers in light of seat belt use utilising multivariate ordered-response and independent probit models. They claim that drivers tend to offset the benefits of the restraint systems such as properly worn seat belts through driving more aggressively. In their research, Bose et al. analysed NASS-CDS data along with the data gathered from the US National Household Travel Survey in 2009 to shed light on the injuries sustained by female and male rear-seat passengers in frontal crashes [29]. Their findings point out mostly thorax injuries.

In some earlier research work, researchers presented results mainly obtained from descriptive statistical analysis of crash data of female and male occupants, where vehicles that were involved in those collisions appeared to be mostly devoid of air bags [20, 30, 31]. The aforementioned studies reveal that, in the absence of air bags, secondary impact between the driver and the steering wheel appears to be a major cause of severe injury, particularly for the unrestrained driver.

Apart from numerous medical articles that generally report single cases of seat belt injury for either female or male occupants, Song et al. reported a systematic review of seat belt trauma to the breast of female occupants [11]. The researchers reviewed the cases of 42 patients, who suffered from one or more of the injuries in the form of pain, swelling, open wounds,

haemorrhage, fat necrosis and cleft deformity. Five patients were also diagnosed with breast cancer.

Some researchers utilised anthropomorphic test devices (ATDs) in crash tests to investigate various crash variables including seat belt use and injury criteria. Tencer et al. investigated the factors affecting pelvic and thoracic forces in near-side impacts collected from ATDs during US-NCAP crash tests by using multiple linear regression analysis and unpaired t-test. They compared their data against NASS-CDS and CIREN data [32]. Motozawa et al. used the commercial ATD representing a pregnant woman, MAMA-2B, in order to estimate the effects of seat belt use on abdominal pressure during impacts. They claimed that properly wearing seat belt reduced abdominal pressure of a pregnant woman in case of a crash [33]. Acar and Esat reviewed various patents taken for novel seat belt designs that claim to provide some sort of protection for pregnant women in the event of a crash, and came up with a novel classification for similar seat belt devices [34]. They also showed the effectiveness of properly using the seat belt for a pregnant women on reducing strain, and thus, injury levels at the utero-placental interface by employing the computational pregnant woman model 'Expecting' [35].

Review of the literature reveals that there is a paucity for the statistical analyses of seat belt injuries particularly carried out for female occupants. Due to anatomical differences between genders, observations and statistical analyses that involve both genders fail to address various different injury types sustained specifically by women. Therefore, this study aims to contribute to the understanding of relationships between crash variables and seat belt related injuries sustained particularly by female occupants involved in full- and oblique-frontal impacts, as well as to highlight the importance of wearing seat belts properly for all occupants in road motor vehicles.

3. METHODOLOGY

In order to investigate various factors that affect injuries sustained by female occupants, a comprehensive database is formed via utilising NHTSA's Crash Injury Research Engineering Network (CIREN) data. The CIREN platform brings together not only a detailed accumulation of data regarding various road vehicle accidents in the USA, but also reports, analyses, and investigates the injuries sustained [36]. Several engineering and medical institutions across the USA contribute to the CIREN data collection. CIREN database contains various separate sets of data, some of which are based on and developed around the injured subjects, their features, and condition; whereas some others are based on the crash cases that took place.

At the time of generating the database, 1439 CIREN subjects were investigated, amongst whom 782 occupants were females. As the group is narrowed down to full- and oblique-frontal impacts; namely, subjected to collisions with the specific Principle Direction of Forces (PDoFs) ranging between 330 (i.e. -30) and 30 degrees, the final database is comprised of a final figure of 463 females. PDoFs for the final cases of interest can be seen in Figure 1, representing frontal collisions.

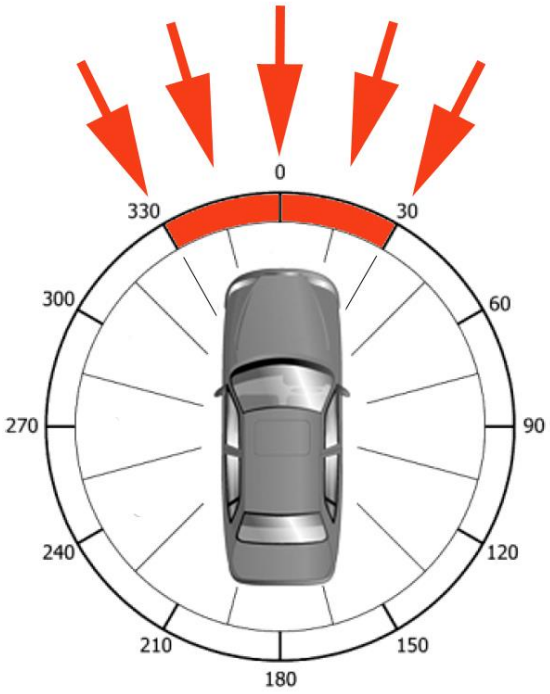


Figure 1. Principle Direction of Forces (PDoFs) ranging between 330 (i.e. -30) and 30 degrees (in clockwise rotation)

The data in the CIREN platform are restored in the form of a Statistical Analysis System (SAS) files. Authors' database is formed within the IBM SPSS Statistics v24, which can utilise the CIREN SAS files. The variables selected from four different CIREN data sets are used to develop authors' specific database aimed to investigate female subjects' injuries and related factors in frontal impacts. The variables selected for the database are summarised in Table 1.

Descriptive statistics of the female subjects' features and conditions within the authors' database such as age, weight, pregnancy status, and fatality status are provided in Table 2. CIREN subjects' age distribution in years, truncated to the last whole year, can be seen in Figure 2. According to these analyses, female subjects' age range between 0 - 88 years, whereas mean age in the authors' database is 45.39 years with a standard deviation of 21.29. Majority of the subjects were not pregnant with 97.0%, and their conditions were not fatal after the accident with 97.0%.

Table 1. Variables selected for the database generated

CIREN Database File*	Variable	Short Description
CASE	CIRENID	CIREN case (individual subject person) unique identifier
	CASENO	NASSMAIN crash case identifier
	CASEYEAR	calendar year when crash occurred
	AGE_MNTH	age in months
	AGE_YR	age in years
	SEX	sex, including pregnancy status for females
	WEIGHT	weight in kilograms
	STATURE	standing height in centimetres
	FATAL	fatality status
	EDUC	highest level of education
	BT_THRX	highest AIS score in BioTab body region “thorax”
	BT_T_SPN	highest AIS score in BioTab body region “thoracic spine”
	BT_ABD	highest AIS score in BioTab body region “abdomen”
	BT_L_SPN	highest AIS score in BioTab body region “lumbar spine”
	MAIS	maximum single Abbreviated Injury Scale (AIS) score
	ISS	Injury Severity Score (ISS)
VE	CASENO	NASSMAIN crash case identifier
	PDOF1	clock direction for PDOF in degrees (highest CDC)
	PDOF2	clock direction for PDOF in degrees (2nd highest CDC)
OA	AGE	age of occupant
	CASENO	NASSMAIN crash case identifier
	MANAVAIL	manual belt system availability
	MANFAIL	manual belt failure mode during accident
	MANUSE	manual belt system use
	SEATPOS	occupant's seat position
INJURY	CIRENID	CIREN case (individual subject person) unique identifier
	AISCODE	AIS code
	ICDM1	first International Classification of Disease (ICDM) code
	ICDM2	second ICDM code
	ICDM3	third ICDM code
	INJRANK	injury severity rank

*CIREN Database Files: CASE: based on the subject, contains demographic/anthropometric data, injury and airbag data; VE: based on the crash case, vehicle exterior data; OA: based on the crash case, occupant assessment data; INJURY: based on the subject, contains injury data

Table 2. Descriptive statistics of the subjects’ features and conditions assessed in the database

	N or Frequency	Min	Max	Mean	St. Dev.
Age (years)	463	0	88	45.39	21.29
Weight (kg)	463	5	179	73.27	24.27
Standing height (cm)	462	53	185	161.22	14.92
Pregnancy status	463		Percentage		
Not pregnant	449		97.0		
Pregnant – 1st trimester	4		0.9		
Pregnant – 2nd trimester	2		0.4		
Pregnant – 3rd trimester	8		1.7		
Fatality status	463		Percentage		
Not fatal	449		97.0		
Fatal due to crash injuries	14		3.0		

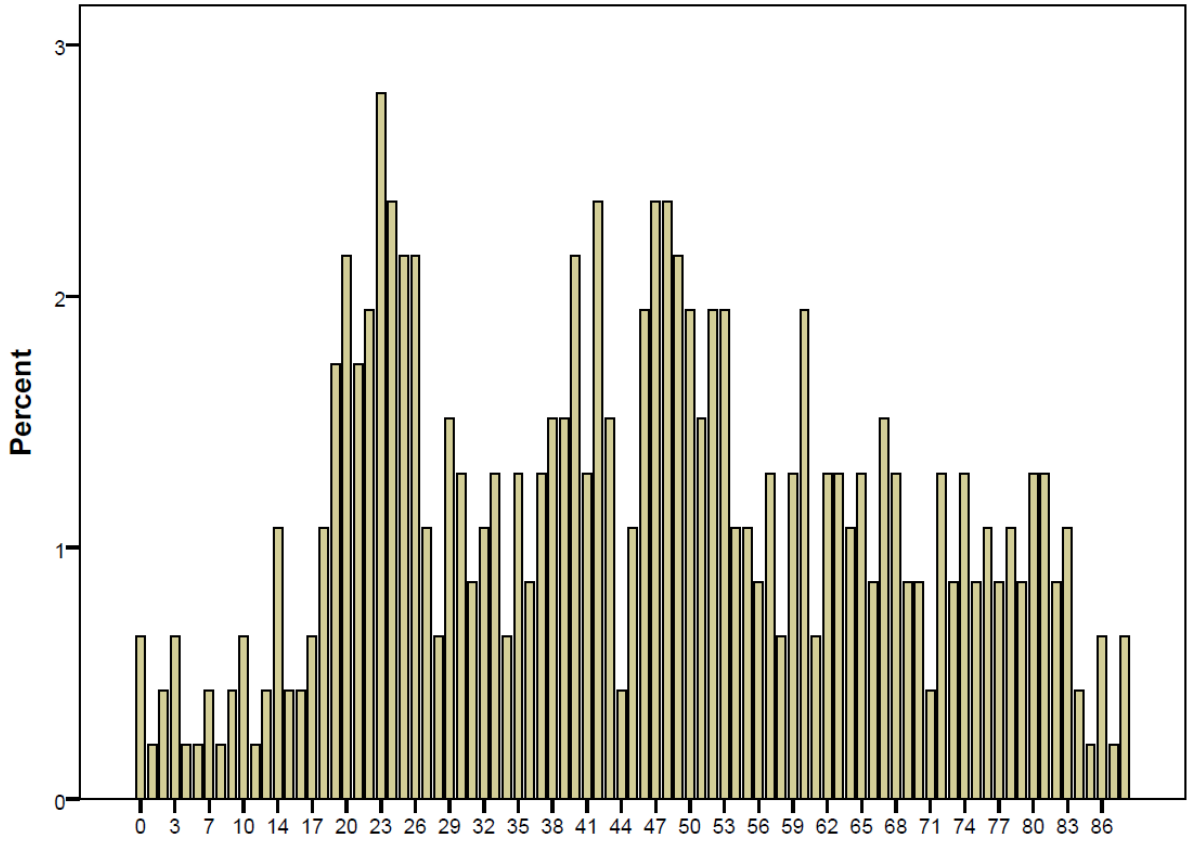


Figure 2. CIREN subjects' age in years, truncated to the last whole year

4. RESULTS AND DISCUSSION

Authors's database contain maximum single Abbreviated Injury Scale (AIS) injury scores for the occupants, as well as subjects' thorax-related maximum AIS scores for the Biotab regions of thorax, thoracic spine, abdomen, and lumbar spine. AIS severity scores range from 1 to 6, values being; (1) minor, (2) moderate, (3) serious, (4) severe, (5) critical, and (6) maximum. Biotab regions, which were designated by a group of researchers, are based on injury causation scenarios that not only embody factors for occurrence of injury, but also contain factors that add to the likelihood and/or severity of an injury [37]. Statistics for the AIS scores of the injuries sustained by the subjects is given in Table 3, and the percentages of the CIREN subjects' highest single AIS scores are shown in Figure 3. The CIREN subjects' maximum AIS scores for the separate Biotab regions of thorax, thoracic spine, abdomen, and lumbar spine are presented in percentages in Figure 4.

Table 3. Statistics for the AIS scores of the injuries sustained by the subjects

	N or Frequency	Min	Max	Mean	St. Dev.	Median
Highest single AIS scale score	463	1	6	3.13	0.816	3
The CIREN subjects' maximum AIS scale score for the specific Biotab regions:						
Thorax	463	0	6	1.50	1.607	1
Thoracic spine	463	0	5	0.17	0.636	0
Abdomen	463	0	5	0.83	1.333	0
Lumbar spine	463	0	5	0.38	0.897	0

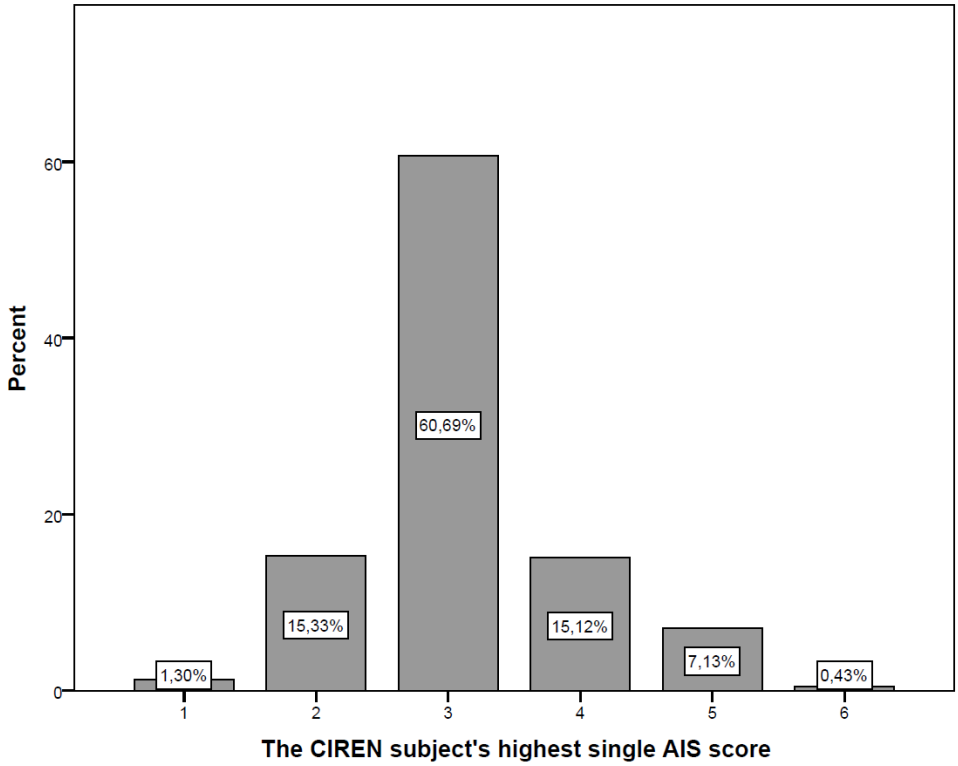


Figure 3. Percentages of the CIREN subjects' highest single AIS scores

Mean highest single AIS score experienced by the subjects appears to be 3.13 with a standard deviation of 0.816. This can be interpreted as the mean severity amongst the subjects is in serious to severe injury levels, with 60.69% of the injured occupants suffer a serious AIS 3 injury level. As the CIREN subjects' maximum AIS scores for the aforementioned specific Biotab regions are investigated, thorax region appears to be most affected from injuries when compared to the other specific Biotab regions of thoracic spine, abdomen, and lumbar spine.

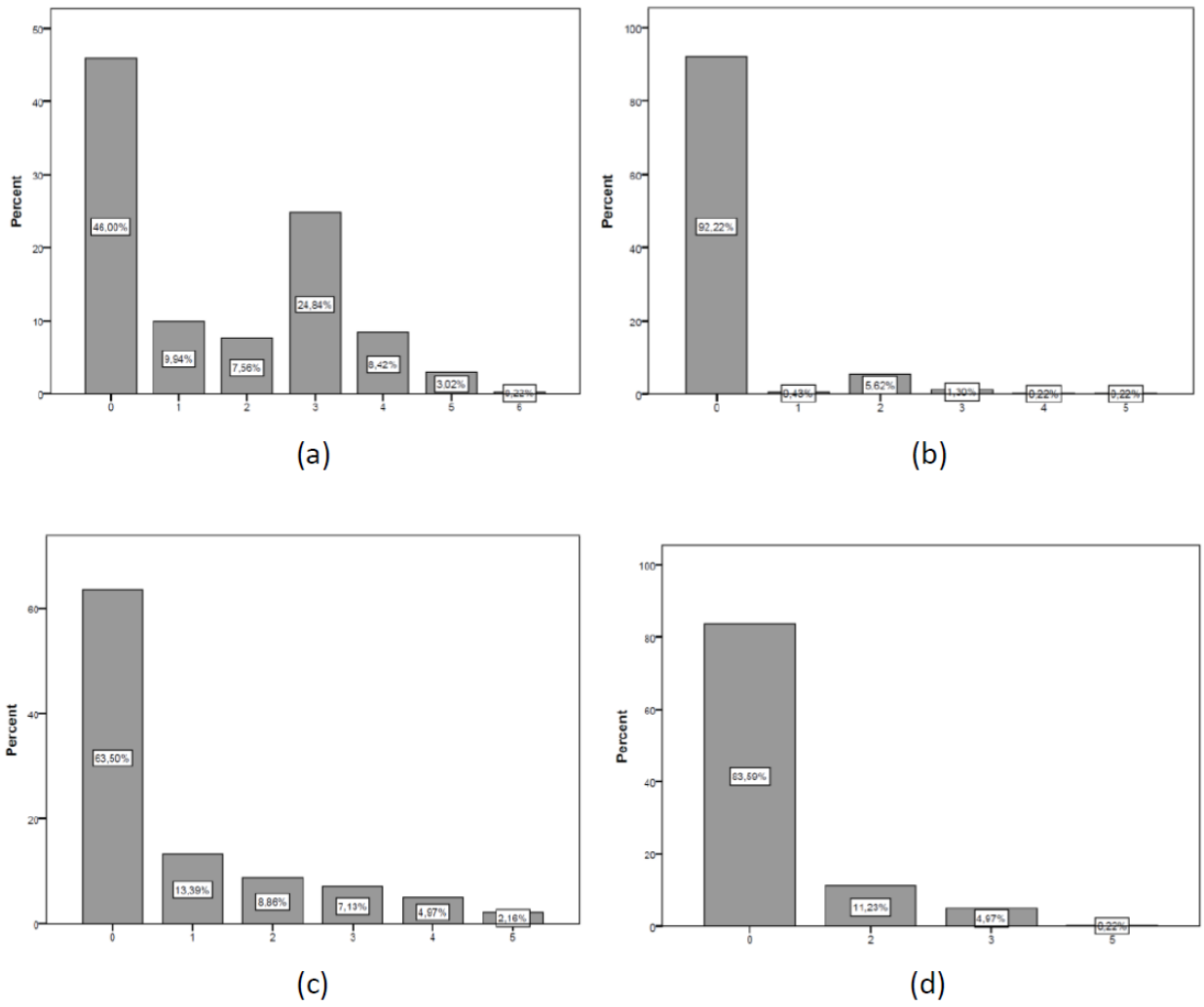


Figure 4. The CIREN subjects' maximum AIS scores for the Biotab regions of; (a) thorax, (b) thoracic spine, (c) abdomen, and (d) lumbar spine.

Figure 5 summarises seat belt related data in the generated database. The percentages of occupants' seating position in the vehicle is shown in Figure 5a, which exhibits that most of the occupants investigated sit on the front left side with 71.08%, being the driver side of the car. The second mostly occupied seat is the front right side with 21.41%, being the front passenger side. Manual seat belt use of the subjects is given in Figure 5b. According to the data, 77.68% of the occupants wore their lap and shoulder belts, while 20.31% did not use their seat belt or it was not available to them. Only a few subjects just wore lap belts, or used some sort of child seat. The data on the manual belt failure mode reveal that no failure occurred in 78.62% of the seat belts, whereas 20.49% of the belts were not used / available. Only a few of the belt systems experienced torn webbing or broken buckle / latch failures.

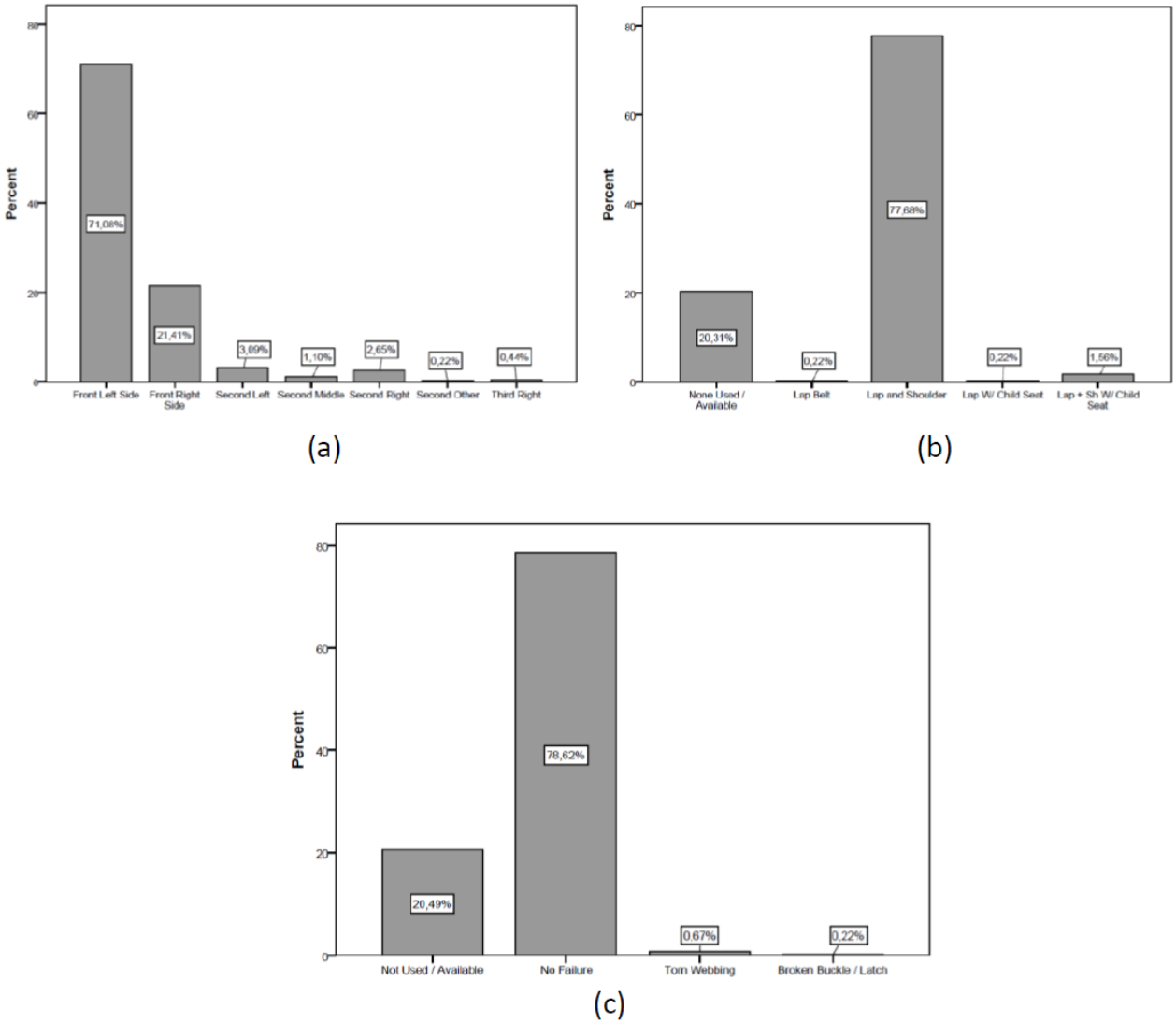


Figure 5. Seat belt related data; (a) occupant's seat position, (b) manual belt system use, and (c) manual belt failure mode during accident.

Frequencies of the injuries sustained by all occupants in the authors' database based on the AIS injury code system used are shown in Figure 6. Most frequently sustained injuries by the subjects are also tabulated in Table 4. The descriptions of the AIS codes are taken from the National Automotive Sampling System (NASS) Injury Coding [38] resource. According to the list of most frequently sustained injuries, the leading injuries appear to be hip skin/muscle contusion (hematoma) with 5.0% of the subjects suffering, and shoulder skin/muscle contusion (hematoma) with 4.2% of the subjects suffering. Other common injuries turn out to be thigh/lower limb skin/muscle contusion (hematoma), hip skin/muscle abrasion, elbow skin/muscle contusion (hematoma), transverse process fracture, shoulder skin/muscle abrasion, metatarsal/tarsal fracture, and abdomen skin/muscle contusion (hematoma). With all the aforementioned injuries, seat belt loading arguably plays a critical role as supported by the

injury code explanations in the National Automotive Sampling System (NASS) Injury Coding resource.

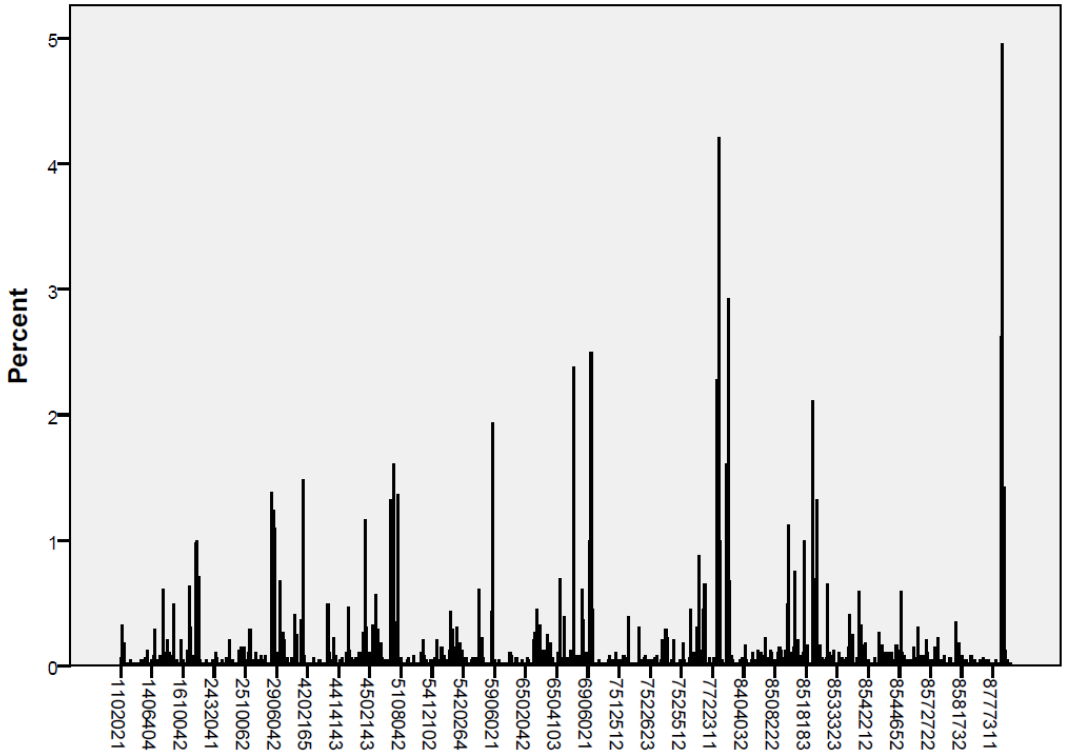


Figure 6. Frequencies of the injuries sustained by all occupants in the database based on the AIS injury code system used

Table 4. Most frequently sustained injuries by the subjects

AIS Code	Injury Description	Frequency	Percentage (%)
890402.1	Hip skin/muscle contusion (hematoma)	244	5.0
790402.1	Shoulder skin/muscle contusion (hematoma)	207	4.2
810402.1	Thigh/lower limb skin/muscle contusion (hematoma)	144	2.9
890202.1	Hip skin/muscle abrasion	129	2.6
710402.1	Elbow skin/muscle contusion (hematoma)	123	2.5
650620.2	Transverse process fracture	117	2.4
790202.1	Shoulder skin/muscle abrasion	112	2.3
852200.2	Metatarsal/tarsal fracture	104	2.1
590402.1	Abdomen skin/muscle contusion (hematoma)	95	1.9

Pearson's chi-squared tests are performed to assess the null hypothesis that the evaluated variables are independent. Typically, a significance value, p, less than 0.05 is considered as "significant". Table 5 provides Pearson's chi-squared test results through cross-tabulation of selected data of seat belt use vs highest single AIS score of the subjects. The test reveals that only the following findings appear to be dependent:

- Subjects' self-reported highest level of education vs seat belt use

- Seat belt use of front left (driver) and front right (passenger) seating subjects vs max. AIS score in the abdomen region

Similarly, Table 6 presents Pearson's chi-squared test results through cross-tabulation of selected data of seat belt failure mode during accident vs highest single AIS score of the subjects. Evaluation of the test results show that only the following findings appear to be dependent:

- Seat belt failure mode during accident for the front left (driver) occupant vs highest single AIS score
- Seat belt failure mode during accident for the front right (passenger) occupant vs max. AIS score in the thoracic spine region
- Seat belt failure mode during accident for the front left (driver) occupant vs max. AIS score in the abdomen region

Table 5. Pearson's chi-squared test results through cross-tabulation of selected data: seat belt use vs AIS score

Variables			Value	df	Significance, p
Row variable 1	Row variable 2	Column variable			
Subjects' self-reported highest level of education		Seat belt use	377.148	40	**0.000**
Seat belt use		Highest single AIS score	12.587	20	0.894
Occupant's seat position					
➢ Front left	Seat belt use	Highest single AIS score	6.186	4	0.186
➢ Front right			3.986	10	0.948
➢ Second left			8.988	8	0.343
➢ Second middle			5.000	4	0.287
➢ Second right			10.453	9	0.315
➢ Third right			2.000	1	0.157
Occupant's seat position					
➢ Front left	Seat belt use	Maximum AIS score – thorax Biotab region	5.402	5	0.369
➢ Front right			10.991	12	0.530
➢ Second left			4.321	8	0.827
➢ Second middle			1.875	2	0.392
➢ Second right			9.333	12	0.674
➢ Third right			2.000	1	0.157
Occupant's seat position					
➢ Front left	Seat belt use	Maximum AIS score – thoracic spine Biotab region	5.829	3	0.120
➢ Front right			1.377	2	0.502
➢ Second left			1.296	4	0.862
➢ Second middle			1.875	2	0.392
➢ Second right			5.244	6	0.513
➢ Third right			-	-	-
Occupant's seat position					
➢ Front left	Seat belt use	Maximum AIS score – abdomen Biotab region	17.235	5	**0.004**
➢ Front right			18.415	10	**0.048**
➢ Second left			4.321	6	0.633
➢ Second middle			5.000	4	0.287
➢ Second right			10.933	12	0.535
➢ Third right			2.000	1.0	0.157

Occupant's seat position					
➢ Front left			3.169	3	0.366
➢ Front right		Maximum AIS score – lumbar spine Biotab region	3.571	4	0.467
➢ Second left	Seat belt use		-	-	-
➢ Second middle			1.875	2	0.392
➢ Second right			3.111	6	0.795
➢ Third right			-	-	-

Table 6. Pearson's chi-squared test results through cross-tabulation of selected data: seat belt failure mode during accident vs AIS score

Variables			Value	df	Significance, p
Row variable 1	Row variable 2	Column variable			
Occupant's seat position					
➢ Front left			27.071	12	**0.008**
➢ Front right	Seat belt failure mode during accident	Highest single AIS score	15.287	10	0.122
➢ Second left			6.741	4	0.150
➢ Second middle			2.222	2	0.329
➢ Second right			5.778	3	0.123
➢ Third right			2.000	1	0.157
Occupant's seat position					
➢ Front left			20.229	15	0.163
➢ Front right	Seat belt failure mode during accident	Maximum AIS score – thorax Biotab region	12.408	12	0.413
➢ Second left			1.296	4	0.862
➢ Second middle			0.833	1	0.361
➢ Second right			2.044	4	0.728
➢ Third right			2.000	1	0.157
Occupant's seat position					
➢ Front left			5.990	9	0.741
➢ Front right	Seat belt failure mode during accident	Maximum AIS score – thoracic spine Biotab region	7.674	2	**0.022**
➢ Second left			0.389	2	0.823
➢ Second middle			1.875	1	0.171
➢ Second right			4.593	2	0.101
➢ Third right			-	-	-
Occupant's seat position					
➢ Front left			34.109	15	**0.003**
➢ Front right	Seat belt failure mode during accident	Maximum AIS score – abdomen Biotab region	11.334	10	0.332
➢ Second left			1.296	3	0.730
➢ Second middle			2.222	2	0.329
➢ Second right			4.889	4	0.299
➢ Third right			2.000	1	0.157
Occupant's seat position					
➢ Front left			3.597	9	0.936
➢ Front right	Seat belt failure mode during accident	Maximum AIS score – lumbar spine Biotab region	4.299	4	0.367
➢ Second left			-	-	-
➢ Second middle			0.833	1	0.361
➢ Second right			1.037	2	0.595
➢ Third right			-	-	-

Multivariate General Linear Modelling (GLM Multivariate) test is used to facilitate regression analysis and analysis of variance through modelling the two dependent variables in the form of highest single AIS score and Injury Severity Score (ISS) based on their relationships with the fixed factor predictors; namely, seat belt use (to be called as MANUSE), and seating position of the occupant (to be called as SEATPOS). Table 7 summarises the results of the

multivariate tests for the aforementioned design. The significance values for the main effects of seat belt use (MANUSE), and seating position of the occupant (SEATPOS), and their combined interaction effect of (MANUSE*SEATPOS) are all above 0.05, indicating that none of the effects of these predictors contribute to the severity of injury when measured in the form of highest single AIS score and Injury Severity Score (ISS). However, multivariate test results of between-subjects effects on the selected data as shown in Table 8 exhibit that combined interaction effect of (MANUSE*SEATPOS) on highest single AIS score is less than 0.05, indicating that both factors together affect the injury severity sustained. In a similar fashion, effect of the corrected model on highest single AIS score is very close to 0.05 (0.052 to be exact), showing all predictors and their interactions affect the injury severity sustained.

Table 7. Multivariate test results for the design based on the selected data: seat belt use and seating position of the occupant vs CIREN subject's highest single AIS score and Injury Severity Score (ISS)

Effect		Value	F	Hypothesis df	Error df	Significance
Intercept	Pillai's Trace	0.493	208.411	2.000	429.000	0.000
	Wilks' Lambda	0.507	208.411	2.000	429.000	0.000
	Hotelling's Trace	0.972	208.411	2.000	429.000	0.000
	Roy's Largest Root	0.972	208.411	2.000	429.000	0.000
MANUSE	Pillai's Trace	0.013	0.711	8.000	860.000	0.682
	Wilks' Lambda	0.987	0.711	8.000	858.000	0.682
	Hotelling's Trace	0.013	0.710	8.000	856.000	0.683
	Roy's Largest Root	0.011	1.216	4.000	430.000	0.303
SEATPOS	Pillai's Trace	0.022	0.813	12.000	860.000	0.638
	Wilks' Lambda	0.978	0.812	12.000	858.000	0.638
	Hotelling's Trace	0.023	0.811	12.000	856.000	0.639
	Roy's Largest Root	0.017	1.237	6.000	430.000	0.286
MANUSE * SEATPOS	Pillai's Trace	0.044	1.385	14.000	860.000	0.154
	Wilks' Lambda	0.956	1.396	14.000	858.000	0.148
	Hotelling's Trace	0.046	1.408	14.000	856.000	0.143
	Roy's Largest Root	0.045	2.774	7.000	430.000	0.008

Table 8. Multivariate test results of between-subjects effects on the selected data: seat belt use and seating position of the occupant vs CIREN subject's highest single AIS score and Injury Severity Score (ISS)

	Source	Type III Sum of Squares	df	Mean Square	F	Significance
Corrected Model	The CIREN subject's highest single AIS score	17.915	17	1.054	1.635	0.052
	The CIREN subject's Injury Severity Score (ISS)	2242.185	17	131.893	1.176	0.280
Intercept	The CIREN subject's highest single AIS score	149.262	1	149.262	231.635	0.000
	The CIREN subject's Injury Severity Score (ISS)	3124.351	1	3124.351	27.866	0.000
MANUSE	The CIREN subject's highest single AIS score	0.629	4	0.157	0.244	0.913
	The CIREN subject's Injury Severity Score (ISS)	308.938	4	77.235	0.689	0.600
SEATPOS	The CIREN subject's highest single AIS score	4.222	6	0.704	1.092	0.366
	The CIREN subject's Injury Severity Score (ISS)	427.405	6	71.234	0.635	0.702
MANUSE * SEATPOS	The CIREN subject's highest single AIS score	12.502	7	1.786	2.772	0.008
	The CIREN subject's Injury Severity Score (ISS)	1483.179	7	211.883	1.890	0.070

5. CONCLUSIONS

This research is aimed at building a database that contains crash variables and seat belt related injuries sustained particularly by female occupants involved in full- and oblique-frontal impacts. By using descriptive and inferential statistical techniques, relationships between database variables are evaluated. Informative results are collected that shed light to various conditions and habits during driving.

Statistical analyses show that occupants' highest level of education and their seat belt use habits are clearly dependent. Various results suggest that seat belt use of the driver and the front passenger and the injury severity at specific regions of the upper body are also somewhat dependent. The same trend is valid for seat belt failure modes as well. However, similar dependence cannot be observed for rear seat occupants. This may be due to lack of data for the significantly lower number of occupants who are seated in the rear seats, constituting only 7.5% of the whole subjects investigated in this research. Therefore, additional data is

potentially required to bring a better understanding to the injuries sustained by the occupants in the rear seats.

The ISS score, which is measured via summing the squares of the highest AIS values for each of the three most severely injured regions, is another injury severity index. ISS score can possibly range from 0 to 75. The analyses results show that AIS injury severity values attained by the occupants appear to be somewhat dependent with seat belt use, seat belt failure, and seating position; whereas, ISS does not show the same trend.

Although use of seat belt can cause some lower severity injuries in case of impact collisions, wearing seat belts properly saves lives of occupants in road motor vehicles and protects from higher severity injuries.

ACKNOWLEDGEMENTS

The authors gratefully acknowledge Design School of Loughborough University for funding and supporting the research project.

REFERENCES

[1] **K. A. Abay, R. Paleti and C. R. Bhat, (2013)**, “The joint analysis of injury severity of drivers in two-vehicle crashes accommodating seat belt use endogeneity,” *Transportation Research Part B,* vol. 50, pp. 74-89.

[2] **World Health Organization (WHO), (2018)**, “Global Status Report on Road Safety,” WHO Press, Geneva.

[3] **Insurance Institute for Highway Safety, “General Statistics,” (2017)**. [Online]. Available: https://www.iihs.org/iihs/topics/t/general-statistics/fatalityfacts/overview-of-fatality-facts. [Accessed 07 04 2019].

[4] **European Transport Safety Council (ETSC), (2018)**, “Ranking EU Progress on Road Safety,” ETSC, Brussels.

[5] **Department for Transport, “Reported road casualties in Great Britain: main results (2017)**, ” [Online]. Available: https://assets.publishing.service.gov.uk/government/uploads/system/uploads/attachment_data/file/744077/reported-road-casualties-annual-report-2017.pdf. [Accessed 07 04 2019].

[6] **European Transfer Safety Council (ETSC) , “News,” ETSC, 25 04 2015**. [Online]. Available: http://etsc.eu/new-survey-reveals-many-europeans-still-dont-take-seatbelt-laws-seriously/. [Accessed 21 08 2017].

[7] **National Highway Traffic Safety Administration (NHTSA)**, “Seat Belts,” NHTSA, [Online]. Available: https://www.nhtsa.gov/risky-driving/seat-belts. [Accessed 21 08 2017].

[8] **P. R. Carter and V. K. Maker, (2010)**, “Changing Paradigms of Seat Belt and Air Bag Injuries: What We Have Learned in the Past 3 Decades,” *Journal of the American College of Surgeons,* vol. 210, no. 2, pp. 240-252.

[9] **M. A. Bjurlin, R. J. Fantus, R. J. Fantus, M. M. Mellett and D. Villines, (2014)**, “The Impact of Seat Belts and Airbags on High Grade Renal Injuries and Nephrectomy Rate in Motor Vehicle Collisions,” *The Journal of Urology,* vol. 192, pp. 1131-1136.

[10] **V. Bansal, C. Conroy, G. T. Tominaga and R. Coimbra, (2009)**, “The Utility of Seat Belt Signs to Predict Intra-Abdominal Injury Following Motor Vehicle Crashes,” *Traffic Injury Prevention,* vol. 10, no. 6, pp. 567-572.

[11] **C. T. Song, I. Teo and C. Song, (2015)**, “Systematic review of seat-belt trauma to the female breast: A new diagnosis and management classification,” *Journal of Plastic, Reconstructive & Aesthetic Surgery,* vol. 68, pp. 382-389.

[12] **L. Al-Ozaibi, J. Adnan, B. Hassan, A. Al-Mazroui and F. Al-Badri, (2016)**, “Seat belt syndrome: Delayed or missed intestinal injuries, a case report and review of literature,” *International Journal of Surgery Case Reports,* vol. 20, pp. 74-76.

[13] **B. Cakir, N. Tuncbilek, E. Unlu and L. Doganay, (2003)**, “Seat belt injury of the breast: MR mammographic follow-up,” *European Journal of Radiology Extra,* vol. 45, pp. 13-16.

[14] **I. Teo, D. Dujon and I. Azmy, (2014)**, “Seat belt injury causing bisection of the breast: A case report,” *J Plastic Reconstr Aesthetic Surg (JPRAS),* vol. 67, no. 7, pp. 1008-1009.

[15] **N. C. Petrie, (2015)**, “Response to “Seat belt injury causing bisection of the breast: A case report",” *J Plastic Reconstr Aesthetic Surg (JPRAS),* vol. 68, no. 3, pp. 429-431.

[16] **I. Kocijancic, M. Rener and K. Vidmar, (2000)**, “Simultaneous occurrence of fat necrosis and carcinoma after breast injury in a traffic accident,” *European Journal of Ultrasound,* vol. 11, pp. 213-216.

[17] **R. N. W. Chan and R. G. M. Duffield, (1975)**, “Subclavian artery rupture: an unusual seat belt injury,” *Injury: the British Journal of Accident Surgery,* vol. 7, no. 1, pp. 29-32.

[18] **M. Assenza, L. Centonze, L. Valesini, G. Campana and M. Corona, (2012)**, “Traumatic subclavian arterial rupture: a case report and review of literature,” *World Journal of Emergency Surgery,* vol. 7, no. 18, pp. 1-6.

[19] **A. Kurgan, H. Abramowitz, J. Shapiro and A. I. Auer, (1997)**, “Traumatic axillary and subclavian vein thrombosis after seat belt injury,” *Journal of Vascular Nursing,* vol. 15, no. 4, pp. 134-135.

[20] **R. J. Newman, (1984)**, “Chest wall injuries and the seat belt syndrome,” *Injury: the British Journal of Accident Surgery,* vol. 16, no. 2, pp. 110-113.

[21] **A. A. Keizer and V. J. Leferink, (2015)**, “Pectoralis major tear at its sternal origin after a seat-belt trauma,” *Journal of Plastic, Reconstructive & Aesthetic Surgery,* vol. 68, pp. e205-e206.

[22] **A. Myhre, T. Pohlman and K. E. Dee, (2002)**, “Hemorrhage into the Breast in a Restrained Driver After a Motor Vehicle Collision,” *AJR Am J Roentgenol,* vol. 179, no. 3, p. 690.

[23] **T. Sircar, P. Mistry, S. Harries, D. Clarke and L. Jones, (2010)**, "Seat-belt trauma of the breast in a pregnant woman causing milk-duct injury: a case report and review of the literature," *Ann R Coll Surg Engl,* vol. 92, pp. 1-2.

[24] **B. Madden, M. Phadtare, Z. Ayoub and R. B. Chebl, (2015)**, "Hemorrhagic shock from breast blunt trauma," *International Journal of Emergency Medicine,* vol. 8, no. 33, pp. 1-4.

[25] **A. J. Murday, (1982)**, "Seat belt injury of the breast - a case report," *Injury: the British Journal of Accident Surgery,* vol. 14, no. 3, pp. 276-277.

[26] **B. D. G. Morgan, (1996)**, "Breast implant rupture and seat belts," *British Journal of Plastic Surgery,* vol. 49, no. 7, p. 501.

[27] **N. Yoganandan, M. W. J. Arun, D. E. Halloway, F. A. Pintar, D. J. Maiman, A. Szabo and R. W. Rudd, (2014)**, "Crash Characteristics and Injury Patterns of Restrained Front Seat Occupants in Far-side Impacts," *Traffic Injury Prevention,* vol. 15, no. Supp 1, pp. S27-S34.

[28] **C. W. Müller, D. Otte, S. Decker, T. Stübig, M. Panzica, C. Krettek and S. Brand, (2014)**, "Vertebral fractures in motor vehicle accidents–a medical and technical analysis of 33,015 injured front-seat occupants," *Accident Analysis and Prevention,* vol. 66, pp. 15-19.

[29] **D. Bose, J. Crandall, J. Forman, D. Longhitano and C. Arregui-Dalmases, (2017)**, "Epidemiology of injuries sustained by rear-seat passengers in frontal motor vehicle crashes," *JournalofTransport&Health,* vol. 4, pp. 132-139.

[30] **E. Arajarvi, (1988)**, "A Retrospective Analysis of Chest Injuries in 280 Seat Belt Wearers," *Accident Analysis & Prevention,* vol. 20, no. 4, pp. 251-259.

[31] **J. R. Hill, G. M. MacKay and A. P. Morris, (1994)**, "Chest and Abdominal Injuries Caused by Seat Belt Loading," *Accident Analysis & Prevention,* vol. 26, no. 1, pp. 11-26.

[32] **A. F. Tencer, R. Kaufman, C. Mack and C. Mock, (2005)**, "Factors affecting pelvic and thoracic forces in near-side impact crashes: a study of US-NCAP, NASS, and CIREN data," *Accident Analysis & Prevention,* vol. 37, p. 287–293.

[33] **Y. Motozawa, M. Hitosugi, T. Abe and S. Tokudome, (2010)**, "Effects of seat belts worn by pregnant drivers during low-impact collisions," *Am J Obstet Gynecol,* vol. 203, no. 62, pp. e1-e8.

[34] **B. S. Acar and V. Esat, (2009)**, "Seat Belt Designs to Protect Pregnant Vehicle Occupants," *Recent Patents on Mechanical Engineering,* vol. 3, no. 1, pp. 1-10.

[35] **B. S. Acar and V. Esat, (2009)**, "Computational Modelling and Simulation for pregnant occupant safety," *Journal of Biological Physics and Chemistry,* vol. 9, no. 4, pp. 155-161.

[36] **N. H. T. S. A.** "Crash Injury Research Engineering Network (CIREN)," NHTSA, [Online]. Available: https://one.nhtsa.gov/Research/Crash-Injury-Research-(CIREN).

[37] **L. W. Schneider, J. D. Rupp, M. Scarboro, P. F., K. B. Arbogast, R. W. Rudd, M. R. Sochor, J. Stitzel, C. Sherwood, J. B. Macwilliams, D. Halloway, S. Ridella and R. Eppinger, (2011)**, "BioTab--a new method for analyzing and documenting injury causation in motor-vehicle crashes," *Traffic Inj Prev,* vol. 12, no. 3, pp. 256-265.

[38] **N. H. T. S. A. (NHTSA), (2000)**, “2000 NASS Injury Coding Manual,” NHTSA, Washington.

IMPROVING THE SAFETY OF LONDON BUS USERS THROUGH DESIGN

Jo BARNES *j.barnes@lboro.ac.uk,* Loughborough University, UK

Laurie BROWN *l.a.brown2@lboro.ac.uk* Loughborough University, UK

Andrew MORRIS *a.p.morris@lboro.ac.uk* Loughborough University, UK

ABSTRACT

Over 5.04 billion bus passenger journeys were made in Great Britain in one year (2015-2016), and around half of the bus passengers in the UK are passengers of London buses. In 2015, 1,594 bus and coach occupant casualties were reported by the Metropolitan Police Service (MPS). However, some 6,096 incidents not requiring police intervention were also reported by London's Bus Operators to Transport for London (TfL) in 2016, suggesting that there is a more of a problem of passenger injury than is suggested by the MPS figures.

In this study, quantitative data was analyzed to derive a better understanding of the nature and circumstances of injuries and how they can be prevented and/or mitigated by design. Additionally, countermeasures were developed in consultation with designers, engineering, human factors and vehicle safety experts. These were then presented to stakeholders to determine priority solutions i.e., those that would have the most impact on preventing bus occupant injuries together with the feasibility of implementing them.

Five years-worth of police collision data were analyzed in total The data identified that bus accidents in the London area resulting in reported bus passenger injuries had increased during a five-year period, rising from a 31% share of the total STATS19 bus accidents in 2012 to 44% in 2016 Department for Transport, 2017). Most passenger injury incidents resulted from non-collision incidents. The data also allowed identification of the passenger position in the bus in one of four categories which can help to identify the bus movement at the time of the incident. The analysis identified that alighting and boarding mainly occurs when the vehicle is "waiting to go", "parked" or "moving off". However, injuries sustained while seated, which on average represent 41% of the casualties, most often occurred when the vehicle is "going ahead" or "slowing / stopping". Standing injuries, which account for half of the total casualties, occurred most frequently when the vehicle was "slowing / stopping", "going ahead", or "moving off".

KEYWORDS: Bus Safety, Slips, Trips and Falls, Non-Collision Injuries

INTRODUCTION

There were an estimated 5.04 billion bus passenger journeys in Great Britain (2015-2016), and a high proportion of these were made in the city of London (Department for Transport, 2017). In total, over 300 million vehicle miles are travelled by the London buses per annum equating to some 6 billion passenger miles per year. Around half of the bus passengers in the UK are passengers of London buses with 1,594 bus and coach occupant casualties reported by the Metropolitan Police Service (MPS) in 2015. These were categorized as one fatality, 70 seriously injured and 1,523 slightly injured casualties as defined within the STATS19 reporting system of 'Slight', 'Serious' and 'Fatal' casualties. Other incidents with injuries not requiring police intervention are reported by London's Bus Operators to Transport for London (TfL) and are published on the TfL's website (Transport for London, 2015). In 2016, 6,096 injuries were reported on London's contracted bus services ranging from those described as 'injuries treated on scene' to 'fatalities'. These figures suggest that many more injury incidents occur beyond the officially reported STATS19 data.

AIMS OF THE RESEARCH

The aims of this research were as follows:

- To derive a better understanding of the nature and circumstances of injuries and how they can be prevented and/or mitigated:
- To provide an in-depth understanding of the safety issues which confront bus passengers in London and consider countermeasures to such safety challenges.

METHODOLOGY AND DATA SOURCES

To provide a quantitative analysis of bus passenger incidents access to relevant Greater London Area datasets was necessary as outlined in Table 1 below. Department for Transport **STATS19** data is available freely online (Department for Transport, 2017); therefore, data for 2012-2016 (inclusive) was downloaded for analysis. It was decided not to analyze the linked police-hospital dataset involving STATS19 and HES (Hospital Episode Statistics) at this stage as the available dataset is relatively old and is not directly comparable to the STATS19 time period for this project. Permission was sought to access the TfL's Incident Reporting Information System (IRIS) incident data, which was released by Transport for London to analyze specific incidents and injury cases for the same 2012-2016 period. These datasets

were used to achieve the first aim of providing a quantitative analysis of bus passenger incidents in the Greater London Area.

Table 1: Data sources for the project

Data Source	Availability	Source partner	Analysis	Data
STATS19	Publicly available	Loughborough	Quantitative - Loughborough	Year 2012-2016
TfL	Available on request	London TravelWatch	Quantitative - Loughborough	Year 2012-2016 (or what is available)
STATS19+HES linked data	Potentially available on request (DfT) permissions required	Loughborough	Quantitative - Loughborough	Available years if permission granted

Other data sources were needed for qualitative analysis of data and such data is held by Bus Operators, but this data is not included within this paper. Meetings were initiated through London TravelWatch to enable Loughborough University to access this data. A preliminary meeting was held with Go-ahead to discuss the feasibility of a study of this kind. Discussions also centered around accessing additional necessary data, identifying potential pitfalls and examining the quality of the data that could be released for analysis. A subsequent follow up meeting organized by London TravelWatch involved representatives from three Bus Operators (Go-Ahead, Abellio and StageCoach) together with Transport for London. At this meeting, the project outline was presented by Loughborough University and project requirements were stipulated with potential data access requirements determined for each of the Bus Operators. The Bus Operators agreed on the provision of several incident reports and CCTV clips that could be accessed (Table 2). Additionally, the operators agreed that they would undertake a 'mail-out' to all passengers identified in the incident reports to invite them to take part in a telephone interview with researchers from Loughborough University.

Table 2: Agreed data to be provided to Loughborough University

Phase	Data Type	Bus operator 1 Go Ahead	Bus operator 2 Stagecoach	Bus operator 3 Abellio
Phase 2 (expected to receive)	Incident reports	300	150	150
	CCTV footage	30	15	15
Phase 3 (expected to mail out)	Passenger interviews	300	150	150

For ease of presentation the project is presented in three distinct phases with the methods and results for each phase described in each section.

IRIS is the database used by TfL to capture all incidents that occur on buses whilst operating a service using a consistent reporting methodology. The IRIS database includes road traffic collisions, slips, trips and falls, vandalism, assault etc. IRIS data for the years 2012-2016 (inclusive) was provided to Loughborough University for analysis for this study.

The raw data was initially 'cleaned' to remove (for example) duplicate records or blank rows in the dataset. The data was then further filtered to remove irrelevant incidents such as assaults and bus-soiling. Finally, injuries to drivers or other non-passengers were removed so that only incidents that resulted in injury to bus passengers were included in the sample for analysis. Microsoft Excel was used for analyzing the IRIS dataset.

As with the STATS19 analysis, two subsets of data were created in order to analyze variables on either an 'incident' or a 'casualty' basis:

- Incidents occurring on TfL operated buses between 2012-2016 [n=20,490].
- Casualties injured on TfL operated buses between 2012-2016 [n=21,998].

Analysis was carried out using descriptive statistics on the dataset as a whole; the distribution of values across the different variables was analyzed and presented as a proportion of the total sample. The variables analyzed included; total number of incidents or casualties, injury event type, sub-category of injury event type, age of casualty, type of injury, body region injured.

Additionally, cross-tabulations of some variables were analyzed to give more detail on exactly where and how injuries were occurring and provide more insight on where to target countermeasures.

RESULTS

The key highlights are reported below;

In total, there were 20,490 incidents involving passengers on London buses between 2012-2016, resulting in 21,998 injured passengers. The number of incidents and injuries has generally increased across time, albeit a slight reduction in 2013.

Table 3 presents a summary of the event types and subcategories which shows that 'slip trip falls' are the highest occurring event type.

Table 3: Original and condensed event types (IRIS data)

Original Event Type	Condensed Event Type	Proportion per event category
Slip Trip Fall	Slip Trip Fall	58%
Knock, Trip or Fall within bus		
Fall downstairs		
Collision	Collision	9%
Collision Incident		
Alighting Incident	Alighting and Boarding	17%
Boarding Incident		
Personal Injury Event	Personal Injury Event	16%
Wheelchair/ Buggy Incident		
Struck by Object		

Most events involved adult passengers, followed by an even split between child and elderly passengers. Youths (16-25 years) are under-represented within the bus incident data. This is surprising given that according to 2015 TfL data, 71% of Londoners aged 24 and under use London buses as a form of transport (Transport for London, 2017).

For some of the data a further sub-category of event type was defined. When this data was analyzed, the large ‘slip/trip/fall’ event now revealed that 27% of incidents are attributed to a ‘fall on the same level’. Also, within the ‘personal injury’ event it was established that passengers are predominantly injured through being struck or hitting an object (14%) or trapping limbs (7%).

Furthermore, age was also compared across the event subcategories. The proportion of incidents in elderly passengers is high in the ‘while boarding’ (30%) and ‘while alighting’ sub-categories (25%) in comparison to children and youth. It is worth noting that the proportion of ‘while boarding’ incidents in elderly passengers is nearly the same as adults. Incidents in the ‘on the same level’ sub-category are relatively high in elderly passengers, compared to children and youths.

Data on the body region where the injury was sustained was available for some of the data (approximately one fifth). the body region with the highest proportion of injuries was the lower extremity (24%), with injuries to the head also relatively common (22%).

There are interesting trends within the body regions affected in incidents when comparing ages of the passengers. For example, youths have the highest proportion of incidents involving the lower extremities, as well as injuries to the back. Equally, children have the highest proportion of head and face injuries of all the age categories.

There are several interesting findings when comparing body regions affected between the condensed event types. A large proportion of the body regions affected in alighting and boarding incidents were the lower extremities and the same pattern was found in personal

injury events. With slip/trip/fall events, the main body region affected was the head, with injuries to both upper and lower extremities comprising most of the remaining incidents in this event type.

The mixed method approach identified various aspects of injury causation on London buses. What was immediately evident was the disparity between the numbers of casualties officially reported in STATS19 data involving a bus in London and the threefold increase in casualty figures for the TfL reported IRIS data. Although the types of incidents vary between the reporting in IRIS and STATS19, there still is an apparent higher number of incidents and injured casualties in London which has steadily increased during the analysis period. Predominantly, the casualties are a result of non-collision incidents and would account for the lower STATS19 numbers. Furthermore, there is an over representation of females, and the age distribution of casualties is skewed towards older occupants. This is expected, and reflects the general demographics seen amongst bus passengers. However, it does raise the question whether there are underlying physiological differences that render females to be more at risk than males of sustaining an injury.

One of the problems in the data is the limitations in describing the actions of the bus and what the passenger intent is resulting in a reliance on assumptions to be formed about the data. This makes it difficult to define countermeasures when broad categories of standing and seated are used in addition to alighting and boarding. There is no allowance for the detail about the actual problem with seated passengers; for example, sudden deceleration can be assumed if the bus is slowing but is not captured in detail in STATS19. One of the other differences in the reporting is the injury descriptions used which again do not lend themselves easily to assist in countermeasure design. STATS19 reported nearly all the casualty incidents as minor and no further detail whereas IRIS can report the ‘type’ of injury sustained within the ‘minor’ category. Unfortunately, the reporting of injury in IRIS data is not consistent and is even unhelpful when looking at injury trends as many of the descriptors used are mechanisms of injury; for example, ‘bump’, ‘crush’ and ‘knock’ rather than an injury for example bruise or abrasion. In injury terms ‘crush’ is a specific kind of injury that would align with sustaining serious injury but is often mis-used in cases where the injuries are ‘minor’ and not what would be expected from such a description. Additionally, the use of ‘slip / trip/ fall’ category is overused and appears as a ‘catch-all’ category. There have been amendments to the IRIS data collection system to enable sub-categorization below this to describe falls on the same level etc., however, it is incomplete. Where it was possible to consider the body-area injured, the head and face in children and face and lower/ upper extremity for elderly passengers were commonly reported. Most of the lower extremity injuries in the subcategory of data were caused in alighting and boarding incidents. The interpretation of this data again relies on

assumptions to understand the data as the detail is not present. Intuitively, head and face injuries in children could be buggy-related or, following the CCTV review, could be attributed to hitting the seat in front as children tend to be thrown forwards during braking, usually head/ face first due their physiology and possibly since they are lighter in weight than adults thus affecting their kinematics.

DISCUSSION

From the quantitative analysis it is evident there are many discrepancies that make it difficult to develop a broad and full understanding of injuries on London buses in any specific detail. Even with perceived improvements and adding sub-categories to the IRIS data, it is argued that the data is not adequate to obtain a full representation of injury on buses. The qualitative data analysis added value to the quantitative data as it attempted to add meaning to the data such as the example of child head / face injuries noted above.

INTERIOR DESIGN FACTORS

What is limiting in the datasets was the passenger and bus movement which helps inform assumptions about injury causation, but the detail is not present compared to the qualitative data whereby it was noted that certain seats were deemed to be 'problem seats' on the bus. These problem seats cannot be isolated in the datasets to identify if passengers who sit in them are more prone to injury compared to other seated passengers. Adding the interpretation of the qualitative data to the dataset analysis accounted for certain passenger and driver behaviours which could contribute to the injury outcome of the passengers. For 'boarding' incidents it is evident that this could be at any stage, from the passenger physically stepping onto the bus, to the point where they are sat down. Ultimately during this period, the bus is' stationary', 'moving off 'or could 'brake sharply' for whatever reason. This now expands the notion of boarding incidents and the causative factors up to the point the passenger is seated; attempting to board when doors are closing or tripping on the platform or falling over because the bus has not been knelt at the stop, all of which one would assume the bus is 'stationary' at the time. The additional factors here are the passenger and driver behaviours which could exacerbate these incidents including the driver closing the doors too early or by mistake, the passenger not being cautious of the doors or being impaired due to the height of the step; and bus factors if the driver has a blind spot and cannot see an approaching passenger on the nearside of the bus. These surmises can be extrapolated for the passengers' next phase of boarding which is the progression through/down the bus to find a seat. The problems here

have been highlighted above and the 'moving off' from the stop and not waiting for passengers to be seated before this happens was a major problem but was also considered to be a priority and a feasible problem to fix by the stakeholder workshop. The nearside blind-spot should in theory be helped by the new proposed EU regulations for HGV mirrors which have been proposed for inclusion in the new bus safety standard following the work of Summerskill et al (2019).

TECHNOLOGY DESIGN FACTORS

Slowing down was another category identified in the datasets and was found to contribute to many of the incidents in the qualitative data. This was often described as 'harsh braking' but few of such incidents were for emergency-stop purposes although a higher proportion were needed to avoid collisions. Whatever reason for braking, the actual 'sharpness' of the bus movement is a major concern for passenger injury causation whether seated or standing. The findings suggest that a lot of 'minor passenger injuries' due to harsh braking could easily be avoided if slight changes in passenger and driver behaviour occurred, or there was assistive technology to help drivers avoid braking harshly. The use of ADAS, specifically forward collision warning devices (e.g., Mobileye) on bus fleets would have a preventative effect on passenger injury as harsh braking would then be avoided and injury risks subsequently reduced. As an injury prevention strategy, this was considered feasible within the short to mid-term time period but relies on investment to enable the retrofit on a large fleet of buses. There is a confounding factor to this which is the proposed fitment of AEBS brakes to the bus fleet as part of TfL's new Bus Safety Standard (Transport for London, 2018). The benefit to vulnerable road users is the driving force behind this recommendation; however, the impact on bus occupants needs to be reviewed in detail to understand passenger kinematics and the potential risk of injury if they were to be fitted as standard.

What was evident from this study was the multifaceted nature of injury causation to bus occupants whereby some design solutions are possible to help prevent them but might incur large costs. In the immediate period there needs to be a general shift-change in passenger and driver behaviour to understand needs and expectations from both perspectives. This was evident when the drivers do not wait for passengers to sit down after boarding and the passenger believing the driver must wait for them - but this is not actual bus operator policy. Thus, innovative and targeted information campaigns would help change long-term passenger behaviours and embedding policy in the big red book and including empathy training elements in driver training would further help to enable drivers to make informed decisions.

CONCLUSIONS

Overall, the analysis of the data has shown that variances exist between the data collected in police reported incidents in STATS19 and the TfL reported incidents in the IRIS dataset. STATS19 reports on some 7,043 casualties in the 5-year period compared to the IRIS dataset through which 21,988 casualties were reported in the same time period. Notably most of all casualty incidents are reported as 'slight/minor' but whereas STATS19 provides no further detail other than this basic descriptor, IRIS has the ability to report the 'type' of injury sustained within the 'minor' category. Other differences exist with the expansion between the passenger locations in STATS19 as a choice of four descriptors but in the IRIS data there were 11 descriptors before being condensed into the 4 analysis categories. Furthermore, the use of subcategory events in the IRIS dataset provides additional specific event information of the event; however, some of these variables contained actual injury descriptors rather than the mechanism of injury or 'event' type. These discrepancies make it difficult to develop a full and broad understanding of injuries on London buses in any specific detail. It is envisaged that the qualitative analysis of actual collision incidents from the Bus Operators will help provide a better understanding of the types of events and injuries sustained in the context of the IRIS dataset.

A summary of the main findings from the STATS19 and IRIS datasets are presented below;

- Both data sets showed a small but distinct upwards turn in the number of people injured on buses in London over the 5-year period;
- Bus only (non-collision) incidents predominate in STATS19 data, mostly on single carriage roads, whereas 'slip trip fall' is the main injury event in the IRIS data;
- Passengers who were recorded as standing or seated dominated the passenger position at the time of injury in STATS19;
- It was difficult to assign passenger position in the IRIS data apart from the comparable alighting and boarding incidents;
- The use of sub-categories helped to specify some other events or injury types, but these were not complete across the whole IRIS dataset;
- When the injury data was recoded for analysis 'minor' injury dominated the type of injuries sustained and included cuts and abrasions or bruises. The injury descriptions could not be analysed in greater detail as some 35% were injury mechanisms; for example, 'trapped' or 'crush' or 'bump' but providing no injury details.
- STATS19 is not designed to capture injury data beyond the severity of the incident; in this regard it is similar to the IRIS data 'minor' injury which was the main type recorded;

- Analysis of subcategory data identified specific body-regions to be at risk of injury; these were mainly head and face in children (probably from buggy falls) and face and lower/ upper extremity for elderly passengers. The majority of the lower extremity injuries in the subcategory of data were caused in alighting and boarding incidents.

Age categories greater than 25 years represented a larger proportion of the data relative to younger passengers, though there is a need to tie this into usage to determine whether older people are more likely to be injured compared with younger people, or merely more likely to use the bus.

REFERENCES

Boyatzis, R.E., (1998). *Transforming Qualitative Information:* Thematic Analysis and Code Development. Thousand Oaks, Calif; London Sage Publications

Flick, U., (2009). *An introduction to Qualitative Research.* 4th Ed., Los Angeles; London: Sage

Martin, B., and Hanington, B., (2012). *Universal Methods of Design*. Beverley; Rockport Publishers

Robson, C., (2002.) *Real World Research:* 2nd Ed., Madden, Mass: Oxford Blackwell

Summerskill, S. et al., 2019. The definition, production and validation of the direct vision standard (DVS) for HGVS. Final Report for TfL review. Version 1.1. London: Transport for London.

Department for Transport (DfT) https://www.gov.uk/government/statistics/annual-bus-statistics-year-ending-march-2017

Transport for London (TfL) Department for Transport (DfT)
https://www.gov.uk/government/statistics/annual-bus-statistics-year-ending-march-2017

Bus Safety Standard: Executive Summary; TfL October 2018; ISBN: 978-1-912433-62-9

ACKNOWLEDGEMENTS

We are grateful to London TravelWatch and the Road Safety Trust who provided funding for the research included in this paper



E-SCOOTER SAFETY STUDIES AND A USER TRIAL STUDY

Sally MAYNARD, *s.e.maynard@lboro.ac.uk*, School of Design and Creative Arts, Loughborough University, LE11 3TU, England

Graham HANCOX, *graham.hancox@nottingham.ac.uk* Digital Technology Services, University of Nottingham, Nottingham, NG7 2RD, England (formerly School of Design and Creative Arts, Loughborough University)

Andrew MORRIS, *a.p.morris@lboro.ac.uk*, School of Design and Creative Arts, Loughborough University, LE11 3TU, England

B. Serpil ACAR, *B.S.Acar@lboro.ac.uk,* School of Design and Creative Arts, Loughborough University, LE11 3TU, Leicestershire, UK

ABSTRACT

E-scooters (electric scooters) are becoming more popular around the world, as people seek alternatives to travelling by car to reduce carbon emissions, have better mobility around congested cities and save money. Several e-scooter rental trials are currently running in some areas in the UK. Despite the benefits the use of e-scooters brings, there were 3 fatalities and 931 casualties in accidents involving e-scooters in the UK in 2021. Hence the safety issues becomes increasingly significant.

The small footprint of the e-scooter can make the rider feel uncomfortable when sharing the roadway with cars, however, in a similar way to e-scooter riders feeling disproportionately vulnerable on roads compared to cars. Safety issues include e-scooter riders' erratic and unpredictable behaviour when switching from one travel mode to another.

Extensive literature review of this study also reveals that the environmental impact of e-scooters is still subject to debate with most e-scooter trips replacing walking rather than polluting vehicles.

A trial where 22 participants evaluated their e-scooter interaction has favourable results with participants rating the e-scooter highly for safety in general, with some contrasting feedback suggesting potential concerns from users.

Keywords: e-scooters, electric scooters, road safety, accidents, incidents, safety.

1. INTRODUCTION

This paper reports a project to study outcomes and factors related to safety and compliance with operational rules of one particular brand of electric scooters (e-scooters) currently part of a trial in the UK, and the implications of those on both users and non-users. The aim of the research was to investigate use of this brand of e-scooters in predetermined areas in the UK and to consider safety recommendations. The research involved the following tasks:

- Systematic literature review
- Questionnaire survey of e-scooter riders
- Interviews with e-scooter riders
- User trials

This paper will concentrate on the literature review and user trials aspects of the project.

E-scooters are becoming increasingly popular around the world, as people seek alternatives to travelling by car to reduce carbon emissions, have better mobility around congested cities and save money. As a result, several e-scooter rental trials are currently running in some areas in the UK, in which riders over the age of 16 years who have a full or provisional driving licence can hire e-scooters for use on the road and on cycle lanes. In the UK at the time of writing, it is illegal to ride an e-scooter on the pavement; this also includes scooters which are part of the rental trials. In areas not covered by one of the trials, e-scooters can only be ridden on private land with the landowner's permission.

Despite the benefits the use of e-scooters may bring, there were 931 casualties in accidents involving e-scooters in the UK in 2021. Of these 732 were e-scooter users, 3 were killed (all of them were e-scooter riders) and there were 253 seriously injured and 675 slightly injured casualties (Department for Transport, 2021).

In countries where e-scooters are already used widely, various approaches are being taken to address safety, including encouraging users to ride e-scooters safely and wear a helmet, introducing a minimum age for users and restricting the use of e-scooters to cycle lanes and roads. In the UK, it has been advocated that e-scooter providers and local authorities involved in the rental trials should implement robust systems that swiftly identify when accidents and incidents have occurred. This is important to enable any issues, such as damaged or misplaced e-scooters, to be rectified quickly, and will also contribute to a collective understanding of e-scooter usage and incidents. Providers and councils also need to recognise and minimise the opportunity for e-scooter users to misuse and ignore practical standards in the current trials. Good discipline by riders now will create a culture of good user behaviour in the future, and training opportunities for e-scooter riders are an important part of this, along with an encouragement that riders wear helmets.

The UK remains one of the last territories in the world to legalise e-scooters. However, UK cities, and in particular London are amongst the most densely populated cities in the world, where the streets are designed for the car and pedestrian binary. Light vehicles and public transit may be the only way future cities will be able to cope with the growing population, mobility requirements and air-quality targets, but without more space for lighter vehicles like bikes and scooters, it will be difficult to promote a change.

There has been some concern regarding the introduction of e-scooters to UK roads and pathways. A report released by the Parliamentary Advisory Council for Transport Safety (PACTS) in March 2022 detailed why e-scooters both differ from cycles and need their own regulations to keep people safe. The report was concerned with private use of e-scooters rather than current rental schemes and highlights that e-scooters "*are propelled entirely by electric power; they have much smaller wheels and the rider's centre of gravity is located further forward; and the severity of head injuries is greater. e-scooters and pedal cycles should not be classified in the same way*," (Winchcomb, 2022). The report makes recommendations that if private e-scooters are to be legalised, then there should be minimum design thresholds met such as having a maximum possible speed of 12.5mph; anti-tampering mechanisms, minimum front wheel size of 12 inches (30.5cm) and minimum rear wheel size of 10 inches (25.5cm), along with two independently controlled braking devices, one on each wheel with lighting to be mandatory at all times. The report also suggests that certain behaviours should be mandatory, such as helmet wearing, and riders be at least 16 years of age. Other behaviours were suggested to be prohibited such as riding on the pavement, carrying of passengers, drink driving and handheld mobile phone use while riding.

2. SYSTEMATIC LITERATURE REVIEW

The search

A systematic literature review was conducted using the search terms ("electric scooter" sharing OR rental) entered into both Web of Science and Scopus. 164 results came up in Web of Science and 62 in Scopus. After articles had been read by title and abstract there were 52 relevant in Web of Science and 40 from Scopus, a further 17 were removed due to being duplicated in both search results.

The 24 most relevant studies (12 from each database) were then selected and read in depth; a summary of the results is presented here.

Barriers to use

A key barrier to e-scooter use has been shown to be cost, a factor reported across multiple studies (Almannaa et al., 2021; Aman, Smith-Colin, and Zhang, 2021; Sellaouti, Arslan and Hoffmann, 2020). Aman, Smith-Colin, and Zhang (2021) found that, along with cost, the means

of payment – the requirement to have a debit or credit card to access the e-scooters – also proved a barrier for some. The perception of needing a certain degree of knowledge, such as to unlock and lock the e-scooter, to navigate through the registration process etc. also acted as a barrier.

Another barrier is insufficient infrastructure (Almannaa et al., 2021; Glavić et al., 2021), for example, lack of roads (such as cycle lanes etc.) required for e-scooter use. Inability to meet the users' mobility needs was a further cited reason for non-use (Eccarius and Lu, 2020; Zhang et al, 2021), together with a lack of perceived safety (Almannaa et al., 2021; Zhang et al, 2021).

Transport replaced by e-scooters

Current literature suggests use of e-scooters predominantly replaces walking; this was within the top three modes of transport that would have been used had e-scooters not been available (Buehler et al., 2021; Glenn et al., 2020; James et al., 2021; Laa and Leth, 2020). The other modes of transport most frequently cited as being replaced by e-scooters was ride hailing services (taxi, uber Lyft etc.) (Almannaa et al. 2021; James et al. 2021) and public transport (James et al.,2021; Laa and Leth, 2020).

The extent to which e-scooters replaced cars varied widely in the literature with some studies reporting only 2% of e-scooter journeys being in place of a car (Buehler et al., 2021), while others had much higher percentages ranging from 7%- 45% (Glenn et al, 2020; James et al., 2021; Laa and Leth, 2020).

Gebhardt, Wolf and Seiffert (2021) used actual trip data with self-report elements in Germany to find that theoretically 10.1% of all motorised individual transport (usually car) trips in Germany could be replaced by e-scooter usage. A higher proportion of motorised individual transport (MIT) trips could be substituted by e-scooters in more sprawling cities compared with compact and densely populated ones where walking or public transport already account for many journeys.

Reasons for use

The main reason for using e-scooters is currently thought to be for leisure trips/ entertainment purposes, where the user is riding the e-scooter due to the perceived fun of doing so (Almannaa et al., 2021; Bielinski and Wazna, 2020; Buehler et al., 2021; Gebhardt, Wolf and Seiffert, 2021; Glenn et al., 2020; McKenzie, 2019). Unsurprisingly, another factor influencing reasons for use is whether the e-scooter is owned or rented, for example, Laa and Leth (2020) found through questionnaires a big difference in number of trips between those who owned e-scooters compared to rented e-scooters. Of those who rented scooters, only 4.5% reported using them several times per week, whereas owners reported using them daily (25%) or several times per week (46%).

Preference for riding location

With regard to where e-scooter users currently ride, a questionnaire survey (Glenn et al, 2020) found that riding behaviour was equally mixed between on the street, on the path, and equal amounts of both. When analysing New Jersey trip data Zhang et al (2021) found e-scooter riders covered the greatest distance on cycle paths (59% longer), multi-use paths (29%), tertiary roads (15%), and one-way roads (21%). This suggests e-scooter riders, given free choice, prefer the use of cycle paths over any other option, and look for simpler routes. They are not deterred by gradients, which is likely to be a result of not requiring increased physical exertion to operate an e-scooter.

Typical e-scooter users

With regard to the typical e-scooter user, there is some consensus that they tend to be young (Bielinski and Wazna, 2020; Huo et al, 2021) and relatively well off, with McKenzie (2019) finding those on lower incomes were less likely to be using the scooters, with the fewest number of scooter-share and bike-share trips home to the lowest income families and largest percentage of African Americans in the district. There is a lack of research on the gender breakdown of e-scooter users. A questionnaire survey by Laa and Leth (2020) also found that e-scooters were predominantly used by residents as opposed to tourists, with 80% of users being residents of Vienna and only 3.7% being tourists. The remainder were commuters or business travellers.

Safety

As e-scooters are a relatively new form of transport the impact they can have on the safety (both actual and perceived) of riders and other stakeholders is crucial. Gibson, Curl, and Thompson (2021) conducted interviews with e-scooter users and pedestrians in New Zealand, where e-scooter riders are permitted to travel in spaces designed for car drivers, cyclists and pedestrians leading them to be able to “go everywhere but belong nowhere,”. The study describes many of the issues that e-scooters now raise with regards to safety. They note e-scooter riders can “transform” into pedestrians when it suits them, dismounting the scooter and walking with it to cross lights and so on and then immediately mounting it again, so they may “‘play’ with road rules and boundaries in urban spaces to maintain their momentum,”. This can lead to erratic and unpredictable behaviour as they switch from one mode to another. The small footprint of the e-scooter can make the rider feel uncomfortable when sharing the roadway with cars, as the cars often do not respect personal space and pass by much closer than they do for a moped. This led to e-scooter riders reporting ‘retreating’ to the footpath to increase their feeling of safety. However, in a similar way to e-scooter riders feeling disproportionately vulnerable on roads compared to cars, pedestrians reported the same

feeling on footpaths when encountering e-scooters, noting the difference in speed and an electric vehicle compared to them on foot. This can mean pedestrians do not feel safe when sharing a space with e-scooters, a finding also noted by Buehler et al. (2021), who found this effect to be even greater for those pedestrians who had not experienced an e-scooter compared to those who had.

Aman, Smith-Colin, and Zhang (2021) identified that the main safety concerns mentioned by e-scooter riders included confusion about laws, and therefore not knowing how to choose the correct paths, and users preferring not to ride next to cars or pedestrians. Buehler et al. (2021) found differences between riders' and non-riders' feelings of safety when being a pedestrian around e-scooters with 13% of riders feeling unsafe as a pedestrian compared to 43% of non-riders feeling unsafe in this context.

Through observations in Brisbane Australia (where helmet use is mandatory for both cycle and e-scooter users and where bicycles can use path or road and e-scooters must use the path), Haworth, Schramm and Twisk (2021) found rental e-scooters may have more safety issues than privately owned ones, "illegal riding (not wearing a helmet, riding on the road, or carrying a passenger) was more prevalent among shared scheme (rental) than private e-scooters (49.6 % vs. 12.2 %)". At least for helmet non-use, the results suggest that risky behaviours are more prevalent among users of shared schemes, and that this difference is accentuated for e-scooters. Todd, Krauss, Zimmermann, and Dunning's (2019) observations of e-scooter users in Los Angeles showed helmets were worn by only 10.9% percent of the riders. Of the e-scooters being operated on the roadway, a total of 6.8% travelled against the flow of traffic, demonstrating that, except for helmet use, rider violations of rules and regulations were noted to be rare.

With regard to accidents a picture is building of e-scooter injuries and the circumstances under which they occur, with many studies comparing and contrasting these to those that would be expected in bicycle injuries. For example, Shah et al (2021) compared e-scooter accidents to those encountered by bicycle riders and found most e-scooter and bicycle incidents occurred in daylight. However, the second most common incidence for e-scooters was night-time in lit areas, whereas for bicycles it was night-time in unlit areas (likely due to bicycles being taken further afield whereas e-scooter use tended to be in the built-up and well-lit areas). Both modes of transport had more accidents in summer months, likely due to increased usage. The proportion of e-scooter crashes involving females was higher than for bicycle crashes (29% vs. 13%). More than 60% of e-scooter- and bicycle-motor vehicle collisions occurred at intersections. More specifically "of all e-scooter crashes, 54% occurred at an intersection with a motor vehicle traveling straight or turning right and an e-scooter rider entering the crosswalk from the right". Conversely, Toofany et al's (2021) systematic literature review of e-scooter

accidents found (from the ten papers that reported how incidents happened) that 92.8% were found to be single road user events, and only 7.1% were injured in multiple road user events. Falls were the most common cause (94.6%), suggesting stability issues may be the safety area in need of most urgent attention. On a pathway (as opposed to road or bike lane) was found to be the most common place for the incidents to occur.

In terms of injuries sustained in the event of a crash Toofany et al (2021) found the most commonly injured body parts were the “head, upper extremities and lower extremities. The chest and abdomen were consistently the two least common injured regions. This injury pattern is similar to that observed in certain non- motorised mobility devices such as skateboards and non-motorised scooters.”

User and non-user perceptions

It seems both being exposed to e-scooters and having actual experience of using an e-scooter can positively impact perceptions of them. Buehler et al. (2021) found non-rider perceptions about convenience, cost, safety, parking, rider behaviour, and usefulness of the e-scooters were more positive after the launch of the scheme than before, suggesting exposure to usage, such as through pilot schemes, may alter opinion favourably. However, satisfaction was still low with only 36% of non-riders reporting ‘proper riding’ after the scheme launched as opposed to 30% predicting e-scooters to be ridden well beforehand. This was higher for intended and actual riders with 72% expecting good riding and 82% reporting good riding after trial introduction. Differences between riders and non-riders were also seen for feelings of safety when being a pedestrian around e-scooters with 13% of riders feeling unsafe as a pedestrian compared to 43% of non-riders feeling unsafe. James et al’s (2021) survey found only 11% of responders felt unsafe being a pedestrian next to cyclists as opposed to 56% reporting feeling unsafe next to e-scooters. This difference was even greater between those who had never used an e-scooter (76% feeling unsafe around them, as opposed to just 24% feeling unsafe if they had used an e-scooter). Similar results were found for car drivers with 16% feeling uncomfortable around bicycles while driving as opposed to 67% feeling uncomfortable driving around e-scooters. Again, experience of using e-scooters affected this with 80% of non-riding car drivers being uncomfortable or very uncomfortable as opposed to 47% for drivers who had also ridden an e-scooter.

Environmental considerations

Current literature has raised some concerns as to how environmentally friendly e-scooters may be. Buehler et al. (2021) found e-scooters replaced walking in 81% of journeys followed by 9% replacing bus trips and only 2% replacing car journeys, so the ecological benefits of e-scooter introduction may be brought into question. Dias, Arsenio, and Ribeiro’s (2021) systematic

literature review found that although e-scooters replacing cars could have a benefit to the environment, current e-scooter systems in place often mean they have a relatively high C02 output in total, and there is a need to improve the engineering of the device and their batteries to reduce this as they currently have a short life span. Schemes which use fossil-fuelled vehicles to pick up the scooters contribute to the emissions problem and charging of e-scooter batteries can also confound the problem if this is not achieved through renewable sources.

3. USER TRIALS

In February 2022 a user trial (n=22) with two e-scooters of the brand being investigated was conducted in a coned off section of Loughborough Design School's grounds to derive feedback from users on several parameters. Special permission was gained since e-scooters are not otherwise permitted on the campus. For health and safety reasons it was not possible for users to experience the e-scooters on varied roads and with traffic and pedestrians, but the set up used did allow participants to experience the e-scooters at full speed and practice difficult U-turn manoeuvres. Participants were provided with a helmet and shown the e-scooter controls before setting off. They were asked to ride one of the e-scooters for as long as they wished; they then completed a short usability questionnaire (see Appendix) with both closed and open-ended responses.

Overall feelings of safety

Figure 1 shows that there was a very positive response from users for their feelings of safety when using the e-scooter with over 80% of respondents giving a rating of neutral or above. There was some mention in the open-ended section of the questionnaire that this was helped by the trial being in a closed off area "*While I felt safe testing it in this little blocked off section with low traffic, I would feel less comfortable in a city on pavement*".

There were some positive comments that might reflect why users felt safe such as "*solidly built*," "*Excellent – very robust, adding to the safety assurance*," "*Easy to control and handle*," "*Good size platform and solid structure*."

Some comments which highlight why users might not rate the feeling of safety quite so highly include "*Felt unstable until more comfortable*," "*A little bumpy over paving*," "*I did not feel in control of the scooter, while it was fun to use the controls seemed intuitive, I felt quite unsafe using it*." "*Twitchy handling and rapid acceleration made overall experience nerve racking*."



Figure 1: Feelings of safety overall

Braking

The comments relating to feelings of safety were then broken down into a number of components, starting with braking. It can be seen in Figure 2 that braking was not considered a safety problem for most respondents with more than 90% reporting feeling neutral or above with regard to safety. Comments about the brakes included "*Brakes are good, not too responsive, other than that feels the same as all others*," "*Not sure if it was just this scooter but the low power on the front brake, compared to the rear, was helpful to not worry about it tipping over*," "*Brakes are sharp*," "*Brakes did not inspire confidence – unsure which was front or rear without experimenting*."

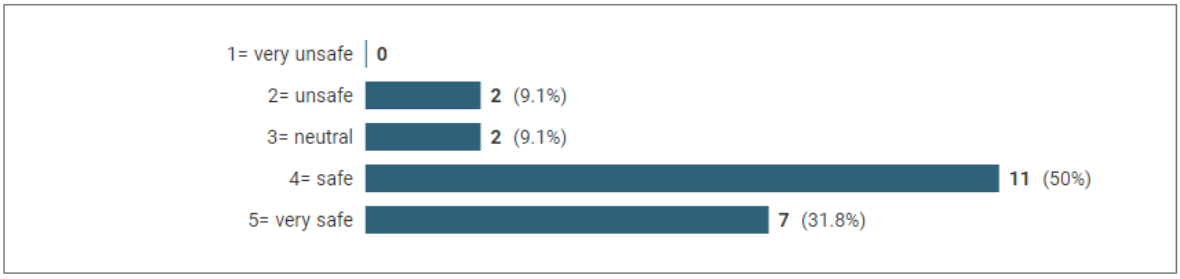


Figure 2: How safe did you feel using the brakes?

Participants were also asked about their experience of using the brakes, and how difficult they found this process. As shown in Figure 3 most users were very satisfied, with only two responders (9.1%) reporting anything less than a neutral opinion. The majority (50%) reported using the brakes to be very easy.

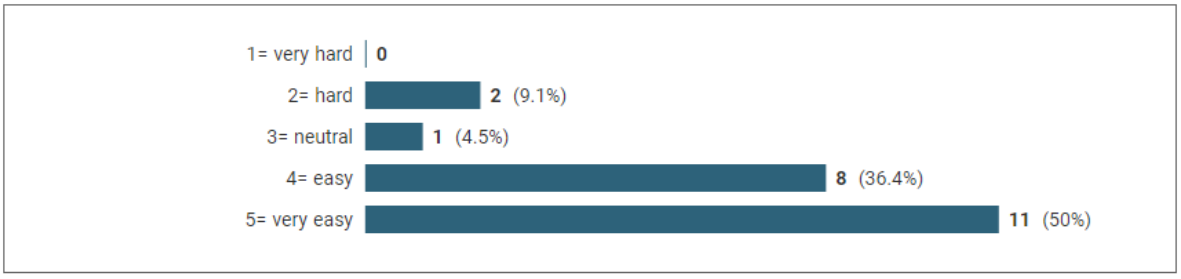


Figure 3: How easy was it to use the brakes?

Steering

When asked how safe participants felt when steering the e-scooter there was a mixed response. Most (68.2%) reported neutral or above with most (54.6%) rating safe or very safe. However, 31.8% were less confident when steering and rated that they felt unsafe (Figure 4). This may have partly been due to the setup of the trial, with the participants having to perform a 180-degree U-turn in a relatively tight space, a scenario that may not be encountered, especially upon first use, when renting an e-scooter at a test site. In the free text box, comments about steering included "*I found turning a little daunting. I think I would feel safe once I was used to using it and got used to speed controls*.", "*I can imagine getting used to it but turning felt like I needed a large turning circle*." "*I needed to get my weight to transfer to get it steering how I like (sticking my inside leg out in turns) but once adapted it steered fine- sharp turns did have the front wheel sliding due to steering angle*." "*Steering is excellent*" "*Easy to use except when turning, took a while to learn how to turn 360*." "*Turning circle was very large – had to reduce speed dramatically*" "*Turning uphill is particularly hard*", "*Turning is scariest part as hard to predict turning circle*," "*Really hard to steer, didn't know if needed to use accelerator or not to keep the balance*." "*Under-steer feeling*."

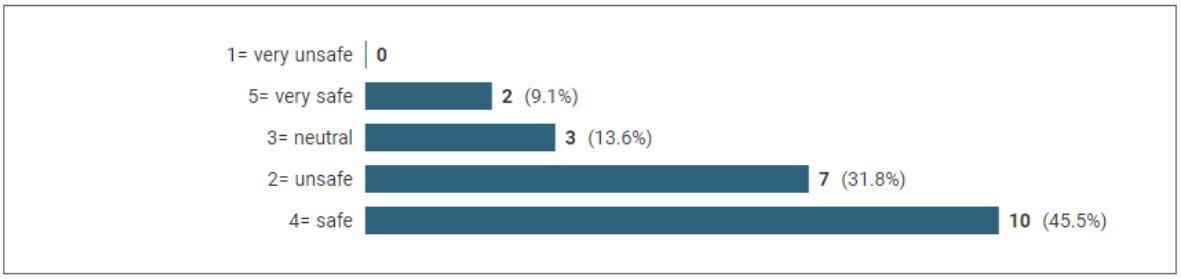


Figure 4: How safe did you feel steering the e-scooter?

Use of the controls

When asked how easy they felt it was to operate the controls of the e-scooter there were very favourable responses with 90.9% rating it easy or very easy and the lowest rating given was neutral (9.1%) (Figure 5). Comments included "*Very user friendly*," "*Took a while to start (initially)/ had to learn kick-off*," "*Kick off is difficult first time*," "*Brakes are hard to activate with thumb near throttle*." "*I found it difficult to do slow control which was made worse as any brake use cuts power*."

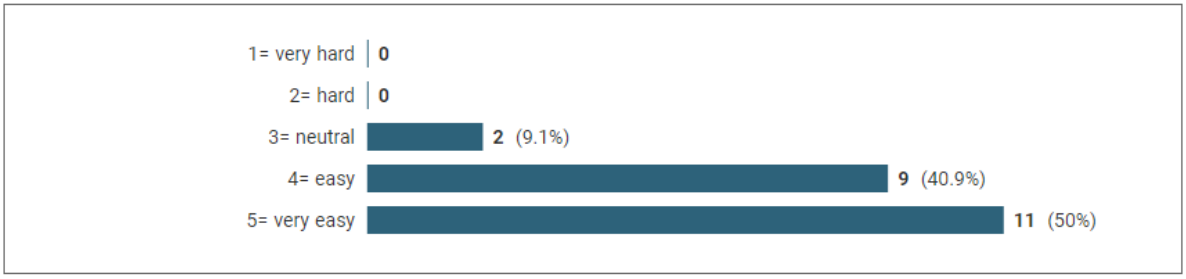


Figure 5: How easy was it to use the controls?

Ease of Acceleration

Participants had a positive opinion of how easy it was to accelerate with 90.9% rating it as easy or very easy (Figure 6). However, the open ended feedback identified a few issues around acceleration "*Almost too easy – I would want the calibration the other way around, a 'soft' start and power later", "Quick acceleration instead of the preferred gradual*," "*Speed took a while to kick in then all of a sudden all comes on*." "*Difficult to control the speed in the curves*", "*You have to push a bit to get it started*", "*The speed is quite jumpy*," "*Accelerator is very sudden*," "*Not smooth so jolts a lot*," "*Acceleration could be 'gentler'*".

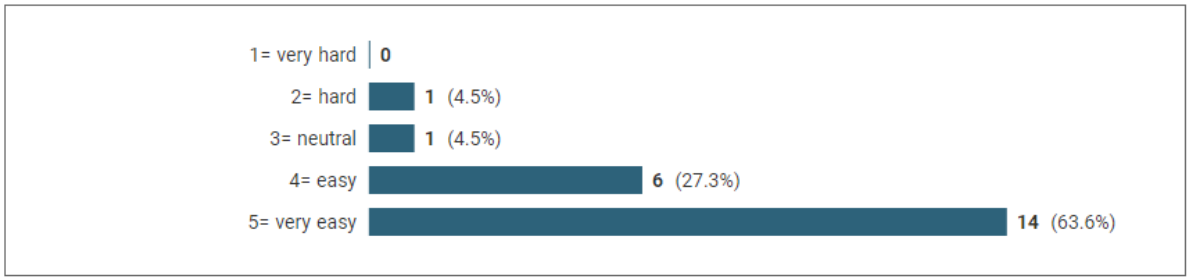


Figure 6: How easy was it to speed up?

Recommending the e-scooter to others

When asked if they would recommend the e-scooter brand to a friend the majority (54.5%) reported that they would. A smaller proportion, 31.8%, were unsure and only 13.6% said no.

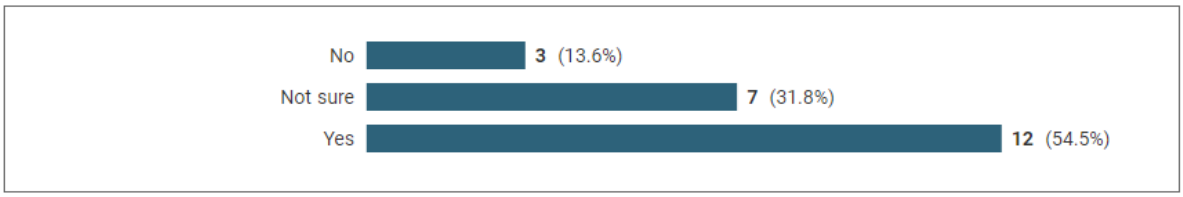


Figure 7: Would respondents recommend the e-scooter to a friend?

4. CONCLUSIONS

In the design or improving the design of any transport vehicle, it Is very important to understand the current transport system and the vehicle's role, its effect and the factors which might effect the vehicle and the system as a whole. Therefore, the vehicle's environment (such as road network, other vehicles, natural environment), the elements which directly interacts with it (such as users), as well as its own subsystems such as its stability, breaks, acceleration systems, visibility, parking, other control systems and mechanic and electrical interfaces. In particular user perceptions and usability issues and user activities are often connected to safety. For this reason an extensive literature review has been conducted on e-scooter safety and sets of data were collected directly in this study.

It has been shown that there is a growing body of literature on e-scooters which perhaps reflects their increasing popularity around the world. It also echoes the concerns around safety which have attached themselves to this new form of transport.

The literature discussed here covers a wide range of issues, including barriers to, and reasons for, e-scooter use, the journeys replaced by e-scooters, typical users, perceptions of both users and non-users, environmental considerations and safety.

Furthermore, the usability trials showed that users have a very positive opinion about e-scooters in terms of usability and safety. As might be expected, issues were identified which could be investigated further to optimise the product and service's usability and safety.

5. REFERENCES

Almannaa, M. H., Alsahhaf, F. A., Ashqar, H. I., Elhenawy, M., Masoud, M., & Rakotonirainy, A. (2021), "Perception analysis of E-scooter riders and non-riders in Riyadh, Saudi Arabia: Survey outputs", Sustainability, Vol.13, No.2, p863.

Aman, J. J., Smith-Colin, J., & Zhang, W. (2021), "Listen to E-scooter riders: Mining rider satisfaction factors from app store reviews", Transportation Research Part D: Transport and Environment, Vol.95, 102856.

Bieliński, T. & Ważna, A. (2020), "Electric scooter sharing and bike sharing user behaviour and characteristics", Sustainability (Switzerland), Vol.12, No.22, pp. 1-13.

Buehler, R., Broaddus, A., Sweeney, T., Zhang, W., White, E., & Mollenhauer, M. (2021), "Changes in Travel Behavior, Attitudes, and Preferences among E-Scooter Riders and

Nonriders: First Look at Results from Pre and Post E-Scooter System Launch Surveys at Virginia Tech", Transportation Research Record, Vol.2675, No. 9, pp335-345.

Department for Transport (2021). *National statistics reported road casualties Great Britain: e-Scooter factsheet year ending June 2021.* Last updated November 2021. Accessed 4th May 2022. https://www.gov.uk/government/statistics/reported-road-casualties-great-britain-e-scooter-factsheet-year-ending-june-2021/reported-road-casualties-great-britain-e-scooter-factsheet-year-ending-june-2021.

Dias, G., Arsenio, E., & Ribeiro, P. (2021), "The role of shared E-Scooter systems in urban sustainability and resilience during the COVID-19 mobility restrictions", Sustainability, Vol.13, p7084.

Eccarius, T. & Lu, C.-C. (2020), "Adoption intentions for micro-mobility – Insights from electric scooter sharing in Taiwan", Transportation Research Part D: Transport and Environment, Vol.84, 102327.

Gebhardt, L., Wolf, C., & Seiffert, R. (2021), "'I'll Take the E-Scooter Instead of My Car'—The Potential of E-Scooters as a Substitute for Car Trips in Germany", Sustainability, Vol.13, 7361.

Gibson, H., Curl, A., & Thompson, L. (2021), "Blurred boundaries: E-scooter riders' and pedestrians' experiences of sharing space", Mobilities, Vol.17, No.1, pp69-84.

Glavić, D., Trpković, A., Milenković, M. & Jevremović, S. (2021), "The e-scooter potential to change urban mobility – Belgrade case study", Sustainability (Switzerland), Vol.13, No.11, 5948.

Glenn, J., Bluth, M., Christianson, M., Pressley, J., Taylor, A., Macfarlane, G.S. & Chaney, R.A. (2020), "Considering the potential health impacts of electric scooters: An analysis of user reported behaviors in provo, Utah", International Journal of Environmental Research and Public Health, Vol.17, pp1-15.

Haworth, N., Schramm, A., & Twisk, D. (2021), "Comparing the risky behaviours of shared and private e-scooter and bicycle riders in downtown Brisbane, Australia", Accident Analysis and Prevention, Vol.152, 105981.

Huo, J., Yang, H., Li, C., Zheng, R., Yang, L. & Wen, Y. (2021), "Influence of the built environment on E-scooter sharing ridership: A tale of five cities", Journal of Transport Geography, Vol.93, 103084

James, O., Swiderski, J. I., Hicks, J., Teoman, D., & Buehler, R. (2019), "Pedestrians and e-scooters: An initial look at e-scooter parking and perceptions by riders and non-riders", Sustainability, Vol.11, No.20, 5591.

Laa, B., & Leth, U. (2020), “Survey of E-scooter users in Vienna: Who they are and how they ride”, Journal of transport geography, Vol.89, 102874.

McKenzie, G. (2019), “Spatiotemporal comparative analysis of scooter-share and bike-share usage patterns in Washington, D.C.”, Journal of Transport Geography, Vol.78, pp.19-28.

Sellaouti, A., Arslan, O. & Hoffmann, S. (2020), “Analysis of the use or non-use of e-scooters, their integration in the city of Munich (Germany) and their potential as an additional mobility system”, 2020 IEEE *23rd International Conference on Intelligent Transportation Systems*, ITSC 2020, 9294224.

Shah, N. R., Aryal, S., Wen, Y., & Cherry, C. R. (2021), “Comparison of motor vehicle-involved e-scooter and bicycle crashes using standardized crash typology”, Journal of safety research, Vol.77, pp. 217-228

Todd, J., Krauss, D., Zimmermann, J., Dunning, A. (2019), “Behavior of electric scooter operators in naturalistic environments”, SAE Technical Papers, 2019-April (April), 2019-01-1007.

Toofany, M., Mohsenian, S., Shum, L. K., Chan, H., & Brubacher, J. R. (2021), “Injury patterns and circumstances associated with electric scooter collisions: a scoping review”, Injury Prevention, Vol.27, No.5, 490-499.

Winchcomb, M. (2022), “The safety of private e-scooters in the UK final report”, Parliamentary advisory council for transport safety (PACTS). https://www.pacts.org.uk/the-safety-of-private-e-scooters-in-the-uk-pacts-research/

Zhang, W., Buehler, R., Broaddus, A., & Sweeney, T. (2021), “What type of infrastructures do e-scooter riders prefer? A route choice model”, Transportation Research Part D: Transport and Environment, Vol.94, 102761.

OCCUPANT PROTECTION IN SEATS WITH FIXED RECLINERS IN REAR-END COLLISIONS

Selçuk HİMMETOĞLU, *s.himmetoglu@hacettepe.edu.tr* Hacettepe University, Turkey

ABSTRACT

This paper presents the development of an energy-absorbing car seat with fixed recliner that can mitigate whiplash risk in rear-end collisions. The developed seat has a proactive head restraint and an energy-absorbing device under the seatpan. The seat produces neck shear forces lower than 120 N when subjected to the medium and high severity crash pulses of EuroNCAP. Additionally, a very high severity crash pulse with a velocity change (delta-V) of 35 km/h is applied and the largest neck-shear force at this severity is only 189 N. The developed seat gets maximum points from the dynamic whiplash assessment protocol of European New Car Assessment Programme (EuroNCAP).

Keywords: Seats with fixed recliner, Rear seat, Rear-end collisions, Integrated safety

1. INTRODUCTION

Car seats with fixed recliners are found typically in the rear section of passenger cars as rear seats or as forward facing seats in sports cars and rear facing seats in vans such as ambulances. Recent real-world crash data indicate that rear seats are mainly occupied by children and adolescents with a mean age of 14.3 years old since rear seats are the safest place for them; it was also found that about 55% of rear seat occupants are females whereas occupants above 20 years old constitute only 21% of rear seat occupants [Durbin et al., 2015; Parenteau et al., 2021]. Real-world crash data from United States and Australia show that in the last twenty years, rear seat occupants are having higher injury risk overall and higher risk of serious injuries and fatality in comparison to front seat occupants; this is partly attributed to the fact that rear seats have not benefited enough from the advances in restraint systems compared to those of front seats [Durbin et al., 2015; Mitchell et al., 2015]. More than half of the serious injuries and fatalities in the rear seat were found among unrestrained occupants [Durbin et al., 2015] indicating that the use of seatbelt among rear seat occupants is still lacking.

Durbin et al. (2015) investigated vehicle crashes including injured front and rear seat occupants in the same vehicle between 2001 and 2011 in New South Wales, Australia and calculated adjusted risk ratios (ARR) of rear seat compared to front seat. ARRs were found by using regression analysis stratified by vehicle. Considering all types of crashes, the risk of neck injuries (ARR: 1.23), thorax injuries (ARR: 1.37), spine - pelvis - lower back injuries (ARR: 2.81) were higher for rear seat occupants in comparison to front seat occupants. On the other hand, regarding all types of crashes, the risk of head injuries (ARR: 0.44), upper extremity (ARR: 0.73) and lower extremity (ARR: 0.58) injuries were lower for rear seat occupants. For minor neck injuries (i.e. whiplash), the ARR was found to be 1.53 for all types of crashes. In vehicle to vehicle rear-end collisions, ARR was found as 1.13 regarding all neck injuries.

Parenteau et al. (2021) analysed National Automotive Sampling System, Crashworthiness Data System (NASS-CDS) in the US between years 1994-2015 for light vehicles with model year 1994+. The focus of this research was non-ejected rear seat occupants. It was found that the number of exposed and serious-to-fatally injured (MAIS3+F) rear seat occupants were highest in frontal crashes whereas rear-end collisions constitute 5.4% of serious-to-fatally injured and 8.7% of exposed rear seat occupants. Around 72% of rear seat occupants experienced rear impacts with a delta-V less than 24 km/h; around 26% of them experienced rear impacts with delta-V between 24 and 48 km/h and only 1.2% of them were exposed to rear impacts with delta-V higher than 48 km/h. In rear impacts with delta-V less than 24 km/h, there were no rear seat occupants with MAIS3+F injuries whereas with delta-V between 24 and 48 km/h, 78% of rear seat occupants had MAIS3+F injuries. In rear impacts with crash severities higher than 48 km/h, 22% of rear seat occupants sustained MAIS3+F injuries. Rear seat occupants with MAIS3+F injuries experienced a crash severity with a mean delta-V of 37.4 ± 3.1 km/h.

Zellmer et al. (2018) investigated the German In-Depth Accident Study (GIDAS) database for frontal crashes involving adult occupants in rearward facing seats. They could find only 5 cases and found out that no whiplash associated disorders occurred in these crashes with delta-V of 25 km/h or lower. It has to be noted that in two of the cases the corresponding vehicles were ambulances which involved special rearward facing seats with almost upright seatbacks to look after the patient.

Hasija et al. (2019) used finite element models of car seat and human-body models simulating rear impacts at 24 km/h and 56 km/h of delta-V and tested seats with compliant recliner and fixed recliner. They evaluated head and chest injury risk only and stated that using fixed recliner, integrated seatbelt and active head restraint helped to reduce injury risk.

Braganza et al. (2011) subjected the BioRID II dummy positioned in a rear seat to rear impacts with a delta-V of 35 km/h. When there was no good support of the upper torso by the upper seatback in a leaning forward position with a backset of 30 cm, maximum upper-neck positive and negative shear forces were recorded as 526 N and 441 N respectively. The maximum upper-neck tension force was measured as 1597 N.

Simms et al. (2009) improved rigid wheelchair (with fixed recliner) design by integrating different head restraints to the seatback. In the wheelchairs, the seatbacks were almost upright hence the gap between upper torso and seatback was minimal. The BioRID II was positioned on the wheelchairs and subjected to the medium severity crash pulse of the European New Car Assessment Programme [EuroNCAP, 2021]. In the tests, there was zero backset between the head and the head restraint, and the top of the head restraints was not lower than the top of the head. Under these conditions, the largest positive and negative upper-neck shear forces were found as 75 N and 100 N, respectively.

EuroNCAP states that since rear seat occupancy rates are lower than those of front seats, whiplash associated disorders are rare in the rear seat compared to those in front seats. Therefore, EuroNCAP applies only a static assessment of head restraint height and backset for the rear seats [EuroNCAP, 2018] whereas dynamic assessment of front seats is required. For these reasons, advanced anti-whiplash front-seat designs including adaptive ones have been developed in the last decade [Himmetoglu et al., 2011; Himmetoglu, 2017; Kaya, 2022] but on the other hand such designs for rear seats have not been explored.

In forward facing frontal car-seats, recliner is a major energy absorbing element but a car seat with fixed recliner has to be redesigned to absorb crash energy and reduce whiplash risk. In this study, an energy-absorbing car-seat with fixed recliner is introduced which provides comfort and neck protection for crash severities up to 35 km/h of delta-V in rear impacts. This seat with fixed recliner is dynamically assessed using the whiplash test protocol of EuroNCAP for front seats. The seat-occupant simulations show that the proposed seat successfully satisfies all whiplash assessment criteria even for the very high severity crash pulse with a delta-V of 35 km/h which is not included in EuroNCAP whiplash test protocol for front seats.

2. DEVELOPMENT OF A CAR SEAT WITH FIXED RECLINER

The development of the car seat with fixed recliner started with the modification of an anti-whiplash front seat which absorbs most of the crash energy by its plastically deforming recliner mechanism (R) and the energy absorbing device (D) under the seatpan (SP) as shown in Figure 1. This anti-whiplash front seat has a typical integrated head-restraint (HR),

seatback (SB) and seatpan (SP) foam and suspension. The design methodology that this front seat is based on, are given in the following references [Himmetoglu et al., 2011; Himmetoglu, 2017]. A biofidelic rear-impact 50th percentile male multi-body human model [Himmetoglu et al., 2009], as shown in Figure 1, is used in developing the anti-whiplash front seat and the seat with fixed recliner in this paper. The simulations are performed by using the multi-body dynamics software MSC VisualNastran 4D.

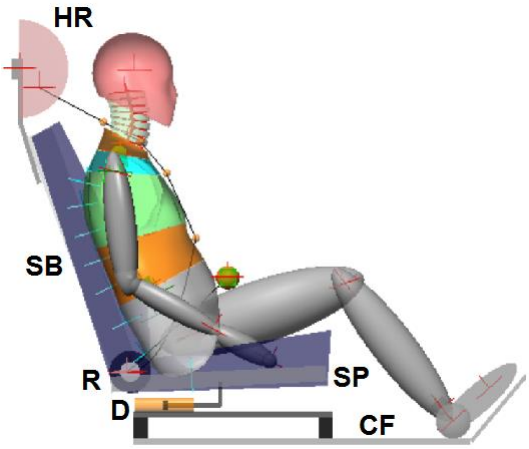


Figure 1. Anti-whiplash front seat and occupant model

The anti-whiplash front seat in Figure 1 is transformed into a seat with fixed recliner by rigidly fixing its recliner (R) and the energy absorbing device (D) such that no relative motion between the seatback (SB), seatpan (SP) and car floor (CF) occurs. The 3-point seatbelt in the front seat is replaced by an integrated seatbelt so that the seat can be moved within the occupant compartment in autonomous cars. Three crash pulses are used in the simulations: 1) SN(16): EuroNCAP medium severity pulse with a delta-V of 16 km/h, mean and peak accelerations of 5 g and 10 g respectively; 2) TR(24): EuroNCAP high severity pulse with a delta-V of 24 km/h, mean and peak accelerations of 6.5 g and 7.5 g respectively [EuroNCAP, 2021]; 3) HS(35): a very high severity pulse with a delta-V of 35 km/h, mean and peak accelerations of 7 g and 16 g respectively [Viano, 2002]. This pulse with a delta-V of 35 km/h is referred as very high severity for rear impacts since about 98% of rear impacts occur with delta-V's less than 35 km/h according to recent crash data reported in the NASS-CDS database in the US [Parenteau et al., 2021]. Therefore, EuroNCAP designates SN(16) and TR(24) pulses as medium severity and high severity crash pulses for rear impacts, respectively.

As shown in Figure 1, the seatback angle is 20 deg from the vertical, and the backset (the horizontal gap between the head and the head-restraint) is 6 cm in both the anti-whiplash front seat and the seat with fixed recliner. In both seats, the occupant has the same posture as shown in Figure 1. When the seat with fixed recliner was subjected to EuroNCAP medium severity crash pulse SN(16), the largest upper-neck shear force was recorded to be around

400 N, which is high considering that the capping limit for upper-neck shear force is 360 N for SN(16) in the whiplash assessment criteria of EuroNCAP [EuroNCAP, 2021]. Capping limit represents an unacceptable high risk of injury. The posture of the human-body in Figure 1 can be comfortable for the occupant but this posture produces a gap between the upper torso and the upper seatback. Hence, the head and the upper torso are not well supported by the head restraint and the upper seatback. Moreover, since the seatback is not allowed to recline and extend the time to absorb crash energy in the seat with fixed recliner, there is not much time to develop full reflex muscle contraction in the neck as the head interacts with the head restraint. Consequently, the head and the upper torso attain high velocities with respect to the seat, and the head restraint bottoms out leading to high neck-shear forces. Similar amounts of shear forces were also found in the work of Braganza et al. (2011) when the BioRID II dummy was leaning forward in a rear seat before the rear impact. Therefore, the motion of the head and upper torso with respect to the seat should be restricted. For this reason, the seat with fixed recliner is further modified such that the motion of the torso with respect to the seatback is eliminated by ideal restraints as shown in Figure 2. These ideal restraints comprise a rigid head-restraint with zero backset, seatback and seatpan with rigid surfaces without any foam and suspension, rigid thorax and lumbar torso-plates eliminating completely the motion of the torso with respect to the seatback and seatpan. The integrated seatbelt and thorax torso-plate prevents ramping up the seatback. With these ideal restraints, the head and torso of the occupant move together with the seat and vehicle under rear impact. This theoretical analysis reveals that the seat with fixed recliner and ideal restraints produces largest upper-neck shear forces of 80.4 N for the crash pulse SN(16), 60 N for the crash pulse TR(24) and 127.9 N for the crash pulse HS(35). These results are in accordance with the rigid wheelchair rear impact tests performed by Simms et al. (2009).

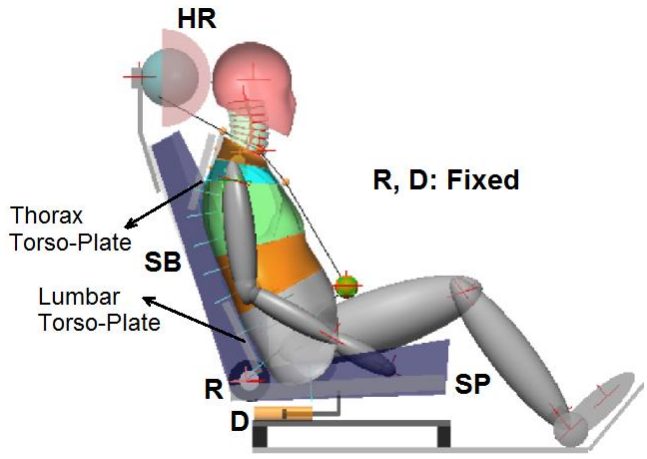


Figure 2. Seat with fixed recliner and ideal restraints

It can be argued that the seat with ideal restraints may not be comfortable, therefore an alternative approach is sought. This approach involves maximisation of energy absorption by

the seat in spite of the presence of a fixed recliner while providing comfort for the occupant during normal daily use. In order to close the gap between head and head-restraint at the start of the impact, a proactive head-restraint (PHR) which consists of a damper (with a viscous damping coefficient of 175 kg/s) and a pre-compressed spring (with a stiffness of 12.5 kN/m) is designed; such designs are used in commercial cars in the market [Hartlieb et al., 2007]. The head restraint is released forward to travel about 6 cm in 40 ms to provide early support of the head while maximising energy absorption by the head restraint. The head restraint is covered with a foam of 7 cm in thickness A relatively harder foam and suspension are used for the seatback which allow the human-body to sink into the seatback by an amount of 1.5 cm during impact. This proposed energy-absorbing seat with fixed recliner is shown in Figure 3.

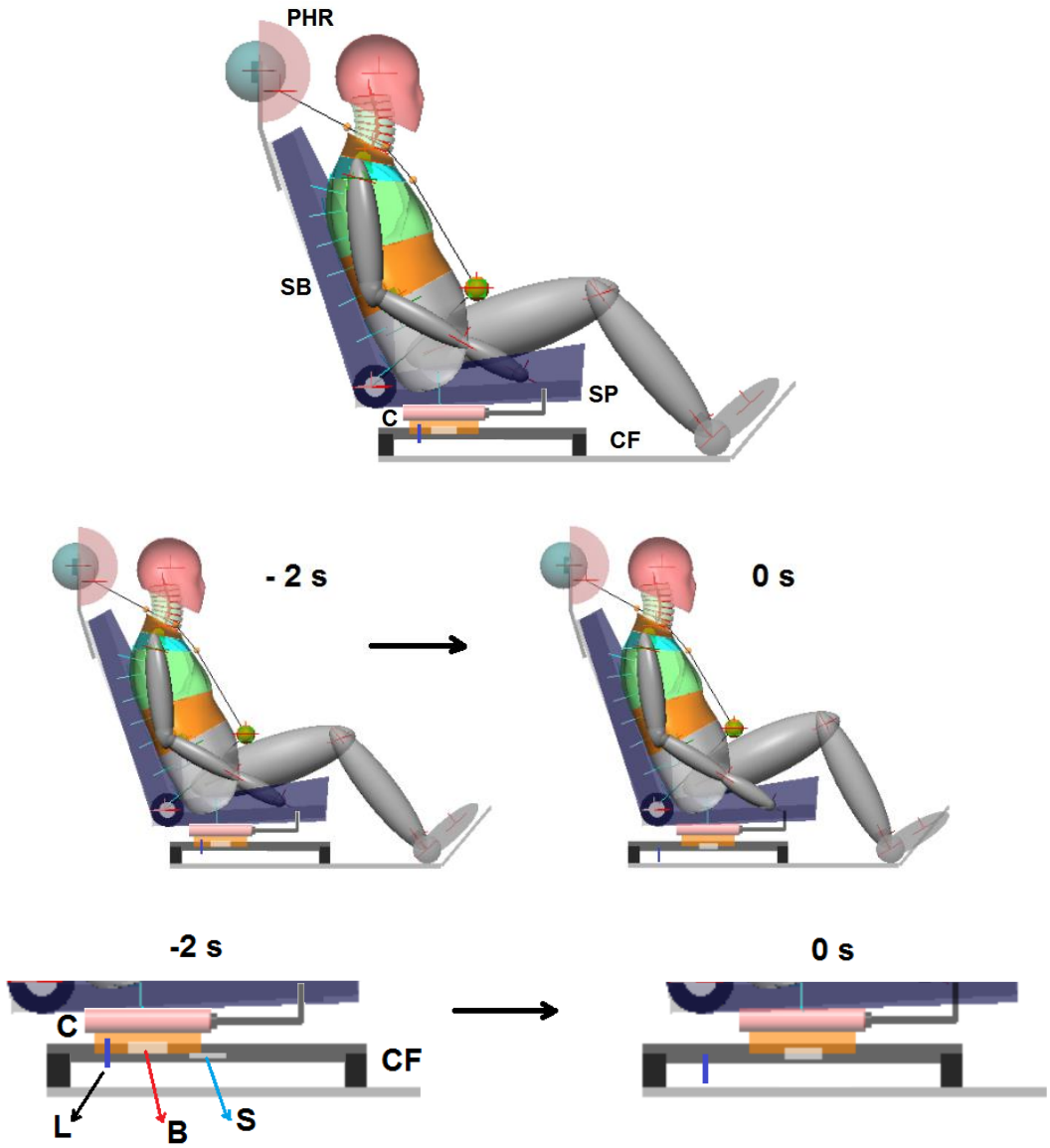


Figure 3. Proposed energy-absorbing seat with fixed recliner

Before the impact occurs, the seatpan is moved forward 20 cm in 2 seconds with respect to the car floor (CF) with the aid of an electric motor, as shown in Figure 3. An energy

absorbing device C is installed under the seatpan (SP) which involves a damper (with a viscous damping coefficient of 1500 kg/s) coupled with a constant force deformation element (with a resistive force of 4250 N). Constant force deformation elements have been used in the literature as energy absorbing devices for impact applications [Zhang and Zhou, 2016]. The seatpan is allowed to displace backward at most 20 cm once the impact occurs hence the net backward displacement of the seat is only 10 cm at most. During normal daily use, the seatpan is secured to the car floor (CF) by a lock pin (P). When the car sensors detect an imminent crash 2 seconds before the impact, the lock pin is released electro-mechanically. There is a spring resisted block (B) within the energy absorbing device (C) and this block moves together with C until it fits into a slot (S) in CF during the forward motion of the seatpan before the impact. Once the block fits into the slot, the forward motion of the seatpan is terminated and the motor is switched off. The impact then starts at time equals zero. The change in the posture of the human-body model with respect to the seat is negligible before the impact during forward travel of the seatpan since the seatpan is moved forward with low levels of acceleration as shown in Figure 4 (an average car accelerates with 0.5 g in the first gear; an average electric car accelerates with 0.55 g at most [Jazar, 2002; Unlusoy, 2016]).

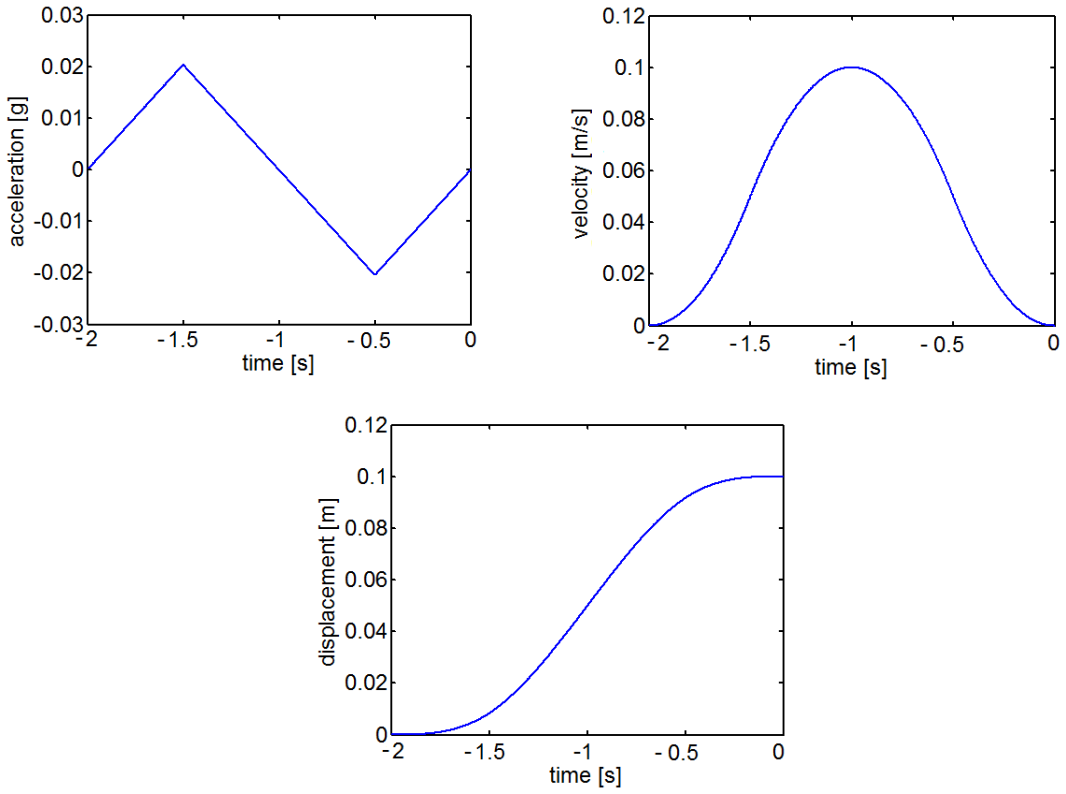


Figure 4. Motion of the seatpan relative to the car floor before the impact

3. PERFORMANCE OF THE PROPOSED SEAT WITH FIXED RECLINER

The proposed energy-absorbing seat with fixed recliner is subjected to the crash pulses SN(16), TR(24) and HS(35) with medium, high and very-high severities, respectively. In order to evaluate the performance of the proposed seat, the whiplash assessment criteria of EuroNCAP for front seats are used [EuroNCAP, 2021]. The corresponding injury assessment reference values (IARVs) for these criteria are presented in Table 1 for both SN(16) and TR(24) pulses which comprises NIC (Neck Injury Criterion), Nkm, v_r (head rebound velocity), $Fsh^{(+)}$ (largest upper-neck positive shear force), $Fsh^{(-)}$ (largest upper-neck negative shear force), Ftn (maximum upper-neck tension force), MyU (largest upper-neck moment), FshL (largest lower-neck shear force), MyL (largest lower-neck moment), T1a (largest acceleration of the first-thoracic-vertebra (T1)), HrCt (head restraint contact time). Nkm is an injury criterion which utilises a combination of upper-neck shear force and moment. NIC is an injury criterion associated with the S-shape-like deformation in the neck and v_r is the maximum resultant velocity of the head with respect to car floor (CF) during which the head begins to rebound from the head restraint and travels in forward direction with respect to the car floor [EuroNCAP, 2021]. For some of the criteria, higher performance limit (HL) and lower performance limit (LL) values are specified regarding seat performance. For the remaining criteria, capping limits (CL) are specified. In general, when a capping limit for an assessment criterion is exceeded, the seat loses all points from the test in the whiplash assessment protocol of EuroNCAP. Capping limit represents an unacceptable high risk of injury. EuroNCAP protocol does not have IARVs for the very-high severity pulse HS(35) since most of the rear-end collisions occur at crash severities below 25 km/h of delta-V but it is reported that the mean delta-V for MAIS3+F injuries is around 35 km/h [Parenteau et al., 2021].

Table 1. Injury assessment reference values (IARVs) for whiplash [EuroNCAP, 2021]

Pulse		SN(16)			TR(24)		
	Unit	HL	LL	CL	HL	LL	CL
NIC	m^2/s^2	11	24	27	13	23	25.5
Nkm	-	-	-	0.69	-	-	0.78
v_r	m/s	-	-	5.2	-	-	6
$Fsh^{(+)}$	N	30	190	290	30	210	364
$Fsh^{(-)}$	N	-	-	360	-	-	360
Ftn	N	360	750	900	470	770	1024
MyU	Nm	-	-	30	-	-	30
FshL	N	-	-	360	-	-	360
MyL	Nm	-	-	30	-	-	30
T1a	g	-	-	15.55	-	-	17.8
HrCt	ms	-	-	92	-	-	92

The performance of the proposed energy-absorbing seat with fixed recliner is presented in Table 2 for all crash severities. In this table, Ds represents in cm the maximum rearward displacement of the seatpan with respect to the car floor during impact. The terms given in Table 1 and Table 2 are also explained in the Appendix.

Table 2. Performance of the proposed energy-absorbing seat with fixed recliner

Pulse	NIC	Nkm	v_r	$Fsh^{(+)}$	$Fsh^{(-)}$	Ftn	MyU	FshL	MyL	T1a	HrCt	Ds
Unit	m^2/s^2	-	m/s	N	N	N	Nm	N	Nm	g	ms	cm
SN(16)	6.38	0.28	1.69	8.66	112.7	102.1	8.28	123.3	8.36	9.45	27	5.75
TR(24)	5.23	0.31	1.58	11.8	117.6	57.4	7.55	112.6	9.64	10.1	24	11.1
HS(35)	9.56	0.45	1.95	15.5	189.7	158.8	12.6	160.1	10.1	14.5	22	19.3

Figure 5 shows the seat-occupant at the start of the rear impact (zero time) and when the head first contacts the head restraint at 25 ms in response to the crash pulse TR(24). Figure 6 shows the system and the corresponding time instants when the maximum seatpan displacement and the maximum torso extension occur at all crash severities.

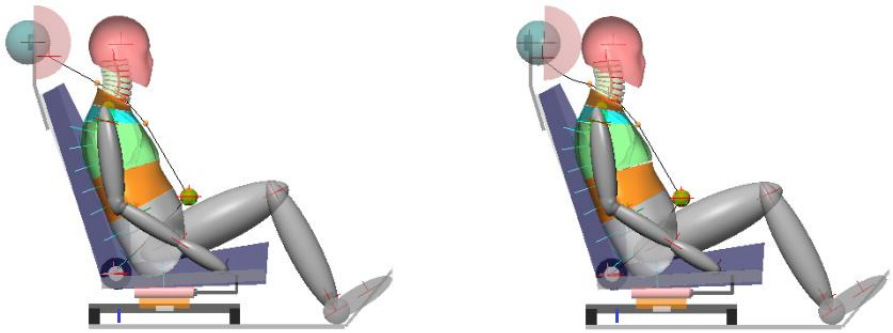


Figure 5. Seat-occupant response in the first 25 ms of the impact

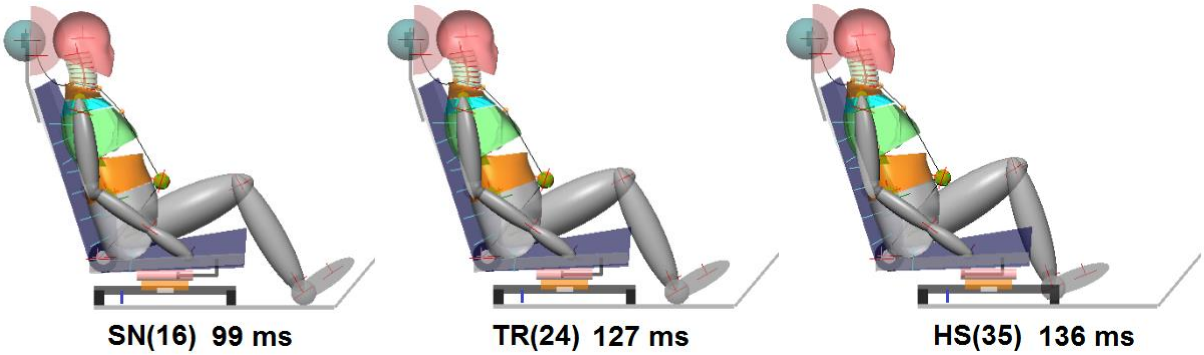


Figure 6. Seat-occupant response at maximum seatpan and torso extension

4. DISCUSSION

When the performance of the proposed seat given in Table 2 is compared with the IARVs given in Table 1, it can be seen that NIC, $Fsh^{(+)}$ and Ftn values are lower than the higher seat performance limits and the remaining IARVs are all below the corresponding capping limits for all three crash pulses involving medium, high and very-high severities. Hence, the proposed seat gets maximum points from the dynamic assessment of EuroNCAP whiplash protocol for front seats. In the simulations, S-shape-like deformation in the neck (head retraction with respect to upper torso) is insignificant as indicated by the low values of NIC and $Fsh^{(+)}$. The loads on the head-and-neck are low during head contact with the head restraint as shown by the values of Nkm, $Fsh^{(-)}$, Ftn, MyU, FshL and MyL. The acceleration of T1 (the first thoracic vertebra) is lower than the corresponding capping limits due to the energy absorbing device under the seatpan. Head restraint contact times (HrCt) are low due to the presence of the proactive head-restraint. The net rearward displacement of the seat with respect to the car floor is no more than 9.3 cm at the very-high severity crash pulse. The rebound velocities of the head as given by v_r are low since the recliner is fixed. If there was an energy-absorbing recliner mechanism, its spring-back during unloading of the seatback would increase head rebound velocities. Table 1 does not involve any IARVs for the very high severity crash pulse HS(35) since IARVs for this pulse are not established in the literature, however the proposed seat have whiplash assessment criteria values all below the established IARVs for both the medium and high severity crash pulses.

Seats with fixed recliners, such as rear seats, cannot absorb crash energy by the plastic deformation of the recliner mechanism since the seatback is not allowed to rotate with respect to the seatpan. Therefore, in a seat with fixed recliner, the other elements that can absorb energy are the head restraint and the energy absorbing device under the seatpan. In order to maximise the energy absorbing potential of these elements, the seatpan and the head restraint are deployed forward before the crash and in the initial stages of the impact, respectively. The 10 cm forward displacement of the seatpan with respect to the car floor is a reasonable distance which the geometry of the occupant compartment can easily afford considering that autonomous cars will have moveable and rotatable seats. The use of the proactive head-restraint and the energy-absorbing device under the seatpan lengthens the time for reflex muscle activation to develop which protects the neck against rear impact for a relaxed unaware occupant.

With good upper torso support from the seatback coupled with close head restraint support, very good performance from seats with fixed recliners, such as rear seats, can be achieved. This has been shown in this paper and in other studies in the literature. Hence, seats with fixed recliners should not be used with larger seatback angles. Considering the seatback

angle and backset distance used in the simulations, the posture of the human-body model can be considered to be slightly out-of-position for a rear seat but this posture can be comfortable for the occupant. Hence, the proposed seat with fixed recliner can provide improved neck protection for out-of-position postures as well.

5. CONCLUSIONS

In this study, an energy-absorbing seat with fixed recliner is developed which utilises the principles of active and passive safety by employing a proactive head-restraint and an energy absorbing device under the seatpan which is deployed forward before the impact. Currently, there is no dynamic assessment of seats with fixed recliners in the regulatory and consumer crash tests for whiplash but the proposed seat gets full points from the dynamic whiplash assessment protocol of EuroNCAP for front seats with deformable recliner mechanisms. The developed seat can provide both comfort and protection when the upper torso is not fully supported by the upper seatback due to the posture of the occupant. Hence, the proposed seat has the potential to accommodate neck protection for a wider range of postures. The proposed energy-absorbing seat with fixed recliner is designed to be forward facing with protective devices against rear impacts. The design principles used in this study can be used for seats with fixed recliners especially in autonomous cars in which seats can be moveable and rotatable.

REFERENCES

1. **Durbin, D.R., Jermakian, J.S., Kallan, M.J., McCartt, A.T., Arbogast, K.B., Zonfrillo, M.R., and Myers, R.K., (2015),** "Rear Seat Safety: Variation in Protection by Occupant, Crash and Vehicle Characteristics", Accident Analysis and Prevention, Vol.80, pp 185-192.

2. **Mitchell, R.J., Bambach, M.R., and Toson, B., (2015),** "Injury Risk for Matched Front and Rear Seat Car Passengers by Injury Severity and Crash Type: An Exploratory Study", Vol.82, pp 171–179.

3. **Parenteau, C.S., Viano, D.C., and Lau, E.C., (2021),** "Rear-seat Occupant Demographics in Rear Impacts: Analysis of NASS-CDS", Vol.22, No.3, pp 218–223.

4. **Zellmer, H., Lubbe, N., and Sander, U., (2018),** "Assessing the Injury Risk of Car Occupants on Rearward Facing Seats – An Analysis of GIDAS Cases", Proc. of 8th ESAR Expert Symposium on Accident Research Conference, Hannover, Germany.

5. **Hasija, V., Kelkar, R., and Takhounts, E.G., (2019),** "Simulation Assessment of Injury Trends for 50th Percentile Males Using Potential Seating Configurations of Future

Automated Driving System (ADS) Equipped Vehicles", Proc. of 26th ESV Conference, Eindhoven, The Netherlands, paper 19-000345.

6. **Braganza, J., Tavakoli, M.S., and Brelin-Fornari, J., (2011),** "Investigation of Rear Occupant Head Restraint Interaction in High-Severity Rear Impact using BioRID and HIII", SAE Paper 2011-01-0273.

7. **Simms, C.K., Madden, B., FitzPatrick, D., and Tiernan, J., (2009),** "Rear-impact Neck Protection Devices for Adult Wheelchair Users", Journal of Rehabilitation Research & Development, Vol.46, No.4, pp 499-514.

8. **EuroNCAP, (2021),** European New Car Assessment Programme - Assessment Protocol - Adult Occupant Protection, Version 9.1.3.

9. **EuroNCAP, (2018),** European New Car Assessment Programme - Rear Whiplash Test Protocol, Version 1.1

10. **Himmetoglu, S., Acar, M., Bouazza-Marouf, K., and Taylor, A.J., (2011),** "Car-seat Design to Improve Rear-impact Protection", Proc. IMechE Part D Journal of Automobile Engineering, Vol.225, No.4, pp 441-459.

11. **Himmetoglu, S., (2017),** "An Adaptive Car-seat to Mitigate Whiplash in Rear Impacts", Proc. of the 21st International Scientific Conference Transport Means, Juodkrante, Lithuania, pp 32-38.

12. **Kaya, A.G., (2022),** "Adaptive Car Seat Control for Whiplash Mitigation", PhD Thesis, Hacettepe University, Mechanical Engineering Department, Ankara, Turkey.

13. **Unlusoy, Y.S., (2016),** ME465 Automotive Engineering, Lecture Notes, METU, Mechanical Engineering Department, Ankara, Turkey.

14. **Jazar, R.N., (2008),** Vehicle Dynamics: Theory and Application, Springer Science +Business Media, LLC.

15. **Himmetoglu, S., Acar, M., Bouazza-Marouf, K., and Taylor, A.J., (2009),** "A Multibody Human Model for Rear-Impact Simulation", Proc. IMechE Part D Journal of Automobile Engineering, Vol.223, No.5, pp 623-638.

16. **Viano, D.C., (2002),** Role of the Seat in Rear Crash Safety, Society of Automotive Engineers, Warrendale, PA, USA.

17. **Hartlieb, M., Bihler, E., Breitner, R., Bürkle, H., Hirth, A., Scheunert, D., and Wörner, U., (2007),** "Neck-PRO Mercedes Benz Active Head Restraint", Proc. of International Conference on Neck Injuries in Road Traffic and Prevention Strategies, Munich, Germany.

18. **Zhang, X. and Zhou, Q., (2016),** "An Energy-Absorbing Sliding Seat for Reducing Neck Injury Risks in Rear Impact - Analysis for Prototype Built", Traffic Injury Prevention, Vol.17, No.3, pp 313-319.

19. **EuroNCAP, (2021),** European New Car Assessment Programme - The Dynamic Assessment of Car Seats for Neck Injury Protection Testing Protocol, Version 4.1.1.

APPENDIX

NOTATION

NIC	neck injury criterion
Nkm	injury criterion having a combination of upper-neck shear force and moment
v_r	head rebound velocity
$Fsh^{(+)}$	largest upper-neck positive shear force
$Fsh^{(-)}$	largest upper-neck negative shear force
Ftn	maximum upper-neck tension force
MyU	largest upper-neck moment
FshL	largest lower-neck shear force
MyL	largest lower-neck moment
T1a	largest acceleration of the first-thoracic-vertebra (T1)
HrCt	head restraint contact time
Ds	maximum rearward displacement of the seatpan with respect to the car floor
HL	higher performance limit
LL	lower performance limit
CL	capping limit
SN(16)	EuroNCAP medium severity crash pulse with a delta-V of 16 km/h
TR(24)	EuroNCAP high severity crash pulse with a delta-V of 24 km/h
HS(35)	very high severity crash pulse with a delta-V of 35 km/h

EXPERIMENTAL STUDIES ON THERMAL DEGRADATION, IGNITION AND COMBUSTION OF LOW-VULNERABILITY GUN PROPELLANTS

Léo COURTY, *leo.courty@univ-orleans.fr* Univ. Orleans, PRISME EA 4229, Bourges, France

Samuel DELBARRE, *samuel.delbarre@univ-orleans.fr* Univ. Orleans, PRISME EA 4229, Bourges, France

ABSTRACT

The development of insensitive gun propellants can lead to ignition issues. Detailed understanding of the thermal behavior of such materials is therefore necessary and is investigated in this paper to present activation energies. Laser ignition appears to be a good alternative to overcome ignition issues. These propellants are ignited in a closed reactor to obtain ignition and combustion characteristics. Experiments are performed for different initial pressures, surrounding atmospheres and laser powers. Results show that ignition and combustion characteristics are better under argon than nitrogen. Indeed, overpressures can be 42 % higher under argon for some initial pressures. For a laser power of 5 W, ignition energies are of 92.63 mJ under argon and of 107.65 mJ under nitrogen. Laser power plays a role on ignition characteristics but has little effect on combustion characteristics.

Keywords: insensitive gun propellants, RDX, thermal analysis, laser ignition, activation energy, ignition energy

1. INTRODUCTION

Gun propellants are a family of energetic materials. In these materials, oxidizer and fuel are included. Their decompositions, that are redox reactions, give huge amounts of gases in a small period, that are generally used in the form of mechanical work to propel a projectile. The increasing of safety in the logistical phases (transport, storage), lead to the development of low-vulnerability -or insensitive- gun propellants. These new gun propellants belong to the Low-Vulnerability Ammunition (LOVA) family. The accidental or criminal ignition probabilities of these new materials are very low compared to classical gun propellants, along with collateral damage in case of ignition. On the contrary, these materials are more difficult to ignite using classical ignition devices. It is therefore very important to study in details their decomposition

and ignition behavior. The experimental study presented in this paper focuses on the laser ignition of these materials, thanks to the deposition of thermal energy on the gun propellant using a laser diode. This ignition technique is an alternative to the classical pyrotechnic ignition techniques, enabling the safe deposition of enough energy to compensate for the loss of sensitivity. Laser ignition also allows a precise location of the ignition point and few thermal losses, that increase again safety.

First studies on laser ignition of energetic materials were published by Brish et al. [1] in the 60's and this technique is still the topic of several research work [2-5]. Studied gun propellants are composed of RDX (1,3,5-trinitro-1,3,5-triazinane) and HTPB (hydroxyl terminated polybutadiene). RDX is an explosive (Research Department eXplosive, cyclotrimethylenetrinitramine) but mixed with HTPB it makes a low-vulnerability gun propellant. For decades, cyclic nitramine explosives like RDX have been used in propellants because of their important energetic properties [6]. To overcome the issues of impact and friction sensitivities, several polymeric binders have been tested and selected to be added in these explosives [7]. One of the most used polymeric binder is the hydroxyl terminated polybutadiene (HTPB), which acts like a matrix and keeps the energetic material and other additives together in a solid gun propellant [8].

Gun propellants are firstly characterized using a classical thermal analysis device, thermogravimetric analysis apparatus (TGA), and the kinetic parameters are obtained. The kinetic parameters of these materials are linked to their performances. Several activation energies are calculated with three models: Ozawa, ASTM E698 and isoconversional method. Data obtained with such thermal analysis processes provide essential results on the thermal behavior of these propellants. These data are helpful to study the combustion, the storage or the ageing of these propellants. Results are given under nitrogen and argon atmospheres to compare the impact of the surrounding gases [9].

The reactivity of these gun propellants is also studied by means of laser ignition in a closed volume reactor. Initial pressures, laser powers and atmospheres are varied. Results are presented for the same gases as thermal analysis: nitrogen and argon [10]. Results are presented in this paper for a low-vulnerability gun propellant composed of RDX and HTPB, but other gun propellants composed of nitrocellulose were also studied [11,12]. In this paper, the link between thermal degradation and combustion is studied thanks to thermal analysis studies. Moreover, the feasibility of laser ignition of low-vulnerability propellants is shown for different atmospheres and laser powers.

Both experimental setups and procedures are presented in the next section: thermogravimetric analysis apparatus and the closed volume reactor. Results and discussions are presented in

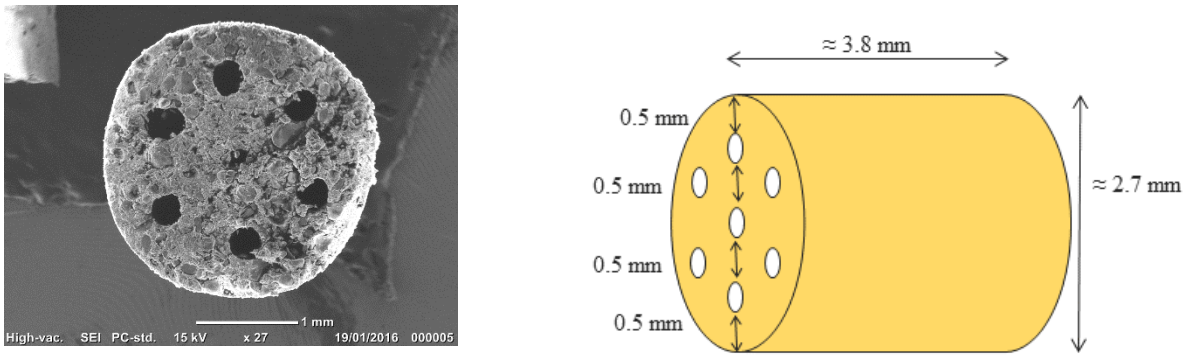
section 3, focusing on thermal analysis results, and overpressures, propagation rates, ignition delays and ignition energies for the laser ignition device.

2. MATERIALS AND METHODS

In this section, the studied materials are presented, along with the different experimental setups used for thermal analyses and laser ignition tests.

2.1 Studied Gun Propellants

All experiments are performed with cylindrical pellets made of RDX (~84 %) and a binder (~16 %, mostly composed of hydroxyl-terminated polybutadiene HTPB). These pellets are commercial propellants provided by ArianeGroup and used as received. Their average diameter, length and mass were respectively 2.7 mm, 3.8 mm and 26 mg. Each cylinder is perforated and contains 7 holes, as shown in Figure 1.



(a) (b)

Figure 1. SEM picture (a) and scheme (b) of the studied gun propellant.

2.2 Thermal analysis setup and procedure

To avoid any gases absorption, the samples are put into an oven heated at 60 °C for a least period of one week before the experiments. The TGA device used for the experiments is a Setsys 16/18 Setaram. Different heating rates are studied, chosen to avoid any thermal runaway behavior. Samples between 1 and 3 mg are exposed to 5 heating rates: 0.3 - 0.5 - 0.8 - 1.0 – 1.2 °C.min^{-1} under a dynamic nitrogen or argon flow rate of 30 mL.min^{-1}. Experiments were conducted between 20 and 400 °C.

Activation energies are obtained using AKTS software, which is a software based on the conventional thermo analytical measurements. The kinetics of solid-phase reactions are usually complex and might include several processes. To obtain a kinetic description of the overall reaction, kinetic parameters like activation energies (Ea) or the kinetic model f(α) are

needed. Here, the study focuses on three different models to reach the activation energies: Ozawa method, ASTM E698 method and Isoconversional method.

Reactions in solid phase are usually described using Equation 1 [13]:

$$\frac{d\alpha}{dt} = k(T).f(\alpha) \quad (1)$$

where α is the conversion rate, t is time (s), T the temperature (K), k(T) is the constant rate which depends on the temperature and f(α) is often called the model of the reaction. Arrhenius expression gives an expression of k(T) using Equation 2:

$$k(T) = A.\exp\left(\frac{-Ea}{RT}\right) \quad (2)$$

In Equation 2, A is the pre-exponential factor (s^{-1}), Ea the activation energy ($J.mol^{-1}$) and R the universal gas constant ($J.K^{-1}.mol^{-1}$). Equation 1 can be written in its differential form:

$$\frac{d\alpha}{f(\alpha)} = k(T).dt \quad (3)$$

Equation 1 can also be written in its integral form:

$$g(\alpha) = \int_0^{\alpha} [f(\alpha)]^{-1} d\alpha = k(T)\, t \quad (4)$$

where g(α) is the reaction model under its integral form.

- Ozawa approach

The first method used in the present study is the Ozawa approach. This author took the logarithm of Equation 4 and used the Doyle's approximation to obtain Equation 5 [14], where β is the heating rate and defined as β= dT/dt.

$$log\beta = \log\left(\frac{A\,Ea}{g(\alpha)R}\right) - 2.315 - 0.457\,\frac{Ea}{RT} \quad (5)$$

- ASTM E698 approach

The variable program rate method of Ozawa is the basis of the ASTM E698 kinetic approach, requiring three or more experiments at different heating rates. An Arrhenius behavior and first order reaction kinetics are assumed in this approach. With β= dT/dt being the heating rate, it is also possible to rearrange Equation 3:

$$\beta\frac{d\alpha}{dT} = A\exp\left(\frac{-Ea}{RT}\right) f(\alpha) \quad (6)$$

The data required for determining the activation energy is obtained from plotting the natural logarithm of the heating rate versus the peak temperature [15]:

$$\ln(\beta) = \frac{-Ea}{R}\,\frac{1}{T} + B \quad (7)$$

- Isoconversional approach

The last method of interest here is the isoconversional approach. The most famous one is the Friedman method, which is based on the following equation for a linear nonisothermal program [16]:

$$\ln\left[\beta_i\left(\frac{d\alpha}{dT}\right)_{\alpha,i}\right] = ln[f(\alpha)A\alpha] - \frac{E\alpha}{RT_{\alpha,i}} \quad (8)$$

The results of Equation 8 assumes that Tα,i changes linearly with the time by following the heating rate βi. At each given α, the value of Eα is calculated from the slope of ln(dα/dt)α,i against 1/Tα,I. The index i is identified as an individual heating rate. Since the differential isoconversional methods do not use any approximations, they are supposed to be more accurate than the integral method. The application of the differential method to integral data as TGA can also be inaccurate due to the background noise of the experiment. Thus, even if this method does not present approximations, the differential method should not be considered more accurate than the integral one.

2.3 Ignition and combustion setup

The experimental setup consists of a stainless steel cylindrical reactor coupled to a laser diode, an optical system and a pressure sensor. An overview of the setup is presented in Figure 2. The internal volume of the reactor is 55 cm^3 and it is possible to open it from the control room to ensure the users' safety. A Coherent laser diode (FAP-I-P1396) operating at 808 nm is used for ignition studies. An optical fiber transports the laser beam to the optical system that consists of two lenses forming a laser spot size of 1.25 mm on the sample. The two lenses have focal lengths of respectively 16 and 25 mm. A pressure sensor (Kistler, 603B) and a photodiode are connected to a digital oscilloscope (Agilent Technologies, DSO-X 3034A).

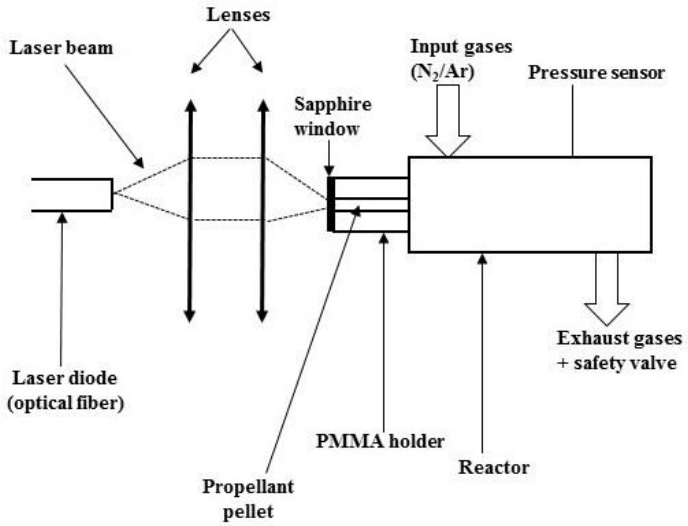


Figure 2. Scheme of the ignition and combustion setup.

A typical experiment is conducted as follows: a propellant sample is placed in a PMMA holder (internal diameter 3 mm, length 50 mm); this holder is placed in the reactor and closed with a sapphire window. Samples are placed so that there is no space between the sample and the window. The reactor closed with the sapphire window was tested to resist to a pressure of 250 bars during 15 minutes. The selected initial pressure of the gaseous atmosphere is set, the laser is fired and the pressure is recorded if ignition occurs. Nitrogen and argon are used as gaseous atmospheres, and the initial pressure is varied between 10 and 70 bars for both gases. Laser pulse durations can be varied with the Coherent laser diode. Laser power can be varied by changing the laser current; laser temperature is fixed at 20 °C. Five powers were studied: 1.43, 2.86, 5.00, 6.42 and 9.95 W corresponding respectively to current intensities of 10, 12, 15, 17 and 22 A. Overpressures, ignition delays and propagation rates are deduced from the pressure signal for each shot. An example of the obtained pressure signal and images of flame propagation is illustrated in Figure 3: the pressure signal is in blue, laser pulse in red and the ignition delay is the time between the beginning of the laser pulse and beginning of the pressure increase. Overpressure ΔP is defined as maximal pressure minus initial pressure and propagation rate as $1/m \cdot (d\Delta P/dt)max$.

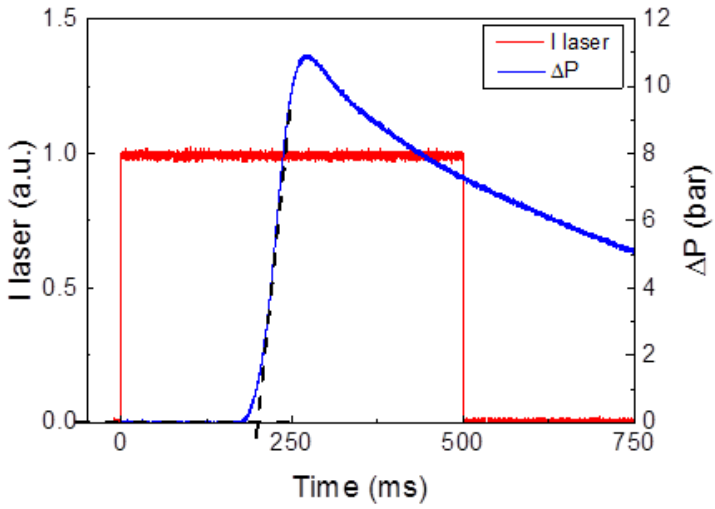


Figure 3. Example of the obtained pressure and laser pulse signals (initial mass 27.2 mg and initial pressure 50 bar).

Ignition probabilities as function of deposited energies are studied in this paper for different power lasers. For a given power, energies giving 50 % of ignition probabilities (E_{50}) are investigated. To do so, ignition is firstly obtained with high energies before decreasing them. The main drawback of this method is that many shoots are necessary to obtain the searched energy. It is therefore interesting to apply statistical methods that link the ignition threshold to

the ignition probability. Different methods are available and the most used are Bruceton and Langlie methods for pyrotechnic mixtures ignition tests. The Langlie method [17] has been adopted in this work and more precisely the “revised” Langlie method proposed by the GTPS [18]. This method is based on the dichotomy principle and relies on a statistical repartition of ignition threshold following a standard normal distribution. Thanks to this method, E_{50} parameter can be obtained with 20 to 30 shoots.

3. RESULTS AND DISCUSSIONS

Results obtained with the different experimental setups presented in the previous section are presented in this section and discussed.

3.1 Thermal Analysis Results

Figure 4 shows a plot of the mass loss (%) over the temperature (°C) for the studied gun propellant under argon atmosphere. The decomposition takes place at lower temperature as the heating rate decreases.

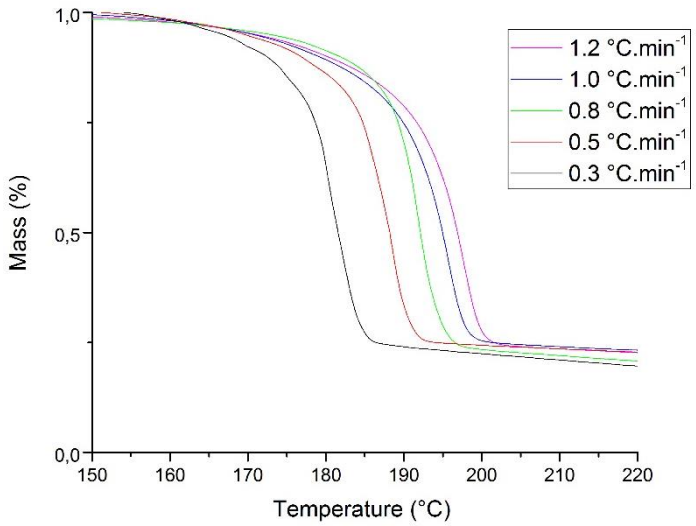


Figure 4. TGA results for the RDX based gun propellant under argon.

Table 1 presents the main events obtained under nitrogen and argon: the maximum peak temperature (Tp), the Onset temperature (Ton) and the Offset temperature (Tof).

Table 1: TGA results for the RDX based propellant under argon and nitrogen.

Material	β (°C.min^{-1})	Peaks (°C)		
		T_p	T_{on}	T_{of}
Argon atmosphere	1.2	195.88	195.19	196.56
	1.0	191.65	191.01	192.17
	0.8	189.93	189.06	190.20

	0.5	186.06	185.6	186.40
	0.3	181.46	177.55	185.29
Nitrogen atmosphere	1.2	195.33	191.87	198.38
	1.0	193.83	189.06	197.54
	0.8	190.99	190.45	191.42
	0.5	187.63	185.71	189.92
	0.3	183.25	177.96	186.94

Table 2 presents the activation energies calculated with the TGA measurements under argon and nitrogen. The differences between Ea under nitrogen and argon are minor for ASTM E698 and isoconversional method, while differences with the Ozawa approach are a bit higher.

Table 2: Calculated E_a for TGA on the RDX based gun propellant depending on the surrounding atmosphere.

Method	Ozawa	ASTM E698	Isoconversional (α = 0.5)
E_a under argon ($kJ.mol^{-1}$)	152.3	150.6 $R^2 = 0.976$	176.9
E_a under nitrogen ($kJ.mol^{-1}$)	170.2	161.6 $R^2 = 0.994$	188.3
ΔE ($kJ.mol^{-1}$)	- 17.9	- 11.0	- 11.4

Note: ΔE is the value of the difference between E_a in argon and nitrogen,
$\Delta E = E_a(argon) - E_a(nitrogen)$

Concerning the experiments under nitrogen, Abd-Elghany et al. [19] have recently published similar results using Differential Scanning Calorimeter (DSC). They exposed a RDX/HTPB solid to several heating rates (2, 4, 8, 16 °C.min-1) and calculated the activation energies. They calculated an activation energy of 157.8 kJ.mol-1. It can also be noticed that the activation energy values are higher in nitrogen than in argon. This can be explained by the thermal conductivity of the gases. Nitrogen is a diatomic molecule and argon is just made of a single atom. However, the molar heat capacity (for a constant volume, calculated from the NASA polynomials from the LNLL thermodynamic database) of argon is lower than the one of nitrogen (e.g., at 773 °C: Cv(Ar) = 12.5 J.K-1.mol-1 and Cv(N2) = 20.7 J.K-1.mol-1).

3.2 Overpressures, Propagation Rates And Ignition Delays

The results on the overpressures, ignition delays and propagation rates are presented in this section for two laser powers: 1.43 and 2.86 W. Overpressures divided by the initial mass of propellant samples as function of the initial pressures for these two laser powers are presented respectively in Figure 5 (a) and (b). Firstly, it can be noticed that overpressures are higher in argon than in nitrogen for all initial pressures and laser powers. As already noticed in thermal analysis section, it can be concluded that argon can be seen as a combustion enhancer for this kind of propellant probably due to its thermal effect. Secondly, authors can note that overpressures are increasing with initial pressures, except for some initial pressures. These "critical" initial pressures depend on the laser power and initial atmosphere. At 1.43 W, the decrease of overpressure occurs at 50 bar under argon and 35 bar under nitrogen. At 2.86 W, it occurs at 45 bar under nitrogen and at 60 bar under argon. For some initial pressures, a decrease in the overpressure can be observed, which probably indicates a weak propagation rate due to an imperfect ignition. This explanation is confirmed by the presence of unburnt residues for these cases. Experiments for these "critical" initial pressures were performed between 5 and 7 times and were reproducible (with a gap between each experiment higher than the one for the other cases due to the presence of unburnt residues).

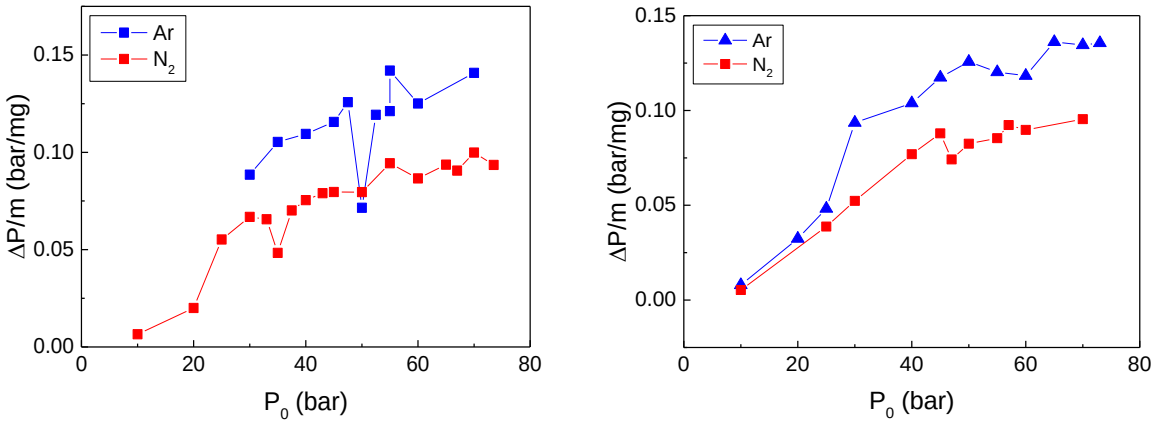
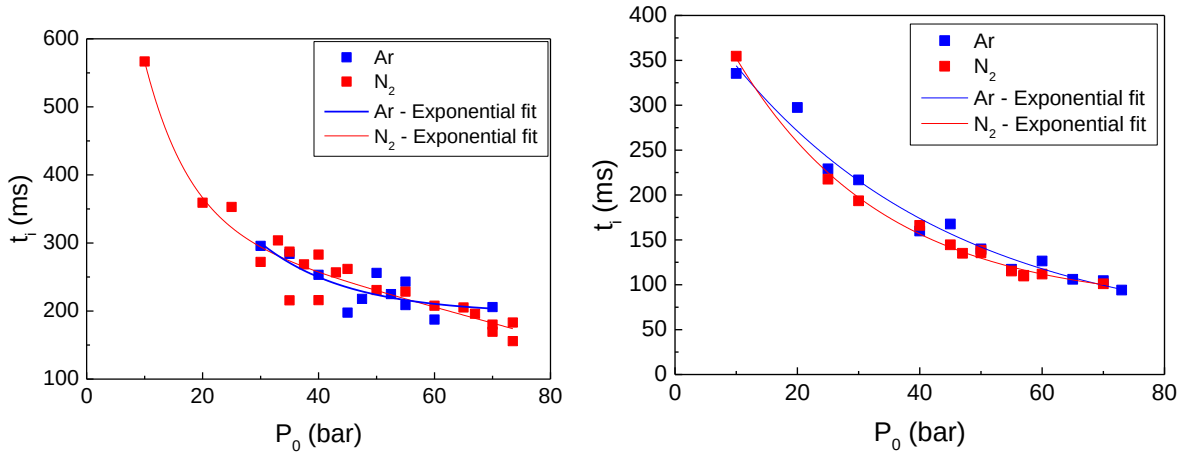


Figure 5. Overpressures as function of initial pressures for a laser power of 1.43 W (a) and 2.86 W (b).

Ignition delays t_i versus the initial pressure for laser powers of 1.43 and 2.86 W are presented respectively in Figures 6 (a) and (b) for the two studied atmospheres, along with exponential fits. At 1.43 W, best fits are obtained with $t_i = t_0 + a_1 \cdot exp^{-P_0/p_1} + a_2 \cdot exp^{-P_0/p_2}$. The following coefficients are obtained: $a_1 = 754.3$, $p_1 = 15.13$, $t_0 = 196.2$, $a_2 = 0$, $p_2 = 0$ under argon atmosphere and $a_1 = 884.9$, $p_1 = 7.782$, $t_0 = -6.136 \cdot 10^6$, $a_2 = 6.163 \cdot 10^6$, $p_2 = 2.642 \cdot 10^6$ under nitrogen atmosphere. At 2.86 W, a one-order fit correctly predicts ignition delays and the

following coefficients are obtained: a_1 = 398.6, p_1 = 36.37, t_0 = 41.23 under argon atmosphere and a_1 = 416.7, p_1 = 24.06, t_0 = 77.48 under nitrogen atmosphere.

For a given laser power, the effect of initial atmosphere on ignition delays is very low. At 2.86 W, it can clearly seen that t_i are decreasing when the initial pressures are increasing. This can be easily explained since an increase in pressure increases the reaction rates and therefore decreases the time to ignition. The results are similar for a lower laser power (1.43 W). As expected, ignition delays decrease with increasing laser power. For instance, under nitrogen, ignition delays are 1.6 times lower at 2.86 W than at 1.43 W at 10 bar and 1.7 times lower at 70 bar. At 1.43 and 2.86 W, ignition delays are respectively 3.3 and 3.5 times higher at 10 bar than at 70 bar.



(a) *(b)*

Figure 6. Ignition delays as function of the initial pressures for a laser power of 1.43 W (a) and 2.86 W (b): experimental data (dots) and exponential fit (straight lines).

Propagation rates give an estimate of the combustion velocity. They are presented in Figures 7 (a) and (b) as function of the initial pressure for two atmospheres and for laser powers respectively of 1.43 and 2.86 W. It can be noticed that combustion rates are higher in argon than in nitrogen for all initial pressures and laser powers. The propagation rate is increasing with initial pressure, except for some cases. Contrary to the ignition delays, propagation rates are almost independent of the laser power. For instance, in argon at 40 bar, the difference of propagation rates between 1.43 and 2.86 W does not exceed 4 %.

3.3 Ignition Energies

Energies giving an ignition probability of 50 %, E_{50}, are studied for different initial pressures and laser powers under nitrogen and argon atmospheres. These energies are presented as function of laser powers for an initial pressure of 50 bars in Figure 8.

E_{50} are decreasing when laser power is increasing for all studied conditions. Nevertheless, it can be noticed that above 6.42 W, E_{50} remains almost constant. Interestingly, standard deviations (represented as error bars in Figure 8) are also decreasing when laser power is increasing. Here again, authors can notice that argon is a combustion enhancer for this kind of propellant, since E_{50} values are higher in nitrogen than in argon. For low (1.43 W) and high (9.95 W) laser powers, it can be noted that the difference between argon and nitrogen is lower than the one for intermediate power values.

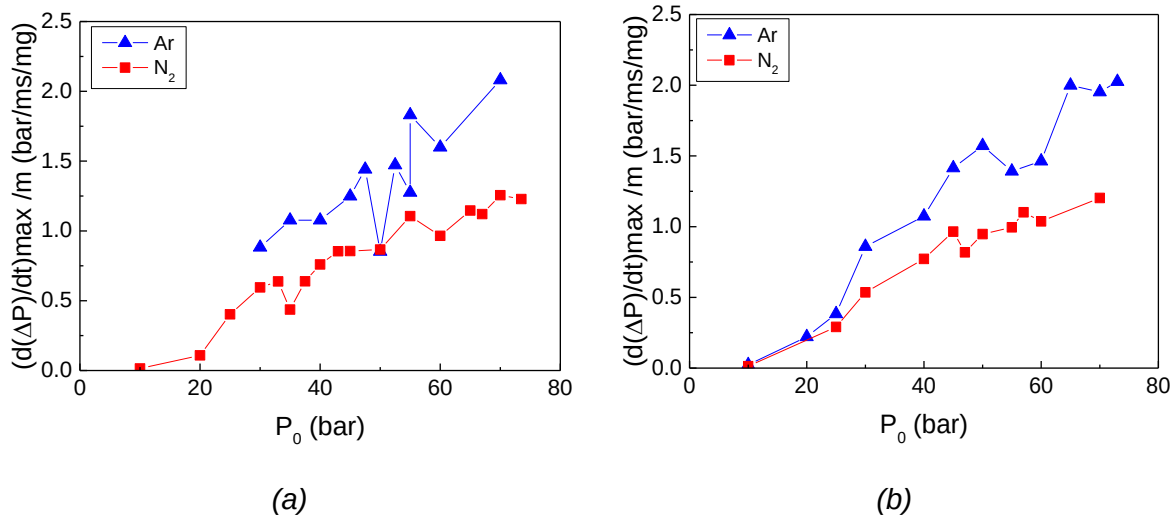


Figure 7. Propagation rates as function of the initial pressure for a laser power of 1.43 W (a) and 2.86 W (b).

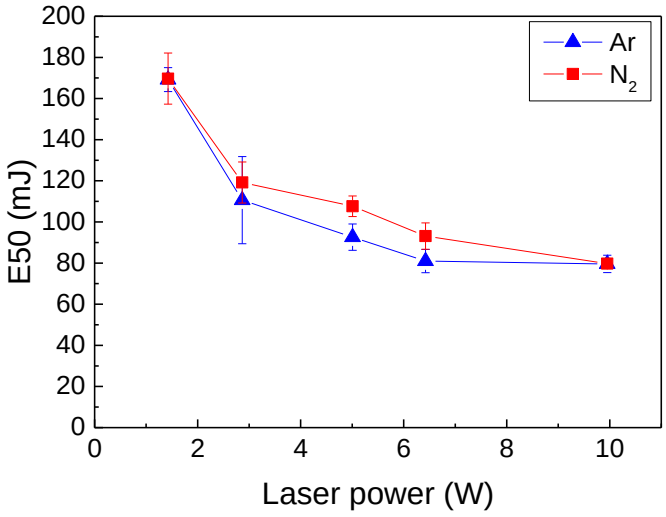


Figure 8. E_{50} as a function of laser power under Ar and N2 atmospheres for an initial pressure of 50 bar.

4. CONCLUSION

Thermal degradation, laser ignition and combustion characteristics of a low-vulnerability gun propellant mainly composed of RDX are experimentally investigated. Thermogravimetric experiments are performed under nitrogen and argon atmospheres for different heating rates and activation energies are extracted. Combustion properties -such as overpressures and propagation rates- along with ignition characteristics -such as ignition delays and ignition energies- are also investigated in a closed volume reactor for different initial pressures of nitrogen and argon. It is shown the role of the surrounding atmosphere is important for this kind of materials. Other gun propellants with different compositions (nitrocellulose) were also tested using the same methodology. In an ongoing work, ignition and combustion processes of low-vulnerability gun propellants using detailed kinetics chemistry for the gas phase are being modelled. Present results will be the basis for the experimental validation of overpressures or propagation rates obtained with the model.

REFERENCES

[1] **Brish, A.A., Galeev, I.A., Zaitsev B.N. et al. (1696),** “Mechanism of initiation of condensed explosives by laser radiation”, Combustion, Explosion and Shock Waves, Vol.5, pp 326-328.

[2] **Herreros, D.N. and Fang, X. (2017),** “Laser ignition of elastomer-modified cast double-base (EMCDB) propellant using a diode laser”, Optics & Laser Technology, Vol.89, pp 21-26.

[3] **Dasa, J., Shem-Tov, D., Zhang, S., Gao, C.Z., Zhang, L., Yao, C., Flaxer, E., Stierstorfer, J., Wurzenberger, M., Rahinov, I. and Michael Gozin, M. (2022),** “Power of sulfur – Chemistry, properties, laser ignition and theoretical studies of energetic perchlorate-free 1,3,4-thiadiazole nitramines”, Chemical Engineering Journal, Vol.443, 136246.

[4] **Uhlenhake, K.E., Gomez, M., Collard, D.N., Örnek, M. and Son, S.F. (2022),** “Laser Ignition of Solid Propellants Using Energetic nAl-PVDF Optical Sensitizers”, AIAA SCITECH 2022 Forum, San Diego, USA.

[5] **Tang, P., Zhu, W., Qiao, Z., Yang, G., Li, X., Tang, Y. and Zhang, H. (2021),** “Laser-induced energetic material ignition with various fluorinated graphenes: Theoretical and experimental studies”, Applied Surface Science, Vol.570, 151187.

[6] **Ulas, A., Lu, Y.C. and Kuo, K.K. (2003)**, “Ignition and combustion characteristics of RDX-based pseudopropellants”, Combustion Science and Technology, Vol.175, pp 698-720.

[7] **Celina, M., Minier, L. and Assink R. (2002),** “Development and Application of Tools to Characterize the Oxidative Degradation of AP/HTPB/Al Propellants in a Propellant Reliability Study”, Thermochimica Acta, Vol.384, pp 343-349.

[8] **Caro, R. (2006),** "Hydroxyl-terminated polyether binders for composite rocket propellants", PhD Thesis, Cranfield University.

[9] **Ehrhardt, J., Courty, L., Gillard, P. (2019),** "Thermal degradation and kinetic parameter of two insensitive propellants: an experimental study", International Journal of Energetic Materials and Chemical Propulsion, Vol.18, pp 51-65.

[10] **Gillard, P., Courty, L., De Persis, S., Lagrange, J.F., Boulnois, C., Gökalp, I. (2018),** "Combustion properties of a low-vulnerability propellant: an experimental and theoretical study using laser ignition", Journal of Energetic Materials, Vol.36, pp 362-374.

[11] **Courty, L., Lagrange, J.F., Gillard, P., Boulnois, C. (2018),** "Laser Ignition of a Low Vulnerability Propellant Based on Nitrocellulose: Effects of Ar and N2 Surrounding Atmospheres", Propellants, Explosives, Pyrotechnics, Vol.43, pp 986-991.

[12] **Courty, L., Gillard, P., Ehrhardt, J., Baschung, B. (2021),** "Experimental determination of ignition and combustion characteristics of insensitive gun propellants based on RDX and nitrocellulose", Combustion and Flame, Vol.229, 111402.

[13] **Vyazovkin, S. (2000),** "Computational aspects of kinetic analysis.: Part C. The ICTAC Kinetics Project — the light at the end of the tunnel?", Thermochimica Acta, Vol. 355, pp 155-163.

[14] **Vyazovkin, S. and Dollimore, D. (1996),** "Linear and Nonlinear Procedures in Isoconversional Computations of the Activation Energy of Nonisothermal Reactions in Solids", Journal of Chemical Information and Computer Sciences, Vol.36, pp 42-45.

[15] **Peyser, P. and Bascom W.D. (1974),** "Kinetics of an Anhydride-Epoxy Polymerization as Determined by Differential Scanning Calorimetry", Analytical Calorimetry, Vol.3, pp 537-554.

[16] **Vyazovkin, S., Burnham, A.K., Criado J.M., Pérez-Maqueda L.A., Popescu C. and Sbirrazzuoli N. (2011),** "ICTAC Kinetics Committee recommendations for performing kinetic computations on thermal analysis data", Thermochimica Acta, 520, pp. 1-19.

[17] **Langlie, H.J. (1962),** "A reliability test method for one shot items", Ford Motor Company Aeronutronic – Publication n° U1792.

[18] **GTPS, (1993),** "Méthode statistique, approche dichotomique", Groupe de Travail de la Pyrotechnie Spatiale, Document n° 11E.

[19] **Abd-Elghany, M., Elbeih, A. and Hassanein S. (2016),** "Thermal Behavior and Decomposition Kinetics of RDX and RDX/HTPB Composition Using Various Techniques and Methods", Central European Journal of Energetic Materials, Vol.13, pp 714-735.

RE-DEFINING TEMPERATURE SET-POINT OF AN HVAC SYSTEM BASED ON THERMAL COMFORT ZONE OF STUDENTS IN A UNIVERSITY STUDY HALL

Cihan TURHAN, *cihan.turhan@atilim.edu.tr* Atilim University, 06830, Ankara, Turkey

Mehmet Furkan ÖZBEY, *furkan.ozbey@atilim.edu.tr* Atilim University, 06830, Ankara, Turkey

ABSTRACT

The main purpose of the Heating, Ventilating and Air-Conditioning (HVAC) systems is to satisfy thermal comfort to the occupants. However, thermal comfort and thermal sensation could be different due to the cultural difference, climatic adaptations, body mass index, gender and age. The gap between thermal comfort and sensation causes higher energy consumption for the HVAC systems. To this aim, this paper aims to investigate thermal comfort temperature of the occupants in temperate climate zone. The experiments are conducted on 1062 students in a university study hall in Ankara/Turkey during heating season. The Actual Thermal Sensations (ATS) of the students are collected on a developed mobile application while the objective measurements of indoor air temperature are conducted via an industrial globe thermometer. The results showed that the thermal comfort temperature is 21.03°C and 20.68°C for female and male students, respectively. According to the simulation results, 243 kWh energy could be saved if new comfort temperature of the students would be used instead of a constant 22°C set-temperature of the HVAC system.

Keywords: Thermal Comfort, Actual Thermal Sensation, Comfort Temperature, HVAC Systems

1. INTRODUCTION

The huge gap between thermal comfort and sensation is discussed from past to present, i.e. in [1-3]. This gap causes increased number of energy consumption of the Heating, Ventilating and Air-Conditioning (HVAC) systems [4,5]. The researchers indicate that the reasons of this gap might be cultural differences [6], climatic adaptations [7], psychology [8], age and gender [9]. Thermal comfort is traditionally measured via thermal comfort sensors using Predicted Mean Vote (PMV)/ Predicted Percentage of Dissatisfied (PPD) index [10]. The PMV index refers to a thermal comfort scale which runs between -3 and +3. 0 value of the PMV means

that the occupant has a fully comfortable environment. On the other hand, international standards such as ISO 7730 [11] and ASHRAE 55 [12] accept the range of [-0.5: +0.5] of the PMV value as comfortable in a specific zone. However, performance of the PMV/PPD method is better in air-conditioned buildings [13]. For non-air conditioned and mixed mode buildings, adaptive models are developed and used in order to increase the accuracy of the thermal comfort models [14].

Thermal sensation is based on actual votes of the occupants via 7-point thermal sensation scale [12]. Surveys are collected from the occupants and then the results are evaluated in order to adjust temperature set-points of the Heating, Ventilating and Air-Conditioning (HVAC) systems. However, determining a constant temperature set-point of an HVAC system is always not a good solution for a good thermal sensation. The researchers stated that perceptions of the occupants in different climate zones could be different from the measured PMV value [15]. For instance, Yao et al. [16] represented that occupants in China prefer lower values than the measured PMV value. On the other hand, Turhan and Akkurt [17] found that the temperature of the 20.9°C could be fully comfortable temperature for the Turkish occupants in a university in Izmir. Therefore, adjusting temperature set-point of the HVAC systems according to perceptions of the occupants could save great amount of energy.

This study purposes to determine thermal sensation profiles of the occupants in a university in Ankara/Turkey and adjust the set-temperature of the HVAC system according to neutral comfort temperatures.

2. METHODS

A university study hall in Ankara/Turkey was selected as a case building. The city of Ankara is classified as warm-summer Mediterranean climate (Csb) according to Köppen-Geiger Climate Classification [18]. The average temperatures of the heating and cooling seasons are 19.2 °C and 4.8 °C, respectively [19].

A 10 m^2 area in the middle of the case building was selected as an experimental zone. The 365m^2 case building includes a large continuous window facing to the north direction. The case building is a mixed-mode building and mechanical ventilation is not existed in the building. The heating of the building is operated with 10 radiators with a 22°C set point temperature. The specifications of the building elements are depicted in Table 1.

Table 1. Specifications of Building Elements

Building Elements	Thickness (m)	Materials Used	U Value (W/m^{2}K)
External and Internal Walls	0.25	Pumice Concrete Cement Plastering Glass Wool Paint	2.86
Window (PVC Frame)	0.07 (13 mm Air – Gap)	Double Glazed Window	4

The indoor environmental parameters: air temperature (T_a), relative humidity (RH_{in}), air velocity (v_a), and mean radiant temperature (T_r), were measured with 1 minute interval via Delta Ohm HD 32.3 TCA [20]. It is crucial to emphasize that the T_r is defined as “the temperature of a uniform, black enclosure that exchanges the same amount of heat by radiation with the occupant as the actual enclosure” [1]. In addition, the data were collected with a height of 1.1m, as ASHRAE-55 [12] standard recommended, between 09:30 and 16:30 for each working day. It is important to mention that the Delta Ohm HD 32.3 TCA [20] is a calibrated device and compatible with the international standards [11,21,22]. Moreover, the outdoor environmental parameters: outdoor temperature (T_{out}) and outdoor relative humidity (RH_{out}) were collected via environmental data logger which contains DHT-22 [23] sensor inside. Collected data from students and devices were used to measure indoor and outdoor environmental data and were stored in a webserver. The thermal comfort sensor specifications can be seen in Table 1 and their locations are illustrated in Figure 1.

Table 2. Specifications of Thermal Comfort Sensor and Environmental Data Logger [20, 23]

DELTA Thermal Comfort Sensor OHM HD32.3TCA [20]	Globe Temperature	Type of Probe	TP3276.2 probe
		Measuring Range	-10 to 100 °C
		Accuracy	±0.1 °C
		Resolution	0.1 °C
	v_a	Type of Probe	AP3203.2 probe
		Measuring Range	0.02 to 5 m/s
		Accuracy	± (0.05 + 5% of the measurement) m/s
		Resolution	0.01 m/s
	T_a, T_r and RH	Type of Probe	HP3217.2R probe
		Measuring Range	Temperature: -40 to 100°C RH: 0-100%
		Accuracy	Temperature: ±0.1 °C RH: ±1,5%
		Resolution	Temperature:0.1 °C RH:0.1%
Environmental Data Logger DHT-22 [23]	T_a and RH	Range	-40 °C to 80°C
		Accuracy	<±0.5 °C

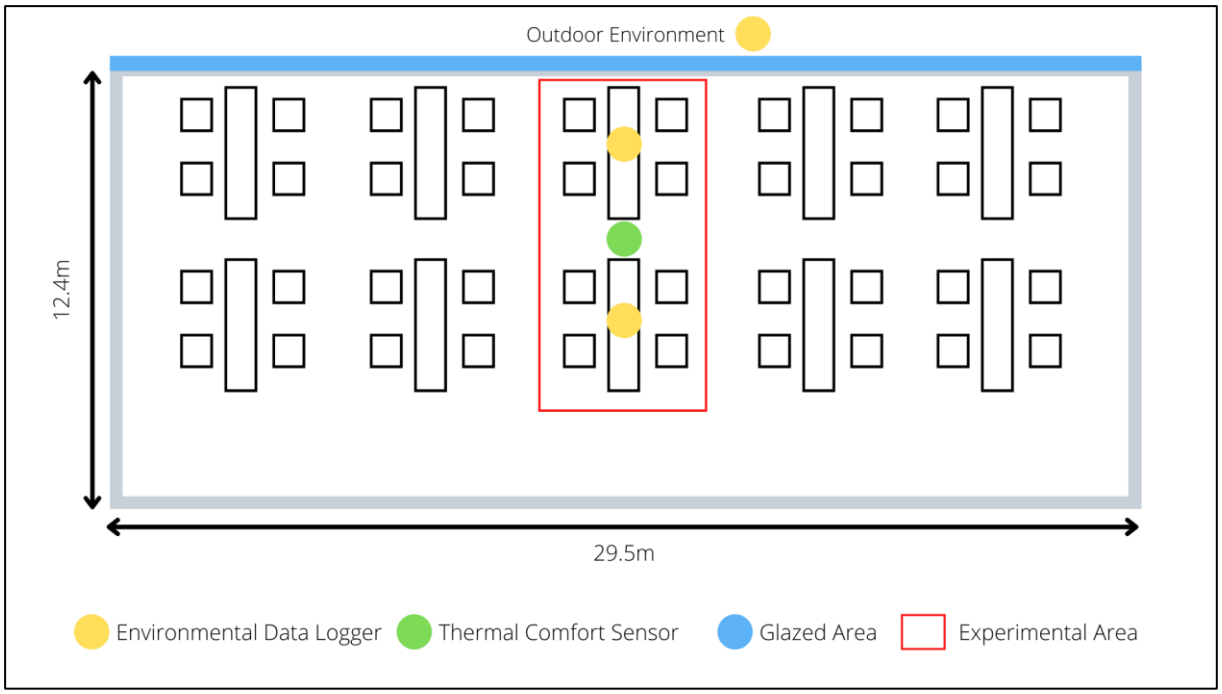


Figure 1. Locations of the Used Sensors

519 healthy male and 543 healthy female students were participated the experiments between on 15th October 2021 to 15th April 2022. Before the study, permissions were taken from the students and Ethics Committee of the University to conduct the experiments. Moreover, the occupants were informed about the aim and experimental procedures, and they were requested to avoid caffeine, alcohol, smoking, and intense physical activity at least 12 hours before experiments. The measurement campaign and surveys were conducted after 30 minutes-resting time since the high metabolic rate level of students after arriving at the study hall by cycling, running, and walking could affect their thermal sensation. The design of experiments is illustrated in Figure 2.

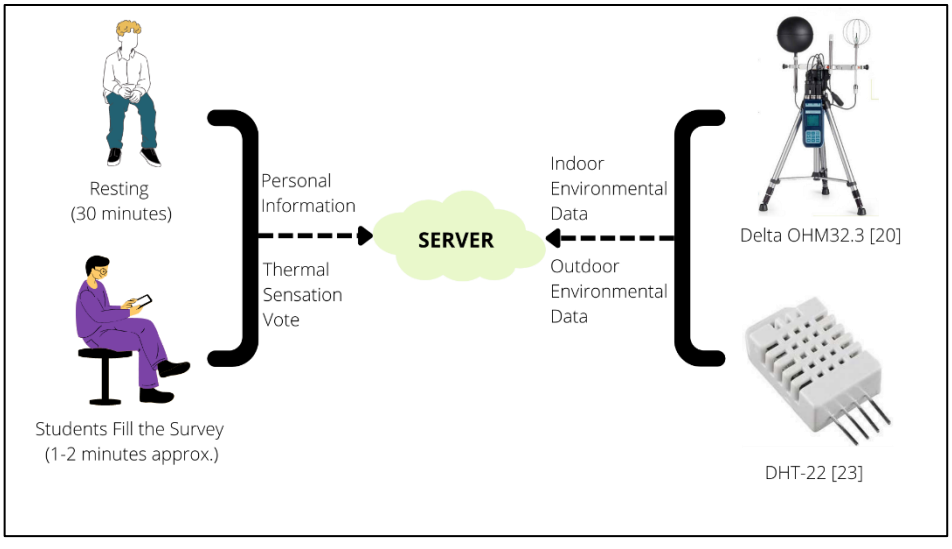


Figure 2. Design of Experiments

A mobile application was developed for the students to fill the surveys easily and rapidly. Personal information of the students – age, gender, weight and height –, the information about their garments and thermal sensation votes of the students were collected via developed mobile application. A 13 – point thermal sensation scale [24] was used instead of commonly used 7 – point thermal sensation scale to obtain more accurate results.

The metabolic rate of the participated students was taken as 1.1 met (65 W/m^2) since the students were in a seated-typing position. Moreover, the clothing value of the occupants were calculated according to their garments which were asked via a survey in a mobile application.

After obtaining the environmental and personal data the comfort temperature was determined with independent (T_a) and dependent (AMV) variables via Linear Regression Analysis [25,26]. The linear regression model is expressed in Equation 1.

$$y = \beta_0 + \beta_1 x + e \qquad (1)$$

Here, β_0 defines the intercept, β_1 signifies the slope, e signifies the error, which is the difference between the observed value of the y and the straight line (β_0+ $\beta_1 x$) and x and y are independent and dependent variables respectively [25,26].

An X-Y chart was plotted to perform a regression analysis with the T_a and AMV data using the MATLAB [27] to determine the relationship between a dependent and independent variable. The regression model fit line was achieved through the middle of all points in the X-Y chart via MATLAB [27]. In addition, Determination of Multiple Coefficient (R^2) was utilized to understand the relation of the AMV and T_a. The R^2 is calculated by Equation 2 [17].

$$R^2 = 1 - \frac{\sum_i |t_i - o_i|^2}{\sum_i (o_i)^2} \qquad (2)$$

Here, t_i represents the target, o_i signifies the output and p defines the number of input output pairs of the i^{th} data [17].

The energy simulations are conducted via Design Builder [28] which is a dynamic simulation software. It is worth to note that the model of the case building is calibrated based on ASHRAE Guideline 14 [29].

3. RESULTS AND DISCUSSIONS

A total number of 1062 each data (T_a, T_o, PMV, ATS, RH_{in} and RH_{out}) was collected during the measurement campaign. Table 3 depicts minimum, maximum, and mean values of the parameters.

Table 3. Data Statistics

	T_a (°C)	T_r (°C)	RH_{in} (%)	T_{out} (°C)	RH_{out} (%)	PMV	ATS
Maximum	26.40	29.10	94.10	39.00	98.00	0.92	3.00
Minimum	16.90	17.90	9.70	-10.50	8.70	-1.41	-2.50
Average	21.77	21.88	32.42	10.67	58.85	-0.45	0.19
Standard Deviation	1.41	1.38	8.66	8.47	20.89	0.26	0.81

The average T_a values is found as 21.77°C even though set-temperature of the HVAC system is 22°C. The reason of this small difference is the high volume of the case building. Mean PMV value is calculated as -0.45 on the cooler side, however, the ATS is found as 0.19 on warmer side. The reason is the cultural and climatic adaptation of the students in temperate climate zone. This result indicates that the ranges of thermal comfort acceptance of occupants (TSV) are higher than the calculated PMV values. It is crucial to mention that high relative humidity values cause lower evaporation and increased skin temperature, which affects the convective heat loss and radiation heat loss from the human body [30]. In this study, the difference of the averages between the RH_{in} and RH_{out} (26.43%) indicates that occupants faced with more dry air than outdoor environment. Hence the difference of the averages between the RH_{in} and RH_{out} caused higher evaporation and decreased skin temperature of the occupants in indoor environment. Figure 3 represents the change of T_a, T_o and T_r with respect to data sample.

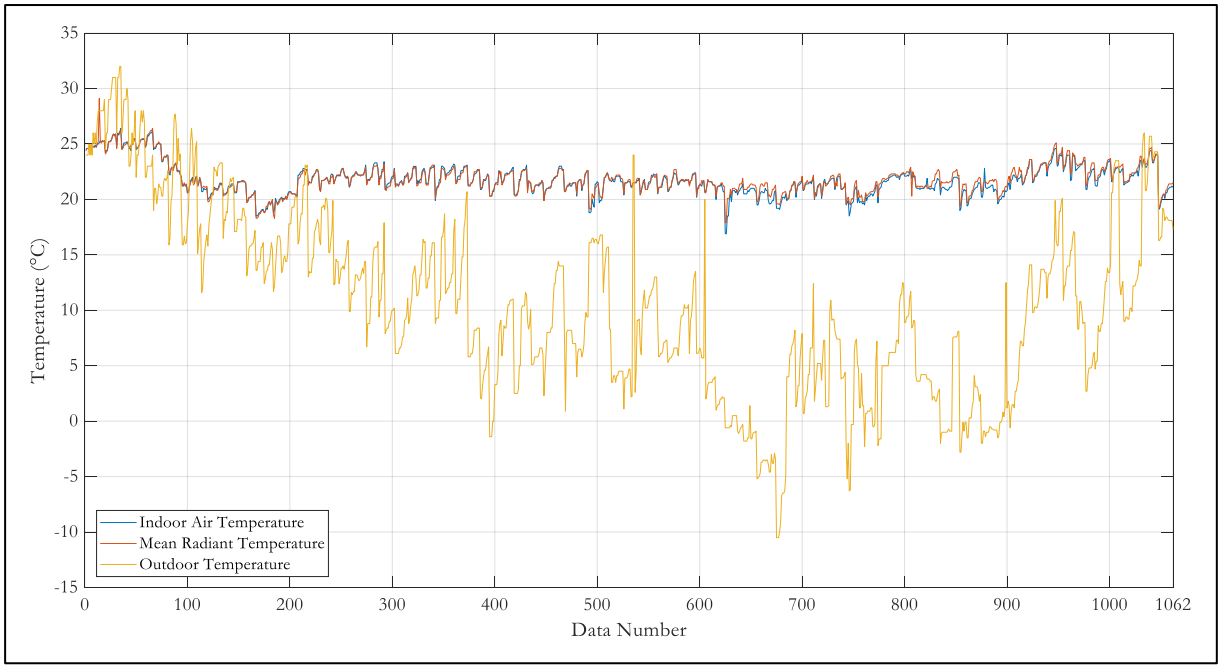


Figure 3. Collected T_a, T_r and T_{out} values.

As it is expected, T_a and T_r are affected from T_o values. However, due to the heating system, the T_a values never decrease under 16.9°C even at T_o values of -10.5°C. Table 4 shows neutral temperatures at ATS=0 line for each gender.

Table 4. Neutral Temperatures of the Case Building

	ATS=0	Thermal Comfort Range [AMV= -0.5;0.5]
General	20.92	[18.48; 23.36]
Female	21.03	[19.04;23,01]
Male	20.68	[18.06; 23.29]

Based on the calculations, the neutral temperature of the case building is calculated as to be 20.92°C while thermal comfort range is found as between 18.48°C and 23.36°C. These calculated values conclude that students in temperate climate perceive higher thermal sensation than calculated PMV values. It is worth to note that this gap results with higher energy consumption in case building as previous research supports [4,5,31,32]. Equation 4 gives linear regression between the ATS and PMV.

$$ABS = 1.09\,PMV + 0.2374 \quad (4)$$

The slope is found as 1.09 which indicates students in temperate climate zone perceive an environment at a higher thermal sensation. For instance, for a PMV value of zero (PMV=0), the students feel 0.23 of ATS. The R^2 of the correlation is 94% for all data.

Another interesting result in this study is that males feel warmer than female ones in case building. So that, the set-temperature of the HVAC system could be decreased when only male students exist in the case building.

In order to understand the energy saving potential of new comfort temperature, the case building is simulated via Design Builder [28]. However, the set-temperature of the HVAC system is given as 20.92°C in place of a constant 22°C to the software. The results indicated that a total of 243 kWh energy could be saved if new comfort temperature of the students would be used instead of a constant 22°C set-temperature of the HVAC system. Some discussions can be stated for the results of this study. Climate change in worldwide will change the perspective of the energy consumption trends. Therefore, decreasing set-temperature of the heating systems according to the thermal comfort range of the occupants will be vital. Study halls are special places where students should be in neutral thermal comfort during studying a major. Therefore, new comfort temperatures should be defined in different climatic zones. Thus, energy consumption of the buildings could be decreased.

4. CONCLUSION

This study investigates neutral thermal comfort temperatures of the students in a study hall in temperate climate zone. The case hall is monitored between 15th October 2021 and 15th April 2022. Thermo-hygrometric parameters of the indoor environment and the PMV and TSV indices of students are assessed with the help of the standards. The result of the study evidently shows that students in temperate climate zone prefer cooler environments than the comfortable PMV values in heating season. Therefore, decreasing set-temperature of the HVAC systems could decrease energy consumption, specifically, high thermal mass buildings such as university and school buildings. Even though this study is limited to one study hall, the study still gives an idea for an interrelation between optimal thermal comfort and energy consumption in temperate climate zone. Future studies will cover a detailed investigation on neutral thermal comfort temperature on different formation of buildings such as residential and industrial. Thereby, the results of these studies would help to develop personalized thermal comfort controllers for the HVAC systems instead of constant set-temperature PID systems.

ACKNOWLEDGEMENT

The collected data in this study is a part of a The Scientific and Technological Research Council of Turkey (TÜBİTAK) project with a number of 120M890. The authors would like to thank TÜBİTAK for funding. Additionally, the authors would like to thank all participants for the contribution to this study.

It is worth to note that this study is conducted under the Approval of Ethics Committee of Atılım University as result of meeting on 14.11.2019.

REFERENCES

1. **Broday, E. E., Moreto, J. A., de Paula Xavier, A. A., and de Oliveira, R. (2019)**, “The approximation between thermal sensation votes (TSV) and predicted mean vote (PMV): A comparative analysis”, International Journal of Industrial Ergonomics, Vol. 69, pp 1-8.

2. **Del Ferraro, S., Iavicoli, S., Russo, S., and Molinaro, V. (2015),** “A field study on thermal comfort in an Italian hospital considering differences in gender and age”, Applied Ergonomics, Vol. 50, pp 177-184.

3. **Larriva, M. T. B., Mendes, A. S., & Forcada, N. (2022),** “The effect of climatic conditions on occupants’ thermal comfort in naturally ventilated nursing homes”, Building and Environment, Vol. 214, 108930.

4. **Yang, D., J. Xiong, and W. Liu. (2017),** "Adjustments of the adaptive thermal comfort model based on the running mean outdoor temperature for Chinese people: A case study in Changsha China", Building and Environment, Vol. 114 pp 357–365.

5. **Forgiarini, R., N. Giraldo, and R. Lamberts. (2015),** "A review of human thermal comfort in the built environment", Energy and Buildings, Vol. 105 pp 178–205.

6. **Faheem, M., Bhandari, N., and Tadepalli, S. (2022),** "Adaptive thermal comfort in naturally ventilated hostels of warm and humid climatic region, Tiruchirappalli, India", Energy and Built Environment, DOI: 10.1016/j.ergon.2018.09.007.

7. **Thapa, S. (2022),** "Investigation of thermal comfort and adaptation among the residents of cold climate in the lower Himalayan region of eastern India", Indoor and Built Environment, 1420326X211067136.

8. **Turhan, C., & Özbey, M. F. (2021),** "Effect of pre-and post-exam stress levels on thermal sensation of students", Energy and Buildings, Vol. 231, 110595.

9. **Indraganti, M., & Humphreys, M. A. (2021),** "A comparative study of gender differences in thermal comfort and environmental satisfaction in air-conditioned offices in Qatar, India, and Japan". Building and Environment, Vol. 206, 108297.

10. **Fanger, P. O. (1970),** "Thermal comfort. Analysis and applications in environmental engineering. Danish Technical Press, Copenhagen, Denmark.

11. **ISO 7730 (2005),** "Ergonomics of the thermal environment−Analytical determination and interpretation of thermal comfort using calculation of the PMV and PPD indices and local thermal comfort criteria", International Standardization Organization, Geneva.

12. **ASHRAE (2020)**, "Thermal Environmental Conditions for Human Occupancy, ASHRAE Standard 55–2020", American Society of Heating, Refrigerating and Airconditioning Engineers, Atlanta, GA.

13. **Khan, M. H., and Pao, W. (2015),** "Thermal comfort analysis of PMV model prediction in air conditioned and naturally ventilated buildings", Energy Procedia, Vol. 75, pp 1373-1379.

14. **Nicol, F., Humphreys, M., and Roaf, S. (2012),** "Adaptive thermal comfort: principles and practice". Routledge.

15. **Sekhar, S. C. (2016),** "Thermal comfort in air-conditioned buildings in hot and humid climates–why are we not getting it right?" Indoor Air, Vol. 26(1), pp 138-152.

16. **Yao, R., Liu, J. and Li, B. (2010),** "Occupants' adaptive responses and perception of thermal environment in naturally conditioned university classrooms", Applied Energy, Vol.87 (3), pp 1015–1022.

17. **Turhan, C. & Akkurt, G. G. (2018),** “Assessment of thermal comfort preferences in Mediterranean climate: A university office building case”, Thermal Science, Vol. 22 (5), pp 2177-2187.

18. **Kottek, M., Grieser, J., Beck, C., Rudolf, B., and Rubel, F. (2006),** “World Map of the Köppen-Geiger climate classification updated”, Meteorol. Z., Vol. 15, pp 259-263.

19. **Turkish State Meteorological Service (2022)**, “Extreme Maximum, Minimum and Average Temperatures Measured in Long Period”, https://www.mgm.gov.tr/eng/forecast-cities.aspx?m=ANKARA (Accessed: May 29, 2022).

20. Delta OHM Thermal Comfort Data Logger HD32.3TC – HD32.3TCA – Thermal Microclimate PMV-PPD / WBGT, Italy. https://www.deltaohm.com/wpcontent/uploads/document/DeltaOHM_HD32.3TC_datasheet_ENG.pdf (Accessed on: May 29, 2022).

21. **ISO 7726 (1998)** “Ergonomics of the thermal environment - instruments for measuring physical quantities”, International Standardization Organization, Geneva.

22. **ISO 7243 (2017)** “Ergonomics of the thermal environment — Assessment of heat stress using the WBGT (wet bulb globe temperature) index”, International Standardization Organization, Geneva.

23. DHT22 Temperature and Relative Humidity Sensor, https://www.sparkfun.com/datasheets/Sensors/Temperature/DHT22.pdf, (Access Date: 29.05.2022).

24. **Buratti, C., Palladino, D., and Ricciardi, P. (2016).** “Application of a new 13-value thermal comfort scale to moderate environments”, Applied Energy, Vol. 180, pp 859-866.

25. **G.A. Seber, and A.J. Lee (2003),** “Linear regression analysis”, Ney Jersey, USA: John Wiley & Sons, pp.139-163.

26. **D.C. Montgomery, E.A. Peck, and G.G. Vining (2012),** “Introduction to linear regression analysis”, New Jersey, USA: John Wiley & Sons, pp.17-113.

27. **Mathworks (2022),** MATLAB ver. R2022b.

28. **DesignBuilder Software Ltd (2022),** Design Builder v7.0.

29. **ASHRAE (2002),** “Measurement of Energy and Demand Savings, ASHRAE Guideline 14-2002”, American Society of Heating, Refrigerating and Airconditioning Engineers, USA.

30. **Jing, S., Li, B., Tan, M., & Liu, H. (2013).** Impact of relative humidity on thermal comfort in a warm environment. Indoor and Built Environment, 22(4), 598-607.

31. **Yang, Liu, Haiyan Yan, and Joseph C. Lam**. "Thermal comfort and building energy consumption implications–a review." Applied energy 115 (2014): 164-173.

32. **Tweed, C., Dixon, D., Hinton, E., & Bickerstaff, K. (2014).** Thermal comfort practices in the home and their impact on energy consumption. Architectural Engineering and Design Management, 10(1-2), 1-24.

DESIGN OF AN ACTIVE MAGNETIC BEARING SPINDLE FOR MICRO-MILLING APPLICATIONS

Kazi Sher AHMED, *kazisherahmed@sabanciuniv.edu* Sabanci University, 34956, Istanbul, Turkey

Bekir BEDIZ, *bbediz@sabanciuniv.edu* Sabanci University, 34956, Istanbul, Turkey

ABSTRACT

The application of micro-milling for the fabrication of micro-scale parts/features from a plethora of materials has found significantly increased usage. In this fabrication process, miniaturization of mechanical components requires smaller machine tools with ultra-high rotational speeds. For such speeds, active magnetic bearing is a promising technology because it enables high-speed and contact-free rotation with active control of the spindle dynamics. Considering the application of the micro-milling process, we present the design of major components of magnetic bearing spindle including radial and axial magnetic bearing, air turbine, and rotor. Conventionally used analytical models, as well as three-dimensional finite element models, were used to aid the design process. A Pareto front using a genetic algorithm for radial magnetic bearing based on bearing force and volume is also determined to aid the selection of manufacturing dimensions based on the relative importance of bearing performance metrics.

Keywords: Magnetic bearings, High-speed micro-milling, Spindle, Air turbine, Pareto front.

1. INTRODUCTION

There has been an increasing demand for (complex) three-dimensional (3D) components with micro-scale features, especially in the fields of bio-engineering, aerospace, energy conversion, and robotics [Ehmann et al., 2005] Functionality, material savings, small dimensions, and reduced masses motivate the miniaturization of components. In addition to being a well-established need of industrial sectors, the focus on miniaturization also aligns with the recently published European Union missions and policies on climate change [European-Commission, 2021] . In this context, miniaturized products require less specific energy.

To effectively fabricate these components, mechanical micro-milling is widely used. Compared to other methods, micro-milling provides benefits in terms of freedom of material selection, intricate part geometry, relative accuracy, and cost efficiency.

One of the main issues that hinders the exploitation of the potential of this process is arising from the bearings that are used in commercially available systems. Initially, contact bearing systems are used in miniature spindles, however, due to the continuous contact, there are problems such as heating (which leads to thermal deformation) and spindle speed limitations. More recently, air bearings are implemented and rotational speeds up to 400,000 rpm can be achieved [Bediz et al., 2014]. Although ultra-high rotational speeds can be achieved with air bearings, these are passive systems. Thus, the spindle error motions (that are radial, axial, and tilt motions of the spindle) are the main problems since they lead to low process accuracy. To overcome these limitations, active magnetic bearing (AMB) is a promising approach since it allows high rotation speeds required by the process and high accuracy since it enables monitoring the process and thereby controlling the micro-tool motions to increase the positional accuracy.

Micro-milling spindles require relatively very high rotational speeds (above 60,000 rpm) compared to the macro-scale milling machines to provide the same quality of machining and tool edge cutting speed (i.e., to achieve process quality and efficiency). In conventional bearings, the mechanical contact between stator-rotor limits the rotational speed due to heat generation and deformation. In contrast, AMBs enable a non-contact, lubrication-free, energy-efficient, and ultra-high-speed rotation with an ability to control the spindle dynamics [Lee & Chen, 2016]. Among machining-focused implementations of AMBs, [Kimman et al., 2010] realized a miniature milling spindle supported by permanent magnet (PM) biased homopolar magnetic bearings with a target speed of 150,000 rpm. The spindle was driven by a commercial permanent magnet synchronous motor. [Park et al., 2012] constructed a prototype of an air turbine-driven miniature spindle that reached up to 200,000 rpm with a tool orbit of less than 10 μm. [Knospe, 2007] experimented with two AMB test-rigs for active suppression of machining chatter. Typical AMB-supported spindles involve slender and stepped rotors. The stepped segments of the rotor are necessary to accommodate spatially separated components including radial bearings, sensors, backup bearings, axial bearing, and motor drive. Most AMB spindles are based on this configuration.

In this study, we present a comprehensive design of AMB spindle components including radial and axial magnetic bearings, rotor, and air turbine. The radial bearing design is aided by an analytical as well as a three-dimensional finite element model. Further, a Pareto front is

developed to allow the designers to manufacture the bearing based on the relative importance of performance metrics. This paper is organized as follows: Section 2 establishes the application requirements imposed by the high-speed micro-milling process. Section 3 presents the design of components and material selection based on these requirements and aided by analytical and 3D FE models followed by a Pareto front for radial bearing performance. Afterward, the assembly of the setup and manufacturing recommendations are described in Section 4. Section 5 concludes the paper.

2. APPLICATION REQUIREMENTS

The spindle design is aimed at the application of a high-speed mechanical micro-milling process. The process and control dynamics impose certain requirements on the component design such as rotational speed, milling forces, and negative stiffness which are addressed in this section.

Rotational speed

The small diameter cutting tools used in micro-milling result in a reduced material removal rate compared to that of macro-scale (conventional) milling. Therefore, to achieve higher removal rates and suitable cutting speeds to effectively cut material, cutting tools must rotate at higher rotational speeds [Chae et al., 2006]. This leads to the use of high-speed spindles with rotational speeds above 60,000 rpm in many cases. In this study, based on a typical micro-milling tool diameter of 200 μm and a typical cutting speed of 130 m/min which is sufficient for machining of common materials, a theoretical rotational speed of 206,901 rpm (3450 Hz) is required. However, acknowledging that *(1)* the rotational speed limits the rotor diameter due to centrifugal stress; *(2)* enough space on the thrust disc, and hence its diameter, is required to accommodate the axial thrust bearing; a lower rotational speed of 150,000 rpm (2500 Hz) is aimed.

Milling forces

The cutting forces experienced by the tool are important in the design of the AMB spindle and depend on cutting mechanics. Machining conditions such as depth of cut, feed rate, spindle speed, etc. as well as tool geometry affect these forces [Ehmann et al., 2005].

We used the cutting forces predictions made by [Kimman et al., 2010] where a vertical slot milling was performed with a 200 μm cutting tool in tool steel, with an HRC of 55. The feed rate of 5 μm per tooth and depth of cut of 5 μm was considered. The static components of cutting forces were obtained as 0.08 N and 0.05 N along lateral axes. Moreover, a higher static

component of 0.5 N acting along the axial axis was found. The dynamic force amplitude stayed around 0.3 N in all directions.

Negative stiffness

Based on the milling forces found above, a closed-loop bearing stiffness of 1.4×10^5 N/m is aimed to compensate for static cutting forces. As a rule of thumb mentioned by [Molenaar, 2000], a negative bearing stiffness of the same magnitude, or at most one order of magnitude lower, can be selected. Therefore, a negative stiffness in the range 1×10^4 -1×10^5 N/m is aimed in this study.

Rotor unbalance

In the sub-critical operation, the rotor has a frequency below the closed loop bandwidth of the system and bearings try to force the rotation around the geometrical center of the rotor. However, in the super-critical operation, the rotor frequency is above the closed loop bandwidth of the bearings and the rotor rotates around its inertial axis while the bearings are unable to compensate for this unbalance force considering the bandwidth limitations [Kimman et al., 2010]. Therefore, precision and dynamic balancing of the rotor is necessary to attain an acceptable spindle run-out during high-speed operation. For estimates of runout, [Park et al., 2012] achieved orbits of less than 10 μm at 200,000 rpm while (Kimman et al., 2010) achieved radial bearing errors of 7.5 μm at 125,000 rpm. Considering other sources of uncertainties, we aim to achieve a spindle runout of less than 10 μm at the selected rotational speed.

3. COMPONENT DESIGN AND MATERIAL SELECTION

The magnetic circuit model, 3D FE model for the radial magnetic bearings, and 1D finite element model for rotordynamics were used to aid the design of AMB spindle components based on the application requirements. The material selection is again influenced by the application requirements as well as convenient availability in the local market. A detailed treatment of component design is treated in this section.

Rotor

Rotor rotation leads to stresses resulting from centrifugal forces which may limit the safely attainable speeds. The maximum attainable rotational speed $\Omega_{\max}$ is related to the rotor disc radius r as given by [Larsonneur, 1990]:

$$\Omega_{\max} = \frac{1}{r}\sqrt{\frac{8\sigma_o}{(\nu+3)\rho}} \tag{1}$$

σ_o is yield strength, ν is the Poisson's ratio, and ρ is the rotor material density. Since ultra-high rotational speeds make the use of electrical steel laminations challenging due to high centrifugal stresses, a solid rotor is used here. Using ferritic SS of annealed AISI 430F as rotor material with σ_o = 275 MPa, ν = 0.27, and ρ = 7750 kg/m^3, a maximum allowed disc diameter of 37.5 mm is obtained for a rotational speed of 150,000 rpm. However, considering the material inhomogeneities in the rotor material, a factor of safety is applied to select 30 mm as the disc diameter. Next, the rotor segments facing the radial bearings are dimensioned to have 16 mm of diameter in response to the minimum target diameter of the selected displacement sensors. This diameter can also accommodate typical micro-machining tool shank diameters. The rotor segment for the air turbine is kept at 12 mm based on the design of the air turbine to be explained in a later subsection. The overall rotor length places the first bending (flexural) mode around 7 times more than the target closed-loop AMB bandwidth of 300 Hz and also out of the operating speed range as seen in the rotor Campbell diagram drawn in Figure 1. The estimate of bandwidth is taken from [Kimman et al., 2010] and [Allaire et al., 2017]. An open-source rotordynamic code [Ahmed & Mushtaq Ahmad, 2019] was used to model the rotor and extract its Campbell diagram. The rotor schematic and CAD model are shown in Figure 2. The relevant parameters of the rotor are listed in Table 1.

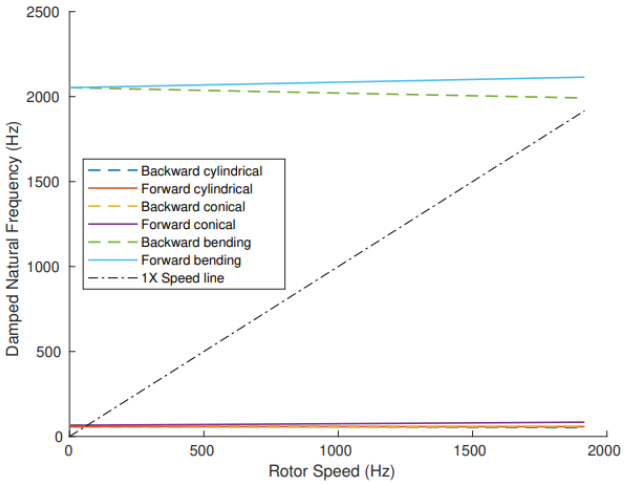


Figure 1. Rotor Campbell diagram showing the rigid body and bending modes variation with rotor speed. 1X speed line represents the synchronous excitation line.

Table 1. Rotor parameters.

Parameters	Values
Total length (mm)	150
Diameter at bearing locations (mm)	16
Diameter (mm)	12
Axial thickness of disc (mm)	3
Diameter of disc (mm)	30
Material	AISI 430F
Weight (N)	2.1

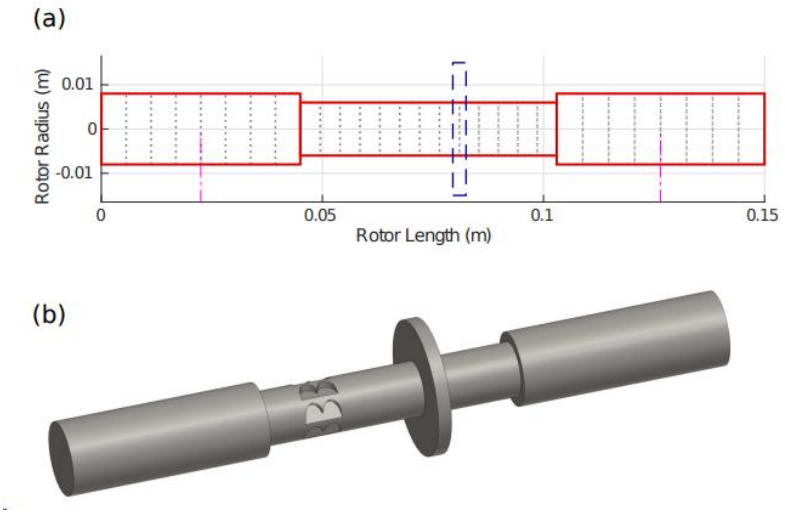


Figure 2. Slender rotor geometry: (a) Schematic with dashed blue lines illustrating the thrust disc and vertical dash-dotted lines showing the bearing locations, (b) CAD model.

Air Turbine

In spindles, the most common drive methods for the rotor include electric motors and air turbines. [Kimman et al., 2007] used a permanent magnet synchronous motor while [Park et al., 2012] utilized an air turbine. For our study, we designed an air turbine to be driven by compressed air. The design method is inspired by the work of (Li et al., 2019). The procedure involves selecting the turbine diameter first while avoiding the supersonic flow. This is followed by torque calculations based on the applied pressure from the nozzle connected to the compressor.

Next, the turbine blade profiles on the rotor are drawn by following the procedure given by [Solemslie, 2016]. The turbine blade profiles and nozzle fixtures are shown in Figure 3 and parameters are listed in Table 2.

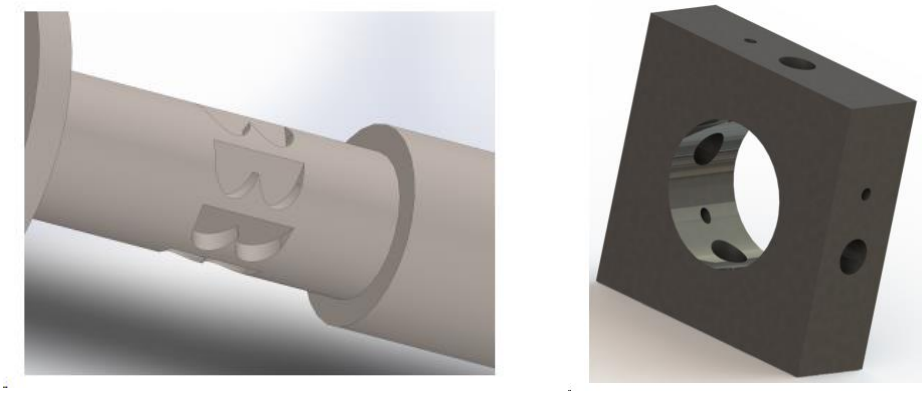


Figure 3. (Left) Air turbine blades on rotor. (Right) Nozzle fixture showing smaller holes as air inlets and larger holes as air outlets.

Table 2. Air turbine parameters.

Parameters	Values
Turbine diameter (mm)	12
Pitch diameter (mm)	10
Nozzle diameter (mm)	1.5
Number of nozzles	4
Inlet pressure (MPa)	0.3

Radial Bearing

For a high-speed rotation, a permanent magnet (PM) biased homopolar magnetic bearing is preferred due to relatively lower losses compared to heteropolar magnetic bearings. To dimension and optimize the bearing for micro-milling requirements defined in Section 2, we first used the magnetic circuit model and linearized the dependence of electromagnetic force on current and rotor displacement [Park et al., 2012]. The bearing topology and flux directions with the assembly are shown in Figure 4.

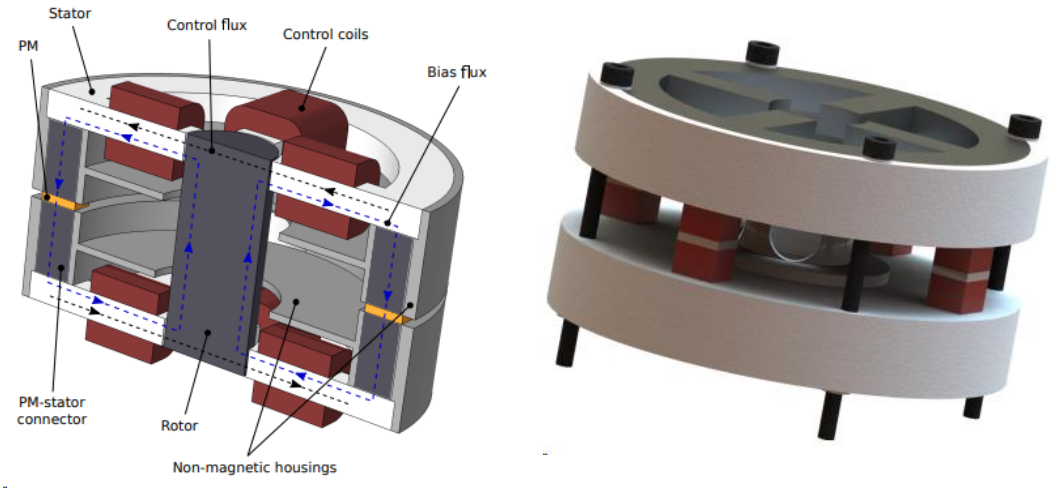


Figure 4. (Left) Radial bearing half-section view with bias and control flux directions in dashed lines. (Right) Radial bearing assembly with housings and lock nuts.

However, the magnetic circuit model does not consider the effects of the following: *(i)* non-linear dependence of magnetic flux density (B) on magnetic field (H), *(ii)* magnetic saturation limits of rotor and stator materials, and *(iii)* flux leakage. Therefore, correction factors are warranted so that the magnetic circuit model can also be used for optimization purposes. These correction factors can be determined by using numerical methods such as three-dimensional (3D) finite element (FE) models which consider the above-mentioned effects. We developed such a model in COMSOL using its *magnetic fields (mf)* interface.

For the application of linear control theory to operate the bearing, the flux density levels need to stay in the linear range of B-H curves of the materials used, *i.e.,* up to 1 T. Using a usual rule of thumb [Yoon et al., 2013] to fix the bias flux levels, we set airgap bias flux density at around 0.5 T, *i.e.,* at 50 percent of the linear B-H range. Assuming a well-balanced rotor and accounting for space needed for backup bearings, the radial airgap length is kept at 0.4 mm. The NdFeB grade N52 PM blocks, connected to the stator with annealed AISI 430F steel, are used to provide the bias flux. Annealing is important to improve the soft magnetic properties of the material. Electrical steel laminations are selected for the stator part to have minimum eddy current losses. Although the radial machining forces on the tool are limited to a static component of 0.08 N and a dynamic amplitude of almost 0.3 N, we generously set the lowest bearing radial load capacity as at least 10 N accounting for unbalance (considering the rotor weighs 2.1 N) and possible disturbances. Another reason for setting this load capacity (with such a large factor of safety) is machining operations involving depths of cut larger than 5 μm considered in Section 2 and the possibility of using harder workpiece materials. Furthermore, as outlined in Section 2, radial negative stiffness between $1x10^4$ and $2x10^5$ N/m needs to be ensured. We compared the results from the magnetic circuit model and 3D FE model to decide

on the correction factor of 0.7. Afterwards, the corrected magnetic circuit model was used to develop a Pareto front.

Pareto Front: To allow the designers to dimension the radial bearing based on the relative importance of performance metrics, a Pareto front is developed here for the objective functions of bearing force and volume. A higher bearing force and lower volume are desired. Selecting the stator geometry and PM thickness as design variables with suitable bound constraints, the multi-objective genetic algorithm in MATLAB was used to prepare the Pareto front as shown in Figure 5. The negative stiffness was used as a non-linear constraint to only get the solution points that do not violate the negative stiffness application requirements.

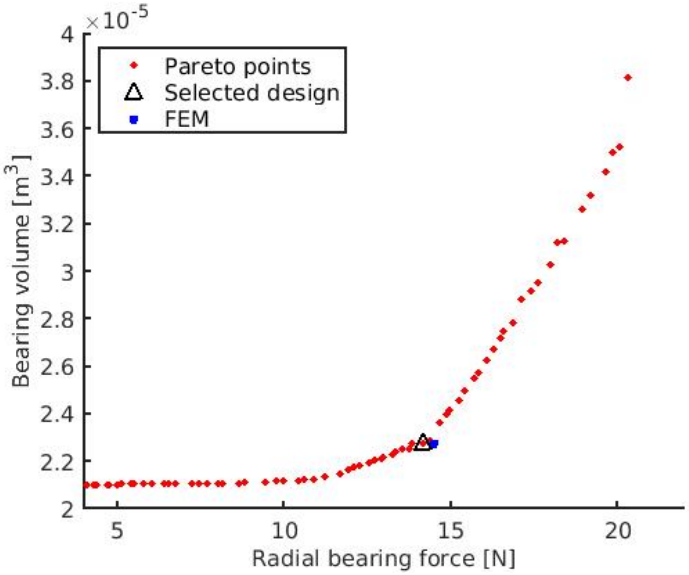


Figure 5. Pareto front of the bearing radial force and volume.

For discussion, a solution on the Pareto front was selected as a design that is a compromise between force capacity and volume as shown in Figure *5*. 3D FEM analysis was conducted to first compare this selected solution with the result from FEM. An acceptable error of 2.45% was found in radial force comparison. Further, FEM analysis was used to ensure that components do not saturate magnetically as shown in Figure 6. Once the magnetic path is magnetically saturated, effective control of the rotor is not possible. In some regions, the maximum flux density levels reach around 1.2 T which is below the magnetic saturation limit. The bearing parameters of the selected design are shown in Table 3.

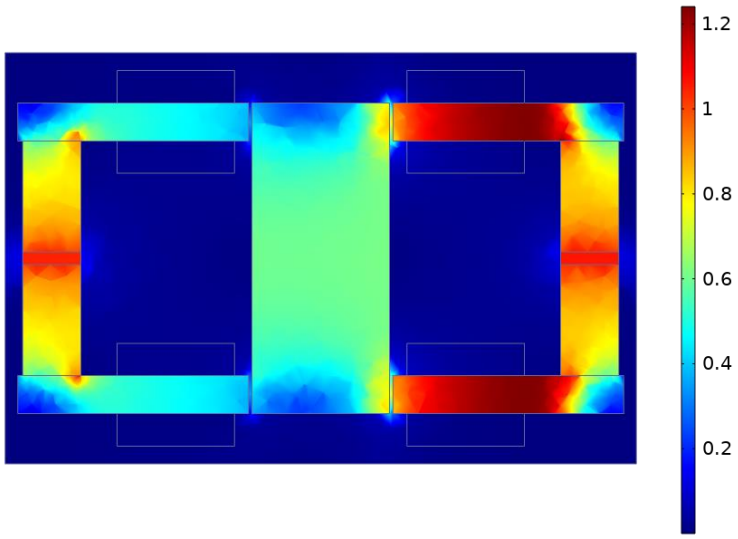


Figure 6: Magnetic flux density (T) on half-section view of the bearing.

Table 3. Parameters of radial bearing.

Parameters	Values
Pole shoe surface area (mm^2)	40.79
Airgap length (mm)	0.4
PM cross-sectional area (mm^2)	224
Coil wire size	AWG 16 *(1.291 mm diameter)*
Number of coil turns per pole	30
Maximum coil current (A)	2.98
PM remanent flux density (T)	1.44

Axial Thrust Bearing

This bearing consists of two u-shaped reluctance actuators with coils wound tangentially. With simple geometry, this bearing type is mostly dimensioned using widely used linearized force relations. The linearized force F_a acting on the thrust disc is given by:

$$\mathrm{F_a} = \mathrm{K_i i_p} + \mathrm{K_z z} \tag{2}$$

where K_i and K_z are open-loop current gain (force-current dependency) and negative stiffness (force-displacement dependency or open-loop stiffness), respectively, and are given as:

$$K_\mathrm{i} = \frac{\mu_\mathrm{o} n^2 A_\mathrm{p} i_\mathrm{b}}{l_o^2} \tag{3}$$

$$K_z = \frac{\mu_o n^2 A_p i_b^2}{l_o^3} \quad (4)$$

where μ_o is the relative permeability of air, n is the number of coil turns, A_p is the area of each pole, i_b is the bias current, and l_o is the nominal airgap length.

The relevant application requirements from Section 2 include: *(i)* static component of milling force at 0.5 N, dynamic force amplitude of 0.3 N, and weight of the rotor at 2.1 N, and *(ii)* negative stiffness in the range 1×10^4 - 1×10^5 N/m. The bearing is dimensioned iteratively to meet these requirements. The airgap length is kept as 0.3 mm. Considering that electrical laminations are challenging to be used for axial bearings, a good magnetic material such as annealed AISI 430F is preferred to develop this bearing. The CAD model of one axial actuator is shown in Figure 7. The final axial bearing parameters are listed in Table 4.

Table 4. Axial thrust bearing parameters.

Parameters	Values
Pole shoe surface area (mm^2)	70
Airgap length (mm)	0.3
Coil turns (per actuator)	35
Bias current (A)	2
Open loop current gain (N/A)	9.57
Negative stiffness (N/m)	$6.38x10^4$

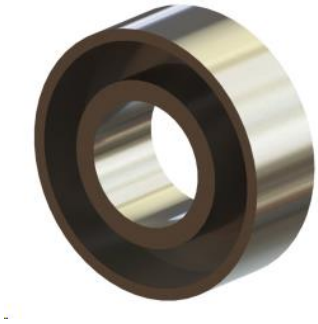


Figure 7. CAD of axial thrust actuator.

4. ASSEMBLY AND MANUFACTURING RECOMMENDATIONS

All major components designed in this study are assembled as depicted in Figure 8. Two radial bearings, positioned at the ends of the rotor, control the rotor in the radial direction. Beneath the top radial bearing, the air turbine nozzles are present for compressor connections. Below that, two axial bearing actuators are placed near the rotor thrust disc for axial control of the

spindle. Vibration-resistant locknuts with wedge-locking washers are used to hold the components together. The material for the side plates is aluminum for strength and low weight.

A round bar material for the rotor needs to be acquired in annealed conditions for better magnetic performance. After general machining, a grinding process is required to give better tolerance and surface for the displacement sensor target. Dynamic balancing of the rotor is necessary. More annealing may be required based on levels of prior annealing. It should be noted that annealing may also soften the material.

The laminated electrical steel for the radial bearing stator needs to be cut with electrical discharge machining to give the best actuator performance during bearing operation. However, laser cutting is also known to give suitable cutting without burring the edges of the laminations. Considering no use of laminations in the axial stator, it can be machined through conventional means.

Considering that the spindle assembly will be mounted on linear stages with high accelerations, fiber lock nuts are recommended that resist loosening due to vibrations and torque. Additionally, wedge-locking washers are recommended.

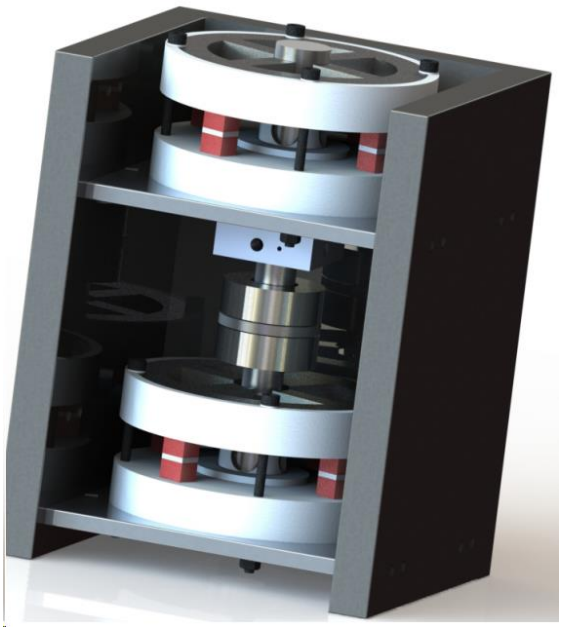


Figure 8. Assembly of the spindle.

5. CONCLUSION

Aiming for the immediate next steps of spindle manufacturing, this study presents the design of major AMB spindle components such as radial and axial bearing, air turbine, and rotor. The design is aided by the conventionally used magnetic circuit models for magnetic actuators and 3D FE models. The micro-milling application requirements influenced the design process. A Pareto front for the bearing performance metrics is also developed to demonstrate that a suitable design point can be selected based on the relative importance of either maximizing the bearing force or minimizing the volume.

REFERENCES

1. **Ahmed, K.S. and Mushtaq Ahmad, S., (2019),** “VibronRotor, an Opensource Rotordynamic Code: Development and Benchmarking”, Measurement, Vol.131, pp 546-558.
2. **Allaire, P., Nichols, B., Dimond, T., Cao, J., and Mushi, S., (2017)**, “Low Cost Active Magnetic Bearings-Concepts and Examples”, ISMB15.
3. **Bediz, B., Arda Gozen, B., Korkmaz, E., and Burak Ozdoganlar, O., (2014),** “Dynamics of Ultra-High-Speed (UHS) Spindles Used for Micromachining”, International Journal of Machine Tools and Manufacture, Vol.87, pp 27-38.
4. **Chae, J., Park, S. S., and Freiheit, T., (2006),** “Investigation of Micro-Cutting Operations”, International Journal of Machine Tools and Manufacture, Vol.46, No.3-4, pp 313-332.
5. **Ehmann, K., Bourell, D., Culpepper, M., and Hodgson, T., (2005),** “International Assessment of Research and Development in Micromanufacturing”, World Technology Evaluation Center (WTEC), Inc.
6. **European-Commission, (2021),** Horizon Europe-Work Programme 2021-2022: Digital, Industry and Space.
7. **Kimman, M. H., Langen, H. H., and Munnig Schmidt, R. H., (2010),** “A Miniature Milling Spindle with Active Magnetic Bearings”, Mechatronics, Vol.20, No.2, pp 224–235.
8. **Kimman, M. H., Langen, H. H., Van Eijk, J., and Munnig Schmidt, R., (2007),** “Design and Realization of a Miniature Spindle Test Setup with Active Magnetic Bearings”, IEEE/ASME International Conference on Advanced Intelligent Mechatronics, pp 1-6.
9. **Knospe, C.R., (2007),** “Active Magnetic Bearings for Machining Applications”, Control Engineering Practice, Vol.15, No.3 SPEC. ISS., pp 307-313.
10. **Larsonneur, R., (1990),** “Design and Control of Active Magnetic Bearing Systems for High Speed Rotation”, Doctoral Dissertation, ETH Zurich.
11. **Lee, R.-M. and Chen, T.-C., (2016),** “Adaptive Control of Active Magnetic Bearing Against Milling Dynamics”, Applied Sciences, Vol.6, No.2, pp 52.

12. **Li, W., Liu, M., Ren, Y. H., and Chen, Q., (2019),** “A High-Speed Precision Micro-Spindle Use for Mechanical Micro-Machining”, International Journal of Advanced Manufacturing Technology, Vol.102, No.9-12, pp 3197-3211.
13. **Molenaar, L., (2000),** “A Novel Planar Magnetic Bearing and Motor Configuration Applied in a Positioning Stage”, Doctoral Dissertation, TU Delft.
14. **Park, J.-K., Kyung, J.-H., Shin, W.-C., and Ro, S.-K., (2012),** “A Magnetically Suspended Miniature Spindle and its Application for Tool Orbit Control”. International Journal of Precision Engineering and Manufacturing, Vol.13, No.9, pp 1601–1607.
15. **Solemslie, B. W., (2016),** “Experimental Methods and Design of a Pelton Bucket”, Doctoral Dissertation, Norwegian University of Science and Technology, Trondheim, Norway.
16. **Yoon, S. Y., Lin, Z., and E. Allaire, P., (2013),** Control of Surge in Centrifugal Compressors by Active Magnetic Bearings. Springer.

INVESTIGATION OF DIMENSIONALITY REDUCTION METHODS FOR CHATTER DETECTION WITH SVM

Kerem Utku DEMİR, *keremutkudemir@etu.edu.tr* TOBB University, 06560, Ankara, Turkey

Batıhan ŞENER, *batihansener@etu.edu.tr* TOBB University, 06560, Ankara, Turkey

Hakkı Özgür ÜNVER, *hounver@etu.edu.tr* TOBB University, 06560, Ankara, Turkey

ABSTRACT

Chatter vibrations significantly affect the quality and efficiency of machining operations. Machine learning algorithms for intelligent chatter detection are viable options when there is sensor data available at the machine tool level. Most machine learning methods require a feature engineering phase where the most valuable data should be extracted and prepared as input for a machine learning classifier. The selection of the proper dimensionality reduction method at this early stage enhances the performance of the classifier.

This study aims to investigate the effectiveness of several dimensionality reduction methods when using Support Vector Machine (SVM) as a classifier. Vibration signals collected during slot milling are binary labeled as stable (0) and chatter (1). Signals were reshaped to 0.5-second segment and 0.1-second segment. Ten-dimensional (10D) statistical time-domain features extracted from signals were reduced to three-dimensional (3D) feature space with Principal Component Analysis (PCA), t-Distributed Stochastic Neighbor Embedding (t-SNE), and Autoencoder (AE) dimensionality reduction methods. Signals were classified by SVM classification with various training distributions.

The effectiveness of different dimensionality reduction techniques and different training distributions were compared for chatter detection. Furthermore, it was observed that dimensionally reduced features were classified quicker and more accurately than statistical time-domain features.

Keywords: Dimensionality Reduction; Machine Learning; Milling; Chatter

1. INTRODUCTION

Machining is the most common subtractive method in manufacturing. End milling is a material removal process including rotary cutting tools with a single or multiple cutting teeth and is one of the most widely used machining operations in industrial manufacturing. In milling processes, surface quality and efficiency have direct effects on cost and chatter is one of the most common limitations for productivity and part quality. Three different types of vibrations are observed in milling operations which include free, forced, and self-excited. Free vibrations are a result of shock and forced vibrations that are caused by unbalanced machine tool assemblies. Detection and suppression of free and forced vibrations are easier than self-excited vibrations because of the complicated character of self-excited vibrations which are not understood entirely. The machine tool chatter is a self-excitation vibration between the tool and the workpiece because of the complex, non-linear and non-stationary characteristics of the machining process. Moreover, chatter vibrations are one of the major limiting factors in increasing the material removal rates of the machine tools and they are also a cause of unstable machining. Mostly manual additional operations are required to clean the chatter marks left on the surface. Due to these reasons, it is critical to determine and prevent chatter during machining operations.

Tlusty [Tlusty, 1963] and Tobias [Tobias, 1969] marked the beginning of mechanistic modeling of self-excited vibrations in orthogonal cutting. They identified the most robust source of regenerative chatter associated with the mechanics of the machine tool and the feedback between following cuts on the same cutting surface. Koenigsberger and Tlusty [Koenigsberger, 1967] used the orthogonal chatter model [Tlusty, 1963] studying the average number of teeth in cut and an average direction in the early milling stability analysis. Opitz et al. [Opitz, 1970] identified an enhanced estimation. Budak [Budak, 1994] performed a stability method that indicates the analytical determination of stability limits in milling that was verified by numerical and experimental results. Chatter could be detected using stability lobes [Altintas, 1995] and other analytical models [Budak, 2006]. However, analytical detection models could not predict chatter precisely due to the complex character of self-excited vibrations and nonlinearities [Altintas, 2004]. Because of market demand and labor cost, automation in machining has become the most incentivizing way to balance production and economic cost [Altintas, 2012]. During machining operations, effective unmanned manufacturing techniques could be a feasible option via using automatic and advanced machining state monitoring methods [Smith, 1991]. In addition, artificial intelligence (AI), machine learning (ML), and deep learning (DL) methods are applied with machining sensor data in intelligent chatter detection. Image features [Chen, 2019], wavelet spectrograms [Yao, 2010; Li, 2019; Kvinevskiy, 2020], signal processing techniques [Kuljanic, 2009; Kuntoglu, 2021], multi-feature fusions [Cao, 2017; Wan, 2021], and

feature selection methods [Lamraoui, 2015; Fu, 2019] are used with neural networks [Gupta, 2020; Postel, 2020] and classification algorithms [Oleaga,2018; Liu, 2018; Dalzochio, 2020]. In this study, three different dimensionality reduction methods were applied and their effects with SVM classification accuracy were investigated. The dimensionality reduction is crucial to accelerate and improve the machine learning algorithms and precision of results especially for high dimensional data interpretation however, it is noticed that there is not a sufficient comparison for chatter detection and aimed to provide awareness besides a guideline with distinctive quality. All analyses and training were implemented with the data collected from a machining center at TOBB-ETU Advanced Manufacturing Laboratory.

2. METHODOLOGY

The proposed method of chatter detection consists of the following three steps, 1) Data Acquisition and Labeling, 2) Feature Engineering, and 3) Support Vector Machine (SVM) Classification. The flowchart of the methodology is presented in Figure 1.

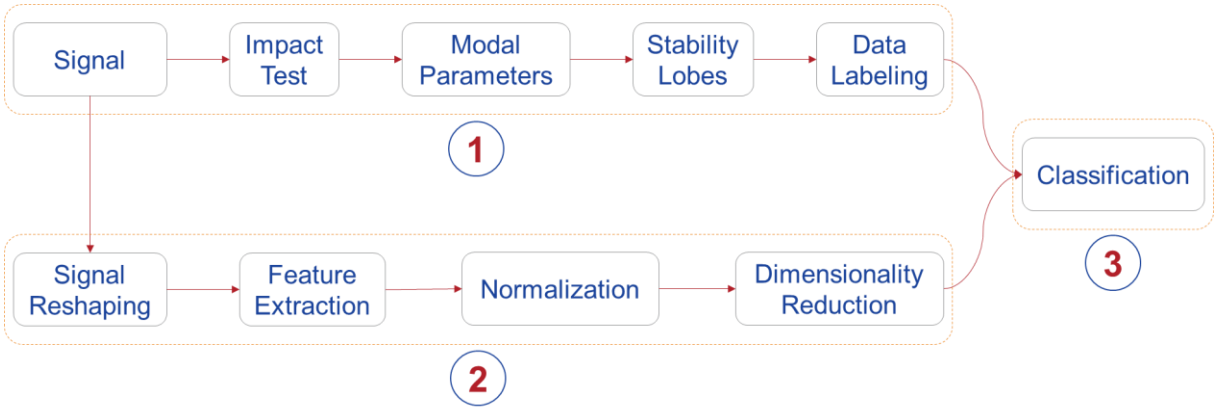


Figure 1. Outline of the Chatter Detection Process

In the first step, vibration signal data were collected from milling operations and labeled with the application of impact test, modal parameters, and stability lobes respectively. In feature engineering, which is the most important part of the study, features are extracted from reshaped signals and normalized before the application of dimensionality reduction. In the last part, both extracted features and dimensionally reduced features are classified with different labeled training and test distributions on SVM classification for the prediction of chatter.

2.1 Data Acquisition and Labeling

The experiments were performed on a medium-sized 5-axis vertical machining center. A 10 mm diameter 3-fluted tungsten-carbide cutting tool was preferred for shoulder milling operations with 50% radial engagement. The shoulder milling operations were performed on Al 7075 stocks. A three-axial PCB accelerometer is used to collect vibration data during cutting operations, and a PCB impact hammer and the aforementioned accelerometer are used to

obtain modal parameter extractions which are required for stability lobe calculations of the system. A data acquisition (DAQ) system NI™ 9234 collects data from sensors and transfers it to LabVIEW™ software. The accelerometer is attached to the spindle case. The sampling rate for both milling and impact tests is 51200 Hz. In this study, a time-domain simulation for the numerical solution-based milling problem is used to generate the stability lobes diagram (SLD). The stability lobes diagram corresponds to the model-based solution developed by Smith and Tlusty [Smith, 1991]. The selection of 24 different cutting combinations in the 6250-16000 RPM cutting speed range, 4-7 mm depth of cut range, the cutting parameters, and the assigned classes are given in Table 1.

Experiment Number	Time (s)	Cutting Depth (mm)	Spindle Speed (RPM)	Classification Class
1	9	7	6250	Stable (0)
2	9	6	6250	Stable (0)
3	5	6	7600	Stable (0)
4	4	6	10000	Stable (0)
5	7	5	6250	Stable (0)
6	6	5	7600	Stable (0)
7	5	5	9000	Stable (0)
8	4	5	10000	Stable (0)
9	3	5	13000	Stable (0)
10	8	4	6250	Stable (0)
11	6	4	7600	Stable (0)
12	5	4	9000	Stable (0)
13	3	7	13000	Chatter (1)
14	3	7	14500	Chatter (1)
15	3	7	16000	Chatter (1)
16	5	6	9000	Chatter (1)
17	3	6	11000	Chatter (1)
18	3	6	13000	Chatter (1)
19	2	6	14500	Chatter (1)
20	3	6	16000	Chatter (1)
21	3	5	11000	Chatter (1)
22	2	5	14500	Chatter (1)
23	2	5	16000	Chatter (1)
24	2	4	16000	Chatter (1)

Table 1. Cutting Parameters and Corresponding Labels of the Experiment Set

2.2 Feature Engineering

In this paper, feature engineering consists of the following two steps, feature extraction from signal and dimensionality reduction. Vibration signals were collected using the mentioned accelerometer attached to the spindle housing with a sampling rate of 51200 Hz and labeled with the stability lobes diagram (SLD). Acquired raw data are processed with signals reshaped as 0.5-second and 0.1-second segments**.** The reshaping procedure is applied to observe various signal length effects, the lack of data, and especially the insufficient amount of chatter data. Indicators extracted from the segments are required and affected the performance of the chatter detection model as much as the conventional chatter detection methods. The monitoring signals change in the time domain. Ten-dimensional statistical time-domain features were extracted from reshaped signal data such as root mean square (RMS), crest factor, impulse factor, index of dispersion, peak value (Pv), variance (Var), skewness, kurtosis, clearance factor, and shape factor. Statistical time-domain features and their notations are also provided in Table 2.

Feature	Notation	Feature	Notation
Root Mean Square (RMS)	$\sqrt{\frac{1}{N}\sum_{n=1}^{N} S_n^2}$	Variance (Var)	$\frac{1}{N}\sum_{n=1}^{N}(S_n-\bar{S})^2$
Crest Factor	$\sqrt{\frac{P_v}{RMS}}$	Skewness	$\frac{\frac{1}{N}\sum_{n=1}^{N}(S_n-\bar{S})^3}{Var^{3/2}}$
Impulse Factor	$\frac{P_v}{\frac{1}{N}\sum_{n=1}^{N}\lvert S_n\rvert}$	Kurtosis	$\frac{\frac{1}{N}\sum_{n=1}^{N}(S_n-\bar{S})^4}{Var^2}$
Index of Dispersion	$\frac{\frac{1}{N}\sum_{n=1}^{N}(S_n-\bar{S})^2}{\frac{1}{N}\sum_{n=1}^{N}S_n}$	Clearance Factor	$\frac{P_v}{\frac{1}{N}\sum_{n=1}^{N}\lvert S_n\rvert^2}$
Peak Value (Pv)	$\frac{1}{2}[max(s_n)-min(s_n)]$	Shape Factor	$\frac{RMS}{\frac{1}{N}\sum_{n=1}^{N}\lvert S_n\rvert}$

Table 2. Statistical Time-Domain Features

Distributions of normalized statistical time-domain features with data set are given in Figure 2. Stable (0) and Chatter (1) samples are shown in the colors blue and red for each distribution figure.

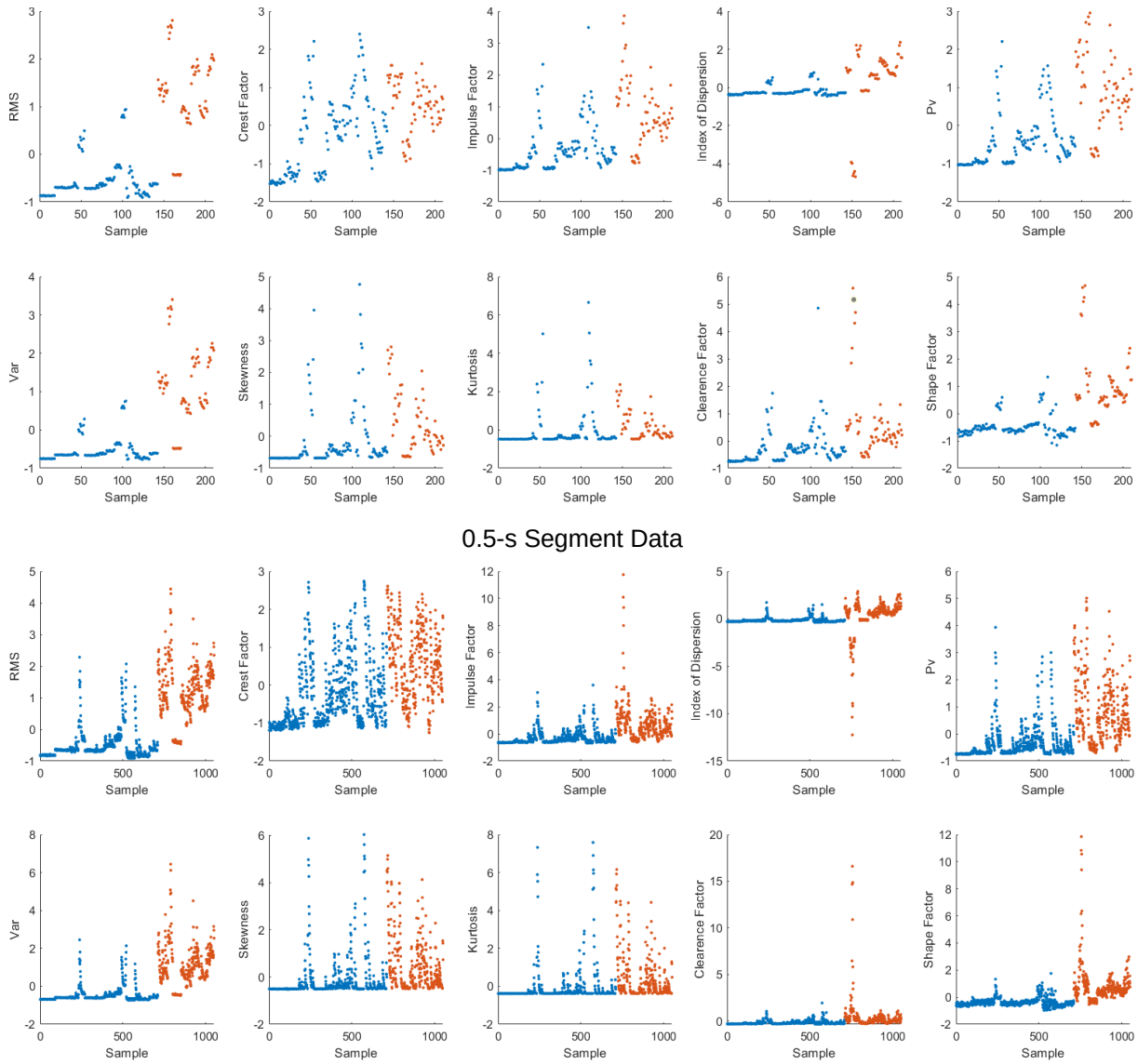
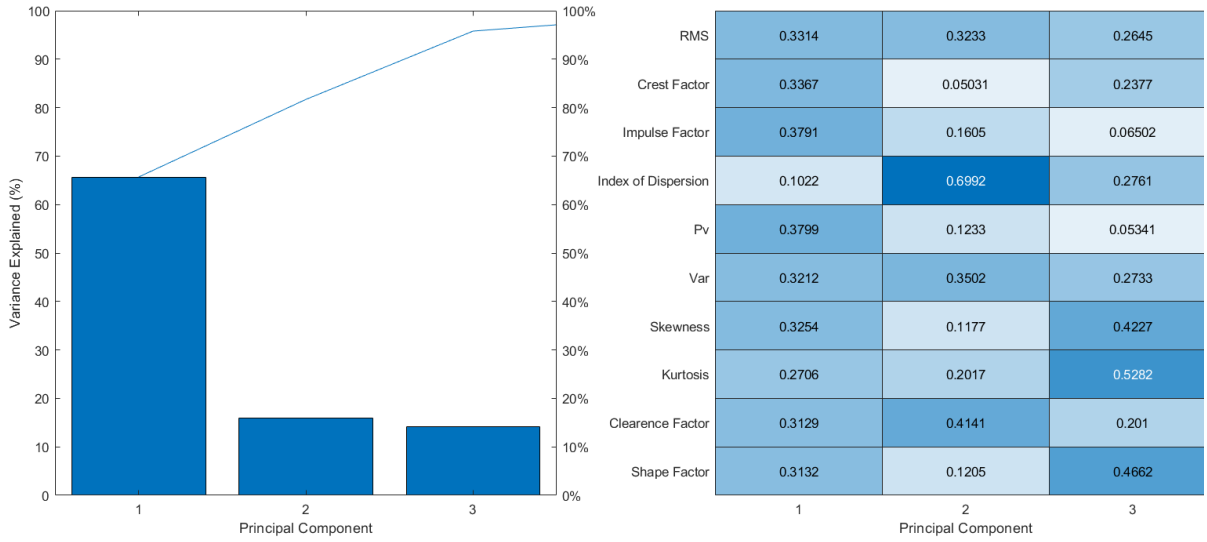


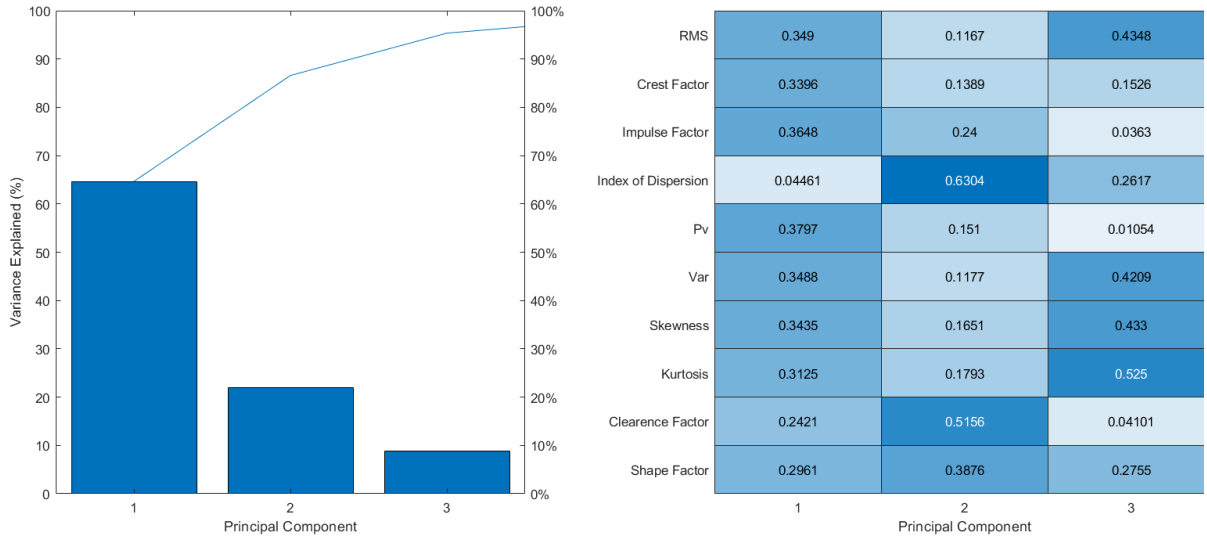
Figure 2. Extracted Statistical Time-Domain Feature Distributions with Data Set

Dimensionality reduction techniques reduced the size of the dataset while keeping the variation. Three dimensionality reduction methods are applied to statistical time-domain features including Principal Component Analysis (PCA), t-Distributed Stochastic Neighbor Embedding (t-SNE), and Autoencoder (AE). Ten-dimensional statistical features are reduced to three-dimensional feature space with each method. Principal Component Analysis (PCA), also known as the Karhunen–Loeve transformation**,** is a commonly used method for lossy data compression, feature extraction, and dimensionality reduction. PCA was initially described by Pearson [Pearson, 1901] and Hotelling [Hotelling, 1933] enhanced individually. As a dimensionality reduction algorithm, PCA is a linear method that transforms a set of correlated variables into a smaller number of the variation in the original dataset. The purpose of PCA is to identify a set of unrelated features known as principal components. PCA can be used for dimensionality reduction by discarding the principal components beyond a chosen threshold

of explained variance. Each PC is a linear combination of the original features and there is no redundant information because PCs are orthogonal to each other. Only significant PCs keep maximum information that could be used to visualize data in low dimensional space. The first principal components represent the largest variation of the original data and decrease the dimensionality of feature space. For the sum of the variances of the first few principal components, it is commonplace to exceed 80% of the total variance of the original data [Jolliffe, 2002; Bishop, 2006; Ilin, 2010; Vidal, 2016]. PCA results are provided in Figure 3.



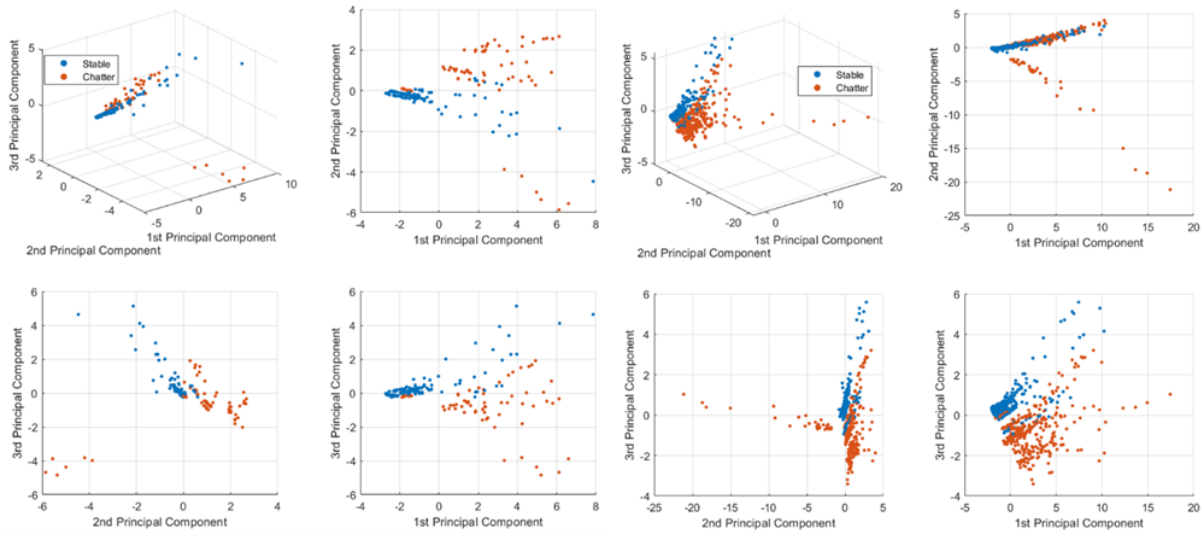
(a)



(b)

Figure 3. PCA Results of (a) 0.5-s Segment Data and (b) 0.1-s Segment Data

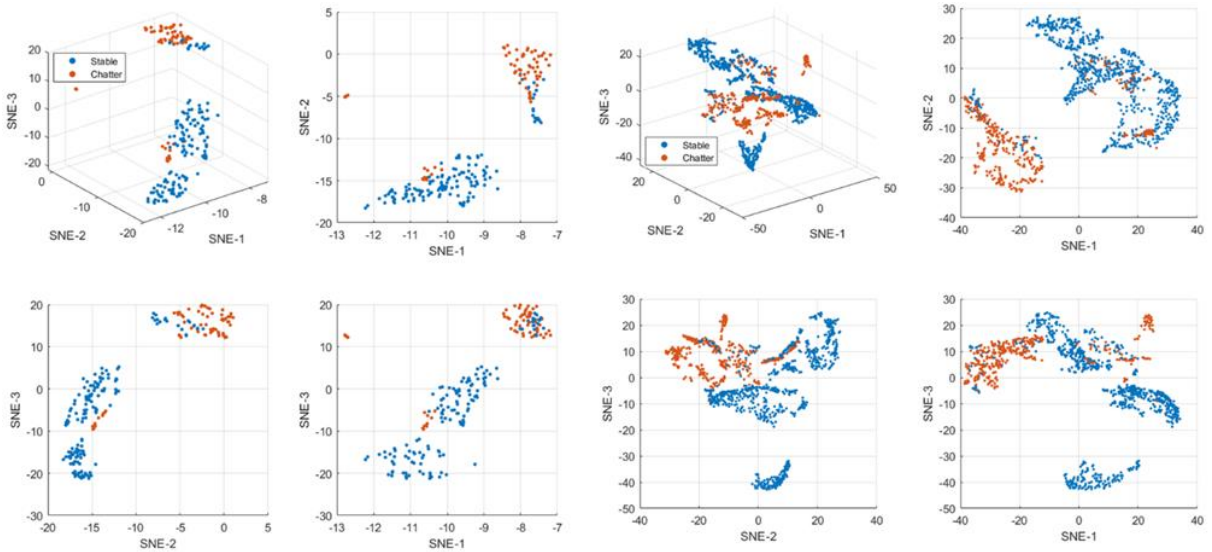
As shown in Figure 3, the first three principal components constitute more than 95% of the variance for each reshaped data. In PCA data distributions are given in Figure 4.



(a) (b)

Figure 4. PCA Data Distributions of (a) 0.5-s Segment Data and (b) 0.1-s Segment Data

t-Distributed Stochastic Neighbor Embedding (t-SNE) [Maaten, 2008] is a non-linear dimensionality reduction technique that is an improved variation of stochastic neighbor embedding (SNE). t-SNE is an unsupervised and probabilistic embedding technique that is generally used for high-dimensional data visualization. Similar to SNE, t-SNE aims at minimizing the Kullback-Leibler divergence between a distribution measuring the pairwise similarity of input objects and the distribution measuring the pairwise similarities in corresponding low-dimensional embedding. Also, t-SNE uses the symmetrized pairwise distance between these input objects [Maaten, 2008; Hamid, 2019]. Data distributions of t-SNE are provided in Figure 5.



(a) (b)

Figure 5. t-SNE Data Distributions of (a) 0.5-s Segment Data and (b) 0.1-s Segment Data

From Figure 5, it could be more predictable to notice the distribution of data in (b) 0.1-s Segment than in (a) 0.5-s Segment because the classifier might distinguish between the chatter and the stable with a decision boundary with a smaller amount of loss. Also, the non-linearity of the t-SNE method may conceivably identify. SNE-1 and SNE-2 features are separated more effectively compared to others for each segment.

Autoencoders are unsupervised learning algorithms and a specific type of feed-forward neural network that tried to reproduce its input (Figure 6). Autoencoders consist of three components which are encoder, code, and decoder. The encoder compresses the input and produces a lower-dimensional code, also known as the latent space representation or bottleneck. Autoencoders are utilized for synthetic data generation, image restoration, data denoising, feature extraction, and dimensionality reduction. Lower-dimensional codes are used for dimensionality reduction and feature selection [Hinton, 2006; Proteau, 2020; Nasir, 2021].

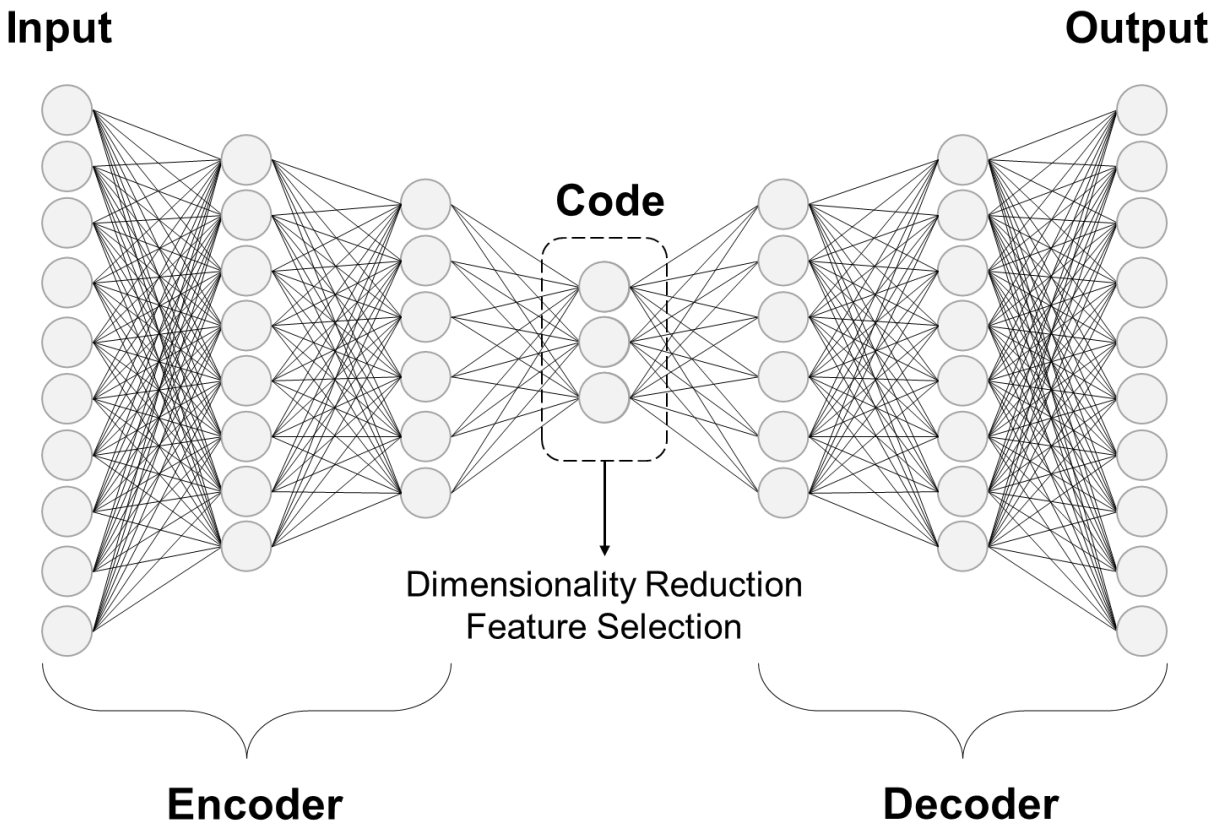
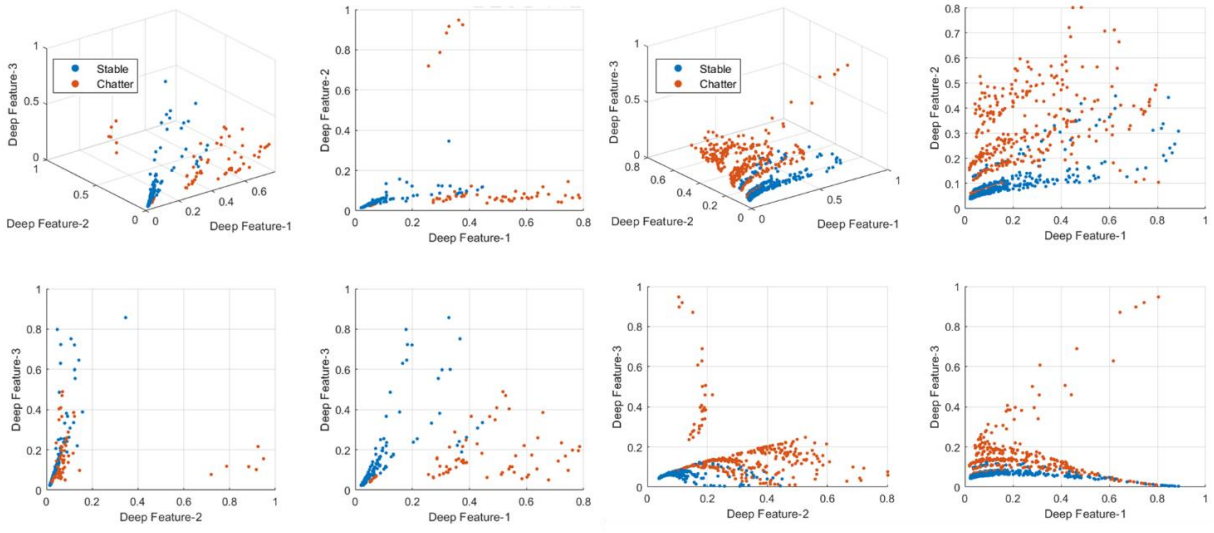


Figure 6. Schematic of the Autoencoder Network

In this study, statistical time-domain features are used as input, and the encoder compresses this input to a three-dimensional hidden layer. Thus ten-dimensional time-domain features are reduced to three-dimensional space. Autoencoder applied data distributions are provided in Figure 7.



(a) (b)

Figure 7. AE Data Distributions of (a) 0.5-s Segment Data and (b) 0.1-s Segment Data

As seen in Figure 7, It is conceivable to recognize the pattern of (b) 0.1-s Segment Data than (a) 0.5-s Segment Data since the borders are more significant to classify. Besides the effect of dimensionality reduction can be perceptible clearly from feature separation.

2.3 Support Vector Machine (SVM) Classification

Chatter detection is a classification problem. Classification is a supervised machine learning method. In this study, Support Vector Machine (SVM) using as a binary classification algorithm. Binary classes are 0 (Stable) and 1 (Chatter). SVM [Cortes, 1995] is a linear model for classification and regression problems. It is capable of solving both linear and non-linear problems. SVM algorithm creates a line or a hyperplane which separates data into classes. In this study, a linear SVM is used for classification, since it gives better classification results than non-linear SVM models. SVM was applied to ten-dimensional statistical time-domain features and PCA, t-SNE, and AE were applied to three-dimensional dimensionally reduced features. Dataset is separated into training and test data with different training distributions. Vibration data sizes are 210 for two segments per second and 1050 for ten segments per second. SVM applied to two segments per second data with 110 train (55 Stable-55 Chatter), 100 test (87 Stable-13 Chatter) and 125 train (85 Stable-40 Chatter), 85 test (57 Stable-28 Chatter) distributions. SVM applied to ten segments per second data with 630 train (315 Stable-315 Chatter), 420 test (395 Stable-25 Chatter), and 630 train (426 Stable-204 Chatter), 420 test (284 Stable-136 Chatter) distributions.

3. RESULTS AND DISCUSSION

A linear SVM classification model was used to predict stable cutting conditions or chatter during the milling operation. Several feature reduction techniques were investigated to find the optimal method. Different signal reshaping lengths and training distribution were used to compensate

for the lack of data. The confusion chart and used classification metric are provided in Figure 8.

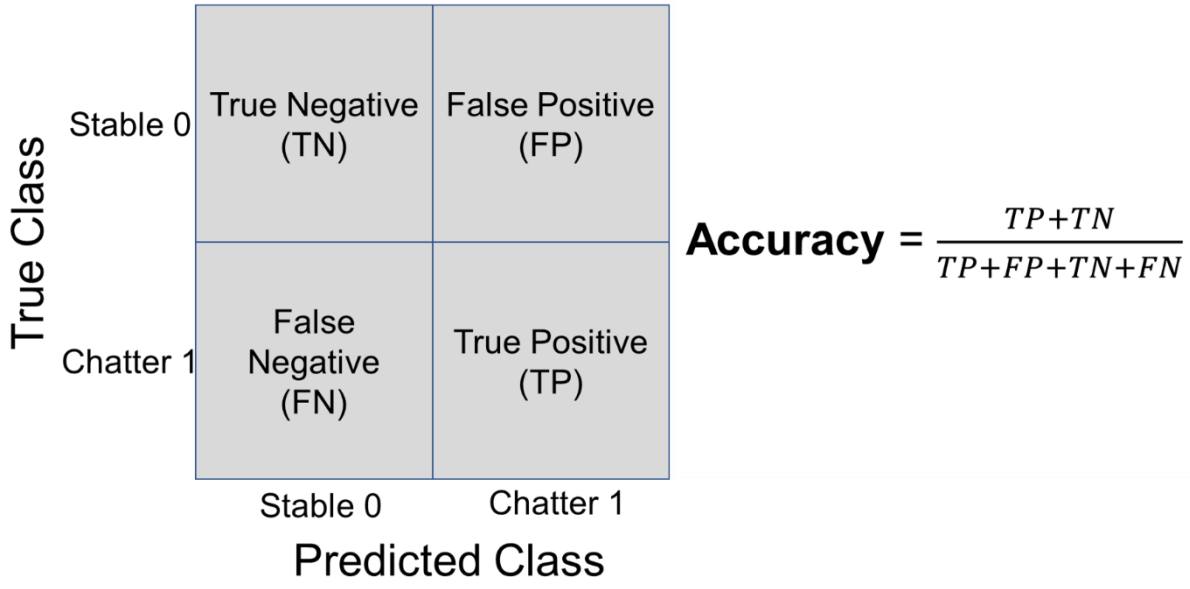


Figure 8. Confusion Chart and Notation of Accuracy

In Figure 9, confusion charts on top belong to 55 stable/55 chatter, and bottoms belong to 85 stable/40 chatter training distributions data for two segments per second data.

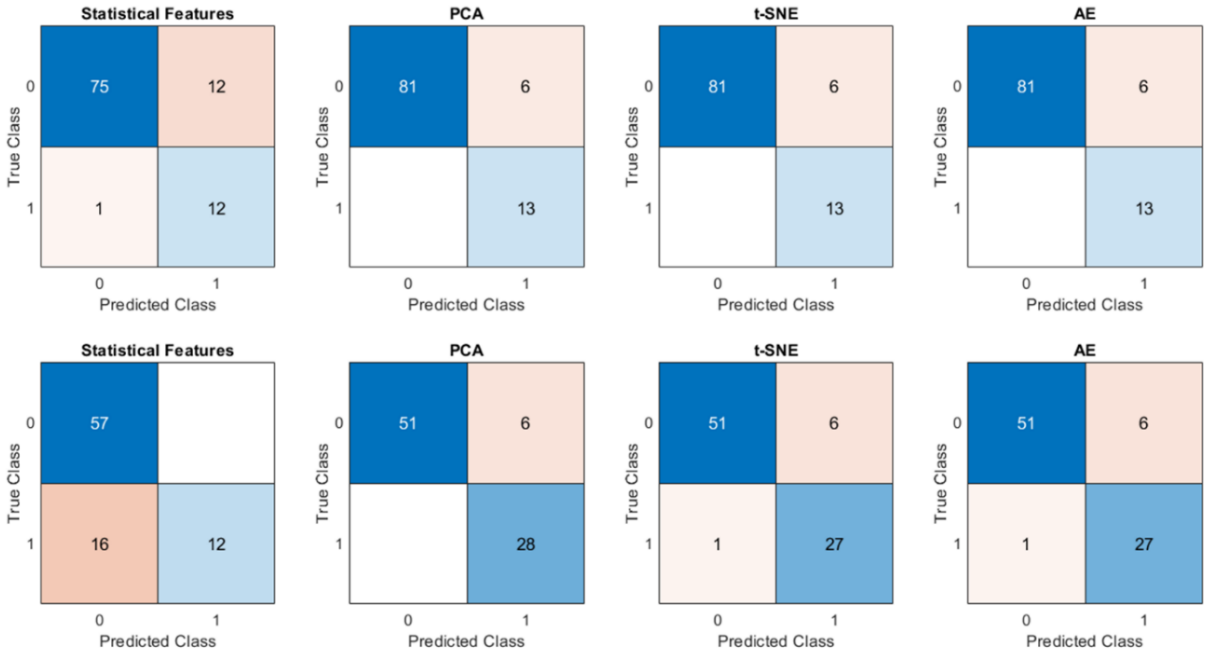


Figure 9. 0.5-s Segment Data Confusion Charts for Test Predictions

SVM classification accuracies for two segments per second data are provided in Figure 10.

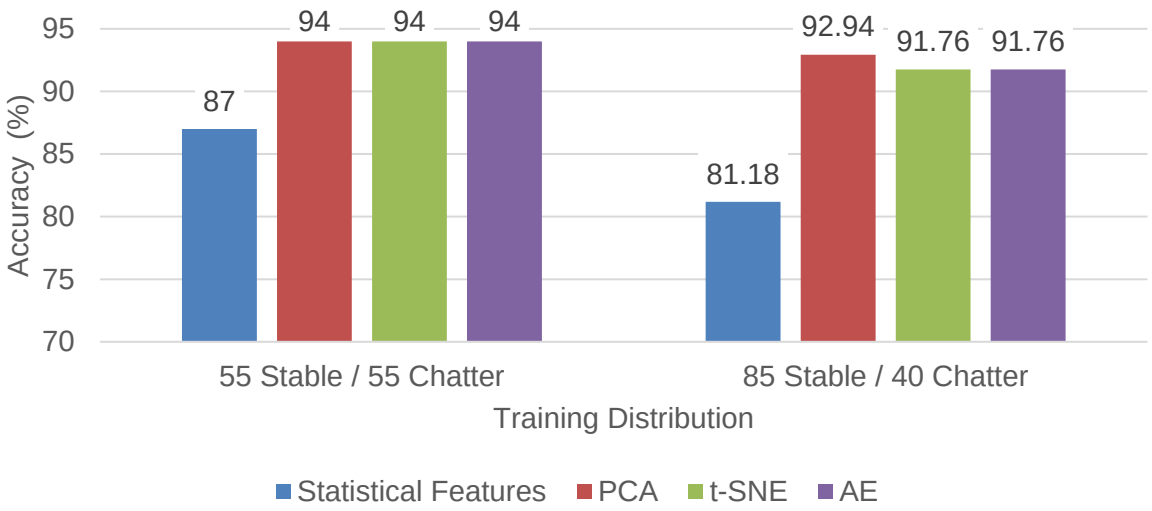


Figure 10. 0.5-s Segment Data SVM Accuracy Bar Chart for Test Predictions

As observed in Figure 9 and Figure 10, PCA, t-SNE, and AE predicted classes identically and accurately than statistical features with 55 stable/55 chatter trained SVM classification for 0.5-second segment data. Also, all reduced data sets predicted both stable and chatter more than the statistical time-domain features data set. PCA has better results than t-SNE and AE with one different chatter prediction and each reduced data set classifies stable samples identical although statistical features have better predictions on stable samples for 85 stable/40 chatter distribution. Accuracies decreased from 55 stable/55 chatter distributions to 85 stable/40 chatter distributions for every 0.5-second segment data set.

In Figure 11, confusion charts on top belong to 315 stable/315 chatter, and bottoms belong to 426 stable/204 chatter training distributions for ten segments per second data.

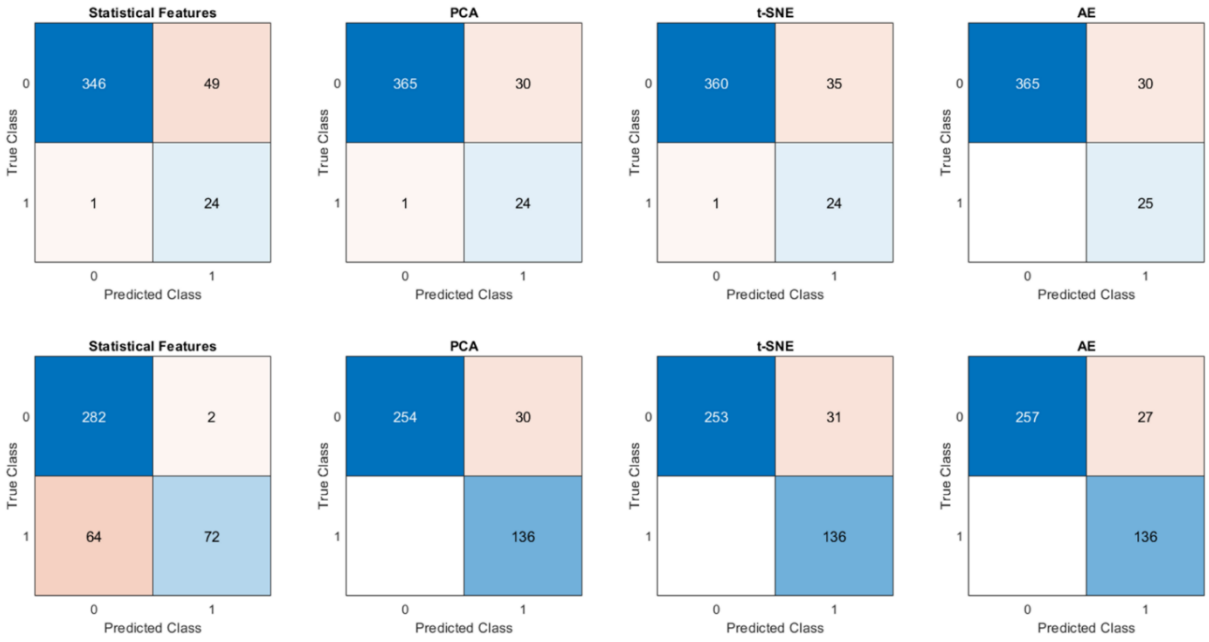


Figure 11. 0.1-s Segment Data Confusion Charts for Test Predictions

SVM classification accuracies for ten segments per second data are provided in Figure 12. These results indicate that the application of dimensionality reduction yielded more satisfactory prediction accuracies with SVM classification.

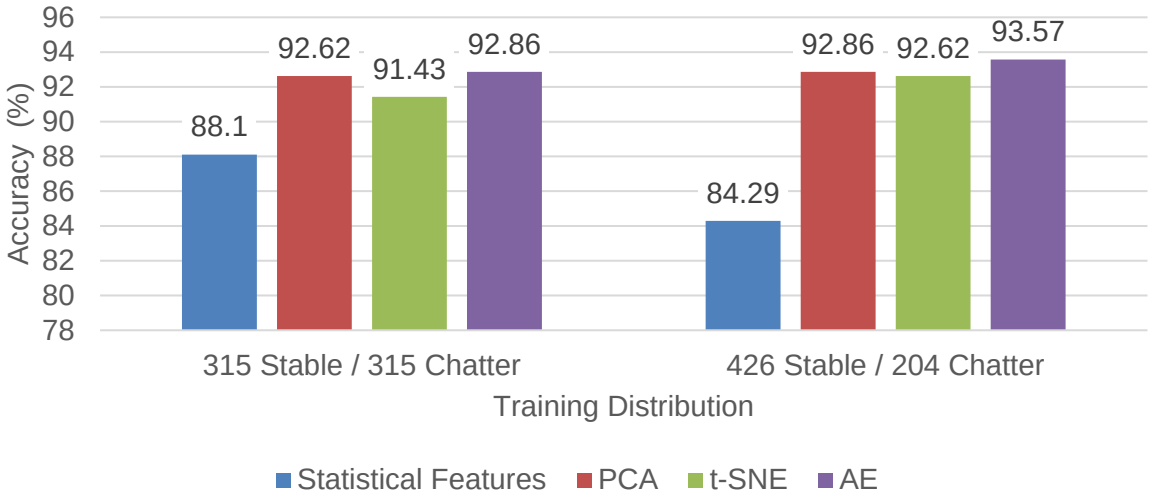


Figure 12. 0.1-s Segment Data SVM Accuracy Bar Chart for Test Predictions

As shown in Figure 11 and Figure 12, PCA and AE applied data identically predicted stable better than t-SNE for 315 stable/315 chatter distribution and AE classify chatter samples better than other data sets. Additionally, statistical features predicted chatter data as same as PCA and t-SNE. For 426 stable/204 chatter data distribution, statistical features predicted stable better than reduced features. The use of dimensionally reduced features compared to statistical features as inputs to the SVM classifier resulted in higher prediction accuracies. These differences between accuracies can only be attributable to dimensional reduction. The main limitation is the lack of data. The findings of the experiment indicate that dimensionality reduction increased accuracy performance and get better prediction results with SVM classification. Also, results demonstrated that PCA and AE yield better outcomes.

4. CONCLUSION AND FUTURE WORK

The effects of dimensionality reduction methods for chatter detection are presented in this paper. Dynamic behavior of the milling process is the main cause of the chatter phenomenon. Vibration signal data were collected from an accelerometer which was fixed on the spindle housing of the CNC machine tool. Labeling was conducted as stable (0) and chatter (1). Vibration signals are reshaped as 0.5-second segment and 0.1-second segment to expand the dataset**,** increase the amount of chatter data, and detection of different signal length effects. Also, two different training-test scenarios were specified to compare their effects on accuracies with different training ratios, and distributions to each reshaped data.

In this study, different types of techniques; PCA (linear), t-SNE (non-linear), and Autoencoder (artificial neural network) are utilized as feature reduction methods to statistical time-domain features which were extracted from reshaped vibration signals, and a linear SVM classification applied for chatter detection. Test accuracies of statistical features were compared to dimensionally reduced features.

Consequently, feature reduction applied data were observed more accurately with SVM classification. As a result, it is concluded that features dimensionally reduced with PCA and AE yield higher classification accuracies than t-SNE when a linear SVM is used as the classifier since t-SNE is a non-linear method.

Future work is planned to use various other machine learning techniques with the best dimensionality reduction techniques identified in this paper.

ACKNOWLEDGMENTS

The authors would like to be grateful to Prof. Dr. Yusuf Altintas for supplying CutPRO™ software and the technical assistance of the MAL Inc. team in this study. The authors also sincerely acknowledge the advanced manufacturing laboratory technician, Mr. Kamil Arslan, for his support throughout the data collection.

This research was supported by The Scientific and Technological Research Council of Turkey, TUBITAK 1001 project no. 118M414 and 2247-C STAR-Intern Researcher Scholarship Program.

REFERENCES

1. **J. Tlusty, M. Polacek, (1963),** “The Stability of Machine Tools against Self Excited Vibrations in Machining,” International research in production engineering, ASME, pp. 465-474.
2. **S. A. Tobias, (1969),** “Machine Tool Vibration,” Blackie, London.
3. **F. Koenigsberger, J. Tlusty, (1967), “**Machine Tool Structures”, Pergamon Press, Oxford.
4. **H. Opitz, F. Bernardi, (1970),** “Investigation and Calculation of The Chatter Behavior of Lathes and Milling Machines”, Annals of the CIRP, Vol. 18, pp. 335–343.
5. **E. Budak, (1994**)**,** “The Mechanics and Dynamics of Milling Thin-Walled Structures”, Ph.D. Dissertation, University of British Columbia.
6. **Y. Altintas, E. Budak, (1995),** “Analytical Prediction of Stability Lobes in Milling”, Manufacturing Automation Laboratory, CIRP Annals, Volume 44, Issue 1, Pages 357-362. https://doi.org/10.1016/S0007-8506(07)62342-7.

7. **E. Budak, (2006),** “Analytical Models for High-Performance Milling. Part II: Process Dynamics and Stability”, International Journal of Machine Tools and Manufacture, Volume 46, Issues 12–13, Pages 1489-1499. https://doi.org/10.1016/j.ijmachtools.2005.09.010.
8. **Y. Altintas, M. Weck, (2004),** “Chatter Stability of Metal Cutting and Grinding“, CIRP Annals, Volume 53, Issue 2, Pages 619-642. https://doi.org/10.1016/S0007-8506(07)60032-8.
9. **Y. Altintas, (2012),** “Manufacturing Automation: Metal Cutting Mechanics”, Machine Tool Vibrations and CNC Design. Cambridge University Press, Cambridge.
10. **S. Smith, J. Tlusty, (1991),** “An Overview of Modeling and Simulation of The Milling Process”, J. Eng. Ind.,113(2): 169-175. https://doi.org/10.1115/1.2899674.
11. **Y. Chen, H. Li, X. Jing, L. Hou, X. Bu, (2019),** “Intelligent Chatter Detection Using Image Features and Support Vector Machine”, Int J Adv Manuf Technol 102, 1433–1442. https://doi.org/10.1007/s00170-018-3190-4.
12. **Z. Yao, D. Mei, Z. Chen, (2010),** “On-line Chatter Detection and Identification Based on Wavelet and Support Vector Machine”, Journal of Materials Processing Technology, Volume 210, Issue 5, Pages 713-719. https://doi.org/10.1016/j.jmatprotec.2009.11.007.
13. **K. Li, S. He, B. Luo, B. Li, H. Liu, X. Mao, (2019),** “Online Chatter Detection in Milling Process Based on VMD and Multiscale Entropy”, Int J Adv Manuf Technol 105, 5009–5022. https://doi.org/10.1007/s00170-019-04478-4.
14. **I. Kvinevskiy, S. Bedi, S. Mann, (2020),** “Detecting Machine Chatter Using Audio Data and Machine Learning”, Int J Adv Manuf Technol 108, 3707–3716. https://doi.org/10.1007/s00170-020-05571-9.
15. **E. Kuljanic, G. Totis, M. Sortino, (2009),** “Development of An Intelligent Multisensor Chatter Detection System in Milling”, Mechanical Systems and Signal Processing, Volume 23, Issue 5, Pages 1704-1718. https://doi.org/10.1016/j.ymssp.2009.01.003.
16. **M. Kuntoglu, E. Salur, M. K. Gupta, M. Sarikaya, D. Y. Pimenov, (2021),** “A State-of-The-Art Review on Sensors and Signal Processing Systems in Mechanical Machining Processes”, Int J Adv Manuf Technol 116, 2711–2735. https://doi.org/10.1007/s00170-021-07425-4.
17. **H. Cao, K. Zhou, X. Chen, X. Zhang, (2017),** “Early Chatter Detection in End Milling Based on Multi-Feature Fusion And 3σ Criterion”, Int J Adv Manuf Technol 92, 4387–4397. https://doi.org/10.1007/s00170-017-0476-x.
18. **S. Wan, X. Li, Y. Yin, J. Hong, (2021),** “Milling Chatter Detection by Multi-Feature Fusion and Adaboost-SVM”, Mechanical Systems and Signal Processing, Volume 156. https://doi.org/10.1016/j.ymssp.2021.107671.

19. **M. Lamraoui, M. Barakat, M. Thomas, M. Badaoui, (2015),** "Chatter Detection in Milling Machines by Neural Network Classification and Feature Selection", Journal of Vibration and Control, Volume: 21, issue: 7, page(s): 1251-1266. https://doi.org/10.1177/1077546313493919.
20. **Y. Fu, Y. Zhang, H. Gao, T. Mao, H. Zhou, R. Sun, D. Li, (2019),** "Automatic Feature Constructing from Vibration Signals for Machining State Monitoring", J Intell Manuf 30, 995–1008. https://doi.org/10.1007/s10845-017-1302-x.
21. **P. Gupta, B. Singh, (2020),** "Local Mean Decomposition and Artificial Neural Network Approach to Mitigate Tool Chatter and Improve Material Removal Rate in Turning Operation", Applied Soft Computing Journal, Volume 96, Issue C. https://doi.org/10.1016/j.asoc.2020.106714.
22. **M. Postel, B. Bugdayci, K. Wegener, (2020),** "Ensemble Transfer Learning for Refining Stability Predictions in Milling Using Experimental Stability States", Int J Adv Manuf Technol 107, 4123–4139. https://doi.org/10.1007/s00170-020-05322-w.
23. **I. Oleaga, C. Pardo, J. J. Zulaika, A. Bustillo, (2018),** "A Machine-Learning Based Solution for Chatter Prediction in Heavy-Duty Milling Machines", Measurement, Volume 128, Pages 34-44. https://doi.org/10.1016/j.measurement.2018.06.028.
24. **C. Liu, Y. Li, G. Zhou, W. Shen, (2018),** "A Sensor Fusion and Support Vector Machine Based Approach for Recognition of Complex Machining Conditions", Journal of Intelligent Manufacturing, Volume 29, Issue 8, pp 1739–1752. https://doi.org/10.1007/s10845-016-1209-y.
25. **J. Dalzochio, R. Kunst, E. Pignaton, A. Binotto, S. Sanyal, J. Favilla, J. Barbosa, (2020),** "Machine Learning and Reasoning for Predictive Maintenance in Industry 4.0: Current Status and Challenges", Computers in Industry, 123, 103298. https://doi.org/10.1016/j.compind.2020.103298.
26. **K. Pearson, (1901),** "LIII. On Lines and Planes of Closest Fit to Systems of Points in Space", The London, Edinburgh, and Dublin Philosophical Magazine and Journal of Science: Vol. 2, No. 11, pp. 559-572. https://doi.org/10.1080/14786440109462720.
27. **H. Hotelling, (1933),** "Analysis of a Complex of Statistical Variables into Principal Components", Journal of Educational Psychology, 24, 417-441. https://doi.org/10.1037/h0071325.
28. **I. T. Jolliffe, (2002),** "Principal Component Analysis", Springer.
29. **C.M. Bishop, (2006),** "Pattern Recognition and Machine Learning", Springer.
30. **A. Ilin, T. Raiko, (2010),** "Practical Approaches to Principal Component Analysis in the Presence of Missing Values", Journal of Machine Learning Research, 11, pp. 1957-2000.
31. **R. Vidal, Y. Ma, S. S. Sastry, (2016),** "Principal Component Analysis in Generalized Principal Component Analysis", New York, Springer.

32. **L. Maaten, G. Hinton, (2008),** “Visualizing Data using t-SNE”, Journal of Machine Learning Research 9, 2579-2605. http://jmlr.org/papers/v9/vandermaaten08a.html.
33. **Y. Hamid, M. Sugumaran, (2019),** “A t-SNE based Non-linear Dimension Reduction for Network Intrusion Detection”, Int. j. inf. technol. 12, 125–134. https://doi.org/10.1007/s41870-019-00323-9.
34. **G. E. Hinton, R. R. Salakhutdinov, (2006),** “Reducing the Dimensionality of Data with Neural Networks”, Science, 504-507. https://doi.org/10.1126/science.1127647.
35. **A. Proteau, R. Zemouri, A. Tahan, M. Thomas, (2020),** “Dimension Reduction and 2D-Visualization for Early Change of State Detection in a Machining Process with a Variational Autoencoder Approach”, Int J Adv Manuf Technol 111, 3597–3611. https://doi.org/10.1007/s00170-020-06338-y.
36. **V. Nasir, F. Sassani, (2021),** “A Review on Deep Learning in Machining and Tool monitoring: Methods, Opportunities, and Challenges”, Int J Adv Manuf Technol 115, 2683–2709. https://doi.org/10.1007/s00170-021-07325-7.
37. **C. Cortes, V. Vapnik, (1995),** “Support-Vector Networks”, Machine learning, 20, p.273-297. https://doi.org/10.1007/BF00994018.

DEVELOPMENT OF AN ONTOLOGY BASED DYNAMIC PROCESS PLANNING AND SCHEDULING METHODOLOGY FOR DISRECETE MANUFACTURING SYSTEMS

Elaf Riyadh Resen Al-HUMAIRI, *elafella915@gmail.com,* Atilim University, 06830, Ankara, Türkiye

Bahram LOTFI, *Bahram.lotfi@atilim.edu.tr,* Atilim University, 06830, Ankara, Türkiye

Saman AMİNBAKHSH, *saman.aminbakhsh@atilim.edu.tr,* Atilim University, 06830, Ankara, Türkiye

ABSTRACT

Manufacturing companies are being pushed toward flexible manufacturing systems by tough global market rivalry and constantly changing client expectations. Process planning and scheduling procedures are therefore extremely important for manufacturers. These processes become even more crucial in the case of flexible job shops with volume and product type flexibility. "Industry 4.0" introduces new possibilities by merging computer and information technologies with manufacturing systems to cope with increasing competition and improve process planning and scheduling efficiency. In this research, an ontology-based metal cutting domain model is created and the reasoning rules for generating feasible solution(s) for the process planning phase are developed. Outcoming results from this process are injected into the Lekin scheduling program to produce the most optimized scheduling solution for the problem.

Keywords: Dynamic process planning and scheduling, ontology-based modelling, SPARQL, Lekin.

1. INTRODUCTION

Process planning is concerned with the selection of manufacturing processes, such as tooling, fixtures, machines, operation sequences, and assembly [1]. Process planning is dealing with setting the sequence of necessary tasks, selection of machine tools, calculation of operations' duration, required tools etc. are performed. The outcome of process planning is routing sheets,

which previously were prepared manually by process planners. Today this complicated process is mostly carried out with the help of computer systems called “Computer-aided Process Planning (CAPP)”. CAPP systems are quite effective especially in small-sized batches with higher numbers of varieties in production. However, for a CAPP system for being highly effective, it is inevitable to work coherently with related Computer-Aided Design (CAD) and Computer-Aided Manufacturing (CAM) systems and obtained results should always be inspected by the human factor [1].

CAPP systems based on their approaches to solve process planning problems, are divided into four main groups called; generative, semi-generative, variant methods and expert systems [2, 3]. In “Variant” method, Group Technology (GT) which is used which tries to find similarity between products and categorize them according to these similarities and prepare equivalent process plans with minimal changes. While, in “Generative” method process plan is generated based on given part geometries, defined algorithms and rules [4]. Semi-generative approaches are in fact a mixture of generative and variant methods, in which as they get benefited from the GT advantages, at the same time they also apply generative approach to create new process plan accordingly [5]. The last category, called “expert systems or knowledge-based” systems. These systems are developed mostly after 1980’s where Artificial Intelligent (AI) tools are started to being used in most of fields and one of these fields was CAPP [5]. As it is clear from the name these systems are essentially based on available knowledge and system’s past experiences. Several studies are carried out to integrate Artificial Intelligent (AI) into CAPP systems to enhance their capabilities in making various decisions particularly when they are dealing with new parts [6]. AI actually imitates the behavior of an intelligent expert by involving some computations to establish reasonable relations between known information and new encountered experiences. In fact, AI tries to mimic the human being actions and eliminate the necessity for human expert presence in CAPP systems [3]. Implementation of AI in CAPP systems demand several developments in CAPP systems infrastructure. One of the very first attempts to use expert systems reasoning in CAPP and generate a process planning is done by Van’t Erve and Kals (1986) by developing XPlane which uses graph search method and produces alternative process plans according to the shape of the product and by comparing the cost of each alternative selects the optimum choice [7]. But later on, from the 2000s various technologies like; the feature-based technologies, knowledge-based systems, neural network, heuristic and meta-heuristic methods, fuzzy set theory/logic, Petri net (PN), agent-based technologies, Internet-enabled CAPP, STEP-compliant CAPP to enhance the intelligence in process planning procedure and reduce systems dependency on human.

Moving towards the smart future, almost all objects and systems like, phones, TVs, homes, etc. are being upgraded to attain a certain level of intelligence. The word “intelligence” here means these things are becoming gradually self-aware, and by detecting the environmental changes they may autonomously make appropriate decisions and possibly develop and apply new strategies to enhance their performance efficiency. This trend is going to evolve in the future and affects almost all sectors. This future is being formed to be based on the internet of things (IoT) and application of this formation in industry and manufacturing appears under the name of Industry 4.0 which is using the IoT infrastructure for its own purposes. Perhaps the most important building block in such systems is the capability to communicate and reach a mutual understanding between such platform entities which are machines, software, and humans. Therefore, all these entities are ought to use a common language to understand and also be understood by the interlocutor. It is crystal clear that developing such a platform (new language to cover all life clusters and sectors) is impossible and to reach that aim, the most applicable way seems to develop related subjects’ own domain-specific communication platform then integrate these platforms together.

In order to develop a reasonable process plan, CAPP requires acquiring data and information from various data sources like CAD modules, enterprise resource management systems, inventory management etc. and also needs to send data to other modules like CAM, finance, operations management, and probably others. Since each of these departments or modules are dealing with a different type of data, CAPP should be able to interpret these various data types and information and also send formatted data as is required by the receiver department. Thus, to support previously named enabler technologies for expert CAPP systems it is necessary to establish an infrastructure capable of dealing with heterogeneous data sources and enable the communication between these various modules and departments. To this purpose and to improve semantic consistency in CAPP systems, enhance its autonomous reasoning process, and integrate to the other modules the ontology domain modelling is proposed as a potential solution.

In this approach various domains are modelled according to their own requirements and prerequisites, afterwards, a rule-based reasoning process is done and based on these new inference model entities which are deduced during the reasoning procedure, the system may conclude its decision. In the case of process planning, since the manufacturing domain is an extremely vast area, it can be divided further into sub-domains. Then, for each sub-domain, a

separate model can be developed and these sub-domains can be matched and integrated together to form the upper manufacturing ontology domain model.

As mentioned before, process planning selects and assigns necessary resources for required operations. However, in manufacturing enterprises the manufacturing resources (machine, staff, tool or others) are limited and related restrictions must be taken into account in the implementation of a prepared process plan on a manufacturing system. “Scheduling” is targeting to optimize resource usage by arranging, allocating, controlling and distributing works between available resources according to the acquired process plan for operations and tasks [8]. In manufacturing systems to achieve better results and optimize system performance even further, an integration between process planning and scheduling is inevitable [2, 9, 10, 11, 12, 13, 14, and 15]. Especially in Flexible Manufacturing Systems (FMS) where the importance of efficient utilization of resources is much predominantly important, this becomes a necessity rather than a preference [16, and 17].

Later on, these days to respond Industry 4.0 requirements the integration of process planning and scheduling is evolved by the introduction of more sophisticated digital solutions, to the problem of real-time integration of CAPP and scheduling. These approaches, which are agent-based systems, virtualization of manufacturing systems, system simulation by creation of cyber-physical layers, digital twins and others can be named as some of them were applied in several types of research. Continuously changing product order lists, product requirements, and dealing with random uncertainties in the production line like; failure of equipment, maintenance issues etc. turns scheduling problem into a complex problem that needs to be solved dynamically in a real-time manner [18, 19, 20, 21, and 22].

As Marquez and Ribiero are mentioned in their broad review paper on scheduling in manufacturing, there is a huge amount of research in this field and going through all applied methodologies in this area is very cumbersome [23]. On another side, as Hermann et al. have mentioned in their study, there are so many names given to various methodologies which are applied in the literature, but going deeper into the details of these methods, it can be concluded that, most of them are similar methods with negligible variances or the evolved form of another method which should be considered in researches [24]. For instance, Industry 4.0, cyber-physical systems, the internet of things, virtual enterprises, and so many other names are used for more or less similar methods.

Specific scheduling goals, such as the reduction of the make-span, flow-time, or tardiness, or the maximizing of the chance of meeting due dates or machine utilization, can be significantly enhanced by integrating scheduling with other planning functions in order to achieve desired outcomes [25, 26, 27, and 28]. To reach these goals various methodologies are employed to solve scheduling problems. Exact solutions, game theory, bio inspired meta-heuristics, machine learning, and artificial intelligence are the most widely used methodologies for this purpose [29].

The main aim of this research is to provide an integrated dynamic process planning and scheduling platform for a job shop that is capable of realizing limited metal cutting processes only (turning, milling, grinding and drilling). To achieve this goal, at the first step in order to prepare a common communication platform between different entities of the system, an ontology domain model for metal cutting processes is developed. Since this platform targets to respond dynamically it should be able to carry out a reasoning process on sensing any changes in the system instantaneously. To satisfy this requirement, the next step is to add the SWRL rules for the reasoning to the model and enable this model to deduce new inferences. The reasoning process is triggered immediately as the system state changes. For instance, if a new order is entered into the system, the reasoning process immediately starts to construe new inferences and get any new possibilities and alternative processes for better system performance. It is worth mentioning that, system data is also kept in the MySQL database, and on each reasoning, the processing system checks the possible differences between MySQL database and ontology model and if there are any, a synchronization process is started and the model is mapped to the database. However, if before the reasoning process a change comes up in the MySQL database, the system immediately updates the model, then runs the reasoning process and after creating the inference model, it is written again back to the database. Parallel to this database, the SPARQL results for being used in scheduling are formatted in an Excel file. If query results bring any changes the scheduling process is carried out. To reach this aim, Lekin program with multiple built-in heuristics and dispatching rules is employed in this research which targets to reduce overall make-span, maximum tardiness, total flow time and total tardiness according to the changing environmental conditions. The process results in form of Gantt Charts, performance metrics, and list of assigned tasks to each working station are derived at the end of the process.

2. METHODOLOGY

The very first step to developing an ontology model is to define the concepts, classes, and properties. Since the definition of process planning is the selection of the appropriate manufacturing processes, such as tooling, fixtures, machines, operation sequences, and assembly to produce a part or product, clearly it deals with product specs and available equipment. Therefore, the ontology model which is going to be used for process planning purposes should definitely contain parts, available equipment, tools, and also their properties. Considering these facts, the developed ontology model entities and structure is defined in a way to encapsulate all these requirements.

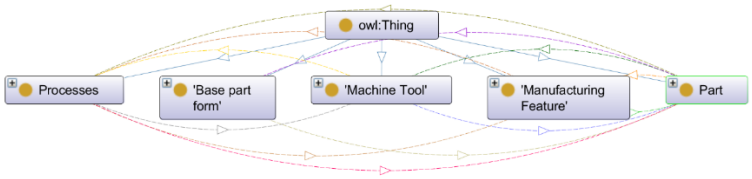


Figure 1. Main classes of ontology model

As shown in Figure 1 five main classes are designed to cover the required functionalities for this model. These classes are; part, base part form, machine tool, process, and manufacturing features. In order to produce a part, the process plan aims to assign required manufacturing processes to the part. Since parts are consisting of one or multiple features and each of these features to be shaped needs different manufacturing processes, thus through these manufacturing feature parts can be related to the required processes. Meanwhile, to realize a process an appropriate machine tool capable of realizing that process also is needed. Therefore, through the process, the part can be related to a specific type of machine tool(s). The base part form actually indicates the hypothetical shape and size of enveloping object prior to start the process. This class is added to ensure that the part could be processed in the selected machine tool and it also may assist to assign any required tool or fixtures during the process planning process.

After classes axioms in the OWL model, the properties are needed to be defined next. There are two types of properties in the OWL DL dialectic. The first one is “object property” which represents the relation between entities in the model. In RDF triples it is also named as “predicates”. Since object properties are connecting (relating) two objects (entities) two each other, they act like functions that have domains and ranges. Or in other words, they relate the domain entity to the range entity and these object properties do also possess a name-space and exactly like other resources in OWL models, they get a URI which is a combination of

model URI and name-space of property. In Listing 1 a sample definition of an object property in the OWL DL model is given.

```
<!-- http://www.semanticweb.org/bahram/ontologies/2021/3/untitled-ontology-2\#machine_processes -->
<owl:ObjectProperty rdf:about="http://www.semanticweb.org/bahram/ontologies/2021/3/untitled-ontology-2#machine_processes">
        <owl:inverseOf rdf:resource="http://www.semanticweb.org/bahram/ontologies/2021/3/untitled-ontology-2#process_needs_machine"/>
        <rdfs:domain rdf:resource="http://www.semanticweb.org/bahram/ontologies/2021/3/untitled-ontology-2#machineTool"/>
        <rdfs:range rdf:resource="http://www.semanticweb.org/bahram/ontologies/2021/3/untitled-ontology-2#processes"/>
</owl:ObjectProperty>
```

Listing 1. RDF/XML machine_processes object property representation

The created object properties for the model, assigned domain and range classes and also the main purpose for conception such a relation is depicted in Table 1.

Table 1 Model object properties, their domain, range, and description.

Object Property Name-space	Domain	Range	Description	Inverse Object Property
Base form is at parts	Base part form	Part	To connect the part(s) with existing base feature	Part has base form of
Feature need process	Manufacturing feature	Processes	To relate enabler processes for the available feature	Process make feature
Features are available at part	Manufacturing feature	Part	To search which part(s) has(have) this feature	Part has features
Machine can work on part	Machine tool	Part	to relates potential parts to the machine tool	Part can be assigned to machine
Machine processes	Machine tool	Processes	connects possible processes to the machine tool	Process needs machine
Part can be assigned to machine	Part	Machine tool	relates potential machine tools to work on the part	Machine can work on part
Part has base form of	Part	Base part form	To relate parts current base form to specified base form category	Base form is at parts
Part has features	Part	Manufacturing feature	To relate all available manufacturing features of the part to the model features	Features are available at part
Part needs process	Part	Processes	To connect all required manufacturing processes to the part	Process is applied on part
Process is applied on part	Processes	Part	To relate all process manufacturing feature of the Processes to the model feature	Part needs process
Process makes feature	Processes	Manufacturing feature	To connect all features which are made by the feature	Feature need process
Process needs machine	Processes	Machine tool	To connect all possible machine tools to carry out the process	Machine processes

Other types of properties which are used in ontology models are datatype properties. This type of property is used to assign literal values to model entities. But like all other entities in owl models, these entities also should be addressed with a specific URI and this URI also should be standardized. Figure 2 depicts the list of used datatypes in the developed ontology model in this research. As shown in this figure, model datatype properties are classified under four main classes. These classes are; “dimensional_props”, “machine_props”, “material_props”, and “mechanical_props”.

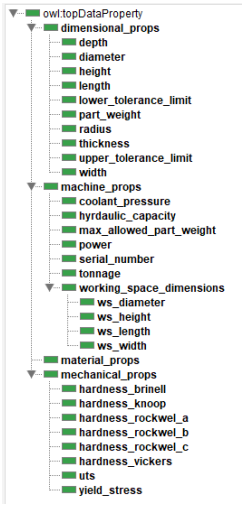


Figure 2. Defined datatype properties in CAPP ontology model

These classes can be altered and updated anytime due to the system's changing requirements. The first datatype properties class (dimensional_props) contains the general measurement and design values. These literal values are mostly floating numbers (xsd:float). The second group is including the machine tools' properties. In this class, various literal values are used for the range of these properties. For instance, the "serial number" has the range of "xsd:string" while the "coolant pressure" property's range is "xsd:float". The "mechanical props" category has the datatype properties regarding mechanical properties like; hardness, compressive and tensile strength values and etc. Here also, various types of literal values are assigned to the properties' ranges according to their usage. The datatype properties, domains are also important and it is certainly vital from a reasoning perspective to assign appropriate domains for these properties.

Transfer model to Jena platform and reasoning

Jena platform is an open-source free java-based programming toolkit that is developed to carry out more detailed actions on ontology models with various standards. Jena platform provides a language-neutral programming interface for ontology development. In Jena, all model information is encoded as RDF triples (as Jena statements) which are stored in the RDF model. The most important advantage of handling ontology models in the Jena platform is to develop an ontology-based application and use a reasoner to infer new statements from the model. Semantic consistency is one of the crucial issues that is utterly important to be checked during the domain ontology model development process. When a domain ontology is developed from heterogeneous data sources, accidentally semantic collisions in the model are inevitable. Therefore, after each modification, it is definitely required to verify the changes and check the

ontology model consistency [30]. In Protégé, the HermiT algorithm is the tool to check the consistency of the model. Parallel to this, a customized consistency algorithm is developed in Jena to check the consistency of the model. HermiT can also handle the added OWL syntax supported rules to the ontology [31]. In order to use HermiT reasoner engine, OWL syntax supported rules which are developed in Semantic Web Rules Language (SWRL) are provided to the ontology in Protégé. Besides, the Jena rules are provided in a specific format in accordance with the requirements of the reasoner engine. Therefore, a list of Jena rules which are equivalents of the SWRL rules are provided and the generic reasoner is implemented for this reason. Totally 28 rules are designed for consistency check and reasoning purposes for process planning.

```
public static void assign_part_to_machine() {

    OntModel model = ModelFactory.createOntologyModel();
    model.read(InferredModelURI, "RDF/XML");
    System.out.println(" ");

    String prismatic_part_size_queryString = "PREFIX rdf: <http://www.w3.org/1999/02/22-rdf-syntax-ns#> "
            + "PREFIX owl: <http://www.w3.org/2002/07/owl#> "
                + "PREFIX rdfs: <http://www.w3.org/2000/01/rdf-schema#> "
                + "PREFIX xsd: <http://www.w3.org/2001/XMLSchema#> "
                + "PREFIX onto: <http://www.semanticweb.org/bahram/ontologies/2021/10/untitled-ontology-2#>"
                + "SELECT  ?part ?x ?y ?z "
                + "WHERE {"
                + "?part rdf:type onto:part . "
                + "?part onto:part_has_length ?x . "
                + "?part onto:part_has_width ?y . "
                + "?part onto:part_has_height ?z "
                + "}";

    Query prismatic_part_size_query = QueryFactory.create(prismatic_part_size_queryString);
    System.out.println("----------------------");
    System.out.println("Sizes Query Result Sheet for Prismatic Parts");
    System.out.println("----------------------");
    QueryExecution qe = QueryExecutionFactory.create(prismatic_part_size_query, model);
    ResultSet results = qe.execSelect();
    ResultSetFormatter.out(System.out, results, prismatic_part_size_query);

    qe.close();
```

Listing 2. Part- Machine size-based-assignment SPARQL query in Jena

Since in this study the ontology model (owl) is based on RDF standards and an RDF store is established to store data and knowledge, to extract data which is in fact the results from the process planning phase, SPARQL query language is used. The scheduling process requires a list of assigned potential parts along with calculated machining duration, needed tools and etc. Therefore, the data from ontology should be extracted and formatted as the scheduling algorithm requested. For this purpose, multiple SPARQL queries are developed and each query is responsible to collect specific information about scheduling algorithm requirements. For instance, Listing 2, illustrates one of the SPARQL queries which intends to find assigned parts to the machines based on their sizes. As described before Jena is a Java-based program and since SPARQL queries are also developed and integrated into the Jena platform, it is written in Java.

After the reasoning process, the process planning information should be sent to the Lekin program for scheduling purposes. The Lekin software accepts special files formats for process planning information therefore, the reasoning outcomes should be formatted accordingly. This process is done with a designed ontology model, Lekin interface and the acquired data is written into two separate files with '. job' and '. mch' extensions for part and machine information, respectively. The first file is including machine park information with a customized extension of (*.mch). The second file includes part information with the (*.job) extension. This file contains job, operation sequence, machining time, release and due dates. In order to send data in form of the requested format, an interface between Jena and the Lekin program is prepared. Figure 3 depicts an example of these two extensions.

```
Shop:           Job
Job:            J1
  RGB:            174;230;197
  Release:        0
  Due:            150
  Weight:         1
  Oper:           Turning;5;A
  Oper:           Milling;3;A
  Oper:           Grinding;3;A
  Oper:           Boring;3;A
  Oper:           Broaching;10;A
  Oper:           Shaping;9;A

Job:            J2
  RGB:            96;64;247
```

a) Data format sample for *.job files

```
Ordinary:
Workcenter:     Turning
  RGB:            108;156;150
  Release:        0
  Status:         A

Workcenter:     Milling
  RGB:            96;25;44
  Release:        0
  Status:         A

Workcenter:     Drilling
  RGB:            38;168;2
  Release:        0
  Status:         A
```

b) Data format sample for *.mch files

Figure 3 Defined datatype properties in CAPP ontology model

Scheduling

The job shop scheduling problem is regarded as one of the most challenging problems to solve from both a theoretical and a practical. Even with a smaller number of machines and job operations, the problem is an NP-hard problem [32, 33, 34, and 35]. As mentioned in the literature the job shop scheduling (JSSP) as one of the most difficult computationally intractable problems is an NP-hard problem type [36, 37, 38, and 39]. The complexity of these problems increases exponentially as the number of machines and operations increases [39, and 40]. Job shop scheduling problems including 10 machines and 10 operations remained unsolved for almost 20 years, till Carlier and Pinson offered an exact integer programming method in 1989 [41]. After that, dynamic programming [42], branch and bound algorithms applications in job shop scheduling [43, and 44] are offered to find the optimal solutions. As the complexity of JSSP increases, exact solutions faces lots of problems and they become

unfeasible to solve. Therefore, a large number of heuristic approaches like; bottleneck heuristic to decompose problems into smaller problems with the aim of minimizing total job accomplishment duration, Hibret Manufacturing and Machine Building Industry (HMMBI), to respond scheduling of flexible production systems with high rates of product type and volume flexibility. This method targets to minimize maximum tardiness or total makespan.

In this study, a flexible dynamic job shop scheduling problem is needed to be solved. Uncertainty is one of the most common issues in manufacturing organizations which cannot be ignored and it should be included in calculations especially in the case of scheduling. However, in order to facilitate the calculations and reduce complex problems to rather simple problems with solutions uncertainty are ignored in most researches. In this study during th process planning phase and assigning potential resources to the requested processes, uncertainties like machine failures, maintenance procedures and others are considered and unavailable resources are ignored during the resources allocation process.

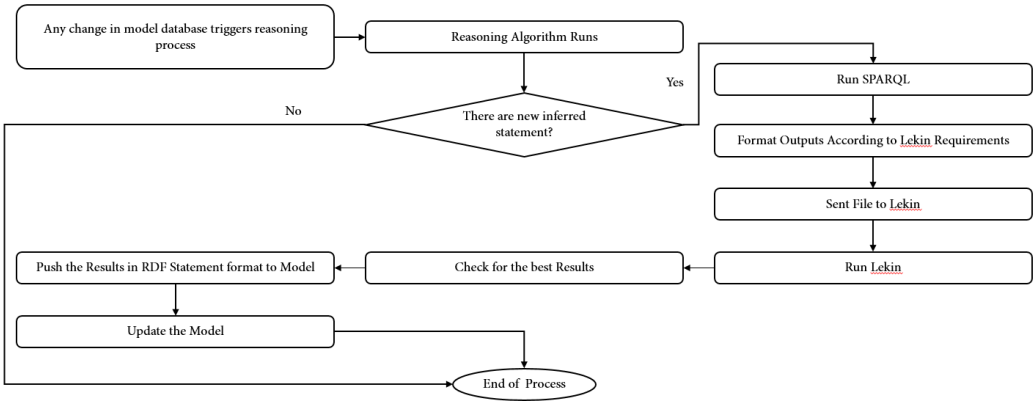


Figure 4 Dynamic Flexible Job Shop Scheduling Process

As shown in Figure 4, in the process planning phase as mentioned before, upon any changes in system data, a new reasoning process is executed and new inferred statements are created and the model is updated. The same approach is followed in the scheduling process. As model data changes, scheduling checks the environmental conditions, and if there are any changes with respect to the last scheduling inputs, the algorithm is run and new scheduling is created and sent to the production department. In this study, Lekin® software is used to obtain various embedded heuristic methods' results. Lekin® is a scheduling software designed and developed by Stern School of Business, New York University and coded by Columbia University Students and partially supported by National Science Foundation (NSF). Then the obtained results from heuristics are analyzed and the best outcome which is the minimum makespan, is selected and the scheduling information, such as; machine program, job routing,

tooling and processing times are set in triples (RDF statements) format and sent to model and the model is updated accordingly.

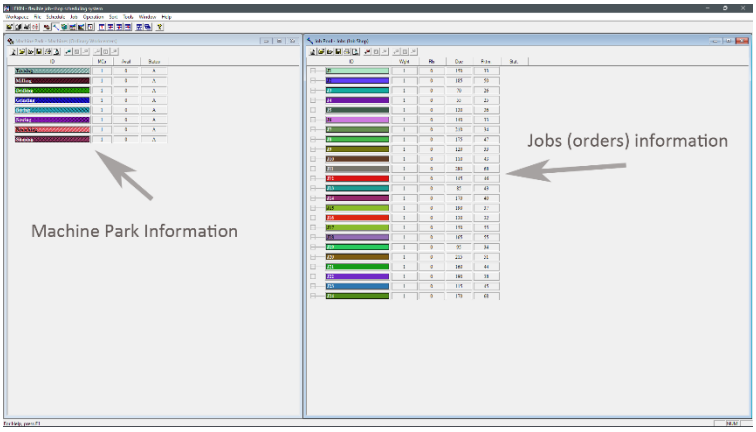


Figure 5 Lekin Graphical User Interface

Figure 5 illustrates the Lekin program graphical user interface (GUI). The imported data from the ontology model are shown in this figure. The left side of this environment contains the machine park information. This information is obtained from the “machine.mch” file. The right side of the environment is depicting the orders or jobs information. Job information is gained from the “jobs.job” file. A sample view of the machine.mch and jobs.job files are given in Figure 3 Both of these sections are updated upon any changes on the model, therefore, each time the scheduling process is executed, it uses different inputs, thus it gives a new scheduling result and update the shop floor scheduling Gantt Chart accordingly.

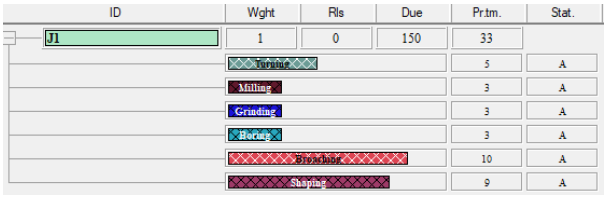


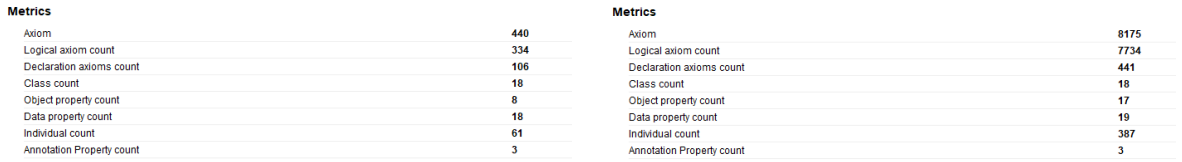
Figure 6 Job (order) process information in Lekin GUI

Figure 6 presents the job (order) information in the Lekin program. Job information contains a list of processes that are required to realize that job, their sequence, the necessary duration for each operation (process), the status of the operation, weight, the due date for that job and also release date. All durations are in minutes and the upper operation is the precedence operation to the lower one. The weight of the job is the importance of that order. By default,

the value “1” is given to all jobs however, if one job has higher priority and is needed to be processed immediately, according to the level of emergency, this weight can be increased. The next important parameter is release date which indicates the date of availability for that specific job. In other words, the order would be available to be processed after the release date. Finally, the job due date is the maximum available time period for processing the job and if overall processing time passes this due date period, a penalty for job tardiness is applied.

3. RESULTS AND DISCUSSIONS

Provided base model in this research as shown in Figure 7a had around 440 axioms. This figure also illustrates that the base model had 18 classes, 8 object properties, 18 data properties, and 61 individuals. However, after running the reasoning algorithm the number of ontology model axioms as shown in Figure 7b increases dramatically to 8175 axioms while the number of classes is the same. During the consistency check, the 9 object properties are added to the model, data properties became 19, and the number of individuals increased more than 6 times to reach 387. As clear from these numbers the ontology model grew almost 20 times after the reasoning process. For instance, before the reasoning process, there was no relation between parts and machine tools, but after the reasoning process, appropriate parts through manufacturing features, base features and manufacturing processes are connected to various machine tools.



Metrics

Axiom	440
Logical axiom count	334
Declaration axioms count	106
Class count	18
Object property count	8
Data property count	18
Individual count	61
Annotation Property count	3

Metrics

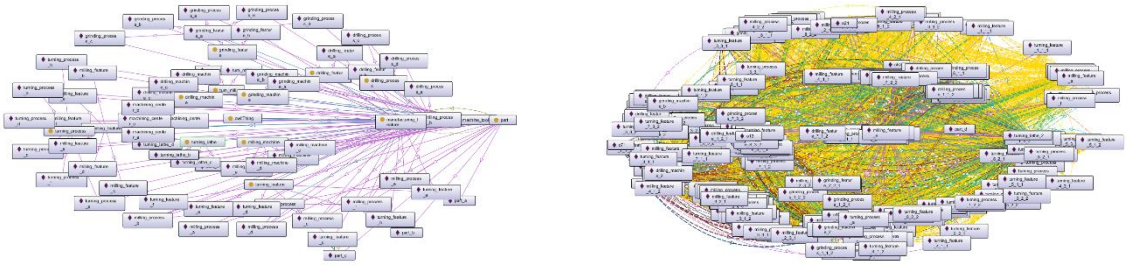
Axiom	8175
Logical axiom count	7734
Declaration axioms count	441
Class count	18
Object property count	17
Data property count	19
Individual count	387
Annotation Property count	3

a) Before Reasoning Process b) After Reasoning Process

Figure 7 Ontology Model Metrics

In order to understand better the results of the reasoning process on the model axioms, it would be helpful to check models’ ontograph (visualization of models) before and after the reasoning process. While Figure 8a is the visualized form of the base model, Figure 8b depicts the inferred model’s ontograph. At first, the most eye-catching issue is the tremendous increase in number of entities and relations in the inferred model in comparison with the base model. But, the important thing here, rather than a huge increase in the number of entities is in the nature of available relations between those entities. Looking carefully at Figure 8b it

seems most of the relations are in the type of “is_a” relation which is shown by the purple colour. However, in Figure 8b, there are various relations among model entities which each of them are distinguished with different colours.



a) Before Reasoning Process b) After Reasoning Process

Figure 8 Ontology Model

Scheduling is carried out by Lekin software with different heuristics, and the results of various heuristics are compared with each other. The performance of each heuristic method will be evaluated with different performance metrics in this section. Obviously, at each run various outcomes would be acquired therefore, the results represented in the following section may not be repeated in the later algorithm runs, however, the main intention here is to compare the results between heuristics rather than concentrating on the obtained individual results. The other important issue is the applied dispatching rules. Any change in dispatching rules affects the heuristic algorithms’ results. The first heuristic which is applied is General Shifting Bottleneck (SB) Routine with the intention to minimize the makespan. The algorithm outcome Gantt Chart and performance metrics are presented in Figures 9 and 10 respectively. Inspecting the results show that after 6 runs this routine obtains an overall makespan of 186 minutes, maximum tardiness of 26 minutes, and Five jobs past the due date.

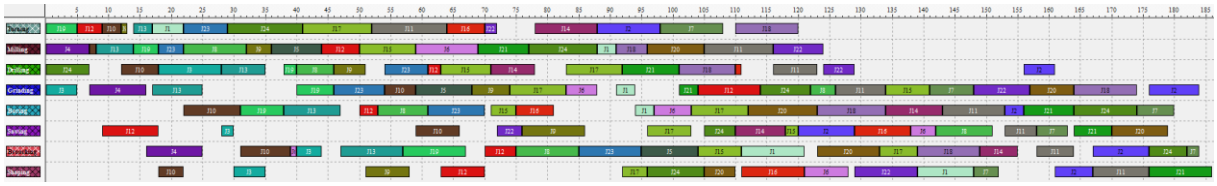


Figure 9 General Shifting Bottleneck Routine with Minimizing Makespan Gantt Chart

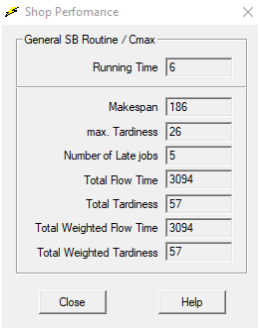


Figure 10 General Shifting Bottleneck Routine with minimizing makespan Performance

Applying the same SB routine with different performance metrics than makespan affects the results marginally. This time instead of makespan, reducing the maximum tardiness is the main target of the algorithm. The total makespan increases to 229 minutes, however, maximum tardiness becomes zero at this point. This means no jobs go beyond their due date and all jobs are delivered to customers on time and no penalty is applicable under these circumstances.

SB routine with minimizing the maximum flow-time gives totally different outcomes. In this scenario, the total makespan is 192 minutes which is longer than the first scenario but much shorter than the second scenario however the main difference is in total flow time which is the main objective of this routine. The total flow time is 2796 minutes which is 200 minutes less than the previous scenario and more than 300 minutes less than the first scenario. The disadvantage of this method is the larger tardiness value and a greater number of jobs with lateness. In this method, 6 jobs are late and pass the assumed due date.

The other important target is to minimize the total tardiness using the SB routine. In this case, the target is to minimize the overall tardiness of all 24 jobs and reduce lateness. In this scenario, the overall makespan becomes 233 minutes, while the maximum tardiness and total tardiness values are zero. The total flow time however, increases drastically to 3109 minutes which is the largest total flow time value among four scenarios up to this point. Larger total flow time means longer usage of the resources and this results in larger energy and human resource consumption which increases the process cost. But, the advantage of this method like minimizing the maximum tardiness is avoiding the penalty due to job lateness and enhancing customer satisfaction. It is worth mentioning the difference between minimizing the maximum tardiness and total tardiness performance metrics. In minimizing the maximum tardiness, the target is to minimize the tardiness of each job regardless of the other jobs tardiness. In this research since both methods give maximum tardiness and total tardiness

values zero, they can be misinterpreted as they are the same but, these methods are different from each other.

The next built-in heuristic of Lekin software that is used in this research is local search with different dispatching rules. Local search heuristic for finding minimum makespan result in a makespan duration of 168 minutes, maximum tardiness of 58, with 9 late jobs, total tardiness of 184 and total flow time of 2988 minutes. Since the target of this algorithm was to minimize the makespan it can be said that the objective is achieved however, the other performance metrics are being deteriorated severely and tardiness, late job numbers, total tardiness and flow time exceeds far beyond SB routine results. Therefore, it can be concluded that although this method performance in minimizing the makespan was successful, the overall performance of this method is not satisfactory.

In the second approach with local search heuristics, an attempt is made to minimize the total flow time. At this approach total flow time decreased considerably by almost 22% to 2332 minutes, while makespan increased 2% and reached 172 minutes. The number of late jobs also decreased from 9 jobs to 1 job which is a huge improvement. Maximum tardiness also enhanced 88% and become 7 minutes. Accordingly, total tardiness falls down more than 96% from 184 minutes to 7 minutes. Considering these two local search algorithms local search with the objective function to minimize the total flow time gives many more satisfactory results than local search with an objective function for minimizing the makespan.

A local search heuristic with the objective of minimizing total tardiness is the next approach that is tested in this research. The total tardiness reduced to zero with a price of a considerable increase in makespan and total flow time. In this method, the makespan value increased 15% from 172 minutes to 197 minutes, the number of late jobs reduced to zero while the previous value was only one. Maximum tardiness is zero which the main intention in this approach was to achieve the minimum value and it can be proved that method has reached its objective. The total flow time increased more than 21% to 2829 minutes which is not acceptable and this will increase the overall production cost.

Table 2 Different Heuristics/ rules performance metrics

Heuristic/ Rule	Makespan	Total Flow Times	Max Tardiness	Total Tardiness	Number of Late Jobs
General SB Routine (Minimize Makespan)	186	3094	26	57	5
General SB Routine (Minimize Max Tardiness)	229	2966	0	0	0
General SB Routine (Minimize Total Flow Time)	192	2796	42	145	6
General SB Routine (Minimize Total Tardiness)	233	3109	0	0	0
Local Search (Minimize Makespan)	170	2918	49	174	8
Local Search (Minimize Total Flow Time)	183	2336	10	17	2
Local Search (Minimize Total Tardiness)	202	2776	0	0	0
MS	204	2913	0	0	0
FCFS	198	2865	88	367	7
LPT	212	4118	137	737	18
SPT	231	2656	58	163	7
CR	211	3193	4	5	2

The overall results as depicted in Table 2, show that Local search heuristic with minimizing total tardiness gives the most optimum solution for this problem. However, by changing problem requirements the results would obviously change as well.

REFERENCES

1. S. Kalpakjian, Manufacturing engineering and technology. Upper saddle river, NJ: Pearson, 2014.
2. M. Kumar and S. Rajotia, “Integration of scheduling with computer aided process planning”, Journal of Materials Processing Technology, vol. 138, no. 1-3, pp. 297–300, Jul. 2003.
3. S. P. L. Kumar, “State of the art-intense review on artificial intelligence systems application in process planning and manufacturing”, Engineering Applications of Artificial Intelligence, vol. 65, pp. 294–329, Oct. 2017.
4. L. Alting and H. Zhang, “Computer aided process planning: The state-of the-art survey”, International Journal of Production Research, vol. 27, no. 4, pp. 553–585, Apr. 1989.
5. P. T. Chang and C.-H. Chang, “An integrated artificial intelligent computer aided process planning system”, International Journal of Computer Integrated Manufacturing, vol. 13, no. 6, pp. 483–497, Jan. 2000.
6. K. Tripathi, “A review on knowledge-based expert system: Concept and architecture”, IJCA Special Issue on Artificial Intelligence Techniques-Novel Approaches & Practical Applications, vol. 4, pp. 19–23, 2011.

7. A. Van't Erve and H. Kals, "XPLANE, a generative computer aided process planning system for part manufacturing", CIRP Annals, vol. 35, no. 1, pp. 325–329, 1986.
8. M. L. Pinedo, "Parallel machine models (deterministic)", in Scheduling, Springer US, Dec. 2011, pp. 111–149.
9. S. Sen and S. Jain, Integration of process planning and scheduling comparison of models approach, 2010.
10. R. K. Phanden, A. Jain, and R. Verma, "Integration of process planning and scheduling: A state-of-the-art review", International Journal of Computer Integrated Manufacturing, vol. 24, no. 6, pp. 517–534, Jun. 2011.
11. R. K. Phanden, A. Jain, and R. Verma, "An approach for integration of process planning and scheduling", International Journal of Computer Integrated Manufacturing, vol. 26, no. 4, pp. 284–302, Jun. 2013.
12. R. K. Phanden, Z. Palková, and R. Sindhwani, "A framework for flexible job shop scheduling problem using simulation-based Cuckoo search optimization", in Lecture Notes in Mechanical Engineering, Springer Singapore, 2019, pp. 247–262.
13. G. Chryssolouris, S. Chan, and N. P. Suh, "An integrated approach to process planning and scheduling", CIRP Annals, vol. 34, no. 1, pp. 413–417, 1985.
14. C. Saygin and S. E. Kilic, "Integrating flexible process plans with scheduling in flexible manufacturing systems", The International Journal of Advanced Manufacturing Technology, vol. 15, no. 4, pp. 268–280, Apr. 1999.
15. H. Lee and S.-S. Kim, "Integration of process planning and scheduling using simulation based genetic algorithms", The International Journal of Advanced Manufacturing Technology, vol. 18, no. 8, pp. 586–590, Oct. 2001.
16. K. Srihari, J. A. Cecil, and C. R. Emerson, "A blackboard-based process planning system for the surface mount manufacture of PCBs", The International Journal of Advanced Manufacturing Technology, vol. 9, no. 3, pp. 188–194, May 1994.
17. S. Jablonski, B. Reinwald, and T. Ruf, "A case study for data management in a CIM environment", in [1990] Proceedings. Rensselaer's Second International Conference on Computer Integrated Manufacturing, IEEE Comput. Soc. Press.
18. Y. F. Zhang, A. N. Saravanan, and J. Y. H. Fuh, "Integration of process planning and scheduling by exploring the flexibility of process planning", International Journal of Production Research, vol. 41, no. 3, pp. 611–628, Jan. 2003.
19. D. N. Šormaz, J. Arumugam, R. S. Harihara, C. Patel, and N. Neerukonda, "Integration of product design, process planning, scheduling, and FMS control using XML data representation", Robotics and Computer-Integrated Manufacturing, vol. 26, no. 6, pp. 583–595, Dec. 2010.

20. S. Wu, J. Fuh, and A. Nee, “Concurrent process planning and scheduling in distributed virtual manufacturing”, IIE Transactions, vol. 34, no. 1, pp. 77–89, Jan. 2002.
21. L. Wang and W. Shen, Journal of Intelligent Manufacturing, vol. 14, no. 5, pp. 429–439, 2003.
22. L.Wang, H.-Y. Feng, and N. Cai, “Architecture design for distributed process planning”, Journal of Manufacturing Systems, vol. 22, no. 2, pp. 99–115, Jan. 2003.
23. C. R. H. Márquez and C. C. Ribeiro, “Shop scheduling in manufacturing environments: A review”, International Transactions in Operational Research, Jan. 2022.
24. M. Hermann, I. Bücker, and B. Otto, “Industrie 4.0 process transformation: Findings from a case study in automotive logistics”, Journal of Manufacturing Technology Management, vol. 31, no. 5, pp. 935–953, Nov. 2019.
25. S. Nourali, N. Imanipour, and M. R. Shahriari, “A mathematical model for integrated process planning and scheduling in flexible assembly job shop environment with sequence dependent setup times”, International Journal of Mathematical Analysis, vol. 6, no. 43, pp. 2117–2132, Jun. 2012.
26. M. Haddadzade, M. R. Razfar, and M. H. F. Zarandi, “Integration of process planning and job shop scheduling with stochastic processing time”, The International Journal of Advanced Manufacturing Technology, vol. 71, no. 1-4, pp. 241–252, Nov. 2013.
27. S. Zhang and T. N. Wong, “Integrated process planning and scheduling: An enhanced ant colony optimization heuristic with parameter tuning”, Journal of Intelligent Manufacturing, vol. 29, no. 3, pp. 585–601, Dec. 2014.
28. L. Jin, C. Zhang, and X. Fei, “Realizing energy savings in integrated process planning and scheduling”, Processes, vol. 7, no. 3, p. 120, Feb. 2019.
29. A. Halty, a. R. Sánchez, V. Vázquez, V. Viana, P. Piñeyro, and D. A. R. and, “Scheduling in cloud manufacturing systems: Recent systematic literature review”, Mathematical Biosciences and Engineering, vol. 17, no. 6, pp. 7378– 7397, 2020.
30. S. Yang, H. Tan, and J. Wu, “Semantic Consistency Checking in Building Ontology from Heterogeneous Sources”, Journal of Applied Mathematics Volume 2014, Article Hindawi Publishing Corporation, doi: http://dx.doi.org/10.1155/2014/181938.
31. B. C. Grau, I. Horrocks, and B. Motik, HermiT Reasoner: Home, 2013.
32. Y. N. Sotskov and N. V. Shakhlevich, “NP-hardness of shop-scheduling problems with three jobs”, Discrete Applied Mathematics, vol. 59, no. 3, pp. 237– 266, May 1995.
33. A. Kononov and S. Gawiejnowicz, “NP-hard cases in scheduling deteriorating jobs on dedicated machines”, Journal of the Operational Research Society, vol. 52, no. 6, pp. 708–717, Jun. 2001.

34. E. Guzman, B. Andres, and R. Poler, “Matheuristic algorithm for job-shop scheduling problem using a disjunctive mathematical model”, Computers, vol. 11, no. 1, p. 1, Dec. 2021.
35. A. M. Ibrahim and M. A. Tawhid, “An improved artificial algae algorithm integrated with differential evolution for job-shop scheduling problem”, Journal of Intelligent Manufacturing, Jan. 2022.
36. J. Kassu and B. Eshetie, “Job shop scheduling problem for machine shop with shifting heuristic bottleneck”, Global Journal of Researches in Engineering: J General Engineering, vol. 15, no. 1, pp. 21–25, 2015.
37. N. Raman and F. B. Talbot, “The job shop tardiness problem: A decomposition approach”, European Journal of Operational Research, vol. 69, no. 1, pp. 187–199, 1993.
38. S. Topaloglu and G. Kilincli, “A modified shifting bottleneck heuristic for the reentrant job shop scheduling problem with makespan minimization”, The International Journal of Advanced Manufacturing Technology, vol. 44, no. 7- 8, pp. 781–794, Jan. 2009.
39. E. Balas and A. Vazacopoulos, “Guided local search with shifting bttleneck for job shop scheduling”, Management Science, vol. 44, no. 2, pp. 262–275, 1998.
40. J. Muth and G. Thompson, Industrial Scheduling, ser. Industrial scheduling. Prentice-Hall, 1963.
41. J. Carlier and E. Pinson, “An algorithm for solving the job-shop problem”, Management Science, vol. 35, no. 2, pp. 164–176, 1989.
42. D. S. Edna Barbosa, C. Michele Gonçalves, D. S. Marilda Fátima, and P. Fabio Henrique, “Evaluation of production sequencing rules in job shop and flow shop environment through computer simulation”, pp. 1–12.
43. J. Adams, E. Balas, and D. Zawack, “The shifting bottleneck procedure for job shop scheduling”, Management Science, vol. 34, no. 3, pp. 391–401, Mar. 1988.
44. I. M. Ovacik and R. Uzsoy, “A shifting bottleneck algorithm for scheduling semiconductor testing operations”, Journal of Electronics Manufacturing, vol. 02, no. 03, pp. 119–134, Sep. 1992.

ON THE FINITE ELEMENT MODELING BEST PRACTICES FOR THE METAL CUTTING SIMULATIONS

Ersen Hatipoglu, *hatipoglue@itu.edu.tr* Istanbul Technical University, 34469, Istanbul, Turkey

Mustafa Bakkal, *bakkalmu@itu.edu.tr* Istanbul Technical University, 34469, Istanbul, Turkey

Erhan Budak, *ebudak@s*abanciuniv.edu Sabanci University, 34956, Istanbul, Turkey

ABSTRACT

Finite element analysis is a widely used method to analyze solid mechanics problems. This method is also popular on metal cutting simulations as cutting process results and characteristics can be obtained in great detail. Despite the modeling and results screening capabilities of this technique, the fidelity of the method is highly dependent to the modeling approach and inputs. In case of metal cutting simulations, modeling may become more challenging due to the excessive work material deformation at high strain rate levels and coupled thermal effects. Different techniques are proposed in literature studies in order to overcome modeling difficulties and improve simulation accuracy but those are mostly proposed for specific problems. The aim of this study is to establish finite element modeling best practices for the metal cutting process which are intended to be generic approaches for different type of problems. For this purpose, detailed evaluation of the tool – work material interaction is performed by considering process geometry and deformation characteristics. FE simulation results are compared with experimental results in order to determine FE modeling best practices in an efficient manner.

Keywords: Metal cutting simulation, Finite element method, Machining process modeling

1. INTRODUCTION

Finite element analysis (FEA) is a substantial computational tool which is used on various problems on both industrial and research purposes. Algorithms and methods keep evolving in order to provide improved and flexible solutions to the scientific and engineering problems. Application of FEA on manufacturing problems are also attractive as the process modeling can be performed in a great detail and results screening is a matchless compared to the analytical or statistical methods. There are numerous examples available in literature regarding to the FEA employment on machining problems. Jin and Altintas (2012) used FE simulations to

obtain cutting force coefficients in order to predict micro milling cutting forces. Authors used Arbitrary Lagrangian Eulerian (ALE) adaptive meshing method in order to overcome excessive element deformation during simulation run. Ozel and Altan (2000) performed 2D plain strain FE simulations to predict cutting forces and evaluate stress and temperature distributions of the cutting tool. As stated previously, detailed result output capability of FEA enabled the evaluation of stress and temperature distributions. In addition to the 2D cutting FE simulations, 3D modeling can also be used. Man et al. employed 3D FEA to predict varying cutting forces due to the tool rotation during milling process. FEA can also be used for different purposes on machining modeling. Constitutive material model accuracy can be evaluated by comparative assessments [4,5]. FEA is also very capable for chip formation characteristics investigations. Shear band formation (serrated chips) can be accurately predicted by implementation of proper material models [4,6]. Different examples regarding to the FE method usage on machining modeling can be found in literature. FE method is also used as a basis for the more detailed assessments such as residual stress modeling, material micro-structure evaluation and surface integrity investigations. Multi-physics modeling and fluid – solid interaction are also FE modeling capability which is useful for investigating cooling mechanisms in machining process.

Despite its wide usage in literature, modeling details of FEA on machining simulations are generally less explained. Usually, specific actions should be taken at modeling phase as the continuous and excessive deformation of machining process leads to challenges during FE modeling. For example, studies about chip formation investigations employ sacrificial layer of work material elements at the tool tip which provides easier chip separation by preventing excessive element deformation. This method may be considered as a practical solution for chip formation simulations but the effectiveness of method degrades with a dominant hone radius geometry. Also, sacrificial element layer removal causes a loss of stress – strain data on the machined surface of work material which makes the method unsuitable for residual stress investigations. Actually, existence of a hone radius on tool geometry is a serious problem for lagrangian type of simulations. Hone radius causes a complex deformation behavior at tool tip and shearing of work material is not easily achieved compared to the simulation cases with sharp or very small hone radius tool geometry. ALE adaptive meshing is a generic solution for this type of problems. Adaptive re-meshing updates mesh structure during simulation at desired frequencies thus ensures proper mesh structure and prevents element folds due to excessive deformation. This is a very important algorithm as folded mesh results negative jacobian at element which causes termination of simulation. There are alternatives to the lagrangian method such as eularian, coupled eularian – lagrangian and meshless methods. These methods do not suffer from mesh distortion problems as work material is not represented with lagrangian mesh elements. However, lagrangian element

representation may be considered as a more desired option due to easier post processing, variety of contact algorithm options and flexible boundary condition imposition.

As stated above, FE modeling of machining process is a challenging task and there are numerous details should be considered during modeling phase. Not only the management of the excessive deformation, the material models, friction model and other required inputs drastically affect the simulation accuracy and make successful simulation run challenging. Considering the information availability about those details in literature studies and problem specific solution proposals, there is a need for a set of practices which can be used as generic solutions for machining simulations. Therefore, the aim of this study is to establish finite element modeling best practices for the metal cutting process which are intended to be a set of generic approaches for different type of problems. The focus of this study is 2D plane strain simulation cases with a tool that has hone radius. Simulations are performed with Abaqus and Deform3D software in order to evaluate explicit and implicit solution algorithms comparatively. In the following section, numerous examples are presented in order to propose guidelines for the modeling and perform sensitivity assessments. Then, simulation results are compared with orthogonal cutting experiments and results are discussed. Lastly, the outcomes of the study are presented.

2. ON THE FE MODELING OF MACHINING PROCESS

This section consists of FE modeling examples which are intended to serve as a list of recommendations for the machining simulations. Each sub-section discusses about some of the important modeling steps on various simulation cases. Examples are established with Abaqus Explicit and Deform3D depending on the interest.

Unit System and Mesh Density

Implementation of the consistent unit system to the FE software is crucial for a correct simulation. For this purpose, consistent Metric or Imperial unit systems are used. For machining problems, modeled feature sizes may become very small. Considering micrometer scale dimensions of the tool hone radius, mesh element dimensions need to be designated even more small in order to achieve accurate deformation and stress results. In case of a kg-m-s metric unit system usage, mesh element dimensions are around 1E-6 m or even less. This condition can result accuracy issues during model pre-processing and round-up errors during solution. In addition to that explicit solution algorithm has an important property which is stable time increment. Stable time increment determines the maximum time increment between explicit solution steps. Stable time increment can be calculated by following equations [7]:

$$\Delta t = \frac{L^e}{c_d} \tag{1}$$

$$c_d = \sqrt{\frac{E}{\rho}} \tag{2}$$

L^e is the characteristic element length and c_d is the dilatational wave speed of the material. Dilatational wave speed is calculated by modulus of elasticity and density (ρ). In case of kg-m-s unit system, stable time increment is calculated around 2E-10 s for a steel material that modeled with 1 um element size. Very small time increment becomes impractical for an explicit solution which is performed for a simulation step times that defined in seconds. Considering the model pre-processing accuracy, potential round-up errors and impractical stable time increment issues for the explicit procedure, it can be said that the kg-m-s or tonne-mm-s metric systems are not well suited for the FE modeling of machining. Therefore, this study proposes the usage of ng-um-us consistent metric system for the machining simulations which are evaluated for micro second level time frames. By introducing ng-um-us unit system, model features can be modeled without accuracy concerns and practical stable time increment levels for explicit analysis procedure can be achieved.

On the other hand, determination of mesh density is also important point. As it is well known, finer mesh grids improve simulation accuracy but it should be noted that at some point further mesh refinement does not provide a significant accuracy improvement. At this point it can be said that mesh convergence is achieved and defined mesh density is sufficient enough to obtain reasonable results. However, it is not that easy to say how fine mesh is enough. Using very fine mesh as a start point may not be a reasonable approach due to the increased computational cost and stable time increment issues in case of explicit solution algorithm. Therefore, mesh sensitivity check has to be performed by performing simulation trials in order to determine mesh convergence. Experimentally validated studies can also be used to determine mesh size but overall model size and geometry should be considered as well. As a general practice, multiple layers of elements at the tool – work material interaction zone is required in order to capture deformation behavior properly.

Additional checks can be applied to evaluate mesh size fidelity. Tool – work material contact pressure distribution can be screened. As it is widely studied, the tool – work material contact pressure distribution has a semielliptical distribution form at the 2nd and 3rd deformation zones [8]. Proper FE model contact pressure distribution should also converge to the semielliptical pressure distribution since deviations or fluctuations at the contact pressure distribution can be resulted from coarse meshing.

Also, the level of contact penetration (interference amount of tool and work material mesh elements at contact zone) between tool and work material can be checked. Ideally, contact penetration amount should be minimal between interacting geometries. Coarse meshes results increased contact penetration and cause contact detection issues between tool and work material. Loss of contact results inaccurate contact pressure and force calculations. Therefore, FE model mesh needs to be refined enough to prevent contact penetration and contact detection issues.

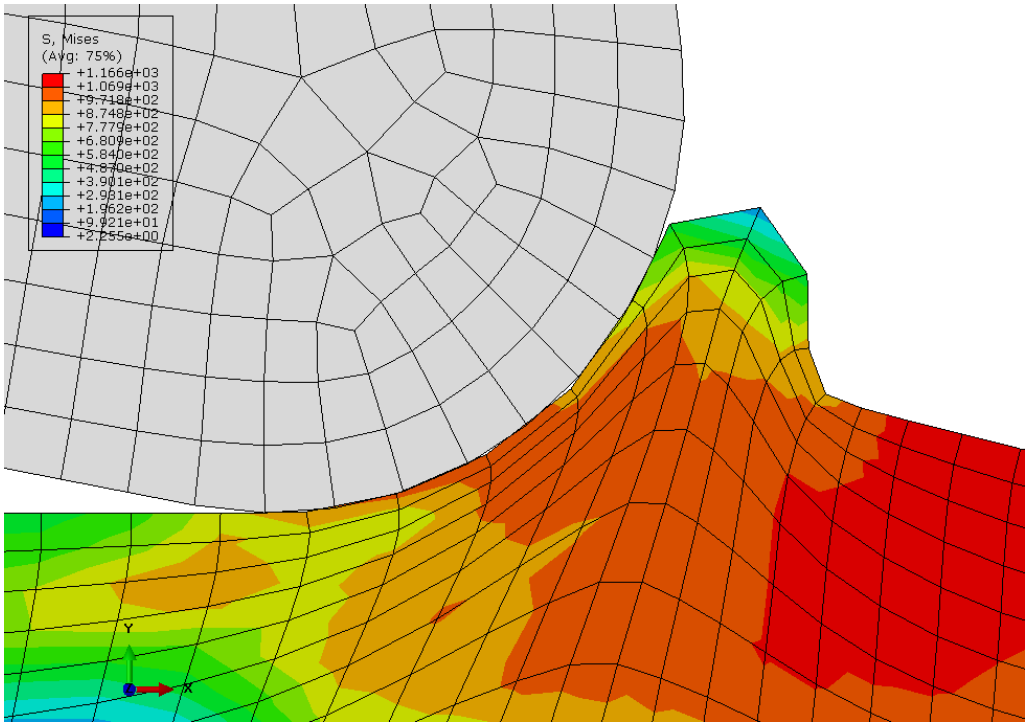


Figure 1. Ploughing simulation of AISI1050 Steel with Abaqus Explicit, contact penetrations are minimal

Figure 1 shows an example of desired contact penetration status between tool and work material. As illustrated, penetration is minimal. On the other hand, Figure 2 shows the opposite example. Chip formation causes excessive deformation thus work material elements are elongated significantly. This condition resulted to a loss of contact for some of the tool nodes. Illustrated condition may not cause a drastic effect on the cutting forces but contact pressure distribution is affected. For such case, further mesh refinement and better adaptive remeshing controls need to be applied.

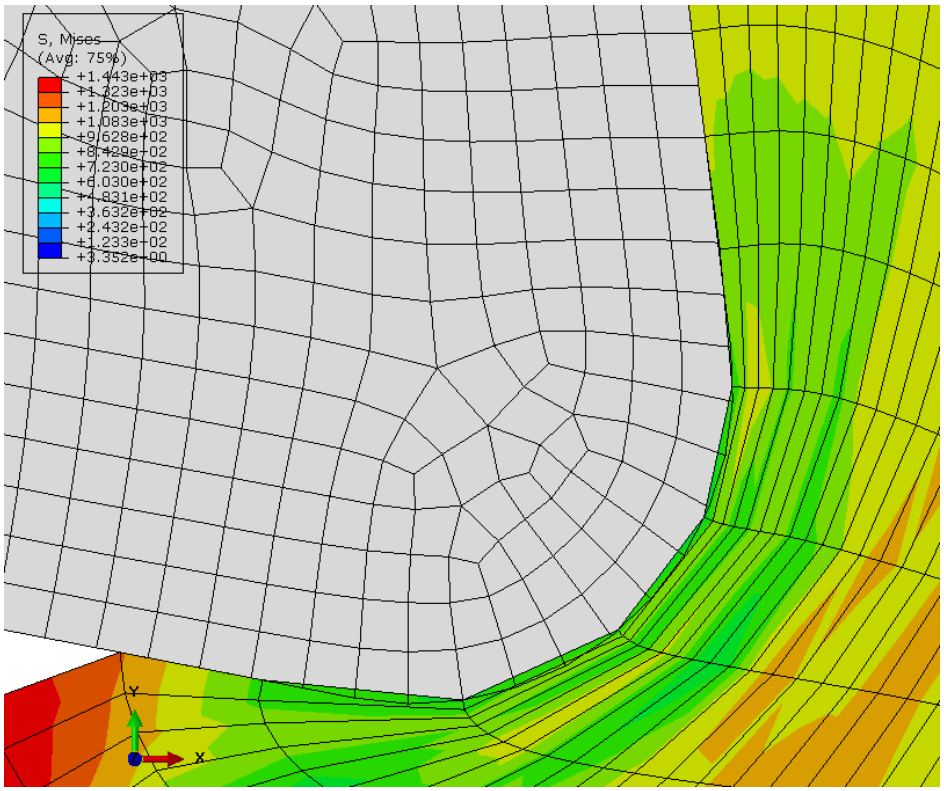


Figure 2. Chip formation simulation of AISI1050 Steel with Abaqus Explicit, contact penetrations are observed

Determination of model size

Generally, a small portion of the machining process geometry is modeled in FE simulations in order to reduce the computational cost of the problem. In order to determine optimum model dimensions, the boundary condition constrains should be away enough from the deformation zone in order to not affect the problem calculations.

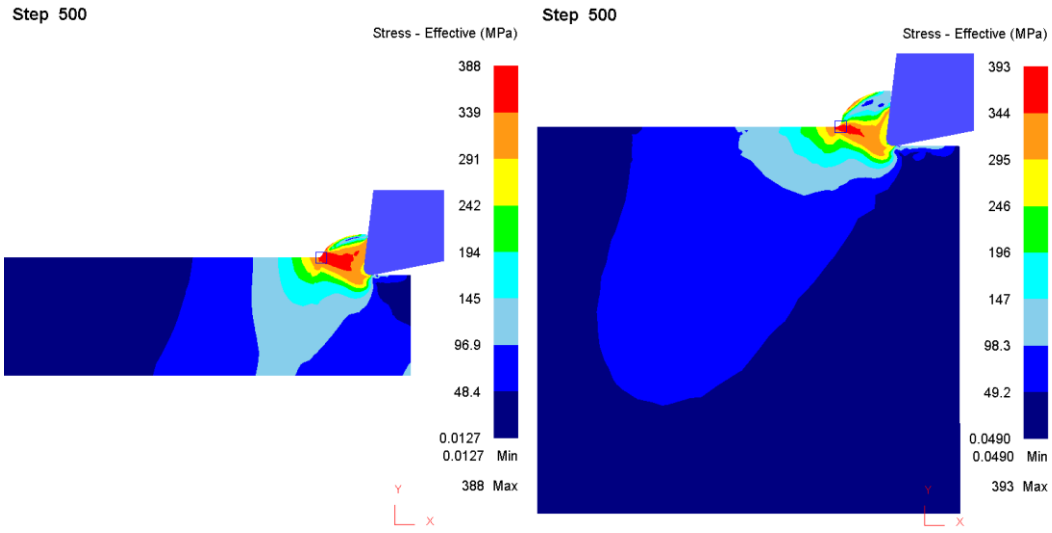


Figure 3. 2D Plain Strain simulation of Al6061 with Deform3D, effect of workpiece model size on equivalent stress distribution

Figure 3 shows the comparison of models with different work material sizes. As explained above, work material model size is insufficient to provide enough room for contact zone stresses to fade out. Additionally, there are imposed boundary conditions on the bottom edge of the work material. It can be seen on the result plot the stress distribution expands to the edge of applied boundary conditions. This condition also affects the stress distribution. In addition to the equivalent stress comparison, cutting force comparison is also performed. Measurements showed that smaller work material geometry resulted ~5% higher cutting forces on tangential and radial directions.

Contact Modeling and Friction

Selection of contact and friction model can be considered as one of the most controversial topics on the modeling of machining process. Different friction models and modeling approaches are available through literature and unfortunately it is not easy to select a best fit friction model that describes the tool – work material interaction properly. Besides that, FE software's contact model algorithms have significant effect on the contact behavior of the interfaces. Widely known examples of the contact models are the constant shear friction and the Coulomb friction models. In many cases, combination of two models at same interface is widely used [4, 8]. Advanced frictional models are also used in studies as an aim of better representation of the tool – work material interaction. Application of static – kinetic friction models by means of decay friction models, models with tangential softening behavior and introducing a shear stress limits are the examples of detailed friction models. Putting the friction models aside, the friction phenomenon has a very complex nature. Contact interface frictional behavior is dependent to almost everything that are included in the problem. Considering the complexity, keeping the frictional model as simple as possible can be considered as a most practical way in case of FE modeling of machining process. At least for the initial simulation trials, frictional effects may be considered in a simplified manner. When the model achieves a reasonable fidelity, fine tuning may be performed by introducing advanced friction models. For some cases like bulk deformation of the material, it may be noticed that satisfactory results can be obtained even with a simple friction model. The accuracy of simple frictional model usage will be shown in the following experimental validation section.

To sum up, following recommendations are proposed for the frictional contact modeling:

Using simple friction models as a starting point is a practical approach for machining process contact modeling. For some cases model accuracy can be satisfactory which may make complex frictional modeling redundant.

Experimental determination of a friction coefficient for specific material couples and physical conditions is a key for improved result accuracy [8].

Coulomb friction model with shear stress limit is quite capable for representation of a sticking/sliding regions at tool – work material interface. Shear stress limit determination may require trial and error procedure as using shear yield stress value directly may not result proper sticking region.

FE contact sliding algorithm details should be reviewed in detail. Proper settings should be defined in order to simulate proper sticking contact condition at high deformation levels.

In addition to the frictional contact mechanical behavior, few comments can be made on thermal contact modelling. Three thermal contact properties can be considered as a major property. First one is the frictional heating which defines the percentage of the frictional energy to be converted to the heat. As a general practice, 100% of the frictional energy is assumed to be converted to heat. Second one is a fraction value that defines the amount of heat to be distributed to contact each contact surface. Proper fraction value can be calibrated from experimental studies. Last property is the contact thermal conductance settings which controls the heat transfer coefficient between contact surfaces. Some literature studies advise considerably high contact conductance values in order to provide improved contact heat transfer. It should be noted that greater contact conductance values reduce stable time increment size in explicit analysis. In this study, effect of contact conductance on contact zone average temperatures are compared for ploughing case of tool (WC) – work material (15-5PH steel) interaction. Simulations are performed with Abaqus Explicit. As illustrated in Figure 4, average contact zone temperatures are very similar for a range of feed rate values. Mean temperature difference between two results sets is 6%.

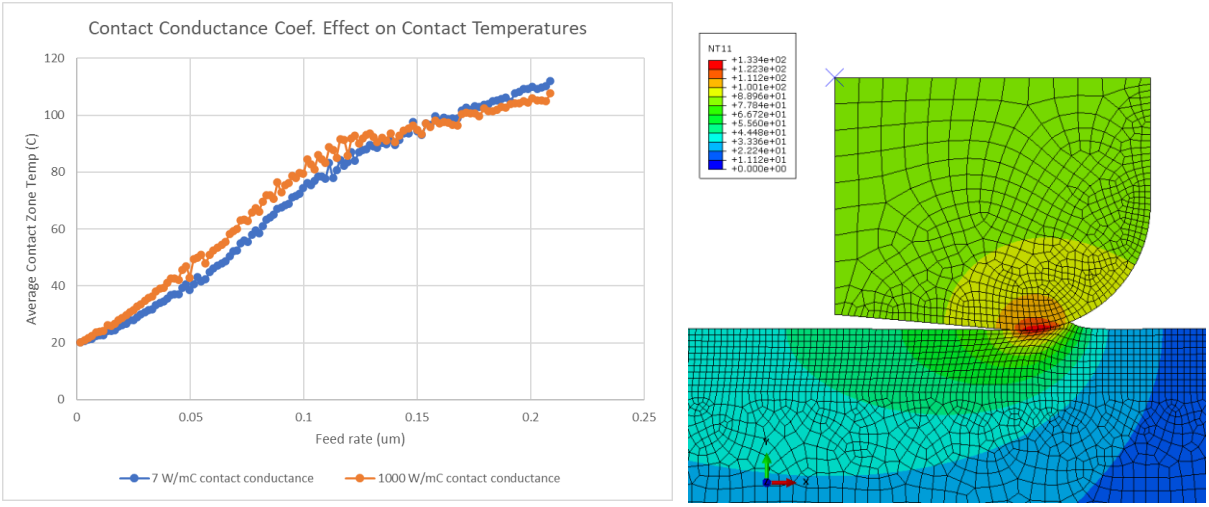


Figure 4. Ploughing simulation of 15-5PH with Abaqus Explicit, contact conductance effect on average contact temperatures

Material model

Correct material data implementation is the backbone of a proper simulation. Elastic, plastic and thermal material properties should be provided to FE model. Johnson – Cook (JC) constitutive model is widely used for the machining simulation as it governs the dynamic – temperature dependent plastic flow data of the material for a wide range of strain rate. Classic form of JC material model does not account for thermal softening at high strain rates therefore modified JC material models are also adopted. The accuracy of JC model may differ for different temperature, strain and strain rate ranges. Therefore, JC model coefficients may need a calibration for a specific deformation range. For this purpose, JC model coefficients are calibrated by applying an inverse method to the orthogonal cutting tests [8]. Calibrated material model results improved accuracy.

Another important material model is the damage model. There are various material damage models are available in literature and FE software packages propose various material model options to implement. Damage model implementation gains importance in case of chip separation simulations. Detailed chip formation model assessments require proper damage model employment [6,11]. Damage models defines the failure strain of the material. In case of implicit methods, when the failure strain is reached material loses its load carrying capability and softening occurs. Explicit methods allow element deletion from the model mesh and damage models are used to trigger element deletion as failure point is reached. Even though, element deletion is an effective way to chip separation simulations it may also cause some problems for the tool – work material interaction especially for a hone radius dominant cutting case. Figure 5 illustrates an example of the element deletion resulted from damage modeling. Elements around tool hone reached to failure point and deleted from mesh. As a result of element deletion proper contact condition is lost.

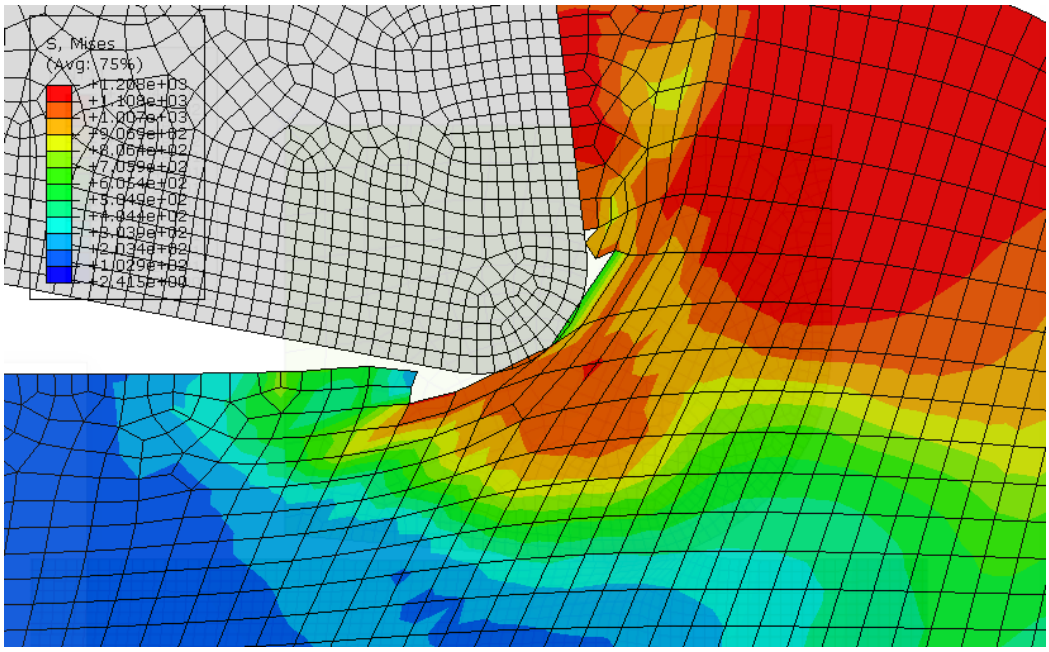


Figure 5. Chip formation simulation of AISI1050 Steel with Abaqus Explicit, proper contact condition is lost due to the element deletion around tool hone

For a small or no hone radius simulation cases, sacrificial element layer is implemented at tool tip level. Purposedly, less capable damage property is defined at sacrificial layer to provide an ease chip separation from work material [11]. However, this method does not work properly for a large hone radius geometry.

In case of pure lagrangian analysis, there is no fully effective solution to this problem. Finer work material mesh can reduce this problem at some level but eventually contact loss problems and excessive deformation issues arise. As it will be shown in experimental validation section, damage model coupled with element deletion improves chip geometry prediction with a cost of force and contact accuracy loss.

Adaptive meshing

Arbitrary Lagrangian Eulerian (ALE) adaptive meshing algorithm provides a very effective solution to the excessive deformation problems. Remeshing is applied with a determined parameters at designated frequencies during simulation run and prevents excessive element distortions. In case of machining simulations with a hone radius tool, it can be said that adaptive meshing algorithm is mandatory for a proper simulation run as pure lagrangian algorithm suffers from element distortion issues. Adaptive meshing algorithm capabilities differs among the FE software packages. In this study, adaptive meshing method is employed in the simulation models. Deform3D uses high capability adaptive meshing algorithm which provides a very effective solution in case of excessive deformation problems. However, Deform3D lacks complete element deletion option due to its implicit algorithm. This limitation can reduce the

chip formation accuracy. On the other hand, Abaqus Explicit allows complete element separation which can result accurate chip formation. However, Abaqus remeshing algorithm is not much flexible compared to the Deform3D and element distortion problems can still occur. Also, damage model and element deletion usage further reduce the adaptive meshing capabilities as the failed domain interface nodes become non-adaptive. Abaqus allows eularian definition on a desired portion of the lagrangian mesh by introducing adaptive meshing constrains but this method requires additional settings and impose of additional boundary conditions. As explained in the introduction section, eularian, coupled eularian – lagrangian and meshfree techniques do not suffer from the excessive element deformation problems but this study's scope is lagrangian based simulations due to the explained rationales.

Implementation of the Initial chip geometry

Implementing an initial chip and tool – work material contact geometry can help for delaying the excessive element distortions. This is especially important for the analysis cases with material failure and element deletion. Due to the progressive deformation at the tool – work material interface, excessive element deformation is inevitable. Adaptive meshing techniques helps to prevent excessive element deformation by remeshing but in case of damage model and element deletion case, mesh adaptivity is not working as desired. Basically, failed elements are out of the remeshing scope therefore, analysis termination may occur. Introducing initial chip and contact geometry helps for delaying the excessive element deformation as initial mesh becomes more suitable for the deformation characteristics of the process. The tool hone and work material elements are aligned better and have better aspect ratios. Also, initial chip section mesh elements are better aligned with the material flow direction.

In this study, an arbitrary value of an initial chip thickness value is selected by considering the feed rate range of the cutting experiments. Simulation results show that chip thickness reach to its process values immediately after the simulation starts. Figure 6 shows the employment of initial arbitrary chip geometry and converged chip thickness during simulation. With the help of initial chip and contact zone geometry employment, tool hone contact condition is improved and chip flow without excessive element deformation is enabled.

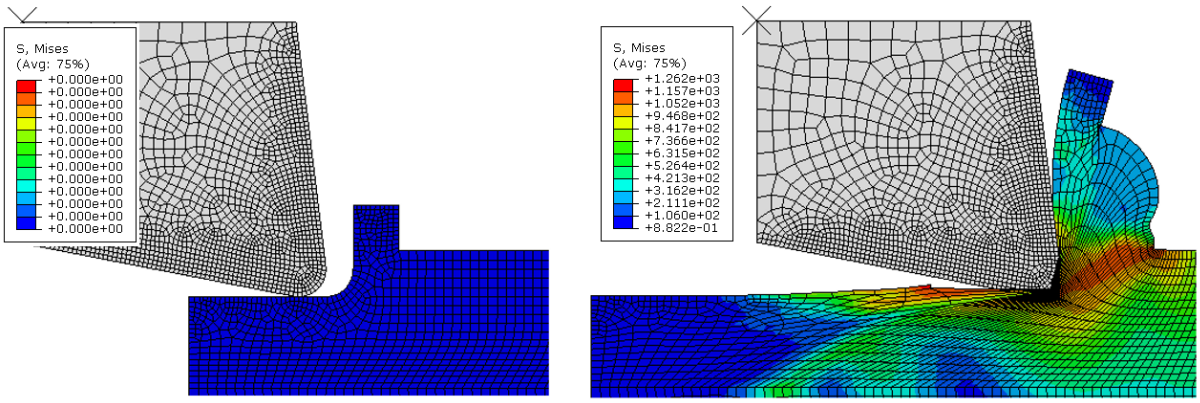


Figure 6. Implementation of the initial chip geometry and convergence of chip thickness to the process conditions as simulation progress

3. EXPERIMENTAL VALIDATION OF THE FE SIMULATIONS

As part of experimental validation efforts, orthogonal cutting test are applied on a tube-shaped specimen which has an 84 mm OD and 2 mm thickness. AISI 1050 steel selected as the work material and TPGN type uncoated turning inserts are used. Two different insert geometry are used with different hone radius, rake and clearance geometries. First insert geometry has 40 um hone radius, 0 degrees rake and 7 degrees clearance angles. Second insert has 60 um hone radius, 7 degrees rake and 11 degrees clearance angles. This selection is mainly intended to observe hone radius effect on the cutting forces (radial and tangential cutting force components). Cutting tests performed at dry condition. Figure 7 shows the test setup.

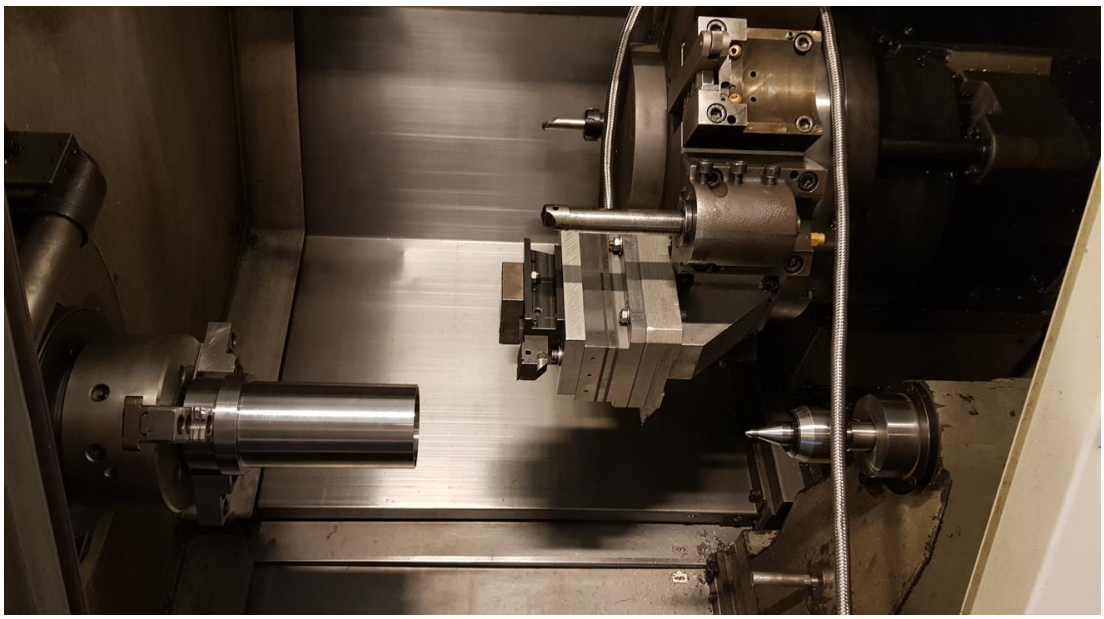


Figure 7. Orthogonal cutting test setup

Cutting force data acquisition is made through a force dynamometer. Cutting tool holder is assembled on a force dynamometer and data acquisition system gathers the cutting forces in three directions. Orthogonal cutting test parameters are given in Table 1:

Test	Hone radius (um)	Cutting Speed (m/min)	t-feed (mm/rev)	depth of cut (mm)
1	60	75	0.02	2
2	60	75	0.05	2
3	60	75	0.1	2
4	60	75	0.15	2
5	40	52	0.005	2
6	40	52	0.01	2
7	40	52	0.02	2
8	40	52	0.04	2
9	40	52	0.06	2
10	40	52	0.08	2
11	40	52	0.1	2
12	40	52	0.15	2

Table 1. Orthogonal cutting test parameters

Cutting force and chip thickness measurements are performed for the tests with 60 um hone radius tool. Tests with 40 um hone radius tool is performed for a wide range of feed rate values. Tests with 60 um tool are intended to evaluate both cutting force and chip formation accuracy of the FE models Tests with 40 um tool are intended to have detailed comparison of cutting forces for a wide range of feed rates.

FE models are prepared with Abaqus Explicit and Deform3D. By this way, two different modeling approach will be compared. Material data for the AISI1050 steel is obtained from literature studies which are considered as reliable as the provided material data used on modeling studies and results are validated by experiments [8, 12]. Material inputs for Abaqus and Deform3D are presented in Table 2:

1050 Abaqus		
Elastic		
Young's Mod. (Mpa)	Poisson Ratio	Temp. (C)
206000	0.3	20
200000	0.3	100
192000	0.3	200
184000	0.3	300
163000	0.3	500
125000	0.3	800
99000	0.3	1000
Density (ng/um^3)		
0.00785		
Thermal Conduct. uW/(um*C)		
49.77		
Specific Heat pJ/(ng*C)		
460		
JC Plastic		
A	880	Mpa
B	500	MPa
n	0.234	-
m	1	-
Tmelt	1460	C
Ttransition	25	C
C	0.013	-
epsilon dot zero	1.00E-06	1/us
JC Damage		
d1	0.06	-
d2	3.31	-
d3	-1.96	-
d4	0.018	-
d5	0.5	-

1050 Deform3D		
Elastic		
Young's Mod. (Mpa)	Poisson Ratio	Temp. (C)
206000	0.3	20
200000	0.3	100
192000	0.3	200
184000	0.3	300
163000	0.3	500
125000	0.3	800
99000	0.3	1000
Density (ton/mm^3)		
7.85E-09		
Thermal Conduct. N/sec/mm/C		
49.77		
Heat Capacity		
3.61885		
JC Plastic		
A	880	Mpa
B	500	MPa
n	0.234	-
m	1	-
Tmelt	1460	C
Ttransition	25	C
C	0.013	-
epsilon dot zero	1.00E-06	1/us

Table 2. AISI 1050 Steel Material input for Abaqus and Deform3D

FE models are prepared by implementing proposed practices in the previous section. Coulomb friction model is defined at tool – work material interface with a friction coefficient 0.5.

60 um hone radius tool experimental and FE model results comparison for the 75 m/min cutting speed is given as follows:

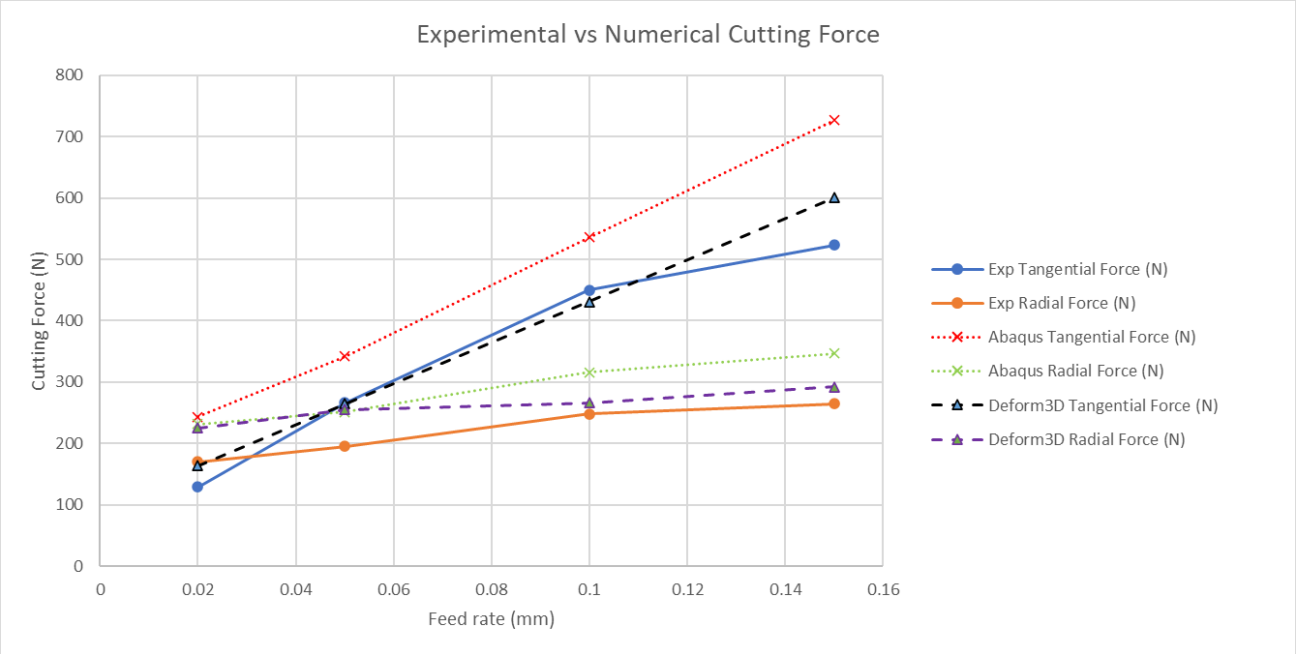


Figure 8. Experimental vs Numerical cutting force comparison
(Hone rad=60 um, Vc=75 m/min)

Figure 8 shows that Deform3D tangential force results have the highest accuracy. For feed rates 0.1 and 0.15 mm/rev Deform3D radial forces also have good accuracy but lower feed rate results have deviation from experimental results. On the other hand, Abaqus simulation results have poor accuracy compared to the Deform3D results. Abaqus results have a similar trend with the experimental force results but with an offset. This condition is thought of as a result of element deletion and contact loss problems occurred in the Abaqus simulations as explained previously. Mean tangential and radial force errors are calculated for Abaqus results as 44% and 31%, for Deform3D results as 9% and 20% respectively.

Chip thickness results are compared. Figure 9 shows that simulation results underestimate the chip thickness values. Unlike force results, Abaqus resulted better accuracy compared to the Deform3D results. This outcome is thought of as a result of element deletion and material failure implementation in Abaqus simulations. In sum, higher flexibility adaptive meshing with implicit method seems to be a good and effective solution for predicting cutting forces. On the other hand, explicit method with damage model and element deletion seems better for predicting chip geometry but stated contact issues due to element deletion degrades the cutting force prediction accuracy.

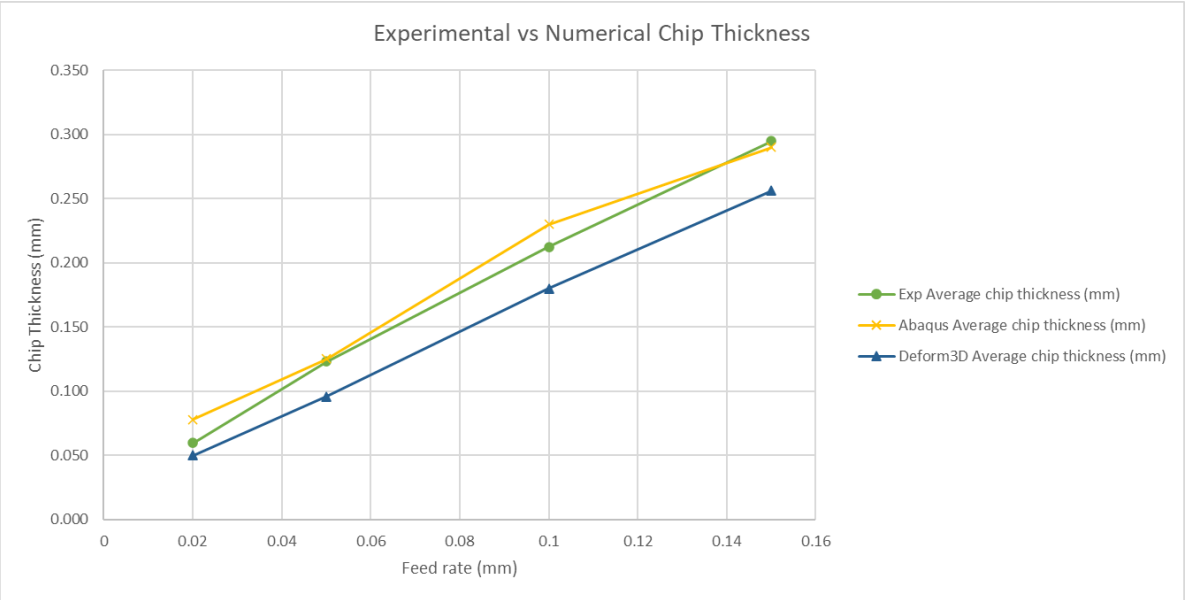


Figure 9. Chip thickness comparison (Hone rad=60 um, Vc=175 m/min)

the Deform3D results. This outcome is thought of as a result of element deletion and material failure implementation in Abaqus simulations. In sum, higher flexibility adaptive meshing with implicit method seems to be a good and effective solution for predicting cutting forces. On the other hand, explicit method with damage model and element deletion seems better for predicting chip geometry but stated contact issues due to element deletion degrades the cutting force prediction accuracy.

As Deform3D resulted a better accuracy for cutting force predictions, second set of experiments are compared only with Deform3D results.

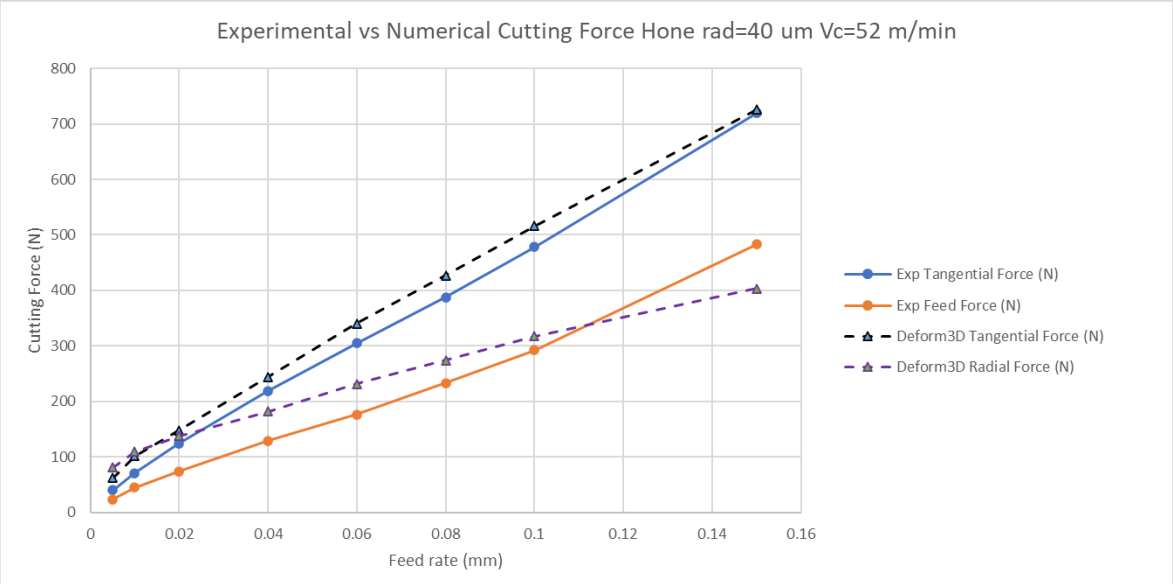


Figure 10. Experimental vs Numerical cutting force comparison

(Hone rad=40 um, Vc=52 m/min)

As illustrated in Figure 10, cutting simulations results have a good agreement with experimental force measurements. Particularly, tangential cutting force accuracy is very high. Similar to the previous assessments, radial cutting force results have some deviation, especially lower feed rates. As stated in previous section, further accuracy improvement may be achieved by fine tuning of the contact interface friction. As a simplified approach, constant 0.5 friction value is implemented. Implementation of an experimentally validated friction coefficient may improve cutting force accuracy further.

4. CONCLUSION

This study is intended to establish a set of best practices for the FE modeling of machining process. For this purpose, important aspects of the lagrangian FE modeling are evaluated and examples are presented. Set of recommendations are proposed to serve as generic approaches to the FE model development for the machining problems. Lastly, experimental validation of the proposed techniques is made to assess weakness and strengths of different modeling approaches. The important outcomes of the study can be listed as follows:

Established set of best practices may serve as a guidance to the future studies and reduce the need for sensitivity studies regarding to the FE modeling approaches on machining simulations.

FE model fidelity can be assessed by checking and comparing the simulation results. By this way experimental validation need can be minimized as the reliability of FE model can be proven with several experiments.

Modeling approach should be determined by considering the expected outcomes from the simulation. As it can be seen on results, a method for better chip formation accuracy may not be a best solution for cutting force prediction.

Study results showed that FE simulations can model cutting process with a satisfactory accuracy as long as proper modeling is incorporated and correct inputs are provided.

REFERENCES

1. **Xiaoliang J and Altintas Y., (2012),** "Prediction of micro-milling forces with finite element method" Journal of Materials Processing Technology, Volume 212, Issue 3, 2012, Pages 542-552.

2. **Tuğrul O. and Taylan A., (2000), "**Process simulation using finite element method — prediction of cutting forces, tool stresses and temperatures in high-speed flat end milling", International Journal of Machine Tools and Manufacture, Volume 40, Issue 5, 2000, Pages 713-738.

3. **Xialin M., Deyao R., Shuji U., Cody J., Troy D. M., (2012),** "Validation of Finite Element Cutting Force Prediction for End Milling", Procedia CIRP, Volume 1, 2012, Pages 663-668.

4. **T. Ozel, S. Yildiz, J. Ciurana., (2009),** "Influence of Material Models on Serrated Chip Formation in Simulation of Machining Ti-6Al-4V Titanium Alloy", Conference: 12th CIRP International Workshop on Modeling of Machining Operations, Volume 1, Pages 123-130.

5. **T. A. Iturbea, E. Giraudb, E. Hormaetxea, A. Garaya, G. Germainb, K. Ostolazac, P.J. Arrazola, (2017),** "Mechanical characterization and modelling of Inconel 718 material behavior for machining process assessment", Materials Science and Engineering: Volume 682, Pages 441-453.

6. **Madalina Calamaz, Dominique Coupard, Franck Girot, (2008),** "A new material model for 2D numerical simulation of serrated chip formation when machining titanium alloy Ti–6Al–4V", International Journal of Machine Tools and Manufacture Volume 48, Issues 3–4, Pages 275-288.

7. "Abaqus Documentation"

8. **Ozlu E., (2008),** "Analytical modeling of cutting process mechanics and dynamics for simulation of industrial machining operations".

9. **S.M. Afazov∗, S.M. Ratchev, J. Segal, (2010),** "Modelling and simulation of micro-milling cutting forces".

10. "Deform3D Documentation"

11. **M.H. Miguélez, X. Soldani, A. Molinari, (2013),** "Analysis of adiabatic shear banding in orthogonal cutting of Ti alloy", International Journal of Mechanical Sciences, Volume 75,Pages 212-222.

12. **Fallah, M. M. & Hamzeloo, Reza, (2019),** " Investigating the Effect of Cutting Condition on the Plastic Energy in Turning Process of AISI 1050", Int J Advanced Design and Manufacturing Technology, Vol. 12

DETERMINATION OF CUTTING PARAMETERS FOR AGGRESSIVE-HIGH PERFORMANCE CHIP REMOVAL OF THE BEVELING MACHINE WITH AUTOMATED WORKPIECE DETERMINATION AND TOOL PATH GENERATION SYSTEM

Can TUNCER, *can.tuncer@gri.com.es*, GESBEY Power Generation Turbine Towers, 10900-Bandirma-Balikesir, TURKEY

Sakıp TÜRKÖZ, *sakip.turkoz@gri.com.es*, GESBEY Power Generation Turbine Towers, 10900-Bandirma-Balikesir, TURKEY

Ali ORAL, *alioral@balikesir.edu.tr,* Balikesir University,10100 Balikesir, TURKEY,

ABSTRACT

The wind turbine tower has a structure consisting of sheet metal plates with welded joining. One of the important factors determining the quality of the welded joining process is the Beveling process. Today, Beveling process is carried out either manually and labor intensively or with CNC machines. The Beveling process carried out under operator control has disadvantages in terms of quality and production time. CNC machines, on the other hand, have disadvantages such as high investment cost and precise part attachment and G code preparation time. For this reason, a fully automatic Beveling machine has been developed that determines the tool path route by recognizing the sheet plate edge geometry with a unique technique. The most important advantages of the developed machine; the lack of a precise part fixing method and G code creation, it has a much lower investment cost than CNC machines, it eliminates operator-induced errors despite manual machines. With the developed machine, edge milling is performed with high volume aggressive chip removal method. Within the scope of the tool wear tests carried out, the relationship between "tool life and machining quality" and "cutting speed and feed rates" was examined and optimum cutting parameters were determined.

Keywords: Beveling machine, milling, aggressive milling, high-volume machining, edge milling, tool life

1. INTRODUCTION

Welding is the process of joining similar or dissimilar metals as inseparable in heat and/or under pressure. Today, the welding process is intensively used in robotics. The success of the welding process in robotic welding depends on the preliminary preparations [1]. One of these preparations is to open a weld bevel in a geometry suitable for the metal to be welded. The bevel formation process is based on the principle of performing deformation with or without chipping by using various methods on certain parts such as edges, corners, surfaces where the joint will take place in the workpieces to be subjected to the welded manufacturing process.

In this study, it is aimed to develop an automatic beveling machine with edge tracking system and determine the cutting parameters to open the bevel in one pass with high volume chip removal by dry process all around the 30mm thick S355JR quality sheet metal plate used in the construction of the wind turbine tower.

2. SCOPE

Today, bevel can be opened with many different methods. Weld beveling application with the most advanced technology is carried out with CNC controlled machines. CNC-controlled beveling machines for edge milling require time-consuming preparation such as good part fixation and G-code preparation.

High-speed cutting makes it possible to remove large amounts of metal and shorten the processing time [2,3]. In our study, an automatic beveling machine that performs high-volume aggressive edge milling has been developed, which does not require a G-code and a perfect part clamping process, has a special algorithm that identifies the plate edges using laser sensors and determines the tool path by creating a mathematical model of the plate geometry.

Weld beveling parameters were determined by chip removal experiments using a cutting tool specially designed for the beveling machine, which was developed to bevel the 30mm thick sheet metal in one pass.

3. MATERIAL - METHOD

The largest piece size aimed to be beveled in the developed machine is 13000 x 3000 (mm x mm). It is aimed that the sum of transport, preparation time and cutting times will be 40 minutes on average. In terms of machine design, the first step is to determine the cutting power in accordance with the cutting geometry. The cutting power can be calculated approximately from Eq. (1) [4].

$$P_c = \frac{a_e, a_p, V_f, k_c}{60, 10^6, \eta} \quad (1)$$

Here,

P_C: cutting power (kW),

a_e: cutting width (mm),

a_p: depth of cut (mm),

V_f: feed rate (mm/min)

k_c: specific shear force (MPa) (≅2500-3000 for steel),

η: efficiency (≅0.75)

The cutting power that is calculated by Equation 1 was found to be approximately 22.5 kW to form the bevel (Figure 1), for one pass on a 30 mm thick plate. It has been decided to use a 30 kW spindle motor on the machine.

For this purpose, a beveling machine with a 30 kW spindle motor, which was developed to be able to open the weld bevel in one pass, was developed, and a cutting tool with a total of 63 cutting inserts in 7 rows with a profile suitable for the weld bevel profile was developed for chip removal. The developed machine is given in Figure 2 and the specially designed cutting tool is given in Figure 3 [5]. Special cutting tools must be used to create different types of bevels.

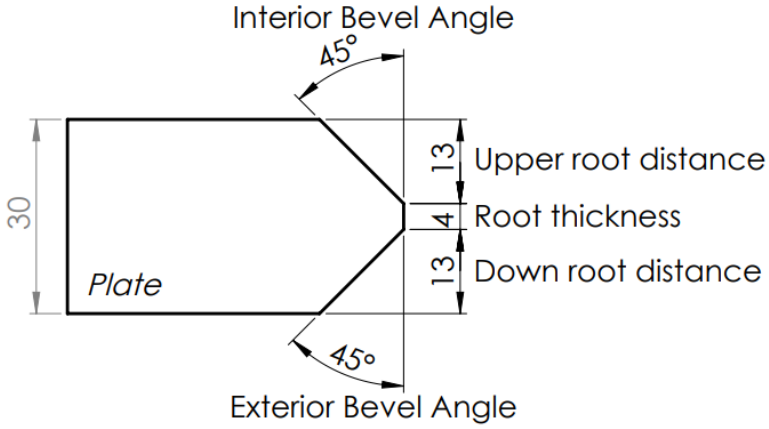
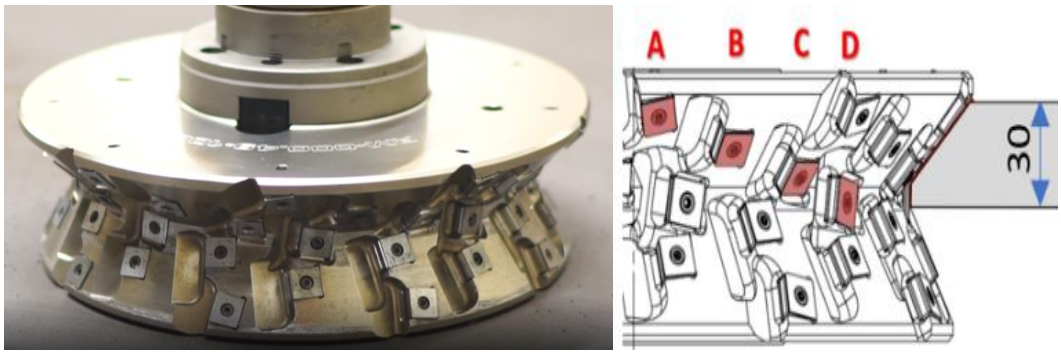


Fig. 1: An example for bevel geometry.



Fig. 2: Beveling machine developed for plate Beveling.



a b

Fig. 3: Cutting tool for Beveling

It has been decided to use an aluminium oxide coated SNHX1406TN08-M12 MP2501 insert seen in Figure 4, as a cutting tool in the beveling process. In the experimental study, the cutting speed value of 200-240 m/min and the feed rate per tooth fz=0.25-0.30 mm/teeth were given by the manufacturer as the cutting parameters. As a result of the first trials on the machine, it was seen that the desired productivity could not be achieved with these values, and it was decided to work on the determination of the cutting parameters that could provide the desired productivity values. In the cutting tool used for this purpose, different cutting speeds occur in each row of the cutting edges, which are arranged in 7 rows. Wear measurements were taken with a Dino-Lite AD4000 series digital microscope with 1/10000 mm sensitivity at 250 times magnification.

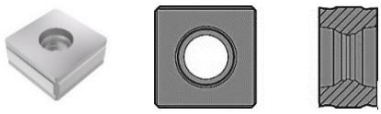


Fig. 4: SECO SNHX1406TN0-M12 MP2501 cutting insert [6]

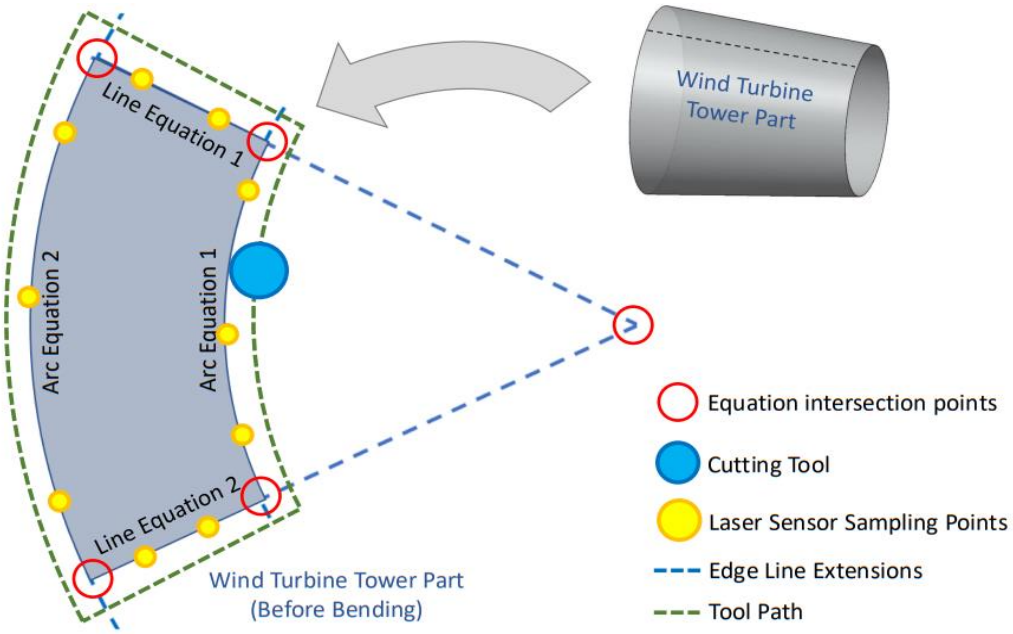
The cutting parameters used for the test runs on the test plate are given in Table 1. In the experimental parameters, the manufacturer's recommendations for the cutting speed were taken into account, and the feed rate was adapted according to the production speed, taking into account the first test results, and it was taken higher than the recommended value.

Table 1: Cutting speed and feed rate values used in the experiments.

Insert ID	1st Experiment Parameter		2nd Experiment Parameters	
	Cutting Speed (m/min)	Feed Rate (mm/min)	Cutting Speed (m/min)	Feed Rate (mm/min)
A	240	820	312	780
B	225	820	292	780
C	210	820	274	780
D	203	820	264	780

The beveling machine operates in X, Y, Z Cartesian coordinates. Movement axes are driven by servo motors. The movement in the X and Y axes is provided by rack and pinion gears, and the movement in the Z axis is realized by the ball shaft mechanism.

After receiving the coordinate information from the part, the geometry of the part is mathematically created in a few seconds with the geometric equations defined in the PLC system and the tool path is obtained. In order to define the part geometry before bevelling process, 3 points from the curved edges and 2 points from the linear edges are taken with the help of laser sensors and sent to the PLC software. Coordinate measurements are made on specific points on the edges. After the geometric dimensions are determined for all the edges, the plate geometry is defined mathematically. The motion route of the tool center, that is, the tool path (Fig. 5), is determined by offsetting the cutting tool radius on the determined geometry. With the PLC system, tool movement is provided with the "point to point" technique and the control of X and Y axis Servo drive motors based on the formula, without the need for G codes and perfect workpiece positioning.



When 3 point coordinates are given, equation of the circular edges of the plate, can be determined by the calculations below;

For given (x1,y1) , (x2,y2) and (x3,y3) first form A,B,C:

$$A = x_1(y_2 - y_3) - y_1(x_2 - x_3) + x_2y_3 - x_3y_2$$

$$B = (x_1^2 + y_1^2)(y_3 - y_2) + (x_2^2 + y_2^2)(y_1 - y_3) + (x_3^2 + y_3^2)(y_2 - y_1)$$

$$C = (x_1^2 + y_1^2)(x_2 - x_3) + (x_2^2 + y_2^2)(x_3 - x_1) + (x_3^2 + y_3^2)(x_1 - x_2)$$

$$D = (x_1^2 + y_1^2)(x_3y_2 - x_2y_3) + (x_2^2 + y_2^2)(x_1y_3 - x_3y_1) + (x_3^2 + y_3^2)(x_2y_1 - x_1y_2)$$

If A=0 then the points are colinear elasewhere using A,B,C you can find center and radius of circle:

$$x_c = -B/2A$$

$$y_c = -C/2A$$

$$r = \sqrt{\frac{B^2 + C^2 - 4AD}{4A^2}}$$

Finally the formula of the circle is:

$$(x - x_c)^2 + (y - y_c)^2 = R^2$$

When 2 point coordinates are given, equation of the linear edges of the plate, can be determined by the calculation below;

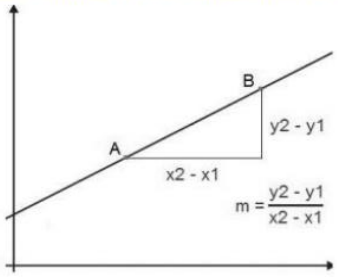


Fig. 5: Flat pattern of sample plate, tool path and edge geometry equations.

The data used by the algorithm that enables the creation of the tool path geometry on the machine are transferred to the PLC system by using the QR codes on the technical drawings by using the hand scanner. Thus, errors that may occur due to the operator's manual entry of numerical values are prevented. These numerical values are plate thickness, edge lengths, outer and inner radius values in conical plates, different root distances desired on each edge.

PLATE NR.	POZ. (IR, DR)	PROJECT PLATE NR.	PLATE THCK.	EDGE 1	EDGE 2	EDGE 3	EDGE 4
76	IR	2733-S1-P6	18.7	10212	2915	10360	2915
TYPE (D,K)	DIAG. LTH.	INT. RAD.	EXT. RAD.	K1 ROOT	K2 ROOT	K3 ROOT	K4 ROOT
K	10691	201638	204553	7	7	7	7

Fig. 6: QR Code sample including the plate parameters.

During the beveling process, the plate with the dimensions of 13000x3000 mm stands on the bench table only with its own weight, no special clamping is done. It was planned to use co-milling in high-volume chip removal, but excessive vibrations occurred in the heavy plate-shaped workpiece during the chip removal process. On the other hand, it was decided to determine the machining method by measuring the vibrations in counter-milling and comparing the vibration measurement results in the chip removal processes performed with both methods. Siemens S7-1500 PLC Automation system manages the servo motors and moves the cutting tool by executing the related equation from point to point with the necessary hardware and software.

After beveling, full circumference measurement, inspection and reporting are carried out with the 2D laser profile sensor, which is seen in Figure 7, located behind the cutting tool in order to monitor whether the weld bevel is opened at the desired dimensions or not. This function, which will be carried out automatically simultaneously with the cutting, eliminates the manual control process of the operator after cutting, and thus it is possible to prevent possible errors and time losses.

4. EXPERIMENTAL STUDY AND EVALUATION

Wear measurements were made after every two passes of metal cutting from all sides circumferentially of the plate with the cutting tool. The wear criterion is based on the flank wear VB=0.3 mm defined in ISO 8688.

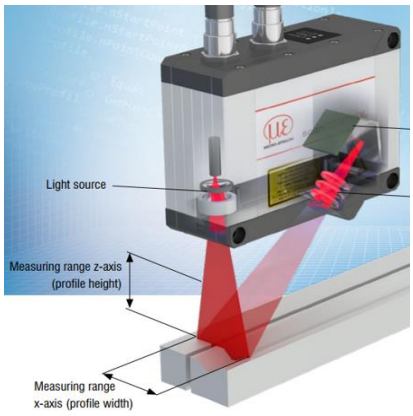
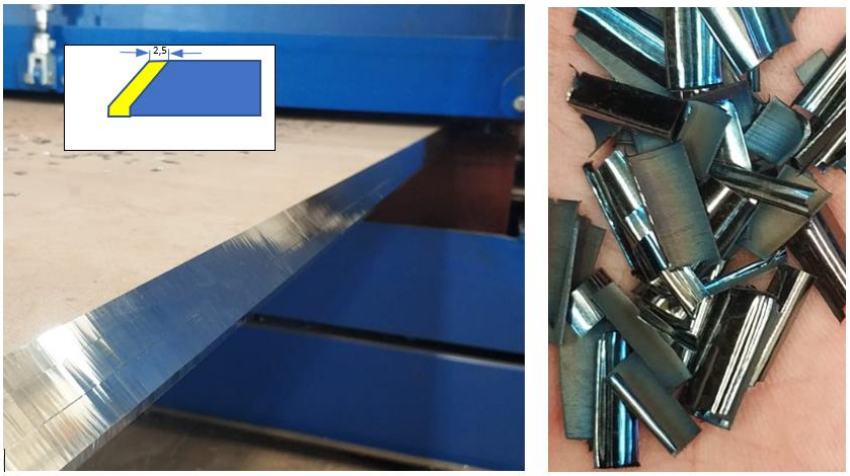


Fig. 7: Laser Profile Sensor [7]

In the study, it is aimed to complete the weld beveling process on the largest plate in around 40 minutes. Experiments were carried out using two different feed rates of 780 mm/min and 820 mm/min, and two different rotational tool speeds of 269 rpm and 350 rpm. The cutting speeds corresponding to these rotations cause the tool in each row to remove chips with a different cutting speed as seen in Table 2, as each cutting insert is placed in different diameters, as seen in Figure 3-b. No cooling fluid was used in the experiments, dry machining was performed. The bevel and the chips obtained during the test studies are given in Figure 8. The wear results obtained in the experiments are given in Table 2, and the wear graphs are given in Figure 9 and Figure 9.



a b

Fig. 8: a- Test plate, b- Chip samples obtained after Beveling [6].

Table 2: Wear measurements obtained at the end of the experiments.

Vf=820 mm/min					Vf=780 mm/min				
Time (min)	A 240 (m/min)	B 225 (m/min)	C 210 (m/min)	D 203 (m/min)	Time (min)	A 312 (m/min)	B 292 (m/min)	C 274 (m/min)	D 264 (m/min)
60.0	0.084	0.059	0.054	0.072	63	0.063	0.049	0.046	0.056
119.0	0.095	0.075	0.094	0.111	125	0.070	0.059	0.063	0.076
178.0	0.105	0.13	0.108	0.176	176	0.087	0.078	0.067	0.087
237.0	0.157	0.151	0.125	0.207	248	0.118	0.110	0.077	0.127
296.0	0.22	0.205	0.136	0.236	310	0.135	0.127	0.097	0.145
355.0	0.23	0.236	0.168	0.255	371	0.157	0.156	0.123	0.189

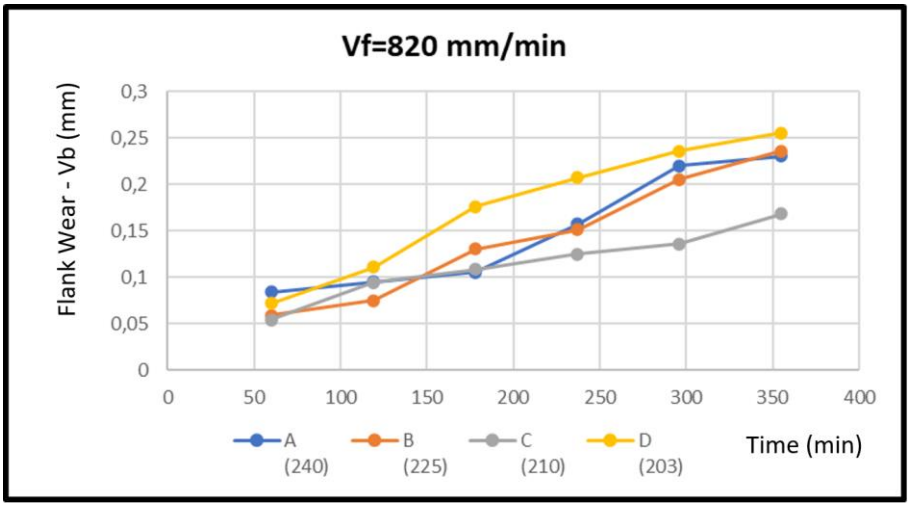


Fig. 9: Wear development of cutting tools at Vf=820 mm/min feed rate (Tuncer 2021).

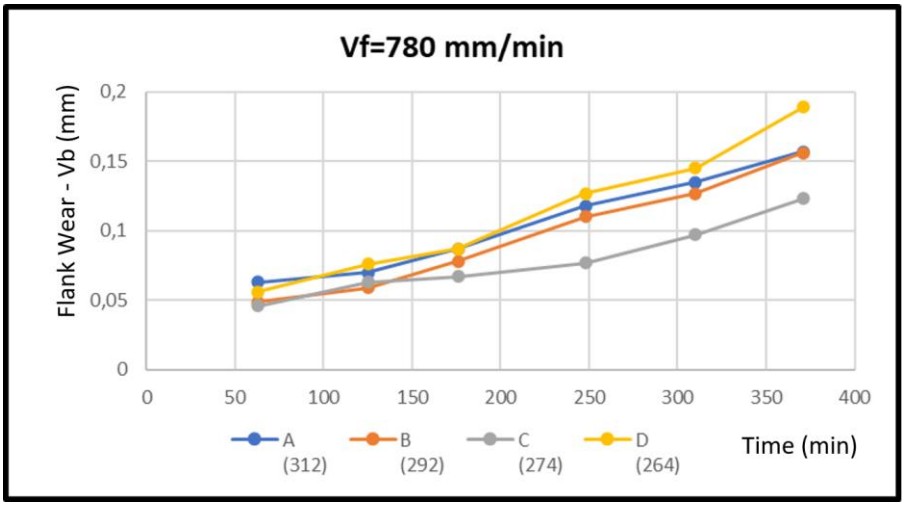


Fig. 10: Wear development of cutting tools at Vf=780 mm/min feed rate (Tuncer 2021).

5. RESULTS

Prototype production studies of the designed automatic beveling machine and working tests carried out under laboratory conditions have been completed and the process of inclusion in the manufacturing processes continues. With this machine, the geometry and position of the plate are automatically determined by the measurements taken over the edges of the plate placed on the machine table. This process is completed in a much shorter time than the time spent for precise placement of a metal plate of 13000x3000 mm, whose mass varies between 6-9 tons depending on the plate thickness. Plate data is transferred to PLC system from technical drawings containing QR code. Thanks to the edge tracking system, the edge to be opened adaptively is monitored and chip removal is performed. Thus, the need for CNC part program in beveling machine technology has been eliminated. In both groups, the highest wear value was recorded despite the lowest cutting speed in the cutting tools that processed the vertical edge in the experiments, and lower cutting speeds were recorded although the cutting speeds of the other tools were higher. In the cutting tool that processes the vertical edge, the approach angle is 90º and in other tools, the approach angle is 45º. This situation, which is seen as a contrary situation with the literature; It has been evaluated that the D tool, which cuts the steep edges due to the approach angle, removes thicker chips and thus is exposed to higher cutting forces and is exposed to more wear.

In the continuation of this study, studies will be carried out to determine the optimum values by repeating the tests for different cutting speeds and feed rates without reducing the production speed.

REFERENCES

1. Lei T., Ronga Y., Wanga H., Huanga Yu. Li M (2020), "A review of vision-aided robotic welding," Computers In Industry, Vol. 123, pp. 1-30

2. Fulemova, J., Hnatik, J.; Kozmin, P., SklenickaJ (2015), "Influence of Cooling Methods On Tool Life During Machining With iMachining Strategy**",** 10th International DAAAM Baltic INDUSTRIAL ENGINEERING" Conference, p.1-6, 12-13 May, Estonia "

3. Schulz, H., (1992), High Speed Machining, Annals of CIRP, Vol. 41(2), pages 642–673

4. https://www.sandvik.coromant.com/tr-tr/knowledge/machining-formulas-definitions/pages/milling.aspx (25.01.2022)

5. Tuncer Can, Turkoz,S. Oral A. (2021), Determination of Cutting Parameters for Peripheral Milling of S355J Sheet Metal with Aggressive-High-Performance Machining Method, 1st

International Conference on Advances in Engineering, Architecture, Science and Technology, p. 677-681, Erzurum Technical University, December 15-17, ERZURUM/TURKEY

6. https://www.secotools.com/article/p_03272731 (30.08.2021)

7. https://www.micro-epsilon.com/download/products/cat--scanCONTROL--en.pdf (25.01.2022)

COMPARISON OF ANN AND RSM IN PREDICTION OF THE TANGENTIAL FORCE IN TURNING OF AISI 4140 HARDENED STEEL CONSIDERING FLANK WEAR

Osman ÖZTÜRK, *osmanozturk@ktun.edu.tr* Konya Technical University, 42250, Konya, Turkey

Ali ÜNÜVAR, *aunuvar@ticaret.edu.tr* Istanbul Ticaret University, 34840, Istanbul, Turkey

ABSTRACT

Turning is one of the industry's most commonly used material removal methods. A significant output of the turning process is the material's surface roughness since the design's functionality depends on the material's surface roughness. The main cutting force during turning is directly related to surface roughness and tool wear. The aim of this study was to predict cutting force by using Artificial Neural Network (ANN) and Response Surface Methodology (RSM). The trained ANN model predicts the critical values of the main cutting force and tool wear. In this model, cutting speed, feed rate, depth of cut, and flank wear were inputs, while the tangential force was output. The results were evaluated by calculating the coefficient of determination, root mean square error, and model predictive error. It was found that the ANN model was better at anticipating the cutting force. The statistical results suggest that ANN and 2nd order RSM model showed higher performance, while the 1st order RSM model indicated very low accuracy. ANN was slightly better than the 2nd order RSM model among better models. Therefore the ANN model was the most effective one among the three models at predicting the cutting force.

Keywords: Artificial neural network, flank wear, machining, turning, response surface methodology.

1. INTRODUCTION

Turning is a widely used manufacturing method because it is both effective for a good surface finish and more energy-efficient than other alternative methods. After a turning operation, the functionality of the design depends on the surface roughness of the material. Surface roughness depends directly on tool condition and cutting parameters. Therefore, cutting parameters must be adjusted carefully before and during the operation for longer tool life. During a turning process, some indicators of tool condition can be measured instantaneously,

such as cutting force and acoustic emission. These outputs depend on the generally used cutting parameters, which are cutting speed, feed rate, and depth of cut. Many researchers worked on different methods to optimize the cutting parameters properly for a high-quality surface finish.

A significant number of the scholars in this subject focused on the modeling and the prediction of cutting force and surface roughness. Bouzid et al. [Lakhdar, 2020] studied the effectiveness of the modeling methods RSM, ANN, and DFA on the turning performance criteria. The resultant surface roughness of the workpiece and the cutting force was chosen as the criteria for AISI D3 hardened steel. Experimental data was based on Taguchi design. ANN method gave better results than the RSM method in terms of the root mean square error, the model predictive error, and the coefficient of determination.

Meddour et al. used ANN and RSM to model the surface roughness and the cutting force for the turning operation of AISI 4140 hardened steel [Meddour, 2018]. Non-dominated Sorting Genetic Algorithm and DFA techniques were also compared as optimization methods. The most satisfying result for the prediction of the minimum value of the surface roughness was found to be the ANN method coupled with Non dominated Sorting Genetic Algorithm. Labidi et al. developed a prediction model for surface roughness, flank wear, and tangential force. ANN and RSM methods were used to develop models that define the relationship between the input parameters and the output dependent variables [Labidi, 2018]. The results indicate that a more accurate model was developed compared to RSM. Hanief et al. developed a regression model and ANN model for the prediction of cutting forces during the turning operation of red brass. ANOVA is used to test the adequacy of the regression model [Hanief, 2017].

As a consequence, the ANN model was more accurate even though the regression model provided acceptable predictions. Mia et al. studied the modeling of surface roughness, cutting force, and feed force during the turning of Ti-6Al-4V under cryogenic conditions [Mia, 2017]. RSM and ANN models were developed and compared in terms of adequacy. On the contrary to other researchers, RSM was found to be a better predictive model than ANN.

Some of the studies in this specific topic focused on the hard turning process. Prediction of the surface roughness and the cutting force components in hard turning of AISI 420 stainless steel using RSM and ANN models was the purpose of the studies conducted by Zerti et al. [Zerti, 2019]. The ANN model showed better accuracy when compared to the RSM model. Paturi et al. investigated the performance of ANN and regression analysis in modeling surface roughness in hard turning of AISI 52100 steel. In this study, the prediction performance of the ANN model was found to be better than regression analysis [Paturi, 2018].

Ulas et al. developed an ANN model for three different materials and compared it with experimental results [Ulas, 2019]. The materials are AISI 304, AISI 420, and AISI 2205, which are austenitic, martensitic, and duplex, respectively. It has been stated that the ANN model is in good agreement with experimental results. Abbas et al. studied the optimization of surface roughness in the turning process of AZ61 magnesium alloy [Abbas, 2018]. It has been concluded that the ANN model reached an accuracy of ±1.35 % for surface roughness. Tebassi et al. compared ANN and RSM for modeling surface roughness and cutting force [Tebassi, 2017]. To determine a better model, lower root mean square error and model predictive error was aimed, while a higher coefficient of determination was desired. Results indicated that the ANN model is better at predicting surface roughness and cutting force. Rajbongshi et al. modeled the surface roughness and flank wear by ANN and RSM [Rajbongshi, 2019]. Two different cutting conditions (dry and forced air-cooling) were investigated. As a result, the ANN model showed better accuracy in terms of the regression coefficient.

The dry machining condition was better for a good surface finish, while the air-cooled condition was better for reducing flank wear. Leo Dev Wins et al. developed an ANN model and evaluated its ability to predict cutting force in the hard turning of H13 steel [Leo Dev Wins, 2021]. Kosaraju et al. used an ANN model to predict cutting force, surface roughness and material removal rate of Titanium alloy Ti6Al4V which is a low machinability material [Kosaraju, 2022].

In this study, an offline adaptive control procedure for cylindrical turning of AISI 4140 hardened steel was developed by regulating the cutting speed and feed rate based on tool condition. In order to regulate cutting parameters, the tangential force and tool wear were measured experimentally. The tangential cutting force and tool wear were modeled by ANN and two types of RSM. The main objective of this study was to lower feed rate and cutting speed to avoid the sudden failure of the cutting tool.

2. EXPERIMENTAL SETUP AND PROCEDURE

Constructing the RSM Model for Tangential Force

In the experimental phase of the study, an appropriate experimental plan was designed for RSM at first. The three main input parameters are cutting speed, feed rate, and depth of cut. The levels of the parameters have been chosen to be suitable for the operating range of the CNC turning machine. A face-centered cubic design was created to build the first and the second order RSM models. The experimental design and the measured responses are given in Table 1. The flank wear (FW) of the insert was also considered. Therefore, cutting speed, feed rate, depth of cut, and FW were input parameters, while tangential force (F_t) was the output response. Length of cut (LOC) for every step of FW was also recorded for later use.

The schematic representation of the procedure of the experimental and the modeling phase is given in Figure 1. According to the procedure, RSM models were built from the data that had been collected from the experimental plan.

Table 1. The experimental design and measured responses for RSM model.

	Input Parameters			Measured Responses					
				FW = 0.01 mm		FW = 0.15 mm		FW = 0.30 mm	
Exp. No.	Cutting Speed ($m \cdot min^{-1}$)	Feed Rate ($mm \cdot rev^{-1}$)	Depth of Cut (mm)	LOC (mm)	F_t (N)	LOC (mm)	F_t (N)	LOC (mm)	F_t (N)
1	250	0.05	0.5	30	87.11	8470	115.05	10395	138.66
2	150	0.2	0.5	30	248.89	6545	274.54	15785	291.19
3	150	0.05	1.5	30	214.39	770	233.53	3080	317.16
4	250	0.2	1.5	30	681.27	1540	694.26	1925	743.67
5	190	0.1	0.87	30	241.23	3080	270.2	9240	298.63
6	190	0.1	0.87	30	222.28	1925	230.56	9240	326.79
7	190	0.1	0.87	30	264.67	3850	284.69	7315	307.65
8	150	0.1	0.87	30	303.61	3080	310.27	13860	336.95
9	190	0.05	0.87	30	158.80	2310	193.15	4235	263.06
10	190	0.1	1.5	30	360.13	1925	376.72	5775	482.75
11	190	0.2	0.5	30	233.40	9625	258.72	20405	307.80
12	250	0.1	0.5	30	135.30	3850	168.34	8470	209.02
13	250	0.2	0.87	30	415.17	1925	424.38	4620	472.27
14	250	0.1	0.87	30	256.82	2310	285.4	3080	322.88
15	190	0.2	0.87	30	423.51	2695	458.14	3850	547.04
16	190	0.1	0.5	30	136.78	5390	147.62	14630	238.74

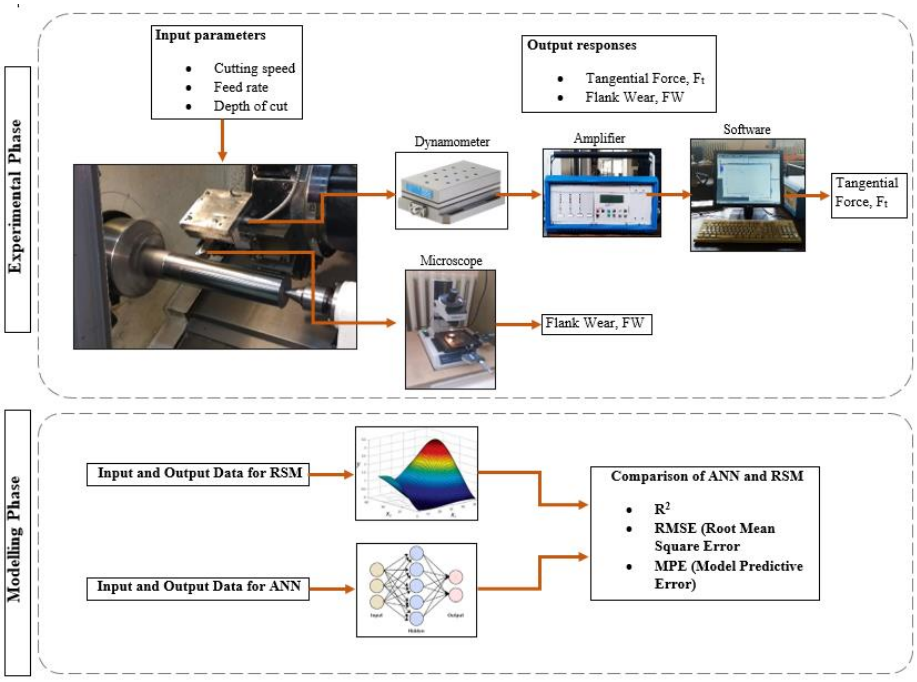


Figure 1. Procedure of the experimental and modeling phase.

Constructing the ANN Model for Tangential Force

There are four main steps in constructing the ANN model for tangential force. The related steps are given below.

Step 1. Design of Experiments. An extra amount of data was required for training, testing, and validating the ANN model. ANN model was built in Alyuda Neurointelligence. The cutting speed, feed rate, and depth of cut (DOC) were given as coded variables. In contrast, input variable length of cut (LOC) and output variable tangential force were given as real variables. The coded and the real values for ANN input variables were defined in Table 2.

Step 2. Classifying the Data. The classification of the data set which was going to be used in training, testing, and validation was made using Alyuda Neurointelligence software. As a result, 92 experiments were used for training, where 21 of them were used for testing and 21 of them were used for validation. Considering all experimental data; 68 %, 16 %, and 16 % of the data were used for training, testing and validation, respectively.

Step 3. Selection of the Best Architecture. The architecture of the neural model was also determined by the software. The criteria were the absolute minimum error of the training, the testing, and the validation results. Among tested architectures, 4-12-1 type was chosen as the best. The absolute error rates are given in Table 3.

Step 4. Choosing the Training Algorithm and the Number of Iteration. Quasi-Newton and Levenberg Marquardt training algorithms were used for comparison [Mukherjee, 2012]. For the data set of this study, It was found that the minimum error rate was acquired by using Quasi-Newton training algorithm and 300 iterations.

Table 2. The real and coded values of input variables for the ANN model.

***v* - Cutting Speed**						
Real Value ($m \cdot min^{-1}$)	150	170	190	210	230	250
Coded Value	-1	-0.51	0	0.32	0.67	1
***f* - Feed Rate**						
Real Value ($mm \cdot rev^{-1}$)	0.05	-	0.1	-	-	0.15
Coded Value	-1	-	0	-	-	1
DOC - Depth of Cut						
Real Value (mm)	0.5	0.7	0.87	1.2	-	1.5
Coded Value	-1	-0.39	0	0.59	-	1

Table 3. The determination of the best ANN architecture for the ANN model of tangential force.

No	Architecture	Weight	Training Error	Validation Error	Test Error
1	4-1-1	9	73.77	63.52	62.79
2	4-13-1	93	8.44	11.31	12.16
3	4-8-1	58	16.02	14.45	15.82
4	4-5-1	37	24.47	13.58	21.14
5	4-11-1	79	10.06	14.53	12.41
6	4-9-1	65	21.38	13.18	19.36
7	**4-12-1**	**86**	**7.7**	**10.78**	**11.33**
8	4-10-1	72	20.62	15.49	19.25

3. EXPERIMENTAL RESULTS

The 1st and 2nd order RSM models are given below. The parameters influencing the output response were cutting speed, feed rate, depth of cut, and flank wear for this case.

$$(F_t)^{1st\ order} = 304.73 + 39.69 \cdot v + 128.50 \cdot f + 140.91 \cdot DOC + 35.61 \cdot FW \quad (1)$$

$$(F_t)^{2nd\ order} = 272.09 - 8.64 \cdot v + 145.54 \cdot f + 142.87 \cdot DOC + 35.27 \cdot FW + 38.6 \cdot v^2 + 53 \cdot f^2 - 9.2 \cdot DOC^2 - 4.3 \cdot FW^2 + 3.7 \cdot v \cdot f + 2.41 \cdot v \cdot DOC - 6.25 \cdot v \cdot FW + 69.37 \cdot f \cdot DOC - 6.41 \cdot f \cdot FW + 9.69 \cdot DOC \cdot FW \quad (2)$$

The overall comparison of RSM and ANN models with experimental data is given in Figure 2. According to these results, the 1st order RSM model was found not to be effective in predicting the experimental force values. However, statistical methods were required to distinguish the performance of the models. Therefore coefficient of determination (R^2), root mean square error (RMSE), and model predictive error (MPE) were calculated from the results given in Figure 2. The statistical results suggested that ANN was better at predicting forces during machining. The results related to R^2 are given in Figure 3, Figure 4 and Figure 5. The overall results for statistical calculations are presented in Figure 6.

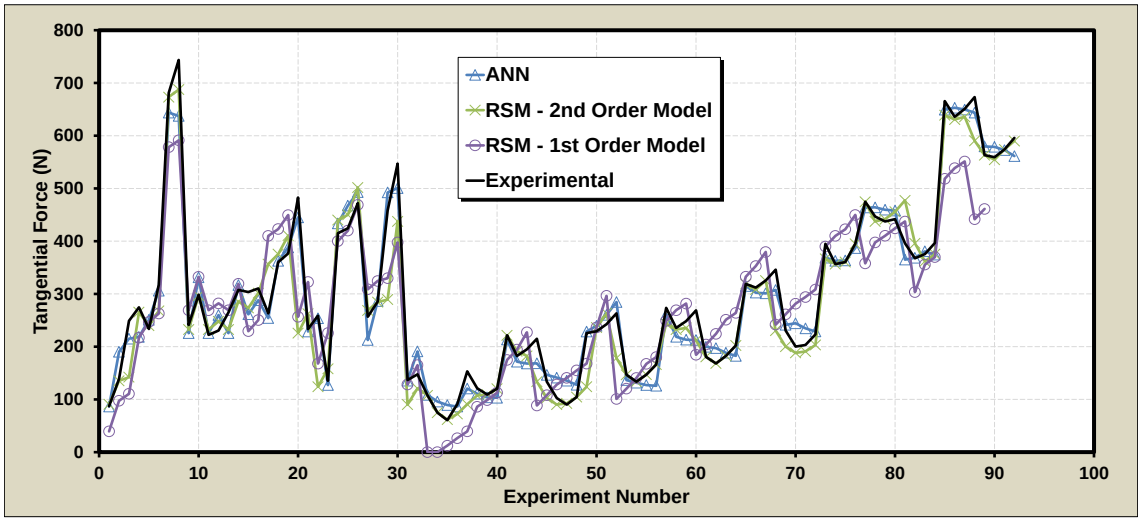


Figure 2. Comparison of ANN and RSM models with experimental data.

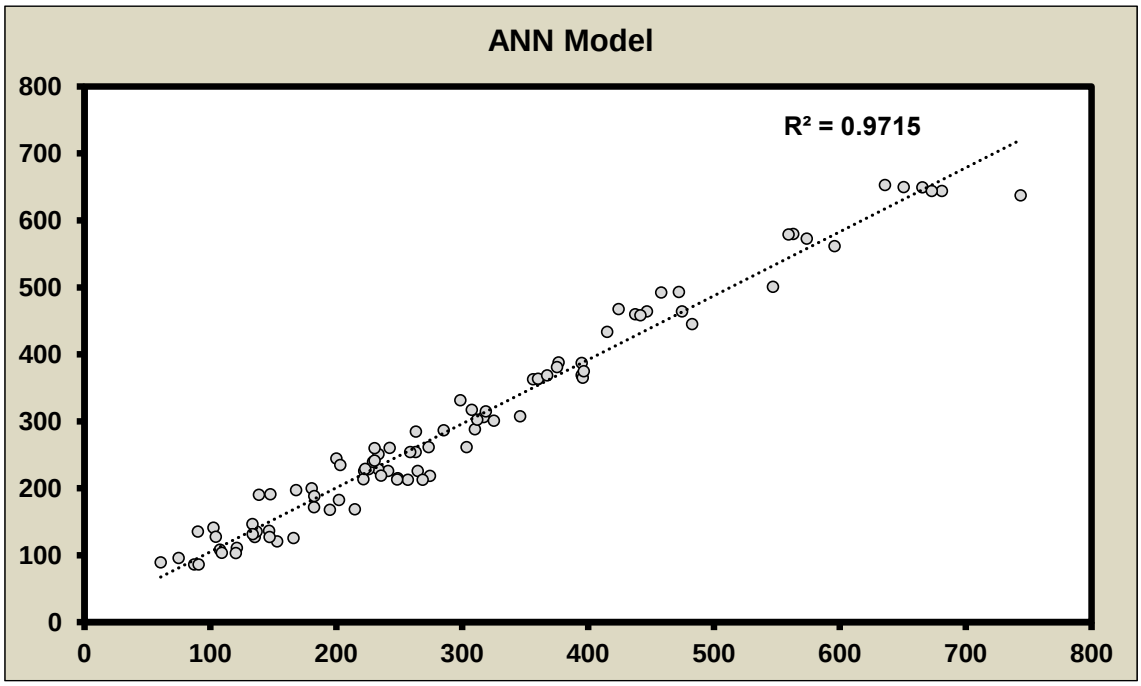


Figure 3. Coefficient of Determination (R^2) for ANN model.

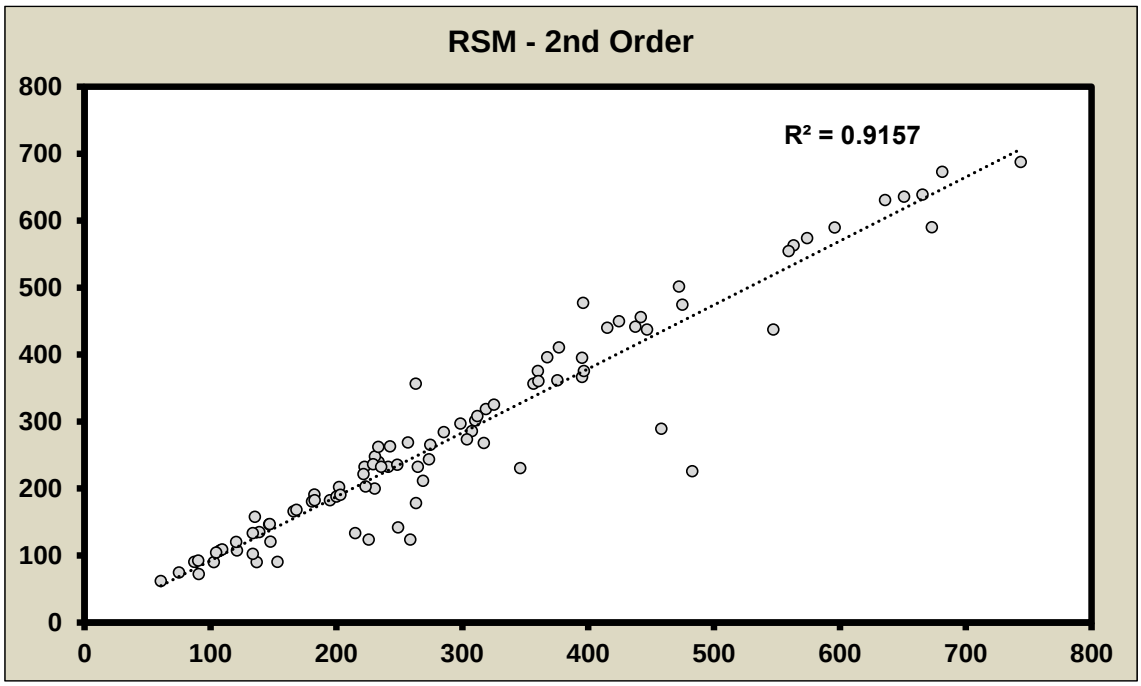


Figure 4. Coefficient of Determination (R^2) 2nd order RSM model.

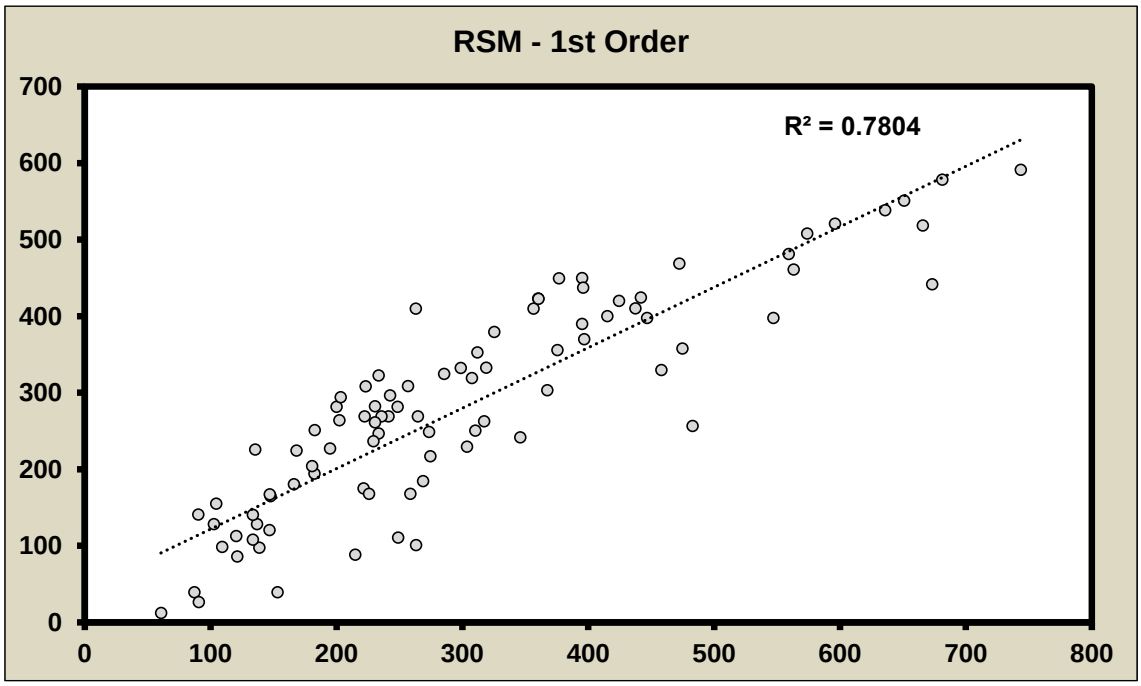


Figure 5. Coefficient of Determination (R^2) 1st order RSM model.

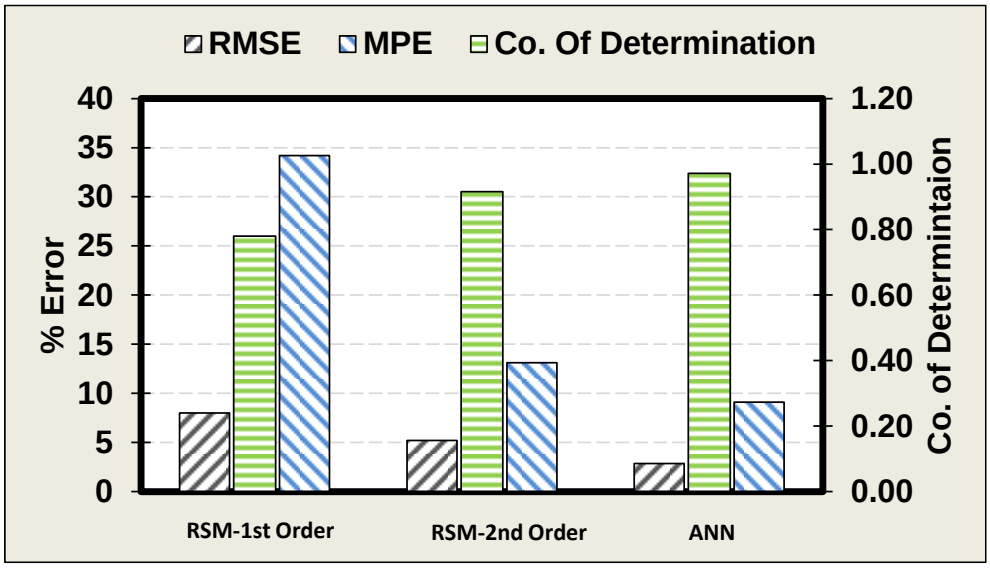


Figure 6. The statistical results of ANN and RSM models.

4. CONCLUSIONS

The aim of this study is to built an ANN and two types of RSM models to predict the tangential forces during turning of AISI 4140 hardened steel. Three common cutting parameters were used as inputs for the models. The tangential force was the output response. The flank wear was also considered as the fourth input in this study, as well as cutting speed, feed rate, and depth of cut, which are commonly used. This study's contribution is considering the effect of tool condition on tangential cutting force. The following results were found in this study.

- It was clear from the experimental data that as flank wear increased, the tangential cutting force also increased. Therefore the output response depends on the tool condition besides commonly used cutting parameters.
- According to the modeling results, the 1st order RSM model was found not to be effective in predicting the experimental force values. ANN and 2nd order RSM models showed better performance forecasting the tangential force, while ANN was slightly better than the 2nd order RSM model. Moreover, this result must have been expressed by numerical values. Therefore the results were statistically investigated.
- The coefficient of determination (R^2), root mean square error (RMSE), and model predictive error (MPE) were calculated for statistical purposes. It was found for the ANN model that R^2, RMSE, and MPE were; 0.97, % 2.86, and % 9.11, respectively. The results for the 1st order RSM model in the same order were; 0.78, % 8.01, and % 34.19. For the last comparison, the results for the 2nd order RSM model in the same order were; 0.92, % 5.19, and %13.12. It was clear that ANN was more accurate in modeling the force in the rough turning operation of hardened steel.

REFERENCES

1. **Lakhdar, B., Athmane, Y. M., Salim, B., and Haddad, A. (2020).** "Modelling and optimization of machining parameters during hardened steel AISID3 turning using RSM, ANN and DFA techniques: Comparative study", Journal of Mechanical Engineering and Sciences, Vol. 14, No. 2, pp 6835–6847.
2. **Meddour, I., Yallese, M. A., Bensouilah, H., Khellaf A. And Elbah M. (2018).** "Prediction of surface roughness and cutting forces using RSM, ANN, and NSGA-II in finish turning of AISI 4140 hardened steel with mixed ceramic tool", Int J Adv Manuf Technol, Vol. 97, pp 1931–1949.
3. **Labidi, A., Tebassi, H., Balhadi S., Khettabi, R. and Yallese M. A. (2018).** "Cutting conditions modeling and optimization in hard turning using RSM, ANN and desirability function.", Journal of Failure Analysis and Prevention, Vol. 18, No. 4, pp 1017-1033.
4. **Hanief, M., Wani, M. F. and Charoo, M. S. (2017).** "Modeling and prediction of cutting forces during the turning of red brass (C23000) using ANN and regression analysis.", Engineering science and technology, an international journal, Vol. 20, No. 3, pp 1220-1226.
5. **Mia, M., Khan, M. A. and Dhar, N. R. (2017).** "Study of surface roughness and cutting forces using ANN, RSM, and ANOVA in turning of Ti-6Al-4V under cryogenic jets applied at flank and rake faces of coated WC tool.", The International Journal of Advanced Manufacturing Technology, Vol. 93, No. 1, pp 975-991.

6. **Zerti, A., Yallese, M. A., Zerti, O., Nouioua, M. and Khettabi, R. (2019).** "Prediction of machining performance using RSM and ANN models in hard turning of martensitic stainless steel AISI 420." Proceedings of the Institution of Mechanical Engineers, Part C: Journal of Mechanical Engineering Science, Vol. 233, No. 13, pp 4439-4462.
7. **Paturi, U. M. R., Devarasetti, H., and Narala, S. K. R. (2018).** "Application of regression and artificial neural network analysis in modelling of surface roughness in hard turning of AISI 52100 steel." Materials Today: Proceedings, Vol. 5, No. 2, pp 4766-4777.
8. **Ulas, H. B., and Murat T. Ö. (2019).** "Turning processes investigation of materials austenitic, martensitic and duplex stainless steels and prediction of cutting forces using artificial neural network (ANN) techniques." Indian Journal of Engineering and Material Sciences, Vol. 26, pp 93-104.
9. **Abbas, A.T., Pimenov, D.Y., Erdakov, I.N., Taha, M.A., Soliman, M.S. and El Rayes M.M. (2018).** "ANN surface roughness optimization of AZ61 magnesium alloy finish turning: Minimum machining times at prime machining costs." Materials, Vol. 11, No .5, 808.
10. **Tebassi, H., Yallese, M. A., Meddour, I., Girardin, F. and Mabrouki, T. (2017).** "On the modeling of surface roughness and cutting force when turning of Inconel 718 using artificial neural network and response surface methodology: accuracy and benefit.", Periodica Polytechnica Mechanical Engineering, Vol. 61, No. 1, pp 1-11.
11. **Rajbongshi, S. K. and Sarma, D. K. (2019).** "A comparative study in prediction of surface roughness and flank wear using artificial neural network and response surface methodology method during hard turning in dry and forced air-cooling condition.", International Journal of Machining and Machinability of Materials, Vol.21, No. 5-6, pp 390-436.
12. **Leo Dev Wins, K., Anuja Beatrice, B., Ebenezer Jacob Dhas, D. S. and Anita Sofia, V. S. (2021).** "Artificial Neural Network and Genetic Algorithm-Based Models for Predicting Cutting Force in Turning of Hardened H13 Steel.", Trends in Manufacturing and Engineering Management, pp 627-635.
13. **Kosaraju, S., Aruri, D., Kolli, M., Sai Kumar, G. and Bobba, P. B. (2022).** "Study on machinability of Ti6Al4V with coated inserts–cutting force, surface finish and material removal rate prediction using ANN.", International Journal on Interactive Design and Manufacturing (IJIDeM), pp 1-11.
14. **Mukherjee, I. and Srikanta R. (2012).** "Comparing the performance of neural networks developed by using Levenberg–Marquardt and Quasi-Newton with the gradient descent algorithm for modelling a multiple response grinding process." Expert Systems with Applications, Vol 39, No. 3, pp 2397-2407.

A METHOD TO OBTAIN THE CROSS-SECTIONAL PROFILE OF THE REGION SWEPT BY A TOROIDAL CUTTER DURING A SCREW MOTION

Ahmet DOĞRUSADIK, *adogrusadik@dogus.edu.tr* Dogus University, 34775, Istanbul, Turkey

ABSTRACT

A model is introduced, which gives the cross-sectional profile of the swept volume of a toroidal cutter that moves along a helical path. The model considers that a milling cutter can be generated by unifying an infinite number of circles along the axis of rotation of the tool since all milling cutters can be represented by the solids of revolution. By obtaining the traces of all circles which undergo helical motion in a reference plane, the equation of the cross-sectional profile of the swept volume is derived as the envelope of these traces. An implicit equation of the cross-sectional profile of the swept volume was obtained. A CAD program was used to verify the model.

Keywords: Toroidal cutter, Helical milling, Helical groove, Profile, Ring torus

1. INTRODUCTION

Helical milling is basically used to create large holes. When a cutter that can machine undercuts, such as a toroidal cutter, is used, it becomes important to calculate the cusp height. The cusp height can be determined approximately by using the geometry of the cutting tool and the pitch of the helical path. This requires the determination of the intersection point of two cross-sectional profiles of the cutter which are aligned vertically with a pitch distance, but this just gives the approximate cusp height. Indeed, the actual cusp height is different from this value every time because the cross-sectional profile of the machined part is different from that of the cutter due to the overcut that occurs during the process. The actual cusp height can be determined as long as the cross-section of the machined surface is calculated. Apart from creating a hole, the same process can be used to create the helical grooves in the sidewall of the workpiece. In this case, it is important to calculate the cross-sectional profile of the groove prior to the process. This cross-section will

obviously be different from the cutter due to the overcut. These two examples indicate the importance of determining the machined part geometry in helical milling.

Several approaches have been introduced for the swept volume generation, such as envelope theory, sweep differential equation (SDE), sweep-envelope differential equation (SEDE), Jacobian rank-deficiency, and others. Wang and Wang [1] introduced an analytical model to obtain the swept volume using the envelope theory, but the model is limited to the regular surfaces. According to the model, the envelope is generated by critical curves that are tangent to the envelope. Blackmore and Leu [2] proposed the SDE method based on the fact that the first-order linear ordinary differential equation can be used to determine the smooth Euclidian motion of an object. Then, Blackmore et al. [3] introduced the SEDE method, an extension of the SDE method. The method decreases the computation time significantly compared to the previous method because it does not require calculating the grazing points at every step. Abdel-Malek and Yeh [4] introduced the Jacobian rank-deficiency method to obtain the swept volumes of geometric entities of multiple parameters, but the method causes high computation cost.

Chiou and Lee [5] introduced a model for the NC verification considering the instantaneous swept profile of APT (automatically programmed tools). The swept profile was defined as the grazing points derived by using the fact that the instantaneous velocity vector at a point on the surface of the solid is perpendicular to the surface normal vector. Then, the swept envelope was constructed by combining the instantaneous swept profiles. Weinert et al. [6] introduced a model to obtain the swept volume for the NC verification. The model is partially derived from Wang's method [1] and uses the boundary representation approach. The swept envelope was obtained as a NURBS (non-uniform rational B-spline) surface by combining instantaneous swept profiles of a fillet-end mill cutter. Gong and Wang [7] introduced a model based on the moving frame method to obtain the swept envelope of the milling cutters modeled by rotating 2D Bezier curves. The grazing points were directly calculated from the cutter location data. Aras [8] proposed a model to determine the swept envelope of the generalized milling cutters. The milling cutter was modeled as a canal surface and decomposed into a set of characteristic and great circles derived from the two-parameter family of spheres. The grazing points were obtained using the relationship between the characteristic and great circles. Lee and Nestler [9] proposed Gauss map approach to obtain the swept volume of a piecewise C^1-continuous shaped cutter for a simultaneous five-axis tool path. The envelope profile is derived in the Euclidean space by using the inverse Gauss function. Rossignac and Kim [10] proposed a method to determine the swept envelope of the canal surfaces which undergo the screw motion. In this work, the authors obtained each grazing point as the intersection of a circle of the tube with the corresponding screw-plane.

Aras [11] developed the closed-form solutions to obtain sub-surface swept profiles of the toroidal and conical milling cutters using the one-to-many strategy that reduces the computation cost due to the fact that a single slice parameter can be utilized to calculate the values of other parameters for a level cut.

The introduced model considers the helical tool path. The reason is that there are previously developed models for arbitrary tool paths, but these models do not exhibit equations that can be directly used to obtain the profile of the machined surface. In addition, most models give an approximation error. The error can be decreased, but this causes higher calculation time. The aim of this work is to obtain the cross-sectional profile of the swept volume by entering the values of the parameters for a toroidal cutter when the tool moves along a helical path.

The helical path of the cutter brings some straightforwardness to the derivation of the machined part surface. Since the tool path is a helix, every cross-section of the machined part is identical. Therefore, it is possible to represent the swept volume based on a cross-section that passes through the screw axis of the helical path. The introduced model is based on the following process. First, the tool surface was decomposed into circles. Then, the traces of the circles moving along a helical path were derived in a reference plane. Lastly, the envelope of the traces was obtained. Following the introduction of the analytical model, a CAD program was used to validate the model.

2. ANALYTICAL MODELING

The surface of a milling cutter can be divided into infinitely many circles along the axis of rotation since the milling cutter can be represented as the solid of revolution. Therefore, it can be said that if the traces of all circles are investigated, the resulting feature can be obtained. First, the trace of a circle that moves along the helical path was investigated to do this.

2.1. Trace of a Circle Moving Along a Helical Path: The trace of a circle that moves along a helical path in the second quadrant of $x-y$ plane can be considered. A circle can be created by rotating the point *I(m,n)* that remains in the first quadrant of x_1-y_1 plane about y_1-axis in the reference coordinate system $O_1x_1y_1z_1$ in Figure 1a and b. The helical path is demonstrated in the reference coordinate system *Oxyz*, and the circle with the reference coordinate system $O_1x_1y_1z_1$ is located to the helical path in Figure 1c and d. The helical path has two parameters. These are the radius of the helix (R) and the pitch of the helix (p). The center of the circle moves along the helical path, and the rotational angle of the center of the circle about the fixed axis of the helix (y-axis) in $x-z$ plane is represented by φ. Based on these assumptions, parametric equations of the circle as the functions of φ in *Oxyz* can be

obtained in Eq. (1) and (2). Eq. (3) is obtained by arranging Eq. (2) and substituting $z = 0$, since the trace of the circle is investigated in the second quadrant of $x - y$ plane. Then, the equation of the upper portion of the trace of the circle in the second quadrant of $x - y$ plane is derived in Eq. (4) by substituting the right side of the first root in Eq. (3) into φ in Eq. (1).

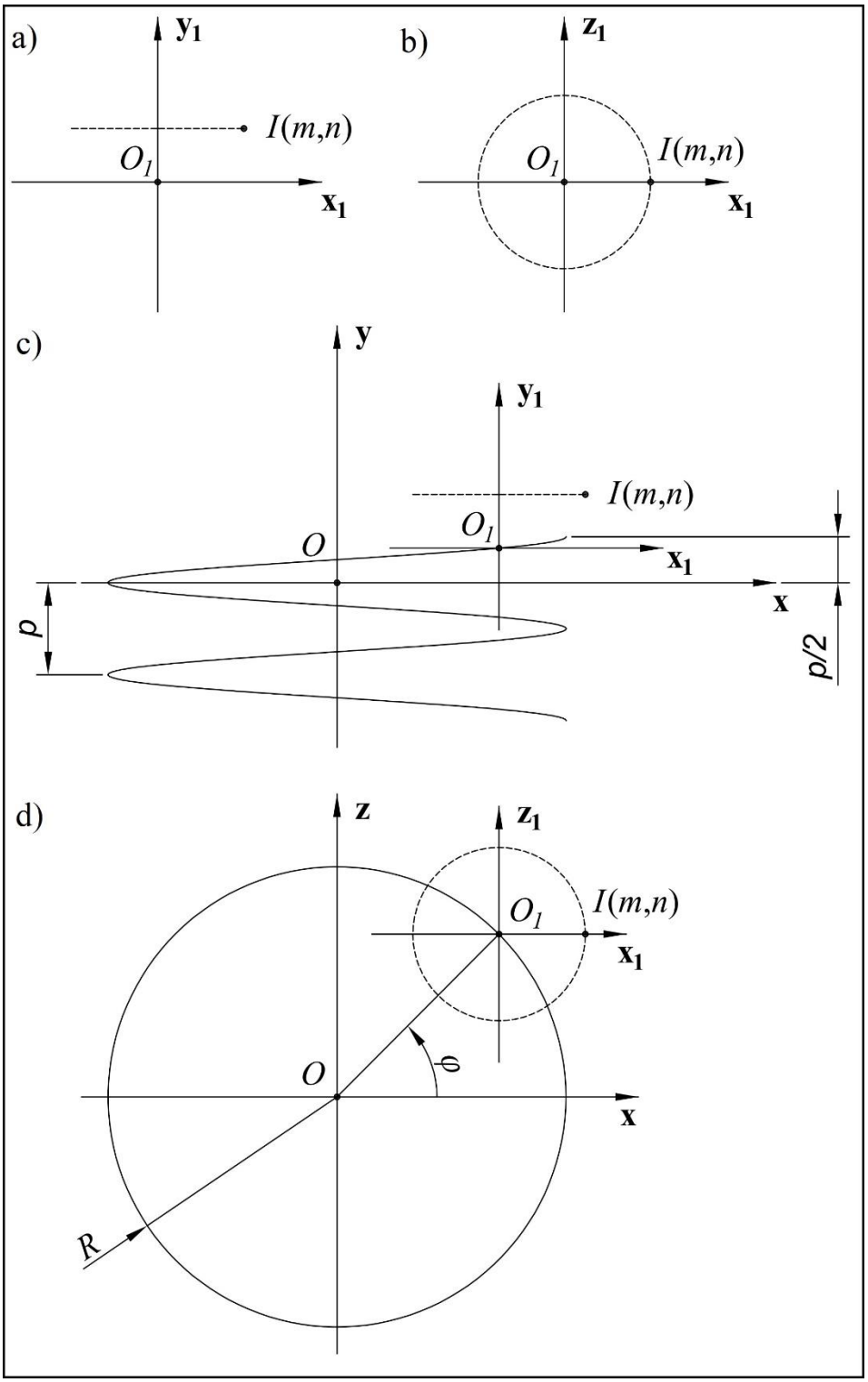


Figure 1. (a) Generated circle in $x_1 - y_1$ plane, (b) Generated circle in $x_1 - z_1$ plane, (c) Helical path in $x - y$ plane, (d) Helical path in $x - z$ plane.

$$y = \frac{p}{2} - \frac{p\varphi}{2\pi} + n \tag{1}$$

$$(x - R\cos\varphi)^2 + (z - R\sin\varphi)^2 = m^2 \tag{2}$$

$$\varphi_1 = \cos^{-1}\left(\frac{x^2+R^2-m^2}{2xR}\right) \text{ and } \varphi_2 = 2\pi - \cos^{-1}\left(\frac{x^2+R^2-m^2}{2xR}\right) \tag{3}$$

$$y = \frac{p}{2} - \frac{p}{2\pi}\cos^{-1}\left(\frac{x^2+R^2-m^2}{2xR}\right) + n \tag{4}$$

An example is given for the circle created by the point $I(10,7)$ in Figure 2a. Setting $R = 25$ mm, $p = 10$ mm, $m = 10$ mm, and $n = 7$ mm in Eq. (4), the upper portion of the trace of a circle that moves along a helical path is given in Figure 2b. The distance between the end points of the trace along x-axis is equal to the diameter of the circle, which is 20 mm, as expected.

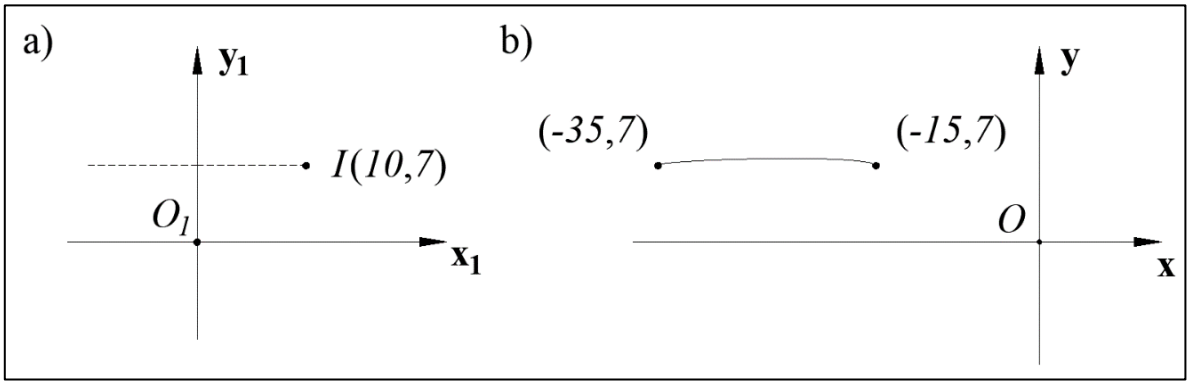


Figure 2. (a) The circle created by rotating the point *I(10,7)* about y_1 axis is shown as the hidden line, and (b) the upper portion of the trace of the circle in the second quadrant of $x - y$ plane is shown with the end points.

2.2. Trace of a Ring Torus Moving Along a Helical Path: The geometrical representation of a toroidal cutter is a ring torus. The ring torus can be obtained by rotating a circle about y_1-axis in Figure 3. The circle will be called generating circle. Two parameters are used to describe a ring torus. These are tube radius a and the distance e between the torus center O_1 and tube center C. I is a point on the circle with coordinates m and n in $x_1 - y_1$ plane. The coordinates of the point I can be written parametrically as the functions of α in Eq. (5) and Eq. (6). Since the ring torus is symmetrical about the x_1-axis and the tool path is a helix, the upper portion of the generating circle can be considered for the analytical model. The whole cross-section of the swept volume can be obtained by mirroring the half cross-sectional profile about x-axis.

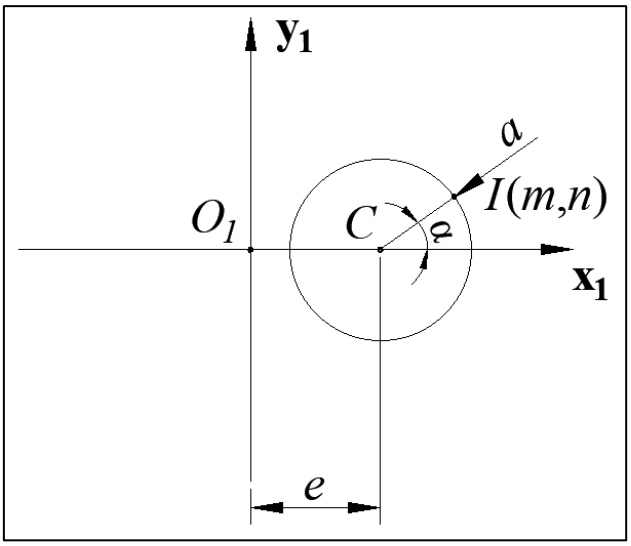


Figure 3. Generation of a ring torus in $O_1x_1y_1z_1$.

$$m = e + a\cos\alpha \tag{5}$$

$$n = a\sin\alpha \tag{6}$$

Previously, only the upper portion of the trace of a circle created by a stationary point I was considered. Since the trace of the torus is investigated, the traces of all possible circles created by the variable point I on the generating circle must be investigated. Substituting the right side of Eq. (5) into m and the right side of Eq. (6) into n in Eq. (4), the equation of the upper portion of the trace of any circle that moves along the helical path and created by rotating the point I on the generating circle about y_1-axis can be obtained in the second quadrant of $x - y$ plane as a function of α in Eq. (7). Figure 4 illustrates the upper portions of the traces of several circles in the second quadrant of $x - y$ plane for several values of α by using $R = 25$ mm, $p = 10$ mm, $e = 10$ mm, and $a = 7$ mm.

$$y = \frac{p}{2} - \frac{p}{2\pi}\cos^{-1}\left[\frac{x^2+R^2-(e+a\cos\alpha)^2}{2xR}\right] + a\sin\alpha \tag{7}$$

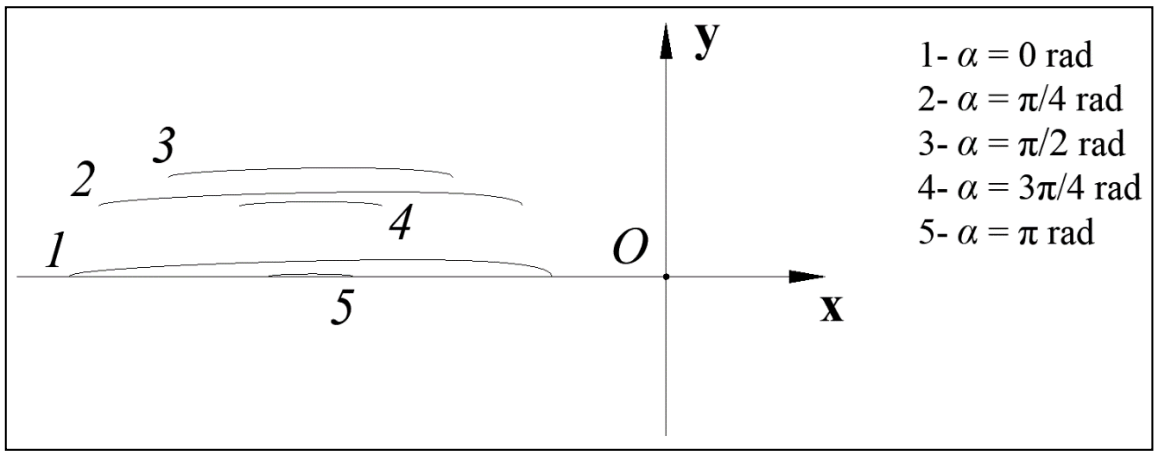


Figure 4. The upper portions of the traces of the circles for several values of α.

As seen in Figure 4, a single trace does not surround the whole region, but the combination of the traces creates the region. Fermat's theorem was applied to Eq. (7) in Eq. (8) to obtain the envelope of the traces of the circles. According to this, when a constant value of x in Eq. (7) is considered, y reaches its highest value for a specific value of α. Differentiating with respect to α and equating to 0, Eq. (9) is obtained in the second quadrant of $x-y$ plane where $x<0$. Arranging Eq. (9) and substituting $t=\cos\alpha$, a polynomial equation with a degree of 6 is derived in Eq. (10). This equation can be solved numerically. After finding an appropriate real root for a specific value of x, α is obtained by using the inverse cosine function. Substituting the value of α into Eq. (7), the corresponding y value is obtained. Thus, the whole curve can be obtained by numerical solution. Figure 5 indicates the cross-sectional profile of the swept volume in the second quadrant of $x-y$ plane for the toroidal cutter ($e=10$ mm and $a=7$ mm), which moves along a helical path ($R=25$ mm and $p=10$ mm). This profile was sketched without considering the shank of the tool. The importance of this cross-section is that both the internal and external groove profiles can be obtained at the same time using a Boolean operation if the aim is to create a helical groove. If this is an internal helical milling process, then the left side of the graph gives the cross-sectional profile of the internal groove. If this is an external helical milling process, then the right side of the graph should be considered.

$$\frac{\partial}{\partial\alpha}\left(\frac{p}{2}-\frac{p}{2\pi}\cos^{-1}\left[\frac{x^2+R^2-(e+a\cos\alpha)^2}{2xR}\right]+a\sin\alpha\right)=0 \tag{8}$$

$$\cos\alpha-\frac{p(e+a\cos\alpha)\sin\alpha}{\pi\sqrt{4R^2x^2-[x^2+R^2-(e+a\cos\alpha)^2]^2}}=0 \tag{9}$$

$$\begin{bmatrix} a^4\pi^2 \\ 4a^3e\pi^2 \\ -a^2p^2+6a^2e^2\pi^2-2a^2\pi^2R^2-2a^2\pi^2x^2 \\ -2aep^2+4ae^3\pi^2-4ae\pi^2R^2-4ae\pi^2x^2 \\ a^2p^2-e^2p^2+e^4\pi^2-2e^2\pi^2R^2-2e^2\pi^2x^2-2\pi^2R^2x^2+\pi^2x^4+\pi^2R^4 \\ 2aep^2 \\ e^2p^2 \end{bmatrix}^T \begin{bmatrix} t^6 \\ t^5 \\ t^4 \\ t^3 \\ t^2 \\ t \\ 1 \end{bmatrix} = [0] \tag{10}$$

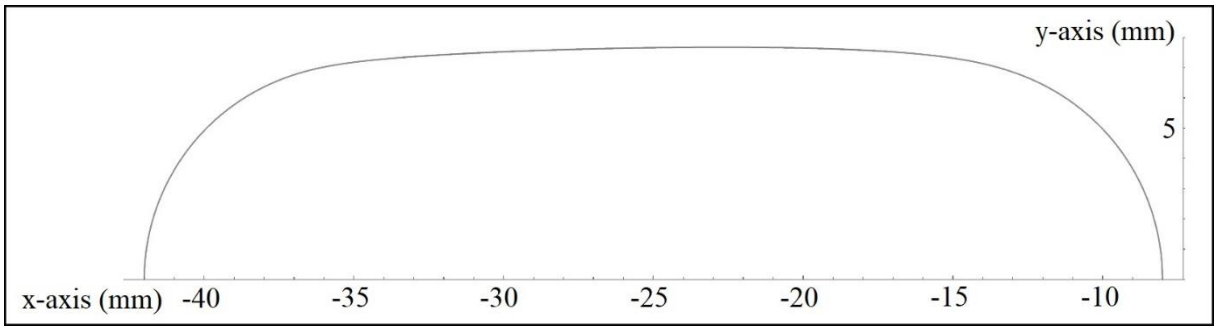


Figure 5. The half cross-sectional profile of the swept volume.

It must be noted that this model only considers the outer surface of the cross-sectional profile. Under certain circumstances, an internal surface may exist in the cross-sectional profile that has not been swept by the ring torus. However, this is not the case for a helical milling operation, whether the aim is to produce a large hole or a groove for the sidewall. The ring torus only represents the cutting edge of the tool, not the entire tool that contains the tool body as well. If this is not considered, the tool body may collide with the workpiece.

3. VERIFICATION OF THE MODEL USING COMPUTER AIDED-DESIGN PROGRAM

Solidworks 2016 was used for the verification. The program contains a “swept cut” command to obtain the remaining portion of a solid after subtracting the swept volume of another solid. However, it just gives the approximate form. In addition, a constraint exists for the swept volume generation of the solids. The solid body must be convex.

In Figure 6a, the workpiece, the helical path, and the toroidal cutter are shown. The internal region of the toroidal cutter was filled to prevent a convex body owing to the constraint. This will not cause a problem when only the outer region of the toroidal cutter performs cutting. One method to provide this is that the workpiece diameter is chosen so that only the outer region of the toroidal cutter engages the workpiece. Using $R = 25$ mm, $p = 20$ mm, $e = 10$ mm, and $a = 7$ mm, an external groove profile was obtained in Figure 6b. The initial workpiece diameter was selected as 30 mm due to the constraint. The maximum overcut value is shown in the figure as 0.80396 mm. According to the introduced model, the overcut value is 0.80397 mm. Therefore, it can be said that the result is compatible with that of the simulation.

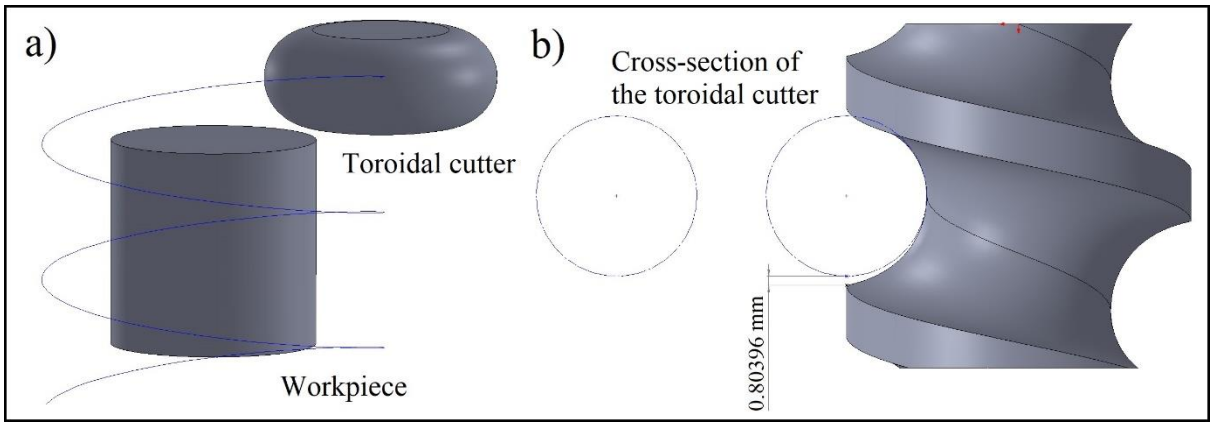


Figure 6. (a) Geometrical representations of the toroidal cutter and the workpiece. (b) The external groove profile is shown with the overcut.

A comparison was also made for the internal groove using the same values ($R = 25$ mm, $p = 20$ mm, $e = 10$ mm, and $a = 7$ mm) for the toroidal cutter and helical path. The setup is

shown in Figure 7. The maximum overcut value was found 0.44938 mm, and the introduced model gives the overcut value as 0.44944 mm. Based on this result, the model and the simulation are congruent.

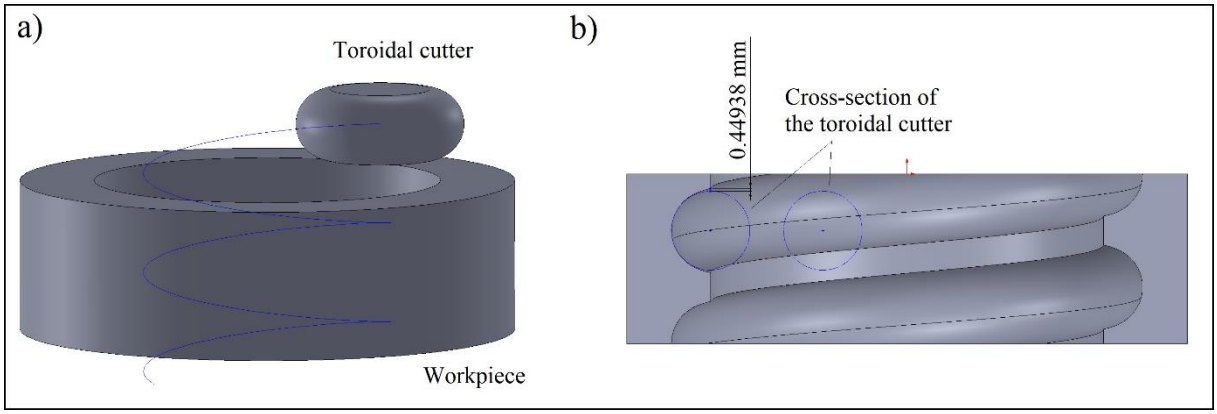


Figure 7. (a) Geometrical representations of the toroidal cutter and the workpiece. (b) The internal groove profile is shown with the overcut.

4. CONCLUSIONS

A model was introduced to obtain the cross-sectional profile of the swept volume of a toroidal cutter during screw motion. The cutting tool was modeled as a ring torus. The model was validated by the CAD program. It was found that the model is highly efficient. The distinct feature of the introduced method is that it gives the equation of the cross-sectional profile, thus, enabling further investigation of the groove profile. Effects of variables such as pitch and radius of the helical path and dimensions of the tools on the generated profile can be directly investigated. It must be noted that the model only considers the screw motion of the cutter and requires a numerical solution.

REFERENCES

1. **Wang, W.P. and Wang, K.K. (1986),** “Geometric modeling for swept volume of moving solids”, IEEE Computer Graphics and Applications, Vol 6, pp 8–17.

2. **Blackmore, D. and Leu, M.C. (1990),** “A differential equation approach to swept volumes”, Proceedings. Rensselaer’s Second International Conference on Computer Integrated Manufacturing, Troy, NY, USA: IEEE Comput. Soc. Press, pp 143–149.

3. **Blackmore, D., Leu, M-C. and Wang, L.P. (1997),** “The sweep-envelope differential equation algorithm and its application to NC machining verification”, Computer-Aided Design, Vol 29, pp 629–637.

4. **Abdel-Malek, K. and Yeh, H-J. (1997),** “Geometric representation of the swept volume using Jacobian rank-deficiency conditions”, Computer-Aided Design, Vol 29, pp 457–468.

5. **Chiou, C-J. and Lee, Y-S. (2002),** “Swept surface determination for five-axis numerical control machining”, International Journal of Machine Tools and Manufacture, Vol 42, pp 1497–1507.

6. **Weinert, K., Du, S., Damm, P. and Stautner, M. (2004),** “Swept volume generation for the simulation of machining processes”, International Journal of Machine Tools and Manufacture, Vol 44, pp 617–628.

7. **Gong, H. and Wang, N. (2009),** “Analytical calculation of the envelope surface for generic milling tools directly from CL-data based on the moving frame method”, Computer-Aided Design, Vol 41, pp 848–855.

8. **Aras, E. (2009),** “Generating cutter swept envelopes in five-axis milling by two-parameter families of spheres”, Computer-Aided Design, Vol 41, pp 95–105.

9. **Lee, S.W. and Nestler, A. (2011),** “Complete swept volume generation, Part I: Swept volume of a piecewise C1-continuous cutter at five-axis milling via Gauss map”, Computer-Aided Design, Vol 43, pp 427–441.

10. **Rossignac, J. and Kim, J.J. (2012),** “HelSweeper: Screw-sweeps of canal surfaces”, Computer-Aided Design, Vol 44, pp 113–122.

11. **Aras, E. (2019),** “Tracing sub-surface swept profiles of tapered toroidal end mills between level cuts”, Journal of Computational Design and Engineering, Vol 6, No.4, pp 629-646.

DESIGN AND MANUFACTURE OF A TWO-COMPONENT DYNAMOMETER TO MEASURE TURNING FORCES

M. Ayberk TÜRK, *c1815402@student.cankaya.edu.tr,* Çankaya University, 06790, Ankara, Turkey

Kaan SONGÜR, *c1615045@student.cankaya.edu.tr,* Çankaya University, 06790, Ankara, Turkey

Suat BENGÜR, *bengur@cankaya.edu.tr,* Çankaya University, 06790, Ankara, Turkey

Samet AKAR, *samet.akar@cankaya.edu.tr,* Çankaya University, 06790, Ankara, Turkey

ABSTRACT

In this study, a dynamometer for turning operation that can measure static and dynamic two directional cutting forces, feed force (F_x) and main cutting force (F_y) by using a strain gauge and the octagonal ring has been designed and manufactured. The orientation of octagonal rings and strain gauge locations has been determined to maximize sensitivity. The developed dynamometer is connected to a data acquisition system. Cutting force signals were captured and processed using a data acquisition system. The obtained results of machining tests performed at different cutting parameters showed that the dynamometer could be used reliably to measure turning forces.

Keywords: Dynamometer, cutting forces, strain gauge, octagonal ring.

1. INTRODUCTION

In this study, the stages of designing a dynamometer to measure the cutting forces that occur during the cutting operation on the turning machine have been described. As a result of specific literature research, a roadmap was drawn for the relevant project topic, problem definition, project requirements, and detailed design were made detailed in this report. Recently, dynamometers that involve piezoelectric systems were used mostly. Piezo works as a pressure converting system. It occurs electrical charge due to the pressure. Since it has a high cost, the industry chooses it rather than the commercial ones. An alternative solution of measuring the cutting force can be expressed as determining the elastic deformation. There are two ways to compute the deformation of the tool. One of the solutions is using a strain gauge directly connected to the cutting tool. Another one includes octagonal rings as

transducers and strain gauge placement on the rings. The first solution is not valid as the second one. It is not able to measure the small forces and has less sensitivity. In this report, octagonal rings and strain gauge-based systems were used. Strain gauges were mounted on the four octagonal rings, rings attached to the two plates (Carbon Steel). Octagonal ring connections are made by using bolts on the plates. The two-plate-shaped system is attached to the cutting tool. Strain gauges are attached to the Wheatstone bridge with cable connections. Those connections are attached to the DAQ system. This system can measure the strain using the differences between the voltage values. The cutting forces acting on a cutting tool are given in figure 1 below.

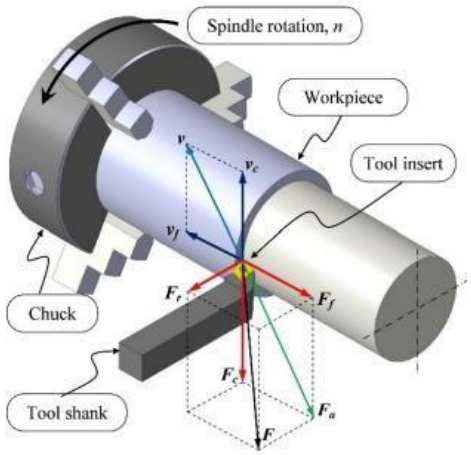


Figure 1.Expression of the forces on the cutting operation

Literature Survey

During the research, it was observed that non-commercial dynamometers were the subject of many studies. In these studies, dynamometer designs were made for different machining processes besides the turning machine and presented to the literature.

Panzere, T. et al. [1] designed and developed a three-component dynamometer to measure turning forces during the turning process. The design is based on a strain gauge system. The strain gauges were placed on the tool post which has a special fabrication and the system was tested with a Kistler model 9257BA dynamometer.

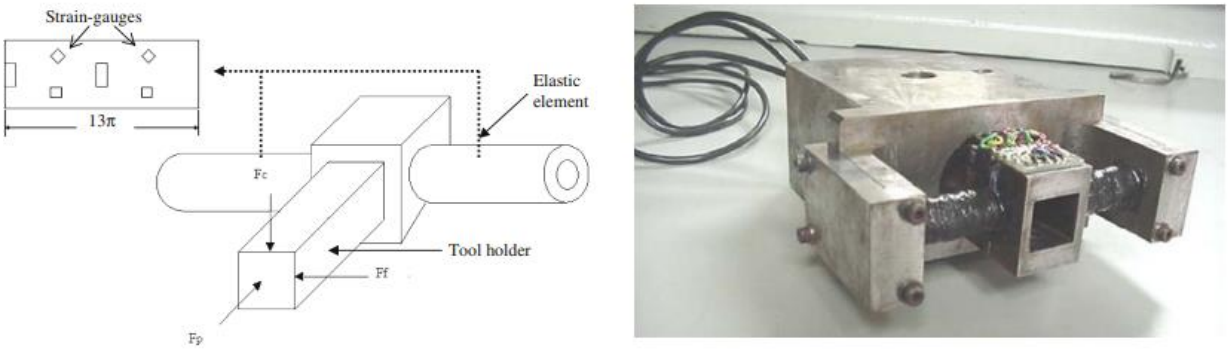


Figure 2. Three-Component Dynamometer [1]

Topal, E.S. & Çoğun, C. & Odabaş, D. [2] worked on a dynamometer design to measure 3-axis cutting forces during the turning process. Strain gauges were placed on the cutting tool and the cutting tool has milled from both sides to obtain sensitive measurements.

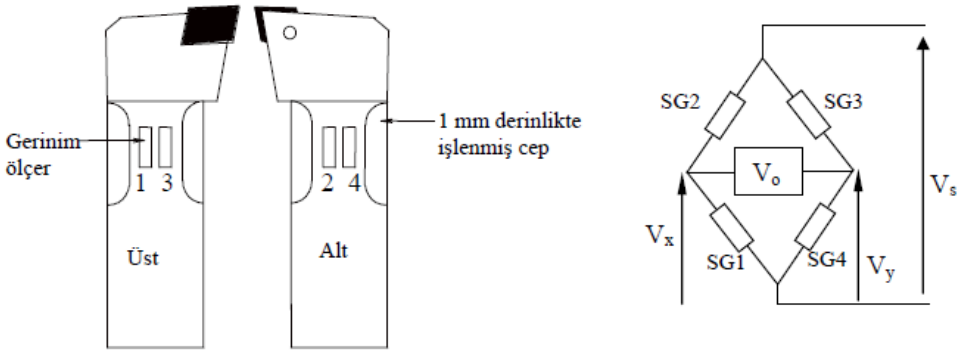


Figure 3. Strain Gauge Placement and Wheatstone Bridge Configuration of the Study [2]

2. PROBLEM DEFINITION AND DESIGN SPECIFICATIONS

Turning machines are used in many machining processes in the manufacturing industry. The general working principle of the turning is to rotate a material fixed to the turning machine chuck and to remove chips by contacting it with the help of a tool attached to the tool post. During this machining process, certain forces act on the tool because of the contact.

The detection of these forces has several advantages. The purposes of determining these forces are to increase the production quality, to determine the life of the used tool and thus prolong the usage life, and to prevent work accidents and material consumption that may occur as a result of overloads.

Problem definition: Design and implementation of dynamometer to monitor the two-dimensional cutting forces (feed force, cutting force) that occur during the cutting process in the turning machine through the deformations acting on the strain gauges placed on the octagonal ring.

The requirements of the design are given below, and design specifications of the products is shown in table 1.

- The designed dynamometer can be used in as many different types of cutting tools as possible.
- Determining the number of strain gauges required to provide the user with a clearer and more accurate result in data calculations.
- Having an ergonomic design planned with a minimum budget.

- Having a design with low error rates.
- Reducing temperature-related data losses to a minimum.
- Measurement of forces up to 1000 newton, with a precision of 10 newtons.

Table 1. Design Specifications of the Dynamometer

DESIGN SPECIFICATIONS	
ASPECT	**SPECIFICATION**
GENERAL	Should be compatible with as many cutting tools as possible The dynamometer must be mountable size to the tool post (110x110x12) Flexible materials need to be used for deformation Easy access to handling and transportation
FUNCTION	2-dimensional cutting forces must be measured Measuring range: 200N to 1000N Precision: 10N DAQ system that should be installed on all computers easily
QUALITY	Strain gauges must be placed in the most deformed point Need to keep cross sensitivity a minimum
ENVIRONMENT	The product needs to be covered for resistance of external factors Dynamometer must be resistant to corrosion, stainless material needs to be used The dynamometer needs to compensate for heat The system should work at a temperature range -30°C to 70°C
TIME	Manufacturing needs to be done in 4 months
COST	Less than 600 USD
TARGET CUSTOMER	Turning machine cutting tool manufacturers Companies engaged in production where the turning machine is actively used

3. CONCEPTUAL DESIGN

The dynamometer consists of two main parts. These are the dynamometer body and data acquisition sections. The materials listed in the design specification section have been used during the creation of the dynamometer. Different models were made during the design phase and these models were revised at certain stages. The reason for these revisions is to achieve correct results in the use of the system.

Concept-1

Figure 2 represents the first conceptual design of the dynamometer body. In this design, the connection bolts were not countersunk or Allen type, that is why the body section could not be connected to the tool post. This was the reason that the related design has not been selected as the best design.

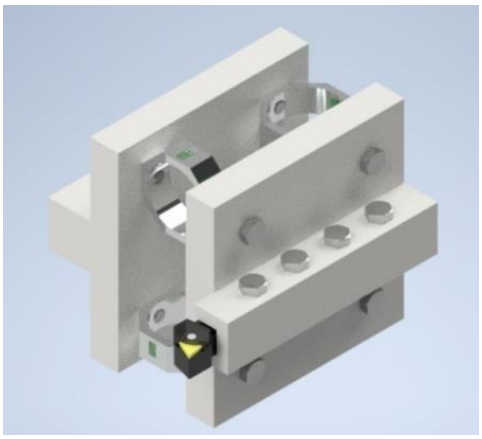


Figure 4:Dynamometer's Concept-1

Concept-2

The dynamometer body part contains two pieces of Carbon Steel plates. Each plate has four holes for the attachment of the octagonal rings. Also, cutting tool holder and tool post mounting has been done by the usage of the plates. Figure 5 shows the best concept dynamometer body. The reason for this design is the selected one, the bolt connection and the tool holder system are much more efficient during manufacturing and implementation.

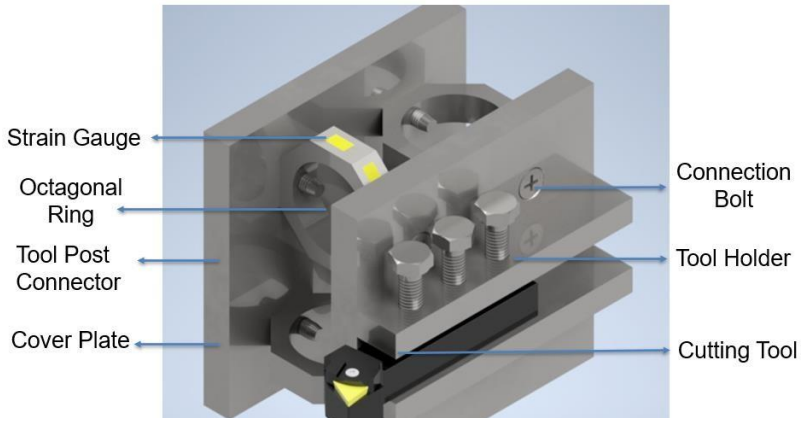


Figure 5. Design Concept-2

4. DETAILED DESIGN

The dynamometer consists of two main sections, these sections are mechanical and electrical. The components included in the electronic and mechanical parts are given in figure 6 below.

Sub-Systems of the Design

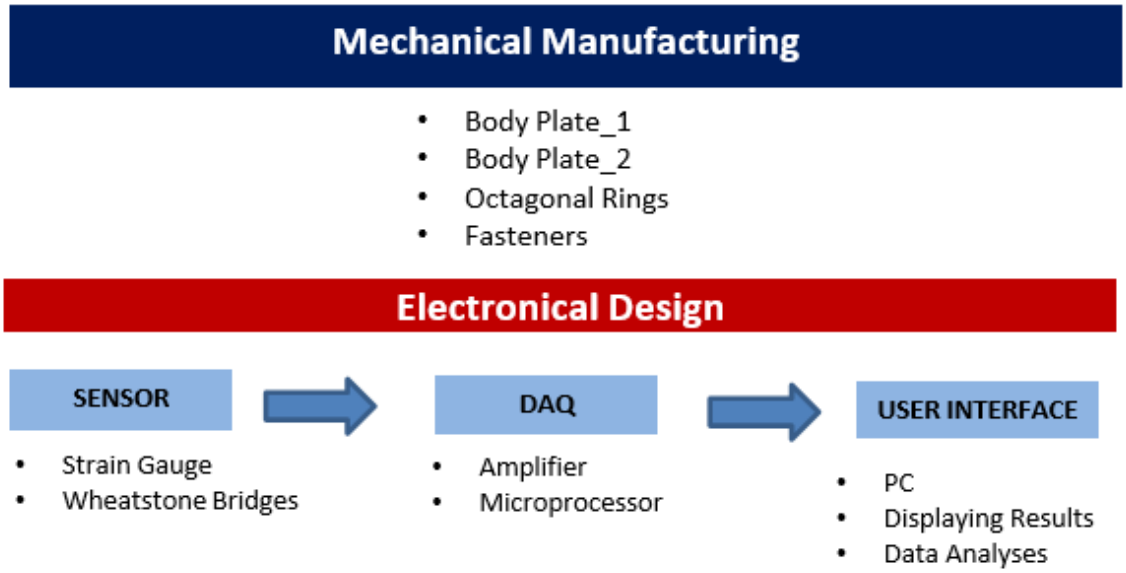


Figure 6. Design Sections

The sub system of the dynamometer is the FASTDAQ Data Logger, which is the product used in the DAQ part. The working features of the DAQ are shown below in table 3. DAQ has its user interface, “GEOGRAM Data Acquisition and Logging Software for FastDAQ “ that shows the strain values and related graphs. Figure 7,8 shows example views of the user interface.

Table 2. FASTDAQ Technical Specifications

FASTDAQ	
Measurement Range	Variable depending on the sensor capacity
Sampling Rate	Configurable
Working Temperature	0-40°C
Power Supply	Through Standard USB Port (PC Connection)
Analog/Digital Conversion Rate	10 bits
Material	Hardened Plastic Enclosure
Software	Requires Excel and PC
Storage	SD Card Support and real time Excel spreadsheet integration

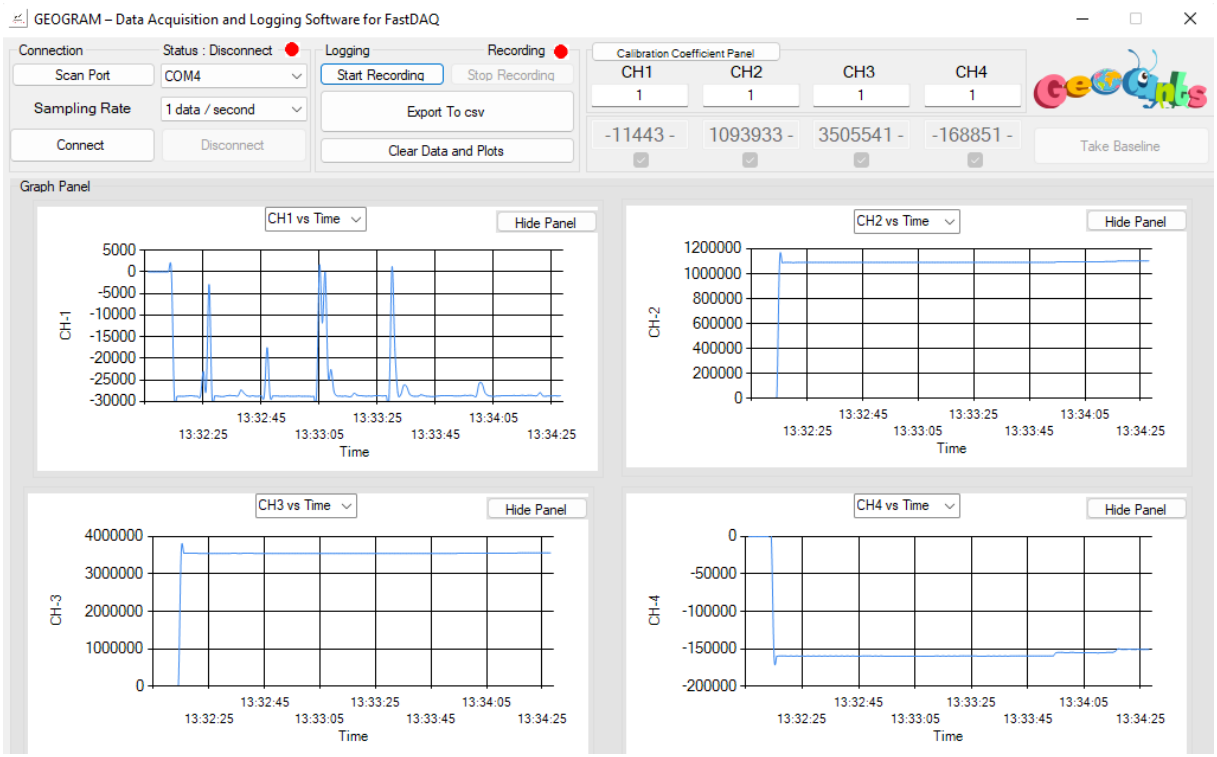


Figure 7. DAQ User Interface

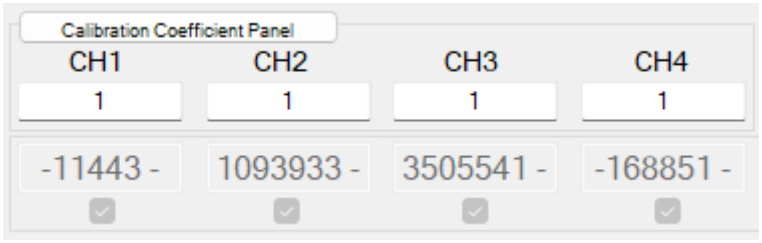


Figure 8. DAQ User Interface / Strain Monitoring Section

There are four channels in the DAQ system and all of them show the strain values in real-time. The calibration Coefficient Panel feature also exists in the system, and it can be changed by the user's desired value.

Theoretical Calculations

In the experiment, octagonal rings were selected as force transducers. It includes a circular ring in the middle of its shape which carries 2 components of the force. One of them is vertical (F_v) other one is horizontal (F_h) values. The figure shows the directions of the acting forces. The octagonal ring's bottom area was assumed as fixed. Forces occur moment with an angle (Ø). Bending moments were calculated as:

$$M_{\emptyset} = \frac{F_v r}{2}\left[\frac{2}{\pi} - sin\emptyset\right] + \frac{F_h r}{2} cos\emptyset \qquad 0 < \emptyset < \pi \qquad (1)$$

$$M_{\emptyset} = \frac{F_h r}{2}\left[\frac{2}{\pi} + sin\emptyset\right] - \frac{F_v r}{2} cos\emptyset \qquad 0 < \emptyset < 2\pi \qquad (2)$$

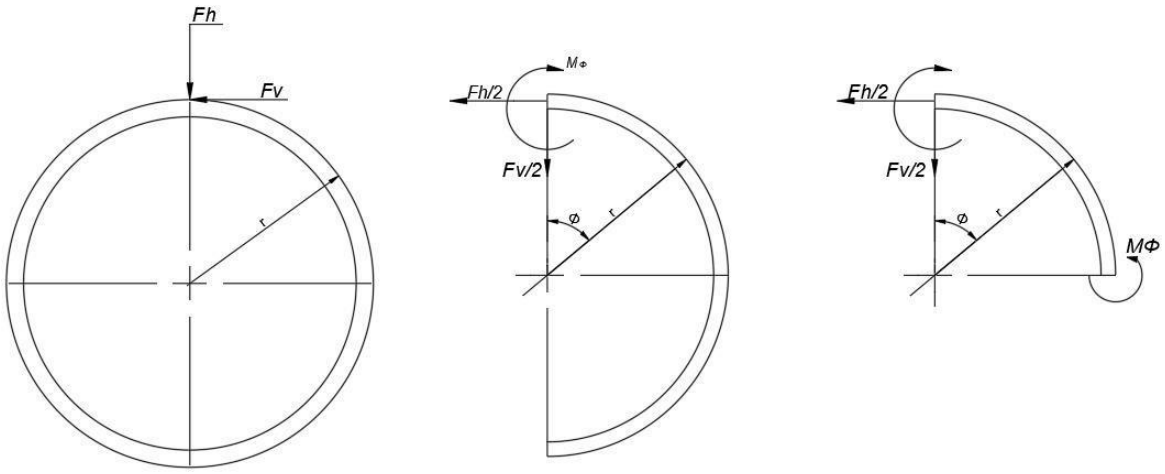


Figure 9.Directional cutting forces on circular shape

Since the system contains strain gauges, location of them should have high priority. They had to be placed where the bending moment is zero [3]. These locations also where the stresses were maximum [3]. So, the formula should be only the function of F_v .Second terms were zero and equation (1) and (2) becomes:

$$\pm \frac{F_h r}{2} cos\emptyset = 0 \quad (3)$$

From the equation of (3), $\emptyset$ can be written as 90. It can easily obtain that strain gauges would be located at $\pm 90°$ clockwise from the top side of the circular shape section to determine the F_v without any side effects from F_h.For equating the F_h both formulas (1) and (2) must be zero. Then the formula becomes:

$$\frac{F_v r}{2}\left[\frac{2}{\pi} \pm sin\emptyset\right] = 0 \quad (4)$$

From equation (4) $\emptyset$ is determined and it included two angles which are $\pm\ 39.5°$ and $\pm\ 140.5°$. It can obtain that the strain gauges were placed at the angles with $\pm\ 39.5°$ and $\pm\ 140.5°$ from the top point of the circular shape when moving in the clockwise direction. Relation between the stress can be expressed as Hooke's Law.

$$\sigma = E\varepsilon \quad (5)$$

The maximum stress at the top point of the circular shape can be expressed as in equations (6), (7):

$$\sigma_c = \frac{Mc}{I} \tag{6}$$

$$I = \frac{bt^3}{12}; c = \frac{t}{2} \tag{7}$$

Where M is the moment of that point, c is the distance between the edge of the octagonal ring and the neutral axis, I, is the moment of inertia is the width of the octagonal ring and t is the thickness of the octagonal ring. By substituting the (6) and (7) to equation (5) the relationship becomes:

$$\varepsilon = \frac{\sigma}{E} = \frac{6M}{Ebt^2} \tag{8}$$

If the angular notation of the gauge nodes ($\emptyset = 39.5° \; and \; 90°$) is substituted in (1) then the equation is:

$$M_{39.5^\circ} = 0.385 F_h r \tag{9}$$

$$M_{90^\circ} = -0.181 F_v r \tag{10}$$

By substituting the (9) and (10) into (8) following equations (11) and (12) occurred:

$$\varepsilon_h = \pm \frac{2.31 F_h r}{Ebt^2} \tag{11}$$

$$\varepsilon_v = \pm \frac{1.086 F_v r}{Ebt^2} \tag{12}$$

Structural failure is an important aspect so it has to be avoided from failure due to overload, maximum stress value must be less than the yield strength of the material structures. By this information, a factor of safety was selected as 2, and the maximum allowable stress occurs in the equation:

$$\sigma_{max} = \frac{S_y}{sf} \tag{13}$$

Where Sy is the yield strength of the steel and sf is the factor of safety. Yield strength is 205 MPa, so allowable maximum stress occurs:

$$\sigma_{max} = \frac{S_y}{sf} = \frac{205MPa}{2} = 102{,}5MPa \quad (14)$$

After that, (5) and (14) were computed and equations (11) and (12) occurred as:

$$F_h max = \frac{44.3bt^2}{r} = \frac{44{,}3.16.(4{,}1^2)}{22{,}07} = 539{,}08\ N \quad (15)$$

$$F_v max = \frac{94{,}38b\ t^2}{r} = \frac{94{,}38.16.(4{,}1^2)}{22{,}07} = 1150{,}1\ N \quad (16)$$

Strain Gauge Arrangement

As a result of these calculations, it can be obtained that the force acting on the top of the dynamometer. It is transducing by using 4 octagonal rings. Since it is carrying and transferring the forces, the whole body could carry almost 2.1 kN. This is the acceptable maximum force that can be acted on the strain gauge-based dynamometer.

Regarding the calculations above, the arrangement of the strain gauges is shown in 2D in figure 10.

- Strain gauges numbered as 1,2 mounted on the Ring-A affected by Feed Force (F_x).
- Strain gauges numbered as 5,6 mounted on the Ring-C affected by Feed Force (F_x).
- Strain gauges numbered as 9,10 mounted on the Ring-B affected by Cutting Force (F_y).
- Strain gauges numbered as 13,14 mounted on the Ring-D affected by Cutting Force (F_y).

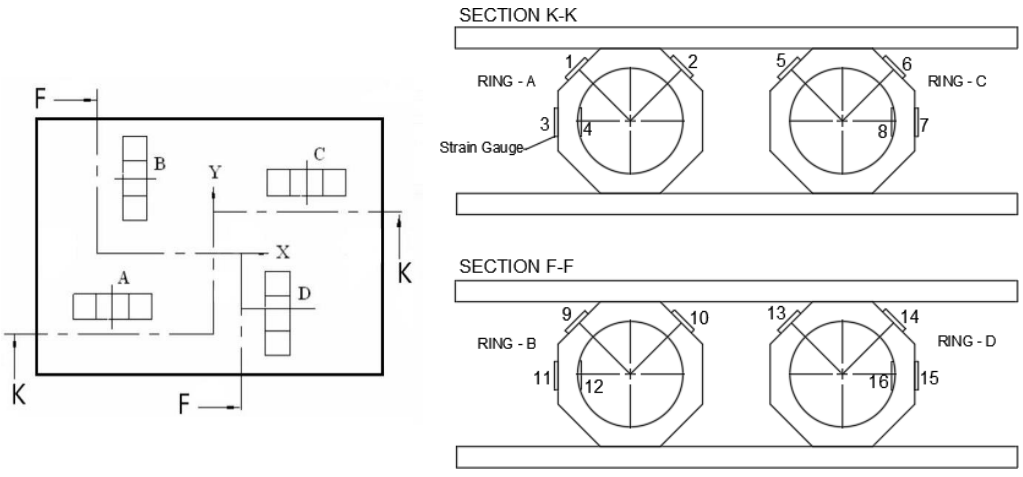


Figure 10. Strain Gauge Arrangement Scheme

Virtual Model of the Design

The solid modeled state of the system, whose design is completed and modeled, is as in the figure the dynamometer body is fixed to the tool post on the turning machine.The cables coming out of the dynamometer body provide the connection between strain gauges and DAQ. Then, the data from the DAQ was transferred to the computer environment.

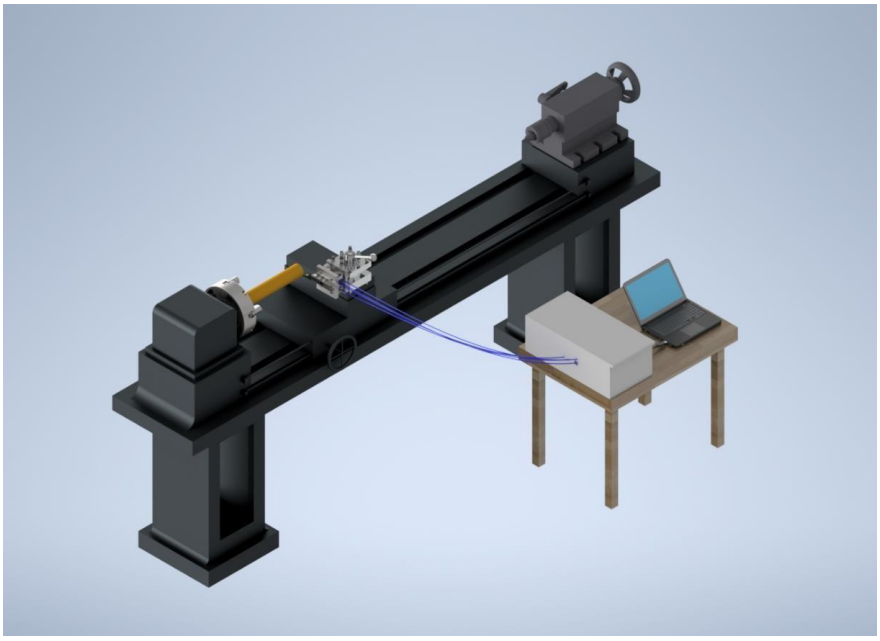


Figure 11. 3D Illustration of the Design

Figure 12 represents the dynamometer body in a closed view. The dynamometer body section and the definitions of them are given below.

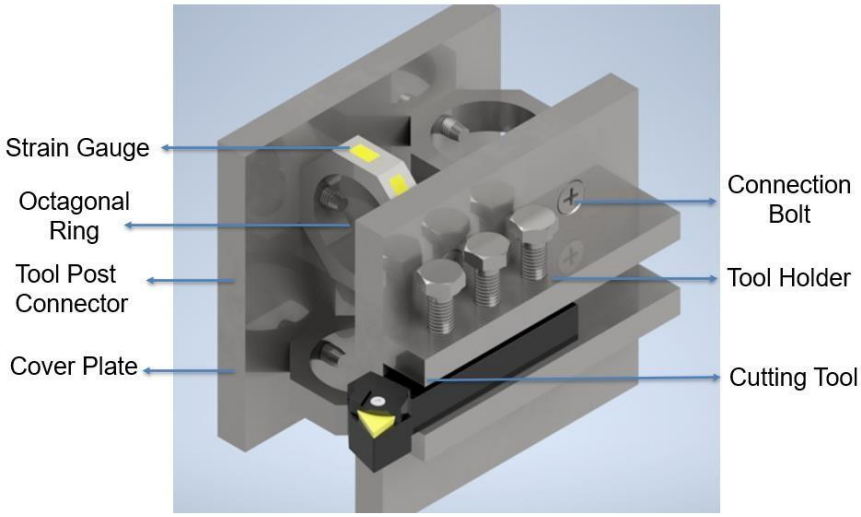


Figure 12. Dynamometer Body Section

5. IMPLEMANTATION

The dynamometer is designed to create a measurement system consisting of different parts. After the completion of the design process, the production phase was started. In the production process, the materials went through the stages described under the title of detailed design. Stages are detailed in the following headings and the product tree is given in figure 13.

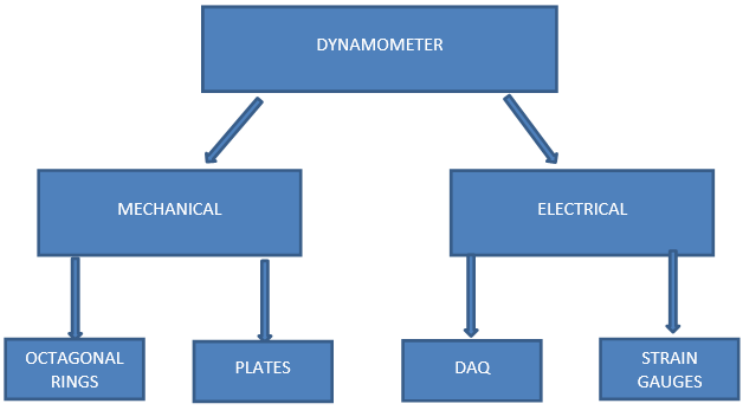


Figure 13. Product Tree of the Dynamometer

Strain Gauge: Strain gauges are sensors used to measure strains on the surfaces of parts. It consists of placing a very small-section conductive wire on a very thin strip in the form of repeating coils. The used strain gauge type in this research is a 120-ohm linear pattern type strain gauge. Sixteen strain gauges were used for the strain measurement. Strain gauges have been placed on the octagonal rings, and they were connected in a full bridge which fully compensates for the errors due to temperature changes [4].

Octagonal Rings: Octagonal rings have been used as a body for the placement of strain gauges. Strain gauges have been placed on the surfaces of the rings. There have been four octagonal rings and four strain gauges have been placed on each ring. The octagonal rings are flexible components so they can easily be deformed. The material of the rings is Stainless Steel 316.

Plates: Sheet plates have been used as the covers of the dynamometer body. Octagonal rings are placed between two plates. Also, the cutting tool will be placed in the tool holder part of the plate and the other side of the sheet has been connected to the tool post.

FAST DAQ System: DAQ system is mounted between the computer and the Wheatstone bridge. Since the system is sensitive, placement should be grounded. The system includes a microprocessor with an embedded motherboard for data capturing. The output of the DAQ is the occurred strain on the gauges.

6. TESTING

Static Calibration

During the static calibration phase, certain weights are hung on the cutting tool for the y-axis and a spring was used to apply force to the dynamometer on the x-axis. The strain occurring in the system was transferred to the computer environment and monitored via DAQ. Specific weights were loaded and unloaded at the same time intervals. The resulting graphs are as follows.

Table 4 shows the specific loads that are applied to the system by using a spring on the x-axis and the monitored force on the user interface. As the values were already known, the calibration equation was calculated by applying the curve fitting process in MATLAB software to reach the calibration coefficient.

Table 3. Load &Monitored Force for Feed F_x

Load (N)	Monitored Force(N)
9,81	10,25
19,62	19,86
29,43	29,83
39,24	39,21
49,05	49,19
58,86	58,68
68,67	68,75
78,48	78,37
88,29	88,78
98,1	99,03

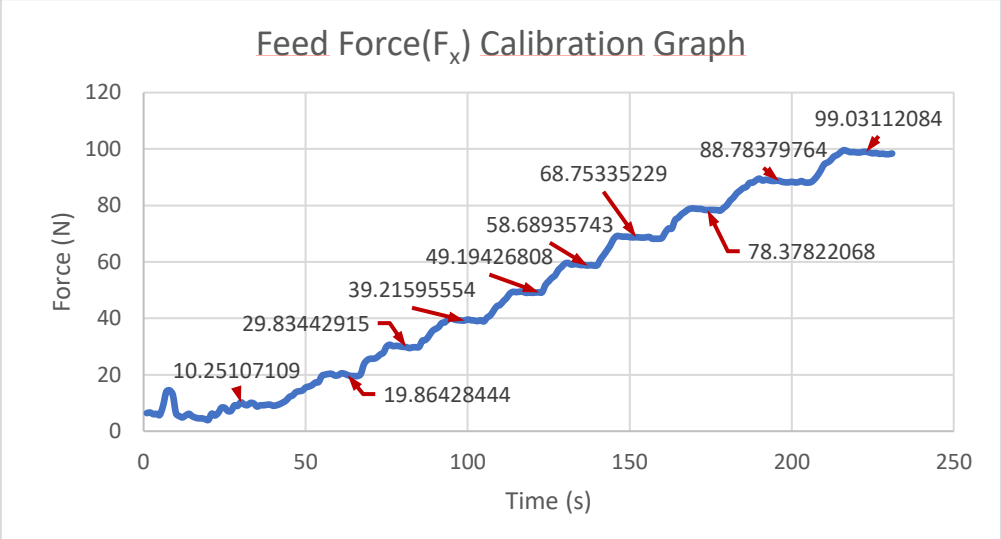


Figure 14.Feed Force (F_x) Calibration Graph

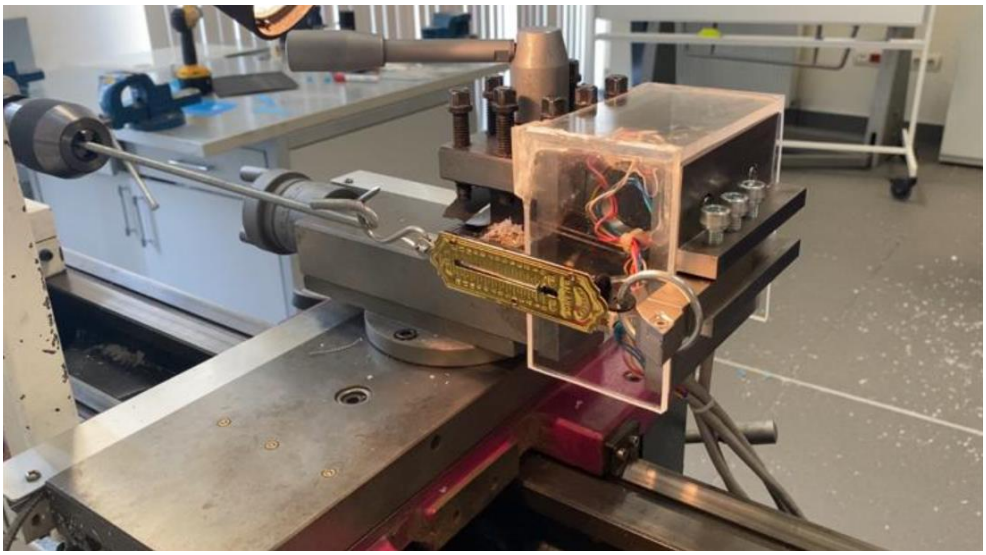


Figure 15. Calibration Setup for F_x

Instead of using spring, specifically known dead weight was hung to the system as the y-axis calibration. The load/monitored force table shows the results of the y-axis calibration.

Table 4.Load &Monitored Force for Feed F_y

Load (N)	Monitored Force(N)
49,05	47,91
68,67	68,69
88,29	88,55
98,1	98,13
107,91	107,1
117,72	116,95
127,53	125,96
137,34	138,37

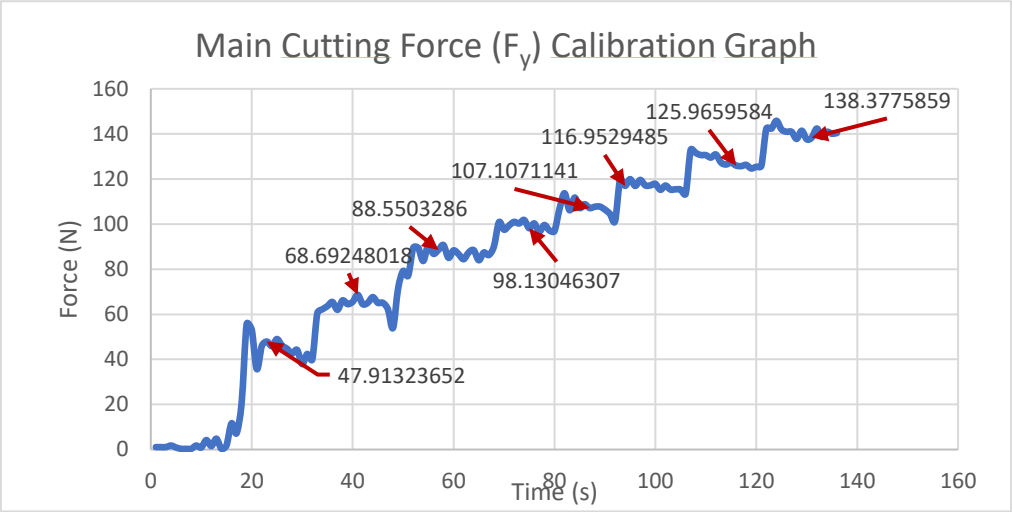


Figure 16. Calibration Graph for F_y



Figure 17. Calibration Setup for F_y

Mechanistic Modelling

Mechanistic modeling is the standardization of a machining process by specifying certain parameters. These parameters contain values that affect the processing to be performed. For example, feed rate, lead angle, depth of cut, etc. This method was used during the

dynamic calibration of the dynamometer. During the use of the method, a previously performed cutting process is referenced. The details of this cutting process are given in table 5 [5].

Table 5. Cutting Coefficient of AL7075-T6 Material

Cutting coefficients Al7075-T6 [5]					
Ktc[N/mm 2]	Kte[N/m m]	Krc[N/mm 2]	Kre[N/m m]	Kac[N/mm 2]	Kae[N/m m]
796	27,7	168,8	30,8	222	1,4

The values given in Table 5 are the details of the cutting process taken as reference from Cascon&Sarasua [5], which describes the dynamical calibration as cutting aluminum bar. The cutting process according to these values was then compared with a high-resolution dynamometer KISTLER. The dynamic calibration of the dynamometer was performed by applying the values in table 6. Al7075-T6 material was used as a specimen of the cutting process.

Table 6. Cutting Conditions of Dynamometers [5]

Cutting Conditions		
	Referenced Model	**Dynamometer**
Material	AL 7075 T6	AL 7075 T6
Cutting Speed	70 mm/min	70.68 mm/min
Feed Rate	0.08 mm/rev	0.056 mm/rev
Depths of Cut	0.8 mm	1.0 mm

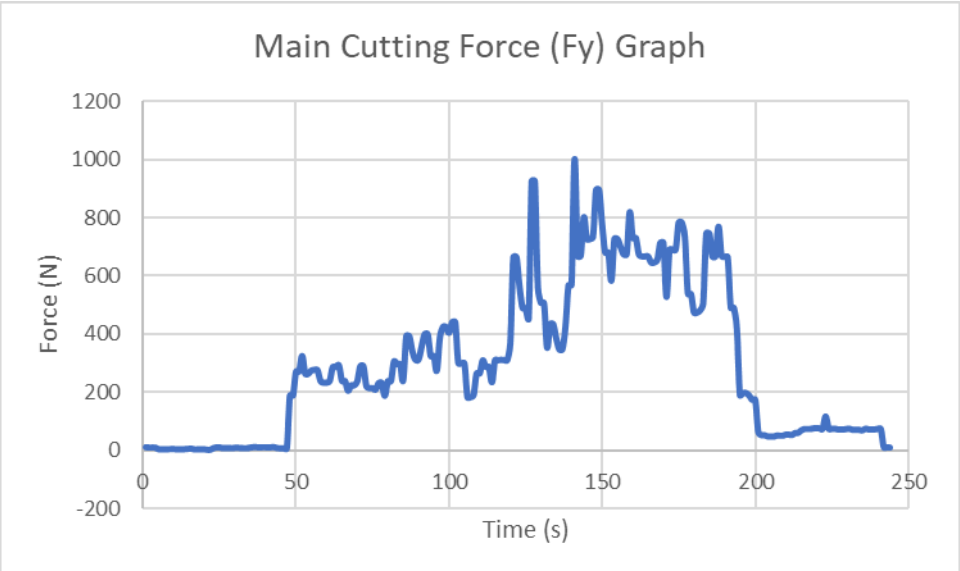


Figure 18. Force vs. Time Graph for F_y

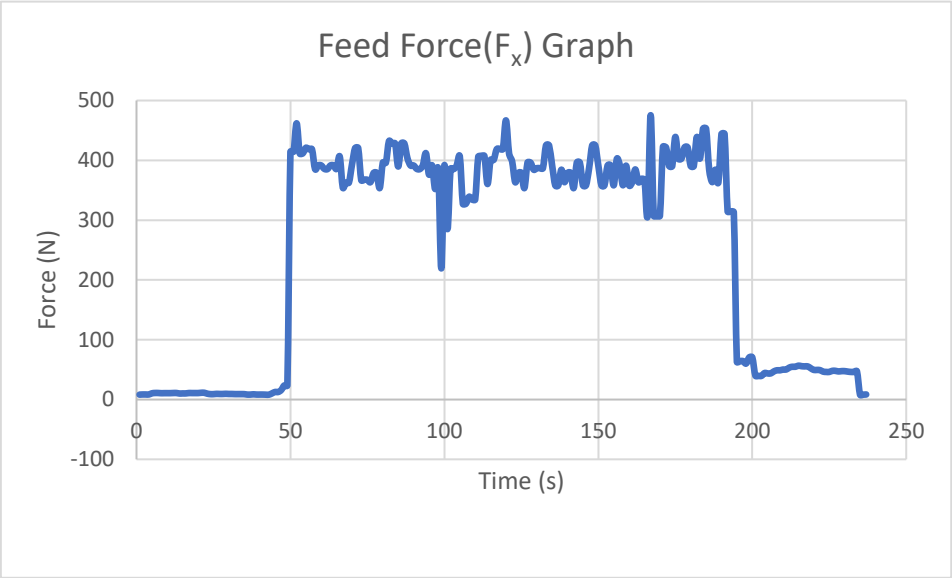


Figure 19. Force vs. Time Graph for F_x

7. CONCLUSION

As a final brief of the study, four octagonal rings and sixteen strain gauge-based systems were used. Two directional cutting forces were examined, cutting and feed force which means x and y directional forces. The manufacturing and implementation phases have tried to be done with maximum sensitivity due to the product should work in the regarding calculations. The test phase includes two parts dynamic and static calibration. Static calibration has been made by hanging dead weights on the dynamometer for y-direction. The process has been held by loading and unloading with unit kilogram weights. The x-axis statical forces were acted on the system by a spring. Output data is monitored on the computer screen by DAQ's software 'GEOGRAM'. Process shared on the testing part with the supporting force graphs. Dynamic calibration has been made by the principles of mechanistic modeling. As a result of the whole process, the designed and implemented dynamometer can operate within a 15% margin of error.

REFERENCES

[1] **Panzera, T. & Souza, Paulo & Campos Rubio, Juan & Abrao, A. & Mansur, Tanius. (2011).** Development of a three-component dynamometer to measure turning force. The International Journal of Advanced Manufacturing Technology. 62. 10.1007/s00170-011-3866-5.

[2] **E. S. TOPAL, C. ÇOĞUN, and D. ODABAŞ**, Tornalama işleminde kesme kuvvetlerini ölçen gerinim ölçer esaslı dinamometre tasarımı ve imalatı, vol. 26, no. 2, Jun. 2010.

[3] **Rizal, Muhammad & Ghani, Jaharah & Husin, Husni & , Husaini. (2018).** Design and construction of a strain gauge-based dynamometer for a 3-axis cutting force measurement in turning process. Journal of Mechanical Engineering and Sciences. 12. 4072-4087. 10.15282/jmes.12.4.2018.07.0353.

[4] **Yaldız, Süleyman & Ünsaçar, Faruk. (2006).** Design, development and testing of a turning dynamometer for cutting force measurement. Materials & Design. 27. 839-846. 10.1016/j.matdes.2005.04.001.

[5] **CASCÓN, Itxaso; SARASUA, Jon Ander**. Mechanistic model for prediction of cutting forces in turning of non-axisymmetric parts. Procedia CIRP, 2015, 31: 435-440.

ACKNOWLEDGEMENT

We would like to thank our advisors Dr. Samet Akar and Suat Bengür who guided us during the study. They provide us invaluable advice and helped us in difficult periods. Their motivation and help contributed tremendously to the successful completion of the study.

RECURSIVE DEFINING OF FORCE COEFFICIENTS IN MILLING PROCESS WITH ACCELEROMETER

Barış ALTUN, e209619@metu.edu.tr Orta Doğu Teknik Üniversitesi, 06800, Ankara

Hakan ÇALIŞKAN, chakan@metu.edu.tr Orta Doğu Teknik Üniversitesi, 06800, Ankara

Orkun ÖZŞAHİN, ozsahin@metu.edu.tr Orta Doğu Teknik Üniversitesi, 06800, Ankara

ABSTRACT

Force coefficients are required for mechanistic force calculations in machining operations. The mainstream method of identification of force coefficients relies on dynamometers. However, using dynamometers is not necessarily applicable. This paper offers a method of force coefficients identification without force measurement. A specially designed workpiece is milled. Its acceleration is utilized together with FRFs obtained on the same milling machine that the acceleration is measured. Force estimation is performed with acceleration data and FRF. Force model is curve-fit with recursive least squares method into force estimation in order to find force coefficients.

Keywords: Machine Tool Structure, Identification, Frequency Response Function, Milling, Cutting Force, Force Coefficients

1 INTRODUCTION

Force coefficients are a set of parameters which are used in mechanistic force models of machining processes. There are databases of force coefficients but, besides workpiece materials there are many factors like tool and process parameters affecting force coefficients. For these reasons, calculation of coefficients for desired conditions from experimental data is usually required. There are wide range of different approaches for force coefficients identification [6] and most of them requires some sort of force measurement, particularly dynamometers. Dynamometers are expensive equipment and cumbersome to set up, methods not based on direct force measurements are required especially for industry applications.

Force calculations without direct force measurement is a research area with multiple approaches. Aggarwal e.t. [3] utilized spindle motor measurements (current) along with inefficiencies on spindle structure to calculate tangential force coefficients. This method requires extensive initial study and only obtains tangential force coefficients. Zhou e.t. [5]

utilizes Kalman filter and tap test results to obtain force calculation. Kalman filter functions to eliminate disturbances and bandwidth problems. Yamato e.t. [4] also utilizes motor current along with encoder readings and applies modelling of feed drive system to obtain force estimation. Load side disturbance observer (LSDO) relies on multiple encoder measurements and tool tip models. The method requires force measurement reference for obtaining system parameters such as mass but process parameters or hammer tests are not involved. However, obtaining measurement from encoders is expected to require quite a strong excitation.

Regarding identification of force coefficients without dynamometer, Pawelko e.t. [2] performed the most prominent research regarding this area. Pawelko e.t. [2] utilizes FRF measurements for force coefficients identification and lists various error factors. The method applied is based on frequency domain representation of force model and workpiece dynamics are assumed rigid. The authors make FRF measurements with tap tests and estimates force excitation based on accelerations measured during operation. The method is only tested numerically and relies on harmonics in frequency domain. Wang e.t. [7] utilizes only one dominant modes of FRF to obtain a mass-spring-damper equation and by applying convolution, a set of linear equations in time domain to be used for least squares are created. The method does not give coefficients and results are accurate in amplitude for high radial engagement.

In this article, a force coefficients identification method based on a specially designed workpiece and FRF measurements has been developed. FRF measurements are taken with tap tests together with 2 accelerometers from 2 perpendicular directions. A single thin wall workpiece is face milled and forces are calculated based on process parameters. Force estimations are calculated based on acceleration obtained during operation and FRFs obtained with tap tests. Force calculations are curve-fit in frequency domain based on recursive least squares method in which force coefficients are identified. Section 2 provides force model, force estimation approach. Section 3 formulates the least square solution oft eh coefficient identification problem. Section 4 explains the experimental test set up and illustrates the use of proposed algorithm. Finally Section 5 concludes the article.

2 MILLING PROCESS AND FORCE MODEL

Cutting force is a direct function of chip thickness which consist of static and dynamic terms. Static (uncut) chip thickness is determined by the feed rate. There are mechanistic models which explains this phenomenon sufficiently to a level that a predictive model is possible. The most well known method approximates the radial chip thickness as $c\sin\theta$ where c is the feed per tooth. Dynamic chip thickness is caused by workpiece and tool vibrations. During a stable cutting process (i.e. no chatter), the vibrations formed at the two consecutive tool vibration

engagement are the same thus the dynamic chip regeneration is insignificant and milling force is assumed to be only related to static chip thickness.

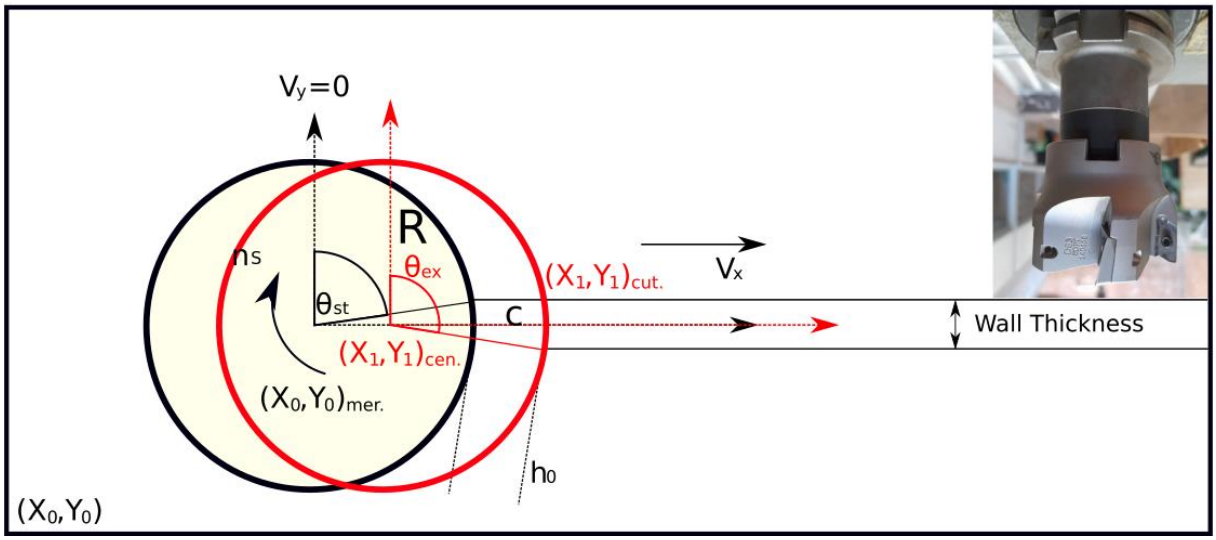


Figure 1 Uncut chip thickness model [6] of workpiece gives a single thin wall aligned with X axis and the wall is cut through X direction. $h_0 = csin\theta$ and c is feed per insert. Cutting tool picture is given.

Using the coordinate definitions given in Figure 1 the milling force generated by the static chip thickness is modeled as follows [1]:

$$\begin{bmatrix} F_x(\theta) \\ F_y(\theta) \end{bmatrix} = \begin{bmatrix} -\cos\theta & -\sin\theta \\ +\sin\theta & -\cos\theta \end{bmatrix} \begin{bmatrix} K_{tc} c \sin\theta + K_{te} \\ K_{rc} c \sin\theta + K_{re} \end{bmatrix} a_p g(\theta) \quad (1)$$

K_{tc} is tangential cutting force coefficient and K_{rc} is radial cutting force coefficient. K_{te} is tangential edge force coefficient and K_{re} is radial edge force coefficient. a_p is axial depth and θ gives cutter angle. $g(\theta)$ is window function and it is one when there is contact with workpiece and cutting tool, otherwise it is zero. c gives feed per insert. The force model given in Eq.(1) utilizes only one insert or one teeth cutter, as utilized in the experiments. Furthermore, angular speed and axial depth are constant. Note that the force mode considers a 0^o helix angle on the cutter and therefore a uniform force distribution throughout the axial depth of cut a_p. This assumption is fairly valid for the square shoulder face mill and insert used in the experiments as shown in Figure 1.

Cutting force equation (1) can be re-written with the unknown cutting force coefficients as a column vector as follows:

$$\begin{bmatrix} F_x(\theta) \\ F_y(\theta) \end{bmatrix} = a_p \begin{bmatrix} -\cos\theta\sin\theta & -\sin^2\theta & -\cos\theta & -\sin\theta \\ \sin^2\theta & -\cos\theta\sin\theta & \sin\theta & -\cos\theta \end{bmatrix} \begin{bmatrix} cK_{tc} \\ cK_{rc} \\ K_{te} \\ K_{re} \end{bmatrix} g(\theta) \quad (2)$$

The workpiece and tool vibrations due to cutting forces can be described by the FRF of X and Y directions as follows

$$\mathbf{X}(\omega) = \begin{bmatrix} X(\omega) \\ Y(\omega) \end{bmatrix} =\cdot \underbrace{\begin{bmatrix} G_{xx}(\omega) & G_{xy}(\omega) \\ G_{yx}(\omega) & G_{yy}(\omega) \end{bmatrix}}_{\mathbf{G}(\omega)} \underbrace{\begin{bmatrix} F_x(\omega) \\ F_y(\omega) \end{bmatrix}}_{\mathbf{F}(\omega)} \tag{3}$$

Considering constant spindle speed, the cutter angular position in Eq. (2) can be expressed as function of time and $\theta = \omega_s t$. Then, by utilizing frequency transformation of the force equation Eq. (2) and then inserting it into the vibration equation (3) one can express the unknown cutting coefficients in terms of the known FRF's and the measured vibrations as follows.

$$\boldsymbol{\omega}_{nx1} = [\omega_1, \omega_2, , \dots, \omega_i, \dots \omega_n]^T \tag{4}$$

$$\hat{\mathbf{F}}(\omega_i)_{2x1} = \begin{bmatrix} G_{xx}(\omega_i) & G_{xy}(\omega_i) \\ G_{yx}(\omega_i) & G_{yx}(\omega_i) \end{bmatrix}^{-1} \begin{bmatrix} X(\omega_i) \\ Y(\omega_i) \end{bmatrix} \tag{5}$$

$$\mathbf{H}(\omega_i)_{2x4} = \begin{bmatrix} c|F_{tc,x}(\omega_i)| & c|F_{rc,x}(\omega_i)| & |F_{te,x}(\omega_i)| & |F_{re,x}(\omega_i)| \\ c|F_{tc,y}(\omega_i)| & c|F_{rc,y}(\omega_i)| & |F_{te,y}(\omega_i)| & |F_{re,y}(\omega_i)| \end{bmatrix} \tag{6}$$

$$\hat{\mathbf{F}}(\boldsymbol{\omega})_{2nx1} \cong a_p \, \mathbf{H}(\boldsymbol{\omega})_{2nx4} \begin{bmatrix} K_{tc} \\ K_{rc} \\ K_{te} \\ K_{re} \end{bmatrix} \tag{7}$$

$\hat{\mathbf{F}}(\boldsymbol{\omega})_{2nx1}$ is force estimation out of the measured acceleration response and FRFs of the system. $\mathbf{H}(\boldsymbol{\omega})_{2nx4}$ provides set of multipliers for force coefficients in given set of linear equations. $\boldsymbol{\omega}$ is nx1 frequency array and ω_i is one frequency value selected and it is a member of array $\boldsymbol{\omega}$.

Equation (7) can be solved for unknown coefficients using least squares. Further simplifications can be done to ease the computation effort. The FRF matrix $\mathbf{G}$ is obtained experimentally with tap tests. The cross effects between the axes are generally small, as a result the off diagonal terms $G_{xy}(\omega)$ and $G_{yx}(\omega)$ are small with respect to the diagonal terms and can be neglected. A diagonal FRF matrix decrease the computation effort for the estimated force $\hat{\mathbf{F}}$ calculation.

$$\hat{\mathbf{F}}(\omega_i)_{2x1} = \begin{bmatrix} \hat{F}_x(\omega_i) \\ \hat{F}_y(\omega_i) \end{bmatrix} = \begin{bmatrix} G_{xx}^{-1}(\omega_i) X(\omega_i) \\ G_{yy}^{-1}(\omega_i) Y(\omega_i) \end{bmatrix} \tag{8}$$

Least squares solution of Eq.(8) can suffer from the ill conditioned case of the $\hat{\mathbf{F}}$ matrix. Considering the case where $\theta = 90^0$ and the thin wall case where the angle difference between the entry and exit tool work piece engagement is small, the $\sin\theta$ terms of $\mathbf{H}$ matrix will die out and the equation (3) can be approximated as follows

$$\mathbf{H}(\omega_i)_{\mathbf{2x4}} = \begin{bmatrix} 0 & c\left|F_{rc,x}(\omega_i)\right| & 0 & \left|F_{re,x}(\omega_i)\right| \\ c\left|F_{tc,y}(\omega_i)\right| & 0 & \left|F_{te,y}(\omega_i)\right| & 0 \end{bmatrix} \tag{9}$$

$$\hat{\mathbf{F}}(\boldsymbol{\omega})_{2nx1} \cong a_p \mathbf{H}(\boldsymbol{\omega})_{2nx4} \begin{bmatrix} K_{tc} \\ K_{rc} \\ K_{te} \\ K_{re} \end{bmatrix} \tag{10}$$

It is seen that the 1st-3rd and the 2nd-4th column pairs of the $\mathbf{H}$ matrix are dependent and the resulting rank is lower than 4. The lower rank $\mathbf{H}$ matrix makes it impossible to solve for the unknown cutting coefficients. Utilizing different engagement angles may seem to solve the lower rank problem, however, in literature it is shown that the $\mathbf{H}$ matrix is ill-conditioned for many cases [2].

3 TWO STEP LEAST SQUARE SOLUTION

In this paper it is proposed to solve the Eq.(7) in two steps. First a reduced order $\mathbf{H}$ matrix will be defined an solved for two intermediate cutting coefficients K_A and K_B. In the second step the unknown cutting coefficients $[K_{tc} \quad K_{rc} \quad K_{te} \quad K_{re}]^T$ are solved from the previously obtained K_A and K_B with different chip thicknesses c. Different chip thicknesses are required to separate force coefficients.

Considering the $\theta = 90^0$ case and approximating $\sin^2\theta \cong \sin\theta$, thus

$$F_{tc,y}(\boldsymbol{\omega}) \cong F_{te,y}(\boldsymbol{\omega}) \tag{11}$$

a reduced order $\mathbf{H}$ matrix is defined as follows

$$\begin{bmatrix} \hat{F}_x(\boldsymbol{\omega}) \\ \hat{F}_y(\boldsymbol{\omega}) \end{bmatrix} \cong a_p \underbrace{\begin{bmatrix} \left|F_{cr,x}(\boldsymbol{\omega})\right| & 0 \\ 0 & \left|F_{ct,y}(\boldsymbol{\omega})\right| \end{bmatrix}}_{\mathbf{H}(\boldsymbol{\omega})} \begin{bmatrix} K_A \\ K_B \end{bmatrix} \tag{12}$$

Here K_A and K_B are the intermediate coefficients and are defined as follows.

$$\begin{aligned} K_A &= K_{rc}c + K_{re} \\ K_B &= K_{tc}c + K_{te} \end{aligned} \tag{13}$$

The general description of the cutting process in this article and work piece to be cut is as shown in Figure 2. A single, thin walled workpiece aligned with X axis $(\theta \approx 90)$ is cut by giving constant feed in the same direction while keeping a constant angular speed at cutting tool. Entry and exit angles $(\theta_{st},\ \theta_{ex})$ are known through geometry of the workpiece and cutter diameter. They are used for window function $g(\theta)$ and keeping them constant ensures a uniform excitation across the milling process in which it helps checking for replicability. Three consecutive tests with different feed per tooth are done. Each test includes multiple tool work piece engagements and used to identify the intermediate coefficients given in Eq. (13). The K_A

and K_B are identified recursively as mentioned in the following section. Then using the 3 test results the cutting coefficients are found.

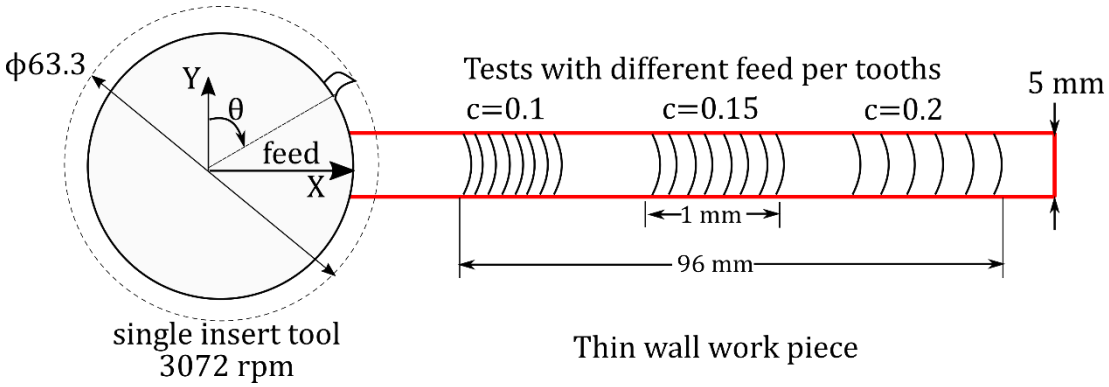


Figure 2 Schematic view of the cutting tool and the thin wall work piece for cutting coefficient identification experiments. 3 tests are performed with different feed rates, while the spindle speed is kept constant.

Figure 3 illustrates the force and acceleration response of a sample engagement. As seen from the figure the cut is equivalent to a single tap test, as it involves one force excitation caused by a single tool-workpiece contact and response in its' entirety until it dampens out. Different from the tap test, here the force is calculated theoretically. Hence its time axis has to be synchronised with the experimentally measured acceleration signal. In order to synchronise the two an acceleration threshold of $5\mathrm{m}/\mathrm{s}^2$ is utilized to place the force date. Note that since the tool have one cutting insert there exits a single excitation in one spindle revolution and the harmonics disappear till the second engagement.

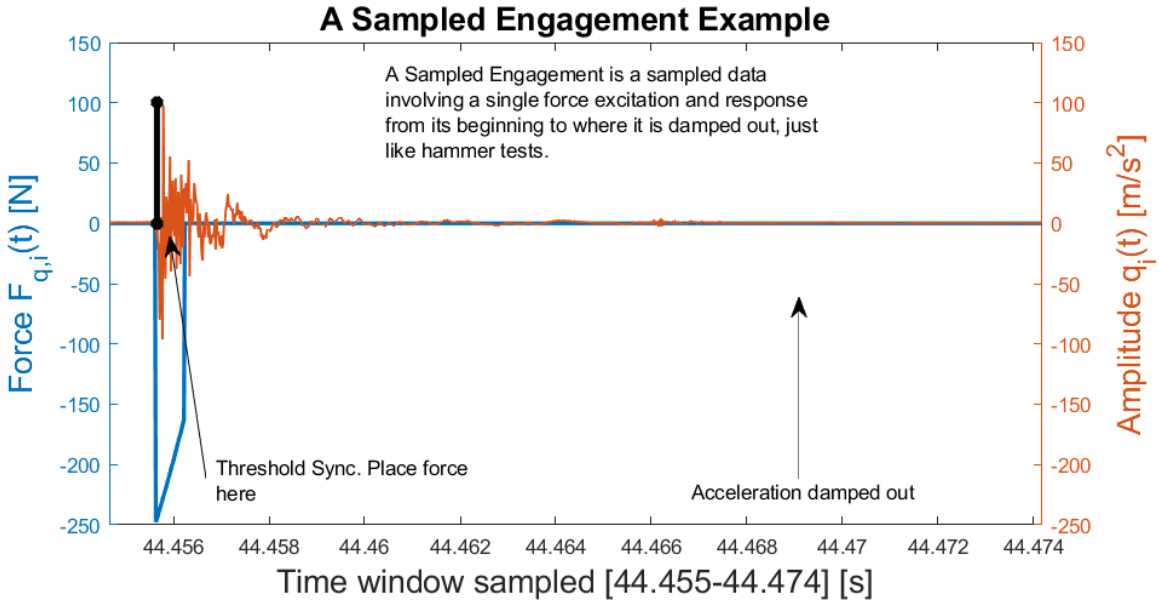


Figure 3 Sampled Engagement Example

3.1 1st Part Solution of Intermediate Coefficients

In the first part; a recursive least squares approach is for each test applied. Each test consists of multiple engagements with constant chip thickness. The intermediate coefficients are calculated recursively for acceleration response of each tool workpiece engagement as shown in Figure 3.

Recursive least square algorithm is given in Eq.(14). The subscript 'i' is used to count the tool and the workpiece engagements. $\mathrm{X_i}(\boldsymbol{\omega})_{\mathrm{n\times 1}}$ and $\mathrm{Y_i}(\boldsymbol{\omega})_{\mathrm{n\times 1}}$ are the frequency domain acceleration response vectors of the corresponding i[th] sample engagement. The response vectors is of size nx1 and are defined for the frequency array $\boldsymbol{\omega}$.

$$\mathbf{P_i} = \left([\mathbf{H}\circ\mathbf{W}]^{\mathrm{T}}\mathbf{H}\right)^{-\mathbf{1}}$$

$$\begin{bmatrix}\mathrm{K_A}\\ \mathrm{K_B}\end{bmatrix}_{\mathrm{i}} = \mathbf{P_i}[\mathbf{H}\circ\mathbf{W}]^{\mathrm{T}}\begin{bmatrix}\mathbf{G_{xx}}(\boldsymbol{\omega})^{-\mathbf{1}}\mathbf{X_i}(\boldsymbol{\omega}) & \mathbf{0}_{\mathrm{nx1}}\\ \mathbf{0}_{\mathrm{nx1}} & \mathbf{G_{yy}}(\boldsymbol{\omega})^{-\mathbf{1}}\mathbf{Y_i}(\boldsymbol{\omega})\end{bmatrix}$$

$$\mathbf{P_{i+1}} = \left(\mathbf{P_i^{-1}} + [\mathbf{H}\circ\mathbf{W}]^{\mathrm{T}}\mathbf{H}\right)^{-\mathbf{1}} \tag{14}$$

$$\mathbf{J_{i+1}} = \mathbf{P_{i+1}}[\mathbf{H}\circ\mathbf{W}]$$

$$\begin{bmatrix}\mathrm{K_A}\\ \mathrm{K_B}\end{bmatrix}_{\mathrm{i+1}} = \begin{bmatrix}\mathrm{K_A}\\ \mathrm{K_B}\end{bmatrix}_{\mathrm{i}} + \mathbf{J_{i+1}}\left(\begin{bmatrix}\mathbf{G_{xx}}(\boldsymbol{\omega})^{-\mathbf{1}}\mathbf{X_i}(\boldsymbol{\omega}) & \mathbf{0}\\ \mathbf{0} & \mathbf{G_{yy}}(\boldsymbol{\omega})^{-\mathbf{1}}\mathbf{Y_i}(\boldsymbol{\omega})\end{bmatrix} - \mathbf{H}\begin{bmatrix}\mathrm{K_A}\\ \mathrm{K_B}\end{bmatrix}_{\mathrm{i}}\right)$$

$\mathrm{P_i}$ is the covariance matrix (alternatively called information matrix) at $\mathrm{i_{th}}$ sampled engagement. In this application matrix size is 2x2. $\mathbf{H}_{\mathrm{2n\times 2}}$ is the regressor matrix (alternatively called basis matrix) which comes from a set of linear equations which in this case are Eq.(12). $\mathrm{J_{i+1}}$ is referred as Kalman gain because recursive least squares work in the same principle as Kalman filter. Finally the intermediate coefficients $[\mathrm{K_A}\quad \mathrm{K_B}\,]^{\mathrm{T}}{}_{\mathrm{i+1}}$ is calculated and the cycle repeats with i increasing by one until all selected sampled engagements are used, finalizing the calculation. Note $[\mathbf{H}\circ\mathbf{W}]$ utilise element-wise multiplication for memory efficiency. This is for saving memory as diagonal weight matrixes are sparse. In order to increase the quality of the estimations a weight matrix $\mathbf{W}_{\mathrm{2nx2}}$, which consists of the amplitude of known FRF itself is utilized.

$$\mathbf{W} = \begin{bmatrix}|\mathbf{G_{xx}}(\boldsymbol{\omega})| & \mathbf{0}_{\mathrm{nx1}}\\ \mathbf{0}_{\mathrm{nx1}} & |\mathbf{G_{yy}}(\boldsymbol{\omega})|\end{bmatrix} \tag{15}$$

3.2 2nd Part Solution of cutting coefficients

The second part is simply utilizing least squares method to separate $\mathrm{K_A}$ and $\mathrm{K_B}$ into cutting and edge coefficients based on chip thickness. With the help of various m-many tests with different

feed per tooths, force coefficients are separated into edge and shear components, as explained equation (16) and (17), completing force coefficients identification.

$$\mathbf{K_A} = \begin{bmatrix} K_{A,1} \\ \vdots \\ K_{A,m} \end{bmatrix} \quad \mathbf{K_B} = \begin{bmatrix} K_{B,1} \\ \vdots \\ K_{B,m} \end{bmatrix} \quad \mathbf{H_1} = \begin{bmatrix} c_1 & 1 \\ \vdots & \vdots \\ c_m & 1 \end{bmatrix} \tag{16}$$

$$\begin{bmatrix} K_{tc} \\ K_{te} \end{bmatrix} = \left(\mathbf{H_1^T} \cdot \mathbf{H_1}\right)^{-1} \cdot \mathbf{H_1^T K_A}$$

$$\begin{bmatrix} K_{rc} \\ K_{re} \end{bmatrix} = \left(\mathbf{H_1'} \cdot \mathbf{H_1}\right)^{-1} \cdot \mathbf{H_1' K_B} \tag{17}$$

4 THE TEST SET UP and EXPERIMENTAL APPLICATION

The proposed method is applied on a Deckel FP5CC, 5 axis CNC milling machine. The CNC is in home retrofitted with Beckhoff control and drive systems. Cutting coefficient are identified for the AL7075 aluminum alloy, which is well known in the aerospace industry. Cutting tool used is EM90 63X6 022 EDPT 140408 (MBC cutting tools, Figure 1) which is a face milling tool with 63.3 mm diameter (with inserts) placed on it. It allows 6 insert but only one of them is used and neither the cutting tool nor insert has no helix angle. Insert used is EDPX 140420-CKN20M (Rapid Maxtools)

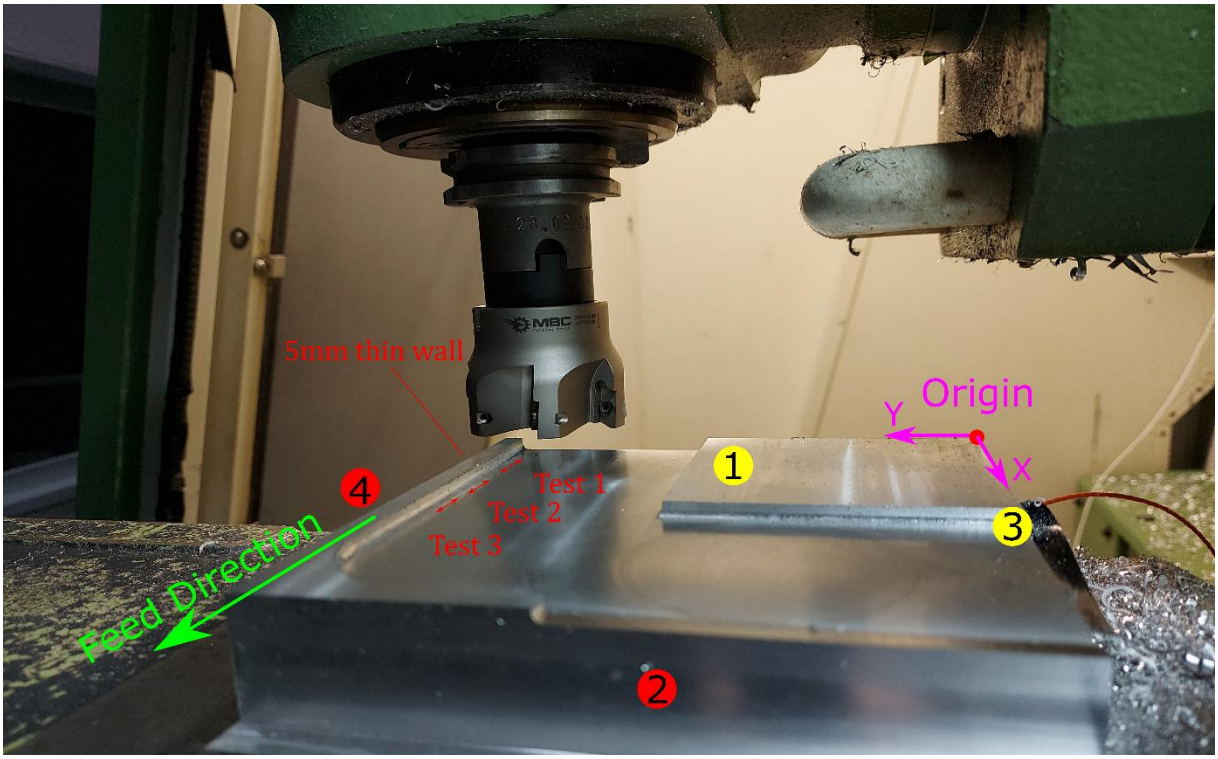


Figure 4 Acceleration locations (1-3) and tap test spots (2-4) are given. Feed is along X direction. Material is AL7075

As hammer, DYTRAN 5800B3T and as accelerometers at X and Y directions PCB 352C23 $(5.12\mathrm{mV/g})$ and DYTRAN 3225F1 $(10.23\ \mathrm{mV/g})$ are used respectively. These accelerometers take data from single direction only. Data acquisition is done through NI 9234 processing card. The schematic view of the tool path along with workpiece engagement was given in Figure 2 and the corresponding experimental test set up view is given in Figure 4. The tool path is along the X-direction. The three consecutive tests with 10mm/s, 7.5mm/s and 5mm/s feed rates and 3072rpm spindle speed are performed along a total 96 mm tool path. In Figure 4, the point 1 and 3 gives acceleration positions and points 2 and 4 gives tap test spots. The tap test results are presented in Figure 5 and Figure 6. Those results verify that neglecting the cross FRF's is a reasonable assumption. Three tests have been performed with different feed per tooth's. Factors applying all tests are given in Table 1 and detailed information regarding tests are presented in Table 2.

Table 1 Test format

Test:1,2,3	Deckel FP5CC	Sampling: 51200 hz
Point 1	Point 3	
Workpiece Accelerometer X 5.12mV/g Gain:1916	Workpiece Accelerometer Y 10.23mV/g Gain:958	Insert: Single
D: 63.3mm	radial offset = 0mm (tool path coincides with wall profile)	

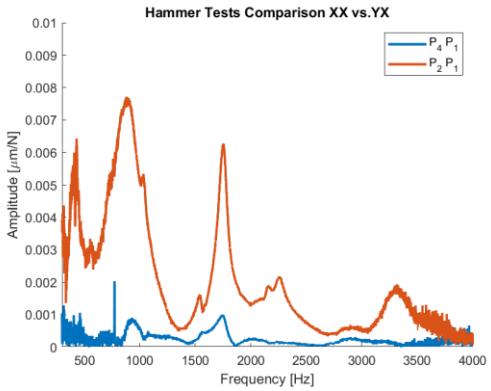


Figure 5 Tap Tests Comparison XX vs. YX.

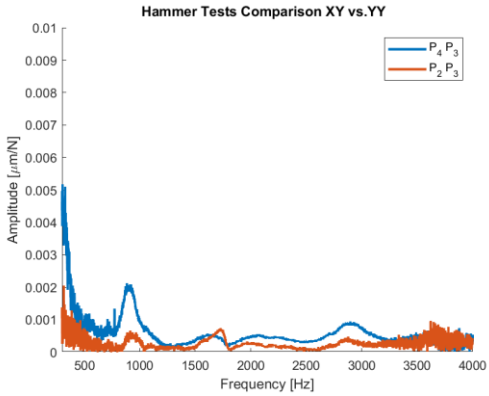


Figure 6 Tap Tests Comparison XY vs. YY.

500-1500 Hz frequency domain is selected for identification due to distinct mode present.

Table 2 Test parameters of cutting force identification

$D = 63.3$ mm		$a_p = 2.9$ mm		wall depth = 4mm	
Test	$V_x \left[\frac{mm}{60s}\right]$	n_s [rpm]	wall thickness[mm]	Sample Position [mm]	Sample Length[mm]
1	300	3072	6	20	1
2	450	3072	6	20	1
3	600	3072	6	20	1

During 3 tests cutting tool center has travelled 32mm in each one. Sample position is taken as 20mm from start of every individual test and a region of 1mm has selected for sampling. Axial depth is $a_p = 2.9mm$. Wall depth is the depth of milled workpiece and this value is higher than axial depth to prevent cutting more than the designated thin wall. Both wall depth and axial depth are constant throught tests.

4.1 Application of the Algorithm

The proposed method is illustrated step by step in Figure 7 by using the data of Test 3.

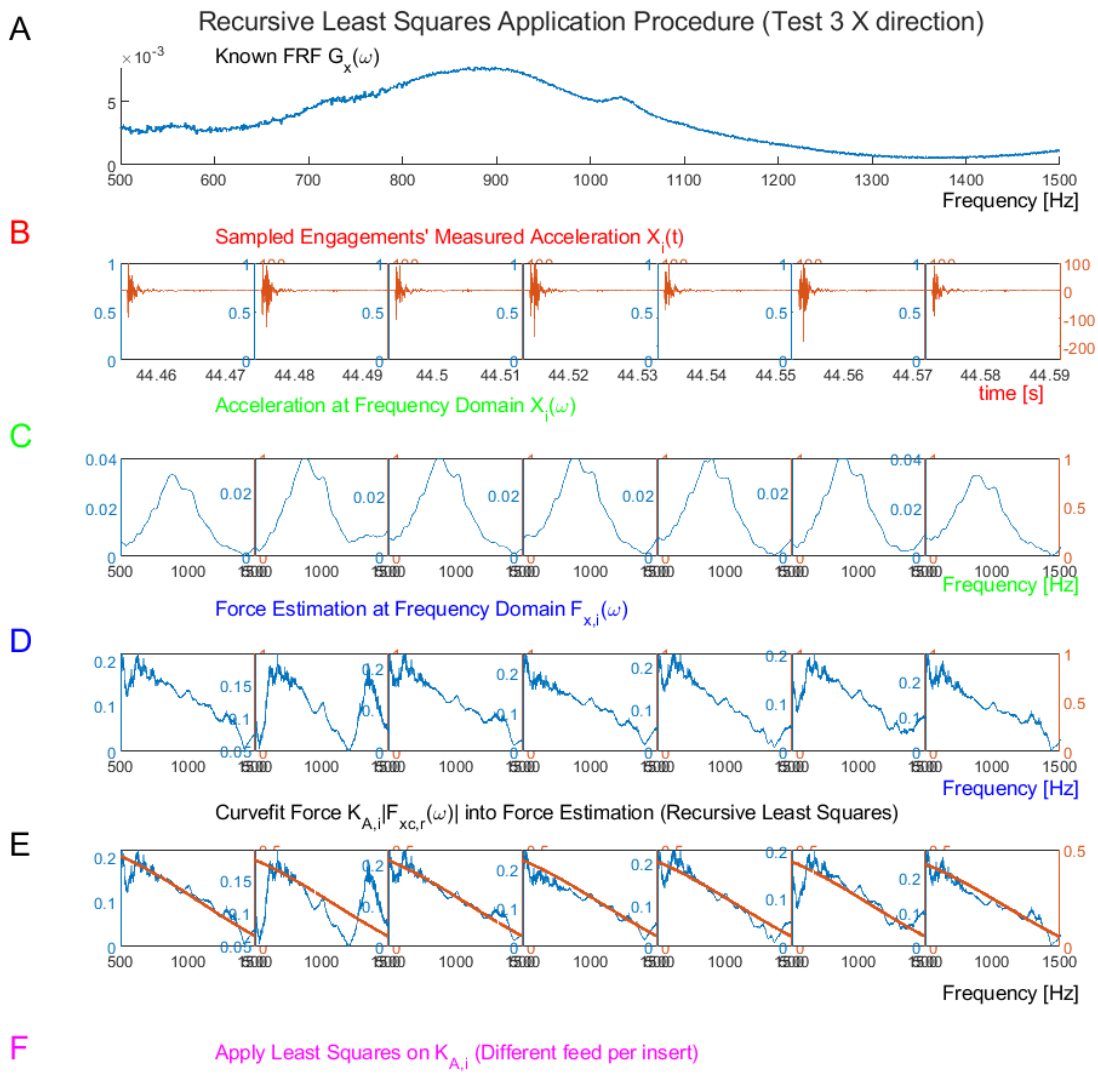


Figure 7 Explanation of cutting coefficients identification is given here(Figures are from the real system)

Explaining the basic framework of the method is as follows:

a. Given as “Known FRF”, an FRF representing behavior of machine-tool structure in which measurement is to be taken is needed for force estimation in following steps. This FRF is obtained through tap tests in this article and they are given in Figure 5 and Figure 6.

b. Measured acceleration $X_i(t)$ is illustrated with 7 windowed time sections. Selection of time sections are determined so that when acceleration response to the force occurred during one contact is in the windowed time frame, from when acceleration starts to rise until acceleration dampens out.

c. The accelerations sampled with 7 windows are represented in frequency domain. For this description, sampling provides 7 seperate acceleration measurements, let’s say for X being

$X_i(t)$ $i = 1,2, \dots ,7$, which were resulted from 7 tool contacts, converted to frequency domain as $X_i(\omega)$ $i = 1,2, \dots ,7$, i representing a sample data.

d. For every sample data, force estimation $\left(\hat{F}_{x,i}(\omega), \hat{F}_{y,i}(\omega)\right)$ is obtained through Eq. (8), which utilize the known FRF matrix $\mathbf{G}(\omega)$ and the sampled acceleration $\mathbf{X}_i(t)$.

e. Together with force model (given in section 2), curve fitting force estimation with force coefficients is applicable. $K_{A,i}$ and $K_{B,i}$ parameters are estimated with this curve fitting. Calculations of curvefit is explained in this section, following paragraphs.

f. Repeating first 5 steps for various tests with different feed per insert values, Recursive Least Squares Method is applied to obtain K_A and K_B and a second least squares method with chip thickness is used to obtain 4 force coefficients.

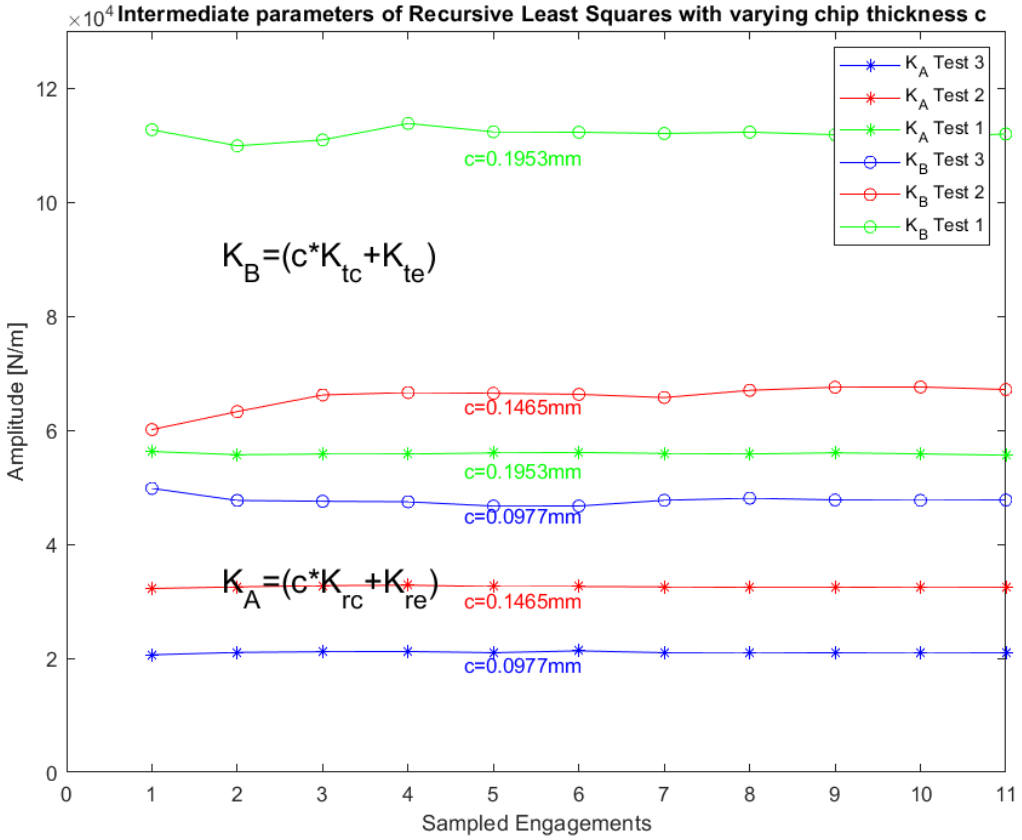


Figure 8 Recursive force coefficients calculation, all tests

Figure 8 gives an example recursive calculation of the intermediate force coefficients $(K_{A,i}, K_{B,i})$ at Test 3. $K_{A,i}$ and $K_{B,i}$ listed in this table are the ones used on step E of Figure 7. As seen from the figure the coefficient estimations converge into a value after a few tool workpiece engagements.

Three tests with different chip thickness values offered 3 sets of K_A and K_B. Using equation (16) and (17), force coefficients are identified as Table 3**.** These force coefficients are final. This value can be compared to what literature says [6].

Table 3 The Identified Force Coefficients

$K_{tc} = 603(MPa)$	$K_{rc} = 244.21(MPa)$
$K_{te} = 28.15 \cdot 10^3 \left(\frac{N}{m}\right)$	$K_{re} = 20.08 \cdot 10^3 \left(\frac{N}{m}\right)$

Figure 9 gives a set of force coefficients taken from a milling force review paper [6]. It is seen that the values found in this article are comparable to the results of the research papers. It should be noted that some of the listed research papers are experimented with extreme conditions such as composite material and very small chip thickness.

From: Milling Force Model for Aviation Aluminum Alloy: Academic Insight and Perspective Analysis

Ref.	Cutter material	Lubrication	Workpiece	K_{tc} (N/mm^2)	K_{te} (N·mm)	K_{rc} (N/mm^2)	K_{re} (N·mm)	K_{ac} (N/mm^2)	K_{ae} (N·mm)
[189]	Cemented carbide	Dry	Al6082-T6	631	13	99	10	273	2. 8
[190]	Cemented carbide	Dry	Al7075-T6	767.01	27.7	168.8	26.6	222	0.7
[160]	Cemented carbide	Dry	Al6061-T6	243.77	7.53	113.5	7.83	–	–
[160]	Cemented carbide	Dry	Al7075-T6	600.46	17.9	180.96	20.42	–	–
[150]	Cemented carbide	mql	AlMgSi0.5	561.2	204.3	194.4	16.2	6.7	2.2
[157]	Cemented carbide	Dry	Al7050-T7451	–	23.4	–	35.16	–	0
[156]	High-speed steel	Dry	Al7075	951.365	11.115	262.597	11.314	323.33	1.105
[47]	Cemented carbide	Dry	Al7075	1319.41	19.65	788.83	26.77	48.75	2.05

Figure 9 A set of force coefficients from [6]

5 CONCLUSION

This article provides a method of force coefficients identification that does not require dynamometers but instead utilizes acceleration measurements and FRFs obtained beforehand. A single thin wall workpiece has been face milled. Data is sampled and force calculations are placed according to process parameters curve-fit is performed with recursive least squares method, leading to identification of force coefficients. The method's results are in accord with the literature. It is concluded that method provides accurate force coefficient estimations.

There is a lot of room for improvement in this method. Reducing number of tests required by identifying 4 force coefficients at the same test would be a significant improvement but a single sample provides ill-conditioned matrix for such an approach and there is work on literature regarding this. [2,7]. Requirement of special workpiece is another improvement area. Nonlinear force models offer better results with shoulder milling. Real-time application of

method should be considered. This is especially true for acceleration measurements from spindle.

6 ACKNOWLEDGEMENT

This research is performed with CNC milling machine retrofit under TUBITAK 1001 project 218M430-Intelligent CNC: Real time Chatter Identificaiton, Detection and Control.

REFERENCE

1. **Altintas, Y.,** "Manufacturing Automation: Metal Cutting Mechanics, Machine Tool Vibrations, And Cnc Design." Cambridge University Press; 2nd edition (March 29, 2012)

2. **Pawełko, P., Powałka, B., & Berczyński, S. (2013),** Estimation of cutting force model coefficients with regularized inverse problem. Advances in Manufacturing Science and Technology, 37(2). https://doi.org/10.2478/amst-2013-0012

3. **Aggarwal, S., Nešić, N. & Xirouchakis, P. (2013),** Cutting torque and tangential cutting force coefficient identification from spindle motor current. Int J Adv Manuf Technol 65, 81–95. https://doi.org/10.1007/s00170-012-4152-x

4. **Yamato, Shuntaro & Imabeppu, Yasuhiro & Irino, Naruhiro & Suzuki, Norikazu & Kakinuma, Yasuhiro. (2019),** Enhancement of Sensor-less Cutting Force Estimation by Tuning of Observer Parameters from Cutting Test. Procedia Manufacturing. 41. 272-279. 10.1016/j.promfg.2019.07.056.

5. **Zhou, Ji & Mao, Xinyong & Liu, Hongqi & Li, Bin & Peng, Yili. (2018),** Prediction of cutting force in milling process using vibration signals of machine tool. The International Journal of Advanced Manufacturing Technology. 99. 10.1007/s00170-018-2464-1.

6. **Duan, Z., Li, C., Ding, W. et al. (2021),** Milling Force Model for Aviation Aluminum Alloy: Academic Insight and Perspective Analysis. Chin. J. Mech. Eng. 34, 18 https://doi.org/10.1186/s10033-021-00536-9

7. **Wang, C., Zhang, X., Qiao, B., Cao, H., and Chen, X. (April 12, 2019),** "Dynamic Force Identification in Peripheral Milling Based on CGLS Using Filtered Acceleration Signals and Averaged Transfer Functions." ASME. J. Manuf. Sci. Eng. June 2019; 141(6): 064501. https://doi.org/10.1115/1.4043362

8. **Bin Li, Hui Cai, Xinyong Mao, Junbin Huang, Bo Luo, (2013),** Estimation of CNC machine–tool dynamic parameters based on random cutting excitation through operational

modal analysis, International Journal of Machine Tools and Manufacture, Volume 71, 2013, Pages 26-40, ISSN 0890-6955, https://doi.org/10.1016/j.ijmachtools.2013.04.001.

A DESIGN IMPROVEMENT AND STRUCTURAL ANALYSIS IN A PRE-DESIGNED HYBRID DRILLING

Mustafa BAKKAL, *bakkalmu@itu.edu.tr* Istanbul Technical University, 34469, Istanbul, Turkey

Mahmut YILMAZ, *mahmutyilmaz@yilmazmachine.com.tr* Yilmaz Machine Inc., 41455, Kocaeli, Turkey

Alper YETER, *alperyeter@yilmazmachine.com.tr* Yilmaz Machine Inc., 41455, Kocaeli, Turkey

Hasan Aytuğ KURT, *hasankurt@yilmazmachine.com.tr* Yilmaz Machine Inc., 41455, Kocaeli, Turkey

ABSTRACT

The load-bearing metal and the composite part drilling process of Al/CFRP, and Ti stacks, on the aircraft wings are crucial for the aircraft industry. During this process, problems such as rapid tool wear, extreme interface consumption, and significant subsurface damage may occur. This process needs to be done either manually or semi-automatically. In this paper, a pre-designed semi-automatical tool is improved with an additional pneumatic driving system and MQL cooling. The last part of the paper focused on the FEM analysis of the selected mechanical sections.

Keywords: Hybrid Drilling, Composites, Tool Design, MQl, FEM

1. INTRODUCTION

Composite materials are used in more than 50% of aircraft structures in the developing aircraft industry. Therefore, problems such as installing such materials and drilling holes have arisen. It is common for composites to be attached to other structural members, but drilling these materials to the desired precision is very difficult. It is very important that especially because of the use of expensive materials.

The burrs that will occur while the CFRP material is drilled may adhere to the drill or the material and cause various blockages. Therefore, it is suitable to work in extremely cold

environments material decreases too much and many forces occur in the material. This causes the material to have a hard and brittle structure, in addition, it makes the chip removal process very difficult. This is prevented by the immersion cryogenic technique. This technique greatly improves machinability by reducing the surface roughness of the drilled parts [Nguyen et al., 2020].

Since titanium is a material with a very high hardness value, scratches, burr removal and changes in the internal structure of the alloy due to overheating are also among the drilling problems. To prevent these, the drilling process is applied by the dipping method in cryogenic (extremely cold) environments, which is also mentioned in CFRP [Boeing, 2006]. Drilling problems of aluminum alloys are generally drilled bit wear and deterioration of hole surface quality. It is seen that PCD (Poly Crystalline Diamond) material is the most suitable choice in the drilling of Aluminum materials with a drill, and it can provide the desired results in terms of tool life and hole surface quality [Campbell, 2006]. Chip formation and chip evacuation are very important issues in drilling and these can vary depending on the workpiece material, drill and insert geometry, coolant pressure, volume, and cutting data. For good chip evacuation, it is necessary to improve chip formation. Excessively long chips are an indicator of insufficient chip formation. This can make chip jamming, deteriorating surface finish, and breaking the tool when grooving, generally in small holes [www.sandvik.coromant.com, 2022]. If there is continuous noise during drilling, chip evacuation is successful, if there is intermittent sound, it can be concluded that the chip evacuation has failed. If the chips are long and bent, there is chip jamming. Ti, CFRP and Al materials all have different properties. The same is true for chips of these materials. For example, high-temperature chips of titanium damage the CFRP material. For this reason, chip evacuation is a very important issue when drilling Ti / CFRP / Al hybrid bundles, especially in the aviation industry where high surface quality is required for drilled parts [web.hitit.edu.tr]. The adaptive drilling method is a common method in hybrid machining processes and consists of two different applications, adaptive speed and adaptive feed. Adaptive speed will show the greatest productivity gains in Al-Ti or CFRP-Ti stacks where drilling time can be reduced by 50% or more. [Hallberg et al., 2017]. Used to prevent chip jamming in long chipping materials and when drilling deep holes (> 3xDC). In a horizontal drill, any downward drop across at least 30 cm (11.81 inches) must have a flow of coolant exiting the drill without it [www.kennametal.com]. When drilling multi-layer stacks consisting of Al alloys, CFRP, and Ti alloys, parameters such as tool wear, chip formation, cutting force, and hole quality are taken into consideration, and the through-feed (internal) cooling technique gives better results. Internal coolant applications are superior to dry drilling. Internal helical coolant channels are a common means of delivering high-pressure coolant

directly to the cutting edge to increase the transfer of heat away from the cutting edge and to aid with chip evacuation [Johns et al., 2014]. To increase cutting efficiency, coolant is used in three separate but interrelated must fulfill functions:

1) Lubrication;

2) Cooling,

3) Anti-weld functions [www.guvensanpetrol.com].

In this paper, a pre-designed semi-automatical tool is improved with an additional pneumatic driving system and MQL cooling. The last part of the paper focused on the FEM analysis of the selected mechanical sections.

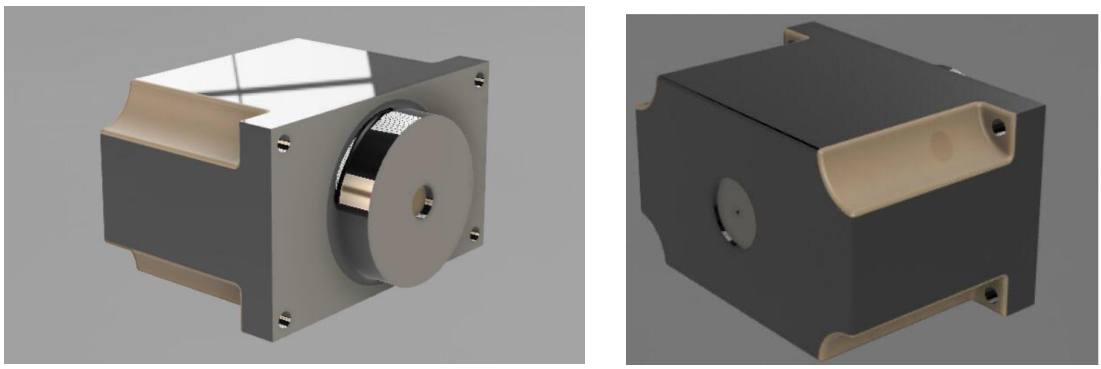
2. MATERIAL, METHOD, IMPROVEMENTS, AND INTEGRATIONS

2.1. Pneumatic Cylinder Integration Into System:

The pneumatic cylinder is the element that controls the compressed air into a linear motion. When converting pneumatic energy into mechanical energy, these cylinders consist of a combination of parts such as the front and back cover, cylinder tube, piston rod, and seals.

The pneumatic systems can be integrated with modem control systems easily [www.pnomatikithalat.com].

Since systems using pneumatic cylinders are much lighter and simpler than electrical power tools, they were preferred for this study as a power system (Fig.1).



(a) front side view (b) backside view

Figure 1. Pneumatic cylinder design.

A pneumatic cylinder was integrated into the drilling machine system to control the feed drive gear that controls the spindle feed gear as seen on Fig. 2.

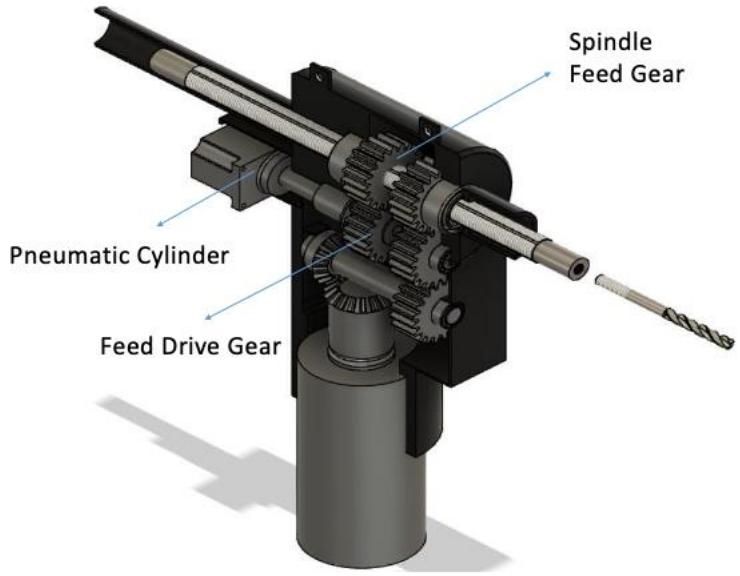


Figure 2. Pneumatic cylinder integrated into the system.

2.2. Minimum Quantity Lubrication (MQL):

MQL is the process of applying a minimum amount of lubricant directly to the cutting tool/workpiece interface. MQL minimizes environmental impact by significantly reducing fluid usage and eliminating the need for coolant treatment and disposal. MQL lubrication method is selected in current design.

During the design (Fig.3) below given considerations are taken into account:

• Ventilation gaps were considered in the machine body section in order to prevent overheating and help to proper heat dissipate.

• Cooling system which include tubes, nuts, gaskets, etc. also integrated into spindle drilling tool.

• Chip evacuation tube which helps to evacuate the continuous chips by vacuum action is also added onto the machine body section.

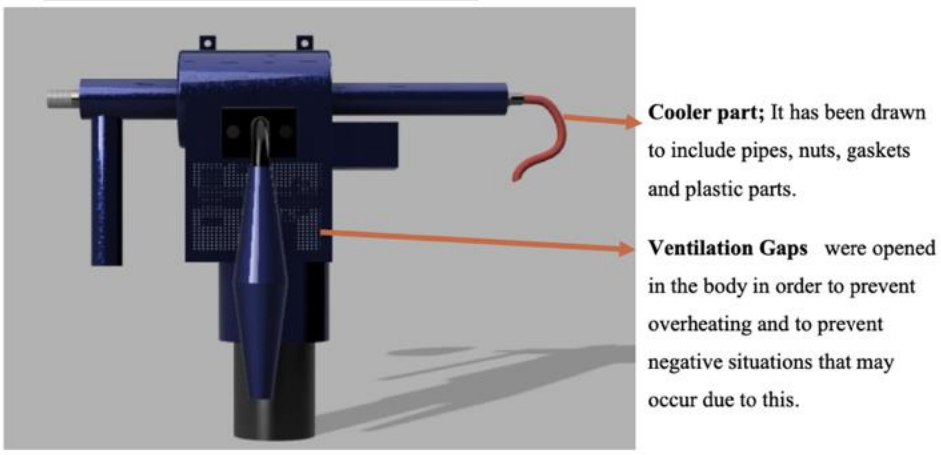


Figure 3. Cooler part and ventilation gaps.

2.3. Hybrid Drilling Machine Working Principle:

A pneumatic cylinder was integrated into the drilling machine system to control the feed drive gear that controls the spindle feed gear.

In Fig. 4, the spindle allows tool to move, with grooves and teeth on this spindle. There are two types of gears attached to the spindle which are spindle gear and feed gear. The spindle gear is connected to the spindle with grooves. Both of these gears are always fixed on the spindle and provide the rotational motion of the spindle. The connected feed gear onto the spindle can move forward and backward (retracted) on the spindle.

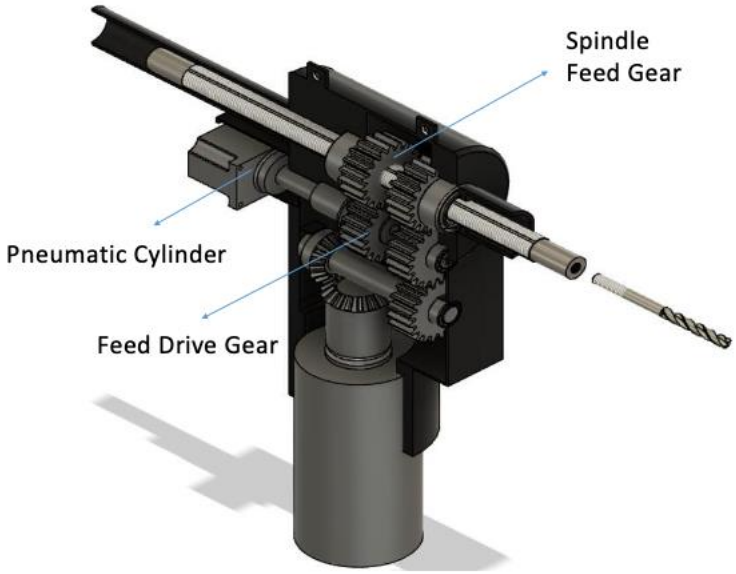


Figure 4. Cross-section of the drilling machine with newly designed additional systems.

For the spindle to move forward, the angular speed of the feed gear must be higher than the spindle gear. If the spindle gear rotates faster than the feed gear, the spindle will retract. The structure of the spindle and feed gear can be seen in Fig. 5 below:

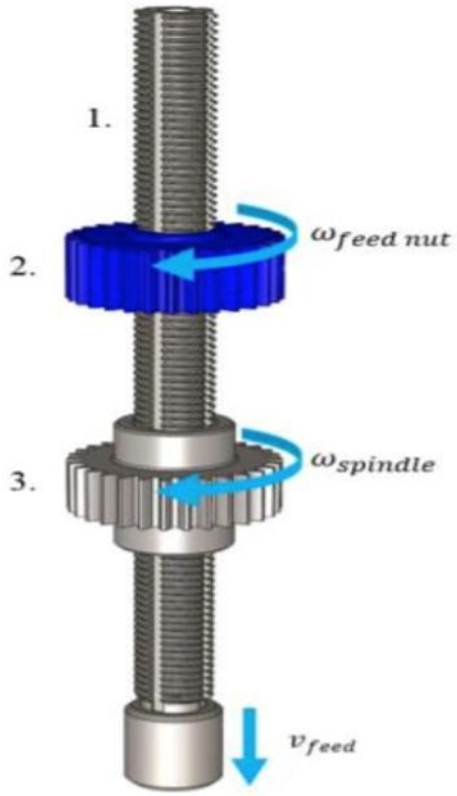


Figure 5. Illustration of The Spindle Mechanism, Spindle (1) With Translational Feed $vfeed$, Feed Nut (2) With Rotational Speed $wspeed$, And Speed Gear (3) With Rotational Speed $wspindle$.

The power from the pneumatic motor is transferred to the shaft with bevel gears (Fig.4). The spur gear on this shaft transmits the power to the spindle drive gear. The spindle drive gear transfers the power to the spindle gear on the spindle. Next to the spindle drive gear, there is a feed drive gear connected to a separate axial moving shaft. The axial moving shaft, on which the feed drive gear is located, is controlled by a pneumatic cylinder. When progress is required in the system, the pneumatic cylinder pushes the axially moving shaft and the feed drive gear and the spindle drive gear are connected by the canine teeth on them, so the power is transferred from the spindle drive gear to the feed drive gear. The feed drive gear transfers the power to the feed gear on the spindle and the feed gear starts to rotate. Thanks to the adjusted gear ratios, the feed gear rotates faster than the spindle gear. In this way, progress takes place. The outer ring of the bearings inside the feed drive gear is movable and the inner ring is fixed. Thus, the axial moving shaft does not rotate. When a retraction is desired, thanks to the pneumatic cylinder that controls the axial moving shaft, the axial shaft

is retracted and the dog tooth connection between the feed drive gear and the spindle drive gear is broken. Housing is designed to stop the feed drive gear so that shortly after the feed drive gear is disconnected, stops the rotation movement and thus the feed gear also stops, and the retraction movement begins.

2.4. Hybrid Drilling Machine Assembly:

A tedious work has been done in order to make the smaller and more ergonomic tool structure and keep all system elements together (Fig.6).

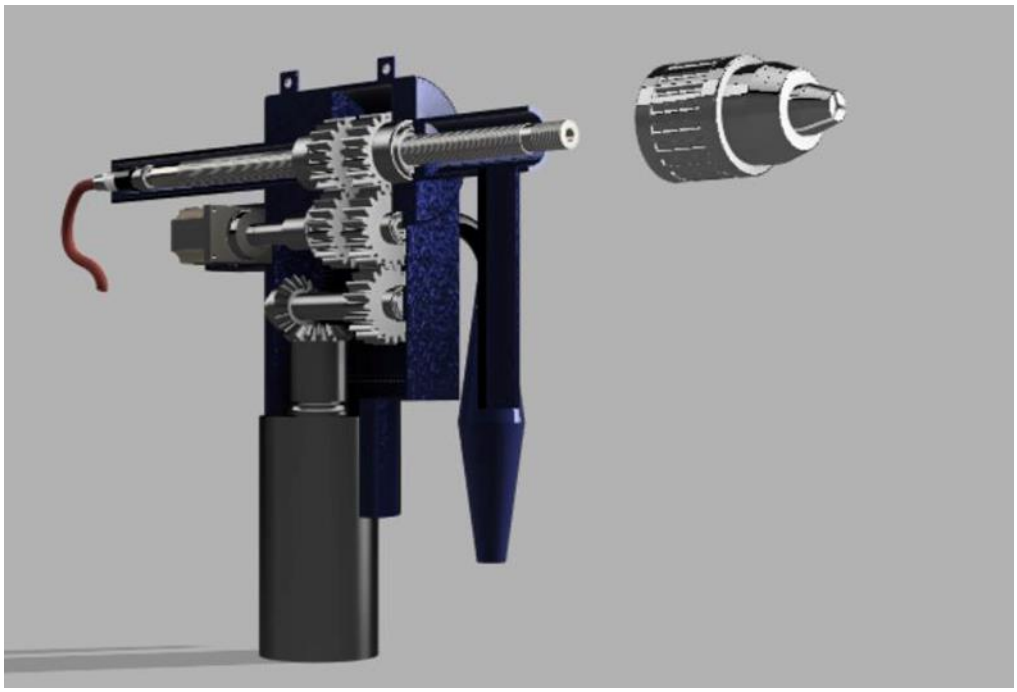
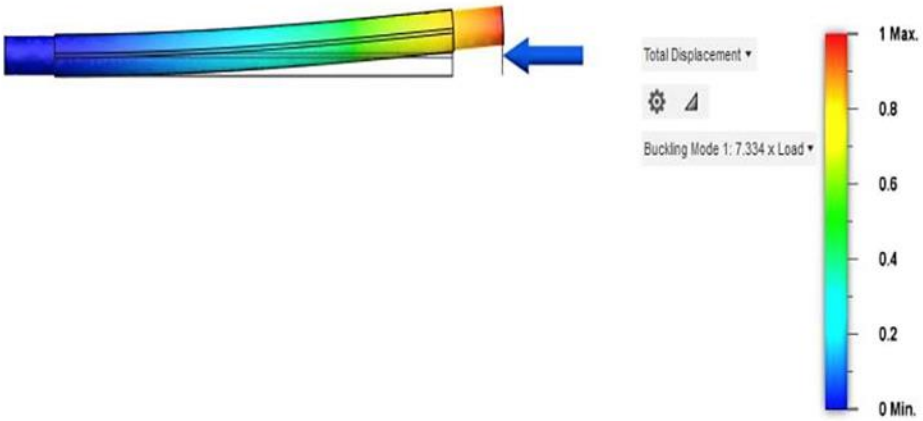


Figure 6. Hybrid drilling machine assembly.

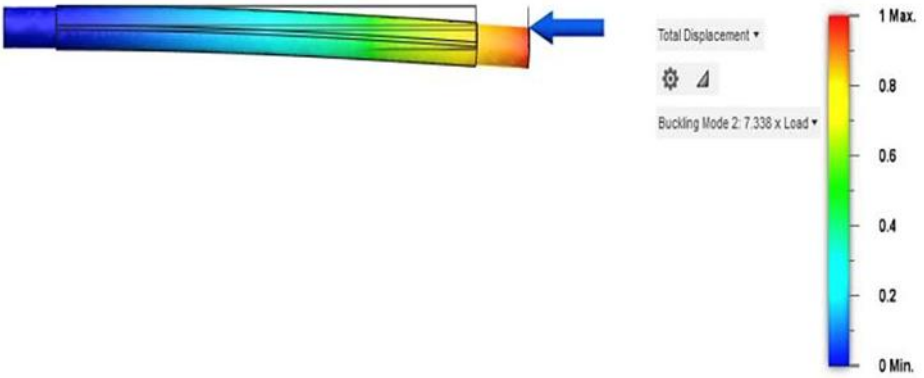
3. ANALYSIS AND RESULTS

3.1. Buckling Analysis of the Spindle:

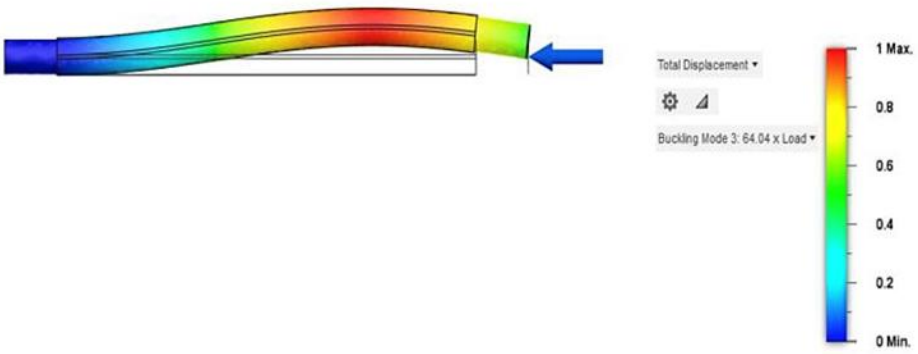
The first of the analyzes for the designed machine was the buckling analysis. When the buckling analysis was performed, the following 3 modes emerged, and according to these results, the system is safe. It has been observed that the force required for the buckling in all 3 modes is quite high Fig.7).



(a) Mode 1



(b) Mode 2



(c) Mode 3

Figure 7. Buckling modes.

3.2. Torsion Analysis of the Spindle:

Looking at the results of the torsion analysis, the safety factor is as high as 15 (Fig.8). Although the factor of safety is very high, this analysis includes only torsion analysis. Thus, in

real application torsion will be affected on the spindle together with buckling and bending forces. As the safety factor is kept very high here, the spindle can withstand high-stress conditions for a long time.

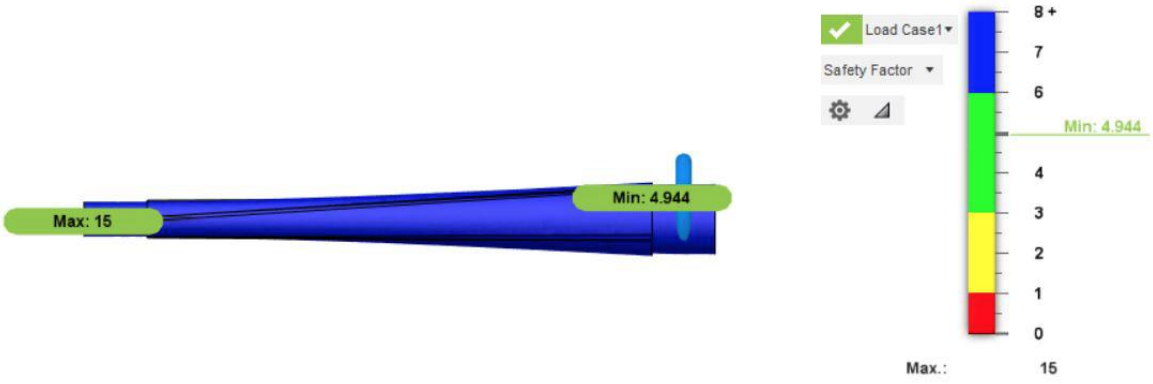
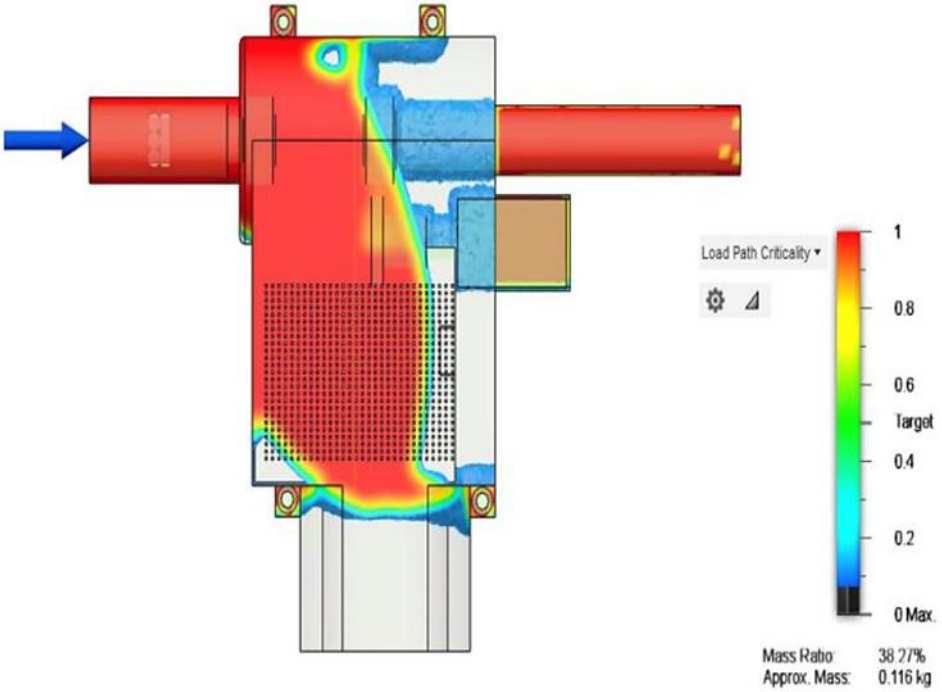


Figure 8. Torsion analysis result of the spindle.

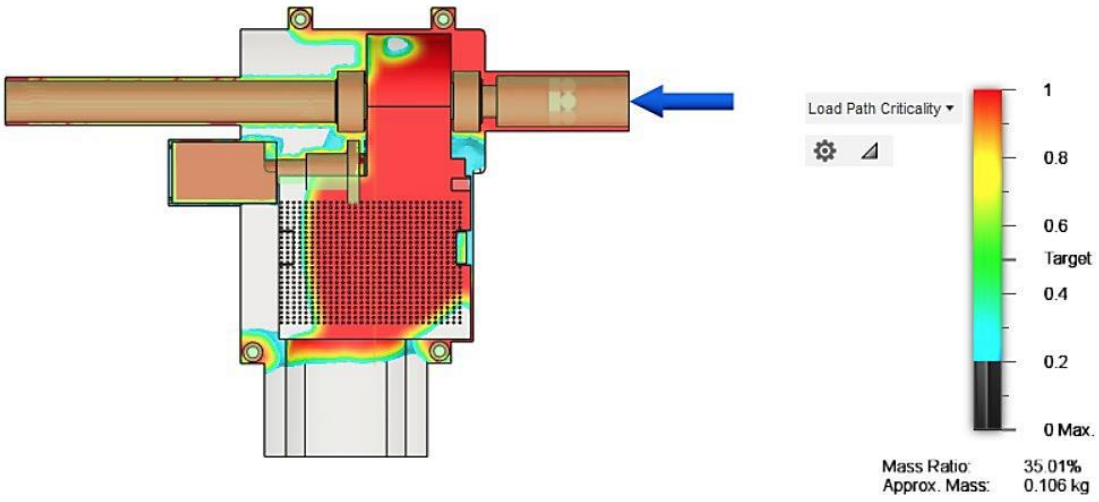
3.3. Topology Optimization of the Drilling Machine:

Topology optimization allows achieving maximum strength by using maximum efficiency. Efficiency includes using minimum material and creating a lightweight product. Furthermore, this also allows for a reduced duration of the design process, which also results in reduced costs.

The topology optimization result of the drilling machine body is given in Fig.9. In order to get a lighter drilling machine, the part thickness and all other dimensions in the design were determined at a minimum level.



(a) Right view



(b) Left view

Figure 9. Result of the topology optimization on machine body

As can be seen in the topology optimization analysis, it has been observed that there is no need for any material reduction in the design. Compared to similar products on the market, the drill design, which is around 3.8 kg, is lighter than many other models. For this topology optimization, it was preferred to use Autodesk Fusion 360 program.

3.4. Stress, Strain, Displacement Analysis of the Machine Handle:

Fig. 10 shows the strain, stress, and displacement analysis results of the newly designed double-sided polyurethane machine handle. Since the stress, strain, and displacement values in the earlier design were high, the handle design is changed reducing all analyzed values by half.

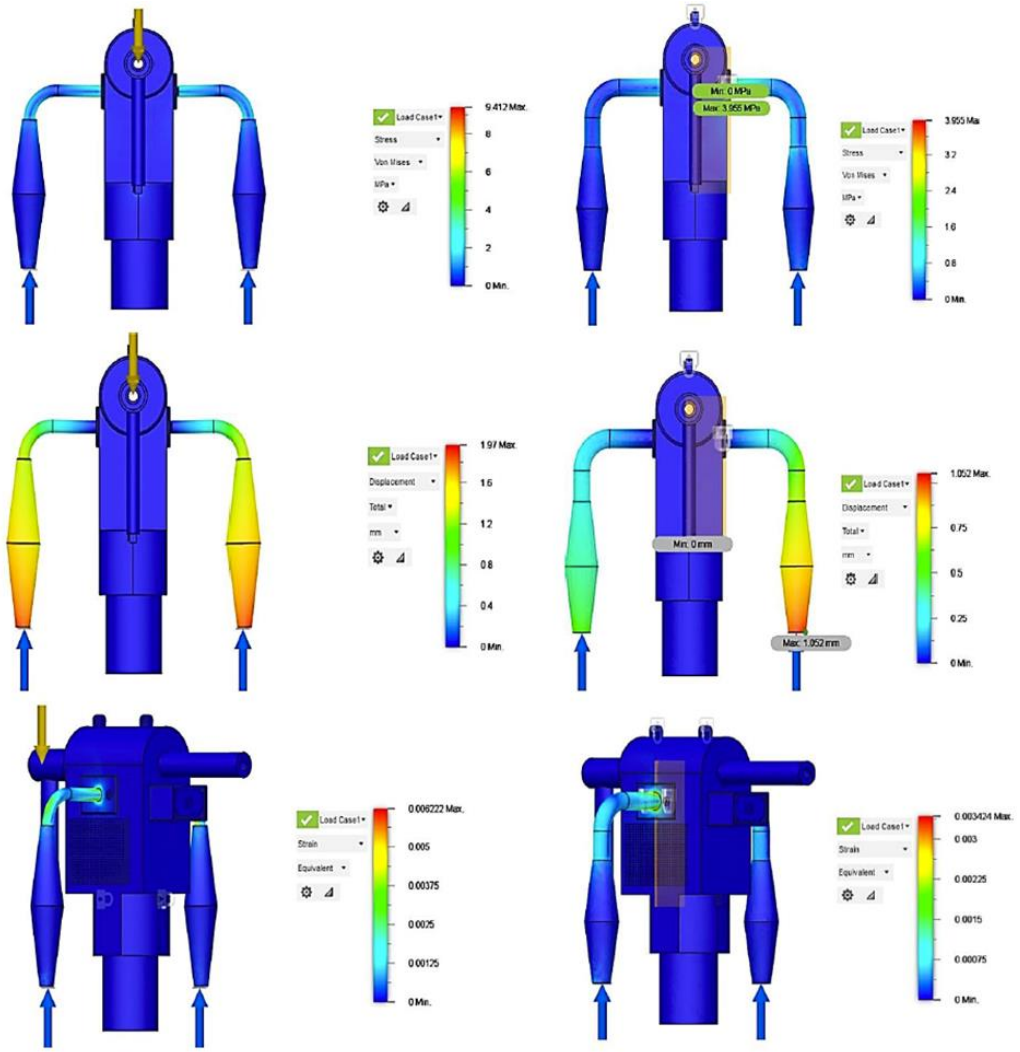


Figure 10. Before (left) and after (right) design change stress, strain and displacement distribution analysis results of the handle.

4. CONCLUSIONS

In order to get a better design of a pre-designed manual stack drilling machine, structural design improvements have been made in this paper. These improvements are a pneumatic drive system, ventilation slots, double-sided handles, chip evacuation, and cooling systems.

Besides the new design, buckling analysis for spindle, static FEM analysis for handles, and topology optimization for machine body have been done.

5. ACKNOWLEDGEMENT

Authors thanks Yilmaz Machine for their valuable support in this design work.

6. REFERENCES

1. **Nguyen, D., Bin Abdullah M.S., Khawarizmi, R., Kim, D. and Kwon, P. (2020),** "The Effect of Fiber Orientation on Tool Wear in Edge-Trimming of Carbon Fiber Reinforced Plastics (CFRP) Laminates", Wear, Volumes 450–451, 2020, 203213, ISSN 0043-1648.

2. **Boeing (2006),** "AERO - Boeing 787 from the Ground Up", Archived from the original on 21 February 2015, Retrieved 7 February 2015.

3. **Campbell Jr, F.C. (2006),** “Manufacturing Technology for Aerospace Structural Materials”, Elsevier Ltd., Missouri.

4. **URL1-** https://www.sandvik.coromant.com/tr-tr/knowledge/parting-grooving/pages/successful-chip-control.aspx

5. **URL 2-** http://web.hitit.edu.tr/dosyalar/materyaller/eminerdin@hititedutrl10520185B2_N4W5Y.pdf

6. **Hallberg, D. and Ringdahl, P. (2017),** “Study on A High Precision Drilling Tool with Focus on Power Source and Driveline”, M. Sc. Thesis, KTH Royal Inst. of Tech., Stockholm.

7. **URL 3-** https://www.kennametal.com/us/en/site-search.html?query=internal+coolant

8. **Johns, A.S., Hewso, R.W, Merson,E., Summers, J.L. and Thompson H.M. (2014)**, “Internal Twist Drill Coolant Channel Modelling Using Computational Fluid Dynamics”, 11th World Congress on Computational Mechanics, WCCM 2014, 20-25 Jul 2014, Barcelona, Spain.

9. **URL 4-** http://www.guvensanpetrol.com/uploads/KesmeSivilari.pdf

10. **URL 5-** https://www.pnomatikithalat.com/pnomatik-silindir/

11. **URL 6-** https://www.luetgert-antriebe.de/luetgert-neu-cn/produkte/taperlock-spannbuchsen/

12. **URL 7-** https://www.desouttertools.com/tools/7/solutions-for-drilling-applications-setitec/71/electric-advanced-drilling-units-evo

13. **URL8-** https://maker.robotistan.com

14. **URL9-** https://www.retmon.com

15. **URL10-** https://devreyakan.com

CHANGES ON SURFACE PROPERTIES OF METALS DUE TO BORON NITRIDE COATINGS

Tuğçe HACALOĞLU, *tugcehacaloglu@gmail.com* Atılım Üniversitesi, 06830, Ankara, Turkey

Asude AYDOĞAN, *asudeaydogan@gmail.com* Atılım Üniversitesi, 06830, Ankara, Turkey

Bilgin KAFTANOĞLU, *bilgin.kaftanoglu@atilim.edu.tr* Atılım Üniversitesi, 06830, Ankara, Turkey

ABSTRACT

Boron nitride (BN) coatings using a physical vapor deposition system with magnetron sputtering are applied on tools, dies and implants to change their surface properties. By changing the coating parameters, different BN allotropes can be produced with different properties. Properties of cubic boron nitride include high coating hardness, good wear resistance whereas the properties of hexagonal boron nitride include low friction coefficient and low hardness. The other allotropes show properties between these extremes. The characterization of the (BN) coatings is carried out to find the thickness, nanohardness, adherence properties using a scratch test, tribometer tests to find friction and wear properties.

Keywords: Coating, Boron Nitride, Magnetron Sputtering, Mechanical Characterization

ÖZET

Magnetron saçtırmalı fiziksel bir buhar biriktirme sistemi kullanan bor nitrür (BN) kaplamalar, yüzey özelliklerini değiştirmek için takımlara, kalıplara ve implantlara uygulanır. Kaplama parametreleri değiştirilerek farklı özelliklerde farklı BN allotropları elde edilir. Kübik bor nitrürün özellikleri arasında yüksek kaplama sertliği, iyi aşınma direnci bulunurken, heksagonal bor nitrürün özellikleri arasında düşük sürtünme katsayısı ve sertlik bulunur. Diğer allotroplar, bu iki allotrop arasında özellikler gösterir. BN kaplamaların karakterizasyonu, kalınlık, nano sertlik, kaplama yapışkanlığını ölçmek için çizik testi, sürtünme ve aşınma özelliklerini bulmak için tribometre testleri yapılarak elde edilir.

Keywords: Kaplama, Bor Nitrür, Magnetron Saçtırma, Mekanik Karakterizasyon

1. Introduction

Depositing thin films is a widely used method for developing surface properties of materials. Surface science has played a very important role and is a multidisciplinary activity intended to tailor the properties of the surfaces of engineering components. Boron (B) is a chemical element which is listed among the metalloid [Habashi, 2010] group in the periodic table. Since Turkey has the largest reserves of boron in the world, this study was initiated to use boron for high technology applications including coatings. Boron Nitride (BN) coating can be defined as a new generation coating which is not yet available at a commercial scale. Boron Nitride (BN) thin film coatings provide wide range of mechanical, optical, electrical, tribological and thermal features for many materials [Gocman et al., 2011]. BN coatings have also recently been found to have antibacterial, antifungal, and osteoblastic properties which are extremely important for medical devices such as implants and surgical equipment. These properties are also useful for the food industry. Depositing BN thin films with a physical vapor deposition (PVD) process can result in a coating containing different allotropes of BN. PVD coating technology has been used to coat different materials such as Ti-Cu-N and Ti-Ni-N for photothermal properties [Prekel et al. 2006].

There are many allotropes (polymorphs) of BN such as, h-BN, w-BN, r-BN, e-BN, t-BN, a-BN, and c-BN. BN is mostly found in two allotropes in the coatings: hexagonal BN (h-BN) and cubic BN (c-BN). c-BN is well known as a super hard material, almost as hard as diamond and h-BN is known as a soft lubricious material like graphite [Kumashiro, 2000]. Crystal structures of some of the allotropes are shown in Figure 1, illustrating that h-BN and r-BN are sp^2 bonded. On the other hand, c-BN and w-BN are sp^3 bonded [Taylor et al., 1997].

BN films have some important properties such as high hardness, wear resistance, low friction coefficient, electrical insulation, transparency with also anti-bacterial, antifungal, and osteoblastic characteristics. The surface of BN film is always covered with sp-bonded BN layers. Mechanical characterization of BN film requires the use of combination of several properties such as nanohardness, thickness, friction coefficient, adhesion (measured by scratch test) measurements. PVD method works at high vacuum conditions and at temperatures less than 3500°C, thereby not effecting the material properties of the substrate (cutting or forming tool). Since c-BN has high hardness and wear resistant properties, it is used for the coating of tools for forming and cutting applications [Ozel et al., 2011]. It provides a thinner coating where complex shapes and cutting edges can easily be deposited without effecting the tool geometry [Ozel et al., 2010]. Many materials are coated with different coating parameters to obtain different BN allotropes to yield different surface properties. Each BN film

obtained using different coating parameters such as coating energy, substrate voltage and temperature is tested for surface characterization and correlations are attempted between coating parameters and characteristics of the BN film. A PVD system for BN coating technology is developed and pilot experiments are conducted for cutting tools and mechanical parts. It is observed that lifetime is increased by a factor of up to four times [Cesur et al., 2009].

In the current research, the changes of surface properties of tools and dies as a result of BN coatings are investigated. Mechanical characterizations of the thin film BN coatings are performed to obtain nanohardness, thickness, adhesion friction and wear characteristics. Fourier Transform InfraRed spectroscopy (FTIR) has been used to find the crystal structure of the BN film. Since the coating is transparent, F20 thin film analyser system is used to measure the thickness using optical properties.

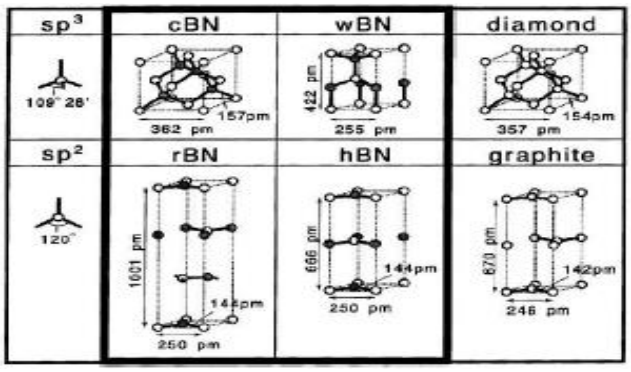


Figure 1 The Four BN Crystals.

2. Experimental Setups

PVD is a method of coating that works under high vacuum (Figure 2). During coating, material which is in the target plate evaporates in the vacuum chamber and intensifies onto the substrate surface. A single crystal growth h-BN target with dimensions of 100 x 250 mm is employed as a cathode. Substrates attached to a substrate holder are connected to a spindle mechanism which provides a planetary motion. The vacuum chamber is evacuated to a base pressure lower than 10^{-2} Torr using a mechanical pump. At this time, hot water is circulated around the system for the evaporation of water molecules in the environment. When vacuum reaches $3x10^{-3}$ Torr, the turbo molecular pump is started. After the vacuum chamber is evacuated to $2x10^{-5}$ Torr, system is filled with Ar gas and plasma cleaning is performed with 250 W RF for approximately 10 min. Then, system is filled with N_2 gas. The ratio of gases (Ar/N_2) is 5 to 1. The flow rate of the working gases is adjusted by controllers installed on the system panel. During the deposition, magnetron power applied to the target plate is increased

up to 900 W RF gradually and maintained at that value till the end of deposition. Substrate RF voltage is also used to control the crystal structure of the coating. Temperature is measured by a thermocouple which is attached to heaters and temperature is kept at 300°C. Holders are designed for each sample to place them properly in vacuum chamber, to attain homogenous coating. Samples deposited for up to six hours with substrate voltage (0-250V) with the magnetron power of 900W. Coatings are characterized by FTIR, thickness, nanohardness, adhesion, tribological tests. BN allotropes are obtained in varying proportions according to the coating parameters.



Figure 2 PVD – Magnetron Sputtering BN Coating System.

Before and after coating, the characterizations are made by the following devices:

- F20 Thin film thickness analyzer
- Scratch Revetest Tester
- Nanoindentation Tester (NHT)
- Standard Tribometer
- Fourier Transform Infrared Spectroscopy (FTIR)

3. Experiments and Characterization of BN Coatings

3.1. Thickness Measurements

The current research shows that BN films are transparent in visible and infrared light. Because of this property, optical techniques can be used. Thickness measurements are performed by F20 thin film analyser which is optical reflectance spectroscope (Figure 3). BN film thicknesses are measured between 20 nm - 4000 nm. Investigations of thickness measurements show that the substrate voltage significantly effects of thickness. Increase of the substrate bias voltage decreases the thickness of the coated film. A typical result is shown in Figure 4.

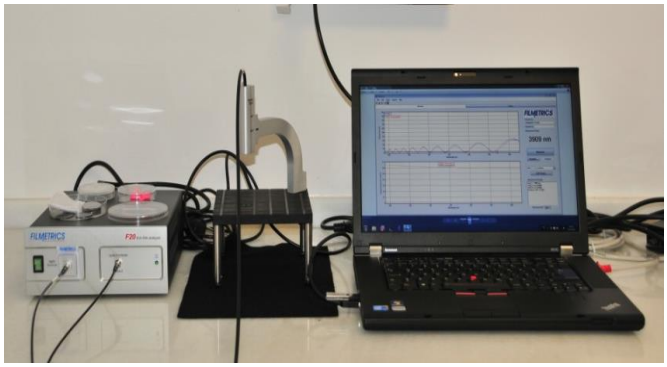


Figure 3 F20 Thin Film Analyzer.

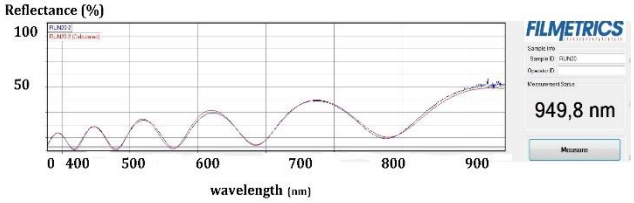


Figure 4 Wavelength vs Reflectance Graph.

3.2. Adhesion Measurements

Scratch tests are widely used to characterize adhesion failure of thin films which is illustrated in Figure 5. Loading is started at 0.5N and progressively increased to 150N. Rockwell diamond indenter type with a radius of 200µm is used. 3mm scratch is formed while indenter is moving at speed of 6mm/min and also acoustic emission (AE), penetration depth (Pd), residual depth (Rd), friction coefficient (µm) are calculated during the test. As shown in Figure 5, adhesion measurement is investigated by BN and TiN coated steel samples. The results showed that BN coating is better than TiN coating for surface adhesion since micro cracks are not formed as for TiN coatings along the scratch as seen in Figure 5.

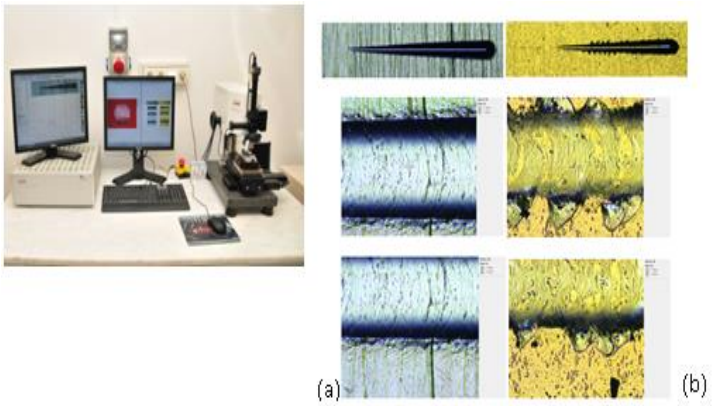


Figure 5 Scratch Revetest Tester and (a) BN Coating on Steel Sample and (b) TiN for Surface Adhesion.

3.3. Hardness Measurements

One of the surface properties is the hardness of the thin film. Hardness measurement of the coating is performed by a nanohardness testing device and Poisson's ratio and elastic modulus are calculated during the test (Figure 6). Hardness of sample is measured before and after the coating operation and results are compared. Depending on coating parameters, hardness of coating changes significantly. According to the observed results, substrate bias voltage plays an important role in hardness. Increasing the voltage can result in a harder coating. Furthermore, the resulting low hardness brings a high thickness. In Figure 6, the indentation mark is demonstrated. Normal force (Fn) - penetration depth (pd) graph is given in Figure 7.

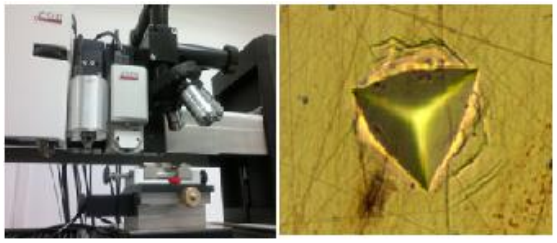


Figure 6 Nanohardness Test Device and Nanohardness Impression on Sample.

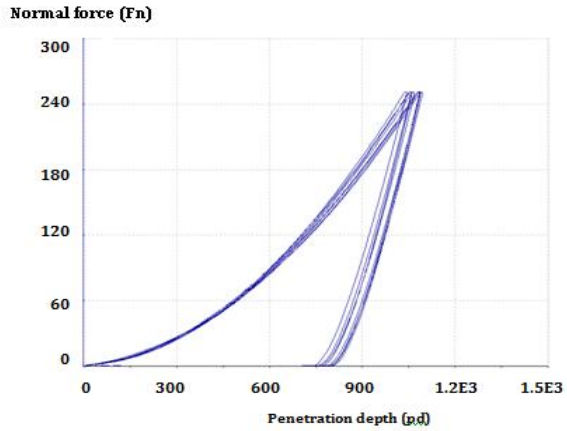


Figure 7 Penetration Depth- Normal Force Graph.

3.4. Friction Coefficient Measurement

Friction coefficients of coatings are measured by a tribometer device that is illustrated in Figure 8. Tests are carried out without lubrication in air environment at room temperature. A pin that is attached on the tribometer device is an alumina ball having a diameter of 6mm. Tests are performed under conditions of normal load of 1N, linear speed of 50mm/s for 50m distance. Radius of circle that is caused by alumina ball is 10 or 12,5mm.

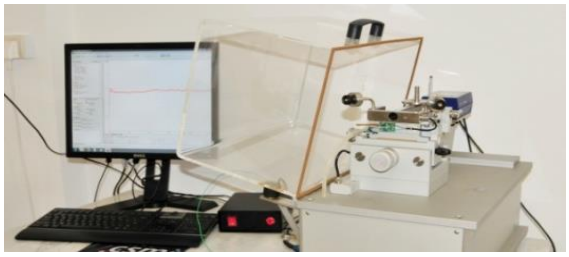


Figure 8 Tribometer Test Device.

Tribological behavior is measured according to tribometer test results. For uncoated AISI D2 steel, friction coefficient is 0.8. Friction coefficient of BN coated samples is between 0.2-0.5. The main parameter of the evaluation is thickness. Distance scale and time scale changes according to thickness. One of the results is shown in Figure 9. In this experiment 50V substrate bias voltage and %20 microwave energy is applied and the friction coefficient of this coating starts from 0.2 and increases to 0.8 as a result of wear. According to tribometer results, the applied coating parameters have been found to be a determining factor.

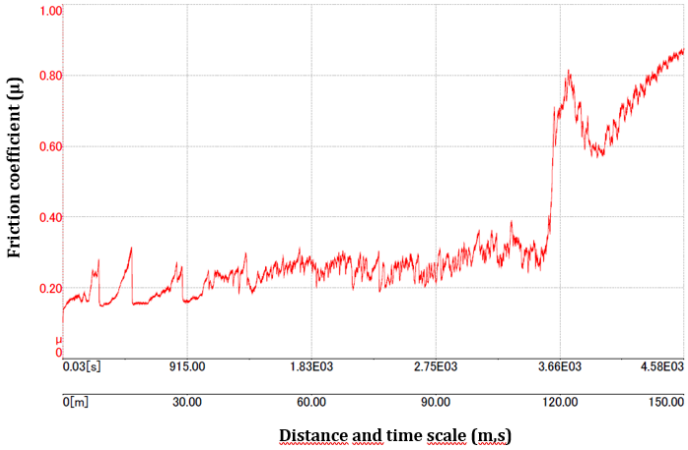


Figure 9 Result of Friction Coefficient Measurement.

3.5. Crystal structure analysis

FTIR measurements are used to examine the internal crystal structure of BN coatings as shown in Figure 10. FTIR is a non-destructive technique for solid and thin films used for quantitative analyses. FTIR spectra for BN thin film coatings are given in Table 1. Broad peak which can be seen in the Figure 10 around wavenumber 1300 cm^{-1} is analyzed by peak fitting method which can be assigned to c-BN. In the same spectra, the bands at about ~775 cm^{-1} which is characteristic of h-BN and at about ~995 cm^{-1} and ~1497 cm^{-1} accepted as a w-BN and a-BN, respectively.

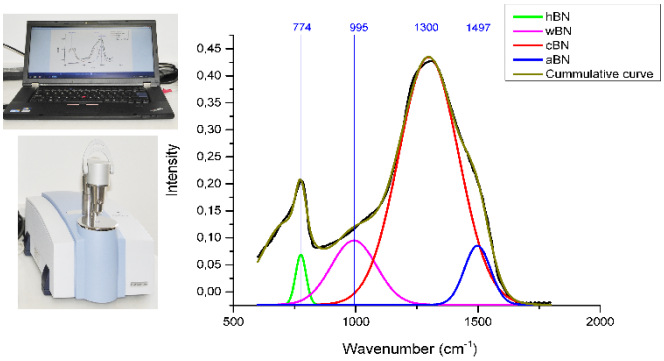


Figure 10 Fourier Transform Infra-Red (FTIR) System and Results of FTIR Measurements.

Table 1 IR Absorption Band of BN.

Phase of BN	*Wavenumber (cm^{-1})*
h-BN bending	760–800
h-BN stretching (TO)	1364-1400
h-BN stretching (LO)	1600
c-BN stretching (TO)	1055-1110
c-BN stretching (LO)	1300
a-B:N	1263-1350
a-B:N	1505-1550
w-BN (TO)	960,1090,1120,1230
w-BN (LO)	1150,1250
e-BN	1400-1450 (s)
	1650-1600,1100
	1020,930 (ms),
	800,1200 (vw)
r-BN	783,1367
r-BN	828,1610
t-BN	934.3,963.8,1331.8
t-BN	738,1032,1155

4. Correlations of Experimental Results of BN Coatings

Correlations are attempted between the coating parameters and coating properties. Figure 11 shows the correlation of nanohardness with substrate bias voltage. It is shown that, hardness increases with increasing substrate bias voltage.

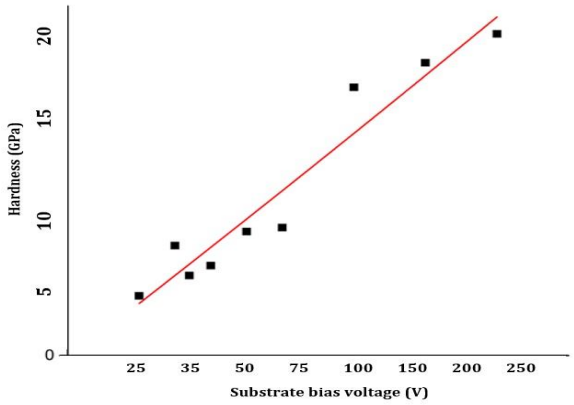


Figure 11 Substrate Bias Voltage and Hardness.

It is also observed that the BN coating thickness decreases as the substrate bias voltage increases as shown in Figure 12.

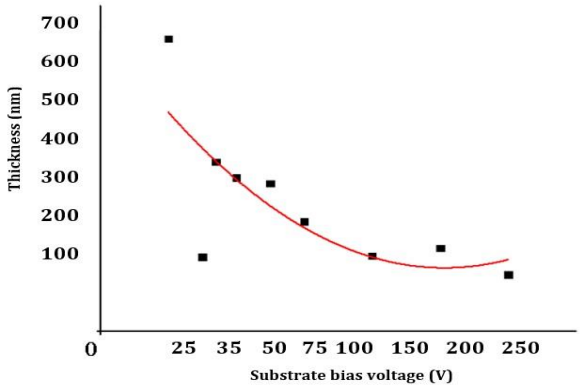


Figure 12 Substrate Bias Voltage vs. Thickness.

5. Discussion of Results

As a result of investigation of BN coatings using different coating parameters, it is observed that thickness decreases and nanohardness increases as substrate bias voltage increases. It is observed that BN coating has a higher adherence compared to TiN coating. Using a BN coating with high substrate voltage in one hour and continuing without substrate voltage for the remaining five hours provides a high performance for shearing dies used for press-hardened materials [Yilmaz et al., 2015]. This kind of composite coating with a high c-BN layer on metal surface topped by a softer h-BN dominated layer is responsible for the improved performance. Coating experiments on cutting tools and dies showed that their lifetime can be extended by a factor of up to about four times [Kaftanoglu et al., 2014]. Surface finish improved by using BN coated milling cutter [Cetin et al., 2015] in milling aluminum since the BN coating provided low friction and prevented the sticking of the chips to the tool. Due to the antibacterial, antifungal, and osteoblastic properties of BN coating, it is preferred for medical applications such as for titanium implants for dental and orthopaedical applications [Gokmenoglu et al.,

2016]. As shown in Figure 5, the adherence of BN coating on steel substrate is better than the TiN coating.

6. Conclusion

BN films are deposited using PVD-magnetron sputtering technique. Samples are characterized by FTIR for crystal structure. Film hardness measurements are carried out by nanohardness test device. Scratch test is performed for adhesion quality. The tribological test is carried out to find friction coefficient and wear. It is seen that BN coating provides a durable surface for cutting tools and dies extending the lifetime up to about four times. Correlations are obtained between coating parameters such as substrate bias voltage with coating properties such as thickness and hardness of the film. Concurrent research also shows that BN coatings can provide antibacterial, antifungal, and osteoblastic properties for implants and surgical equipment in the medical sector.

ACKNOWLEDGEMENT

This research was funded with the BAP Project at Atilim University. (ATU-BAP-A-1213-02). The authors would like to thank the Metal Forming Centre of Excellence (MFCE) and BOREN Centre of Competence for Boron Coating at Atilim University, for the support and the facilities used in the experiments.

REFERENCES

1. **Habashi, F. (2010),** 'Metals: typical and less typical, transition and inner transition', Foundations of Chemistry, Springer, pp.31-39.

2. **Gocman, K., Kałdoński, T., Mróz, W., Burdyńska, S., and Prokopiuk, A., (2011),** 'Structural and mechanical properties of boron nitride thin films deposited on steel substrates by pulsed laser deposition', Journal of KONES, Vol.18, pp.149-156.

3. **Prekel, H., Klopfstein, M. J., Giesselbach, M., Patzelt, S., Ghisleni, R., Lucca, D. A., and Stock, H. R., (2006),** 'Photothermal Investigation of Ti-Cu-N and Ti-Ni-N PVD Films', CIRP Annals-Manufacturing Technology, Vol. 55 No.1, pp.585-588.

4. **Kumashiro Y. (2000**), Electric refractory materials, CRC Press.

5. **Taylor II, C. A., and Clarke, R., (1997),** 'Growth kinetics of cubic boron nitride films and composites', in Diamond Based Composites, Springer, Netherlands, pp. 63-113.

6. **Ozel, T., Thepsonthi, T., Ulutan, D., and Kaftanoglu, B., (2011),** 'Experiments and finite element simulations on micro-milling of Ti–6Al–4V alloy with uncoated and cBN coated micro-tools', CIRP Annals-Manufacturing Technology, Vol. 60 No.1, pp.85-88.

7. **Ozel, T., Sima, M., Srivastava, A. K., and Kaftanoglu, B., (2010),** 'Investigations on the effects of multi-layered coated inserts in machining Ti–6Al–4V alloy with experiments and finite element simulations', CIRP Annals-Manufacturing Technology, Vol.59 No.1, pp.77-82.

8. **Cesur H. and Kaftanoglu B., (2009),** 'An Experimental Study about CBN Formation for Cutting Tools', 5th International Conference and Exhibition on Design and Production of Machines and Dies/Molds, Kusadasi, Turkey, pp.257-261.

9. **Cesur H. and Kaftanoglu B., (2009),** 'Machining Performance of CBN Coated Cutting Tools for Die/Mold Applications', 5th International Conference and Exhibition on Design and Production of Machines and Dies/Molds, Kusadasi, Turkey, pp.263-267.

10. **Yilmaz, I., Kaftanoglu, B., Hacaloglu, T., and Kilickan, M., (2015),** 'Integration of Press Hardening with Cold Trimming', 5 ICAFT /22 SFU 2015, Chemnitz, Germany, pp.105-118.

11. **Kaftanoglu, B., and Dokmetas, N., (2014),** 'An environmentally friendly method of cutting and forming of materials by boron nitride coated tools', International Journal of Sustainable Manufacturing 10, Vol.3 No.2, pp.143-155.

12. **Cetin, B., Kiricioglu O., Koseoglu E., Dokmetas N., Hacaloglu T., Kilickan M., and Kaftanoglu B., (2015),** 'Tool Life Improvement of End Mill Cutters with BN Coating by PVD Method', 8th International Conference and Exhibition on Design and Production of Machines and Dies/Molds, Kusadasi, Turkey, pp.211-216.

13. **Gokmenoglu, C., Ozmeric, N., Cakal, G., Dokmetas, N., Ergene, C., and Kaftanoglu, B., (2016),** 'Coating of titanium implants with boron nitride by RF-magnetron sputtering', Bulletin of Materials Science, Vol.39 No.5, pp.1363-1370.

INFLUENCE OF PUNCH PROPERTIES ON CONTACT MECHANICS OF COATED SUBSTRATES

Mehmet N. BALCI, *mehmetbalci@hacettepe.edu.tr* Hacettepe University, 06800, Ankara, Turkey

ABSTRACT

The contact mechanics between a deformable elastic punch and a coated half-plane substrate model is examined. The half-plane substrate is made of Ti6Al4V metallic alloy and coating is the ceramics named as ZrO_2. Ti6Al4V/ZrO_2 coating substrate model is in contact between a deformable punch made of Si_3N_4. The displacement and stress expressions are derived based on theory of elasticity and the equilibrium equation. Boundary and interface continuity conditions are determined. To obtain contact and subsurface stresses, finite element method is utilized. The accuracy of the developed computational solution is tested by employing mesh independence study. Then, parametric analyses are carried out to reveal elastic punch properties, coefficient of friction and thickness of the coating on stress distributions. It is demonstrated that punch modulus has a profound impact on results, hence designing of punch material is critical to avoid surface related damages.

Keywords: Contact mechanics, Elastic coating, Deformable punch, Coefficient of friction, Finite Element Method.

1. INTRODUCTION

Protective coatings are widely used in tribological applications since they are sensible option to keep the substrate material from harsh environmental surface conditions. Material scientists continue on studying new material designs involving coatings to meet the increased demand in materials of today's world. The use of ceramics coating on metallic substrate provides improved surface properties such as high stiffness, strength, fatigue life, resistance to wear and corrosion. Hence, the machine life can be prolonged due to the successful applications of coatings. Several type of coatings with their manufacturing methods were explained in Hogmark [1]. The most common coating materials are oxides, nitrides and carbides such as Al_2O_3, ZrO_2, SiC, BN, TiN, TiB_2 [2]. Since failures generally arise from surface related damages, contact stress behavior of coated structures are crucial in design of such components.

Johnson [3] provided some benchmark solutions to the variety of contact problems. Gladwell [4] and Hills et al. [5] studied the contact problems of homogenous materials. Chen [6] adopted

analytical method to find exact stresses and displacements in a linear elastic half-plane consisting of one or two layers bonded to another homogenous half-plane. Chen and Engel [7] analytically obtained stresses in multilayered media under the effect of impact and contact load. Contact stresses in a layered transversely isotropic half-plane were examined by Kuo and Keer [8]. Guler [9] provided analytical formulation for the contact mechanics problem between two deformable solids. Guler and Erdogan [10] solved the contact problem between two deformable bodies involving coatings made of functionally graded material (FGM). Apart from analytical studies, Komvopoulos [11] used finite element method to solve the contact problem between a layered elastic solid subjected to normal contact with a rigid surface. Kral and Komvopoulos [12] obtained the surface deformation and surface stresses in an elastic-plastic layered medium exposed to sliding contact conditions based on three dimensional finite element method. Lovell [13], Morrow and Lovell [14] developed a method based on finite element analysis to find stress and deformation in coated structures. Hence, finite element method seems powerful tool in the solution of different type of contact problems. It was reported that the main failure mechanism appearing in homogenous coatings was the delamination and subsequent spallation at the coating-substrate interface [9]. Hence, subsurface stress distributions should be computed during the design stage. Thorough search in the literature showed that there has been very limited study related to the contact mechanics between deformable punch and metallic substrate with ceramics coating, and influence of punch properties on contact mechanics of such problems have not been explicitly presented yet. Hence, in this study, contact and subsurface stresses are computed within the coating/substrate system for various punch properties using finite element method.

2. PROBLEM DESCRIPTION

Ti6Al4V is an attractive material due to its low density, good corrosion resistance and high relative strength, and this alloy is widely used in aerospace and biomaterial applications [15-16]. However, working temperature is generally below 500 $^{\circ}C$ and resistance to frictional wear is poor [17]. ZrO_2 ceramics can be applied as a coating to keep this alloy form harsh surface conditions. The schematics of the contact problem between a deformable punch made of Si_3N_4 and the ZrO_2/Ti6Al4V coating/substrate system is depicted in Figure 1. The homogenous elastic coating is perfectly bonded to the elastic substrate, and thickness of the coating is shown by h. Points a and b respectively denote trailing and leading ends of the contact, and p_h is the height of the deformable punch. Contact length between the coating and the deformable punch is $(b-a)$, and deformable punch stands at a distance e away from the coordinate axis. Deformable punch is pressed against the coating by a force P and lateral force Q is developed due to the friction between punch and the coating surface. The lateral

force is applied to the deformable punch at its trailing edge. E_S, ν_S show the elastic modulus and the Poisson's ratio of the metallic substrate, E_C, ν_C indicate the elastic modulus and the Poisson's ratio of the ceramics coating and E_P, ν_P express the elastic modulus and the Poisson's ratio of the deformable punch.

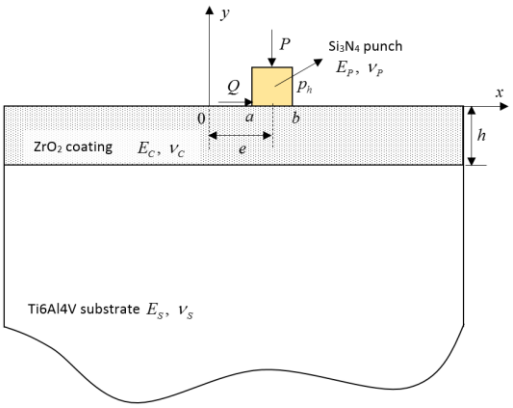


Figure 1. Schematics of the frictional contact problem between Ti6Al4V/ ZrO_2 system and deformable silicon nitride (Si_3N_4) punch.

Since punch is deformable, stress field in the homogenous ceramic coating and metallic substrate and the punch can be written as follows:

$$\sigma_{XX}{}^{i} = \frac{\mu_i}{\kappa_i - 1}\left((\kappa_i + 1)\frac{\partial u_i}{\partial x} + (3 - \kappa_i)\frac{\partial v_i}{\partial y} \right), \quad i = C, S, P, \tag{1}$$

$$\sigma_{YY}{}^{i} = \frac{\mu_i}{\kappa_i - 1}\left((3 - \kappa_i)\frac{\partial u_i}{\partial x} + (\kappa_i + 1)\frac{\partial v_i}{\partial y} \right), \quad i = C, S, P, \tag{2}$$

$$\sigma_{XY}{}^{i} = \mu_i\left(\frac{\partial u_i}{\partial y} + \frac{\partial v_i}{\partial x} \right), \quad i = C, S, P, \tag{3}$$

$$y = \begin{cases} -h < y < 0, & i = C \\ y < -h, & i = S \\ 0 < y < p_h, & i = P \end{cases} \tag{4}$$

In a two-dimensional (2D) case, the equilibrium equations can be written as follows:

$$\frac{\partial (\sigma_{xx})^{i}}{\partial x} + \frac{\partial (\sigma_{xy})^{i}}{\partial y} = 0, \quad i = C, S, P, \tag{5}$$

$$\frac{\partial (\sigma_{xy})^{i}}{\partial x} + \frac{\partial (\sigma_{yy})^{i}}{\partial y} = 0, \quad i = C, S, P. \tag{6}$$

Where subscripts and superscripts C, S and P are used to identify coating, substrate and the punch, respectively. When stresses provided in Eqs. (1)-(3) are substituted into Eqs. (5)-(6), the following Partial Differential Equation (PDE) system is obtained:

$$\left(\frac{\kappa_i+1}{\kappa_i-1}\right)\frac{\partial^2 u_i}{\partial x^2}+\frac{2}{\kappa_i-1}\frac{\partial^2 v_i}{\partial x\partial y}+\frac{\partial^2 u_i}{\partial y^2}=0, \quad i=C,S,P, \tag{7}$$

$$\frac{\partial^2 v_i}{\partial x^2}+\frac{2}{\kappa_i-1}\frac{\partial^2 u_i}{\partial x\partial y}+\frac{\kappa_i+1}{\kappa_i-1}\frac{\partial^2 v_i}{\partial y^2}=0, \quad i=C,S,P, \tag{8}$$

In order to solve the given PDE system, the interface and boundary conditions should be determined. Horizontal and vertical displacements should be equal at the interface, which reads:

$$u_C\left(x,-h\right)=u_S\left(x,-h\right), \quad -\infty<x<\infty, \tag{9}$$

$$u_C\left(x,-h\right)=u_S\left(x,-h\right), \quad -\infty<x<\infty, \tag{10}$$

Normal and shear stresses should be equal at the interface, which requires:

$$\sigma_{YY}{}^{C}\left(x,-h\right)=\sigma_{YY}{}^{S}\left(x,-h\right), \quad -\infty<x<\infty, \tag{11}$$

$$\sigma_{XY}{}^{C}\left(x,-h\right)=\sigma_{XY}{}^{S}\left(x,-h\right), \quad -\infty<x<\infty. \tag{12}$$

The free surfaces apart from the contact zone are stress free. Hence, following conditions are valid.

$$\sigma_{YY}{}^{C}\left(x,0\right)=\sigma_{XY}{}^{S}\left(x,0\right)=0, \quad -\infty<x<a, \tag{13}$$

$$\sigma_{YY}{}^{C}\left(x,0\right)=\sigma_{XY}{}^{S}\left(x,0\right)=0, \quad b<x<\infty, \tag{14}$$

$$\int_a^b \sigma_{YY}{}^{P}\left(x,p_h\right)dx=-P, \quad a<x<b, \tag{15}$$

$$Q=\eta P, \quad x=a, \quad y=0. \tag{16}$$

In addition to these conditions, the solution should satisfy the regularity condition. This condition means that all the field quantities should vanish at far field boundaries, i.e. $\sqrt{x^2+y^2}\to\infty$. In order to solve the PDE system under prescribed boundary and interface conditions, analytical methods such as Fourier transform and a singular integral equation (SIE) technique can be used. However, derivation of the analytical formulation and getting the solution is very hard and time consuming. Hence, the addressed contact problem is solved by

means of finite element method. The applied finite element procedure is explained in the next chapter.

3. FINITE ELEMENT MODEL AND THE SOLUTION

Since contact problem involves two elastic deformable bodies, derivation of the analytical formulation and its solution is very hard and time consuming. Instead, computational approach based on finite element methods is adopted. The finite element analyses are carried out using general purpose finite element software ANSYS [18]. The finite element model for the contact problem between the coating and deformable punch is depicted in Figure 2(a). The solution domain is discretized by 6-noded quadrilateral triangular elements called as PLANE183. As illustrated in Figure 2(b), the 6-noded triangle version of the quadrilateral element is formed by merging the three nodes of the quadrilateral element at a single point. In the contact zone, contact line elements are utilized to discretize the contact surface. This discretization is performed by using CONTA172 and TARGE169 elements. Each CONTA172 element has three nodes, as shown in Figure 2(b). As shown in Figure 2(a) L_w, L_h and h denote substrate length, substrate height and coating thickness, respectively. In order to model the half-plane geometry and minimize the dimensional effects on results, punch width is kept small when compared to substrate dimensions. Hence, $(b-a)/L_w = 1/40$ and $(b-a)/L_h = 1/20$. Coating thickness is adjusted such as $(b-a)/h = 2,\ 1,\ 0.\overline{6},\ 0.5$ and 0.4 to observe the influence of this parameter on stress results.

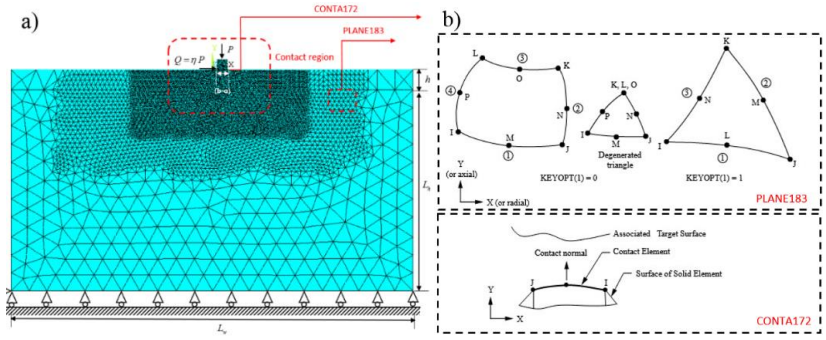


Figure 2. (a) Finite element model for the contact problem, (b) (a) PLANE183 and CONTA172 elements available in ANSYS [18].

Moreover, the mesh density is increased around the contact region to capture the sharp variations of the stress components due to the flat punch contact.

4. NUMERICAL RESULTS

Material properties of Ti6Al4V, ZrO_2 and Si_3N_4 are provided in Table 1. The punch material is assumed to be silicon nitride (Si_3N_4) since this material is widely used in tribological applications [19-20]. Poisson's ratio ν for the substrate, coating and the punch is assumed as

0.30 in all the simulations [21]. Contact stress and subsurface stress results are presented for various values of elastic punch properties, coefficient of friction and coating thickness. Contact and subsurface stress distributions are normalized using the averaging normal stress which reads:

$$\sigma_0 = P/(b-a), \tag{17}$$

Horizontal axis x is normalized using the parameter $(2x-(b+a))/(b-a)$, where $x=a$ shows '-1' (the trailing end) and $x=b$ indicates '1' (the leading end) of the contact as provided in Dag and Erdogan [22]. Subsurface stress is presented towards to thickness of the coating and the medium. Hence, the vertical axis- y is normalized using a new parameter as follows:

$$r = (y/h) - 1. \tag{18}$$

Table 1. Elastic modulus of materials used in simulations [21, 23].

Property	**Ti6Al4V**	**ZrO_2**	**Si_3N_4**
Elastic modulus [GPa]	66.2	117	320

The parameter r starts from -1 and ends at 1 where $r=-1$ points the contact surface, $r=0$ indicates the coating and substrate interface, and $r=1$ indicates the interior point $y=-2h$.

4.1. Mesh independence study

In order to observe the accuracy of the results, a convergence analysis is performed, where contact mechanics analyses are performed for four different finite element models with different element numbers. These four models and related total number of finite elements are given in Table 2. Subsurface contact stress results pertaining to this convergence study are displayed in Figures 3(a)-(b) where the former one shows the subsurface normal stress and the latter one indicates the subsurface shear stress. As can be inferred from the figures, normal and shear subsurface stresses are very close to each other, which implies developed computational procedures provide convergent stress results. Detailed numerical comparison between stresses obtained for Model #1, Model #2, Model #3 and Model #4 is performed. Since Model #4 involves highest number of elements, results of this model are assumed as the most accurate and it is used as a reference model in percent difference calculations.

Table 2. Models consisting of different number of elements.

Model no	**Elements in total**
#1	12066
#2	34388
#3	42506
#4	84278

Tables 3 and 4 display the comparison study for subsurface normal and shear stresses, respectively. $\sigma_{XX}{}^{S}$ and $\sigma_{XY}{}^{S}$ show the subsurface normal and shear stresses through the thickness of the coated substrate. The superscript *'s'* implies subsurface stress and subscripts *1,2,3* and *4* stand for the model number. $\varepsilon_i\%$ shows the percent difference between stress of that model and the reference model (Model#4). When subsurface normal stress provided in Table 3 is examined, highest level of difference is observed for Model #1 which includes least number of elements. Generally, the percent difference values are gradually getting smaller for Model#2 and then Model#3. The same trend is observed for the subsurface shear stress given in Table 4. Further increase in the number of elements from Model#3 to Model#4 does not provide significant level of accuracy in stress values but it results in remarkable increase in computational time. Hence, computation and the parametric analyses are proceeded with the Model#3 consisting of 42506 elements.

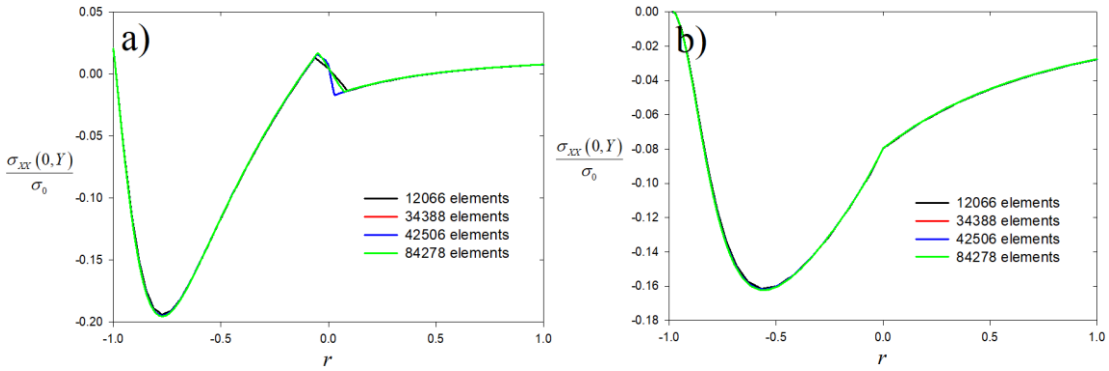


Figure 3. (a) Subsurface lateral, (b) Subsurface shear stress distribution using different number of finite elements for the contact problem between Ti6Al4V/ZrO_2 and Si_3N_4 punch, $\eta = 0.1$, $(b-a)/h = 0.5,\ e/h = 0.5.$

Table 3. Relative difference between subsurface normal stress results based on reference model.

r	$\left(\frac{\sigma_{XX}{}^{S}}{\sigma_0}\right)_1$	$\varepsilon_1\%$	$\left(\frac{\sigma_{XX}{}^{S}}{\sigma_0}\right)_2$	$\varepsilon_2\%$	$\left(\frac{\sigma_{XX}{}^{S}}{\sigma_0}\right)_3$	$\varepsilon_3\%$	$\left(\frac{\sigma_{XX}{}^{S}}{\sigma_0}\right)_4$
-0.9	-0.1295	**2.5515**	-0.1323	**0.4372**	-0.1324	**0.4195**	-0.1329
-0.7	-0.1839	**0.5769**	-0.1845	**0.2905**	-0.1844	**0.2937**	-0.1850
-0.5	-0.1165	**0.4465**	-0.1158	**0.1357**	-0.1158	**0.1458**	-0.1160
-0.3	-0.0497	**1.5626**	-0.0492	**0.6409**	-0.0492	**0.6313**	-0.0489
-0.1	0.0046	**15.3943**	0.0050	**6.8416**	0.0050	**6.8004**	0.0054
0.1	-0.0131	**3.0994**	-0.0128	**1.1951**	-0.0128	**1.1905**	-0.0127
0.3	-0.0047	**7.0382**	-0.0045	**2.3190**	-0.0045	**2.3163**	-0.0044
0.5	0.0008	**16.9166**	0.0009	**3.3615**	0.0009	**3.3678**	0.0009
0.7	0.0044	**3.0067**	0.0044	**1.6143**	0.0044	**1.6170**	0.0045
0.9	0.0068	**1.0590**	0.0068	**0.4338**	0.0068	**0.4338**	0.0069

Table 4. Relative difference between subsurface shear stress results based on reference model.

r	$\left(\frac{\sigma_{XY}}{\sigma_0}^{S}\right)_1$	ε_1 %	$\left(\frac{\sigma_{XY}}{\sigma_0}^{S}\right)_2$	ε_2 %	$\left(\frac{\sigma_{XY}}{\sigma_0}^{S}\right)_3$	ε_3 %	$\left(\frac{\sigma_{XY}}{\sigma_0}^{S}\right)_4$
-0.9	-0.0347	**3.4066**	-0.0357	**0.4368**	-0.0358	**0.3991**	-0.0359
-0.7	-0.1438	**1.5329**	-0.1456	**0.3270**	-0.1456	**0.3189**	-0.1461
-0.5	-0.1602	**0.1489**	-0.1601	**0.2307**	-0.1601	**0.2307**	-0.1604
-0.3	-0.1380	**0.0396**	-0.1379	**0.0009**	-0.1379	**0.0034**	-0.1379
-0.1	-0.1027	**0.0183**	-0.1025	**0.1237**	-0.1025	**0.1294**	-0.1027
0.1	-0.0708	**0.2670**	-0.0706	**0.0868**	-0.0706	**0.0952**	-0.0706
0.3	-0.0562	**0.7967**	-0.0560	**0.3182**	-0.0560	**0.3150**	-0.0558
0.5	-0.0452	**0.4123**	-0.0450	**0.0217**	-0.0450	**0.0190**	-0.0450
0.7	-0.0367	**0.2954**	-0.0367	**0.1506**	-0.0367	**0.1474**	-0.0366
0.9	-0.0304	**0.5443**	-0.0303	**0.2660**	-0.0303	**0.2640**	-0.0302

4.1. Contact stress result

In this section, contact and subsurface stress results are presented for various values of elastic modulus of the deformable punch E_P, coefficient of friction η and thickness of the coating h. Since punch is flat, contact stresses around punch ends tend to be quite high and these high stresses should be controlled to avoid any surface related damages such as surface cracking or propagating of the previously occurred cracks. Figure 4 illustrates the normalized normal stress contours around the contact region for various values of E_P/E_C ratio for the ZrO_2 coated Ti6Al4V substrate system in frictionless case.

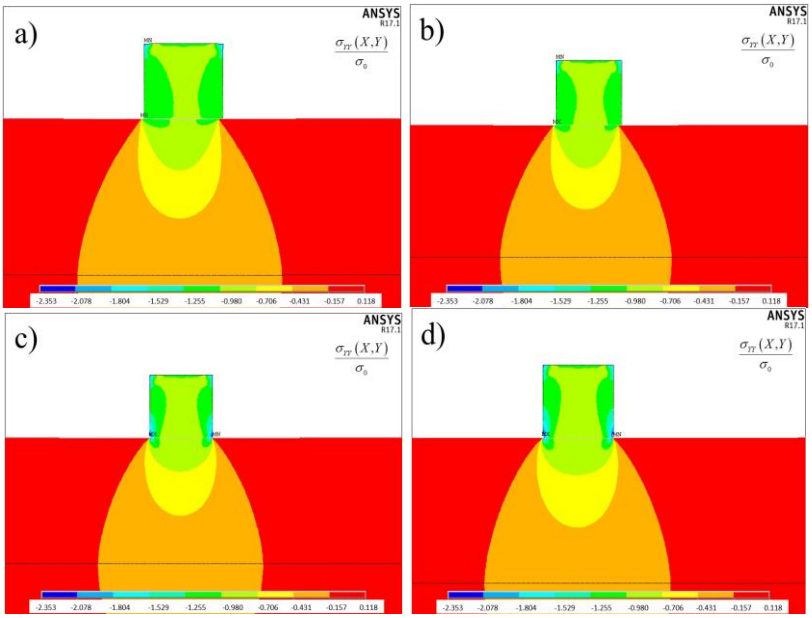


Figure 4. Contour plots of the normal stress around the contact region between Ti6Al4V/ZrO_2 and elastic punch with different elastic modulus; (a) $E_P/E_C = 1/10$, $E_P/E_C = 1/5$, $E_P/E_C = 5$, $E_P/E_C = 10$, $\eta = 0.0$, $(b-a)/h = 0.5$, $e/h = 0.5$.

When $E_P/E_C<1$, the stiffness of the punch is less than that of coating and if $E_P/E_C>1$, the stiffness of the punch is greater than that of coating. As E_P/E_C is increased from 1/5 to 10, normal stress within the deformable punch increases and this stress reaches a considerable level at punch edges as seen in Figure 4(c)-(d). When Figures 4(a)-(b) and Figures 4(c)-(d) are compared, normal stress contour shown by green expanded regions on the contact surface tends to be shrink around the contact ends, which implies the severity of the stress at punch ends as stiffness of the punch is increased. Figure 5 displays the contours of shear stress for various values of the coefficient of friction.

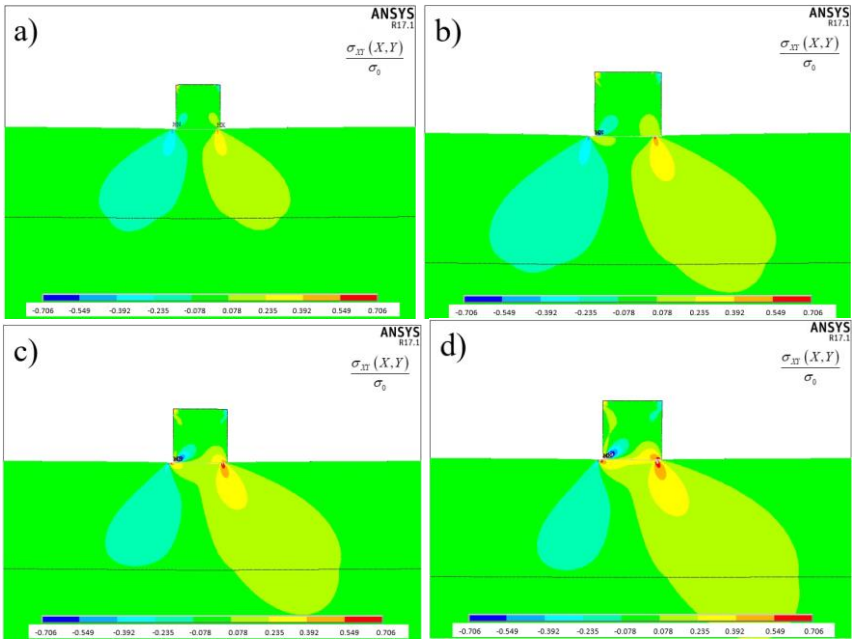


Figure 5. Contour plots of the shear stress around the contact region between Ti6Al4V/ZrO_2 and Si_3N_4 punch; (a) $\eta=0.0$, (b) $\eta=0.1$, (c) $\eta=0.3$, (d) $\eta=0.4$, $(b-a)/h=0.5$, $e/h=0.5$.

In this case, the punch material is Si_3N_4 and contacting body is ZrO_2 coated Ti6Al4V substrate. In all cases, there is a negative shear stress around the trailing edge of the punch $x=a$, whereas shear stress around the leading edge of the punch $x=b$ is positive. As coefficient of friction is increased, shear stress increases and disperses within the deformable punch and this can be seen in Figures 5(a)-(d). When the coating is examined, increase in the coefficient of friction leads to considerable increase in the positive shear stress observed around the leading end of the contact, resulting in expansion of positive shear stress region. While negative shear stress around the trailing edge of the punch increases considerably, this negative shear stress around the trailing end of the contact slightly decreases, hence this region slightly shrinks within the coating medium. Figure 6(a)-(b) show normal and lateral contact stresses for various values of the punch elastic modulus in frictionless case. As the ratio E_P/E_C is increased, normal stress in the middle of contact decreases from high

compressive values, and normal stress around contact ends tend to be asymptotic. If punch is rigid, stresses are singular. The same behavior is observed for the lateral contact stress in $\left(2x-\left(b-a\right)\right)/\left(b+a\right)\in\left[-1,1\right]$. However, there is no remarkable change in the lateral contact stress outside the contact region as inferred from Figure 6(b). Figures 6(c)-(d) show the subsurface normal and shear stresses. Increase in the elastic modulus of the punch does not change stresses significantly. There is a slight increase in these stresses between $r\in\left[-1,-0.5\right]$.

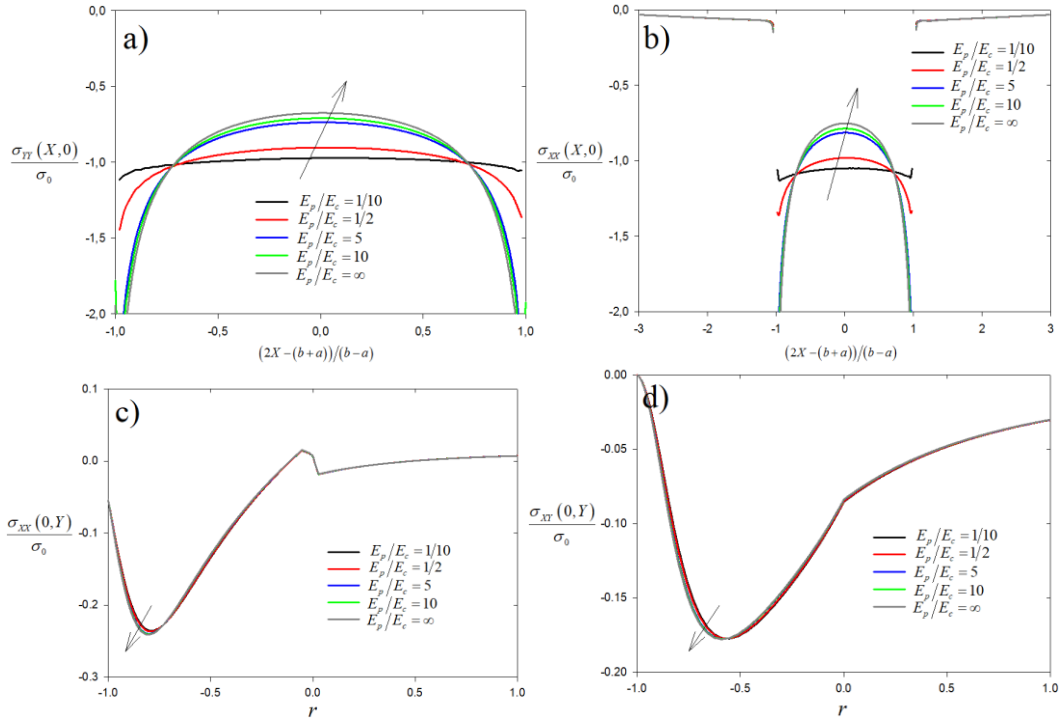


Figure 6. The influence of punch elastic modulus on stress distributions; (a) Normal contact stress, (b) Lateral contact stress, (c) Subsurface lateral stress, (d) Subsurface shear stress, $\eta=0.0,\ \left(b-a\right)/h=0.5,\ e/h=0.5.$

Figure 7 demonstrates the contact and subsurface stresses in frictional case where $\eta=0.3.$ When the punch is less stiff, normal contact stress slants towards the trailing end of the contact as shown in Figure 7(a). As E_P/E_C is increased, normal stress increases compressively around trailing end and normal stress exhibits a curly distribution. The similar trend is observed for the lateral contact stress in the contact region where $\left(2x-\left(b-a\right)\right)/\left(b+a\right)\in\left[-1,1\right]$. When subsurface stresses are examined, there is almost no change apart from the slight increase around $r\in\left[-1,-0.5\right]$. The influence of coefficient of friction on contact and subsurface stress distributions is examined in Figure 8. In this case, punch material is Si_3N_4 and contacting material is ZrO_2/Ti6Al4V coating substrate system. As coefficient of friction is increased, the

lateral force applied at the trailing edge of the deformable punch is increased and normal stress within the contact region decreases especially around $\left(2x-\left(b-a\right)\right)/\left(b+a\right)\in\left[-1,0\right]$, as shown in Figure 8(a). Hence slanted curves for normal stress are obtained. Figure 8(b) indicates the lateral contact stress for various values of coefficient of friction. As coefficient of friction is increased, lateral stress in the contact region decreases and stress curves slightly slants towards trailing end. Increase in the coefficient of friction leads to increase in the magnitude of lateral stress ahead of the contact and it results in increase in tensile lateral stress behind the contact.

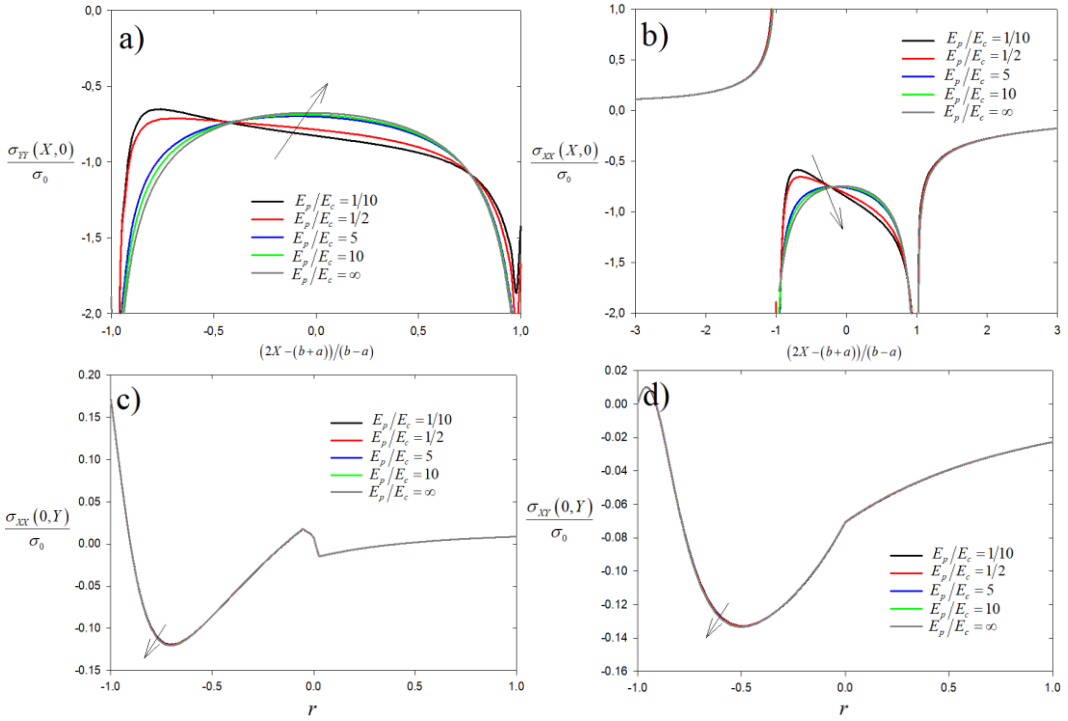


Figure 7. The influence of punch elastic modulus on stress distributions; (a) Normal contact stress, (b) Lateral contact stress, (c) Subsurface lateral stress, (d) Subsurface shear stress, $\eta=0.3,\ \left(b-a\right)/h=0.5,\ e/h=0.5.$

This tensile stress can reach critical levels for greater values of coefficient of friction and it can be responsible for possible surface related damages such as surface cracking or propagation of previously existing cracks. Hence, this tensile lateral stress should be taken into account to avoid surface related damages. Figure 8(c)-(d) respectively show the normal and shear stresses towards the thickness for different coefficient of friction values. When coefficient of friction is increased, normal and shear stress decrease in the region $r\in\left[-1,0\right]$. The similar behavior is observed in the studies conducted by Apatay et al. [24], Balci et al. [25] where punch material was assumed as rigid. The point $r=0$ indicates the interface between the coating and the substrate. While going away from the contact, influence of coefficient of friction on subsurface stresses tends to diminish.

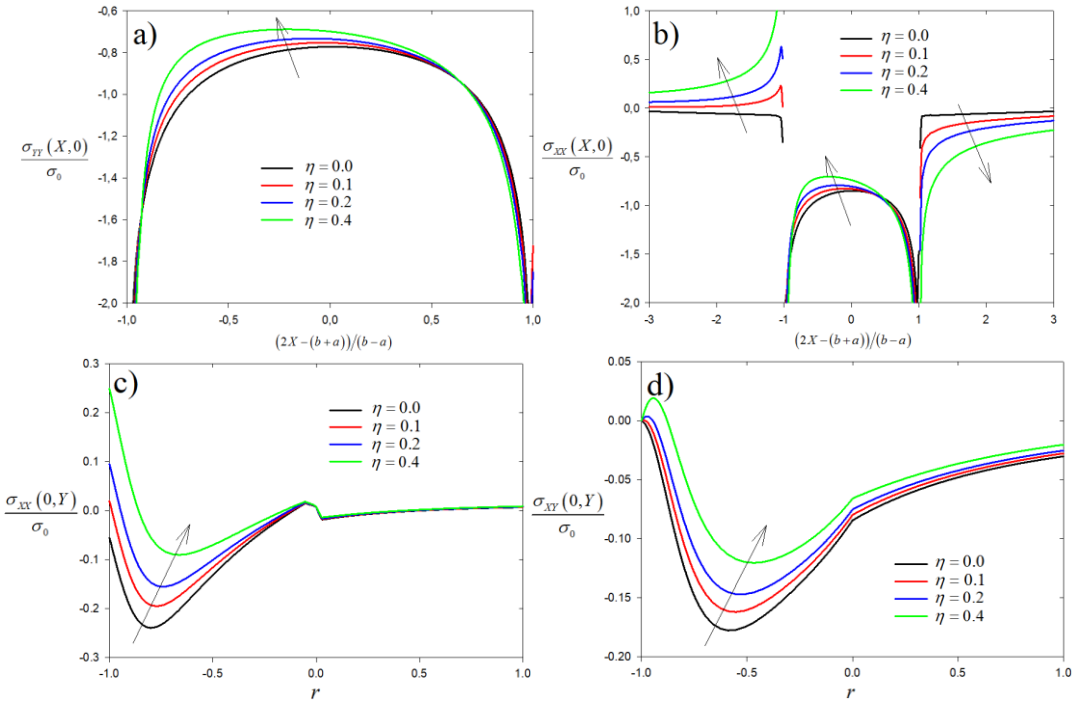


Figure 8. The influence of punch elastic modulus on stress distributions; (a) Normal contact stress, (b) Lateral contact stress, (c) Subsurface lateral stress, (d) Subsurface shear stress,

$$E_P/E_C = 2.735,\ (b-a)/h = 0.5,\ \ e/h = 0.5.$$

Figure 9 illustrates the contact and subsurface stress distributions for various values of the coating thickness in frictionless case. Punch material is Si_3N_4 and contacting material is ZrO_2/Ti6Al4V. In simulations, punch width is kept constant and coating thickness value (h) is changed parametrically. Thus, when coating thickness is increased, the ratio $(b-a)/h$ is decreased. As coating thickness is increased, normal contact stress is slightly increased as can be observed in Figure 9(a). As shown in Figure 9(b), the lateral contact stress outside the contact region decreases from slight tensile levels and lateral stress in the contact region also decreases in the case of higher thickness of the coating. Subsurface normal and shear stresses through the thickness are depicted in Figure 9(c)-(d). As coating thickness is increased, subsurface stresses tend to be gradually higher in the close vicinity of the contact zone and it decreases in a more sharp way, which implies the utilization of thin coatings may be beneficial to alleviate the sharp stress gradients within the coating material. On the other hand, if the coating is relatively thin, it may suffer from the normal stress discontinuity at the interface as shown by black solid line in Figure 9(c).

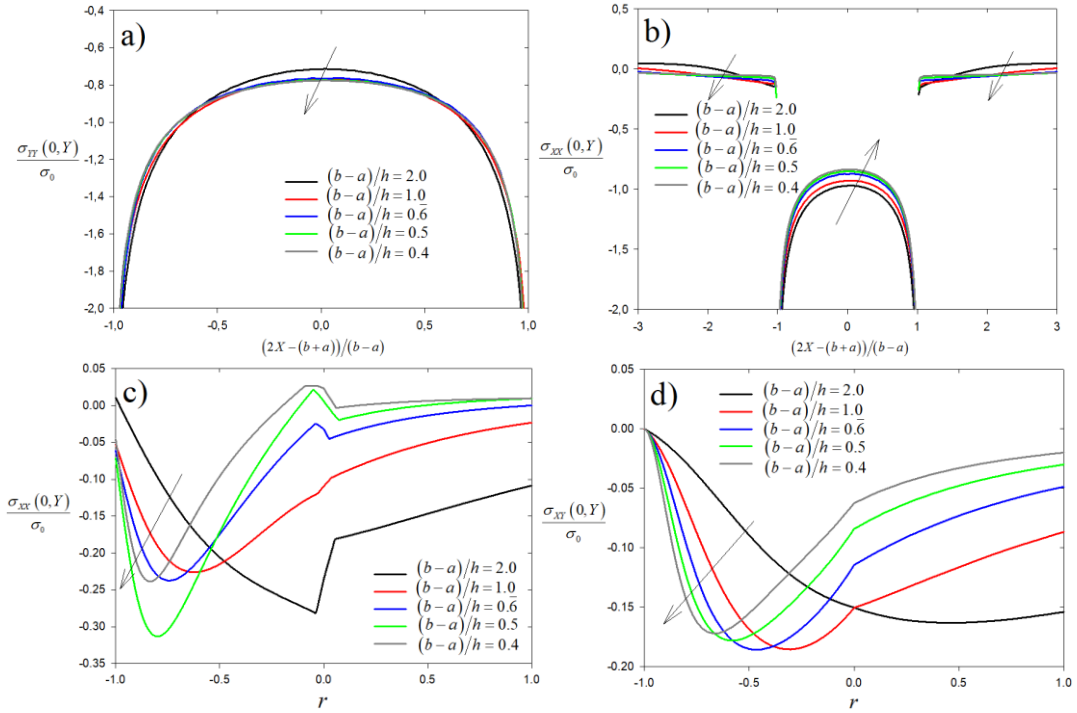


Figure 9. The influence of punch elastic modulus on stress distributions; (a) Normal contact stress, (b) Lateral contact stress, (c) Subsurface lateral stress, (d) Subsurface shear stress,

$$E_P/E_C = 2.735,\ \eta = 0.3,\ (b-a)/e = 2.$$

5. CONCLUSION

This study examines the effect of punch stiffness, coefficient of friction and thickness of the coating on contact and subsurface stresses. The following conclusions can be drawn from this research:

- Increase in the elastic modulus of the punch results in a formation of greater normal stress within the deformable punch and severity of normal stress is enhanced around punch edges. If punch is assumed rigid, normal stresses on the coating are singular at these edges.
- As coefficient of friction is increased, normal stress slightly leans towards the trailing end and magnitude of normal stress decreases at these region. Lateral contact stress achieves high tensile levels behind the contact region, which may be critical for any kind of surface related damages.
- Increase in the coating thickness results in formation of high compressive normal and shear stresses in close proximity of contact surface and these stresses decrease sharply, which means high stress gradients. Utilization of very thin coating may lead to discontinuity in the normal stress, which can be critical for delamination/spallation type failure.

REFERENCES

1. Hogmark, S., Jacobson, S. and Larsson, M. (2000), "Design and evaluation of tribological coatings", Wear, Vol. 246, pp 20-33.

2. Choy, K.L. (2003), "Chemical vapour deposition of coatings", Prog. Mater. Sci., Vol. 48, pp. 57-170.

3. Johnson, K.L. (1985), Contact Mechanics, Cambridge University Press, Cambridge, UK.

4. Gladwell, G.M. (1980), Contact Problems in the Classical Theory of Elasticity, Kluwer Academic Publishers, Dordrecht.

5. Hills, D.A. Nowell, D., Sackfield, A. (1993), Mechanics of Elastic Contacts, Butterworth, Heinemann, Oxford.

6. Chen, W.T. (1971), "Computation of stresses and displacements in a layered elastic medium", Int. J. Engng. Sci., Vol. 9, pp. 775-800.

7. Chen W.T. and Engel, P.A. (1972), "Impact and contact stress analysis in multilayered media", Int. J. Solids Struct., Vol. 8, pp. 1257-1281.

8. Kuo, C.H. and Keer, L.M. (1992), "Contact stress analysis of a layered transversely isotropic half-space", ASME J. Tribol., Vol. 114, No. 2, pp. 253-261.

9. Guler, M.A. (2001), "Contact Mechanics of FGM Coatings", Ph.D. Thesis, Lehigh University, Betlehem, PA, USA.

10. Guler, M.A. and Erdogan, F. (2004), "Contact mechanics of two deformable elastic solids with graded coatings", Mech. Mater, Vol. 38, pp. 633-647.

11. Komvopoulos, K. (1988), "Finite elements analysis of a layered elastic solid in normal contact with a rigid surface", ASME J. Tribol., Vol. 110, No. 3, pp.447-485.

12. Kral, E.R. and Komvopoulos, K. (1996), "Three dimensional finite element analysis of surface deformation and stresses in an elastic-plastic layered medium subjected to indentation and sliding contact loading", ASME J. Appl. Mech., Vol. 63, pp. 365-375.

13. Lovell, M.R. (1998), "Analysis of contact between transversely isotropic coated surfaces: Development of stress and displacement relationship using FEM", Wear, Vol. 214, pp. 165-174.

14. Morrow, C. and Lovell M. (1999), "Numerical contact analysis of transversely isotropic coatings", Wear, Vol. 236, pp. 360-367.

15. Ochonogor, O.F., Akinlabi, E.T., DidierNyembwe. (2017), “A review on the effect of creep and microstructural change under elevated temperature of Ti6Al4V alloy for turbine engine application”, Materials Today: Proceedings, Vol. 4, pp. 250-256.

16. Saleem S., Ahmad, R., Ayub, R., Ikhlaq, U., Jin, W., Chu, P.K. (2017), “Investigation of nano-structured Zirconium oxide film on Ti6Al4V substrate to improve tribological properties prepared by PIII&D”, Appl. Surf. Sci., Vol. 394, pp. 586-597.

17. Li, H., Sun, Y., Zhang, J. (2015), “Effect of ZrO2 particle on the performance of micro-arc oxidation coatings on Ti6Al4V”, Appl. Surf. Sci., Vol. 342, pp. 183-190.

18. ANSYS (2016), “Ansys mechanical APDL theory reference”, Ansys Inc., Release 17.1, Canonsburg.

19. Ai, X., Gao, D.-Q., Chen, W., Lv, Z.-L. (2016), “Tribological Behavior of Si3N4-Hbn Ceramic Materials Against Metal with Different Sliding Speeds”, Ceram. Int., Vol. 42, pp. 10132-10143.

20. Geng, X., Zhang, Z., Barthel, E., Dalmas, D. (2010), “Mechanical Behavior of Stiff Coating on Glass under Sliding Contact”, Wear, Vol. 269, pp. 351-361.

21. Choi, H.J. and Paulino, G.H. (2008), “Thermoelastic contact mechanics for a flat punch sliding over a graded coating/substrate system with frictional heat generation”, J. Mech. Phys. Solids, Vol. 56, pp. 1673-1692.

22. Dag, S., Erdogan, F. (2002), “A surface crack in a graded medium loaded by a sliding rigid stamp”, Eng. Fract. Mech., Vol. 69, pp. 1729-1751.

23. Yildirim, B. (2004), “Investigation of Thermally Shock Fracture in an Edge-cracked Functionally Graded Layer using Finite Element Method”, J. Fact. Eng. Arch. Gazi Univ., Vol. 19, No. 3, pp. 235-245.

24. Apatay, T., Dag, S., Guler, M.A., Gulgeç, M. (2010), “Fonksiyonel Derecelendirilmiş Kaplamalarda Sürtünmeli Rijit Zımba Etkisiyle Oluşan Yüzeyaltı Temas Gerilmeleri”, J. Fact. Eng. Arch. Gazi Univ., Vol. 25, No. 3, pp. 611-623.

25. Balci, M.N., Dag, S., Yildirim, B. (2017), “Subsurface stresses in graded coatings subjected to frictional contact with heat generation”, J. Therm. Stresses, Vol. 40, No. 4, pp. 517-534.

NUMERICAL DETERMINATION OF THE NECKING PHENOMENON USING STRESS WAVE PROPAGATION TECHNIQUE

Şehram DİZECİ, *Sehram.dizeci@tedu.edu.tr* TED University, 06420, Ankara, Turkey

Bahman PAYGOZAR, *Bahman.paygozar@tedu.edu.tr* TED University, 06420, Ankara, Turkey

ABSTRACT

Generally, the stress wave method is based on the propagation of the waves inside the solids which under some conditions cause the material to undergo the necking phenomenon. The numerical method by the way needs to employ dynamic explicit solver to be able to show the necking phenomenon. However, the most important step regarding the solutions in this method is to give applicable material properties to obtain the acceptable results for the time and the place of the necking. Therefore, the material properties implemented to the numerical model should be modified specifically for the points after the necking. This study compares some of the correction methods affecting the necking time and shows that without suitable correction factor, the explicit solver will not be able to define the necking appropriately.

Keywords: Stress wave propagation, Necking, Sheet metal, Correction methods

1. INTRODUCTION

The initiation of plastic instability in the sheet metal is related to the point where bifurcation from the fundamental loading path takes place. There are different methods to define the onset of diffuse necking in the metals. There was considerable interest in the subject of necking development under plane stress through the two important theoretical criteria of Swift and Hill [1]. However, since they provided criteria only for the onset of instabilities, the necking development and the imperfection evolution during plastic deformation could not be described. In this respect, another study published later by Marciniak & Kuczyński [2] assumed that an imperfection existing in the specimen would start a necking development during the plastic deformation. To predict the occurrence of the necking phenomenon, there are several other methods based on some theoretical formulations, among which the Considère criterion is the simplest one demonstrating the time of necking using Holloman's hardening equation. He

proposed that the necking occurs when the force reaches to its maximum value then by small calculations:

$$\bar{\sigma} = K\bar{\varepsilon}^{n} \quad (1)$$

where $\bar{\sigma}$ is the equivalent true stress, K is the strength coefficient, $\bar{\varepsilon}$ is the equivalent plastic strain and n is the hardening index. If P is the load applied in the tensile test,

$$P = \bar{\sigma}.A = K\bar{\varepsilon}^{n}.A \quad (2)$$

Taking the natural logarithm from both sides and differentiating,

$$dP = 0, \Rightarrow \bar{\varepsilon} = n \quad (3)$$

Which means at the necking point the equivalent strain is equal to hardening index of the material.

Yasnikov et al. [3] modified the theorem to be applicable for most of the materials considering the dislocation movements. Armstrong & Walley [4] studied the necking under high-rate loadings where the criteria provide the framework for the understanding of neck formation. Necking in the metallic materials can be divided into two types: diffuse necking, and localized necking. The former is the most prevalent one and known as the necking in the literature, whereas the latter is a more complicated phenomenon and occurs when a material endures higher levels of stress. It is worth mentioning that the localized necking is far more complex and occurs much later than the onset of diffuse necking [5]. In other words, diffuse necking occurs when the plastic deformation of a sample changes to non-uniform due to stress triaxiality, whereas the localized necking occurs slightly before fracturing the sample.

The finite element methods (FEM) employ dynamic explicit solvers to model the necking phenomenon by numerical methods. Abaqus explicit solver [6] takes the material properties in two different tables for elastic and plastic regions. However, there is not any specific criterion to define the onset of the necking. The method is based on two different speeds inside the material: deformation speed and stress wave propagation speed. The stress waves affect the material behavior by differing the material's deformation speed. The deformation speed tends to rise in order to follow or reach the stress values given as material properties by the user and implemented as stress wave propagation in the dynamic explicit solutions. The bilateral interaction between deformation speed and the velocity of plastic waves inside the material leads to instability of the material in an almost arbitrary location in the samples [7].

For an elastic wave the wave velocity will be constant because in the elastic region the stress-strain relation is linear, whereas in the plastic region the stress-strain relationship will instead be non-linear. It means that the velocity of plastic waves is lesser than elastic waves since the velocity declines with diminishing slope and strain hardening [8]. It should be noted that the

amplitude of a stress wave and the rate of application of the load increases with the passage of time up to the necking point. If the rising deformation speed of the material affected by higher amplitude of the waves due to hardening effect passes the declining velocity of the plastic waves (eqn. 4), the instability will start. The plastic wave velocity is:

$$C_p = \sqrt{\frac{d\bar{\sigma}/d\bar{\varepsilon}}{\rho}} \tag{4}$$

where, C_p is the plastic wave speed and ρ is the density of the material.

Generally, in most of the materials the non-linear plastic deformation curve has a declining slope which means at one point there will be a necking in the part under tensile loading. The time of the necking or in other word the equivalent strain ($\bar{\varepsilon}$) in which the necking starts can not be accurately determined unless the input material properties reflect the exact behavior of the material.

2. CORRECION METHODS

Since the material behavior is normally extrapolated for the post-necking region by Hollomon (eqn. 1) or other hardening formulations, it is apparently assumed that the loading condition is uniaxial up to the fracture point which is not practically correct. Therefore, the necking determined by the FEM solution will not reflect the actual conditions consequently. To overcome this drawback, so many correction factors have been proposed for post-necking behavior.

Bridgman [9] offered a correction method to the diffuse neck of a flat sheet tension sample with a rectangular cross-section as:

$$k_r = \frac{1}{1+\ln\left(1+\frac{h}{4r}\right)} \tag{5}$$

where h is the current thickness of the narrowest cross-section of the sheet metal and r is the radius of curvature in the neck profile. However, the deformation of inside a neck in a flat sheet tension sample is often far from the plane strain condition assumed by Bridgman and the actual morphology of the neck so the correction factor does not reflect the necking phenomenon correctly.

Yang and Tang [10] summarized most of the hardening models utilized to model the behavior of a sheet metal. The Swift model and linear hardening they have compared in their work are shown in equations (6) and (7) respectively.

$$\bar{\sigma} = \sigma_u(1 + \bar{\varepsilon} - \varepsilon_u) \tag{6}$$

where briefly linear hardening proposes that the hardening after the necking turns to a line with the constant slope of the stress-strain curve at necking point.

$$\bar{\sigma} = K(\bar{\varepsilon} + \varepsilon_y)^n \quad (6)$$

where, ε_y is the strain at yield point and sometimes is assumed to be equal to 0.002.

There are so many other correction methods like the study Majzoobi et al. [11] proposed where the correction factor is obtained in terms of the initial specimen radius, the neck radius and the z-strain on the neck surface. The curve produced with this method stands between Swift and linear hardening model too.

3. EXPERIMENTAL METHOD

The specimens of mild steel with respect to ASTM E8 were prepared and tested at 10 mm/min rate. The material properties obtained has been summarized in Table 1 as follows,

Table 1. mechanical properties of Mild steel

Material	E (Gpa)	Poisson's ratio	Yield strength (MPa)	UTS (MPa)	Strength Coefficient (MPa)	Strain hardening index
Mild Steel	194	0.29	255	375	638	0.243

The corresponding stress-strain curve and the curves for implemented correction methods have been presented in Fig. 1. The points for onset of necking in experimental test and Considere' criterion have been shown on the true stress-strain curve as well.

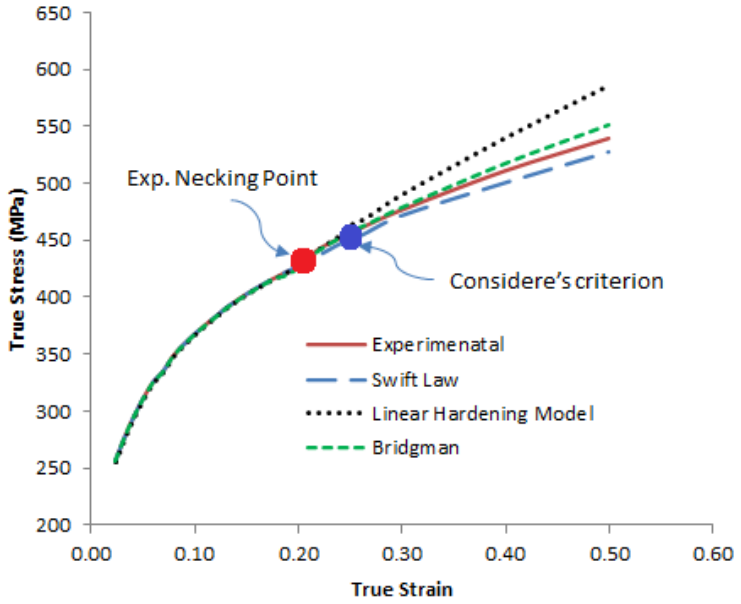


Fig. 1. Plastic deformation curves with corresponding correction methods

4. NUMERICAL METHOD

To simulate the specimens studied in the research, three-dimensional (3D) parts were analyzed using ABAQUS/Explicit solver. Then different meshing scheme were utilized to investigate the mesh independency and validate the numerical solutions based on the experimental results. The suitable mesh size is $0.5 \times 0.3 \times 0.25\ mm$ where there are four elements in thickness direction. Also, the ratio of the internal energy to kinetic energy was tested to be above 10 to assure the analysis is in quasi static condition.

5. RESULTS AND DISCUSSIONS

The stress-strain relation implemented to the numerical models need to be modified for post-necking region because of the variation in the loading history of the elements. This modification is applied using different types of correction factors. In this study four different criteria were used to determine onset of the necking in the specimens.

Considere's criterion is showing the necking to happen when $\bar{\varepsilon} = 0.243$ which is late determination clearly shown on the curve in Fig. 1.

All the correction methods have been implemented to Abaqus/explicit to capture the necking point. All of them have shown the necking but the time o the necking is different for them. It is obviously shown in Fig. 2 that explicit solver can show the stress and strain localization during the process successfully.

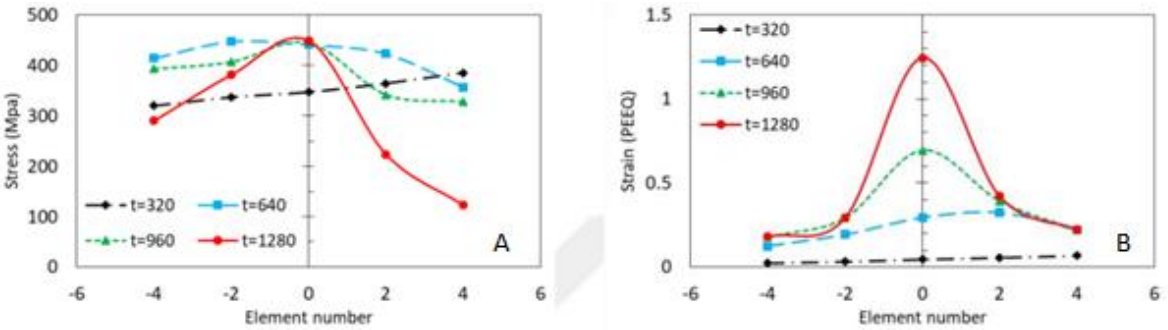


Fig.2. Corresponding stress and strain propagation in the necking area at different time frames. (Zero shows the necked element)

The equivalent plastic strains in the specimens have been compared for four different conditions in Fig. 3 at the time when the equivalent strain starts to localize in the neck region. As it is obvious, Linear hardening model has predicted the necking very late comparing to the others. The results are as expected for this model which gives the upper bound solution for the predictions because it assumes that $d\bar{\sigma}/d\bar{\varepsilon}$ remains constant for the post-necking conditions

which is not the case. However, it defines that all the correction methods will somehow produce the curves which stays below this curve because in all the correction methods $d\bar{\sigma}/d\bar{\varepsilon}$ is decreasing.

Bridgman correction method also has given late prediction comparing to the experimental data. It should be noted that for sheet metal conditions, Bridgman method assumes that the post-necking is a plane strain condition, and this assumption is not literally correct.

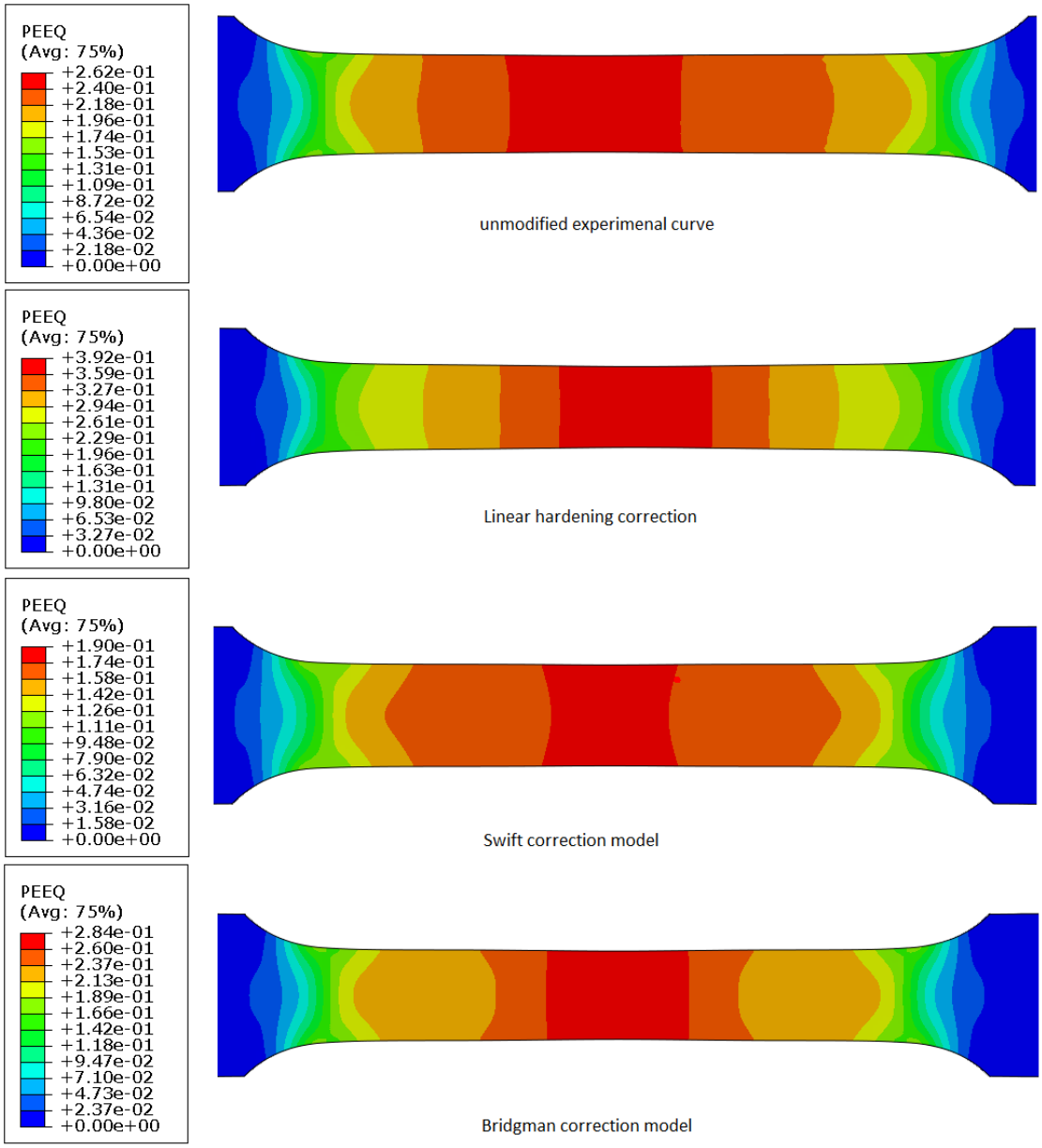


Fig.3. Comparison between different correction factors considering equivalent strain at necking

The best results considering equivalent plastic strain and displacement at necking, was obtained using Swift model as shown in the figure where $\bar{\varepsilon} = 0.19$was achievd. As a general rule, if Considere's criterion shows higher number comparing to experimental data, the correction factor needs to decrease the slope of the curve meaning post-necking curve should be below the experimental one which is the case for swift model for this material. The opposite condition is valid if Considere's criterion shows lower number and then the correction factor needs to increase the slope of the curve to better catch the necking point.

6. CONCLUSIONS

The Necking phenomenon is studied using stress wave propagation technique by implementing explicit finite element solvers.

It is concluded that most of the times the experimental stress-strain curve will not capture the post-necking behavior of the material due to extrapolation applied for that region. Instead, a correction factor needs to be employed to better model the process and determine the necking accurately.

Generally, Considere's criterion is not giving the accurate necking equivalent strain and other correction factors need to be applied instead. For mild steel studied in this work, Swift model gave better results comparing to linear hardening and Bridgman correction methods.

7. REFERENCES

1. **Swift, H. W. (1952).** Plastic instability under plane stress. Journal of the Mechanics and Physics of Solids, Vol. 1, pp 1-18.
2. **Marciniak, Z., & Kuczyński, K. (1967).** "Limit strains in the processes of stretch-forming sheet metal". International Journal of Mechanical Sciences, Vol. 9, pp 609-620.
3. **Yasnikov, I. S., Vinogradov, A., & Estrin, Y. (2014).** "Revisiting the Considère criterion from the viewpoint of dislocation theory fundamentals". Scripta Materialia, Vol.76, pp 37-40.
4. **Armstrong, R., & Walley, S. M. (2008).** "High strain rate properties of metals and alloys". International Materials Reviews, Vol. 53, pp 105-128.
5. **Hwang, J.-K. (2020)**. "Revealing the small post-necking elongation in twinning-induced plasticity steels". Journal of Materials Science, Vol. 55, pp 8285-8302.
6. **Hibbitt, Karlsson and Sorenson, (2011)**, "ABAQUS/Explicit: user's manual".

7. **Christopher, J., & Choudhary, B. K. (2018). "**On the onset of necking instability in tempered martensitic 9% Cr steels". Mechanics Research Communications, Vol. 94, pp 114-119.
8. **Macaulay, M. (2012).** "Introduction to Impact Engineering", Springer Netherlands.
9. **Bridgman P.W. (1952),** "Studies in Large Plastic Flow and Fracture"**,** McGraw-Hill, New York.
10. **Yang S.-Y., W. Tong, (2009),** "A finite element analysis of a tapered flat sheet tensile specimen". Exp. Mech., Vol. 49, pp 317-330.
11. **Majzoobi G., Fariba F., Pipelzadeh M. and Hardy S.J., (2014),** "A new approach for the correction of stress–strain curves after necking in metals", J. Strain Analysis, pp 1-13.

ANALYSIS OF ACOUSTICALLY ACTUATED SEDIMENTATION PREVENTION SYSTEM FOR SYRINGE PUMPS

Arda KAYA, *kaya.arda@metu.edu.tr* Middle East Technical University, 06560, Ankara, Turkey

Güven ÖNER, *guven.oner@metu.edu.tr* Middle East Technical University, 06530, Ankara, Turkey

Ö. Faruk ERGÜVEN, *erguven.omer@metu.edu.tr* Middle East Technical University, 06530, Ankara, Turkey

Ender Yıldırım, *yender@metu.edu.tr* Middle East Technical University, 06530, Ankara, Turkey

F. Ginaz Almus, *ginaz@metu.edu.tr* Middle East Technical University, 06530, Ankara, Turkey

ABSTRACT

The design and analysis of a sedimentation prevention system for a syringe pump is presented in this paper. The aim of the design is to prevent sedimentation inside the syringe placed on a syringe pump by utilizing acoustophoresis technique. Analysis performed for the design of the syringe is provided. The analyses are done using COMSOL Multiphysics software. Piezo electric transducer providing 2.4 MHz with the supply of 220 V of electric potential is determined to prevent sedimentation of particles with 1100 kg m^{-3} density and 10 μm diameter.

Keywords: Acoustophoresis, Sedimentation, Syringe Pump, Piezo electric transducer

1. Introduction

Syringe pumps are widely used for microfluidic applications to actuate fluid. They utilize a syringe as a fluid reservoir. By using a linear motion system, force is transferred to the piston of the syringe and fluid is pressurized. Conventionally, stepper motors are used as motion source and rotational motion is converted to the linear motion via a lead screw with small lead value. Although, they provide better control on flowrates [Byun et al., 2014], they have some operational restrictions and problems.

One of the problems is to prevent sedimentation of particles inside the syringe. Sometimes operating time of the syringe pump can be long. During the operation, particles inside the syringe could accumulate at the bottom of the syringe and distort the homogeneity of the fluid inside.

For some studies made in the microfluidics field homogeneity is important since it is directly related with viscous effects [Shanko et al., 2021]. For these reasons and to make the assumptions legitimate, accumulation of particles is not desired. So, homogeneity of the fluid is an important parameter in the microfluidic applications.

Since, syringe is totally closed reservoir, preventing the sedimentation inside is a design problem. To prevent the sedimentation, it is needed to mix the fluid without any contact with it. Some designs utilize a rotation mechanism to rotate the syringe about its axial axis. [Lane et al., 2019] However, this type of solutions requires complicated designs, mechanisms, and machine elements. They increase the complexity of the system and complicates the user interface of the pump. Thus, simpler solutions that requires minimum number of components is desired. Particles should be actuated without direct physical interaction with the syringe or fluid. Therefore, as a contactless method, acoustic actuation of the particles could be utilized.

In this study, analysis of an acoustophoretic sedimentation prevention system for a syringe pump is presented. Two different types of analyses were done. One of the analyses was done to calculate the normal displacement on the syringe caused by the acoustic pressure field of piezoelectric transducer. The other analysis was performed to calculate the sedimentation and the acoustophoretic radiation forces on particles. From the displacement analysis, displacement on the syringe wall is given as an input to the sedimentation analysis. These analyses are performed using COMSOL Multiphysics software.

2. Sedimentation

Aim of the project is to prevent sedimentation inside the syringes during the operation time. To achieve this, acoustophoresis is used. Acoustophoresis tries to counter the gravitational effects using acoustic pressure. In the design process piezo electric transducer needed to be chosen. For this choice two parameters were used. One of them is the acoustic pressure field transducer creates inside the syringe, the other one is the normal displacement it creates on the walls of the syringe. For these parameters computational analyses were performed using COMSOL Multiphysics program. COMSOL Multiphysics program utilizes finite element method in its solver. Both the normal displacement analysis and the acoustic analysis were performed on COMSOL Multiphysics.

2.1. Displacement Analysis

System is analysed using COMSOL Multiphysics' pressure acoustics module, solid mechanics module and electrostatic module. The aim of this analysis is to determine the normal displacement on the syringe wall caused by the piezoelectric effect with the changing voltage. The domain names and the material assigned to these domains can be seen in Figure 1.

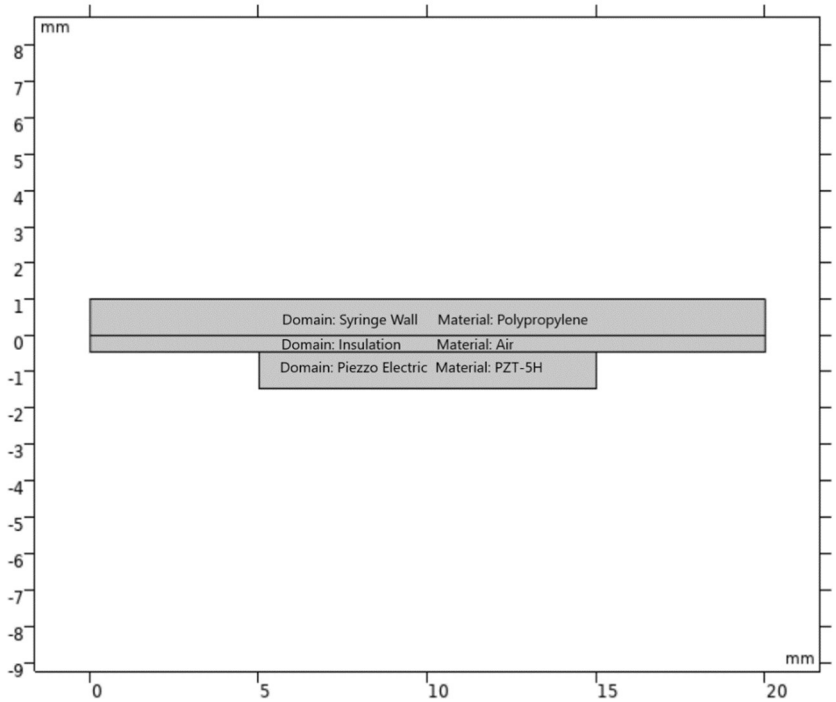


Figure 1. Domain Names and Assigned Materials for the Normal Displacement Analysis.

On the domains where solid mechanics is solved, each edge should contain at least 3 mesh elements for an accurate solution. On the domains where pressure acoustics is solved, meshing should be done such that a wavelength contains at least 6 mesh elements. For simplicity the meshing is done by using the minimum mesh requirement. To have an accurate result maximum mesh element size is defined as 0.1mm for 2.4 MHz of frequency. Close up view of the mesh can be seen in Figure 2. On these domains, multiple physics were used and according to the interaction of these domains COMSOL Multiphysics were defined. Pressure acoustics physics in frequency domain is used in the insulation domain. As the reference pressure and the reference speed of sound air is used. During the solution of this physic only impedance boundary condition is defined for the air. The boundaries of the insulation domain are defined as acoustic structure boundary.

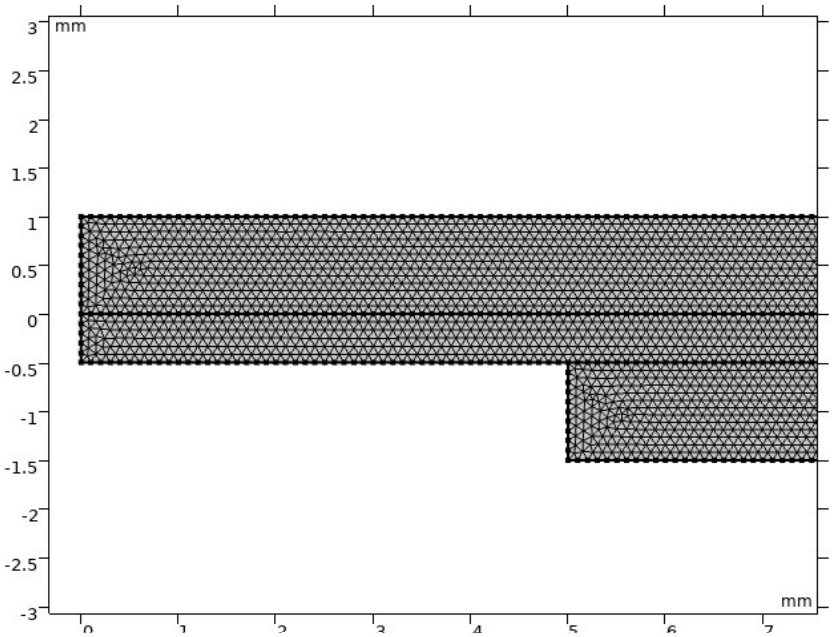


Figure 2. Close View of Meshes Defined for the Solid Mechanics

Solid mechanics physics is used in both piezo electric and syringe wall domains. For the piezoelectric domain, piezoelectric material boundary condition is defined. This boundary condition automatically calculates the stresses due to the electrical charges. Electrostatics physics is defined for the piezo electric domain. For this physics, ground and electric potential boundary conditions are defined for the bottom and top of the piezo electric domains respectively. For the electric potential boundary condition 220 V was given. The voltage is determined iteratively by trying the possible voltages that can be given to the piezo electric

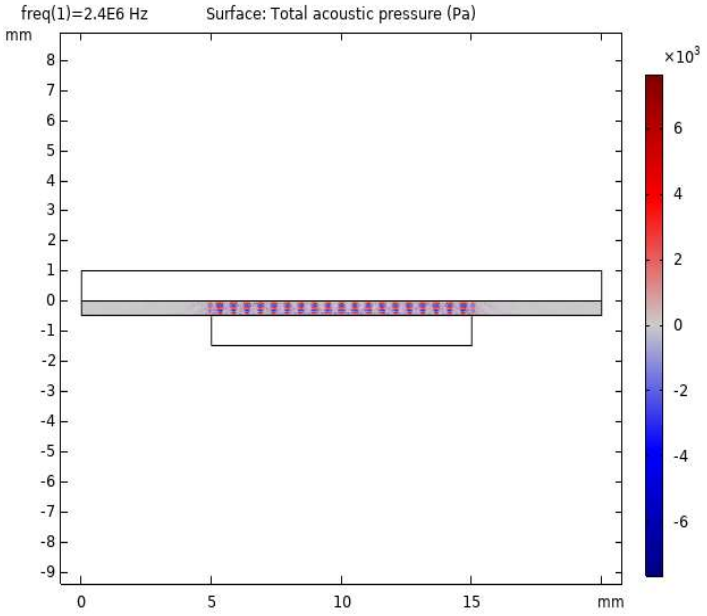


Figure 3. Acoustic Pressure Field of the Insulation of Normal Displacement Analysis

transducers. To couple the solid mechanics module and electrostatic module for the piezoelectric boundary condition, piezoelectric effect COMSOL Multiphysics is defined on the piezoelectric domain.

These physics are solved using the frequency domain for 2.4 MHz of frequency. Acoustic pressure field of insulation domain caused by the 2.4 MHz of frequency can be seen in Figure 3.

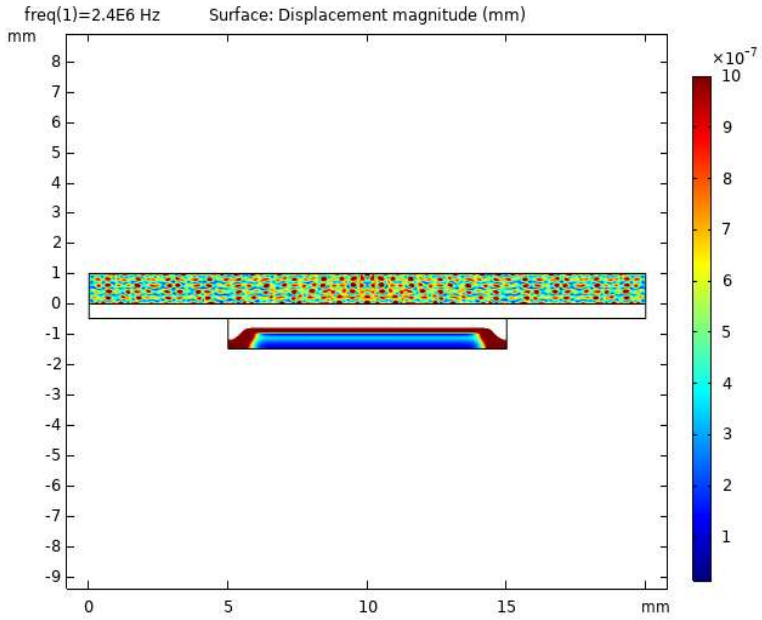


Figure 4. Normal Displacement on the Syringe Walls

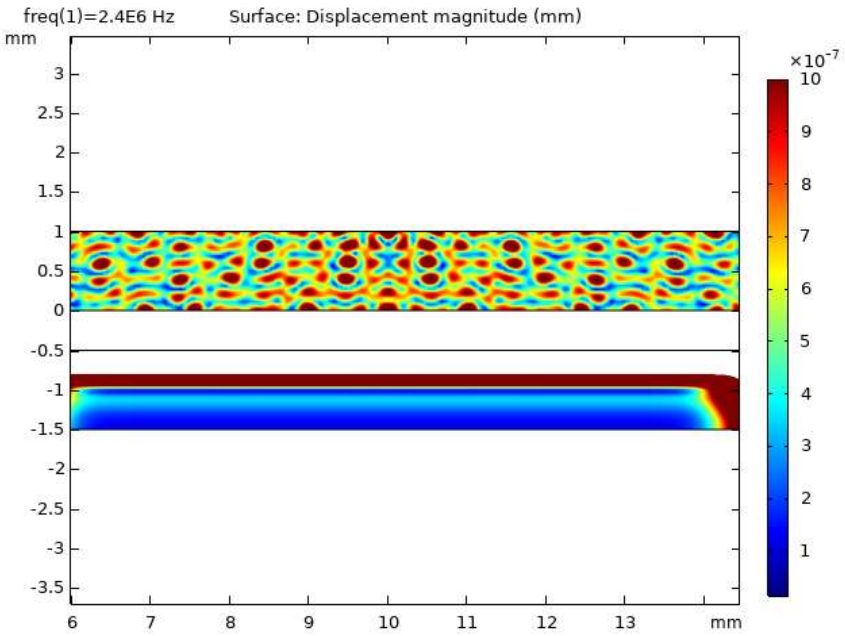


Figure 5. Close View of the Normal Displacement on the Syringe Walls

In Figure 4, the displacement on the syringe walls and on piezo electric material can be seen with the ranges clipped such that the displacement distribution on the syringe walls can be seen better. Close up view of the displacement on the syringe walls can be seen in Figure 5.

As can be seen from Figure 4 or Figure 5, displacement on the syringe wall varies in the order of 10^{-7} mm. This variation is caused by high frequency and high number of nodes it causes. For the acoustic analysis, normal displacement is taken as the average 0.4 nm.

2.2. Sedimentation Analysis

The resulting frequency is determined as 2.4 MHz with 0.4 nm of normal displacement occurring at the syringe wall. During the analysis it was determined that acoustic pressure field tries to move the particles its effecting towards to the nodes of the pressure field. Therefore, having high number of nodes will provide a homogenous distribution inside the syringe. As observed from the analysis having high frequency also provides with higher number of nodes, which is beneficial to achieve homogeneity.

System is analysed using COMSOL Multiphysics' thermoviscous acoustics module coupled with particle tracking module. Thermoviscous physics is chosen because of its solver's ability to solve linearized Navier-Stokes equations. This solver can calculate viscous effects for a geometry with small dimensions. Due to the lack of computational resources and for the ease of analysis, analysis was performed in 2D and for the water domain only, additionally only a part of the syringe was considered to neglect the effects of the piston and the hub of the syringe.

Meshing is done such that a wavelength contains at least 6 mesh elements. Close up view of the meshing done can be seen in Figure 6. Maximum mesh element size is taken as 0.1 mm which is calculated according to 2.4 MHz of frequency. Triangular meshing is used for the mesh type.

For the thermoviscous acoustics physics, reference pressure and speed of sound is chosen for water. Normal impedance boundary condition is defined for the boundaries with water interaction. Velocity boundary condition was defined from the bottom of the syringe since piezo electric materials are implemented to that boundary. For the magnitude of the velocity boundary condition, angular frequency which is calculated by the solver and the normal displacement on the inside of the syringe wall caused by the piezo electric material is considered. After the analysis performed to determine, the normal displacement is assumed to be 0.4 nm.

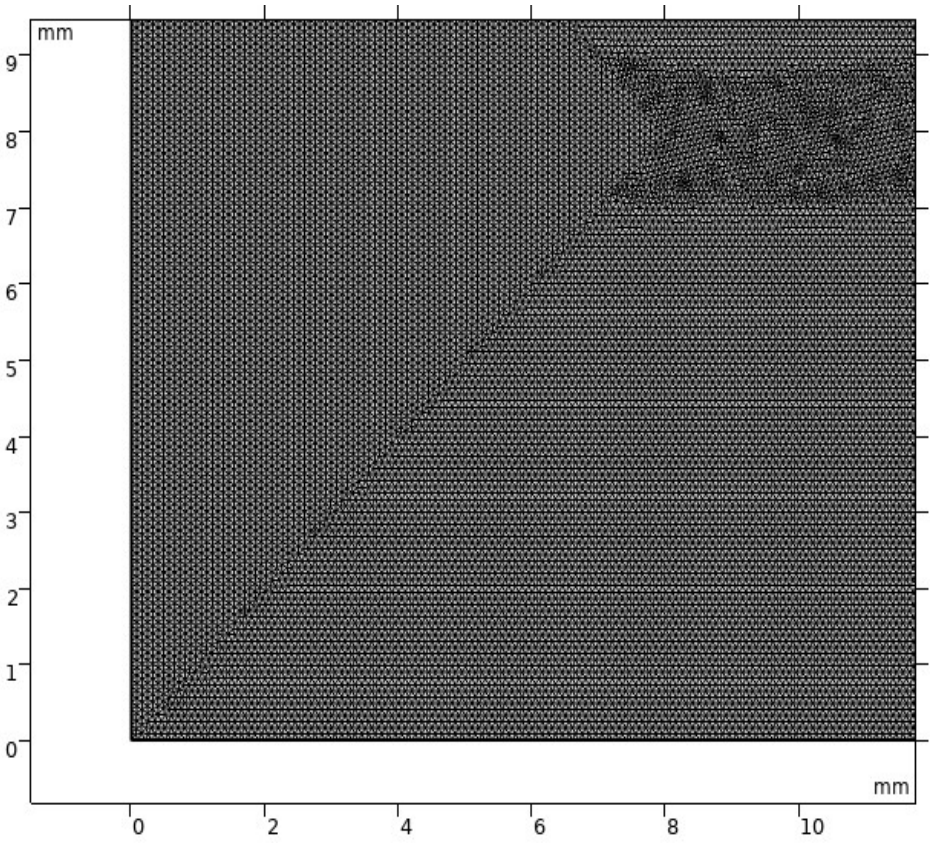


Figure 6. Close up View of the Mesh of Sedimentation Analysis

For the particle tracking, drag force, gravitational force and acoustophoretic radiation force were defined as the forces imposing on the particles. Gravitational force is constant and calculated by the solver. The drag force and the acoustophoretic radiation force is automatically calculated by the solver according to the location and the velocity of the particle. Particles to be examined are released from a predefined grid. Particles have been assumed to have 1100 kg m^{-3} with the diameter of 10 μm. Particles properties are chosen as the properties of the red blood cell [Connor et al., 1994].

Two different solvers were used in this analysis. Thermoviscous acoustics physics were solver using frequency domain solver and particle tracking is solver by a time dependent solver.

The resulting acoustic pressure field is given in Figure 7. In Figure 7's legend it can be seen that the pressure changes in the order of 10^4. A closer view of the pressure field can be seen in Figure 8. It can be seen that the pressure field contains high number of nodes, which was desired.

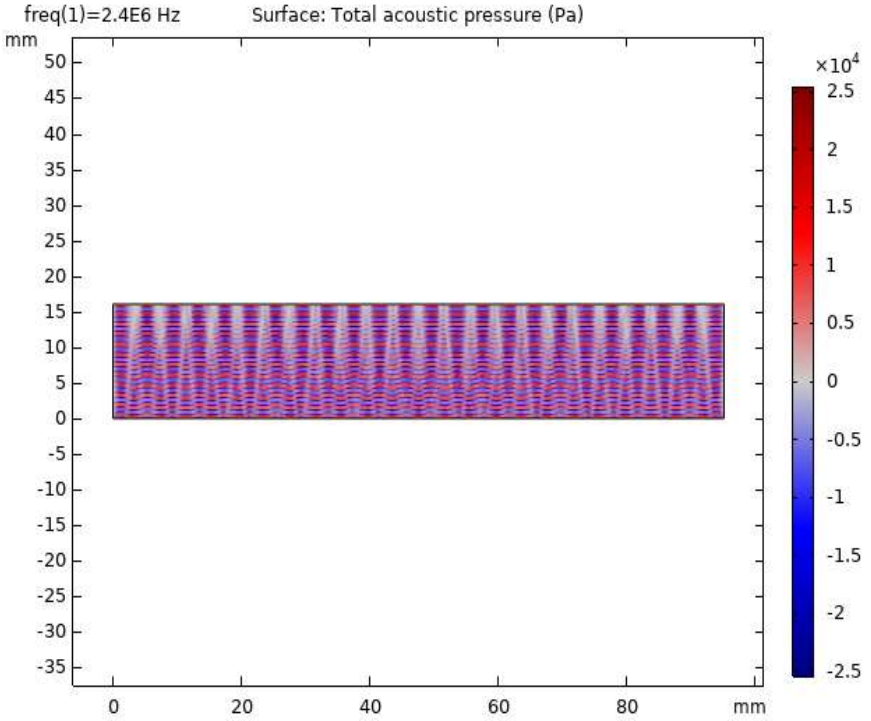


Figure 7. Acoustic Pressure Field of Sedimentation Analysis

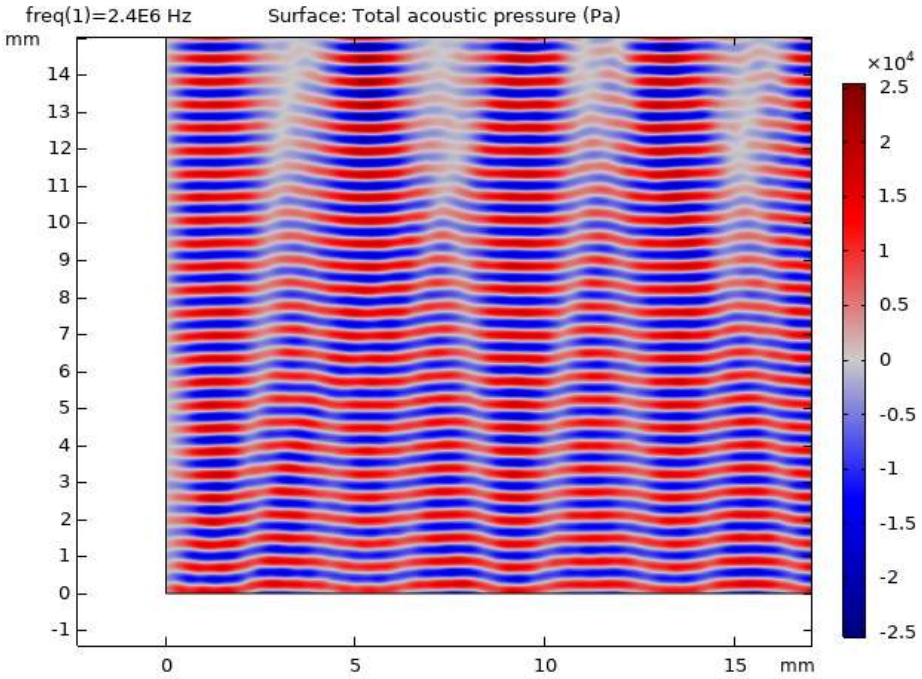


Figure 8. Close Up View of the Acoustic Pressure Field of Sedimentation Analysis

From the solution of the particle tracking physics, forces acting on the particles can be determined. In Figure 9, acoustic radiation force acting in the positive y direction on the

particles can be seen. As the legend of the Figure 9 indicates the force acting on the particle is in the order of 10^{-14} and in some areas 10^{-13}.

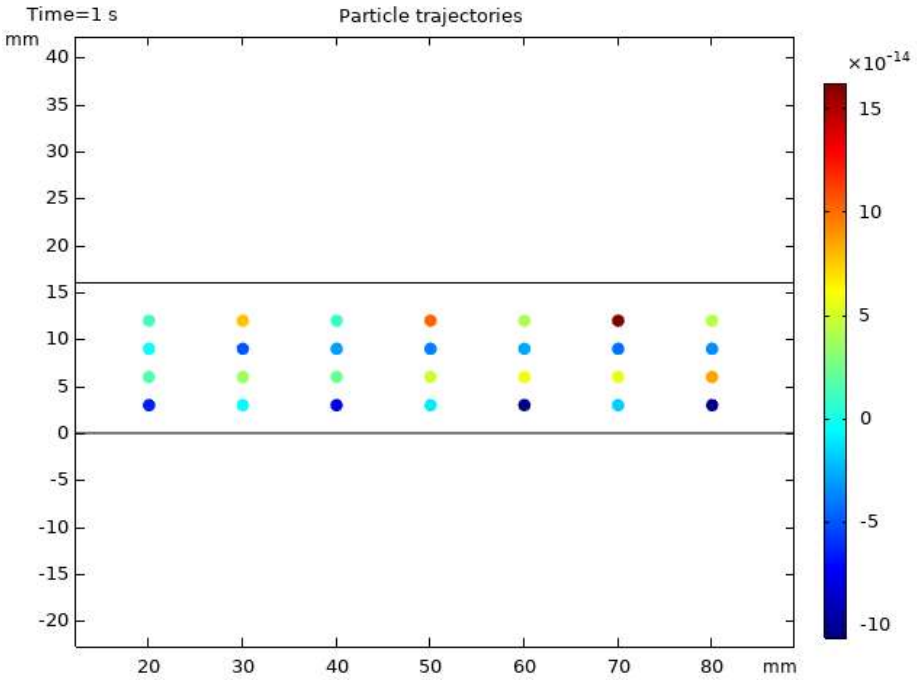


Figure 9. Acoustic Radiation Force Acting on the Particles

In Figure 10, gravitational force acting on the particles can be seen. As can be seen in the legend of the Figure 10, gravitational force is in the order of 10^{-13}.

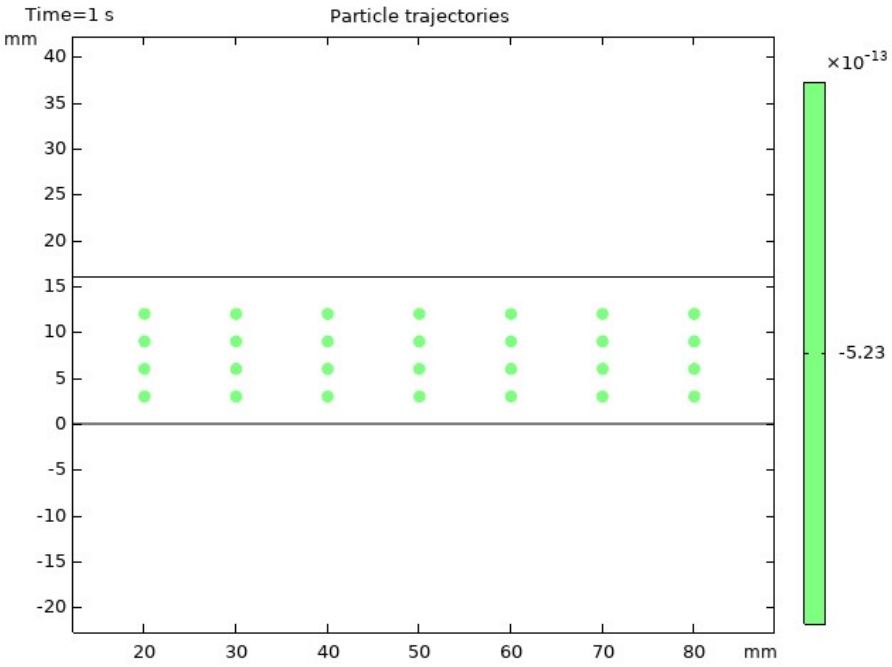


Figure 10. Gravitational Force Acting on the Particles

In Figure 11, drag force acting on the particles in positive y direction can be seen. As can be seen in the legend of the Figure 11, drag force is in the order of 10^{-13}.

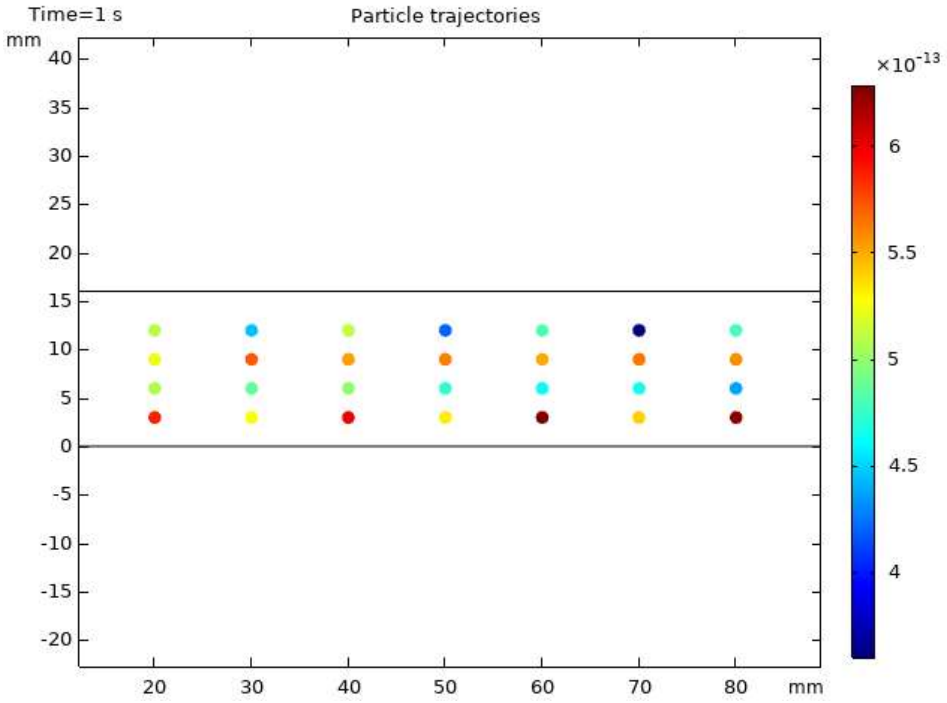


Figure 11. Drag Force Acting on the Particles

From the force analysis performed on the particles, it can be determined that acoustic force acting in some places are enough to slow down the sedimentation. Since the pressure field contains high number of nodes, the acoustic force applying on the particles changes rapidly inside the pressure field; therefore, although currently on some particles acoustic force applying is not enough to slow down the particle movement, as the particle moves through the pressure field the acoustic force applying to the particle increases and decreases according to the location of the particle and in some places of the pressure field particle will be slowed down thus preventing sedimentation of the particles.

3. Optimization

During the analysis it was determined that, with increasing voltage and frequency normal displacement on the syringe wall increased [Mao et al., 2019]. With increasing normal displacement and frequency, acoustic pressure increases. Therefore, during the process solution parameters are obtained iteratively.

Before beginning the analyses, available commercial products were examined and the possible frequencies that can be obtained were determined. During the product search five different applicable ultrasonic piezo transducers with different resonance frequencies are

found. These frequencies are 40 kHz, 107 kHz, 113 kHz, 1.7 MHz, and 2.4 MHz. Transducer with 40 kHz is used for ultrasonic distance sensors while others are ceramic piezo discs used for humidification and water atomization applications. The voltage requirements and the frequency of these products were given as input to the normal displacement analysis.

According to the displacement obtained, sedimentation analysis was performed as the normal displacement and frequency as the input. Results obtained from the sedimentation analysis were examined to determine whether the acoustophoretic radiation force is sufficient. If the radiation force is not sufficient, frequency of the sedimentation analysis increased according to a new piezo electric transducer. If the increased frequency is capable of preventing sedimentation, normal displacement analysis was performed for the new piezo electric transducer. From the obtained normal displacement, sedimentation analysis was performed again to check the change in the normal displacement had an impact on the acoustophoretic radiation force. If the acoustophoretic radiation force is decreased such that it is no longer capable of preventing sedimentation, voltage applied the piezo transducer increases to increase the displacement. Even if with the increase of the voltage the displacement is not sufficient, then a new piezo electric transducer will be tried with higher voltage capable of providing similar frequency.

4. Test

A Test is made by preparing an experimental set-up using ceramic piezo discs operating at 2.4 MHz. Diagram of the circuit is as shown in Figure 12, which is an oscillator circuit. Circuit is powered by a power supply with 25 to 30 Volts. Piezo discs are placed on top, and bottom of the syringe. Barrel of the syringe is filled with water and black pepper particles.

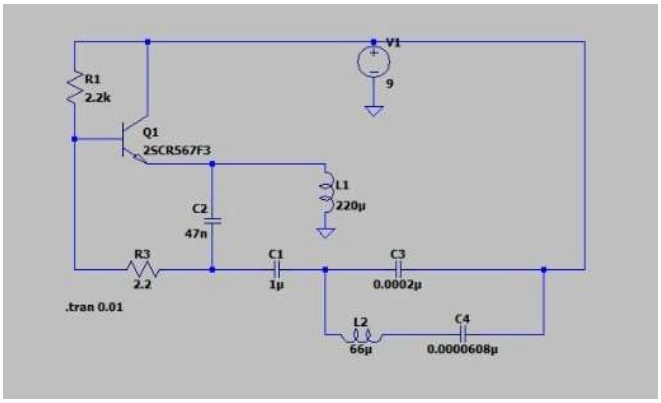
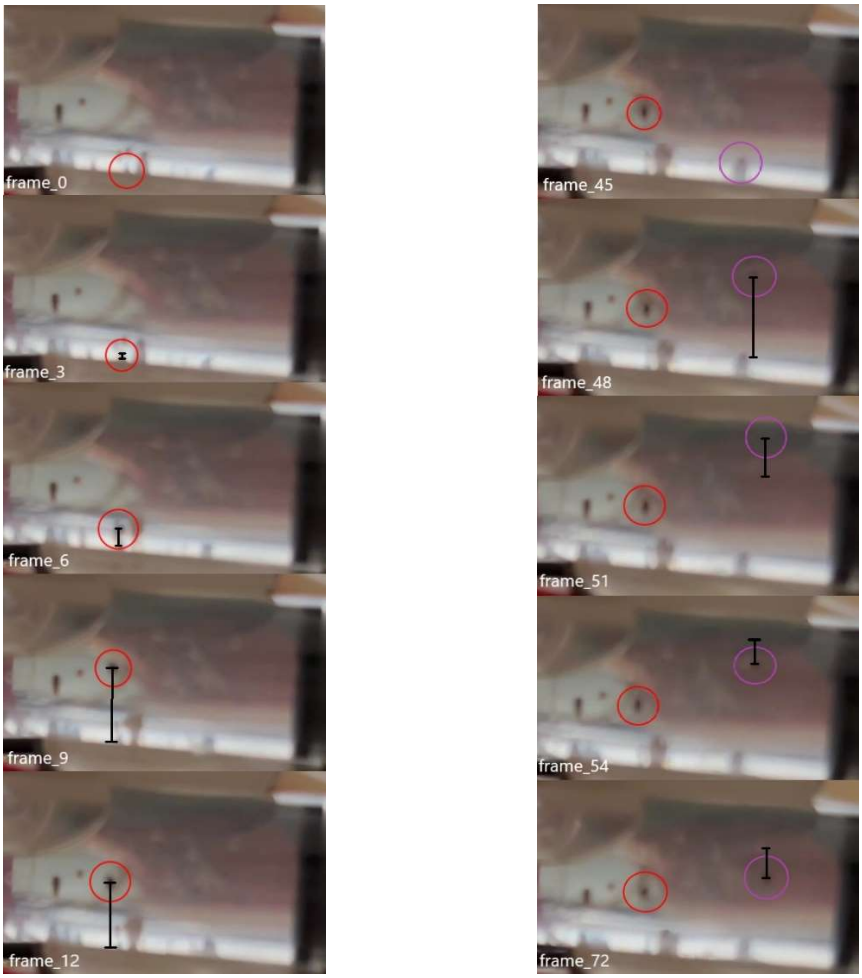


Figure 12. Circuit Diagram of Piezo Discs

Test is recorded with a 60 fps camera and examined frame by frame. Figure 13. (a) shows a black pepper particle with time intervals of 3 frames and height of the particle with respect to first position of it. Initial time (frame_0) is the exact moment of power up. Figure 13. (b) shows another black pepper particle with time intervals of 3 frames and height difference of the particle with respect to previous position of it. Last interval is 18 frames for clarifying slow descend. Initial time of it is 45 frames after power up.



(a) (b)

Figure 13. Examination of Black Pepper Particles, a) Holding Node, b) Slower Sedimenting

Particle in Figure 13. (a) is initially at the base of the syringe. Particle started to ascend immediately after power up, continued to rise until 9 frames. It is observed that the particle stayed at the same height after 9 frames and did not start to descend until power off. Examination shows that the particle took hold to a node at its final height.

Particle in Figure 13. (b) is also initially at the base of the syringe. Particle started to ascend 45 frames after power up. Particle reached the top of the syringe after 6 frames and descended

a small vertical distance for a long period of 21 frames. It is observed that particle continued to descend very slowly until power off.

5. Conclusion

In this study, analysis of an acoustically actuated sedimentation prevention system designed for the syringe pumps is presented. Normal displacement analysis is done by using COMSOL Multiphysics' pressure acoustics module, solid mechanics module and electrostatic module to determine the normal displacement that is induced on the syringe walls. A test set-up is prepared, and first tests are concluded. From displacement analysis, displacement is approximated as 0.4nm. Normal displacement obtained is used to find acoustic pressure and acoustic radiation force values created inside of the barrel. From the initial calculations acoustic radiation force created seems to slow down the sedimentation, and applied test supports this. As a next step, further experimental validations of these analysis will be done. In these experiments, a similar particle of polystyrene is aimed to be used. Throughout the process using these particle concentration control will be made.

Acknowledgement

Authors would like to acknowledge the help and advice of Adil Berkay Temiz (adilberkaytemiz@gmail.com, Ankara, Turkey) and equipment support of Micromanufacturing Laboratory of METU Mechanical Engineering Department.

REFERENCES

1. **Byun, C.K., Abi-Samra, K., Cho, Y.-K. and Takayama, S. (2014),** "Pumps for Microfluidic Cell Culture", ELECTROPHORESIS, Vol.35, No.2-3, pp 245-257.
2. **Shanko, E. S., Ceelen, L., Wang, Y., van de Burgt, Y., & den Toonder, J. (2021). "**Enhanced Microfluidic Sample Homogeneity and Improved Antibody-based Assay Kinetics Due to Magnetic Mixing", ACS Sensors, Vol.6, No.7, pp 2553-2562.
3. **Lane, S. I., Butement, J., Harrington, J., Underwood, T., Shrimpton, J., & West, J. (2019).** "Perpetual Sedimentation for the Continuous Delivery of Particulate Suspensions", Lab on a Chip, Vol.19, No.22, pp 3771–3775.
4. **Connor J, Pak CC, Schroit AJ. (1994)** "Exposure of Phosphatidylserine in the Outer Leaflet of Human Red Blood Cells. Relationship to Cell Density, Cell Age, and

Clearance by Mononuclear Cells", The Journal of Biological Chemistry, Vol.269, No.4, pp 2399-404.

5. **Mao, Y., Yang, J., Liu, H., Liu, Y., & Xu, W. (2019).** "Study on Radial Vibration of Circular Piezoelectric Ceramic", In Journal of Physics: Conference Series, IOP Publishing, Vol. 1187, No.2.
6. **COMSOL Multiphysics [Computer software] (2014).** Retrieved from https://www.comsol.com/

DESIGN OF AN ANTI-SEDIMENTATION SYRINGE PUMP FOR MICROFLUIDICS APPLICATIONS

Eminalp KOYUNCU, *eminalp.koyuncu@metu.edu.tr* Orta Doğu Teknik Üniversitesi, 06800, Ankara

A. Tardu KOÇUM, *tardu.kocum@metu.edu.tr* Orta Doğu Teknik Üniversitesi, 06800, Ankara

Enes KOÇ, *enes.koc@metu.edu.tr* Orta Doğu Teknik Üniversitesi, 06800, Ankara

Cem KÜÇÜKGENÇ, *cem.kucukgenc@metu.edu.tr* Orta Doğu Teknik Üniversitesi, 06800, Ankara

Baturay KURTOĞLU, *baturay.kurtoglu@metu.edu.tr* Orta Doğu Teknik Üniversitesi, 06800, Ankara

Oğuzhan KARAKAŞ, *oguzhan.karakas@metu.edu.tr* Orta Doğu Teknik Üniversitesi, 06800, Ankara

Ender KURUKAHVECİ, *ender.kurukahveci@metu.edu.tr* Orta Doğu Teknik Üniversitesi, 06800, Ankara

Bülent ÖZCAN, *bulent.ozcan@metu.edu.tr* Orta Doğu Teknik Üniversitesi, 06800, Ankara

Ender YILDIRIM, *yender@metu.edu.tr* Orta Doğu Teknik Üniversitesi, 06800, Ankara

F. Ginaz ALMUS, *ginaz@metu.edu.tr* Orta Doğu Teknik Üniversitesi, 06800, Ankara

ÖZET

Mikroakışkan sistemler, üzerinde küçük hacimli sıvı numunelerin işlendiği platformlardır. Mikroakışkanları yönlendirme ve kontrol etme yöntemleri son zamanlarda kritik hale gelmiştir. Sıvıyı bir mikroakışkan sistemden geçirmek için en iyi tanımlanmış yöntem, şırınga pompalarını kullanmaktır. Şırınga pompaları, sıvı yüklü bir şırınganın pistonunu önceden tanımlanmış bir hızda iterek akış oluşturan tezgah üstü ekipmanlardır. Bu cihazların pahalı olması, sınırlı kaynaklara sahip laboratuvarda şırınga pompalarını bulmayı zorlaştırmaktadır. Ek olarak, partikül çözeltilerindeki mikroakışkan uygulamalarda şırınga haznesindeki partiküllerin çökelmesi de dikkate alınması gereken bir diğer konudur. Yavaş akış ve sürecin hassas ve genellikle uzun süreli tamamlanması da bu çökelmelerin oluşumunda önemli faktörlerdir. Bu duruma farklı çözümler geliştirilmeye devam edilmektedir. 3B baskı kullanılarak çeşitli açık kaynaklı alternatif şırınga pompası sistemleri üretilebilir ve oluşturulabilir. Bu makale, partikül çökelmesini önleyen açık kaynaklı bir şırınga pompası tasarlamak ve üretmek için basit ve ekonomik bir yöntem sunar.

Anahtar Kelimeler: Şırınga Pompası, Mikroakışkan, Sedimantasyon, Titreşim, Parçacık, 3B Baskı

ABSTRACT

Microfluidic systems are platforms on which small volumes of liquid samples are processed. Today, methods of directing and controlling Microfluidics have become critical. The best-defined method for pushing liquid through a microfluidic system is to use syringe pumps. Syringe pumps are benchtop equipment that creates flow by pushing the plunger of a liquid-laden syringe at a predefined rate. The expensiveness of these devices makes it challenging to find them in laboratories with limited resources. In addition, precipitation of particles in the syringe barrel is another issue to consider in microfluidic applications in particle solutions. The slow flow and the sensitive and generally long-term completion of the process are also essential factors in the formation of these sedimentations. Different solutions for this situation continue to be developed. Various open-source alternative syringe pump systems can be fabricated and created using 3D printing. This article presents a simple and economical method to design and manufacture an open-source syringe pump that prevents particle precipitation.

Keywords: Syringe Pump, Microfluid, Sedimentation, Vibration, Particle, 3D Printing

INTRODUCTION

In the recent years, microfluidics as a branch of science and technology has been getting more and more attention. With number of chronic diseases and cancer cases on the rise, studies in microfluidic applications are a much-necessitated tool for engineers worldwide. Microfluidic systems work with fluid flow in the ranges of milliliters to microliters, regarding continuous flow of the fluids as essential, hence commercial products to be used in laboratory work environments such as syringe pumps become exceedingly functional for enactments of drug delivery, particle manipulation, droplet generation. [Zhang, Xia & Ji, 2020]

These microfluidic systems used in many essential sectors of varied industries necessitate a uniform mixing of the fluids introduced into the system when this fluid material is of a liquid suspension type whereby differently sized particles with differing properties coexist within the liquid medium. To achieve this desired uniform mixing, hence the prevention of sedimentation there are numerous solutions such as using blade mixers, high shear components, rotation, vibration etc. This article studies implementing the solution of vibration by making use of a vibration motor in contact with the syringe that contains the liquid. [Menbari & Hashemnia, 2019]

This article will discuss the properties of the designed system wherein the operating principle of the syringe pump product will be elaborated upon and essential aspects of the design that makes it unique will be discussed. In the latter stages of the article the methods and advanced analysis techniques utilized to reach significant conclusions with regards to prevention of sedimentation within a liquid suspension medium in a microfluidic application will be articulated. Further, the setup that is made use of in order to conduct a physical test to observe the effects of the vibratory solution on the condition of sedimentation will be explained and the results of the experiment will be shared.

MATERIALS AND METHODS

Operating Principle

The design aims to transfer liquid automatically and reversibly from the syringe to the microfluid channel at different flow rates, namely performing infusion/withdrawal through remote control. The syringe barrel will be fixed to the system by the means of a screw clamp whereby the top fixture, consisting of springs and a guide shaft, compresses the barrel with the compressive force of the springs. In this way, it is also helpful for placement of syringes of different models and sizes without wasting time on setup. Also, for the parts such as screw clamp and fixtures, additive manufacturing methods were utilized similar to Baas and Saggiomo [Baas, S., & Saggiomo, V., 2021] due to the various advantages of using this manufacturing method. In addition, the vibration motor positioned on the screw fixture will operate at a specific frequency during the process, and possible sedimentations will be prevented. The syringe plunger is fixed with the help of an e-slide mount, which is specially designed and can be used for different syringe models. In this way, the syringe plunger is connected to the threadless screw. The design of the threadless screw mechanism was inspired by, and the relevant engineering calculations and the decisions of respective parameters were made in accordance with the article of Chung-Wei Lee and co. [Lee & Chou, 2020] With the threadless screw, the force from the NEMA 17 micro stepper motor is

transferred to the syringe's piston. In this way, infusion and withdrawal events take place. When the process ends with the help of the button on the design, the system stops itself.

Important Aspects of the Design

The syringe pump design was created in line with literature surveys. Detailed analyses and research have been made to find plausible solutions to prevent sedimentation. As a result of these, it was deemed appropriate to use a vibration motor to prevent sedimentation. For the purpose of getting the maximum efficiency from the vibration motor, the syringe barrel is positioned as close as possible in its specific location at the top fixture to be in contact at all times. Isometric and front view of the design as well as its components are shown below figures.

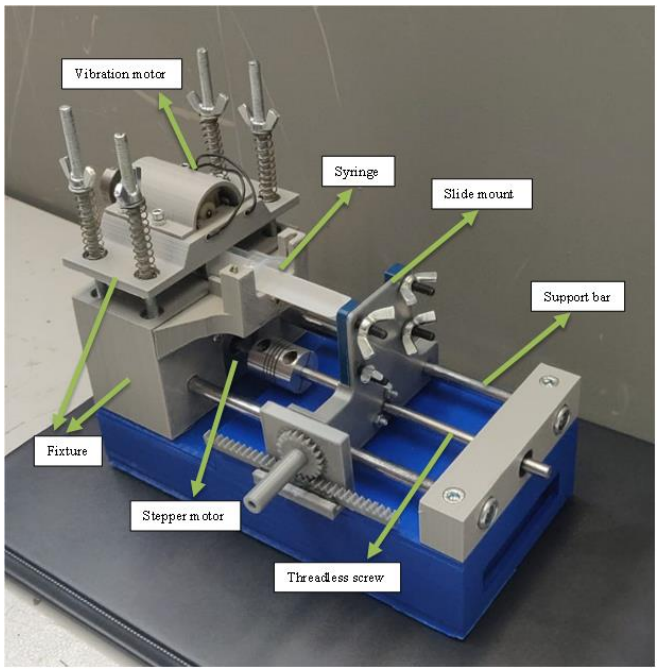


Figure 1. Isometric view of the design

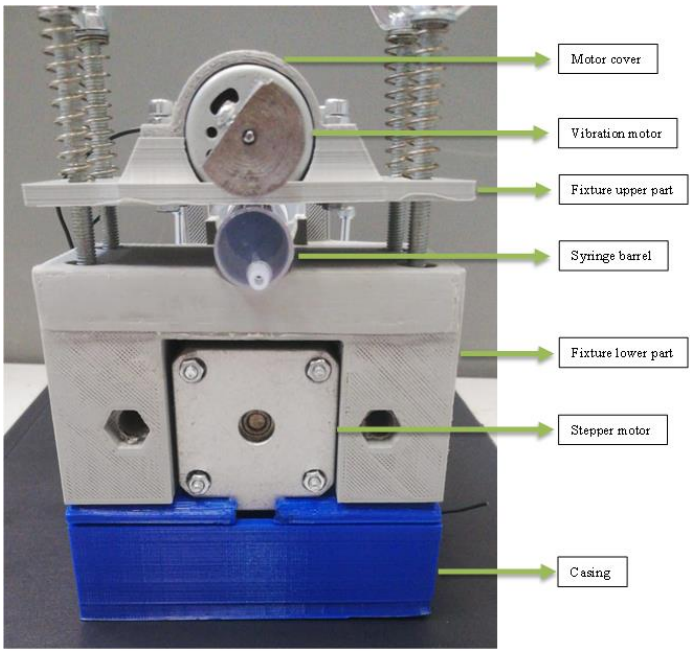


Figure 2. Front view of the design

Flow Range Control

As seen in similar syringe pump designs, it is evident that a stepper motor in this design drives the syringe pump. The design requirements provide a working flow range between 1µl/min and 20ml/min. Since the current design does not have any variable transmission components between the stepper motor and the input shaft of the threadless screw mechanism, the only possible strategy to achieve the desired input shaft rpm values is to change the rotational speed of the motor. For the purpose of confirming these flow rate values, image processing is utilized with the help of a simple MATLAB code. The cross-sectional area of the test tube is known, therefore, with the measured displacement of the liquid inside the test tube, flow rate is calculated analogous to Atay's work. [Atay et al, 2021]

Low-cost syringe pumps are analyzed in the literature by Samokhin [Samokhin, A. S., 2020]. According to Samokhin [Samokhin, A. S., 2020], Arduino Nano, Arduino Uno, Board with ATmega328P and Raspberry Pi are common controllers for these syringe pumps. In this article, a low-cost syringe pump which is remotely controlled is aimed to be designed. In the current syringe pump design, the stepper motor is actuated by using an ESP8266 microcontroller and its corresponding stepper library since the ESP8266 microcontroller has built-in Wi-Fi module. The ESP8266 microcontroller is connected to a micro stepper that drives the stepper motor. The micro stepper allows the corresponding stepper motor to work at as low as 1/32 of a step that the motor has typically. The increased step count using a micro stepper allows the stepper motor to turn slower than it usually can without increasing the pulsation effect. This process also has some drawbacks, dramatically decreasing the motor torque as the step count increases. This phenomenon can be seen in the article of Collins [Collins, D., 2019]. This does not pose a massive problem for the current syringe pump design because the flow rates are meager in the minimum flow rate condition. Since the flow rates are so low, the torque needed to drive the system is much lower due to backpressure decreasing as the flow rate decreases. So, to adjust the flow rate, the potentiometer present in the stepper motor controller and the micro-step actuator are satisfactory.

Preventing Sedimentation

The syringe pump designed for this product will be used in MEMS applications, where there is a possibility of using liquid suspensions in MEMS applications. In these applications, the particles inside the suspension must be distributed homogeneously across the carrying fluid during the infusion process. Thus, the syringe pump should prevent sedimentation inside the fluid. To prevent sedimentation, the syringe is vibrated with enough excitation frequency and amplitude. Vibration analysis is conducted with different vibration motor speeds and torques to determine the vibration frequency and amplitude. After the motor is selected, the selection is confirmed with CFD simulation, where the suspension inside the syringe is modelled and excited with the determined parameters.

Vibration Analysis

In order to prevent sedimentation, a vibration motor is decided to be employed. According to the excitations provided by the motors, CFD analysis is run, and the selected motor and the design of the upper fixture are optimized accordingly.

To model the system, First, a structural analysis is run on the upper fixture and syringe barrel to find their stiffnesses.

The syringe barrel is structurally analyzed by creating a finite element model on MSC Apex. [MSC Software, 2021] The model is clamped at the sides, and 1 N force is given at the surface. After getting the translational displacements, Stiffness is calculated as shown below:

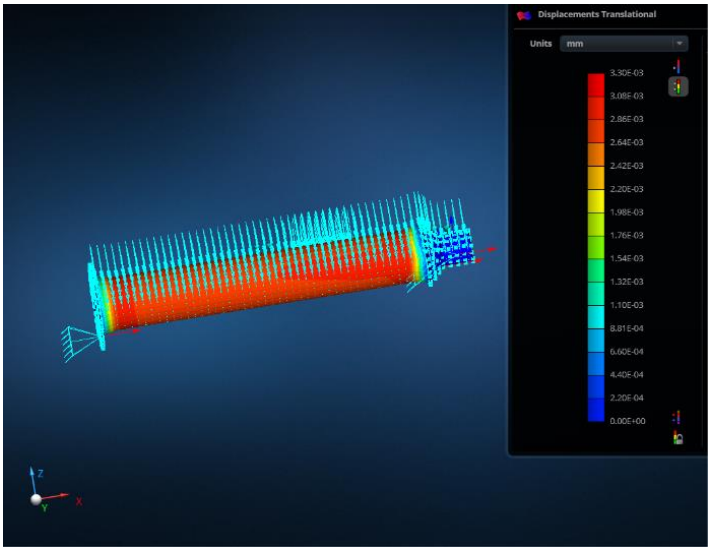


Figure 3. Structural Analysis of the Syringe

$$k = \frac{F}{x} \tag{1}$$

$$k_1 = \frac{1}{4.76*10^{-6}} = 2.101 * 10^5 \frac{N}{m} \tag{2}$$

To create vibration, it is decided to employ a DC motor and handmade unbalance. The properties of the selected motor at the end of the iterations and the unbalance that is decided to place at the shaft of the vibration motor is given below:

Frequency

$$\omega = \frac{20000}{60} = 333.33\ Hz \tag{3}$$

Mass of the motor

$$M = 0.05\ kg \tag{4}$$

Mass of unbalance

$$m = 1381 * 10^{-9} * 8000 = 0.011\ kg \tag{5}$$

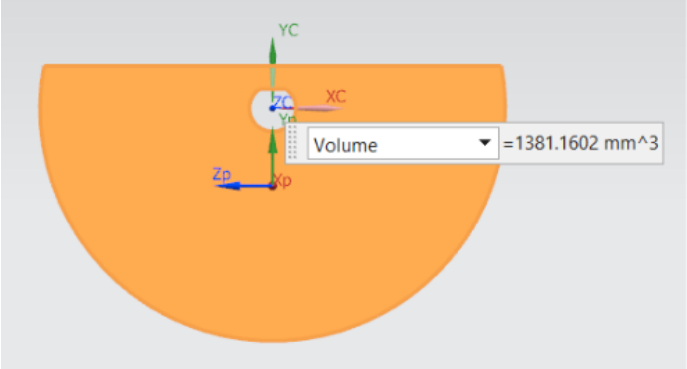


Figure 4. Unbalance

Unbalance distance

$$e = 0.005\ m \tag{6}$$

Then the vibration calculations are made according to mathematical model.

Natural Frequency

$$\omega_n = \sqrt{\frac{k}{M}} = 2.462 * 10^3\ Hz \tag{7}$$

From the Medel's work [Medel, 2022] on Polymer Testing, damping ratio for the PLA material which is used for 3D printing of parts can be assumed as 0.02.

Damping ratio

$$\zeta = 0.02 \tag{8}$$

Magnification factor

$$H = \frac{1}{\sqrt{\left(1-\frac{\omega^2}{\omega_n^2}\right)^2+\left(2*\zeta*\frac{\omega}{\omega_n}\right)^2}} = 1.019 \tag{9}$$

Phase angle

$$\theta = atan2\left(\left(1-\frac{\omega^2}{\omega_n^2}\right),\left(2*\zeta*\frac{\omega}{\omega_n}\right)\right) = 0.006 \tag{10}$$

Magnitude of force provided by the motor

$$F_0 = m * e * \omega^2 = 6.138\ N \tag{11}$$

Amplitude of displacement

$$X_0 = \frac{F_0}{k} * H = 2.1 * 10^{-5}\ m \tag{12}$$

Magnitude of transmitted force function

$$F_T = F_0 * \sqrt{1 + \left(2 * \zeta * \frac{\omega}{\omega_n}\right)^2} * H = 6.253\ N \quad (13)$$

Transmitted force

$$F_T(t) = F_T * \cos(\omega * t - \theta) = 6.253 * cos(333.33 * t - 0.006)\ N \quad (14)$$

Sedimentation Analysis

In order to check whether the selected motor is enough to prevent sedimentation inside the syringe, a CFD simulation is conducted on the syringe. The following problem domain is used for the simulation. Note that, the simulation is conducted on the ANSYS Fluent software. [ANSYS Inc., 2022]

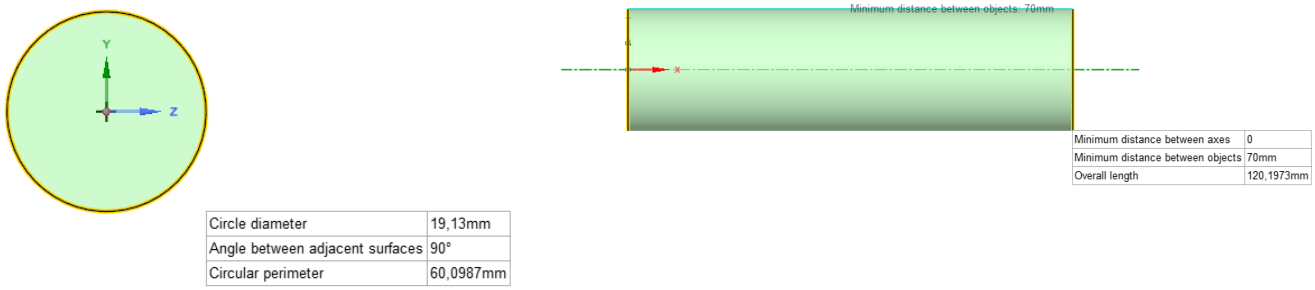


Figure 5. Problem Domain

As it can be seen from the problem domain, the simulation is conducted on a 3D domain. The domain represents the fluid volume inside the 20 mL syringe. The following mesh and boundaries are used for this simulation.

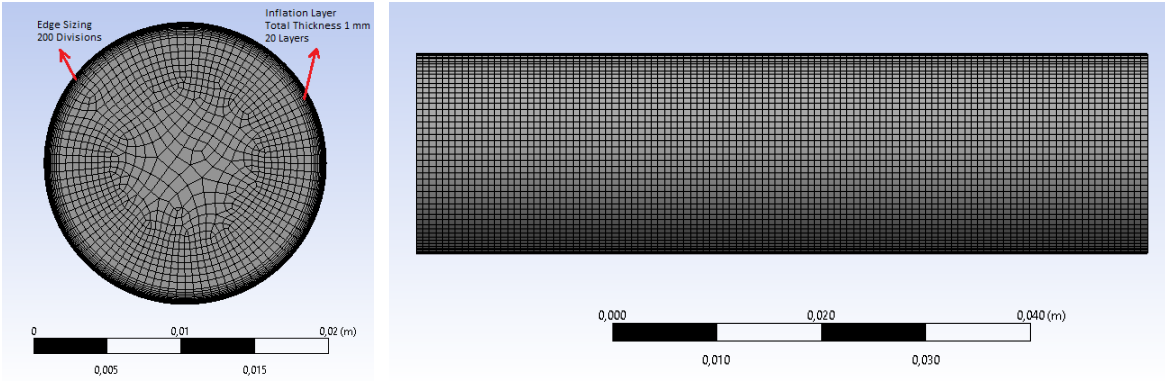


Figure 6. Overview of the Mesh

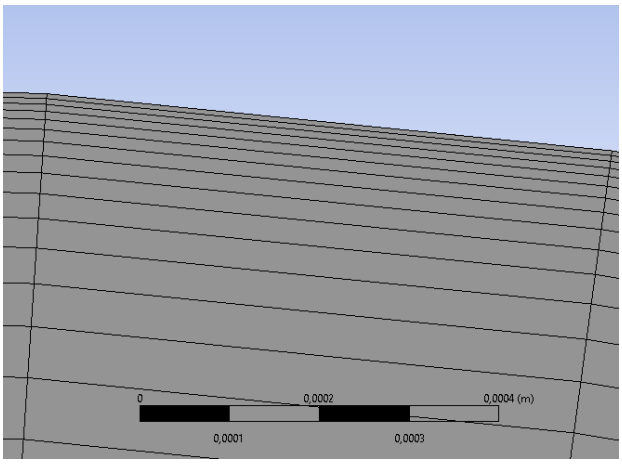


Figure 7. First Layer Thickness

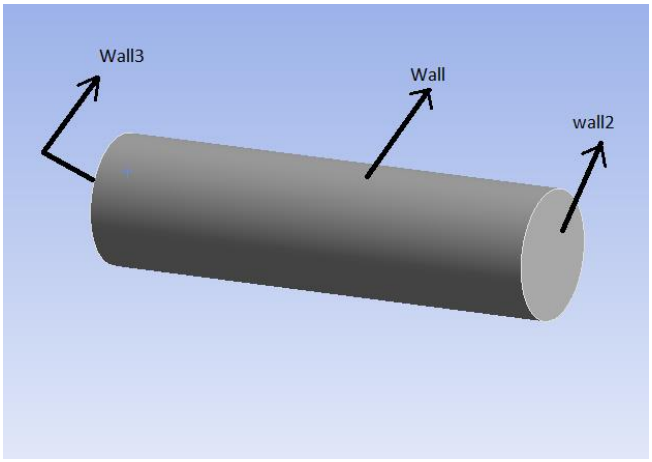


Figure 8. Problem Domain Boundaries

Statistics	
Nodes	329734
Elements	322560

Figure 9. Mesh Statistics

From above figure, a total number of 322560 elements is used in this mesh. Also, the first layer thickness of the mesh is kept at a small value since the vibration causes turbulent activity inside the problem domain. To simulate the vibration effects on the particles, the transient k-ϵ model is used with enhanced wall treatment. Also, the discrete phase solver is enabled to simulate the particles. Particles are injected to the problem domain at t=0 within a volume lying at the bottom of the problem domain (syringe). At the discrete phase solver, the pressure gradient forces and interaction of the particles with the continuous phase is enabled. All the boundaries are defined as “wall” boundary condition and they are set to reflect the particles with conserving the momentum. The continuous phase (fluid) is defined as water with default properties and the particles are defined as inert anthracite particles with a diameter of 50 μm. The vibrational effects are given to the system as time varying gravitational field. From above calculations, vibration motor speed and syringe displacement were determined as,

$$\omega = 14600\, rpm \Rightarrow\ f = 233\, Hz\ ,\ \delta = 0.049\, mm \tag{15}$$

So, the position of the syringe can be determined as,

$$y(t) = \delta \sin\,(2\pi f t) \tag{16}$$

So, the acceleration of the syringe becomes,

$$\ddot{y}(t) = -\delta(2\pi f)^2 \sin\,(2\pi f t) \tag{17}$$

Overall gravitational acceleration becomes,

$$g_{field} = -g - \delta(2\pi f)^2 \sin(2\pi f t)\,[\tfrac{m}{s^2}] \tag{18}$$

Where g is the gravitational acceleration 9.81 m/s^2. The overall gravitational acceleration is given to the simulation. So, the vibration on the syringe is modelled as the time varying gravitational field. The time step of the simulation is selected as 0.0009 seconds to ensure that the calculation is repeated a few times in a vibration cycle. The solver settings are given in the figures below.

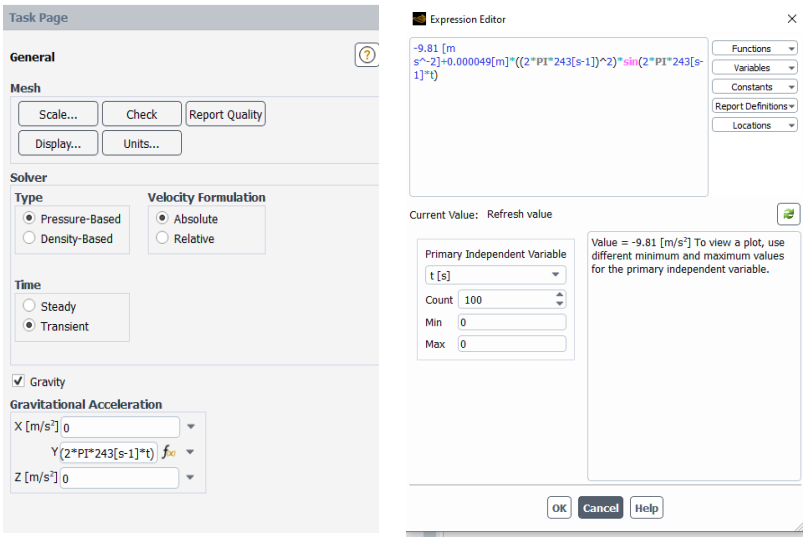


Figure 10. Solver Settings and Gravity Expression

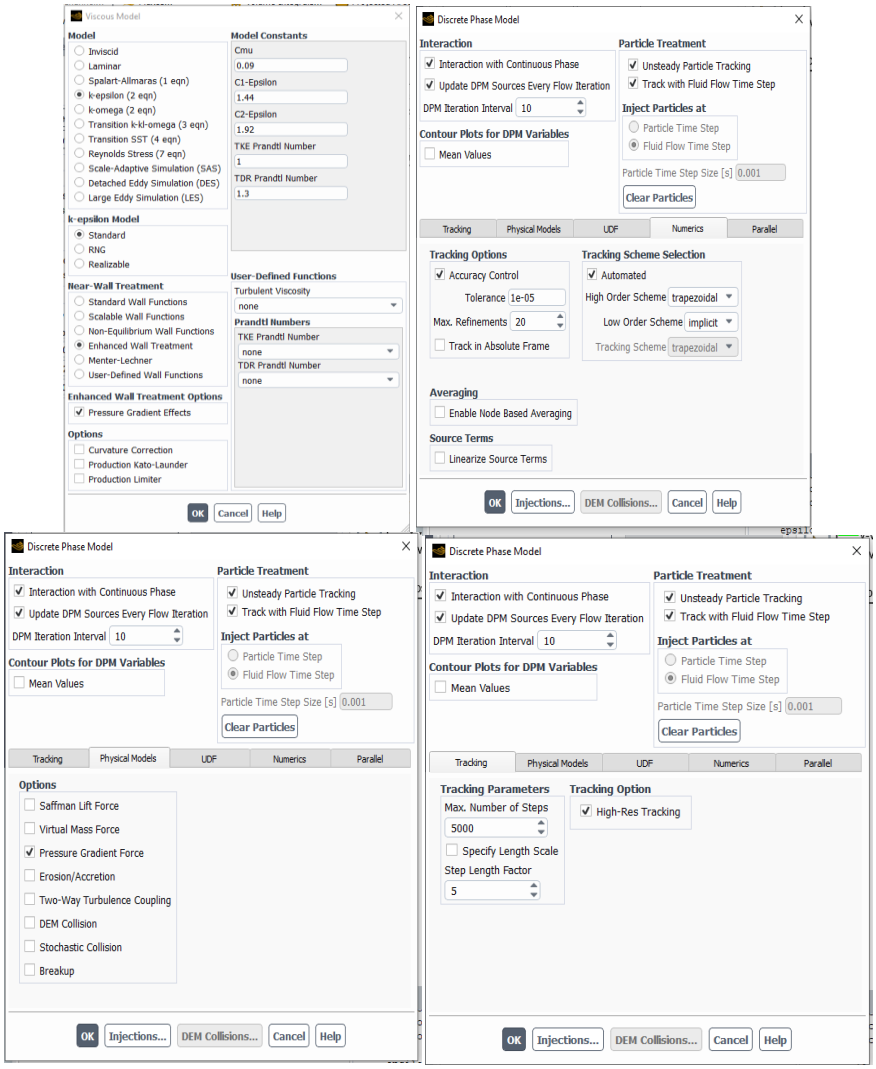


Figure 11. Viscous and Discrete Phase Solver Settings

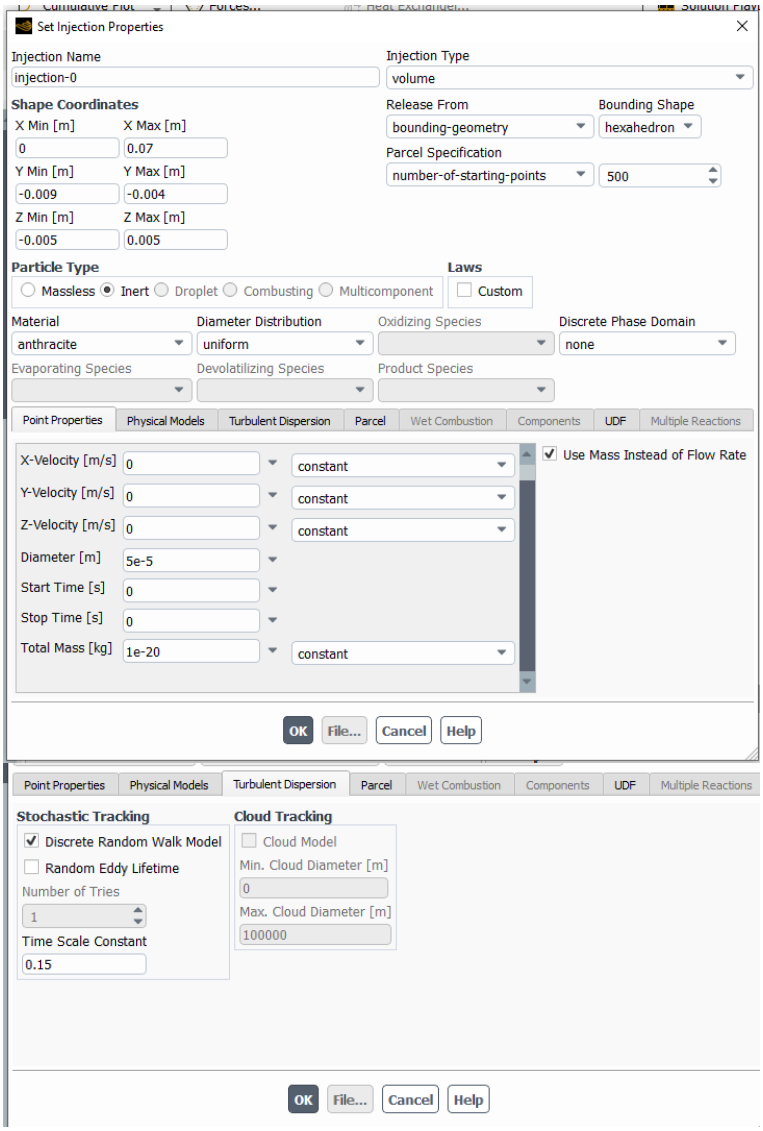


Figure 12. Injection Properties

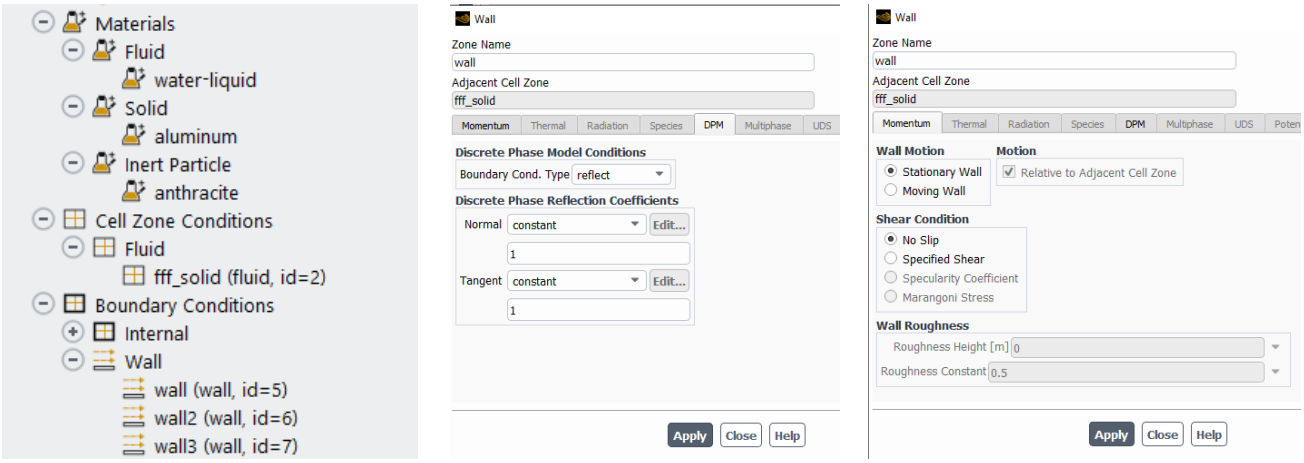


Figure 13. Boundary Conditions

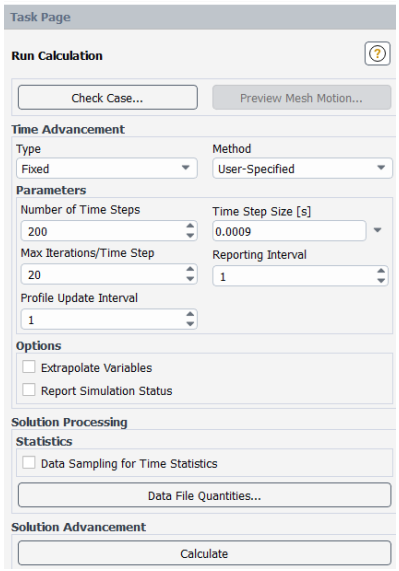


Figure 14. Solver

RESULTS AND DISCUSSION

Motor Selection as a Result of Vibration Analysis

The DC motor list is given below. Green painted DC motor is selected after several iterations discussed in the vibration analysis section of Materials and Methods, and by considering CFD results, cost, and weight.

Table 1. DC motor selection

No	Motor Model	Motor Speed [rpm]	Motor Dimension (Length x Width) [mm]	Motor Mass [g]	Unbalance Mass [g]	Unbalance Distance [mm]	Displacement [mm]	Force [N]
1	Emay Center RS385 Dc Motor 12-36V 12000 Rpm	12000	38x27.5	-	11	5	0.007	2.23
2	Emay Center RS385 Dc Motor 12-24V 8000 Rpm	8000	38x27	72.8	11	5	0.003	0.986
3	MLS RS385 12-24V Dc Motor 15000RPM	15000	43x27	-	11	5	0.052	3.513
4	Johnson 508100 3F1756	20000	40x25	50	11	5	0.021	6.141
5	Mabuchi RS-540SH-3780 Redüktörsüz DC Motor	9600	50x35	157	11	5	0.005	1.433
6	Motorbit RS550-2 14.4V 21000Rpm Redüktörsüz DC Motor	21000	60x35	-	11	5	0.024	7.324
7	RS545 14.4V 25000Rpm Redüktörsüz DC Motor	25000	54x35	-	11	5	0.035	10.626

CFD Simulation Results

The simulation explained in detail in the sedimentation analysis section of Materials and Methods is run for 200 time steps. The residuals plot is given below

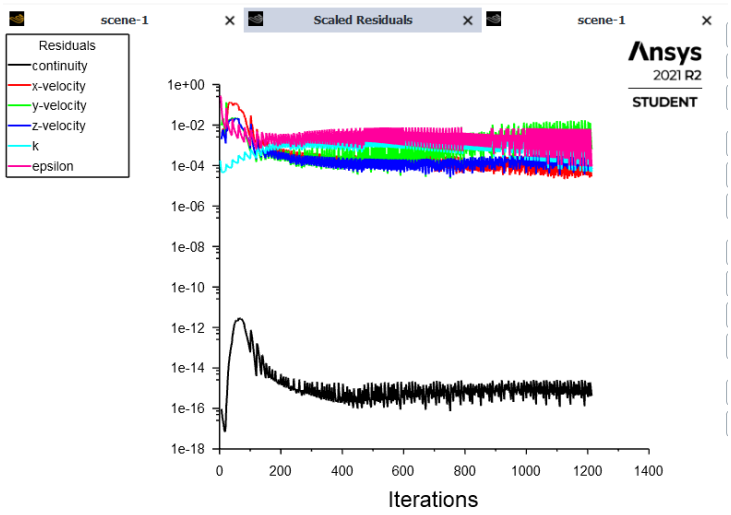


Figure 15. Residuals

The particle distribution inside the syringe at the start of the simulation (time step 1, t = 0.0009 sec) is given below. Note that the black face is the outer face of the syringe.

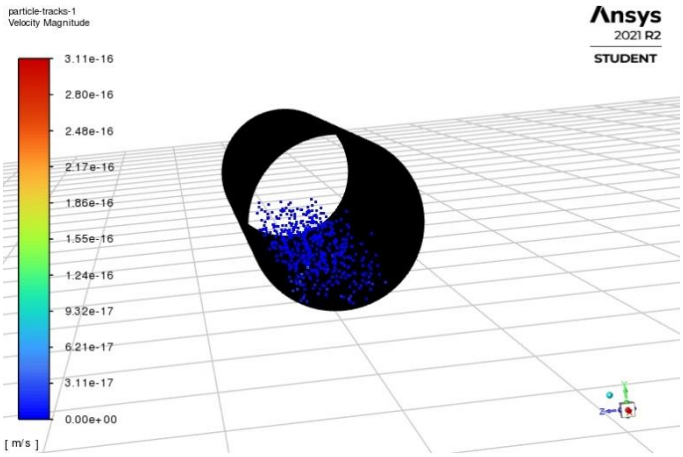


Figure 16. Particle Distribution at Time Step 0

The particle distribution at the end of the simulation (time step 200, t = 0.18 sec) is given below.

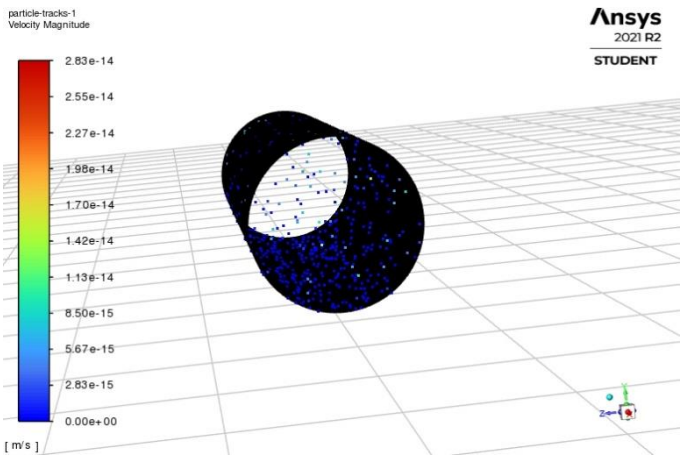


Figure 17. Particle Distribution at Time Step 200

Preventing Sedimentation Test

The test setup consists of the upper and lower fixtures locating the syringe firmly. The syringe is filled with the liquid suspension of black pepper powder infused water which is used in order to imitate a circumstance of laboratory work. The black pepper powder particles have a size of 500 microns diameter. [n.d.,2022]

To conduct the test, the DC vibration motor is run at 6 volts with the help of an external power supply. This voltage corresponds to 11000 RPMs in the DC vibration motor, and it proves to be more than enough to prevent sedimentation of a particle infused liquid. Following figures provide the observations for the initial mixing stage and the latter mixing stages which clearly help the reader to visualize the particles being homogeneous mixed within the fluid medium.

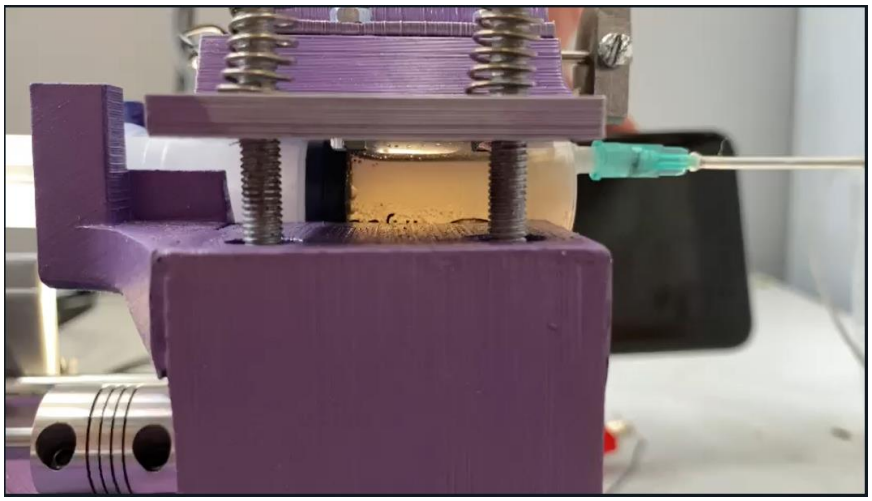


Figure 18. The test setup when the vibration motor is off

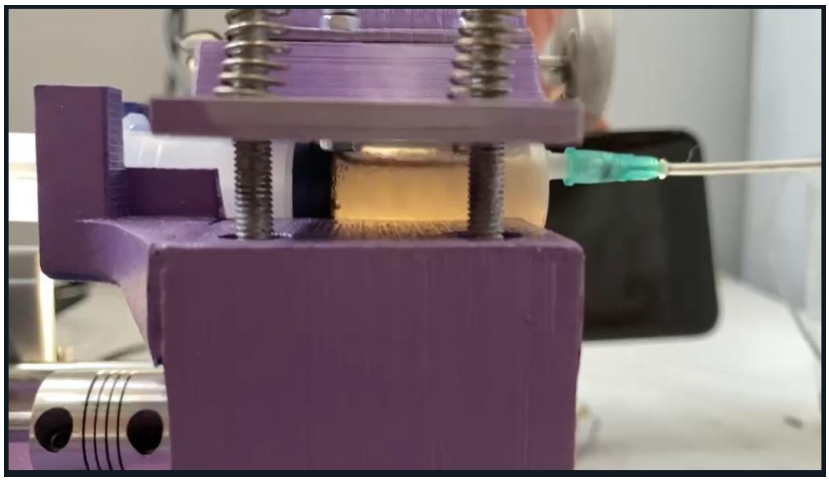


Figure 19. The vibration motor rotating at lower RPM range

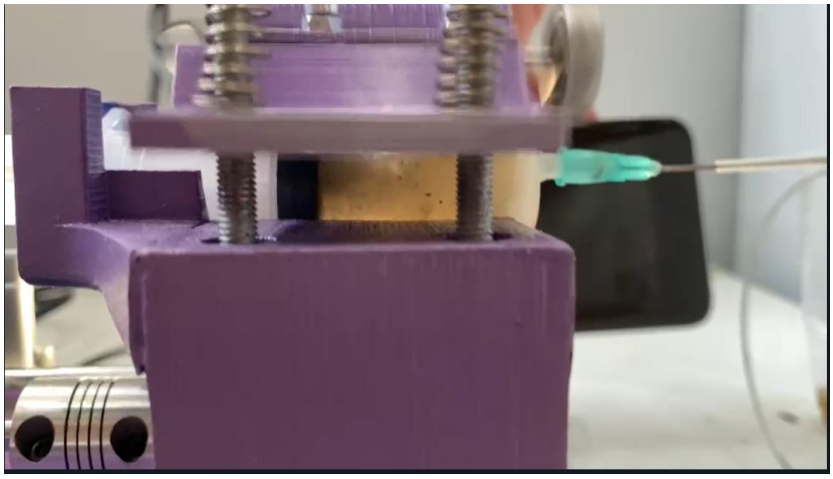


Figure 20. The vibration motor rotating at 11000 RPMs, where the mixing of particles, hence prevention of sedimentation is observable

CONCLUSIONS

This article has provided all the details with respect to the properties of the designed system, relevant engineering calculations, and the related analyses. As a result of all the work, the authors have put into designing the syringe pump product, quite a lot of experience and practice have been accumulated. Overall design at this last stage of the process incorporates aspects of vibratory systems to prevent sedimentation, unconventional yet effective mechanical systems such as a threadless screw to deal with power transmission, and electronic components for handling the control algorithms. All of the features involved in the design have been put there to meet the requirements and corresponding specifications initially laid out for the product, on top of the thought processes that ensured that the final system would be able to keep clear of potential failures.

Taking into consideration all of this, the authors believe that the final design presented will be capable of providing accurate flow rates at the desired values reliably by making use of the combination of a threadless screw mechanism and a stepper motor with micro-stepping; and preventing a large portion of sedimentation owing to the vibration motor and its placement on the system, which would otherwise adversely develop within the liquid medium. Although so many of the problems the syringe pump might be due facing in its workings have been thoroughly investigated, some slight concerns the authors have towards this design are one, whether or not the motor and the mechanical systems will be powerful enough to fully overcome the relatively large back pressures generated in the microfluidic channels and two, if the prolonged flow rates and thus the equally slow rotation of the stepper motor will cause significant fluctuations and pulsations in the flow.

FUTURE WORK

In order to find the optimum motor speed for the sedimentation prevention, the simulation process should be repeated with different motor speeds. Then some metric can be defined to show the sedimentation prevention efficiency. One can define sedimentation prevention efficiency S as the ratio of the standard deviation of the number of particles in XZ-plane vs. Y-axis graph for the unshaken syringe to the standard deviation of the number of particles in XZ-plane vs. Y-axis graph for the shaken syringe. Example graphs and calculation are given below. The mentioned axes and problem geometry is same as in *Figure 5. Problem Domain*.

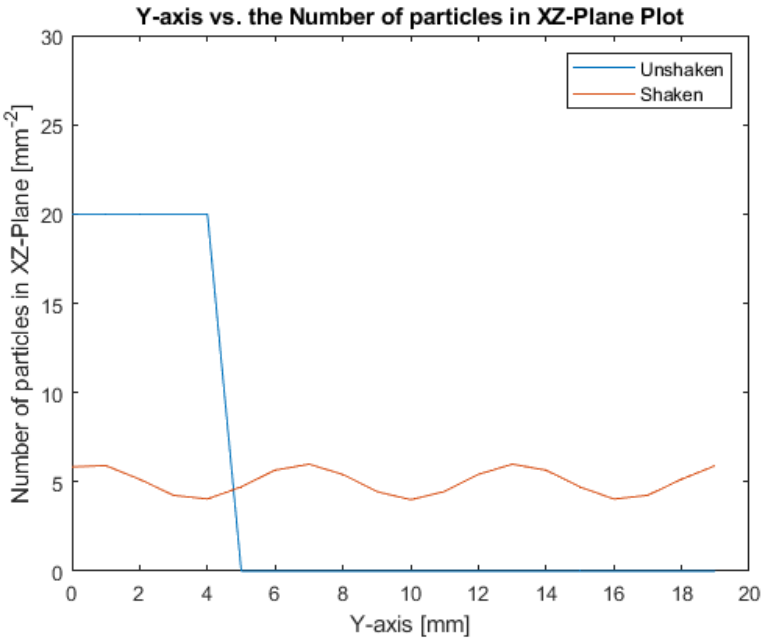


Figure 21. Y-axis vs. the Number of particles in XZ-Plane Plot

$$\sigma_{unshaken} = 8.88 \tag{19}$$

$$\sigma_{shaken} = 0.73 \tag{20}$$

$$S = \frac{8.88}{0.73} = 12.16 \tag{21}$$

The blue curve on the graph represents the unshaken syringe. The particles are sedimented at the bottom of the syringe, so the particle concentration is high at the bottom, and it is zero afterwards. On the other hand, the orange curve represents a well shaken syringe, and the concentration is more homogeneous over the y-axis. Note that the curves are drawn discretely, so each data point represents the number of particles inside a 1 mm thick plate over the y-axis. Also, for the plots, the data points should be the time average of the simulation since the simulation is transient.

A higher sedimentation prevention efficiency implies that the sedimentation is prevented more effectively. After running simulations with different motors, the motor with higher sedimentation prevention efficiency can be selected.

ACKNOWLEDGEMENTS

First and foremost, we want to thank Associate Professor Ender Yıldırım for providing supervision as well as accommodating this study in his laboratory, and F. Ginaz Almus, our teaching assistant, who guided us through this piece of work. They assisted and gave us priceless advice. The study was successfully finished, largely thanks to their inspiration and assistance. Additionally, we would like to express our gratitude to ME407 Lab and METU MEMS Lab for allowing us to design the system and perform our tests.

REFERENCES

1. **ANSYS Inc., (2022),** Students. Ansys for Students. Retrieved 2022, from https://www.ansys.com/academic/students
2. **Atay, A., Topuz, A., Sarıarslan, B., Yıldırım, E., Charmet, J., Couling, K., & Çetin, B. (2021),** Flow rate-controlled pipetting for microfluidics: second-generation flexible hydraulic reservoir (FHRv2). *Microfluidics and Nanofluidics*, *25*(1). https://doi.org/10.1007/s10404-020-02402-x
3. **Baas, S., & Saggiomo, V. (2021),** Ender3 3D printer kit transformed into open, Programmable Syringe Pump Set. https://doi.org/10.26434/chemrxiv.14718183.v2
4. **Collins, D. (2019),** *Microstepping for Stepper Motors. Linear Motion Tips*. Retrieved August 11, 2022, from https://www.linearmotiontips.com/microstepping-basics/
5. Ground black pepper: 32 mesh black pepper. Troyer's Spices. (n.d.). Retrieved July 7, 2022, from https://troyersspices.ca/shop/pepper-black-32-mesh/
6. **Lee, C. W., & Chou, J. H., (2020),** Developing a Novel Miniature 3D-Printed TLBS with High Mechanical Efficiency and Better Controllability. *Micromachines*, 11(7), 662. https://doi.org/10.3390/mi11070662
7. **Medel, F., Abad, J., & Esteban, V. (2022),** Stiffness and damping behavior of 3D printed specimens. *Polymer Testing*, 109, 107529. https://doi.org/10.1016/j.polymertesting.2022.107529
8. **Menbari, A., & Hashemnia, K., (2019),** Effect of vibration characteristics on the performance of mixing in a vertically vibrated bed of a binary mixture of spherical particles. *Chemical Engineering Science*, 207, 942–957. https://doi.org/10.1016/j.ces.2019.07.026
9. **MSC Software, (2021),** Student Editions. *MSC Software Student Editions*. Retrieved 2022, from https://www.mscsoftware.com/student-editions
10. **Samokhin, A. S. (2020),** Syringe Pump Created using 3D Printing Technology and Arduino Platform. *Journal of Analytical Chemistry*, *75*(3), 416–421. https://doi.org/10.1134/s1061934820030156
11. **Zhang, X., Xia, K., & Ji, A., (2020),** A portable plug-and-play syringe pump using passive valves for microfluidic applications. *Sensors and Actuators B: Chemical*, 304, 127331. https://doi.org/10.1016/j.snb.2019.127331

INVESTIGATION OF THE EFFECT OF HUB CURVE ON THE PERFORMANCE OF RADIAL COMPRESSOR FOR HIGH SPEED TURBOMACHINERY

O. Deniz YILMAZ, *okan.yilmaz@trmotor.com.tr,* TRMOTOR INC., 06800, Ankara, Turkey

ABSTRACT

This paper presents the design of a radial compressor with vaneless diffuser for high speed turbomachinery. The aim of this paper is to design a radial compressor with improved aero dynamic performance with better hub curve. The design process starts with the aerodynamic analysis of blade design and continue with structural and modal analysis of integrated disk and blades. A special attention is applied to meridional profile has a significant effect on surge/stall performance the compressor. The hub curve is optimized by using Bezier curve with 4 (x,y) control points and fitted to the arc segment. The verification of the aero design has been conducted using CFX software with focusing on a blade passage and vaneless diffuser. The structural integrity of blade and disk have been carried out at maximum rotational speed with Al2124-T851 material.

Keywords: Centrifugal compressor, hub curve, stress analysis, computational fluid dynamics, Al2124-T851

1. INTRODUCTION

Today's companies with heavy duty otto and diesel cycle reciprocating engines are still cost-effective options compared to popular hybrid electric vehicle rivals. These engines still attain levels of quality in term of low fuel consumption, better engine response, low initial costs, and long life cycle, meet the specified emission targets. These options require controllable and smooth engine power to meet the impending emission regulations such as nitrogen oxide (NO_x).

Nowadays, commercial heavy duty engines use a high performance turbocharger to satisfy the requirements in engine design. Turbochargers has a direct impact on specific fuel consumption, exhaust emission as well as to control engine power so development of high efficient turbochargers with more efficient radial turbine and compressor are emerging trend to improve economic impact of these engines. This can be achieved by designing an efficient radial blades which improve the inlet air flow of engine which ensure controlling exhaust emission in an accurate way [1].

Main components of a turbocharger are a radial compressor, main shaft and radial turbine. Turbine is rotated by an external combustion gases and compressor is driven by the turbine and torque is transmitted over main shaft. The system of this components are ideal because the compressor works no any pressure on other part. This is why that radial compressors should design in an efficient way with full understanding [2].

It is essential to understand behavior of radial compressor but it is not too easy just by using test setup and calculation. Since, researchers used different approach such as computational fluid dynamics, optimization algorithm and developed empirical equations to design radial impeller. These all researches were based on blade geometry and passage of the radial impeller [3-6]. However, the support of this techniques are not enough validation of actual performance of impellers due to high experimental cost, difficulties to in confirmatory test benches. Moreover, air flow in blade passage is very fast so complex and the air flow is moving through positive pressure gradient. That’s is why, air flow is slowing down along the mean line of blade passage so this result in dramatically loss of impeller performance [7].

The second issue in the blade passage that air flow reaches critical relative Mach number when approaching tip of impellers which means some area near inlet might be choked. This issue is mostly occur in high pressure ratio radial compressor because air flow must spends more time in blade passage to accelerate enough to gain desired pressure ratio. Jet and wake flows is generated in this issue due to pressure and velocity different through inlet to outlet of blade passages. This case can be solved adding splitter blades at the tip of the flow passage. However, splitter blade is not directly addressed this problem due to not ensure of jet and wake

flow locations. Hence, Stahler [8] proposed that the critical relative Mach number at the tip should not be greater 0.8 to do not face efficiency loss.

The third issue while designing radial compressor impeller is its diffuser afterwards. Compressor-diffuser arrangement is the same relation as rotor-stator matching; therefore, leaving air flow from the compressor tip is non-uniform as expected so there is another major loss in the diffuser section. Interestingly, researches in the literature is mostly focusing on predicting the losses at the diffuser to improve efficiency [9-11].

The final issue is its manufacturing cost based on design perspectives. In industry, radial compressor is restrained due to fact that impeller design is based on to meet the required mass flow and efficiency stated by turbine work and it should be producible and low cost. Another concern for designer is the manufacturing technique. Integrated bladed disk should be manufactured by casting or cnc milling. Casting is highly cost effective if the number of production is numerous. However, casting is restricting the blade angles so flow capacity and efficiency is limiting. On the other hand, designer can work with high blade angles or lean angles to improve flow rate and efficiency [12] by cnc milling but cost and production time would be risky concern.

Turbocharges generally provide average 80% percent total to total isentropic stage efficiency (inlet to outlet) while total pressure loss is mostly coming from in diffuser and volute profile so demand in industry would be better flow range and increase in stage isentropic efficiency. Kurauchi and Barbosa [13] proposed the design of radial compressor for natural gas in their design perspectives. Firstly, 1d calculation of impeller sizing and blade angles is completed. Second stage is continuing with blade passage flow analysis in the meridional plane. Finally, CFD analysis of pre-design is verified to improve final design.

Aungier model is one of the best guideline for preliminary design in the open literature. He [14] gave the initial and efficient approach for blade angles at hub and shroud. He also suggested that hub profile in the meridional plane should properly studied because it is essential to improve impeller efficiency [14]. Another importance parameter of impeller design is the inlet, outlet area, flow, blade angles, inlet Mach number and outlet mass flow rate which defines the overall efficiency that is correlated using empirical equation by Aungier [14].

By the way, there is also key parameters about the structural integrity of impeller. According to Aungier [14], the tip speed is key parameter to define the material as well as structural integrity. Increasing backsweep angle at tip is decreasing stress level while increasing temperature ratio of stage. Therefore, designer should be aware of the required pressure and mass flow range to correctly define the backsweep angle and tip speed. However, the back sweep angle should be kept at minimum to improve mass flow capacity so Aungier defines the

work input coefficient to control tip speed. Zahed and Bayomi [15] indicated that higher back sweep angle decrease flow capacity. The relation between tip speed, back sweep angle, mass flow range, pressure ratio and temperature ratio can be used as an optimization parameter to improve efficiency by ensuring the structural integrity of the compressor.

2. IMPELLER DESIGN

The impeller of the compressor has a 97.4 mm b-width exducer diameter with a tip speed of 489.6 m/s. The diameters of leading edge are 18 mm at hub and 70 mm at tip, respectively. The stage flow coefficient of 0.2, isentropic efficiency 87% and total pressure ratio 4.6 has been taken as design parameter for 1D flow calculation.

Table 1. Main Parameters of a Radial Compressor Impeller

Term	Definition	Term	Definition
T01 = 288.15	Inlet stagnation (Total) Temperature at SLS [K]	Pr = 4.6	Desired Pressure ratio
P01 = 101325	Inlet stagnation (Total) Pressure at SLS [Pa]	n = 0.87	Desired isentropic efficiency
mdot = 0.68	Mass flow rate [kg/s]	w = 96000	Rotational speed [rev/s]
Q_0 = 0.833	Inlet Volume flow [m^3/s]	fi = 0.2024	Stage flow coefficient
M_i = 0.755	Inlet Mach Number at mean	M_U = 1.4387	Mach Number at exit
d_h = 18	Hub diameter at inlet[mm]	d_s = 70	Shroud diameter [mm]
d_2t = 97.4	Exducer diameter [mm]	C_a1 = 177.42	Axial inlet [m/s]

The fluid properties are taken standard atmospheric conditions for 1D calculations that known as a standard sea level (SSL) term. The main parameters of a radial compressor is shown in Table 1. The calculation in preliminary design should include the effect of various losses caused by tip clearance, recirculation and friction loss. After the consideration of design requirements and losses, the blade, flow angle, temperature, pressure and initial geometry could be found for the preliminary part. The blade, flow angle and the design constraint is shown in Table 2.

Furthermore, the awareness of the velocity triangles at hub, mean and tip gives the quick insight to stress, temperature and pressure provide detailed design constraint. Moreover, the meridional profile of hub and shroud should be connected while increasing air velocity throughout leading edge to trailing edge because meridional view has an imperious effect on overall requirements [16]. The hub curve is generated with Bezier curve by using four control points and fitted to the arc segment and shroud curve is design with spline curve. Shroud profile is not optimized due to fit previous casing to conduct experiment. The meridional profile of hub and shroud profile with vaneless diffuser can be seen in Figure 1.

Additionally, the back swept angle that is the beta2, improve the flow capacity of the compressor for wide range of shaft speed [17]. Another positive effect of backswept blades decrease the stress level at tip. However, high backswept blade increase the temperature as expected so design should be aware of the thermal gradient at blade tip. Since, some the material like aluminum is highly nonresistant to high temperatures.

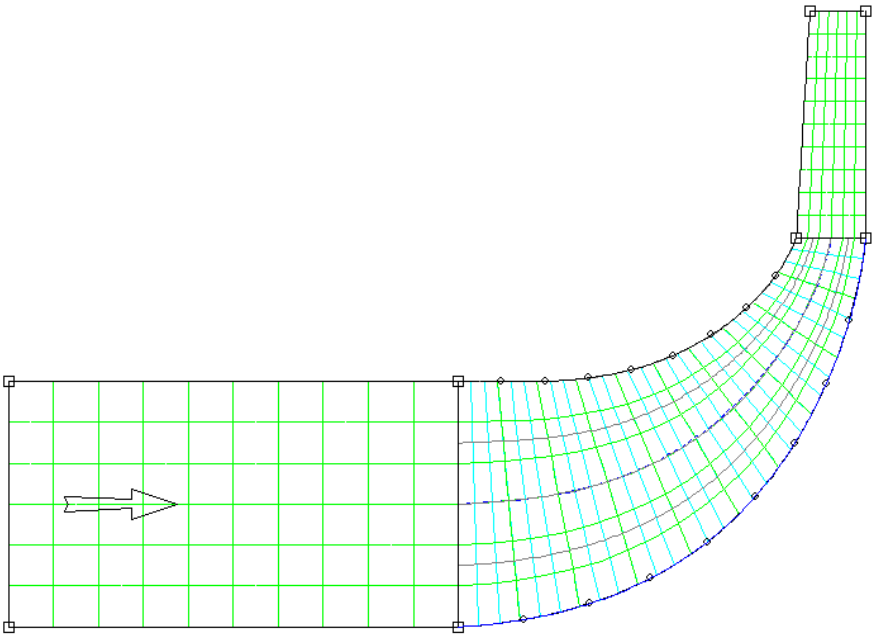


Figure 1. The meridional profile of hub and shroud profile with vaneless diffuser

BladeGen tool has been used to create 3d model of the radial impeller after determination of 1D model. Splitter blades are inserted by controlling flow velocity through leading to trailing edge. Since, short splitter blades minimize flow range, increase blade loading at main blades so become useless. The blade to blade view at hub and shroud can be seen in Figure 2, respectively.

Table 2. Blade, Flow Angles and Design Constraints

Term	Definition	Term	Definition
ns = 1.7644	Specific speed	ds = 1.8485	Specific diameter
Rr = 0.7136	is the ratio of impeller eye to tip diameter	Z = 14	Number of impeller
T03 = 470.2	Diffuser stagnation (Total) Temperature [K]	P03 = 466.1	Diffuser stagnation (Total) pressure [kPa]
beta2 = 42	Backswept angle [°]	slip = 0.841	Slip factor
P1 = 83.34	Pressure at inlet [kPa]	P2 = 235.03	Pressure at exit [kPa]
P02 = 522.4	Total (Stagnation) pressure at tip [kPa]	ro_2 = 2.195	Density at tip [kg/m^3]
b_1h = 62.98°	Blade angle at inlet hub	a_2h = 17.5°	Flow angle at exit hub
b_1 = 34.63°	Blade angle at inlet mean	a_2 = 20.4°	Flow angle at exit mean
b_1t = 26.92°	Blade angle at inlet tip	a_2t = 22.9°	Flow angle at exit tip

Blade angle at inlet and outlet is the major constraints to represent real life aerodynamics performance therefore the detailed decision of it must be accurate off course. It is essential to know that the blade angle at theta direction should converge at trailing edge because it excessively increase blade loading at High Mach number so work input prediction become pointless. Thus, matching turbine work output to compressor input would be nightmare for the designers. The blade angle at theta direction and thickness of the blade can be shown in Figure 3.

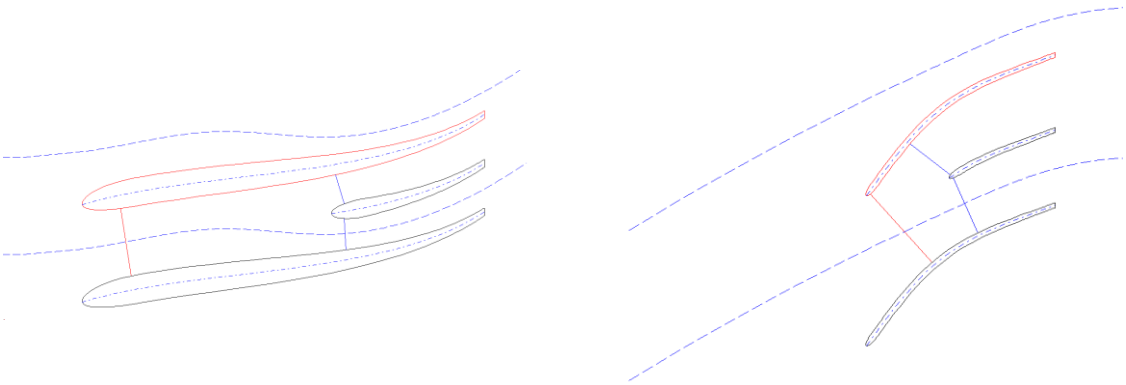


Figure 2. The blade to blade view at hub (left) and shroud (right)

Lastly, blade thickness should withstand the centrifugal load and gas load so appropriate thickness should be chosen for initial design.

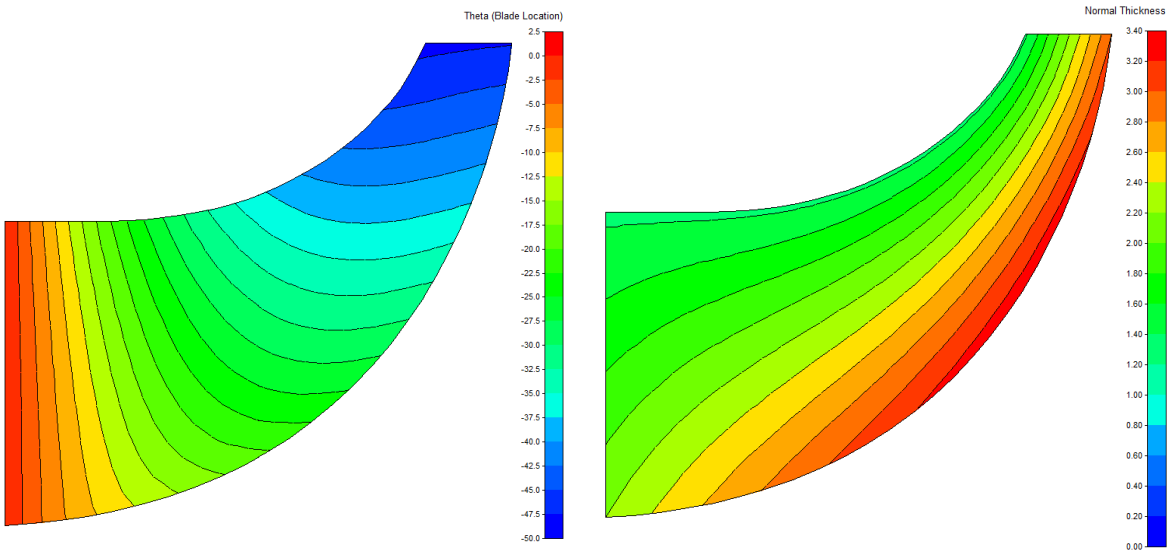


Figure 3. The blade angle at theta direction and thickness of the blade

After creating model of impeller, we continue to generate the mesh of impeller. The geometry is exported through TurboGrid which is a powerful blade mesh tool. These meshes are used in the workflow to solve complex rotating blade passage problems. Tip clearance is added while meshing the geometry. The tip clearance is taken as 0.25 at leading edge and 0.45 at trailing edge millimeter, respectively. Mesh information can be seen in Table 3.

Table 3. Mesh Information of CFD calculation

Total Nodes	1324160	Total Elements	1248828
Minimum Face Angle	27.2445°	Maximum Face Angle	152.756°
Maximum Element Volume Ratio	12.4458	Minimum Volume [m^3]	2.49e-15
Maximum Edge Length Ratio	572.169	Maximum Connectivity Number	10

3. AERODYNAMIC PERFORMANCE

3D flow analysis of radial compressor is compulsory for initial assessment of prepared radial impeller. The model needs to validated by compressible viscous flow solver to estimate performance. Even if the experimental techniques are more reliable for a such application but the iteration of design stage should be eliminated by viscous flow solver. In this present design, Ansys CFX flow solver with shear stress transport (k-ω SST) turbulence model is used to estimate the performance of a radial blades because it is best model for rotating for in the literature [18].

The CFD simulation completed with blade passage and vaneless diffuser passage. Inlet is extended 50 mm from the blade leading edge and diffuser diameter is taken as 150 mm. Tip clearance is changing through leading edge (0.25 mm) to trailing edge (0.45 mm). The result of simulation is paramount importance but review of the solution is more important. The meridional velocity, absolute and relative Mach number through leading to trailing edge, pressure and temperature should be evaluated to ensure the expected air flow. The meridional velocity and total pressure can be seen in Figure 4.

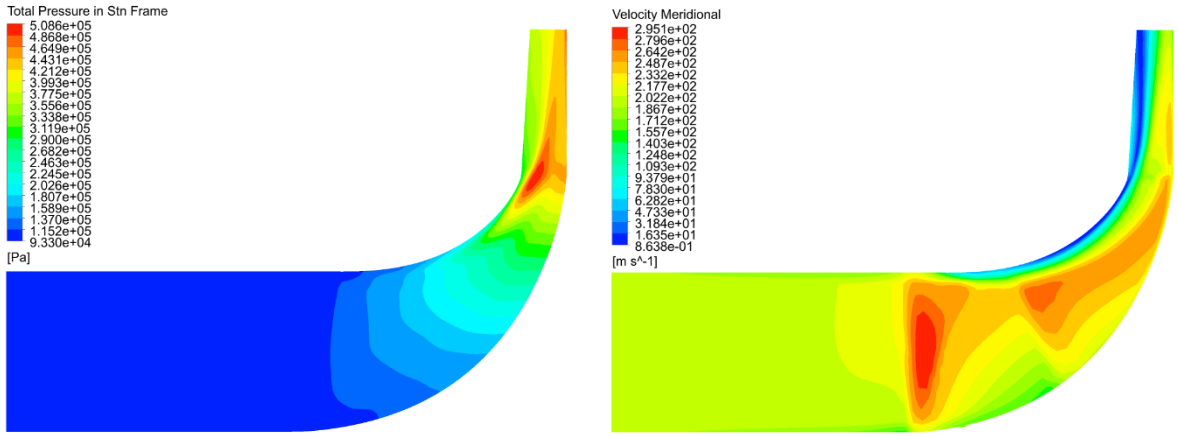


Figure 4. Meridional view of Total Pressure (top) and Velocity (bottom)

The meridional plots show that the result is quite similar to 1D calculation of preliminary design. The pressure and velocity increase through meridional profile. The blade loss is excessive near to 0.8 span due to tip clearance which negatively affect the flow passage [19]. The tip clearance can minimize by increasing quality of manufacturing but the cost is always would be major concern. Since, designer should be aware of its advantage against cost.

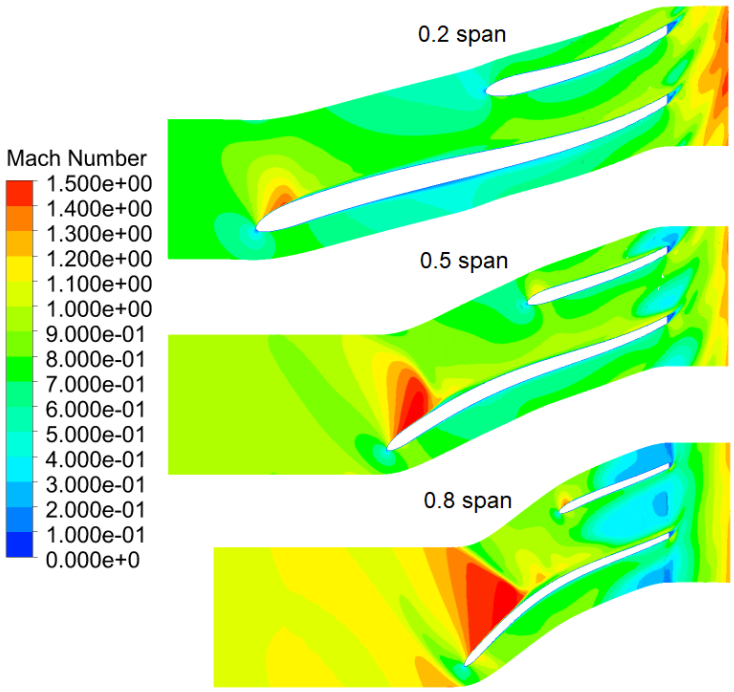


Figure 5. The Mach number at 0.2, 0.5 and 0.8 span

The Mach number at 0.2, 0.5 and 0.8 span show that is always increasing in Figure 5 and these result is similar to general air flow [20].

4. STRUCTRUAL INTEGRITY

Integrated bladed radial compressor must withstand the gas, centrifugal, thermal and maneuver load for operation. The finite element structural analysis of radial impeller has been simulated to divide into 7 cyclic sector. The aluminum 2124-T851 has been used evolution of the model that has a minimum yield strength of 358 MPa at 130 °C with density of 2780 kg/m^3. The geometry has been meshed can be seen in Figure 6.

The validation of stress intensity is proportional to centrifugal load so validation of stress has been calculated at a speed of 96000 rev/min.

The equivalent von-misses stress, total deformation and temperature can be seen in Figure 7 and Figure 8, respectively. The maximum von-mises stress appears the root of the blade and it is equal to 346 MPa. The temperature is nearly 50° where the maximum stress appears. The maximum temperature is appeared the tip of the blade and it is equal to 130°. The stress is nearly 276 MPa there and it is well below the yield stress of the material.

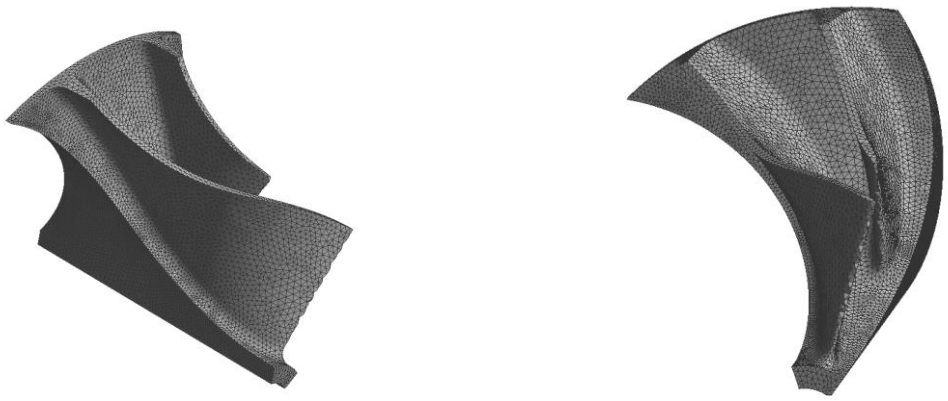


Figure 6. Finite Element Mesh

6. CONCLUSION

The requirement of radial compression with high pressure ratios can be achieved with small radius at speeds of 96000 rpm. In a high speed turbomachinery application such radial compressor achieves outstanding stage isentropic efficiency and can be used to maximize to boost for higher power and can be also operated at low rotational speed with acceptable power without surging. The procedure of the design should begin with 1D calculation and continue with generating hub and shroud curves. The results show that hub profile in the meridional plane has a huge effect on impeller efficiency. Moreover, the better hub curve decreases the stress level.

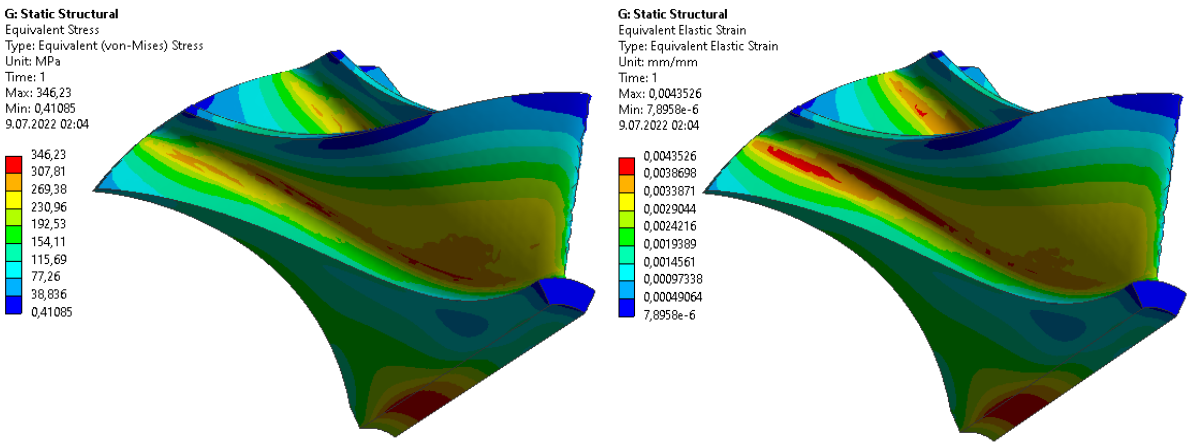


Figure 7. Equivalent (von-mises) stress and total deformation

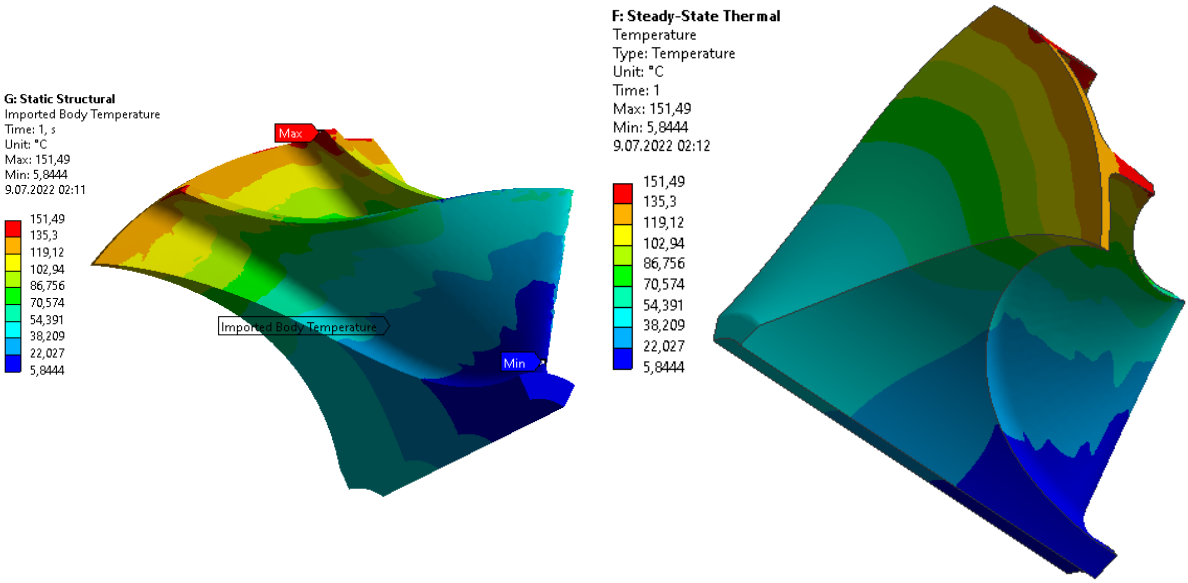


Figure 8. Temperature Distribution

7. ACKNOWLEDGEMENT

The author wish to thank the Teknofest 2019 for their support and contributions to this research. All supports are gratefully acknowledged.

REFERENCES

1. **Frese, F., Einzinger, J., and Will, J. (2012),** "Design optimisation of an impeller with CFD and Meta-Model of optimal Prognosis (MoP)". in 10th International conference on turbochargers and turbocharging, London, England.

2. **Aungier, R. H. (2000),** "Centrifugal compressors. ASME press New York.

3. **Cosentino, R. (2001),** "Expert system for radial impeller optimisation". in Proceedings of the 4th European Conference on Turbomachinery, 2001.

4. **Perdichizzi, A. and Savini, M. (1985),** "Aerodynamic and geometric optimization for the design of centrifugal compressors". International journal of heat and fluid flow, 6(1): p. 49-56.

5. **Xu, C. and Amano, R. S. (2012),** "Empirical design considerations for industrial centrifugal compressors". International Journal of Rotating Machinery, 2012.

6. **Cho, S.-Y., Ahn, K.-Y., Lee, Y.-D., and Kim, Y.-C. (2012),** "Optimal design of a centrifugal compressor impeller using evolutionary algorithms". Mathematical Problems in Engineering, 2012.

7. **Bhinder, F. and Ingham, D. (1974),** "The effect of inducer shape on the performance of high pressure ratio centrifugal compressors". in Turbo Expo: Power for Land, Sea, and Air. American Society of Mechanical Engineers.

8. **Stahler, A. F. (1961),** "Transonic flow problems in centrifugal compressors. SAE Technical Paper.

9. **Ebaid, M. S. Y. and Al-Hamdan, Q. Z. M. (2017),** "Design of a single stage centrifugal compressor as part of a microturbine running at 60000 rpm, developing a maximum of 60 kW electrical power output". American Journal of Aerospace Engineering, 4(2): p. 6-21.

10. **Brown, W. B. and Bradshaw, G. R. (1947),** "Method of designing vaneless diffusers and experimental investigation of certain undetermined parameters. FLIGHT PROPULSION RESEARCH LAB CLEVELAND OH.

11. **Stanitz, J. (1951),** "Some theoretical aerodynamic investigations of impellers in radial-and mixed flow centrifugal compressors". ASME.

12. **Tough, R., Tousi, A., and Ghaffari, J. (2010),** "Improving of the micro-turbine's centrifugal impeller performance by changing the blade angles". ICCES, 14(1): p. 1-22.

13. **Kurauchi, S. and Barbosa, J. (2013),** "Design of a Centrifugal Compressor for Natural Gas". Revista de Engenharia Térmica, 12(2): p. 40-45.

14. **Aungier, R. H. (2000),** "On the Effectiveness of Aerodynamic Design and Analysis for Centrifugal Compressors". in ASME International Mechanical Engineering Congress and Exposition. American Society of Mechanical Engineers.

15. **Zahed, A. H. and Bayomi, N. N. (2014),** "Design procedure of centrifugal compressors". isesco journal of science and technology, 10(17): p. 77-91.

16. **Xu, C. and Amano, R. (2012),** "Meridional considerations of the centrifugal compressor development". International Journal of Rotating Machinery, 2012.

17. **Barr, L., Spence, S., and Eynon, P. (2009),** "Design and Analysis of a Radial Turbine with Back Swept Blading, in Fluid Machinery and Fluid Mechanics. Springer. p. 115-121.

18. **Röyttä, P., Grönman, A., Jaatinen, A., Turunen-Saaresti, T., and Backman, J. (2009),** "Effects of different blade angle distributions on centrifugal compressor performance". International Journal of Rotating Machinery, 2009.

19. **Casey, M., Krähenbuhl, D., and Zwyssig, C. (2013),** "The design of ultra-high-speed miniature centrifugal compressors". in European Conference on Turbomachinery Fluid Dynamics and Thermodynamics ETC.

20. **Tamaki, H., Unno, M., Kawakubo, T., and Hirata, Y. (2010),** "Aerodynamic design of centrifugal compressor for AT14 turbocharger". IHI engineering review, 43(2): p. 70-76.

AN EXPERIMENTAL And NUMERICAL STUDY OF MULTI-STAGE HOT FORGING PROCESS OF CW617N BRASS ALLOY

Hakan COŞKUN, *hakan.coskun@torunmetal.com* Torun Bakır Alaşımları Metal Sanayi ve Ticaret A.Ş., 41480, Kocaeli, Turkey

Tayfun ORHAN, *tayfun.orhan@torunmetal.com* Torun Bakır Alaşımları Metal Sanayi ve Ticaret A.Ş., 41480, Kocaeli, Turkey

Sami KURAL, *sami.kural@torunmetal.com* Marmara University, 34722, Istanbul, Turkey

Yusuf KAYNAK, *yusuf.kaynak@torunmetal.com* Marmara Üniversity, 34722, Istanbul, Turkey

ABSTRACT

The multi-stage hot forging is critical as it enables the production of a large number of brass fittings. Experimental analysis is performed by examining microstructure and hardness characteristics of multi-stage hot forged specimens. Numerical simulation of this process and predicted outputs such as strain distribution through using SIMUFACT software are presented. Experimental results reveals that the metal flow lines is regular and no dead metal areas are found. The results obtained from the study will contribute to a good understanding of the forging load, the metal flow lines and the forming conditions for the designers at both forging stages.

Keywords: Multi-stage hot forging process, Metal flow line, Effective strain-stress distribution, Numerical analysis, Brass alloy

1. INTRODUCTION

The multi-stage hot forging process is one of the most low-cost methods used in the production of fittings, depending on the part size. The fittings are commonly used in production industry [Mebmer, et al. (2007), Gangopadhyay, et al. (2011)]. Brass material is the most common type of material used in the production of fittings due to its high corrosion resistance, good machinability and good mechanical properties. Brass materials with high copper content (more than 60%) are generally used in forging processes in order to give enough plastic deformation to the material [Fadhil, et al. (2018)]. If the annual production volume is generally over 20,000 pieces, multi-stage hot forging process is preferred

depending on the part sizes. The multi-stage horizontal forging technology is used in hot, warm and cold forging processes [Mebmer, et al. (2007)].

Several finite element (FE) and finite volume (FV) programs have been developed to understand process faults such as pre-draft form of part during hot forging, material flow into the die cavities, incomplete filling of the die cavities, press loads, stresses and the effect of excessive material usage. It has been observed that such analysis studies are widely used in the literature in the analysis the multi-stage horizontal hot/cold forging process. Ohdar et al. [Gangopadhyay, (2011)] have used the DEFORM 3D program to analyze multi-stage hot forging of rail wheels, including blow molding, forging, and punching processes. They used finite element method with rigid-viscoplastic material model for thermo-mechanical analysis of the process. They have shown that three-dimensional finite element simulations can be used efficiently in the analysis, design and optimization of process complexities for the multi-stage rail system wheel production process, instead of traditional analysis methods. Han-Sung and Shao-Yi, [Huang, (2016)] developed a process to solve crack transformation problems in the gas connection part caused by poor forging process design in the cold forging process. They used the DEFORM 3D analysis program in their work and carried out microscopic examinations with an optical microscope and SEM method to observe the internal micro-crack formation and the distribution of metal flow lines. They presented the stress and strain distributions formed in the gas fittings by using the metal forming program. They reported that the narrower the metal flow lines, the more easily the work piece would be damaged [Huang, (2016)]. Qiang et al. [Chen, (2017)] have worked on the production of deep blind hole brass parts in a 6-step multi-stage cold forging process. They used a finite element simulation to validate the multi-stage cold forging process and to show strain distributions and flow lines. They designed and produced the forging dies according to the simulation results they obtained. In their experimental studies, they have shown that the effect of the strain hardening that occurs in cold forming and the distribution of the flow lines are compatible. As a result of these studies, they significantly increased production efficiency. Shao-Yi and Yu-Tuan [Hsia, (2015)] conducted analytical and experimental studies on the development of the cold forging process of hex nuts. They used the DEFORM 3D program to analyze the process at different stages in their analytical work. They applied compression tests in order to compare the differences between the equation defined in the simulation program and the experimental results. At the same time, they performed hardness and metallographic tests to understand the cold forming properties of the forged part. The results of the research revealed that it is beneficial for the machine companies to recognize the forming conditions and forging load at various stages before forming the fastener. Xu et al. [Zuo, (1999)] reported the contribution of FEM simulation to metal forming and discussed

the critical techniques of three-dimensional FEM simulation for the multi-stage forging process. They developed a CAD / CAE integration system to simulate the industrial multi-stage metal forming process. They simulated the complex multi-stage forging process to analyze the three-dimensional metal flow of the lever shaft using solid models of forging dies. Simulation results showed consistency with the workpiece. Jin-Hee et al. [Lee, (1996)] designed a process sequence for multi-stage cold forging to be used to shape the workpiece using the rigid-plastic finite element method. The numerical approach in this study deals with axially symmetrical deformations. In the study, forging loads, effective strain distributions and velocity distributions, which provide useful information for process design, were examined. Hongwei et al. [Jiang, (2020)] studied over distribution of the metal flow lines during the hot forging of the bearing ring part. They have applied two different hot forging processes in order to eliminate and optimize the irregularities of the flow lines brought about production method for the bearing ring. They have demonstrated with simulation and experimental studies that the punching die and punch recess position has a notable effect on the metal flow line transformation. In addition, they investigated that the flow lines in the given direction have shown mechanical anisotropy in the tensile direction of the bearing ring part. Joun et al. [Joun, (1998)] presented a simulation technique for the forging process with a spring-added die. At the end of the studies, they showed that the die with spring added reduces the forging load and its effects on metal flow lines.

Xiao et al. [Shen, (2015)] applied that experiments and finite element method to study metal flow in shaping the rail wheel. They proposed axially symmetrical modeling in the wheel rolling process to predict metal flows in the radial direction. According to the results of the research, they showed that the axial symmetric method is effective for estimating the metal flows in the radial direction and analyzing the movement relations of the tools during the wheel rolling. Lee and Joun, [Lee, (2009)] combined two and three dimensional simulation techniques to analyze the multi-stage automatic cold forging process steps in their work. They used the forging simulation known as AFDEX on the basis of the rigid-plastic finite element method. Quadrilateral elements were used for two-dimensional simulations while tetrahedral elements were used for three-dimensional simulations. They demonstrated that the importance of using two- and three-dimensional integrated simulations in terms of solution precision, accuracy and computational efficiency.

In this study, the hot forging characteristics of the brass alloy were investigated by simulating the two-stage hot forging process. The distribution of the strain, stress and the forging flow lines occurring in the brass part during the two-stage hot forging process and their resulting effects on the forging process were presented. The microstructure images showing the

distribution of metal flow lines were obtained through the experimental studies. Afterward, the microstructural images obtained were compared and evaluated with the simulation results.

2. MATERIALS AND METHODS

Experimental Method

In this study, CuZn40Pb2 (CW617N) brass material was used as a workpiece. The chemical composition of this material is presented in Table 1. The microstructure of the workpiece material includes average grain size of about 50 μm and 60 μm for transverse direction and longitudinal direction respectively, as depicted in Fig 1. The microstructure images were obtained at 1000X magnification. Microstructures of transverse and longitudinal direction are both the alpha-beta phase with Pb particle. Lead (Pb) particles usually precipitate within the alpha phase [Hsieh, (2013)]. The samples were grinded and polished, respectively before the etching. For microstructural observations the samples were etched with 30 mL aqueous solution, 3.5 mL hydrogen peroxide and 4.25 g ammonium persulfate for about 30 seconds. For macro observations (as metal flow line) the longitudinal cross sectioned of the part was etched with 10 mL nitric acid and 90 mL aqueous solution for about 4 minutes. Hardness of specimens were measured under 100 g applied load for 10 seconds and the average value of five mesaurements is reported.

Numerical Method

SolidWorks program is used to create the 3D geometric model of dies, punches and workpieces. The solid parts are transformed into the SIMUFACT forming program for simulation of the two-stage hot forging process. Fig 2 displays the two-stage hot forging process of the analyzed brass part. The two-stage hot forging process consists of preforming and final forging stages. The first stage is the preformation of the brass part and the second stage is the base metal working process. Fig 3 shows that FV simulation model for the two-stage hot forging process.

Table 1 Chemical composition and physical properties of the studied brass alloy [Sarbak, (2018)]

Composition	Cu	Zn	Pb	Sn	Fe	Ni	Al	others	
CuZn40Pb2 (CW617N)	59.0	Rem.	2.5	0.3	0.3	0.3	0.05	0.2	
Physical properties	**Phase Structure**	**Modulus of Elasticity** *(GPa)*		**Density** *(g/cm^3)*		**Thermal connectivity** *(W/(m.K))*		**Thermal expansion coefficient** *(10^{-6}, 1/K)*	

α, β	96	8.43	113	21.1

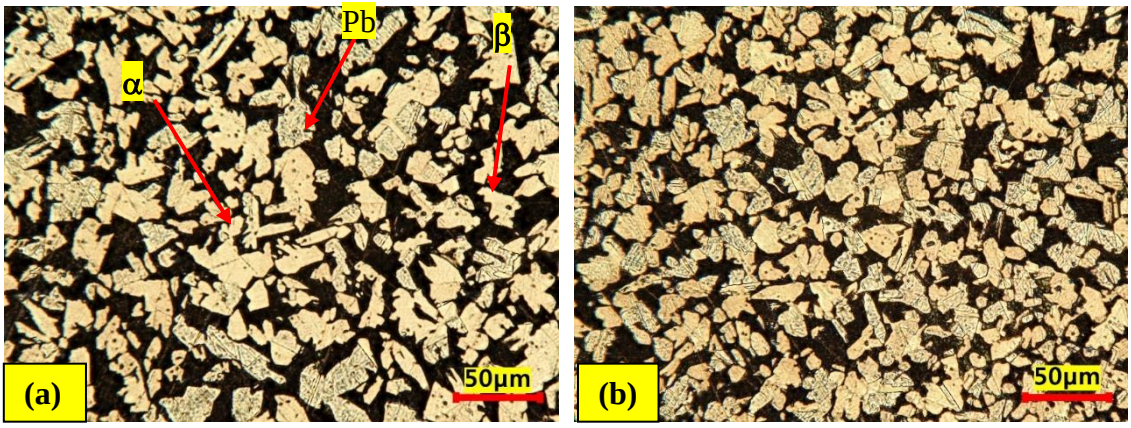


Figure 1 Microstructure of the brass alloy, (a) Longitudinal direction, (b) Transverse direction

The three-stage horizontal hot forming machine with maximum load of 900 kN was used for forward and backward processing movements in the slider-crank mechanism. Horizontal multi-stage forging press used in this study have an integrated shearing facility, which enables the induction-heated bars to be sheared to the required length [Mebmer, (2007)]. The work material, die and simulation parameters used to analyze for the two-stage hot forging process are displayed in Table 2. In this study, it was used the coulomb and shear stress friction model (stated as the combined friction) as friction model approach. This approach comprises the possibility to designate the biggest value to the frictional shear stresses for high contact stresses [Behrens, (2011)]. The interface friction factor value is taken into account as 0.18 for lubricated conditions as stated by Burte's work [Burte, (1990)].

Table 2 Simulation parameters for the Simufact Forming analysis

Workpiece / Die prope	Elastic-Plasticity / Rigidi
Die Temperature	200 *(°C)*
Workpiece Temperature	700 *(°C)*
Mesh numbers	14.750
Punch speed	394 *(mm/s)*
Interface friction factor	0.18
Friction model	Combined (Coulomb and Shear stress) friction

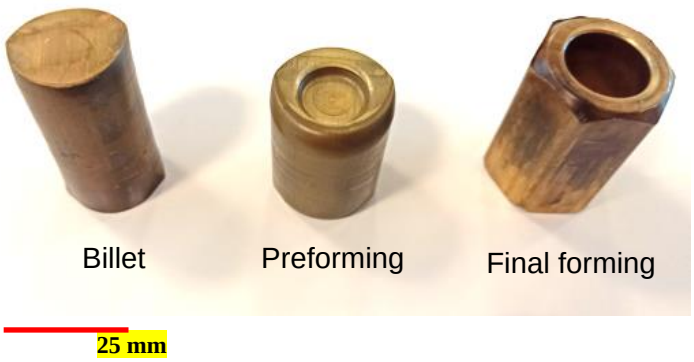
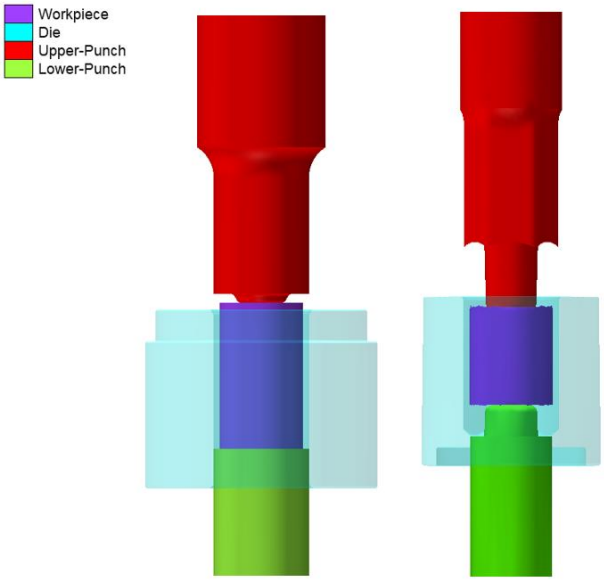


Figure 2 The forging workpieces in the different stages



(b)

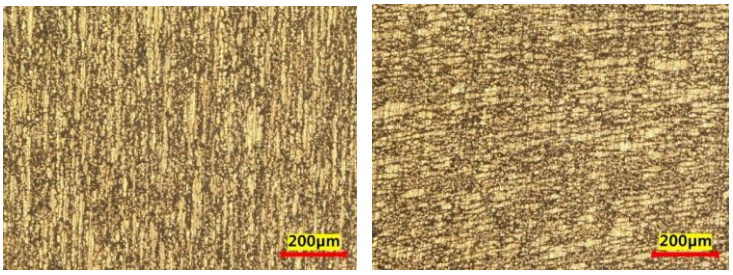
Figure 3 Finite volume (FV) simulation representation for the two-stage hot forging process in 3D, (a) Preforming process, (b) Final forming process

3. RESULTS AND DISCUSSION

Microstructural Examination

The microstructures of the forged brass workpiece are depicted in Fig 4. As can be seen from the microstructures, the grains are elongated with respect to deformation direction. This elongation of the grains will add anisotropic property to the material. The elongated grain extent at the sub-section of the forged brass material is small. Accordingly the grains are comparatively coarse as shown Fig 5(d). Hardness value of bottom surface and internal wall of the forged brass workpiece is 130 HV and 125 HV, respectively. Hardness value of the billet and the preform material is 106 HV and 108 HV, respectively. The two-stage hot forging

process is capable of increasing the mechanical properties of the brass alloy. Hereby, the forged brass workpiece has high hardness and mechanical strength.



(a) (b)

Figure 4 Microstructure images at the longitudinal and transverse direction of the hot forged brass material, (a) the longitudinal cross-section, (b) the transverse cross-section

Distribution Of Metal Flow Lines

The hot metal deformation has an substantial effect on the development of the metal flow lines. During plastic deformation, the hot metal primary flows in the direction where the value of the principal stress is the highest. The directions of the shear stresses are perpendicular to the directions of the flow lines [Chen, (2017)], [Jiang, (2020)]. Metal flow lines for certain regions extracted from the experimental study and the cross section of the forged brass material are shown in Fig 5. It is shown that there are no any flaw at corners and the critical section of the workpiece. The experimental results show that the distribution of the flow lines in the forged brass material is suitable as no hot deformation defects and this flow lines are distributed uniformly during the two-stage hot forging process. In the experimental examinations, no dead metal zone were seen due to the restriction of the metal flow line.

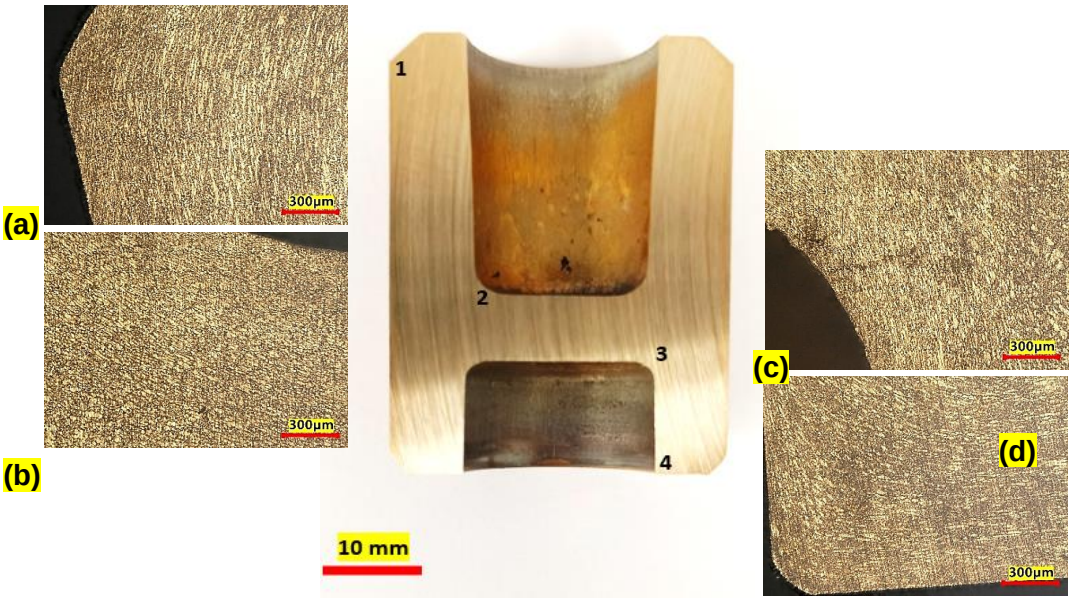
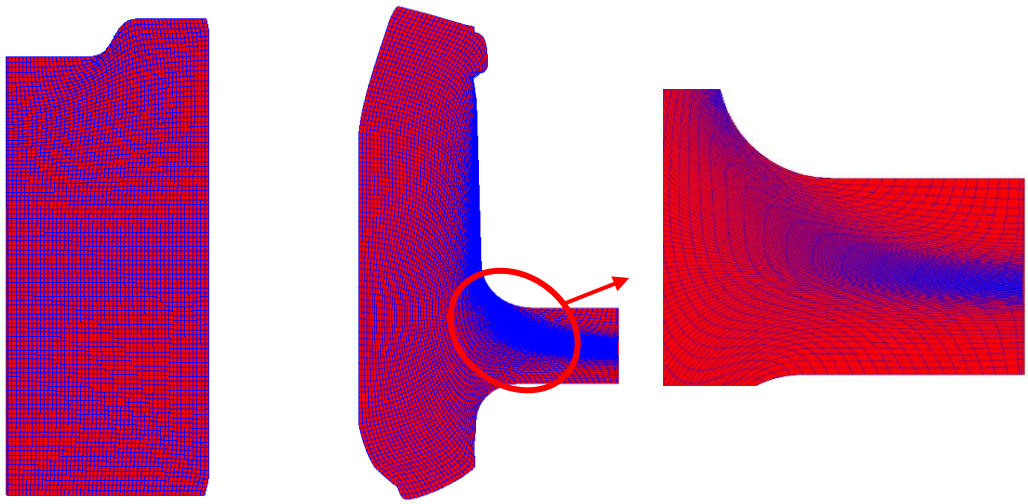


Figure 5 The longitudinal section view of the forged brass part and the microstructural images of the metal flow lines (microstructure images of the metal flow lines in the regions indicated by 1, 2, 3 and 4 are respectively stated in (a), (b), (c) and (d))

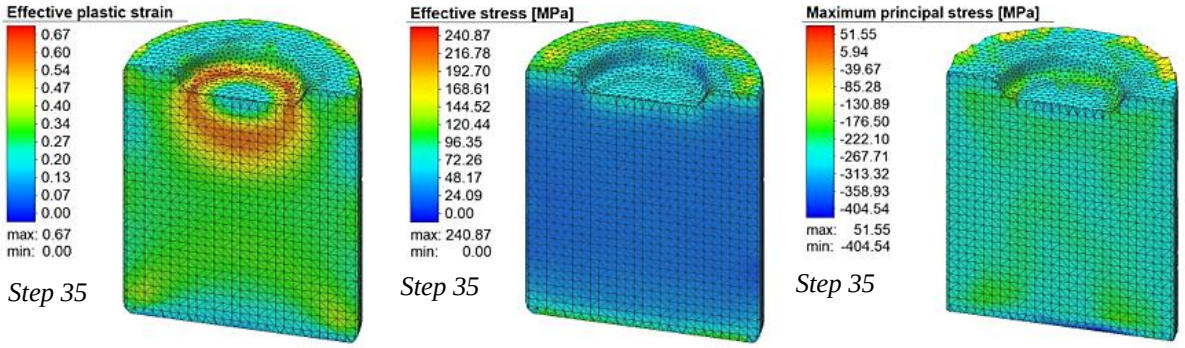
Simulation Studies

The distribution of the flow lines in forged brass material is similar to simulation results shown in Fig 6. The flow line distribution at regions where the workpiece contacted with the upper punch is curved for final stage forming as seen in Fig 6(c). Also, it's seen that the shape of the forged workpiece is fairly close to the simulation results. In order to examine the effects of the press load and deformation rate on the brass workpiece during hot forging, the effective strain, stress and the maximum principal stress analyses have been made for the two-stage hot forging process. It's shown that evolution of the effective plastic strain, the effective stress and the maximum principal stress contours of the workpiece for the two-stage in Fig 7 and Fig 8. Stroke distances are for the first and final stage, 11.80 mm and 23.80 mm, respectively. The boundary conditions of the simulation are stated that after the forging begin, the upper punch moves down throughout the die/lower punch as the lower punch and the die are fastened as depicted in Fig 3. The workpiece obtained from the first process was employed to simulate the final process. The maximum effective plastic strain value is about 0.67 mm/mm in the preforming stage as depicted in Fig 7(a). The plastic strain of the preforming process is not distributed uniformly. The maximum effective plastic strain value is about 2.29 mm/mm in the final forming stage as depicted in Fig 8(a). The maximum effective plastic strain of the brass part emerged the area where the upper punch entered. The zone of the maximum plastic strain centred around the formed hole wall of the brass part. Deformations at this zone were increased by the upper punch. At the first stage, the maximum value of the effective stress were focused on the top of the upper punch and the bottom surface of the workpiece as shown in Fig 7(b). At the second stage, the maximum value of the effective stress were focused on the top of the upper and lower punch, in which thin-walled area between the upper and lower punch as depicted in Fig 8(b). It is observed that the compressive stress between the top of the upper and lower punch has the maximum value of the principal stress. The maximum value of the principal stress was focused on the punch head, in which the brass part directly touched as shown Fig 7(c). It has been seen that the maximum value of the compressive principal stress has centred around the thin wall surfaces between the upper and lower punch. The tensile principal stresses was dispensed on the circumference of the brass part as shown Fig 8(c).



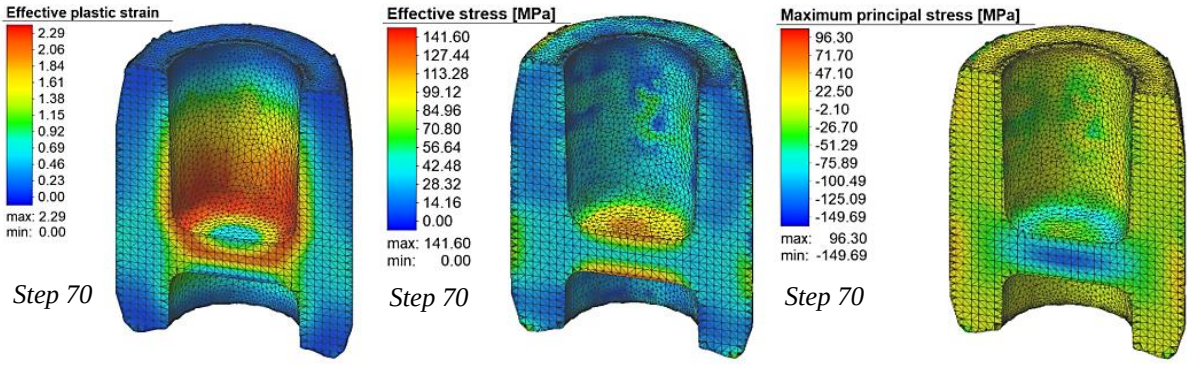
(a) (b) (c)

Figure 6 Flow lines obtained by simulation studies (2D axisymmetrical view with half of the workpiece), (a) Preforming, (b) Final forming, (c) The detailed view of the metal flow line



(a) (b) (c)

Figure 7 Simulation results of the first process in the three dimesional: (a) Effective plastic strain, (b) Effective stress, (c) Maximum principal stress



(a) (b) (c)

Figure 8 Simulation results of the final process in the three dimensional: (a) Effective plastic strain, (b) Effective stress, (c) Maximum principal stress

CONCLUSION

This paper presents the results of the experimental and numerical simulation on the two-stage hot forging process. The following conclusions are obtained.

The distribution of metal flow lines is regular and no dead metal areas are found. As regards the metallographic test results, the metal flow line simulated with program is compatible with the results obtained from the experiments.

The simulation results revealed that the effective strain, stress and maximum compressive stress are higher in the areas where the workpiece comes into contact with upper and lower punch.

It is planned to examine the effects such as the hot deformation characteristic of the ferrous and non-ferrous material types in the multi-stage hot forging process for future studies.

REFERENCES

1. **Mebmer, G. and Huber, S., (2007),** “Hot forging on horizontal multi-stage presses machine technology”, (1st ed.) [Online]. Available: https://www.semanticscholar.org/paper

2. **Gangopadhyay, T., Ohdar, R., Pratihar, D. and Basak, I., (2011),** “Three-dimensional finite element analysis of multi-stage hot forming of railway wheels”, The International Journal Advanced Manufacturing Technology, Vol. 53, pp 301–312.

3. **Fadhil, A.A., Ghattas, M.S., Iskander, B.A., Ajeel, S.A. and Enab T.A., (2018),** “Structural characterization and detecting processes of defects in leaded brass alloy used for gas valves production”, *Alexandria Engineering Journal*, Vol. 57, No. 3, pp 1301-1311.

4. **Huang, H. and Hsia, S.Y., (2016),** “New design of process for cold forging to improve multi-stage gas fitting”, *Advances in Mechanical Engineering*, Vol. 8, No. 4, pp 1–12.

5. **Chen, Q., Hu, H., Lin, J., Huang, S., Wu, Y., Shu, D., Huang, W. and Mingbo, Y., (2017)**, “Multi-stage cold forging process for H68 brass cylindrical shell part with deep blind hole: simulation and experiment”, The International Journal of Advanced Manufacturing Technology, Vol. 91, pp 3789–3798.

6. **Hsia, S. and Chou, Y., (2015)**, “Fabrication improvement of cold forging hexagonal nuts by computational analysis and experiment verification,” Mathematical Problems in Engineering, Vol. 2015, pp 1-11.

7. **Zuo, X., Wei, Y., Chen, J., Zeng, L. and Ruan, X., (1999),** “3D FEM simulation of multi-stage forging process using solid modeling of forging tools”, Journal of Materials Processing Technology, Vol. 91, pp 191–195.

8. **Lee, J., Kang, B. and Lee, J.H., (1996),** "Process design in multi-stage cold forging by the finite-element method", Journal of Materials Processing Technology, Vol. 58, pp 174-183.

9. **Jiang, H., Wu, Y., Gong, X., Shan, D. and Zong, Y., (2020)**, "Control of flow lines during the forging process of bearing outer rings with a deviated groove", The International Journal of Advanced Manufacturing Technology, Vol. 106, pp 753-764.

10. **Joun, M., Lee, S. and Chung, J., (1998)**, "Finite element analysis of a multi-stage axisymmetric forging process", International Journal of Machine Tools and Manufacture, Vol. 38, pp 843-854.

11. **Shen, X., Chen, W., Yan, J., Zhang, L. and Zhang, J., (2015)**, "Experiment and simulation of metal flow in multi stage forming process of railway wheel", Journal of Iron and Steel Research International, Vol. 22, No. 1, pp 21-29.

12. **Lee, M., Chung, S., Joun, M., (2009)**, "Automatic and precise simulation of multi-stage automatic cold-forging processes by combined analyses of two- and three-dimensional approaches", The International Journal of Advanced Manufacturing Technology, Vol. 41, pp. 1-7.

13. **Hsieh, C., Wang, J., Wu, P. and Wu, W., (2013)**, "Microstructural development of brass alloys with various Bi and Pb additions," Metals and Materials International, Vol. 19, pp 1173–1179.

14. **Sarbak Inc. (2018),** *Brass alloy technical data sheet* [Online]. Available: https://sarbak.com.tr/dokuman/alasimlar/en/S617.pdf

15. **Behrens, B., Bouguecha, A., Hadifi, T. and Mielke, J., (2011)**, "Advanced friction modeling for bulk metal forming processes," Production Engineering, Vol. 5, pp 621–627.

16. **Burte, P., Im, Y., Altan, T. and Semiatin, S., (1990),** "Measurement and analysis of heat transfer and friction during hot forging," Journal of Manufacturing Science and Engineering, Vol. 112, No. 4, pp 332-339.

BULK PASSIVE SENSORLESS SORTING OF COMPLEX CYLINDRICAL COMPONENTS WITH INTERNAL FEATURES AND SYMMETRICAL EXTERNAL TAPERS

Toby WILLIAMS, *t.williams@lboro.ac.uk* Loughborough University, Loughborough, LE11 3TU, United Kingdom

Kaddour BOUAZZA-MAROUF, *k.bouazza-marouf@lboro.ac.uk* Loughborough University, Loughborough, LE11 3TU, United Kingdom

ABSTRACT

In robotic assembly, manipulators can be used extensively to undertake all the different facets of the process, however, this can be expensive and space inefficient. Instead, reduced intricacy in sensing and control (RISC) can be adopted involving minimal use of manipulators with parts of the process undertaken using passive methods.

A novel tooling method has been developed to passively orientate complex shaped cylindrical components with symmetrical external tapers in bulk transit. The design of the tooling is component specific, however, this method can be applied to generic components. This technique has been successfully tested in an industrial assembly system.

Keywords: Sensorless, Bulk sorting, Orientation filtering

1. INTRODUCTION

In robotic assembly systems it can be difficult and costly to correctly orientate and assemble a bulk set of components. Optimal design considers, the total cost of the assembly cell, the reliability of the process, and the space occupied by the system.

In complex bulk manufacturing and sorting systems a reduction in unnecessary intricacy in control is desired (RISC) [Canny and Goldberg, 1994]. RISC is especially important for components where false positive orientations could cause significant damage to downstream machinery or could cause expensive complications to the components end application, the most robust and operationally simple engineering solution is desirable.

The two categories of component manipulation are active and passive orientation. Active orientation is defined by the use of a feedback system that generally consists of sensors and manipulators. This can increase the modular cost, the operation cycle time, and the rate of false positive orientations of a bulk set of components compared to passive orientation filtering. It is evident that the use of passive sensorless component orientation techniques are more desirable when possible.

The most common method of bulk feeding and orientation of components is the use of vibratory bowl feeders. Vibratory bowl feeders consist of a base, a bowl with an internal helical track, and suspension springs. The springs are excited, usually via an electromagnet, causing the bowl to vibrate in small reciprocating arcs that forces the components within the bowl to climb up the internal spiral [Selig and Dai, 2005].

Due to their simple and robust structure they are used in over 80% of automated small part delivery systems used in manufacturing plants [Hofmann, Huang, and Reinhart, 2013]. Most interest, from an academic viewpoint, has been focused on either the mechanism used in the motion of parts using vibrating tracks [Huang and Mason, 1997; Lim, 1998] or the optimisation of established tooling methods, depending on the shape and dimensions of the component [Hofmann, Huang, and Reinhart, 2013]. The 'tooling' of a vibratory bowl feeder refers to the shaping of section(s) of the component path so that only the components with the correct orientation are allowed to proceed, with the rejected components being rejected and recirculated.

Therefore, tooled vibratory bowl feeders can be thought of as a combined bulk to single-file transformation and a part orientation filter. Each possible component orientation can be assigned a numerical state, and only one state (or more if the part has a plane of symmetry) is outputted. This can be achieved by using a combination of fences and traps to alter the path of the components as required.

In this paper, a new vibratory bowl feeder tooling method for the orientation of small lightweight cylindrical components with thick walled internal features and symmetrical external tapers is proposed. The design has been successfully implemented in a robotic assembly system being used in an industrial environment.

2. CYLINDRICAL COMPONENTS WITH INTERNAL FEATURES AND SYMMETRICAL EXTERNAL TAPERS

In this section, the design for vibratory bowl feeder tooling for lightweight cylindrical components with thick walled internal features and external tapers is detailed. A test case

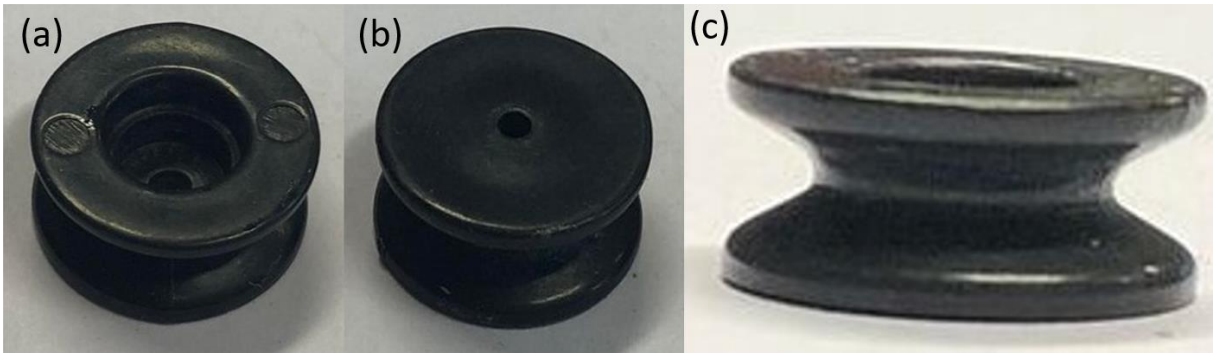


Figure 1. Test Case Component: (a) Correct Orientation, (b) Incorrect Orientation, (c) Side View.

component is shown in Figure 1. The cylindrical component with thick walled internal features is shown in the correct output orientation in Figure 1(a) and the incorrect output orientation in Figure 1(b). The 'hourglass' external tapers of the same component are shown in Figure 1(c). The component is manufactured of a relatively low-density plastic and is 12 mm in external diameter and 6 mm in height.

There are accepted standard tooling methods that can be used to alter the orientation of different component shapes. However, for components that require more complex methods of tooling (i.e. non-polygonal), it is first required that the components are arranged to be single layered, and in single file before the orientation/rejection process.

Methods of single layering and single filing are relatively universal between component shapes. Single layering is usually achieved using a fence suspended above the path of the components, referred to as a wiper. Depending on the exact shape of the components, the wiper should be suspended about 1.25 to 1.5 of the height of the component above the track. This allows for only a single layer of components to pass, with additional layers being rejected back into the bottom of the bowl feeder. It is also to be noted that when dealing with cylindrical components where their diameter is greater than their height (as is the case with the test case component), the wiper may also be used to reduce the possible number of orientations that are fed into the orientation tooling. This is done by forcing components on their side to either be knocked under the wiper onto one of their faces or to be driven off the track into recirculation.

For low-density light-weight components single filing is generally achieved by introducing a notch cut out of the inside of the bowl feeder track so that only a single outer row of components may pass. This reduces the volume of components being fed into the upstream orientation filter by forcing inner rows of components off the track, through the notch, to recirculate.

Most standard vibratory bowl feeder tracks have two gradients comprised of a 5° radial and a 10° helical pitch angle. The radial gradient ensures that the components remain on the track, against the outer wall of the bowl, unless otherwise influenced. This has the adverse effect

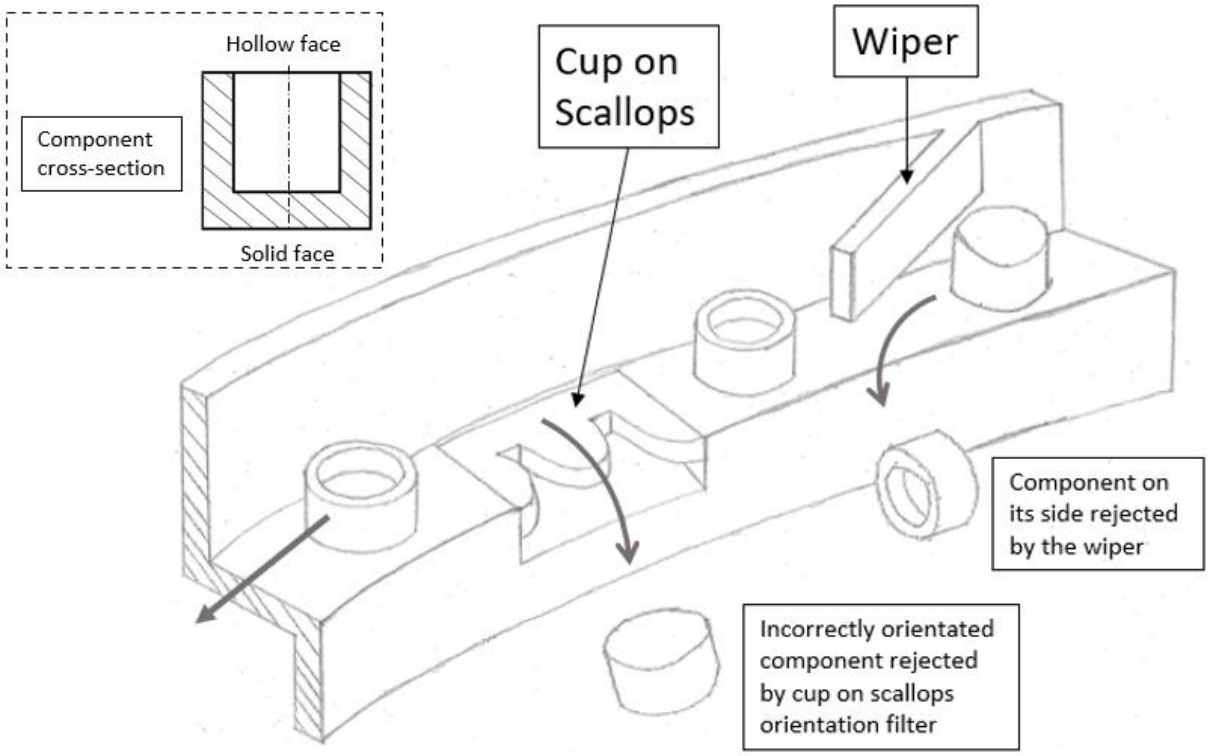


Figure 2. Cup on Scallops Bowl Feeder Tooling for Cylindrical Components with Thin Walled Internal Features [Adapted from Automation Devices INC.].

that, if the component is small and of low density, the force transmitted to the part via the vibration of the vibrating bowl feeder is not great enough to move the component both up the track and out away from the wall. As a result, a queue of components is formed producing back pressure among the components. This can reduce feed rates, promotes pinching, and reduce the effectiveness of some component orientation methods.

The limit for the individual mass of a component at which the climbing of the radial gradient becomes an issue, is a function of the gradient of the slope, the amplitude and frequency of the bowl feeder, and the type of transport regime that acts upon the components [Lim, 1998].

The most applicable orientation selection tooling method for cylindrical components with internal features is to use the cup on scallops method, see Figure 2 [Akella and Mason, 1998; Yeong and De Vries, 1994]. This tooling technique is designed to orientate cylindrical components with internal features via passive rejection of incorrectly orientated components. When the component is solid face down the scallops provide support to the component beyond its centre of mass and allow it to pass, while when the component is hollow side down, the scallops do not provide support for the component beyond its centre of mass and the component falls from the track. The incorrectly orientated component falls from the track because the gaps in the scallops are wider than the wall thickness of the components, which effectively removes any support under the component beyond its centre of mass. This technique requires that tooling is already in place that prevents the components from entering



Figure 3. Component Queuing Causing Component Pinching.

the cup on scallops orientation filter on their side. This is represented in Figure 2 via the use of a wiper upstream of the cup on scallops that does not allow components on their side to pass.

The cup on scallops orientation method is not appropriate for all cylindrical components with different external features. The test case component is lightweight with symmetrical external tapers. As a result, when the vibratory bowl feeder operates with a large number of the components, single filing and selective orientation tooling creates component queuing, where components coalesce, pushing against each other due to the flow restrictions introduced by the tooling. Because of the symmetrical external tapers, shown in Figure 1(c), the queuing can cause components to partially rise up on top of one another, becoming locked together and lifting a single component completely off the track as shown in Figure 3.

The arrangement of the pinching phenomenon displayed in Figure 3 shows an incorrectly orientated component raised off the surface of the vibratory bowl feeder track by two correctly orientated components. The outcome of this arrangement using the cup on scallops filtering method would result in an incorrectly orientated component to pass through. A method to overcome this scenario is described in Section 3 below.

3. PASSIVE SENSORLESS ORIENTATION FILTER DESIGN

The inter component pinching described in the previous section can cause incorrectly orientated components to pass through, making the system not reliable. Therefore, in order to reliably, continuously, passively filter the orientation of the components the inter component pinching must either be prevented from occurring during the orientation filtering and/or the raised component removed. However, with lightweight components, pinching can occur at any

point on the vibratory bowl feeder track; therefore, simply removing the pinched components before the filtering (using a wiper) is not sufficient to prevent false positive outcomes. Pinching must be prevented during the whole of the filtering process.

For cylindrical components with internal features and symmetrical external tapers there are two cases; one where the external diameter of the component is less than the height of the component, and the other where the external diameter is greater than the height of the component.

For the first case where the external diameter of the component is less than the height of the component, pinching during the cup on scallop orientation filtering can be prevented by using a height limiter over the whole of the orientation filter. So, if pinched components are removed before the orientation filtering and a height limiter is employed during the whole of the orientation filtering each incorrectly orientated component can be reliably rejected.

In the second case, where the component's diameter is greater than its height, a height limiter would prevent the rejection mechanism of the cup on scallops filter from functioning properly. This is because the cups on scallops rejection mechanism works by rotating an incorrectly orientated component off the track, but because of the external diameter being greater than the height of the component, the rejected component would contact against the height limiter during its rotation and is thus prevented from falling.

A robust alternate approach for the orientation filtering would be to decouple any pinching components, and subsequently limit the number of components in contact with each other during the orientation filtering to two components. For clarity, a minimum of three components are required for pinching to occur, therefore, if only two components are in contact during the filtering process pinching cannot occur.

Pinching components can be decoupled by forcing the components to undergo an in-path rotation, which can be achieved by a sharp change in incline, as illustrated in Figure 4. As the leading component, of the pinched set of components, is forced to rotate through angle θ it is forced to decouple from the pinched (trailing) component. Angle θ must be greater than or equal to the angle of the external taper of the component, but not be so great as to prevent the component from climbing the incline.

The inter component decoupling only occurs at the point of elevation past the upper angle of transition, as shown in Figure 4. Therefore, the cup on scallops orientation filtering method, in Figure 2, can be used reliably by positioning it immediately after the transition point, but it must be ensured that pinching cannot occur from the upstream components. This can be achieved by introducing a step drop immediately after the orientation filtering. By having a change in

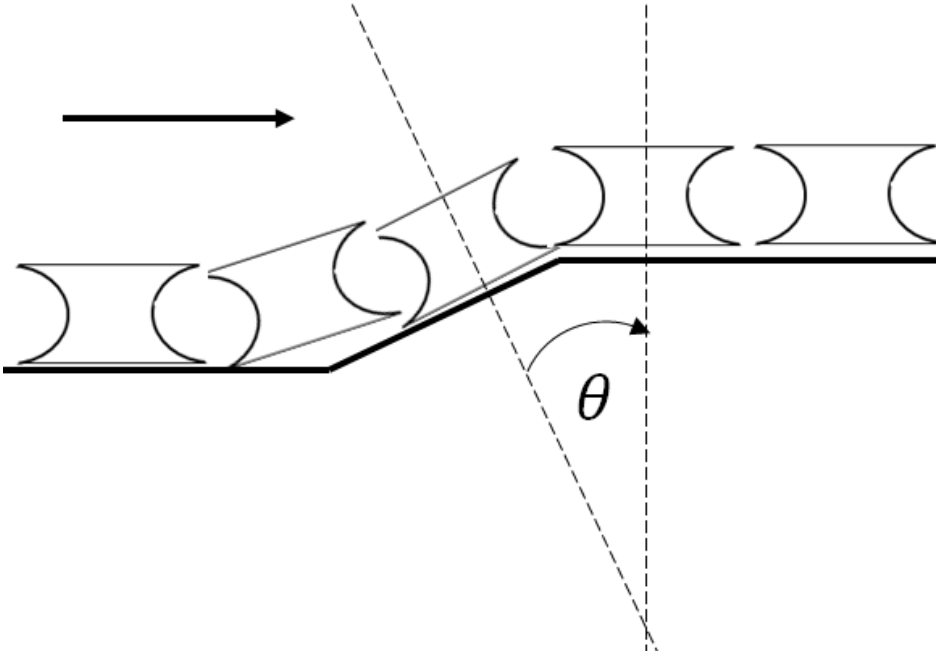


Figure 4. Decoupling of Cylindrical Components with Symmetrical External Tapers via a Step Change in Incline.

elevation both before and after the orientation filtering, the filtering process is isolated from inter component forces and component back pressure, as depicted in Figure 5.

The height of the step drop downstream of the orientation filtering is determined by the shape and dimensions of the external taper of the component. it should not be so great as to allow the falling component to change orientation during the fall, or to allow the following component to mount the components preceding it. This condition is given in Equation 1, with reference to Figure 6.

Figure 6 gives the resulting design to satisfy the passive orientation filtering for a cylindrical component with internal features and symmetrical external tapers. The generic dimensions a, b, c, and θ are given based on their relation to the generic component internal diameter, d, external diameter, D, and taper angle, ϕ, in Equations 1 to 4.

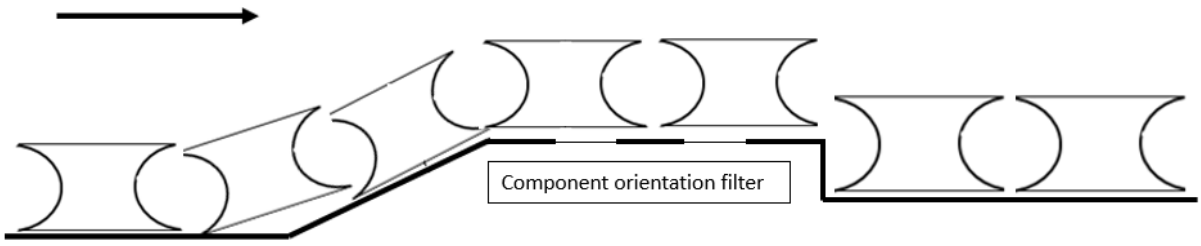


Figure 5. Cylindrical Components with Symmetrical External Tapers with Orientation Filtering for Internal Features.

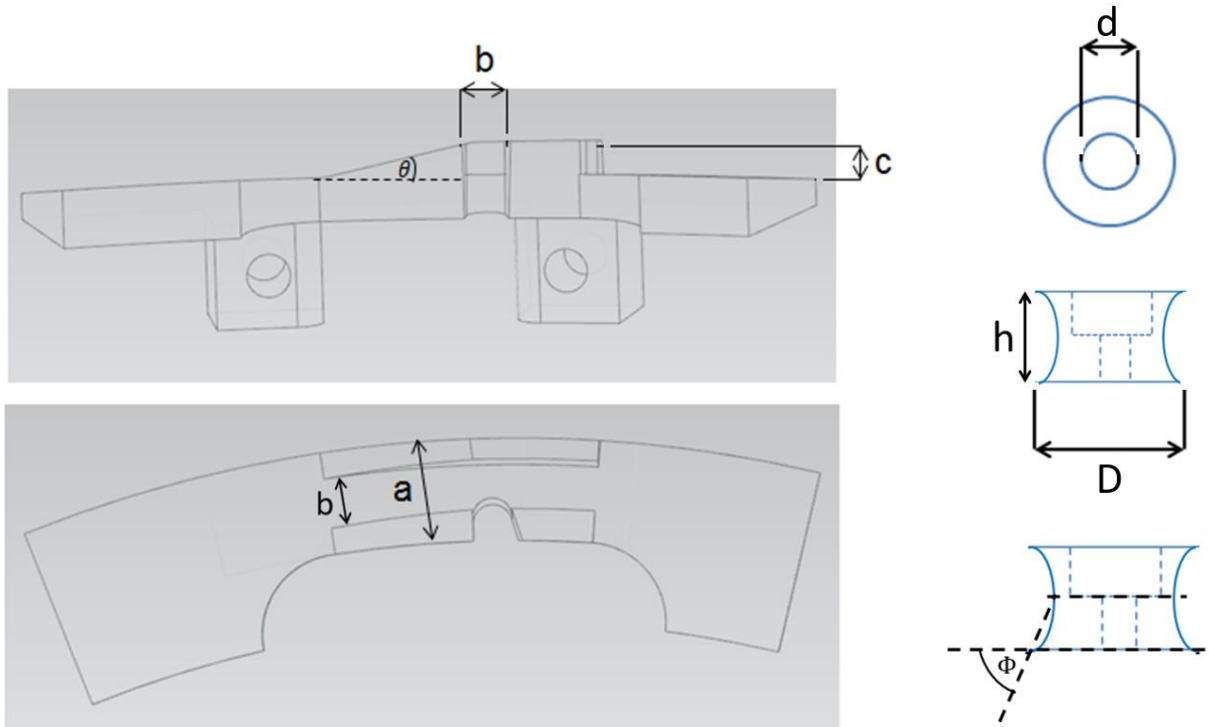


Figure 6. Orientation Tooling for Cylindrical Components with Internal Features and External Tapers.

$$c < \begin{cases} \frac{D}{2}, & h > \frac{D}{2} \\ h, & h < \frac{D}{2} \end{cases} \quad (1)$$

$$a = \frac{D + d}{2} \quad (2)$$

$$b = \frac{D - d}{2} + tol. \quad (3)$$

$$\theta \approx \phi \quad (4)$$

4. DISCUSSION

The vibratory bowl feeder orientation filter tooling design for cylindrical components with internal features and symmetrical external tapers outlined in Figure 6 has been 3D printed using an Ultimaker^{2+} for the test case component in Figure 7. The designed orientation filtering system was run for 5000 components using a machine vision system to assess the orientation of the outputted components. All components outputted by the system were in the correct orientation and all observed pinching was decoupled by the step angle change, discussed in Section 3. Periodically the output from the bowl feeder was intentionally blocked to simulate

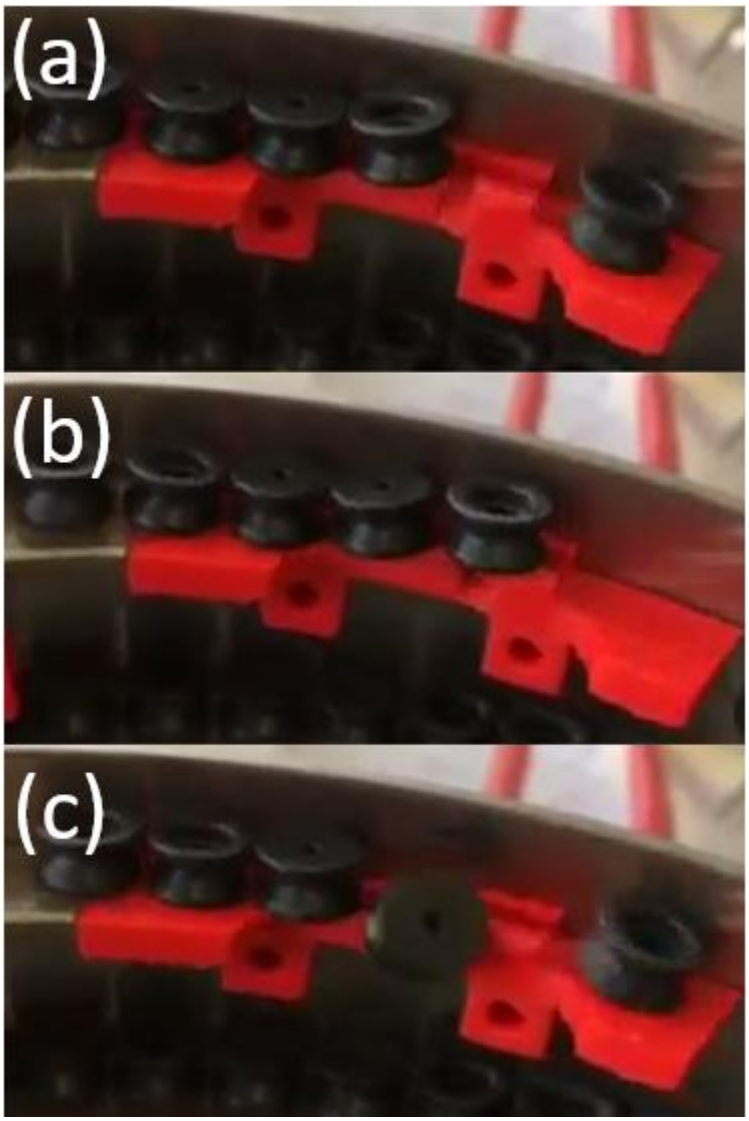


Figure 7. Rejection Mechanism for Incorrectly Orientated Components: (a) Correctly Orientated Component Passing the Orientation Filter, (b) Incorrectly Orientated Component Approaching the Orientation Filter, (c) Incorrectly Orientated Component Being Rejected by the Orientation Filter.

real world scenarios, when the assembly rate is slower than the feed rate of the separate components. The change in step height, described in Section 3, was observed to efficiently prevent pinching from occurring during the orientation filtering. The rejection mechanism for incorrectly orientated components is shown in Figure 7.

A vibratory bowl feeder with the orientation filtering tooling described in this paper was successfully incorporated into an industrial robotic assembly system which included other vibratory bowl feeders for less complex components.

5. CONCLUSION

Conventional vibratory bowl feeder tooling for the orientation of cylindrical components with internal features utilises cut-outs and grooves on the vibratory bowl feeder track to reject incorrectly orientated components. However, if pinching occurs due to symmetrical external tapers, then traditional tooling methods cannot guarantee successful orientation filtering.

A novel technique has been developed to passively filter the orientation of small lightweight circular components with internal features and symmetrical external tapers using vibratory bowl feeders. The dimensions of the tooling can be calculated for a generic component geometry using the equations stated in this paper. This unique tooling design has been successfully tested on a robotic assembly system in a production line for over 1 year without failure.

REFERENCES

1. **Canny, J. and Goldberg, K.Y., (1994),** "RISC for Industrial Robotics: Recent Results and Open Problems", Proceedings of IEEE International Conference on Robotics and Automation (ICRA), San Diego, pp 1951-1958.

2. **Selig, J.M. and Dai, J.S., (2005),** "Dynamics of Vibratory Bowl Feeders", Proceedings of IEEE International Conference on Robotics and Automation (ICRA), Barcelona, pp 3288-3293.

3. **Hofmann, D., Huang, H. and Reinhart, G., (2013),** "Automated Shape Optimization of Orientating Devices for Vibratory Bowl Feeders", Journal of Manufacturing Science and Engineering, Vol.135, No.5.

4. **Huang, W.H. and Mason, M., (1997),** "Mechanics for Vibratory Manipulation", Proceedings of IEEE International Conference on Robotics and Automation (ICRA), Albuquerque, pp 2391-2396.

5. **Lim, G.H., (1998),** "On the Conveying Velocity of a Vibratory Feeder", Computers and Structures, Vol.62, No.1, pp 197-203.

6. **Yeong, M.Y. and De Vries, W.R., (1994),** "A Methodology for Part Feeder Design", Annals of the CIRP, Vol.43, pp 19-22.

7. **Akella, S. and Mason, M.T., (1998),** "Posing Polygonal Objects in the Plane by Pushing", The International Journal of Robotics Research, Vol.17, No.1, pp 70-88.

OPTIMUM DESIGN OF AN AIRPLANE BRACKET USING TOPOLOGY AND SHAPE OPTIMIZATION METHODS

Betül Sultan YILDIZ, , *betulyildiz@uludag.edu.tr*, Makine Mühendisliği Bölümü, Uludağ Üniversitesi, 16059, Bursa

ABSTRACT

A design phase of products significantly impacts the entire production process when examined in terms of production and maintenance costs, product quality, and time. The efficiency of the product design process is increased by catching the optimum designs; it is aimed to reduce the cost, increase the quality and reduce the total product production time. In this study, the optimum dimensions of the airplane bracket used in airplanes were obtained by making topology and shape optimization, respectively.

Keywords: Topology optimization, Shape Optimization, Bracket

1. INTRODUCTION

In the design process of a product, it is taken into account that the component is capable of fulfilling its primary function for its intended use and that it performs these functions without any damage during the determined life. In addition, in today's difficult conditions, where using limited resources most efficiently is one of the most significant imperatives, the costs must remain within a determined limit while meeting these expectations. The pre-design alternatives created are evaluated, and the optimum product designs are tried to be caught. Today, optimization methods, which are added to the literature daily, can be counted as frequently used tools.

Trivets of engineering designs; If we determine functionality, cost, and life, we can obtain a design close to the optimum when we examine these features and their interrelationships according to the constraints and conditions at hand. What is expected from the design obtained under all these conditions; it is not unnecessarily safe with the cost above the expected or not having the quality that does not contain the desired safety conditions by reducing the cost. It is essential to design the optimum by considering both aspects.

When the production process of engineering products is considered in terms of cost, it is seen that the design stage is the most influential stage in product life. Considering that a large part of the total cost of the product is determined during the design phase, the design of products with the desired qualities at this stage will increase efficient and effective production. Considering that the design stage has a large share in terms of time, effort and cost spent for the entire production process of a product; it is evident that the decisions taken at this stage will have an impact on the product cost and time to market. On the contrary, the deficiencies and mistakes made during the design phase will adversely affect future processes. For this reason, choosing the optimum under the determined conditions among the alternative designs obtained during the design is highly important in production.

This study aims to apply an optimization technique based on material distribution to shorten product design times and obtain the best product design model' with the desired qualities under specified conditions. For this purpose, topology and shape optimization of the airplane bracket part, respectively, has been made.

2. OPTIMUM DESIGN OF A BRACKET

Various analytical and numerical solution methods are proposed in the literature to solve engineering design optimization problems [1]. There are various studies on design optimization in this area.[2-5]. With the developing technology, optimization techniques based on material distribution are frequently used in optimization issues, especially with computer support. One of these methods is used in structural topology optimization.The first study in the literature on structural topology optimization methods dates back to 1904 [6]. The main logic in topology optimization is to increase the rigidity of the part, provided that there is no change in the external dimensions of the part under consideration. At the same time, the material is discharged from certain areas in the figure and ultimately obtains the optimum design. Topology optimization aims to find the material distribution where the stiffness is maximum (minimum compliance), or the natural frequency is maximum. The method, which is called the homogenization method and was developed by Bendsoe and Kikuchi in 1988, has provided great convenience in solving topology optimization problems [7]. Another method that is frequently used in solving topology optimization problems is R.J. Yang and C.H. It is a material distribution method developed by Cuhang in 1993 [8].

In the homogenization method, the optimum material distribution in the elastic design area is found under the specified conditions while providing the constraints. In the homogenization method, compliance minimization (rigidity maximization) or natural frequency maximization is chosen as the objective function, and material reduction is chosen as the constraint function,

with material density being the design variable. According to this method, a microstructure is classified into three groups; generalized porous material containing no material (hole size =1), isotropic material (hole size = 0), and orthorhombic material (0 < hole size < 1). The distribution of voids, pores, and solid microstructures indicates a structure's topology. In the material distribution method, the density of each finite element is accepted as a design variable, unlike the homogenization method. Similar to the homogenization method, the topology design in this method aims to minimize compliance, which is equivalent to the maximum stiffness.

The process steps for topology optimization are given below:

Step1: Creating a three-dimensional model of the part to be optimized

Step2: Determining the element type to be used in optimization

Step3: Determining the regions to be optimized and not to be optimized.

Step4: Applying the boundary conditions to the part

Step5: Checking the optimization process

Step6: Viewing the obtained results

After the topology optimization was performed, a shape optimization study was carried out on the new airplane bracket model. In this study, in which topology optimization is performed, an airplane bracket is taken as a sample application, and the steps followed are explained in the subsections below. The topology optimization was started with the creation of the finite element model of the first draft part, whose three-dimensional model was obtained and is shown in Figure 1, and the current boundary conditions applied to the part are given in Figure 3. The finite element model of the structure is given in Figure 2.

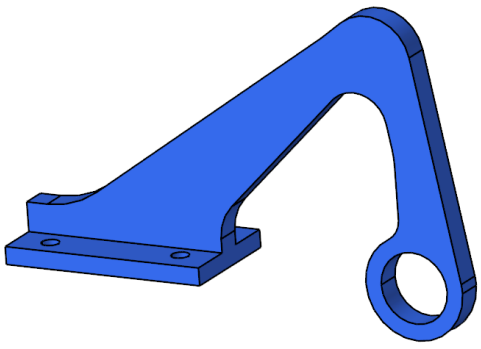


Figure 1. Initial design model of the Airplane bracket

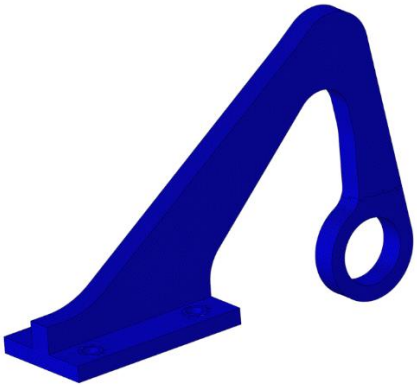


Figure 2. Airplane bracket finite element model



Figure 3. Boundary conditions of the bracket

This optimization study determined compliance minimization as the objective function, and 50% volume reduction was determined as the constraint.

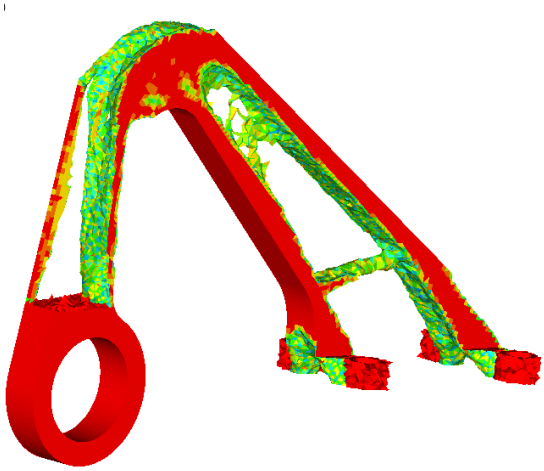


Figure 4. Material distribution after topology optimization

The unloading process was carried out in the three-dimensional model of the part, and the analysis was made under the current boundary conditions. The maximum stress and displacement values resulting from the analysis and the mass and volume values of the part are given in Table 2. A metaheuristic algorithm was used for shape optimization after topology optimization. Since the yield stress of the material in question is 350 N/mm2, it is not a problem

to increase the stress a little more to reduce the mass of the part. For this purpose, shape optimization of the airplane bracket part has been made. The lower and upper limits of the design parameters used in shape optimization are given in Table1.

Table 1. Lower and upper limits of design parameters

Design parameters	Lower limits (mm)	Initial values (mm)	Upper limits (mm)
R1	1	2	3
R2	2	3	4
R3	1	2	3
R4	1	2	3

In the shape optimization, the values listed in table 1 for the design variables given in figure 5 were taken as the lower and upper limits of the design parameters. In the shape optimization, the minimization of the mass was determined as the objective function, and the maximum stress value not exceeding 350 N/mm2 was determined as the constraint, and a solution was made under these conditions.

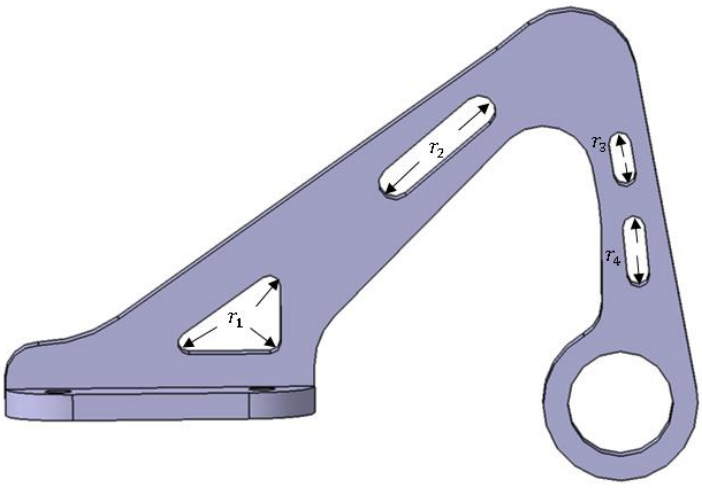


Figure 5. Design variables

As given in Figure 6, the stress analysis of the airplane bracket part, of which optimum dimensions were obtained, was carried out. The stress and displacement values and their distributions under current boundary conditions are given in figures 7 and 8.

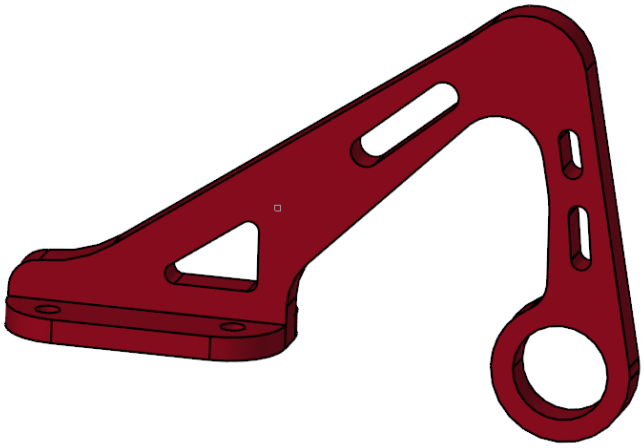


Figure 6. Redesigned bracket

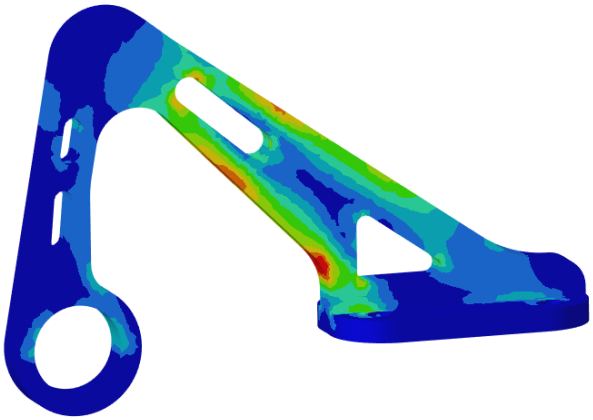


Figure 7. Stress distribution of optimum bracket design

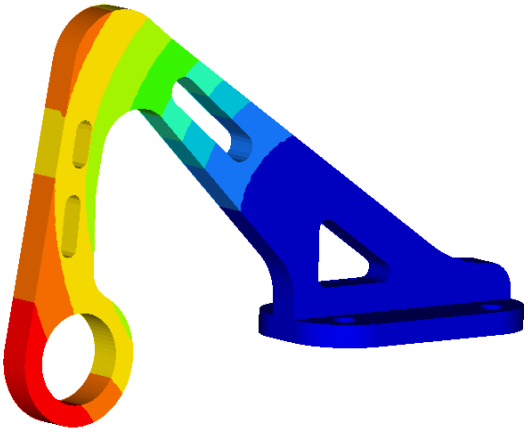


Figure 8. Displacement distribution of the optimum bracket design

Table 2. Results before and after optimization

Airplane Bracket	Mass (gr)	Max Stress (N/mm2)	Max Displacement (mm)
Initial design	239,7	244,2	0,3954
Topology optimization	212,03	271,15	0,4153
Shape optimization	203,96	301,49	0.4327

The weight of the optimum design obtained as a result of shape optimization is 203,96 grams, while the weight of the intial design is 239.7

5. CONCLUSIONS

The results obtained before and after the optimization of the first design model of the airplane bracket part examined in this study, in which the topology optimization was carried out, are given comparatively in Table 2. Compared to the initial conditions of the part, its weight is decreased by .14.9%. The results obtained in this study show the contribution of the use of the material distribution-based approach in topology optimization in the design of an aircraft component. The bracket can be designed using topology optimization for additive mabufacturing as a future work. It will show a comparison between traditional topology optimization and topology optimization for additive manufacturing approaches.

REFERENCES

1. **Steen, K., Niels O. and John R., (1989),** “Concept of an optimisation system”, Computer Aided Optimum Design of Structures Springer, pp 79-88.
2. **Torsten, B.,(1989),** “Application of structural optimisation software in the design process”, Computer Aided Optimum Design of Structures, Springer, pp 13-22.
3. **Jean, T., (1999),** “CAD meets CAE”, Mechanical Engineering, Vol. 121, No. 10, pp 66-70.
4. **Yıldız, B. S., (2020), ‘’**Slime mould algorithm and kriging surrogate model-based approach for enhanced crashworthiness of electric vehicles’’, International Journal of Vehicle Design, Vol.83, No.1, pp. 54-68.
5. **Yıldız, B. S., Pholdee, N., Panagant, N., Bureerat, S., Yildiz, A. R., & Sait, S. M,. (2022),** "A novel chaotic Henry gas solubility optimization algorithm for solving real-world engineering problems." Engineering with Computers Vol. 38,No.2,pp 871-883.

6. **Michell, A. G. M.,** “The limits econmy in frame structures”. Philo. Mag. Sect. 6, 8, 589 .
7. **Bendsoe, M.P. and Kikuchi, N., (1988),** “Generating Optimal Topologies in Structural Design Using A Homogenization Method”, Comput. Meth. Appl. Mech. Engng, Vol. 71,pp 197-224.
8. **Yang, R.J. and Chuang, C.H., (1993),** “Optimal Topology Design Using Lineer Programming”, Structural Optimization,Vol.68, pp 265-290.

THE OPTIMUM STRUCTURAL DESIGN OF AIRCRAFT COMPONENTS FOR ADDITIVE MANUFACTURING

Betül Sultan YILDIZ, , *betulyildiz@uludag.edu.tr*, Makine Mühendisliği Bölümü, Uludağ Üniversitesi, 16059, Bursa

ABSTRACT

Today, with the development of technology, traditional production methods used in the industry have been developed and changed, or new techniques have been discovered. Additive manufacturing or 3D printing technology, which has been used frequently in recent years, is one of them. Thanks to additive manufacturing, it has become possible to manufacture parts that are difficult to manufacture, costly, and time-consuming compared to other methods. It is widely used in areas where technology is constantly developing, such as aviation and automotive. In addition, topology optimization methods have been developed to reduce the mass of the manufactured parts and thus lower material consumption. After topology optimization, another method called lattice optimization is frequently applied to change the lattice structures of the parts and make them safe for the applied loads.

Within the project's scope, the drone arm, the connecting element of an unmanned aerial vehicle, was examined. Topology and lattice optimizations were applied, and it was aimed to reduce the mass of the arm. The stress values, masses, and displacements at the initial state and after the optimization were compared.

Keywords: Additive manufacturing, optimization, production, lattice structures, topology optimization.

1. INTRODUCTION

Vehicle design and production process in the aviation industry, it is necessary to minimize the product development processes by obtaining optimum designs at the design stage to keep the product cost to a minimum.

The expectation of obtaining optimum designs during the design development phase led the researchers to different searches, and as a result, optimization methods were developed. In this study, the topology optimization approach was used to reach the optimum designs during

the design phase. The drone arm design study was examined to ensure that the product could be produced with a 3D printer using the lattice structure.

2. TOPOLOGY OPTIMIZATION

The topology optimization method is based on the unloading of the part to be optimized from certain regions without any change in the external dimensions of the part, without disturbing the rigidity of the part. As can be understood from this expression, the main difference between topology optimization from shape optimization is that it allows the volume to be reduced without reducing the outer dimensions of the part. Topology optimization theory investigates the placement of void and solid regions in a Ω domain that maximizes the stiffness corresponding to the minimization of structural compliance (Fig. 1) [1].

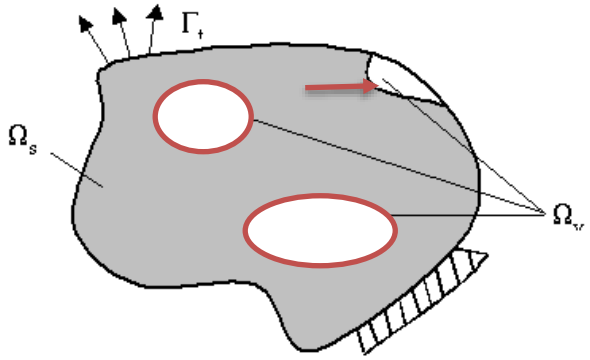


Figure 1. Field Model for Topology Optimization Problem

In order to show randomly selected configurations of Ω_s's, the indicator function expressed by Equation 1 is created. [8].

$$\begin{cases} 1 \quad x \quad \epsilon \quad \Omega_s \text{ için} \\ 0 \quad x \quad \epsilon \quad \Omega_v \equiv \dfrac{\Omega}{\Omega_s} \text{ için} \end{cases}$$

$$\chi : \Omega \rightarrow \{ 0,1 \}\ \chi(x) \qquad (1)$$

The Ω_v region is the space-containing region of Ω. t, b, and u denote surface traction, body force, and displacement vectors, respectively. Γ_t and Γ_u denote the tension and displacement at the boundaries of Ω, respectively. The flexibility of an elastic structure is measured by compliance. Compliance is expressed by Equation (2).

$$J = \int_{\Gamma_t} (\bar{t}.u)d\Gamma - \int_{\Gamma_u} (t.\bar{u})d\Gamma + \int_{\Omega} (b.u)d\Omega \quad (2)$$

The homogenization method was first developed in the literature by Kikuchi and Bendsoe in 1988 [1]. This method finds the optimum material distribution in the design area while providing the objective function and constraints. In the homogenization method, the structure is considered as the composition of periodic microstructures, and equivalent material properties are determined by a boundary process involving a reduction in microscopic size. In addition, the material axes' orientation must be considered in defining material properties. Thus, the elastic material properties of a structure can be defined by the orientation and size of the microstructural holes. In the optimization process, the microstructures alternate between solid and void. If the amount of material available is certain, the material can move from one part of the structure to another. Therefore, the topology design of structures can be considered as finding the optimal material distribution within the determined structural area [1].

Yang and Chuang developed the density method in 1993 [2]. Unlike the homogenization method, the density method considers the density of each finite element as a design variable. Similar to the homogenization method, the topology design in this method aims to minimize compliance, which is equivalent to the maximum stiffness. A volume restrictor restricts material usage.

3. LATTICE OPTIMIZATION

Although the essential feature of the additive manufacturing method is the ability to produce detailed and complex parts easily, lattice systems can be given as advanced examples. Lattice structures are produced by repeating cell shapes or types using only a 3D printer.

They have some desirable features by design. For example, thanks to its vast structural network, it provides better strength and rigidity to the model. They can also be applied to absorb impact energy, reduce weight while maintaining rigidity, and insulate from vibration and noise. In addition to these, since they have low density, they can be used effectively as heat insulators.

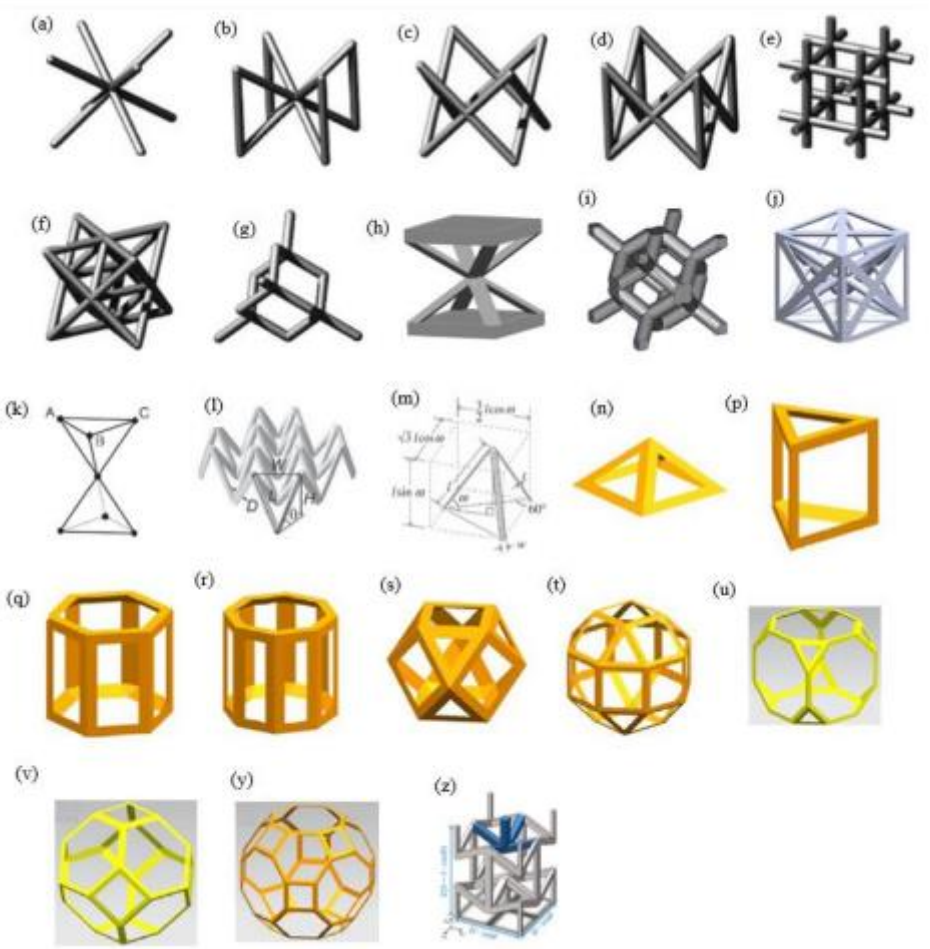


Figure 2: Different Types of Lattices[13]

Strut-based beam structures;

a) hmk b) hmkd c) ymk d) ymkd e) cubic f) octal lattice g) diamond h) G7 (i) dodecahedral shape with rhombic surface (j) ymk-hmk (k) 3-dimensional Kagome (l)) pyramid (m) tetrahedral structure (n) square pyramid (p) triangular prism (q) hexagonal prism (r) octagonal prism (s) octagonal cube (t) rhombic surface, eight-sided cube (u) cut cube (v) cut octahedron (y) cut octahedron cube (z) auxetic lattice structure

4. OPTIMUM STRUCTURAL MODEL AND LATTICE STRUCTURE OF THE DRONE ARM

This study was carried out to determine the optimum structural model of the vehicle slider arm, which allows the sliding doors of commercial vehicles to slide on a determined axis on the slide during opening-closing.

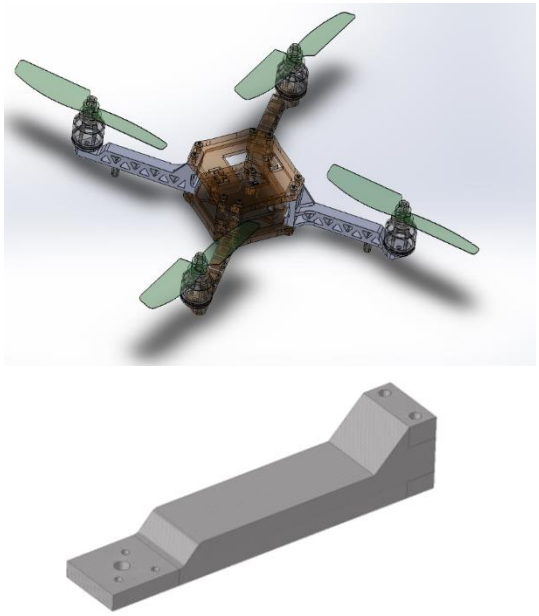


Figure 3. Drone Arm Initial Design Model

The initial design model shown in Figure 3 is topology optimization under current boundary conditions. In the topology optimization, a load of 30 N was applied. Compliance minimization is considered as the objective function.

As a result of topology optimization, the material distributions seen in Figure 3 were obtained. In these distributions, the red areas show where the material should remain, and the blue-colored regions show where the material should be extracted.

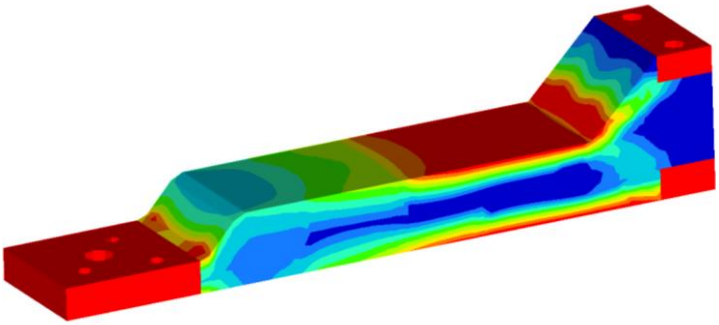


Figure 4. The model obtained as a result of topology optimization

The design obtained as Figure 4 is analyzed under the current boundary conditions, and the stress distribution is shown in Figure 5, and the displacement distribution seen in Figure 6 is obtained.

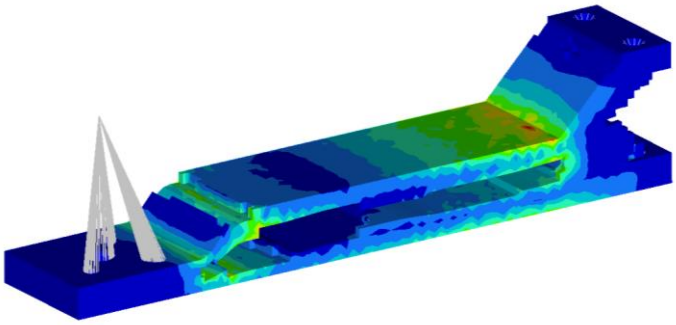


Figure 5. Stress distribution of redesign drone arm

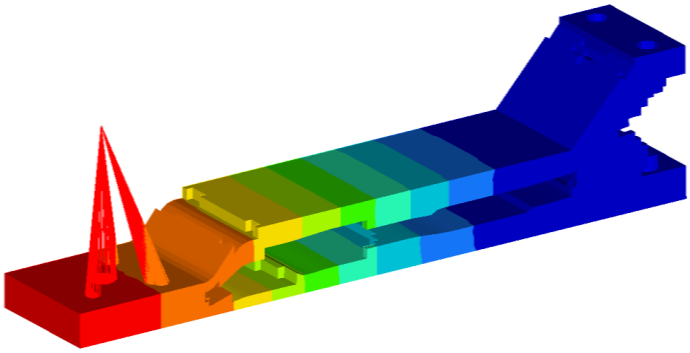
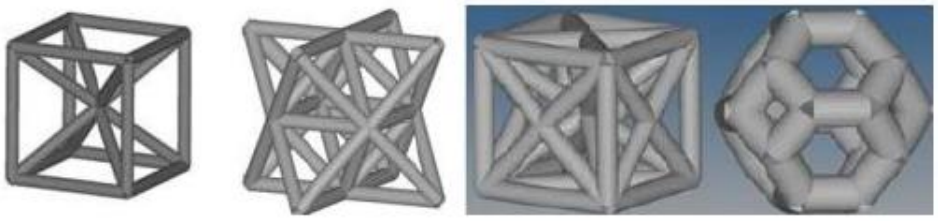


Figure 6. Displacement distribution of redesign drone arm

In the second step of this research, lattice structures are embedded to initial design using topolgoy optimization for additive manufacturing tool of a software.

Four types of the lattice shown in figure 7 are available in the software. In this research, type 1 is used.



Type 1 Type 2 Type 3 Type 4

Figure 7. Lattice types in the software

The optimized structures are better values for weight reduction. Stress and displacement distribtion of the second optimzied design are shown in figure 8 and 9, respectively.

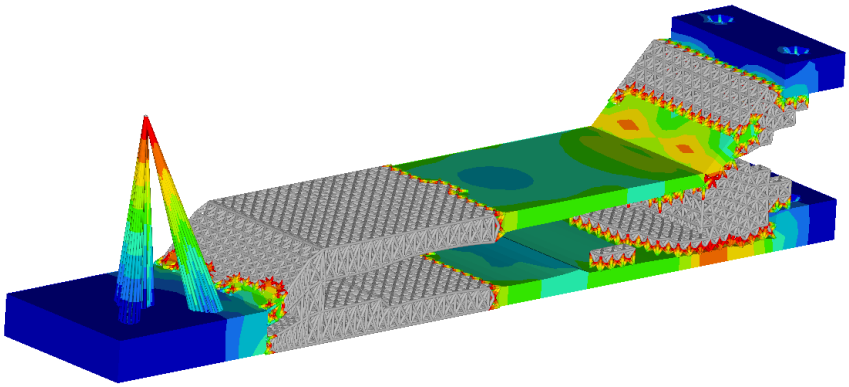


Figure 8. Stress distribution of the design obtained by lattice optimization

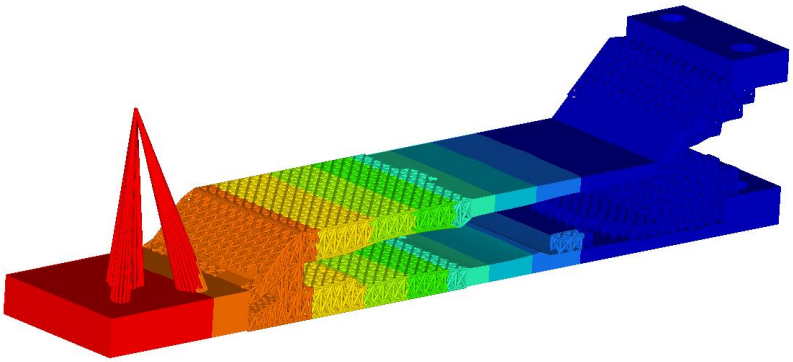


Figure 9. Displacement distribution of the design obtained by lattice optimization

The comparative results on the design obtained as a result of structural optimization and lattice optimization are given in Table 1.

Table1. Comparative Results

	Initial Design	Topology Optimization	Lattice
Mass (gr)	169.2 gram	106.7 gram	77.07 gram
Maximum stress (Mpa)	5.95 Mpa	14.86 Mpa	7.94 Mpa
Maximum displacement	**1.16 mm**	3.1 mm	1.409 mm

The rate of change shows that lattice optimization provide an important weight reduction for drone arm design. The weight of the intial drome arm design is 169.2 gram. The wight of the optimzied design as additive manufacturing is 77.07 gram.

5. CONCLUSIONS

In this study, but traditional topology optimization and topology optimzieiton for additive manfacturing are used to determine the optimum structural model of the drone arm. A new design is created according to the distribution obtained as a result of the optimization, and the

determination of the optimum model is carried out by lattice structures. The results of the design criteria and constraints of the current model are given in Table 1 comparatively. The results show the topology optimization for additive manufacturing has important superiority as traditional topology optimization and it can be used in design studies in the industry. As a future work of this study, shape optimization using metaheuristics will significantly contribute to reducing the part's weight.

REFERENCES

1. **Bendsoe, M.P. and Kikuchi, N., (1988),** “Generating Optimal Topologies in Structural Design Using A Homogenization Method”, Comput. Meth. Appl. Mech. Engng, Vol. 71,pp 197-224.
2. **Yang, R.J. and Chuang, C.H., (1993),** “Optimal Topology Design Using Lineer Programming”, Structural Optimization,Vol.68, pp 265-290.
3. **Diaz, A. and Kikuchi, N., (1992),** “Solutions to Shape And Topology Eigenvalue Optimization Problems Using A Homogenization Method”, Int. J. Numer. Meth. Engng, Vol. 35, pp 1487-1502.
4. **Jog, C. S. , Haber, R.B, and Bendsoe, M.P., (1994),** “Topology Design With Optimized, Self-Adaptive Materials”, Int. J. Numer. Meth. Engng, Vol.37, pp 1323-1350.
5. **Yildiz, A.R. and Saitou, K., (2011), “**Topology Synthesis of Multicomponent Structural Assemblies in Continuum Domains”, ASME Journal of Mechanical Design, Vol.133, No.1.
6. **Yildiz, B.S., Lekesiz, H. and Yildiz, A.R., (2016), “**Structural Design of Vehicle Components Using Gravitational Search and Charged System Search Algorithms”, Vol.58, No.1, pp 79-81.
7. **Yildiz, B.S. and Yildiz, A.R., (2018), “**Comparison of Grey Wolf, Whale, Water Cycle, Ant Lion and Sine-Cosine Algorithms for The Optimization of A Vehicle Engine Connecting rod”, Materials Testing, Vol.60, No.3, pp. 311–315. .
8. **Karagöz S. and Yildiz, A.R., (2017),** “A Comparison of Recent Metaheuristic Algorithms for Crashworthiness Optimisation of Vehicle Thin-walled Tubes Considering Sheet Metal Forming Effects”, International Journal of Vehicle Design,Vol.73, No.1-3, pp 179-188.
9. **Nantiwat T., Bureerat S. and Yildiz A.R., (2017),** “Hybrid Real-Code Population-Based İncremental Learning and Differential Evolution for Many-Objective Optimisation of An Automotive Floor-Frame”, International Journal of Vehicle Design,Vol. 73, No.1-3, pp 20-53.

10. **Yildiz A.R., (2013), "**Comparison of Evolutionary Based Optimization Algorithms for Structural Design Optimization", Engineering Applications of Artificial Intelligence, Vol. 26, No.1, pp 327–333.
11. **Kiani M. And Yildiz A.R., (2016),** "A Comparative Study of Non-Traditional Methods for Vehicle Crashworthiness and NVH Optimization", Archive and Computational Methods Engineering , Vol.23, pp. 723-734, DOI:10.1007/s11831-015-9155-y.
12. **Maconachie, T., Leary, M., Lozanovski, B., Zhang, X., Qian, M., Faruque, O., Brandt, M. 2019.** "SLM lattice structures: Properties, performance, applications and challenges", Materials and Design, 183: 108-137.
13. **Yıldız, A. R., Kaya, N., & Öztürk, F.** (2003a). "Taşıt elemanlarının optimum topoloji yaklaşımı ile tasarımı", Mühendis ve Makina, 44 (516).
14. **Yildiz, A. R., Öztürk, N., Kaya, N., & Öztürk, F.** (2003b). "Integrated optimal topology design and shape optimization using neural networks", Structural and Multidisciplinary Optimization, 25 (4), 251-260.

Modeling and Simulation of Active Double-Acting Hydro-Pneumatic Suspension System Using Fuzzy Logic Controller for 6x6 Terrain Vehicle

K. Berke ULUSOY, *kaan.ulusoy@metu.edu.tr* HİDROAN, METU, 06800, Ankara, Turkey
Bensu DEĞİRMENCİ, *bensu.degirmenci@metu.edu.tr* HİDROAN, METU, 06800, Ankara, Turkey

Erkin FİLİZ, *erkin.filiz@metu.edu.tr* HİDROAN, METU, 06800, Ankara, Turkey

Derin TÜREDİ, *derin.turedi@metu.edu.tr* METU, 06800, Ankara, Turkey

Mustafa KARAMAN, *mkaraman@hidroan.com.tr* HİDROAN, GAZİ University, 06560, Ankara, Turkey

Ahmet H. ALKAN, *aalkan@hidroan.com.tr* HİDROAN, 06935, Ankara, Turkey

E. İlhan KONUKSEVEN, *konuk@metu.edu.tr* METU, 06800, Ankara, Turkey

1. ABSTRACT

Active suspension systems are widely used in terrain vehicle applications because of their outstanding road holding and ride comfort characteristics. In this paper, an active double-acting hydro-pneumatic suspension system with the fuzzy logic controller is studied. In order to compare the performance of both active and passive suspension systems, a two DOF quarter car model of a 6x6 terrain vehicle is simulated on three different road conditions. To observe more realistic results, the kinematic relations between the sprung and unsprung masses are included in the model.

Keywords: Double-Acting Hydro-Pneumatic Suspension, Active Suspension, Fuzzy Logic Control, Dynamic Modeling, Quarter Car for Rough Terrain Vehicles

2. NOMENCLATURE

h_0: Initial vertical distance between the two connection points of the arm rod

l_{arm}: length of the arm rod that connects the tire with both sprung mass and suspension system

θ_{arm}: Angle of the arm rod with respect to the vertical axis

γ: Angle between the force F_{susp} acts on the unsprung mass and horizontal axis

α: Angle between the force F_{susp} acts on the sprung mass and horizontal axis

β: Angle between the horizontal line and the l_{cons}

$F_{tspring}$: Force exerted on the tire due to its spring effect

$k_{tspring}$: Tire spring coefficient

F_{susp}: Suspension force

F_{ac}: Actuator force

A_{fp}: Floating piston area

A_{pis}: Main piston area

A_{pr}: Remaining area between piston and rod

A_r: Piston rod area

A_{v1}, A_{v2}: Area of the first and second orifices

P_{atm}: Atmospheric pressure

P_{30i}, P_{40i}: Initial accumulator pressures

M_{fp}: mass of the floating piston inside the accumulator

V_{30i}, V_{40i}: Initial volume of the gas inside the accumulator

k: Polytropic gas constant

ρ: Density of the hydraulic fluid

3. INTRODUCTION

Suspension systems connect wheels to the vehicle body. Their task is to temporarily store and dissipate energy induced by the irregularities on the road, such as bumps. How much the suspension system achieves this task is vital to riding performance. Fulfilling all requirements of the ride performance with a suspension design having fixed parameters is a complex task since performance metrics such as ride comfort and traction require parameters to be set in contradicting manner. These contradictions pose a significant challenge for engineers and scientists.

Passive suspension systems are most common because of their simplicity and low cost [Sağlam and Ünlüsoy, 2014]. Engineers conduct optimization studies to achieve balanced ride performance using passive systems, but it is limited due to fixed parameters. This limitation becomes more apparent in applications involving widely varying road or loading conditions, such as trucks and military vehicles.

Various designs with different working principles are developed to alter the parameters of suspension systems. These designs can be grouped into semi-active and active by the ability to adjust the response of the suspension system. While the damping and stiffness of semi-active suspension systems can be adjusted during operation, additional introduction or removal of energy via an actuator is also possible for active systems. Even though using semi-active or active systems can significantly increase ride performance, they are more complex and expensive.

Hydro-pneumatic suspension systems were developed to meet the extensive requirements of varying conditions while keeping the simplicity of passive systems. This suspension system was used commercially for the first time by Citroën and became widespread for tanks, trucks, and trains.

Even though different configurations are developed, hydro-pneumatic systems consist of a hydraulic cylinder, accumulator, and orifice in their simplest form. The hydraulic cylinder is connected to the wheel. Oil in the cylinder flows to the accumulator when the road displaces the wheel, and the oil removed from the cylinder compresses the gas in the accumulator. The energy is temporarily stored in the compressed gas; hence the effect of spring is achieved. The oil displaced to the accumulator flows back to the cylinder via an orifice while the wheel returns to its neutral position, dissipating the energy stored in the gas [Reddy et al., 2014].

The force needed to compress a gas rises with increasing pressure [Bauer, 2011]. This inherently nonlinear behavior of gases provides a significant advantage to hydro-pneumatic suspension systems. Compressing gas gets harder with increasing wheel displacement or vehicle load; hence spring gets stiffer. Parameters of the semi-active hydro-pneumatic suspension system are adjusted spontaneously without the need for an external controller.

Vehicles with a hydro-pneumatic suspension system are generally built with a hydraulic reservoir and pump to adjust pressure. Drive height can be adjusted using this hydraulic system without any additional investment. It is also possible to add or remove energy by changing the volume of oil in the chamber, so active control of the system is also possible.

Double-acting configuration of the hydro-pneumatic suspension is shown in Figure 1, which is modeled as connected between the vehicle and suspension arm to increase allowable wheel displacement. Since displacement and forces are drastically affected, kinematics of the arm is also incorporated into the model.

There are various approaches in the literature for the controller design of suspension systems depending on the objective to be achieved. In general, linear standard suspension systems are taken into account to develop innovative algorithms while preserving the simplicity [Doğan et al., 2015] [Khodadadi and Ghadiri, 2018]. On the other hand, for the complex non-linear systems a general approach is to consider a linearized model of the suspension system and perform an optimal control strategy that penalizes the position, velocity, and actuation input at the same time [Kirk, 2004]. However, it is crucial to emphasize that the linearization of hydro-pneumatic suspension around an equilibrium point will make the system lose its significance for rough terrain applications. Furthermore, especially for vehicles with an articulated suspension system, the kinematic relationship between the sprung mass and the tire causes extra non-linearity.

According to the Bhangal's study, the fuzzy logic controlled active suspension exhibits more effective results than the LQR method [Bhangal and Raj, 2016]. Son relies on the same argument and indicates that for nonlinear systems, the fuzzy logic controller achieves a better response with respect to LQR method for higher speeds [Son and Isik, 1996]. In his study, Allam reaches the same outcome and states that in the same suspension working space, the fuzzy logic controller has significant improvements in comparison with LQR, by means of body acceleration and tire deflection [Allam et al., 2010]. Other than linearization approaches, Sağlam presented the method of SDRE (State Dependent Ricatti Equation), which to solve nonlinear characteristics of spring and damper effects [Sağlam, 2016]. Based on the results presented in the literature and the mathematical model of the system, a fuzzy logic controller is developed, which inputs are the displacement and velocity of the suspension.

4. MODEL

The mathematical model is derived to analyze the behavior of the vehicle suspension system together with the control algorithms. The controller needs to be adaptable, simple, and realistic for easier controllability and reduced computational power. In the literature, the studies on quarter car models, the suspension is directly connected to the vehicle chassis and the wheel, therefore; do not include the kinematic effects of suspension structures such as double wishbone MacPherson or multi-link. In this study, the suspension arm kinematics and the tire size effects are included [Ulusoy et al., 2022]. The dynamic effects of the connection elements, such as friction, are neglected to keep the model simple.

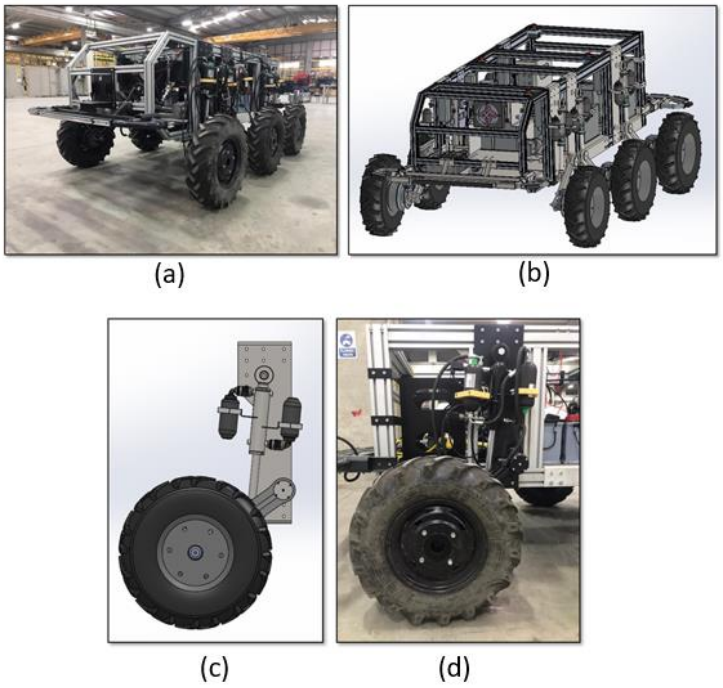


Figure 1 6x6 Test Vehicle

Kinematic Relations

The displacement of the wheel and hydraulic cylinder (suspension system) is uneven, as the suspension system is connected to the arm rather than the wheel itself directly. The angle defining the proportion of the wheel displacement to the hydraulic cylinder contraction can be calculated using suspension geometry Figure 2-a. The mathematical relation is described in Equation 1, which represents the initial vertical displacement between the connection point of the arm rod with the sprung mass and the unsprung mass center.

$$cos\theta_{arm} = \frac{z_s - z_{us} + h_0}{l_{arm}} \quad (1)$$

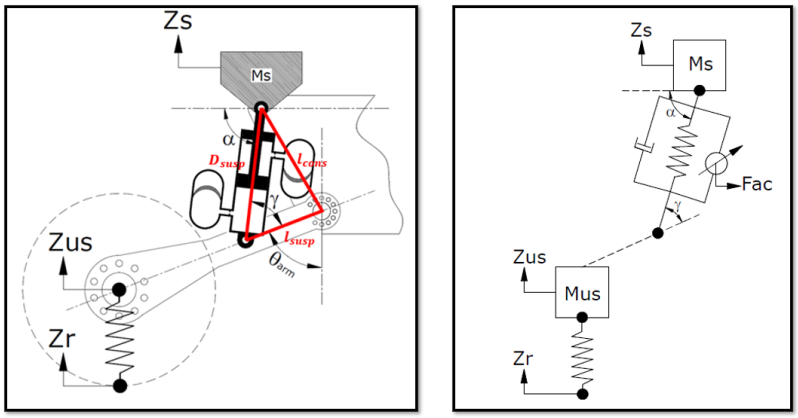


Figure 2 a) Kinematic Relation of Hydro-pneumatic Suspension, b) Simplified Kinematic Relationship of Suspension System

The suspension displacement can be determined with the angle θ_{arm} and Cosine theorem as shown in Equation 2. The notation β represents the angle between the horizontal line and the l_{cons}. Edges of the triangle are lines between connection points of the arm, hydro-pneumatic cylinder, and vehicle. Edges of the triangle are lines between connection points of the arm, hydro-pneumatic cylinder, and vehicle. As shown in Figure 2-a, velocities of sprung and unsprung masses can be obtained by differentiating displacements.

$$D_{susp}^2 = l_{susp}^2 + l_{cons}^2 - 2l_{susp}l_{cons}\cos(\beta + 90 - \theta_{arm}) \quad (2)$$

The establishment of kinematic relations can be completed by defining the angles at which suspension forces act on the sprung and unsprung masses, as demonstrated in Figure 2-a. Angles γ and α can be calculated with the Equations 3 and 4.

$$sin\gamma = \frac{l_{cons}\sin(\beta + 90 - \theta_{arm})}{D_{susp}} \quad (3)$$

$$\alpha = 90 - \theta_{arm} + \gamma \quad (4)$$

Equation of Motion and Free Body Diagram of The Unsprung Mass

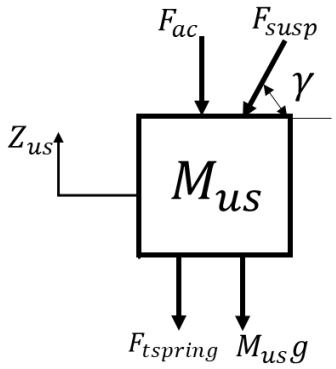


Figure 3 Unsprung Mass Free Body Diagram

Figure 3 shows the free body diagram of the unsprung mass. The corresponding equation of motion can be defined by Equation 5 with the help of kinematic relations established in the previous section.

$$+\uparrow \sum F_z = m_{us}\ddot{z}_{us} \Rightarrow F_{tspring} - m_{us}g - F_{susp}sin\gamma = m_{us}\ddot{z}_{us}$$
$$\Rightarrow k_{tspring}(z_r - z_{us}) - m_{us}g - F_{susp}sin\gamma - F_{ac} \quad (5)$$

$F_{tspring}$ is the force exerted by the tire of the 6x6 test vehicle. The approximate stiffness is obtained from similar tires that have more or the less same geometry, size, and pressure, presented in the literature.

Total suspension force F_{susp} is composed of spring and damping forces which are denoted as F_{spring} and F_{damper} respectively. Detailed derivation of these forces is presented in the sprung mass section.

Total unsprung mass consists of $m_{tire} = 30\ kg$, $m_{motor} = 10\ kg$, $m_{arm} = 8\ kg$ and $m_{aux} = 1\ kg$. The center of gravity is very close to the center of the wheel; therefore, it is assumed to be on the central axis.

Equation of Motion and Free Body Diagram of The Sprung Mass

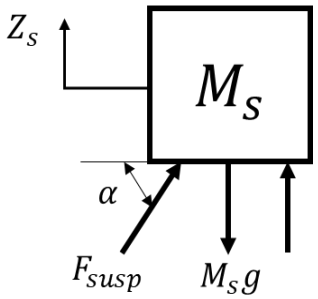


Figure 4 Sprung Mass Free Body Diagram

Figure 4 shows the free body diagram of the sprung mass $(m_s = 225\ kg)$, equation of motion can be defined as shared in equation 6.

$$+\uparrow \sum F_z = m_s\ddot{z}_s - m_s g = F_{susp}\sin(\alpha) + F_{ac} \quad (6)$$

The suspension force F_{susp}:

$$F_{susp} = F_{spring} + F_{damper} \quad (7)$$

The pre-charge pressure of the accumulators must be defined first to obtain spring stiffness. Relation between the pre-charge pressures of accumulators connected to the upper and lower chamber of the cylinder is:

$$P_{30} = \left(\frac{\frac{m_s g}{\sin(\alpha)} + \left(\frac{(P_{40} + P_{atm})A_{fp} - M_{fp} g}{A_{fp}} A_{pr} \right) A_{fp}}{A_{pis}} - M_{fp} g \right) A_{fp} + P_{atm} \quad (8)$$

Pressure P_{40} is determined by considering vehicle properties such as mass with the suspension parameters presented in [Sağlam, 2016].

The stiffness of the spring also depends on the initial gas volume of accumulators V_{30}, V_{40} and the area of the upper- and lower-cylinder chambers A_{pis}, A_{pr}. The mathematical relation relating stiffness to the area, pressure, and volume is presented in Equation 9.

$$k_{spring} = \frac{A_{pis}^2 P_{30} V_{30}^k k}{\left(V_{30} + A_{pis}(z_s - z_{us}) \right)^{k+1}} + \frac{A_{pr}^2 P_{40} V_{40}^k k}{V_{40} - A_{pr}(z_s - z_{us})^{k+1}} \quad (9)$$

The suspension force can be obtained using spring stiffness [Joo, 1991]. A certain amount of suspension compression occurs to balance the vehicle's weight. For this reason, the static compression amount is also added to the dynamic response equation.

Damping force is created by the oil flow through the orifices while the cylinder contracts or extends. The amount of damping force exerted can be altered by changing the diameter of the orifices. The relation between the orifice area and damping force can be described as:

$$F_{damper} = A_{pis} \left(\frac{A_{pis}(\dot{z_s} - \dot{z_{us}})}{C_d A v_2} \right)^2 \frac{\rho}{2} \times sign(\dot{z_p} - \dot{z_{us}}) + A_{pr} \times \left(\frac{A_{pr}(\dot{z_s} - \dot{z_{us}})}{C_d A v_1} \right)^2 \frac{\rho}{2} sign(\dot{z_p} - \dot{z_{us}}) \quad (10)$$

4. FUZZY LOGIC CONTROLLER

Fuzzy logic controller (FLC) is an efficient method of controlling complex, nonlinear or undefined systems with a much faster and simple way that requires a good background knowledge for defining the input-output relations and the boundaries [Son and Isik,1996]. The reason of such kind of requirement is because the fuzzy logic approach mimics a person's decisions that need to be well defined.

The FLC composed of three stages these are fuzzification, fuzzy inference, and defuzzification. In the first stage, the crisp inputs are converted into fuzzy sets. Subsequently, based on the pre-defined rules, the fuzzy inference stage processes the fuzzy input sets and computes the controller output. In the last step (defuzzification), by using the centroid method,

output fuzzy sets are converted into real output numbers in between the pre-defined control limits. The idea behind the centroid method is to compute the center of mass of the contributing fuzzy sets to obtain the real output control values [Stříbrský et al., 2003] [Allam et al.,2010].

In the literature, fuzzy logic controller is widely used to examine the suspension characteristics under different road conditions. However, most of these studies conducted for standard suspension systems which are naturally linear because of their constant spring and damping coefficients [Lin et al., 1993] [Hyniova, 2016]. In this study, a fuzzy logic controller is implemented on the non-linear hydro-pneumatic suspension model to observe more realistic results.

Active Double Acting Hydro-pneumatic Suspension System

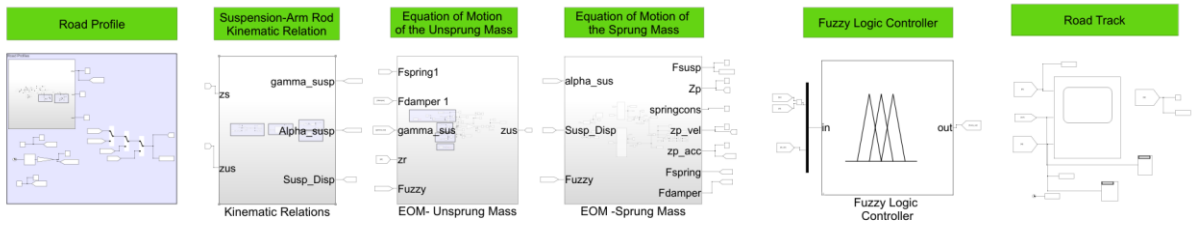


Figure 5 Complete Hydro-Pneumatic Suspension System with Fuzzy Logic Controller MATLAB/Simulink Model

Single acting hydro-pneumatic suspensions using the oil flow as a controlled input is a straightforward procedure. However, in a double-acting hydro-pneumatic suspension system, there are two chambers to be controlled at the same time to avoid negative pressure at one side. That is why, in this study, to focus on the behavior of both passive and active suspension system, the output is treated as force required to achieve desired road holding performance (Figure 5) [Şerifoğlu and Kasnakoğlu, 2021].

In this study, suspension displacement (Dp) and velocity(V) values are used as the input of the FLC. Each input consists of three Membership Functions (MF) which are presented in Figure 6-a and 6-b. In order to consider all of the input combinations, five different MFs are used for the output force (Figure 6-c). The “z” and “s” shaped MFs are preferred for the limits of both inputs and output, whereas for the intermediate changes a triangular shaped MF for the inputs and generalized bell-shaped MFs for the output are used. The rule base considered in this study is presented in Table 1 as linguistic terms. These linguistic expressions are NL (Negative Large), NM (Negative Medium), N (Negative), M (Medium), P (Positive), PM (Positive Medium), and PL (Positive Large).

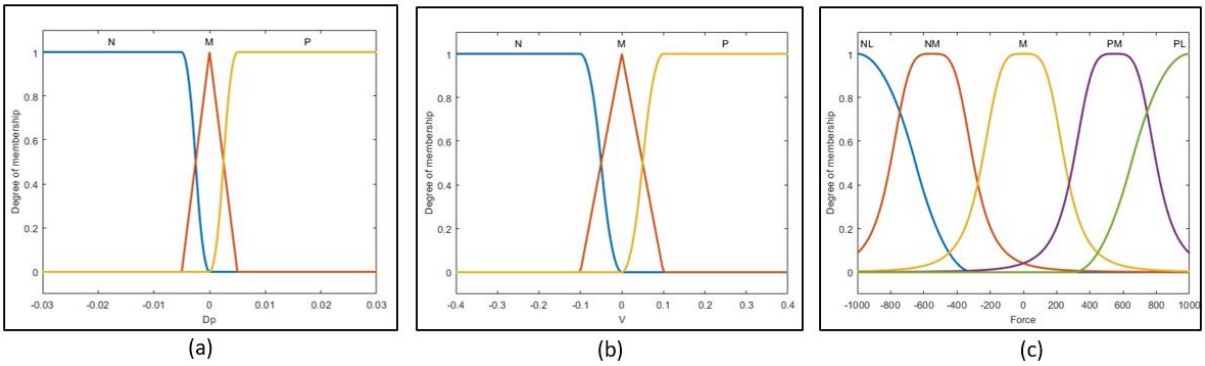


Figure 6 a)-b) Membership Functions of FLC, c) Output Force

Table 1 Fuzzy Logic Controller Rules

Velocity (V) / Displacement (Dp)	N	M	P
N	**PL**	**PM**	**NM**
M	**PM**	**M**	**NM**
P	**M**	**NM**	**NL**

5. RESULTS AND DISCUSSIONS

The dynamic model of double acting hydro-pneumatic suspension system with a fuzzy logic controller is simulated, in order to analyze the position and acceleration of the sprung mass with respect to different road profiles. The simulation results presented in this paper show the travel of vehicle body. Furthermore, to see the performance enhancement numerically, RMS values for the travel of sprung mass and its acceleration are calculated.

Three different road scenarios are used in this simulation. A single bump and a single pothole with a height of 10 cm is supplied to the system while cruising at 20km/h speed to visualize the performance alteration. [Hassaan, 2014] To observe the effects of non-uniformities on road surfaces, a third random road profile is taken into account as well [Sağlam, 2016].

The most apparent superiority of double acting suspension systems is having a minimum spring stiffness at a specific amount compression, for which the spring stiffness gets a higher value for further compression or expansion. To visualize this feature, the plot of spring stiffness versus suspension displacement is presented in Figure 7-a. Moreover, a typical damping characteristic of a hydro-pneumatic suspension system is shared in Figure 7-b [Oscarsson, 2015].

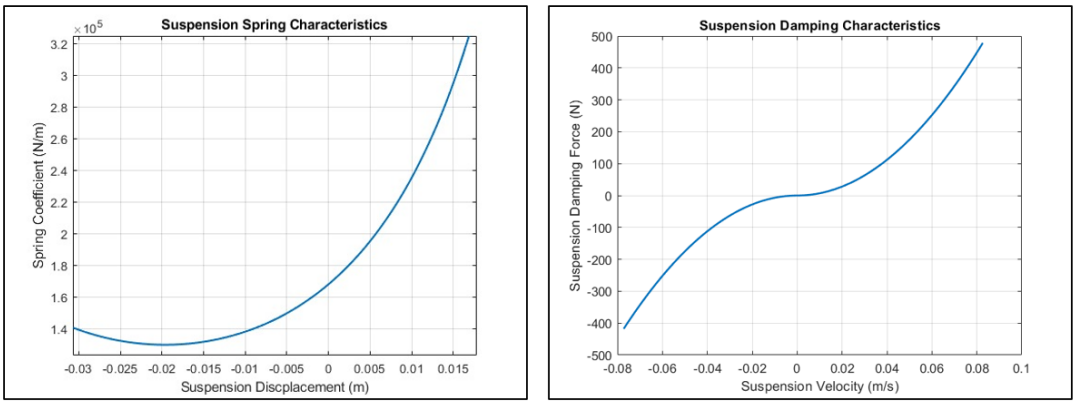


Figure 7 a) Behavior of Spring Characteristics b) Behavior of Damping Characteristics

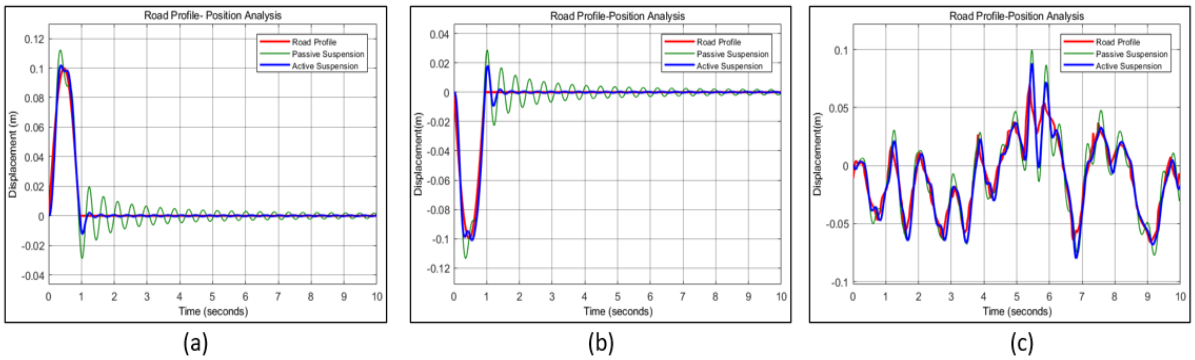


Figure 8 a) Bump Road Profile, b) Pothole Road Profile, c) Random Road Profile

In the case of single bump and single hole conditions, the passive hydro-pneumatic suspension system performs rather oscillatory behavior. Even after 10 seconds simulation, the suspension system cannot absorb the effect of the excitation completely. However, as it is shown in the Figure 8-a, 8-b, the presented active suspension system with FLC yields better results by means of road holding while preserving the ride comfort. According to the position and acceleration RMS values given in Table 2, for the road surface with a single bump, the active suspension tracks the road two times better while decreasing the acceleration at the same rate. On the other hand, for the road surface with a single pothole, again the active suspension performs better results for both position and acceleration but this time the performance of FLC decreases slightly compared to former road conditions. According to the ISO-2631-1 standard, the acceleration RMS values for the above explained cases, are below the uncomfortable threshold for human exposure [ISO 2631-1, 1997].

In order to observe the performance of the FLC on unmaintained natural road surfaces, passive and active suspension characteristics are also shared together with the RMS values. Even for sudden direction changes on the road surface, the fuzzy logic controller performs better results in comparison with the passive suspension system. However, to see the effects on oscillations,

a flat surface should be considered after the excitation, as examined in the first two road conditions.

Table 2 RMS Value of Passive and Active Suspension

		Bump	Pothole	Random Road
Passive Suspension	Position $[m]$	0.0064	0.0066	0.0135
	Acceleration $[m^2/s]$	1.3684	1.4304	3.2194
Active Suspension	Position $[m]$	0.0030	0.0039	0.0098
	Acceleration $[m^2/s]$	0.7334	0.9930	2.6738

6. CONCLUSION

Fuzzy logic controlled active double acting hydro-pneumatic suspension system with two DOFs is simulated for a 6x6 terrain vehicle with an articulated suspension mechanism. The nonlinear effects caused by both kinematic relations and hydro-pneumatic suspension are included to have more realistic model. The flexibility of the fuzzy logic controller is demonstrated for three different road profiles. The simulation results showed that the proposed fuzzy logic controller is very effective on damping characteristics for terrain vehicles. In the future, more advanced fuzzy logic controller, that can also adjust the orifice opening instantaneously, can be developed.

7. ACKNOWLEDGEMENT

The study is conducted under the project “Design and Development of a Modular Height Adjustable Land Platform with 6x6 Tactical Wheels” that is supported by
HİDROAN Ankara Hydraulic. We appreciate HİDROAN Ankara Hydraulic for their support.

REFERENCES

1. Sağlam, F., and Ünlüsoy, Y.S., (2014), “Hidro-Pnömatik Süspansiyonlu Araçlar İçin Tümleşik Sürüş Konforu ve Yükseklik Kontrolü”, OTEKON 14, No. 7, Bursa, pp 26-27.

2. Reddy, C.V., Shankapal, S.R. and Gowda, M.H., (2014), “Modelling and Simulation of Hydropneumatic Suspension for a Car”, SASTech-Technical Journal of RUAS, Vol. 13, No.1, pp 24-30.

3. Bauer, W., (2011), “Hydropneumatic Suspension Systems”, Springer, Berlin.

4. Doğan, H., Kaplan, K., Kuncan, M. and Ertunç, H. M., (2015), “Araç Süspansiyon Sistemi Kontrolüne PID ve Bulanık Mantık Yaklaşımları PID”, Otomatik Kontrol Ulusal Toplantısı, Denizli, pp 699-704.

5. Khodadadi, H., and Ghadiri, H., (2018), “Self-Tuning PID Controller Design Using Fuzzy Logic for Half Car Active Suspension System”, International Journal of Dynamics and Control, Vol.6, No 1, pp 224-232.

6. Kirk, D. E. (2004), Optimal control theory: an introduction. Dover Publications, Inc., Mineola, New York.

7. Bhangal, N. S., and Raj, K. A., (2016), “Fuzzy Control of Vehicle Active Suspension System”, International Journal of Mechanical Engineering and Robotics Research, Vol. 5, No. 2, pp 144-148.

8. Son, S. I., and Isik, C., (1996), “Application of Fuzzy Logic Control to an Automotive Active Suspension System”, In Proceedings of IEEE 5th International Fuzzy Systems, Vol. 1, pp 548-553.

9. Allam, E., Elbab, H. F., Hady, M. A. and Abouel-Seoud, S., (2010), “Vibration Control of Active Vehicle Suspension System Using Fuzzy Logic Algorithm”, Fuzzy Information and Engineering, Vol. 2, No.4, pp 361-387.

10. Sağlam, F., (2016), “Optimization of ride comfort for vehicles equipped with passive and active hydro-pneumatic suspensions”, PhD Thesis, METU, Ankara.

11. Ulusoy, K.B., Değirmenci, B., Filiz, E., Türedi, D., Karaman, M., Konukseven, E.İ., (2022), “Modeling and Simulation of Double Acting Hydro-Pneumatic Suspension System for 6x6 Terrain Vehicle with Different Performance Parameters”, Proceedings of ISUDEF'22 Symposium, Madrid.

12. Joo, F.R., (1991), “Dynamic Analysis of a Hydropneumatic Suspension System”, PhD Diss., Concordia University Mech. Eng. Dept., Montreal.

13. Stříbrský, A., Hyniová, K., Honců, J. and Kruczek, A. (2003), “Using Fuzzy Logic to Control Active Suspension System of One-Half-Car Model”, Acta Montanistica Slovaca, Ročník, 8.

14. Lin, Y. J., Lu, Y. Q. and Padovan, J., (1993), "Fuzzy Logic Control of Vehicle Suspension Systems", International Journal of Vehicle Design, Vol.14, No.5-6, pp. 457-470.

15. Hyniova, K., (2016) "Vibrational Analysis Of Suspension System For One-Half-Car Model With Fuzzy Logic Controller", Scientific**,** pp.82-85.

16. Şerifoğlu, A. M., and Kasnakoğlu, C., (2021), "Fuzzy Logic Controlled Active Hydro-Pneumatic Suspension Design Simulation and Comparison for Performance Analysis", 3rd International Congress on Human-Computer Interaction, Optimization and Robotic Applications, Ankara, pp. 1-5.

17. Hassaan, G.A., (2014), "Car Dynamics Using Quarter Model and Passive Suspension, Part I: Effect of Suspension Damping and Car Speed", International Journal of Computer Techniques, Vol. 1, No.2, pp 1-9.

18. Oscarsson, M., (2015), "A Hydropneumatic Suspension Parameter Study on Heavy Multi-Axle Vehicle Handling"**,** M. Sc. Thesis, KTH, School of Engineering Sciences (SCI), Stockholm.

19. **ISO 2631-1, (1997),** International Organization for Standardization, Mechanical Vibration and Shock—Evaluation of Human Exposure to Whole Body Vibration—Part 1: General Requirements, ISO 2631-1:1997, 1997.

DESIGN OF A TWO-SPEED DUAL-CLUTCH TRANSMISSION FOR ELECTRIC VEHICLES

S. Can Becerikli, *s.canbecerikli@gmail.com* Atilim University, 06830, Ankara, Turkey

Hatice Erdoğan, *haticerd98@hotmail.com* Atilim University, 06830, Ankara, Turkey

Mustafa B. Bayram, *mustafabayram99@hotmail.com* Atilim University, 06830, Ankara, Turkey

Ozan Tekin, *ozan.tekin@atilim.edu.tr* Atilim University, 06830, Ankara, Turkey

Ramin Barzegar, *ramin.barzegar@atilim.edu.tr* Atilim University, 06830, Ankara, Turkey

ABSTRACT

This paper deals with the design of a two-speed dual-clutch transmission (DCT) system for electric vehicles. In contrast to the two concentric clutch assembly used in conventional DCTs which is very complex and costly, in this study a novel approach was proposed in which two electromagnetic clutches were mounted on parallel shafts. The design and analysis of the transmission components were carried out by means of analytical approach. The results indicated that compared to a single-speed transmission which required 64 seconds to reach from zero to 55 km/h, the application of the two-speed transmission in the electric car resulted in the decrease of the acceleration time to 30 seconds. Also, it was found that the two-speed transmission system resulted in 37 kJ energy save during the acceleration.

Keywords: Dual-Clutch, Transmission, Electric Vehicle, Acceleration, Energy Saving

1. INTRODUCTION

Unlike internal combustion engines which their torque characteristics are highly dependent on engine speed, the electric motors can reach high torque values from the start. As a result, a single gear pair acting as a torque multiplier is common in electric vehicles (EV). Single-speed transmission has additional advantages including less weight, small space, and less cost compared to a multi-speed transmission system (Ehsani et al., 2004; Miller, 2004; Husain, 2010; Hu, Martinez and Yang, 2017). However, owing to the fact that the efficiency of an electric motor depends on its speed, the motor cannot run in the high-efficiency range in both

the high and low speed ranges, resulting in poor energy transmission efficiency (Ren, Crolla and Morris, 2009). Several studies have shown that addition of a two-speed transmission to an electric vehicle can increase the vehicle torque by 34% and its top speed by 24% (Sorniotti, Holdstock, Pilone, Viotto, Bertolotto, Everitt, Robert J. Barnes, et al., 2012). The comparison between the energy consumption of EVs with a variable and fixed ratio transmission under regular driving cycle has proven that when equipped with a multi-speed gearbox, the overall energy efficiency can be enhanced by about 5 to 12% (Ruan, Walker and Zhang, 2016). Therefore, including a multi-speed transmission allows not only high torque at lower speeds but also increase in the efficiency and maximum speed of EV.

Another important issue affecting vehicle efficiency is during gear shift. The shifting mechanism should be designed so that its operation be quick and efficient to avoid power flow interruption. The automatic transmission is almost unaffected by momentary torque drops thanks to its fast gear shift. But its efficiency can only reach up to 86%. The manual transmission, on the other hand, causes a power flow discontinuation for a short period of time during gear shifting, but its efficiency is as high as reach 97%. Dual-Clutch Transmission (DCT) transmission offers the convenience of the automatic transmission and efficiency of a manual transmission system (Vacca et al., 2017). Owing to its pre-selected gears, the DCT operates quickly at shifting (Walker, Zhu and Zhang, 2017). In manual transmissions, the gear shifting process takes place in three steps: the clutch separates the connection between the engine and transmission, the next gear is selected and the speed difference between gears is synchronized with the help of the synchronizer, and finally, the clutch re-engages and the connection between engine and transmission is re-established. However, in DCTs this process takes place in two-step: while one clutch is engaged and the power flows from one set of gears, the next gear set will be pre-selected and gear shifting is achieved by simply changing the operating clutch. In this way, the transition phase will be minimum with small power loss during gear shift and it also provides driving comfort. (Sorniotti, Holdstock, Pilone, Viotto, Bertolotto, Everitt, Robert J Barnes, et al., 2012)

There are two well-known brands that put the idea of installing transmissions in EVs into the practice. The most well-known one is the Porsche Taycan, which is still on the market, and the other one was the first-generation Tesla Roadster, which is not very well-known because it was on sale for a short period of time. The transmission produced by Tesla was a two-speed manual dry clutch transmission. The problem with this transmission was that the dry clutch could not cope with the sudden increase in torque of the electric motor. As a result, Tesla quickly turned to the use of a single-speed gearbox. On the other hand, Porsche used a gearbox consisting of two sets of planetary gears with multiplate clutches (Fietkau, Kistner and Munier, 2020). Thanks to the multiplate clutch assembly, the power transmission from the

electric motor to the wheels was achieved seamlessly. Comparing the torque values of these two marketed vehicles which is 1050 N-m for the most powerful version of the Taycan and 400 N-m for the most powerful version of the Roadster, since it is difficult to control sudden fluctuations in these high torque values, the roadster with dry clutch was withdrawn from the market, while the Taycan with multi-plate clutch reached high sale figures.

Review of the literature revealed that application of a dual-clutch transmission system in EVs has not been studied. Therefore, this study aimed to design and develop a two-speed electronically controlled DCT for EV in order to improve its acceleration and reduce energy consumption. Additionally, in conventional DCTs, the two clutches are assembled concentrically which makes it very complicated and expensive. In contrast, the DCT designed in this study utilizes two separate clutches on parallel shafts. The calculations were carried out by means of analytical methods for an EV with power and torque values of 4 kW and 13 N-m, respectively.

2. MATERIALS AND METHODS

A two-speed DCT was designed for a lightweight EV using an electric motor with the power output of 4 kW, the maximum torque of 13 N-m and the maximum speed of 3000 rpm. Helical gear type was selected since helical gears are able to operate with the efficiencies as high as 99.7% (Petry-Johnson et al., 2008; Kim et al., 2020), also their operation creates less noise and vibration. The material used for the gears were AISI 8650 steel alloy which is one of the steel types commonly used in gear production. It has high strength suitable for hardening and surface smoothing. The material used for the case were Al-6061 and Al-5750 aluminum alloys. Al-6061 was chosen for the main walls to carry the axial forces caused by the helical gears. Al-5750, on the other hand, was chosen as the sheet metal material to be used to cover areas that will carry relatively less load.

In order to calculate the maximum speed that the vehicle can reach with the 4 kW motor, the drag force and rolling resistance were calculated based on the following equations:

$$F_{air} = \frac{1}{2} \cdot \rho \cdot C_d \cdot A \cdot V^2 \quad (1)$$

$$F_{roll} = f_R \cdot g \cdot m \quad (2)$$

Considering these forces, the first and second gear ratios of the vehicle were determined. After finding the number of teeth of the gears according to the gear ratios, the helix angle (Ψ) was selected considering the ease of production and its effect on the axial load. In order to obtain

the gear module, the maximum loading force (F_Y) and the tangential force that the gear can handle (F_t) were calculated as follows:

$$F_Y = \frac{P \cdot 60{,}000}{\pi \cdot M_n \cdot Z \cdot N} \cdot C_s \tag{3}$$

$$F_t = \sigma_s \cdot b \cdot Y \cdot M_n \tag{4}$$

The maximum tangential force handles by the gear is calculated according to the Barth equation:

$$F_{tmax} = F_t \cdot C_v \tag{5}$$

F_Y must be smaller or equal to the F_{tmax} since the only unknown value is the normal module which was calculated by using these two equations. The gear module (M_t), pitch diameter (d_p), pitch line velocity (V), and transmitted load (W_t) were calculated based on the following equations:

$$M_t = \frac{M_n}{\cos \Psi} \tag{6}$$

$$d_p = \mathrm{Z} \cdot M_t \tag{7}$$

$$V = \frac{\pi \cdot d_p \cdot N}{60} \tag{8}$$

$$W_t = \frac{60{,}000 \cdot H}{\pi \cdot d_p \cdot N} \tag{9}$$

The pressure angle in the direction of rotation (Φ_t) is:

$$\Phi_t = tan^{-1} \frac{tan\Phi}{cos\Psi} \tag{10}$$

The radial and axial components of the transmitted load were calculated based on the following equations:

$$W_r = W_t \cdot tan\, \Phi_t \tag{11}$$

$$W_a = W_t \cdot tan\, \Psi \tag{12}$$

Thus, the forces in all directions caused by the power transmission through the gears were found. Additionally, the bearings to support the shafts to which the gears are connected were selected and the lifetime calculations were made for these bearings as follows:

$$L_{10h} = \frac{L_r}{60 \cdot N} \cdot \left(\frac{C_{10}}{F_e}\right)^3 \tag{13}$$

Finally, the bending stress value was calculated by using the AGMA equation. This value is required for material selection and the factor of safety calculation.

$$\sigma = W_t \cdot K_v \cdot K_o \cdot K_s \cdot \frac{P_t}{F} \cdot \frac{K_m \cdot K_B}{J_p} \tag{14}$$

Based on the obtained results from the analytical calculations, the gear models were created. Then, the case design was made in suitable dimensions and strength to carry the loads. Two electromagnetic clutches were selected according to the required torque values of the electric motor.

3. RESULTS AND DISCUSSION

By applying the described analytical procedure, the maximum speed of the vehicle using a 4-kW electric motor was calculated to be 82 km/h. The cruising speed of the vehicle was set to 55 km/h according to the maximum obtainable efficiency of the electric motor. Figure 1 represents the relation between the torque and speed of the vehicle. As can be seen, the optimum speed at which the gear shift should occur was calculated as 58 km/h in which the motor speed was reached up to 2880 rpm. According to the output data for the vehicle, the gear ratios for the first and second gears in the transmission system were calculated to be 1.38 and 0.92, respectively. Multiplied these ratios by the differential ratio of 4, the overall ratio of the first gear was 5.52 and the second gear was 3.68. Based on the abovementioned equations, using only the second gear set, the required energy during acceleration was calculated as about 108 kJ in 63 seconds, while adding the first gear set reduced the needed acceleration energy to 71 kJ in 30 seconds which resulted in 37 kJ energy save during acceleration as can be seen in Figure 2.

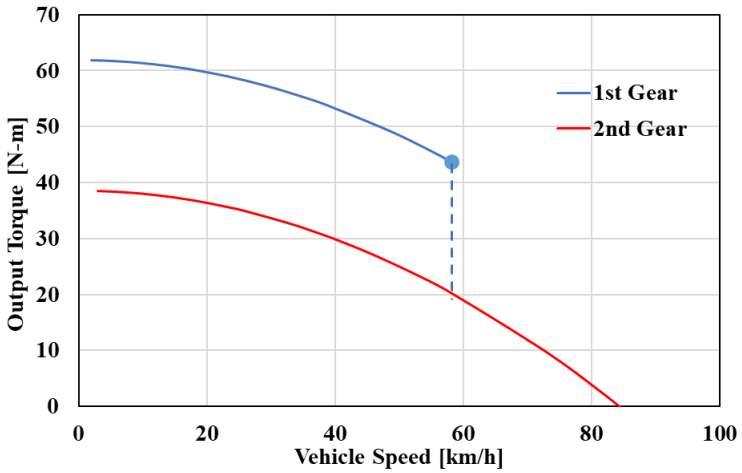


Figure 1. Comparison of output torque with engine speed and gear shift position

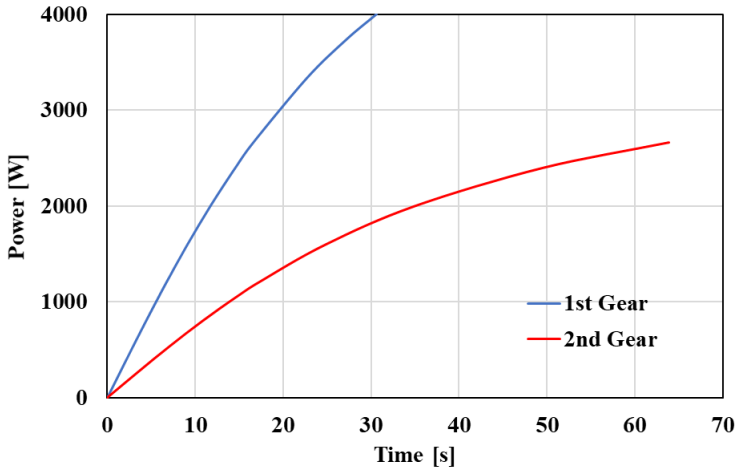


Figure 2. Consumed power during acceleration at different gear ratios

The schematic of the designed DCT is shown in Figure 3. This diagram shows the arrangement and number of teeth of the gears and the position of the electromagnetic clutches. Activating the upper clutch results in power flow from the upper shaft and switching between the clutches results in the power flow direction to the lower shaft. An electric control system was used for the accurate timing of the clutch switch.

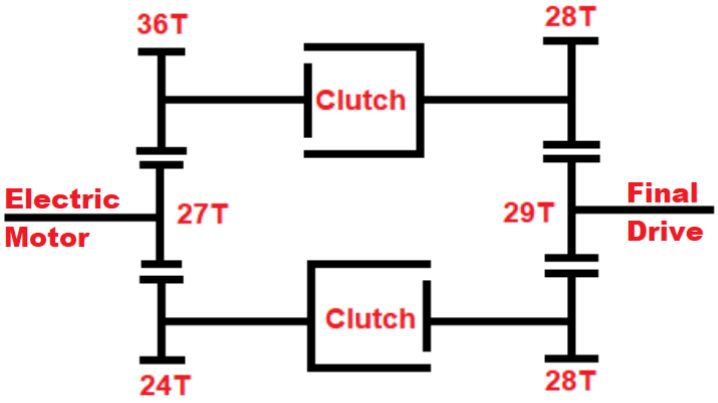


Figure 3. Schematic of the designed DCT

The gears were designed based on the calculated ratios as well as considerations regarding the space limitations. The normal modulus value was found to be 2 mm by using equations (3), (4) and (5) in the previous section. Transmitting power from the motor through helical gears results in occurrence of three forces which can be seen in Figure 4. These forces were calculated for the pinion gear using equations (9), (11) and (12). The transmitted load was

332.2N with the axial component of 120.8N and the radial component of 128.6N. The reaction forces at the two points where the gear shaft will be fixed were calculated as well and the results can be seen in Figure 4.

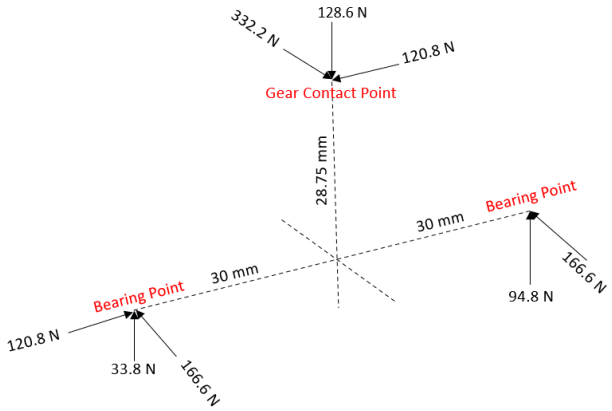


Figure 4. Free-body diagram of the motor shaft

In order to be able to support the shaft to which the gear is connected, the selection of bearings and the lifetime calculations were carried out based on equation (13). As a result, a lifecycle of 10000 hours was found in case the bearing number SKF16004 was selected. The final analytical calculation for the gears was assessing the bending stress. According to AGMA's equation, the bending stress value of the pinion gear was 44.4 MPa. This value was far lower than the strength of AISI4140 steel chosen as the gear material. However, because of the space limitations which mainly was the clutch diameter, the gear diameters could not be reduced further.

Figure 5 represents the designed gear train for the input and output of the transmission system. In both groups, it was critical that the centers of the outermost gears be equidistant because the shafts had to be parallel to each other. The final assembly of the designed DCT is shown in Figure 6. The arrangement of the gears, clutches and other components can be seen as well as the parts designed to mount the gearbox on the vehicle.

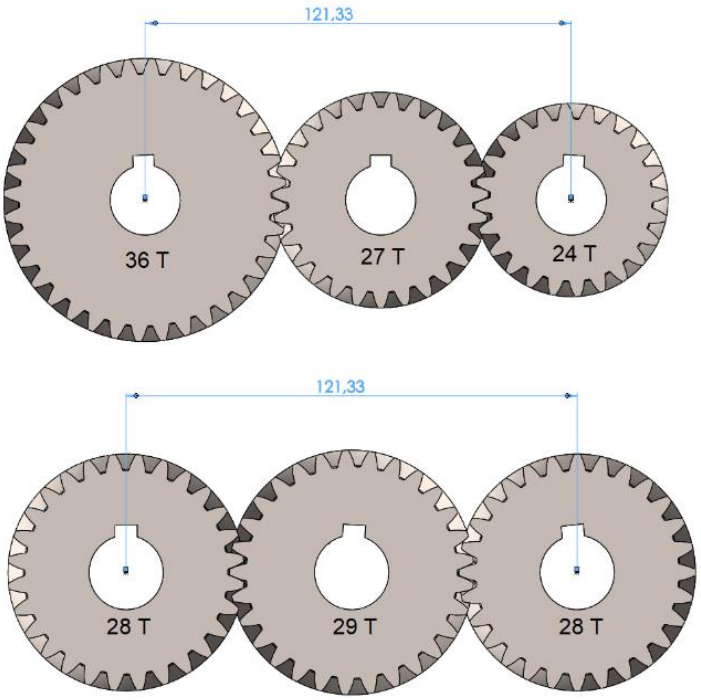


Figure 5. Input and output gear trains of the DCT

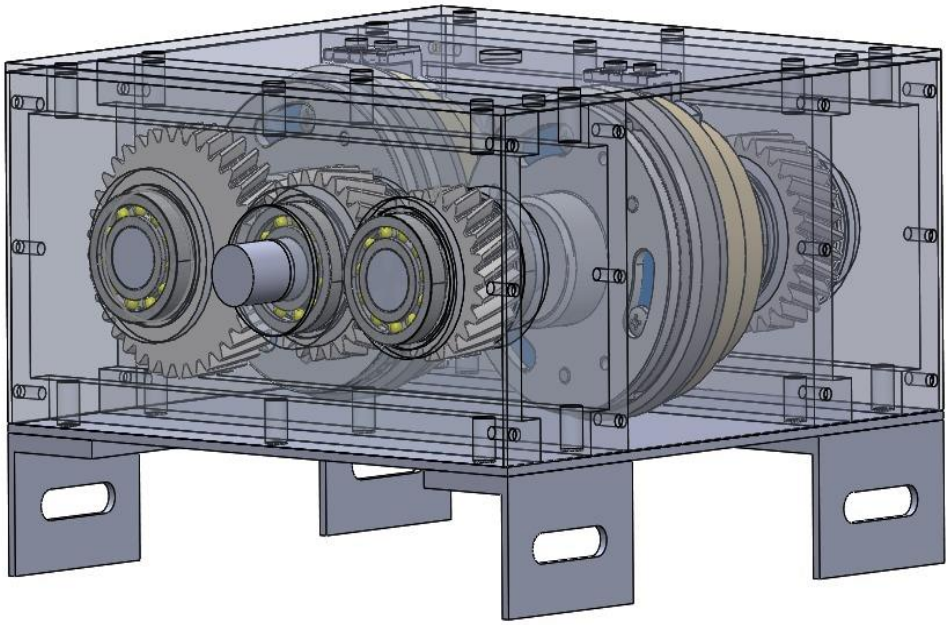


Figure 6. Final assembly of the designed DCT

4. CONCLUSION

In this paper a new type two-speed dual-clutch transmission system was proposed to be used in electric vehicles. In contrast to the conventional DCTs which have concentric clutches which

require complex and costly design, in this design, two electromagnetic clutches were mounted on parallel shafts. The calculations regarding the transmission components were carried out analytically for an electric motor with the power and torque of 4 kW and 13 N-m, respectively. It was seen that application of a two-speed clutch decreased the acceleration time by more than 50% and also reduced the energy consumption during acceleration by about 37 kJ.

5. REFERENCES

Ehsani, M. *et al.* (2004) *Modern electric, hybrid electric, and fuel cell vehicles: Fundamentals, theory, and design*, *Modern Electric, Hybrid Electric, and Fuel Cell Vehicles: Fundamentals, Theory, and Design*.

Fietkau, P., Kistner, B. and Munier, J. (2020) 'Virtual powertrain development', *Proceedings of the Institution of Mechanical Engineers, Part D: Journal of Automobile Engineering*, 234(14), pp. 3288–3301. doi: 10.1177/0954407020936797.

Hu, X., Martinez, C. M. and Yang, Y. (2017) 'Charging, power management, and battery degradation mitigation in plug-in hybrid electric vehicles: A unified cost-optimal approach', *Mechanical Systems and Signal Processing*, 87. doi: 10.1016/j.ymssp.2016.03.004.

Husain, I. (2010) *Electric and Hybrid Vehicles*. CRC Press. doi: 10.1201/9781439894972.

Kim, S. chul *et al.* (2020) 'Macro geometry optimization of a helical gear pair for mass, efficiency, and transmission error', *Mechanism and Machine Theory*, 144. doi: 10.1016/j.mechmachtheory.2019.103634.

Miller, J. M. (2004) *Propulsion Systems for Hybrid Vehicles*, *Propulsion Systems for Hybrid Vehicles*. doi: 10.1049/pbpo045e.

Petry-Johnson, T. T. *et al.* (2008) 'An experimental investigation of spur gear efficiency', *Journal of Mechanical Design, Transactions of the ASME*, 130(6). doi: 10.1115/1.2898876.

Ren, Q., Crolla, D. A. and Morris, A. (2009) 'Effect of transmission design on Electric Vehicle (EV) performance', in *5th IEEE Vehicle Power and Propulsion Conference, VPPC '09*. doi: 10.1109/VPPC.2009.5289707.

Ruan, J., Walker, P. and Zhang, N. (2016) 'A comparative study energy consumption and costs of battery electric vehicle transmissions', *Applied Energy*, 165. doi: 10.1016/j.apenergy.2015.12.081.

Sorniotti, A., Holdstock, T., Pilone, G. L., Viotto, F., Bertolotto, S., Everitt, M., Barnes, Robert J, *et al.* (2012) 'Analysis and simulation of the gearshift methodology for a novel two-speed transmission system for electric powertrains with a central motor', *Proceedings of the*

Institution of Mechanical Engineers, Part D: Journal of Automobile Engineering, 226(7), pp. 915–929. doi: 10.1177/0954407011431415.

Vacca, F. *et al.* (2017) 'On the energy efficiency of dual clutch transmissions and automated manual transmissions', *Energies*, 10(10). doi: 10.3390/en10101562.

Walker, P., Zhu, B. and Zhang, N. (2017) 'Powertrain dynamics and control of a two speed dual clutch transmission for electric vehicles', *Mechanical Systems and Signal Processing*. Academic Press, 85, pp. 1–15. doi: 10.1016/J.YMSSP.2016.07.043.

AN INVESTIGATION OF THE CRASHWORTHINESS OF MULTI-CELL FILLED BATTERY SIDE BEAMS

İsmail YAY, *ismlyay@gmail.com* Bursa Technical University, 16350, Bursa, Turkey

Emre DEMİRCİ, *emre.demirci@btu.edu.tr* Bursa Technical University, 16350, Bursa, Turkey

ABSTRACT

In this study, the crashworthiness of the battery side beam structures for battery safety of electric vehicles was numerically tested. L profile was chosen for the side beam structure cross-section. Three different multi-cell geometries were investigated to examine the effect of filling multi-cell structures in the battery side beam on the crash resistance. In addition, multi-cell structures with different thicknesses and different materials are also examined. The crash analysis was carried out with a cylindrical rigid impactor. As a result, it was determined that multi-cell structures increased the crash efficiency for the battery side beam.

Keywords: Crashworthiness, Multi-Cell Structure ,Battery Side Beam, Electric Vehicle

1. INTRODUCTION

The internal combustion engine (ICE) vehicles have dominated the transportation sector for nearly a century, and in the last decade, electric vehicles have started to replace the internal combustion engine vehicles. Since electric vehicles have much lower emission levels than ICE vehicles, many countries encourage investments in electric vehicle production. The battery component is one of the most important parts of the electric vehicle. With the widespread use of electric vehicle batteries, vehicles have to undergo some revisions on certain issues such as crash safety and fire resistance. Therefore, the battery case frame of electric vehicles must be reliable and robust.

Li-ion batteries are often preferred in electric vehicles due to their efficiency. Since Li-ion batteries used in electric vehicles have a high explosion tendency when exposed to impact, serious research studies on the safety of battery components have become an issue in the literure. For example, in the study of Palvoelgyi and Stangl [Palvoelgyi and Stangl,1990], a new energy management system was developed for a GM G-VAN model vehicle to reduce the

crash severity of frontal impact. Energy absorbing elements were designed to dissipate the kinetic energy of the impact on the battery box. In a different study, a new battery box platform was developed to protect the battery with a multi-layered protection structure. [Uwai et al., 2009].

In the literature review on energy absorption and crushing efficiencies for multi-cell structures, which are considered to be used within the scope of this research, the back-buffer structures called crash boxes are frequently used. In the study of Yong Xiao et al., the energy absorption of carbon fiber reinforced plastic (CRFP) beams in aluminum honeycomb filled structures was investigated. As a result of the study, it was observed that CRFP beam structures filled with aluminum honeycomb significantly increased energy absorption and specific energy absorption compared to empty structures [Xiao et al., 2018]. In another study, researchers investigated the behavior of honeycomb structure in the axial compression condition. Honeycomb materials of different thicknesses were used in their studies and the effect of reinforcement plates was also investigated. The results were compared experimentally and using the finite element method [Tiwari et al., 2018]. In the study of H.J. Rathbun et al., the behavior of the square profile honeycomb structure made of stainless steel material in sudden shock loading was investigated. Both experimental and finite element methods were used in the study. According to the results, it has been observed that sandwich structures with honeycomb increase the impact resistance [Rathbun et al., 2006]. Acar et al., evaluated some multi-cell design structures to improve the crash performance of crash boxes [Acar et al., 2019]. In another study, different wall lengths of crash boxes with multi-cell structure was investigated to improve the crashworthiness [Albak, 2021]. Navale et al. investigated the mechanical behavior of the battery box in various vehicle crash scenarios [Navale et al., 2021]. In another research, to reduce the risk of battery explosion, honeycomb structure filling material that absorbs impact energy is proposed to be applied on the sides of the batteries [Setiawan and Salim, 2017].

In this study, battery box side protector profiles were investigated numerically under the high-speed impact condition. The L profile structure was chosen as the battery side protector beam profile and the impact effects were observed by supporting it with multi-cell structures in different geometries. The multi-cell structure to be used in these studies was modeled in Solidworks, a computer aided drawing program, and simulations were carried out with Radioss software.

2. GEOMETRIC DESIGN CONCEPTS

In the battery box design, the length and height of the L profile structure were determined based on the side sill length of the Toyota Yaris 2010 vehicle model. The three support profiles

at the back of the L profile structure represent the side profile support and battery separator beams used in the battery box. The length of the L profile is 1235 mm. Side view and dimension of L beam can be seen in Figure 2. The components of the L profile structure include aluminum alloy, structural steel and multi-cells structure. Comparison of multi-cell structures with 0.5 and 1.5 mm thick aluminum material with different geometries was investigated. Multi-cell structures were designed in three different type as hexagonal (honeycomb), quadrangular and triangular. Design parameters of the multi-cell structures are shown detail in Figure 3.

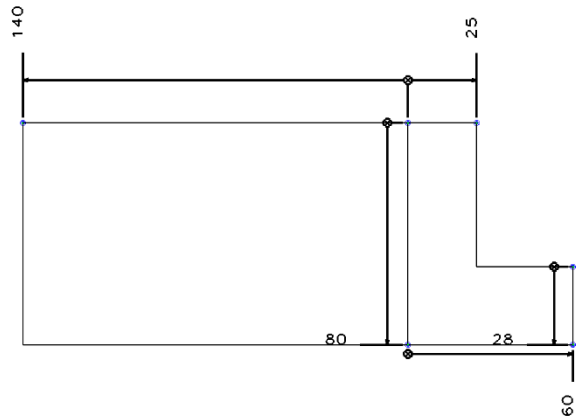


Figure 2. Side View and Dimensions of the L profile beam

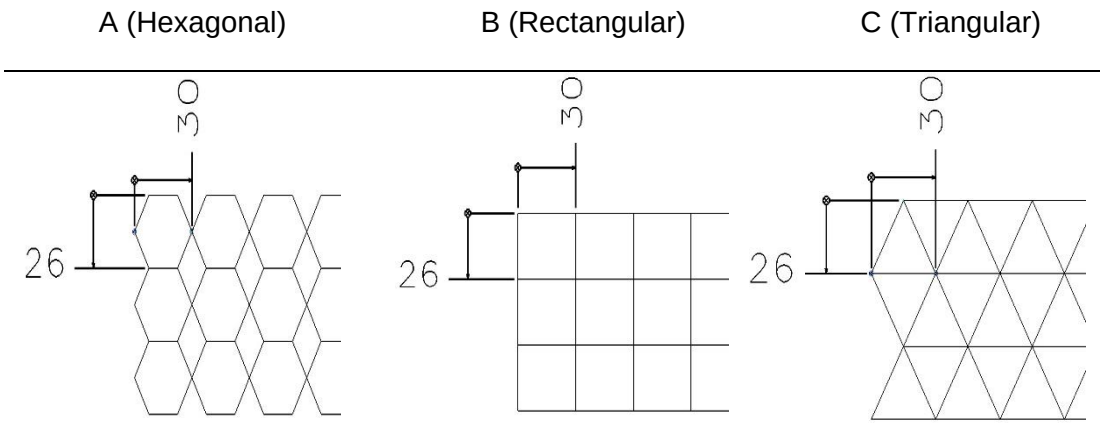


Figure 3. Geometry and Measurements of the Multi-cells Structures

3. FINITE ELEMENT METHOD

Validation

The validation of the finite element model was tested with the experimental data from a study in the literature [Altin et al., 2017]. As part of the validation process, the empty aluminum 6063 material circular tube was used. Finite element model of a circular tube model was created in accordance with the experimental study and the boundary conditions were determined in

HyperMesh software. Detailed information about experimental test and boundary conditions can be found in Ref. [Altin et al., 2017]. The results of validation study was shown in Figure 5.

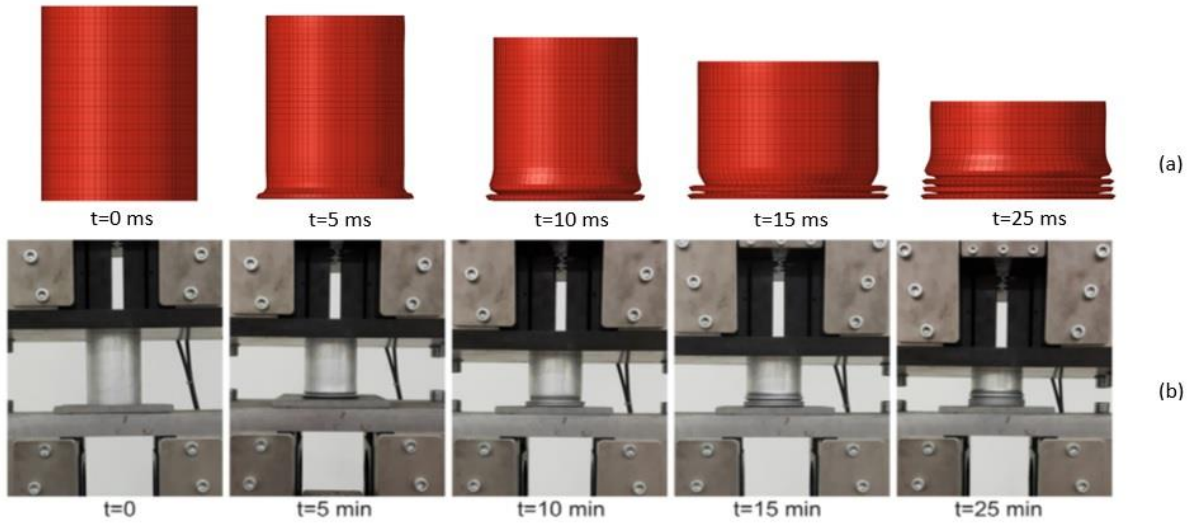


Figure 5. (a) Numerical study (b) Experimantal Study of Validation Model [Altin,2017]

When the results in the figure are examined, it was seen that there was a positive correlation between the results of the experimental study and the numerical finite element analysis (FEA) study. In addition, the crush force - displacement curves of the material used in the experimental study and the FEA study are shown in Figure 6. The FEA results are in good agreement with the experimental results.

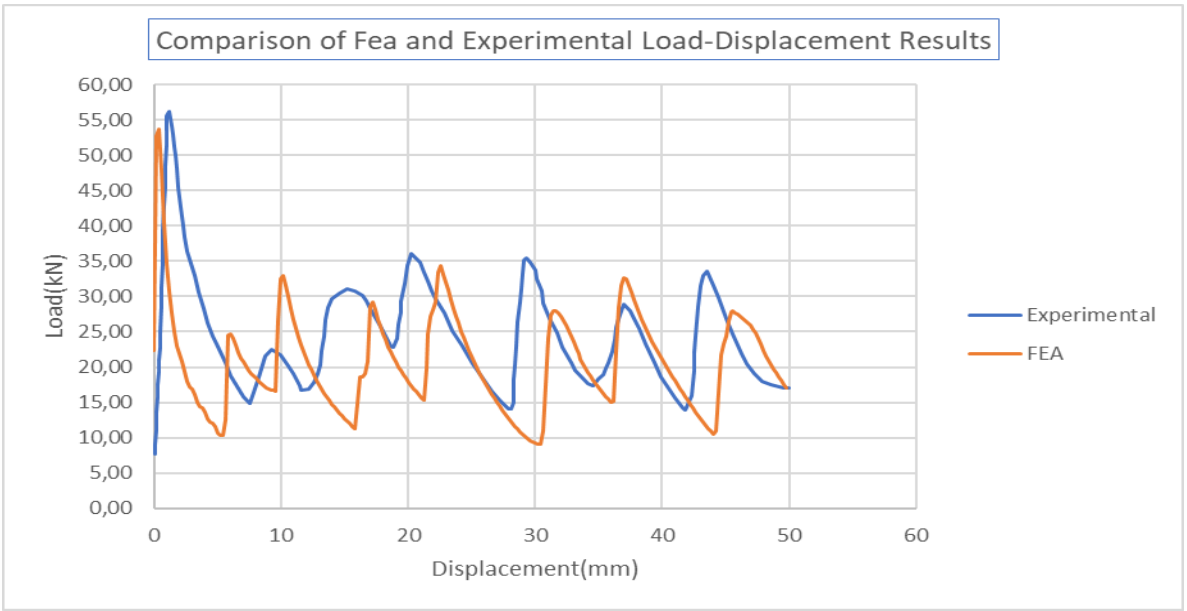


Figure 6. Load-Displacement curves of experimental [Altin et al. ,2017] and FEA studies

Finite Element Model of Battery Side Beam

The general features of the created simulation test L profiles are as follows; Profiles filled with hexagonal multi-cells are named as A_(Material type)_thickness, rectangular filled multi-cells B_(Material type)_thickness, multi-cells filled with triangles are named C_(Material type)_thickness. L shaped battery side beam and multi-cell structures were design as shell and all shell parts were formed into meshes with element dimensions of 3 x 3 mm. The cylindrical solid impactor model was created by meshing with a 6-node tetra mesh process. The rigid cylindrical 254 mm diameter barrier crashed with the profile at a speed of 15 m/s. The contact between impactor, side beam and multi-cell structure were defined by using the Type 2 interface in HyperMesh. *M36_PLAS_TAB isotropic elasto-plastic material card was selected for the aluminum shell structures and multi-cell structures in the created model. Material properties were calculated according to the Quadrangular ElastoPlastic Physical Hourglass Control (QEPH) formula for aluminum shell structures. The displacement and rotational degrees of freedom at the bottom side of the support structures were constrained in all directions. The finite element model of the crash analysis system is given in Figure 7.

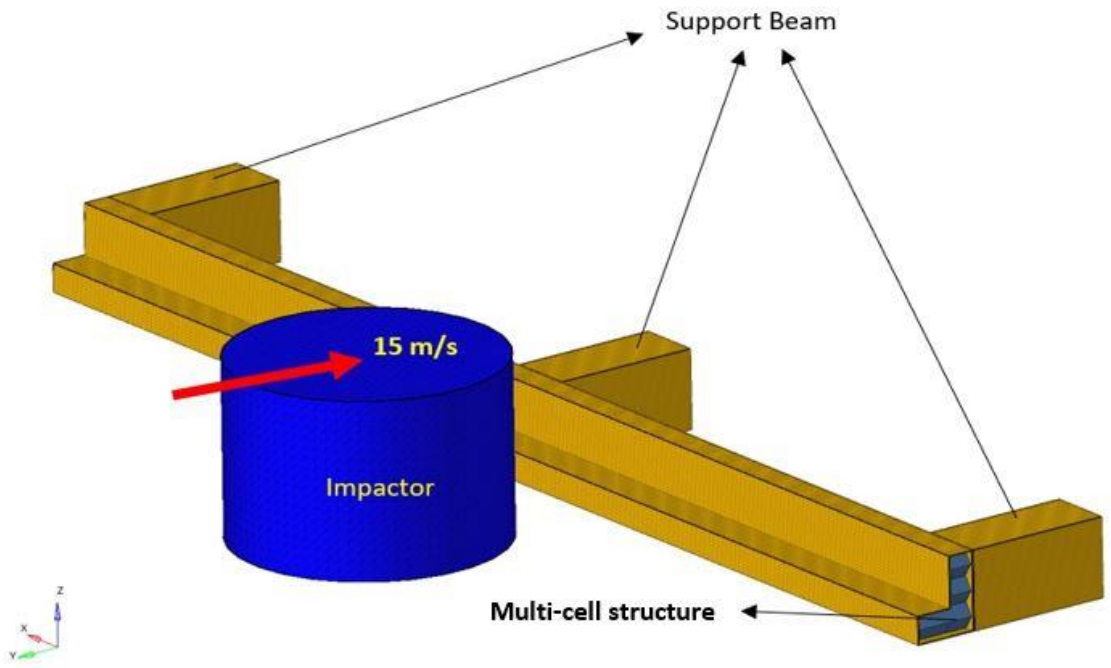


Fıgure 7. General Geometry of the crash analysis system

Material Definitions

Aluminum alloy materials are obtained by mixing different materials at different rates. Aluminum 7003 material is obtained by mixtures of Al–Zn–Mg materials [Hoang et al., 2022]. Al-Mg-Si materials can be used for aluminum 6063 material. Aluminum materials are frequently used in the automotive industry due to their light weight. In addition, these materials are used

in many different sectors [Alaneme and Aluko, 2011]. Dual Phase steels are also frequently preferred in the automotive industry. The ferrite and martensite phases give the dual phase steel its name. These steels have high strength and high deformation properties [Tian et al., 2020]. There are four types of materials used in this study. Crash analysis was performed by using materials in different variations. 2 mm thick DP800 material was used for L shaped battery side beam and support structures. Aluminum alloy 7003, aluminum alloy 6063 and DP800 AHSS steel materials are used in multi-cell structures. The mechanical properties and the true stress and true strain curves of the materials used in this study are given in Table 1 and Figure 8, respectively.

Table 1. Mechanical Properties of Used Materials

	Young's Modules *GPa*	Poisson's Ratio -	Density *g/cm³*
Aluminum 7003	*71*	*0.33*	*2.77*
Aluminum 6063	*68.2*	*0.3*	*2.7*
DP 800 AHSS Steel	*210*	*0.3*	*7.85*
DP 1000 AHSS Steel	*210*	*0.3*	*7.85*

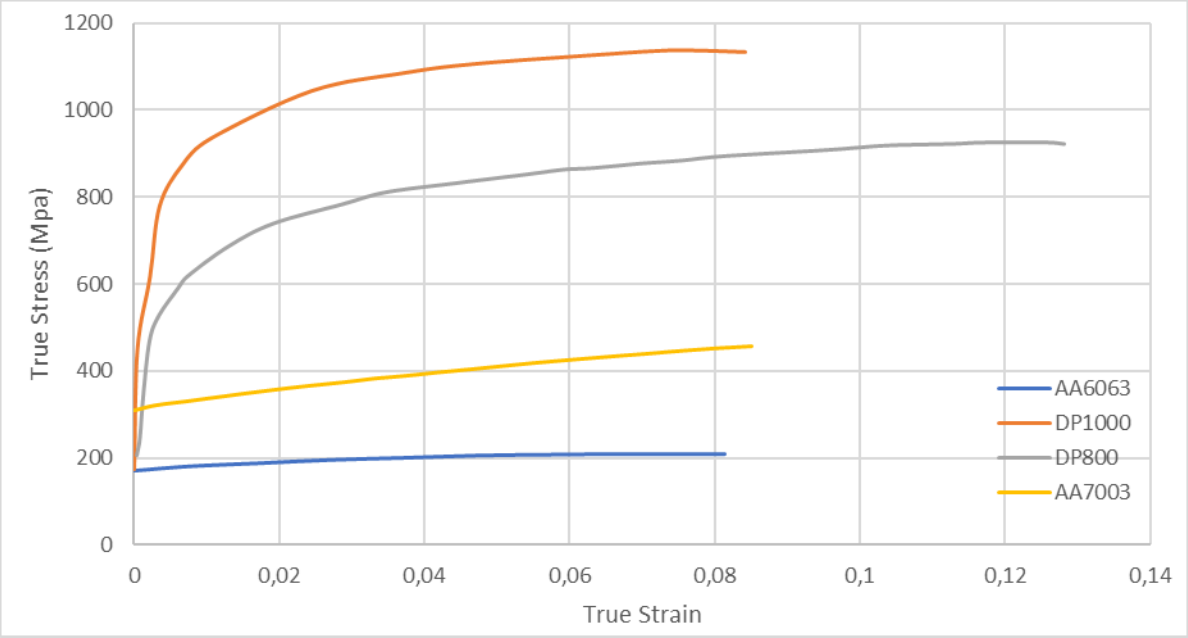


Figure 4. True stress and true Strain of used materials

Crash Simulation

A 71 kg cylindrical rigid impactor with an initial velocity of 15 m/s was crashed with L shaped battery side beam. Specific energy absorption values and maximum force values were determined for the deformation in the L profile, which is caused by a 60 mm displacement of the cylindrical impactor.

The specific energy absorption is calculted by dividing the absorbed energy by the mass of the battery side beam before it deforms. The formulas used in this calculation are given in equation below [Demirci and Yildiz, 2018]:

$$SEA = \frac{EA}{m} = \frac{\int_{d_0}^{d_{max}} Fds}{m} \quad (1)$$

According to this formula, the less the mass of the structure, the higher the specific energy absorption value will be.

4. RESULTS

Firstly, the empty L shaped battery side beam was subjected to crash analysis and the results were given in Table 2. Then battery side beam was filled with the multi-cell structures and crash analysis was repeated over and over.

Table 2. Empty battery side beam FEA simulation results

Empty L Profile	Material Thickness(mm)	Mass (kg)	SEA (kJ/kg)	Fmax (kN)	Absorbed Energy (kJ)
DP 800	2	7,229	0,686	246,100	4,960

Table 3. Hexagonal multi-cell filled battery side beam FEA simulation results

Hexagonal Multi-cell	Material Thickness(mm)	Mass (kg)	Sea (kJ/kg)	Fmax (kN)	Absorbed Energy (kJ)
AA 6063	1.25	8,513	0,761189	185,2	6,48
	1.50	8,769	0,707036	202,7	6,20
AA 7003	1.25	8,546	0,727826	239,9	6,22
	1.50	8,809	0,736747	257	6,49
DP 800	1.25	10,94	0,624314	284,6	6,83
	1.50	11,68	0,600171	294,6	7,01

It has been determined that the best crash performance in the hexagonal multi-cell filled structure is the A_Al6063_1.25 structure. It absorbed approximately %4 more specific energy than A_Al7003 materials and %23 more than A_DP800 materials. Figure 7 shows the crush force-displacement curves for the hexagonal multi-cell filled battery side beams with different materials.

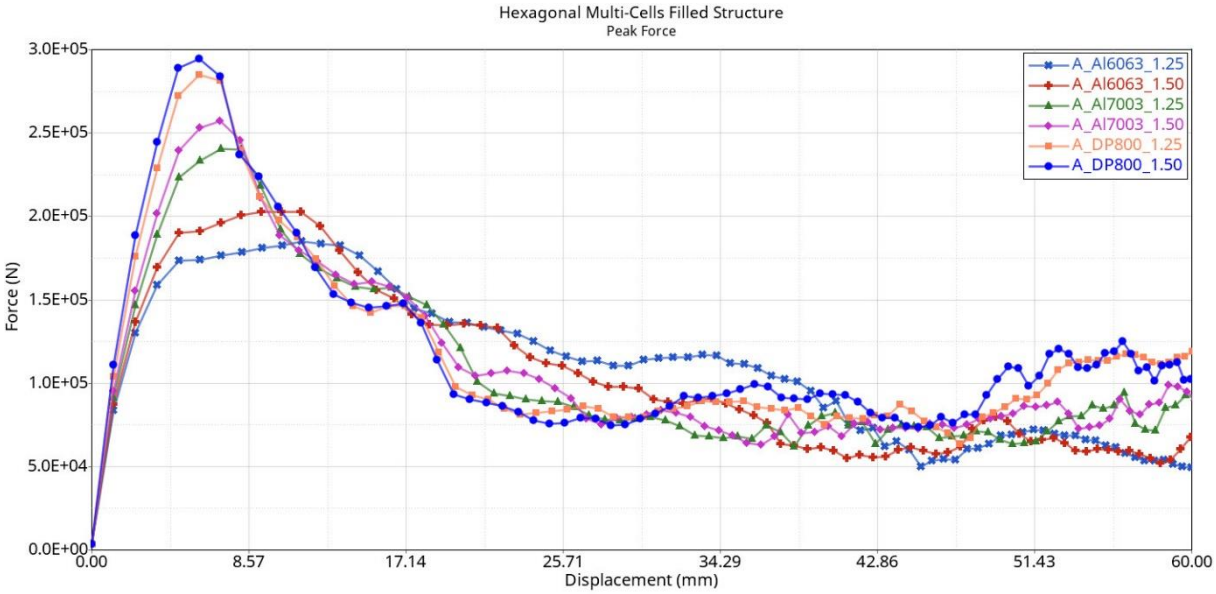


Figure 7. Force-Displacement curve of hexagonal multi-cell filled battery side beams

As seen in Figure 7, it is observed that the peak force is 294,6 kN in A_DP800_1.50 material at first contact. When we compare it with aluminum alloy materials, it is seen that it is 45-58% higher than A_Al6063 materials and 14-23% higher than A_Al7003 material.

Table 4. Rectangular multi-cell filled battery side beam FEA simulation results

Rectangular Multi-cell	Material Thickness(mm)	Mass (kg)	SEA (kJ/kg)	Fmax (kN)	Absorbed Energy (kJ)
AA 6063	1.25	8,745	0,824471	205	7,21
	1.50	9,049	0,791248	220,7	7.16
AA 7003	1.25	8,785	0,816164	246,9	7,17
	1.50	9,096	0,814644	263,7	7,41
DP 800	1.25	11,61	0,635659	296,3	7,38
	1.50	12,49	0,592474	308,5	7,40

For the rectangular multi-cell filled structure, it was observed that the best specific energy absorption value was the B_Al6063_1.25 structure. It is approximately %2 more than B_Al7003 materials and %32 more than B_DP800 materials.

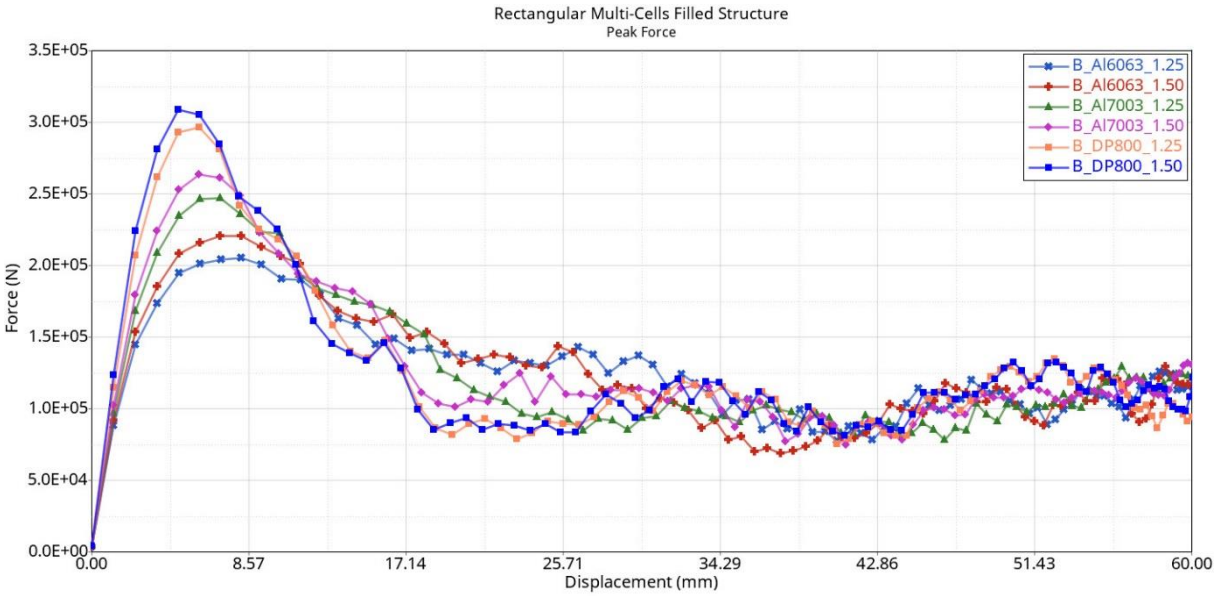


Figure 8. Force-Displacement curve of rectangular multi-cell filled battery side beams

When the force displacement graph is examined, it is seen that the peak force is 308.5 kN in A_DP800_1.50 material during the first impact. When we compare it with aluminum alloy materials, it is seen that it is 17-25% higher than A_Al7003 materials and 40-50% higher than A_Al6063 material.

Table 5. Triangular multi-cell filled battery side beam FEA simulation results

Triangular Multi-cells	Material Thickness(mm)	Mass (kg)	SEA (kJ/kg)	Fmax (kN)	Absorbed Energy (kJ)
AA 6063	1.25	9,013	0,704538	219,27	6,35
	1.50	9,37	0,708645	221,51	6,64
AA 7003	1.25	9,059	0,728557	274,21	6,60
	1.50	9,425	0,702387	288,7	6,62
DP 800	1.25	12,38	0,544426	326,7	6,74
	1.50	13,41	0,509321	335	6,83

The highest specific energy absorption value in the triangle multi-cell filled material was C_Al7003_1.25 structure. Compared to other materials, it is approximately %35 more than C_ DP800 material and %3 more than C_Al7003 materials.

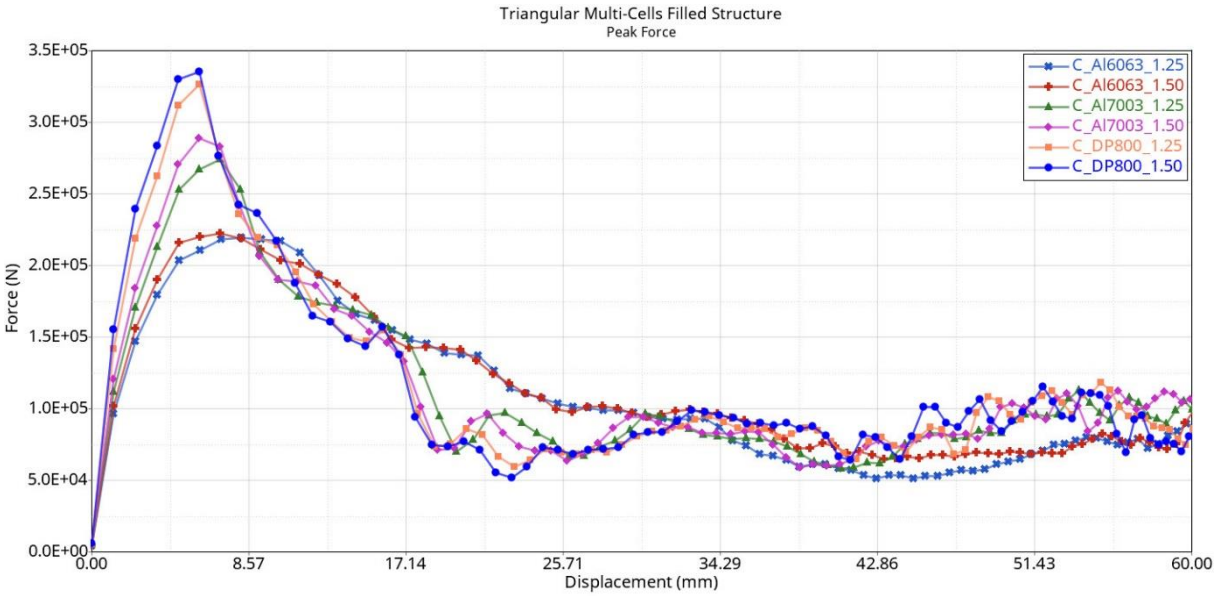


Figure 9. Force-Displacement curve of triangular multi-cell filled battery side beams

When the force displacement graph is examined, it is seen that the peak force is 335 kN in A_DP800_1.50 material. When we compare it with aluminum alloy materials, it is seen that it is 16-22% higher than A_Al7003 materials and 51-53% higher than A_Al6063 material.

5. CONCLUSIONS

As a result of the study, multi-cell structures in different geometries were compared among themselves (material change and thickness change) and with each other (different geometries). Different materials have been defined, and as a result of crashed multi-cell structures of different thicknesses with a cylindrical rigid barrier, their energy absorption capacities, maximum forces and specific energy absorptions have been evaluated and the following results have been reached;

- When multi-cell structures with different geometries are compared with each other, it has been observed that triangle multi-cells filled structures increase relatively more weight than other structures.
- The energy absorption performance per unit mass of the multi-cell filled L shaped battery side beams as a result of crash was high in B_Al6063_1.25 structure.
- As it seen form the results, the highest energy absorption occurred in the B_Al7003_1.50 and B_DP800_1.50 structure with respectively 7,41 kj and 7,40 kj.

- It has been observed that the maximum strength is higher in dual-phase steel materials. Due to the hard structure of the steel material, the result of the analysis was as expected.
- When the spesific energy absorption values of the empty L battery side beam and the materials filled with different geometries are compared, it has been observed that Aluminum Alloy 6063 materials increase 10,9-3,0% in the hexagonal multi-cells filled structure, 20,2-15,3% in the rectangular structure and 3,3-2,7% in the triangular structure. All results are shown in Table 6.

Table 6. Spesific energy absorption change rate of multi-cell filled battery side beams compared to empty beam

	Material Thickness(mm)	Hexagonal Multi-cells	Rectangular Multi-cells	Triangular Multi-cells
AA 6063	1.25	10,9%	20,2%	2,7%
	1.50	3,0%	15,3%	3,3%
AA 7003	1.25	6,1%	19,0%	6,2%
	1.50	7,4%	18,7%	2,4%
DP 800	1.25	-9,0%	-7,4%	-20,7%
	1.50	-12,5%	-13,6%	-25,8%

REFERENCES

1. **Palvoelgyi, S. and Stangl, P.K., (1990),** “Crashworthiness of the Electric G-Van” , International Congress and Exposition, Detroit, Michigan
2. **Uwai, H., Isoda, A., Ichikawa, H., and Takahashi**, **N., (2009),** “Development Of Body Structure For Crash Safety Of The Newly Developed Electric Vehicle”, Automotive Engineers of Japan, Vol. 63, No. 9, pp 67-72.
3. **Xiao, Y., Hu, Y., Zhang, J., Song, C., Liu, Z., and Yu, J. (2018),**” Dynamic bending responses of CFRP thin-walled square beams filled with aluminum multi-cells”, Thin-Walled Structures, Vol.132, pp 494–503.
4. **Tiwari, G., Thomas, T., and Khandelwal, R. P. (2018),** “Influence of reinforcement in the multi-cells structures under axial compressive load”, Thin-Walled Structures, 126, pp 238–245.
5. **Rathbun, H. J., Radford, D. D., Xue, Z., He, M. Y., Yang, J., Deshpande, V., Fleck, N. A., Hutchinson, J. W., Zok, F. W., and Evans, A. G. (2006),** “Performance of

metallic multi-cells-core sandwich beams under shock loading", International Journal of Solids and Structures, Vol.43, No.6, pp 1746–1763.

6. **Acar, E., Altin, M. and Güler, M.A., (2019),** "Evaluation of various multi-cell design concepts for crashworthiness design of thin-walled aluminum tubes", Thin-Walled Structures, Vol.142, pp. 227-235.
7. **Albak E.İ., (2021),** "Multi-objective crashworthiness optimization of thin-walled multi-cell tubes with different wall lengths", International Journal of Crashworthiness, Vol. 26, No. 4, pp. 438-455.
8. **Navale, A.B., Chippa, S.P., Chougule, D.A. and Raut, P.M. (2021),** "Crashworthiness aspects of electric vehicle design", International Journal of Crashworthiness, Vol. 26, No. 4, pp. 368-387.
9. **Setiawan, R. and Salim, M.S. (2017),** "Crashworthiness Design for an Electric City Car against Side Pole Impact", Journal of Engineering and Technological Sciences, Vol. 49, No. 5, pp. 587-603.
10. **Altin, M., Güler, M. A., and Mert, S. K. (2017),** "The effect of percent foam fill ratio on the energy absorption capacity of axially compressed thin-walled multi-cells square and circular tubes", International Journal of Mechanical Sciences, 131–132,pp 368–379.
11. **Hoang, N. H., Morin, D. and Langseth, M. (2022),** "Testing and modelling of butt-welded connections in thin-walled aluminium structures", Thin-Walled Structures, Vol.171.
12. **Alaneme, K.K. and Aluko,A.O. (2011),** "Production and Age-Hardening Behaviour of Borax Premixed SiC reinforced Al-Mg-Si alloy Composites developed by Double Stir-Casting Technique", The West Indian Journal of Engineering, Vol.34, No.1/2, pp.80-85.
13. **Tian, C., Ponge, D., Christiansen, L., and Kirchlechner, C. (2020),** "On the mechanical heterogeneity in dual phase steel grades: Activation of slip systems and deformation of martensite in DP800", Acta Materialia, Vol.183, pp 274–284.
14. **Simhachalam,B., Srinivas,K. and Lakshmanarao,C. (2013),** "Compression Behavior and Energy Absorption of Aluminum Alloys and Steel for Automotive Application". Symposium on International Automotive Technology .
15. **Saai, A., Hopperstad, O. S., Granbom, Y., and Lademo, O.-G. (2014),** "Influence of Volume Fraction and Distribution of Martensite Phase on the Strain Localization in Dual Phase Steels" Procedia Materials Science, Vol.3,pp 900–905.

16. **Demirci, E. and Yıldız, A. R.,(2018),** "An experimental and numerical investigation of the effects of geometry and spot welds on the crashworthiness of vehicle thin-walled structures" Materials Testing, vol. 60, no. 6, pp. 553-561.

DESIGN AND ANALYSIS OF A LIGHTWEIGHT CHASSIS FOR AN ELECTRIC VEHICLE

Özgür AKDENİZ, *ozgur.akdeniz.97@gmail.com* Atilim University, 06830, Ankara, Turkey

Mert ALPAR, *mertalpar@yahoo.com.tr* Atilim University, 06830, Ankara, Turkey

İsmail U. HOROZOĞLU, *utkuhorozoglu@gmail.com* Atilim University, 06830, Ankara, Turkey

Ozan TEKİN, *ozan.tekin@atilim.edu.tr* Atilim University, 06830, Ankara, Turkey

Ramin BARZEGAR, *ramin.barzegar@atilim.edu.tr* Atilim University, 06830, Ankara, Turkey

ABSTRACT

The purpose of this paper is to design a modular ladder frame chassis for an electric vehicle. The factors considered in the design of the chassis were obtaining a lightweight structure that not only could carry the static loads but also provide structural integrity under the dynamic loads of different crash scenarios. The analysis was carried out by means of linear FEA (Finite Element Analysis) for static loads and non-linear FEA for crash tests. Three different crash scenarios including frontal impact, side impact, and roof strength test were taken into account according to Insurance Institute for Highway Safety (IIHS) test protocols. The designed chassis provided survival space for occupants and no fracturing occurred in the structure.

Keywords: Chassis, Electric Vehicle, Static and Dynamic Analysis, Crash Tests

1. INTRODUCTION

Transportation is the second highest energy consumer sector and is driven mainly by the liquid fossil fuels (Alimujiang and Jiang, 2020). Climate change and its adverse consequences on the environment is primarily due to the release of greenhouse gas emissions from burning fossil fuels (Breuer *et al.*, 2021). Electric vehicles (EV) especially battery electric vehicles (BEV) are booming in recent years to tackle this issue and are considered as a viable solution for sustained mobility. Not only they are more efficient than

internal combustion engine vehicles (ICEV), but also, they can run on electricity generated from renewable energy resources. Since BEVs only create emissions during production and recycling, with negligible emissions during operation, if charged with electricity generated from renewable resources, they can result in significantly lower emissions than ICEVs (Hoekstra, 2019). Consequently, they are seen as the solution for zero emission and sustainable transportation systems.

One of the major issues with BEVs is that they are more expensive than ICE powered vehicles. Considering a 20 year lifespan for a vehicle, it was calculated that for compact sized vehicles, BEVs cost 44% more than their ICEV counterparts while mid-size BEVs have 60% higher cost compared to ICEV (Brennan and Barder, 2016). This makes BEVs out of reach for most consumers in need of a personal vehicle. Another problem of BEVs is the fact that they are considerably heavier than ICEVs due to added mass of the battery pack. This results in increased energy consumption as well as stronger and heavier structure is required for BEVs.

One of the major parts in a vehicle is chassis and it plays a crucial role in the design of the entire vehicle. Therefore, designing a lightweight chassis for electric vehicles is of great importance. In order to reduce the weight of the structure, alloys of aluminum are extensively used throughout the entire chassis while at critical parts where strength of the material is important, structural steel is used as well. Safety is a major aspect is in chassis design and it should be designed to absorb most of the impact energy during accident. Several safety scenarios such as frontal impact, side impact, and roof strength tests should be passed by a vehicle in order to ensure its structural integrity. Insurance Institute of Highway Safety (IIHS) standard specialized in crash tests provides an elaborate and thorough test protocols for vehicle safety (Insurance Institute for Highway Safety, 2014, 2020, 2021).

Among several types of chassis, the ladder frame chassis is cost effective and easy to design and manufacture (Begum and Murty, 2016). Also, owing to its modular design advantage, with simple modifications on the structure, different configurations can be obtained which does not add a serious challenge on the production line. This modularity allows research and development costs spread across multiple vehicle models and configurations, ultimately reducing the price of the individual model.

In this study, a lightweight ladder frame chassis was designed for an electric vehicle by means of numerical approach. The linear FEA was used in order to assess the strength of the chassis under static loads of the vehicle. Also, non-linear FEA method was employed to simulate the chassis strength under different crash scenarios. Based on the obtained results,

adjustments were made to enable the chassis to absorb the crash energy without any fracture.

2. MATERIALS AND METHODS

The materials used for the chassis were 6063-T5 Aluminum alloy for the main body (Silva and Perera, 2012) and structural steel for the roll-cage component (Yao and Wang, 2022) with the characteristics given in Table 1. For non-linear analysis, the material properties of aluminum in the plastic region was obtained from (Yun, Wang and Gardner, 2021). A multi-linear stress-strain curve was used in analyzing the structure behavior during crash.

Table 1: Properties of materials used on construction of the chassis

	Aluminum 6063-T5	Structural Steel
Young's Modulus (MPa)	71000	200000
Poisson's Ratio	0.33	0.3
Tensile Yield Strength (MPa)	142	406
Tensile Ultimate Strength (MPa)	182	585

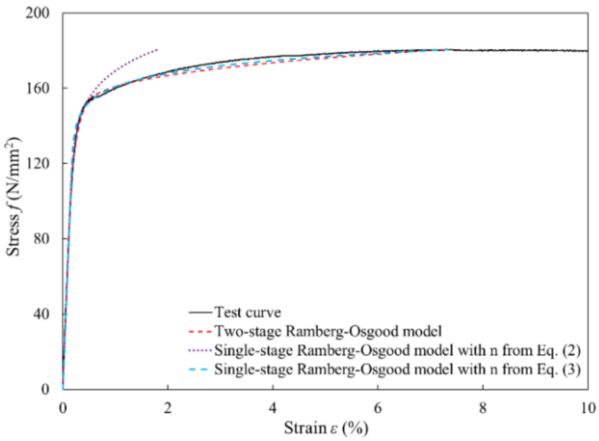


Figure 1: Stress-strain curve of Aluminum 6063-T5 (Yun, Wang and Gardner, 2021)

The vehicle components to be mounted on the chassis were determined and their weights were calculated and applied to the chassis in appropriate locations as point masses with the values given in Table 2. Mesh independency analysis was carried out in the mesh size range of 4-10 mm and the proper value was determined. The linear FEA analysis was performed in order to obtain the structure capable of withstanding the static loads of the weight of vehicle components. Additionally, in order to assess the behavior of the structure during crash, non-linear FEA analysis was conducted. The IIHS test scenarios including frontal crash, side

crash and roof strength test were applied, and adjustments were made on the chassis to absorb the crash energy based on the obtained results.

Table 2: Point mass values of the vehicle components

Component	Mass (kg)	Component	Mass (kg)
Body Shell	70	Driver + Seat	90
Passenger + Seat	90	Differential	20
Electric Motor	15	Transmission	15
Battery Pack	38		

3. RESULTS AND DISCUSSION

3.1. Static Analysis

In order to ensure the fidelity of analysis results, the mesh independency test was conducted with mesh sizes ranging from 4 to 10mm. Mesh sizes and their corresponding attributes as well as stress values from the analysis results are shown in Table 3. Based on the obtained results, 5mm mesh size was chosen for analysis. Figure 2 shows the generated gird.

Table 3: Mesh independency analysis results

Mesh Size (mm)	Number of Elements	Number of Nodes	Stress (MPa)
4	682305	1580729	173
5	447082	1044217	116
6	334105	779639	108
7	288606	666425	118
8	263935	600198	89
9	250868	561999	94
10	240119	529708	95

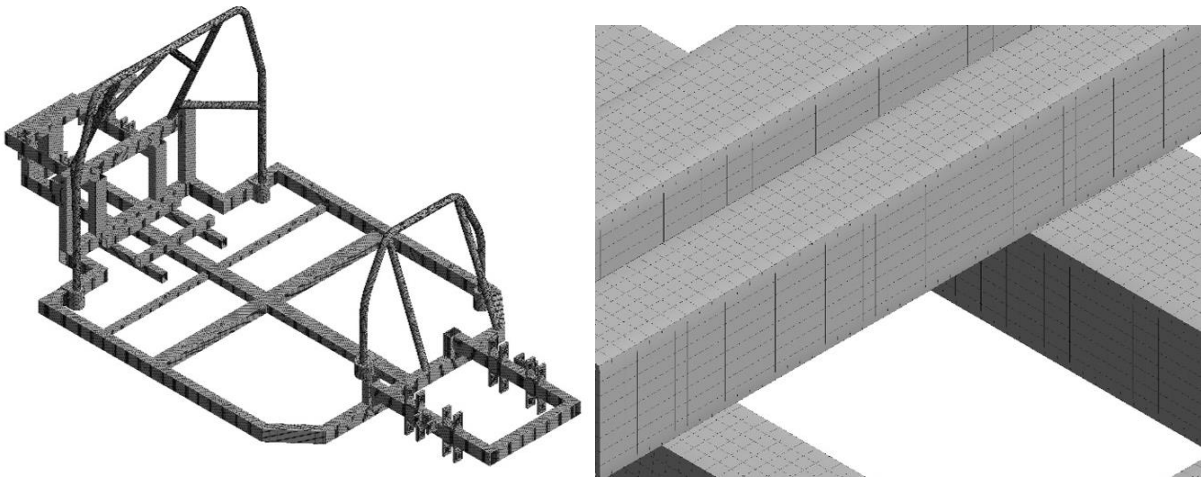


Figure 2: Generated grid for the chassis

The static structural analysis was performed for the designed chassis considering the weight of the chassis and the vehicle components under gravitational force. The chassis structure, the point masses, the direction of gravitational force, and the vertical deformation and von-misses stress values are shown in Figure 3. The obtained results indicated that the equivalent stress value was 58 MPa and the vertical directional deformation of was 4mm. Comparing the stress values to the yield stress value of the aluminum alloy from Table 1, a safety factor of 2.45 was obtained. It can be concluded that the structure can safely withstand the static loads of the vehicle.

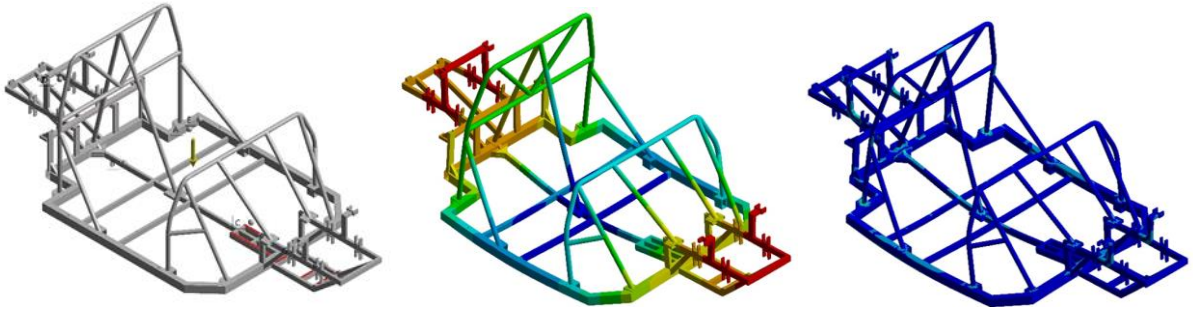


Figure 3: Chassis structure, vertical deformation, and von-misses stress under static load

3.2. Frontal Crash

The frontal impact test was simulated according to IIHS Moderate Overlap Frontal Crashworthiness Evaluation Crash Test Protocol (Insurance Institute for Highway Safety, 2014). The main consideration was that the crash energy should be completely absorbed by the chassis and no fracture should occur. The total weight of the vehicle was considered as 300 kg and the cruise speed of the vehicle was 60 km/h. The crash impact time was set to 0.2 seconds based on the suggestions from literature (Montalvao and Moore, 2014). The

vehicle deceleration during crash and the impact force can be calculated based on the following equations:

$$a = (V - V_0)/t \quad (1)$$

$$F = m \cdot a \quad (2)$$

According to the calculations, the deceleration during crash was found to be 83.3 m/s^2 and the impact force was 25 kN. Therefore, 25 kN of force was applied from the front of the chassis in 0.2 seconds. Figure 4 represents the configuration of a rigid body mounted in the front of the vehicle by which the force was exerted. The maximum von-misses stress reached during crash was found as 340 MPa and the deformation in the direction of the vehicle was about 30 mm and the permanent deformation was 17 mm. These results were obtained after several adjustments to the structure to prevent fracture during crash.

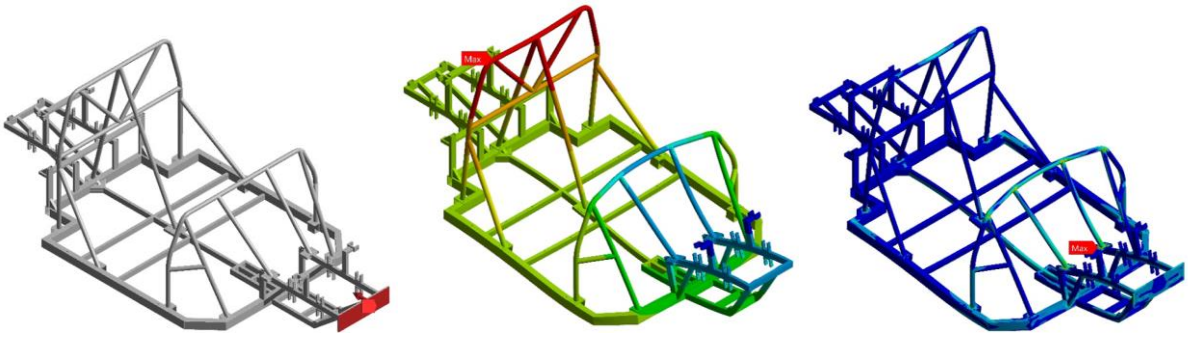


Figure 4: Frontal crash test analysis results

3.3. Side Crash

The side crash test was carried out according to IIHS Side Impact Crashworthiness Evaluation Crash Test Protocol (Insurance Institute for Highway Safety, 2020). In this analysis it was assumed that a vehicle of 300 kg at 60 km/h was crashed to the chassis from side. The impact force was set to 25 kN and the crash duration was considered to be 0.2 seconds. Figure 5 shows the rigid body mounted in the side of the vehicle by which the force was applied. The maximum von-misses stress was obtained as 150 MPa and the directional deformation was about 54 mm with permanent deformation of 40 mm ensuring that the structure was capable of absorbing side impact as well. The deformation and stress values during crash can be seen in Figure 5.

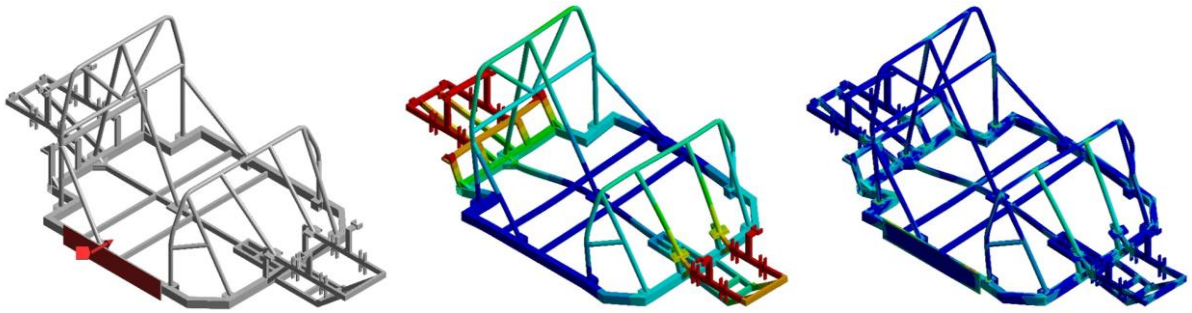


Figure 5: Side crash test analysis results

3.4. Roof Strength Test

The roof strength test was analyzed according to IIHS Crashworthiness Evaluation Roof Strength Test Protocol (Insurance Institute for Highway Safety, 2021). Based on this test, a vehicle must be able to carry four times of its own weight while the roof has a deformation less than or equal to 5 inches (127mm). The main component of the structure to withstand this load was the roll-cage assembly mounted on the chassis. The force applied to the roof of the vehicle was calculated to be about 12 kN and was exerted over the structure as seen in Figure 6. The maximum von-misses stress during impact was found as 402 MPa and the deformation was about 54 mm with the permanent deformation of 30 mm. Figure 5 also represents the deformation and stress values during crash.

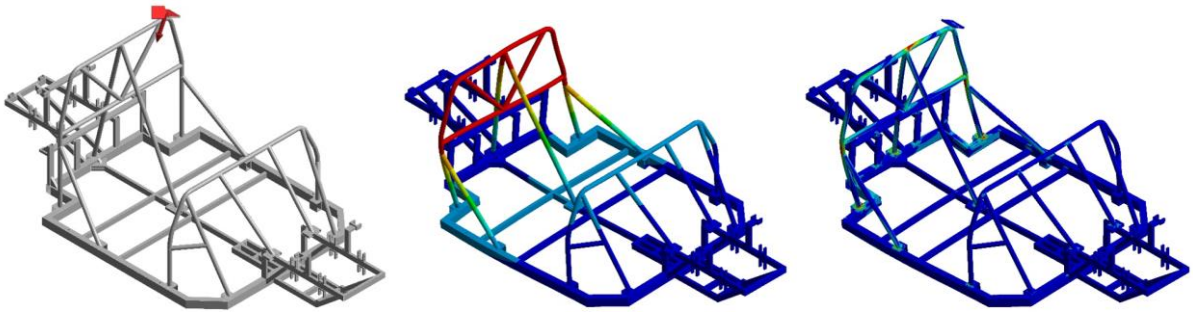


Figure 6: Side crash test analysis results

4. CONCLUSION

In this paper a modular ladder frame chassis for an electric vehicle was designed with the focus on structural integrity to absorb dynamics loads during different crash scenarios. Frontal impact, side impact, and roof strength test were carried out according to IIHS protocols. The designed structure was capable of carrying static loads with safety factor of 2.45. Additionally, several adjustments were made on the structure to ensure it can withstand

the dynamic loads under different crash scenarios. The obtained chassis was a lightweight structure providing survival space for occupants with no fracturing during impact.

5. REFERENCES

Alimujiang, A. and Jiang, P. (2020) 'Synergy and co-benefits of reducing CO2 and air pollutant emissions by promoting electric vehicles—A case of Shanghai', *Energy for Sustainable Development*, 55, pp. 181–189. doi: 10.1016/j.esd.2020.02.005.

Begum, S. N. and Murty, S. P. B. (2016) 'Modelling and Structural Analysis of Vehicle Chassis Frame Made of Polymeric Composite Material', *International Research Journal of Engineering and Technology*, 3(8), pp. 574–582. Available at: https://www.irjet.net/archives/V3/i8/IRJET-V3I8106.pdf.

Brennan, john W. and Barder, T. E. (2016) 'Battery Electric Vehicles vs . Internal Combustion Engine Vehicles : A United States-Based Comprehensive Assessment', *Arthur D. Little*, p. 48.

Breuer, J. L. *et al.* (2021) 'How to reduce the greenhouse gas emissions and air pollution caused by light and heavy duty vehicles with battery-electric, fuel cell-electric and catenary trucks', *Environment International*, 152(March), p. 106474. doi: 10.1016/j.envint.2021.106474.

Hoekstra, A. (2019) 'The Underestimated Potential of Battery Electric Vehicles to Reduce Emissions', *Joule*, 3(6), pp. 1412–1414. doi: 10.1016/j.joule.2019.06.002.

Insurance Institute for Highway Safety (2014) *Moderate Overlap Frontal Crashworthiness Evaluation Crash Test Protocol*.

Insurance Institute for Highway Safety (2020) *Side Impact Crashworthiness Evaluation 2.0 Crash Test Protocol (Version I)*. Available at: https://www.iihs.org/media/0027a26d-8dd2-4de4-affc-0eb98338c6ba/cLjh9w/Ratings/Protocols/current/test_protocol_side-2.0.pdf.

Insurance Institute for Highway Safety (2021) *Crashworthiness Evaluation Roof Strength Test Protocol*.

Montalvao, D. and Moore, M. (2014) 'Computational Analysis of a Car Chassis Frame under a Frontal Collision', *International Journal of Engineering Research and Technology*, 3(2), pp. 39–43.

Silva, G. I. P. De and Perera, W. C. (2012) 'Improvement of the Mechanical Properties of Aluminum 6063 T5 Extrudates By Varying the Aging Condition Cost-Effectively', (July 2020),

pp. 62–64.

Yao, Z. and Wang, W. (2022) ‘Full-range strain-hardening behavior of structural steels: Experimental identification and numerical simulation’, *Journal of Constructional Steel Research*, 194(April), p. 107329. doi: 10.1016/j.jcsr.2022.107329.

Yun, X., Wang, Z. and Gardner, L. (2021) ‘Full-Range Stress–Strain Curves for Aluminum Alloys’, *Journal of Structural Engineering*, 147(6), pp. 1–38. doi: 10.1061/(asce)st.1943-541x.0002999.

DEVELOPMENT OF AN IMAGE PROCESSING SYSTEM FOR THE AUTOMATIC QUALITY CONTROL OF VEHICLE AIRBAG PLASTIC PARTS

Bilgin DALLI, *bilgin.dalli@dakamak.com* Daka Mühendislik, 16240, Bursa
M. Cemal ÇAKIR, *cemal@uludag.edu.tr* Bursa Uludağ Üniversitesi, 16240, Bursa

ABSTRACT

In this study, an automatic vision-based defect inspection and sorting system has been developed for a plastic injection mold component called side passenger airbag, which is a critical component in automotive safety. In order to detect the defects on the plastic part, the necessary mechanical and automation system for the industrial image processing system has been developed. A part-specific image processing algorithm was created and faults were detected in 1.28 seconds instead of 45 seconds. Thanks to the developed system, all defects on the plastic product, which is a vital and safety component, could be detected, and the safety part was sent to the end user faultless.

Keywords: Image processing, Plastic Injection, Quality control

INTRODUCTION

Industrial image processing is concerned with the design of integrated mechanical, optical, electrical, and software systems to identify faults, enhance product quality, operational efficiency, and safety, and to operate with natural objects and materials, human artifacts, and manufacturing processes.

The concept of integrating industrial image processing systems in measurement and control activities has enabled these systems to be employed in a variety of applications in new industries. While no industrial image processing technology currently or in the near future can compete with human interpretation, industrial vision is more efficient than people in repeated activities such as measuring under closely regulated settings. While industrial image processing tools can evaluate basic, well-defined, mass-produced objects at high speeds, it is extremely difficult for individuals to make consistent judgements under these settings.

Al Kamal and Al-Alaoui (Al-Kamal and Al-Alaoui 2004) provided a concept for an online machine vision system capable of detecting faults in the rubber coating of metal caps during manufacturing in their study. The designed system was a simple and economical system that consists of a CCD camera installed on a conveyor belt and connected to a PC through FireWire (IEEE 1394). A novel pattern recognition system was developed in the research by Blackledge and Dubovitskiy (Blackledge and Dubovitskiy 2008) to monitor the quality of steel sheet manufacturing in a rolling mill. The system was built on the utilization of an imaged object's Euclidean and Fractal geometric features to generate training data, which was then utilized in conjunction with a supervised learning based on the application of a fuzzy inference engine.

In his work Oechsle (Oechsle 2009) investigated how vision software may be automatically developed using Genetic Programming (GP), a technique that learns how to write programs while emulating Darwinian evolution. This study went beyond demonstrating the applicability of evolutionary learning to specific image processing tasks to address the topic of how to develop more "complete" vision systems utilizing GP.

Nicolas Bonnot et al (Bonnot et al. 2004) attempted to detect flaws on metallic industrial parts with striated surfaces. The orientation of these parallel lines was absolutely arbitrary. Scratches and a lack of processing were the defects sought. To show the specific surface properties investigated, a customized industrial image processing system was built. The designed machine vision system was tested in an industrial production line, delivering 2% underdetection and 16% oversensing. The work of Chen et al. (Chen et al. 2016) is closely related to the production quality of metal can containers and product safety in the food and beverage industry. To address the quality control criteria, a real-time supervised image processing system was described in this paper.

Singh and Kaur's (2012) work was a significant quality determination research in industries that deal with surfaces as the main feature of products, such as visual inspection of material surface quality, plywood, metal, tile, glassware, and many others. A sample from the tile industry was tested in the presented study. The automated visual inspection system checked cracks, holes, stains, foreign objects, and extra material on the tile surface. The approach entailed detecting surface flaws using image processing techniques based on the statistical features of the defects observed on the surfaces. Mkwelo developed a machine vision-based method to evaluate the size distribution of pebbles on a conveyor belt in his research (Mkwelo 2004). The acquired findings were comparable with an RMS error of 2.37 percent in the test set.

Nashat et al. (Nashat et al. 2014) investigated biscuits or baked items with uneven color distribution and textured backgrounds using a machine vision system. The Canny-Deriche filter was employed in this investigation to emphasize the fracture and eliminate noise. Pithadiya et al. (2009) examined the few optimum edge detection approaches utilized to assess the top and bottom fill level of the bottle in the industrial vision system in their study. The study not only discussed quality control, but also methods and ways for examining the fill level and below the bottle utilizing various edge detection techniques. The findings of several optimum edge detection algorithms, such as the Marr-Hilderth LoG algorithm, the Canny algorithm, and the Shen Castan algorithm, were shown to be far superior to standard template-based approaches such as the Sobel and Kirsch operators.

Sawadisavi et al (Sawadisavi et al. 2009) focused on employing an industrial image processing system to detect abnormalities and faults in wood fasteners, rail anchors, cradle ballast, and turnout components, based on consultation with the American Association of Railroad Researchers. The system has been designed to be audited in accordance with FRA track safety rules as well as rail-specific rail standards, which may contain extra criteria. Seulin et al. (Seulin et al. 2001) conducted research to identify surface flaws in industrial products with highly reflecting surfaces. Dents, lumps, and scratches were examples of surface flaws. The dimensions of the industrial portion were 200 x 50 mm, and the fault surface is less than 1 mm^2.

Li et al. (2010) investigated weld bead profile measuring, tracking, and flaw identification using a structured light-based image inspection system. Image processing and extraction algorithms for laser profiles and feature points were presented. During multilayer welding procedures, the dimensional characteristics of the weld bead were measured, and welding flaws were found. Zhang et al. (Zhang et al. 2018) described a novel and effective inspection system comprised of three modules, as well as a particle tracking and classification method based on an adaptive local weighted-collaborative sparse model.

n this study, unlike all the above-mentioned studies, an automatic vision-based defect inspection and sorting system has been developed for a plastic injection mold component called the side passenger airbag, which is a critical component in terms of automotive safety. The appropriate mechanical and automation system for the industrial image processing system has been built in order to detect faults on the plastic part. A part-specific image processing algorithm was created and errors were detected.

MATERIALS AND METHOD

The created system validates the net component depicted in the picture prior to injection (Figure 1). The cartesian robot takes a piece of net from a workbench (shown in Figure 9) and places it in front of the camera. If the mesh piece is appropriate, it is placed into the mold; otherwise, it is tossed into the NOK box. After injection in the system that was planned and manufactured, the side passenger airbag component is also regulated (Figure 2). Following the injection, the cartesian robot retrieves the item from the mold, places it in front of the camera, and, if the component is satisfactory, places it on the conveyor in front of the operator. If the part is not suitable, it is placed in the NOK box. Furthermore, if even one component of the net section has an error, the entire system is stopped, and all net components are asked to be replaced. The system resumes where it left off after replacing all of the net components on the workbench with new ones.

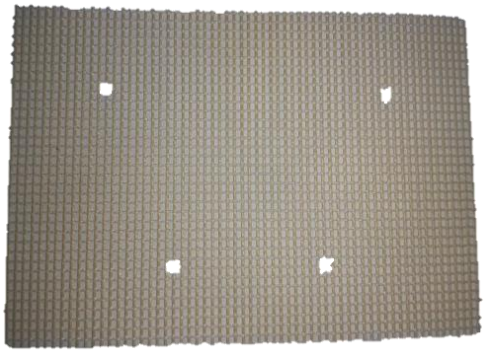


Figure 1 – Net

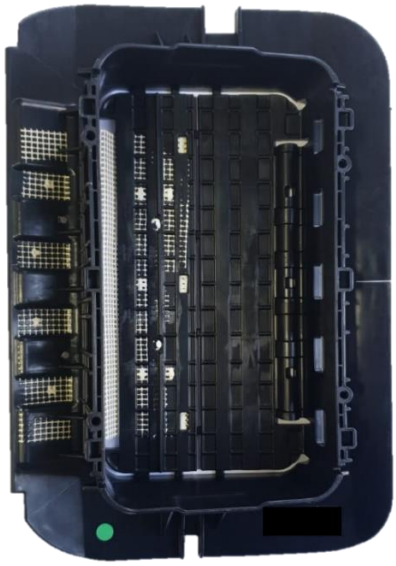


Figure 2 - Side passenger airbag

When the enjection die is opened, a check is performed on it, as well as the mesh and side passenger airbag components. If something gets in the path of the die as it closes, the mechanism stops and shuts down the injection machine. After the issue has been resolved and the checks have been done again, the system restarts where it left off after being restarted.

Figure 3 depicts the measurements of the net component that must be examined by placing them in a box. The precision of these measures is 0.5 mm. Controlling incorrect lateral and vertical cutting while cutting the net is more important than dimensional control. This mistake resulted in the airbag bursting.

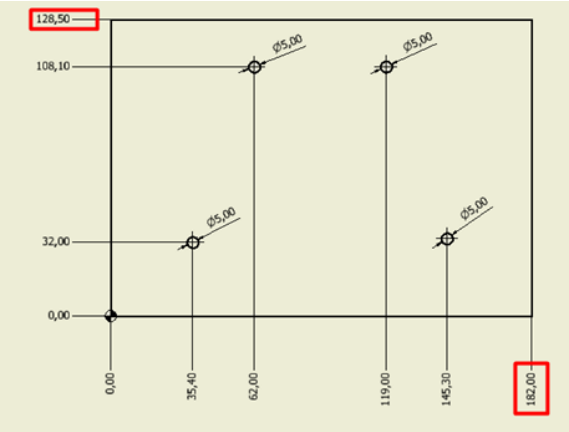


Figure 3 – Net Dimensions

The FOV, or field of view, must first be established in order to choose the camera needed to control the mesh component. The following equation can be used to determine the field of view:

FOV = Biggest part size + placement tolerance + necessary blank distance + aspect ratio of the camera sensor

The biggest piece size in this case is 182 mm. 1 mm is the positioning tolerance, 2 mm of empty space must also be needed.

$FOV_{vertical}$ can be calculated as 182 + 1 + 2 = 185 mm and $FOV_{horizontal}$ as 185 x 3/4 = 138.75 mm.

The following formula can be used to determine the resolution by field of view:

$FOV \times (N_f / S_f) = R_C = FOV / R_S$

FOV : Field of View

N_f : The number of pixels in the smallest element

S_f : The smallest element

R_C : Camera Resolution

R_S : Spatial Resolution

$RC_{vertical}$: 185 millimeters x 1 pixel / 0.25 millimeters = 740 pixels and $RC_{horizontal}$: 1 pixel x 0.25 mm x 138.75 mm = 555 pixels

For the net control, the Omron STC-MCE132U3V model camera with a resolution of 1280 x 1024 pixels was utilized. The lens that would be used to control the net component was chosen using the chart in Figure 4. The horizontal axis in the chart represents the position suited for the field of vision, and the vertical axis represents the working distance from the component. With an estimated field of vision of 185 mm and a working distance of 300 mm, the product with the code FZ-LEH12 was chosen. Figure 5 illustrates the dimensions of the component to be measured. Similar calculations were performed in the same manner as those for the net component and the appropriate lens was selected.

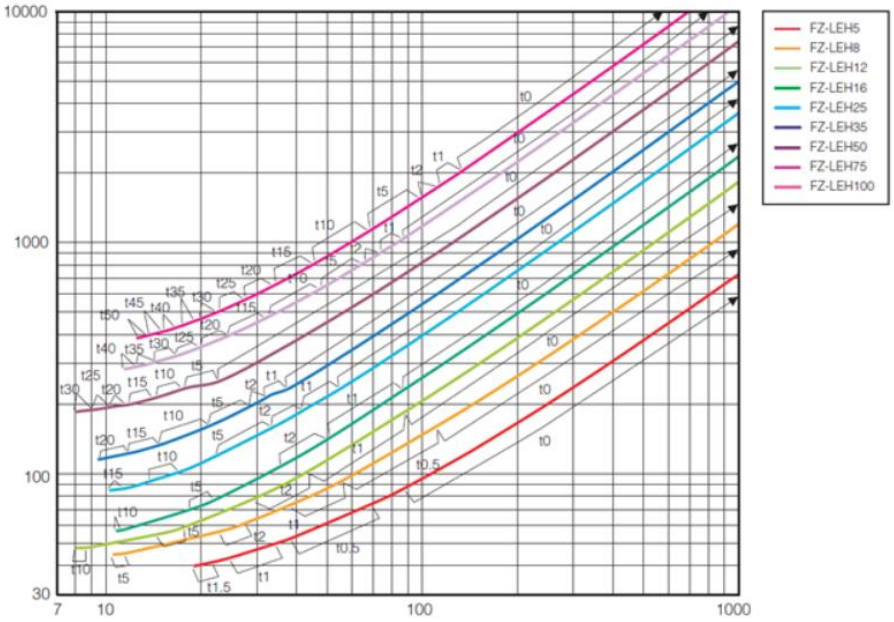


Figure 2 - Lens Selection Chart (Omron)

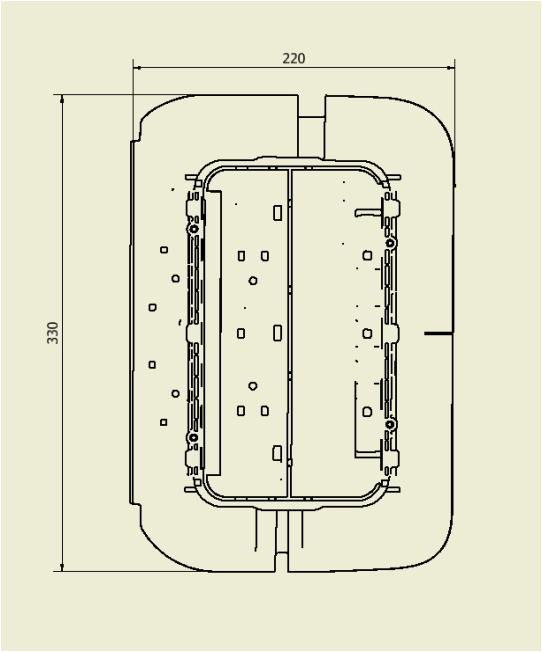


Figure 3 - Part Dimensions

Following the selection of the cameras and lenses, lighting tests on the parts indicated that ring lighting was perfect for the net component (Figure 6), while direct illumination with a hole in the center for the camera was suitable for the side passenger airbag (Figure 7). In-mold cameras, on the other hand, make use of direct illuminations that are angled (Figure 8).

The net bench, where the nets will be placed, served as the system's starting point. The design was built in such a manner that the Cartesian robot would always assume the correct position by making use of the reference holes on the nets (Figure 9).

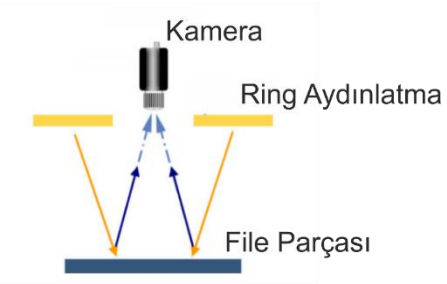


Figure 4 - Ring Lighting

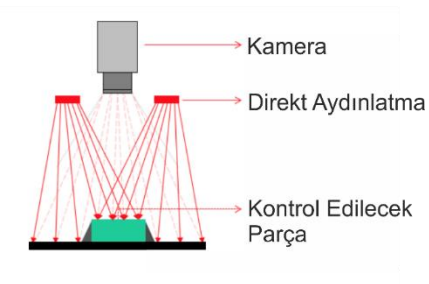


Figure 5 - Direct Lighting

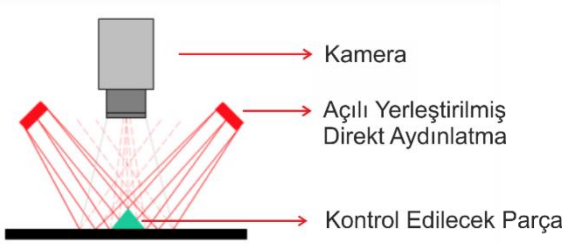


Figure 6 - Angled Direct Lighting

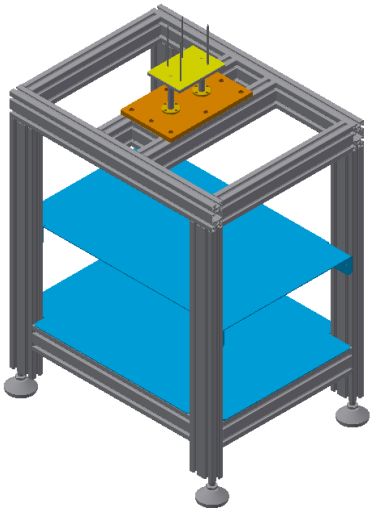


Figure 7 – Net Bench Design



Figure 8 – Net Bench

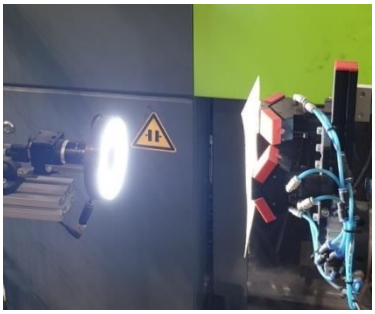


Figure 9 - Camera 1 to control the net

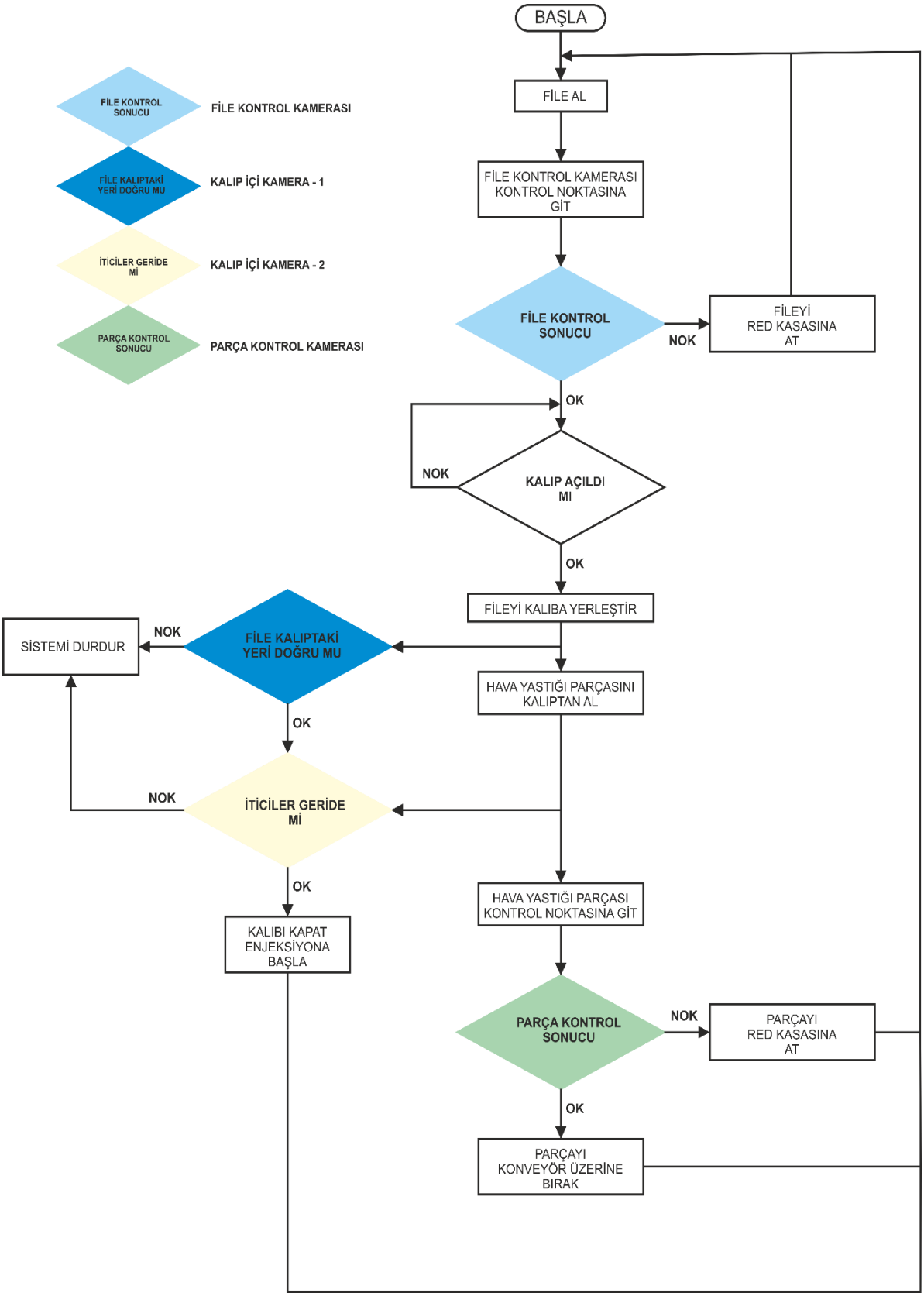


Figure 10 – System FlowChart

Figure 10 illustrates the production drawing for the net loom. The picture also depicts the NOK component box, which will be used to discard the faulty net part and the side air passenger bag pieces. To start the system, the net is removed from the bench. While the control is running, the net is validated in front of the camera (Figure 11). The flowchart of the industrial image processing system is shown in Figure 12.

During this control, the net's positioning, hole widths, and outside dimensions are evaluated. If the net is appropriate, it is placed into the die; otherwise, it is tossed into the NOK box shown in Figure 10. Another camera confirms that the net is properly positioned. Figure 13 and Figure 14 show photographs shot with cameras.

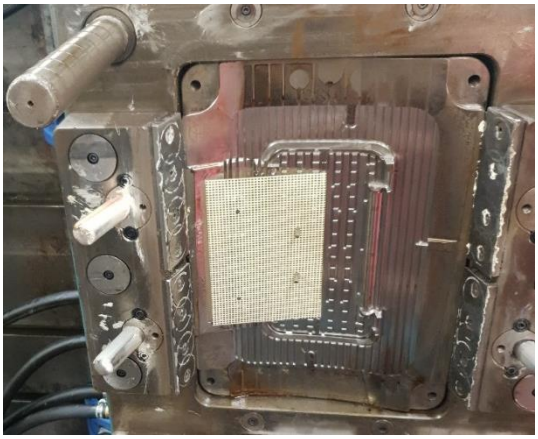


Figure 11. In-Mold Net Inspection



Figure 12. In-Mold Ejector Inspection

Meanwhile, the cartesian robot pulls the finished item from the die and positions it in front of the part inspection camera. After the finished item is withdrawn from the die, the pushers are removed. Another camera within the die verifies that the ejectors are in place and that there are no impediments to the die closing.

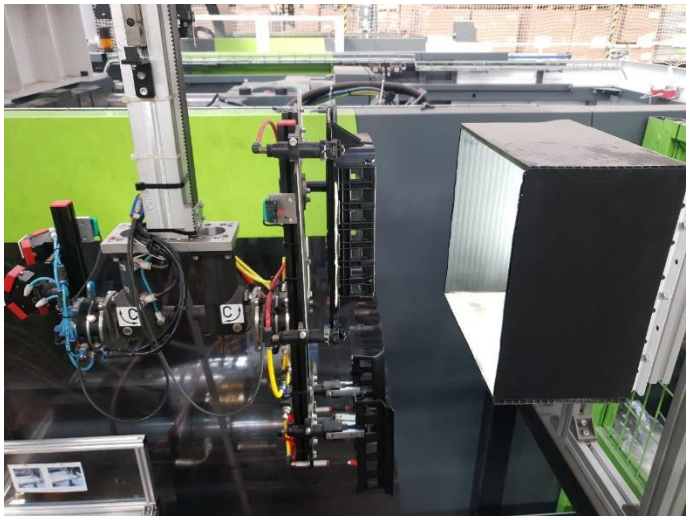


Figure 13 Part control has been completed.

DISCUSSION AND CONCLUSION

Quality control is crucial in many manufacturing areas in today's highly competitive economy. The human eye is often utilized as a quality control tool, however it does have limitations. Industrial image processing solutions are being developed to address these difficulties.

An autonomous vision-based defect inspection and sorting system for a plastic injection component known as a side passenger airbag, a vital component in vehicle safety, was created in this work. In order to detect faults on the plastic part, the appropriate mechanical and automation system for the industrial image processing system was built. While developing a part-specific image processing method, flaws were discovered. The designed system detects all flaws on the components, and fault types in all parts are recorded and notified in real time.



Figure 14 - Failure Modes

Figure 16 (Left-Top) shows a form of inaccuracy that is extremely difficult to identify during a human eye test. While this fault category accounted for 50% of the errors recorded before to this investigation, it was reduced to zero owing to the established method. The fault types depicted in Figure 16 can be identified with 100 percent accuracy in the part's controls.

Figure 16 (Left-Top) shows a form of inaccuracy that is extremely difficult to identify during a human eye test. While this fault category accounted for 50% of the errors recorded before to

this investigation, it was reduced to zero owing to the established method. The fault types depicted in Figure 16 can be identified with 100 percent accuracy in the part's controls.



Figure 17. Errors in net cut direction

a) Correct Net Cut Direction b) Incorrect Net Cut Direction

Table 1. Timeframes necessary for the operator and the industrial image processing system to make the identical controls

Control	**Operator Control (Second)**	**Industrial Image Processing System (Second)**
Net Cut Direction	5	0,120
Net Dimension	12	0,180
In-Mold	5	0,220
Short Shot injection	8	0,330
Burr	8	0,425
Net Errors After Injection	7	0,225
Total Time	45	1,5

Burrs and partial injection faults account for 40% of the faults in components given to the OK case in the human eye assessment. The developed industrial image processing system can identify small burrs or partial injection faults that the human eye cannot detect.

The net cut direction error and dimensions errors in the net component account for 10% of the overall faults (Figure 17). Following the system's commissioning, all file errors were eradicated. Situations managed by in-mold cameras occur only 1-2 times per year in the plant, and the cause is generally a negligent operator. If this occurs, however, manufacturing would be delayed for several weeks, and the expense of fixing the mold will be prohibitively high. As a result, even if the component is not verified, only the in-mold camera system is intended to be compatible with all of the factory's plastic injection machines.

The timeframes necessary for the operator and the industrial image processing system to make the identical controls are shown in Table 1. The operator must execute all of the controls in 45 seconds. 1.5 seconds looks to be adequate for an industrial image processing system on the surface. However, the system may provide net controls (mesh cutting direction control, net size control) as well as in-mold controls at the same time. As a consequence, the created system requires only 1.28 seconds to complete.

The following are the main contributions of this study: The lighting system developed in the study makes it easier to detect flaws in dark-colored materials. It may also be used to identify scratches in plastic materials. As a consequence, all faults on the plastic product, which is a critical safety component manufactured by this system, were discovered, and the safety part was stopped from reaching the end user unintentionally. Furthermore, waste is reduced by recycling improperly created raw materials.

REFERENCES

AIA, EMVA, JIIA, 2013. Global Machine Vision Interface Standards, http://www.emva.org/cms/upload/Marketing_edocs_download/FSF_Vision_Standards_Brochure_A4_screen.pdf (Erişim Tarihi: Nisan 2022).

Bonnot, N., Seulin, R., Merienne, F. 2004. Machine vision system for surface inspection on brushed industrial parts. *Machine Vision Applications in Industrial Inspection,* 5303: 64-72.

Kamal, I.A., Alaoui, A.A. 2008. Online Machine Vision Inspection System for Detecting Coating Defects in Metal Lids. Proceedings of the International MultiConference of Engineers and Computer Scientists, 19-21 March, 2008, Hong Kong.

Li, Y., Li Fu, Y., Wang, Q.L., Tan, M. 2010. Measurement and Defect Detection of the Weld Bead Based on Online Vision Inspection. *Transactıons On Instrumentatıon And Measurement,* 59(7): 1841-1849.

Nashat, S., Abdullah, A., Abdullah, M.Z. 2014. A Machine Machine vision for crack inspection of biscuits featuring pyramid detection scheme. *Journal of Food Engineering* 120 (2014): 233–247.

Oechsle, O. 2009. Towards the Automatic Construction of Machine Vision Systems using Genetic Programming. *Doktora Tezi*, University of Essex, School of Computer Science and Electronic Engineering, England.

Omron, Vision Accessory Catalog, https://www.ia.omron.com/data_pdf/cat/flv_fl_q198-e1_12_6_csm1017729.pdf?id=3284(Erişim Tarihi:Nisan 2022)

Sawadisavi, S.V., Edwards, J.R., Resendiz, E., Hart, J.M. 2008. Machine-Vision Inspection of Railroad Track. Federal Railroad Administration. Illinois.

Singh, S., Kaur, M. 2012. Machine Vision System for Automated Visual Inspection of Tile's Surface Quality. *IOSR Journal of Engineering,* 2(3): 429-432.

SYSTEM OPTIMIZATON OF BATTERY DISCHARGE STATE USING ARTIFICIAL NEURAL NETWORK IN AN ELECTRIC VEHICLE POWERTRAIN

Mehmet Onur Genç, onur.genc@btu.edu.tr, Bursa Technical University, Mechatronics Engineering Department, 16310, Bursa, Turkey

Necmettin Kaya, necmi@uludag.edu.tr, Bursa Uludag University, Mechanical Engineering Department, 16059, Bursa, Turkey

ABSTRACT

In this study, the physical modeling of the real vehicle is used to create DT (Digital Twin) model by using Artificial Neural Network (ANN). Than, the obtained DT model is used as the objective function in SA (Simulated Annealing) algorithm to find optimum DoD (Depth of Discharge) value based on the defined parameters in the electric powertrain system. The electric vehicle powertrain system is modeled as 1-D, and battery DoD status are observed based on system inputs. After that, the modeled battery system is subjected to Design of Experiment (DOE) study using Latin Hypercube distribution which enables to have system behavior data in wide range, which provides the data pool for ANN model. Obtained data pool from DOE including the vehicle weight, roll friction coefficient and wind speed is modeled with ANN structure in Python language. Trained ANN model, also called 'Digital Twin' of the system, then is used within System Optimization using Simulated Annealing (SA) Algorithm as objective function. Afterwards, the obtained parametric model is confirmed and compared with physical modeling. The deviations between the 1-D models and optimized ANN model from SA algorithm are found with maximum 7.5% deviation ratio. According to results of the performed methodology, ANN adaptation and System Optimization in Vehicle powertrain system enables to predict desired comfort parameters and optimized the modeled vehicle system.

Keywords: Electric Vehicle Battery System, Artificial Neural Network, System Optimization, Latin Hypercube distribution, Digital Twin, Simulated Annealing Algorithm

1. INTRODUCTION

Battery management in electric vehicles has high importance to provide both optimized electric consuming and safe driving. Increased battery life and balanced 'Depth of Discharged' (DoD) are set the desired system design of 'State of Charge' (SoC) status of an electric vehicle. Artificial Intelligence is one of the potential for Automotive technologies which also enables the system modeling more precise, clear and time and cost saving instead making experimental test load. In parallel, Artificial Neural Network (ANN) is the potential concept to consolidate with dynamic systems to make more precise parameter assumption with the support of wide experienced data pool. Recently Artificial Intelligence (AI) studies have started to take place in engineering problem solving area both in system or design point of views. Artificial Neural Network models have one of the major possible area that representing the physical model of the real system. Nowadays 'Digital Twin' concept is leading virtual representative method for engineering systems that provides to make predict in behalf of the model behavior. ANN modeling is one of the methodology to create 'Digital Twin' for the physical models and provide physical prediction without using either real model or physical model so called 1-D model.

In literature there are several studies exist based on the modeling and the optimization of the BMS and electric drivetrain. Osornio et. al. [1] modeled the BMS (Batery Management System) control map and define the optimization methodology. In thier study, they used Multi-Objective Genetic Algorithm optimization to control the BMS workflow. Kostopoulos et. al. [2] made comparison the physical modeling of the real-driving conditions based on the BMS. They made the investigation for the performance behavior of the BMS range between %20 - %80 and %80 - %100 the State of Charge (SoC) operation modes. Janiaud et. al. [3] studied on the electric powertrain simulation developed under Matlab-Simulink, with the intention of optimizing performances and powertrain efficiency. The modeled is used to choose battery technology and dimensioning according to criteria and driving cycles. Han et. al. [4] studied a generalized formulation for determining the optimal operating strategy and cost optimization for battery. They investigated the explicit expression of the average cost rate is derived for battery lifetime. Saldana et. al. [5] investigated the compares and contrasts electrical equivalent circuit models, impedance models, and runtime models for battery-based EV applications based on the characteristics, advantages and disadvantages in the field of electromobility. Hu et. al. [6] investigated and studied in thier study the BMS control and energy consumption review based on the road-slope conditions including up-hill and down-hill condition. Eckert et. al. [7] studied different EV driveline based on the different configurations. They used GA (Genetic Algorithm) to perform electric engine vs. reductor (transmission) gear ratio optimization. Liu et. al. [8] performed battery analysis based on capacity loss optimization. Genetic algorithm selected as

optimization methodology and sensivity analysis methodology was also proposed. Pan et. al. [9] developed a new mathematical framework to study the optimal design of air electrode microstructures for lithium-oxygen (Li-O2) batteries. They investigated that how an air electrode microstructures affect the discharge capacity of Li-O2 batteries. Perger et.al. [10] stuided the physical model of the energy consumption of the electric vehicle including heating, air conditioning, and other additional loads. The Street network is modeled as a network with nodes and weighted edges in order to apply a shortest path algorithm that finds the route with the smallest edge costs. Sayed et.al. [11] stuided on the energy-saving of each driving distance for battery electric vehicle (BEV) applications, by developing a more e_ective energy management strategy (EMS), under different driving cycles. Fuzzy logic control (FLC) is suggested to control the power management unit (PMU) for the battery management system (BMS) for BEV applications.

Figure 1 explains the methodology followed in this study. The electric vehicle powertrain system was first modeled via 1-D model library by indicating the key parameters in BMS by using LMS AMESim. As next step, the system model was defined with parameter tolerances, and totally 100 experimental set was defined by using Latin Hypercube method in order to have more sensitive distribution that provides precise input for ANN model. As next step, the obtained results from 1-D model was transferred to ANN model, so that the model predict the estimated battery DoD based on the input data. This methodology creates opportunity to expect realized system model results in design phase instead to making too much several experimental study causing time and cost consuming by using trained ANN model as DT model behaving like Responce Surface (RS). The methodology makes a new contribution to the literature and an electric vehicle battery discharge behavior is first investigated based on ANN model integrated SA algorithm. The methodology provides the system estimation by using ANN called Digital Twin and system optimization using ANN as objective function.

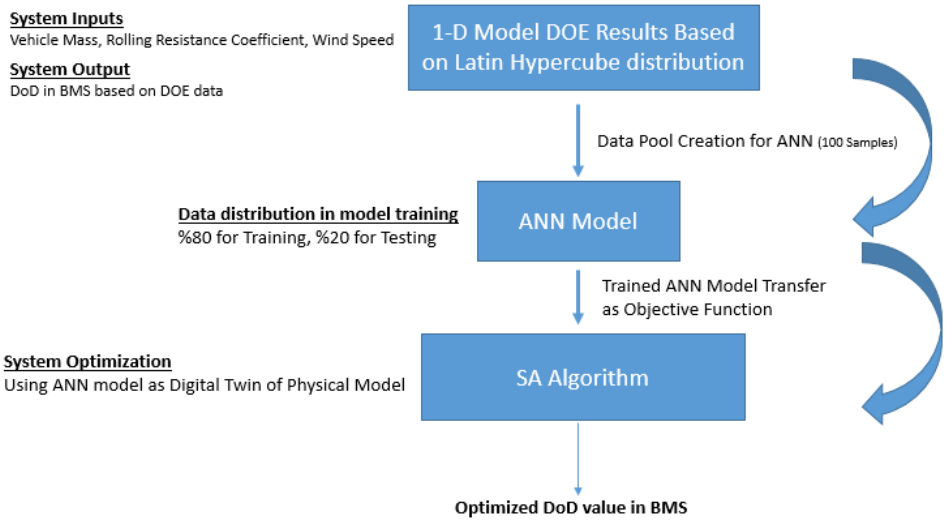


Figure 1. General Flow Followed in the Study

2. VIRTUAL MODELING

Based on the input data (vehicle weight, rolling friction coefficient, wind speed), the output was defined as battery Depth of Discharge (DoD) reading by Battery Management System (BMS). Figure 2 shows the main tasks and functions of the BMS. Depth of Discharge (DoD) prediction has high importance on for drivers to estimate milage capacity. This sensitivity and importance of DoD composes the motivation of this study with comparative using Artificial Neural Network (ANN) for prediction.

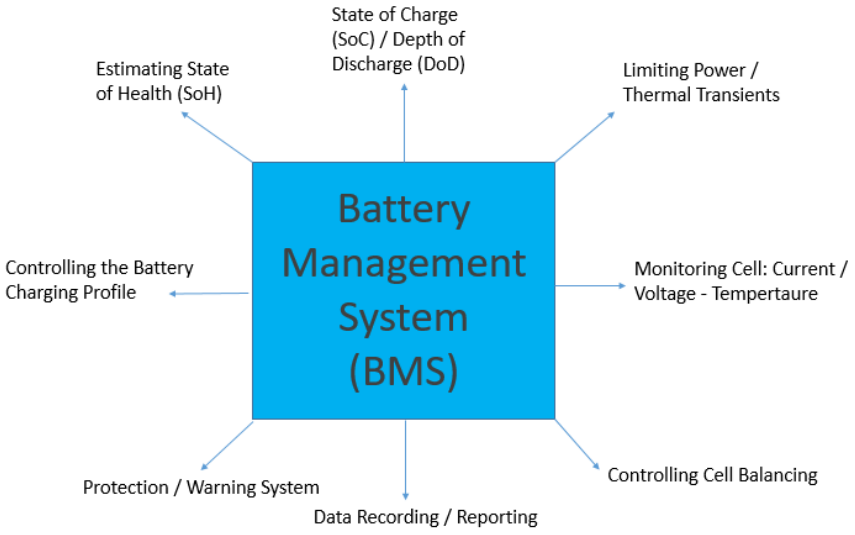


Figure 2. Battery Management System Functions in an Electric Vehicle

DoD explains the instant situation of the remained battery charge in terms of percentage in the running vehicle. DoD is affected by the key parameters of the vehicle directly based on different impact levels and managed by 'Battery Management System' (BMS). Figure 3 explains the modeled electric vehicle powertrain main sections as electrical and mechanical system sections.

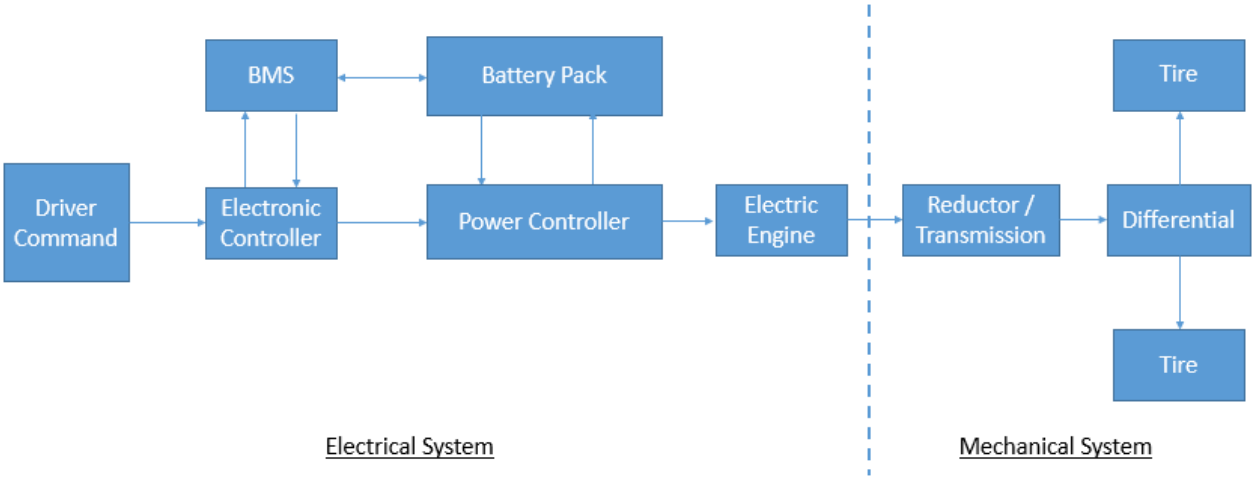


Figure 3. Powertrain System in the Electric Vehicle Analysed in the Study

This section explains the virtual modeling study of the real product. Virtual model, also called physical model, was created as 1-D model in AMESim programme. Figure 4 shows the modeled powertrain system. In this study, as system parameter totally 3 different values were taken into account. These parameters are in order; Vehicle total weight (tonne), Rolling friction coefficient and Wind speed (m/sn). The model represents the medium range passenger car with electric powertrain. The 1-D model reads the Depth of Discharge (DoD) data from Battery Management System (BMS) based on the selected signal intervals. Table 1 shows the parameters within the tolerance values of key parameters. The tolerance range was defined based on the passenger car design ranges in EV.

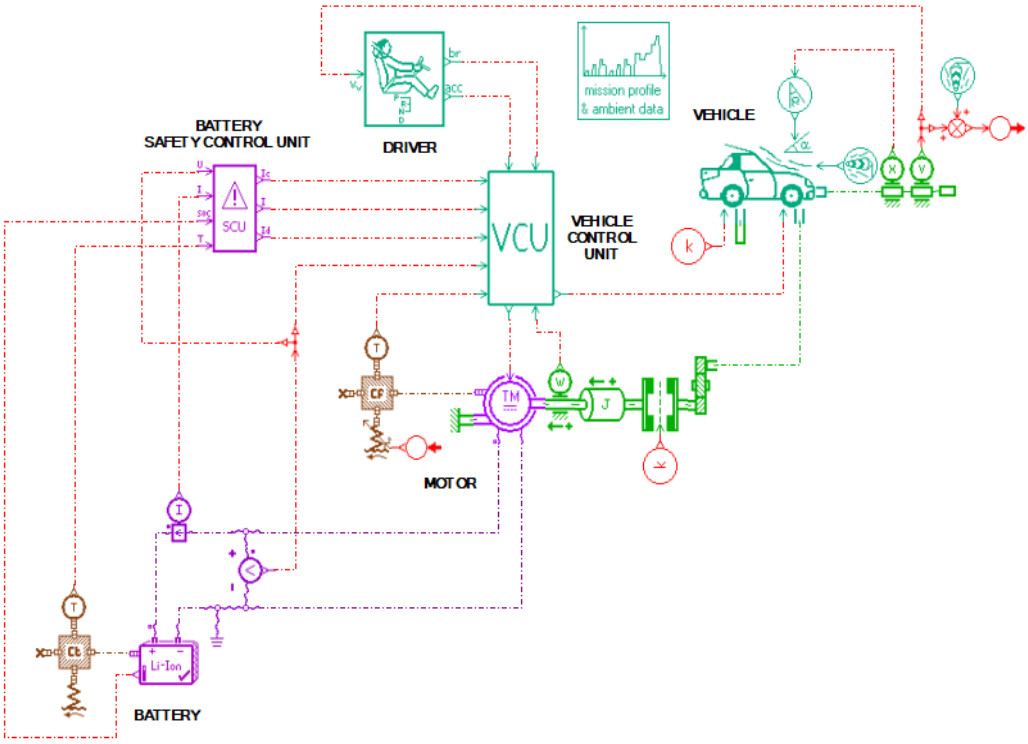


Figure 4. AMESim 1-D Model with BMS (Battery Management System)

Table 1. System Parameters using in 1-D Modeling

System Parameters	Min Value	Max Value
Vehicle Weight	0.5	1.5
Rolling Friction Coefficient	0.01	0.05
Wind Speed	0	30

3. ARTIFICIAL NEURAL NETWORK (ANN) MODELING and TESTING

Artificial Neural Network (ANN) represents the biological brain by making interacting with each artificial neurons and transmit the signals to the other in the physical models. In general, the information flow between the neurons can be provided just the signal can exceed the threshold value. Figure 5 shows the classical ANN model consists of; Input, Hidden and Output layers. Hidden layers represent the non-linear transformation section that strength the model

consistency for the input values. Hidden layers strength the model estimation in case the more non-linear data exist in the pool.

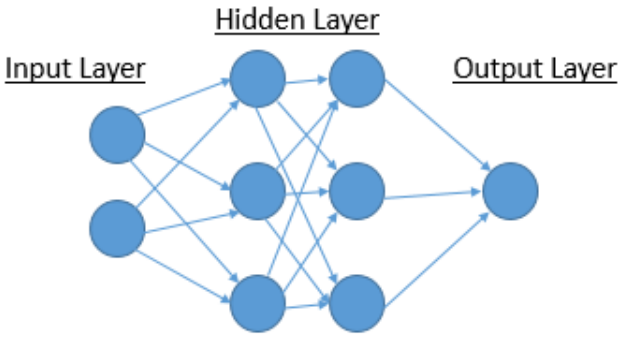


Figure 5. Information Flow in ANN

ANN modeling also ables to represent the real and physical modeling. This situation can be named as Digital Twin (DT) which represents the virtual twin of a physical model and can allow the make prediction based on the real or virtual model. In this study, in order to create base information data for 'Digital Twin', the virtual model was modeled as 1-D and DOE (Design of Experiment) study was performed by using Latin Hypercube distribution methodology. Figure 6 explains the 'Digital Twin' (DT) concept by comparable with real and virtual systems. DT concept enables the simulate real product and its phsysical modeling during system and design optimization phases.

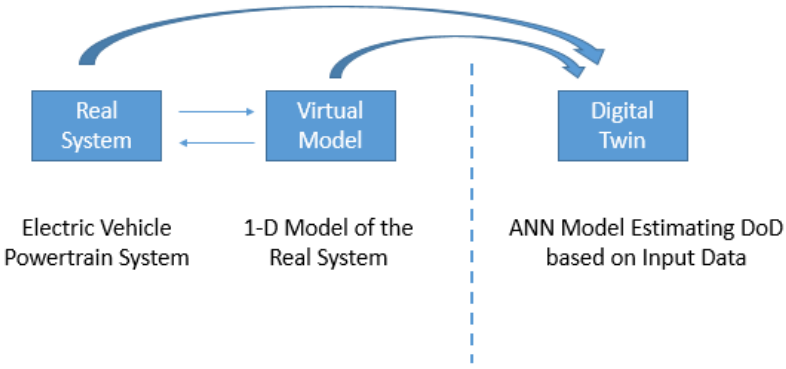


Figure 6. Digital Twin Concept Followed in the Study

In this section the ANN modeling study is introduced and explained. Figure 7a shows the DOE data used in 1-D modeling as representative for first and last five values within the 100 samples represent the 100 (one hundred) batch run via 1-D system model. Figure 7b indicates Latin Hypercube distribution coefficients as sample for first and last five values as the base coefficients of the value in 7a. These data were sent to ANN model and enabled the model to get read it via 'Pandas' module.

	Vehicle Weight (tonne)	Rolling Friction Coefficient	Wind Speed (m/sn)
1	0,765	0,011	22,35
2	1,185	0,0318	0,045
3	0,985	0,027	12,45
4	0,875	0,0322	14,25
5	0,965	0,0234	4,05
96	0,805	0,0266	23,55
97	1,365	0,0142	25,05
98	1,045	0,0114	16,35
99	1,355	0,0458	18,75
100	0,625	0,0354	7,95

a) 1-D Modeling DOE parameters

1	[0.265 0.025 0.745]
2	[0.685 0.545 0.045]
3	[0.405 0.425 0.415]
4	[0.375 0.555 0.475]
5	[0.465 0.335 0.135]
96	[0.305 0.415 0.785]
97	[0.865 0.105 0.835]
98	[0.545 0.035 0.545]
99	[0.855 0.895 0.625]
100	[0.125 0.635 0.265]

b) Latin Hypercube distrubition factors

Figure 7. DOE Input Parameters distributed by Latin Hypercube Theory

Figure 8 shows the ANN model flow performed in the study. The obtained DOE results coming from the 1-D modeling first are being read by the model, than the model is randomly splitted into two groups. First group is used for training, and covers the 80% of the data. The remain 20% of are used for testing the performance of the trained data. Afterwards, the layer definition for the Artificial Neurons (AN) is done including hidden layers according to expected performance from the model. Keras ANN module library was used to make prediction based on Depth of Discharge (DoD) and the 'Digital Twin' model was represented by Artificial Neurons. As activation function between the neurons 'Relu Activation Function' was used to provide interactions between the layers. As next step, the optimizer and loss method definition take place. 'Adam' optimization methodology and 'Mean Squared Error' are selected, after that the model fit is provided and tested to provide model prediction at last step.

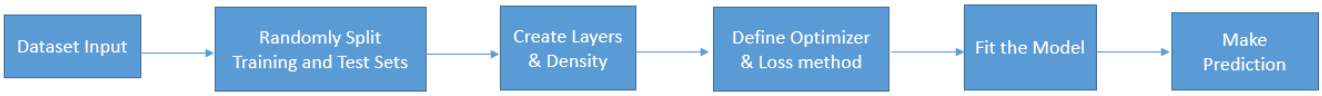


Figure 8. ANN Model Flow

Table 2 shows the random 3 batch results taken from the 1-D batch results. The results were compared between the trained ANN results and the 1-D results, then the deviation results were obtained. The deviations between the trained ANN model, so called DT model, and the physical model was found in average as 2.93%. The results can be considered as meaningfull and useful for system engineering point of view.

Table 2. Trained ANN Model Random Results vs. Comparison with 1-D Modeling

System Parameters			ANN Results (DoD)	1-D Results (DoD)	Deviation (%)
1st Random Trial	Vehicle Weight	0.965	**13.90**	**13.52**	**2.8%**
	Rolling Friction Coefficient	0.0234			
	Wind Speed	4.05			
2nd Random Trial	Vehicle Weight	1.485	**11.05**	**11.44**	**3.5%**
	Rolling Friction Coefficient	0.0102			
	Wind Speed	0.15			
3rd Random Trial	Vehicle Weight	1.355	**18.12**	**18.59**	**2.5%**
	Rolling Friction Coefficient	0.0458			
	Wind Speed	18.75			

4. SYSTEM OPTIMIZATION USING SIMULATED ANNEALING ALGORITHM

SA is an optimization algorithm accepted as a global optimization method and is a methodology for constrained multivariable optimization. The name of 'Simulated Annealing' refers to the simulating the behavior of metals during the annealing process. The optimization process starts by generating a random initial solution. The temperature decreases from an initial positive value to zero. During these intervals, the algorithm randomly chooses a solution close to the current one, and selects better or worse solutions according to Boltzmann probability. Accepting worse move (worse objective function values) by Boltzmann probability factor is shown in Eq. 1. f (xtemp) is the new move and f(x_i) is the new current solution. T_t is the temperature at the current location (m). As m becomes larger (towards the end), the output becomes smaller, so the probability in accepting new worse moves is reduced.

$$\text{Boltzmann equation} = 1 \Big/ \left(e^{\left(\frac{f(\overline{x_{tmp}}) - f(\overline{x_i})}{T_t} \right)} \right) \quad (1)$$

Figure 9 shows the general operation steps of the ANN integrated SA algorithm. Trained ANN model is used as objective function within the algorithm flow to provide DoD optimization. The

SA algorithm takes the input parameters ‘Vehicle Weight’, ‘Rolling Friction Coefficient’, ‘Wind Speed’ into consideration as starting search point. The objective function (trained ANN model) is subjected optimization iterations and final optimum value is found based on the defined SA definition parameters ‘Starting temperature’ and search intervals.

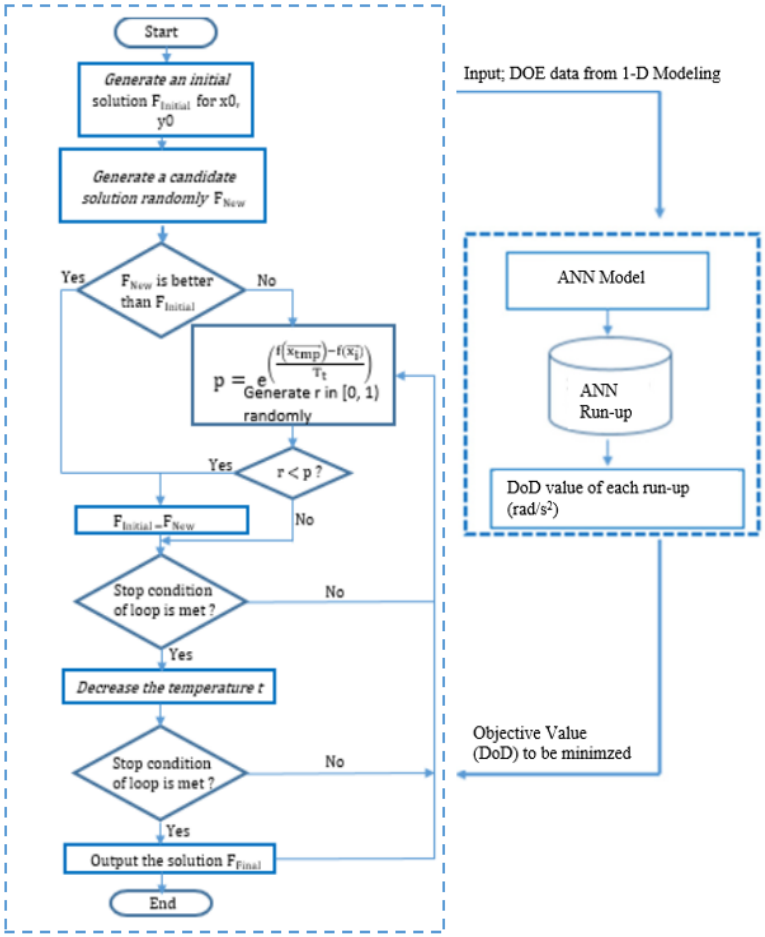


Figure 9. SA Algorithm using the ANN Trained Model to Optimized DoD Values

Figure 10 shows the sample behavior of trained ANN as objective function within the SA algorithm flow. In order to find global minimum value and ensure system optimization, the ANN model behaves like in the Figure 10. The integrated SA algorithm model finds the minimum DoD value after several iterations designed based on the SA algorithm logic flow.

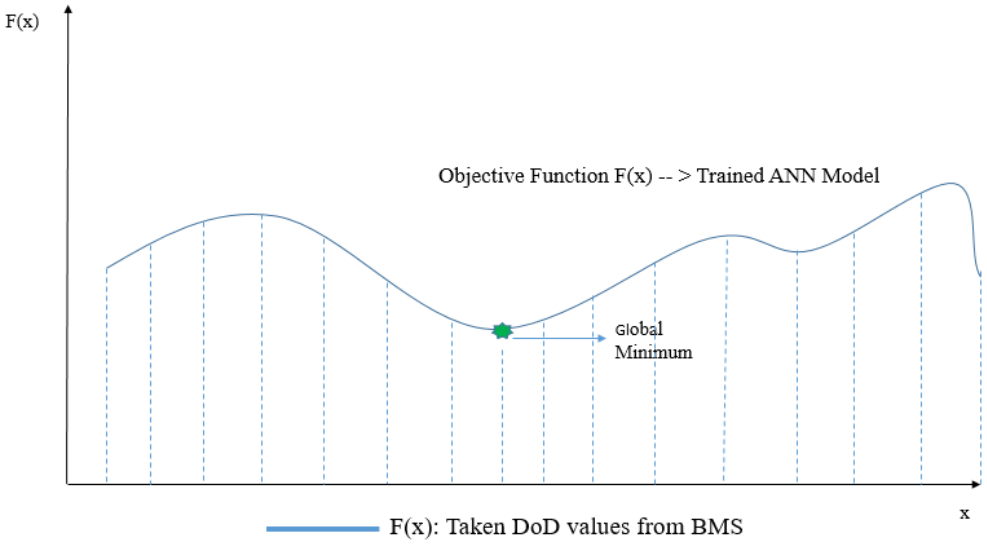


Figure 10. Trained ANN Model as Objective Function in SA Algorithm Concept

Table 3 shows the random three values also based on the found ANN in Table 2. The optimization flow starts with the random starting point for Vehicle Weight, Rolling Friction and Wind Speed. Afterwards, found optimized DoD values are compared with 1-D model results to observe the deviation between the optimized % DoD value and 1-D model results. The average deviation for three random choices are found 5.73 %.

Table 3. SA DoD Optimized Results based on Trained ANN Model vs. 1-D Model Comparison for Final Values

	Random Starting Point for Searching	Final Points	Initial DoD ANN Result %	Optimized DoD ANN Result %	1-D Result at Final Points for Optimized DoD %	Deviation
Vehicle Weight	0.965	0.756	**13.90**	**9.65**	**10.11**	**4.5%**
Rolling Friction (coeff.)	0.0234	0.0123				
Wind Speed	4.05	2.1				
Vehicle Weight	1.485	1.256	**11.05**	**8.62**	**9.32**	**7.5%**
Rolling Friction (coeff.)	0.0102	0.0098				
Wind Speed	0.15	0.11				
Vehicle Weight	1.355	0.956	**18.12**	**13.92**	**13.22**	**5.2%**
Rolling Friction (coeff.)	0.0458	0.022				
Wind Speed	18.75	9.51				

Table 4 makes general comparison between the trained ANN model (DT model) estimation deviation and Optimized trained ANN model results from SA algorithm. According to results, while the DT model (trained ANN) shows 2.93% average deviation between the 1-D of the physical model, the optimized DoD values shows 5.73% deviation. The deviation results (5.73%) obtained from SA algorithm can be accepted as useful, and has meaningful estimation based on system and design sensivity.

Table 4. Deviations Digital Twin (trained ANN model) vs. Optimized (from SA algorithm) Digital Twin (trained ANN model) results between 1-D Modeling

	Deviation ratio for DoD result btw. Trained ANN model vs. 1-D Model	**Deviation ratio for DoD result btw. Optimized Trained ANN model from SA algorithm vs. 1-D Model**
Random Trial 1	**2.8%**	**4.5%**
Random Trial 2	**3.5%**	**7.5%**
Random Trial 3	**2.5%**	**5.2%**
Average	**2.93%**	**5.73%**

5. CONCLUSION

In this study, the parametric optimization model was created and trained ANN model was integrated to this model to find optimum DoD value within defined parameter tolerance range. In order to find optimum DoD behavior, 1-D model was run by preparing Design of Experiment (DoE) study based on Latinhypercube distribution. Totally 100 (one hundred) different configuration was tested by batch run, then the data-pool transfered to ANN model in order to train the model. The trained model first compared with 1-D results to see how much the DT model can closely estimate the DoD value. Then the randomly selected three (3) ANN points are subjected and integrated to SA algorithm to find optimum DoD value in order to find optimum design parameters in the electric vehicle system. According to obtained results, the trained ANN model estimates the battery discharge state with 2.93 % average deviation. This deviation can be accepted useful during system and design engineering phases. Afterwards, the ANN model was integrated into the SA model as objective function to find optimum DoD value, and the found values were compared with the 1-D results in order to test consistency between the SA optimization algorithm and ANN model. The deviation was found as 5.73% between the optimized DoD results obtained from SA model and the 1-D model results of the input parameters. 5.73% average deviation result also can be acceptable considerably, because the less deviation occured despite of the out of parameter selection from DoE data-

pool subjected to 1-D batch multiple model run. This model can be used in the design process in future studies and also for optimization purposes to eliminate many real-vehicle testing and bench test, and provides system parameter estimation using ANN model as 'Digital Twin' concept.

REFERENCES

1. Osornio, C., Villereal, R. C., Molina, A, Estavillo, J., Santillan, S.D., (2013), "Optimization of Power Train and Control Strategy of a Hybrid Electric Vehicle for Maximum Energy Economy" Engineering Investigation of Technology, Volume: 14, Issue: 1, pp.65-80.

2. Kostopoulos, E., Spyropoulos, G., Kaldellis, J., (2020), "Real-world study for the optimal charging of electric vehicles" Energy Reports, Volume:6, pp.418-426.

3. Janiaud, N., Vallet, F., Petit, M., Sandou, G., (2011), "Electric Vehicle Powertrain Simulation to Optimize Battery and Vehicle Performances" IEEE Conference on Vehicle Power and Propulsion (VPPC)-IEEE Online Journal, 978-1-4244-8218-4.

4. Han, Y., Wang, J., Zhao, Q., Han, P., (2014), "An Optimal Operating Strategy for Battery Life Cycle Costs in Electric Vehicles" Journal of Applied Mathematics , Volume 2014, Article ID 305905, 6 pages, http://dx.doi.org/10.1155/2014/305905.

5. Saldana, G., Martin, J., Zamora, I., Asensio, F., Onederra, O., (2014), "Analysis of the Current Electric Battery Models for Electric Vehicle Simulation" Energies, Volume: 12, doi:10.3390/en12142750.

6. Hu, T., Li, Y., Zhang, Z., Zhao, Y., Liu, D., (2021), "Energy Management Strategy of Hybrid Energy Storage System Based on Road Slope Information" Energies, Volume: 14, doi:10.3390/en14092358.

7. Eckert, J., Silva, L., Costa, E., Santiciolli, F., Dedini, F., Correa, F., (2015), "Electric vehicle drivetrain optimization" IET Electrical Systems in Transportation, Volume: 7, Issue: 1, pp. 32-40.

8. Liu, C., Liu, L., (2017),"Optimal Design of Li-Ion Batteries through Multi-Physics Modeling and Multi-Objective Optimization" Journal of The Electrochemical Society, Volume: 164, Issue: 11, pp. 3254-3264.

9. Pan, W., Yang, X., Bao, J., Wang, M., (2017), "Optimizing Discharge Capacity of Li-O2 Batteries by Design of Air-Electrode Porous Structure: Multifidelity Modeling and Optimization" Journal of The Electrochemical Society, Volume: 164**,** Issue: 11, pp. 3499-3511.

10. Perger, T., Auer, H., (2020), "Energy efficient route planning for electric vehicles with special consideration of the topography and battery lifetime" Energy Efficiency, Volume: 13, https://doi.org/10.1007/s12053-020-09900-5, pp.1705–1726.

11. Sayed, K., Kassem, A., Saleeb, H., Alghamdi, A., (2020), "Energy-Saving of Battery Electric Vehicle Powertrain and Efficiency Improvement during Different Standard Driving Cycles" Sustainability, Volume: 12, doi:10.3390/su122410466.

12. M, Cavalcanti., M, Schmal., Giudici, R., R, Alves., (2019), ''A catalyst selection method for hydrogen production through Water-Gas Shift Reaction using artificial neural networks.'' Journal of Environmental Management, Vol.237, pp. 585–594.

13. L, Cheng., D, Quin., Y, Wang., (2017), ''Modeling and simulation of pure electric bus based on Modelica'' Automobile Technology, 48(8), pp. 43–48.

14. D, Quin. J, Li., T, Wang., D, Zhang., (2019), "Modeling and Simulating a Battery for an Electric Vehicle Based on Modelica'' Automotive Innovation, Vol.2, pp. 169–177.

15. K, P, Somashekhar., N, Ramachandran., Jose, Mathew., (2010), "Optimization of material removal rate in Micro-EDM using artificial neural network and genetic algorithms" Materials and Manufacturing Processes, Vol.25, pp.467-475.

16. L, Lu., X, Han., J, Li., J, Hua., M, Ouyang., (2013), "A review on the key issues for lithium-ion battery management in electric vehicles'' Journal of Power Sources, Vol. 226, pp.272–288

DESIGN OF MODULAR PLANETARY GEARBOX WITH TWO-STAGE PLANET GEARS FOR USE IN VALVE ACTUATORS

Seher SEVEN, *seher.seven@novumek.com* Novumek Technology Corp., Ankara, Turkey

Muhammed Mahbub İBİŞ, muhammedibis@ksb.com.tr, KSB Corp. Ankara, Turkey

Evren COŞKUNER, evrencoskuner@ksb.com.tr KSB Corp. Turkey, Ankara, Turkey

Besim BARANOĞLU, *besim.baranoglu@novumek.com* Novumek Technology Corp., Ankara, Turkey

ABSTRACT

A method to help design a planetary gearbox for use in valve actuators is presented. In the method AGMA criteria are employed along with the assembly requirements of the gearbox. A three-arm planet system with planets split into two separate wheels is considered instead of a simple planetary gear train. A MATLAB program is coded to help the design and with this code it becomes possible to obtain two- and more staged inline gearbox system.

Keywords: Planetary gearbox, modular, valve actuator

1. INTRODUCTION

Many machines and mechanisms in various applications require gearboxes in power transmission. There are various types of gears and gearboxes for different applications, and a special type of gearing is the planet (or epicyclic) gear trains. The fundamental difference of epicyclic gears is in the degrees of freedom it presents: two [Söylemez, 2009]. Therefore, they can be employed by either fixing one degree of freedom, or, can be used as a differential which either sums or subtracts the two input powers [Heisler, 2002]. Several advantages of the epicyclic gears can be given as, (1) it has a compact structure, (2) it's lightweight and has high power density [Chen, 2014]. Also, it is an advantage of the planetary gearboxes that they can give higher reduction-to-weight ratio than a parallel shaft gearbox while keeping the input and output shafts coaxial [McFadden, 2016]. And the planetary gearbox is well suited to carrying high torques [McFadden, 2016]. The main disadvantage can be stated as its lower efficiency relative to the simple gearboxes [Chen, 2014]. Other two disadvantages can be stated as:

(1) they are maintenance intensive and have higher mean time to repair when compared to parallel shaft gears, and (2) they are more complex in design [Forsthoffer, 2011].

This study mainly focuses on a modular gearbox to be installed in a valve actuator system. The actuator is composed mainly of an input module, where the power is created (by an electric motor and its driver) which is transferred/transformed in the transmission module to the exit module where different types of valves can be attached. In the transmission module, there is a multi-stage gearbox where all stages are interconnected inline through their input and output shafts. In the transmission module, every stage is an epicyclic gear. This way, it becomes possible to avoid shaking torques and moments along the main transmission axis.

A gearbox design can be done for several different requirements: For strength [Shim, 2014, Mandol, 2018], for shape and weight [Daoudi, 2016] or for dynamic analysis [Yuan, 2018] and/or modal analysis [Lingtao, 2015], which are designed for several applications: for use in a wind turbine [Mohsine, 2016], or helicopters [Kaynar, 2017], etc. The main aim of the present study is to obtain a scalable two or more stage planetary gearbox design tool that can be used in the design of the gearbox module for use in valve actuators. The design procedure follows the standards of AGMA [ANSI/AGMA 2001-D04 (2004)]. A generalized MATLAB code is written to follow the rules stated in the following text. With the help of this code, it becomes possible to design different gearboxes for different input actuators and different output requirements as well as change the number of stages. The design is made with planets split into two separate wheels to increase the output drive ratio with minimal increase in volume and not increasing the moving parts.

2. CONCEPTUAL DESIGN

The main reason for selecting planetary gears in modular valve actuator's transmission module is that two (or more) planetary gearboxes can easily be assembled in series along their input and output shafts (Figure 1). To minimize the off-axis forces and moments on the input and output shafts, equidistant assembly of identical planets are used in many designs, and to minimize (or theoretically make zero) the inline force on the main shaft, spur gears are used.

Instead of a simple epicyclic gear (Figure 2a) a single arm-carrier associated mechanism with the planets split into two separate wheels (Figure 2b) is used in this study to increase the drive ratio with a minimal volume change of the gearbox. The mechanism drawing which is given in Figure 2b, is a subset of the 12 possible epicyclic gear mechanism which are stated by [Levai, 1968] (Figure 3).

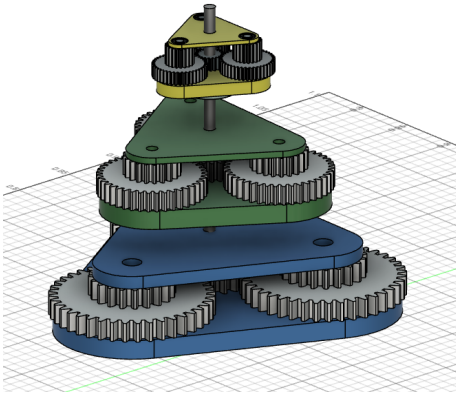


Figure 1. Three planet gears (grounded rings not shown) assembled in aligned shafts

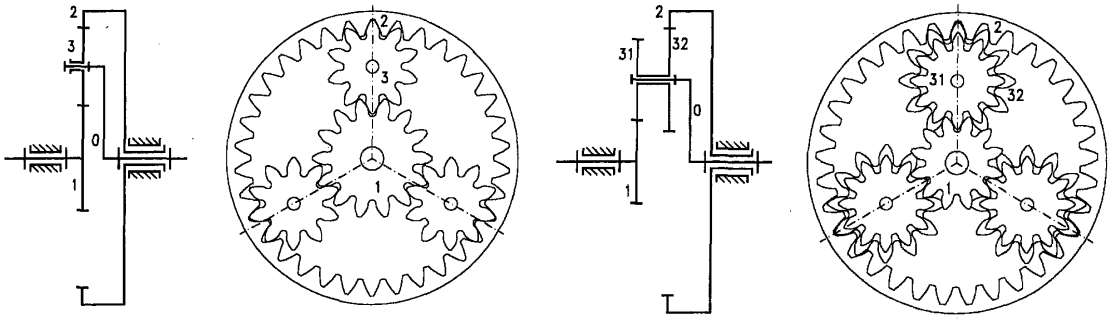


Figure 2. The simple (a) and compound (b) epicyclic gears, reprinted from [Juvinall 2012].

The drive ratio is dependent on the selection of the gear diameters. It can be shown that a higher drive ratio can be obtained with compound epicyclic gears in a single stage.

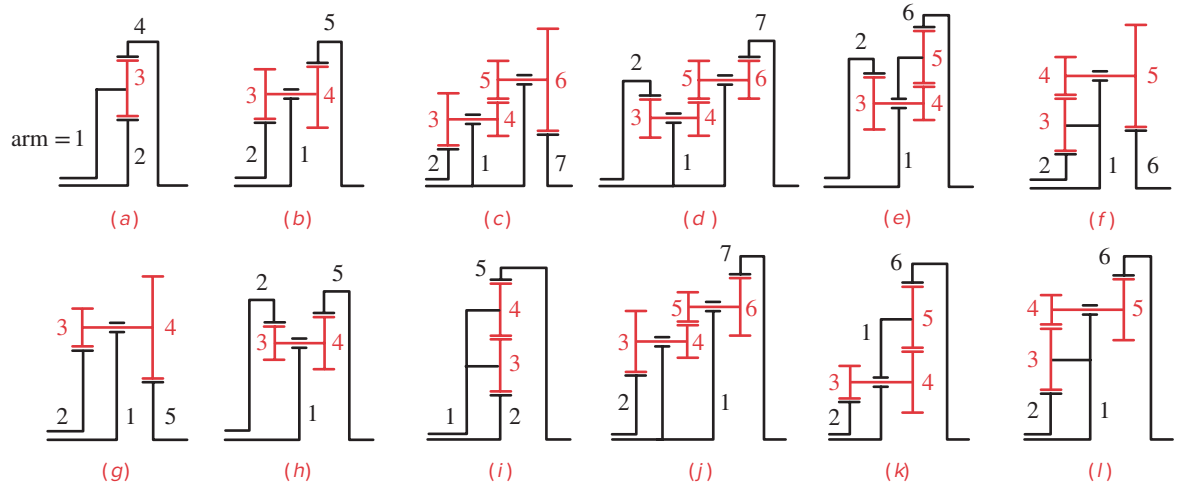


Figure 3. The 12 possible epicyclic gear constructions by Levai, reprinted from [Norton, 2020]

There are infinite possibilities in selecting the gear sizes and number of planets in the epicyclic gear, yet these possibilities are narrowed by two conditions: (1) the available space, e.g., the

tooth tips of the adjacent planets should not touch (see Figure-4a where equidistant four planets are coinciding), and (2) alignment of the planets, e.g., each planet should mesh properly with the sun and the ring (Figure 4b where in the case of a four equidistant planets, two mesh with the sun and the ring properly, while the other two does not mesh with the ring). For a further discussion, see [Juvinall 2012].

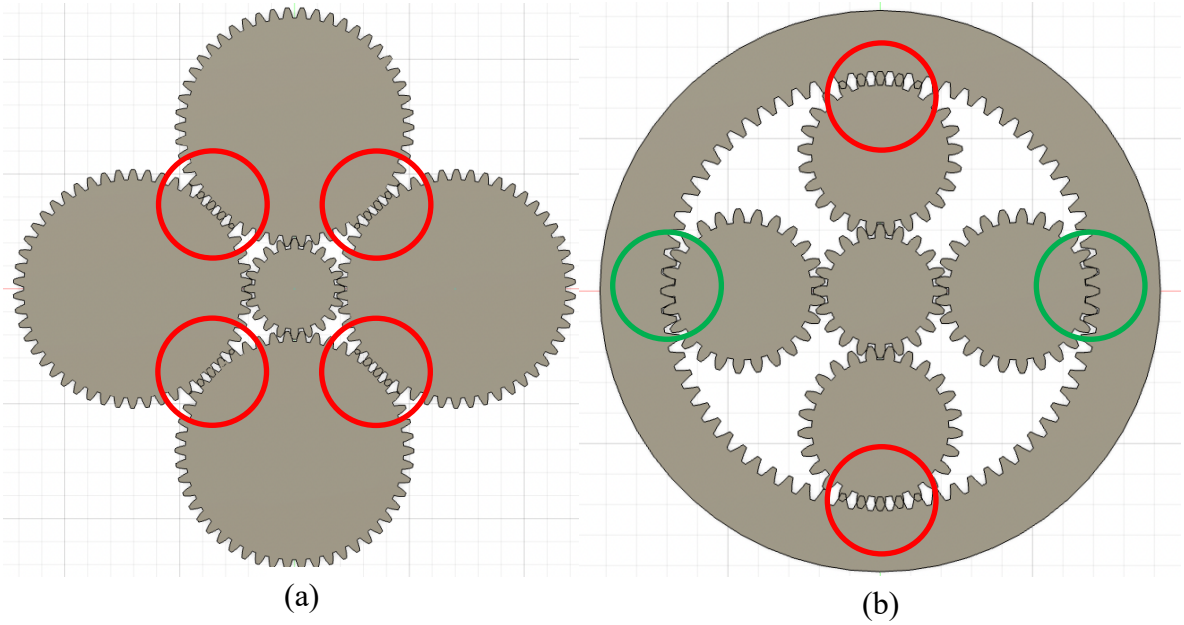


Figure 4. The size problem, where the planets touch the adjacent planets (a) and alignment problem where the planets mesh correctly with the sun but two of the planets cannot mesh with the ring (b).

In the present design, a 3-equidistantly disposed planet structure is preferred. Designating the number of teeth of the sun gear as z_s , the number of teeth of the ring as z_r and the numbers of teeth of the planet z_{ps} and z_{pr} for the sun and the ring sides consecutively (see Figure-5), the assembly of the planets is ensured through the relation [Simionescu, 1998]:

$$(z_s \cdot z_{pr} + z_r \cdot z_{ps})/n = |A_1 \cdot z_{pr} \pm A_2 \cdot z_{ps}| \qquad (1)$$

where $0 < A_1 < z_{ps}/D$ and $0 < A_2 < z_{pr}/D$ are integers. In these equations, D is the greater common divider of z_{pr} and z_{ps} and n is the number of equidistant planets. Note that, if $z_{pr} = z_s$ and $z_{ps} = 2z_{pr}$, which would require $z_r = 4z_s$, Equation 1 would read

$$(z_s^2 + 8\, z_s^2)/3 = |A_1\, z_s \pm 2\, A_2 z_s| \qquad (2)$$

which is possible with $A_1 = 1$ and $A_2 = 1$ where both obeys the requirement since $D = z_s$. Therefore, with these parameters, a scalable design of epicyclic gears is possible (e.g., selection of the number of gears in the sun would yield to an epicyclic gear that can be assembled without problem).

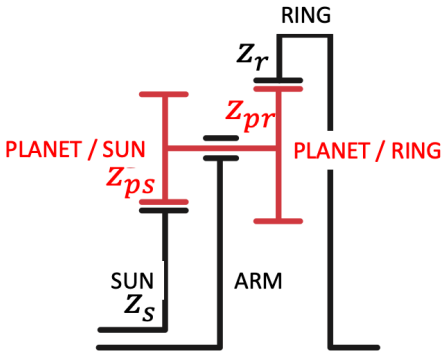


Figure 5. Gear number of teeth designations for an epicyclic gear train with planets split into two separate wheels

The minimum number of teeth for the sun gear can be obtained from the relation [Budynas, 2011] considering the interference:

$$N_p = \frac{2k}{(1+2R)\sin^2\phi}\left(R + \sqrt{R^2 + (1+2R)\sin^2\phi}\right) \tag{3}$$

where, assuming full-depth teeth, $k = 1$, $\phi = 20°$ is the pressure angle and $R = 2$ is the ratio of the pinion (sun) and the gear (planet). The minimum integer value in this case is obtained as 15. At this point, any selection of teeth number larger than or equal to 15 would be free of interference with the above proportions between sun, planets, and the ring gear.

Table 1. Conceptual design parameters

Number of planets	3
Number of teeth for sun, z_s	20
Number of teeth for the planet in sun side, $z_{ps} = 2\,z_s$	40
Number of teeth for the planets in ring side, $z_{ps} = z_s$	20
Number of teeth for the ring, $z_r = 4\,z_s$	80
Pressure angle, in degrees	20
Calculated drive ratio	9

The selection of the proper number of teeth for the sun (and for the planet on the ring side) requires a consideration on the geometry factor in AGMA equations for which the graph is given in AGMA218.01 standard (see Figure14-6 in [Budynas, 2011]). It can be seen from the geometry factor graph that for number of teeth that is less than 18, the geometry factor steeply drops. Therefore, a selection of number of teeth that is greater than 18 would be proper. For the mating gear being twice the pinion, the sun gear number of teeth, $z_s = 20$ would be a

proper choice giving the geometry factor, $J \cong 0.33$. Thus, conceptually, the parameter for each module is selected as given in Table 1.

3. MODULAR SCALABLE DESIGN

In the conceptual design, several design parameters are selected. These parameters can be used to estimate the final design of the modular planetary gearbox. The basic requirement would be the input power and speed (or, more precisely, input torque and speed) of the gearbox.

Each module of the gearbox would decrease the speed by 1:9 of the input speed of that module while the power will be transmitted with the reduction due to efficiency:

$$P_{out} = \eta \cdot P_{in} \tag{3}$$

where the efficiency of the planetary gearbox can be estimated as [Norton, 2020]:

$$\eta = \frac{R\,E_0 - 1}{R - 1} \tag{3}$$

where E_0 is the efficiency of the gear pairs connected. In case of a spur gear, this efficiency can be assumed approximately as $E_0 = 0.98$. Note that there are 6 pairs of gear contact, which would make $E_0 = 0.98^6 \cong 0.89$. With $R = 9$ the total expected efficiency would be $\eta = 0.88$.

The free body diagrams (FBD), in 2-D space (disregarding the planet shaft off-axis forces and moments) is be given in Figure 6 assuming efficiency is 1. This case incorporates the maximum power transmitted, thus a design that is safe with this efficiency would be safe under less efficiency values.

When the FBD are considered, it can be easily seen that, if no manufacturing/assembly imperfections are considered, the shaft off-axis forces in all centers reduce to zero. This makes it possible to use simple roller bearings or lubricated bushings (which, is not discussed in this study). This also allows to design the shafts considering only the torque transmitted.

This study focuses on the gear calculations. For this, a MATLAB code is developed for evaluating the AGMA equations [ANSI/AGMA 2001-D04, 2004]. The algorithm of the code is given in Figure 7. The code then presents the results and state if the design is safe. As the input power and speed is specified, the code first assumes a prescribed module and face width of the gears, then by changing first the face width and then the module finds an admissible pair for those two parameters. Admissible module values are selected from a table of standard values [Budynas, 2011].

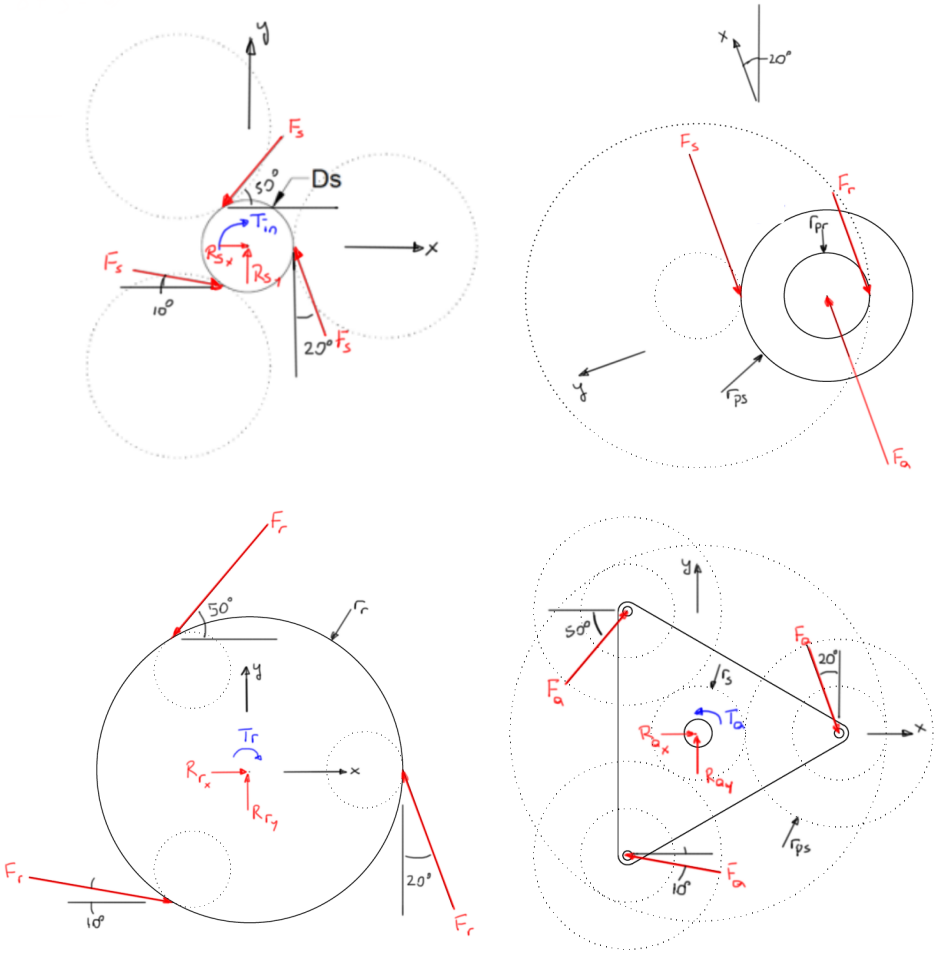


Figure 6. Simplified FBD of the sun (upper left), the planets (upper right), the ring (lower left) and the arm (lower right).

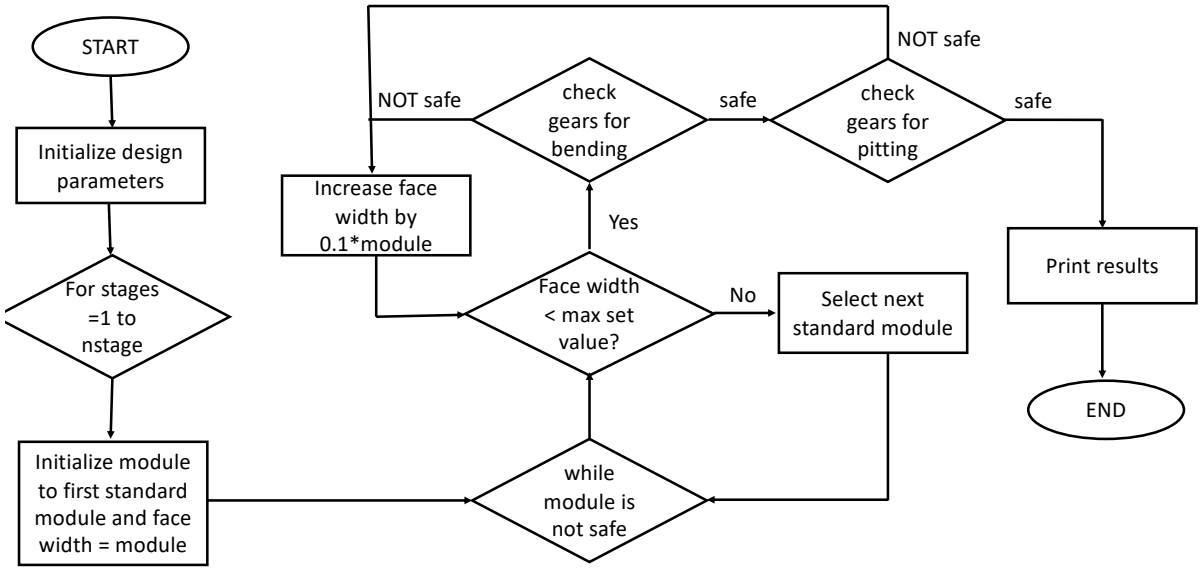


Figure 7. The algorithm of the MATLAB code

4. CASE STUDIES

Two examples to design a modular gearbox is presented in this section. The first is the 300W actuated (at 1200rpm) 3 – stage gearbox. The total reduction in speed is 1:729, thus a 1200 rpm input will be reduced to approximately 1.65 rpm at the output. The input torque of the actuator is approximately 2.39Nm at 1200 rpm, which, for cases to cover stall conditions, this torque is increased by 50%. The calculations results are presented in Table-2. Note the safety factor being very close to 3, which is a required parameter for exiting the loops. If this safety factor is decreased or increased, the values change. The reliability of the gearbox is selected as %99.9. In AGMA calculations Q5 quality for surface is assumed (which can be changed in the code).

As a second example, a two-stage gearbox design is considered for a 1.25 kW motor (at 1200 rpm) for which the input torque is estimated as 10Nm. Assuming a 20% increased stall torque, the design is created using 12Nm. A change of design results with changing safety factor is presented in Figure 8. The sharp changes in the face width indicate increase in module. The module change when the face width hits the maximum value is evident in the graph.

In both case studies, it can be concluded that the resulting design is valid.

4. DISCUSSION AND CONCLUSION

A design procedure and a tool for helping the design is presented in this study for use in valve actuators' transmission module. The following notes are in place for the given study:

- The design procedure is effective in multi stage gearboxes where in all stages a 1:9 planetary gearbox is employed. The assembly of the gearbox is ensured if $z_{ps} = 2\,z_s$ and $z_{pr} = z_s$ where z_s is the the number of teeth of the sun gear, and z_{ps} and z_{pr} are the the numbers of teeth of the planet gears for the sun and the ring sides consecutively. The number of teeth in the ring gear, $z_r = 4z_s$ is a calculated value from the above values.
- The designed gearboxes have three equidistantly placed planets in the construction. This way the off-axis forces and moments are minimized which leads to minimized shaking moments and torques. Aside from manufacturing and/or assembly tolerances and errors, no shaking moments and torques are expected.
- In the design spur gears are used, which leads to theoretically no axial forces on the main shafts of the gears, resulting in the lesser needs for the bearings and/or bushings.
- All design is based on AGMA standards, no further analysis (numerical or theoretical) is given. Since the surface condition is given as Q5 quality in the design (which is a very low surface condition), a numerical analysis presents no additional benefit.

Table-2: Calculations for the first evaluation example

Stage 1	Safety factor=	3	2	1.5
Input Torque (Nm)		3.581	3.581	3.581
Calculated module (mm)		1	1	1
Calculated face width (mm)		5.1	3.40	2.6
Lowest safety factor (for planet in bending)		3.02	2.02	1.55
Highest safety factor (for sun in pitting)		8.19	6.71	5.86
Stage 2	Safety factor=	3	2	1.5
Input Torque (Nm)		32.228	32.228	32.228
Calculated module (mm)		1.5	1.25	1.25
Calculated face width (mm)		18.3	17.25	12.63
Lowest safety factor (for planet in bending)		3.00	2.00	1.51
Highest safety factor (for sun in pitting)		8.17	6.68	5.79
Stage 3	Safety factor=	3	2	1.5
Input Torque (Nm)		290.06	290.06	290.06
Calculated module (mm)		3	3	2.5
Calculated face width (mm)		42.6	27.00	29.25
Lowest safety factor (for planet in bending)		3.00	2.00	1.51
Highest safety factor (for sun in pitting)		8.17	6.67	5.80

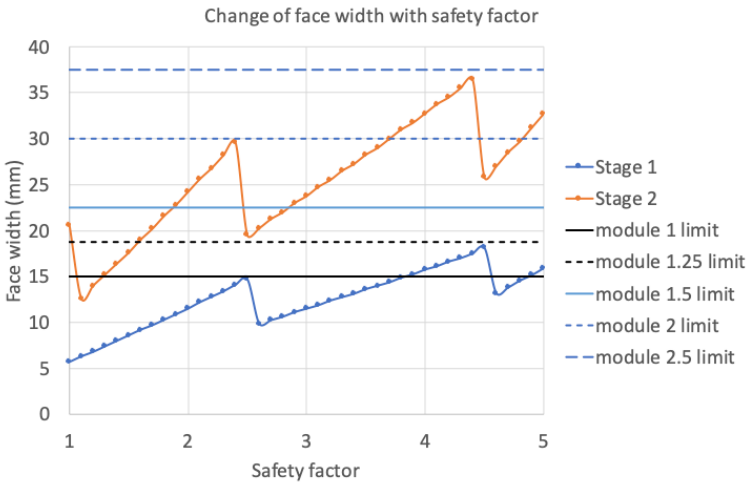


Figure 8. The change of face width with changing safety factor

- The preconditions of the analysis can be changed easily to render the procedure to any other material (for the gears), any other criteria for safety, reliability, surface condition, total expected number of cycles, etc. With new analysis, multi stage gearboxes can be constructed with the given procedure.

The main assumption in the procedure is that the face width of the sun gear and those of the gears in the planets are the same. This is a practical condition for decreased manufacturing costs in mass production. This condition may be loosened by changing the algorithm of the procedure.

A future study may be suggested by enhancing the procedure obtain a general procedure for any number of equidistantly placed planets ensuring assembly. Also, with three equidistantly placed planets, alternative teeth numbers can be worked on to establish a general rule.

REFERENCES

1. **Söylemez, E. (2009),** Mechanisms, 4th Ed., Middle East Technical University Pub., Ankara, Turkey.
2. **Chen, C., Chen, J. (2014),** "Power analysis of two-dof epicyclic gear transmission and experimental validation", International Gear Conference, 26 – 28 August 2014, Lyon.
3. **Heisler, H. (2002),** Advanced vehicle technology, 2nd Ed., Butterworth-Heinemann.
4. **McFadden, S., Basu, B. (2016),** Offshore wind farms – technologies, design and operation, Woodhead Publishing.
5. **Forsthoffer, W. E. (2011),** Fossthoffer's best practice handbook for rotating machinery, Butterworth-Heinemann.
6. **Shim, J-H, Han, S. G., Shin, Y. I., Yoon, C. H. (2014),** "Strength verification of the planetary gear system", Proceedings of the 2014 International Conference on Mechanics, Fluid Mechanics, Heat and Mass Transfer, 22 – 24 February, Interlaken, Switzerland.
7. **Mandol, S., Dan, P. K., Mondal, M. K. (2018),** "Modeling for optimality in design of planetary ring gear to reduce stress development - A Response Surface Methodology based Parametric Modelling Approach", 3rd International Conference for Convergence in Technology (I2CT), 6 – 11 April, Pune, India.
8. **Daoudi, K., Boudi, E. M. (2016),** "Shape optimization of a planetary gear train based on the minimum weight", International Renewable and Sustainable Energy Conference (IRSEC), 14-17 November, Marakkesh, Morocco.
9. **Yuan, Y. (2018),** "Dynamic Analysis of Planetary Gear Train Based on ADAMS", MATEC Web of Conferences 175, 03051, DOI:1051/matecconf/201817503051

10. **Lingtao, L., Chao, M., Shaohong, W. (2015),** "Modal analysis of modified planetary gear transmission based on real meshing stiffness", IEEE 12th International Conference on Electronic Measurement & Instruments, 16-18 July, Qingdao, China.
11. **Mohsine, A., Boudi, E. M., Marjani, A. E. (2016),** "Modeling and structural analysis of planetary gear of a wind turbine", International Renewable and Sustainable Energy Conference (IRSEC), 14-17 November, Marakkesh, Morocco.
12. **Kaynar, E. (2017),** Helikopterlerde planet dişli sistemi rulmanı profil optimizasyonu, M.Sc. Thesis, Gazi University.
13. **Budynas, R. G., Nisbett, J. K. (2011),** Shigley's Mechanical Engineering Design, 9th Ed. in SI units, McGraw-Hill, Singapore.
14. **Juvinall, R. C., Marshek, K. M. (2012),** Machine Component Design, 5th Ed., John Wiley & Sons Inc., Singapore.
15. **Simionescu, P. A. (1998),** "A unified approach to the assembly condition of epicyclic gears", Trans. ASME, J. of Mechanical Design, v.120, pp 448-452.
16. **Norton, R. L. (2020),** Design of machinery: an introduction to the synthesis and analysis of mechanisms and machines,
17. **Levai, Z. (1968),** "Structure and Analysis of Planetary Gear Trains.", Journal of Mechanisms, v.3, pp 131-148.
18. **ANSI/AGMA 2001-D04 (2004),** Fundamental Rating Factors and Calculation Methods for Involute Spur and Helical Gear Teeth, American Gear Manufacturers Association, Virginia.

CANCELLATION OF SINGULARITIES OF RRRRP PLANAR PARALLEL ROBOTS

Mustafa ÖZDEMİR, *mustafa.ozdemir@marmara.edu.tr* Department of Mechanical Engineering, Faculty of Engineering, Marmara University, Recep Tayyip Erdoğan Campus, 34854 Maltepe, İstanbul, Türkiye, ORCID iD: https://orcid.org/0000-0002-4981-9573

Sinan Yalçın ÖNAL, *sinanonal@marun.edu.tr* Department of Mechanical Engineering (English), Institute of Pure and Applied Sciences, Marmara University, Göztepe Campus, 34722 Kadıköy, İstanbul, Türkiye, ORCID iD: https://orcid.org/0000-0002-1646-0912

Corresponding author: Mustafa ÖZDEMİR, Tel.: +90 216 777 3741

ABSTRACT

Parallel robots have many advantages compared to their conventional serial counterparts such as high accuracy and precision, high rigidity, low energy consumption and high payload carrying capacity. Their major disadvantage, however, is the existence of Type II singularities within the workspace. When approaching to these singularities, the magnitudes of the Lagrange multipliers and of the actuator forces and/or torques go to infinity, and hence controllability of the robot is lost. This paper studies conditions for cancellation of Type II singularities of the RRRRP-type planar parallel robot from its dynamic model. The RRRRP robot belongs to the five-bar parallel robot family.

Keywords: Parallel robot, Planar parallel robot, Singularity, Singularity cancellation

1. INTRODUCTION

The biggest disadvantage of parallel robots, which have many advantages such as high accuracy and precision, high rigidity, low energy consumption and high load-carrying capacity [Merlet, 2006], is the existence of “Type II singularities” inside their workspace [Gosselin and Angeles, 1990]. The magnitudes of the Lagrange multipliers and of the actuator forces and/or torques tend to infinity when approaching to these singularities, which are not encountered in conventional serial robots and arise due to the loop-closure constraints. As a solution to this problem, it was proposed in the literature [Ider, 2005; Jui and Sun, 2005; Briot and Arakelian, 2008] to plan the velocity and acceleration trajectories in a way to ensure that the equations of

motion are consistent at the singular configuration to be passed through. Later, Özdemir [2017] proved that maintaining the consistency of the dynamic model at the singularity does not guarantee alone the boundedness of the Lagrange multipliers and of the actuator forces and/or torques and developed a complete singularity removal theory for parallel robots by deriving the additional necessary conditions in this regard. This paper contributes to the literature by applying this theory to RRRRP planar parallel robots, where R and P stand for the revolute and prismatic joints, respectively.

The RRRRP-type planar parallel robot consists of a five-bar mechanism with two degrees of freedom. Two-degree-of-freedom planar closed-loop mechanisms have emerged as a prominent class of parallel robots that are used to generate desired planar coupler curves [Gao et al., 1998]. The two-degree-of-freedom mechanism with the minimum number of links that can be achieved using only lower kinematic pairs is the five-bar mechanism [Tanık and Söylemez, 2006].

Two-degree-of-freedom planar parallel mechanisms are used in many different areas, including (but not limited to) pick-and-place operations [Li-xin and Yong-gang, 2014; Bourbonnais et al., 2015], medical robotics [Lessard et al., 2007; Szep et al., 2009], and agricultural transplanting [Rahul et al., 2019; Zhao et al., 2020]. The previous studies on these mechanisms can be classified according to their subjects as follows:

a) Workspace [Feng et al., 1996; Cervantes-Sánchez and Rendón-Sánchez, 1999]

b) Mechatronic [Giberti et al., 2013] and concurrent [Cervantes-Culebro et al., 2017; 2021] design

c) Kinematic [Alici, 2002; López et al., 2021] and dynamic [Mermoud, 2000; Qi et al., 2012; Wu et al., 2013] analyzes

d) Uncertainties and clearances [Le et al., 2013; Lara-Molina et al., 2018a; Quintero et al., 2019]

e) Calibration [Joubair et al., 2013; Schütz et al., 2013]

f) Optimization [Liu et al., 2006a; 2006b; 2006c; 2007; Villarreal-Cervantes et al., 2010; Jin et al., 2015; Wang et al., 2019; Vezvari et al., 2021]

g) Singularities [Alıcı, 2000; Cervantes-Sánchez et al., 2000; Liu et al., 2006d; Macho et al., 2008; Özdemir, 2019]

h) Joint flexibility [Lara-Molina et al., 2018b]

2. MATHEMATICAL MODEL OF THE ROBOT

The RRRRP planar parallel robot is illustrated in Figure 1. The revolute joint variables θ_1, θ_2, θ_4, and the constant angular parameter α_3 of the robot are defined in the figure. The vector of joint variables is

$$\mathbf{q} = \begin{bmatrix} \theta_1 & \theta_2 & s_3 & \theta_4 \end{bmatrix}^{\mathrm{T}} \tag{1}$$

where the superscript T denotes the transpose, and the prismatic joint variable is defined as $s_3 = |CD|$. The base revolute joint and the prismatic joint are actuated. Therefore, the vectors of active and passive joint variables are, respectively,

$$\mathbf{q}^{\mathrm{a}} = \begin{bmatrix} \theta_1 & s_3 \end{bmatrix}^{\mathrm{T}} \tag{2}$$

$$\mathbf{q}^{\mathrm{p}} = \begin{bmatrix} \theta_2 & \theta_4 \end{bmatrix}^{\mathrm{T}} \tag{3}$$

The origin of the fixed Cartesian coordinate system xy is located at point A. The symbols used to represent the constant link lengths of the mechanism are explained in Table 1.

The complex loop-closure equation can be written by using the Euler formula as follows:

$$a_1 e^{i\theta_1} + a_2 e^{i\theta_2} = a_0 + s_3 e^{i\alpha_3} + a_4 e^{i\theta_4} \tag{4}$$

where i is the unit imaginary number; that is, $i = \sqrt{-1}$.

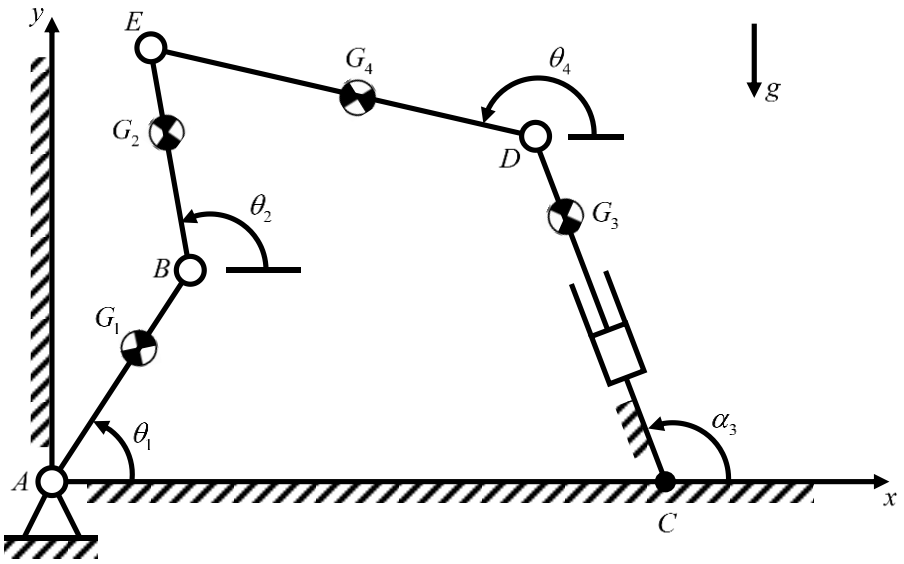


Figure 1. RRRRP Planar Parallel Robot.

Table 1. Symbols used for denoting the constant link lengths of the robot.

Symbol	Definition
a_0	$\lvert AC \rvert$
a_1	$\lvert AB \rvert$
a_2	$\lvert BE \rvert$
a_4	$\lvert DE \rvert$

Complex equation (4) can be separated into its real and imaginary parts as follows:

$$a_1 \cos(\theta_1) + a_2 \cos(\theta_2) = a_0 + s_3 \cos(\alpha_3) + a_4 \cos(\theta_4) \tag{5}$$

$$a_1 \sin(\theta_1) + a_2 \sin(\theta_2) = s_3 \sin(\alpha_3) + a_4 \sin(\theta_4) \tag{6}$$

By differentiating equation (4) with respect to time t, we obtain

$$i\dot{\theta}_1 a_1 e^{i\theta_1} + i\dot{\theta}_2 a_2 e^{i\theta_2} = \dot{s}_3 e^{i\alpha_3} + i\dot{\theta}_4 a_4 e^{i\theta_4} \tag{7}$$

Here and in the rest of the paper, the overdot denotes the time derivative. The real and imaginary parts of complex equation (7) can be written separately as

$$-\dot{\theta}_1 a_1 \sin(\theta_1) - \dot{\theta}_2 a_2 \sin(\theta_2) = \dot{s}_3 \cos(\alpha_3) - \dot{\theta}_4 a_4 \sin(\theta_4) \tag{8}$$

$$\dot{\theta}_1 a_1 \cos(\theta_1) + \dot{\theta}_2 a_2 \cos(\theta_2) = \dot{s}_3 \sin(\alpha_3) + \dot{\theta}_4 a_4 \cos(\theta_4) \tag{9}$$

Equations (8) and (9) can be expressed in the following matrix-vector form:

$$\mathbf{J}\dot{\mathbf{q}} = \begin{bmatrix} 0 \\ 0 \end{bmatrix} \tag{10}$$

where $\mathbf{J}$ is the Jacobian of the scalar loop-closure equations, which is given by

$$\mathbf{J} = \begin{bmatrix} -a_1 \sin(\theta_1) & -a_2 \sin(\theta_2) & -\cos(\alpha_3) & a_4 \sin(\theta_4) \\ a_1 \cos(\theta_1) & a_2 \cos(\theta_2) & -\sin(\alpha_3) & -a_4 \cos(\theta_4) \end{bmatrix} \tag{11}$$

In terms of the time derivatives of the vectors that are defined by equations (2) and (3), equation (10) can be rewritten as

$$\mathbf{J}^{\mathrm{a}}\dot{\mathbf{q}}^{\mathrm{a}} + \mathbf{J}^{\mathrm{p}}\dot{\mathbf{q}}^{\mathrm{p}} = \begin{bmatrix} 0 \\ 0 \end{bmatrix} \tag{12}$$

where the submatrices of the $\mathbf{J}$ matrix that appear in the above equation are as follows:

$$\mathbf{J}^{\mathrm{a}} = \begin{bmatrix} -a_1 \sin(\theta_1) & -\cos(\alpha_3) \\ a_1 \cos(\theta_1) & -\sin(\alpha_3) \end{bmatrix} \tag{13}$$

$$\mathbf{J}^{\mathrm{p}} = \begin{bmatrix} -a_2 \sin(\theta_2) & a_4 \sin(\theta_4) \\ a_2 \cos(\theta_2) & -a_4 \cos(\theta_4) \end{bmatrix} \tag{14}$$

Using the approach presented by Ider [2005], and recalling that the link lengths cannot be zero, Type II singularities of the robot can be determined from

$$\Delta = \det\left(\mathbf{J}^{\mathrm{p}}\right) = a_2 a_4 \sin(\theta_2 - \theta_4) = 0 \tag{15}$$

as the configurations where $\theta_4 = \theta_2 \pm n\pi$ for $n = 0, 1, 2, 3, \ldots$. It is worth noting that at these configurations, $\mathrm{rank}\left(\mathbf{J}^{\mathrm{p}}\right) = 1$. In other words, the $\mathbf{J}^{\mathrm{p}}$ matrix of the robot is rank-deficient by one at its Type II singular configurations.

In the mechanism, link 0 is the fixed link, and links 1, 2, 3 and 4 are the moving links. The moving link j ($j = 1, 2, 3, 4$) has mass m_j and mass center G_j. The mass center distance of each moving link is given in Table 2. The centroidal mass moments of inertia of links 1, 2 and 4 that experience rotation are I_1, I_2 and I_4, respectively. The gravitational acceleration g is supposed to act along the negative y-axis. By choosing the vector of joint variables to be the vector of generalized coordinates and using Lagrange's equations with Lagrange multipliers [Greenwood, 2003], the equations of motion of the robot can be obtained as

$$M_{11}\ddot{\theta}_1 + M_{12}\ddot{\theta}_2 + N_1 = T_1 - a_1 \sin(\theta_1)\lambda_1 + a_1 \cos(\theta_1)\lambda_2 \tag{16}$$

$$M_{21}\ddot{\theta}_1 + M_{22}\ddot{\theta}_2 + N_2 = -a_2 \sin(\theta_2)\lambda_1 + a_2 \cos(\theta_2)\lambda_2 \tag{17}$$

$$M_{33}\ddot{s}_3 + M_{34}\ddot{\theta}_4 + N_3 = F_3 - \cos(\alpha_3)\lambda_1 - \sin(\alpha_3)\lambda_2 \tag{18}$$

$$M_{43}\ddot{s}_3 + M_{44}\ddot{\theta}_4 + N_4 = a_4 \sin(\theta_4)\lambda_1 - a_4 \cos(\theta_4)\lambda_2 \tag{19}$$

where T_1 is the motor torque actuating the revolute joint at A, F_3 is the linear actuator force at the prismatic joint, and λ_1 and λ_2 are the Lagrange multipliers. Note that while deriving this model, we assumed that there are no external nonconservative forces and moments other than T_1 and F_3. The expressions for M_{11}, M_{12}, M_{21}, M_{22}, M_{33}, M_{34}, M_{43}, M_{44}, N_1, N_2, N_3 and N_4 are given by equations (20) to (29). The derivation details of the equations of motion of the robot are presented in the Appendix.

Table 2. Symbols used for denoting the mass center distances of the moving links.

Symbol	Definition
r_1	$\lvert AG_1 \rvert$
r_2	$\lvert BG_2 \rvert$
r_3	$\lvert DG_3 \rvert$
r_4	$\lvert DG_4 \rvert$

$$M_{11} = m_1 r_1^2 + I_1 + m_2 a_1^2 \tag{20}$$

$$M_{12} = M_{21} = m_2 r_2 a_1 \cos\left(\theta_1 - \theta_2\right) \tag{21}$$

$$M_{22} = m_2 r_2^2 + I_2 \tag{22}$$

$$M_{33} = m_3 + m_4 \tag{23}$$

$$M_{34} = M_{43} = m_4 r_4 \sin\left(\alpha_3 - \theta_4\right) \tag{24}$$

$$M_{44} = m_4 r_4^2 + I_4 \tag{25}$$

$$N_1 = m_2 r_2 a_1 \dot{\theta}_2^2 \sin\left(\theta_1 - \theta_2\right) + \left(m_1 r_1 + m_2 a_1\right) g \cos\left(\theta_1\right) \tag{26}$$

$$N_2 = -m_2 r_2 a_1 \dot{\theta}_1^2 \sin\left(\theta_1 - \theta_2\right) + m_2 r_2 g \cos\left(\theta_2\right) \tag{27}$$

$$N_3 = -m_4 r_4 \dot{\theta}_4^2 \cos\left(\alpha_3 - \theta_4\right) + \left(m_3 + m_4\right) g \sin\left(\alpha_3\right) \tag{28}$$

$$N_4 = m_4 r_4 g \cos\left(\theta_4\right) \tag{29}$$

3. CONDITIONS FOR CANCELLATION OF SINGULARITIES OF THE ROBOT FROM THE LAGRANGE MULTIPLIERS, FROM THE MOTOR TORQUE AND FROM THE LINEAR ACTUATOR FORCE

Let point $E\left(x_E, y_E\right)$ be the endpoint of the robot. So, the vector of task variables is $\mathbf{x} = \begin{bmatrix} x_E & y_E \end{bmatrix}^{\mathrm{T}}$. Given a task described by $\mathbf{x} = \mathbf{x}(t)$ such that no inverse kinematic singularities occur for that task, the required $\mathbf{q}$ can be computed by simultaneously solving the task equations and the loop-closure equations. To determine the required motor torque and the

required linear actuator force, a two-step procedure can be employed (see, e.g., [Özgören, 2001]). In the first step, equations (17) and (19) are solved for the Lagrange multipliers as

$$\lambda_1 = -\frac{a_4 \cos(\theta_4)\left(M_{21}\ddot{\theta}_1 + M_{22}\ddot{\theta}_2 + N_2\right) + a_2 \cos(\theta_2)\left(M_{43}\ddot{s}_3 + M_{44}\ddot{\theta}_4 + N_4\right)}{\Delta} \tag{30}$$

$$\lambda_2 = -\frac{a_4 \sin(\theta_4)\left(M_{21}\ddot{\theta}_1 + M_{22}\ddot{\theta}_2 + N_2\right) + a_2 \sin(\theta_2)\left(M_{43}\ddot{s}_3 + M_{44}\ddot{\theta}_4 + N_4\right)}{\Delta} \tag{31}$$

After that, in the second step, the required motor torque T_1 and the required linear actuator force F_3 are calculated, respectively, from equations (16) and (18) as follows:

$$T_1 = M_{11}\ddot{\theta}_1 + M_{12}\ddot{\theta}_2 + N_1 + a_1 \sin(\theta_1)\lambda_1 - a_1 \cos(\theta_1)\lambda_2 \tag{32}$$

$$F_3 = M_{33}\ddot{s}_3 + M_{34}\ddot{\theta}_4 + N_3 + \cos(\alpha_3)\lambda_1 + \sin(\alpha_3)\lambda_2 \tag{33}$$

As Δ goes to zero; that is, as a Type II singularity is approached, the limits of λ_1 and λ_2, and hence the limits of T_1 and F_3, do not have a finite value unless the quotients on the right-hand sides of equations (30) and (31) are indeterminate of the form 0/0 at that singularity. It follows from this that the condition for consistency of the equations of motion of the RRRRP planar parallel robot at a Type II singular position is

$$M_{43}\ddot{s}_3 + M_{44}\ddot{\theta}_4 + N_4 = \sigma\left(\frac{a_4}{a_2}\right)\left(M_{21}\ddot{\theta}_1 + M_{22}\ddot{\theta}_2 + N_2\right) \tag{34}$$

where

$$\sigma = \begin{cases} -1, & \text{for } n = 0,\ 2,\ 4,\ 6,\ \ldots \\ 1, & \text{for } n = 1,\ 3,\ 5,\ 7,\ \ldots \end{cases} \tag{35}$$

Note that the condition given by equation (34) can be equivalently obtained based on the linear dependence of the equations of motion at the singular positions [Ider, 2005].

As long as equation (34) holds at a Type II singularity, l'Hôpital's Rule can be applied to find the limits of the Lagrange multipliers as that singularity is approached. It follows from l'Hôpital's Rule that the limit of an indeterminate quotient of two functions is equal to the limit of the quotient of their derivatives [Krantz, 2018]. Therefore, the limits of the Lagrange multipliers as a Type II singularity is approached are finite if equation (34) and the following condition are both satisfied at that singularity:

$$\dot{\Delta} \neq 0 \tag{36}$$

The additional condition (36) obeys the general theory developed by Özdemir [2017] for removal of singularities of parallel robots. Interested readers are referred to [Özdemir, 2017; 2019; 2021] for further details on this theory and its application to explore the “high-order singularities” or “hypersingularities” of parallel robots.

4. CONCLUSIONS

This paper contributes to the literature by studying the cancellation of Type II singularities of the RRRRP-type planar parallel robot from the Lagrange multipliers, from the motor torque and from the linear actuator force. This can be achieved if two conditions, namely conditions (34) and (36), hold simultaneously at the singular configuration. Equation (34) gives the condition for consistency of the equations of motion of the robot at the singularity. By substituting equations (21), (22), (24), (25), (27) and (29) into it, we obtain

$$\begin{aligned} m_4 r_4 \sin(\alpha_3 - \theta_4)\ddot{s}_3 + (m_4 r_4^2 + I_4)\ddot{\theta}_4 + m_4 r_4 g \cos(\theta_4) = \sigma\left(\frac{a_4}{a_2}\right)\Big[& m_2 r_2 a_1 \cos(\theta_1 - \theta_2)\ddot{\theta}_1 \\ & + (m_2 r_2^2 + I_2)\ddot{\theta}_2 - m_2 r_2 a_1 \dot{\theta}_1^2 \sin(\theta_1 - \theta_2) \\ & + m_2 r_2 g \cos(\theta_2)\Big] \end{aligned} \tag{37}$$

Differentiating equation (15) with respect to time gives

$$\dot{\Delta} = a_2 a_4 (\dot{\theta}_2 - \dot{\theta}_4)\cos(\theta_2 - \theta_4) \tag{38}$$

Noting that at a Type II singularity,

$$\cos(\theta_2 - \theta_4) = \begin{cases} 1, & \text{for } n = 0,\ 2,\ 4,\ 6,\ \ldots \\ -1, & \text{for } n = 1,\ 3,\ 5,\ 7,\ \ldots \end{cases} \tag{39}$$

condition (36) can be equivalently expressed as

$$\dot{\theta}_4 \neq \dot{\theta}_2 \tag{40}$$

The RRRRP-type planar parallel robot can pass through a Type II singular configuration if equation (37) and condition (40) are satisfied together at that singular configuration. It is worth mentioning that the singularity removal conditions derived in this paper for the RRRRP planar parallel robot obey the general singularity removal theory developed by Özdemir [2017] for parallel robots. The cancellation of Type II singularities of other five-bar planar parallel robots can be studied in a similar manner. For example, interested readers can see Ider [2005] for the “consistency condition” and Özdemir [2019] for high-order singularities of the planar 5R parallel mechanism.

ACKNOWLEDGEMENTS

This paper is based on a part of the Master of Science Thesis of the second author (Sinan Yalçın ÖNAL), which is in preparation in the Department of Mechanical Engineering (English) at Marmara University Institute of Pure and Applied Sciences under the supervision of the first author (Assoc. Prof. Dr. Mustafa ÖZDEMİR).

APPENDIX

Lagrange's equations with Lagrange multipliers [Greenwood, 2003] can be applied to the RRRRP planar parallel robot as follows:

$$\frac{d}{dt}\left(\frac{\partial L}{\partial \dot{q}_j}\right)-\frac{\partial L}{\partial q_j}=Q_j+J_{1j}\lambda_1+J_{2j}\lambda_2,\quad j=1,\,2,\,3,\,4 \tag{41}$$

where L is the Lagrangian of the robot and Q_j is the nonconservative generalized force associated with q_j. Here, q_j is the j th element of the generalized coordinate vector $\mathbf{q}$, $\dot{q}_j$ is the j th element of the generalized velocity vector $\dot{\mathbf{q}}$, and J_{kj} is the element of the matrix $\mathbf{J}$ in the k th row and j th column. The Lagrangian of the robot can be expressed as

$$\begin{aligned}L=&\frac{1}{2}\left(I_1+m_1r_1^{\,2}+m_2a_1^{\,2}\right)\dot{\theta}_1^{\,2}+\frac{1}{2}\left(I_2+m_2r_2^{\,2}\right)\dot{\theta}_2^{\,2}+\frac{1}{2}\left(m_3+m_4\right)\dot{s}_3^{\,2}+\frac{1}{2}\left(I_4+m_4r_4^{\,2}\right)\dot{\theta}_4^{\,2}\\&+m_2a_1r_2\dot{\theta}_1\dot{\theta}_2\cos\left(\theta_1-\theta_2\right)+m_4r_4\dot{s}_3\dot{\theta}_4\sin\left(\alpha_3-\theta_4\right)-\left(m_1r_1+m_2a_1\right)g\sin\left(\theta_1\right)-m_2r_2g\sin\left(\theta_2\right)\\&-\left(m_3\left(s_3-r_3\right)+m_4s_3\right)g\sin\left(\alpha_3\right)-m_4r_4g\sin\left(\theta_4\right)\end{aligned} \tag{42}$$

Taking the necessary derivatives and substituting them into equations (41) gives the dynamic model of the robot in the form of equations (16)-(19) supplemented by equations (20)-(29). Notice that we have $Q_1=T_1$, $Q_3=F_3$, and $Q_2=Q_4=0$ since it is assumed that there are no external nonconservative forces and moments other than T_1 and F_3.

REFERENCES

1. **Merlet, J.-P. (2006),** Parallel Robots, 2nd edition, Springer, Dordrecht, The Netherlands.

2. **Gosselin, C. and Angeles, J. (1990),** "Singularity Analysis of Closed-Loop Kinematic Chains", IEEE Trans. Robot. Autom., Vol.6, No.3, pp 281-290.

3. **Ider, S.K. (2005),** "Inverse Dynamics of Parallel Manipulators in the Presence of Drive Singularities", Mech. Mach. Theory, Vol.40, No.1, pp 33-44.

4. **Jui, C.K.K. and Sun, Q. (2005),** “Path Tracking of Parallel Manipulators in the Presence of Force Singularity”, Trans. ASME, J. Dyn. Sys., Meas., Control, Vol.127, No.4, pp 550-563.

5. **Briot, S. and Arakelian, V. (2008),** “Optimal Force Generation in Parallel Manipulators for Passing through the Singular Positions”, Int. J. Robot. Res., Vol.27, No.8, pp 967-983.

6. **Özdemir, M. (2017),** “Removal of Singularities in the Inverse Dynamics of Parallel Robots”, Mech. Mach. Theory, Vol.107, pp 71-86.

7. **Gao, F., Liu, X. and Gruver, W.A. (1998),** “Performance Evaluation of Two-Degree-of-Freedom Planar Parallel Robots”, Mech. Mach. Theory, Vol.33, No.6, pp 661-668.

8. **Tanık, E. and Söylemez, E. (2006),** “Değişken Stroklu Yedi Uzuvlu Bir Mekanizma Tasarımı”, Makina Tasarım ve İmalat Dergisi, Vol.8, No.2, pp 76-79.

9. **Li-xin, X. and Yong-gang, L. (2014),** “Investigation of Joint Clearance Effects on the Dynamic Performance of a Planar 2-DOF Pick-and-Place Parallel Manipulator”, Robot. Comput.-Integr. Manuf., Vol.30, No.1, pp 62-73.

10. **Bourbonnais, F., Bigras, P. and Bonev, I.A. (2015),** “Minimum-Time Trajectory Planning and Control of a Pick-and-Place Five-Bar Parallel Robot”, IEEE/ASME Trans. Mechatron., Vol.20, No.2, pp 740-749.

11. **Lessard, S., Bigras, P. and Bonev, I.A. (2007),** “A New Medical Parallel Robot and Its Static Balancing Optimization”, Trans. ASME, J. Med. Devices, Vol.1, No.4, pp 272-278.

12. **Szep, C., Stan, S.-D., Csibi, V., Manic, M. and Balan, R. (2009),** “Kinematics, Workspace, Design and Accuracy Analysis of RPRPR Medical Parallel Robot”, Proceedings of the 2nd International Conference on Human System Interaction (HSI 2009), Catania, Italy, May 21-23, 2009, IEEE, pp 75-80.

13. **Rahul, K., Raheman, H. and Paradkar, V. (2019),** “Design and Development of a 5R 2DOF Parallel Robot Arm for Handling Paper Pot Seedlings in a Vegetable Transplanter”, Comput. Electron. Agric., Vol.166, 105014.

14. **Zhao, X., Guo, J., Li, K., Dai, L. and Chen, J. (2020),** “Optimal Design and Experiment of 2-DoF Five-Bar Mechanism for Flower Seedling Transplanting”, Comput. Electron. Agric., Vol.178, 105746.

15. **Feng, G., Xiao-Qiu, Z., Yong-Sheng, Z. and Hong-Rui, W. (1996),** “A Physical Model of the Solution Space and the Atlas of the Reachable Workspace for 2-DOF Parallel Planar Manipulators”, Mech. Mach. Theory, Vol.31, No.2, pp 173-184.

16. **Cervantes-Sánchez, J.J. and Rendón-Sánchez, J.G. (1999),** "A Simplified Approach for Obtaining the Workspace of a Class Of 2-DoF Planar Parallel Manipulators", Mech. Mach. Theory, Vol.34, No.7, pp 1057-1073.

17. **Giberti, H., Cinquemani, S. and Ambrosetti, S. (2013),** "5R 2DoF Parallel Kinematic Manipulator – A Multidisciplinary Test Case in Mechatronics", Mechatronics, Vol.23, No.8, pp 949-959.

18. **Cervantes-Culebro, H., Cruz-Villar, C.A., Martinez Penaloza, M.-G. and Mezura-Montes, E. (2017),** "Constraint-Handling Techniques for the Concurrent Design of a Five-Bar Parallel Robot", IEEE Access, Vol.5, pp 23010-23021.

19. **Cervantes-Culebro, H., Chong-Quero, J.E., Padilla-Garcia, E.A. and Cruz-Villar, C.A. (2021),** "Concurrent Design of a 2 Dof Five-Bar Parallel Robot a Hybrid Design of Rigid and Flexible Links", IEEE Access, Vol.9, pp 17450-17462.

20. **Alici, G. (2002),** "An Inverse Position Analysis of Five-Bar Planar Parallel Manipulators", Robotica, Vol.20, No.2, pp 195-201.

21. **López, E.J., Servín De La Mora-Pulido, D., Servín De La Mora-Pulido, R., Ochoa-Estrella, F.J., Acosta Flores, M. and Luna-Sandoval, G. (2021),** "Modeling in Two Configurations of a 5R 2-DoF Planar Parallel Mechanism and Solution to the Inverse Kinematic Modeling Using Artificial Neural Network", IEEE Access, Vol.9, pp 68583-68594.

22. **Mermoud, O. (2000),** "Dynamics of a Planar Parallel Mechanism: The Equilateral Five Bars Linkage", Dyn. Stab. Syst., Vol.15, No.4, pp 387-399.

23. **Qi, H., Liwen, G. and Jianxin, W. (2012),** "Dynamic Performance Evaluation of a 2-DoF Planar Parallel Mechanism", Int. J. Adv. Robot. Syst., Vol.9, No.6, 250.

24. **Wu, J., Wang, L. and Guan, L. (2013),** "A Study on the Effect of Structure Parameters on the Dynamic Characteristics of a PRRRP Parallel Manipulator", Nonlinear Dyn., Vol.74, No.1-2, pp 227-235.

25. **Le, T.D., Kang, H.-J. and Suh, Y.-S. (2013),** "Chattering-Free Neuro-Sliding Mode Control of 2-DOF Planar Parallel Manipulators", Int. J. Adv. Robot. Syst., Vol.10, No.1, 22.

26. **Lara-Molina, F.A., Koroishi, E.H., Steffen, V. and Martins, L.A. (2018a),** "Kinematic Performance of Planar 5R Symmetrical Parallel Mechanism Subjected to Clearances and Uncertainties", J. Braz. Soc. Mech. Sci. Eng., Vol.40, No.4, 189.

27. **Quintero, H.F., Mejia, L.A. and Diaz-Rodriguez, M. (2019),** "End-Effector Positioning Due to Joint Clearances: A Comparison Among Three Planar 2-DOF Parallel Manipulators", J. Mech. Sci. Technol., Vol.33, No.7, pp 3497-3507.

28. **Joubair, A., Slamani, M. and Bonev, I.A. (2013),** "Kinematic Calibration of a Five-Bar Planar Parallel Robot Using All Working Modes", Robot. Comput.-Integr. Manuf., Vol.29, No.4, pp 15-25.

29. **Schütz, D., Raatz, A. and Hesselbach, J. (2013),** "Adapted Task Configuration of a Reconfigurable Binary Parallel Robot with PRRRP Structure", Robotica, Vol.31, No.2, pp 285-293.

30. **Liu, X.-J., Wang, J. and Pritschow, G. (2006a),** "On the Optimal Kinematic Design of the PRRRP 2-DoF Parallel Mechanism", Mech. Mach. Theory, Vol.41, No.9, pp 1111-1130.

31. **Liu, X.-J., Wang, J. and Pritschow, G. (2006b),** "Performance Atlases and Optimum Design of Planar 5R Symmetrical Parallel Mechanisms", Mech. Mach. Theory, Vol.41, No.2, pp 119-144.

32. **Liu, X.-J., Wang, J. and Zheng, H.-J. (2006c),** "Optimum Design of the 5R Symmetrical Parallel Manipulator with a Surrounded and Good-Condition Workspace", Robot. Auton. Syst., Vol.54, No.3, pp 221-233.

33. **Liu, X.-J., Guan, L. and Wang, J. (2007),** "Kinematics and Closed Optimal Design of a Kind of PRRRP Parallel Manipulator", Trans. ASME, J. Mech. Des., Vol.129, No.5, pp 558-563.

34. **Villarreal-Cervantes, M.G., Cruz-Villar, C.A., Alvarez-Gallegos, J. and Portilla-Flores, E.A. (2010),** "Differential Evolution Techniques for the Structure-Control Design of a Five-Bar Parallel Robot", Eng. Optimiz., Vol.42, No.6, pp 535-565.

35. **Jin, S., Kim, J. and Seo, T. (2015),** "Optimization of a Redundantly Actuated 5R Symmetrical Parallel Mechanism Based on Structural Stiffness", Robotica, Vol.33, No.9, pp 1973-1983.

36. **Wang, L., Zhang, Z., Shao, Z. and Tang, X. (2019),** "Analysis and Optimization of a Novel Planar 5R Parallel Mechanism with Variable Actuation Modes", Robot. Comput.-Integr. Manuf., Vol.56, pp 178-190.

37. **Vezvari, M.R., Nikoobin, A. and Ghoddosian, A. (2021),** "Perfect Torque Compensation of Planar 5R Parallel Robot in Point-to-Point Motions, Optimal Control Approach", Robotica, Vol.39, No.7, pp 1163-1180.

38. **Alıcı, G. (2000),** "Determination of Singularity Contours for Five-Bar Planar Parallel Manipulators", Robotica, Vol.18, No.5, pp 569-575.

39. **Cervantes-Sánchez, J.J., Hernández-Rodríguez, J.C. and Rendón-Sánchez, J.G. (2000),** "On the Workspace, Assembly Configurations and Singularity Curves of the RRRRR-Type Planar Manipulator", Mech. Mach. Theory, Vol.35, No.8, pp 1117-1139.

40. **Liu, X.-J., Wang, J. and Pritschow, G. (2006d),** "Kinematics, Singularity and Workspace of Planar 5R Symmetrical Parallel Mechanisms", Mech. Mach. Theory, Vol.41, No.2, pp 145-169.

41. **Macho, E., Altuzarra, O., Pinto, C. and Hernandez, A. (2008),** "Workspaces Associated to Assembly Modes of the 5R Planar Parallel Manipulator", Robotica, Vol.26, No.3, pp 395-403.

42. **Özdemir, M. (2019),** "High-Order Singularities of 5R Planar Parallel Robots", Robotica, Vol.37, No.2, pp 233-245.

43. **Lara-Molina, F.A., Dumur, D. and Assolari Takano, K. (2018b),** "Multi-Objective Optimal Design of Flexible-Joint Parallel Robot", Eng. Comput., Vol.35, No.8, pp 2775-2801.

44. **Greenwood, D.T. (2003),** Advanced Dynamics, Cambridge University Press, Cambridge.

45. **Özgören, M.K. (2001),** "Motion Control of Constrained Systems Considering Their Actuation-Related Singular Configurations", Proc. IMechE Part I: J. Syst. Control Eng., Vol.215, No.2, pp 113-123.

46. **Krantz, S.G. (2018),** Transition to Analysis with Proof, CRC Press, Taylor & Francis Group, Boca Raton, Florida.

47. **Özdemir, M. (2021),** "Hypersingularities of 3-RRR Planar Parallel Robots", Proc. Ro. Acad., Series A, Vol.22, No.4, pp 353-360.

INVESTIGATING EFFECTS OF POLARIZATION AND DIMENSIONS OF MAGNETIC COUPLING ON TRANSMITED TORQUE BY FINITE ELEMENT ANALYSIS

S. H. POUR RAHMATI KHALEJAN, hamed.pourrahmati@hktm.com.tr Hidropar Hareket Kontrol Teknolojileri Merkezi A.Ş. (HKTM), 41400, Kocaeli, Turkey

ABSTRACT

In this study, a 3-dimentional Finite Element Analysis (FEA) model is developed to investigate of the torque transmission capability of 16 radial magnetic couplings with different polarizations and magnet dimensions (height, thickness, and the gap between two sets of magnets). As theoretical model, Coulomb model is presented. The results show that increasing polarization of the magnet by 20% (from 1.11 to 1.33 T) resulted in 45% increase in the transmitted torque. In addition, 50% increase in the gap size between two sets of the magnets causes 18% decrease in the transmitted torque. On the other hand, when height or thickness of the magnet is increased 50%, the transmitted torque increases 55% and 85% respectively.

Keywords: Magnetic coupling, Finite Element Analysis, Torque transmission, Polarizations

1. INTRODUCTION

A magnetic coupler transmits torque between two rotating parts using a magnetic field rather than a physical contact. Prevent transmission of vibration, axial and radial loads through the drive shaft are the other advantages of magnetic coupling. Radial coupling form with two concentric sets of magnets, which rotate around the same axis. The geometry of each set is ring-shaped and presents periodic radial magnetic polarizations. The torque of magnetic coupling depends on geometrical dimensions of the coupling, the gap between two sets, magnetization characteristics of the magnets, the numbers of poles and the position of the rotors [1-3].

There are studies, which theoretically and experimentally investigate parameters of magnetic couplings;

Ravaud et al. (2009) studied the torque transmitted between tile permanent magnets, which was uniformly magnetized, based on the three-dimensional Coulomb model [4]. Li et al. (2019) computed the pull-out torque of conical permanent magnet coupling based on a multi-section two-dimensional model [5]. In study of Mulyaseputra et al. (2013), magnetic field distribution

of each magnetic element on the first rotor disc with each second rotor disc magnetic element was discussed [6]. Charpentier et al. (2015) calculated mechanical behaviour of ironless permanent magnet couplings by using semi numerical magnetic pole theory method [7] Ose et al. (2011) studied the performance of a magnetic coupler with rectangular permanent magnets. In their study, the influence of permanent magnets' width and number on the mechanical torque was investigated [8]. Mei et al. (2006) calculated the magnetic field. In their study, the main problems of designing magnetic mechanisms was discussed [9]. Chaojun et al. (2014) calculated the electromagnetism characteristics of magnetic coupling such as the distributions of induced current, torque by using the ANSOFT software [10].

In this research, the 3D FEA model is performed to study and compare the torque transmission of the radial magnetic coupling with different dimensions and characteristics of the magnets.

2. MATERIALS AND METHODS

Radial magnetic coupling (Figure 1) includes inner and outer iron rings, each ring carry magnets (in this study, 10 magnets are used for each ring). The arrangement of each ring is the alternating north and south poles of magnets. Due to the barrier, that separates the inner and outer parts, the shaft seals are not required in the magnetic coupling.

16 magnetic couplings with same numbers but different dimensions and magnetic characteristics of magnets are compared and simulated.

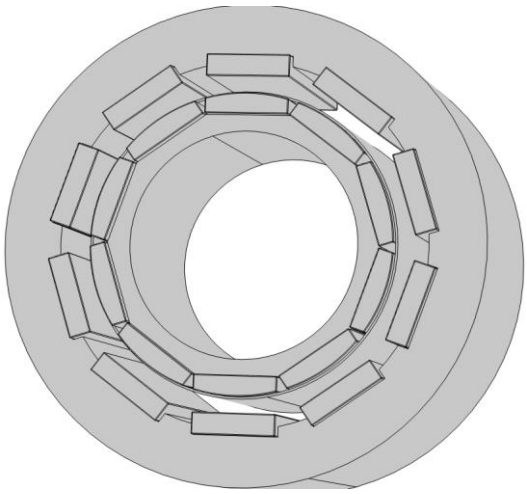


Figure 1. Image of magnetic coupling with inner and outer rings.

2.1 The Analytical model

Based on the Coulomb model of a magnet, FEA for the calculation of transmitted torque was performed between two rotating parts using magnetic field equations. FEA is a popular method

for numerically solving differential equations arising in engineering and mathematical modeling.

Maxwell's equations compute the distribution of the electromagnetic field. The vector potential and the scalar potential formulation can be used to solve Maxwell's equations.

By introducing magnetic vector potential (A), the magnetic flux density and the electric field can be defined as [5]:

$$\mathbf{E} = -\frac{\partial \mathbf{A}}{\partial \mathrm{t}} \tag{1}$$

$$\mathbf{B} = \nabla \times \mathbf{A} \tag{2}$$

With Eq.1 and Eq. 2, Faraday's law and the magnetic flux conservation law can be calculated. In addition, these equations can be written as:

$$\nabla \times \mathbf{E} = -\frac{\partial \mathbf{B}}{\partial \mathrm{t}} \tag{3}$$

$$\nabla \times \mathbf{B} = 0 \tag{4}$$

The magnetic flux conservation can be written as:

$$\mathbf{B} = \mu_0 \mu_r \mathbf{H} + \mathbf{B_r} \tag{5}$$

$$\mathbf{B_r} = |B_r| \frac{\mathbf{e}}{|e|} \tag{6}$$

Where μ_0 is magnetic permeability of free space, μ_r is the ratio of the permeability of a specific medium to the permeability of free space, and Br is flux density.

The equation to be solved is Ampère's law:

$$\nabla \times \mathbf{H} = \mathbf{J} \tag{7}$$

J is illustrate the polarizations of magnet.

In our models, in order to calculate of torque, the following parameters are used:

- $\mathbf{r_1}$, $\mathbf{r_3}$= inner radius of the inner and outer permanent magnet [m]
- $\mathbf{r_2}$, $\mathbf{r_4}$= inner and outer radius of the outer tile permanent magnet [m].
- $\mathbf{z_1}$,$\mathbf{z_3}$= lower axial coordinate of the inner and outer permanent magnet [m].
- $\mathbf{z_2}$,$\mathbf{z_4}$= upper axial coordinate of the inner and outer permanent magnet [m].
- θ_1, θ_3= angular coordinate of the inner magnet [rad].
- θ_2, θ_4= angular coordinate of the outer magnet [rad].
- $\mathbf{J_1}$, $\mathbf{J_2}$= Polarizations of the inner and outer magnets [T].

The coordination of inner and outer magnets are given in Figure 2.

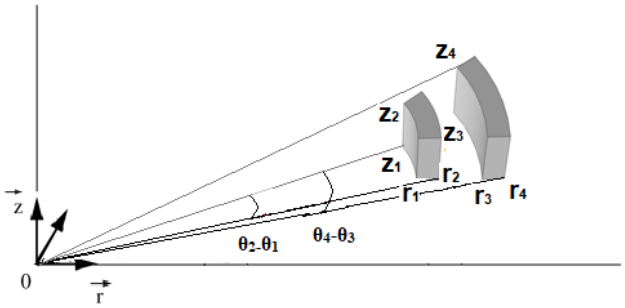


Figure 2. Coordinates of the inner and outer magnets.

Figure 3 is represented radial polarization of the permanent magnet, which two charged planes located on the inner and outer faces of it.

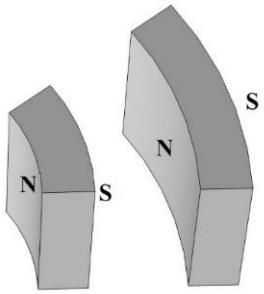


Figure 3. Two tile permanent magnets with radial polarizations.

The transmitted torque (T) on the inner magnet can be calculated by considering the azimuthal field (H_θ (r, θ, z)), which is created by the outer magnet [4];

$$T = -J_2 r_1^2 \int_{z_1}^{z_2}\int_{\theta_2}^{\theta_2} H_\theta(r_1, \theta, z)\, d\theta\, dz + J_2 r_2^2 \int_{z_1}^{z_2}\int_{\theta_2}^{\theta_2} H_\theta(r_2, \theta, z)\, d\theta\, dz \quad (8)$$

Where

$$H_\theta(r, \theta, z) = \frac{J_1}{4\pi\mu_0\mu_r}\{\sum_{i=3}^{4}(-1)^{i+1} \times \int_{z_3}^{z_4}\int_{\theta_3}^{\theta_4} \frac{r_i^2 \sin\theta\, d\theta\, dz}{(r^2 + r_i^2 + 2rr_i\cos\theta + z^2)^{\frac{3}{2}}}\} \quad (9)$$

Note that the operator $\sum_{i=3}^{4}(-1)^{i+1}$ changes sign of the azimuthal field.

By considering Equation 9 in Equation 8, the transmitted torque is:

$$T = -\frac{J_1 J_2}{4\pi\mu_0\mu_r}\sum_{i,k,m=1}^{2}\sum_{j,l=3}^{4}(-1)^{i+j+k+l+m}\, A + \frac{J_1 J_2}{4\pi\mu_0\mu_r}\sum_{i,k,m=1}^{2}\sum_{j,l=3}^{4}(-1)^{i+j+k+l+m}\, B \quad (10)$$

With

$$A = -\sqrt{a_{ijkl}}\,\mathbf{E}\,[\Phi, m] \quad \text{and} \quad \left(\Phi = \frac{\theta_m - \theta_n}{2}\ ,\ m = \frac{-4r_i r_j}{a_{ijkl}}\right) \tag{11}$$

$$B = (z_l - z_k)\int_{\theta_3}^{\theta_4} \log\left(\sqrt{b_{ijkl} - 2r_i r_j \cos(\theta_m - \theta)} - (z_l - z_k)\right) d\theta \tag{12}$$

where

$$\mathbf{E}\,[\Phi, m] = \int_0^{\Phi} \sqrt{1 - m\sin(\theta)^2}\ d\theta \tag{13}$$

and

$$a_{ijkl} = (z_k - z_l)^2 + (r_i - r_j)^2 \tag{14}$$

$$b_{ijkl} = (z_k - z_l)^2 + r_i^2 + r_j^2 \tag{15}$$

2.2. Methods

For the calculation of torque, 16 types of magnetic couplings with different geometries and magnetic properties were selected. All cases have 10 number of magnetics in each set with these geometries:

$\mathbf{r_2}$-$\mathbf{r_1}$=$\mathbf{R_1}$, $\mathbf{r_4}$-$\mathbf{r_3}$=$\mathbf{R_2}$ and $\mathbf{r_3}$-$\mathbf{r_2}$ = gap between two sets
$\mathbf{z_2}$-$\mathbf{z_1}$=$\mathbf{Z_1}$, $\mathbf{z_4}$-$\mathbf{z_3}$=$\mathbf{Z_2}$

Magnets geometry and characteristics belong to each coupling are same (Figure 4), then:

$\mathbf{R_1}$=$\mathbf{R_2}$=$\mathbf{R}$
$\mathbf{Z_1}$=$\mathbf{Z_2}$=$\mathbf{Z}$
θ_3- θ_1= θ_4- θ_2=0
$\mathbf{J_1}$=$\mathbf{J_2}$=$\mathbf{J}$



Figure 4. The geometry of magnetic coupling.

FEA for the calculation of transmitted torque was performed between two rotating parts using Comsol program via these steps:

- Using form assembly, the geometry is finalized.
- An identity pair is created between the inner and outer rotors.

- Magnetic flux conservation is applied everywhere.
- Force and torque are computed via force calculation features.
- Continuity is applied at the identity pair.

In summary, geometry dimensions, boundary conditions and magnet properties of each magnet of couplers as data were adjusted, then model implemented in comsol.

3. RESULTS AND DISCUSIONS

In this section, in order to calculate of transmitted torque, 16 magnetic couplings with different thicknesses, heights, gaps and polarizations are analysed and compared. The results are presented in Table 1.

Table 1. Calculations of maximum torque (T_{max}) for different couplings.

Number of Magnetic coupling	**R** (mm)	**Z** (mm)	Gap (mm)	**J** (T)	$\mathbf{T_{max}}$ (N.m)
1	5	50	4	1.11	17
2	5	50	4	1.33	25
3	5	50	6	1.11	14.5
4	5	50	6	1.33	21
5	5	75	4	1.11	27
6	5	75	4	1.33	39
7	5	75	6	1.11	22.5
8	5	75	6	1.33	32.5
9	7.5	50	4	1.11	32
10	7.5	50	4	1.33	46
11	7.5	50	6	1.11	27
12	7.5	50	6	1.33	39
13	7.5	75	4	1.11	51
14	7.5	75	4	1.33	72.5
15	7.5	75	6	1.11	42.5
16	7.5	75	6	1.33	60.5

Table 1 indicates the torque results for different couplings, where each coupling has 2 sets of 10 magnets with different geometries (thicknesses, heights and gaps) and characteristics (polarizations) of magnets. The range of thickness and height of magnets is from 5 to 7.5 mm and 50 to 75 mm respectively. In addition, the range of the gap between two sets and the polarization of couplings are 4 to 6 mm and 1.11 to 1.33 T respectively.

3.1. Effects of air gap and polarization

For investigating the gap and polarization effects of magnetic couplings on T_{max}, data from Table 1 can be arranged as Table 2:

Table 2. Data Arrange by thickness and height with different Gap and polarizations.

Group	**R** (mm)	**Z** (mm)	**T_{max}** (N.m) (Gap= 4mm **J**= 1.11 T)	**T_{max}** (N.m) (Gap= 6mm **J**= 1.11 T)	**T_{max}** (N.m) (Gap= 4mm **J**= 1.33 T)	**T_{max}** (N.m) (Gap= 6mm **J**= 1.33 T)
A	5	50	17	14.5	25	21
B	5	75	27	22.5	39	32.5
C	7.5	50	32	27	46	39
D	7.5	75	51	42.5	72.5	60.5

As seen in Table 2, each group of couplings have own thickness and height. The transmitted torque decreases as the gap between two sets of magnets increases. In addition, by increasing the polarization of magnets, the torque is increased. Figure 5 shows the effects of gap on maximum transmitted torque for groups with different polarizations.

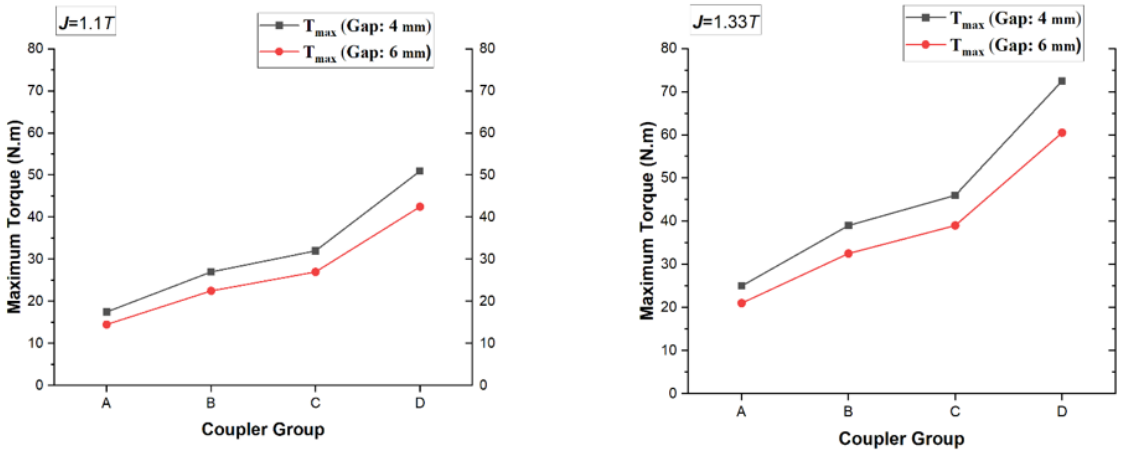


Figure 5. Effects of the gap on maximum transmitted torque for group of couplings with different polarizations; left: J=1.11 T, right J=3.33 T.

As shown in Figure 5, increasing the gap in each group with its own R and Z decreases the maximum torque in two scenarios of polarization. By extending the gap from 4 to 6 mm in couplings A, B, C, and D with 1.11 T polarization, the maximum torque decreases from 17 to 14.5, 27 to 22.5, 32 to 27, and 51 to 42.5 N.m, respectively. Furthermore, in couplings A, B, C, and D with 1.33 T polarization, increasing the distance from 4 to 6 mm decreases the maximum torque from 25 to 21, 39 to 32.5, 46 to 39, and 72.5 to 60.5 N.m, respectively. One can note that increasing 50% in gap size causes about an 18% decrease in transmitted torque.

Figure 6 shows the effects of magnet's polarization on maximum transmitted torque for groups with different gaps.

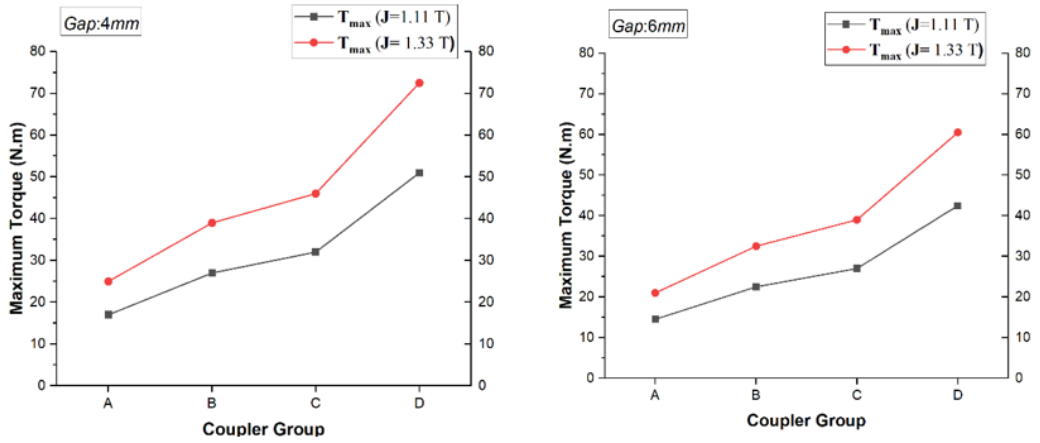


Figure 6. Effects of polarizations on maximum transmitted torque for group of couplings with different gaps; left: gap=4 mm, right: gap=6mm.

As shown in Figure 6, the maximum torque increases with the increase in polarization of the magnet in each group with its own R and Z. In couplings A, B, C, and D with a gap of 4 mm, by increasing polarization from 1.11 to 1.33 T, the maximum torque decreases from 17 to 25, 27 to 39, 32 to 46, and 51 to 72.5 N.m, respectively. In addition, in couplings A, B, C, and D with a gap of 6 mm, by increasing polarization from 1.1 to 1.33 T, the maximum torque increased from 14.5 to 21, 22.5 to 32.5, 27 to 39, and 42.5 to 60.5 N.m, respectively. By increasing the polarization of the magnet from 1.11 to 1.33 T, the transmitted torque increases by about 45%.

3-2- Effects of magnet's height (Z) and thickness (R)

In order to investigate the effect of height and thickness of magnets on the maximum torque, Table 1 can be arranged as Table 3, where each group has its own gap and polarizations with different thicknesses and heights:

Table 3. Data Arrange by gap and polarizations with different height and thicknesses.

Group	**Gap** (mm)	**J** (T)	$\mathbf{T}_{max}$ (N.m) (**R**= 5mm **Z**= 50mm)	$\mathbf{T}_{max}$ (N.m) (**R**= 5mm **Z**= 75mm)	$\mathbf{T}_{max}$ (N.m) (**R**=7.5 **Z=** 50mm)	$\mathbf{T}_{max}$ (N.m) (**R**= 7.5mm **Z**= 75 T)
E	4	1.11	17	27	32	51
F	4	1.33	25	39	46	72.5
G	6	1.11	14.5	22.5	27	42.5
H	6	1.33	21	32.5	39	60.5

As seen in Table 3, by increasing height (Z) and thickness (R) of magnet, the transmitted torque increases.

Figure 7 shows the effects of magnet's height on maximum transmitted torque for these groups with different thicknesses.

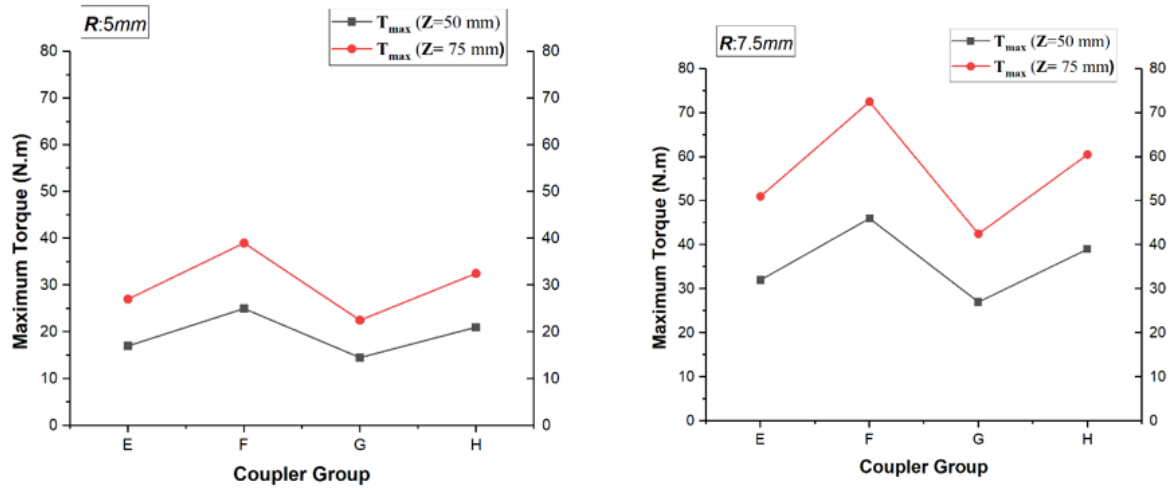


Figure 7. Effects of height on maximum transmitted torque for group of couplings with different thicknesses; left: R= 5 mm, right R= 7.5 mm.

Figure 7 indicates that the maximum transmitted torque increases with the height of magnet in each group with its own gap and polarization. In couplings E, F, G and H with a thickness of 5 mm, by increasing height from 50 to 75 mm, the maximum torque increases from 17 to 32, 25 to 46, 14.5 to 27 and 21 to 39 N.m respectively. In addition, in couplings E,F,G and H with height of 7.5 mm, by increasing height from 50 to 75 mm, the maximum torque increase from 32 to 51, 46 to 72.5, 27 to 42.5 and 39 to 60.5 N.m respectively.

By increasing 50% height of magnet, the transmitted torque increases by about 55% in all cases.

As shown in Figure 8, the maximum transmitted torque increases by the increase of the magnet's thickness in each group with its own gap and polarization. The maximum torque increased from 17 to 27, 25 to 39, 14.5 to 22.5, and 21 to 32.5 N.m as the thickness increased from 5 to 7.5 mm. In addition, in couplings E, F, G, and H with a height of 75 mm, by increasing the thickness from 5 to 7.5 mm, the maximum torque increases from 27 to 51, 39 to 72.5, 22.5 to 42.5, and 32.5 to 60.5 N.m respectively.

In these groups, by increasing the magnet height by 50%, the transmitted torque increases by about 85% in all cases.

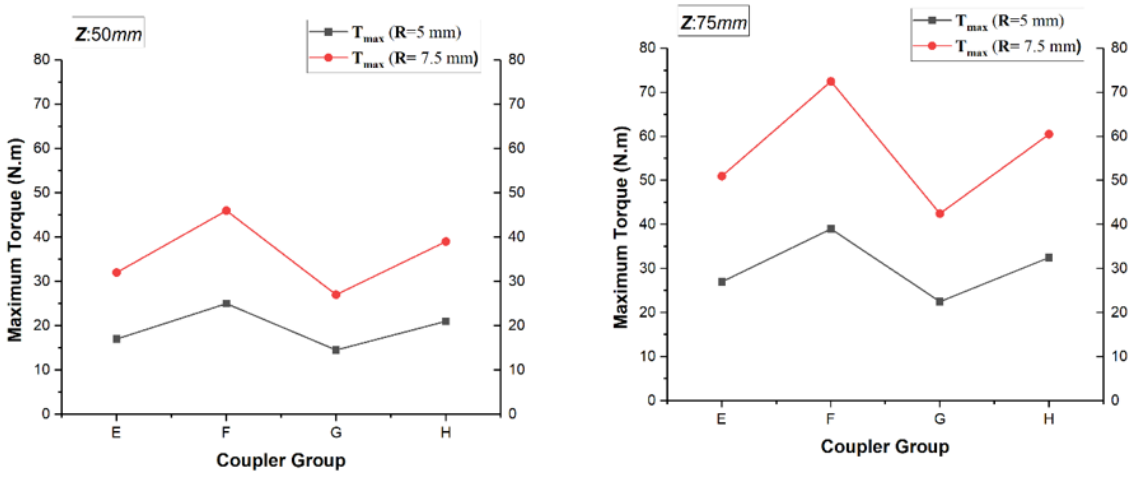


Figure 8. Effects of thickness on maximum transmitted torque for group of couplings with different height; left: Z= 50 mm, right Z= 75 mm.

Increasing 50% of height is more efficient than increasing 50% of thickness because increasing height has 30% more effect than increasing thickness.

4. CONCLUSIONS

In this work, analysis of the torque transmission of the radial magnetic coupling with different dimensions and magnetic characteristics has been performed by using the 3D FEA model.

The main results of this study are summarized as below:

- The transmitted torque decreases as the gap between two sets of magnets increases.
- A 50% increase in the gap size between two sets of magnets results in an 18% decrease in transmitted torque.
- The torque is increased by increasing the polarization of magnets.
- The transmitted torque is increased by approximately 45% by altering the polarization of the magnet from 1.11 to 1.33 T.
- The transmitted torque increases as the magnet's height (Z) and thickness (R) increase.

- Increasing the magnet's thickness by 50%, increases the transmitted torque by around 55% in all cases.
- Increasing the height of the magnet by 50%, increases the transmitted torque by about 85% in all cases.
- To increase transmitted torque, it is better to increase height of magnets instead of its thickness, because increasing height has 30% more effective than increasing thickness.

In magnetic coupling, the geometrical dimensions and magnet characteristics play important roles in determining the transmitted torque value. To find efficient torque, different combinations (thickness, height, gap and polarization) have been used in this study.

ACKNOWLEDGEMENTS

I would like to thank Assoc Prof. Evren Samur, Mr. Tolga Cankurt, Mr. Ömer Faruk Uysal and Ms. Ayça Muştu, for their help in this study and for their motivation and support. I feel myself lucky to have such an opportunity to work with them.

In addition, I would like to acknowledge the support provided by the research and development center of Hidropar Hareket Kontrol Teknolojileri Merkezi (HKTM), for the financial support of this project.

REFERENCES

[1] Chueng G. (2005), Permanent magnets applied to magnetic coupling, *World pump*, no 468, pp. 19.

[2] W. Y. Lin, L. P. Kuan, W. Jun and Han, D. .(2013), Near-optimal design and 3-D finite element analysis of multiple sets of radial magnetic couplings, IEEE Trans. Magn., vol. 44, no. 12, pp. 4747–4753.

[3] L.Thierry, and S.Mezani, (2012). Simple Analytical Expres sions for the Force and Torque of Axial Magnetic Couplings. *IEEE Transactions on Energy Conversion.*

[4] Ravaud, R., Lemarquand, G., Lemarquand, V. and Depollier, C. (2009). Torque in permanent magnet couplings: Comparison of uniform and radial magnetization. *Journal of applied physics*, 105(5), 053904.

[5] Li, Y., Hu, Y., Song, B., Mao, Z. and Tian, W. (2019). Performance analysis of conical permanent magnet couplings for underwater propulsion. *Journal of Marine Science and Engineering,* 7(6), 187.

[6] Mulyaseputra, P. S., Wijaya, F. D. and Hadi, S. P. (2013). Magnetic field distribution simulation on two permanent magnet rotor discs with twelve pole pairs. In 2013 3rd International Conference on Instrumentation, Communications, *Information Technology and Biomedical Engineering* .(pp. 178-183). IEEE.

[7] Charpentier, J. F. and Lemarquand, G. (2001). Calculation of ironless permanent magnet couplings using semi-numerical magnetic pole theory method. *COMPEL-The international journal for computation and mathematics in electrical and electronic engineering.*

[8] Ose, B., Pugachov, V., Orlova, S. and Vanags, J. (2011). The influence of permanent magnets' width and number on the mechanical torque of a magnetic coupler with rectangular permanent magnets. *IEEE International Symposium on Industrial Electronics* (pp. 761-765). IEEE.

[9] Mei, S., Zhang, Z. and Xiao, R. (2006). Methods for Calculating the Transmission Torque of Magnetic Transmission Mechanisms. *In International Conference on Programming Languages for Manufacturing* (pp. 631-636). Springer, Boston, MA.

[10] Yang, C. J., Zhou, Y. H., Chen, X. P., Kong, L. Y. and Du, Y. (2014). Electromagnetic properties analysis of field-modulated asynchronous magnetic couplings. *In Applied Mechanics and Materials* (Vol. 535, pp. 192-197). Trans Tech Publications Ltd.

INVESTIGATION OF PERMANENT MAGNET SYNCHRONOUS MOTORS WITH THREE DIFFERENT SLOT-POLE COMBINATIONS FOR SCOOTER APPLICATION

Hayatullah NORY,*hayatullah.nory@voltmotor.com.tr* Volt Electric Motor, 35735, İzmir, Turkey

Serhat AKŞUN, *serhat.aksun@voltmotor.com.tr* Volt Electric Motor, 35735, İzmir, Turkey

Cansu AKSOY, *cansu.aksoy@voltmotor.com.tr* Volt Electric Motor, 35735, İzmir, Turkey

Salih ÇELİK, *salih.celik@voltmotor.com.tr* Volt Electric Motor, 35735, İzmir, Turkey

ABSTRACT

In this paper, analysis of three permanent magnet synchronous motors (PMSM) has been carried out using the Simcenter Speed program, which is based on the finite element method (FEM). This motor has 500W shaft power, 9.1Nm shaft torque and 525 rpm to be used in electric scooters. Noiseless, vibration-free, smooth and efficient operation are the forefront requirements for scooters, for this reason, three different combinations of stator slot-rotor poles (36-40, 36-38 and 36-34) have been tried in this paper. The results obtained by numerical calculation and finite element method (FEM) were compared. Comparison results are given in the next sections in order.

Keywords: Design, Analysis, Simcenter Speed, BPM, PMSM, PM, Outer rotor, Hub Motor, FEM, Analytic calculation, Back EMF, Slot, Pole

INTRODUCTION

Electric motors are one of the inevitable and indispensable parts of our lives. Different sizes are used for different purposes. For example, it is used in household appliances, such as refrigerators, washing machines, dishwashers, cooker hoods, fans, dryers, and in industry, machines such as automation, CNC machine, saw, scissors and lathe. The use of electric motors in electric vehicles, which is the most widespread and frequently used, is rapidly gaining popularity. To give an example for this situation, PMSM motors are rapidly gaining use in automobiles, mopeds, electric motorcycles, electric bicycles, electric buses and mini electric vehicles such as scooters. In this study, the design and analysis of the scooter motor with 500W and 9.1Nm and 14A and 36Vdc values were carried out. By law and for safety reasons,

scooter vehicles should not exceed 25km-h speed [Directing, 2021], therefore, the scooter motor was designed at 525 rpm rated speed. The designed motor operates in the constant torque region. There is no field weakening on the driver's side. There are many reasons why scooter vehicles are so popular. For example, since it uses electrical energy, it does not harm nature as it does not produce harmful gases, it prevents the use of vehicles such as automobiles for short distances, and it enables terrorists to visit many places in a short time. It causes a decrease in traffic accidents and traffic density. For this purpose, it is possible to design the electric PMSM motor with inner and outer rotors (Hub Motor). In order to minimize the weight of the scooter vehicle in order not to cover much space, to avoid extra costs and to prevent damage, it was considered to be placed inside the wheel by designing with an outer rotor. Factors such as the noiseless and vibration-free operation of the motor are important in such vehicles. For this reason, care has been taken to reduce these factors and at the same time not increase the cost during the design and analysis process. Slot-pole combination is one of the most important issues for harmonic, cogging torque and torque ripple, for this reason, three different combinations were tried. The results of all of them were obtained and compared among themselves. Analytical calculations were performed for the relevant motor. For this process, the flow diagram given in Figure 1. was followed. [Duan 2010].

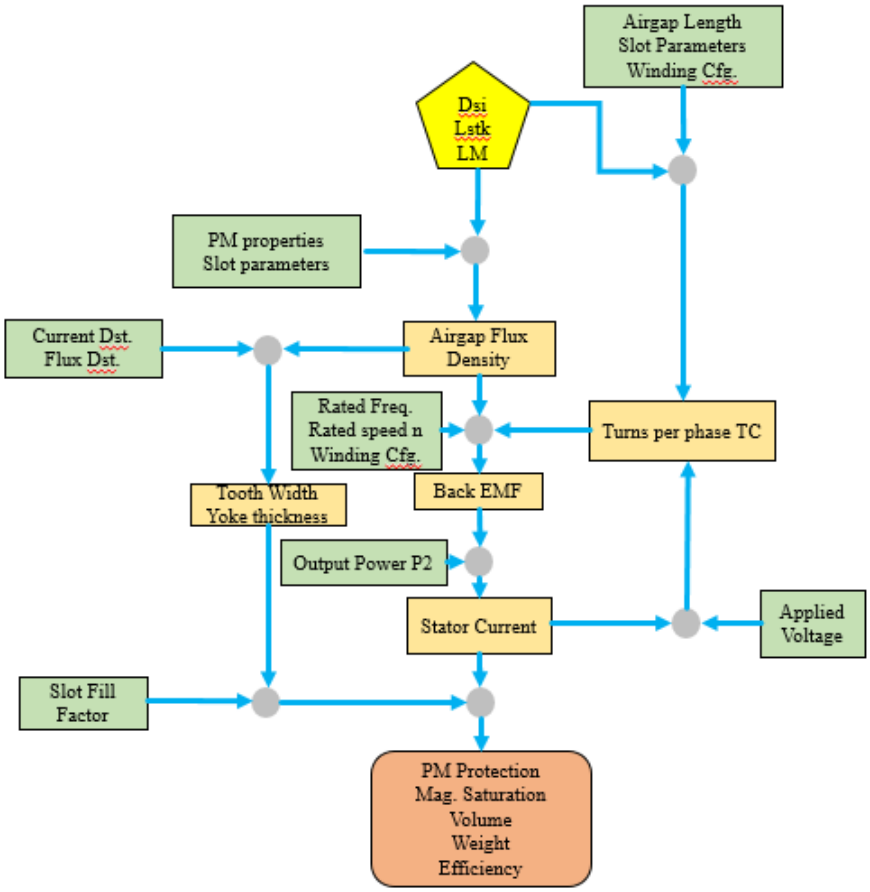


Figure 1. Design Flow Diagram

DIMENSIONAL PARAMETERS AND NUMERIC CALCULATIONS

In this section, information about the general structure of the motor is given. Physically, an electrical motor basically consists of four main components; It consists of stator, rotor, permanent magnet (PM) and stator winding wires. Their dimensions are most important factor in the electrical and electromagnetic design and analysis stages.

Stator: Stator lamination design and dimensional calculations are important in PMSM. In order to ensure that no magnetic saturation occurs, no leakage fluxes available and that the material is used effectively, detailed analyzes are made with the FEM after the analytical calculation thus the optimum dimensions are determined. Based on our previous experience, the following equations can be used for stator slot sizing. These dimensions which are shown in Figure 2. do not differ for outer rotor or inner rotor motors [Nory, Akyün, 2020].

As explained in Equation (1) each slot pitch is obtained by dividing the number of stator outer circumference to the stator slot numbers.

$$\tau_s = \frac{\pi \cdot D_{si}}{N_{slot}} \tag{1}$$

Where D_{si} Stator outside diameter, N_{slot} number of stator slots.

The stator tooth thickness (t_s) can be in the range given in Equation (2) [Nory, Akyün, 2020].

$$0.4\tau_s \le t_s \le 0.6\tau_s \tag{2}$$

The stator slot depth (d_s) can be in the range given in Equation (3) [Nory, Akyün, 2020].

$$3t_s \le d_s \le 7t_s \tag{3}$$

The stator slot opening (b_{s0}) can be in the range given in Equation (4) [Nory, Akyün, 2020].

$$b_{s0} \approx (0.1 \cong 0.5)(\tau_s - t_s) \tag{4}$$

The d_{s0} and d_{s1} values may be in the ranges given in Equations (5) and (6), respectively.

$$d_{s0} \approx (0.1 \cong 0.5)(\tau_s - t_s) \tag{5}$$

$$d_{s1} \approx (0.1 \cong 0.5)(\tau_s - t_s) \tag{6}$$

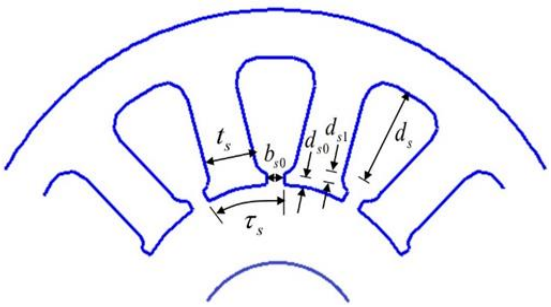


Figure 2. Notation of Stator Slot Dimensions

Rotor: Since rotor leakage fluxes and magnetic flux short circuits do not occur in surface magnet synchronous motors, rotor design is quite simple compared to embedded brushless permanent magnet (BPM) motors.

Permanent Magnet: Permanent Magnet sizing is critical and important. PM sizes directly affect the air gap flux density and the shaft torque curve and the Back-EMF curve. By determining the optimum values, the air gap flux density can be increased, the Cogging torque value can be minimized, the Back-EMF curve can be simulated to a sinus, the harmonics can be reduced, and the ripple in the torque curve can be minimized. With the word rough and ready, the magnet thickness can be 5-10 air gap times [Handershot, Miller, 2010]. In addition, one of the points to be considered in magnets is that they are demagnetization. This usually occurs when the motor is overloaded and in case of faults [Handershot, Miller, 2010]. In order not to encounter these undesirable situations, attention should be paid to the high coercivity value of the magnets to be used.

Stator Winding Wire: Stator Winding wires can be in different insulations such as B, F and H [IEC60034-2-1, 2014]. These insulations are each based on different temperatures. It can be used by selecting the appropriate wire according to the magnet coercivity value.

Airgap Length: A short airgap length (g) maximizes the airgap flux density for a given thickness of magnet, but is also requires closer mechanical tolerances, increases cogging torque and increase inductance. It is one of the advantages of surface-magnet brushless motors that they can tolerate an airgap length at least two or three times greater than in a comparable induction motor or switched reluctance motor, due to the high coercivity of new technology PM. At the same time, however, a greater airgap may be necessary to accommodate a retaining bandage or can, especially when it is desired to make the most of the reluctance torque or to maximize the inductance for flux-weakening purposes at high speed. With test factors in mind, it is unusual to find brushless motors with extremely small airgap lengths, and 0,1-1 mm is common in small motors. In larger machines of course, it scales up [Handershot, Miller, 2010].

Stator slot and Rotor Pole Combination: The choice of stator slot-rotor pole combination is one of the most important and critical points for the design process. This selection determines the geometrical dimensions of the motor. The important factors to be considered while choosing the slot-pole combination can be listed as winding scheme, torque ripple, harmonics, winding factor, cogging torque value, symmetric number in the winding scheme, iron loss, revolution number (rpm) and frequency value. In addition, the size of the motor must be considered when choosing the slot-pole. Selecting a high combination for a small circumference motor and a low combination for a large circumference motor may not be

appropriate. Table 1. shows the winding factor, (Least Common Multiple) LCM value, winding scheme symmetric number and number of slots per pole per phase (q1) for 7x7 different slot-pole combinations. The reason why these combinations are given here is to make comparisons among themselves [Emetor, 2022].

Table 1. 7x7 Stator Slot- Rotor Pole Combination

Number of slot / Number of poles		32	36	38	40	42	44	46
27	Winding Factor	0.915	0.866	0.766	0.695	0.617	0.525	0.429
	Number of slots per pole per phase	0.281	0.25	0.237	0.225	0.214	0.205	0.196
	Number of symmetries	1	9	1	1	3	1	1
	Least common multiple	864	108	1026	1080	378	1188	1242
30	Winding Factor	0.951		0.874	0.866		0.711	0.64
	Number of slots per pole per phase	0.313		0.263	0.25		0.227	0.217
	Number of symmetries	2		1	10		2	1
	Least common multiple	480		570	120		660	690
33	Winding Factor	0.954		0.928	0.903		0.866	0.778
	Number of slots per pole per phase	0.344		0.289	0.275		0.25	0.239
	Number of symmetries	1		1	1		11	1
	Least common multiple	1056		1254	1320		132	1518
36	Winding Factor	0.945		0.956	0.945	0.966	0.902	0.87
	Number of slots per pole per phase	0.375		0.316	0.3	0.286	0.273	0.261
	Number of symmetries	4		1	4	3	2	1
	Least common multiple	288		684	360	252	396	828
39	Winding Factor	0.917		0.954	0.954		0.936	0.917
	Number of slots per pole per phase	0.406		0.342	0.325		0.295	0.283
	Number of symmetries	1		1	1		1	1
	Least common multiple	1248		1482	1560		1716	1794
42	Winding Factor	0.89		0.945	0.953		0.953	0.945
	Number of slots per pole per phase	0.438		0.368	0.35		0.318	0.304
	Number of symmetries	2		1	2		2	1
	Least common multiple	672		798	840		924	966
45	Winding Factor	0.858		0.927	0.945	0.951	0.955	0.955
	Number of slots per pole per phase	0.469		0.395	0.375	0.357	0.341	0.326
	Number of symmetries	1		1	5	3	1	1
	Least common multiple	1440		1710	360	630	1980	2070

Concentrated winding Unbalanced winding

Hall Effect Sensors: Hall effect sensors are generally placed at 120 electrical angles, three in total. Since the Hall effect sensor positioning and the PCBs used affect the cost, the layout calculation of this type of sensors is explained. Generally, hall sensors are placed in the middle of the just three stator teeth. They generate 0-1 signals according to the magnetic field. It is placed on the stator teeth according to the slot-pole combination as explained in Equation (7), (8), (9) and respectively [Honeywell International Inc, 2012], [Texas Instruments Incorporated., 2021] and [Viramontes, 2010].

Number of pole pairs are calculated as,

$$pp = \frac{P}{2} \tag{7}$$

Where P, is the pole number.

Mechanical degrees (n), the rotor spins to make one complete is calculated as,

$$n = \frac{360}{pp} \tag{8}$$

Because of 120 electrical degree (edge) hall effect sensor placement, it is need to find the number of mechanical degree (mdeg) per 120 edeg. So Equation (8) is divided by 3.

$$m = \frac{n}{3} \text{ (mdeg/120edeg)} \tag{9}$$

To mount the hall sensors on the stator slots, it is need to find the number of mdeg per slot,

$$x = \frac{360}{Nslot} \text{(mdeg/slot)} \tag{10}$$

Now it is need to multiply m by integer (I) until to find an integer number, that is the slots between hall effect sensors. Number of slots between two hall effect sensors are calculated,

$$hall_{slot} = \frac{m \cdot I}{x} \tag{11}$$

Electrical degree apart of hall effect sensor,

$$edeg = x \cdot hall_{slot} \tag{12}$$

RESULTS

In this section, numerical and FEM results obtained from Simcenter Speed program are given for all slot-pole combinations. All the results were compared among themselves. These comparisons were made as Electrical, Electromagnetic, Mechanical and cost.

Numerical Calculation results

Numerical calculation results for all three models are given side by side in the table below.

Table 2. Performance results of 36-32, 36-38 and 36-40

Definition	Abb.	36-slot-32 pole	36-slot-38 pole	36-slot-40 pole
Shaft Torque	T_{shaft} [Nm]	9.1	9.1	9.1
Shaft Power	P_{shaft} [W]	500	500	500
Airgap flux density	Bg_{AvOC} [T]	0.77	0.75	0.79
Stator teeth peak flux density	B_{st} [T]	1.63	1.6	1.72
Stator yoke peak flux density	B_{sy} [T]	1.23	1.01	1.02
Efficiency	Eff [%]	92.1	91.9	92
Total Losses	W_{tatol} [W]	43.2	44	43.4
Iron Losses	W_{Fe} [W]	9.4	10.3	12.6
Cupper Loss	W_{Cu} [W]	33.8	33.8	30.8
Total Mechanical Loss	$M_{echLoss}$ [W]	9.4	10.3	12.6
Line rms current	I_{Lrms} [A]	12.8	12.8	12.3
Current Density	J_{rms} [A/mm^2]	7.3	7.2	6.9
RMS Fundamental Generated EMF per phase	E_{q1} [V]	13.3	13.2	13.9
Back-EMF constant	kE [Vs/Rad]	0.57	0.57	0.6
Torque Constant	kT [Nm/A]	0.51	0.51	0.54
Fundamental Winding Factor	Kw1	0.945	0.953	0.945
PM Weight	W_Mag [kg]	0.198	0.198	0.198

According to the above analytical results, it is seen that the 36-40 combination has better performance results since the kT and kE and Eq1 values are high. In addition, in the next section Cogging Torque and Harmonics and torque ripples in the torque graph are also investigated.

FEM Results and Graphics

In addition to the cogging torque FEM results and flux density distribution harmonics, torque vs. rotor position, Back-EMF numerical result graphs are also given respectively in this section. As seen in Figure 3. the combination with the least cogging torque value is 36-38, 36-40 can be preferred as the second option. 36-32 is too high to be preferred compared to others. According to the results of Figure 3. and Table 2. 36-38 may be the best combination up to now.

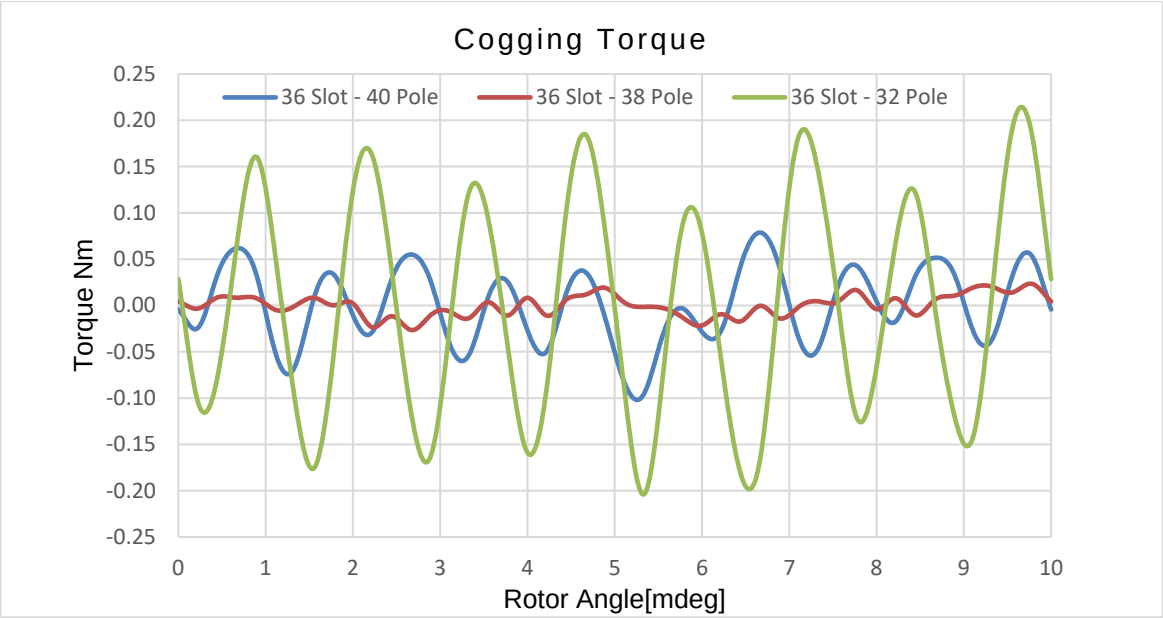


Figure 3. Cogging Torque Graphics of 36-40, 36-38 and 36-32 Slot-Pole Combination

In Figure 4, 5, 6, 7, 8 and 9 the flux distribution and flux path of 36-40, 36-38 and 36-32 combinations are shown respectively.

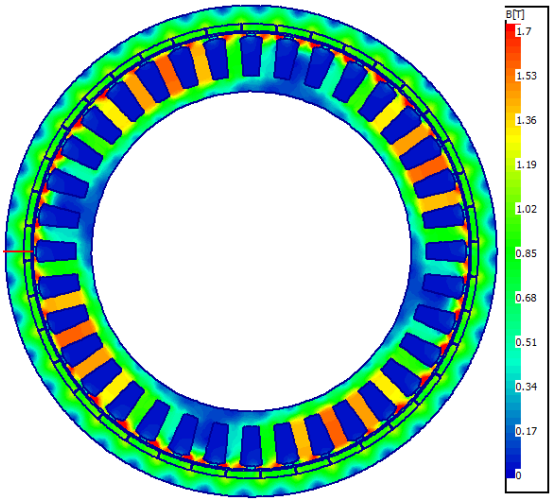


Figure 4. Flux Distribution of 36-40 Combination

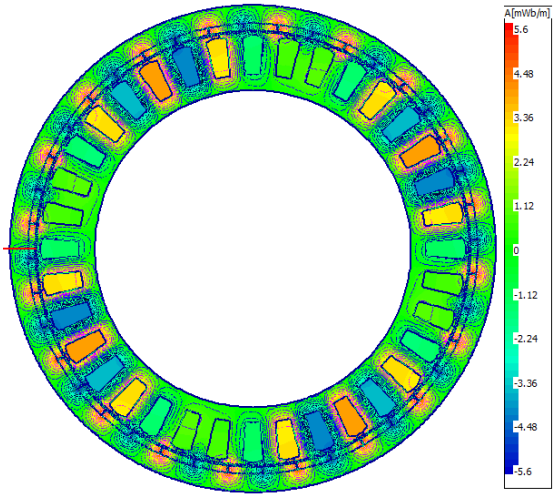
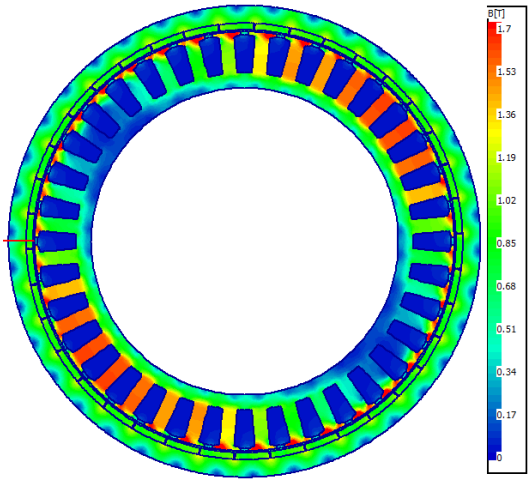


Figure 5. Flux Path of 36-40 Combination



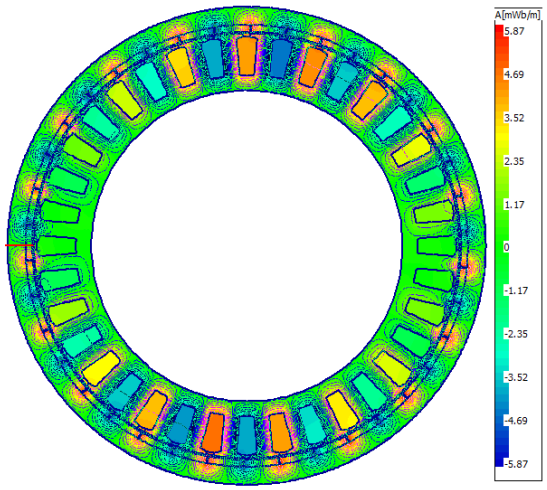


Figure 6. Flux Distribution of 36-38 Combination

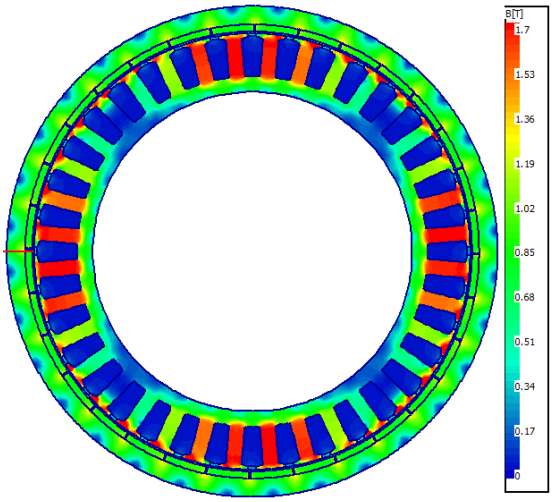


Figure 7. Flux Path of 36-38 Combination

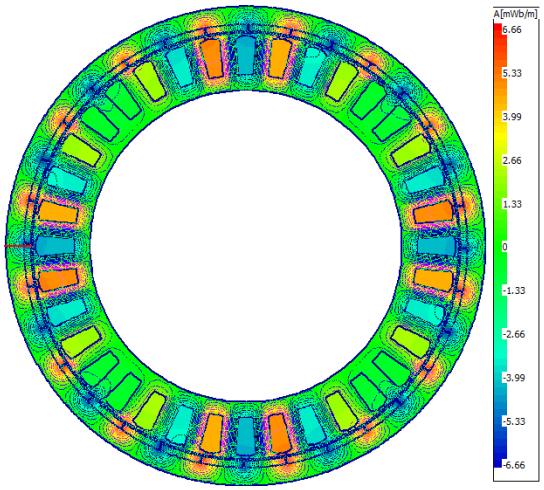


Figure 8. Flux Distribution of 36-32 Combination

Figure 9. Flux Path of 36-32 Combination

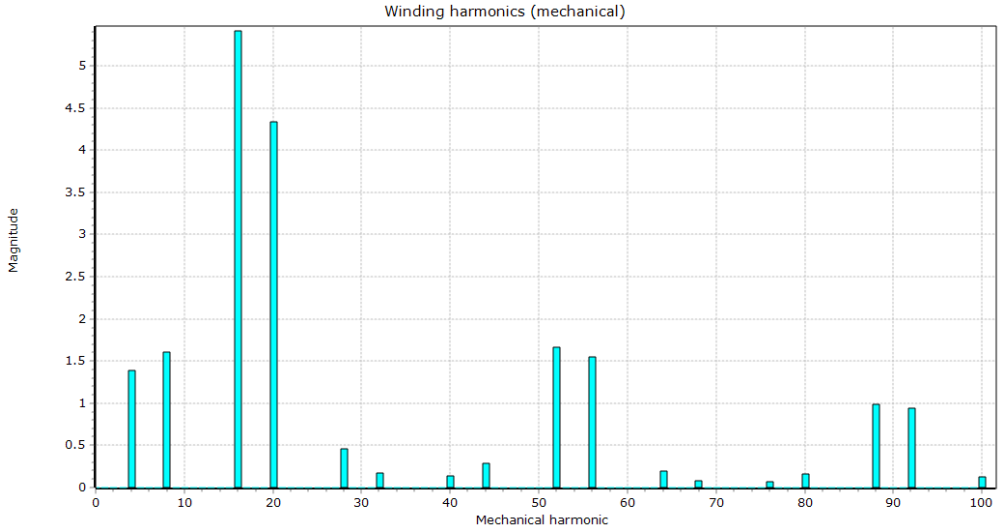


Figure 10. Shows the Winding Harmonics for 36-40 combination

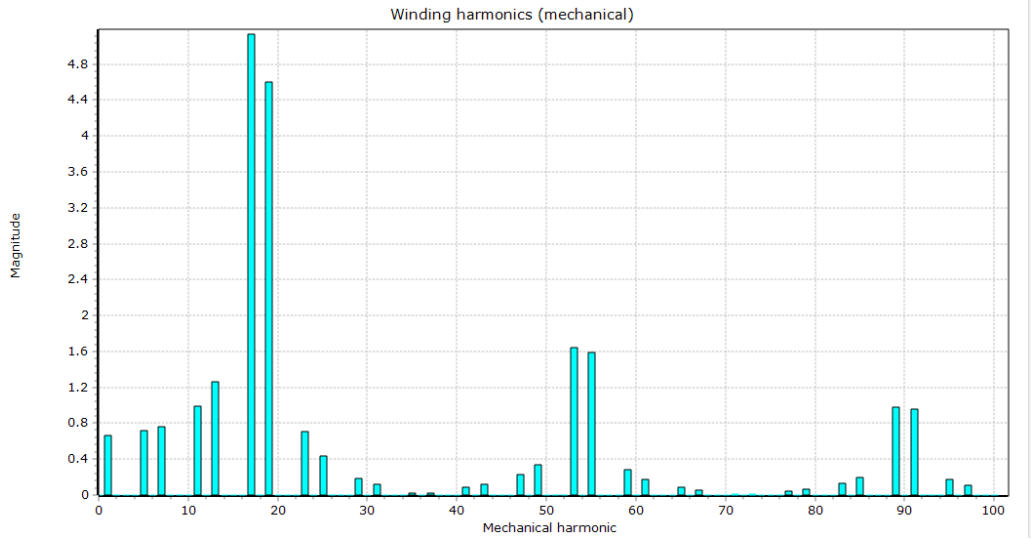


Figure 11. Shows the Winding Harmonics for 36-38 combination

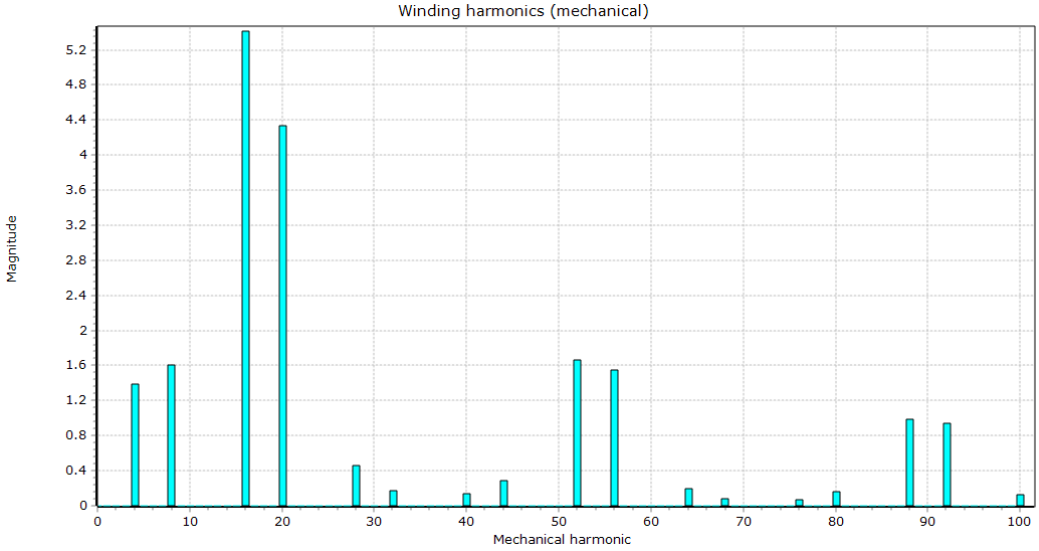


Figure 12. Shows the Winding Harmonics for 36-32 combination

Figures 10, 11 and 12 refer to slot-pole combinations 36-40, 36-38 and 36-32, respectively. According to these results, the most winding harmonic is found in 36-38 combination. According to the winding harmonic results, combinations of 36-40 and 36-32 can be preferred. In Figure 13. winding harmonics of 36-40, 36-38 and 36-32 are plotted on top of each other.

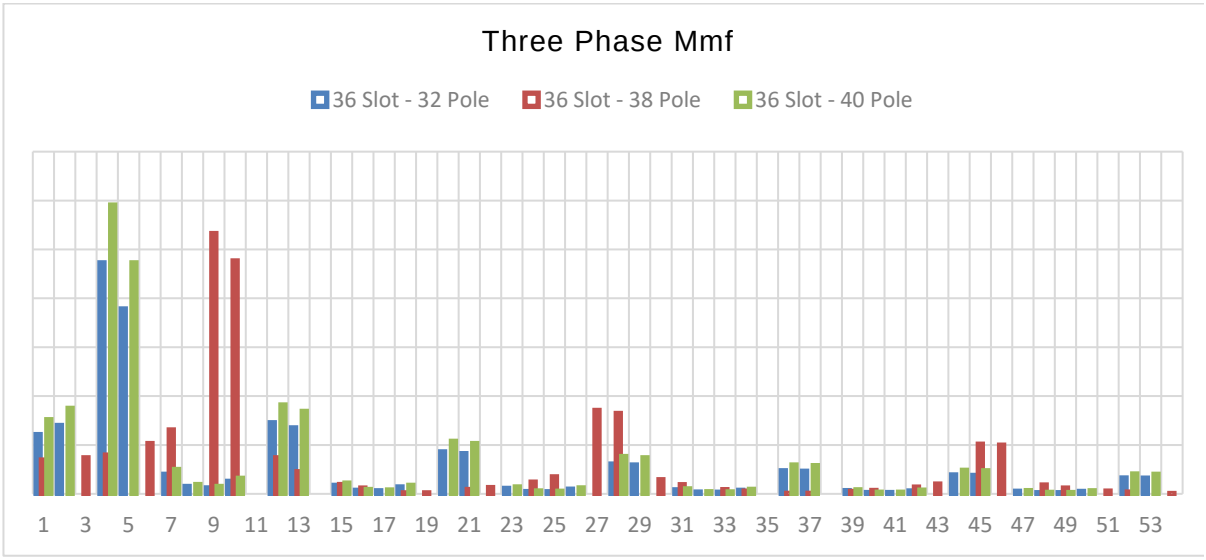


Figure 13. The winding harmonic results of 36-40, 36-38 and 36-32 slot-pole combinations are plotted for comparison purposes.

In Figures 8, 9, and 10. Torque vs. Rotor Position and Torque ripple vs. Rotor Position are given for 36-40, 36-40, and 36-32 respectively. Green line shows alignment torque and red line shows cogging + EM torque. As seen the cogging torque is causing torque ripple on torque cures. To select noiseless and no less vibration combination the motor should have less torque ripple.

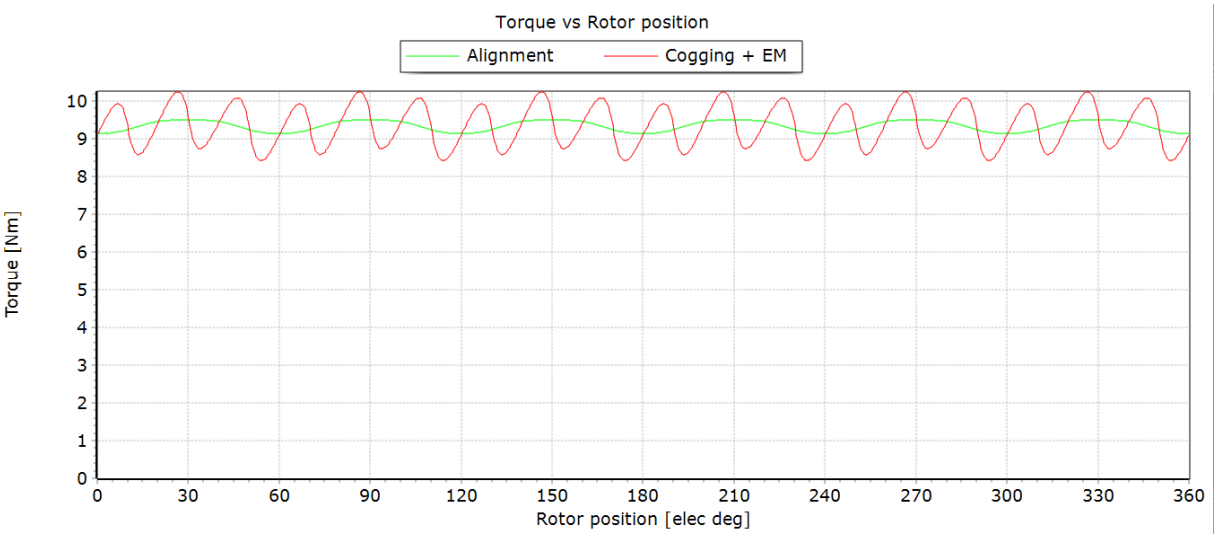


Figure 14. Torque vs. Rotor Position for 36-40 combination

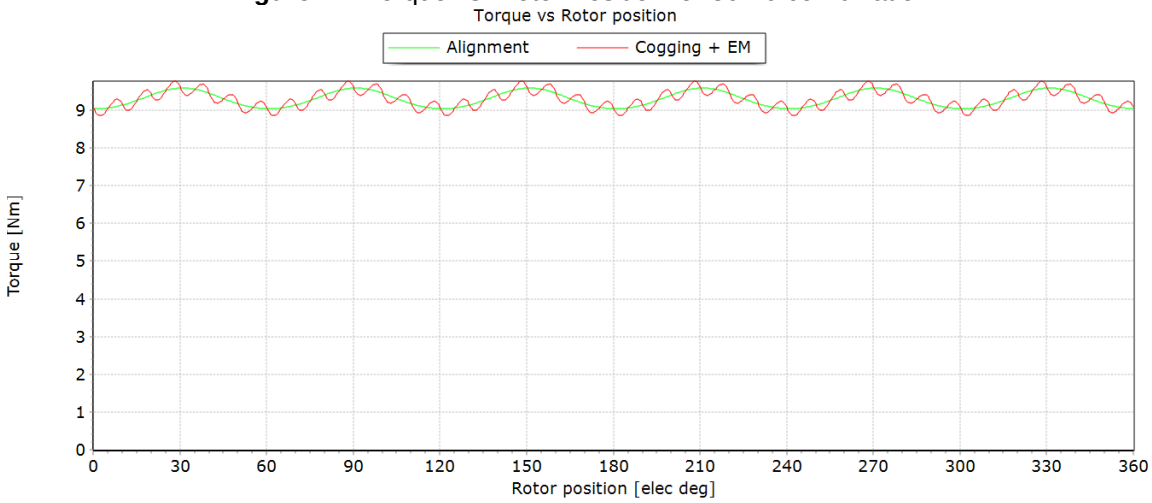


Figure 15. Torque vs. Rotor Position for 36-38 combination

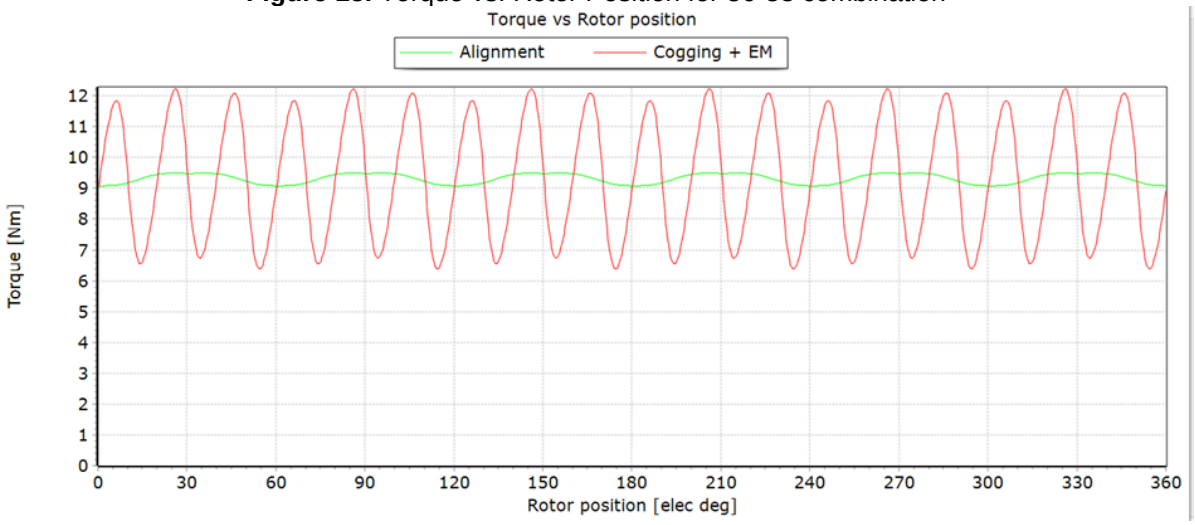


Figure 16. Torque vs. Rotor Position for 36-32 combination

In Figure 17. Back-EMF results are obtained for all three 36-40, 36-38 and 36-32 combinations. Obtained results are plotted on top of each other for comparison.

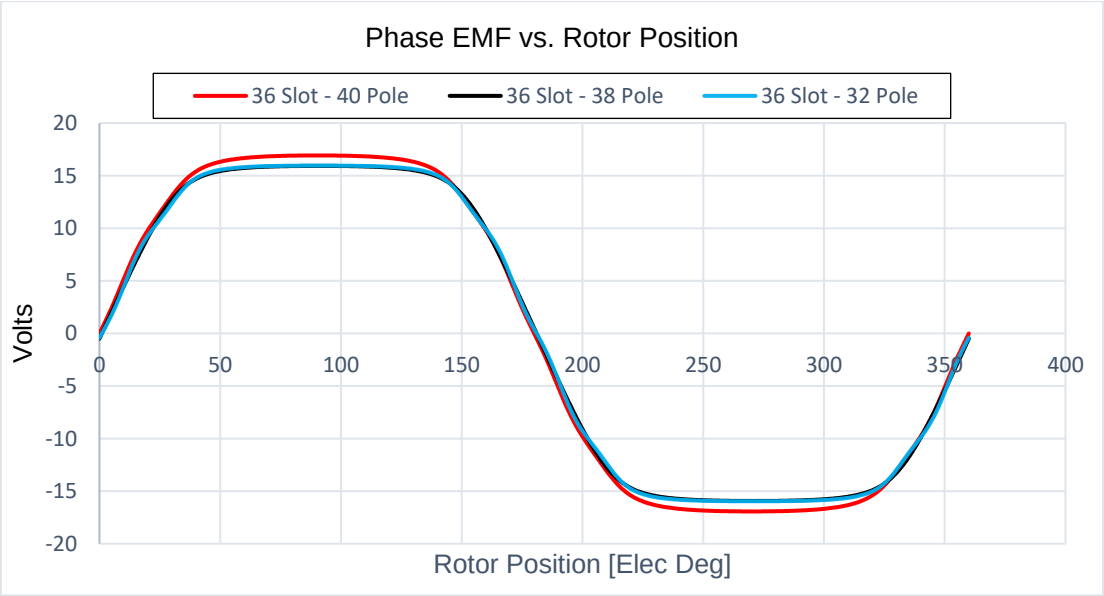


Figure 17. Shows Phase BEMF for 36-40, 36-38 and 36-32 combinations

As stated at the beginning, three hall effect sensors are generally used in this type of motor. Positioning of these sensors is done according to the calculations in Equation (7-12). Although the hall sensors are located closer to each other, it means less cost and less labor. Hall effect sensor every 12 slots in 36-38 and 36-32 combinations, but only 3 slots in 36-40 combinations can be placed. In other words, the PCB produced for 36-40 combination will be smaller, so it will be realized with less cost. Finally, to summarize, according to the results obtained, 36-40 can be preferred in terms of cost and 36-38 in terms of performance.

Acknowledgement

Sources and licensed Simcenter Speed software of Volt Electric Motor have been used for this publication. In addition, one prototype for each 36-40 and 36-38 combination motor is planned to be made.

REFERENCES

1. **Yönetmelik (2021),** "Elektrikli Skuter Yönetmeliği", Resmî Gazete. Sayı: 31454.

2. **Yao, D. (2010),** "Method For Design and Opiimizatıon of Surface Mount Permanent Magnet Machines and Induction Machines", PHD. Thesis. Georgia Institute of Technology .

3. **Hayatullah N., Yakup A., (2020),** "Experimentally Constrained Design Parameters Approach for PMSM and BLDC Motor", Conference, pp. 123-129,

4. **James R. H, and T. Miller., (2010),** "Design of Brushless Permanent-Magnet Machine", Book, Venice, Florida.

5. **IEC60034-2-1., (2014), "**Rotating Electrical Machines - Part 2-1: Standard Methods for Determining Losses and Efficiency from Tests (Excluding Machines for Traction Vehicles)", 2014-12.

6. **EMETOR,** "https://www.emetor.com/", Free Electrical Machine Design Resources, 2022.

7. **Honeywell International Inc., (2012),** "How to Select Hall-Effect Sensors for Brushless DC Motors", 005959-1-EN, December 2012

8. **Texas Instruments Incorporated., (2021),** "Brushless DC Motor Commutation Using Hall-Effect Sensors", 2021 Texas Instruments.

9. **Eduardo, V. SS443A., (2010),** " BLDC Motor Control with Hall Effect Sensors Using the 9S08MP ", Do. NO. AN4058, Rev. 0, 4/2010.

19. ULUSLARARASI MAKİNA TASARIM VE İMALAT KONGRESİ

BİLDİRİ KİTABI

Editörler

Metin AKKÖK
Besim BARANOĞLU
Cemal ÇAKIR
S. Engin KILIÇ
E. İlhan KONUKSEVEN
Bahram LOTFİ
Ali ORAL
Ulvi ŞEKER
Hakkı Özgür ÜNVER
Volkan ESAT
Selcuk HIMMETOĞLU

umtik 2022

31 Ağustos- 03 Eylül 2022

KAPADOKYA- TURKİYE

MATİMAREN
MAKİNA MÜHENDİSLİĞİ BÖLÜMÜ
ORTA DOĞU TEKNİK ÜNİVERSİTESİ
ANKARA-TÜRKİYE

Bu bildiri kıtabın yayın hakkı Orta Doğu Teknik Üniversitesi'nindir. Bu Kitapta yayımlanan bildirilerin aynen yayımlanması, yazarlardan ve editörlerden yazılı izin almak koşulu ile mümkündür.
Alıntı için kaynak göstermek yeterlidir.

Bu Bildiri Kitabı

UMTIK
Mechanical Engineering Department
Middle East Technical University
06800 Ankara- Turkey

Manufacturing Engineering Department
ATILIM University
06830 Ankara- Turkey

Adreslerinden sağlanabilir.

Kapak Baskı:

ODTÜ- Ankara

Baskı ve Cilt:

ODTÜ- Ankara

Matbaa Adı:

ODTÜ

ISBN

TÜRKÇE BİLDİRİLER

PAPERS IN TURKISH

3-DENKLEMLİ TÜRBÜLANS GEÇİŞ MODELİNİN JENERİK GÖVDE GEOMETRİSİ İLE BAŞARIM DEĞERLENDİRMESİ

Hediye ATİK, *hediye.atik@atilim.edu.tr* Atılım Üniversitesi, 06830, Ankara

ÖZET

Reynolds-ortalamalı Navier Stokes (RANS) denklemlerine dayalı laminar-türbülans geçiş modelleri arasında bulunan 3-denklemli *k-kl-ω* ismiyle adlandırılan geçiş modelinin incelenmesi, hava ve su araçlarının gövdesini temsil eden jenerik gövde modeli kullanılarak gerçekleştirilmiştir. Bu modelin değerlendirilmesi 6.5 x 10^6 Reynolds sayısında ve 5 derece hücum açı koşulunda, en yaygın kullanılan γ-Re_Θ türbülans geçiş modeli analiz sonuçları ve halihazırda mevcut deneysel veri sonuçları kullanılarak yapılmıştır. Eksenel kuvvet ve normal kuvvet katsayılarının yüzey çözüm ağı büyüklüğünden kaynaklı ayrıklaştırma belirsizlik bandı Ağ Yakınsama Endeks (İng. Grid Convergence Index, GCI) metoduyla bulunmuştur. Geometrinin hesaplanan integral aerodinamik katsayı parametrelerinin yanı sıra yüzey basınç ve sürtünme katsayılarının değişimi de incelenmiştir. *k-kl-ω* türbülans geçiş modeli γ-Re_Θ modeline göre eksenel kuvvet katsayısını yaklaşık %50, normal kuvvet katsayısını ise yaklaşık %30 fazla tahmin etmektedir. *k-kl-ω* türbülans geçiş modeli ile elde edilen sonuçlar etrafındaki belirsizlik bandı tahmini ise normal kuvvet katsayısında daha fazla iken γ-Re_Θ modeli eksenel kuvvet katsayısı etrafındaki bandı daha büyük bulmaktadır.

Anahtar Kelimeler: Türbülans geçiş modeli, ayrıklaştırma hatası, küremsi geometri, türbülans geçiş yeri, aerodinamik katsayı

ABSTRACT

One of the Reynolds-averaged Navier Stokes (RANS) based transition model, which is called *k-kl-ω* model, is investigated using a generic body geometry of air/water vehicles. This model evaluated at 6.5 x 10^6 Reynolds number at 5 degree angle of attack with the results obtained with widely accepted γ-Re_Θ transition model and an available experimental study. Discretization uncertainty band around the axial and normal force coefficients due to surface mesh sizes are found using Grid Convergence Index (GCI) method. Besides integral

aerodynamic coefficients, variation of surface pressure and friction coefficients are evaluated. The *k-kl-ω* transition model finds axial force coefficient approximately 50%, and normal force coefficient approximately 30% larger than the γ-Re_Θ transition model results. While the *k-kl-ω* transition model gives greater uncertainty band around normal force coefficient, γ-Re_Θ transition model gives larger uncertainty band around axial force coefficient.

Keywords: Transition model, discretization error, spheroid geometry, transition location, aerodynamic parameters

1. GİRİŞ

Hava ve su aracı tasarımlarında aero/hidrodinamik katsayılarının yeteri doğrulukta tahmin edilmesi kritik öneme sahiptir. Bu araçların tasarım sürecinin önemli bir kısmında sayısal analiz yöntemleri kullanarak kuvvet ve moment katsayıları tahmin edilmektedir. Bu katsayıların doğruluk derecesi aynı zamanda uçuş performans analizlerinin doğruluk seviyesini de belirlemektedir. Tasarımlar sırasında sayısal analizleri doğrulamak amacıyla rüzgar tüneli testleri yapılıyor olsa da rüzgar tüneli testlerinin sayısal analizlere göre maliyetinin yüksek olması sebebiyle, analizler rüzgar tüneli testlerinin tasarımında da kullanılmaktadır. Akış koşul aralıkları, kritik akış koşulları ve akış benzetimlerinin doğru yapılabilmesi amacıyla türbülans geçiş bölgelerinin yer tahmini gibi bilgiler sayısal analizlerden elde edilmektedir. Dolayısıyla sayısal analizlerin doğruluk seviyesi tasarımın başarısında önemli katkıya sahiptir.

Laminar akıştan türbülanslı akışa geçişin görüldüğü birçok mühendislik uygulamaları bulunmaktadır. Örneğin, insansız hava araçlarının ve yenilenebilir enerji sistemlerinde kullanılan rüzgar türbini pallerinin akış rejiminde türbülans geçisi görülmektedir ve tasarımında bu olayın doğru modellenmesi önemlidir. Rüzgar tüneli testlerinde ölçeklendirilmiş modellerin kullanılması sebebiyle test koşulları gerçek Reynolds sayısında gerçekleştirilememekte, bunun yerine laminar-türbülans geçisi model üzerinde geçiş bandlarıyla zorlanmaktadır. Test verilerinin gerçeğe yakın elde edilebilmesinde türbülans geçiş yerinin sayısal analizler ile doğru tahmin edilmesine ihtiyaç vardır.

Laminar akıştan türbülanslı akışa geçiş oldukça karışık bir olaydır çünkü akışta bu olayı tetikleyen birçok bozucu etki bulunmaktadır [Schlicting ve Gersten, 2000; Sengupta, 2012]. Türbülanslı akışa geçiş farklı uygulamalarda farklı merkanizmalarla gerçekleştiğinden bu geçiş tahmini oldukça güçtür. Sayısal olarak direkt sayısal simülasyon (İng. direct numerical simulation, DNS [Versteeg ve Malalasekera, 2007]) yöntemi, hiçbir türbülans modeli kullanımını gerektirmediğinden bu olayın tahmininde kullanılması için akla gelen ilk

yöntemdir. Büyük ölçekli türbülans yapılarının çözümlendiği fakat küçük ölçekli yapıların modellendiği büyük girdap simülasyon (İng. Large eddy simulation, LES [Versteeg ve Malalasekera, 2007]) yöntemi de bu olayın tahmininde kullanılabilecek metodlar arasındadır. Fakat bu metodta da DNS yönteminde olduğu gibi duvara yakın bölgelerde türbülans modeli kullanımı yerine akış direkt olarak çözülmektedir. Bu sebeple, DNS ve LES metodları birçok pratik problemler için yüksek hesaplama maliyeti sebebiyle kullanılamamaktadır [Wauters ve Degroote, 2018]. Bu sebeple, karışık geometriler etrafındaki türbülanslı (veya türbülansa geçişin olduğu) akışlar için kullanılan en genel geçer matematiksel model halen türbülans modeli ile tamamlanmış Reynolds-ortamalı Navier-Stokes (RANS) denklemleridir. RANS yönteminde akışın tümüyle türbülanslı olduğu varsayıldığından bu yöntem ile türbülans geçişin olduğu Reynolds sayısı ve geçişin ne şekilde olduğu doğru bir şekilde tahmin edilememektedir [Eça ve Hoekstra 2008].

Açık kaynaklarda, RANS denklemleri ile birlikte kullanılan birçok geçiş modellerinin çalışıldığı görülmektedir. Bu yöntemlerin değerlendirildiği Pasquale vd. (2009), Boiko vd. (2015), ve Krumbein vd. (2015) tarafından yapılmış inceleme makaleleri bulunmaktadır. Kaynaklar incelendiğinde türbülanslı akışa geçiş tahmini için en çok kullanılan modelin Menter vd. (2006) ve Langtry ve Menter (2009) tarafından geliştirilmiş bölgesel korelasyon geçiş modeli (İng. local correlation transition method (LCTM)) olduğu görülmektedir. γ-Re_θ geçiş modeli olarak adlandırılan bu modelde türbülans aralıklılık, γ (İng. intermittency) ve türbülans geçiş başlangıç kriter korelasyonu için taşınım denklemleri çözülmektedir [Langtry ve Menter, 2009]. Bu model, sınır tabaka ayrılmasından, basınç değişiminden ve serbest akış türbülans yoğunluğundan kaynaklı türbülans geçiş olayının benzetimlerinde kullanılmak üzere yaygın olarak kullanılan iki-denklemli Shear-Stress Transport (SST) k–ω modeli [Menter, 1994] ile birleştirilmiştir. γ-Re_θ geçiş modeli birçok araştırma ve ticari hesaplamalı akışkanlar dinamiği (HAD) (İng. Computational Fluid Dynamics, CFD) yazılımlarına entegre edilerek farklı sınama durumları ile başarımı incelenmiştir [Vaz vd., 2009, Lopes vd. 2021, Seyfert 2011]. Atik (2022), γ-Re_θ geçiş modelini 6:1 küremsi sınama geometrisi kullanarak 6.5 milyon Reynolds sayısında yüzey çözüm ağından kaynaklı çözümleme sonuçlarındaki ayrıklaştırma belirsizlik bandını tahmin ederek, modelin türbülans geçiş başarımını deneysel veri ile karşılaştırmıştır. Çalışmada küremsi geometri üzerinde tespit edilen türbülans geçiş bölge geometrisinin deneysel sonuçlarla farklılık gösterdiği, özellikle basınç tarafında türbülans geçişinin yakalanmadığı görülmüştür.

Walter ve Cokljat (2008) tarafından çalışılan bir diğer LCTM konseptine dayalı türbülans geçiş modeli k-kl-ω olarak adlandırılmıştır. Yukarıda bahsi geçen γ-Re_Θ geçiş modelinde olduğu gibi k-ω türbülans modeline dayalı olmasına rağmen ek olarak laminar kinetik enerji

(k_L) taşınım denklemi çözülmektedir. Sınır tabaka içerisinde laminar kinetik enerji dinamiği türbülans geçişi ile ilişkili olduğundan bu modelin ampririk yaklaşımdan ziyade türbülans geçiş fiziğine dayalı olduğu belirtilmektedir. Walter ve Cokljat (2008) çalışmasında, geliştirdikleri modeli 2-boyutlu farklı düz plaka üzeri akışlar ve farklı su damlası kesitleri etrafındaki akışlarla sınayarak modelin türbülans geçişini makul bir şekilde yaratabildiğini göstermişlerdir.

Bu çalışmanın amacı, en yaygın kullanılan γ-Re_Θ geçiş modeli ve türbülans geçiş fiziğine dayalı olduğu belirtilen *k-kl-*ω türbülans geçiş modelinin jenerik gövde modeliyle su ve hava araçları için türbülans geçiş olayı simülasyonlarındaki başarımının tahmin edilmesidir. Bu değerlendirme esnasında Atik (2022) çalışmasında kullanılan 6:1 küremsi (İng. spheroid) geometri kullanılmıştır. Bu geometri farklı akış olaylarının çalışılmasında yaygın olarak kullanılan oldukça basit bir geometri olmasının yanı sıra, su ve hava araçlarının gövdesini temsilen kullanılan bir geometridir. Meier vd. (1980), 6:1 küremsi geometri ile türbülans akış geçişini farklı akış koşullarında düşük hızlı rüzgar tünelinde test etmiştir. Bu çalışmada, 6.5 x 10^6 Reynolds sayısında 5^o hücum açısında yapılan deneysel sonuçlar kullanılmıştır.

Türbülans geçiş modellerinin kullanımı rutin HAD analizlerine göre daha küçük boyutta çözüm ağına ihtiyaç duymaktadır. Tüm HAD uygulamalarında olduğu gibi sayısal analizlerde belirsizlik analizlerinin yapılması hidro/aerodinamik katsayılardaki belirsizliklerin belirlenmesinde büyük öneme sahiptir. Bu çalışmada model başarımının deneysel veri ile karşılaştırılması öncesinde çözüm ağı kaynaklı ayrıklaştırma belirsizliklerinin bulunması amaçlanmıştır. Her iki geçiş modeli için yüzey çözüm ağı etkisinin hidro/aerodinamik katsayılara olan etkisi gösterilmiştir. Ayrıklaştırmadan kaynaklı belirsizlik oranları Grid Convergence Index (GCI) metodu [Celik vd., 2008] kullanılarak bulunmuştur.

2. YÖNTEM

Bu çalışmada yapılan tüm hesaplamalar sonlu hacim metodu kullanan Ansys® Fluent, Versiyon 20.1 yazılımı ile gerçekleştirilmiştir. Yazılım karışık geometriler etrafındaki sıkıştırılabilir ve sıkıştırılamaz akış problemlerini çözmektedir. Fluent yazılımı ağdasız, laminar ve türbülanslı akışları çözebilme kabiliyetine sahiptir. Ayrıca yazılımda laminar-türbülans geçiş tahminleri için γ, γ-Re_Θ ve *k-kl-*ω modelleri bulunmaktadır. Yazılım basınç veya yoğunluk tabanlı çözücü seçimine izin vermektedir. Bu çalışmada basınç tabanlı birleşik algoritma kullanılmıştır. Basınç için ikinci dereceden ayrıklaştırma metodu seçilirken, momentum, türbülans kinetik enerji, laminar kinetik enerji, özgül dağılım oranı, aralıklılık ve Reynolds momentum kalınlık parametreleri için ikinci derece akış yönünde (İng. upwind)

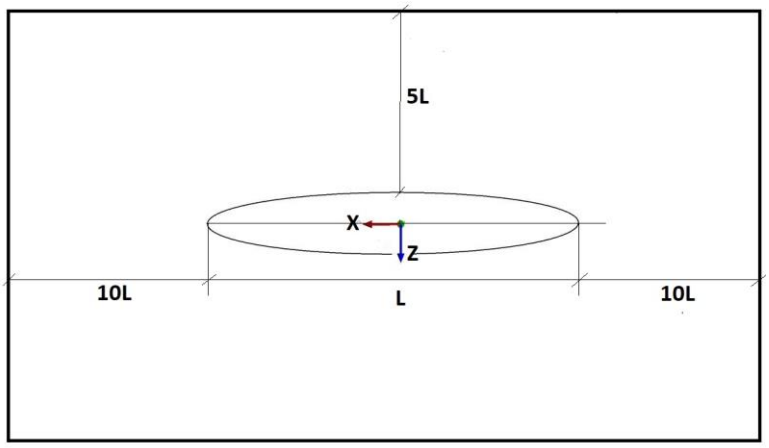
ayrıklaştırma şeması kulanılmıştır. Parametrelerin değişim ve türevlerinin hesaplanmasında hücreye dayalı en küçük kare (İng. least square cell based) metodu kullanılmıştır. Tüm analizler zamandan bağımsız gerçekleştirilmiştir.

Çalışmada γ-$Re\theta$ geçiş modeli, laminar-türbülans geçişi konusunda çalışan geniş bir kullanıcı kesimi tarafından kabul görmesi ve birçok araştırma ve ticari yazılımlarda kullanılması sebebiyle *k-kl-ω* modellinin başarım değerlendirilmesine dahil edilmiştir. Atik (2022) tarafından 5^o hücum açısında elde edilen sonuçlar çalışmada yapılan analiz karşılaştırmalarında kullanılmıştır. Atik (2022) çalışmasında kullanılan çözüm ağları, sınır koşul türbülans parametreleri, yakınsama kriterleri ve karşılaştırma yapılan deneysel çalışma sonuçları benzer şekilde bu çalışmada da kullanılmıştır.

Kullanılan hibrid-düzensiz çözüm ağı, geometri üstünde üçgen, üzerine prizmatik elemanlar ve devamında da dörtyüzlü elemanlar kullanılarak elde edilmiştir. GCI yöntemi üç farklı düzey çözüm ağının kullanımına ihtiyaç duymaktadır. Celik vd. (2008) yöntemin uygulamasında dikkat edilecek hususları belirtmişler ve yöntemin uygulanması sırasında bu hususlar dikkate alınmıştır. Yöntemin tarifi ve uygulanması ile ilgili detaylı bilgiler Atik (2022) makalesinde verilmiştir. Çalışmada yüzey çözüm ağından kaynaklı ayrıklaştırma belirsizliği elde edilmesi amaçlandığından farklı çözüm ağı düzeyleri farklı yüzey eleman büyüklükleri ile elde edilmiştir. Sınır tabakayı içerisine alan prizmatik çözüm ağının özellikleri türbülans modeline uygun olarak elde edilmiştir. Yüzey üzerindeki en büyük y+ değerinin 1'den küçük olmasına dikkat edilmiş, açılma oranı da 1.1 olarak kullanılmıştır. Kullanılan çözüm ağı özellikleri Tablo 1'de, çözüm hacminin boyutları Şekil 1'de verilmiştir. Çalışmada deneysel veri ile karşılaştırma bulunduğundan sınır koşullarının deneysel koşullara benzer şekilde yaratılmasına dikkat edilmiştir. Özellikle sınır yüzeylerdeki türbülans parametreleri önemli olmaktadır. Sınır koşulu olarak türbülans yoğunluğu % 0.2 ve türbülans viskozite oranı 50 kullanılarak 6:1 küremsi yapının burnunda %0.15 türbülans yoğunluğu elde edilmiştir. Böylece deneysel çalışmada [Kreplin v.d., 1980] belirtilen türbülans yoğunluğu aralığının ortalaması burun civarında elde edilmiştir.

Tablo 1 Çözüm Ağları ve Özellikleri [Atik, 2022]

Çözüm Ağı	Yüzey Eleman Büyüklüğü (mm)	Prizmatik Ağ (Sınır Tabaka)			Eleman Sayısı	Düğüm Sayısı
		İlk Eleman Kalınlığı (m)	Genişleme Oranı	Katman Sayısı (Kalınlık)		
Düzey-1	3	5x10-6 (y+<0.3)	1.1	56 (10.3 mm)	9,480,052	4,467,923
Düzey-2	6				3,466,306	1,597,635
Düzey-3	12				1,131,851	506,715



Şekil 1 Çözüm Hacmi Boyutlarının Şematik Gösterimi

3. BULGULAR VE DEĞERLENDİRMELER

Aerodinamik Katsayı Değerlendirmeleri

k-kl-ω türbülans geçiş modeli kullanılarak 6.5 x 10^6 Reynolds sayısında ve 5 derece hücum açısında gerçekleştirilen sayısal analiz kuvvet katsayı sonuçları γ-Re_θ geçiş modeli sonuçları [Atik, 2022] ile Tablo 1'de karşılaştırılmıştır. Tabloda *k.* düzey çözüm ağı için düğüm sayısı *Nk*, *k.* düzey çözüm çözüm ağı için katsayı değerleri Φ_k ve çözüm ağı küçültme oranları *r* (çözüm ağı eleman büyüklük oranı) ile verilmiştir. Tabloda verilen *p*, çözümlemeler sonucu gerçekleşen hassasiyet derecesini, $\Phi^{21}_{ext,}$ çözüm ağı eleman büyüklüğünün sıfıra gitmesi durumunda tahmin edilen parametre değerini, e^{21}_a, yaklaşık göreceli hatayı, e^{21}_{ext}, tahmini göreceli hatayı, *GCI* ise sık çözüm ağı ile elde edilen çözüm etrafındaki hata bandı büyüklüğünü vermektedir [Celik vd., 2008].

Tablo 1 Yüzey Çözüm Ağı Kaynaklı Eksenel Kuvvet Katsayısı Ayrıklaştırma Hataları.

	Eksenel Kuvvet Katsayısı		Normal Kuvvet Katsayısı	
	γ-Re_θ	*k-kl-*ω	γ-Re_θ	*k-kl-* ω
N1	9,480,052	9,480,052	9,480,052	9,480,052
N2	3,466,306	3,466,306	3,466,306	3,466,306
N3	1,131,851	1,131,851	1,131,851	1,131,851
r_{21}	1.398	1.398	1.398	1.398
r_{32}	1.452	1.452	1.452	1.452
Φ_1	-3.1359E-04	-4.6605E-04	-2.1524E-04	-2.8514E-04

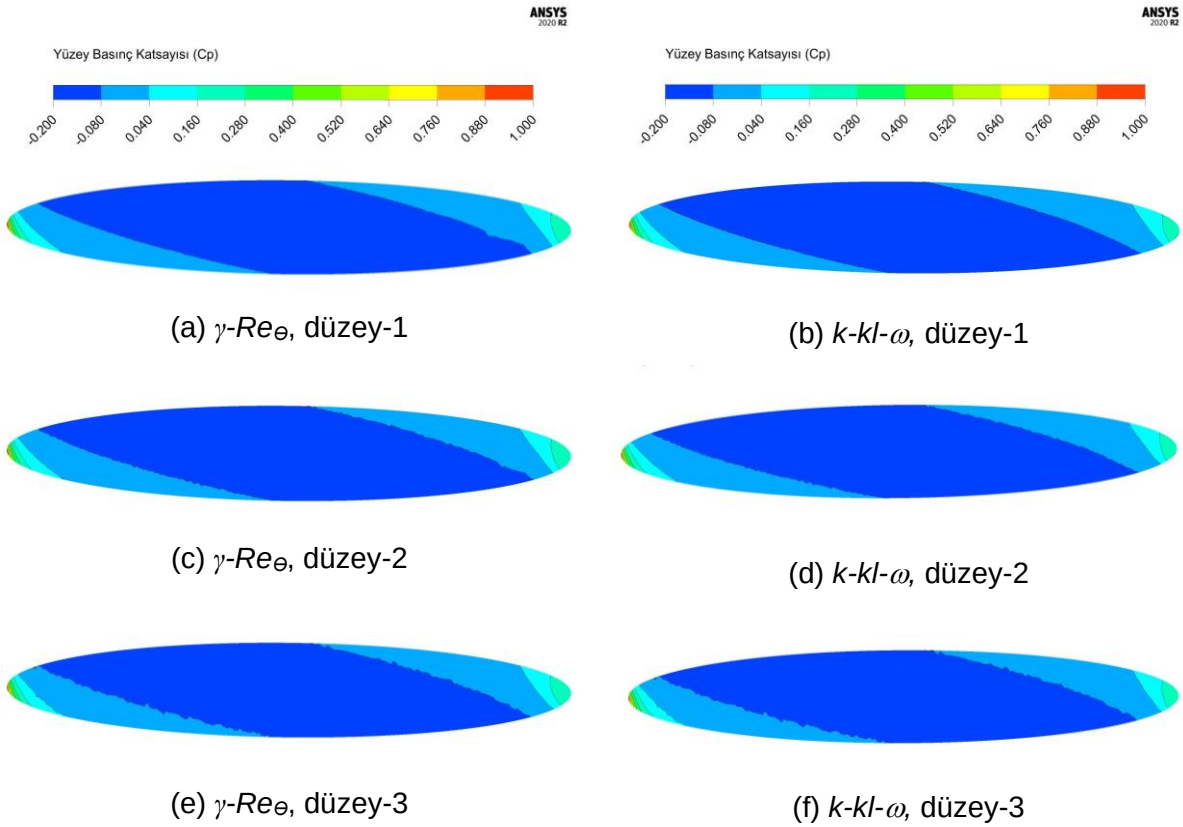
Φ_2	-3.3214E-04	-4.7950E-04	-2.1756E-04	-3.0632E-04
Φ_3	-4.4966E-04	-5.3239E-04	-2.3086E-04	-3.7915E-04
p	2.74	3.52	4.57	3.15
Φ^{21}_{ext}	-3.0130E-04	-4.6010E-04	-2.1460E-04	-2.7387E-04
e_a^{21}	%5.92	%2.89	%1.1	%7.42
e_{ext}^{21}	%4.09	%1.29	%0.3	%4.11
GCI_{fine}^{21}	%4.92	%1.60	%0.37	%4.94
GCI_{fine}^{32}	%11.62	%5.06	%1.70	%13.24

Farklı çözüm ağları ile elde edilen eksenel kuvvet katsayıları arasındaki farklar incelendiğinde γ-Re_Θ ve *k-kl-* ω geçiş modelleri ile elde edilen sonuçların monotonik yakınsadığı ($0 < \frac{\varepsilon_{21}}{\varepsilon_{32}} < 1$), görülmektedir [Phillips ve Roy, 2014]. Gerçekleşen hassasiyet derecesi, *p*, her iki model için teorik değer olan 2'den büyük hesaplanmıştır ve bu durum sayısal sonuçların asimptotik davranmadığını göstermektedir. En yaygın kullanılan γ-Re_Θ modeli için en küçük yüzey eleman büyüklüğüne sahip düzey-1 çözüm ağı için belirsizlik bandı, GCI^{21}_{fine}, %5 görülürken düzey-2 çözüm ağı için belirsizlik bandı, GCI^{32}_{fine}, %12'ye artmaktadır. *k-kl-* ω geçiş modeli kullanıldığında belirsizlik bandları düzey-1 çözüm ağı için %1.60'a, düzey-2 çözüm ağı için %5 civarına düşmektedir. Geçiş modellerinin tahmin ettiği eksenel kuvvet katsayıları karşılaştırıldığında, *k-kl-*ω türbülans geçiş modelinin katsayı büyüklüğünü γ-Re_Θ geçiş modeline göre yaklaşık %50 fazla bulduğu görülmüştür.

Normal kuvvet katsayıları incelendiğinde sonuçların her iki model kullanımında eksenel kuvvet katsayısında olduğu gibi monotonik yakınsağı ve asimtotik davranmadığı görülmektedir. γ-Re_Θ geçiş modeli düzey-1 çözüm ağı ile elde edilen normal kuvvet katsayısı etrafındaki belirsizlik bandını %1 altında verirken, *k-kl-*ω türbülans geçiş modeli %5 civarı tahmininde bulunmuştur. Normal kuvvet katsayı değeri *k-kl-*ω türbülans geçiş modeli ile yine daha fazla bulunmuştur.

Yüzey Basınç ve Sürtünme Katsayı Değerlendirmeleri

Yüzey basınç katsayı dağılımı tüm çözümlemeler için Şekil 1'de verilmiştir. Şekiller incelendiğinde görsel olarak basınç dağılımlarının farklı düzey çözüm ağları için benzer olduğu görülmektedir.



(a) γ-Re_{Θ}, düzey-1

(b) *k-kl-ω,* düzey-1

(c) γ-Re_{Θ}, düzey-2

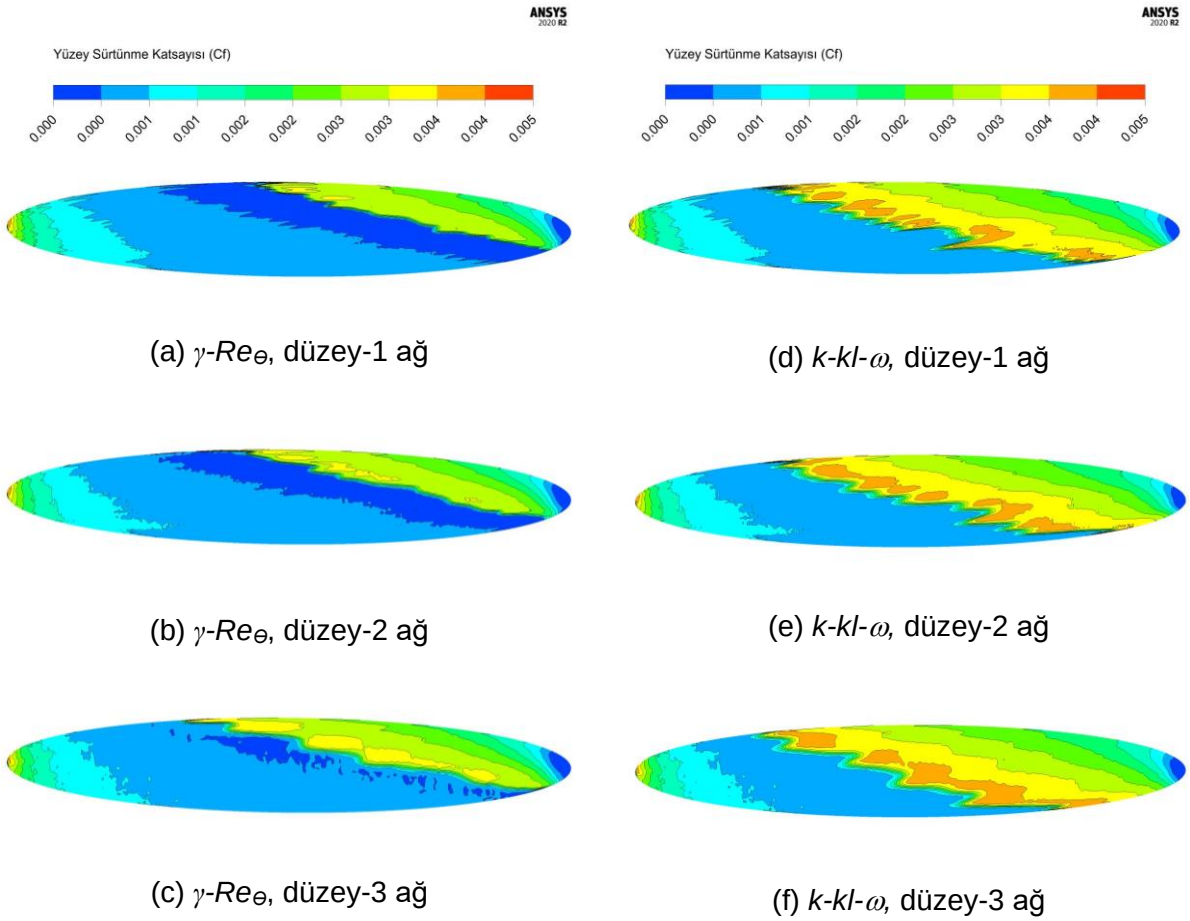
(d) *k-kl-ω,* düzey-2

(e) γ-Re_{Θ}, düzey-3

(f) *k-kl-ω,* düzey-3

Şekil 1 Yüzey Basınç Katsayı Dağılımı.

Tüm analiz sonuçları ile elde edilen yüzey sürtünme katsayı dağılımı Şekil 2'de verilmiştir. Her iki türbülans geçiş modeli sonuçlarında türbülans geçiş bölgesi yerlerinin farklı çözüm ağı düzeyleri için farklılık gösterdiği görülmektedir. Yüzey çözüm ağı eleman büyüklüğü arttıkça geçiş yerinin geometrinin burnuna (sol) doğru kaydığı gözlemlenmektedir. γ-Re_{Θ} geçiş modeli sonuçlarında gövdenin üst tarafında yaklaşık boyun yarısında türbülans geçişinin oluştuğu, akışın geldiği gövdenin alt kısmına inildikçe geçişin arkaya doğru kaydığı hatta tam alt kısımda geçişin oluşmadığı görülmektedir. *k-kl-ω* geçiş modelinde gövdenin alt kısmında geçişin daha önde oluştuğu alt kısma ilerlerken yine geçişin arkaya kaydığı görülmüştür. Bu modelde farklı olarak türbülans geçisinin gövdenin alt kısmında oluştuğu görülmektedir.



(a) γ-Re_Θ, düzey-1 ağ

(d) *k-kl-*ω, düzey-1 ağ

(b) γ-Re_Θ, düzey-2 ağ

(e) *k-kl-*ω, düzey-2 ağ

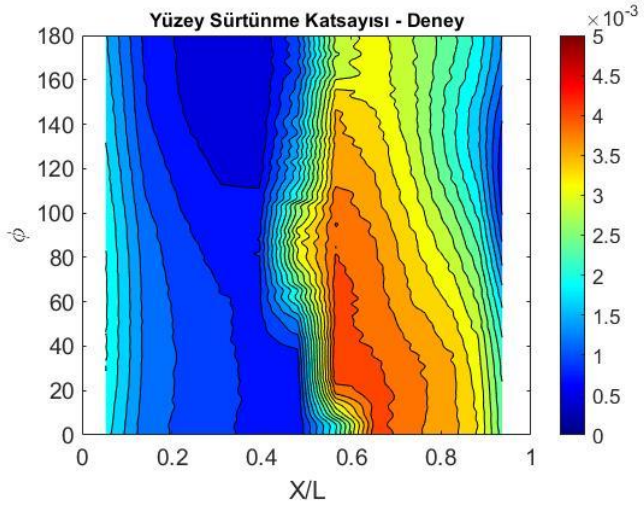
(c) γ-Re_Θ, düzey-3 ağ

(f) *k-kl-*ω, düzey-3 ağ

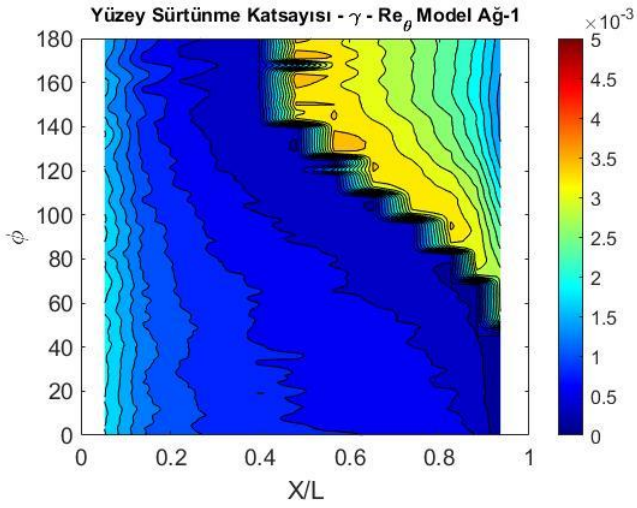
Şekil 2 Yüzey Sürtünme Katsayı Dağılımı.

Kreplin v.d. (1985) tarafından yapılan deney sonuçları düzey-1 çözüm ağı ile elde edilen analiz sonuçları ile Şekil 3'te karşılaştırılmıştır. Deneysel çalışamada sunulan tablolar incelendiğinde her bir eksenel pozisyondaki ölçüm noktaların birbirine göre farklı çevresel açılarda (ϕ) ve farklı sayılarda olduğu görülmüştür. Ölçüm noktalarının düzensiz olmasının yanı sıra, sayısal çalışmada düzensiz çözüm ağının kullanılması ve farklı çözüm ağı büyüklüklerinin olması sebebiyle tüm sonuçların birbiriyle aynı noktalarda karşılaştırılabilmesi için sonuçların belli noktalarda iç kestirim metoduyla elde edilmesi gerekmiştir. Sayısal analizlerde elde edilen yüzey parametreleri deneysel sonuçlarda olduğu gibi on iki eksenel pozisyon (x/L) için ayıklanmıştır. Sonrasında parametreler, tüm eksenel pozisyonlarda 0^o ila 180^o çevresel açı aralığında 1^o aralıkla üçüncü dereceden iç kestirim yöntemiyle hesaplanmıştır. Böylece hem deneysel hem sayısal sonuçlar için 181 x 12 veri seti elde edilmiş ve Şekil 3'te görülüğü şekilde yüzey dağılımları elde edilmiştir.

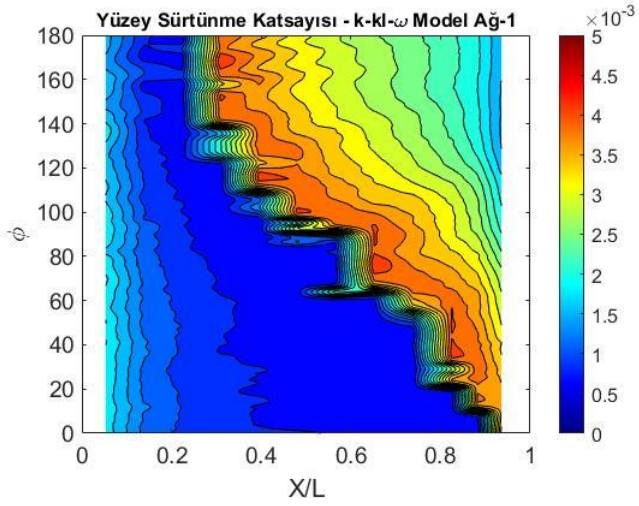
Şekil 3(a)'da verilen deneysel veri incelendiğinde türbülans geçişinin yaklaşık boyun yarısında olduğu, üst tarafın buruna biraz daha yakın olduğu gözlenmektedir. Şekil 3(b) ve Şekil 3(c)'de γ-Re_Θ ve k-kl-ω geçiş modeli sonuçlarındaki farklar daha belirgin görünmektedir. k-kl-ω geçiş modelinde geometrinin üst tarafında türbülans geçisi deneysel veriye göre daha önde oluşmaktadır. Gövdenin alt yüzeyine inildikçe γ-Re_Θ modelinde olduğu gibi geçişin arkaya doğru kaydığı görülse de alt kısımda türbülans deneysel veride olduğu başladığı görülmektedir. Fakat k-kl-ω geçiş modelinin geçiş yer tahmini deneysel veriye göre oldukça arkadadır.



(a) Deneysel veri



(b) γ-Re_Θ



(c) k-kl-ω

Şekil 3 Yüzey Sürtünme Katsayı Dağılımının Deneysel Veri ile Karşılaştırılması (Düzey-1 Çözüm Ağı).

4. SONUÇ

Bu çalışmada, k-kl-ω türbülans geçiş modelinin düzensiz çözüm ağ kullanılarak 6:1 küremsi geometri üzerinde başarım değerlendirmesi, 6.5 x 10^6 Reynolds sayısında ve 5^o hücum açısında yapılmıştır. Değerlendirmede, yaygın kullanılan γ-Re_Θ türbülans geçiş modeli ve deneysel ölçümlerle elde edilmiş sonuçlar kullanılmıştır. Geçiş modelinin etkisi eksenel kuvvet, yanal kuvvet, yüzey basınç ve sürtünme katsayıları kullanılarak gösterilmiştir. Ayrıca, elde edilen kuvvet katsayıları etrafındaki hata band tahmini GCI metodu kullanılarak gerçekleştirilmiştir. k-kl-ω türbülans geçiş modeli γ-Re_Θ modeline göre eksenel kuvvet katsayısını yaklaşık %50, normal kuvvet katsayısını ise yaklaşık %30 fazla tahmin etmektedir. k-kl-ω türbülans geçiş modeli ile elde edilen sonuçlar etrafındaki hata bandı tahmini ise normal kuvvet katsayısında daha fazla olduğu tespit edilmiştir. Fakat γ-Re_Θ modeli eksenel kuvvet katsayısı etrafındaki belirsizlik bandını daha büyük bulmaktadır.

Geçiş modellerinin kullanılması yüzey basınç katsayılarında önemli bir değişiklik yaratmamıştır. Fakat yüzey sürtünme katsayısında önemli değişiklikler gözlemlenmiştir. Yüzey sürtünme katsayılarının ani değişimleri türbülans geçişine işaret etmesi sebebiyle yüzey üzerinde geçişin olduğu yerlerde de önemli farklılıklar görülmektedir. Çözüm ağı büyüklüğünün azalması geçiş bölgesini her iki modelde de arkaya doğru kaydırmaktadır. Geçiş bölgesi geometrisi, bir başka deyişle gövde üzerindeki türbülans geçiş yerleri hem çözüm ağına hem de modele göre farklılıklar göstermektedir. Fakat çözüm ağı büyüklüğüyle değişimin k-kl-ω türbülans geçiş modelinde daha belirgin olması bu modelin çözüm ağı büyüklüğüne daha hassas olduğunu göstermektedir.

Deneysel olarak elde edilen yüzey sürtünme katsayıları ile geçiş modelleri kullanılarak elde edilen yüzey sürtünme katsayıları karşılaştırıldığında modellerin geometrinin üst yüzeyindeki türbülans geçiş yerini deneye göre daha önde buldukları, k-kl-ω türbülans geçiş modelinin geometrinin alt kısmında geçişi tahmin edebildiği halde deneye göre arkada bulduğu tespit edilmiştir. Bu farklılık geçiş modellerinin halen iyileştirmeye açık olduğunu göstermektedir. Geçiş model kullanıcılarının modelleri kullanmadan önce ilgilendikleri akış durumları için farklı geçiş model sonuçlarını karşılaştırılmaları, mümkün olduğunca benzer geometri ve akış durumlarında elde edilmiş deneysel sonuçlarla başarımlarını karşılaştırmaları tavsiye olunur.

KAYNAKÇA

1. **Schlichting, H., and Gersten, K., (2000),** Boundary-Layer Theory, 8th ed., Springer-Verlag, Berlin, Heidelberg.

2. **Sengupta, T. K., (2012),** Instabilities of Flows and Transition to Turbulence, CRC Press, Boca Raton.

3. **Versteeg, H.K., and Malalasekera, W., (2007),** An Introduction to Computational Fluid Dynamics, The Finite Volume Method, Pearson Education Limited. ISBN: 978-0-13-127498-3.

4. **Wauters, J., and Degroote, J. (2018),** "On the Study of Transitional Low-Reynolds Number Flows over Airfoils Operating at High Angles of Attack and Their Prediction Using Transitional Turbulence Models", Progress in Aerospace Sciences, Vol. 103, pp. 52–68.

5. **Eca L., Hoekstra M. (2008),** "The Numerical Friction Line", Journal of Marine Science and Technology, Vol. 13, No.4, pp. 328-345.

6. **Pasquale, D. D., Rona, A., and Garrett, S. J. (2009),** "A Selective Review of CFD Transition Models", 39th AIAA Fluid Dynamics Conference, San Antonio, Texas, AIAA Paper 2009-3812.

7. **Boiko, A. V., Kirilovskiy, S. V., Maslov, A. A., and Poplavskaya, T. V. (2015)**, "Engineering Modelling of the Laminar-Turbulent Transition: Achivements and Problems (Review)", Journal of Applied Mechanics and Technical Physics, Vol. 56, No. 5, pp. 761–776.

8. **Krumbein, A., Krimmelbein, N., Grabe, C., and Shengyang, N., (2015),** "Development and Application of Transition Prediction Techniques in an Unstructured CFD Code", AIAA 2015-2476, AIAA Aviation 45th AIAA Fluid Dynamics Conference, Dallas, TX, 22-26 June 2015.

9. **Menter, F. R, Langtry, R. B., Likki, Y. B., Suzen, Y. B., Huang, P. G. and Volker, S. (2006),** "A Correlation-Based Transition Model Using Local Variables: Part I — Model Formulation", Journal of Turbomachinery, 128(3), pp. 412-422.

10. **Langtry, R. B,. and Menter, F. R. (2009),** "Correlation-Based Transition Modeling for Unstructured Parallelized Computational Fluid Dynamics Codes", AIAA Journal, Vol. 47, No. 12, pp. 2894–2906.

11. **Menter, F. R. (1994), "**Two-Equation Eddy-Viscosity Turbulence Models for Engineering Applications", AIAA Journal, Vol. 32, No. 8, pp. 1598–1605.

12. **Vaz, G., Jaouen, F., and Hoekstra, M. (2009),** “Free-Surface Viscous Flow Computations: Validation of URANS Code FreSCo”, 28th International Conference on Ocean, Offshore and Arctic Engineering, Vol. 43451, 2009, pp. 425–437.

13. **Lopes, R., Eca, L., Vaz, G., and Kerkvliet, M. (2021),** “Assessing Numerical Aspects of Transitional Flow Simulations Using the RANS Equations”, International Journal of Computational Fluid Dynamics, Vol. 135, No. 3, pp. 157-178.

14. **Seyfert, C., Krumbein, A. (2012, January),** “Correlation-Based Transition Transport Modeling For Three-Dimensional Aerodynamic Configurations”, In 50th AIAA Aerospace Sciences Meeting including the New Horizons Forum and Aerospace Exposition (p. 448).

15. **Atik, H. (2022),** “Estimation of Discretization Uncertainty using the γ-Reθ Transition Model for Transitional Flows on 6:1 Spheroid”, ASME Journal of Fluids Engineering, Vol. 144, pp. 111501-1-12.

16. **Walters, D. K., and Cokljat, D. (October 24, 2008).** "A Three-Equation Eddy-Viscosity Model for Reynolds-Averaged Navier–Stokes Simulations of Transitional Flow." ASME. J. Fluids Eng, Vol. 130(12), pp 121401.

17. **Meier, H. U., and Kreplin, H. P. (1980),** “Influence on Free-Stream Turbulence on the Boundary Layer Development”, AIAA Journal, Vol. 18, No. 1, pp. 11-15.

18. **Celik, I.B., Ghia, U., Roache, P. J., Freitas, C. J., Coleman, H., and Raad, P. E. (2008),** “Procedure for Estimation and Reporting of Uncertainity Due to Discretization in CFD Applications”, Journal of Fluids Engineering, Vol. 130, pp. 078001-1-4.

19. **Phillips, T. S., and Roy, C. J., (2014),** "Richardson Extrapolation-Based Discretization Uncertainty Estimation For Computational Fluid Dynamics", Journal of Fluids Engineering Vol. 136 No. 12, pp. 21401-1-10.

DAİRE TESTERE TEZGAHLARINDA, KESİCİ TAKIM ÜZERİNDE OLUŞAN TİTREŞİMİN İŞ PARÇASINA ETKİSİNİN İNCELENMESİ

ÖZET

Testere tezgâhları, üretimde kullanılacak metal iş parçalarını kesme işlemi ile istenilen ölçülere getiren makinelerdir. Endüstride yaygın olarak kullanılan testere tezgâhları, üretim hatlarının ilk kısmında yer almaktadır. Bu sebeple, iş parçasının istenilen toleranslarda kesilememesi durumunda ciddi üretim ve malzeme kayıpları oluşmaktadır. Bu çalışmada, kesici takım üzerinde oluşan titreşimin, ölçü toleransına ve yüzey pürüzlüğüne olan etkisi incelenmiştir.

Anahtar Kelimeler: Testere tezgâhı, ölçü toleransı, yüzey pürüzlülüğü, titreşim

ABSTRACT

Saw benches are machines that bring the workpieces to be used in production to the desired dimensions by cutting. Saw benches, which are widely used in the industry, are located in the first part of the production lines. For this reason, if the workpiece cannot be cut within the desired tolerances, serious production and material losses occur. In this study, the effect of vibration on the cutting tool on perpendicularity tolerance and surface roughness was investigated.

Keywords: Saw bench, length tolerance, surface roughness, vibration

1. GİRİŞ

Takım tezgâhları ile malzeme üzerinden talaş kaldırma işlemleri esnasında meydana gelen ve kontrol edilemeyen titreşimler, elde edilen üründeki ölçü tamlığını, yüzey kalitesini, kesici takım ömrünü ve takım tezgahını etkilemektedir [1].

Talaş kaldırmada sürekli olarak, zorlanmış ve kendiliğinden oluşan olmak üzere iki türlü titreşim mevcuttur. Zorlanmış titreşim, takım tezgahının mekanik hareketlerinin toplam etkisinin sonucu ortaya çıkan titreşimdir. Kendiliğinden doğan titreşim ise talaş kaldırmadan dolayı, tezgâhtan ve dış çevreden bağımsız olarak oluşur. Bu şekildeki titreşime tırlama titreşimi denilmektedir. Bu titreşim esas itibariyle kesme hızı artığında kesme kuvvetinin

azalmasından meydana gelir. Tırlama titreşimi, iş parçalarında, boyutsal tamlıkta azalma, düşük işleme hassasiyeti, kesici takım aşınmaları ve kırılmaları, takım tezgahının zarar görmesi gibi üretimi sınırlayan etkenlere sebep olur [2].

GGG50 döküm malzemenin torna tezgâhında dört ayrı ilerleme ve kesme hızları referansında yapılan bir çalışmada, titreşimin, ses şiddetinin ve yüzey pürüzlülük değerlerinin karşılaştırılması yapılmıştır. İlerleme değeri artıkça titreşim değerinin, yüzey pürüzlülük değerinin ve ses şiddetinin arttığı görülmüştür.

Kesme hızı arttırıldığında ise titreşim ve ses şiddetinde kısmen bir azalma görülürken, yüzey pürüzlülük değerlerinden önemli bir değişiklik olmadığı saptanmıştır [3].

Benzer bir çalışmada, 34CrNiMo6 çeliğin farklı kesme parametreleri ile frezelenmesinde; iş yüzeyinde oluşan pürüzlülük değerleri ve tezgâhta oluşan titreşim değerleri incelenmiştir. Yapılan deneyler sonucunda, ilerleme miktarının artmasıyla yüzey pürüzlülük değerinin de artığı gözlemlenmiş kesme hızı ve talaş derinliğinin yüzey pürüzlülüğü değişiminde önemli bir etkisi olmadığı görülmüştür. Kesme hızı ve talaş derinliğinin artması durumunda titreşim değerinin arttığı tespit edilmiştir [4].

Bu doğrultuda, kesici takım üzerindeki ivme sensörü ile titreşim değerleri ölçülerek, titreşimin ölçü tamlığı ve yüzey kalitesine olan etkisi incelenmiştir.

2. MATERYAL VE METOT

Metal kesimi için şerit testere ve daire testere tezgâhları kullanılmaktadır. Şerit testereler, daha fazla esneklik gerektiren işlemler için idealdir. Çok çeşitli metal türlerini ve kalitelerini kesmede etkilidir. Titanyum ve nikel bazlı alaşımlar gibi sert metallerde de düzgün kesimler sağlar. Daire testereler ise yüksek hızlı ve tekrarlayan kesimler için uygundur. Titanyum, nikel gibi sert metalleri kesmede şerit testerelerin aksine etkili değildir.



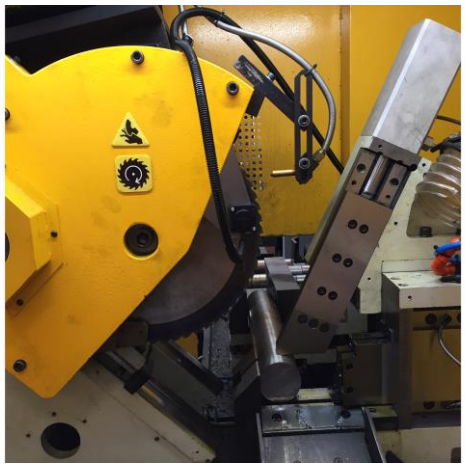
Şekil 1. Daire Testere Tezgahı



Şekil 2. Şerit Testere Tezgahı

Şerit testere makinelerinde, doğrusal kesim yapılması esnasında, kesici takımını karşıdan görecek şekilde konumlandırılan endüktif mesafe sensörleri sayesinde kesici takımın doğrusal hareketi kontrol edilmektedir. Bu sayede şerit testere makinelerinin doğrusal kesim yapması sağlanırken, daire testere makineleri ile gerçekleştirilen dairesel kesim işleminde bu uygulama kullanılamamaktadır. Bunun en büyük sebebi daire testere makinesinin yapı ve konstrüksiyonu nedeniyle şerit testere makinelerinde kullanılan sensörlerin daire testere makinelerine konumlandırılmasının mümkün olamamasıdır. Daire testere makineleriyle seri imalat yapıldığı göz önüne alındığında, kesim işlemi esnasında oluşan herhangi bir hata veya sapma nedeniyle oldukça ciddi üretim, malzeme kaybı yaşanmakta ve dolayısıyla hatalı kesime bağlı maliyet ve işlem süreleri oldukça artmaktadır. Bu sebeple kesici takım üzerinde konumlanan kola ivme sensörü yerleştirerek, ölçü tamlığı ve yüzey pürüzlülüğü arasındaki incelenmiştir.

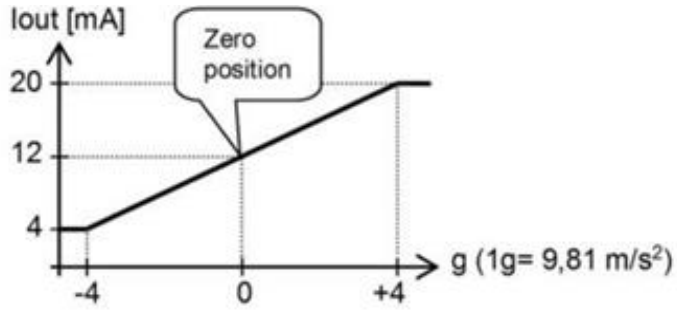
İvme sensörleri, ivme, titreşim ve mekanik şok değerlerini ölçmede kullanılan elektromekanik elemanlardır. İvme sensörlerinin farklı çalışma yöntemleri vardır. Bazı ivme sensörleri pieozoelektrik etkiyi kullanır. İçerdikleri mikroskobik kristal yapılar ivmesel kuvvetle gerilir; bu da voltaj üretilmesini sağlar. Bir başka yol da kapasitedeki değişimi algılamaktır. Birbirine yakın iki mikro yapı arasında kapasitif etki oluşur ve kapasitans değeri açığa çıkar. Kapasitif ivmeölçer; kapasitif iletim prensibi kullanılır. Sismik kütle olarak bir diyafram kullanılabilir. Bir ivme etkidiği zaman sabit elektrot ile sismik elektrot arasındaki mesafe değişir. Mesafenin değişmesiyle kapasitans değişir ve ivme ile orantılı bir çıkış elde edilir [5]. İvme sensörleri doğrudan titreşen nesnenin üzerine uygulanır, böylece ivme sensörünün titreşim enerjisini, nesnenin anlık ivmesi ile orantılı bir elektrik sinyaline dönüştürmesi sağlanır.



Şekil 3. BMDO 100 XS Daire Testere Tezgahı

Deney donanımı olarak; Beka-Mak firmasına ait BMDO 100 XS daire testere tezgâhı, DIS-Sensors firmasına ait QG serisi ivme sensörü kullanılmıştır. Sonuçlar analog input modulü üzerinden kontrolcüye aktarılmış ve çıktılar gözlenmiştir.

QG serisi sensörler 3 eksende ivme ölçme kabiliyetine sahiptir. Bu sensörler, kapasitans farklılıklarının bir mikro-mekanik sensör çipi içinde bir analog voltaja dönüştürülebildiği MEMS teknolojisine dayanmaktadır. MikroElektroMekanik sistemler (MEMS), Entegre Devre (IC) uyumlu toplu işleme teknikleri kullanılarak geliştirilen, elektrik ve mekanik bileşenlerle ilgili entegre mikro cihazlar veya sistemlerdir. Bu sistemler, mikro ölçekte algılama, kontrol etme ve harekete geçirme ve makro ölçekte efektler oluşturmak için ayrı ayrı veya diziler halinde işlev görme/çalıştırma yeteneğine sahiptir [6].



Şekil 4. QG40N Çalışma Aralığı

Kullanılan ivme sensörü 12 mA'da 0 g, 10 mA'da +4 g, 4 mA'da -4 g değerini vermektedir.

Kesici takım üzerinde yerleştirilen ivme sensörüyle z eksenindeki g değişimi dikkate alınarak titreşimin kesim boyu toleransı ve yüzey pürüzlülüğüne olan etkisi incelenmiştir. Deneyler, 2 farklı kesici takım (kullanılmış, yeni) ile sabit kesme ve ilerleme hızlarıyla toplamda 6 adet ∅70 mm Ck45 malzemeyle yapılmıştır.

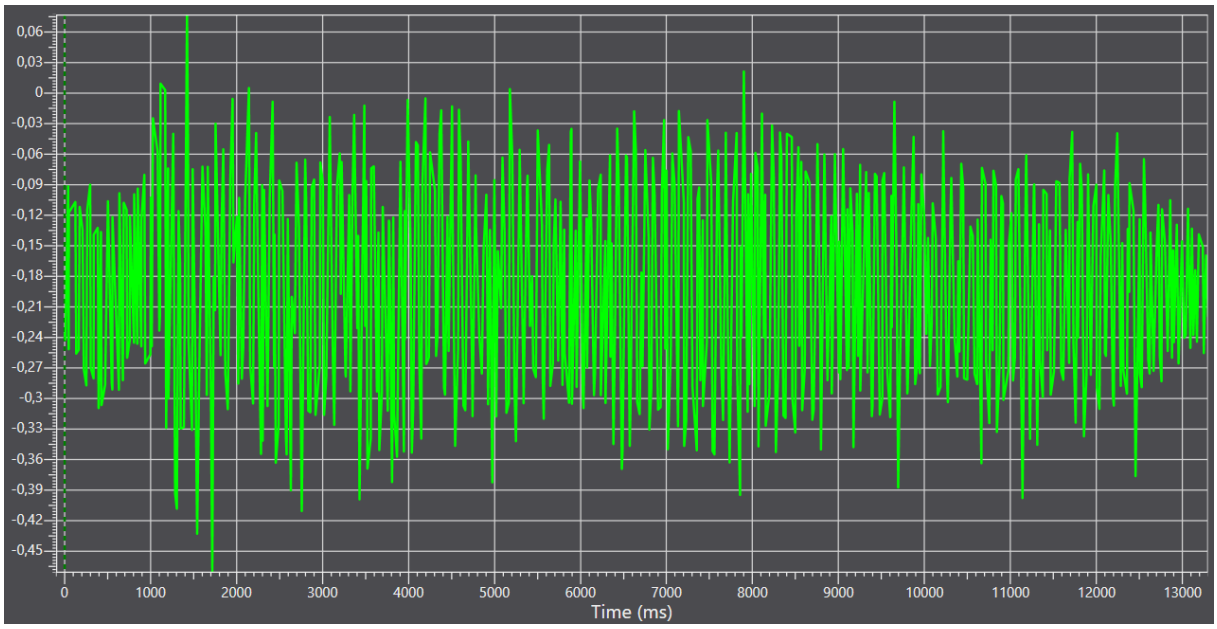
3. BULGULAR

Sysmac Studio programı ile sensör verileri gerçek zamanlı alınmış olup, data trace ile grafik haline getirilmiştir. Yer çekimi ivmesinin (z ekseninde), zaman domeninde değişimi incelenerek, maksimum sapma miktarı tespit edilmiştir. Yer çekimi ivmesindeki değişim ile kesme boyu toleransı ve yüzey pürüzlülüğü arasında matematiksel model oluşturularak programa entegre edilmiştir.

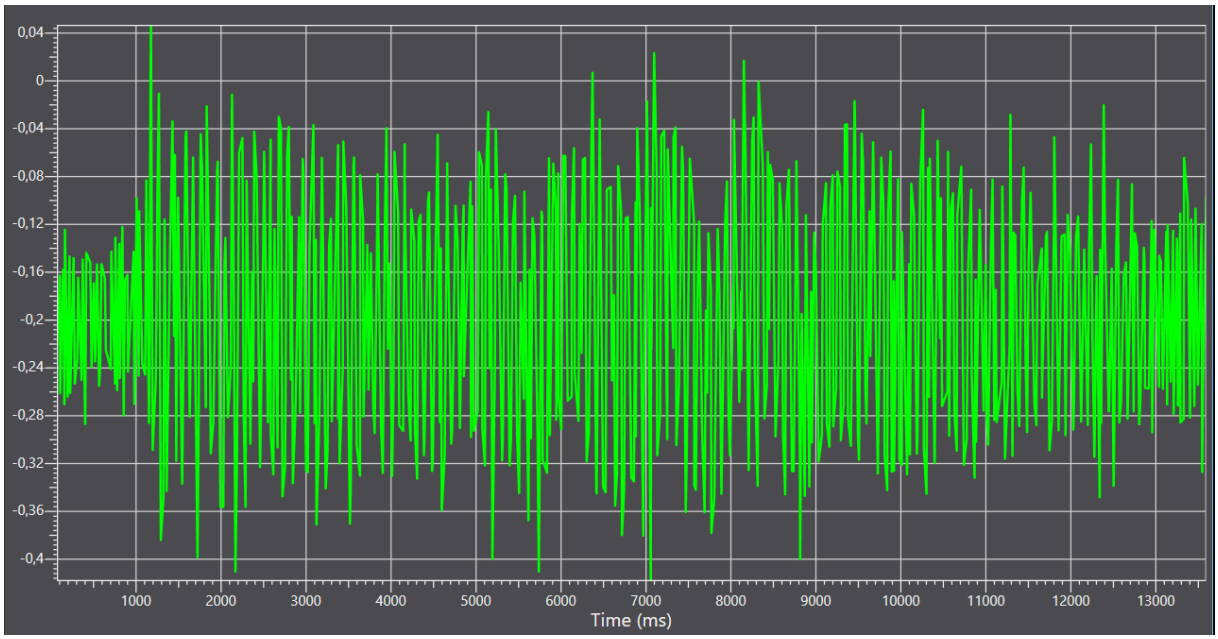
İlk 3 deney dişleri aşınmış kesici takım ile yapılırken, diğer 3 deney yeni kesici takım ile yapılmıştır. z eksenindeki g değişimleri ve yüzey pürüzlülüğü Ra cinsinden tabloda verilmiştir.

Tablo 1. g ve Ra değişimi

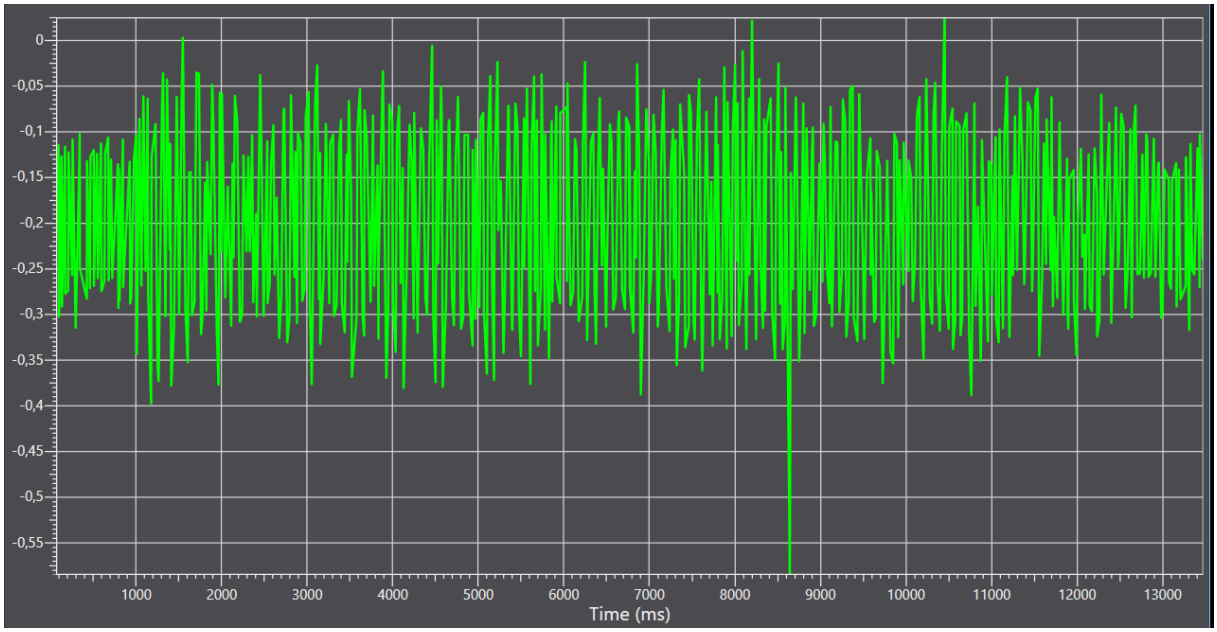
	g (+)	g (-)	g Değeri Sapma (1g = 9,81m/s2)	Ra (µm)
1.	0,079	0,474	0,474	1,44
2.	0,049	0,420	0,420	1,48
3.	0,028	0,587	0,587	1,7
4.	0,059	0,419	0,419	1,30
5.	0,015	0,409	0,409	1,44
6.	0,026	0,358	0,358	1,3



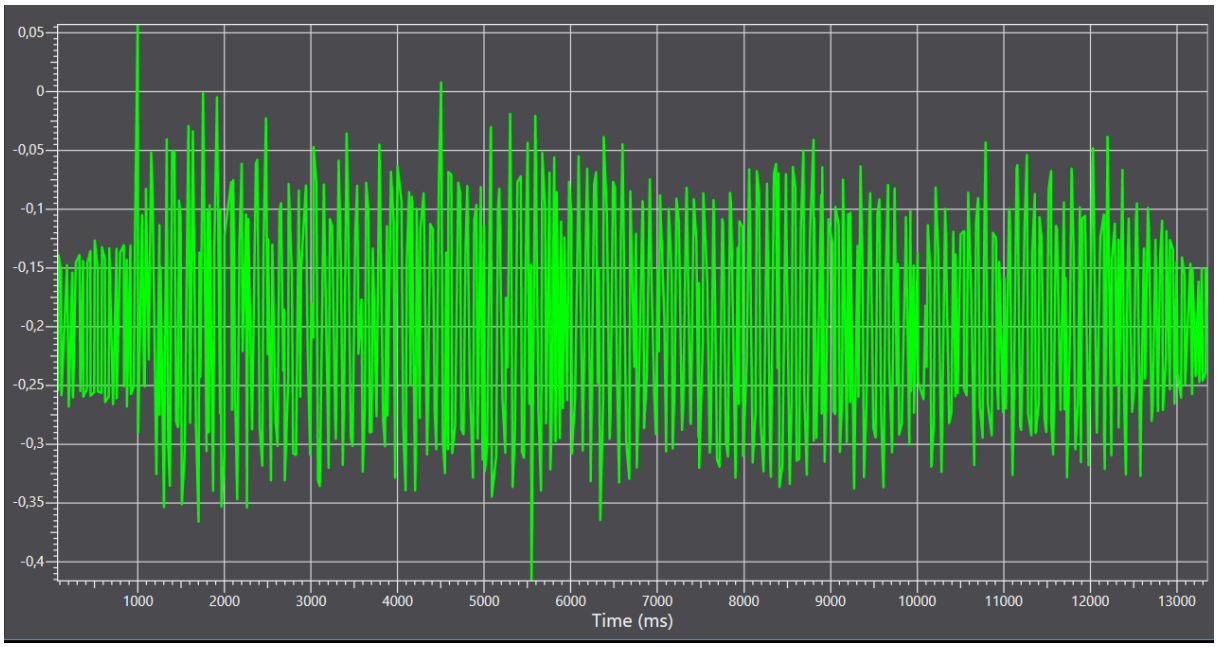
Şekil 5. Deney No 1



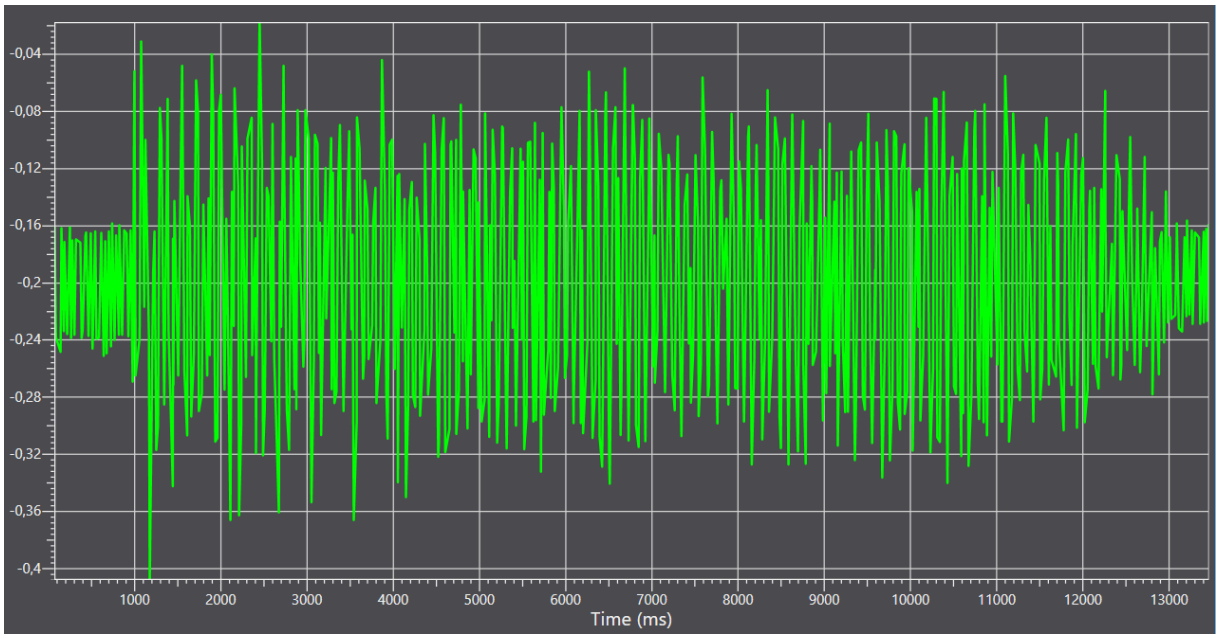
Şekil 6. Deney No 2



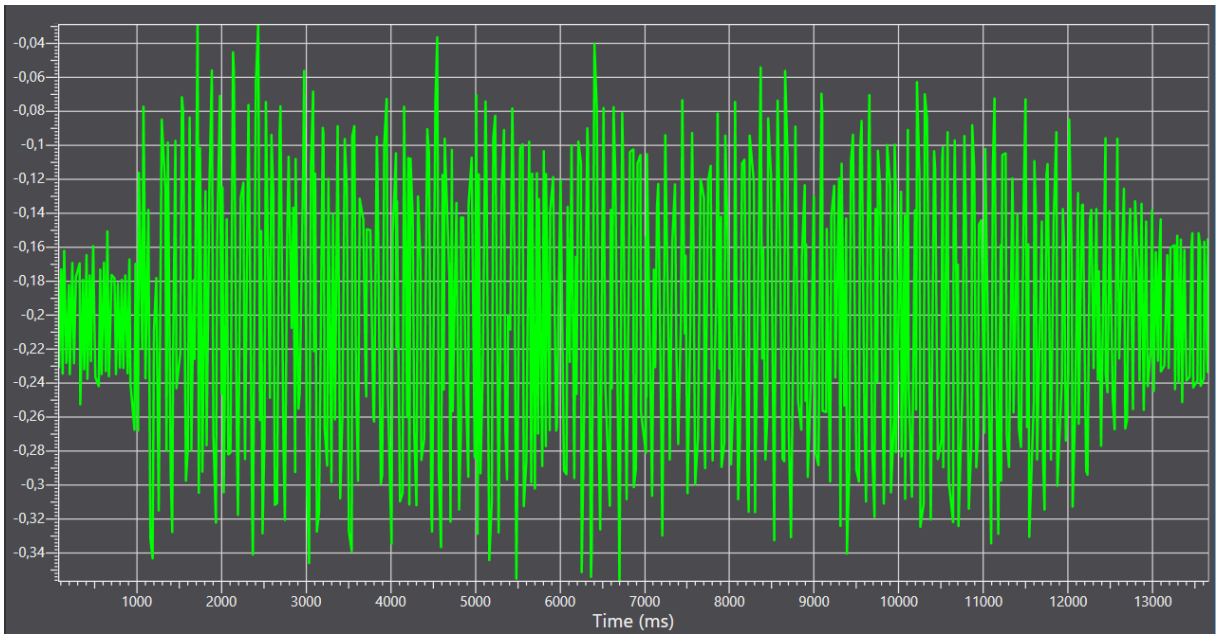
Şekil 7. Deney No 3



Şekil 8. Deney No 4

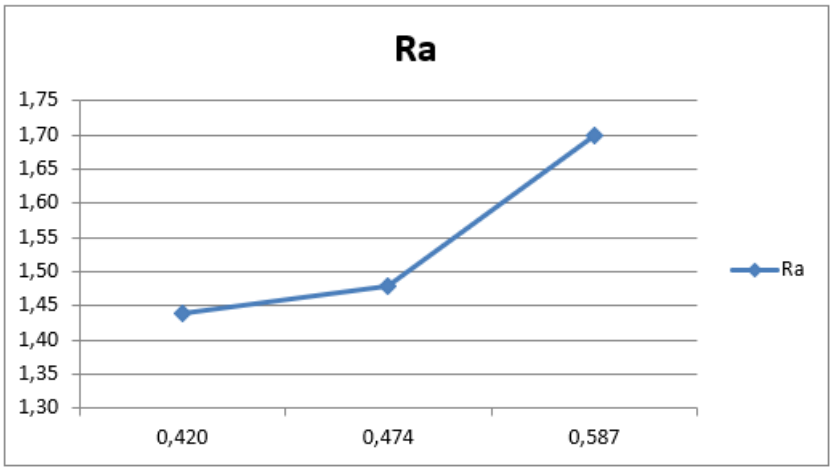


Şekil 9. Deney No 5

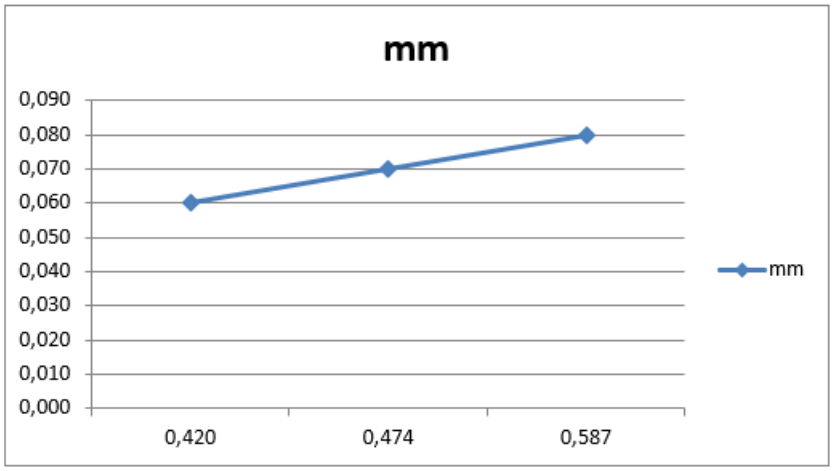


Şekil 10. Deney No 6

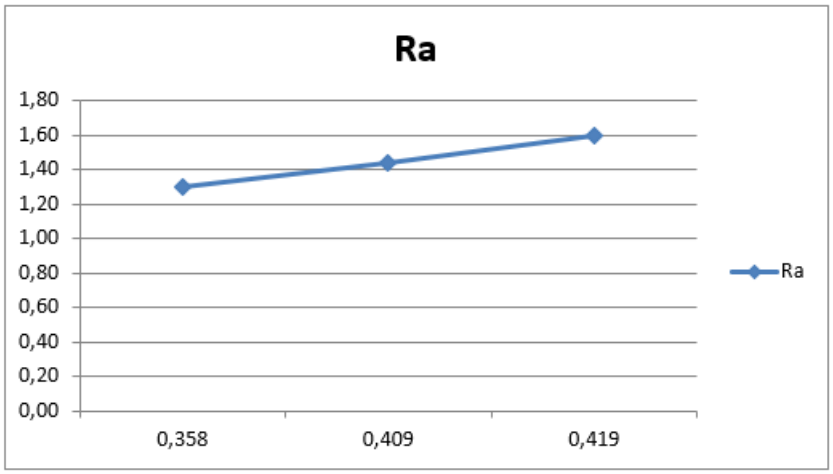
Aşınmış kesici takım ve yeni kesici takım ile yapılan test kesimlerinde, g değerindeki sapmanın aşınmış kesici takımda daha yüksek değerlerde olduğu gözlenmiştir. Maksimum sapma 3. Deneyde oluşurken, minimum sapma 6. deneyde oluşmuştur. Aşınmış kesici takımdaki ortalama sapma değeri 0,587.g iken, yeni kesici takımda bu değer 0,358.g'dir.



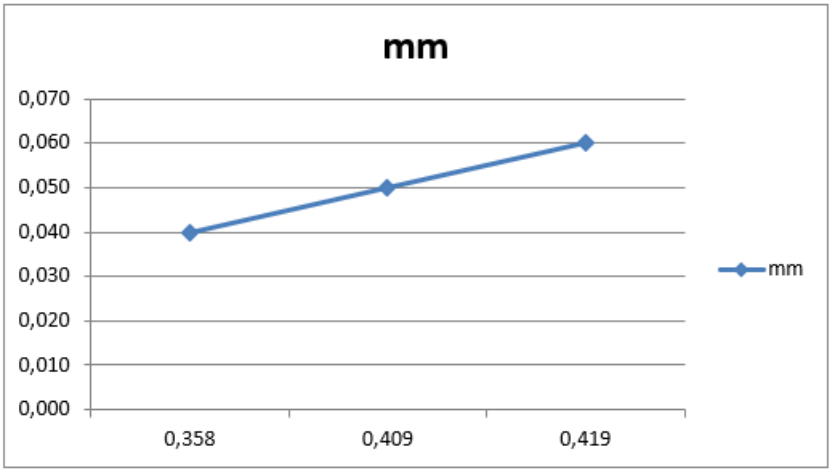
Şekil 11. Aşınmış Kesici Takım Ra Değişimi



Şekil 12. Aşınmış Kesici Takım Kesim Ölçüsü Değişimi



Şekil 13. Yeni Kesici Takım Ra Değişimi



Şekil 14. Yeni Kesici Takım Kesim Ölçüsü Değişimi

4. SONUÇLAR

Çalışma, titreşim genliğinin ölçü tamlığı ve yüzey pürüzlülüğü üzerinde büyük bir etkiye sahip olduğunu ortaya koymuştur. Artan takım aşınması ile titreşim büyüklüğündeki artış, ölçü tamlığını azaltırken, yüzey pürüzlülük değerini artırmaktadır. Aşınmış ve yeni kesici takıma ait g değişimi ile, kesim ölçüsü ve yüzey pürüzlülüğü arasında lineer bir değişim gözlenmiştir.

Gelecekte deney sayılarının arttırılması ile daha hassas sonuçlara ulaşılabilecektir. Sonuçların kuvvet ölçümü ile de zenginleştirilerek anlamlandırılması ile de makine yazılımları değiştirilebilecektir.

KAYNAKÇA

1. **Sezan ORAK, Erol TÜRKEŞ, "**Tornalamada Ortogonal Kesme İçin Tırlama Titreşimi ve Kararlılığın Lineer Analizi", Eskişehir Osmangazi Üniversitesi Müh.Mim.Fak.Dergisi C.XIX, S.2, 2006
2. **Volkan YILMAZ (2014), "**Frezeleme İşlemlerinde Titreşimi ve Yüzey Pürüzlülüğünü Etkileyen Parametrelerin Optimizasyonu", SDU Teknik Bilimler Dergisi, Cilt 4, Sayı1, Sayfa 37-44
3. **A. Şahinoğlu, A. Güllü, A. Dönertaş**, "GGG50 Malzemenin Torna Tezgâhında İşlenmesinde Kesme Parametrelerinin Titreşim, Ses Şiddeti ve Yüzey Pürüzlülüğü Üzerinde Etkisinin Araştırılması", Sinop Üniversitesi Fen Bilimleri Dergisi, cilt 2(1), sayfa 67-79, Şubat 2017.
4. **M. Erbaş, A. Güllü**, "34CrNiMo6 Çeliğinin Frezelenmesinde Kesme Parametrelerinin Titreşim ve Yüzey Pürüzlülüğüne Etkilerinin İncelenmesi", Politeknik Dergisi, cilt 22(3), sayfa 633-939, 2019.
5. ***Tevfik KADIOĞLU1, Hasan DİNÇER2, "***İvme Sensörü Uygulaması***"***
6. **Manish Kumar Mishra**, "MEMS Technology: A Review", Research Scholar, School of Engineering and Technology, Career Point University, Kota, Rajasthan, 2019

TAVLAMA BENZETİMİ YÖNTEMİ VE YANIT YÜZEY METODU KULLANILARAK YÜZEY PÜRÜZLÜLÜĞÜ İÇİN İŞLEME PARAMETRELERİNİN OPTİMİZASYONU

Y. Emre NEHRİ, *yunusnehri@balikesir.edu.tr* Balıkesir Üniversitesi, 10145, Balıkesir

Enes EZME, *eezme@alp.com.tr* Alp Havacılık, 26110, Eskişehir

Gülşen AYDIN KESKİN, *gülsen.keskin@balikesir.edu.tr* Balıkesir Üniversitesi, 10145, Balıkesir

Ali ORAL, *a.oral@balikesir.edu.tr* Balıkesir Üniversitesi, 10145, Balıkesir

ÖZET

Üretimin temel yapı taşlarından biri talaşlı imalattır. Üretilen parçaların kendilerinden beklenen fonksiyonları yerine getirebilmesi için yüzey kalitesi ve toleransların önemi bilinmektedir. Endüstride yaygın şekilde kullanılan AISI 304L paslanmaz çelikler tornalanırken kesme parametrelerinin optimizasyonu üzerinde çok fazla çalışma bulunmamaktadır. Bu çalışmada, AISI 304L paslanmaz çelikler tornalama işlemine tabi tutulmuştur. Kesme parametreleri optimize edilerek en iyi yüzeyin elde edilmesi yani yüzey pürüzlülüğünün minimum seviyede tutulması amaçlanmıştır. Çalışmada kullanılan kesme parametreleri olarak kesme hızları, ilerleme ve paso değerleri alınmış olup bunların sonucunda oluşan yüzey pürüzlülük değerleri ölçülmüştür. Giriş parametreleri için tam faktöriyel deney tasarımı oluşturulmuştur. Giriş parametrelerinden yüzey pürüzlülüğü üzerinde etkin olan parametre ilerleme olarak belirlenmiştir. Minimum yüzey pürüzlülüğü için tavlama benzetimi yöntemi kullanılmış ve optimum kesme parametreleri olarak 132 m/dak kesme hızı, 1,5 mm paso ve 0,11 mm/dev değerleri elde edilmiştir.

ABSTRACT

One of the basic elements of production is machining. The importance of surface quality and tolerances is known so that the manufactured parts can perform the functions expected from them. There are not many studies on optimization of cutting parameters when turning AISI 304L stainless steels, which are widely used in the industry. In this study, AISI 304L stainless steels were machined. By optimizing the cutting parameters, it is aimed to obtain the best surface, that is, to keep the surface roughness at a minimum level. Cutting speeds, feed, and depth of cut values were taken as the cutting parameters used in the study, and the resulting surface roughness values were measured. A full factorial experimental design was created for

the input parameters. The parameter that is effective on the surface roughness was determined as the feed. Simulation Annealing method was used for minimum surface roughness and optimum cutting parameters were obtained as 132 m/min cutting speed, 1,5 mm depth of cut and 0,11 mm/rev.

GİRİŞ

Talaşlı imalat, önceden dizaynı yapılıp standartlara uygun olarak projelendirilmiş teknik resmi referans alınarak uygun talaşlı imalat tezgahlarında, belirlenmiş kesici takımlar yardımı ile, parça üzerinden farklı şekil ve büyüklüklerde talaş kaldırılarak istenilen geometrik şekli verme işlemidir. Temel amaç, geometrik şekli vermekle birlikte tasarlanan ürünlerin en düşük maliyetle, en yüksek kalitede ve en verimli yöntemle, ölçü tamlığına uygun bir şekilde elde edilmesidir. Bu amacın yerine getirilmesi için talaş kaldırma işleminde uygun kesici takımın seçilmesi ve ayrıca kesme parametrelerinin en iyilenmesi gerekir. Doğru kesici takım seçilmiş olmasına rağmen kesme parametreleri uygun değil ise işleme süreleri artabilecek, yüzey kalitesi bozulabilecek ve dahası iş parçası ıskartaya ayrılabilecektir. Bu çalışmada da endüstride yaygın bir şekilde kullanılan AISI 304L paslanmaz çeliğinin işlenmesi için kesme parametreleri incelenmiştir.

Shunmugesh K ve diğ. çalışmalarında, 11SMn30 otomat çeliğini tornalamak için farklı kesme hızı, ilerleme ve talaş derinliği değerlerini kullanarak Taguchi yöntemiyle yüzey pürüzlülüğü için varyans analizi ve optimizasyon yapmışlardır. İlerlemenin yüzey pürüzlülüğü üzerinde en etkin parametre olduğu sonucuna varmışlardır [1].

Lalwani ve diğ. çalışmalarında, MND250 çeliğini tornalamak için farklı kesme hızı, ilerleme ve talaş derinliği değerlerini kullanarak yanıt yüzey metoduyla yüzey pürüzlülüğü ve kesme kuvveti için varyans analizi ve optimizasyon yapmışlardır. İlerlemenin yüzey pürüzlülüğü üzerinde en etkin parametre olduğu sonucuna varmışlardır [2].

Sahithi ve diğ. çalışmalarında, farklı alüminyum alaşımlarını (6061,6063 ve 6082) tornalarken farklı kesme hızı, ilerleme ve talaş derinliği değerlerini kullanarak Taguchi yöntemiyle yüzey pürüzlülüğü için optimum işleme parametrelerini belirlemişlerdir. Al 6063 ‘ün diğerlerine göre daha kolay işlenebildiği sonucuna varmışlardır [3].

Sahu ve Choudhury çalışmalarında, AISI4340 çeliğini kaplamalı ve kaplamasız kesici uçlar kullanarak tornalarken farklı kesme hızı, ilerleme ve talaş derinliği değerleri kullanarak Taguchi

yöntemiyle yüzey pürüzlülüğü için optimum işleme parametrelerini belirlemişlerdir. Yüksek kesme hızı ve düşük ilerleme değerinde yüzey pürüzlülüğünün daha iyi olduğu ve ilerlemenin yüzey pürüzlülüğü üzerinde en etki parametre olduğu sonuçlarına varmışlardır [4].

Mozammel ve diğ. çalışmalarında, AISI1060 çeliğini minimum miktarda yağlamayla tornalarken farklı kesme hızı, ilerleme ve talaş derinliği değerleri kullanarak Taguchi yöntemiyle yüzey pürüzlülüğü, aşınma ve talaş kaldırma oranı için varyans analizi ve optimizasyon yaparak optimum parametreleri belirlemeye çalışmışlardır [5].

Wika ve diğ. çalışmalarında, AISI304L paslanmaz çeliği kesme sıvısı ve minimum miktarda yağlamayla kritik karbondioksit soğutmayla işlerken farklı kesme hızı ve ilerleme değerleri kullanarak kesme parametrelerinin yüzey pürüzlülüğü, takım aşınması, mikro sertlik ve yan yüzey kalıntı gerilmeleri üzerindeki etkilerini incelemişlerdir. Kullanılan soğutma yöntemiyle takım ömründe iyileşmeler olduğu sonucuna varmışlardır [6].

Gupta ve Kill çalışmalarında, cam fiber kompozitleri işlerken farklı kesme hızı, ilerleme ve kesme derinliği değerlerini kullanarak deney tasarımı yapılıp, radyal kuvvet için varyans analizi yaptıktan sonra tavlama benzetimi algoritmasıyla da optimizasyon yapmışlardır. Çalışmalarının sonucunda kesme derinliğinin radyal kuvvet üzerinde en büyük etkiye sahip olduğu sonucuna varmışlardır [7].

Kolahan ve Abachizadeh çalışmalarında, tornalamada işleme parametrelerini optimize etmek için tavlama benzetimi algoritmasını geliştirmişlerdir. Son ürün parçasını minimum toplam maliyetle elde etme, amaçları arasındadır. Hesaplama sonuçları, önerilen optimizasyon prosedürünün, toplam operasyonu önemli ölçüde iyileştirdiğini göstermişlerdir [8].

Kolahan ve diğ. çalışmalarında, St 50-2 çeliğini tornalarken farklı kesme hızı, ilerleme ve kesme derinliğini kullanarak Grey ilişkisel analiz ve tavlama benzetimi algoritmasıyla yüzey pürüzlülüğü ve talaş kaldırma oranını optimize etmişlerdir. Geliştirdikleri çok amaçlı modelde (multi objective models) kesme hızının en etkin parametre olduğu sonucuna varmışlardır [9].

Jabri ve diğ. çalışmalarında, farklı kesme hızı, ilerleme, kesme derinliği ve kesme derinliği değerlerini kullanarak tornalama işlemini yapmışlardır. Maliyet ve kalite için Hibrit Genetik Tavlama Benzetimi Algoritmasını kullanarak çok geçişli tornalama işleminin optimizasyonunu sağlamışlardır [10].

Rudrapati ve diğ. çalışmalarında, paslanmaz çelikleri taşlarken farklı iş hızı, yüzeye doğru ilerleme ve boyuna ilerleme değerlerini kullanarak yanıt yüzey metoduyla matematiksel model

oluşturup tavlama benzetimi algoritmasıyla yüzey pürüzlülüğü için optimizasyon yapmışlardır. Yüzey pürüzlülüğü üzerinde iş hızının daha etkili olduğu sonucuna varmışlardır [11].

Bu çalışmada, AISI 304L paslanmaz çeliklerin işleme parametrelerinin yüzey pürüzlülüğü üzerinde nasıl etkiye sahip oldukları ve minimum yüzey pürüzlülüğünü sağlamak için optimizasyon çalışması yapılmıştır. Kesme parametrelerinin yüzey pürüzlülüğü üzerindeki etkileri için varyans analizi yapılmış, yanıt yüzey metoduyla da matematiksel model oluşturulup minimum yüzey pürüzlülüğü değerini elde etmek için tavlama benzetimi yöntemi kullanılarak kesme parametrelerinin optimizasyonu yapılmıştır.

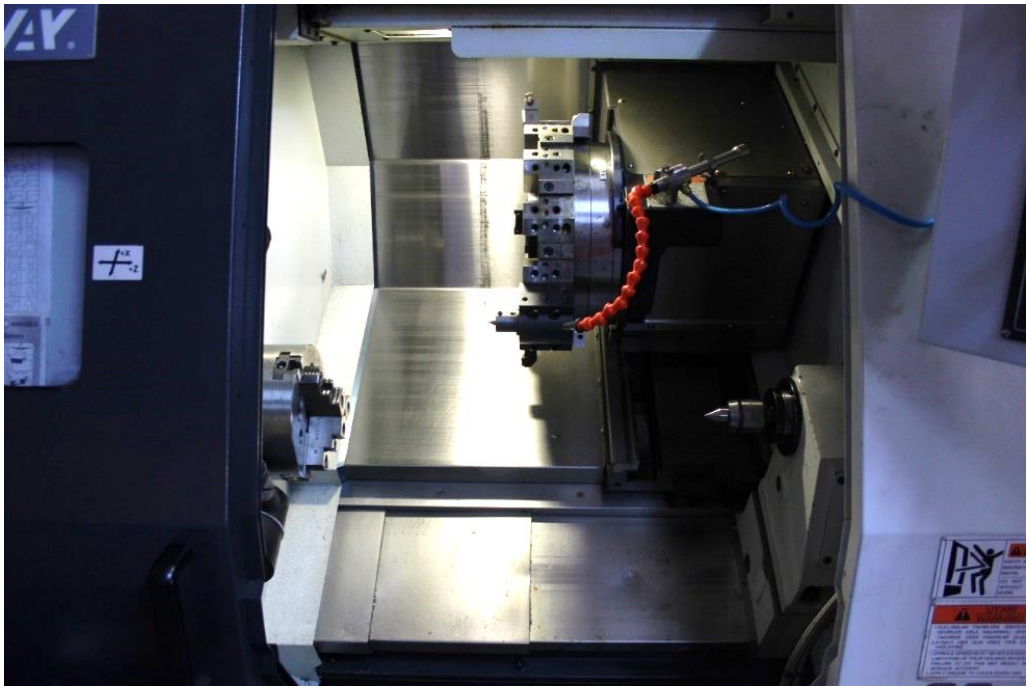
MATERYAL METOT

Deneyler, özellikleri Tablo 1'de verilen Goodway GS-200 torna tezgahında (Şekil 1) ϕ25 mm AISI 304L paslanmaz çeliklerin (

Tablo 2 ve Şekil 2) 100 mm tornalanmasıyla gerçekleştirilmiştir. Tornalama işlemi için farklı kesme parametreleri kullanılarak deney tasarımı (Tablo 3) oluşturulmuştur. İşleme yapılırken, daha önce ön deneyleri yapılmış ve farklı özelliklere sahip kesici uçlar arasında karşılaştırma yapılarak seçilmiş olan Al2O3+TiNC kaplamaya sahip CVD SUMITOMO kesici uçları kullanılmıştır.

Tablo 1 CNC tezgaha ait özellikler

Modeli	Kontrol Ünitesi	Motor Gücü (kW)	Max. İş Mili Devri (d/dak)
GS-200	Fanuc	11	4800

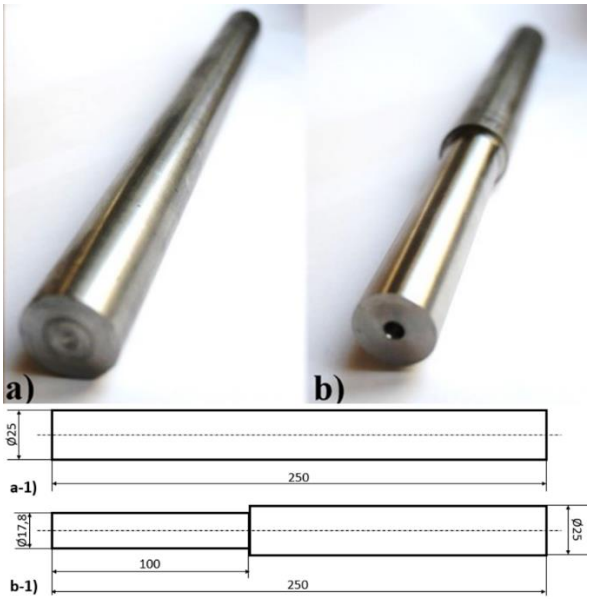


Şekil 1. CNC tezgahı

Tablo 2 AISI 304L paslanmaz çeliğin mekanik ve kimyasal özellikleri

Mekanik Özellikleri							
Malzeme		Akma Mukavemeti (N/mm^2)		Çekme Mukavemeti (N/mm^2)		Sertlik (HB)	
304L Paslanmaz Çelik (1.4307/X2CrNi18-9)		205		515		232	
Kimyasal Özellikleri (%)							
C	Si	Mn	Cr	Ni	P	S	N
0,01	0,57	1,86	18,07	8,19	0,03	0,024	0,088

Tam faktöriyel tasarımda giriş parametrelerinin hepsini birbiriyle ilişkili olacak şekilde bir tasarım sunmaktadır. Giriş parametrelerinin sonuçların üzerindeki etkileri varyans analizi (ANOVA) ile ortaya konulup incelenebilmektedir. Yanıt yüzey metodu, deneysel faktörlerin uygunluğunu, giriş parametreleri arasındaki performansı ve matematiksel modeli oluşturmada yardımcı olmaktadır. Giriş parametreleri ile çıkış parametreleri arasındaki matematiksel modeli oluşturmaktadır [12].



Şekil 2 Deney numunesi (a-işlenmemiş, b-işlenmiş)

Tablo 3 Deney tasarımı

Kesme Hızı (m/dk)	100	120	140	160	180
İlerleme (mm/dev)	0,11			0,15	
Kesme Derinliği (mm)	0,9		1,2		1,5

Tavlama benzetimi algoritması, çok değişkenli fonksiyonların maksimum ve minimum değerlerinin bulunması ve birçok yerel minimumu olan doğrusal olmayan fonksiyonların minimum değerlerinin bulunması için tasarlanmıştır. Algoritma, tavlama işlemi temelinde oluşturulmuştur. Fiziksel anlamda malzeme, tavlama sıcaklığına kadar ısıtılıp malzemenin iç yapısını daha kullanılabilir hale getirip sonrasında kademeli soğutulma işlemi yapılır. Tavlama benzetimi, mutlak minimum iç enerji yapısına ulaşmak için tavlama sürecini kullanarak oluşup büyüyen kristallerin istatistiksel sürecini simüle eden bir yaklaşımdır. Tavlama işlemindeki sıcaklık yavaşça düşürülmediği takdirde ve her sıcaklıkta yeterli zaman geçirilmezse, işlem iç enerji için yerel bir minimum durumda sıkışabilir. Ortaya çıkan kristal yapılar birçok iç kusura sebep olabilir. Sistemlerin optimizasyonu için tavlama benzetimi yöntemi uygulanabilir. Yeterince uzun bir süre çalıştırıldığında bu algoritma sürekli-ayrık-tamsayı değişkenli doğrusal olmayan programlama problemleri için global minimumları bulur.

Tavlama işlemine bu algoritmanın uygulanması, belli olan en iyi noktanın etrafında rastgele noktalar oluşturmak ve oradaki amaç fonksiyonlarını değerlendirmektir. Fonksiyon değeri mevcut en iyi değerden küçükse en iyi amaç fonksiyon değeri güncellenir. Eğer fonksiyon değeri bilinen en iyi değerden yüksekse o nokta ve karşılık gelen fonksiyon değeri genellikle

reddedilir. Noktanın kabulü, Boltzmann-Gibbs dağılımının olasılık yoğunluk değerine dayanmaktadır. Ancak bazı durumlarda, olasılık yoğunluk fonksiyonu rastgele bir sayıdan büyükse, fonksiyon değeri bilinen en iyi değerden yüksek olsa da deneme noktası kabul edilir. Olasılık yoğunluk fonksiyonu hesaplanırken sıcaklık parametresi kullanılır. Optimizasyon işleminde bu sıcaklık, kullanılacak fonksiyonun optimum değeri için hedef olarak kullanılabilir. İlk olarak daha büyük bir hedef değer seçilir işleme devam edilir. Denemeler ilerledikçe hedef değer yani sıcaklık düşürülür. Buna da soğutma program denir. Soğutma programında denemler yapıldıktan sonra süreç sonlandırılır. Soğutma işleminde sıcaklık düşüşüyle Kabul olasılığı sıfıra düşer. İlk aşamalarda metot bazen daha kötü tasarımları tercih ederken son aşamalarda daha kötü tasarımlar sürekli reddedilir. Bu durum da yerel minimumlardan kaçınmaya yardım eder.

Algoritmanın temel adımları;

1- Başlangıç sıcaklığı T_0 (fonksiyon için beklenen global minimum) ve uygulanabilir deneme noktası $x^{(0)}$ seçin. Sonra $f(x^{(0)})$'ı hesapla. L (beklenen minimum değere ulaşmak için deneme sayısının limiti) tamsayısı ve r<1 parametresi seçin. K=0 ve k=1 iterasyonlarını başlat.

2- Belirlenen nokta yakınlarında rastgele yeni $x^{(k)}$ noktası üret. Eğer nokta uygun değilse, uygun olana kadar rastgele nokta oluştur. $f(x^{(k)})$ ve $\Delta f=f(x^{(k)})-f(x^{(0)})$ hesapla.

3- Eğer $\Delta f<0$ ise $x^{(k)}$'yı en iyi nokta olarak $x^{(0)}$'a atayın, $f(x^{(0)})=f(x^{(k)})$ eşitliğini kur ve 4. Adıma git. Aksi takdirde muhtemel yoğunluk fonksiyonunu hesapla;

$$P(\Delta f) = \exp\left(\frac{\Delta f}{T_K}\right) \tag{1}$$

[0-1] arasında eşit olarak dağıtılmış rastgele bir *z* sayısı üret. $z<p(\Delta f)$ ise $x^{(k)}$'yı en iyi nokta olarak $x^{(0)}$'a ata ve 4. Adıma geç. Aksi takdirde 2.adıma geri dön.

4- Eğer k<L ise, k=k+1 olarak ayarla ve 2.adıma git. k>L ve durdurma kriterlerinden herhangi biri karşılanıyorsa durun. Aksi durumda 5. Adıma git.

5- K=K+1 ve k=1 eşitliğini, $T_k=rT_k$-1 eşitliğini kur ve 2. Adıma git.

Tavlama benzetimi yöntemi, daha önceden belirlenmiş kullanılacak fonksiyonu ve kısıt fonksiyonlarını değerlendirmektedir. Yöntem fonksiyonun sürekliliğine veya türevlenebilirliğine

ihtiyaç duymamaktadır. Bu yöntem, türevlenemeyen problemler, gradyanların hesaplanamadığı ve hesaplanması çok maliyetli olan problemler için faydalı olabilmektedir.

Sıcaklığın düşmesiyle sistem düşük enerjiye doğru odaklanır. Tavlama süreci; optimizasyon problemini, sıcaklık; iterasyon sayısını kontrol eden kontrol parametresini, fiziksel sistem durumu; problemin çözümünü, içinde bulunan durumun enerjisi; amaç fonksiyonunun değerini, hızlı soğutma işlemi; optimal çözümü ve minimum enerji ise optimum çözümü sunmaktadır [13]–[16].

Deneyler için tam faktöriyel deney tasarımı kullanılmıştır. Deneyler yapılırken her deneyde 3 paso talaş kaldırılmış olup her paso sonunda yüzey pürüzlülüğü değeri ölçülerek kesme parametrelerinin yüzey pürüzlülüğü üzerindeki etkileri incelenmiştir. Yanıt yüzey metodu kullanılarak matematiksel modeller oluşturulmuştur. Elde edilen matematiksel model, Tavlama benzetimi algoritmasıyla optimizasyon için kullanılmış ve optimum kesme parametreleri belirlenmiştir (**Error! Reference source not found.**).



Şekil 3 Yüzey pürüzlülüğünün minimum değeri için uygulanan işlem adımları

BULGULAR VE TARTIŞMA

Tam faktöriyel deney tasarımı ile oluşturulmuş deney tasarımında her bir deney yapılarak yüzey pürüzlülük değerleri ölçülmüştür. Yüzey pürüzlülüğü üzerinde kesme hızı, ilerleme ve pasonun etkileri varyans analizi ile ortaya konulmuştur (

Tablo 4). F- Değeri sütunu, numune ortalamaları arasındaki varyasyonun numuneler içindeki varyasyona oranıyla elde edilir ve bu değerin büyük olması p değerinin düşük olmasını sağlamaktadır [11]. Değerlendirme sonucunda yüzey pürüzlülüğü üzerinde %83,41 oranıyla en etkin parametrenin ilerleme olduğu görülmüştür. İncelenen deneylerin %95 güven

aralığında %92,33 açıklama gücüne sahip olması tahmin edilen yüzey pürüzlülüklerinin doğruluğunu kanıtlar niteliktedir.

Tablo 4 Varyans Analizi (ANOVA)

Terimler	S.D	Karelerin Ardışık Toplamı	Katı Oranları	Düzeltilmiş Kareler Toplamı	Düzeltilmiş Ortalama Kareler	F-Değeri	P-Değeri
Model	8	1,65589	92,33%	1,65589	0,20699	31,61	0,000
Lineer	3	1,58564	88,41%	1,58564	0,52855	80,71	0,000
Kesme Hızı	1	0,02489	1,39%	0,02489	0,02489	3,80	0,065
İlerleme	1	1,49589	83,41%	1,49589	1,49589	228,42	0,000
Paso	1	0,06487	3,62%	0,06487	0,06487	9,90	0,005
Kareler	2	0,01547	0,86%	0,01547	0,00774	1,18	0,326
Kesme Hızı*Kesme Hızı	1	0,01425	0,79%	0,01425	0,01425	2,18	0,155
Paso*Paso	1	0,00122	0,07%	0,00122	0,00122	0,19	0,670
İkili Etkileşim	3	0,05477	3,05%	0,05477	0,01826	2,79	0,066
Kesme Hızı*İlerleme	1	0,00371	0,21%	0,00371	0,00371	0,57	0,460
Kesme Hızı*Paso	1	0,01914	1,07%	0,01914	0,01914	2,92	0,102
İlerleme*Paso	1	0,03192	1,78%	0,03192	0,03192	4,87	0,039
Hata	21	0,13753	7,67%	0,13753	0,00655		
Toplam	29	1,79341	100,00%				

Varyans analizi de göz önünde bulundurularak yanıt yüzey yöntemiyle giriş parametreleri ile çıkış arasında matematiksel denklem oluşturulmuştur (**Error! Reference source not found.**). Yöntemin matematiksel denkleminde, giriş parametrelerinin kendi etkileri ve ikili ilişkiler de bulunmaktadır (Şekil 4).

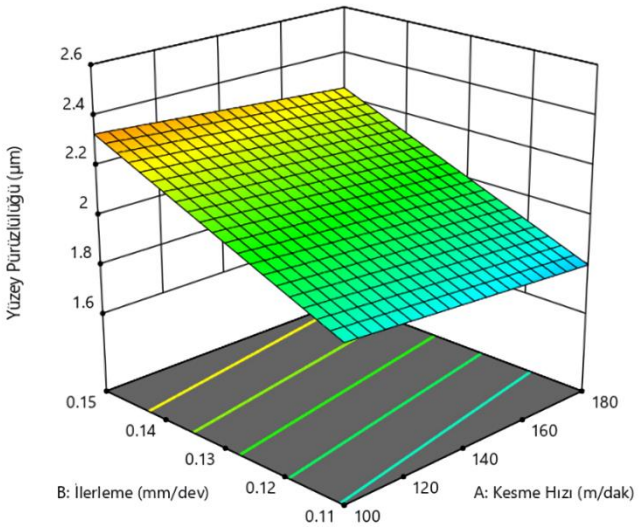
Tablo 5 Matematiksel model

$$\text{Yüzey Pürüzlülüğü} = 0{,}568 - 0{,}01195*Vc + 21{,}91*f + 0{,}527*ap + 0{,}000033*Vc*Vc - 0{,}151*ap*ap - 0{,}0197*Vc*f + 0{,}00365*Vc*ap - 6{,}66*f*ap \quad (2)$$

Vc : Kesme hızı (m/dak)

f : İlerleme (mm/dev)

ap : Paso (mm)



Şekil 4 Kesme hızı ve ilerlemenin yüzey pürüzlülüğü ile etkileşimi

Matematiksel denklem (denklem 2), sınır işleme şartları içerisindeki en iyi yüzey pürüzlülüğü değerini elde etmek için optimum işleme parametrelerinin bulunmasına yardımcı olmaktadır. Matematiksel denklemi çözmek için tavlama benzetimi yöntemi kullanılmıştır. Yöntemde amaç fonksiyonu olarak denklem 2 kullanılmıştır. Giriş parametrelerinin başlangıç noktaları, başlangıç sıcaklığı (500^{o}C), maksimum iterasyon sayısı (max iter:3000), giriş parametrelerinin üst ve alt sınır değerleri girilmiştir. Tavlama benzetimi yönteminin 1854 iterasyon sonunda bulmuş olduğu tornalama parametreleri; 132,01 m/dak kesme hızı, 0,11 mm/dev ilerleme ve 1,5 mm paso şeklindedir. Bu parametreler sonucunda yüzey pürüzlülüğü değeri ise 1,7642 µm olarak bulunmuştur.

SONUÇLAR

Deneysel sonuçlar göz önünde bulundurularak, tam faktöriyel deney tasarımıyla, tavlama benzetimi yöntemine dayanan ve yanıt yüzey yöntemi kullanarak yüzey pürüzlülüğünün minimum değeri için aşağıdaki sonuçlara varılmıştır.

Varyans analizi sonuçlarından, ilerlemenin diğer giriş parametrelerine oranla yüzey pürüzlülüğü üzerinde daha büyük etkiye sahip olduğu görülmüştür.

Yüzey pürüzlülüğü tahmini için yanıt yüzey yönteminden elde edilen matematiksel model kullanılabilir. Böylece %95 güven aralığında %92,33 açıklama gücüne sahip sonuçlar elde edilebilecektir.

Yüzey pürüzlülüğünün minimum değeri için tavlama benzetimi yöntemi kullanılarak elde edilen kesme parametre değerleri: 132,01 m/dak kesme hızı, 0,11 mm/dev ilerleme ve 1,5 mm paso şeklindedir.

KAYNAKÇA

[1] K. Shunmugesh, K. Panneerselvam, M. Pramod, and A. George, “Optimization of CNC Turning Parameters with Carbide Tool for Surface Roughness Analysis Using Taguchi Analysis,” *Res. J. Eng. Sci.*, vol. 3, no. 6, pp. 1–7, 2014.

[2] D. I. Lalwani, N. K. Mehta, and P. K. Jain, “Experimental investigations of cutting parameters influence on cutting forces and surface roughness in finish hard turning of MDN250 steel,” *J. Mater. Process. Technol.*, vol. 206, no. 1–3, pp. 167–179, Sep. 2008, doi: 10.1016/J.JMATPROTEC.2007.12.018.

[3] V. V.D. Sahithi, T. Malayadri, and N. Srilatha, “Optimization of turning parameters on surface roughness based on taguchi technique,” *Mater. Today Proc.*, vol. 18, pp. 3657–3666, 2019, doi: 10.1016/j.matpr.2019.07.299.

[4] S. Sahu and B. B. Choudhury, “Optimization of Surface Roughness Using Taguchi Methodology & Prediction of Tool Wear in Hard Turning Tools,” *Mater. Today Proc.*, vol. 2, no. 4–5, pp. 2615–2623, 2015, doi: 10.1016/j.matpr.2015.07.218.

[5] M. Mia, G. Singh, M. K. Gupta, and V. S. Sharma, “Influence of Ranque-Hilsch vortex tube and nitrogen gas assisted MQL in precision turning of Al 6061-T6,” *Precis. Eng.*, vol. 53, no. December 2017, pp. 289–299, Jul. 2018, doi: 10.1016/j.precisioneng.2018.04.011.

[6] K. K. Wika, P. Litwa, and C. Hitchens, “Impact of supercritical carbon dioxide cooling with Minimum Quantity Lubrication on tool wear and surface integrity in the milling of AISI 304L stainless steel,” *Wear*, vol. 426–427, no. September 2018, pp. 1691–1701, Apr. 2019, doi: 10.1016/j.wear.2019.01.103.

[7] M. Gupta and S. K. Gill, “Prediction of cutting force in turning of UD-GFRP using mathematical model and simulated annealing,” *Front. Mech. Eng.*, vol. 7, no. 4, pp. 417–426, 2012, doi: 10.1007/s11465-012-0343-2.

[8] F. Kolahan and M. Abachizadeh, “Optimizing turning parameters for cylindrical parts using simulated annealing method,” *World Acad. Sci. Eng. …*, vol. 36, no. December, pp. 436–439, 2008, [Online]. Available: http://profdoc.um.ac.ir/paper-abstract-1005069.html.

[9] F. Kolahan, R. Golmezerji, and M. A. Moghaddam, “Multi objective optimization of turning process using grey relational analysis and simulated annealing algorithm,” *Appl. Mech. Mater.*, vol. 110–116, pp. 2926–2932, 2012, doi: 10.4028/www.scientific.net/AMM.110-116.2926.

[10] A. Jabri, A. El Barkany, and A. El Khalfi, “Multipass Turning Operation Process Optimization Using Hybrid Genetic Simulated Annealing Algorithm,” *Model. Simul. Eng.*, vol. 2017, 2017, doi: 10.1155/2017/1940635.

[11] R. Rudrapati, A. Bandyopadhyay, P. K. Pal, and L. Rathod, “Analysis, modeling and optimization of surface roughness in cylindrical traverse cut grinding using factorial design, RSM and simulated annealing algorithm,” *IOP Conf. Ser. Mater. Sci. Eng.*, vol. 814, no. 1, 2020, doi: 10.1088/1757-899X/814/1/012016.

[12] D. C. M. Christine Anderson-Cook, Raymond Myers, *Response surface*

methodology process and product optimization using designed experiments. Canada: New Jersey: john wiley & sons, 2008.

[13] J. S. Arora, “Discrete Variable Optimum Design Concepts and Methods,” in *Introduction to Optimum Design*, Elsevier, 2004, pp. 513–530.

[14] H. Foerster and G. Wäscher, “Simulated annealing for order spread minimization in sequencing cutting patterns,” *Eur. J. Oper. Res.*, vol. 110, no. 2, pp. 272–281, 1998, doi: 10.1016/S0377-2217(97)00257-9.

[15] Y. Eren, İ. B. Küçükdemiral, and İ. Üstoğlu, “Introduction to Optimization,” in *Optimization in Renewable Energy Systems*, Elsevier, 2017, pp. 27–74.

[16] S. Sieniutycz and J. Jeżowski, “Brief review of static optimization methods,” in *Energy Optimization in Process Systems*, Elsevier, 2009, pp. 1–43.

ISIL İŞLEM UYGULANAN AISI 420 PAZLANMAZ ÇELİĞİN TORNALAMA İŞLEMİ ÜZERİNDE CBN UÇLAR İLE YÜZEY PÜRÜZLÜLÜĞÜ ARAŞTIRMASI

Hasan Safa ÇAVUŞOĞLU, *safa.cavusoglu@novumek.com*, NOVUMEK Teknoloji A.Ş., Ankara

Seher SEVEN, *seher.seven@novumek.com* , NOVUMEK Teknoloji A.Ş., Ankara

Besim BARANOĞLU, *besim.baranoglu@novumek.com*, NOVUMEK Teknoloji A.Ş., Ankara

ÖZET

Bu araştırmada ısıl işlem görmüş AISI-420 paslanmaz alaşımlı silindirik şaft malzemenin CBN kesici uçları ile işlenerek kesici uç ve yüzey pürüzlülüğünü incelenmiştir. İşlemlerde kullanılan iş parçasının yüzeyden indüksiyon ısıl işlem ile sertleştirmesi yapılarak bu işlem sonrasında yüzey sertliği 55 HRC olarak ölçülmüştür. İşlemler belirlenen matrislere uygun olarak farklı ilerleme, kesme hızı/devir ve talaş miktarları ile gerçekleştirilmiş ve bu parametrelerin yüzey kalitesine etkisi incelenmiştir. Yapılan işlemler ve incelemelere göre devir hızı arttıkça yüzey pürüzlülüğünün azaldığı, bunun yanında ilerleme ve talaş kaldırma miktarı arttıkça ise pürüzlülüğün buna doğru orantılı olarak arttığı gözlemlenmiştir.

Anahtar sözcükler: CBN, CNC Tornalama, Yüzey Pürüzlülüğü

ABSTRACT

In this study, heat-treated AISI-420 stainless steel cylindrical shaft material's are machined (turned) with CBN cutting tools and the surface roughness were observed. The workpiece utilized in the operations was hardened from the surface using induction heat treatment, and the surface hardness after this process was measured to be 55 HRC. Inline with the specified matrices, the operations were carried out with varying feed, cutting speed/revolution, and depth of cut, and the impacts of these factors on the surface quality

were investigated. According to the procedures and research, the surface roughness lowers as rotation speed increases, whereas it grows correspondingly when feed and chip removal quantity increases.

Keywords: CBN, CNC Turning, Surface roughness

GİRİŞ

Talaşlı imalat, özellikle ülkemizde oldukça yoğun olarak kullanılan imalat yöntemlerinden biridir. Torna ile silindirik şaftların imalatı ise yine talaşlı imalat alanında önemli bir yer tutmaktadır. Günümüzde CNC (Computer Numerical Control) torna işlemleri de sektörde oldukça yaygınlaşmıştır. Bununla birlikte, özellikle yüzey pürüzlülüğü kontrolü ve ölçüsel toleransların elde edilebilmesi amacıyla çoğunlukla silindirik taşlama işlemi, torna ile talaşlı imalat sonrasında uygulanmaktadır. Ancak, silindirik taşlamanın (CNC olsa dahi) torna ile imalata göre oldukça yüksek olan imalat zamanı, giderek artan imalat adetleri dolayısı ile alternatif arayışını gerekli kılmaktadır.

Taşlama yöntemi ile üretilen parçaların talaşlı imalat ile doğrudan imalatına yönelik çalışmalar özellikle yakın zamanda gündeme gelmektedir. Yakın zamanda Davies ve arkadaşları tarafından yapılmış bir çalışmada kritik helikopter parçalarında talaşlı imalatın doğrudan uygulanmasının taşlama yönteminin uygulanmasına göre yorulma ömrü ve kalıntı gerilmeler açısından daha avantajlı olduğu gösterilmiştir [Davies, 2014]. Aynı çalışma Tablo 1'de gösterilen sonuçları da göstermektedir. Bu sonuçlara göre silindirik taşlama ile imalata alternatif olarak tornada talaşlı imalat ile üretilen silindirik şaftlarda yorulma direncinin arttığı ve kalıntı gerilmelerin düştüğü gözlemlenmiştir. Ayrıca aynı çalışmada numunelerdeki standart sapma ve varyasyonun da tornalamada daha düşük olduğu görülmüştür.

Tablo 1. Silindirik taşlama ve tornalama ile üretilen parçaların karşılaştırılması

Talaşlı imalat	Yorulma dayanımı (MPa)	Numune varyasyonu	Numune standart sapması	Kalıntı gerilme (MPa)
Taşlama	10.40	5.30	2.30	-183
Tornalama	11.09	1.74	1.32	-103

Bu çalışmada gösterilen bir başka sonuç da ilerleme hızının (feed rate) artmasının, talaş kaldırma miktarının son (finish) tornalamada aynı olarak tutulmasına rağmen, yüzey kalitesinde daha kötü sonuçlara yol açtığıdır [Davies, 2014]. Bununla birlikte, doğru proses parametreleri seçildiğinde talaşlı imalatın yüzey kalitesinde taşlama kadar iyi sonuçlar verebildiği söylenebilir [Oberg, 2016].

Gerek taşlama işleminin yavaşlığı, gerekse kesme işlemi sonrasında tekrar bağlama zamanından tasarruf etme gereklilikleri, uygun imalat süreleri ve maliyetleri açısından taşlama işlemi yerine aynı sonucu elde edebilecek şekilde torna ile imalat üzerine çalışmaların yoğunlaşmasına sebep olmuştur. Özellikle çelik malzemelerin ısıl işlem görmesi sonrasında başlangıçta 20 HRC seviyelerinde olan sertliklerinin 60 HRC seviyelerine çıkarılabilmesi dolayısı ile kesme işleminin parametreleri sadece hızlanma açısından değil, aynı zamanda takım aşınması açısından da incelenmelidir [Uhlmann, 2009]. Bu durum sadece yüksek mukavemetli metal malzemeler için değil, aynı zamanda metal matris kompozitler için de geçerlidir [Ciftci, 2004].

CBN (Cubic Boron Nitride) ve diğer seramikler özellikle bu noktada talaşlı imalat için uygun alternatifleri oluşturmaktadır. Pek çok çalışma gerek CBN (veya farklı bir seramik) kaplama gerekse CBN ve benzeri diğer seramik malzemelerden imal edilmiş uçların kesme performanslarını özellikle yüzey pürüzlülüğü, kesme kuvvetleri ve/veya takım aşınması açısından incelemektedir [Chen, 2000, Zoya, 2000, Chou, 2002, Arunachalam, 2004]. Benzer şekilde CBN ve diğer seramik uçların karşılaştırmalı çalışmaları da mevcuttur [Sahin,

2009]. Kullanılacak olan takımların imalatına yönelik de çalışmalar önemlidir; örneğin Özel CBN kesici uçların kesici kenarının hazırlanmasını sonlu elemanlar yöntemi ile modellemiştir [Özel, 2003].

Yukarıda özetlenen çalışmalar özelinde dikkat çeken husus şudur: gerek CBN gerekse diğer seramik uçlar ile talaşlı imalatta yüksek devir ve düşük ilerleme altında istenilen yüzey kalitesi elde edilebilmekte ve istenilen ölçüsel toleranslara ulaşılabilmektedir. Kesme hızının artması ile malzemeden kaldırılan talaş miktarının azalması ile daha düşük yüzey pürüzlülüğünün düştüğü gözlemlenmiştir. Çalışmalarda kesme hızı arttıkça yüzey pürüzlülüğü düşerken ilerleme arttıkça pürüzlülük arttığı görülmüştür

Bu çalışmanın temel motivasyonunu da bu gözlem oluşturmaktadır. Belirli bir süreç dahilinde öncelikle talaşlı imalatla üretilerek indüksiyon sertleştirmesi yapılan ve ardından silindirik taşlama ile son ölçüsel toleranslarına ve yüzey pürüzlülüğüne ulaştırılan silindirik şaft ürünlerin CNC torna üzerinde ve CBN uç ile silindirik taşlama işlemi olmadan imalatı konu alınmaktadır. Bu sayede imalat sürelerinin oldukça kısalması ve imalat masraflarının kısılması söz konusu olabilecektir.

2. DENEYSEL ÇALIŞMALAR VE BULGULAR

Deneysel çalışmalar için farklı firmalardan çeşitli çaplarda AISI-420 malzeme tedariği sağlanmıştır (Tablo 2, 3 ve 4, sırasıyla AISI-420 malzeme standardını, temin edilen malzemenin mekanik özelliklerini ve temin edilen malzemenin alaşım miktarlarının ölçüm sonuçlarını göstermektedir). Hammadde olarak alınan malzeme öncelikle tornalama işlemine tabii tutulmuş, daha sonrasında ise yüzey üzerinden indüksiyon ile ısıl işlem uygulanmıştır. Isıl işlem sonrası yüzeyden içeriye doğru 0.5mm kalınlığında bir bölgede ölçülen değerler 48-55 HRC arasındadır. Deneylerde, otomatik punta özellikli, 15 kVa gücüne sahip Hyundai CNC Torna (Resim 1) tezgahı kullanılmıştır. Takım 1 ve Takım 2 olarak iki farklı firmalardan CBN uç alınarak deneyler yapılmıştır. İki köşeli olan CBN uçlar, DNMG uç ve DNMG Kateri kullanılarak uygulanmıştır. (Resim 2 ve Resim 3).



Resim 1. Hyundai CNC Torna

Tablo 2. 420 Malzeme Özellikleri/Içeriği (standart)

Kimyasal Analiz							
%Base	% C	% SI	% Mn	% P	% S	% Cr	%Fe
	0.43-0.5	Max 1	Max 1	Max 0.04	Max 0.03	12.5-14	Rest
Fe	0.449	0.39	0.289	0.019	0.0276	12.6	Kalan

Tablo 3. 420 Malzeme Özellikleri/Içeriği

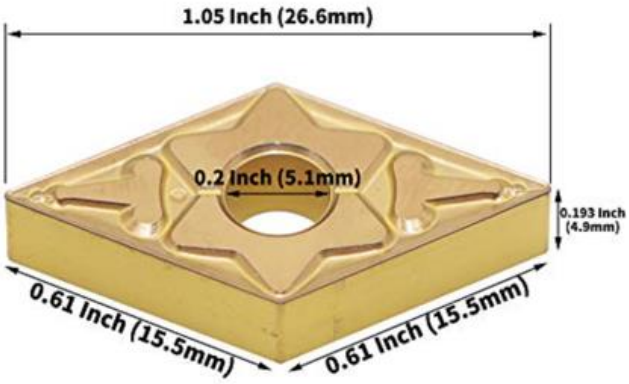
Mekanik Özellikler				
Red Area Z %	Yield Strength Rp 0.2 % Mpa	Tensile Strength RM Mpa	Elongation %	Hardness HB
47	655	792	15	228

Tablo 4. 420 Malzeme Özellikleri/Içeriği (ölçüm)

Kimyasal Bileşimi						
Kalite	C	Mn	P	S	Si	Cr
420 (1.4034)	0.46	1.0 max	0.04 max	0.03 max	1.0 max	13.0



Resim 2. DNMG Kater



Resim 3. DNMG Uç

Mitutiyo SJ 301 Surftest (Resim 4) ve Mahr Ps10 (Resim 5) ölçüm cihazlarıyla yüzey pürüzlüğü ölçülmüştür. 5 bölgeden alınan yüzey ölçümleri, Ra ve Rt olarak değerlendirilmiştir. Ölçümlerde ilk olarak parça eksenel olarak ölçülmüştür. İkinci olguda ise Cut off the lenght λc=0,85 olarak ayarlanmış ve 3'er kez ölçülerek ortalaması alınmıştır.



Resim 4. Mitutiyo Sj-301 Surftest



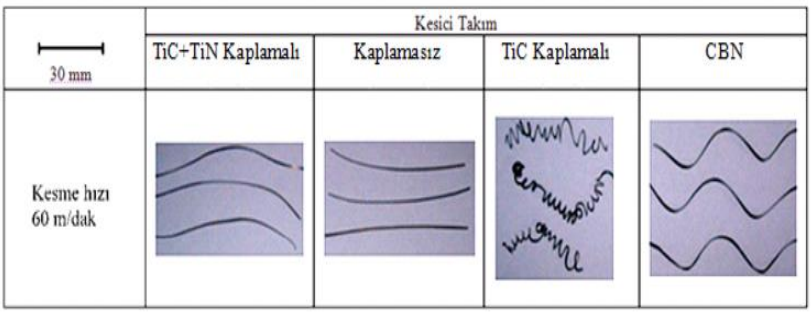
Resim 5. Mahr Ps10

AISI-420 malzemesinin işleme sırasındaki yüzey pürüzlülüğünü değerlendirmek için uçların fabrika verileri ve CNC torna tezgahına uygun olabilecek parametreler belirlenmiştir.

Çalışmada belirlenen farklı kesme hızları, ilerleme hızları ve talaş kaldırma miktarları ile matris parametreleri belirlenmiştir. Belirlenen değerler bir deney matrisi oluşturacak şekilde Tablo 5'te verilmiştir. Bunların birlikte yapılan diğer çalışmalardar farklı kullanılan uçların talaş kaldırma miktarlarının takım üzerindeki etkileri incelenmiştir (Resim 6).

Tablo 5. Matris parametreleri

Kesme Hızı	İlerleme Miktarı	Talaş Kaldırma Miktarı
3500	0.01	0.2
3500	0.01	0.3
3500	0.02	0.2
3500	0.02	0.3
3400	0.01	0.2
3400	0.01	0.3
3400	0.02	0.2
3400	0.02	0.3
3300	0.01	0.2
3300	0.01	0.3
3300	0.02	0.2
3300	0.02	0.3
3200	0.01	0.2
3200	0.01	0.3
3200	0.02	0.2
3200	0.02	0.3



Resim 6. Talaş kaldırma miktarının kesici takım malzemesinin ve kaplama üzerinde olan etkileri [Özer, 2009]

3. SONUÇLAR ve TARTIŞMA

Isıl işlem görmüş AISI-420 paslanmaz alaşımlı silindirik şaft malzemenin, CNC Torna Tezgâhında, soğutma sıvısı kullanılmadan, CBN uçlarla tornalanarak yapılan deneysel çalışmaya ait notlar aşağıdaki gibidir:

Deneylerde, Takım 1 ve Takım 2 firmalarından 0.2, 0.4 ve 0.8 mm radyusları sahip farklı uçlar kullanılmıştır. Ek olarak sadece kaba işleme denemeleri de yapılmış, bu denemelerde farklı hızlar ve talaş kaldırma miktarları da denenmiştir. 2 tip ve 2 köşeli CBN uçlar, kaba işler için seçilmiştir. Kaba işlem ile yapılan denemelerde ilk uç ile ortalama 490 adet parça toleranslar dahilinde işlenmiştir. İkinci uç ile ise 150 adet deneme yapılmıştır. İlk uç soğutma sıvısı kullanılmadan işleme yapılmış olup ilk 400 parçada Ra değeri ortalama 0.24 µm ile 0.32 µm arasında olduğu görülmüştür. İkinci uç ise ilk 75 parçada 0.25 µm ile 0.35 µm arasında olup 75'den sonra Ra değerleri 0.49 µm ile 0.68 µm arasında olduğu görülmüştür. Kaba işlemi yapılan parçaların bazılarına ise finish yüzey atma işlemi uygulanmıştır. Bu denemelerde 0.8, 0,4 ve 0.2 radyuslu CBN uçlar kullanılmıştır. Kaba işlemleri yapılan parçalarda belirlenen matris parametreleri uygulanmıştır. Bu parametreler 3 ana temelde belirlenmiştir (Kesme Hızı, İlerleme hızı ve talaş kaldırma miktarı). Yapılan işlemlerde CBN uç radyusu ne kadar büyük olur ise Ra değeri ortalama üstü veya ortalama üstüne yakın, radyus küçüldükçe ise ilk parçalarda Ra değeri ortalama değerlerin oldukça altındayken bir süre sonra uç kırılması/erimesi gibi etkenlerden dolayı Ra değerinin ortalama üstüne çıktığı gözlemlenmiştir. Alınan ölçümlerde, Ra değerleri 0.089 µm ile 0.19 µm, Rt değerleri ise 0.8 µm ile 1.2 µm arasındadır. Deneylerde, parçalara doğrudan finish atma işlemi yapılıp, kaba işlem sonrası da finish atma işlemi yapılmıştır. Bu iki işlem arasında Ra ve Rt değerlerinde değişkenlik gözlenmenmekte ancak bu gözlemlenen değişikliğin gözardı edilebileceği değerlendirilmektedir. Bunun yanı sıra en önemli değişim CBN ucun ömründe artışlarında gözlenmiştir.

Elde edilen sonuçlar ışığında, tornalama işleminin gerek ölçüsel toleransları elde etme gerekse istenilen yüzey pürüzlülüğü değerlerine ulaşma amacı ile taşlama işlemine alternatif olarak kullanılabileceği değerlendirilmektedir.

TEŞEKKÜR

KSB Pompa ArmatürSan. ve Tic. A.Ş. imalat ekibine, ve NOVUMEK Teknoloji A. Ş.'deki çalışma arkadaşlarımıza bu araştırma sürecindeki yardım ve desteklerinden dolayı teşekkür ederiz.

KAYNAKÇA

1. **Davies, D. P., Jenkins, S. L., Legg, S. J. (2014),** "The effect machining processes can have on the fatigue life and surface integrity of critical helicopter components", 2nd CIRP 2nd CIRP Conference on Surface Integrity (CSI), 28 – 30 May, Notttingham, England.
2. **Oberg, E., Jones, F. D., Horton, H. L., Ryffel, H. H. (2016),** Machinery's handbook, 30th Ed., Senior Ed. McCauley, C. J., Industrial Press, USA.
3. **Uhlmann, E., Oyadenel Fuentes, J. A., Keunecke, M. (2009),** "Machining of high performance workpiece materials with CBN coated cutting tools", Thin Solid Films, v.518, pp 1451 – 1454.
4. **Ciftci, I., Turker, M., Seker, U. (2004),** "CBN cutting tool wear during machining of particulate reinforced MMCs", Wear, v.257, pp 1041 – 1046.
5. **Chen, W. (2000),** "Cutting forces and surface finish when machining medium hardness steel using CBN tools", International Journal of Machine Tools & Manufacture, v.40, pp 455 – 466.
6. **Zoya, Z. A., Krishnamurthy, R. (2000),** "The performance of CBN tools in the machining of titanium alloys", J. of Materials Processing Technology, v. 100, pp 80 – 86.
7. **Chou, Y. K., Evans, C. J., Barash, M. M. (2002),** "Experimental investigation on CBN turning of hardened AISI 52100 steel", J. of Materials Processing Technology, v. 124, pp 274 – 283.

8. **Arunachalam, R. M., Mannan, M. A., Spowage, A. C. (2004),** “Residual stress and surface roughness when facing age hardened Inconel 718 with CBN and ceramic cutting tools”, International Journal of Machine Tools & Manufacture, v.44, pp 879 – 887.
9. **Sahin, Y. (2009),** “Comparison of tool life between ceramic and cubic boron nitride (CBN) cutting tools when machining hardened steels”, J. of Materials Processing Technology, v. 209, pp 3478 - 3484.
10. **Özel, T. (2003),** “Modeling of hard part machining: effect of insert edge preparation in CBN cutting tools”, J. of Materials Processing Technology, v. 141, pp 284 – 293.
11. **ÖZER, A BAHCECİ. E. (2009).** “Machinability of Aisi 410 martensitic stainless steels depending on cutting tool and coating”, *Journal of the Faculty of Engineering and Architecture of Gazi University*, *24*(4), 693-698.

EKLEMELİ İMALAT TEKNOLOJİSİYLE ÜRETİLMİŞ INCONEL 718 VE Ti6Al4V 'nin MİKRO FREZELENMESİNDE KESME KOŞULLARININ ETKİSİNİN ARAŞTIRILMASI

Ahmet HASÇELİK, *ahascelik@aku.edu.tr* Afyon Kocatepe Üniversitesi, 03200, Afyon

Kubilay ASLANTAŞ, *aslantas@aku.edu.tr* Afyon Kocatepe Üniversitesi, 03200, Afyon

Mohd DANISH, *mdanish@uj.edu.sa* Cidde Üniversitesi, 21589, Cidde

ÖZET

Eklemeli imalat teknolojileri, karmaşık geometriye sahip parçaların kolaylıkla üretilebilmesine imkan tanıyarak geleneksel imalat yöntemlerine göre ön plana çıkmaktadır. Fakat yetersiz yüzey kalitelerinden dolayı iş parçasının son bir yüzey düzeltme işleminden geçirilmesi gerekmektedir. Bu çalışmada Seçici Lazer Ergitme (SLM) yöntemi ile üretilen Inconel ve Ti6Al4V iş parçalarının 4 farklı kesme koşulunda (kuru kesme, MQL, bor yağı ve soğutulmuş CO_2) mikro frezelenmesi durumunda kesme kuvvetleri, yüzey pürüzlülüğü ve takım aşınmasındaki farklılıklar incelenmiştir. Her iki iş parçası için de en iyi sonuçlar MQL şartlarında elde edilmiştir. Inconel iş parçasındaki takım aşınmasının, kesme kuvvetlerinin ve yüzey pürüzlülüğünün Ti6Al4V'a göre daha fazla olduğu gözlenmiştir.

Anahtar Kelimeler: Seçici Lazer Ergitme, Mikro Frezeleme, Kesme Kuvvetleri, Takım Aşınması, Yüzey Pürüzlülüğü

INVESTIGATION OF THE EFFECT OF CUTTING CONDITIONS ON MICRO MILLING OF INCONEL 718 AND TI6AL4V MADE WITH ADDITIVE MANUFACTURING TECHNOLOGY

ABSTRACT

Additive manufacturing technologies stand out compared to traditional manufacturing methods by allowing parts with complex geometries to be produced easily. However, due to insufficient surface qualities, the workpiece has to undergo a final surface finishing process. In this study, the differences in cutting forces, surface roughness and tool wear were investigated in case of micro-milling of Inconel and Ti6Al4V workpieces produced by Selective Laser Melting (SLM) method under 4 different cutting conditions (dry, MQL, coolant

and chilled CO2). The best results for both workpieces were obtained under MQL conditions. It has been observed that tool wear, cutting forces and surface roughness in Inconel workpiece are higher than Ti6Al4V.

Keywords: Selective Laser Melting, Micro Milling, Cutting Forces, Tool Wear, Surface Roughness

1. GİRİŞ

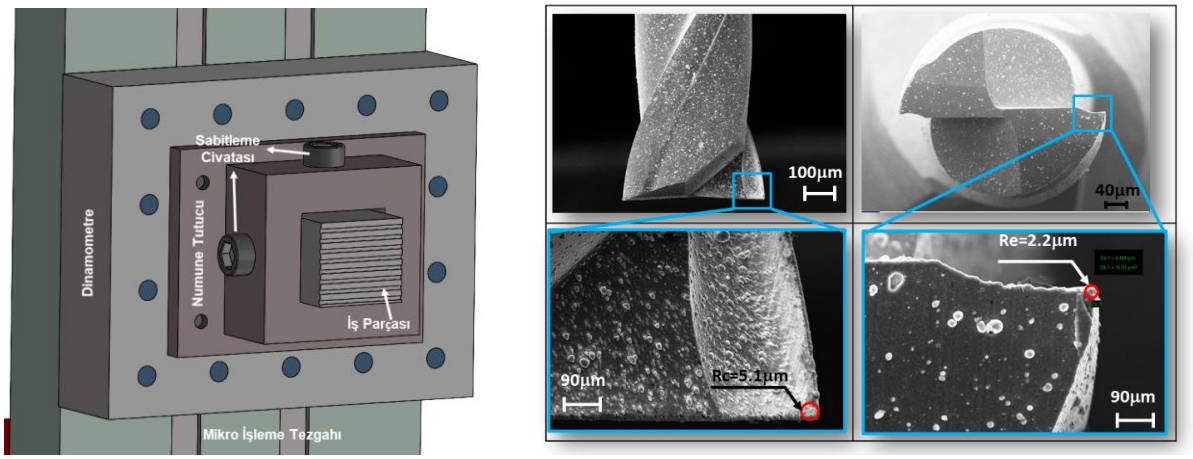
Nikel alaşımları, olağanüstü mekanik ve fiziksel nitelikleri nedeniyle havacılık, kimya, otomotiv, uzay ve tıp endüstrilerinde yaygın olarak kullanılmaktadır. Titanyum ve alaşımları, daha düşük ısıl iletkenliği nedeniyle daha yüksek işleme sıcaklıklarına ve daha düşük kesme kuvvetlerine sahiptir. Ayrıca yüksek sıcaklıklarda ve kimyasal reaktivitede mukavemetini sürdürme eğilimindedir [Korkmaz et. al. 2020]. Eklemeli imalat, karmaşık geometriye sahip parçaların üretimini mümkün kılması, yüksek tasarım özgürlüğü ve sağladığı ekonomik faydalar ile son yıllarda sıklıkla tercih edilen bir teknoloji haline gelmiştir [Busachi 2017] [Brandt 2017]. Seçici lazer ergitme (SLM) yöntemi ise özellikle metalik malzemeleri üretmek için kullanılan en yaygın eklemeli imalat yöntemlerinden biridir [Bodziak 2019] [Shipley 2018]. Araştırmacılar, eklemeli imalat teknolojisi ile üretilen nikel ve titanyum alaşımlarından oluşan çeşitli bileşenlerin mikro frezelenmesi ile ilgili birçok çalışma yapmıştır [Kassim et. al. 2020] [Korkmaz et. al. 2019]. Sreeram et. al. (2006), çelik malzemelerin mikro frezelemesinde kesme parametrelerini optimize etmek amacıyla bir dizi çalışma yapmışlardır. Kuram ve Ozcelik (2015), aynı deneysel koşullarda Inconel 718 ve Ti6Al4V'un mikro frezeleme performansını kıyaslamışlardır. Takım aşınması, kesme kuvvetleri ve yüzey pürüzlülüğüne en çok etkiyen değişkenlerin kesme parametreleri olduğunu belirterek optimum kesme parametrelerini tespit etmişlerdir [Kuram ve Ozcelik 2015]. Sun et. al. [2006], titanyum alaşımının işlenmesinde kesme koşullarının etkilerini araştırmışlar ve MQL teknolojisinin takım ömrü artırdığını, kesme kuvvetlerini ise azalttığını belirtmişlerdir. Kasım et al. [2014], Inconel 718'in frezelenmesinde MQL teknolojisinin daha iyi bir yüzey kalitesi sağladığını belirtmişlerdir. Li et al. [2006], MQL kesme koşulunda kaplamasız bir karbür kesici kullanılarak kesme işleminde aşınma davranışlarını incelemişlerdir. Bunun sonucunda göze çarpan aşınma türünün yanak aşınması olduğunu ve MQL kesme koşulunun takım ömrünü büyük ölçüde artırdığını belirtmişlerdir. Da Silva et al. [2011] düşük karbonlu çeliklerin işlenmesinde, ıslak, kuru ve MQL kesme koşullarının işleme performansı üzerindeki etkilerini incelemişlerdir. MQL tekniğinin, malzeme kaldırma oranını (MRR) en üst seviyeye çıkarmak için avantajlı olduğunu gözlemlemişlerdir. Bu çalışmanın özellikle havacılık sektöründe

sıklıkla tercih edilen bu iki malzemenin farklı kesme koşullarında mikro frezelenmesi durumunda araştırmacılara yol göstermesi beklenmektedir.

2. MATERYAL ve METOT

2.1. İş Parçaları ve Kesici Takım:

Çalışmada SLM tekniği ile üretilen Nikel ve Titanyum alaşımları sabit kesme parametrelerinde ve farklı kesme şartlarında mikro frezeleme işleminde tabi tutulmuştur. 10 mm x 10 mm x 30 mm boyutlarındaki, Inconel 718 ve Ti6Al4V iş parçaları, mikro freze tezgahındaki dinamometre üzerine sabitlenen bir fikstür üzerine yerleştirilmiştir (Şekil 1a). Kesme deneylerinde kullanılan iki kanallı karbür parmak freze kesici takımların çapı ve 500 µm ± 10 µm, burun yarıçapı 5,1 µm ±0,4 µm ve kenar yarıçapı 2,2 µm ±0,2 µm olarak ölçülmüştür (Şekil 1b).

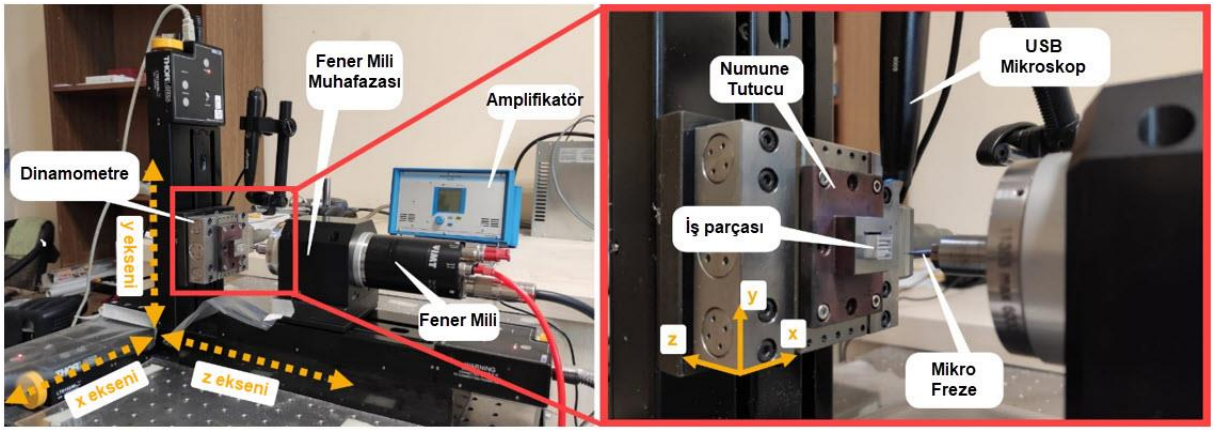


Şekil 1 Kesme deneylerinde kullanılan fikstür ve mikro takımın SEM görüntüleri

2.2. Deney Düzeneği:

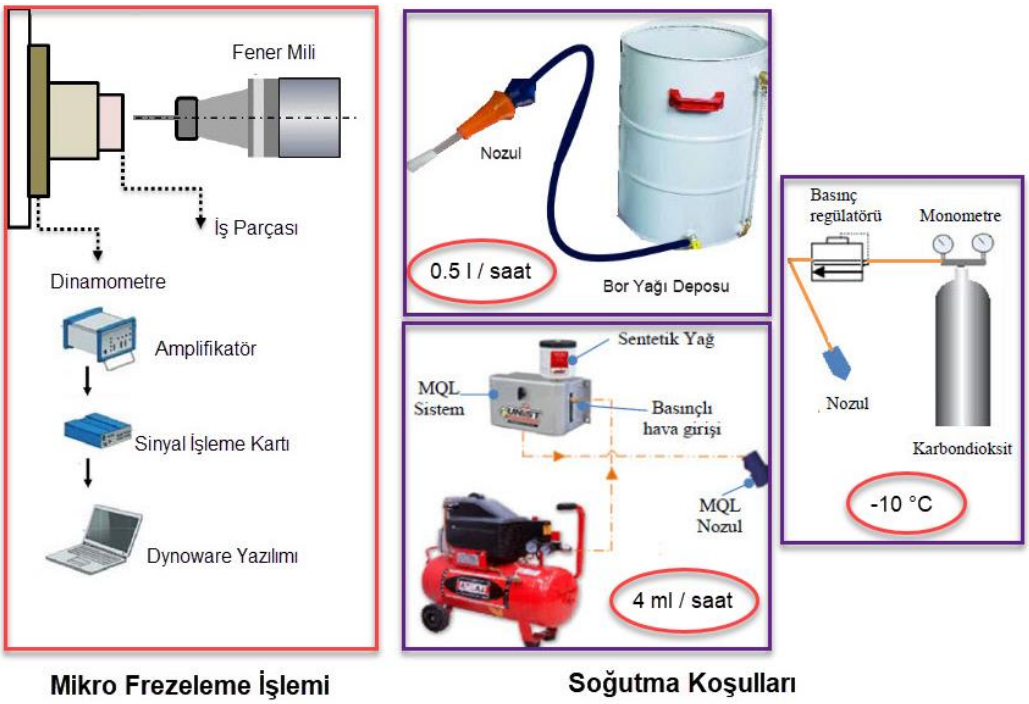
Çalışmada yüksek kesme hızlarında mikro işleme yapabilmek için tasarlanmış özel bir deney düzeneği kullanılmıştır (Şekil 2). Yatay bir işleme merkezine benzemekte olan deney düzeneğinde, mikro kesici takım, pnömatik hava basıncı yardımıyla fener miline sabitlenmiştir. Kullanılan IMT marka fener mili maksimum 60000 dev/dk'ya kadar çıkabilmekte ve devir ayarı kendine ait bilgisayar yazılımı ile hassas olarak elde edilebilmektedir. Eksen hareketleri için mikro step motorlarla desteklenmiş lineer kızaklar (Thorlabs) kullanılmıştır. Kızakların maksimum hareket mesafesi 150 mm olup, hassasiyeti ise 0.1 µm' dur. Fener mili, talaş derinliğinin de ayarlandığı Z ekseni boyunca hareket

etmektedir. İş parçasının yerleştirildiği fikstür, kesme kuvvetleri verilerini elde ederek bilgisayar ortamına aktarmak için kullanılan mini dinamometre (Kistler-9119AA1) üzerine konumlandırılmıştır. Mini dinamometre, Y eksenini ifade eden kızak üzerine sabitlenmekte, ilerleme ise X ekseni boyunca olmaktadır. Deney düzeneğinde her eksenin çözünürlük doğruluğu 0.1 µm ve tekrarlanabilirlik doğruluğu 0.4 µm'dir. Deneylerde hem kesme bölgesinin hem de takım aşınmasının daha net olarak gözlemlenebilmesi, adına 20-800 arasında büyütme yapabilen bir USB mikroskop kullanılmıştır.



Şekil 2 Mikro frezeleme deney düzeneği

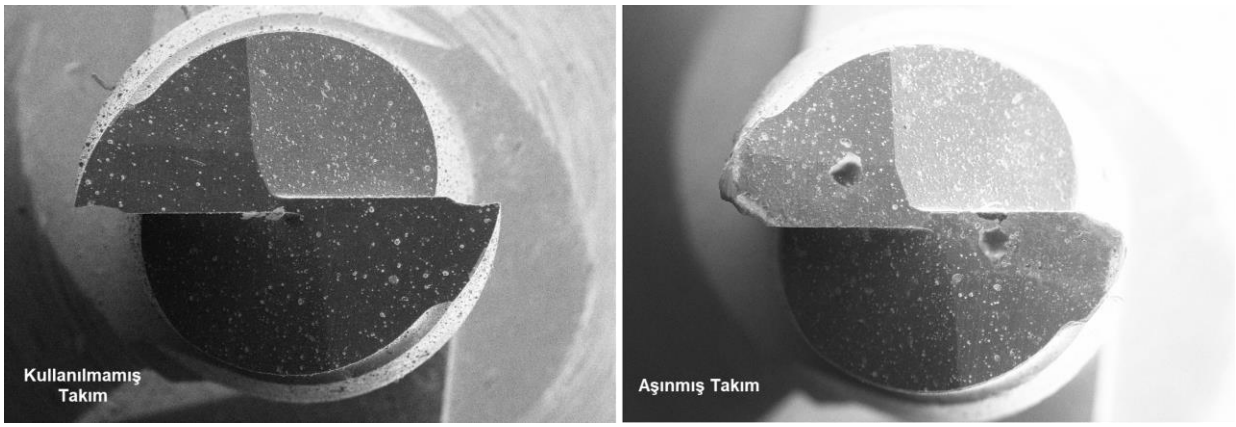
Bu çalışmada; kuru kesme, minimum miktarda yağlama (MQL), karbondioksit ile soğutma ve bor yağı olmak üzere dört farklı kesme koşulu uygulanmıştır (Şekil 3). Öncelikle kuru kesme koşulu için kesme deneyleri gerçekleştirilmiştir. Kuru kesme koşulunun tüm deneyleri tamamlandıktan sonra, MQL kesme koşulunu uygulayabilmek için UNIST Coolubricator düzeneği kullanılmıştır. Coolube 2210 modeli yağlayıcı ile optimum soğutma-yağlayıcı etkisi elde edilerek MQL kesme koşulu için kesme deneyleri tamamlanmıştır. Kesme esnasında 4 bar hava basıncında saatte 4 mL yağ püskürtülmüştür. Soğuk havanın kullanıldığı kesme koşulunda ise kesme bölgesinde $C0_2$ gazı uygulanmıştır. Termokupl kullanılarak, gaz sıcaklığı -10°C'ye ulaştıktan sonra kesme işlemi başlatılmıştır. Son kesme koşulu olan bor yağı ile soğutma işleminde ise, oranı %4 olan bor yağı-su karışımı kullanılmıştır. Kesme işlemi süresince, kesme bölgesinin tamamını kapsayacak şekilde soğutma işlemi gerçekleştirilmiştir. Tüm kesme koşullarında, nozul, iş parçası ile yaklaşık 15 mm uzaklıkta ve 45° açı ile konumlandırılmıştır.



Şekil 3 Mikro frezeleme işlemi ve kesme koşulları

2.3. **Çıktı Parametreleri:**

Mikro frezeleme yöntemiyle kesme işlemi esnasında mini dinamometre ile kesme sinyalleri Amplifikatör yardımıyla sayısal değerlere çevrilerek, Dynoware yazılımı ile bilgisayara kaydedilmiştir. Kesme kuvvetlerinin ölçülmesinde herhangi bir filtreleme yapılmamıştır. Kesme deneyleri sabit kesme parametrelerinde (devir sayısı = 40000 dev/dk, kesme derinliği 100 µm, ilerleme hızı 1µm / diş) ve 10 mm kesme mesafesi boyunca full slot olarak gerçekleştirilmiştir. Takım çapı öncelikle taramalı elektron mikroskobu kullanılarak hassas bir şekilde ölçülmüş, bu ölçüm sonucuna göre USB mikroskop kalibre edilmiştir. Takım aşınmasını ölçebilmek için bu USB mikroskop kullanılmıştır ve ölçüm hassasiyeti 1 µm'dur. USB mikroskobu deney düzeneğinde sabit bir noktaya yerleştirilmiştir. Belirli kesme mesafelerinde deney durdurularak, kesici takım mikroskop pozisyonuna getirilmiştir. Böylece kesme mesafesi boyunca takım aşınması ölçülerek not edilmiştir. Kesme deneyleri sonucunda taramalı elektron mikroskobu (SEM) kullanılarak aşınmış takım geometrisi incelenmiştir (Şekil 4).



Şekil 4 Kullanılmamış ve aşınmış takım SEM görüntüleri

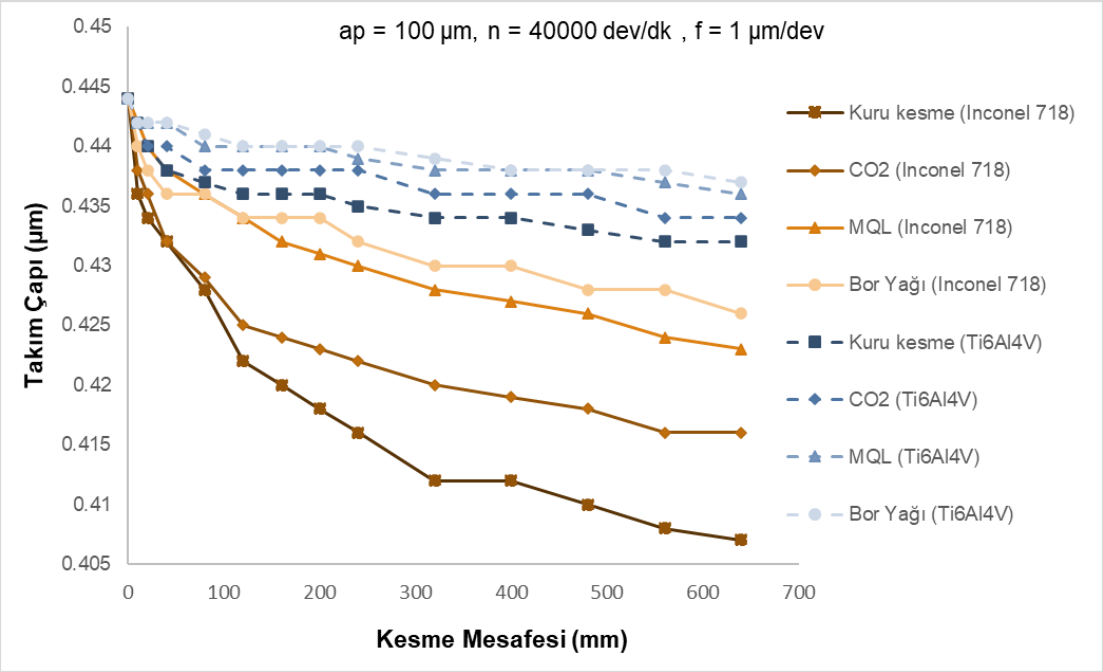
Ayrıca kesme deneylerine başlamadan önce ve kesme deneyleri sonucunda kesici takımın Taramalı elektron mikroskobu (SEM) kullanılarak görüntüleri alınmıştır. Takımın aşınma durumu, kenar ve burun yarıçapı ölçümleri yapılmıştır. İş parçası kesme kanallarındaki alansal yüzey pürüzlülüğünün ölçümü için, yuva genişliği boyunca üç boyutlu yüzey taraması yapılmıştır. Bu işlem için Nanovea-ST400 3D Optik profilometre cihazı kullanılmıştır. Kesme kanalları üzerinden alınan ölçüm sonuçları not edilerek, alansal tarama parametreleri olan Sa ve Sz yüzey pürüzlülük parametreleri elde edilmiştir.

3. SONUÇLAR VE TARTIŞMA

3.1. **Takım Aşınması:**

Bu çalışmada, 640 mm kesme mesafesi boyunca, sabit kesme parametrelerinde Inconel 718 ve Ti6Al4V iş parçalarına dört farklı kesme koşulunda mikro frezeleme işlemi yapılmıştır. Bu iki iş parçası için, kesme koşulunun takım aşınmasına etkisi incelenmiştir. Kesme mesafesi arttıkça kenar yarıçapı artmakta, buna bağlı olarak ise takım çapı azalmaktadır. Şekil 5'de, kesme mesafesine bağlı olarak farklı kesme koşullarında takım çapındaki değişim her iki iş parçası için ayrı ayrı gösterilmektedir. Tüm soğutma şartlarında Inconel 718'deki takım aşınması, Ti6Al4V'dan daha fazladır. Inconel 718'in özgül ağırlığı (8.19 gr/cm^3) nın Ti6Al4V'un özgül ağırlığından (4.43 gr/cm^3) daha fazla olmasının aşınma farklılığına büyük bir etken olduğu düşünülmektedir. İş parçasından bağımsız olarak MQL ve Bor Yağı uygulandığında takım aşınması minimumken, kuru kesme şartında takım aşınması maksimumdur. Takım-talaş ara yüzünde kesme koşulunun etkisiyle sürtünme azalmış, bu da takım aşınmasına olumlu etki yapmıştır. Tüm kesme koşullarında takım çapındaki azalmanın, başlangıçtaki 100 mm'lik kesme mesafesinde daha fazla olduğu görülmüştür. Özellikle kuru kesme şartında bu net olarak gözlenmektedir. Tüm kesme koşullarında İlk 100

mm'lik kesme mesafesinde takım çapındaki azalma, toplam aşınmanın yüzde 40'ı ila 60'ı arasında değişmektedir. Soğutulmuş karbondioksit kullanılarak yapılan kesme işleminde takım aşınması, kuru kesme şartına göre az olsada, diğer iki (MQL ve Bor yağı) kesme koşuluna göre oldukça fazladır. Bu durumda soğutulmuş hava koşulunun kuru kesme koşuluna göre takım aşınması üzerinde bariz bir farklılık yaratmadığı görülmüştür. MQL ve Bor yağı soğutma koşulu kuru kesme ile kıyaslandığında takımın talaşa yapışıp kaynamasını engelleyerek kesici takım ömrünün uzamasına da katkı sağladığı gözlenmiştir [Liao vd., 2007]. Ayrıca bu iki kesme koşulunun takım aşınması önemli ölçüde azalttığı ve birbirine çok yakın sonuç verdiği gözlenmiştir. MQL'in ekonomik ve çevresel faydaları göz önüne alındığında, bor yağına göre daha avantajlı olduğu düşünülmektedir.

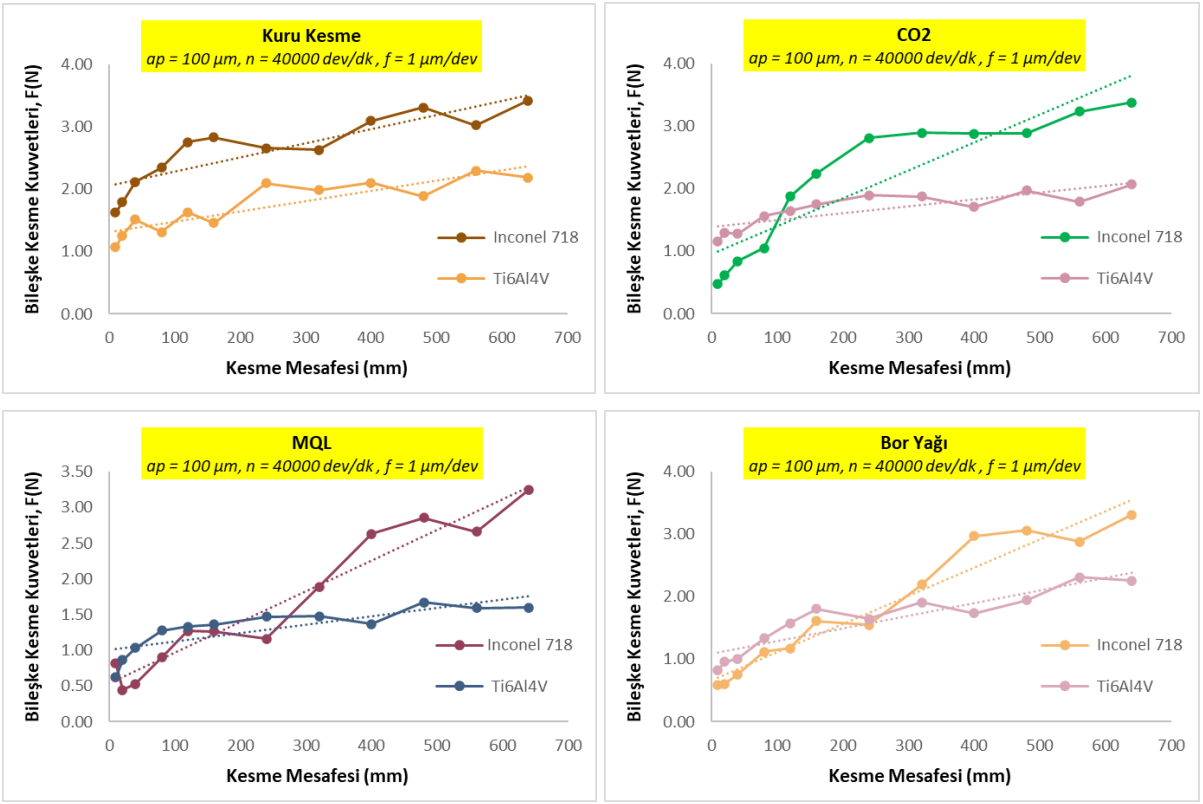


Şekil 5 Farklı kesme koşullarında kesme mesafesine bağlı olarak takım çapının değişimi

3.2. **Kesme Kuvvetleri:**

Ti6Al4V ve Inconel 718 iş parçalarının mikro frezelenmesinde, belirli kesme mesafelerinde kesme kuvvetlerinin değişimi incelenmiştir. Çalışmada kesme esnasında oluşan asıl kesme (Ft) ve ilerleme (Ff) kuvvetleri kullanılarak bileşke kesme kuvveti elde edilmiştir (Şekil 6). Ortaya çıkan kesme kuvveti, mikro frezelemede spesifik kesme enerjisini hesaplamak için sıklıkla kullanılır [Haq et. al. 2020]. Mikro frezeleme işleminde yüksek kesme hızları kullanıldığından, takım aşınması daha kısa bir zaman diliminde gelişebilir [Chinchanikar et. al. 2021]. Takım geometrisindeki bu değişikliğe bağlı olarak kesme kuvvetleri yükselir. Bu

sebeple Şekil 6'da de görüldüğü üzere kesme mesafesi arttıkça kesme kuvvetleri artmaktadır. Ayrıca tüm kesme koşullarında Inconel 718'deki kesme kuvvetlerinin Ti6Al4V dan daha fazla olduğu görülmektedir. Bu sonuç aynı kesme parametreleri kullanılarak bu iki iş parçasının mikro frezelendiği literatürdeki çalışmalarla uyuşmaktadır [Kuram ve Ozcelik 2015]. Inconel için özellikle ilk 100 mm'lik kısımda düşük olan kesme kuvvetleri, kesme mesafesi arttıkça bariz bir artış göstermiştir. Ti6Al4V'daki kesme mesafesine bağlı artış eğimi ise Inconel 718'e göre daha azdır. Bunun, ilk 100 mm'lik kesme mesafesinde Inconel 718'deki takım aşınmasının, Ti6Al4V'a göre oldukça fazla olmasından kaynaklı olduğu düşünülmektedir. Kesme koşulları karşılaştırıldığında ise en büyük bileşke kuvvetin kuru kesme koşullarında elde edildiği görülmüştür. Her iki iş parçasında da Bor yağı ve MQL kesme koşullarında kesme kuvvetlerinin düşük olduğu görülmüştür.

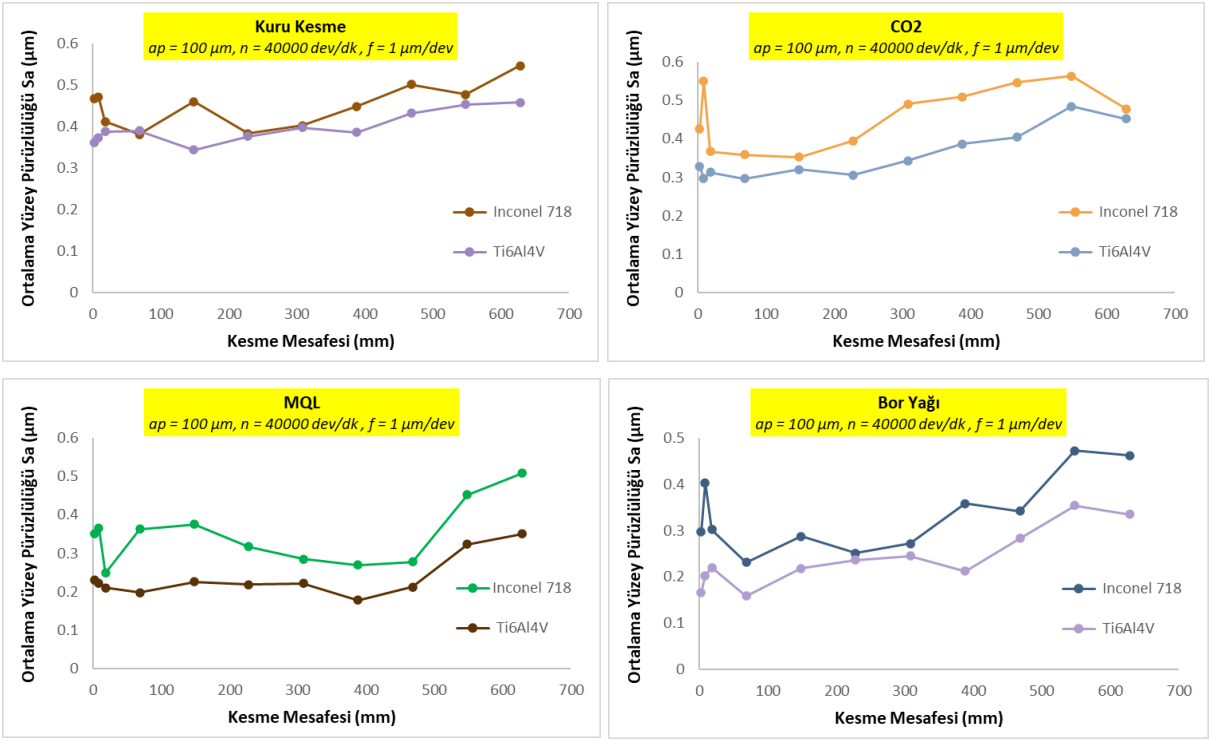


Şekil 6 Farklı kesme koşulları için kesme mesafesi ile ortaya çıkan kesme kuvveti değişimi

3.3. **Yüzey Pürüzlülüğü:**

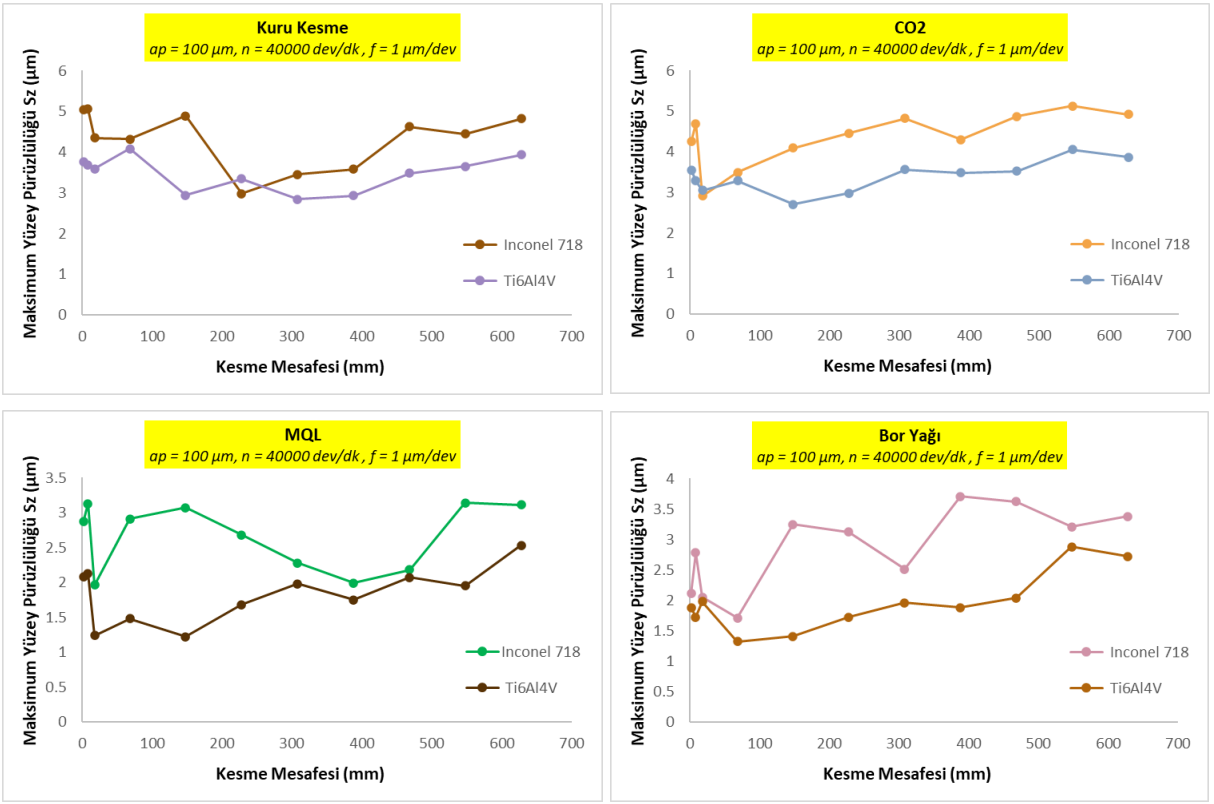
Kesme işlemi sonucunda iş parçası yüzeyinin mümkün oldukça pürüzsüz olması istenir. Kesme parametreleri ve kesme koşulları yüzey pürüzlülüğüne doğrudan etki eder. Bu çalışmada kesme parametreleri sabit tutularak kesme koşullarının etkisi incelenmiştir. Ayrıca Inconel 718 ve Ti6Al4V iş parçaları kullanılarak birbirleri arasındaki farklılıklar da incelenmiştir. Inconel 718 ve Ti6Al4V, benzer kesme koşullarında karşılaştırıldığında

ortalama yüzey pürüzlülüğü değerinin Inconel 718 için daha yüksek olduğu görülmektedir (Şekil 7). Inconel 718'de aşınmanın fazla olması ve buna bağlı olarak kesme kuvvetlerinin de yüksek çıkması, yüzey pürüzlülüğünü de artırmaktadır. En iyi yüzey koşulları MQL ve Bor yağı ile kesme koşullarında görülmüştür. Soğutulmuş CO_2 'nin kuru kesmeye göre yüzey pürüzlülüğünü azalttığı görülse de bariz bir farklılığın olmadığı açıktır. İlk kanallarda (0-20mm) elde edilen Sa değeri sonrasında bir miktar düşse de, 300 mm'den sonra bariz bir şekilde artış göstermektedir. 0-300 mm'deki azalma burun yarıçapının artmasıyla ilişkilendirilebilir. 300 mm'den sonra kenar yarıçapının artmasıyla kazınma etkisi artmış, bu da yüzey pürüzlülüğün artmasına neden olmuştur.



Şekil 7 Farklı kesme koşullarında kesme mesafesine bağlı ortalama yüzey pürüzlülüğü

İki iş parçası maksimum yüzey pürüzlülüğü açısından incelendiğinde ise, ortalama yüzey pürüzlülüğü ile benzer sonuçlarla karşılaşılmaktadır. Aynı kesme koşullarında Inconel 718'deki maksimum yüzey pürüzlülüğü, Ti6Al4V'dan fazladır. Bor yağı ve MQL kesme koşulu, her iki iş parçasında da kuru kesme ve soğutulmuş CO_2 kesme koşuluna göre maksimum yüzey pürüzlülüğünü yarı yarıya azaltmaktadır. Kesme mesafesine bağlı olarak ise maksimum yüzey pürüzlülüğünün bir miktar arttığı gözlenmiştir (Şekil 8). Kesme mesafesine bağlı olarak yüzey pürüzlülüğünün artması takım aşınması ile ilişkilendirilebilir.



Şekil 8 Farklı kesme koşullarında kesme mesafesine bağlı maksimum yüzey pürüzlülüğü

4. SONUÇ

Bu çalışmada sabit kesme parametrelerinde farklı kesme koşullarında Ti6Al4V ve Inconel 718 iş parçalarına mikro frezeleme deneyleri gerçekleştirilmiştir. Kesme koşullarının takım aşınmasına, kesme kuvvetlerine ve yüzey pürüzlülüğüne etkisi incelenmiştir. Buna göre;

- Inconel 718'in her kesme koşulunda Ti6Al4V a göre kesme kuvvetleri, takım aşınması ve yüzey pürüzlülüğü fazladır.
- Kesme mesafesine bağlı olarak Inconel 718'deki kesme kuvvetleri artışının Ti6Al4V'den fazla olmasının sebebi, Inconel 718'deki takım aşınmasının Ti6Al4V'a göre daha fazla olmasına bağlı olduğu düşünülmektedir.
- Takım aşınması ve kesme kuvvetleri açısından Ti6Al4V'un en kötü performansı (kuru kesme), Inconel 718'in en iyi performansından (bor yağı), dahi daha iyi sonuçlar vermiştir. Kesme koşulundan bağımsız olarak Ti6Al4V işlenmesindeki takım ömrü Inconel 718'den fazladır.

- Her iki malzeme için de kuru kesme koşulunda takım aşınması maksimumken, MQL ve bor yağı kullanılan kesme koşulunda takım aşınmasının minimum olduğu görülmüştür.
- Soğutulmuş CO_2'nin kuru kesmeye göre biraz daha iyi sonuçlar verdiği ancak bariz bir katkı sağlamadığından dolayı işlevsel olmadığı gözlenmiştir.
- Takım aşınması, kesme kuvvetleri ve yüzey pürüzlülüğü açısından Bor Yağı ve MQL in birbirine yakın sonuçlar vermiş, en optimum sonuçlar ise bu iki kesme koşulunda Ti6Al4V için elde edilmiştir.

5. TEŞEKKÜR

Bu çalışma 22.Fen.Bil.22 nolu proje kapsamında Afyon Kocatepe Üniversitesi Bilimsel Araştırmalar Birimi (BAP) tarafından desteklenmiştir. Kuruma desteklerinden dolayı teşekkür ederiz.

KAYNAKÇA

1. **Korkmaz, M.E. Yasar, N., Günay, M. (2020),** "Numerical and experimental investigation of cutting forces in turning of Nimonic 80A superalloy", Eng. Sci. Technol. Int. J., Vol. 23, pp 664-73.

2. **Korkmaz, M.E. Günay M, Verleysen, (2019),** "Investigation of tensile Johnson-Cook model parameters for Nimonic 80A superalloy", J Alloy Compd, Vol. 801, pp 542-9.

3. **Busachi, A. Erkoyuncu, J. Colegrove, P. Martina, F. Watts, C. Drake, R. (2017), "**A review of additive manufacturing technology and cost estimation techniques for the defence sector", Cirp J. Manuf. Sci. Tech., Vol.19, pp 117-28.

4. **Brandt, M. (2017),** "Laser additive manufacturing, materials, design, technologies, and applications", Elsevier, pp. 475.

5. **Bodziak, S. Al-Rubaie, KS. Valentina, LD. et al. (2019),** "Precipitation in 300 grade maraging steel built by selective laser melting: aging at 510 °C for 2 h.", Mater. Charact., Vol. 151, pp 73-83.

6. **Shipley, H. McDonnell, D. Culleton, M. Coull, R. Lupo, R, et al. (2018),** "Optimisation of process parameters to address fundamental challenges during selective laser melting of Ti-6Al-4V: a review", Int. J. Mach. Tools Manuf., Vol.128, pp 1-20.

7. **Kassim, S. Saulo, M. Alexsandro, R. José, M. Paiva, Mohamed A. Elbestawi, Stephen, C. (2020), "**Machinability of SLM-produced Ti6Al4V titanium alloy parts Journal of Manufacturing Processes", Vol. 57, pp 768-786.

8. **Sreeram, S, Senthil Kumar, A, Rahman, M, (2006),** "Optimization of cutting parameters in micro end milling operations under dry cutting conditions using genetic algorithms", Int. J. Adv. Manuf. Tech. 2006, Vol. 30, pp 1030-1039.

9. **Kuram, E. Ozcelik, B. (2017),** "Optimization of machining parameters during micro-milling of Ti6Al4V titanium alloy and Inconel 718 materials using Taguchi method", Proceedings Of The Institution Of Mechanical Engineers Part B-Journal Of Engineering Manufacture, Vol. 231, No.2, pp 228-242.

10. **Sun, J. Wong, Y.S. Rahman, M. Wang, ZG, et al. (2006),** "Effects of coolant supply methods and cutting conditions on tool life in end milling titanium alloy", Mach. Sci. Technol., Vol. 10, pp 355-70.

11. **Kasim, M.S. Che Haron, C.H. Ghani, J.A. et. al. (2014),** "Prediction Of Cutting Force In End Milling Of Inconel 718", Journal of Engineering and Technology, Vol. 5, No. 2, pp 63-70.

12. **Liao, Y. Lin, H. (2007),** "Mechanism of minimum quantity lubrication in high-speed milling of hardened steel", Int. J. Mach. Tool. Manuf., Vol. 47, 1660-1666.

13. **Haq, M.A. ul, Hussain, S. Ali, M.A. Farooq, M.U. Mufti, N.A. Pruncu, C.I. Wasim, A. (2020),** "Evaluating the effects of nano-fluids based MQL milling of IN718 associated to sustainable productions", J. Clean Prod. 2021, Vol. 310, 127463.

14. **Chinchanikar, S. Kore, S.S. Hujare, P. A. (2021),** "A review on nanofluids in minimum quantity lubrication machining", J. Manuf. Process 2021, 68, 56-70.

15. **Li, H.Z. Zeng, H. Chen, X.Q. (2006),** "An experimental study of tool wear and cutting force variation in the end milling of Inconel 718 with coated carbide inserts", J. Mater. Process. Technol. Vol. 180, pp 296-304.

16. **Da Silva, R. B. Vieira, J. M. Cardoso, R. N. Carvalho, H. C. et al. (2010),** "Tool wear analysis in milling of medium carbon steel with coated cemented carbide inserts using different machining lubrication/cooling systems", Vol. 271, pp 2459–65.

.

AlCrN ESASLI PVD KAPLAMANIN ENJEKSİYON KALIP YÜZEY KALİTESİNE ETKİLERİ

Yusuf ASLAN, *yusuf.aslan@oerlikon.com* Oerlikon Balzers Kaplama San. ve Tic. Ltd. Şti., 16145, Bursa

Şükran KATMER, *sukatmer@gmail.com* Gazi Üniversitesi, 06500, Ankara

Ulvi ŞEKER, *useker@gazi.edu.tr* Gazi Üniversitesi, Teknoloji Fakültesi, İmalat Mühendisliği Bölümü, 06500, Ankara

ÖZET

Farklı PVD kaplamaların (TiN, ZrN, Ti-Al-N, WC-C, CrN, TiCN, DLC, vb.) ve bunların tek veya çok katmanlı uygulamalarının, kalıpların yüzey kalitesi, korozyon direnci, aşınma direnci gibi özelliklerine etkileri, son yılların araştırma konularından biridir. Bu çalışmada, AlCrN esaslı bir PVD kaplamanın bir plastik enjeksiyon kalıbının yüzey kalitesine etkisi, yüzey pürüzlülüğü üzerinden deneysel olarak araştırılmıştır. Kalıplama malzemesi olarak PA6/GF30 ve PA6/GF50 malzemeler kullanılmıştır. Sonuçlar, PVD kaplamanın, kaplama sonrasında yüzey pürüzlülüğünü artırdığını, ancak sağladığı aşınma dayanımı ile enjeksiyon kalıplama sürecinde yüzey pürüzlülüğünün artışını sınırlandırdığını ortaya koymuştur.

Anahtar Kelimeler: PVD Kaplama, Plastik Enjeksiyon Kalıplama, Yüzey Pürüzlülüğü, Baskı Sayısı

ABSTRACT

In recent years, it is one of the research topics that effects of different PVD coatings (TiN, ZrN, Ti-Al-N, WC-C, CrN, TiCN, DLC, etc.), and their single or multi layers applications on the surface quality, the corrosion resistance, the wear resistance etc. of moulds. In this study, it was investigated that the effects of a PVD coating, which is based on AlCrN, on surface quality of a plastic injection mould via surface roughness, experimentally. PA6/GF30 and PA6/GF50 were used as the moulding materials. The results showed that the PVD coating limited the increasing of surface roughness during injection moulding process because of its wear resistance although it made increasing the surface roughness after the coating.

Keywords: PVD Coatings, Plastic Injection Moulding, Surface Roughness, Cycle Counts

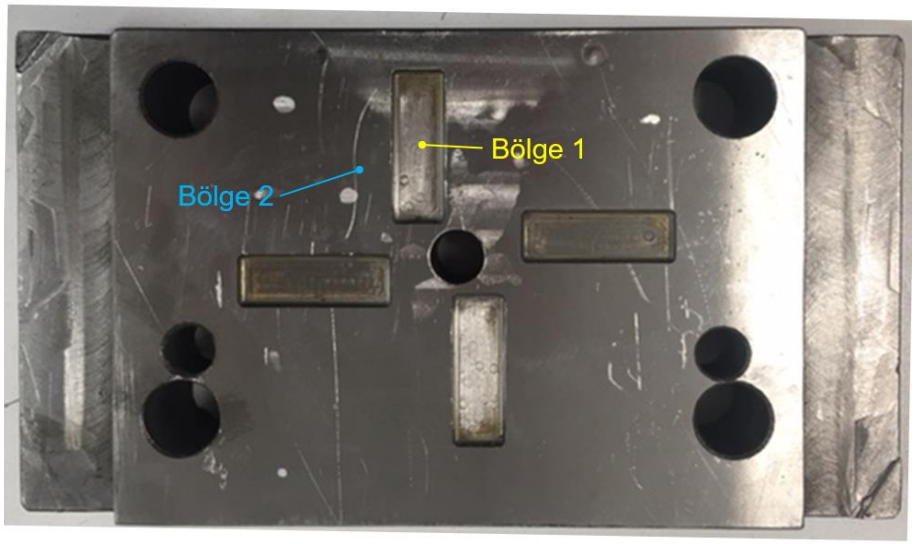
1. GİRİŞ

Plastik enjeksiyon kalıplama süreci kalıbın kapanması, dolum, ütüleme, soğutma ve mal alma ile kalıbın açılarak parçanın çıkartılması safhalarından oluşur. Plastik enjeksiyon kalıpları, kalıplama sürecinin dolum safhasında yüksek kuvvetlere maruz kalmaktadır. Bu kuvvetler; ergiyik plastik veya farklı katkı, dolgu veya liflerle güçlendirilmiş ergiyik plastik malzemenin kalıp içerisindeki akışı esnasında kalıba uyguladığı kuvvetler ve enjeksiyon makinasının kalıp kilitleme kuvvetidir [Huang and Lin 2017]. Özellikle kalıbı dolduran akışkanın göreceli dar olan yolluk, dağıtıcı, giriş kanalları ve kalıp boşluğunda akmaya zorlanması ile akışkan ve kalıp yüzeyi arasındaki sürtünme katsayısına bağlı olarak akış kuvvetleri artmaktadır. Bu kuvvetler her seferinde akışkan içerisindeki varsa katkı, dolgu veya liflerin de etkisiyle kalıp yüzeylerinde yüzey bozulmaları ve daha ileri durumlarda aşınmanın temelini oluşturmaktadır. Akışkan ergiyiğin aşındırma etkisine direnç göstermesi için kalıp yüzeyinin sert ve sürtünme katsayısının düşük olması beklenmektedir [Van Stappen, Vandierendonck et al. 2001, Golabczak, Jacquet et al. 2013]. Bunun için plastik enjeksiyon kalıplarına çeşitli yüzey işlemleri uygulanmaktadır [Steinebrunner, Emmerich et al. 1996, Golabczak, Jacquet et al. 2013, Hopmann, Weber et al. 2015]. Uygulanabilecek yüzey işlemleri seçilen kalıp malzemesinin özellikleriyle doğrudan ilişkili olup, izin verdiği ölçüde çeşitlenebilmektedir [Heinze 1998]. Bu işlemler, yüzey sertleştirme (sementasyon, nitrürasyon vb.) veya sert kaplamalar (kimyasal buhar çöktürme (CVD), fiziksel buhar biriktirme (PVD)) olabilmektedir. PVD kaplama olarak AlTiN, TiN, CrN/Cr, CrN/Nb, ZrN, Ti-Al-N, WC-C, CrN, TiCN, CrCN, DLC gibi kaplamalar uygulanabilmektedir [Kleer, Kaiser et al. 1996, Van Stappen, Vandierendonck et al. 2001, Jacquet, Gołąbczak et al. 2012, Deflorian, Rossi et al. 2013, Silva, Martinho et al. 2014, Moravec 2017, D'Avico, Beltrami et al. 2018]. Beş farklı PVD kaplamanın (AlTiN, TiN, CrN/Cr, CrN/Nb, ZrN), kalıpların korozyon ve yüzey dayanım özelliklerine etkisinin araştırıldığı bir çalışmada titanyum esaslı kaplamaların plastik ve kauçuk kalıplarında daha yüksek korozyon direnci ve yüzey özellikleri sağladığı rapor edilmiştir (D'Avico, Beltrami et al. 2018). CrN/CrCN/DLC çok katmanlı PVD kaplama cam elyaf takviyeli poliproplenin kalıplama çevriminde, kaplamasız kalıba nazaran çok yüksek (58,2 kat) aşınma dayanımı sergilemiştir [Silva, Martinho et al. 2014].

Bu çalışmada, cam elyaf ile güçlendirilmiş aşındırıcı etkisi yüksek plastik matriksli kompozitlerin kalıplanmasında AlCrN esaslı bir PVD kaplamanın kalıp yüzey durumlarına etkisi yüzey pürüzlülüğü üzerinden deneysel olarak araştırılmıştır [Aslan 2022]. Bu sayede, yüksek aşındırıcılıktaki bir malzeme ile çalışan bir kalıbın istenen yüzey özelliklerini muhafaza etmesinde, dolayısıyla istenen parça yüzey kalitesini sağlamasında AlCrN esaslı bir PVD kaplamanın etkin olup olmadığı ortaya konmuştur.

2. DENEYSEL ÇALIŞMA

Bu çalışmada, plastik enjeksiyon kalıbı olarak dört boşluklu bir plastik enjeksiyon kalıbı kullanılmıştır. Kalıbın dişi plakasının üst görünüşü Şekil 1'de gösterilmiştir. Dişi plaka dış ölçüleri 30 mm x 125 mm x 200 mm olup, PVD kaplamaya uygun, DIN 1.2738 plastik takım çeliğinden (Impax) imal edilmiştir. Dişi plakanın imal edildiği çelik malzemenin (DIN 1.2738), PVD kaplama süreci açısından önemli bazı özellikleri Tablo 1'de sunulmuştur. Kalıp imalatından sonra ve deneysel çalışmanın farklı aşamalarında Şekil 1'de gösterilen bölgelerden yüzey pürüzlülük ölçümleri Stylus Profilmetre (Mahr SD26) ile (DIN EN ISO 4287) alınmıştır. Bunlar; 1. Bölge, kalıp boşluğu ve 2. Bölge, kalıp kapanma yüzeyidir.



Şekil 1. Plastik enjeksiyon kalıbı ve yüzey pürüzlülüğü ölçümü alınan bölgeler

Tablo 1. DIN 1.2738 malzemenin özellikleri

Malzeme Kimyasal Bileşenleri	Karbon	Krom	Molibden	Silisyum	Mangan	Nikel
	C	Cr	Mo	Si	Mn	Ni
	0,40	2,00	0,20	0,30	1,50	1,10
Malzeme Isıl İşlem Bilgisi		Sıcaklık		Ortam		Sertlik
	Yumuşatma Tavlaması	710 - 740 °C		Fırın		235 HB
	Gerilim Giderme	500 - 550°C		Fırın		

Dişi plaka, kalıp boşlukları ve kalıp kapanma yüzeyine PVD Ark metodu ile AlCrN esaslı PVD kaplama (Balinit Alcrona Pro, Oerlikon Balzers) yapılmıştır. Kaplama işlemi sadece dişi plakaya uygulanmıştır. Uygulanan PVD kaplamanın bazı özellikleri Tablo 2'de belirtilmiştir.

Tablo 2. AlCrN esaslı PVD kaplamanın özellikleri [10]

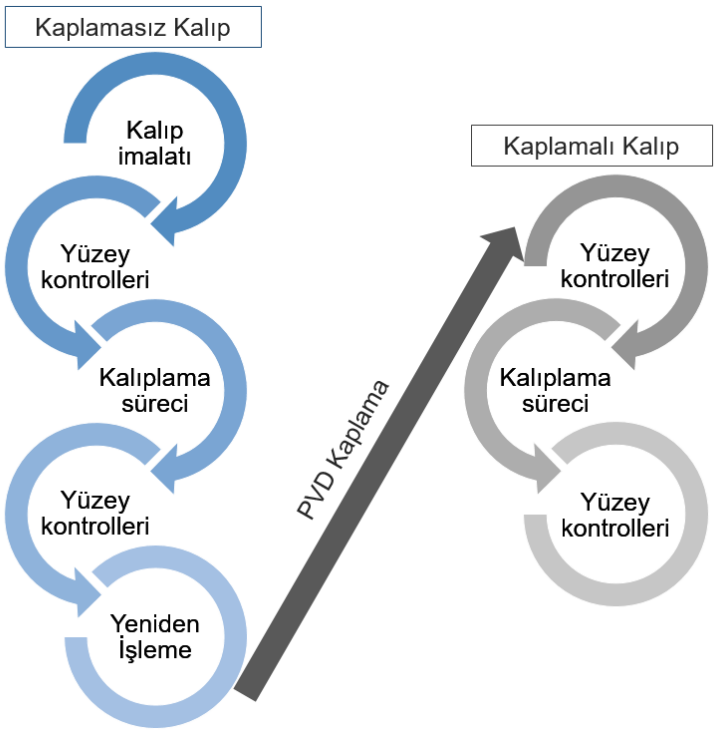
Kaplama malzemesi	AlCrN esaslı
Kaplama yöntemi	Arc
Kaplama rengi	Parlak gri
Kaplama kalınlığı HIT[GPa]*	36 +/-3
Sürtünme katsayısı (kuru) - çelik**	~0.6
İçsel stres [GPa]***	-3 +/-1
Maks. servis sıcaklığı [°C]****	1,100
Kaplama sıcaklığı [°C]	< 500

ºVerilen tüm veriler yaklaşık değerlerdir, uygulamaya, ortama ve test koşullarına bağlıdır.
**Kaplama kalınlığı HIT[GPa] ISO 14577'ye göre nano iz ile ölçülmüştür Çoklu katmanlar için farklı katmanların sertliği değişir.*
***Sürtünme katsayısı (kuru) – çelik ASTM G99'a göre bir Çelik bilyayla kuru koşulda diskte bilya testiyle belirlenmiştir. Alıştırma sırasında verilen değerler aşılabilir.*
****İç stres [GPa] XRD veya bükme yöntemiyle ölçülür (Stoney denklemi). Hesaplanan termal stres çıkarılmıştır.*
*****Maks. servis sıcaklığı [°C] olarak belirtilen değerler alan dışı yaklaşık değerlerdir. Termodinamik yasalarından dolayı uygulamada bir basınç bağımlılığı vardır [10].*

Kalıplama malzemesi olarak %30 cam elyaf takviyeli polyamid 6 (PA6/GF30; Tecomid® NB40 GR30 BK005 IM E) ve %50 cam elyaf takviyeli polyamid 6 (PA6/GF50;Tecomid® NB40 GR50 BK005 IL) malzemeler kullanılmıştır. Kalıplanan termoplastik kompozit malzemelerin bazı özellikleri Tablo 3'de sunulmuştur. Deneysel çalışmada, kalıbın kaplamasız ve kaplamalı çalışma sürecinde, PA6/GF30 malzemeden 60.000 baskı, PA6/GF50 malzemeden 10.000 baskı yapılmıştır. Böylece kaplamasız ve kaplamalı kalıbın çalışma şartları ve yüzey kaliteleri toplamda, her iki durum için de ayrı ayrı, 70.000 adet baskı sayısı sonunda kontrol edilmiştir. Baskı, kalıbın bir çevrim çalışması (kalıp kapanması, enjeksiyon, ütüleme, soğutma ve kalıbın açılıp parçanın çıkartılması) sürecini ifade etmektedir. Yüzey durumu kontrolleri tek kalıp gözü üzerinden yapıldığı için ürün sayısı yerine baskı sayısı ifadesi kullanılmıştır. Tüm deneysel çalışma sürecinde, kalıp üzerinde yapılan işlemler ve sıralamaları Şekil 2'de şematize edilmiştir.

Tablo 3. PA6/GF30 ve PA6/GF50 malzemelerin özellikleri

Özellik	PA6/GF30	PA6/GF50
Yoğunluk (g/cm^3)	1,30	1,54
Ergiyik akış hızı (2,16kg, 270 ^{o}C) (g/10´)	-	-
Nem Alma (50% RH, 23 ^{o}C) (%)	1,6	1,4
Ergime sıcaklığı (10 K/min) (^{o}C)	223	223
Yük altında ısıl deformasyon sıcaklığı (0,45 MPa) (^{o}C)	210	220
Enjeksiyon sıcaklığı (^{o}C)	250-270	250-270
Kalıp sıcaklığı (^{o}C)	60-100	60-100
Enjeksiyon hızı	Yüksek	Yüksek



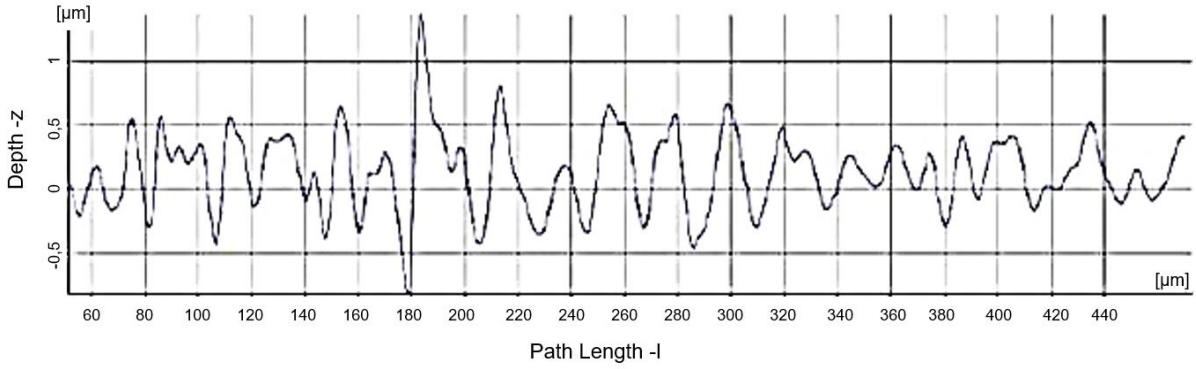
Şekil 3. Kalıp üzerinde yapılan işlemler süreci

3. DENEYSEL BULGULAR

Deneysel bulgular Şekil 3'de sunulan şematik gösterimde belirtilen sıra ile bu başlık altında verilmiştir.

Kaplamasız kalıp kalıplama öncesi yüzey kontrolleri

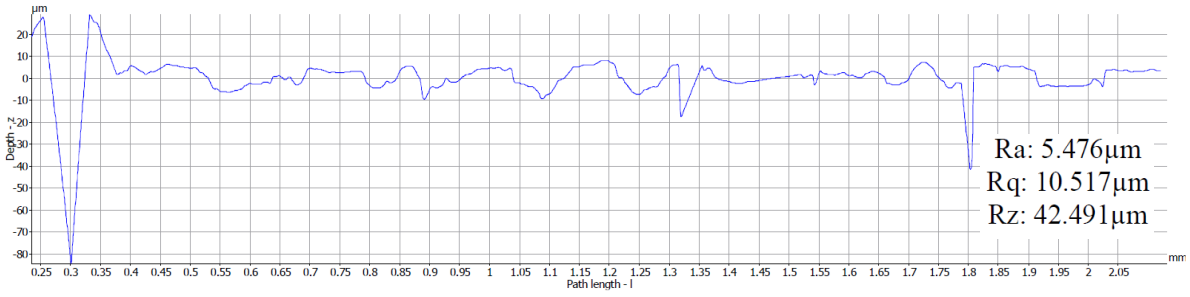
Enjeksiyon kalıp imalatından sonra, Şekil 1'de gösterilen 1. Bölgeden kalıbın yüzey pürüzlülük ölçümü yapılmıştır. Maksimum yüzey pürüzlülüğü (Rz) 1,1602 µm, ortalama yüzey pürüzlülüğü (Ra) ise 0,2531 µm olarak ölçülmüştür (Şekil 4).



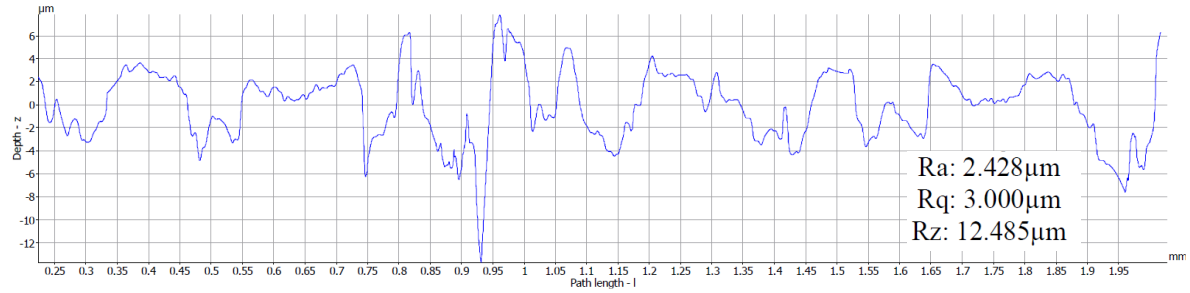
Şekil 4. Kaplamasız kalıp kalıplama öncesi yüzey pürüzlüğü değeri

Kaplamasız kalıp kalıplama sonrası yüzey kontrolleri

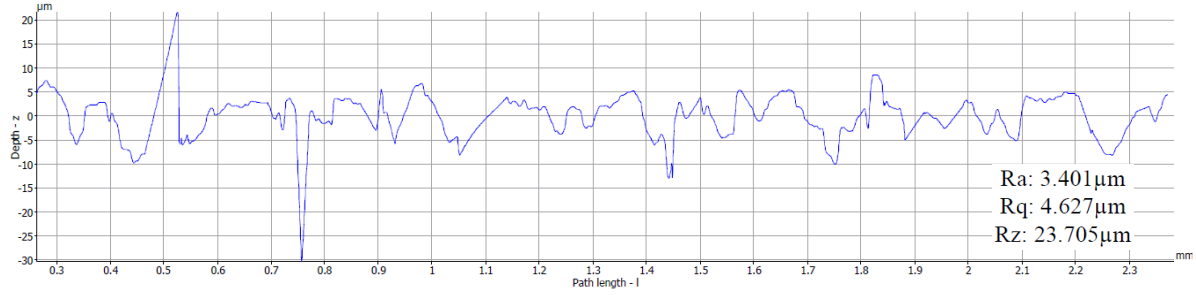
Kaplamasız kalıpla ikinci bölümde açıklandığı gibi toplamda 70.000 baskı yapılmış ve işlem sonunda 1. Bölgeden yüzey pürüzlülük ölçümleri alınmıştır. Kalıp boşluğu yüzey durumu plastik akış yönüne paralel (Şekil 5a), plastik akış yönüne dik (Şekil 5b) ve kalıp gözü merkezinden noktasal (Şekil 5c) ölçümlerle incelenmiştir. Yüzey pürüzlülüğü sonuçları Şekil 5'te her bir ölçüm yönü için ayrı ayrı sunulmuştur. Maksimum yüzey pürüzlülüğü (Rz); akış yönüne paralel ölçümde 42,491 µm, akış yönüne dik ölçümde 12,485 µm ve kalıp gözü merkezinden noktasal ölçümde 23,345 µm olarak ölçülmüştür. Ortalama yüzey pürüzlülüğü (Ra) ise; akış yönüne paralel ölçümde 5,476 µm, akış yönüne dik ölçümde 2,428 µm ve kalıp gözü merkezinden noktasal ölçümde 3,401 µm olarak tespit edilmiştir.



(a)



(b)

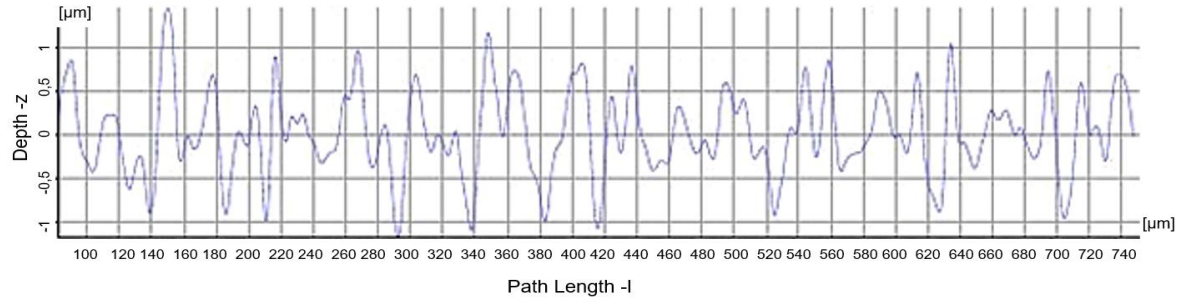


(c)

Şekil 5. Kaplamasız aşınmış kalıbın yüzey pürüzlülüğü (a) plastik akış yönüne paralel, (b) plastik akış yönüne dik, (c) kalıp gözü merkezinden noktasal

Kaplamalı kalıp kalıplama öncesi yüzey kontrolleri

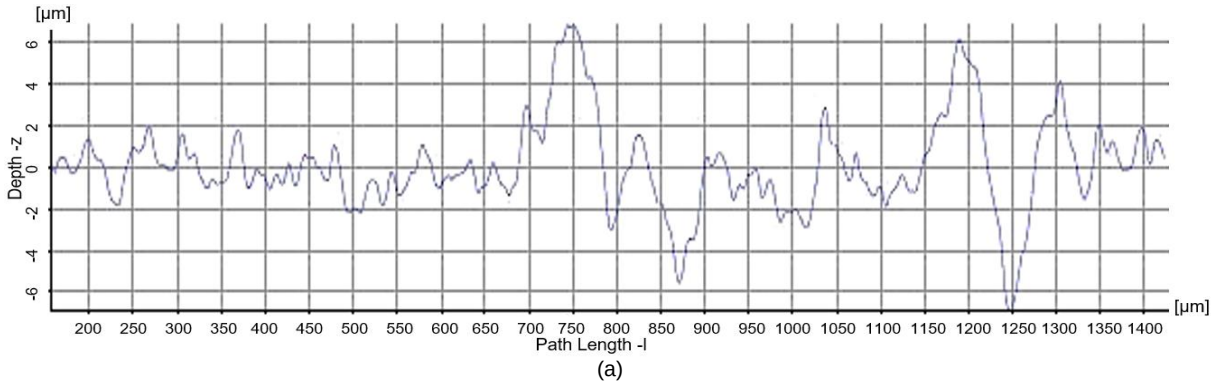
Kaplamasız kalıp yeniden işlenmiş ve kalıp kapanma yüzeyi ile kalıp boşlukları PVD kaplanmıştır. PVD kaplama işlemi sonrasında 1. Bölgeden yüzey pürüzlülük ölçümleri yapılmıştır. Elde edilen sonuçlar Şekil 6'daki grafikte verilmiştir. Ra 0,3691; Rq 0,4719; Rz 2,1672 µm ölçülmüştür.



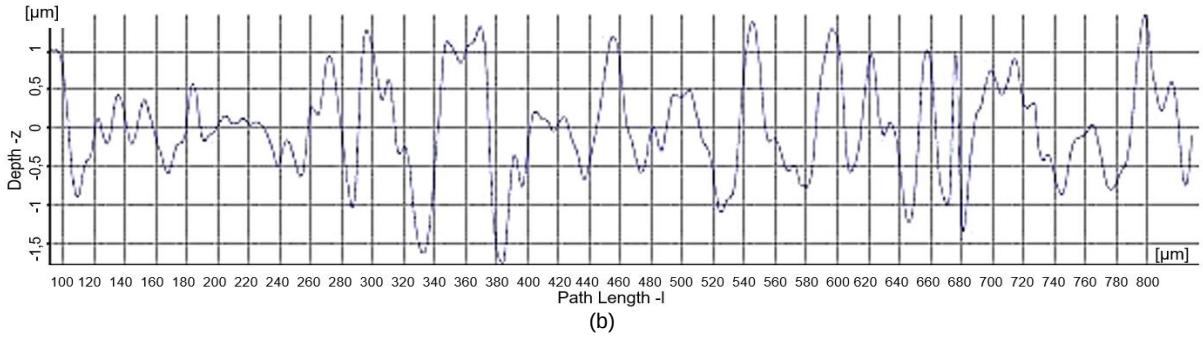
Şekil 6. Kaplamalı kalıp, kalıplama öncesi yüzey pürüzlülük değeri

Kaplamalı kalıp kalıplama sonrası yüzey kontrolleri

PVD kaplanmış kalıba da, kaplamasız kalıp gibi, toplamda 70.000 baskı sonunda Şekil 1'de belirtilen bölgelerden yüzey pürüzlülük ölçümleri yapılmıştır. Yapılan yüzey pürüzlülük ölçümlerinde 1. Bölgeden alınan değerler (Ra 1,5192; Rq 2,1711; Rz 7,6295 µm) Şekil 7a'da, 2. Bölgeden alınan değerler (Ra 0,5165; Rq 0,6502; Rz 2,6142 µm) Şekil 7b'de gösterilmiştir.



(a)

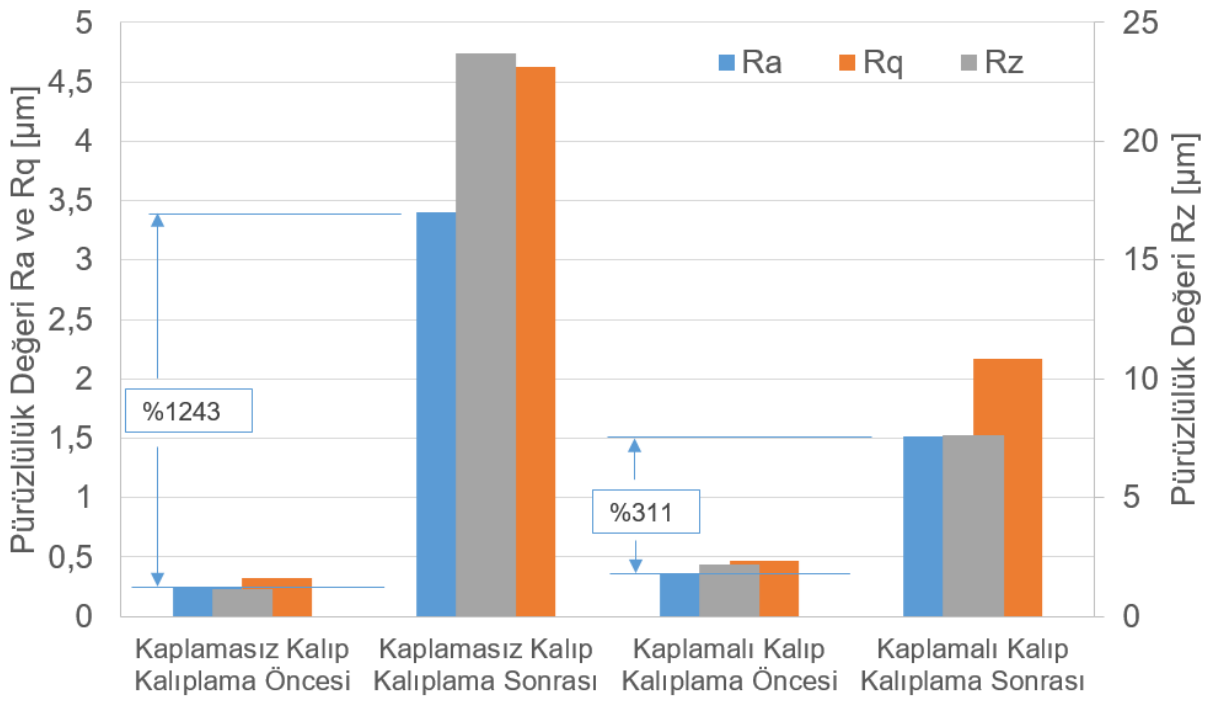


(b)

Şekil 7. Kaplamalı kalıp, kalıplama sonrası yüzey pürüzlülük değeri (a)1. Bölge, (b) 2. Bölge

Kaplamasız kalıp ve kaplamalı kalıbın, kalıp boşluğundan alınan (1. Bölge) tüm yüzey pürüzlülük ölçümleri Şekil 8'deki grafikte karşılaştırılmıştır. Grafikte Ra ve Rq sol düşey eksende, Rz sağ düşey eksende gösterilmiştir. Öncelikle kaplamasız ve kaplamalı kalıplarda ortalama yüzey pürüzlülükleri (Ra) kalıplama öncesi ve kalıplama sonrası olarak kendi içinde değerlendirilmiştir. Buna göre, kaplamasız kalıpta 70.000 baskı sonunda yüzey pürüzlülüğü %1243 artış gösterirken PVD kaplamalı kalıpta bu artış %311 olmuştur.

Kaplamasız ve kaplamalı kalıplardaki Ra değerleri, kalıplama öncesi ve kalıplama sonrasında karşılaştırıldığında, sonuçlar, PVD kaplamalı kalıbın yüzey pürüzlülüğünün kalıplama öncesi %45,8 daha yüksek olduğunu gösterirken, kalıplama sonrasında ise %55,3 daha düşük gerçekleşmiştir (Şekil 8).



Şekil 8. Yüzey pürüzlülük değerlerinin karşılaştırılması

4. SONUÇLAR

AlCrN PVD kaplamanın bir plastik enjeksiyon kalıbının yüzey pürüzlülüğüne etkisinin araştırıldığı bu çalışma, PVD kaplamanın, kaplamanın atomik düzeyde yüzeyde biriktirilmesi nedeniyle kalıp yüzeyinde yüzey pürüzlülüğünü artırdığını ancak sağladığı aşınma dayanımı ile baskı esnasında kalıpta yüzey pürüzlülüğünün artışını sınırlandırdığını ortaya koymuştur.

Bu çalışmanın sonuçlarına dayanarak, özellikle belirli bir yüzey deseninin veya parlaklığının istendiği kalıplarda AlCrN PVD kaplama uygulanmasının kalıpta yenilenme ihtiyacını

azaltacağı ve baskı sayısını artıracağı söylenebilir. Benzer bir çalışmanın, PVD kaplamaların, farklı yüzey desenlerine ve parlaklık derecelerine sahip kalıplardaki etkilerini incelemek için yapılabilir olduğu öngörülmektedir.

KAYNAKÇA

Aslan, Y. (2022), "AlCrN Esaslı Bir Kaplamanın Plastik Enjeksiyon Kalıp Ömrüne Etkisinin Deneysel Olarak Araştırılması", Gazi Üniversitesi.

D'Avico, L., Beltrami, R., Lecis, N. and Trasatti, S. (2018), "Corrosion Behavior and Surface Properties of PVD Coatings for Mold Technology Applications", Coatings 9(1).

Deflorian, F., Rossi, S., Maines, L. and Straffelini, G. (2013), "Industrial PVD coatings for improving corrosion protection of components for polymeric injection moulding", Corrosion Engineering, Science and Technology 42(3): 266-271.

Golabczak, M., Jacquet, P., Nouveau, C. and Fliti, R. (2013), "Tribological Investigations of TiC+a-C:H Coatings Manufactured on X38CrMoV5-1 Steel Using PVD Technology", Defect and Diffusion Forum 334-335: 97-104.

Heinze, M. (1998), "Wear resistance of hard coatings in plastics processing", Surface and Coatings Technology 105: 38–44.

Hopmann, C., Weber, M., Schöngart, M., Schäfer, C., Bobzin, K., Bagcivan, N., Brögelmann, T., Theiß, S., Münstermann, T. and Steger, M. (2015), "Injection moulding of optical functional micro structures using laser structured, PVD-coated mould inserts".

Huang, M.-S. and Lin, C.-Y. (2017), "A novel clamping force searching method based on sensing tie-bar elongation for injection molding", International Journal of Heat and Mass Transfer 109: 223-230.

Jacquet, P., Gołąbczak, M. and Lourdin, P. (2012), "Experimental characterizations of non-seizing solutions for plastic moulding tools", Applied Surface Science 261: 824-829.

Kleer, G., Kaiser, E. and Döll, W. (1996), "Behaviour of Ti-A1-N coatings for tools applied in the thermoplastic moulding of inorganic glasses", Surface and Coatings Technology 79: 95-102.

Moravec, J. (2017), "Increase of the operating life of active parts of cold-moulding tools", Tehnicki vjesnik - Technical Gazette 24(Supplement 1): 143-146.

Silva, F. J. G., Martinho, R. P. and Baptista, A. P. M. (2014), "Characterization of laboratory and industrial CrN/CrCN/diamond-like carbon coatings", Thin Solid Films 550: 278-284.

Steinebrunner, J., Emmerich, T., Heck, S., Munder, I. and Steinbuch, R. (1996), "A novel impact tester operating at elevated temperatures for characterising hard coatings", Surface and Coatings Technology 86-87: 748-752.

Van Stappen, M., Vandierendonck, K., Mol, C., Beeckman, E. and De Clercq, E. (2001), "Practice vs. laboratory tests for plastic injection moulding", Surface and Coatings Technology 142-144: 143-145.

TEŞEKKÜR

Bu çalışma Ata Kalıp San ve Tic A.Ş.' tarafından, firma bünyesinde yürütülen 7190209 numaralı TÜBİTAK TEYDEB 1507 projesi kapsamında desteklenmiştir.

GÖRSEL LAZER NOKTA KAYNAĞI UYGULAMALARINDA AÇISAL KONUMLANDIRMA HATALARININ KAYNAK KALİTESİNE ETKİSİNİN İNCELENMESİ

Emre ŞERİFAĞAOĞLU, *emreserifagaoglu@gmail.com* Evinoks Servis Ekip. 16245, Bursa

Murat Erkin AKYÜZ, *erkinakyuz@gmail.com* Evinoks Servis Ekipmanları, 16245, Bursa

Barış KOYAŞ, *bkoyas@evinoks.com* Evinoks Servis Ekipmanları, 16245, Bursa

Murat REİS, *reis@uludag.edu.tr* Bursa Uludağ Üniversitesi, 16059, Bursa

ÖZET

Paslanmaz ince malzemelerin görsel kusur oluşturmayacak şekilde birleştirilmesi için gerekli kaynak parametrelerinin belirlenmesi oldukça hassas bir işlemdir. Zira, kaynak işleminin görsel kusur olmayacak kadar narin olması istenirken, diğer yandan da bağlantının cihazın ömrü boyunca dayanacak kadar güçlü olması beklenir. Bu çalışmada paslanmaz (inox) mutfak ve otel ekipmanlarının mikro lazer punta kaynak uygulamalarında açısal konumlandırma hatalarının kaynak kalitesine etkisi deneysel olarak incelenmektedir. Manuel kaynak işlemlerinde en yaygın operatör hatası, lazer ışını ile plaka yüzeyi arasındaki açısal konumlandırma hatasıdır. Çalışmada lazer sinyali şiddet ve süresi gibi diğer kaynak parametreleri sabit tutulmuş, farklı lazer ışın açıları için kaynak numuneleri hazırlanmış ve numunelerde her bir kaynak noktasının taşıyabileceği maksimum yükler ölçülmüştür. Deneyler, kritik kaynak açısından daha küçük açılarda ince paslanmaz sac üzerinde yeterince geniş bir kaynak alanı oluşturulamayacağını, buna karşın kritik kaynak açısından büyük açılarda ince paslanmaz malzemenin görünür yüzeyinde ısı kaynaklı izler veya mikro deformasyonlar oluştuğunu göstermektedir. Deneysel sonuçlar kullanılarak, mevcut lazer kaynak parametreleri için optimum torç açısı aralığı belirlenmiştir. Sonuçlar, görsel lazer kaynak uygulamalarında, lazer ışını açısının, operatörün gözle ayarlayamayacağı kadar dar bir açı aralığında doğru bir şekilde kaynaklanabileceğini göstermektedir.

Anahtar Kelimeler: inox, paslanmaz, sac, mikro lazer, kaynak

ABSTRACT

It is a very sensitive process to determine the necessary welding parameters for joining stainless thin materials in a way that does not create visual defects. Because while it is desired that the welding process be delicate enough to not have visual defects, on the other hand, the connection is expected to be strong enough to last for the life of the device. In this study, the effect of angular positioning errors on welding quality in micro laser spot welding applications of stainless (inox) kitchen and hotel equipment is investigated experimentally. The most common operator error in manual welding processes is the angular positioning error between the laser beam and the plate surface. In the study, other welding parameters such as laser signal intensity and duration were kept constant, welding samples were prepared for different laser beam angles and the maximum loads that each welding spot could carry were measured in the samples. Experiments show that a sufficiently large weld area cannot be formed on the thin stainless sheet at angles smaller than the critical weld angle, whereas heat-induced traces or micro-deformations are formed on the visible surface of the thin stainless material at angles greater than the critical weld angle. Using the experimental results, the optimum torch angle range was determined for the available laser welding parameters. The results show that in visual laser welding applications, the laser beam angle can be welded accurately in an angle range that is too narrow for the operator to adjust with the eye.

Keywords: inox, stainless, sheet metal, micro laser, welding

1. GİRİŞ

Yüksek enerjili lazer kaynağı uygulaması dar bir bölgenin ısıdan etkilenmesi, düşük kalıntı gerilmeleri, tek tip tane yapısı, yüksek verimlilik ve geleneksel kaynak işlemlerine kıyasla düşük işletme maliyetleri nedeniyle ince cidarlı paslanmaz yüzeylerin birleştirilmesinde sıklıkla kullanılmaktadır. Lazer kaynağı hassas ısı kontrolü sayesinde minimum termal bozulma, iyi mekanik özellikler ve mükemmel tekrarlanabilir gibi avantajlara sahiptir [Luangpaiboon 2011, Tsukamoto 2003]. İnce sac metal kaynağı için başarılı bir şekilde kullanılabilmesine rağmen, derin nüfuz etme kabiliyetine de sahiptir [Chen 2009]. Bu avantajların bir sonucu olarak lazer kaynağı, geleneksel ark kaynağına kıyasla daha yüksek kaynak hızı ve verimliliği sunar. Görselliğin ön planda olduğu inox mutfak ve otelcilik ekipmanlarının üretiminde bu kriterlere ek olarak, kaynak işleminin ince levhanın görünen yüzünde ısı izi bırakmayacak kadar da narin yapılabilmesi gerekmektedir. Ancak, paslanmaz ince metal levhaları görünür yüzeylerinde ısı izi oluşmayacak şekilde lazerle birleştirmek için, özel kaynak yöntemlerinin kullanılması gerekir. Aksi halde aşırı ısının etkisi ile ince metal

levhaların küçük kalınlıkları mikro kaynakta dahi görünür ısı izlerinin oluşumuna neden olabilir. Bu nedenle ince saca minimum ısı girdisi hem teknik hem de ekonomik açıdan oldukça etkilidir. Teknik olarak, görünür olmayan yüzeyden görünür yüzeye doğru huni formunda bir ergime hacmi oluşacak şekilde mikro lazer kaynağı uygulaması yapılır. Bu sayede görünür ince paslanmaz sac ısıdan daha az etkilenir. Bu uygulama ekonomik olarak, daha az ısı girişi, daha az ekipman yatırımı ve düşük çalıştırma maliyeti ile ilişkili olarak daha düşük lazer gücü gerektirir.

Östenitik paslanmaz çeliklerin lazerle mikro kaynağına odaklanan literatürdeki çalışmalar, lazer kaynak parametrelerinin kaynak genişliği ve kaynak penetrasyon derinliği üzerindeki etkisini analiz eder. Derin penetrasyonlu lazer kaynaklarında kaynaklı parçanın mukavemetini bozan gözeneklilik sıklıkla gözlenir [Ishide 1999, Katayama 1997,1998,1998]. Lazer kaynak işlemini optimize etmek ve yüksek kaynak kalitesi ve mukavemeti sağlamak için kaynak işleminde gözenekliliğin nasıl oluştuğunu anlamak ve ardından gözenek kusurlarını azaltmak veya ortadan kaldırmak için yöntemler bulmak gerekir. Zhou ve Tsai gözenek oluşumuna yol açan taşıma olaylarını sistematik olarak araştırmak için matematiksel modelleri kullanmak ve lazer kaynağında gözenek oluşumunu azaltmak veya ortadan kaldırmak için olası çözümleri araştırmıştır [Zhou 2006]. Sonuçlar darbeli lazer kaynağında gözenek oluşumunun iki rakip faktörden kaynaklandığını göstermektedir: Bu faktörler erimiş metalin katılaşma hızı ve çökme işlemi sırasında erimiş metalin geri doldurma hızıdır. Sun ve ark. 20 mm kalınlığındaki AISI 304 plakaların lazer dikiş kaynaklarında gözenek oluşumunda farklı koruyucu gazların etkisini incelemiştir [Sun 2017]. Sonuçlar, koruyucu gazın gözenek oluşumunda büyük bir etkiye sahip olduğunu ve Ar kullanıldığında dikiş kaynaklarında birkaç gözenek bulunduğunu, ancak N2 veya gaz kullanılmadığında dikiş kaynaklarında neredeyse hiç gözenek bulunmadığını göstermiştir. Kumar ve ark. AISI 304 ve AISI 316 paslanmaz çelik alaşımlarının lazer dikiş kaynağına ilişkin karşılaştırmalı bir analizini yapmıştır [Kumar 2017]. Sonuçlar, dikiş kaynağının maksimum nihai mukavemetini elde etmek için AISI 316 alaşımına kıyasla AISI 304 alaşımında daha yüksek doğrusal ısı girdisinin gerekli olduğunu göstermiştir. Paslanmaz çelik alaşımlarının lazer mikro nokta kaynağı üzerine az sayıda çalışma yapılmıştır [Siva 2012, Cedeño-Viveros 2018]. Siva Shanmugam ve ark. plaka üzerinde boncuk konfigürasyonunda 2,5 mm kalınlığındaki östenitik AISI 304 paslanmaz çelik levhaların lazer mikro nokta kaynağı için simülasyonu deneysel testlerle karşılaştıran bir sonlu eleman modeli (FEM) sunmuştur [Siva Shanmugam 2012]. Cedeno-Viveros ve ark. örtüşen bir bağlantı konfigürasyonunda 0,254 mm kalınlığında östenitik AISI 302 paslanmaz çelik levhalarda lazer mikro nokta kaynaklarında lazer gücünün ve odak mesafelerinin etkisini deneysel olarak incelemiştir [Cedeno-Viveros 2018]. Kumar ve

ark. Inconel 718 ince folyolarını kalın 410 çelik yığına birleştirmek için mevcut mikro dirençli nokta kaynağının (mikro-RSW) mikro lazer nokta kaynağı ile değiştirilmesinin çeşitli yönlerini araştırmış ve sonuçları kaynak kalitesi, mekanik mukavemet, mikro yapısal özellikler ve yüksek sıcaklıktaki kaynak mukavemeti temelinde değerlendirmiştir [Kumar 2022].

Özellikle ultra ince folyoların mikro lazer nokta kaynağı için darbeli lazer kaynağı, sürekli dalga lazer kaynağına göre tercih edilen kaynak yöntemidir. Zira, bu yöntem ısıdan etkilenen bölgeyi, artık gerilmeleri ve ısı girdisini azaltan hassas ısı kontrolü sunar [Ventrella, 2010]. Tıbbi cihaz imalatı, ince membranlı sensörler, işaretleyicilerin stentlere kaynaklanması, ultra ince folyolar kullanılarak mikro türbin imalatı vb. dahil olmak üzere çeşitli mikro kaynak uygulamalarında darbeli lazer kaynağı kullanılmaktadır [Kleine 2004, Gillner 2005, Tolinski 2008, Quazi 2021]. Genel olarak, darbeli lazer kaynağı, periyodik bir şekilde art arda malzeme eritmeye ve katılaşmaya odaklanan yüksek yoğunluklu bir enerji ışınının aralıklı bir tedarikidir. Darbeli lazer kaynağındaki işlem parametreleri, tatmin edici kaynak kalitesi elde etmek için kullanılan darbe enerjisi/lazer gücü, darbe genişliği, darbe frekansı, lazer nokta boyutu ve kaynak hızını içerir [Shaikh 2019, Pakmanesh 2018]. Kim ve ark. darbeli bir lazer kullanarak nükleer santraller için Inconel 600 boru şekilli bileşenlerin (1.0 mm ila 1.2 mm Inconel yığını) başarılı bir şekilde kaynaklandığını ilk çalışmanın ardından, Inconel gibi sıcaklık dayanımı yüksek malzemelerin mikro lazer kaynak yöntemi ile paslanmaz çelikle birleştirilmesi konusu son yılların popüler araştırma konularındandır [Kim 2001, Ahmad 2020, 2021, Yan 2022]. Buna benzer olarak, Inconel alaşımlarının farklı çelikler ile birleştirilmesi konusunda da literatürde çalışmalar mevcuttur [Srikanth 2020, Cheepu 2020, Sidharth 2019, Lin 2021, Kumar 2022]. Ventrella ve ark. 100 m kalınlığında AISI 316L paslanmaz çelik folyonun mikro lazer kaynağında lazer enerjisinin etkisini araştırmışlar ve lazer darbe enerjisinin hassas bir şekilde kontrol edilmesiyle mikro yapısal ve mekanik güvenilirliğin sağlanabileceği sonucuna varmışlardır [Ventrella 2010]. Buna karşılık, Lertora ve ark. 0,4 mm ila 1,6 mm arasındaki Inconel 718 levhalar arasındaki CO2 lazer bindirme bağlantılarını araştırmış ve mikro çatlaklara rağmen bindirme kaynaklarının yorulma davranışlarının uçak motorlarının gereksinimlerine uygun olduğunu bildirmişlerdir [Lertora 2014]. Metal yüzeylere çarpan yüksek ışınımlı lazerler, metalin yüksek yansıtıcıdan güçlü emiciye hızla değişebildiği karmaşık, dinamik bir süreç yaratır. Bu etki Simonds ve ark. tarafından deneysel bir çalışmada ele alınmıştır [Simonds 2018].

Manuel mikro nokta lazer kaynağında sac malzemelerin birleşen yüzeyleri arasındaki boşluk ve torç tutuş açısı (lazer ışını ve kaynak yüzeyi arasındaki açı) görünür yüzeyde ısı izi oluşturmadan yeterli kaynak mukavemeti elde etmek için anahtar değişkenlerdir. Lazer kaynağında kaynak dikişi geometrisi ile ilgili etkiler zaten iyi anlaşılmış olsa da, görsel mikro

lazer kaynağının ayrıntılı özellikleri yeterince açıklığa kavuşturulmamıştır. Bu çalışmada lazer ışını ile kaynak yüzeyi arasındaki açısal konumlandırma hatalarının kaynak kalitesine etkisi deneysel olarak incelenmektedir. Zira manuel mikro lazer uygulamalarında torç tutuş açısı (lazer kaynak açısı) hataya en açık kaynak değişkenidir. Deneysel sonuçlar, lazer kaynak açısının ince paslanmaz sac yüzeylerde istenen kaynak kesitinin oluşumunu etkileyen en önemli parametrelerden biri olduğunu ve açısal konumlandırma hassasiyeti sağlanmadan görsel mikro kaynak uygulaması yapmanın uygun olmayacağını göstermektedir. Üretimde bu görsel kusurları gidermek için yüzeye uygulanan işlemler üretim hızını düşürerek maliyetleri artırmakta, yüksek ısı ve yüzeye iz gidermek için uygulanan işlemler paslanmaz yüzeyin korozyon direncini düşürmektedir.

2. MATERYAL METOD

Paslanmaz test numunelerinin görsel mikro lazer kaynağında Sekil 1.a da gösterilen Turcweld LP300 serisi, Nd:Yag Lazer tip kaynak makinesi, Şekil 1.b de gösterilen manuel el torçu ile birlikte kullanılmaktadır. Bu sistemde grafit uçlar, kaynak parçası için özel olarak tasarlanır ve operasyon fikstür gerektirmediği için oldukça ekonomiktir. Ergonomik tasarımı ile ulaşılması zor bölümlerde kaynak uygulamasını kolaylaştırır. Endüstriyel mutfak ekipmanlarının görünür yüzeylerinin sabitlenmesinde manuel mikro nokta lazer kaynağı sıklıkla kullanılmaktadır. Görsel mikro lazer nokta kaynağı endüstriyel uygulama örneği Şekil 2.a ve 2.b de gösterilmiştir. Bu uygulamada 0,8 mm kalınlıktaki ince sacın görünür olmayan yüzeyinde çok kısa süreli ısı artışı sayesinde yeterli kaynak alanı oluşturulurken, görünür ön yüzeyinde ısı izi oluşturmayacak hassasiyetle kaynak yapılması beklenmektedir.

Kaynak test numuneleri mekanik ve kimyasal özellikleri Tablo 2 de verilen 2 mm ve 0,8 mm 305 serisi paslanmaz çelik saclar, Şekil 3.a da gösterilen şekilde birbirleri üzerine tek noktadan Şekil 3.b de gösterilen lazer sinyali ve parametreleri ile birleştirilmiştir. Birbiri üzerinde tek noktadan birleştirilen her numunenin boyutları 80 mm uzunluk, 14 mm genişliktedir. Birleştirme sonrası çekme testine tabi tutulacak birleştirilmiş numunelerinin boyu 110 mm ‘dir. İki sacın kaynak yüzeylerinin boşluksuz teması için, her kaynak numunesi aynı baskı kuvveti ile kaynatılmıştır. Bindirme kaynak numunelerinin kaynak mukavemetini ölçmek için numuneler Bursa Uludağ Üniversitesi Laboratuvarlarında 0,4 N hassasiyetli özel üretim bir mikro çekme cihazı kullanılarak çekme testine tabi tutulmuştur. Kaynak birleşim noktaları kayma zorlanması altında kopartılmıştır. Test sırasında kafa hızı 10 mm/dak olarak ayarlanmış ve numune kırılmasına kadar çekme-kesme kuvveti yavaşça arttırılmıştır.



(a) (b) (c)

Şekil 1. a.) Turcweld LP300 lazer kaynak makinesi, b.) Manuel el torçu kontrol kutusu, c.) El torçu

Tablo 1. Lazer Kaynak Makinesi Teknik Özellikleri

Model	Turcweld LP300
Lazer Üreteci	Nd:YAG Lamba Pompalı
Dalga Boyu	1064 nm
Maksimum Atım Enerjisi	100 J
Maksimum Tepe Gücü	9,9 kW
Maksimum Ortalama Güç	300 W
Darbe Aralığı	200 ms/s
Darbe Frekansı	1-300 Hz
Voltaj	200-500 W
Odak Masefesi	80mm/100mm/120mm/150mm/300mm
Görüntüleme Sistemi	CCD Kamera
Parametre Ayarı Kaydetme	32 Farklı Ayar Ekranı
Enerji Ölçüm Sistemi	Dahili
Kontrolcü	Çoklu Kontrol Sistemi, Hata Kontrol Algoritması, Bakım ve Durum Mesajları İçin Uyarı
Arayüz	RS232
İzole Gaz Desteği	Esnek ve Dairesel Nozul
Soğutma Sistemi	Dahili Su / Hava Isı Eşanjörü
Soğutma Opsiyonları	Dahili Su Soğutma Sistemi + Ayrıştırılmış Soğutucu Sistemi
Elektrik Gereksinimi	AC 380 V ±%10 3p+N+PE 50/60 Hz
Güç Tüketimi	12 kW
Ölçüler (E/B/Y)	650x1330x1000 mm

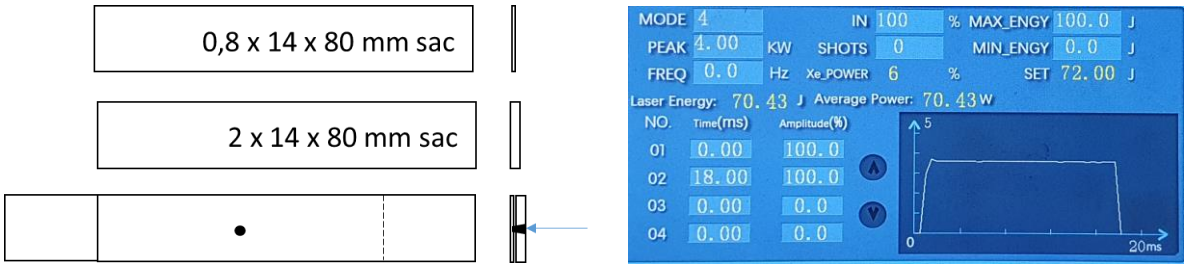
Tablo 1. 304 Paslanmaz Çelik Sac Mekanik ve Kimyasal Özellikleri

Kalite	Kimyasal Bileşim (%)								Kopma Gerilmesi (N/mm2)	Akma Gerilmesi (N/mm2)	Sertlik (HV)
	C	Si	Mn	P	S	Ni	Cr	N			
304/304L/1.4301/1.4307	0,022	0,34	1,38	0,028	0,002	8,01	18,15	0,065	632	274	164



(a) (b)

Şekil 2. İnce inox malzemelerde görsel lazer nokta kaynağı uygulaması. a.) Görünür yüzey (0,8 mm kalınlığında 304 paslanmaz çelik sac), b.) Görünmez yüzey (2 mm kalınlığında 304 paslanmaz çelik sac)



(a) (b)

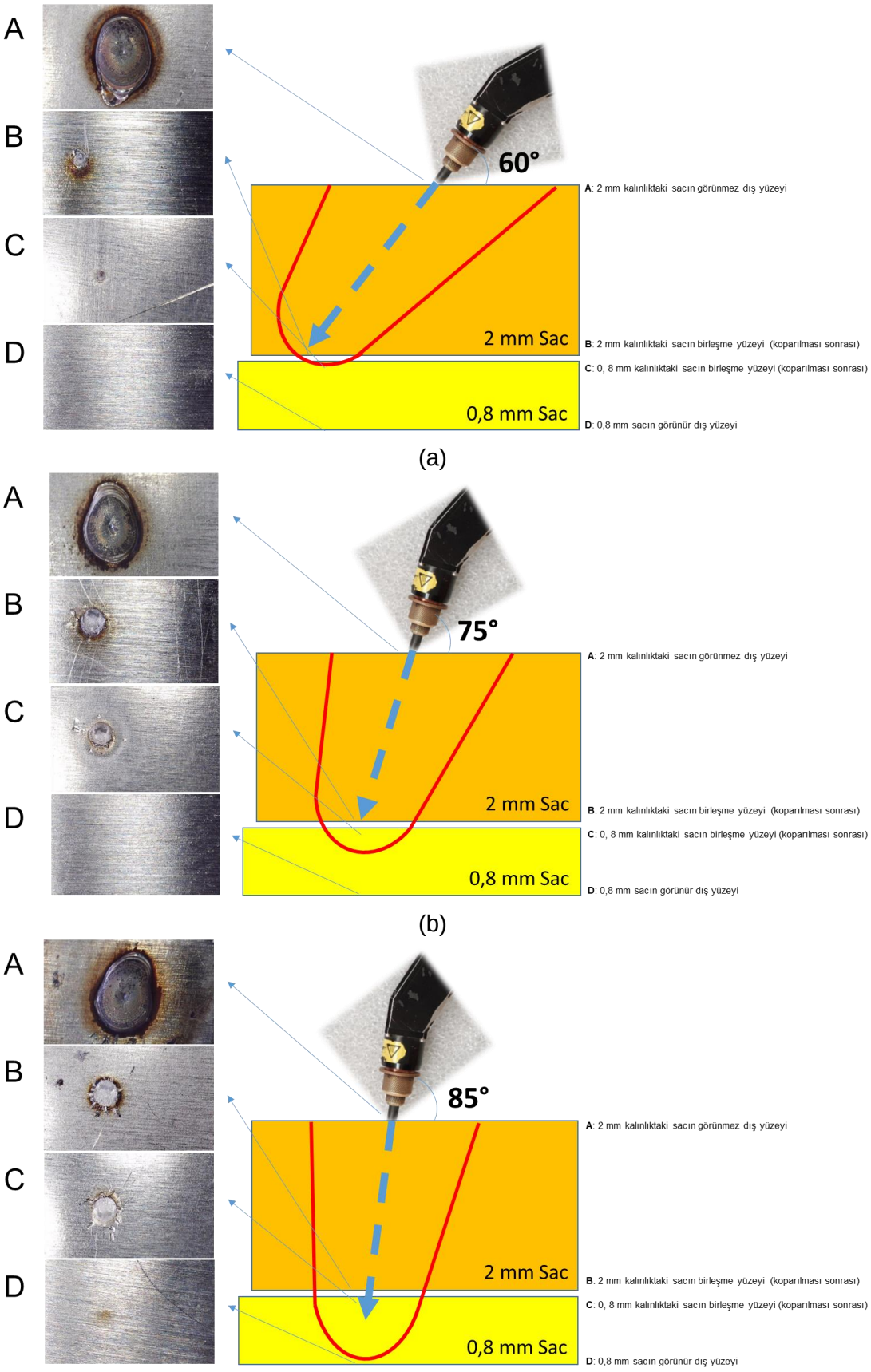
Şekil 3. a.) Test numuneleri boyutları ve 2 mm ve 0,8 mm 305 serisi paslanmaz çelik test numunelerin tek noktadan birleştirilmesi, b.) Lazer kaynak parametreleri ve sinyal formu.

3. SONUÇLAR

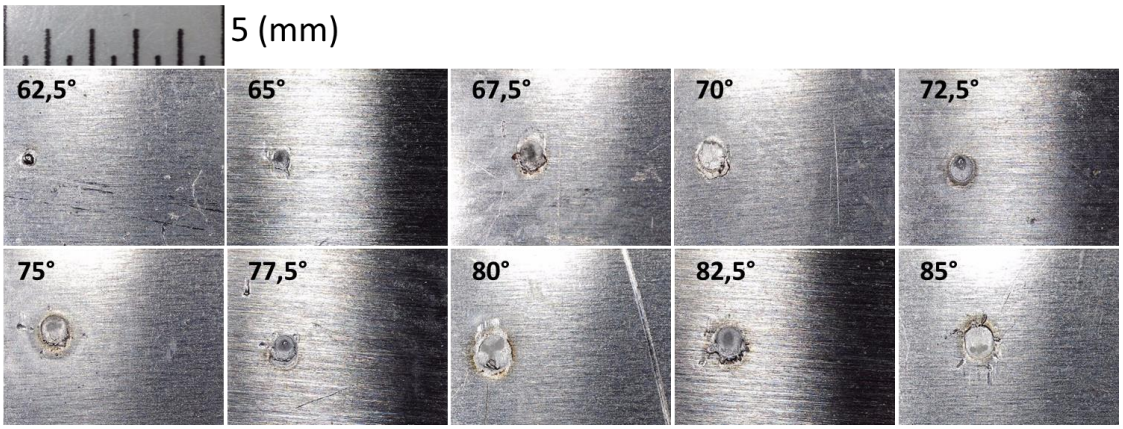
Paslanmaz malzemelerin görsel kusur oluşturmayacak kadar narin bir şekilde kaynak edilmesi ve aynı zamanda da çalışma koşullarında zamanla ortaya çıkacak yüklerinin çalışma ömrü boyunca üstesinden gelinebilmesi için gerekli kaynak açısının tespit edilmesi ve uygun görsel kaynak proseslerinin geliştirilmesi bu çalışmanın temel motivasyonu oluşturmaktadır. Manuel mikro nokta lazer kaynağında sac malzemelerin birleşen yüzeyleri arasındaki boşluk ve torç tutuş açısı (lazer ışını ve kaynak yüzeyi arasındaki açı) görünür yüzeyde ısı izi oluşturmadan yeterli kaynak mukavemeti elde etmek için anahtar değişkenlerdir. Görünür yüzeyde kaynak izlerinin olmaması lazer kaynağının temel şartı iken, bağlantı mukavemeti genellikle kritik kalite kriteridir. Bu nedenle test numunelerini görünür yüzeylerinde ısı izi oluşup oluşmadığı ve kaynak kesitinin boyutu mikroskop altında

incelenmiştir. Şekil 4 'te A, B, C ve D büyük harfleri ile isimlendirilen yüzeyler sırasıyla 2 mm kalınlıktaki sacın görünmez dış yüzeyini, 2 mm kalınlıktaki sacın birleşme yüzeyini (koparılması sonrası), 0, 8 mm kalınlıktaki sacın birleşme yüzeyini (koparılması sonrası) ve 0,8 mm sacın görünür dış yüzeyini ifade etmektedir. 60° daha küçük açılarda ergime hacmi 2 mm lik sacın dışına ulaşamadığı için kaynak işlemi mümkün olmamış ve 60° yatay açılar için test yapılamamıştır. 60°-80° aralığında test yapmak için yeterli kaynak alanı oluşmaktadır ve görünür sac yüzeyinde herhangi bir ısı izi oluşmamaktadır. 82,5° görünür yüzeyde mikro kabarmalar ortaya çıkmaktadır. Belli açılarda ışık yansıması sayesinde belirgin olan bu yüzey izlerinin görüntüleri, mikroskobun aydınlatma açısı bu ışık yansımalarını oluşturacak açıda bulunmadığı için alınamamıştır. Buna karşın 85° den sonra görünür yüzeyde belirgin ısı izleri oluşmaktadır. Şekil 5 'te torç tutuş açısının 60° den 2,5° artımlarla 90° dik tutuş açısına yaklaşmasının kaynak kesitine ve dolayısıyla kaynak kesit alanına etkisi 0,8 mm lik sacın birleşme yüzeyinin kopartılma sonrası mikroskop fotoğrafları ile gösterilmektedir. Testler 90° dik açıda lazer ışınının geri yansıyarak optik sisteme zarar vermemesi için 85° kesilmiştir. Mikroskop fotoğraflarından torç tutuş açısının yüzeye dik hale yaklaşması ile kaynak kesitinin düzgün bir şekilde arttığı görülmektedir.

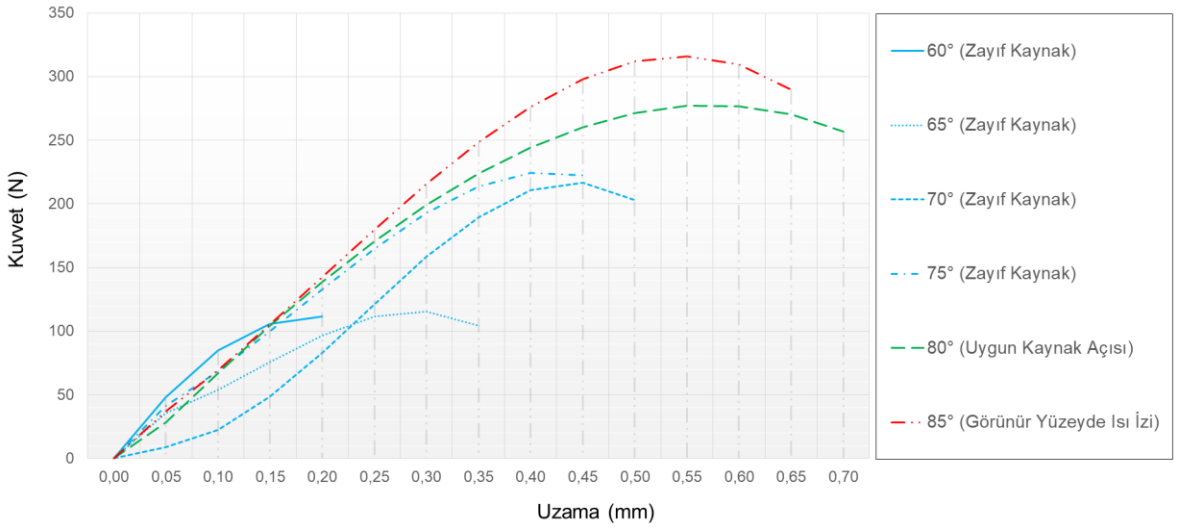
Şekil 6 'de farklı torç açıları için tek nokta kaynağı tarafından taşınan kuvvetin uzama ile değişimi gösterilmektedir. 60° den 85° ye kadar kaynak tarafından taşınan maksimum kuvvetin 100N dan 320N 'a kadar arttığı ve 90° kadar artma eğiliminde olacağı anlaşılmaktadır. Çalışmada görünür yüzeyde ısı izi veya kabarmaların oluşmadığı kaynak mukavemetinin de en yüksek olduğu 80° açı kritik torç açısı olarak anılacaktır. Şekil 7 'de normalize kaynak yükünün torç açısı ile değişimi gösterilmektedir. Normalize kaynak yükü kaynağın kopartılıncaya kadar taşıdığı maksimum kuvvetin yüzeyde ısı izi oluşturmadan ulaşılabilecek maksimum kaynak yüküne oranını ifade etmektedir. Mevcut lazer sinyal parametreleri ile 80° de 277 N luk bir kaynak yüküne ulaşılmaktadır. Grafikte kaynak için uygun olan ve uygun olmayan torç açıları farklı renkler ve açıklamalar ile gösterilmiştir. Torç'un kaynak oluşturamayacak kadar yatay olduğu 60 dereceden küçük ve 120 dereceden büyük açılar grafik alanın dışında kalmaktadır. 60°-77° ve 103°-120° aralıklarında kaynak dayanımı artış eğilimi gösterse de, amaç en iyi kaynak dayanımını elde etmek olduğu için 77 derceden küçük ve 113 dereceden büyük açılar lazer uygulaması için en uygun açılar değildir. 77°-80° derece ve 100°-103° aralıkları görünür yüzde iz oluşturmayan ve kaynak dayanımı en yüksek torç açısal pozisyonlarıdır. Mevcut lazer sinyal parametreleri için en uygun açısal konumun bu aralıklar olduğu değerlendirilmektedir.



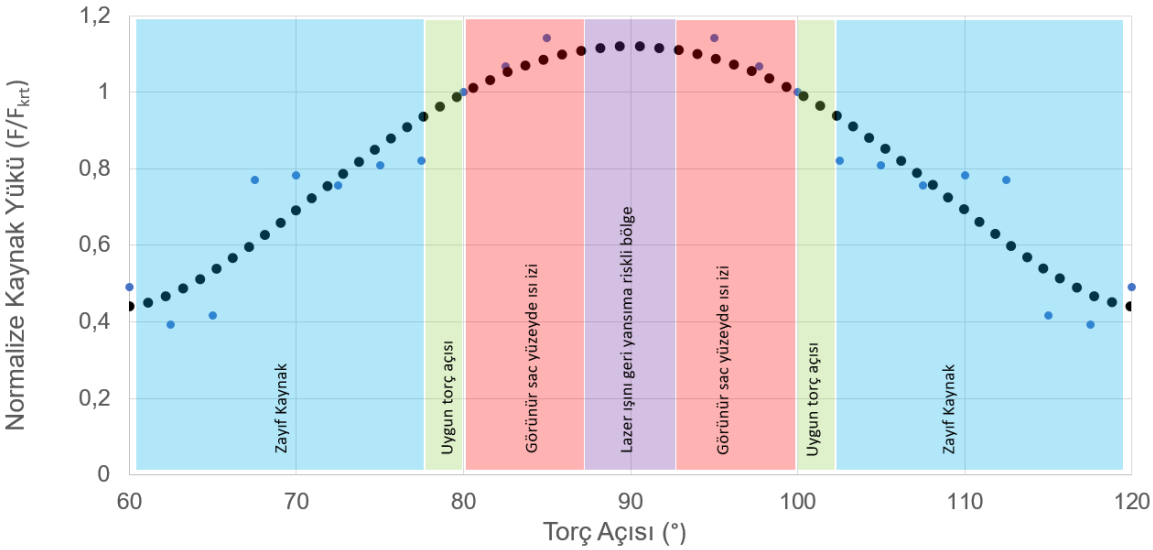
Şekil 4. Farklı kaynak torç tutuş açıları için kaynak izleri ve kaynak kesitleri.
a.) 60° b.) 75° c.) 85°



Şekil 5. Farklı kaynak torç açıları için kopartılma sonrası kaynak kesit alanlarının mikroskop fotoğrafları



Şekil 6. Farklı torç açıları için tek nokta kaynağı tarafından taşına kuvvet ve uzama eğrisi.



Şekil 7. Normalize kaynak yükünün torç açısı ile değişimi.

4. TARTIŞMA

Az sayıda ve çok farklı tipte ürün gamına sahip, müşteri odaklı tasarım ve üretim yapan endüstri alanlarında manuel kaynak yöntemi maliyet ve hız açısından robotik kaynak yöntemine göre daha verimli görülebilmektedir. Zira robotik kaynak hattının ürün değiştikçe revizyonu ve yeniden programlanması üretimi yavaşlatmakta ve maliyetini yükseltmektedir. Lazer sinyali ile ilgili kaynak parametreleri standart olsa da, levhalar arasındaki boşluk ve lazer ışınının levha yüzeyine geliş açısı, yüzey lekeleri ve lazer ışının yansıma oranı gibi faktörler kaynak kalitesini etkilemektedir. Görsel mikro lazer kaynağı uygulamalarında operatörün yeteneğine en bağımlı kaynak parametresi torç açısıdır. Zira, karmaşık geometrili ve farklı yüzey açısına sahip dar alanlarda, operatörün göz kararı ile lazer ışını ve kaynak yüzeyi arasındaki açıyı ayarlaması oldukça zor bir görevdir. Uygulamanın basit ve seri olması, operatörün kontrolsüz işlem yapmasına olanak sağlamaktadır. Üreticiler bu noktada robotik kaynak üretim bandının revize maliyeti ve manuel mikro kaynaktan dolayı ortaya çıkan ıskarta ürün maliyetleri arasında ekonomik bir tercih yaparak üretimi planlamaktadır. Üretim adedinin az olduğu durumda kaçınılmaz olarak manuel kaynak yöntemini tercih edilmektedir.

Bu çalışmada manuel kaynak işleminde görsel kusurların önüne geçmek için kaynak operatörünün torç tutuş açısına odaklanılmış ve operatör tarafından yapılan açısal hatanın kaynak kalitesi ve görsel kusura etkisi incelenmiştir. Kaynak torçu ile kaynak yüzeyi arasındaki açı ne kadar dik olursa kaynak yolu o kadar kısalmaktadır, yolun kısalmasından kaynaklı enerji kayıpları azalmaktadır ve buna bağlı olarak kaynak nüfuziyeti artmaktadır. Bun yanında, kullanılan malzeme kalitesi ve kalınlıkları göz önünde bulundurularak nihai ürünün kozmetik durumunun da istenilen özelliklerde olması gerekmektedir. Zira, aşırı kaynak nüfuziyeti ince sacın görsel yüzeyinde ısı izlerinin oluşmasına sebep olmaktadır. Bu nedenle özellikle inox malzemeler için maksimum kaynak güçü optimum kaliteyi sağlayamamaktadır. Kaynaklı imalat atölyelerinde dikkate alınmasa da, açısal konumun kaynak kalitesi (kozmetik ve dayanım) bakımından en az güç, frekans vb. parametreler kadar önemli olduğu gözlemlenmiştir. Çalışmada belirli lazer güç ve sinyal parametreleri için kozmetik kusur oluşturmayan ve en yüksek kaynak kalitesi oluşturan uygun torç açısı aralığı belirlenmiştir. İlerleyen dönemde lazer açısının operatör tarafından uygun aralıkta tutulması için el torçunun açısal sensörler ve yardımcı sistemler ile donatması mümkün olabilir. Bu sayede manuel mikro nokta lazer kaynak uygulamasında insan hatalarının en aza indirilmesi, endüstriyel mutfak, gıda sanayii, sağlık sektörü gibi geniş bir yelpazede daha hızlı ve daha kaliteli ürün üretme imkânı sağlanabilecektir.

TEŞEKKÜR

Evinoks Servis Ekipmanları San. ve Tic. A.Ş. ‘ye çalışmaya katkılarından dolayı teşekkür ederiz.

KAYNAKÇA

1. **Ahmad, G.N., Raza, M.S., Singh, N.K., Kumar, H. (2020),** "Experimental investigation on Ytterbium fiber laser butt welding of Inconel 625 and Duplex stainless steel 2205 thin sheets", Opt. Laser Technol. 126, 106117.

2. **Ahmad, G.N., Raza,M.S., Singh, N.K., Muvvala, G. (2021),** "Investigating the effect of process parameters on weld pool thermal history and mechanical properties of laser welded Inconel 625 and Duplex stainless steel 2205 dissimilar welds", Optik, 248, 168134.

3. **Simonds, B.J., Sowards, J., Hadler, J., Pfeif, E., Wilthan, B., Tanner, J., Harris, C., Williams, P., Lehman, J. (2018),** "Time-Resolved Absorptance and Melt Pool Dynamics during Intense Laser Irradiation of a Metal", Vol. 10, Iss. 4. DOI: 10.1103/PhysRevApplied.10.044061.

4. **Cedeño-Viveros L.D., García-López E., Vázquez E.V., et al (2018),** "Laser micro-spot welding of AISI 302 stainless steel sheets", In Proceedings of SPIE - Laser -based Micro and Nano processing XII. San Francisco, p 105.

5. **Chen, W., Ackerson P., Molian, P. (2009),** "CO2 laser welding of galvanized steel sheets using vent holes", Mater. Design, 30: 245-251. DOI:10.1016/J.MATDES.2008.05.009

6. **Cheepu, M., Kumar Reddy, Y.A., Indumathi, S., Venkateswarlu, D. (2020),** "Laser welding of dissimilar alloys between high tensile steel and Inconel alloy for high temperature applications", Adv. Mater. Process. Technol. 1–12.

7. **Duley, W.W., (1999),** "Laser Welding", 1st Edn., Wiley-New York, ISBN: 0471246794, pp: 251.

8. **Ion, J.C., (2005),** "Laser Processing of Engineering Materials: Principles, Procedure and Industrial Application", 1st Edn., Butterworth-Heinemann, Boston, ISBN: 0750660791, pp: 556.

9. **Gillner, A., Holtkamp, J., Hartmann, C., Olowinsky, A., Gedicke, J., Klages, K., Bosse, L., Bayer, A. (2005),** "Laser applications in micro technology", J. Mater. Process. Technol. 167, 494–498.

10. **Kannatey-Asibu, E., (2009),** "Principles of Laser Materials Processing", 1st Edn., John Wiley and Sons, Hoboken, N.J., ISBN-10: 0470177985, pp: 819.

11. **Katayama, S., Seto, N., Kim, J., Matsunawa, A., (1997),** "Formation Mechanism and Reduction Method of Porosity in Laser Welding of Stainless Steel", In Proceedings of ICALEO, Sec. G, pp. 83–92.

12. **Ishide, T., Tsubota, S., Nayama, M., Shimokusu, Y., Nagashima, T., Okimura, K., (1999),** "10 kW Class YAG Laser Application for Heavy Components", SPIE High-Power Lasers in Manufacturing, Osaka, Vol. 3888, pp.543–550.

13. **Katayama, S., and Matsunawa, A., (1998),** "Formation Mechanism and Prevention of Defects in Laser Welding of Aluminum Alloys", In Proceedings of CISFFEL 6, Vol. 1, pp. 215–222.

14. **Katayama, S., Seto, N., Kim, J., Matsunawa, A., (1998),** "Formation Mechanism and Suppression Procedure of Porosity in High Power Laser Welding of Aluminum Alloys", in Proceedings of ICALEO, Sec. C, pp. 24–33.

15. **Kim, J.D., Kim, C.J., Chung, C.M., (2001),** "Repair welding of etched tubular components of nuclear power plant by Nd:YAG laser", J. Mater. Process. Tech. 114, 51-56.

16. **Kleine, K.F., Fox, W.J., Watkins, K.G., (2004),** "Micro Welding with Pulsed Single Mode Fiber Lasers", Laser Institute of America: San Francisco, CA, USA, p. M501.

17. **Kumar N, Mukherjee M, Bandyopadhyay A. (2017)**, "Comparative study of pulsed Nd:YAG laser welding of AISI 304 and AISI 316 stainless steels", Opt Laser Technol 88:24–39. https://doi.org/10.1016/j.optlastec.2016.08.018

18. **Kumar, N., Dhara, S., Masters, I., Das, A. (2022),** "Substituting Resistance Spot Welding with Flexible Laser Spot Welding to Join Ultra-Thin Foil of Inconel 718 to Thick 410 Steel", Materials, 15, 3405. https://doi.org/10.3390/ma15093405.

19. **Lertora, E., Mandolfino, C., Gambaro, C. (2014),** "Mechanical Behaviour of Inconel 718 Thin-Walled Laser Welded Components for Aircraft Engines", Int. J. Aer. Eng., 721680.

20. **Lin, J., Wang, X., Lei, Y., Wei, R., Guo, F. (2021),** "Study on hot cracking in laser welded joints of inconel 718 alloy foils", J. Manuf. Process. 64, 1024–1035.

21. **Luangpaiboon, P., (2011),** "Constrained response surface optimization for a laser beam welding process", J.Math Stat, 7: 5-11. DOI: 10.3844/jmssp.2011.5.11

22. **Quazi, M., Ishak, M., Fazal, M., Arslan, A., Rubaiee, S., Aiman, M., Qaban, A., Yusof, F., Sultan, T., Ali, M. (2021),** "A comprehensive assessment of laser welding of biomedical devices and implant materials: Recent research, development and applications", Crit. Rev. Solid State Mater. Sci. 46, 109–151.

23. **Pakmanesh, M.R., Shamanian, M. (2018),** "Optimization of pulsed laser welding process parameters in order to attain minimum under fill and undercut defects in thin 316L stainless steel foils", Opt. Laser Technol. 99, 30–38.

24. **Poprawe, R., (2009),** "Tailored Light 2: Laser Application Technology", 1st Edn., Springer, Berlin London, ISBN-10: 3642012361, pp: 644.

25. **Torkamany, M.J., Hamedi, M.J. Malek F., Sabbaghzadeh, J. (2006),** "The effect of process parameters on keyhole welding with a 400 WNd:YAG pulsed laser", J. Phys. D: Appl. Phys., 39:4563-4563. DOI: 10.1088/0022-3727/39/21/009

26. **Tolinski, M. (2008),** "Lasers seal the deal in medical", Manuf. Eng. 140, LT14–LT20.

27. **Tsukamoto, S., (2003),** "Laser welding", Welding Int., 17:767-774. DOI:10.1533/wint.2003.3172.

28. **Sun, J., Nie, P., Feng, K., Li, Z., Guo, B., Jiang, E. (2017),** "The elimination of pores in laser welds of AISI 304 plate using different shielding gases", J.Mater Process Technol 248:56–63. https://doi.org/10.1016/j.jmatprotec.2017.05.011

29. **Shaikh, U.F., Das, A., Barai, A., Masters, I. (2019),** "Electro-Thermo-Mechanical Behaviours of Laser Joints for Electric Vehicle Battery Interconnects", In Proceedings of the 2019 Electric Vehicles International Conference (EV), Bucharest, Romania, 3–4 October 2019; IEEE: Piscataway, NJ, USA, pp. 1–6.

30. **Siva Shanmugam, N., Buvanashekaran, G,, Sankaranarayanasamy, K. (2012)** "Some studies on weld bead geometries for laser spot welding process using finite element analysis", Mater Des 34:412–426. https://doi.org/10.1016/j.matdes.2011.08.005

31. **Sidharth, D., KV, P.P., Rajendran, R., Narayanan, S. (2019),** "Microstructure and properties of inconel 718 and AISI 416 laser welded joints", J. Mat.. Proc. Tech. 266, 52–62.

32. **Srikanth, S., Parthiban, A. (2020),** "Microstructural analysis of Nd:YAG laser welding for Inconel alloy.Mater", Today Proc. 21, 568–571.

33. **Ventrella, V.A., Berretta, J.R., de Rossi, W. (2010),** "Pulsed Nd:YAG laser seam welding of AISI 316L stainless steel thin foils", J. Mater. Process. Technol. 210, 1838–1843.

34. **Yan, L., Jam, J.E., Beni, M.H., Kholoud, M.J., Baleanu, D., Shahraki, M.E., Ghaemi, F. (2022),** "Effect of laser welding parameters on the temperature distribution, microstructure and mechanical properties of dissimilar weld joint of Inconel 625 and stainless steel 304", Int. Commun. Heat Mass Transf. 131, 105859.

35. **Zhou, J., Tsai, H. (2006),** "Porosity Formation and Prevention in Pulsed Laser Welding", ASME. J. Heat Transfer., 129(8): 1014–1024. https://doi.org/10.1115/1.2724846.

TAŞITLARDA AĞIRLIK AZALTIMINDA HAFİF MALZEME OLARAK ALÜMİNYUM KULLANIMI

Yahya ISIK, *yahya@uludag.edu.tr,* Bursa Uludağ Üniversitesi, 16059 Bursa

Recep ÇAGLAYAN, *recepcaglayan@gmail.com,* Uludağ University 16059 Bursa

ÖZET

Teknolojinin gelişmesi ile birlikte başta güvenlik gereksinimleri olmak üzere konfor ve performans talepleri gibi artan istekler, araçların ağırlığını artırmıştır. Bu çalışmada taşıt ağırlığının zamanla artma nedenleri ve artan taşıt ağırlığı nedeniyle oluşan sorunlar ve ağırlık azaltmada en çok kullanılan hafif metal olarak alüminyum incelenmiştir. Alüminyumun taşıtlarda kullanımı ile sağlanan avantajlar araştırılmıştır. Ağırlık azaltmada alüminyum kullanımının yanında bilgisayar destekli optimizasyon teknikleri, daha iyi sonuçlar elde edilmesini mümkün kılmaktadır. Bu çalışmada örnek model olarak otomobillerde kullanılan salıncak kolu tasarımında, St 37 çelik malzeme yerine Al 5754 alüminyum alaşımı kullanımı ile hafifletme sağlanması incelenmiştir. Yapılan analizler, çelik malzeme yerine alüminyum malzeme kullanımı ile %59 ağırlık azaltımı sağlanmıştır.

Anahtar Kelimeler: Alüminyum, ağırlık, yakıt tasarrufu, taşıt ağırlığı, salıncak kolu

ABSTRACT

With the development of technology, increasing demands such as comfort and performance demands, especially safety requirements, have increased the weight of the vehicles. In this study, the reasons for the increase in vehicle weight over time and the problems caused by the increased vehicle weight and aluminum as the most used light metal in weight reduction were examined. The factors caused by the use of aluminum in vehicles were investigated. In addition to the use of aluminum in weight reduction, computer-aided optimization techniques make it possible to obtain better results. In this study, the use of Al 5754 aluminum alloy instead of St 37 steel material in the design of the swing arm used in automobiles as an example model, was examined. The analyzes showed that 59% weight reduction was achieved by using aluminum material instead of steel material.

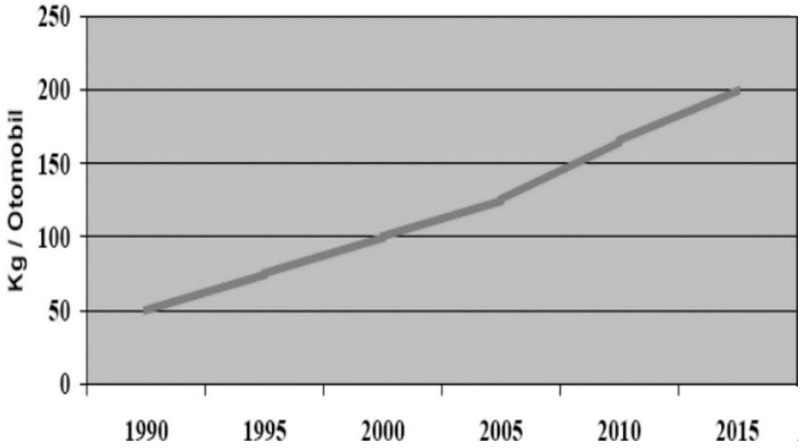
Key words: Aluminum, ağırlık, fuel saving, vehicle weight, wishbone

1. GİRİŞ

Ülkelerin katı çevreci politikaları ve artan rekabet ile birlikte otomotiv üreticileri esas amacı belirli bir yükü belli bir noktaya en az enerji tüketerek ve enerji verimliliğini artırarak taşımak olan taşıtların en az maliyet ile çalışabilmesi için araştırmalar yapmaktadır. Tüketicilerin araç alımında öncelikleri fiyat, yakıt tüketimi ve güvenliktir. Günümüzde otomotiv üreticilerinin asıl sorunları ise çevreyi koruma, yakıt tasarrufu ve güvenliktir. Bu nedenle üreticiler verimli motorlar ve aerodinamik tasarım yapmakta, taşıtları hafifletmekte ve küçültmektedirler. Taşıtların güç ağırlığı (ağırlık/ motor gücü) Avrupa Standartlarına göre 15-20 kg/kw'dir [1]. Ağırlık azaltışında sağlanan başarı ile motor ve aktarma organları küçülmektedir. Araçlarda yapılacak hafifletme ile sağlanacak yakıt tasarrufunun yanında daha az CO_2 doğaya salınmaktadır.

Araçların yakıt tüketimini ve buna bağlı olarakta emisyon oranlarını azaltmada kullanılacak en etkin yol, taşıt ağırlığında hafifletmeler yapılmasıdır. Taşıt ağırlığını azaltmak için taşıt şaseleri yeniden tasarlanmakta, her parça için ağırlık azatlımı yapılmaktadır. Ağırlık azaltımı ile yakıt tüketimi ve karbon salınımı azalmaktadır. Ayrıca; Motor daha verimli çalışır, daha az egzoz salınımı sağlar, titreşim azalır, araç performansı artar, hızlanma ve frenleme performansı artar, kullanılan malzeme maliyetleri düşer. Yakıt tasarrufu alüminyum kullanımı ile sağlanabilir ancak alüminyum ile sağlanan yakıt tasarrufu alüminyumun yüksek fiyatı nedeniyle sınırlanmaktadır. Hafifletme ile aracın toplam ömrü boyunca daha az yakıt tüketilmesi ile yüksek fiyatı toplam ömrü boyunca elde edilen tasarruf ve yüksek verimli geri dönüşümü ile günümüzde alüminyum kullanılabilir hale gelmiştir. Otomotiv üreticileri ağırlık azaltmak için çeşitli çalışmalar yapmakta, değişik malzemeler kullanmakta, optimizasyon, parça eksiltme vb. çalışmalarla daha fazla hafiflik amaçlanmaktadır. King (2007) yaptığı araştırma ile yakıt tüketimini azaltan teknolojik yenilikleri araştırmıştır [2].

Taşıtlarda hafifletme yöntemi, geleneksel çelik gibi ağır malzeme yerine alüminyum, titanyum, magnezyum, yüksek mukavemetli çelik, kompozit, plastik gibi hafif malzemelerin kullanılması ile sağlanır. Bu hafif malzemeler gelecek için büyük bir potansiyel oluşturmaktadır. Günümüzde mevcut taşıtlarda kullanılan çelikler yerine daha hafif malzeme ve tasarımsal değişiklikler ile birlikte taşıt ağırlığında büyük azalmalar sağlanacaktır. Taşıtlarda alüminyum kullanımı kademeli olarak artmakta olup yıllara göre kullanım artışı aşağıdaki Şekil 1'de gösterilmiştir. Taşıtlarda 2030 yılında yaklaşık 250-300 kg alüminyum kullanımı olabileceği ön görülmektedir.



Şekil 1. Yıllara göre alüminyum kullanımının artışı [3]

Otomotiv sektöründe günümüzde sac metal şekillendirme yeteneklerinin artması ile ağırlıklar azalımı artmıştır. Bu nedenle günümüzde taşıt parçaları daha hafif ve sağlam üretilebilmektedir. Hafifletmede kullanılabilecek alternatif malzemeler Tablo 1'de sunulmuştur [4].

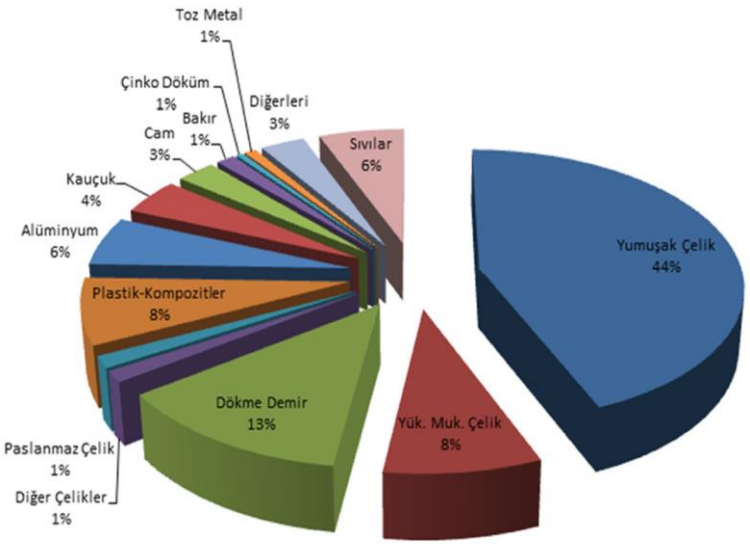
Tablo 1. Hafifletmede kullanılabilecek potansiyel malzemeler [4]

Hafif Malzeme	**Yerine Geçeceği Malzeme**	**Ağırlıktaki Azalma (%)**	**Parça Başına Göreceli Maliyet**
Yüksek Alaşımlı Çelik	Yumuşak Çelik	10	1
Alüminyum	Çelik, Dökme Demir	40-60	1,3-2
Magnezyum	Çelik veya Dökme Demir	60-75	1,5-2,5
Magnezyum	Alüminyum	25-35	1-1,5
Cam Fiber Takviyeli Polimer Kompozit	Çelik	25-35	1-1,5
Grafit Takviyeli Kompozit	Çelik	50-60	2-10+
Titanyum	Alaşımlı Çelik	40-55	1,5-10+
Paslanmaz Çelik	Karbonlu Çelik	20-45	1,2-1,7

Taşıtlarda hafifletme, kullanılan parçaların daha hafif malzemelerden üretilmesi ile mümkün olabilmektedir. Daha büyük oranlarda hafifletmenin sağlanabilmesi için parçaların tasarım aşamasında ele alınarak çeşitli teknikler ile tasarlanması ve optimize edilmesi gerekmektedir. Bu aşamada çeşitli bilgisayar destekli optimizasyon teknikleri kullanılmaktadır. Benzin ve dizel

motorlu araçların ağırlık azaltma çalışmaları hibrit ve elektrikli araçlar için daha fazla önem arz etmektedir. Elektrikli araçlar artan ağırlıkları dolayısı ile hafifletme için daha fazla alüminyum gibi hafif malzemeye ihtiyaç duyarlar. Elektrikli araçlar gücünü bataryadan alıp elektrik motoru yüksek torka ve çok iyi hızlanmaya sahiptir [1]. Hibrit araçlar ise sürüş durumuna göre elektrik ya da benzin motorundan güç almakta ve frenleme enerjisi bataryaları sarj etmekte kullanılır. Yaklaşık olarak benzin ve dizel motorlu araçlar toplam 1300-1600 kg ağırlığında iken elektrikli araçlarda ek olarak 300-600 kg batarya bulunmaktadır. Hibrit modellerde ise batarya yaklaşık 44-120kg'dır. Ticari araçlarda ise batarya 600-1500 kg'dır [5].

Song ve ark. (2009) yaptığı çalışmada alüminyum, çelik ve kompozit malzemelerin denendiği 1 kg'lık cam fiber malzemenin 1,8 kg çelik ve 0,9 kg alüminyum ile aynı rijitlikte olduğu belirtilmiştir [6]. Geleneksel çeliklere göre %50 pahalı olmasına rağmen daha hafif ve daha ince olmaları nedeniyle uygulamalarda et kalınlığının azalımı ile %24 hafifletme yapılabilir [7]. Malzeme seçiminde; güvenilirlik, performans, üretebilme ve maliyet etkilidir. Günümüzde alüminyum başta olmak üzere titanyum, magnezyum, seramik ve plastiklere rağmen çelikler, taşıtta istenen farklı özelliklere cevap verebilmesi, iyi fiyat performansı ile yüksek oranda kullanılmaktadır. Mukavemetin artması ile birlikte çeliklerin şekillendirmesi zorlaşmaktadır. Bu nedenle mukavemet ve işlenebilirlik birlikte ele alınarak malzeme seçilmelidir. Mayyas ve ark. (2012) taşıtı oluşturan malzemelerin ağırlıkça oranlarını aşağıdaki şekil 2'de gösterilmiştir [8].



Şekil 2. Taşıtı oluşturan malzemelerin ağırlıkça oranları [8]

Çelik yaygın kullanımına rağmen alüminyuma karşı başta yüksek yoğunluğu nedeniyle günümüzde hafifletme amacıyla yerini alüminyuma bırakmaktadır. Taşıtlarda geçmişte yoğun

çelik kullanımı yerini günümüzde alüminyum alaşımlarına bırakmıştır. Gelecekte ise yeni kullanım alanları ve yeni üretim yöntemleri ile yeni alaşım hafif alüminyumlara doğru kayması beklenmektedir [8].

2.1. Alüminyumun özellikleri

Alüminyumun günümüzde kullanımın artmasını sağlayan önemli özellikleri bulunmaktadır. Bu özellikler tek başına ve diğer özellikleri ile beraber kullanılarak alüminyum yüzyılımızın stratejik metali olmuştur. Hafiflik, alüminyumun en önemli özelliğidir. Alüminyumun özgül kütlesi 2,70 gr/cm³ iken çeliğin özgül ağırlığı 7,8 gr/cm³'tür. Aynı hacimde çelikten 3,5 kat daha hafif olması alüminyumu hafiflik istenen durumlarda vazgeçilmez kılmaktadır. Böylece %65'lik ağırlık azalımı başarılır. Tek parça olarak taşınamayan parçalar alüminyumdan imal edilerek taşınabilir hale gelmektedir.

Alüminyum saf halde sünek malzeme olup alaşımları saf halinin 15 katı daha mukavemetli olabilmektedir. Brinell Sertliği saf halde 20 iken alaşımlarında 175'e çıkmaktadır. Yüzey sertliği eloksal ile dahada iyileştirilebilir. Alüminyum sıcak, soğuk ve UV ışınlarından etkilenmez. Malzemelerin mukavemeti, bileşim ve içyapısı değiştirilerek arttırılabilir. Saf alüminyumun çekme dayanımı yaklaşık 49 MPa iken 7029 alaşımın çekme mukavemeti 430 MPa, bazı alaşımlar ısıl işlemlerle çekme dayanımı 700 MPa'a çıkarılabilmektedir. Saf halde taşıtlarda kullanılmaya uygun olmayan alüminyum alaşımlandırılarak taşıtlarda kullanılan çeliklerden daha iyi mukavemet değerleri sunmaktadır [9].

Saf alüminyum atmosferde %21 oranında bulunan oksijen ile birleşerek 1-2 mikron kalınlığında pasivasyon özelliği ile alüminyum oksit tabakası oluşturur ve bu tabaka üstün korozyon dayanımının ana sebebidir. Alüminyum oksit tabakası, kararlı durumda dış koruyucu tabaka oluşturduğu için demirdeki pas gibi yüzeyden sıyrılmaz ve kaybolmaz aksine sıyrılma olduğunda hemen oksijen ile birleşerek tekrar oksit tabaka oluşturur. %99,99 oranında saflıkta üretilebilen alüminyum yumuşak, kolay işlenebilir, iyi ısı ve elektrik iletkenliğinde, korozyon dayanımı oldukça yüksektir. Alaşımlı alüminyumlar iyi korozyon direncine sahip olmadıkları için saf alüminyum dışını saracak şekilde giydirilip ısıl işleme tabi tutulabilmektedir.

Alüminyum, akma gerilmesinin düşük olması ve iyi süneklik özellikleri nedeni ile daha az enerji harcanarak istenen karmaşıklıkta üretime izin vermektedir. Yüzey merkezli kübik kristal özelliği sayesinde büyük boyutlu parçalar 360°C ila 620°C'lerde sıcak olarak dövülmekte, karmaşık kesitli parçalar ekstrüzyonlanmakta, çekilebilmekte, saçlar yırtılmadan derin çekilebilmekte ve 6 mikron seviyesine kadarda haddelenebilmekte, boyunun 400 katına kadar esneyebilmektedir.

Alüminyumun, çeliğin 3 katı daha hafif olmasına iyi şekillendirme özellikleri de eklenince kullanım oranı daha da artmaktadır. Alüminyum döküm, ekstrüzyon, dövme, torna, freze gibi tüm üretim yöntemlerinde başarı ile şekillendirilebilir [10]. Tablo 2'de Alüminyum malzemenin mekanik özelliklerinin değerleri görülmektedir.

Alüminyum; kaynak, lehim, perçin, yapıştırma, cıvata somun, geçme vb. uygulamalarla birleştirilebilir. Alüminyum, yüksek basınçlı döküm sayesinde karmaşık şekilli parçalar hızlı şekilde iyi mekanik özelliklerle üretilir. Alüminyum diğer metallerle birleştirmede yaşanan sorunlar nedeniyle soğuk kaplama, daldırma kaplama, elektrolitik kaplama yapılmak suretiyle diğer metallerle birleştirilebilir. Ayrıca alüminyumu diğer metallerle birleştirmede araya ara malzeme kullanılarak ta birleştirme sağlanabilir.

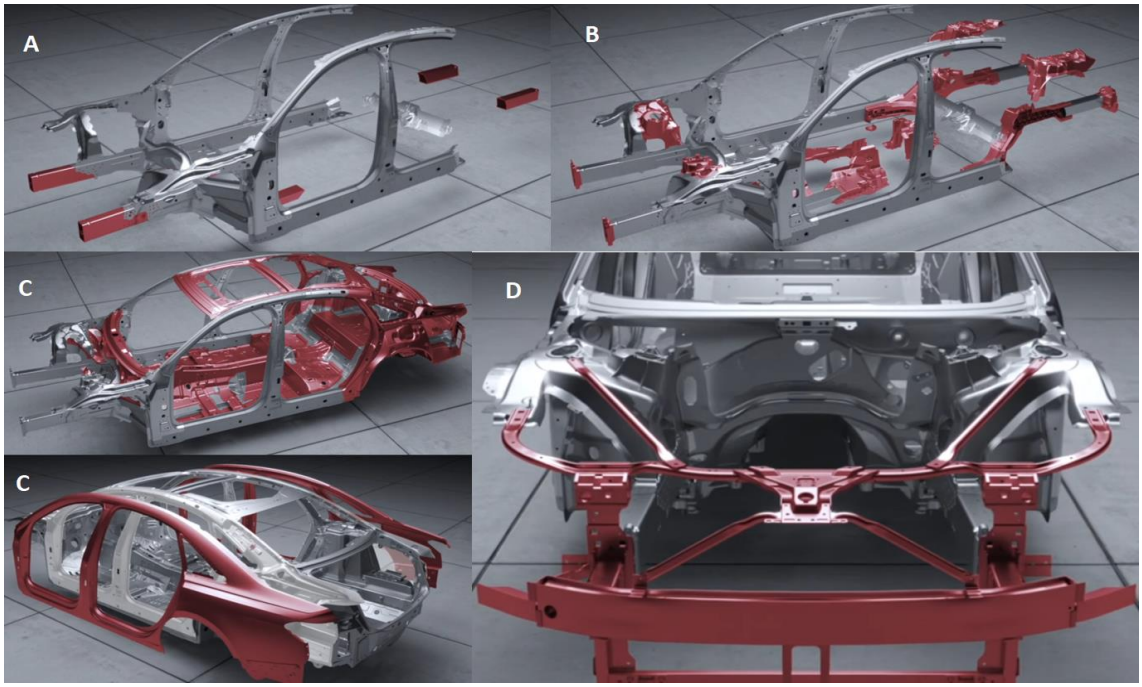
Tablo 2. Alüminyum malzemenin mekanik özelliklerinin değerleri [10]

	Döküm Alüminyum	Hadde Alüminyum	Isıl İşleme Tabi Tutulmuş Alüminyum
Çekme mukavemeti (MPa)	90-120	180-280	70-110
Akma mukavemeti (MPa)	30-40	160-240	50-110
Uzama (%)	18-25	3-5	30-40
Büzülme (%)	40-55	60-85	80-95
Sertlik (Brinell)	24-32	45-60	80-95

Alüminyumun hafifliğine yeni elementlerin eklenmesiyle iyi mekanik özellikli alaşımların eldesi ve yeni imalat yöntemlerinin kullanılmasıyla karmaşık parçaların imali ve seri üretim, otomobillerde geniş kapsamlı alüminyum kullanımına imkân sağlamıştır. Alüminyum alaşımları yüksek ısı iletme kabiliyeti nedeniyle çok iyi soğutma sağlamakta, dökme demir gibi alternatiflerinden daha hafif olması, düşük ısıl genleşmesi ve hafiflik ile beraber atalet kuvvetlerinin daha az olması alüminyum alaşımlarını motor üretiminde parça ve komple olarak alternatif malzeme yapmıştır. Motorların daha yüksek sıcaklıklarda çalışması verimliliği arttırır. Günümüzde gri dökme demir ve küresel grafitli dökme demirden yapılan motor bloğu 32 kg iken aynı özellikteki motor bloğu alüminyum alaşımları sayesinde 23,5 kg'dan yapılmış ve %26,5 hafifletme sağlanmıştır [11].

Alüminyum en çok motor blokları, aktarma organları, ısı uygulamaları, gövde, piston, süspansiyon, fren parçaları ve tekerleklerde kullanılır. Radyatör, ısı eşanjörü ve klima ünitelerinde hafiflik ve iyi ısı iletimi özelliği nedeniyle alüminyum kullanımına sıklıkla başvurulmaktadır. Taşıt

ağırlığının %22-25 taşıt gövdesi oluşturduğu için gövdede yapılacak iyileştirmeler hafifletme çalışmalarına ciddi katkı sunmaktadır [12]. Taşıt kaportalarında St12, St13, St14 çelik malzeme yerine alüminyum kullanımı ağırlık azaltımında en büyük potansiyelin araç gövdesinde olması nedeniyle başlamıştır. Alüminyum paslanmaması nedeniyle çeliğe göre daha fazla dayanıklılık sağlar. Sac malzemenin kullanımında dayanım ve şekillendirebilme özellikleri istenen iki özelliktir. Kaporta ve şasenin tamamen alüminyumdan imali ile %25 yakıt tasarrufu öngörülmektedir. Audi markası 4. nesil A8 modelinde Audi Space Frame adını verdiği teknoloji ile kaportayı tamamen alüminyumdan imal edip şaside %58 oranında alüminyum kullanarak bir önceki nesle göre %24 daha rijit olmasını sağlamıştır. Şekil 3'de kırmızı renk ile farklı üretim teknikleri ile üretilen alüminyumun araçta kullanımı gösterilmiştir [13].



Şekil 3. Şaside alüminyum kullanımı A) Alüminyum profil B) Alüminyum döküm C) Alüminyum levha D) Darbe sönümleyici [13]

Hibrit otobüslere takılan dövme alüminyum jantlar ile 120 kilogramlık hafifletme ile 6-7 aylık süreçte %1,8'e varan yakıt tasarrufu sağlamıştır. Konfigürasyon ve jant sayısına göre ortalama 250 kg kadar hafiflik sağlanabilmektedir [14].

Optimizasyon teknikleri ile daha hafif ürünler tasarlamak mümkün olmaktadır. Örnek vermek gerekirse çelik malzemeden yapılmış parça 7,5 kg, alüminyum alaşımları kullanılarak %60 oranında hafifletilmiş olup daha sonra bu parça tasarım optimizasyonu sayesinde %16 daha hafif hale gelmiştir [4]. Şekil 4'de. Optimizasyon tekniği ile parçanın hafifletilmesi görülmektedir.



Çelik malzeme kullanılmış tasarım 7,5 kg | Alüminyum malzeme kullanılmış tasarım 3 kg | Optimize edilmiş alüminyum malzeme tasarım 2,5 kg

Şekil 4. Optimizasyon tekniği ile parçanın hafifletilmesi [4]

Tüfekçi (2016), hafif ticari araç kapı menteşesi için S355 çelik malzemesi kullanılırken hafifletme için Al7075 alüminyum alaşımı kullanımı üzerine çalışmıştır. Yapılan bu malzeme değişikliği ile 4 adet menteşe toplam 9200 gram iken alüminyum alaşımı kullanımı sayesinde 2880 gram olmuştur. Yapılan bilgisayar destekli simülasyon ve testler ile bu doğrulanmıştır. Malzeme değişikliği ve optimizasyon yöntemleri ile %68 hafifletme sağlanmıştır. Bu hafifletme alüminyumun düşük yoğunluğu ve bilgisayar destekli tasarım ile mümkün olmuştur [15].

3. MATERYAL ve YÖNTEM

Taşıtlarda süspansiyon sistemlerinin asıl görevi, lastiklerle yol arasında sürekli teması sağlayarak sürüş hakimiyetini sağlamaktadır. Böylece süspansiyon sistemleri taşıtların yol tutuşunu sağlar, emniyetli şekilde virajları savrulmadan geçmesini sağlar ve yoldan gelecek sarsıntıları azaltır. Süspansiyon sistemi parçalarından olan salıncak kolları tekerlek takımını gövdeye bağlar. Salıncak kolları tekerlek takımını çukur ve kasislerde sınırlandırıp yukarı aşağı hareketine izin vererek yoldan gelen darbeleri emmeye çalışan önemli bir parçadır. Salıncak kollarının tasarımlarında mekanik özellikler, üretilebilirlik, malzeme temini ve üretim maliyeti göz önünde bulundurularak tasarım yapılır. Karting aracı salıncak kolu St37 (S235JR) çeliğinden imal edilmiştir. St37 çeliği düşük karbon oranı ile kaynak kabiliyeti yüksek, mangan içeriği ile de iyi mekanik özellikler sunmaktadır.

Taşıtlarda sıklıkla 5xxx ve 6xxx seri alüminyum alaşımlar kullanılmaktadır. 5xxx seri alüminyum alaşımlarda esas alaşım elementi magnezyum oranı arttıkça sertlik, korozyon direnci, şekillendirilebilme ve kaynaklanabilme özelliği artar, süneklik azalır. Al 5754 alüminyum alaşımı magnezyum içeriği ile sahip olduğu iyi mukavemet değerleri ve hafifliği nedeniyle basınçlı kap imalinde, gemi inşasında, kimya sanayinde ve otomotiv sanayinde sıklıkla kullanılmaktadır.St37 çeliğin yerine Al 5754 alüminyum alaşımı kullanımı ile karting aracı sac salıncak kolu hafifletilmeye çalışılmıştır. Yaşlandırılmayan Al 5754 (AlMg3) alaşımının kimyasal birleşimi ve mekanik özellikleri aşağıda Tablo 3. ve Tablo 4'de görülmektedir.

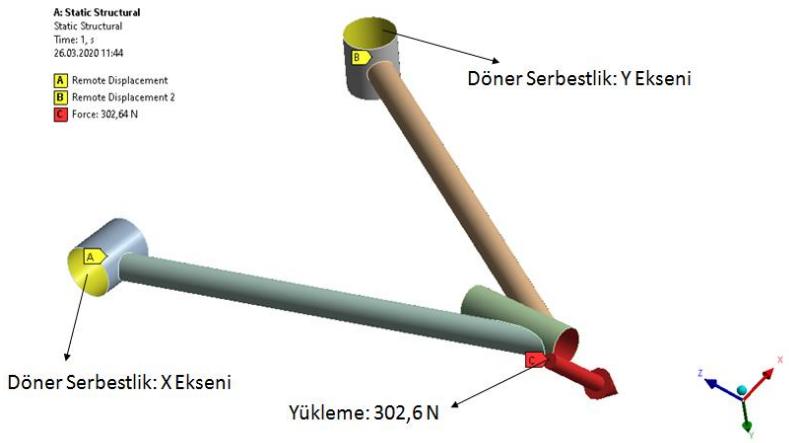
Tablo 3. Al 5754 alüminyum alaşımının kimyasal birleşimi [14]

Al 5754 (AlMg3) Kimyasal Birleşim									
Fe	Si	Cu	Mn	Mg	Zn	Cr	Ti	Diğer	Al
0,4	0,4	0,1	0,5	2,6-3,6	0,2	0,3	0,15	0,15	Kalan

Tablo 4. Al 5754 alüminyum alaşımının mekanik özellikleri [14]

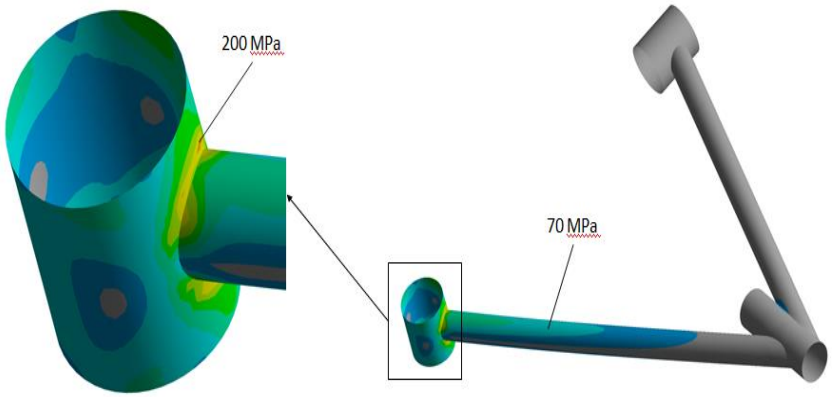
Temper	Akma Mukavemeti (Mpa) Min-Max	Çekme Mukavemeti (Mpa) Min-Max	ama (%50) Min- Max	rtlik (Brinell) Min- Max
0-H111	80-100	190-215	24	50-55
HX2	130-185	220-245	14	65-70
HX4	160-215	240-270	12	73-75
HX6	190-245	265-290	9	80
HX8	250-270	290-315	8	85-90
HX9	300	340	0-4	95

Karting aracının sac salıncak kolunun aracın kendi ağırlığındaki (120 kg) mukavemet analizi Ansys program ile yapılmıştır. Yapı kabuk modellenmiştir ve et kalınlığı 3mm'dir. Salıncak kolu ikinci dereceden 2mm kabuk elemanlarla modellenmiştir. Eleman sayısı 9100 ve düğüm (node) sayısı 25570 olarak Ansys programında belirlenmiştir. Sınır koşulları ve yükleme durumu dikkate alınarak modellenmiştir. Yükleme X ve Y eksenlerinde 214 N olarak verilmiş bileşke kuvvet ise 302 N'dur. Şekil 5.de sac salıncak kolunun sınır koşulları ve yükleme durumu görülmektedir.



Şekil 5. Sac salıncak kolunun sınır koşulları ve yükleme durumu

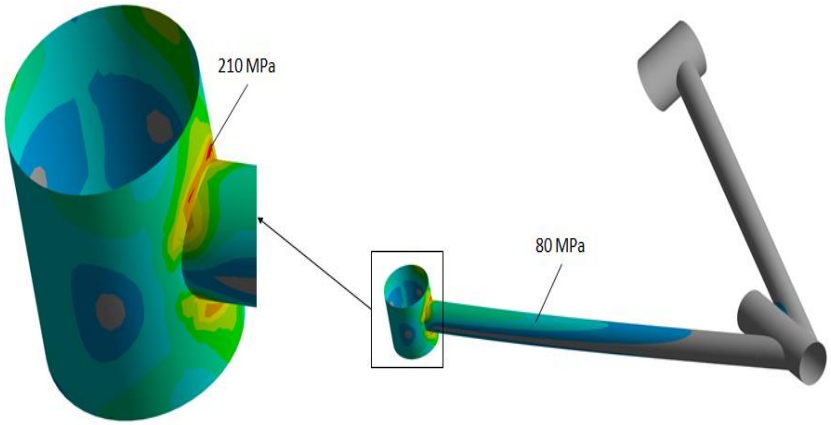
Mevcut tasarımda akma mukavemeti 230 Mpa olan St37 malzemesi 3 mm et kalınlığı ile analizi yapılmıştır. Yapılan analiz ile tespit edilen emniyet katsayısı 1,15'tir. Şekil 6'da 3 mm et kalınlığında St37 çeliğin analizi görülmektedir.



Şekil 6. 3 mm et kalınlığında St37 çeliğin analizi

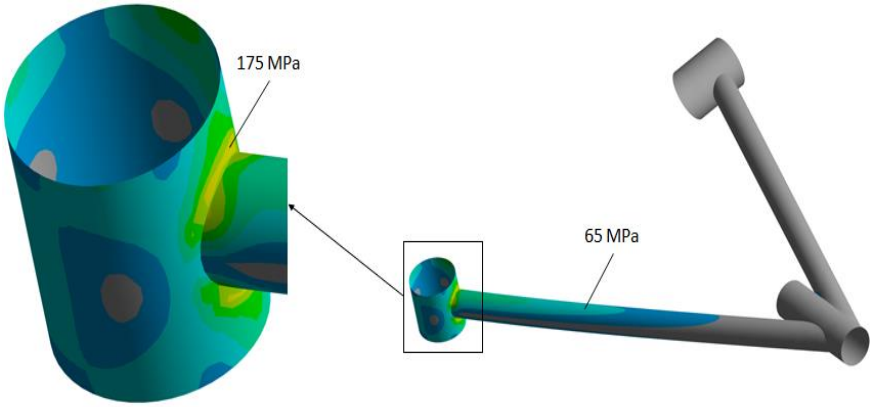
St37 çelik malzemesinin yerine yine 3 mm et kalınlığında akma mukavemeti 200 Mpa olan Al 5754 Hx6 alüminyum alaşımı analiz edilmiştir. Analiz sonucunda 210 Mpa gerilmeler tasarımı yeterli dayanımda olmadığını gösterdiği için kalınlık arttırma yoluna gidilmesi gerektiği

görülmüştür. Şekil 7'de 3 mm et kalınlığında Al 5754 Hx6alüminyum alaşımının analizi görülmektedir.



Şekil 7. 3 mm et kalınlığında Al 5754 Hx6alüminyum alaşımının analizi

Örnek modelde 3mm Al 5754 Hx6 alüminyum alaşımı yeterli dayanımı sağlamadığı için et kalınlığı arttırılarak tekrar analiz yapılmıştır. Et kalınlığı 3,4 mm yapılarak tekrar analiz yapıldığında mevcut St37 çelik tasarımdaki 1,15 emniyet katsayısı sağlanacak şekilde güvenilir bir tasarım Al 5754 Hx6 alüminyum alaşımı ile yapılmıştır. Şekil 8'de 3,4 mm et kalınlığında Al 5754 Hx6 alüminyum alaşımının analizi görülmektedir.



Şekil 8. 3,4 mm et kalınlığında Al 5754 Hx6 alüminyum alaşımının analizi

4. BULGULAR

Günümüzde artan taşıt ağırlığı nedeniyle oluşan sorunlar ve bu sorunların çözümü için yapılan hafifletme çalışmalarında özellikle hafif metal olarak alüminyum öne çıkmaktadır. Ağırlık azaltımında alüminyum kullanımının yanında bilgisayar destekli optimizasyon teknikleri ile daha iyi sonuçlar elde edilebilmektedir. Otomobillerde kullanılan salıncak kolu tasarımında St 37 çelik malzeme yerine Al 5754 alüminyum alaşımı kullanımı ile hafifletme sağlanmaya çalışılmıştır. Yapılan analizler ile salıncak kolunun çeliğin sağladığı aynı emniyet katsayısı ile alüminyumdan imal edilebileceği görülmüştür. Hafifletme amacıyla St37 çelik malzemeden imal edilmiş sac salıncak kolunun Al 5754 alüminyum alaşımdan imal edilmesine karar verilmiştir. Ancak aynı kalınlıklarda akma mukavemetine göre değerlendirildiğinde Al 5754 alüminyum alaşımı emniyetli değildir. Dolayısıyla et kalınlığı toplu olarak 0,4 mm artırıldığında St37 malzeme ile aynı mukavemette bir salıncak koluna ulaşılmıştır. Son durumda %59 kadar bir hafifletme yapılmıştır. Yapılan analizler sonucunda hazırlanan Tablo 4'de sunulmuştur.

Tablo 4. St37 çelik yerine Al 5754 alüminyum alaşım ile imal edilen tasarımda sağlanan ağırlık azaltımı

Malzeme	Kalınlık	Ağırlık	Güvenlik Katsayısı
St37	3 mm	0,87 kg	1,15 Güvenli
Al 5754	3 mm	0,31 kg	0,95 Güvenli Değil
Al 5754	3,4 mm	0,35 kg	1,15 Güvenli

5. SONUÇ

Teknolojinin gelişmesi ile birlikte başta güvenlik gereksinimleri olmak üzere konfor ve performans talepleri gibi artan istekler araçların ağırlığını artırmıştır. Bu çalışmada taşıt ağırlığının zamanla artma nedenleri ve artan taşıt ağırlığı nedeniyle oluşan sorunlar ve hafifletme çalışmaları incelenmiştir. Taşıt ağırlıkları yeni alaşımlar ve alaşımların çeşitlenmesi, yeni imal yöntemleri, hafif alüminyum, hafif alüminyumdan 4 kat daha hafif köpükler, yüksek maliyetlerin azalması, bilgisayar destekli optimizasyon yöntemleri ile sürekli azaltılıp mekanik özellikler iyileştirilmektedir. Hafif malzemeler maliyet artışına neden olurken tasarımların küçülmesi, yakıt sarfiyatının azalması ve geri dönüşüm bu maliyetleri kabul edilebilir hale getirmektedir. Yeni teknolojiler ve yatırımlar ile gelişen uzay havacılık sanayinin bilgi birikimi zamanla diğer sektörlerde de kullanıma

girmesi hafifletme işlemlerini hızlandırmaktadır. Alüminyum uzay ve havacılıkta sağladığı hafiflik ve iyi mukavemet özellikleri ile taşıtlarda da kullanılmaya başlamıştır. Genelde hafif malzeme olarak alüminyum alaşımları taşıtlarda en çok kullanılan geleneksel çeliklerin yerine kullanılmaktadır. Ağırlık azaltmada hafif metal olarak kullanılan alüminyum incelenmiştir. Bu çalışmada örnek model olarak salıncak kolu tasarımında St 37 çelik malzeme yerine Al 5754 alüminyum alaşımı kullanımı ile hafifletme sağlanmaya çalışılmıştır. Yapılan analizler çelik malzeme yerine alüminyum malzeme kullanımı ile %59 ağırlık azaltımı sağlanmıştır.

KAYNAKLAR

1. **Anonim,** (2020), Seykoç Alüminyum Alaşımlar, http://www.seykoc.com.tr/icerik/5754?dil=tr

2. **King, J.,** (2007), The King Review of low-carboncars - Part I: the potential for CO2 reduction, London.

3. **Anonim, (2006).** Alüminyum Raporu.TmmobMetalurji Mühendisleri Odası, Alüminyum Komisyonu 24.Dönem Çalışma Raporu.

4. **Anonim, (2010).** U.S. Department of EnergyVehicle Technologies Program Office of EnergyEfficiencyandRenewableEnergy U.S. Department of Energy, Multi-year Program Plan 2011 – 2015, USA.

5. **Anonim, (**2019), 2015 Model Volvo XC90 Euro NCAP test sonuçları, **https://www.euroncap.com/tr/results/volvo/xc90/209762019.**

6. **Song,** Y.,Youn, R., Gutowski, T.G. (2009), Life cycle energy analysis of fiber reinforced composites. Composites: Part A 40 (2009) 1257–1265.

7. **Yüce, C.** (2013), Yeni Nesil Ticari Araçlar İçin Hafifletilmiş Yolcu Koltuğu Tasarımı Ve Prototip İmalatı.*Yüksek Lisans Tezi*, Uludağ Üniversitesi, Fen Bilimleri Enstitüsü, Bursa.

8. **Mayyas, A.,Qattawi, A., O.M. Shan. (2012).** Design for sustainability in automotive industry: A comprehensive review. Renewable and Sustainable Energy Reviews 16(2012) 1845–1862.

9. **Yıldırım, H. (2006),** Alüminyum Malzemenin Otomotiv Sektöründeki Uygulamaları. *Yüksek Lisans Tezi,* İTÜ, Fen Bilimleri Enstitüsü, İstanbul.

10. **Kazdal Zeytin, H., (2000),** Alüminyum alaşımları, otomotiv endüstrisinde uygulamaları ve geleceği, MAM-MKTAE/OSD, Gebze, Türkiye.

11. **Aghion, E.,Boronfin B., Eliezer D. (2001),** The Role of theMagnesiumIndustry in Protectingthe Environment, *J.Mat. Proc. Tech*., 117, p: 381-385.

12. **Höke, Ö. (2016),** Hafif Ticari Araçlarda Kullanılan Motor Traversinin Yapısal Optimizasyonu.*Yüksek Lisans Tezi,* YTÜ, Fen Bilimleri Enstitüsü, İstanbul

13. **Anonim, (2017).** 2018 Audi A8 alüminyum ağırlıklı gövdesini sergiledi. https://tr.motor1.com/news/142690/2018-audi-a8-aluminyum-video/ (Erişim Tarihi: 12.01.2020).

14. **Anonim, (2020),** 2020 AlcoaWheelsgenel broşür. http://ak-set.com.tr/Dokumanlar/Genel-Brosür.pdf.

15. **Tüfekçi M., (2016).** Hafif ticari araç kapıları için modüler menteşe tasarımı, optimizasyonu ve prototip imalatı.*Yüksek Lisans Tezi*,455507 Uludağ Üniversitesi, Fen Bilimleri Enstitüsü, Bursa.

BİR SİLAH NAMLUSUNDA KOVAN-ATIM YATAĞI ETKİLEŞİMİNİN İNCELENMESİ

Muhammet Mustafa YILMAZ, *mmyilmaz@aselsankonya.com.tr*, Aselsan Konya Silah Sistemleri, 42280, Konya

Sadettin ORHAN, *sadettinorhan@ybu.edu.tr*, Ankara Yıldırım Beyazıt Üniversitesi, 06010, Ankara

ÖZET

Bu çalışmada 30 mm x 173 kalibre NATO standartlarında mühimmat atabilen bir silah namlusu için atım yatağı-kovan etkileşimi incelenmiştir. Deneysel bir yöntem kullanılarak namlunun iç balistik analizi yapılmıştır. İç balistik analizi neticesinde namlu içerisinde, zamana göre basınç değişiminin grafiği elde edilmiştir. Sonrasında kovan ve namlu malzemelerinin mekanik özellikleri belirlenmiştir. Namlu, kalın cidarlı basınçlı kap; kovan, ince cidarlı basınçlı kap kabul edilerek, kovanın namlu ile radyal yönde olan etkileşimi incelenmiştir. Çalışmada “Bilinear Kinematic Hardening” modeli kullanılarak deformasyonlar incelenmiştir. Model kullanılarak ortalama atım yatağı-kovan boşluğu ve deformasyon değeri hesaplanmıştır. Atış yapılmış kovan ve atış yapılmamış kovanın ölçüm sonuçları, model sonuçlarıyla kıyaslanmıştır. Sonuçların hesaplama ile elde edilen değerlerle uyumlu olduğu görülmüştür.

Anahtar Kelimeler: İç Balistik, Namlu, Atım Yatağı, Mühimmat, Kovan, Ateşli Silah, Sevk Barutu

ABSTRACT

In this study, the interaction between the barrel chamber-cartridge case for a gun barrel capable of firing 30 mm x 173 NATO standard ammunition was investigated. Internal ballistic analysis of the gun barrel was carried out by using an experimental method. As a result of the internal ballistic analysis, the graph of the pressure change in the gun barrel versus time was obtained. Afterwards, the mechanical properties of the cartridge case and the gun barrel material were determined. The gun barrel and cartridge case were considered as the thick-walled pressure vessel and the thin-walled pressure vessel, respectively. With this assumption, the interaction between the cartridge case with the gun barrel in radial direction was investigated. In the study, deformations were investigated using the "Bilinear Kinematic Hardening" model. Mean clearance between the barrel chamber and cartridge case and the amount of deformation were calculated by using model. The obtained measurements from the fired cartridge and the unfired cartridge were compared to the results obtained from the model. The results were found to be compatible with the values obtained by the calculation.

Keywords: Internal Ballistic, Gun Barrel, Barrel Chamber, Ammunition, Firearms, Cartridge Case, Propellant

1.Giriş

Balistik, mermi ve roketlerin uçuş davranışını inceleyen ve bunların dinamik davranışlarını ele alan bir bilim dalıdır. “Balistik” kelimesi Yunanca “ballein” Türkçe “atmak” anlamına gelen kelimeden türetilmiştir.

Balistik; iç balistik, ara balistik, dış balistik, hedef balistiği olmak üzere dört alt alana ayrılmaktadır.

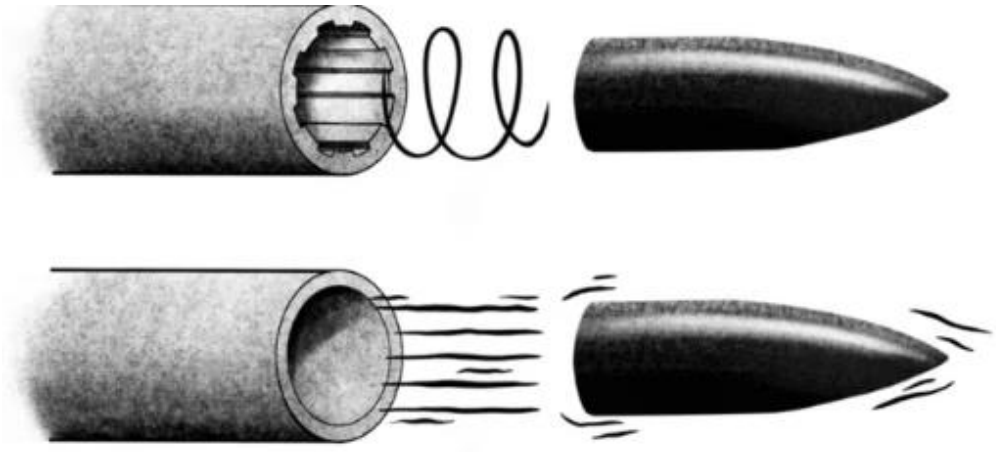
İç balistik, sevk barutunun yanmasıyla oluşan enerjinin mermi çekirdeğini hareket ettirmesiyle oluşan fiziksel ve kimyasal olayların, çekirdek namlu içerisindeyken etkilerini inceleyen balistik biliminin bir alt çalışma alanıdır. İç balistik hesaplamalarından elde edilen sonuçlar ve mühimmat bilgileri kullanılarak silah tasarımları şekillenmektedir.

Ateşli silahların en temel kısmı namludur. Namlu, mühimmatın ateşlendiği ve içerisinde oluşan gaz basıncıyla mermi çekirdeğinin hareketlenmişini sağlayan boru şeklinde parçadır. Ateşli silahlarda mühimmat namlu içerisindeki atım yatağına yerleştirilir ve ateşleme gerçekleşir. Silah namluları kalın cidarlı basınçlı kap şeklinde değerlendirilmektedir [Zhong,2018].

Silah tasarımının ilk adımı namlu tasarımı, dolayısıyla namlu atım yatağı tasarımıdır. Bu alandaki çalışmalar hazır tasarımlar ve tersine mühendislik yöntemleri kullanılarak gerçekleştirilmektedir. Özgün ve geliştirilmiş ateşli silahların tasarlanması için iç balistik, atım yatağı ve namlu tasarım parametrelerinin belirlenmesi gerekmektedir.

Namlular yivli veya yivsiz olabilir (Şekil 1). Farklı tespit arayüzlerine sahip şekilde tasarlanabilir. Ağız baskılı veya ağız baskısız olabilir, yanma odası ayrı veya birleşik olabilir (Şekil 2).

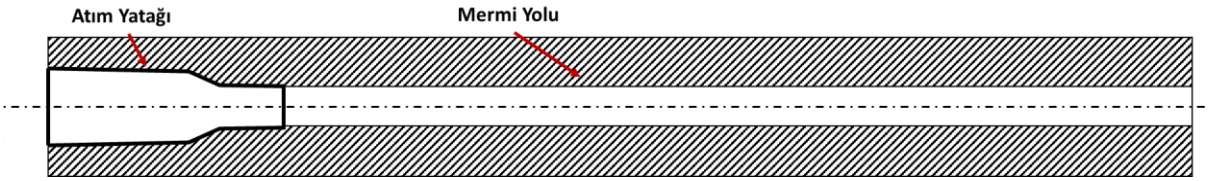
Bahsedilen farklılıklar olsa da namlular temel de iki bölgeye ayrılır. Bu bölgeler atım yatağı bölgesi ve mermi yoludur (Şekil 3).



Şekil 1. Yivli ve Yivsiz Namlular (2)

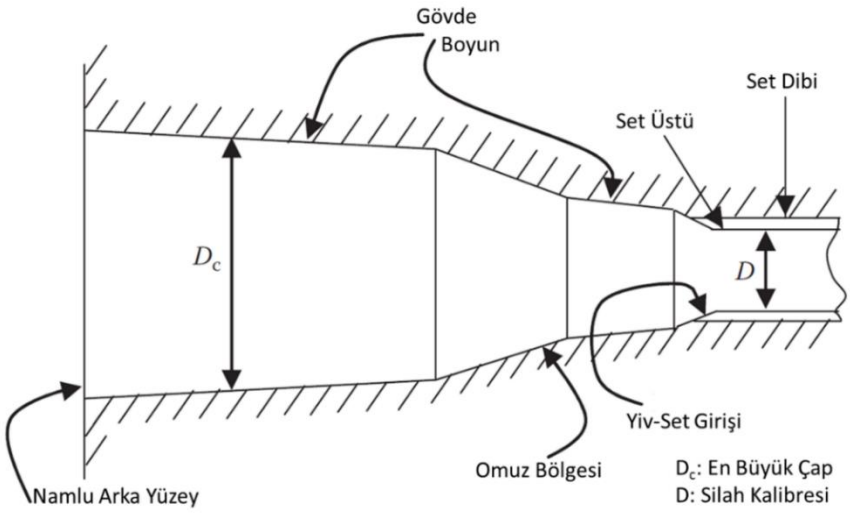


Şekil 2. Birleşik Olmayan Atım Yatağı



Şekil 3. Namlu İç Yapısı

Genellikle tek kullanımlık mühimmatla beslenen askeri namluların atım yatağı yapısı Şekil 4'te belirtildiği gibi olmaktadır.

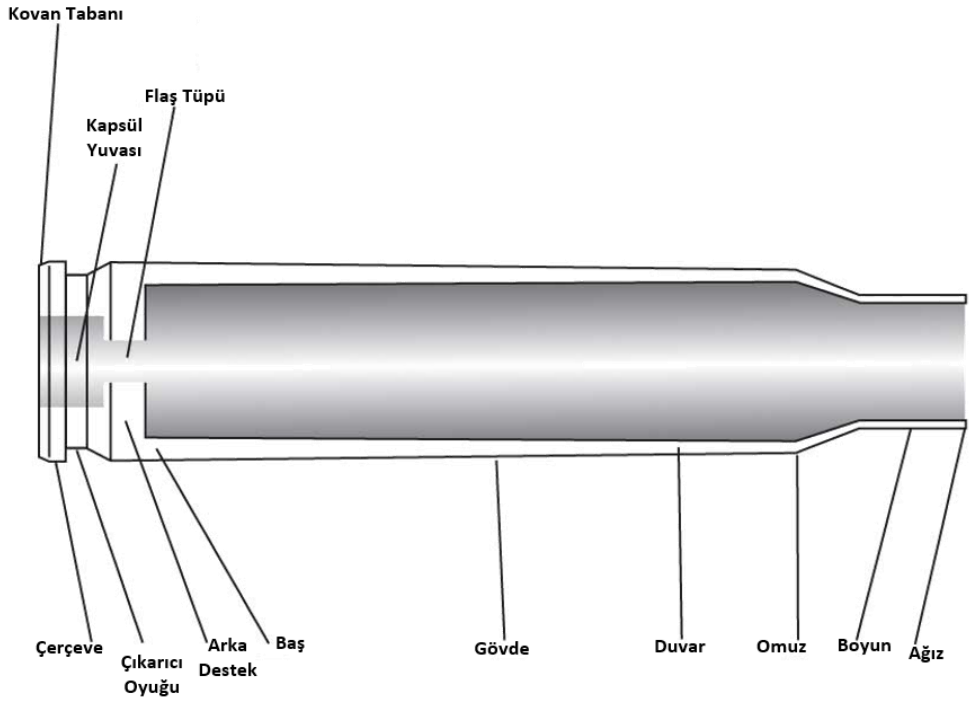


Şekil 4. Atım Yatağı Yapısı

Namlunun dış cidar ölçüleri belirlenirken kalın cidarlı basınçlı kap denklemleri (Lame Denklemleri) kullanılmaktadır [Gündüzer,2011]. Sadece Lame denklemleri kullanılarak yapılan namlu tasarımında, malzemenin yüksek gerinim hızındaki davranışı ve atım yatağı-mühimmat ilişkisini incelenmemektedir. Bahsedilen ilişkilerin incelenmesiyle ağırlıkça hafif namlular tasarlanabilmektedir. Ateşli silah tasarımı yapılırken öncelikle namlunun atım yatağı kısmı tasarlanmalıdır. Daha sonra istenilen özelliklere uygun mermi yolu belirlenmelidir.

Mermi yolu, balistik hesaplamalarda mühimmat çekirdeğinin harekete başladıktan sonra ilerlediği kısmı olarak kabul edilmektedir. Namlu boyu ise atım yatağı birleşik namlularda, mermi yolu ve atım yatağı eksenel ölçüsünün toplamı olmaktadır. Cidar kalınlığı ve diğer namlu tasarım parametreleri daha sonra şekillenmektedir.

Atım yatağının belirlenmesinde namlunun atacağı mühimmatın özelliklerinin iyi bilinmesi gerekmektedir. Özellikle atım yatağı tasarımı için mühimmat kovanının dış ölçüleri, malzemesi ve sertliği bilinmelidir. Farklı kovan tipleri bulunmasına rağmen temel olarak kovan yapısı, bölgelerin işlevi ve tasarım kriterleri tüm kovanlarda benzer özelliklerde olmaktadır. Şekil 5'te genel bir kovanın yapısı ve bölgeleri görülmektedir.



Şekil 5. Kovan Yapısı

Klasik bir kovan; kovan ağzı, kovan boynu, kovan yan duvarları ve kovan başı olarak dört ana bölgeye ayrılmaktadır.

Kovan ağzı, mermi çekirdeğinin tespit edildiği kısımdır**.** Diğer kısımlara göre et kalınlığı ince ve sünektir. Çekirdeğin yeteri miktarda kuvvet sonrası ayrılmasına izin verir ve sızdırmazlığı sağlar.

Kovan omuzu, kovanın atım yatağından çıkmasını kolaylaştıracak şekilde açılıdır. Bazı tip kovanlarda kovanın eksenel hareketini kısıtlar.

Kovan yan duvarları (gövde), kovanın arka kısmına doğru kalınlaşmaktadır. Kovanın omuz kısmına doğru et kalınlığının incelmesinden dolayı kovan, omuz bölgesine yakın bölgede daha fazla sızdırmazlık özellik gösterir. Süneklik ve mukavemet seviyesi iyi ayarlanmalıdır.

Çok sert olursa çıkartma durumunda eksenel olarak kesebilir, atış esnasında çevresel olarak yarılabilir. Çok sünek olursa kovan atım yatağına yapışır. Atım yatağından çıkarma zorluğu yaşanır.

Kovan başı**,** kovanın radyal yönde desteksiz kalan en rijit kısmıdır. Eksenel kuvveti karşılar. Kovanın çıkması için çıkarıcı oyuğu buradadır. Kapsül bileşenlerine yataklık eder.

Günümüzde namlu tasarımları, teknolojiyi geliştirmeyen ülkeler tarafından mevcut tasarımların tersine mühendislik çalışmaları olarak gerçekleştirilmektedir. Namlunun en kritik bölgesi olan atım yatağı bölgesi tasarımlarında askeri ve ticari namlular için bazı kalibrelerde standartlaştırılmış ölçüler bulunmaktadır. Belirtilen standart atım yatağı ölçülerine göre namlu tasarımları ortaya çıkmaktadır.

Standartlaştırılan ölçüler NATO gibi müşterek oluşumlarda temel seviye değiştirilebilirliğin sağlanması ve lojistik kolaylık adına belirlenen ölçülerdir. Aynı kalibrede farklı şekillerde optimize edilmiş namlu tasarımları bulunmaktadır. Belirtilen standartlarda olmayan mühimmatlar için ise herhangi bir bilgi bulunmamaktadır. Aerodinamik olarak optimize edilmiş mühimmatlar ve farklı görev ihtiyacında kullanılabilecek mühimmatlar için herhangi bir standart bulunmamaktadır. Atım yatağı tasarımı için ticari yazılımlar da kullanılmaktadır. Yazılımların kullanılması için teorik bilgi gerekli olmakla birlikte, yazılımlar kısıtlamaya tabi ürün olabilmekte, ambargoya takılmakta, yüksek fiyat, kütüphane ve modüllerinin tamamının temin edilememesi problem teşkil etmektedir. Aynı zamanda yazılımların hesaplamadığı parametreler de bulunmaktadır.

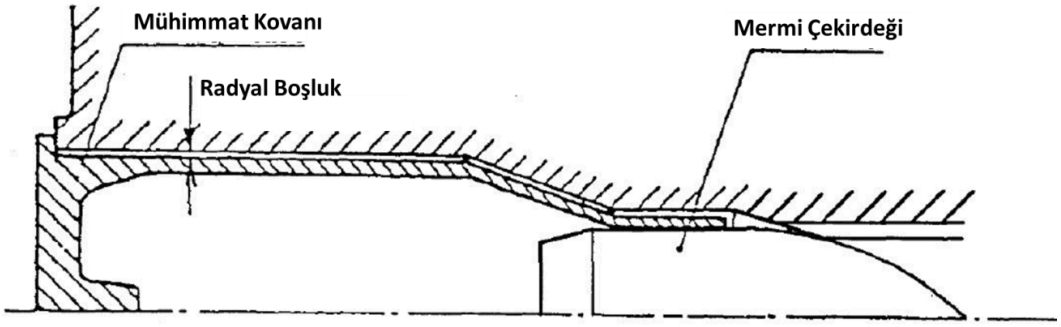
Atım yatağının geri tepme kuvvetine ve namlu tasarımına etkisi ayrı bir çalışma konusudur. Bu çalışmalar neticesinde optimizasyon çalışmaları yapılabilmektedir. Bu sebeplerden dolayı her mühimmat tipine göre atım yatağı tasarlayabilmek ve buna göre optimize edilmiş namlu ve mekanizmalar tasarlamak büyük önem arz etmektedir.

Yapılan çalışmada, söz konusu tasarım süreçlerinin teorisinin ortaya konması ve bu bağlamda her tipte mühimmata uygun atım yatağının tasarlanması ve bu tasarımların optimizasyonlarının gerçekleşmesi ve daha sonra uygun arayüze sahip paket bir programın geliştirilmesi amaçlanmıştır.

2. TEORİ

Kovanın atım yatağına yerleştirildikten sonra fonksiyonunu yerine getirebilmesi için kovan-atım yatağı arasındaki radyal boşluğun ve atım yatağı açısının kovan açısına göre iyi ayarlanması gerekmektedir. Radyal boşluk az olursa kovan, atış sonrası atım yatağına yapışır ve kovanın tahliyesinde problem yaşanır, silah mekanizması fonksiyonunu yerine getiremez. Boşluk fazla olursa kovan desteksiz kalır, yüksek basıncın etkisiyle ince cidarlı kovan üzerindeki gerilme, kovanın çekme dayanımının üzerine çıktığı an kovan yarılır ve silahta arızaya sebep olur.

Şekil 6'da kovan-atım yatağı arasındaki ilişki gösterilmiştir.

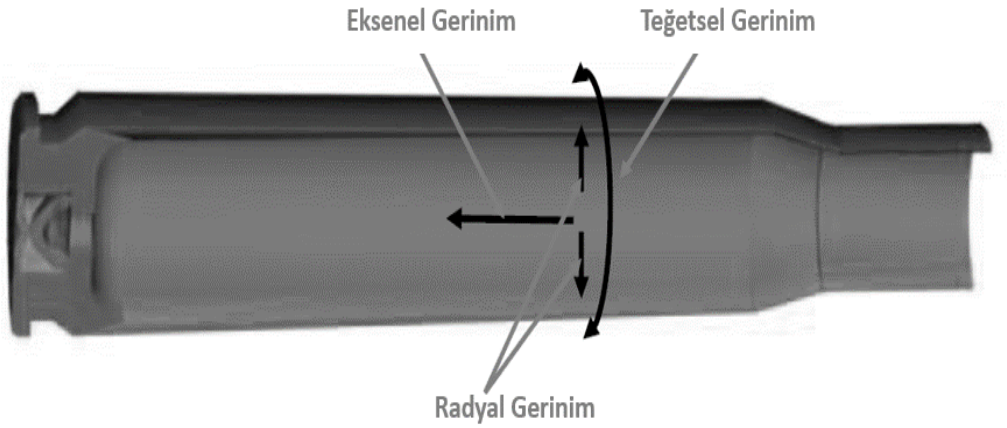


Şekil 6. Kovan-Atım Yatağı Arayüzü Kesit Görünümü

Atım yatağı, mühimmatın kovan kısmından namlu ekseninde yataklanmasına yardımcı olur, sevk barutunun yanmasıyla oluşan yüksek basınç esnasında ince cidarlı kovana destek olur. Kovan ise sevk barutunu içerisinde barındırmakta ve atış esnasında gaz sızdırmazlığını sağlamaktadır. Gaz sızdırmazlığını en çok kovanın boyun bölgesi sağlamaktadır [Zhao,2014].

Tasarlanacak atım yatağının fonksiyonunu yerine getirmesi için kovan üzerindeki gerilmenin çekme dayanımı üzerine çıkmaması gerekmektedir. Kovan tek kullanımlık olduğundan dolayı akma dayanımının üzerine çıkılması problem teşkil etmemektedir. Kovan-atım yatağı arasındaki boşluklar ve deformasyon üzerinden inceleme yapılacağı için maksimum gerinim değeri üzerinden hesaplamaların gerçekleştirilmesi daha uygun olmaktadır.

Atış esnasında kovan üzerinde Şekil 7'de belirtilen gerilmeler oluşmaktadır. Bunlardan eksenel gerilme hesabı, kovan cidar kalınlığına göre kama tasarımı ve mekanizma tasarımı ile değerlendirilmektedir. Radyal gerilme ise ince cidarlı basınçlı kaplar için ihmal edilebilir seviyededir.



Şekil 7. Basınç Altında Kovan Üzerindeki Mekanik Deformasyonlar

Eksenel dayanım için kovan, kovan tipine göre değişen feyyür (headspace) mesafesinden sabitlenir. Kovan üzerinde meydana gelen çekme gerilmesi ve kovanın radyal yönde desteksiz kalabilecek bölgesi değerlendirilerek kovanın namludan çıkma mesafesi belirlenir.

Daha sonra mekanizma ve kama toleransları belirlenir. Bu durum, Şekil 8'de kesilmiş kovan kesitinde gösterilmiştir. Şekil 9'da kovanın radyal destekli kalması gereken bölgeler belirtilmiştir.



Şekil 8. Kovan Üzerine Gelen Eksenel Yük

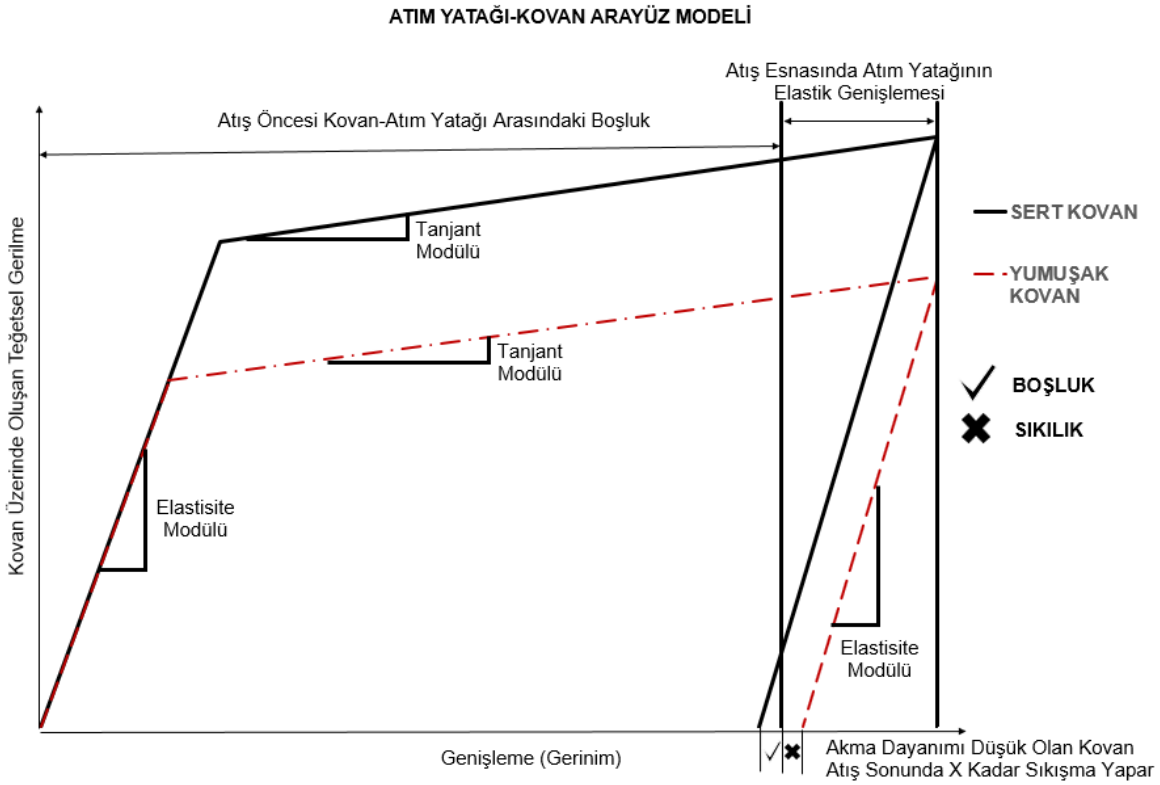


Şekil 9. Kovanın Radyal Destekli Kalması Gereken Bölgeleri

Kovan tek kullanımlıktır. Gerilim değerinin kovan malzemesinin çekme dayanımının üzerine çıkmaması gerekmektedir. Bundan dolayı, hesaplamalarda ve analizlerde "Bilinear Kinematic Hardening" modeli kullanılmaktadır. Modelde malzemenin Von Mises elipsindeki akma yüzeyi genişlemez ama yer değiştirir. Bilinear olması malzemenin plastik bölgede tek bir lineer özellik göstermesini belirtir. Düşük dayanıma sahip kovan malzemesi olarak sıklıkla Cu70Zn30 pirinç malzeme, alüminyum, düşük karbonlu çelikler ve son yıllarda polimerler kullanılmaktadır. Çelik kovan; mukavim olması, ucuz olması ve içerisine daha çok sevk barutu alması sebebiyle orta kalibrelerde tercih edilmektedir. Alüminyum kovan ise, hafiflik açısından avantaj sağlamaktadır.

Bu çalışmada AISI 1020 malzeme düşük karbonlu çelik kovan özellikleri referans alınarak hesaplamalar gerçekleştirilmiştir.

Namlu atım yatağı ve kovan arasındaki ilişkiyi gösteren “Bilinear Kinematic Hardening” modeli Şekil 10’da gösterilmiştir.

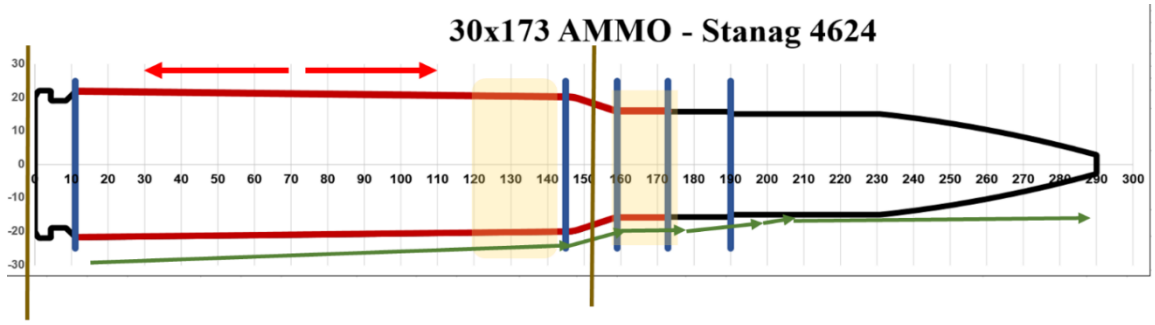


Şekil 10. Kovan-Atım Yatağı Hardening Modeli

Mühimmat bilgisi ve iç balistik hesaplamaları, namlu ve ateşli silahlı tasarımının temel gereksinimleridir. Buradaki zamanlama ve yüklere göre silah mekanizması ve yapısalı tasarlanmaktadır.

Kovan, analizler için Şekil 11’de belirtilen bölgelere ayrılmıştır. Her bölgenin mekanik özellikleri farklıdır. Malzemenin sertlik değeri farklılık göstermektedir. Aynı zamanda katılık değeri de farklıdır. Bundan dolayı hesaplamalar bölgesel olarak yapılmalı ve daha sonra sonuçlar birleştirilmelidir.

Matematiksel model oluşturmak için kovanın parçaları kendi sertliğinde ve katılığında tanımlanmalı, daha sonra sonuçlar birleştirilmelidir. Kovanın Şekil 11’ de belirtilen 120 mm ile 173 mm arasındaki bölgesi kovanın sünek ve en çok genişleyen, sızdırmazlığı sağlayan bölgesidir.

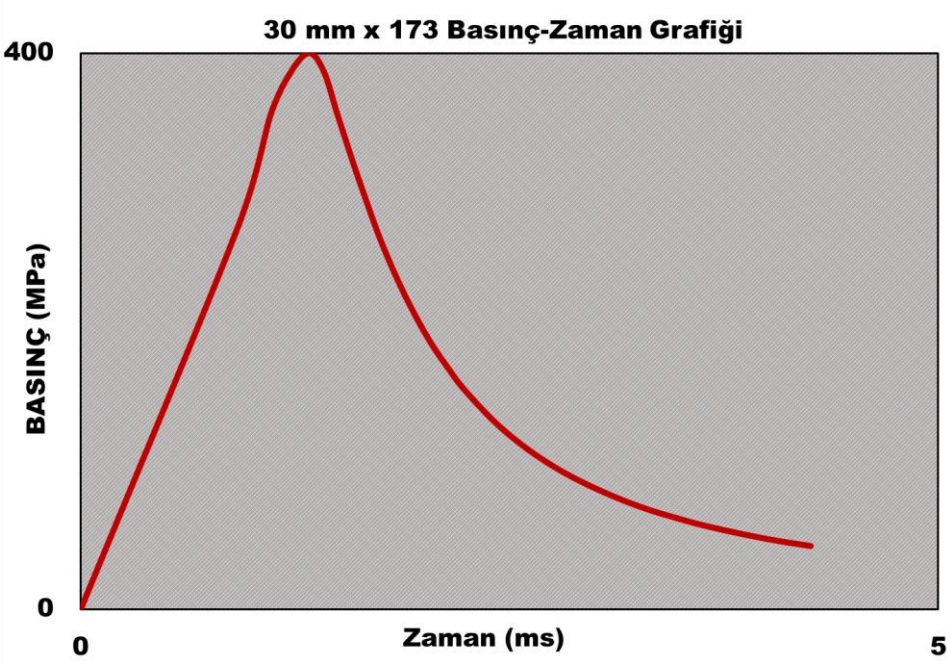


Şekil 11. Mühimmat Kritik Bölgeleri

Namlu tasarımı için mühimmatın namlu içerisindeki davranışı incelenmelidir. Bu davranışı ortaya koymak için iç balistik hesaplamalarının yapılması gerekmektedir.

İç balistik analizleri için, teorik modellerin PRODAS yazılımı gibi paket programa dönüştüğü ticari yazılımlar bulunmaktadır. İç balistik modellerinden termodinamik model, NATO Stanag 4367 ile tanımlanmış, bu model Bear-Frankle modelinin ilerletilmiş metodudur. Literatürde farklı termodinamik ve numerik modeller kullanılmakla birlikte Vallier-Heydenreich gibi deneysel modeller de kullanılmaktadır [Susantez,2020]. Cronemberger 7.62 mm kalibre bir silah için Vallier-Heydenreich ve Bear-Frankle Lumped modelinin sonuçlarını, yapmış olduğu testler ile kıyaslamıştır [Cronemberger,2014]. Akçay, Resal çözümü ile barut geometrisine bağlı olan ilişkiyi incelemiş, deneysel sonuçları Cronemberger çözümleriyle kıyaslamıştır [Akçay,2016]. Çalışmanın zamana bağlı çözümlere girdi olacak şekilde iç balistik analizleri birden çok yöntemle yapılmıştır. Vallier-Heydenreich yöntemi, diğer yöntemlere kıyasla daha az veriye ihtiyaç duymasından dolayı çalışmanın zamana bağlı çözümlerinin ilk aşamasında kullanılmıştır. Zamana bağlı olmayan çözümlerin ilk aşamasında atım yatağı tasarımı için maksimum basınç bilgisi yeterli olmaktadır. Atım yatağı hesaplamalarının sonlu elemanlar çözümlemelerinde, zamana bağlı olacak kovanın ve atım yatağının değişimini incelemek, sıcaklık etkisini zamana bağlı olarak analiz etmek ve atım yatağı-mermi çekirdeği-kovan ilişkisine göre optimum namlu tasarımı yapmak için iç balistik analizi sonucu elde edilen değerler kullanılmaktadır. Bu çalışmada tek atış durumu için namlu içi sıcaklık değeri ihmal edilerek sadece maksimum basınç değeri kullanılmıştır.

Pyhton programlama dilinde Vallier-Heydenreich modeli, paket program haline getirilmiş ve farklı kalibrelere göre girdiler arayüz programına girilerek iç balistik sonuçları elde edilmiştir. Şekil 12'de 30 mm x 173 mühimmatı için Vallier-Heydenreich yöntemi ile gerçekleştirilen iç balistik analizi neticesinde oluşturulan namlu içi 'Basınç-Zaman' grafiği gösterilmiştir. Buna göre 5 ms'den kısa bir sürede mermi çekirdeği namluyu terk etmekte ve çok kısa sürede namlu içerisinde maksimum basınç değerine ulaşılmaktadır.



Şekil 12. İç Balistik Basınç-Zaman Grafiği

Atım yatağı hesaplamalarında kullanılan kısaltmalar Tablo 1'de verilmiştir.

Tablo 1. Hesaplamalarda Kullanılan Kısaltmalar

$\mathbf{E_n}$	Namlu Elastisite Modülü	$\mathbf{E_k}$	Kovan Elastisite Modülü
$\boldsymbol{\nu}$	Poisson Oranı	$\mathbf{E_{kt}}$	Kovan Tanjant Modülü
$\mathbf{r_{nd}}$	Namlu Dış Yarıçapı	$\boldsymbol{\Delta u_n}$	Namlu Deformasyonu
$\mathbf{r_{ni}}$	Namlu İç Yarıçapı	$\boldsymbol{\Delta u_k}$	Kovan Deformasyonu
$\mathbf{r_n}$	Namlu Deformasyonuna Bakılan Yarıçap	$\boldsymbol{\Delta u_{km}}$	Kovan Maksimum Deformasyonu
$\mathbf{r_k}$	Kovan Dış Yarıçapı	$\boldsymbol{\Delta u_{ks}}$	Kovan Sonuç Deformasyonu
$\mathbf{p_d}$	Dış Basınç	$\boldsymbol{\varepsilon_k}$	Kovan Gerinimi
$\mathbf{p_i}$	İç Basınç	$\boldsymbol{\varepsilon_{km}}$	Kovan Maksimum Gerinimi
$\mathbf{c}$	Namlu-Kovan Arası Boşluk	$\boldsymbol{\varepsilon_{ka}}$	Kovan Akma Gerinimi
$\mathbf{t}$	Kovan Et Kalınlığı	$\boldsymbol{\varepsilon_{kd}}$	Kovan Dönüş Gerinimi
$\boldsymbol{\sigma_{ka}}$	Kovan Akma Gerilmesi	$\boldsymbol{\varepsilon_{ks}}$	Kovan Sonuç Gerinimi
$\boldsymbol{\sigma_{km}}$	Kovan Maksimum Gerilmesi	$\mathbf{r_{ks}}$	Kovan Sonuç Yarıçapı

Kalın cidarlı basınçlı kapların hesap yöntemi ile namlu cidar kalınlığı, namlu üzerindeki gerilme ve deformasyon değerleri hesaplanabilmektedir. Silah namlusunda meydana gelen eksenel deformasyon ihmal edilirse, açık uçlu, kalın cidarlı basınçlı kap denklemi kullanılmaktadır. Sıcaklık ihmal edilirse açık uçlu, kalın cidarlı basınçlı kap için radyal deformasyon miktarı aşağıdaki gibi olmaktadır [Öztürk,1972], [Carlucci,2018], [Ugural,2019].

$$\Delta u_n = \frac{r_n}{E_n \cdot (r_{nd}{}^2 - r_{ni}{}^2)} [(1-\nu) \cdot (p_i \cdot r_{ni}{}^2 - p_d \cdot r_{nd}{}^2) + \frac{(1+\nu) \cdot r_{ni}{}^2 \cdot r_{nd}{}^2}{r_n{}^2}] \cdot (p_i - p_d) \quad (1)$$

Atış yapıldıktan sonra kovan, atım yatağı arasındaki boşluğu kapatmakta ve atım yatağına yapışmaktadır. Daha sonra kovan ve atım yatağı birlikte, namlunun iç yüzeyinin deformasyon miktarı kadar daha deformasyona uğramaktadır. Buna göre kovanın deformasyon miktarı, denklem 2'de görüldüğü gibi, ince cidarlı açık uçlu basınçlı kap modeline göre namlunun deformasyon miktarı ve aradaki radyal boşluğun toplamı kadar olmaktadır.

$$\Delta u_n + c = \Delta u_k = \frac{p_i \cdot r_k{}^2}{E_k \cdot t} \quad (2)$$

Buradan yola çıkarak kovanın toplam deformasyon miktarı bulunabilmektedir. Denklem (2)'de verilen "t" sembolü kovanın et kalınlığı olup, kovan tasarımı ve imalatı neticesinde gelmektedir. Kovan bölgesine göre değişmektedir. Değişken kovan kalınlığı bölgeleri incelendiğinde, bölgesel sertlik miktarına göre atım yatağı tasarımında optimizasyona gidilmektedir.

Kovan üzerinde oluşan maksimum gerilme hesaplanırsa;

$$\sigma_{km} = [(\varepsilon_{km} - \varepsilon_{ka}) \cdot E_{kt})] + \sigma_{ka} \quad (3)$$

elde edilir.

Elde edilen gerilme değerinin, kovanın çekme dayanımının altında kalması gerekmektedir. Hesaplamalar atım yatağı-kovan ilişkisinin radyal yönde dayanımı için geçerlidir. Kovanın eksenel yönde dayanımı için, silahın diğer mekanizmalarının da dâhil edildiği hesaplama yöntemlerinin geliştirilmesi ve tüm hesaplamaların beraber değerlendirilmesi gerekmektedir.

Kovanın maksimum basınç değerinde ulaştığı gerilme değeri bulunduktan sonra kovan üzerindeki basınç zamanla azalacak, namlu elastik deformasyona uğradığından dolayı eski haline dönecek, kovan ise plastik deformasyona uğramış olacaktır. Analizi yapılan çalışmada çelik kovan kullanıldığı için, kovanın bazı bölgelerinde yüksek mukavemet bulunmakta ve elastik deformasyona uğramakta, bazı bölgelerinde ise kovan (ince cidarlı, sünek omuz ve boyun bölgelerinde) plastik deformasyona uğramaktadır.

Deformasyon sonucu kovan üzerindeki basınç yükü kalktığında “Bilinear Kinematic Hardening” modeline göre denklem (4)’teki ifade yazılabilir.

$$\varepsilon_{kd} = \frac{\sigma_{km}}{E_k} \tag{4}$$

İnce cidarlı basınçlı kaplar için ise denklem (5), (6), (7) geçerlidir.

$$\Delta u_k = \frac{p_i \cdot {r_k}^2}{E_k \cdot t} \tag{5}$$

$$\sigma_k = \frac{p_i \cdot r_k}{t} \tag{6}$$

$$\varepsilon_k = \frac{\sigma_k}{E_k} \tag{7}$$

Denklemler düzenlendiğinde kovan deformasyonu, maksimum gerinim ve kovan iç çapı cinsinden denklem (8) ve (9)’ da belirtildiği gibi olur.

$$\Delta u_{km} = r_k \cdot \varepsilon_{km} \tag{8}$$

$$\Delta u_{km} + r_k = \Delta u_n + r_{ni} \tag{9}$$

Buna göre kovan-atım yatağı arasındaki boşluk denklem (10) ile belirlenir.

$$c = r_{ni} - r_k \tag{10}$$

Kovanın maksimum deforme olduğu durum ile malzeme modeline göre kovanın plastik deformasyon sonrası üzerindeki yük kalktığında daralması sonucu geriye kalan deformasyon miktarı arasındaki fark hesaplanarak, kovanın atış sonrası davranışı analiz edilir ve kovan-atım yatağı arası boşluklar, denklem (11) ve (12)’den elde edilir.

$$\varepsilon_{ks} = \varepsilon_{km} - \varepsilon_{kd} \tag{11}$$

$$\Delta u_{ks} = r_k \cdot \varepsilon_{ks} \tag{12}$$

Buna göre atış sonucunda kovanın nihai ölçüsü, hesaplanan bölgede denklem (13)‘te belirtildiği gibi olmaktadır.

$$r_{ks} = r_k + \Delta u_{ks} \tag{13}$$

Eğer r_{ks}, atım yatağı çapından büyük olursa, kovan-atım yatağı arasında millerdeki sıkı geçme prensibine göre arayüz basıncı, kovan-atım yatağı arasındaki sürtünme kuvveti ve bu değerlerden kovanın atım yatağından çıkarılması için gerekli kuvvet hesaplanmalıdır. Bu durumda kovan atım yatağına sıkışmaktadır. Çıkarma kuvveti, atım yatağının konik olmadığı durumlarda çok yüksek mertebede olmaktadır. Silahlarda, çalışma mekanizmalarına ve kovan malzemesine bağlı olarak r_{ks} değerinin atım yatağı çapından büyük olduğu durumlar bulunmaktadır.

$r_{ks} \geq r_{ni}$ Durumunda kovan, atım yatağından serbeste çıkamayacaktır.

r_{ks} değerinin atım yatağı çapından küçük olması durumunda ise, kovan atım yatağı arasında boşluk oluşacaktır. Kovanı atım yatağından çıkarmak için yüksek kuvvet gereksinimlerine ihtiyaç duyulmayacaktır.

$r_{ks} \leq r_{ni}$ Durumunda kovan, atım yatağından serbestçe çıkabilecektir.

Kovan arasındaki boşluğun fazla olması kovanın radyal dayanımını, boşluğun az olması ise silah mekanizmasının fonksiyonunu rahatlıkla yerine getirmesini etkilemektedir.

3.MALZEME ÖZELLİKLERİ

Çalışmada, numune kovan olarak AISI 1020 derin çekilmiş düşük karbonlu çelik kullanılmıştır. İki farklı atış yapılmış kovan ve atış yapılmamış kovan için incelemeler gerçekleştirilmiştir. Kovan ölçülerinin net belirlenmesi ve kovanlarda bölgesel sertliğin elde edilmesi için numune kovanlar ortadan ikiye ayrılmıştır.



Şekil 13. Kovanların Ortadan İkiye Ayrılmış Hali

Her üç kovanın da bir yarım dilimi hidrolik pres cihazında düzleştirilmiş, kovanların çeşitli bölgelerinden Ultrasonik sertlik ölçüm cihazı ile sertlik ölçümleri yapılmıştır. Aynı zamanda atış yapılmış bir kovan numunesinin ince sünek bölgesinden kesilmiş parçası bakalite alınmış ve sabit ölçüm cihazında Vickers sertliği ölçülmüştür.



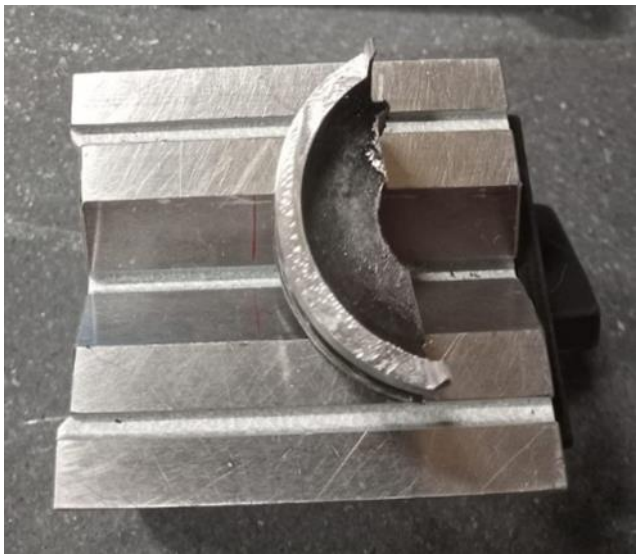
Şekil 14. Düzleştirilmiş Kovan ve Düzleştirilmemiş Kovanın Ölçüm İçin Hazırlanması

Sertlik ölçümleri düzleştirilmiş ve düzleştirilmemiş kovanlarda yapılmıştır. Kovan diliminin et kalınlığının ince olmasından dolayı Ultrasonik ölçüm kovanların ince bölgelerinde da sağlıklı sonuç vermemiştir. Fakat atış yapılmış ve yapılmamış kovanların baş kısmı kesilerek kovanın çekirdek sertliği Ultrasonik ölçümlerle elde edilmiştir. Ultrasonik ölçüm sonuçları tutarlı gelmiştir.



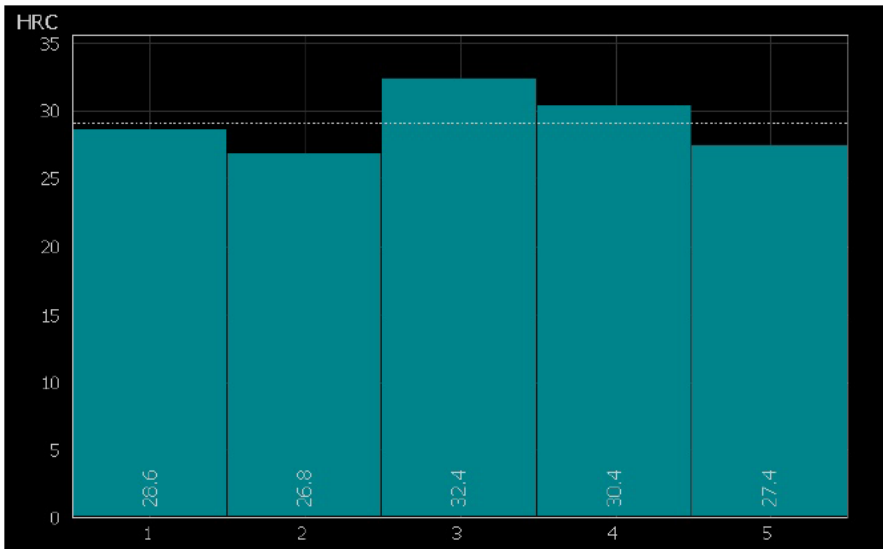
Şekil 15. Kovan Baş Bölgesi

Bakalite alınan atış yapılmış kovan parçasının ince sünek bölgesinden Vickers sertlik ölçümü yapıldığında sonuç Rockwell C ölçeğinde 22-25 HRC olarak elde edilmiştir. Atış yapılmış kovanın baş kısmı sertliği, Ultrasonik ölçüm yöntemi ile ölçüldüğünde 30-32 HRC gelmektedir. Aynı ölçme yöntemi ile atış yapılmamış kovanın baş kısmı sertliği 27-32 HRC aralığında gelmektedir. Atış yapılan kovanın ince bölgelerinde ise Ultrasonik yöntem ile sertlik değeri ölçülememiştir.



Şekil 16. Kovan Baş Bölgesinden Çekirdek Sertliği Ölçümü

Kovan derin çekme yöntemi ile üretilmektedir. Derin çekme imalat yönteminin gerektirdiği gibi, kovanın baş kısmında malzemenin daha sert, boyun bölgelerinde ise yumuşak olduğu gözlemlenmiştir. Çelik malzemelerde sertliğin süneklik ile ilişkisi olduğu gibi, çeliğin çekme dayanımında da etkisi bulunmaktadır. Çeliğin çekme dayanımı sertliğin bir fonksiyonu olarak yazılabilmektedir. Namlu atım yatağı ve kovan arasındaki boşluklar bu kriterler göz önünde bulundurularak ve bölgelere ayrılarak verilmelidir.



Şekil 17. Kovan Sertlik Değerleri

Numunelerin yapısından dolayı çekme testi gerçekleştirilememiştir. Literatürde bulunan değerler temel alınarak hesaplamalarda kullanılan çekme ve akma dayanım değerleri belirlenmiştir. Hesaplamalarda kullanılacak çekme ve akma dayanımı için, malzemenin çekirdek sertliğine göre ISO 18265 Standardında belirtilen değerler değerlendirilmiştir. XRF cihazı ile kovan çeliğinin analizi yapılmıştır.

Dönmez çalışmasında, AISI 1020 çeliğinin, pekleşme neticesinde sertliğine göre mekanik özelliklerinin değişimini belirtmiştir [Dönmez,2003].

Çelik kovan için tanjant modülünün değeri, analitik hesaplarla ve literatürde bulunan değerlere göre elde edilmeye çalışılmıştır [Havron,1989], [Dönmez,2003]. Aynı zamanda elde edilen değerlerin maksimum ve minimum aralığında olmasının hesaplar üzerine etkisi incelenmiştir. Tanjant modülünün değeri 0.8 GPa ile 2 GPa arasında uç değerler girilerek hesaplanmış, literatürden elde edilen verilerle ortalama değer olarak 1 GPa girilmiştir.

Verilen bilgilere göre kovan malzeme özellikleri Tablo 2'de belirtilmiştir.

Kovan malzemesi olarak düşük karbonlu AISI 1020 çelik malzeme kullanılmıştır.

Tablo 2. Kovan Malzemesi Mekanik Özellikleri

AISI 1020 Mekanik Özellikleri	
Çekme Dayanımı	850 MPa
Akma Dayanımı	750 MPa
Elastisite Modülü	210 GPa
Sertlik	25-30 HRC
Yüzde Uzama	%10
Tanjant Modülü	1 GPa
Poisson Oranı	0.3

Tablo 3. Namlu Malzemesi Mekanik Özellikleri

AISI 4140 Mekanik Özellikleri	
Çekme Dayanımı	1180 GPa
Akma Dayanımı	1100 MPa
Elastisite Modülü	210 GPa
Sertlik	40 HRC
Yüzde Uzama	%15
Poisson Oranı	0.3

Analiz için namlu malzemesi olarak AISI 4140 kullanılmıştır.

Denklemler kullanıldığında sonuçlar kovan üzerinde belirlenen numune bölge için tabloda belirtildiği gibi olmaktadır.

4. HESAPLAMA

Kovan - atım yatağı etkileşimi neticesinde oluşan deformasyonlar, kovan-atım yatağı arasındaki nihai boşluk değeri, gerinim ve gerilim değerleri ilgili denklemler kullanılarak hesaplanmış olup Tablo 4, 5 ve 6'da sunulmuştur.

Tablo 4. Namlu Analiz Girdileri

Atım Yatağı Radyal Genişleme			
Atım Yatağı Radyal Genişleme	$\Delta \mathbf{u_n}$	0.057	mm
Atım Yatağı İç Yarıçapı	$\mathbf{r_{ni}}$	20.80	mm
Atım Yatağı İç Çapı	$\boldsymbol{d_{ni}}$	41.6	mm
Atım Yatağı Dış Yarıçapı	$\mathbf{r_{nd}}$	80	mm
Atım Yatağı Dış Çapı	$\boldsymbol{d_{nd}}$	160	mm
İç Basınç	$\mathbf{p_i}$	400	MPa
Dış Basınç	$\mathbf{p_d}$	0.1	MPa

Tablo 5. Kovan Analiz Girdileri

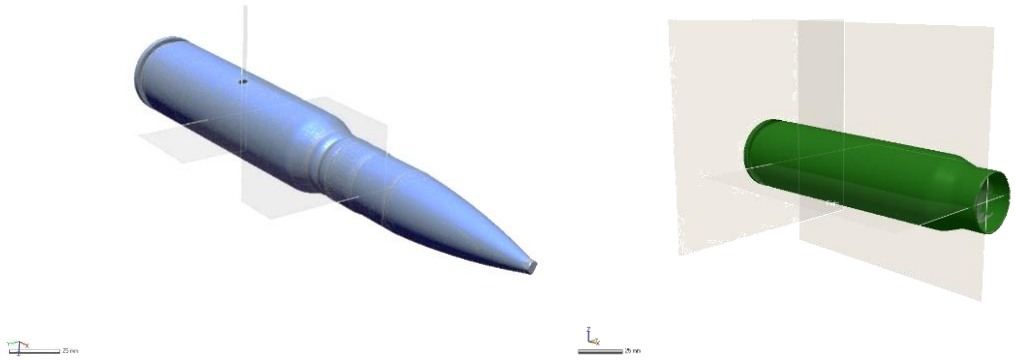
Kovan Radyal Genişleme			
Kovan Dış Yarıçapı	$\mathbf{r_k}$	20.7	mm
Kovan Dış Çapı	$\boldsymbol{d_k}$	41.4	mm
Kovan Akma Gerinimi	$\boldsymbol{\varepsilon_{ka}}$	0.0036	
Kovan Et Kalınlığı	$\mathbf{t}$	1.6	mm

Tablo 6. Ortak Çözüm Sonucu

Analiz			
Genişledikten Sonra Atım Yatağı Yarıçapı	$\mathbf{r_{ni}} + \Delta \mathbf{u_n}$	20.86	mm
Kovan Maksimum Deformasyon	$\Delta \mathbf{u_{km}}$	0.157	mm
Maksimum Kovan Gerinimi	$\boldsymbol{\varepsilon_{km}}$	0.008	
Maksimum Kovan Gerilimi	$\boldsymbol{\sigma_{km}}$	754	MPa
Kovan Dönüş Gerinimi	$\boldsymbol{\varepsilon_{kd}}$	0.0036	
Kovan Sonuç Gerinimi	$\boldsymbol{\varepsilon_{ks}}$	0.004	
Kovan Sonuç Deformasyonu	Δu_{ks}	0.083	mm
Atış Tamamlanınca Kalan Kovan Yarıçapı	$\mathbf{r_{ks}}$	20.78	mm
Nihai Kalan Boşluk	-	0.017	mm

5. DOĞRULAMA

Atış yapılmış ve yapılmamış kovan arasındaki farkın incelenmesi için atış yapılmamış mühimmat ve atış yapılmış mühimmat kovanı Geomagic Design X program kullanılarak 3 boyutlu tarayıcı cihazda taranmıştır.



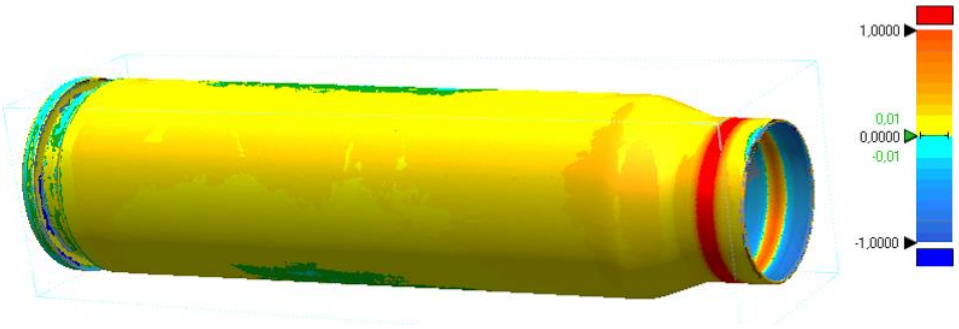
Şekil 18. Kovanların Orjine Hizalanması

Elde edilen verilerin nokta bulutu çıkartılıp mesh yapısı örülmüştür. Daha sonra hazırlanan veri uzayda dönme ekseninden ve en rijit bölgesinden sabitlenmiştir.



Şekil 19. Kovanların Rijit Bölgelerden Hizalanması

Veri setleri daha sonra ayrı bir dosyada manuel olarak üst üste çakıştırılmış, Geomagic Design X Programındaki algoritma ile ortak noktalar tanımlanmış ve hizalama otomatik olarak gerçekleştirilmiştir.

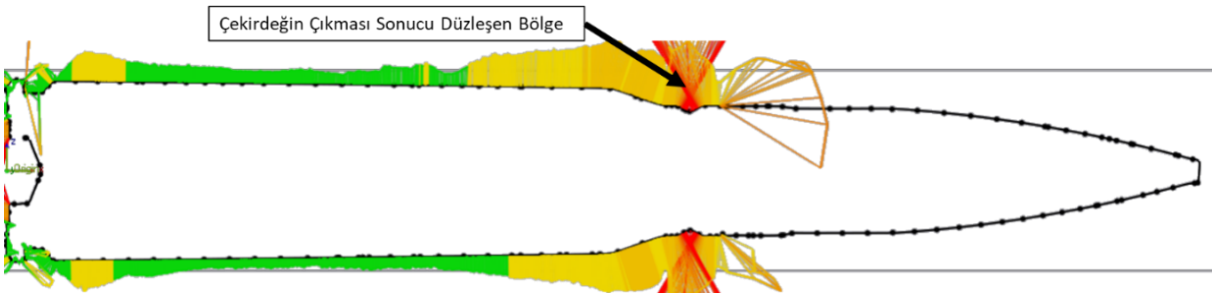


Şekil 20. Boş Kovan Sapma Miktarı



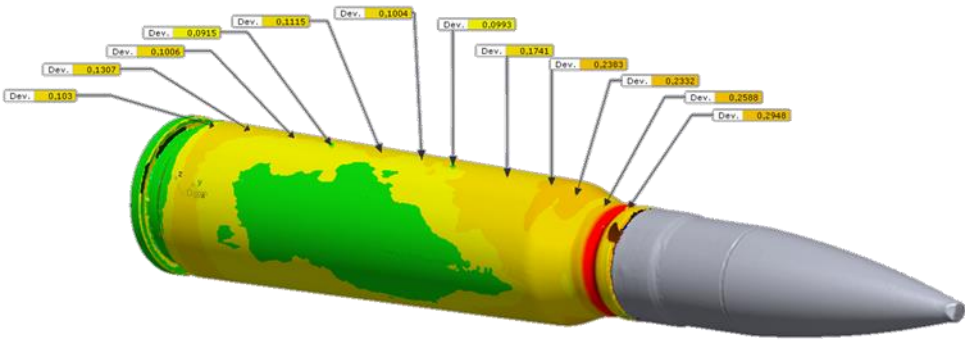
Şekil 21. Kovan Kısmı Sapma Miktarı

Çalışmada Geomagic Control X programı kullanılarak kesitten alınan 2 boyutlu ölçüler kıyaslanmıştır.

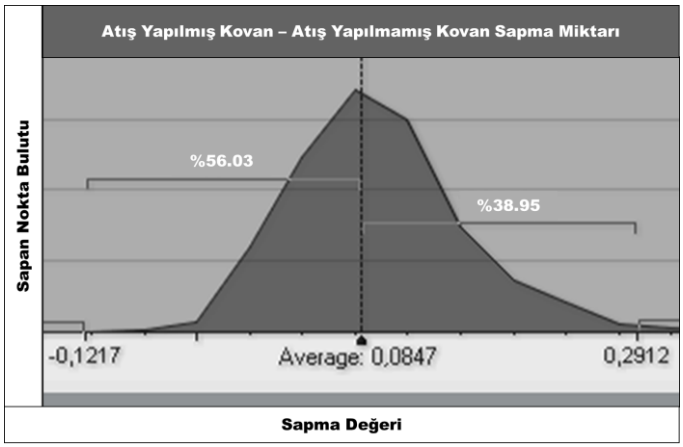


Şekil 22. 2 Boyutlu Sapma Analizi

Çalışmada atış yapılmış kovanın, atış yapılmamış kovandan ne kadar saptığı incelenmiştir ve sonuçlar analitik model ile karşılaştırılmıştır. İstatistiksel sapma miktarı çıkarılmıştır.



Şekil 23. 3 Boyutlu Bölgesel Analiz Sonuçları



Şekil 24. İstatistiksel Olarak Ortalama Sapma Değeri

6. ANALİZ SONUÇLARI

Elde edilen verilerde, genleşmenin en fazla kovanın omuz kısmında gerçekleştiği gözlemlenmiştir. Bu durum, kovanın çekirdek yönü tarafından sızdırmazlığın sağlanması için beklenen bir durumdur. Kovanın arka kısmında ise yine orta kısmına kıyasla daha fazla deformasyon gözlemlenmiştir. Burada kovan süren taşıyıcı mekanizmanın asimetrik yapısının etkisi olduğu değerlendirilmektedir. Tarama sonucunda ortalama kalıcı deformasyon miktarı 0.087 mm'dir. Hesaplama sonucunda ise bu değer 0.083 mm olarak gelmektedir. İncelenen kesitte hesaplama sonucu ve ölçüm sonucunun yakın değerlerde olduğu gözlemlenmiştir. Atış yapılmış kovanda bir miktar sertleşme gözükmektedir.

7. SONUÇ VE TARTIŞMA

Bu çalışmada 30 mm x 173 kalibre mühimmat için atım yatağı tasarım parametreleri incelenmiştir. Çalışmada, standart ölçüsü bulunmayan, elde edilemeyen farklı tip mühimmatlara göre atım yatağının çıkarılması için bir yöntem ortaya konulmuştur. Mühimmatın kovan ölçüleri belirlenmiş, kovan bölgelere ayrılmış, bölgelere göre mühimmatın mekanik özellikleri belirlenmiştir. Daha sonra namlu malzemesi belirlenmiş, mühimmat-atım yatağı arasındaki etkileşim incelenmiştir.

Tasarlanan namlunun iç balistik analizi yapılmış, iç balistik analizi için bilgisayar kodu yazılmıştır. Çalışma basıncına göre atım yatağı tasarımı yapılmıştır. Kovan-atım yatağı arasındaki ölçülen ortalama boşluk değeri için kovanın ortalama ölçüsünü temsil eden bir bölgedeki kesit kullanılmıştır. Atış yapılmış kovan ve atış yapılmamış kovanın ölçüm sonuçları ile hesaplanan sonuçlar kıyaslanmıştır.

Yapılan çalışma, sonlu elemanlar yöntemi ile analiz edilebilir ve analiz sonuçları elde edilen değerlerle kıyaslanabilir. Atım yatağı-kovan arasındaki ilişki ve teori ortaya çıkartıldıktan sonra ikinci aşama olarak, kovan-mekanizma ve atım yatağı-namlu ilişkileri incelenebilir. Tasarlanacak atım yatağı sayesinde dış cidarı daha hafif, geri tepmesi daha az, optimize edilmiş güvenilir silahlar ortaya çıkacaktır. Tüm veriler birleştirildiğinde hesaplamalar paket program haline getirilip, numerik çözümlerle optimizasyon çalışmaları yapılabilir.

TEŞEKKÜR

Yazarlar, çalışmaya vermiş oldukları kıymetli desteklerinden dolayı Aselsan Konya Silah Sistemleri'ne, Mehmet Çağlar ORAKCI ve İsa EROL'a en içten ve samimi teşekkürlerini sunarlar.

KAYNAKÇA

1. Zhong, J.,Xia, W. and Ren, J., (2018), "Theoretical Calculation and Research on the Strength of a Artillery Barrel", ICEESD 2018, Advances in Engineering Research, volume 163.
2. https://gununiversity.com/barrel-rifling-101 - (Erişim: 30.08.2022)
3. Zhao, H., Xie, J., Li, Z., Zhang, H., (2014), "Experiment and Simulation of Launching Process of a Small-Diameter Steel Cartridge Case", Defence Technology 10, 349-353.
4. Susantez, Ç., (2020), "Vallier-Heydenreich Metodu ile Silahların Namlu İç Balistiğinin İncelenmesi", Savunma Bilimleri Dergisi, 19(1): 73-94.
5. Havron, L., (1989), "Finite Element Analysis of 30-mm Cartridge Case", ARDEC, Report AD-A214 396.
6. Dönmez, G., (2003), "Zincir Çeliklerinin Soğuk Çekme Oranına Bağlı Olarak Deformasyon Davranışlarının Belirlenmesi", Yüksek Lisans Tezi, İstanbul Teknik Üniversitesi Fen Bilimleri Enstitüsü
7. Cronemberger, P.O., Junior Lima,E.P., Gois, J.A.M. and Caldeir, A.B., (2014), "Theoretical and Experimental Study of The Interior Ballistics of a Rifle 7.62", EngenheriaTermica (Thermal Engineering), volume 13, No 2, p20-27.
8. Akçay, M., (2016), "Internal and Transitional Ballistic Solution for Spherical and Perforated Propellants and Verification with Experimental Results", Journal of Thermal Science and Technology, 37, 1, 35-44.

9. Ugural, C.A., Fenster, K.S., (2019) “Advanced Mechanics of Materials and Applied Elasticity”, 6th ed., Pearson
10. Budynas, R. G., (1999), “Advanced Strength and Applied Stress Analysis”, 2nd ed., McGraw-Hill
11. Boresi, A. P., Schmidt, R. J., and Sidebottom, O. M., (1993), “Advanced Mechanics of Materials”, 5th ed., John Wiley & Sons
12. Beer, F. P., Johnston, E. R., and DeWolf, J. T., (2016), “Mechanics of Materials”, 4th ed., McGraw-Hill
13. Öztürk, Y., (1972), “Analysis of Axisymmetrically Loaded Cylindrical and Spherical Pressure Vessels for Various Loading Conditions”, Msc Thesis, Naval Postgraduate School
14. Carlucci, D.E., Jacobson S.S., (2018), “Ballistics Theory and Design of Guns and Ammunition”, 3rd ed., CRC Press
15. Akçay, M., (2010), “Balistik”, 1. Baskı, Kazmaz Matbaacılık
16. Gündüzer, O., (2011), “Namlu Cidarı Boyutlandırılmasına İç Balistik Davranışın Etkisi”, Yüksek Lisans Tezi, Gazi Üniversitesi Fen Bilimleri Enstitüsü
17. Baer, P.G. and Frankle, J.M., (1962), “The Simulation of Interior ballistic Performance of Guns by Digital Computers”, Ballistic Research Laboratory
18. Anderson, R.D andFickie, K.D., (1987) “IBHVG2 User’s Guide”
19. Öztürk, A.R., (1984)“İç Balistik”, Makina ve Kimya Endüstrisi Kurumu Genel Müdürlüğü Özel Yayınları
20. Öztürk, A.R., (1988) “Silah Mekaniği ve Mermilerin Hedef Üzerindeki Etkileri”, Makina ve Kimya Endüstrisi Kurumu Genel Müdürlüğü Özel Yayınları.
21. Değirmenci, E., Evci, C., Işık, H., Macar, M., Yılmaz, N., Dirikolu, M.H. ve Çelik, V. (2016). “Thermo-Mechanical Analysis of Double Base Propellant Combustion in a Barrel”, Applied Thermal Engineering, 102, 1287-1299.
22. Stanag 4367, (2000), “Thermodynamic Interior Ballistic Model with Global Parameters”, North Atlantic Treaty Organization, Edition 2.
23. Stanag 4624, (2012), “30 MM x 173 Ammunition”, North Atlantic Treaty Organization, Edition 1.
24. DIN EN ISO 18265, (2004), “Metallic Material – Conversion of Hardness Values”, Deutsches Institut für Normung
25. AEP 97, (2020), “Multi-Calibre Manual of Proof and Inspection (M-CMOPI) for NATO Small Arms Ammunition”, Edition A version 1.
26. Pyhton 3.10.5 Documentation
27. Arrow Tech. Associates, “Projectile Design and Analysis System” (PRODAS V3) Documentation

DÜZLEMSEL BEŞ ÇUBUK MEKANİZMASININ OPTİMİZASYON SONUCUNDA ELDE EDİLEN PARAMETRELERİN DİZAYN EDİLEBİLİRLİĞİNİN İNCELENMESİ

Deniz KAVALA ŞEN, *d.kavalasen@gmail.com* Bursa Uludağ Üniversitesi, 16059, Bursa

Prof. Dr. Osman KOPMAZ, *okopmaz@uludag.edu.tr* Bursa Uludağ Üniversitesi, 16059, Bursa

ÖZET

Düzlemsel beş çubuk mekanizmaları iki serbestlik dereceli paralel manipülatörler olup sanayide kullanılagelmektedir. Böyle bir mekanizmada iş organın(örneğin lazer kesim kafası) bağlı olduğu noktaya dairesel bir yörünge çizdirilmesi durumunda ortaya çıkan sarsma kuvvetleri ve momentlerinin en aza indirgenmesi konusu ele alınmıştır. Bu amaçla parçacık sürüsü optimizasyonu kullanılmıştır. Burada tasarım parametrelerinin tamamı optimizasyon sürecine tabi tutulmuştur. Uzuv kütleleri ve atalet momentleri bağımsız parametreler olarak hesaba katıldığından optimizasyon sonucu elde edilen parametre değerlerine göre mekanizmanın fiziki olarak dizayn edilebilirliği, bir CAD programıyla kontrol edilmesi önem arz etmektedir. Önceki çalışmalardan farklı olarak bu bildiride fiziki gerçeklenebilinirlik konusu ayrıntılı olarak ele alınmıştır.

Anahtar Kelimeler: Sarsma kuvveti, Sarsma momenti, Dengeleme, Optimizasyon, 3D Dizayn

ABSTRACT

Planar five-bar mechanisms are parallel manipulators with two degrees of freedom used in industry. In such a mechanism, the issue of minimizing the shaking forces and moments that occur when a circular trajectory is drawn at the point of attachment of the workpiece (e.g., laser cutting head) is discussed. For this purpose, particle swarm optimization was used. Here, all design parameters have been optimized. Since the bar masses and moments of inertia are considered independent parameters, it is essential to check the physical design of the mechanism according to the parameter values obtained as a result of optimization and to check it with a CAD program. Unlike previous studies, this article discusses the issue of physical realizability in detail.

Keywords: Shaking force, Shaking moment, Balancing, Optimization, 3D Design

1. GİRİŞ

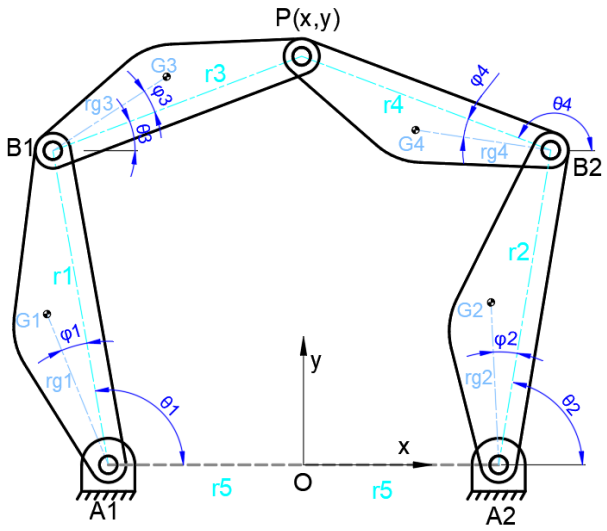
Beş çubuk mekanizmaları, genellikle endüstri alanında yaygın olarak kullanılmakta olup, özellikle pozisyonlama için kullanılmaktadır. Bu mekanizmalar, aktüatörlerin döner veya doğrusal olmasına bağlı olarak çeşitleri bulunmaktadır.(Cervantes-Saâ Nchez & Rendoâ N-Saâ Nchez, 1999)

Bu mekanizmalar tasarlanırken, kinematik ve dinamik konularıyla ilgili birçok problem çözülmesi gerekir. Kinematik konular, çalışma alanının belirlenmesi (Le et al., 2017; Liu et al., 2006) ve yörünge planlaması (Abdelhay & Zakriti, 2019; Oarcea et al., 2021)iken, dinamik konular ise aktüatörlerin torklarının belirlenmesi ile sarsma kuvveti ve momentinin(Alici et al., n.d.; Nehemiah et al., 2012) bulunmasıdır. Bu mekanizmalarda çeşitli optimizasyon yöntemleri uygulanarak tasarım parametrelerinin bulunması ile ilgili bir çok çalışma bulunmaktadır.(Campos et al., 2010; Ganesh & Rao, 2018; Giberti et al., 2013; Mundo et al., 2009; Stan et al., 2007; Zhou & Cheung, 2001)

Bu çalışma, özellikle diğer çalışmalara göre üç boyutlu modelleme yapılarak bulunan tasarım parametrelerinin uygun olup olmadığı tespiti sağlanmıştır. Bu çalışmada, düzlemsel beş çubuk mekanizmasının sarsma kuvvetinin ve momentinin minimize edilmesini sağlayacak bir optimizasyon problemi çözümü yapılmıştır. Bu optimizasyon problemi sonucunda elde edilen tasarım parametrelerini sağlayacak şekilde uzuvların üç boyutlu tasarım yapılmıştır.

2. DÜZLEMSEL BEŞ ÇUBUK MEKANİZMASI

Kapalı devre mekanizmaları, yüksek hızlarda ve hassasiyet istenen işlerde yaygın olarak kullanılmaktadır. Düzlemsel beş çubuk mekanizması, iki serbestlik derecesine sahip kapalı kinematik zincir kullanılarak elde edilir.



Şekil 1 Düzlemsel Beş Çubuk Mekanizması.

Mekanizmanın çevrim denklemi aşağıdaki gibidir.

$$\overrightarrow{OP} = \overrightarrow{OA_1} + \overrightarrow{A_1B_1} + \overrightarrow{B_1P} = \overrightarrow{OA_2} + \overrightarrow{A_2B_2} + \overrightarrow{B_2P} \quad (1)$$

$$x + iy = r_5 e^{i\pi} + r_1 e^{i\theta_1} + r_3 e^{i\theta_3} = r_5 e^{0} + r_2 e^{i\theta_2} + r_4 e^{i\theta_4} \quad (2)$$

2.2. Sarsma Kuvveti Dengelenmesi ve Sarsma Momentinin Minimize Edilmesi

Sarsma kuvveti, sistemin atalet kuvvetlerinin bileşkesi olup, ayrıca sistemin durağan O noktasına göre lineer momentumunun zaman göre değişimi olarak da ifade edilebilir.

$$\overrightarrow{F_s} = -\sum_{i=1}^{4} M_i \ddot{r}_{Gi} = -\frac{d\vec{L}_o}{dt} \quad (3)$$

Sarsma momenti ise sistemin durağan O noktasına göre açısal momentumunun zamana göre değişimidir.

$$\overrightarrow{M_s} = -\sum_{i=1}^{4} (r_{Gi}\, x\, M_i \ddot{r}_{Gi}) + I_{Gi}\, \ddot{\theta}_{Gi} = -\frac{d\vec{H}_o}{dt} \quad (4)$$

2.2.1 Lineer Momentum

Lineer momentum denklemi aşağıdaki gibi olup, bu değer sabit olduğunda sarsma kuvveti sıfırlanırsa kütle dengelenmesi yapılmış olur.

$$\begin{aligned}\vec{L}_o = {} & (i\dot{\theta}_1)e^{i\theta_1}\left(m_1 r_{G1} e^{i\varphi_1} + m_3 r_1 + m_4 \frac{r_1}{r_4} r_{G4} e^{i\varphi_4}\right) \\ & + (i\dot{\theta}_2)e^{i\theta_2}\left(m_2 r_{G2} e^{i\varphi_2} + m_4 r_2 - m_4 \frac{r_2}{r_4} r_{G4} e^{i\varphi_4}\right) \\ & + (i\dot{\theta}_3)e^{i\theta_3}\left(m_3 r_{G3} e^{i\varphi_3} + m_4 \frac{r_3}{r_4} r_{G4} e^{i\varphi_4}\right)\end{aligned} \quad (5)$$

2.2.2. Açısal Momentum

Açısal momentum, denklem (6) deki gibi ifade edilir.

$$\begin{aligned}\vec{H}_o = {} & \dot{\theta}_1[I_{G1} + m_1 {r_{G1}}^2 + m_3 {r_1}^2 \\ & + m_3 r_1 r_{G3} \cos(\theta_1 - \theta_3 - \varphi_3) - m_3 r_1 r_5 \cos\theta_1 - m_1 r_{G1} r_5 \cos(\theta_1 + \varphi_1)] \\ & + \dot{\theta}_3[I_{G3} + m_3 {r_{G3}}^2 + m_3 r_1 r_{G3} \cos(\theta_1 - \theta_3 - \varphi_3) - m_3 r_{G3} r_5 \cos(\theta_3 + \varphi_3)] \\ & + \dot{\theta}_2[I_{G2} + m_2 {r_{G2}}^2 + m_4 {r_2}^2 \\ & + m_4 r_2 r_{G4} \cos(\theta_2 - \theta_4 - \varphi_4) + m_4 r_2 r_5 \cos\theta_2 + m_2 r_{G2} r_5 \cos(\theta_2 + \varphi_2)] \\ & + \dot{\theta}_4[I_{G4} + m_4 {r_{G4}}^2 + m_4 r_2 r_{G4} \cos(\theta_2 - \theta_4 - \varphi_4) + m_4 r_{G4} r_5 \cos(\theta_4 + \varphi_4)]\end{aligned} \quad (6)$$

2. OPTİMİZASYON

Bu optimizasyon problemi; sarsma kuvvetinin ve sarsma momentini minimuma indirgeyecek düzlemsel beş çubuk mekanizmasının yeniden boyutlandırılması için gereken parametrelerin bulunması olarak tanımlanır.

Amaç fonksiyonu:

$$F = \sqrt{\sum \left\| \overrightarrow{F_s} \right\|^2 + \sum \left\| \overrightarrow{M_s} \right\|^2} \tag{7}$$

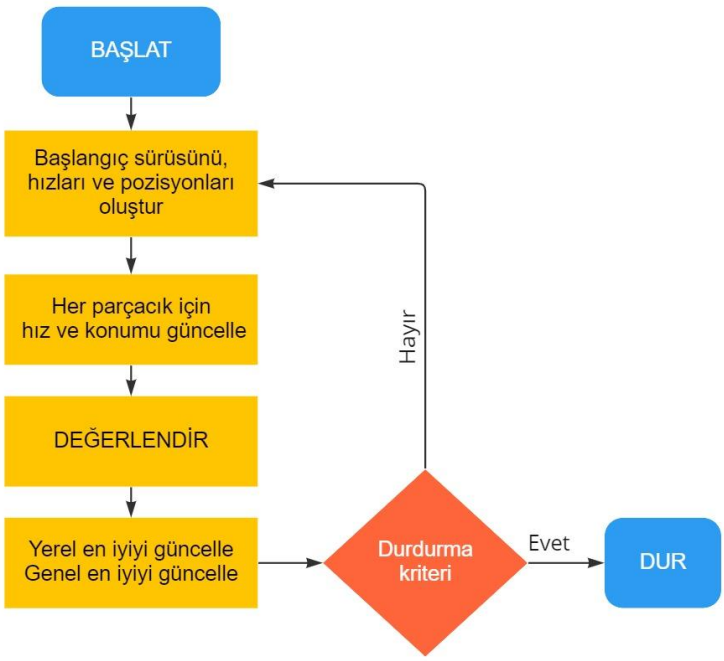
Dizayn değişkenleri:

$$[r_{g1} \quad r_{g2} \quad r_{g3} \quad r_{g4} \quad m_1 \quad m_2 \quad m_3 \quad m_4 \quad I_{g_1} \quad I_{g_2} \quad I_{g_3} \quad I_{g_4} \quad \alpha_1 \quad \alpha_2 \quad \alpha_3 \quad \alpha_4 \quad r_1 \quad r_2 \quad r_3 \quad r_4 \quad r_5] \tag{8}$$

Kısıtlar:

$$\begin{aligned} &0 \le r_{gi} && \text{i=1...4} \\ &0.7m_i \le m_i \le 1.3m_i && \text{i=1...4} \\ &0.7I_{gi} \le I_{gi} \le 1.3I_{gi} && \text{i=1...4} \\ &0 \le \varphi_i \le 2\pi && \text{i=1...4} \\ &0.9r_i \le r_i \le 1.1r_i && \text{i=1...5} \end{aligned} \tag{9}$$

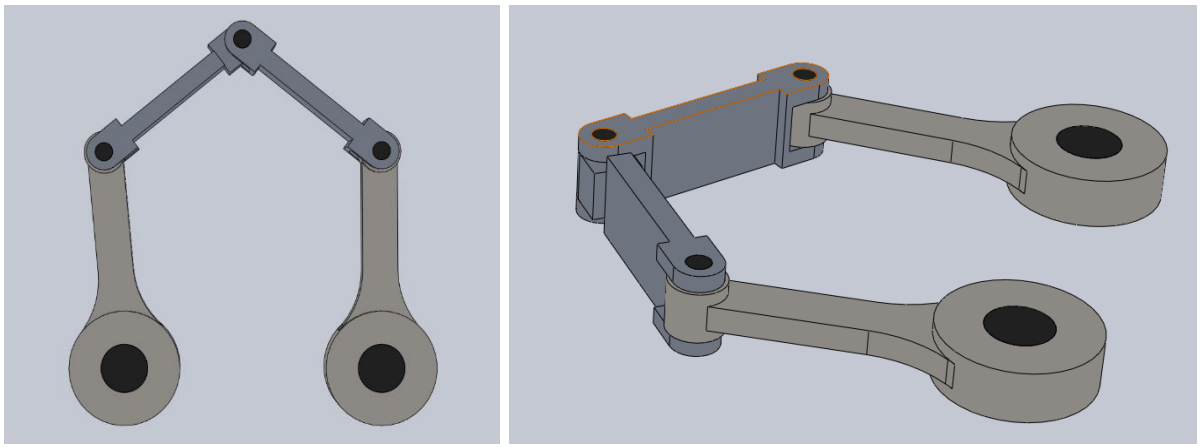
Bu problemde; Parçacık sürüsü optimizasyon (PSO) yöntemi uygulanmıştır. PSO algoritmasının akış diyagramı Şekil 2'de gösterilmiştir.



Şekil 2 PSO Akış diyagramı.

3.1.Optimizasyon Öncesi Üç Boyutlu Tasarım

Düzlemsel beş çubuk mekanizmasının ilk tasarımı, takip etmesi istenen en büyük yörüngenin belirlenmesi, bu mekanizmanın bu yörüngeyi takibi sırasında çalışma bölgesinde yer alması ve tekil noktalar oluşturmaması sağlanarak yapılmıştır. Ayrıca mekanizmanın uç işlevcisinin istenen hız profilinde çalıştırılması sağlanmıştır.

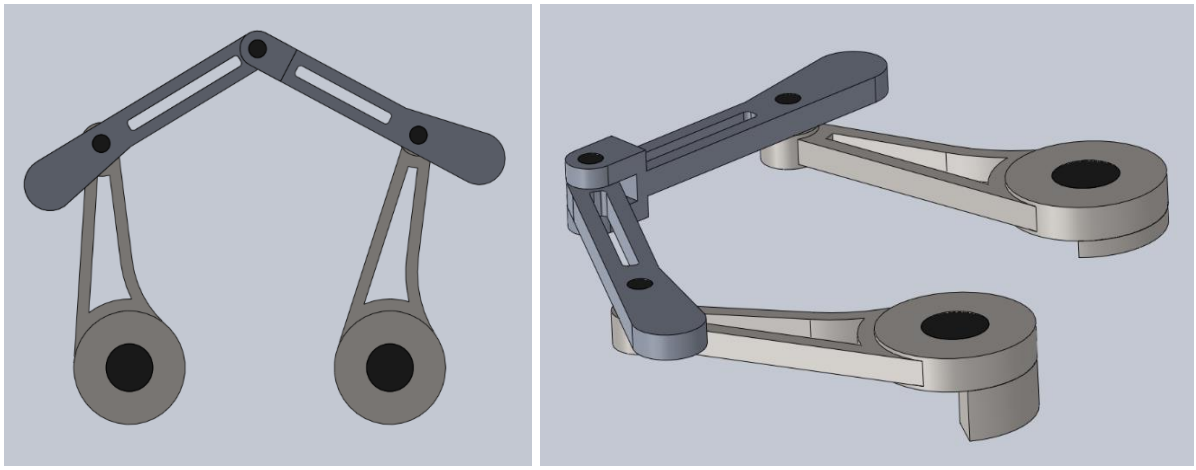


Şekil 3 İlk Tasarım.

3.2. Optimizasyon Sonrası Elde Edilen Parametreler ve En Uygun Üç Boyutlu Tasarım

Optimizasyon sonucu elde edilen parametrelerin üç boyutlu tasarım ile elde edilmesi zor bir tasarım problemidir. Burada, ağırlık merkezinin mafsala olan uzaklığı, ağırlık merkezinin mafsala göre açısı, atalet momenti ve kütlesinin hepsinin aynı anda üç boyutlu tasarım aracılığıyla bulunması istenmiştir.

Yapılan tasarımlarda öncelikli olarak ağırlık merkezinin konumu ve kütlesi dikkate alınmıştır. Daha sonrasında atalet momenti ile ilgili değişimler göz önüne alınarak işlemler tekrarlanmıştır. Fakat optimizasyon sonucundaki parametrelere yüzde yüz yaklaşılmamıştır.



Şekil 4 Optimizasyon Sonrası Tasarım.

3. SAYISAL SONUÇLAR

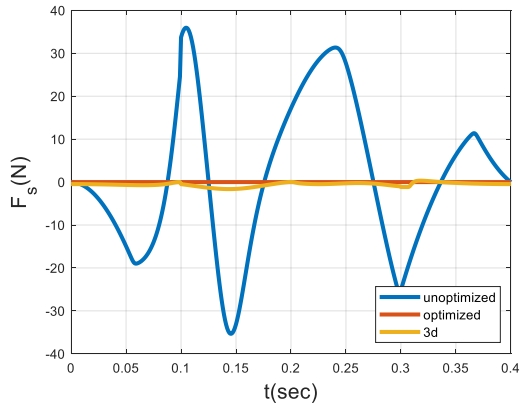
Tasarım parametreleri; ilk koşul, optimizasyon sonucu ve üç boyutlu tasarım ile elde edilen olarak aşağıdaki kıyaslama tablosunda yer almaktadır.

Tablo 1 Tasarım Parametrelerinin Kıyaslaması.

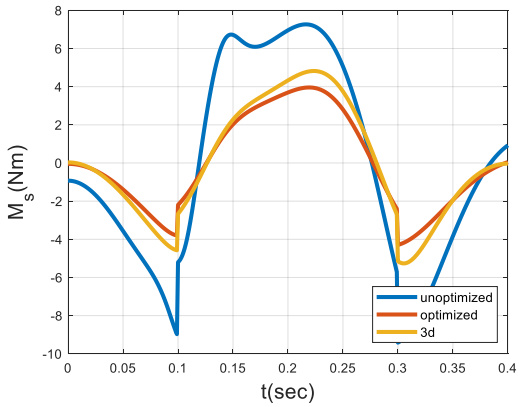
Uzuv i	m_i (kg)			r_i (m)			I_{gi} (kgm^2)		
	İlk	Opt.	3D	İlk	Opt.	3D	İlk	Opt.	3D
1	1.871	2.143	2.1	0.180	0.189	0.189	0.0093	0.0075	0.011
2	1.871	1.588	1.59	0.180	0.196	0.196	0.0093	0.0075	0.010
3	0.326	0.261	0.26	0.150	0.165	0.165	0.0008	0.0006	0.0009
4	0.327	0.262	0.30	0.150	0.164	0.164	0.0008	0.0006	0.001
5	-	-	-	0.110	0.111	0.111	-	-	-

Uzuv i	r_{gi} (m)			φ_i (rad)		
	İlk	Opt.	3D	İlk	Opt.	3D
1	0.077	0.021	0.022	0	3.138	3.12
2	0.077	0.034	0.035	0	3.144	3.13
3	0.075	0.011	0.02	0	0.040	0.03
4	0.080	0.010	0.037	0	3.182	3.17
5	-	-	-	-	-	-

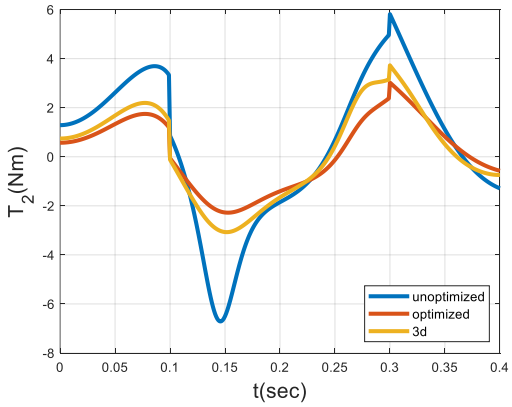
Yapılan çalışmalar, bir daire yörüngesini takip ederken istenen hız profilinde gerçekleştirilmiştir. İlk tasarım, optimizasyon sonucu ve optimizasyon sonrası tasarım ile elde edilen parametreler kullanılarak sarsma kuvveti, sarsma momenti ve torklar aşağıdaki grafiklerde gösterilmiştir.



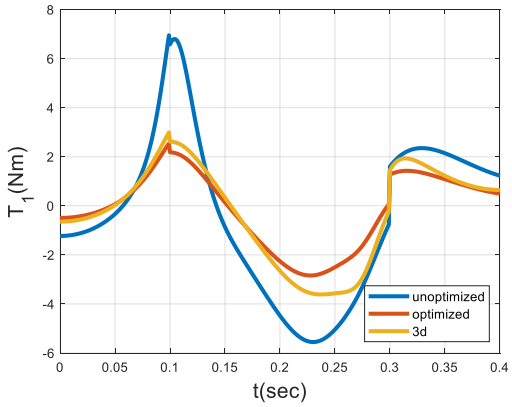
a)



b)



c)



d)

Şekil 4 Optimizasyon Verileri ve Optimizasyon Sonrası Tasarım Verileri ile Elde Edilen Sarsma Kuvveti (a), Sarsma Momenti (b), Birinci Motor Torku (c), İkinci Motor Torku(d) Değişimleri.

5.SONUÇ

Bu çalışmada, optimizasyonla sarsma kuvvetinin ve sarsma momentinin minimize edildiği tasarım parametreleri bulunmuştur. Uzuvların üç boyutlu tasarımı, öncelikli olarak ağırlık merkezinin konumu ve parça kütlesi değerini sağlayacak şekilde yapılmış ve atalet moment değeri kontrol edilerek tasarım onaylanmıştır. Burada özellikle tasarım parametrelerine göre tasarımın en kadar zor yapıldığı tespit edilmiştir. Bununla birlikte, en iyi optimizasyon sonucunun, üç boyutlu tasarımı yapılmadan dizayn edilebilir olmadığı bulunmuştur.

KAYNAKÇA

1. **Abdelhay, S., & Zakriti, A. (2019),** "Modeling of a Quadcopter Trajectory Tracking System Using PID Controller", Procedia Manufacturing, 32, 564–571.

2. **Alici, G., Shirinzadeh, B. (2003),** "Optimum force balancing with mass distribution and a single elastic element for a five-bar parallel manipulator", Proceedings of the 2003 IEEE International Conference on Robotics & Automation

3. **Campos, L., Bourbonnais, F., Bonev, I. A., & Bigras, P. (2010),** "Development of a five -bar parallel robot with large workspace". Proceedings of the ASME Design Engineering Technical Conference, 2(PARTS A AND B), 917–922.

4. **Cervantes-Saâ Nchez, J. J., & Rendoâ N-Saâ Nchez, J. G. (1999),** "A simplified approach

for obtaining the workspace of a class of 2-dof planar parallel manipulators", Mechanism and Machine Theory 34, 1057-1073

5. **Ganesh, S. S., & Rao, A. B. K. (2018),** "Kinematic and Dynamic Optimization of a 2-DOF Parallel Kinematic Mechanism", Procedia Computer Science, 133, 576–584.

6. **Giberti, H., Cinquemani, S., & Ambrosetti, S. (2013),** "5R 2dof parallel kinematic manipulator - A multidisciplinary test case in mechatronics", Mechatronics, 23(8), 949–959.

7. **Le, T., Kang, H., , Quang, D. V., (2013),** "A method for optimal kinematic design of five-bar planar parallel manipulators", 2013 International Conference on Control, Automation and Information Sciences (ICCAIS)

8. **Liu, X. J., Wang, J., & Pritschow, G. (2006)**, "Kinematics, singularity and workspace of planar 5R symmetrical parallel mechanisms", Mechanism and Machine Theory, 41(2), 145 169.

9. **Mundo, D., Gatti, G., & Dooner, D. B. (2009),** "Optimized five-bar linkages with non-circular gears for exact path generation", Mechanism and Machine Theory, 44(4), 751–760.

10. **Nehemiah, P., Sundara Siva Rao, B. S. K., & Ramji, K. (2012), "**Shaking force and shaking moment balancing of planar mechanisms with high degree of complexity", Jordan Journal of Mechanical and Industrial Engineering, 6(1), 17–24.

11. **Oarcea, A., Cobilean, V., & Stan, S. D. (2021)**, "Trajectory planning of a 3-RRRRR planar parallel robot", Proceedings of 2021 9th International Conference on Modern Power Systems, MPS 2021.

12. **Stan, S. D., Mătieş, V., & Bălan, R. (2007), "**Optimization of workspace of a 2 DOF parallel minirobot using genetic algorithms and simulated annealing optimization methods", Proceedings of IEEE Workshop on Advanced Robotics and Its Social Impacts, ARSO, 1108 1113.

13. **Zhou, H., & Cheung, E. H. M. (2001),** "Analysis and optimal synthesis of hybrid five-bar linkages", Mechatronics, 11(3), 283–300.

EKLER

Ek-A :(5) nolu Lineer Momentum Denkleminin Çıkarılması;

Uzuvların ağırlık merkezlerinin konum vektörleri:

$$\begin{aligned}\overrightarrow{r_{G1}} &= r_5 e^{i\pi} + r_{G1} e^{i(\theta_1+\varphi_1)}\\ \overrightarrow{r_{G3}} &= r_5 e^{i\pi} + r_1 e^{i(\theta_1)} + r_{G3} e^{i(\theta_3+\varphi_3)}\\ \overrightarrow{r_{G2}} &= r_5 e^{i0} + r_{G2} e^{i(\theta_2+\varphi_2)}\\ \overrightarrow{r_{G4}} &= r_5 e^{i0} + r_2 e^{i(\theta_2)} + r_{G4} e^{i(\theta_4+\varphi_4)}\end{aligned} \quad \text{(A-1)}$$

Uzuvların ağırlık merkezlerinin hız vektörleri:

$$\begin{aligned}\overrightarrow{V_{G1}} &= (i\dot{\theta}_1) r_{G1} e^{i\varphi_1}\\ \overrightarrow{V_{G3}} &= (i\dot{\theta}_1) r_1 e^{i\varphi_1} + (i\dot{\theta}_3) r_3 e^{\varphi_3}\\ \overrightarrow{V_{G2}} &= (i\dot{\theta}_2) r_{G2} e^{\varphi_2}\\ \overrightarrow{V_{G4}} &= (i\dot{\theta}_2) r_{G2} e^{\varphi_2} + (i\dot{\theta}_4) r_{G4} e^{i\varphi_4}\end{aligned} \quad \text{(A-2)}$$

(2) nolu çevrim denkleminden

$$e^{i\theta_4} = \frac{-2r_5 + r_1 e^{\theta_1} + r_3 e^{\theta_3} - r_2 e^{\theta_2}}{r_4} \quad \text{(A-3)}$$

olarak bulunur. Her iki tarafın zamana göre türevi aşağıdaki gibidir.

$$(i\dot{\theta}_4) e^{i\theta_4} = \frac{(i\dot{\theta}_1) r_1 e^{\theta_1} + (i\dot{\theta}_3) r_3 e^{\theta_3} - (i\dot{\theta}_2) r_2 e^{\theta_2}}{r_4} \quad \text{(A-4)}$$

Buna göre mekanizmanın toplam lineer momentum;

$$\overrightarrow{L_0} = -\sum_{i=1}^{4} M_i \overrightarrow{\dot{r}_{Gi}} \quad \text{(A-5)}$$

Lineer momentumun açık ifadesi şöyledir.

$$\begin{aligned}\overrightarrow{L_0} = \Big(& m_1 r_{G1}\dot{\theta}_1 cos(\theta_1+\varphi_1) + m_3 r_1 \dot{\theta}_1 cos\theta_1 + m_3 r_{G3}\dot{\theta}_3 cos(\theta_3+\varphi_3)\\ & + m_2 r_{G2}\dot{\theta}_2 cos(\theta_2+\varphi_2) + m_4 r_2 \dot{\theta}_2 cos\theta_2 + m_4 \frac{r_1}{r_4} r_{G4}\dot{\theta}_1 cos(\theta_1+\varphi_4)\\ & - m_4 \frac{r_2}{r_4} r_{G4}\dot{\theta}_2 cos(\theta_2+\varphi_4) + m_4 \frac{r_3}{r_4} r_{G4}\dot{\theta}_3 cos(\theta_3+\varphi_4)\Big)\vec{\imath}\\ & + \Big(-m_1 r_{G1}\dot{\theta}_1 sin(\theta_1+\varphi_1) - m_3 r_1 \dot{\theta}_1 sin\theta_1 - m_3 r_{G3}\dot{\theta}_3 sin(\theta_3+\varphi_3)\\ & - m_2 r_{G2}\dot{\theta}_2 sin(\theta_2+\varphi_2) - m_4 r_2 \dot{\theta}_2 sin\theta_2 - m_4 \frac{r_1}{r_4} r_{G4}\dot{\theta}_1 sin(\theta_1+\varphi_4)\\ & + m_4 \frac{r_2}{r_4} r_{G4}\dot{\theta}_2 sin(\theta_2+\varphi_4) - m_4 \frac{r_3}{r_4} r_{G4}\dot{\theta}_3 sin(\theta_3+\varphi_4)\Big)\vec{\jmath}\end{aligned} \quad \text{(A-6)}$$

Ek-B :(6) nolu açısal momentum denkleminin çıkarılması:

$$\vec{H}_o = \vec{k}H_{oz} = \overrightarrow{r_{G1}} x m_1 \overrightarrow{V_{G1}} + \overrightarrow{r_{G3}} x m_3 \overrightarrow{V_{G3}} + \overrightarrow{r_{G2}} x m_2 \overrightarrow{V_{G2}} + \overrightarrow{r_{G4}} x m_4 \overrightarrow{V_{G4}} + \overrightarrow{k}(I_{G1}\dot{\theta}_1 + I_{G3}\dot{\theta}_3 + I_{G2}\dot{\theta}_2 + I_{G4}\dot{\theta}_4) \quad \text{(B-1)}$$

Her bir vektörel çarpım aşağıdaki gibi gösterilir.

$$\begin{aligned}\overrightarrow{r_{G1}} x m_1 \overrightarrow{V_{G1}} &= [(-r_5 + r_{G1}\cos(\theta_1 + \varphi_1))\vec{\imath} + r_{G1}\sin(\theta_1 + \varphi_1)\vec{\jmath}] x m_1 \left[\left(-r_{G1}\dot{\theta}_1 \sin(\theta_1 + \varphi_1)\right)\vec{\imath} + \left(r_{G1}\dot{\theta}_1 \cos(\theta_1 + \varphi_1)\right)\vec{\jmath}\right] \\ &= (-m_1 r_{G1} r_5 \dot{\theta}_1 \cos(\theta_1 + \varphi_1) + m_1 {r_{G1}}^2 \dot{\theta}_1)\vec{k}\end{aligned} \quad \text{(B-2)}$$

$$\begin{aligned}\overrightarrow{r_{G3}} x m_3 \overrightarrow{V_{G3}} = [&(-r_5 + r_1\cos\theta_1 + r_{G3}\cos(\theta_3 + \varphi_3))\vec{\imath} \\ &+ (r_1 \sin\theta_1 + r_{G3}\sin(\theta_3 + \varphi_3))\vec{\jmath}] x\, m_3 \left[\left(-r_1\dot{\theta}_1 \sin\theta_1 - r_{G3}\dot{\theta}_3(\theta_3 + \varphi_3)\right)\vec{\imath}\right. \\ &\left. + \left(r_1\dot{\theta}_1 \cos\theta_1 + r_{G3}\dot{\theta}_3\cos(\theta_3 + \varphi_3)\right)\vec{\jmath}\right] \\ &= (-m_3 r_1 r_5 \dot{\theta}_1 \cos\theta_1 - m_3 r_{G3} r_5 \dot{\theta}_3 \cos(\theta_3 + \varphi_3) + m_3 {r_1}^2 \dot{\theta}_1 + m_3 {r_{G3}}^2 \dot{\theta}_3 \\ &+ m_3 r_1 r_{G3}\dot{\theta}_1 \cos(\theta_1 - \theta_3 - \varphi_3) + m_3 r_1 r_{G3}\dot{\theta}_3 \cos(\theta_1 - \theta_3 - \varphi_3))\vec{k}\end{aligned} \quad \text{(B-3)}$$

$$\overrightarrow{r_{G2}} x m_2 \overrightarrow{V_{G2}} = (m_2 r_{G2} r_5 \dot{\theta}_2 \cos(\theta_2 + \varphi_2) + m_2 {r_{G2}}^2 \dot{\theta}_2)\vec{k} \quad \text{(B-4)}$$

$$\begin{aligned}\overrightarrow{r_{G4}} x m_4 \overrightarrow{V_{G4}} = (&m_4 r_2 r_5 \dot{\theta}_2 \cos\theta_2 + m_4 r_{G4} r_5 \dot{\theta}_4 \cos(\theta_4 + \varphi_4) + m_4 {r_2}^2 \dot{\theta}_2 + m_4 {r_{G4}}^2 \dot{\theta}_4 \\ &+ m_4 r_2 r_{G4}\dot{\theta}_2 \cos(\theta_2 - \theta_4 - \varphi_4) + m_4 r_2 r_{G4}\dot{\theta}_4 \cos(\theta_2 - \theta_4 - \varphi_4))\vec{k}\end{aligned} \quad \text{(B-5)}$$

Açısal momentum, B-6 denklemindeki gibi düzenlenir.

$$\begin{aligned}\vec{H}_o = \dot{\theta}_1[&I_{G1} + m_1 {r_{G1}}^2 + m_3 {r_1}^2 \\ &+ m_3 r_1 r_{G3}\cos(\theta_1 - \theta_3 - \varphi_3) - m_3 r_1 r_5 \cos\theta_1 - m_1 r_{G1} r_5 \cos(\theta_1 + \varphi_1)]\vec{k} \\ &+ \dot{\theta}_3[I_{G3} + m_3 {r_{G3}}^2 \\ &+ m_3 r_1 r_{G3}\cos(\theta_1 - \theta_3 - \varphi_3) - m_3 r_{G3} r_5 \cos(\theta_3 + \varphi_3)]\vec{k} \\ &+ \dot{\theta}_2[I_{G2} + m_2 {r_{G2}}^2 + m_4 {r_2}^2 \\ &+ m_4 r_2 r_{G4}\cos(\theta_2 - \theta_4 - \varphi_4) + m_4 r_2 r_5 \cos\theta_2 + m_2 r_{G2} r_5 \cos(\theta_2 + \varphi_2)]\vec{k} \\ &+ \dot{\theta}_4[I_{G4} + m_4 {r_{G4}}^2 \\ &+ m_4 r_2 r_{G4}\cos(\theta_2 - \theta_4 - \varphi_4) + m_4 r_{G4} r_5 \cos(\theta_4 + \varphi_4)]\vec{k}\end{aligned} \quad \text{(B-6)}$$

İNSANSI YÜZ MİMİKLERİNE SAHİP BİR ANİMATRONİK ROBOT SURAT TASARIMI VE İMALATI

Furkan TÜTÜNCÜ, 501910053@*ogr.uludag.edu.tr* Uludağ Üniversitesi, 16059, Bursa

M. Cemal ÇAKIR, *cemal@uludag.edu.tr* Uludağ Üniversitesi, 16059, Bursa

ÖZET

Bu çalışmada, günümüzde önemi her geçen gün artan ve üzerine yeni çalışmalar gerçekleştirilen insansı robotlar geliştirmek, insan mimiklerini gerçekçi şekilde simüle edecek mekanizmalar tasarlamak ve bu tasarımları gerçekçi boyutlarda bir araya getirerek insansı bir yapı oluşturmak amaçlanmıştır. Bu bağlamda düşük maliyet hedefi ile üç boyutlu yazıcı ve giriş seviyesi elektronik komponentler ile yüz kaslarını simüle edecek mekanizmalar tasarlanmış ve bunlar hareket ettirilerek yüz mimikleri simüle edilmiştir. Çalışma sonucunda herkes tarafından aynı şekilde algılanabilecek seviyede gerçekçi yüz mimikleri elde edilmiş ve amacı doğrultusunda başarılı bir sonuç elde edilmiştir.. Türkiyede benzer konudaki araştırmalar çok kısıtlı sayıda olduğundan, bu proje öncü proje niteliği taşımaktadır.

Anahtar Kelimeler: İnsansı Robot, Mimik, Animatronik, Duygu, Mekanizma

ABSTRACT

In this study, it is aimed to develop humanoid robots, the importance of which is increasing day by day and on which new studies are carried out, to design mechanisms that will simulate human mimics realistically, and to create a humanoid structure by bringing these designs together in realistic dimensions. In this project, mechanisms to simulate facial muscles were designed with a three-dimensional printer and entry-level electronic components because of the goal of low cost, and facial expressions were simulated by moving them. As a result of the study, realistic facial expressions that can be perceived by everyone in the same way were obtained and a successful result was obtained in line with its purpose. Since there are very limited number of studies on similar subjects in Turkey, this project is a pioneering project.

Keywords: Humanoid Robot, Expressions, Animatronic, Gestures, Mechanism

1. GİRİŞ

İnsansı robotlar, şekil ve görev bakımından insana benzeyen ve gün geçtikçe bu benzerliğin daha da artırıldığı robot türleridir. Bu robotlar insan vücudunun hareket ve becerilerini taklit etmek üzere tasarlanmaktadır.

Bu alanda öncü firmalardan biri olan Hanson Robotics 'in Albert HUBO isimli robotu yürüme, koşma gibi insani hareketleri gerçekleştirirken gerçekçi yüz mimikleri ile insansı robotlar arasında öne çıkmaktadır [Oh, Hanson, Kim, 2006; Hanson Robotics, (web)]

Geçmişten günümüze insansı robot yüz ile ilgili çalışmalar incelendiğinde her bir çalışmanın, çok farklı odak noktaları olduğu görülmektedir. Bu çalışmalardan bazıları, görüntü işleme teknolojisi ile kamera tarafından analiz edilen insan hareketlerini taklit etmek üzere tasarlanan robotlardır [Chen, Liu, Li, Zhang, Cangelosi, 2021]. Kamera, derin öğrenme algoritmalarının çalıştırıldığı bilgisayar yardımıyla karşısındaki insanın hareketlerini algılar ve belirli referans noktaları yardımıyla bir sanal iskelet oluşturur. Bu referans noktalarının kameradaki yer değiştirmelerini analiz eden derin öğrenme yazılımı, aynı koordinat değişikliklerini inceleyerek insansı robota taklit etme yeteneği kazandırır. Buradaki en önemli konu, kameranın referans noktalarını net algılayabilmesi için uygun ışık ve koşullara sahip bir kayıt ortamının gerekliliğidir.

Kimi çalışmalar, robotun kendisinden çok, yüz tanıma teknolojisine yönelik çalışmalardır ve amaçları, robot suratlar üzerinde kullanılabilme amacıdır [Ishihara, Ota, Asada, 2017] Bu ve benzeri çalışmalarda ise amaç, bir önceki çalışmada anlatılan referans noktaları için verimli bölgeleri bulmak ve daha iyi veriler elde etmektir. Daha iyi veri, daha doğru konum bilgisi ve daha başarılı taklit yeteneği demektir.

Çalışmaların bir diğer boyutu ise mekanizma tasarımlarıdır. Yüz kaslarını simüle edebilecek mekanizma ve yöntemler üzerine çalışma yapılmasının amacı, görüntü işleme teknolojisi ile elde edilen verileri simüle edecek robotları geliştirmektir. Bu tip çalışmalarda, iki tip odak noktaları mevcuttur. Bunlardan biri, basit ve büyük hareket grubu üzerinde çalışılan ve örneğin ağız bölgesini yalnızca çene aç-kapa hareketi ile simüle eden çalışmalardır [Rusu, Pirpidel, Biris, 2020; Fitzpatrick, 2010]. Bir diğer çalışma türü ise detaylı mimik hareketlerinin simülasyonu üzerine çalışılan, yüz kaslarındaki ufak hareketleri simüle edebilecek kadar detaylı çözümler üretmeyi amaçlayan araştırmalardır [Chen, Hu, Li, Cummings, Lipson, 2021].

İlk bahsettiğimiz basit çalışmalar, genel olarak farklı materyallerden mekanizma tasarımları içermektedir ancak daha detaylı olan çalışmalar için farklı altyapılar söz konusudur. Bu altyapılar, mekanizmalar ile kas hareketi simülasyonu ve kablo sistemi ile kas hareketi simülasyonu şeklinde ayrıştırılabilir. Her iki sistemin de avantaj ve dezavantajları mevcuttur.

Mekanizma tasarımı ile kas hareketini taklit etmek, bize daha kontrollü hareket menzili sağlar. Tasarlanan mekanizmanın hareket sınırları daha kesindir. Ancak bu gibi tasarımlar, daha fazla yer kaplayacağından, insansı boyutlar içerisinde kalmak, hareketi simüle edilebilecek kas sayısını azaltacaktır [Wagshum, Lin, Yen, 2016].

Öte yandan kablo ve kablo kanalları ile oluşturulan insansı robot surat sistemlerinde motorlar, genellikle kafa bölgesi olmak üzere belirli bir alana düzenli şekilde toplu şekilde yerleştirilir. Motor uçlarına bağlanan kablolar, yüzün belirli bölgelerine yerleştirilen kablo kanallarından geçirilir ve yapay yüz derisinin spesifik noktalarına tutturularak bu noktalardan belirli yönlerde hareket verilmesi sağlanır. Kablo kanallarının esnekliği ve yer kaplamaması, tüm motorların daha geniş bir alanda konumlandırılması gibi avantajlar nedeniyle çok daha fazla hareket noktası oluşturulur ve bu da diğer yönteme kıyasla daha fazla yüz kasını simüle edebilme yeteneği anlamına gelir [Chen, Hu, Li, Cummings, Lipson, 2021; Sato, Namba, Yang, Nishida, Ishi, Minato, 2022]. Ancak bu mekanizmalarda az önce avantaj olarak bahsedilen esneklik nedeniyle mekanizma tasarımı kadar kesin ve net hareketler gerçekleştirmek zorlaşmaktadır.

Tüm bu çalışmaların amacı, tasarım anlamında insana yaklaşan robotlar ile gelecekte insanların yaptığı işleri yapacak, özellikle hizmet sektörleri için tasarlanmış robotlara sahip olabilmektir.

“İnsansı Yüz Mimiklerine Sahip Animatronik Robot Surat Tasarımı ve İmaları” başlıklı projemizde duygu durumlarını ifade edebilme kabiliyetine sahip robot surat tasarımı üzerine bir çalışma yapılmıştır. Bu çalışmanın amacı, herkes tarafından algılanabilecek seviyede gerçekçi yüz mimikleri elde etmek ve bu çalışmayı düşük maliyetler ile gerçekleştirebilmektir.

2. ANİMATRONİK ROBOT SURATIN TASARIMI

Bu çalışmada üretilen insansı mimiklere sahip animatronik robot, çeşitli sınırlar belirlenerek tasarlanmıştır. Bu sınırlamalar şu şekildedir:

- Kaşlar iki serbestlik dereceli şekilde, dış eklem kısmı dikey, iç eklem kısmı ise eğimli olarak tasarlanmıştır.
- Göz, 4 farklı hareket gerçekleştirmektedir. Bunlar yukarı, aşağı, sağ ve sol şeklindedir.
- Göz kapağı, kapanma ve açılma hareketini gerçekleştirmektedir.
- Ağız bölümünde çene ve dudak, ayrı şekilde incelenmiştir. Çene, açılma ve kapanma hareketi yaparken öne ve geriye serbestliği verilerek mekanizmada esneklik oluşturulmuştur. Dudak kısmında ise sekiz farklı eklem noktası belirlenmiştir. Bunlardan üçü alt, üçü üst, ikisi de ağız kenarı kısımlarındadır.

2.1 Kaş Bölgesi

Kaşlar, duygu durumlarını ifade etme biçimlerimizde büyük rol oynamaktadır. Her ne kadar yapı gereği diğer bölümlerden daha basit olsa da mimikler açısından en dikkat çeken bölgelerden biridir.

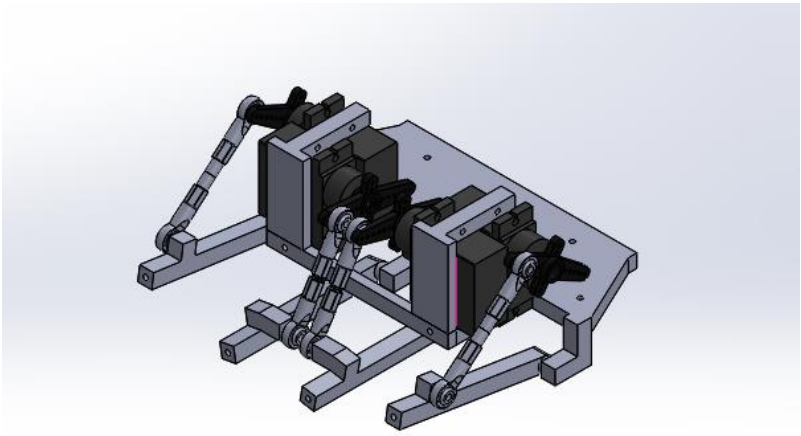
Tasarımsal açıdan inceleyecek olursak temel anlamda iki ayrı eklem bölgesi bulunmaktadır. Şekil 1 ‘de basit anlamda aşağı yönlü (kızgın), nötr ve yukarı yönlü (şaşkın) kaş durumları gösterilmiştir.



Şekil 1 Kaşın Temel Konumları [Fitzpatrick, 2010].

2.2 Kaş Mekanizmasının Tasarımı ve Kaşların Hareketi

İnsan suratına orantısı ve gerçekçi boyutlar göz önüne alınarak çıkartılan hareket şemasını gerçekleştirebilecek bir mekanizma tasarlanmıştır. Mekanizmanın üstündeki alana zıt yönlerde ve arkalı önlü yerleştirilen servo motorlardan kafanın içine bakanlar kaşların iç kısımlarını, dışına bakanlar ise dış kısımlarını hareket ettirmek üzere konumlandırılmıştır. Kaşların iç noktaları daha önce gözlemlendiği ve açıklandığı şekilde 10º ’lik bir açı ile yukarı aşağı hareket etmektedir. Dış tarafta kalan hareket noktaları ise dikey olarak aşağı yukarı hareket ederek asıl duygu durumunu belirten iç hareket noktalarını dengeleyici görev üstlenmektedir. Kaş mekanizmasının izometrik görüntüsü Şekil 2 ‘de gösterilmiştir.

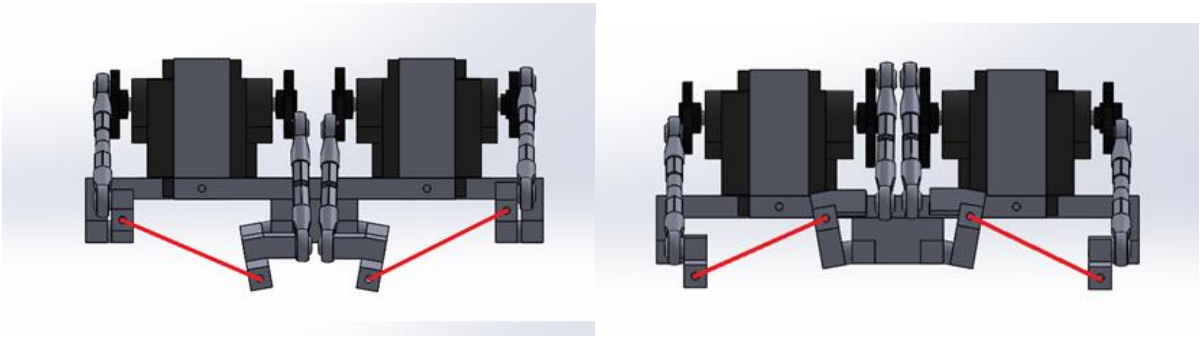


Şekil 2 Kaş Mekanizmasının İzometrik Görünüşü

Burada kullanılan balık gözü mafsallar bulunamadığından mekanizmaya özel ölçülerde yeniden tasarlanıp üç boyutlu yazıcı ile Biopolimer Polilaktik Asit (PLA) malzemeden

üretilmiştir. PLA malzeme seçimindeki en büyük etken Akrilonitril Bütadien Stiren (ABS) malzemeye göre daha kolay basılması ve daha az çarpılma yaşanmasıdır.

Kaş mekanizması, daha önce de belirtildiği üzere az açılı iç eklem ve dikey hareket ile destekleyici dış eklemden oluşur. İç eklem açısı yaklaşık olarak 10º olarak kabul edilmiş ve buna göre tasarım gerçekleştirilmiştir. Kaş mekanizmasının hareket menzili, Şekil 3 ‘de gösterilmiştir.



Şekil 3 Kaş Mekanizmasının Hareket Menzili.

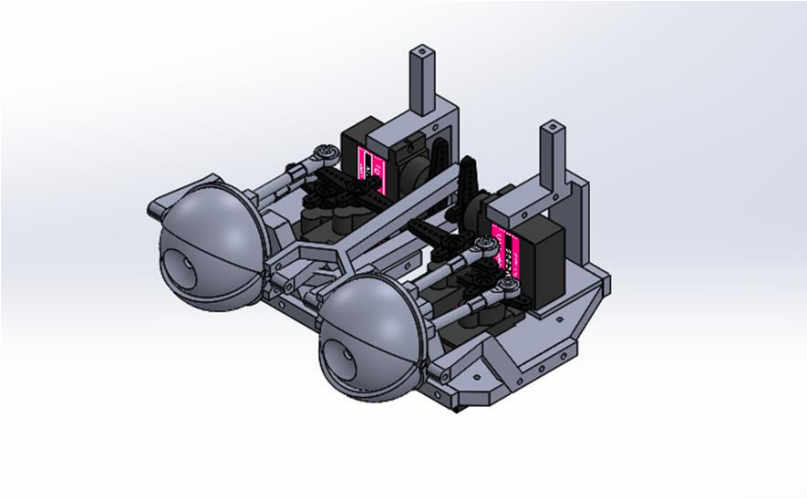
2.3 Göz Bölgesi ve Göz Mekanizmasının Tasarımı

Göz mekanizması projedeki komplike mekanizmalardan biridir. Daha öncesinde çeşitli mekanizma tasarımları yapılmış olsa da hepsinin yalnızca estetik farkları bulunduğu ve temel olarak hareket tasarımlarının benzer özellikte olduğu görülmüştür. Bu konuda çalışmalar yapan Nilheim Mechatronics’in [Cogley, 2019] göz mekanizmasından esinlenilerek revize edilen göz mekanizması, projede diğer bölgelerdeki mekanizma tasarımlarına uygun şekilde montajlanmıştır. Esinlenilen bu mekanizma standartlaştırılmış göz mekanizması olarak kabul görmektedir.

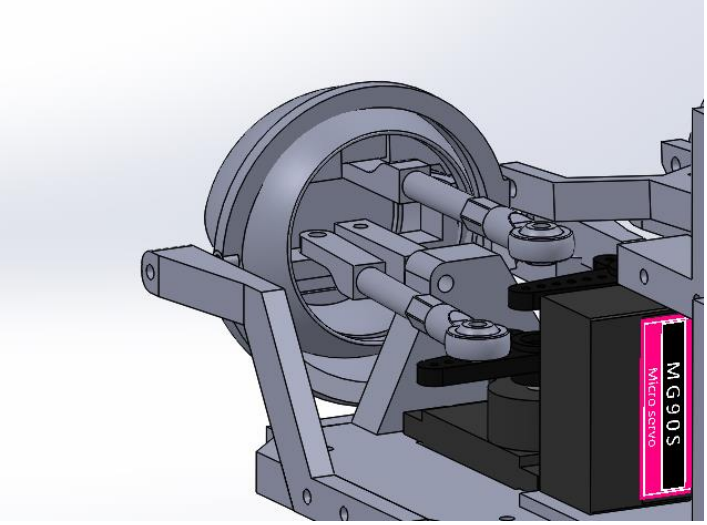
Göz mekanizmasında gözlerin hareketi için 4, göz kapaklarının hareketi için 2 servo motor kullanılmış ve bunlar gözlerin hemen arkasında konumlandırılmıştır. Göz ve kaş mekanizmalarını birbirlerine bağlamak adına göz mekanizmasının dört farklı köşesinden bağlantı parçaları monte edilmiş ve iki mekanizma birbirine bağlanmıştır. Şekil 4 ‘de göz mekanizmasının genel detaylarına yer verilmiştir.

Göz kürelerinin sağ, sol, yukarı ve aşağı hareketleri için Nilheim Mechatronics ‘in mekanizması ile çalışılmış, ancak balık gözü mafsalların bulunabilirlik sorunları nedeniyle bu mekanizma parçaları mafsallı olarak mekanizmaya özel ölçülerle yeniden tasarlanmış ve üç boyutlu yazıcıda PLA malzemesi ile üretilmiştir. Orijinal tasarım yalnızca göz mekanizması odaklı olduğundan gövde parçaları üzerinde de tasarımsal düzenlemeler yapılarak, ağız ve kaş mekanizmaları ile montaj imkanı sunan bir tasarım ortaya koyulmuştur. Göz kürelerinin hareketinde kullanılan mekanizma ve yeniden tasarlanan mafsallar Şekil 5 ‘de gösterilmiştir.

Şekil 5 de de görüldüğü üzere alçakta kalan motor, göz küresinin sağ ve sol hareket tahriğini sağlarken, yüksekte kalan motor, yukarı ve aşağı hareketini kontrol etmektedir.



Şekil 4 Göz Mekanizmasının İzometrik Görünüşü.

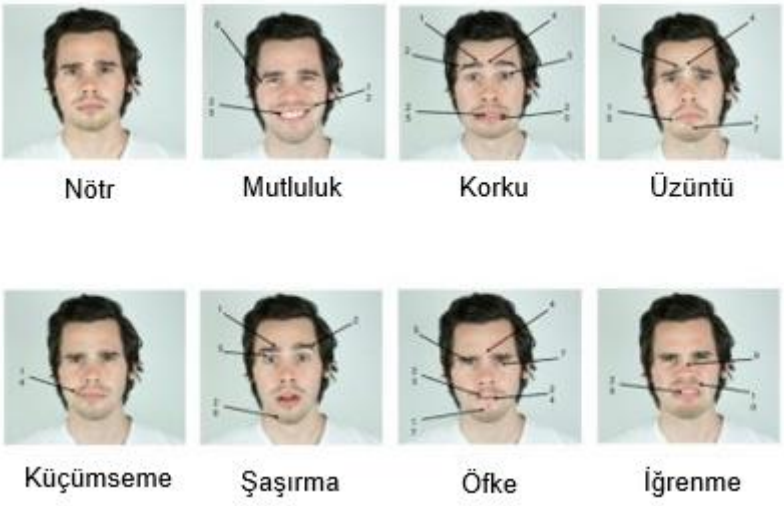


Şekil 5 Göz Kürelerinin Hareket Mekanizması ve Mafsallı Bağlantı Parçaları.

Motor olarak MG90S model koduna sahip mikro servo motorlar kullanılmıştır. Bunun nedeni, projede motor gücüne çok ihtiyaç olmaması, tasarım ve belirli hareketleri gerçekleştirmeye odaklanılmasıdır. Bu nedenle mikro servoların tork değeri yeterli seviyededir.

2.4 Ağız Bölgesi ve Dudakların Hareket Analizi

Her ne kadar dudak ve çene mekanizmaları ayrı ele alınan ve ayrı tasarlanan mekanizmalar olsa da çalışmaları ve insan fizyolojisi anlamında birlikte değerlendirilmeleri gereken mekanizmalardır. Dudaklar, duygu durumlarının belirlenmesinde önemli bir yere sahiptir. İnsanların karşılarındaki kişinin ne düşündüğünü ya da hangi duygu içerisinde olduğunu anlamak için baktıkları ilk bölgelerdendir. Bu nedenle bu proje için önemli bir yere sahiptir. Dudakların hareket analizi Şekil 6 ‘da gerçekleştirilmiştir.

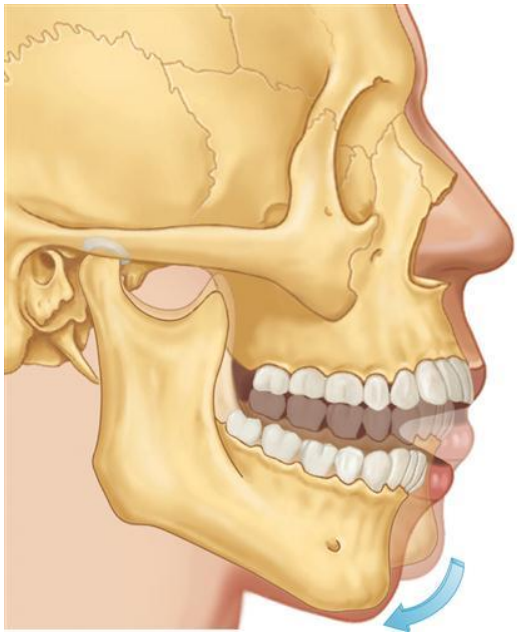


Şekil 6 Farklı Duygu Durumlarında Dudak Hareketlerinin İncelenmesi [Lansley, 2022].

Yukarıda da görüldüğü gibi dudak bölgesinde 8 farklı hareket noktası bulunmaktadır. Daha az hareket noktası ile de belirli simülasyonlar gerçekleştirilebiliyor olsa da bu projede gerçeğe yaklaşmak adına bu 8 hareket noktası seçilmiş ve buna göre tasarım yapılmıştır.

2.5 Çenenin Hareket Analizi

Çene, dudaklar ile senkron çalışması gereken bir bölgedir ve birlikte hareketleri pekiştirmektedirler. Çene temel olarak konuşma, çiğneme vb işlevlerde rol alır ve tüm bu görevler sırasında belirgin şekilde yukarı ve aşağı, daha az belirgin ancak destekleyici şekilde ileri geri hareketlerini gerçekleştirir. Bu hareketler sırasında dişlerin arkasından mesnetli bir hareket yapısına sahiptir. İnsan çenesinin hareket analizi Şekil 7 ‘de gerçekleştirilmiştir.



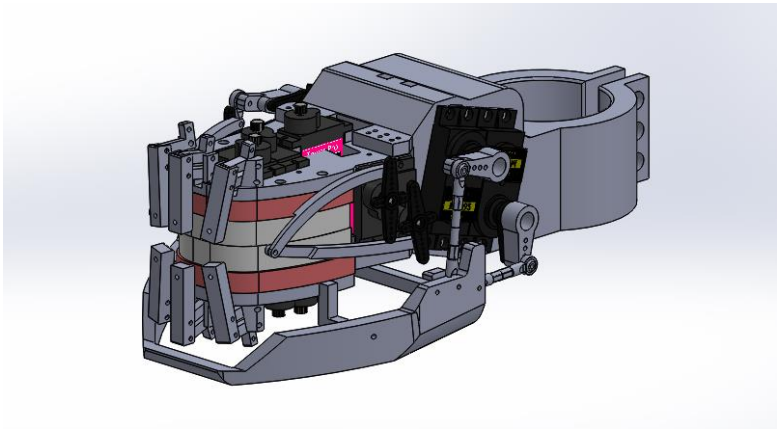
Şekil 7 Çene Eklemi Hareket Analizi [Pocket Dentistry, web].

Çene, aşağı ve yukarı hareketini diş arkasından mesnetli şekilde gerçekleştirir. İleri ve geri hareketi bu hareketi desteklemek ve esneklik açısından gerçekleştirilir. Sağa ve sola hareketi günlük hayatta çok sık kullanılmadığı için mekanizmanın karmaşıklığını azaltmak adına ihmal edilmiştir.

2.6 Çene ve Dudak Mekanizmalarının Tasarımı

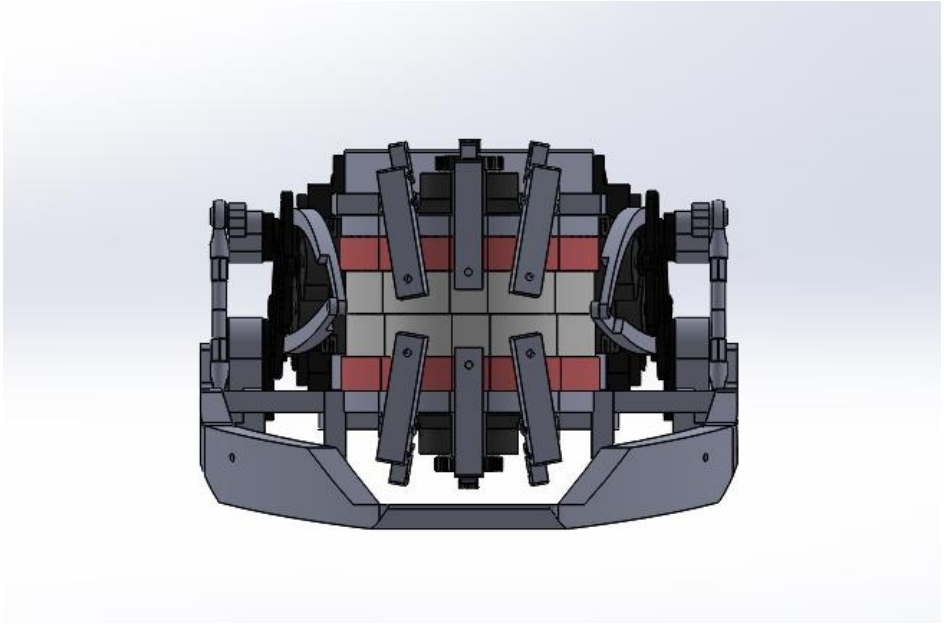
Dudak mekanizmasında daha önce de belirtilen hareket noktaları için gerekli olan tasarım yapılmıştır. Buna göre dudağın üst ve altındaki hareket noktalarına birer motor atanmıştır. İki yanda bulunan ve dudak ile yanağın birleşim noktası olarak duygu durumlarında önemli bir rol alan hareket noktaları için ise ikişer motor kullanılmış ve dudak mekanizmasında toplam 10 adet servo motora yer verilmiştir.

Çene mekanizmasına bakıldığında çene açma, kapama, ileri ve geri olarak dört farklı hareket kabiliyeti bulunması gerekir. Buna uygun gerçekleştirilen tasarımda, hareketin mekanizmaya tek taraflı yük bindirmemesi açısından iki tarafta da motor kullanımı tercih edilmiş, yukarı ve aşağı hareketi için birer, ileri ve geri hareketi için de birer olmak üzere 4 servo motor kullanılmıştır. Ancak bu servo motorlar alt dudak ve alt çeneye ait tüm parçaları taşımakta görev aldıkları için diğer servo motorlara nazaran daha güçlü olan MG995 servo motoru tercih edilmiştir. Bu motorlar boyut olarak geri kalan servo motorlara göre daha büyüktür ancak çene mekanizmasındaki tasarımdan dolayı rahatlıkla kullanılabilmektedirler. Çene mekanizmasının arka tarafına yerleştirilen aparat tasarımı sayesinde robot surat üzerinde çalışırken konumlandırma sorunu çözülmüş ve bir stand üzerine sabitlenmiştir. Ağız mekanizmasının farklı açılardan görüntüleri Şekil 8 ve Şekil 9 ‘da gösterilmiştir.



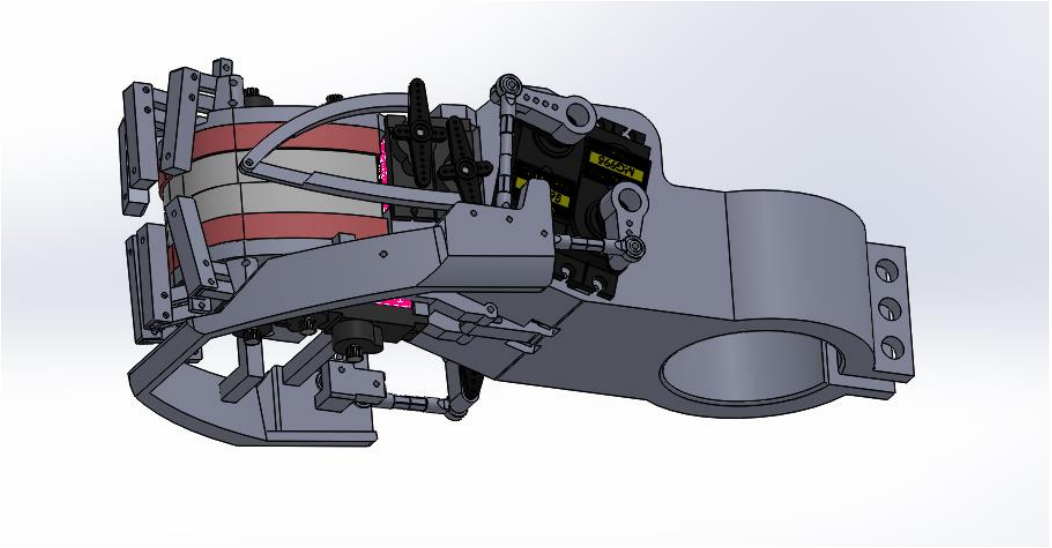
Şekil 8 Ağız Mekanizmasının Genel Tasarımı.

Çenedeki esnekliği sağlamak ve çok kullanılmasa da tasarımın hareket kabiliyetini artırmak amacıyla ileri-geri hareketi, slot benzeri bir tasarımla sağlanmış ve çene motorlarıyla kontrol edilecek şekilde yerleştirilmiştir. Bu sayede çene eklemi sınırlı da olsa gerçeğe yakın hareket kabiliyetine kavuşmuştur.



Şekil 9 Ağız Mekanizmasının Önden Görünüşü.

Yukarıda da bahsedilen çenenin mesnetli hareketi bu slot tarafından sağlanmış ve ileri-geri hareketi sırasında mesnet yapısında herhangi bir problem oluşmaması sağlanmıştır. Bu tasarımın detaylı görünümü Şekil 10 'da gösterilmiştir.



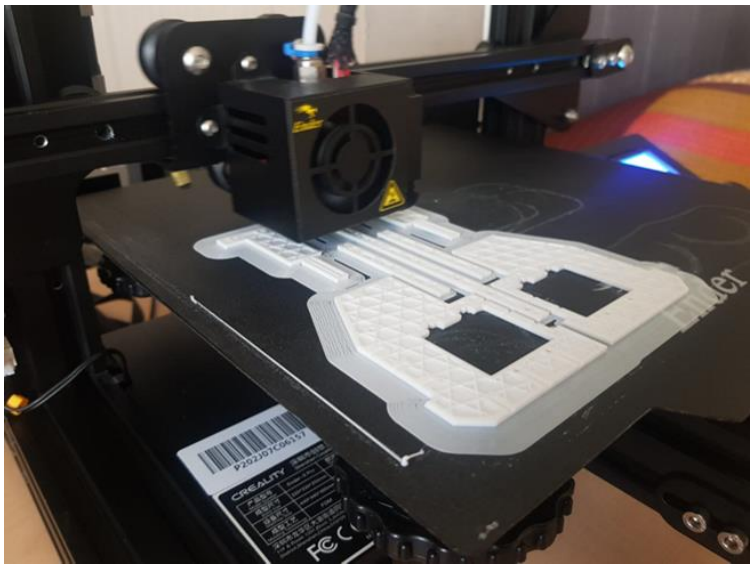
Şekil 10 Çene Mekanizmasındaki Slotlu Tasarımın Detaylı İncelemesi.

Şekilde de görüldüğü gibi, mesnet yapısı dişlerin arkasında kalacak şekilde konumlandırılmış ve arka çene motorlarının yardımıyla ileri-geri hareketini gerçekleştirirken mesnet özelliğinin korunması amaçlanmıştır. Ağız mekanizmasının arkasında yer alan, vida ve somun yardımıyla sıkılığı ayarlanan tasarım, kafayı stand görevi görecek boruya sabitlemede kullanılmıştır.

3. ANİMATRONİK ROBOT SURATIN İMALATI

Günümüzde imal edilen robotlar farklı materyallerden yapılsa da, bu projenin amaçlarından biri olan düşük maliyet nedeniyle üç boyutlu yazıcı ile plastik baskı yöntemi seçilmiştir. Bu yöntemin hassasiyeti diğer yöntemlerden daha düşük olabilir [Şahin, Turan, 2018], ancak genel anlamda mekanizmalar işlevlerini yerine getirebilmekte ve gerçekçi mimikler elde edilebilmektedir.

Mekanizma tasarımları gerçekleştirildikten sonra bu tasarım dosyaları, Standard Triangle Language (STL) formatına getirilerek üç boyutlu yazıcılara yüklenmiş ve PLA malzemeden üretimleri gerçekleştirilmiştir. Bir mekanizmanın üretimine ait örnek görsel Şekil 11 ‘de gösterilmiştir.



Şekil 11 Üç Boyutlu Yazıcıda Örnek Bir Baskı Aşaması.

Yukarıdaki görselde baskının iç yapısı gözlemlenebilmektedir. Baskılar, %20 doluluk oranı ve dinamik baskı kalitesi olarak geçen 0,16 mm baskı kalitesinde alınmıştır. Destek malzemesi seçeneği açık olarak ayarlanmış ve yüzeyle temas etmeyen bölgeler, destek malzemesi ile düzgün şekilde basılabilmiştir. Bu kısımlar, baskı sonrası temizlenerek mekanizmalar kullanıma hazır hale getirilebilmektedir. Örneği verilmiş olan baskı aşaması, elektronik komponentler ve dişler dışarısındaki tüm malzemeler için aynı şekilde gerçekleşmiştir.

3.1 Animatronik Robot Suratın Elektronik Tasarımı

Animatronik robot suratın tasarlanan mekanizmalarını istenilen doğrultuda hareket ettirilebilmesi ve çeşitli mimiklerin simüle edilebilmesi için mikro kontrolcü, motor sürücüsü, konum kontrollü servo motorlar, güç kaynağı gibi elektronik komponentlere ihtiyaç duyulmaktadır. Bu parçalar birbiri ile uyum içinde çalışılmalı ve motorlara ihtiyaç duyulan güç,

kontrollü bir şekilde aktarılmalıdır. Aksi takdirde sağlıklı bir çalışma ortamı oluşturulamamaktadır. Bu bölümde kullanılan komponentler ve özellikleri incelenmiştir.

Mikro Kontrolcü ve Servo Motor Sürücüsü: Maliyet avantajı göz önünde bulundurulduğunda, kontrolcü ve motor sürücü kartının ayrı ayrı kullanıldığı bir tasarım yerine üzerinde kontrolcü çipi bulunan entegre bir servo motor sürücü kartı kullanılmıştır ve bu kart, 32 adet servo motoru aynı anda kontrol edebilmektedir.

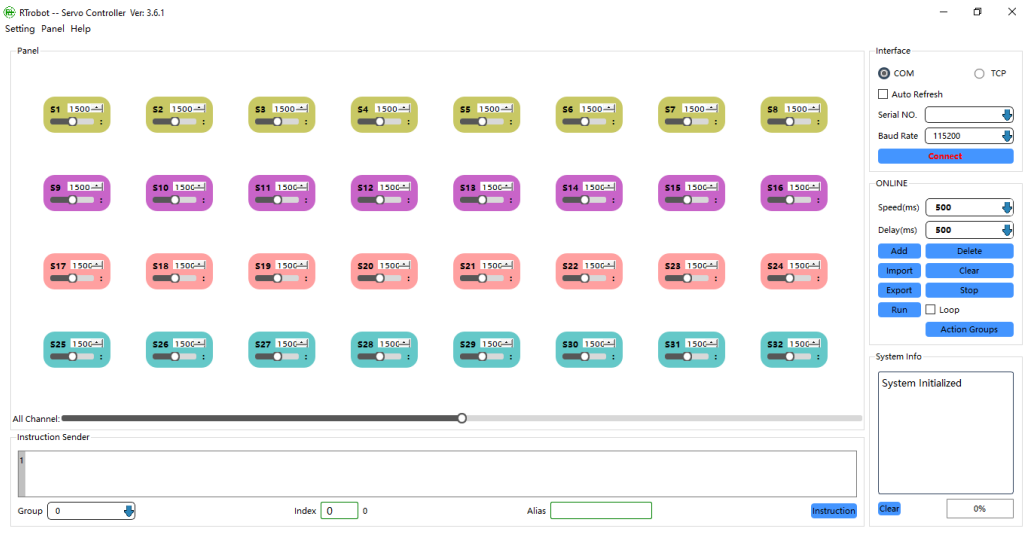
Voltaj Regülatörü: Karta ve motorlara gönderilen gücü kontrol edilebilmek ve yüksek voltajdan kaynaklı bir hasarın önüne geçilebilmek amacıyla, kullanım kolaylığı ve ekstra malzeme ihtiyacı olmaması açısından üzerinde yerleşik gösterge bulunan bir regülatör seçilmiştir.

MG90S Mikro Servo Motor: Boyutu ve maliyet avantajı ile projede sayıca en çok ihtiyaç duyulan servo motorlardır. MG90 mikro servolar yerine MG90S mikro servoların seçilme nedeni metal dişli olmalarıdır. Bu sayede yeterli dayanıklılık elde edilmiştir.

MG995 Servo Motor: Çenede kullanılacak motorların alan anlamında daha serbest olması ve alt çene mekanizmasının ağırlığını taşıyacak olması nedeniyle daha güçlü bir servo motor ihtiyacı doğmuştur. Bu doğrultuda yine metal dişlileriyle dayanıklı ve maliyet olarak optimum seviyede olan MG995 servo motorlar seçilmiştir.

3.2 Animatronik Robot Suratın Yazılımı

Animatronik robot suratta kullanılan kontrolcü kartı, daha önce özelliklerinde belirtildiği gibi arduino, bilgisayar, kablosuz kontrolcü gibi farklı kontrol program ve ekipmanlarıyla kontrol edilebilmektedir. Ancak bu projede kartla uyumlu olması ve kullanım kolaylığı açısından kontrolcü kartın kendi yazılımının kullanımı tercih edilmiştir [RTRobot, web]. Kontrolcü kart yazılımın alınan arayüz ekran görüntüsü, Şekil 12 ‘de gösterilmiştir.



Şekil 12 Kontrolcü Kart Yazılımının Arayüzü.

Yukarıda gösterilen arayüzde çok sayıda kişiselleştirme seçenekleri sunulmuştur. Servolara farklı renkler ve isimler atanabilmekte, yerleri sürükle-bırak yöntemiyle değiştirilebilmekte ve kişisel olarak farklı diyagram şekilleri oluşturulabilmektedir. Bunların dışında kullanılmayan servolar ekran üzerinden kaldırılıp ve aksiyon grubu adlı özellik ile birden fazla servo motor, tek bir görev için eş zamanlı programlanabilmektedir.

4. ANİMATRONİK ROBOT SURATIN MALİYETİ

Animatronik robot suratın hedeflerinden bir diğeri de düşük maliyet kriteridir. Uygun fiyatlı malzemelerle üretilen animatronik robot suratın maliyeti, temel olarak üç ana kısımdan oluşmaktadır. Sarf malzeme, üretim ve elektronik şeklinde sınıflandırabileceğimiz bu maliyetler özellikle üç boyutlu baskı kısmında, irili ufaklı birçok ara bağlantı elemanı olması nedeniyle bölgesel olarak gruplandırılarak hesaplanmıştır. Üç boyutlu baskılara ait maliyet analiz tablosu Tablo1 ‘de verilmiştir.

Tablo 1 Animatronik Robot Suratın Üç Boyutlu Baskı Maliyetleri.

Animatronik Robot Surat Üç Boyutlu Baskı Maliyetleri				
Parça Adı	Baskı Süresi (h)	Filament Miktarı (kg)	Elektrik	Malzeme
Kaş Grubu	6,5	0,027	$ 0,048	$ 0,336
Göz Grubu	11,5	0,06	$ 0,085	$ 0,748
Ağız Grubu	35,5	0,215	$ 0,263	$ 2,681
Bağlantı Aparatları	7	0,025	$ 0,052	$ 0,311

Yukarıda maliyet analizi yapılırken, üç boyutlu yazıcının saatlik elektrik tüketimi 0,1 kW, elektrik ücretleri ortalama 0,074 $/kW ve 1 kg PLA filament ücreti 12,47 $ olarak kabul edilmiştir. Bu değerler günümüz koşullarındaki ortalama değerlerdir.

Maliyet hesabındaki diğer kategori, elektronik kategorisidir. Burada da ürünlerin mevcut fiyatları incelenmiş ve maliyet analizi tablosu oluşturulmuştur. Maliyet tablosu, Tablo 2 ‘de verilmiştir.

Tablo 2 Animatronik Robot Suratın Elektronik Komponent Maliyetleri.

Animatronik Robot Surat Elektronik Komponent Maliyetleri			
Ürün	Adet	Fiyat	Toplam Fiyat
32 Kanal Servo Sürücü Kartı	1	$ 36,474	$ 36,474
Dijital Göstergeli Voltaj Regülatörü	1	$ 3,642	$ 3,642
MG90S Mikro Servo Motor	20	$ 3,266	$ 65,32
MG995 Servo Motor	4	$ 4,351	$ 17,404
DC-DC Adaptör	1	$ 4,117	$ 4,117

Baskı maliyeti B, elektronik maliyeti E, toplam maliyet T olarak kabul edilmiştir.

$$T = (B + E) \quad (1)$$

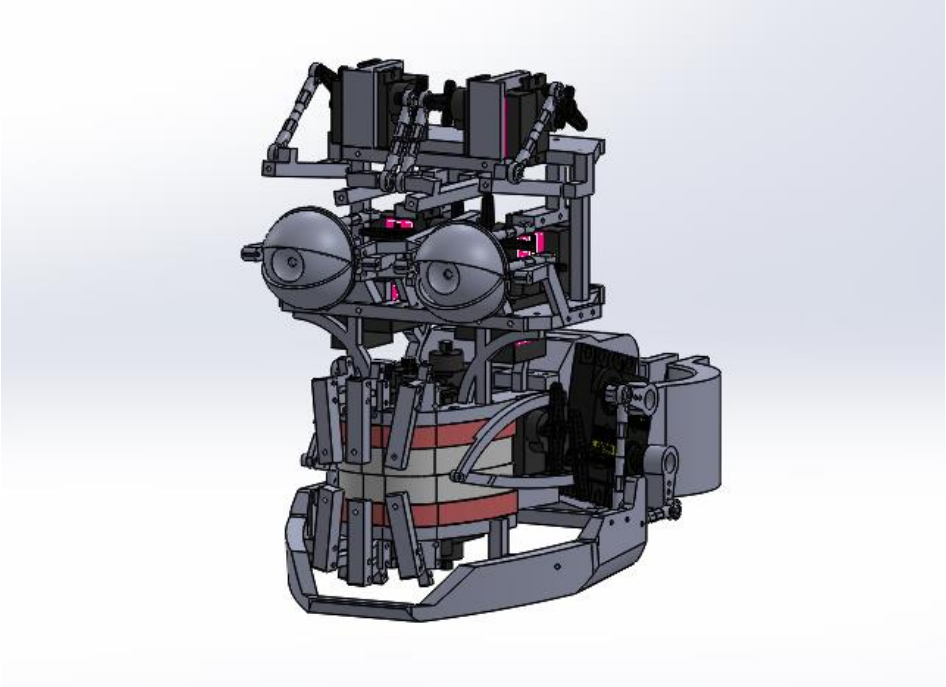
$$T = [1{,}15\ (4{,}524) + 126{,}96] \quad (2)$$

$$T = 132{,}16\ \$ \quad (3)$$

Denklem 2 ‘de de görüldüğü gibi baskı maliyetlerine %15 fire eklenip toplam maliyet dolar kuru üzerinden hesaplandığında animatronik robot suratın günümüz koşullarındaki maliyeti 132,16 $ civarlarındadır.

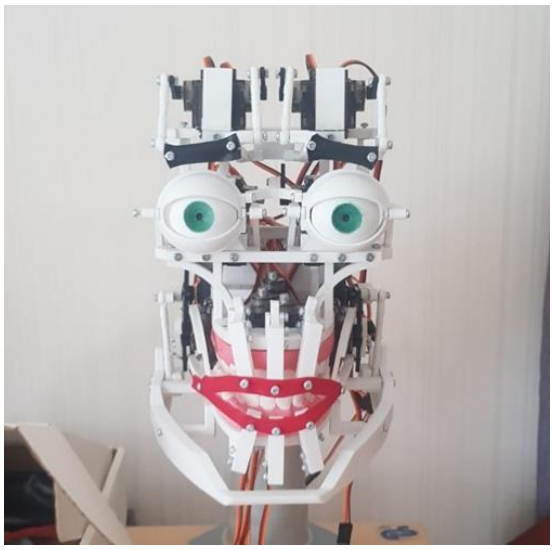
5. SONUÇLAR

Bu projede, insansı yüz mimiklerine sahip animatronik robot surat üzerine tasarım ve üretim çalışmaları gerçekleştirilmiştir. Projedeki temel kriter, tasarımda insana yaklaşmak olduğundan boyut kısıtlarıdır. Bu nedenle kullanılmış olan motorlar ve bu motorların hareket ettirdiği mekanizmalar insan kas yapısına uyumlu, benzer konumda benzer işlevleri gerçekleştirmelidir. Animatronik robot suratın bilgisayar ortamında modellemesi, Şekil 13 ‘de gösterilmiştir.



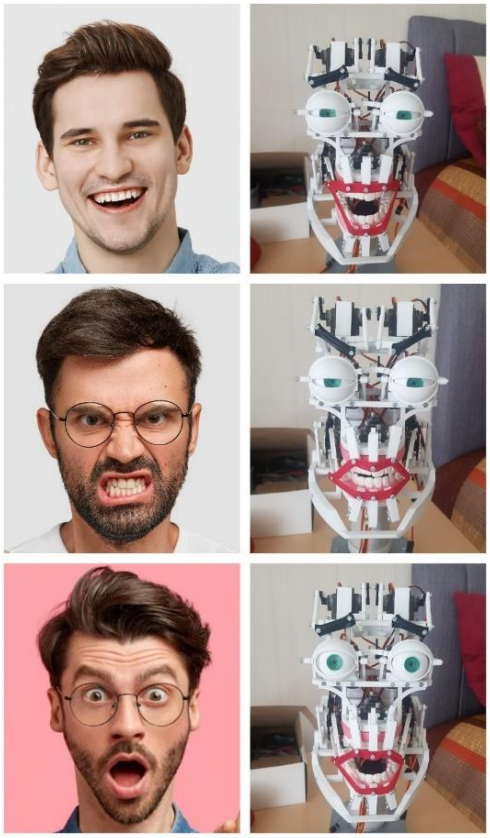
Şekil 13 Animatronik Robot Suratın Bilgisayar Ortamında Modellemesi.

Yüz mimikleri daha belirgin hale getirilmiş haliyle montajı tamamlanan insansı yüz mimiklerine sahip animatronik robot surat, Şekil 14 ‘de gösterilmiştir.



Şekil 14 Animatronik Robot Suratın Tamamlanmış Hali.

Animatronik robot suratın dudak ve kaş bölgeleri belirginleştirilerek, insan mimiklerinin algılanmasında kolaylık sağlanmıştır. Kas yapısı ile benzer tasarlanan mekanizmalar, belirli duygu durumlarını, herkes tarafından anlaşılabilecek seviyede simüle etmeyi başarmıştır. Farklı duygu durumlarının simüle edilmiş halleri, Şekil 15 ‘de gösterilmiştir.



Şekil 15 Animatronik Robot Suratın Farklı Duyguları Simüle Etmesi [Freepik, web].

Yukarıda verilen görselde de görüldüğü gibi bu projede tasarlanan ve üretilen animatronik robot suratta, her bir duygu durumu için yüz kaslarının hareketleri incelenmiş ve bu hareketler doğrultusunda servo motorların konumları programlanarak duygu mimikleri simüle edilmiştir.

Bu çalışmada insansı robot teriminin mekanik tasarımı üzerine çalışılmıştır. İnsansı yüz mimiklerine sahip animatronik robot surat projesi, maliyet sınırları içerisinde Türkiye ’de çok az sayıda çalışma yapılmış bir konudur ve bu nedenle öncü konumundadır.

Daha sonraki çalışmalarda, projenin kapsamı genişletilerek çevresiyle etkileşime geçebilecek bir yapıya getirilebilir ve bu sayede insansı özellikleri artabilir. Bunun için işlemcisinin güçlendirilmesi, bir görüntü sağlayıcısı eklenerek çevresini algılayabilmesi ve yazılımının geliştirilerek yapay zeka eklenmesi gerekmektedir. Giriş kısmında da anlatıldığı gibi yüz kaslarının belirli bölümlerinde, örneğin ağız bölgesi, kablolu tasarıma geçilerek referans noktaları artırılabilir ve daha gerçekçi ağız hareketleri elde edilebilir. Çevreyi algılama kabiliyetinin gelişmesi için boyun mekanizması eklenerek görüş alanı genişletilebilir. Bu sayede proje kapsamı, yüz bölgesinden tüm kafa bölgesine genişletilebilir.

4. KAYNAKÇA

1. **Oh, J.H., Hanson, D., Kim, D., (2006).** “Design of android type humanoid robot Albert HUBO.” Intelligent Robots and Systems, 2006 IEEE/RSJ International Conference on. IEEE, 2006.

2. **Hanson Robotics, (web).** “Albert HUBO”, erişim: 14 Mar 2022, https://www.hansonrobotics.com/albert-hubo.

3. **Chen, Y., Liu, X., Li, J., Zhang, T., Cangelosi, A., (2021).** Generation of Head Mirror Behavior and Facial Expression for Humanoid Robots. 10. 10.54364/AAIML.2021.1110.

4. **Ishihara, H., Ota, N., Asada, M., (2017).** Derivation of simple rules for complex flow vector fields on the lower part of the human face for robot face design. Bioinspiration & Biomimetics. 13. 10.1088/1748-3190/aa8f33.

5. **Rusu, D.M., Pirpidel E., Biris C.M., (2020).** DESIGNING AN ANIMATRONIC HUMANOID ROBOTIC HEAD. 64. 461-466.

6. **Fitzpatrick, R., (2010).** “Designing and Constructing an Animatronic HeadCapable of Human Motion Programmed using Face-Tracking SoftwareTable of Contents,” tech. rep., Worcester Polytechnic Institute, 2010.

7. **Wagshum, A., Lin, C.Y., Yen, S.H., (2016).** Humanoid Head Face Mechanism with Expandable Facial Expressions. International Journal of Advanced Robotic Systems. 13. 1. 10.5772/62181.

8. **Chen, B., Hu, Y., Li, L., Cummings, S., Lipson, H., (2021).** Smile Like You Mean It: Driving Animatronic Robotic Face with Learned Models.

9. **Sato, W., Namba, S., Yang, D., Nishida, S., Ishi, C., Minato, T., (2022).** An Android for Emotional Interaction: Spatiotemporal Validation of Its Facial Expressions. Frontiers in Psychology. 12. 10.3389/fpsyg.2021.800657.

10. **Cogley, W., (2019),** "Compact and Robust 3D Printed Animatronic Eye Mechanism", erişim: 27 Kas 2021 , http://www.nilheim.co.uk/latest-projects-and-blog/compact-and-robust-3d-printed-animatronic-eye-mechanism.

11. **Şahin, K., Turan, B., (2018).** "ÜÇ BOYUTLU YAZICI TEKNOLOJİLERİNİN KARŞILAŞTIRMALI ANALİZİ". Stratejik ve Sosyal Araştırmalar Dergisi. 2. 97-116. 10.30692/sisad.441648.

12. **RTRobot, (web),** "RTRobot Software Ver 3.12", erişim: 05 May 2022, https://rtrobot.org/software.

13. **Lansley H., (2022).** "The Facial Action Coding System", erişim: 13 May 2022, https://www.eiagroup.com/the-facial-action-coding-system.

14. **Pocket Dentistry, (web).** "Mechanics of Mandibular Movement", erişim: 21 Kas 2021, https://pocketdentistry.com/4-mechanics-of-mandibular-movement.

15. **Freepik, (web).** Yüz Mimiklerinin Görselleri, erişim: 18 Nis 2022, https://www.freepik.com.

İŞ MAKİNELERİ TASARIMINDA DÜŞÜK EMİSYONLU ALTERNATİF YAKIT UYGULAMALARI

Ceyhun GÜL, *ceyhun.gul@hidromek.com.tr* HİDROMEK A.Ş., 06935, Ankara
L. Furkan MUMCU, *furkan.mumcu@hidromek.com.tr* HİDROMEK A.Ş., 06935, Ankara
T. Yasin ALTINAY, *yasin.altinay@hidromek.com.tr* HİDROMEK A.Ş., 06935, Ankara
M. Can KATMER, *mehmet.katmer@hidromek.com.tr* HİDROMEK A.Ş., 06935, Ankara
Fatma YALÇIN, *fatma.yalcin@hidromek.com.tr* HİDROMEK A.Ş., 06935, Ankara
Ferhan FIÇICI, *ferhan.ficici@hidromek.com.tr* HİDROMEK A.Ş., 06935, Ankara

ÖZET

Bu çalışmada küresel iklim değişikliğinin en temel nedenlerinden biri olan karbon emisyonunun azaltılması için alternatif yakıt kullanımı üzerine araştırma yapılmıştır. Yapılan çalışmada öncelikle mevcut alternatif yakıt teknolojileri hakkında güncel bilgiler paylaşılmıştır. Daha sonra iş makinesi tasarımında alternatif yakıt teknolojileri uygulama örnekleri; ekskavatör, kazıcı-yükleyici ve yükleyici makinelerinde ayrı ayrı incelenmiştir. Araştırmalar değerlendirildiğinde; otomotiv sektörü gibi iş makinesi sektöründe de alternatif yakıt kullanımının yaygınlaşarak büyümeye devam ettiği ve yakın gelecekte tamamen fosil yakıtların yerini alacağı açıkça görülmektedir.
Anahtar Kelimeler: İş Makineleri, Alternatif Yakıtlar, Elektrikli / Hibrit Araçlar

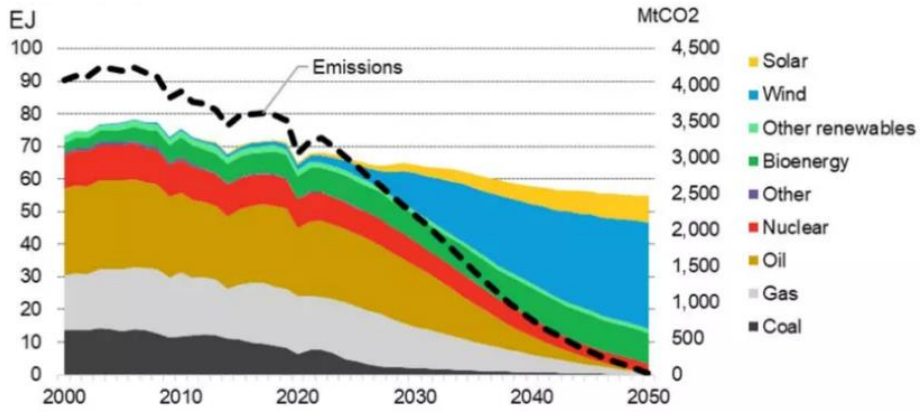
ABSTRACT

In this study, research was conducted on the use of alternative fuels to reduce carbon emissions which one of the main causes of global climate change. At the beginning of the study, up-to-date information about current alternative fuel technologies was shared. Then, alternative fuel technologies application examples in construction equipment design; excavator, backhoe-loader and loader machines were examined separately. When the studies are evaluated; It is clearly seen that the use of alternative fuels in the construction equipment sector, like the automotive sector, continues to expand and grow and will completely replace fossil fuels in the near future.
Keywords: Construction Equipment, Alternative Fuels, Electric / Hybrid Vehicle

1. GİRİŞ

Günümüzde çevre kirliliği ve buna bağlı iklim değişiklikleri, şüphesiz insana ve dünya üzerinde yaşayan birçok canlı hayatına olumsuz temas eden oldukça önemli bir problem

haline gelmektedir. Araştırmalara göre, 2009 yılında bile küresel inşaat sektörünün doğrudan C02 emisyon salınımının kaynağı olarak benzin, motorin, sıvı yakıt yağları ve diğer petrol bileşenlerinin olduğunu göstermiştir. [Huang et al., 2018]. Bu fosil yakıtlar, iş makinelerine ve diğer inşaat ekipmanlarına güç sağlamak için kullanılan yakıtın %99,5'ini kapsamaktadır. İş makineleri, inşaat sektörünün ve ağır sanayinin gelişmesinde önemli bir rol oynamasına rağmen, yüksek enerji tüketimi ve özellikle içten yanmalı motor (İYM) kullanan makinelerde sera gazı emisyonu salınımı ile bir o kadar mevcut problemler doğurmaktadır. Bu nedenle, bilim insanlarının, özellikle emisyon değerlerini azaltabilen ve aynı zamanda enerji verimliliğini artırıp yakıt tüketimini en aza indirebilecek çeşitli alternatif yakıt teknolojileri arayışına girişmesi önem arz etmektedir. Son zamanlarda teknolojik gelişmelerle birlikte İYM'nin kullanımına alternatif olarak Hidrojen, Elektrik, Biyo-Yakıtlar, Hibrit teknolojileri potansiyel bir aday olarak değerlendirilmektedir. Uluslararası Enerji Ajansı'nın (International Energy Agency) araştırmalarına istinaden, 1990'dan 2018'e kadar rüzgâr, solar fotovoltaik (FV) ve hidrojen kaynakları ile yenilebilir elektrik üretimi hızla artmıştır. Hidrojen enerjisinin büyümesinin %97,3 arttığı ve dünyanın en büyük yenilenebilir üretim kaynağı olmaya devam edeceği tahmin edilmektedir. [IEA, 2018] Bu verilere bağlı olarak iş makineleri üreticileri ise alternatif yakıt arayışlarına yönelik çalışmaları incelendiğinde öncelikli araştırmalarının elektrik, hidrojen ve hibrit teknolojilerine odaklandığı görülmüştür. İş makineleri sektöründe, çoğunlukla tahrik sisteminin enerji gereksinimi İYM vasıtasıyla gerçekleştiği ve bu da doğrudan fosil yakıtlara bağımlı olduğumuzu göstermektedir. Hiç şüphesiz fosil yakıtların sınırlı geleceği, alternatif yakıt arayışını her zaman tetiklemiştir. Düşük karbonlu bir ekonomiye geçiş için yenilikçi teknolojileri kapsayan stratejik bir araştırma kuruluşu olan BloombergNEF (BNEF), Avrupa'nın son zamanda yaşanan istikrarsız politik düzenden kaynaklı enerji krizi ve artan iklim tutkusu, politikacılar arasında enerji sistemini çeşitlendirmek ve karbondan arındırmak için yeni bir ivme kazandığını belirtti. BNEF'in Avrupa için Net Sıfır Senaryosuna göre, 2050 yılına kadar fosil yakıtların tamamen ortadan kalkacağı öngörülüyor [BNEF, 2022]. Şekil 1'de de görüldüğü gibi bunun mümkün olabilmesi için temelde elektrifikasyona geçişle rüzgâr, güneş ve doğadan elde edilebilirliği oldukça kolay olan hidrojen enerjisinin kullanılabilirliği ile mümkün olacağı görülebilmektedir. Avrupa Birliği Komisyonu tarafından 2019 yılı sonunda ortaya konulan Avrupa Yeşil Mutabakatı, AB'nin iklim değişikliği sorunuyla mücadele kapsamında geliştirdiği bir eylem planı olarak tanımlanabilmektedir. Ayrıca (Avrupa Yeşil Mutabakatı) AYM ile AB ülkelerinin 2050 yılına kadar iklim/karbon nötr olması hedeflenmektedir [European Commission, 2021]. Metan gazı salınımlarını azaltma taahhütleri 2021'in Kasım ayında Glasgow'da düzenlenen COP26 (Climate Change Conference)'da önemli bir yer tutmuş ve 100'den fazla ülke metan gazı salınımı 2030'a kadar yüzde 30 azaltmayı öngören bir taahhütte uzlaşmıştır.



Şekil 1 BNEF tarafından oluşturulan 2000-2050 yılları arası öngörülen Net Sıfır Senaryosunda Enerji Kaynakları [BNEF, 2022]

2. ALTERNATİF YAKIT TEKNOLOJİLERİ

2.1. Biyoyakıt

2.1.1. Biyodizel

Biyodizel, organik yağların baz ve alkolle karıştırılarak dizel yakıta çevrilmesi sonucu elde edilen üründür. Oksijenli zincir yapısı biyodizeli, petrol kökenli dizel yakıtından ayırır. Biyodizel, dizel yakıtına yakın ısıl değere, dizel yakıtından daha yüksek alevlenme noktasına sahiptir. Bu özellik biyodizeli kullanım, taşıma ve depolamada daha güvenli bir yakıt yapar. Biyodizel üretiminde kullanılmak üzere yetiştirilen bitkilerin doğadan aldıkları karbondioksitle, biyodizelin yanması neticesinde ortaya çıkan karbondioksitin birbirlerini nötürleyici etkisi vardır. Yapılan laboratuvar çalışmaları saf biyodizel (B100) kullanımı neticesinde gözlemlenen karbondioksit salınım oranın, standart motorin kullanımı neticesinde ortaya çıkan karbondioksit salınım oranından %74 oranında az olduğunu göstermektedir. [Biyodizel Sanayi Derneği] Biyodizelin birden fazla çeşidi bulunmaktadır. Bunların en sık kullanılanları Fatty Acid Methyl Ester (FAME) ve Hydrotrated Vegetable Oil (HVO)'dir. FAME genellikle bitkisel ve hayvansal yağlardan elde edilen Fatty Acid Methyl Ester kelimelerinin (Yağ Asidi Metil Ester) kısaltılmasıdır. Üretimi biyokütle kaynaklarının metanol ve potasyum hidroksit katalizörleri ile reaksiyon vermesi ile gerçekleşen transesterifikasyona dayanmaktadır. Bitkisel ve hayvansal yağlar doğrudan hidrojenasyon ile HVO 'ya dönüştürülmektedir.

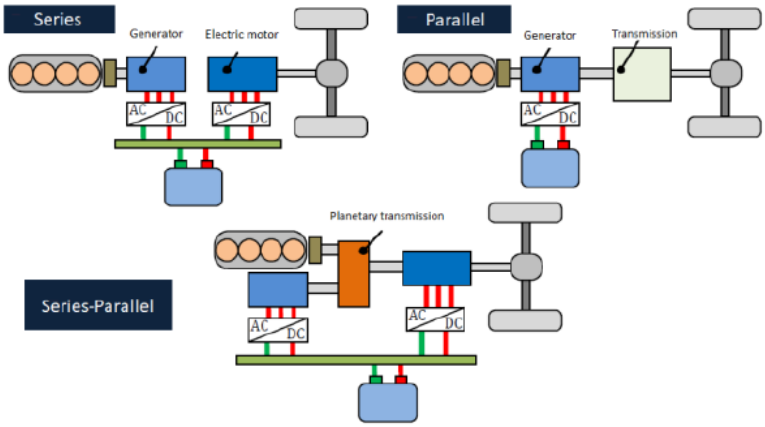
2.1.2. Alkoller

İçten yanmalı motorlarda doğrudan ya da motor yakıtlarının içerisine belirli oranlarda karıştırılarak kullanılabilinmektedirler. İçten yanmalı motorlarda kullanılabilen alkol çeşitleri metanol (CH_3OH), etanol (C_2H_5OH) ve bütanol (C_4H_9OH)'dür. Alkoller motor yakıtlarına göre daha küçük moleküler yapıya sahip olmaları, yapılarında oksijen bulundurmaları, motor yakıtlarında bulunan kükürt, kanserojen maddeler ve ağır metalleri içermemelerinden dolayı

egzoz emisyonlarında olumlu etkilere sebep olmaktadırlar [Akyaz, S., 2007] Yapılan çalışma sonuçları göstermektedir ki, dizel motorlarında alkol yakıtlarının kullanımı sonucunda motor gücü, motor momenti ve egzoz gazı sıcaklığı azalmakta, özgül yakıt tüketimi artmaktadır. Ayrıca CO, NOx, is emisyonlarında düşme, HC emisyonlarını artış görülmektedir. Genel olarak bakıldığında sonuçlar dizel motorlarda alkol kullanılmasının motor performansını azalttığını fakat emisyonlarda iyileşme sağladığını bildirmişlerdir. [Özer ve Özdalyan, 2013]

1.1. Hibrit

Gün geçtikte artan egzoz emisyon standartları nedeni ile iş makinesi üreticileri emisyon değerlerini düşürmek için farklı güç aktarma sistemleri üzerine çalışmalar yapmaktadırlar. Bunların başında hibrit ve elektrikli sistemler gelmektedir. Batarya problemlerinden dolayı elektrikli sistemlere geçilmeden önce ara basamak olarak hibrit sistemler üretilip tüketicilerin kullanımına sunulmaya başlamıştır. Otomobil sektöründe hibrit araçların kullanımı her geçen gün daha da artmaktadır. Alternatif güç aktarma sistemi çözümleri değişebilir ve elektrikli yardımcı güç çıkışlarından, dizel-elektrikli ve dizel-hidrolik çözümlerden birçok hibrit düzene ve akülü-elektrikli, yakıt hücreli-elektrikli ve diğer birçok varyasyona kadar farklı konseptleri kapsayabilir. [KALOCIŃSKI, T., (2022)]



Şekil 2 Hibrit Araç Mimarileri [MERKISZ, J., PIELECHA, I., (2015)]

Seri Hibrit Tahrik Sistemi: İçten yanmalı motor, elektrik motoru ve jeneratör olmak üzere üç ana kısımdan oluşur. İçten yanmalı motor tarafından oluşturulan mekanik enerji, jeneratör tarafından elektrik enerjisine dönüştürülerek elektrik motoru çalıştırılır ve tahrik (hareket) sağlanır.

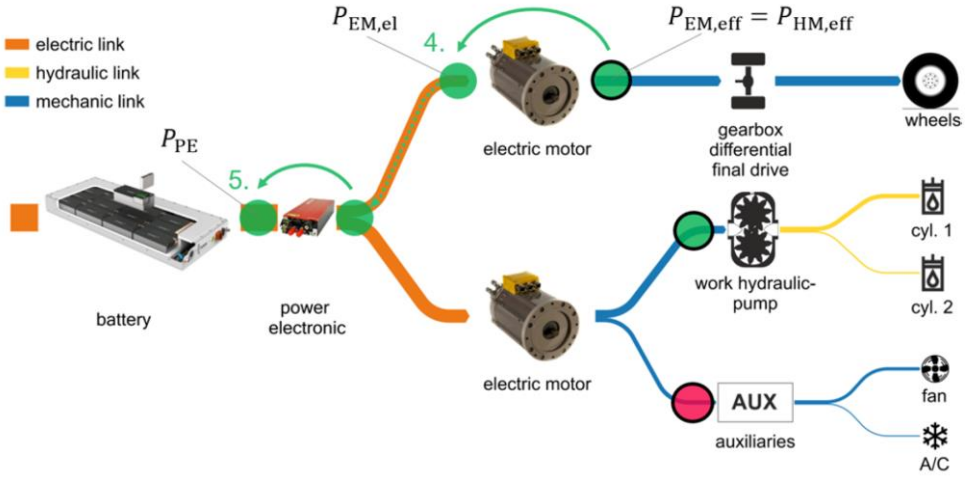
Paralel Hibrit Tahrik Sistemi: Tahrik elektrik motoru ya da içten yanmalı motor ile sağlanır.

Kompleks (Karışık) Hibrit Tahrik Sistemi: Bu sisteme karışık hibrit denmesinin nedeni seri paralel sistemde kullanılan jeneratörün yerine gerektiğinde motor gerektiğinde jeneratör

olarak çalışan bir elektrik makinesiyle değiştirilmiş olmasıdır. [MEPEG Motorlu Araçlar Teknolojisi Alanı, 2014] [MERKISZ, J., PIELECHA, I., 2015] [KALOCIŃSKI, T., 2022]

1.2. Elektrik

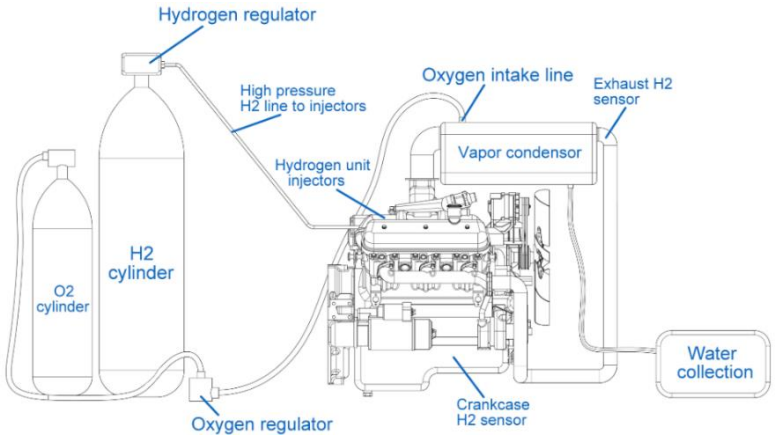
Sistem açısından bakıldığında, güç aktarma organı elektrifikasyonu söz konusu olduğunda tam bir elektrik mimarisi en basit çözümdür. Şekil 3' de gösterildiği gibi, tam bir elektrik mimarisi, araca uygulanan tüm olası mekanik yükleri sürmek için kullanılan tek bir güç kaynağından oluşur: aktarma organları, hidrolik sistem ve tüm PTO'lar (Güç-Kalkış) elektrikle çalıştırılır. Bir elektronik dönüştürücü vasıtasıyla, önceden bir pil paketinde depolanan elektrik enerjisi (DC voltajı ve akımı), kurulu elektrik motoruna (EM) alternatif voltaj ve akım (AC) sağlayacak şekilde düzenlenir.



Şekil 3 Tam Batarya Elektrik İş Makinesinde Güç Aktarım Yapısı [Ratzinger J.M. ve arkadaşları 2021]

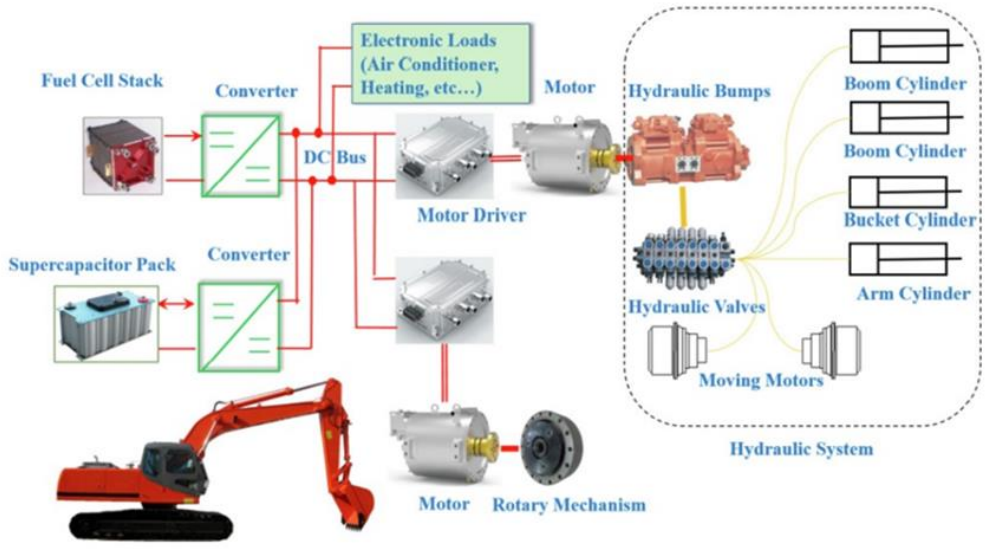
1.3. Hidrojen

Yapılan araştırmalar ışığında genel olarak iş makineleri sektöründe “Hidrojen Yakıt” temelli 2 farklı sistem görülmüştür. İçten yanmalı motorlarda hidrojen kullanımı temelde kimyasal enerjinin mekanik enerjiye dönüştürülmesidir. Hidrojen yakıt sisteminin menzil kapasiteleri elektrikli araçlara göre daha yüksektir. 5 litre hacimli tam dolu depo ile ortalama 65 KW güc ihtiyacı duyan bir araç için tekrar yakıt doldurmaksızın 450 km menzil sağlar. Bu değer iş makineleri kullanım saati için bir veri bulunamasa da elektrikli araçlar için karşılaştırıldığında daha uzun süreli bir kullanım sunacağı düşünülmektedir. Buji ateşlemeli motorlar, büyük modifikasyonlar gerektirmeden hidrojenle çalıştırılabilir. Daha yüksek bir hidrojen yakma hızı, yanmayı iyileştirir ve daha yüksek fren termal verimliliğine izin verir [Subash,2011]. Sistem elemanları ve çalışma yapısı Şekil 4’de gösterilmiştir. İçten yanmalı motorlarda hidrojen beslemesi, optimum koşullar altında %50'nin üzerine çıkabilen CO2, CO, HC ve duman seviyelerinde önemli azalmalar göstermiştir [Seyed Ehsan Hosseini & Brayden Butler, 2019].



Şekil 4 Kapalı Sistem İçten Yanmalı Hidrojen Motor [POCHARI, 2019]

Yakıt Hücresi teknolojisinde ise temelde kimyasal enerjinin elektrik enerjisine dönüşümü ve sonrasında mekanik işe çevrilmesi ile hareket sağlanır. Yakıt hücresinde, hidrojen tankında gelen H2, açık hava ortamından karşılanan oksijen ile teması sonucu elektroliz yöntemi kullanılarak elektronlarının koparılmasıyla elektrik açığa çıkar. Bu enerji ile elektrik motoru beslenir. Tipik bir yakıt hücreli (YH) iş makinesinin önerilen sistemi Şekil 5'de gösterilmiştir. Genel şeması şu şekildedir; ataşmanları besleyen hidrolik sistem ve yürüyüşe tahriki sağlayan güç kaynakları olarak sistem iki kısma ayrılmıştır. Enerji depolama cihazları olarak süperkapasitör ve bataryalara ihtiyaç duyulmaktadır. YH ünitesi, iş makinesinin ani yük taleplerine anında yanıt veremez bu yüzden sistemde süperkapasitör kullanılmaktadır [Tri Dung Dang, Yingxiao Yu, 2019]. Aynı zamanda, salınım aşaması sırasında yerçekimi kuvveti ve frenleme enerjisi ile aşağı doğru hareket ederken bom ve arm silindirlerinden enerjiyi geri kazanabilmek için bir batarya ünitesi mevcuttur [T. Li ve arkadaşları 2018].



Şekil 5 Yakıt Hücresinin Ekskavatörlerde Kullanım Şeması [T. Li ve arkadaşları, 2019]

2. ALTERNATİF YAKITLARIN İŞ MAKİNELERİNDE KULLANIMI

Günümüzde birçok ülke çevre dostu bir algı düzenine geçiş yapmak ve bununla birlikte net sıfır emisyon olgusunu gerçekleştirmek için çalışmalar sürdürmektedir. Bu minvalde iş makineleri sektörü de etkin olarak pillere ve hidrojene dayalı elektrik teknolojilerine yönelik çevre dostu ürünler geliştirmektedir. Bu gelişim süreci Avrupa'da kompakt boyutlu ekipmanlarla başlasa da Amerika ve Asya ülkelerinde orta ile büyük boyutlu ekipmanlara doğru genişlemektedir. Ürün bazlı oluşturulan başlıklar ile yürütülen çalışmalar aşağıdadır.

2.1. Ekskavatör

Orta ve küçük sınıflarda yer alan ekskavatörlerden hidrojen ile çalışan modellerin ARGE çalışmalarına devam edilmektedir. Bunun yanı sıra elektrik ve hibrit modellerle ticarileşen iş makineleri hızla çeşitlenmektedir.



Şekil 4 Hidromek Hicon 7W [Hidromek, 2020]

İş makinesi üreticisi Hidromek, elektrikli iş makineleri konusunda uzmanlaşmak ve ürün portföyünü genişletmek konusunda ciddi kararlar almış ve elektrikli iş makinelerini kategorize etmek amacıyla HİCON alt markasını kurmuştur. Bu markanın ilk modeli de Hidromek Hicon 7W. Çevre dostu ve endüstri 5.0 doğrultusunda teknolojilerle benzenmiş %100 elektrikli ve yerli üretim bir şehir ekskavatörü olarak tasarlanmıştır. Enerjisini yeni nesil Lityum-İon bataryalar ile depolayan Hicon, enerji verimliliği konusunda %97 daha verimli bir çalışma sistemine sahiptir. İşletme maliyetleri olarak yakıt ve servis konusunda çok daha avantajlı olan iş makinesi, bakım maliyetleri olarak dizel iş makinelerine göre çok daha ekonomiktir. Tam şarj ile 8 saat aralıksız çalışma yapabilmektedir [Hidromek, 2022].

Japonya menşeili iş makinesi üreticisi, 2008 yılında dünyanın ilk ticari hibrit ekskavatörünü geliştirdi. Hibrit mimarisi nedeniyle dizel motor 6 silindirden 4 silindire küçültülebilmektedir.

Üreticinin hibrit modelinde, elektrikli döner motor/jeneratör, üst yapı yavaşlarken enerjiyi yakalar ve yeniden üretir ve onu elektrik enerjisine dönüştürmektedir.



Şekil 5 Komatsu Hibrit Ekskavatör [Komatsu, 2022]

Yakalanan enerji, ultra kapasitörde depolanır ve hızlanması gerektiğinde motora yardımcı olmak için jeneratör/motor tarafından kullanılmaktadır. Ultra kapasitör tertibatı, kondansatörde depolamak için jeneratör motorundan ve döner motordan AC elektriği DC elektriğe çeviren bir invertör içerir. Kondansatörler, şarj ve deşarj için elektronların ve iyonların geçişini gerektirdiğinden, elektrik üretmek için kimyasal reaksiyonlar kullanan pillerden çok daha hızlı güç aktarabilirler. Ayrıca üretici firma, hibrit mimarisiyle yakıt tüketiminde %25-41 arasında azalma olduğunu iddia etmektedir [Komatsu, 2022], [KALOCIŃSKI, T., 2022].



Şekil 6 JCB ve Hyundai Hidrojen Ekskavatör [JCB, 2022] [Hyundai CE, 2021]

Son yıllarda çeşitli üreticiler prototip olarak başlatmış oldukları hidrojen içten yanmalı motor çalışmalarında yaklaşık olarak 100 kW gücünde olan dizel motorlarına eş değer güç ve tork değerleri elde etmişlerdir. 2 yıldan uzun bir süredir saha çalışmalarına ve testlere devam edilen ekskavatör modellerinden biri 22-ton ağırlığındadır [JCB, 2022]. Bunun yanı sıra 14-ton lastikli ekskavatör için Yakıt Hücreli sistemin kullanıldığı başka bir çalışma devam etmektedir. 2021 yılında bir fuarda tanıtılan bu çalışma 95 kW çıkış performansına sahip

olduğu iddia edilmektedir. Çalışmayı yürüten üretici firma, lityum pilleri için, pil kapasitesini artırmaya yönelik çeşitli girişimleri sınırlayan yapısal sorunları dile getirmiş ve hidrojen yakıt hücrelerinin genişletilmesinin çok daha kolay olduğunu vurgulamıştır [Hyundai CE, 2022].

2.2. Kazıcı Yükleyici

Tam elektrikli kazıcı yükleyiciler günlük işletme maliyetlerini önemli ölçüde düşürecek, sıfır emisyon üretecek, bakım taleplerini azaltacak ve elektrikli ekipman/araçlarla çalışmak için yerel/proje bazlı teşvikleri karşılayacaktır. İlk yatırım maliyeti daha yüksek olsa da müşterilerin işletme maliyetleri göz önünde bulundurulduğunda yaklaşık olarak beş yıl içinde yatırım ücretini amorti edeceği öngörülmektedir.



Şekil 7 CASE Zeus [CASE, 2022]

İlk olarak tam elektrikli kazıcı yükleyici çalışması 2020 yılında tanıtılmıştır. Bu çalışmada iş makinesi, herhangi bir 220 volt/üç fazlı bağlantıyla şarj edilebilen 480 volt, 90 kilowatt-saatlik bir lityum-iyon pil paketi ile çalışmaktadır. Uygulamalar değişiklik gösterse de her bir şarjda ortalama sekiz saatlik çalışmayı desteklemektedir. Batarya, aktarma organları ve hidrolik motorlara ayrı ayrı güç sağlamaktadır. Bu da dizel motorlu makinelere eşit hidrolik koparma kuvvetleri ve aynı anda yükleyici ve aktarma organları çalışması sırasında iyileştirilmiş performans göstermektedir. Böylece, operatörler dizel motorlu bir makinede elde edilen aynı kazma, yükleme ve kaldırma performansını daha sessiz, emisyonsuz bir çalışma alanında deneyimleyebilecektir [CASE, 2022].



Şekil 8 HUDDIG TIGON [HUDDIG, 2021]

Yakın zamana kadar, iş makineleri için hibrit hidrolik tahrikler, genellikle içten yanmalı bir motorla çalışan hidrolik tahrik ve mekanik tahrik kombinasyonu anlamına geliyordu. Ancak, mobil hidrolik sistemleri çalıştıran elektrik motorlarının sürekli gelişmesiyle birlikte, hibrit aynı zamanda bir hidrolik-elektrikli tahrik kombinasyonu anlamına da geliyor. İsveç kökenli kazıyıcı yükleyici üreticisinin hibrit çalışmalarında, dinamik elektronik hız değiştirme, entegre park ve servis frenlerine sahiptir. Sürüş paketi, elektrik motorunun güç çıkışında tam olarak yararlanmaktadır. Entegre hız kaydırma, motoru her zaman maksimum verimlilik için optimum hız aralığında çalıştırmaktadır. Sıvı soğutmalı 30 kW'lık bir elektrik motoruyla tahrik edilen her bir tekerlekten, 40.000 Nm'lik bir çıkış torku üretebilmektedir. Her tekerleğin hızının ve torkunun bağımsız kontrolü, özellikle çekişin zor olacağı kaygan ve eğimli yüzeylerde kullanışlı olduğu belirtilmektedir. Üretici yetkilileri, dizel ve elektrik gücünü birleştiren tam hibrit teknolojisinin, iş makineleri için daha önce hiç mümkün olmayan bir şekilde enerji üretip yeniden ürettiğini belirtmektedir. Teknoloji daha yüksek verimlilik ve performans üreterek daha düşük yakıt tüketimi, daha yüksek tork, daha sessiz bir makine ve daha çevre dostu bir çalışma yöntemi sağlar [HUDDIG, 2022] [PM, 2018].



Şekil 9 JCB Hidrojen Kazıcı Yükleyici [JCB, 2021]

İş makineleri üreticileri tarafından, pillerin yüksek güç gerektiren ekipmanlar ve kazıcı yükleyiciler gibi uzak yerlerde çalışan makineler için pratik olmadığı düşünülmektedir. Mevcut alt yapı olanaklarıyla, yerinde şarj edilebilir olsa bile piller çok ağır, pahalı ve iş makinelerinin şarj edilme sürelerinin fazla olmasından ötürü elverişli bulunmamaktadır. Halihazırda mevcut bileşenlerle yerleşik motor teknolojisini kullanarak ve uyarlayarak, hidrojen yakılır ve güç, bir dizel motorla tamamen aynı şekilde sağlanabilmektedir. Bu noktada, iş makineleri sektörüne hizmet veren İngiltere menşeili üretici firma, 2021 yılında hidrojen ile çalışan ve 70 kW güç

üreten motor geliştirildiğini bildirmektedir. Aynı zamanda, bu yeni hidrojen motoruyla donatılmış prototip kazıcı yükleyici dizel eşdeğerinin yapabileceği tüm kabiliyetlere sahiptir. Dahası, teknoloji hidrojen yakıt hücresi teknolojisinden çok daha az karmaşıktır. Egzoz borusundan su buharından başka bir şey çıkmamaktadır [JCB, 2021] [DP, 2021].

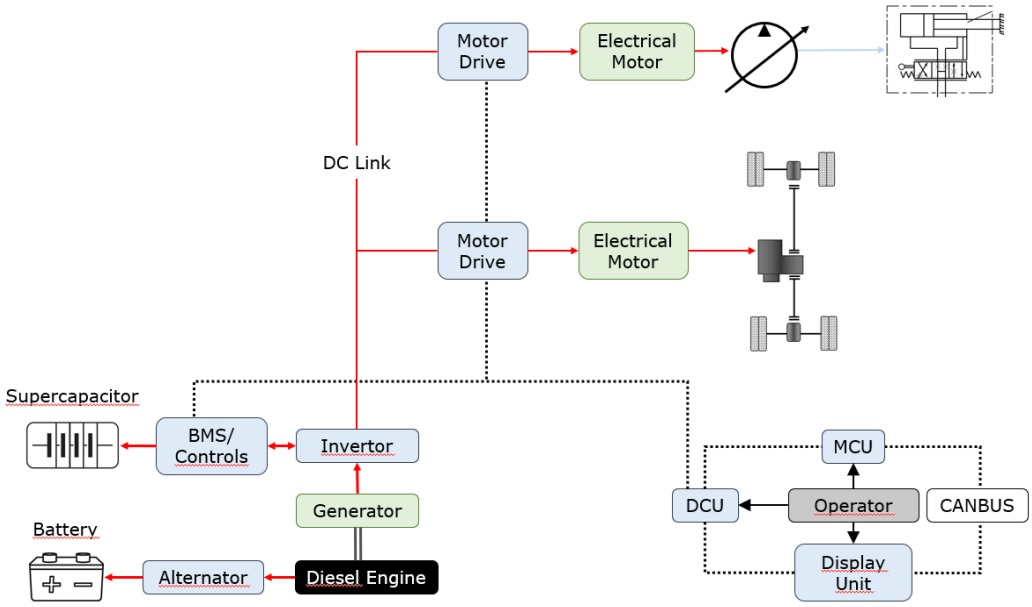
3.3 Lastikli Yükleyici

Enerji kullanımı ve çevre duyarlılığı konusunda tüm dünyada takip edilen stratejiler göz önünde bulundurulduğunda, emisyon seviyeleri ve enerji geri kazanımı ön plana çıkmaktadır. HİDROMEK de pazardaki durumunu daha ileri seviyeye taşımak için birçok teknolojik proje yürütmektedir. Söz konusu proje ile lastikli yükleyici sınıfında Türkiye'de ilk olacak ''Hibrit Lastikli Yükleyici'' iş makinasının hayata geçirilmesi hedeflenmektedir. Bu projede makinenin üretkenliğinden ödün vermeksizin, daha yüksek verimliliğe, düşük yakıt tüketimine ve gürültü seviyesine sahip hibrit lastikli yükleyici makine tasarımı amaçlanmıştır. Konvansiyonel makinelerde dizel motor sürekli değişen ve verimliliğinin düşük olduğu yüksek hızlarda çalıştırılmak durumundadır.



Şekil 10 Hidromek 640 Lastikli Yükleyici [Hidromek, 2022]

Hibrit makinede dizel motor daha stabil ve verimliliğin en yüksek olduğu hız aralığında çalıştırılabilecektir. Aynı kaynaktan (dizel motordan) iki farklı kullanıcının (güç aktarım paketi ve hidrolik sistem pompalarının) sürülmesi makine gelen verimliğini ayrıca düşürmektedir. Hibrit makinede iki ayrı kullanıcı (güç aktarım paketi ve hidrolik sistem pompaları), birbirinden bağımsız elektrik motorları tarafından sürülebilecek ve daha verimli çalışması sağlanacaktır. Tipik lastikli yükleyici çalışma koşullarında fren sistemi sık sık ve yoğun olarak kullanılması gerekmektedir. Frenleme esnasında aracın kinetik enerjisi ısıya dönüşerek atmosfere atılmaktadır. Hibrit yükleyici makinede fren sisteminden geri kazanılan enerji süper kapasitörlerde depolanarak tekrar faydalı işe dönüşmek üzere sistemde kullanılabilecektir, ayrıca sistemin anlık yüksek güç ihtiyaçlarını karşılayarak motorun düşük verimli yüksek devirde çalışması engellenecektir.



Şekil 11 Hidromek hibrit lastikli yükleyici genel yerleşim ve haberleşme modeli [Katmer, M. C. ve arkadaşları, 2021]

Lastikli yükleyici makinelerde kullanılan tork çeviriciler (hidro-dinamik kavrama) yaklaşık %70 verimlilikte çalışmaktadır. Motor volanından alınan enerjinin yaklaşık %30' u faydalı işe dönüştürülmeden şanzıman yağ soğutucusu ile atmosfere ısı olarak atılmaktadır. Hibrit makinede tork çeviricili bir şanzımana ihtiyaç kalmamaktadır. Elektrik motorları şanzımanı direkt olarak tahrik edebilmektedir.

İsveç kökenli iş makineleri üreticisi firma, iş makineleri için sıfır emisyonlu teknolojilerin dağıtımını hızlandırmak amacıyla şantiyelerde pille çalışan Elektrikli kompakt tekerlekli yükleyicisini neredeyse bir yıldır test etmektedir. Hali hazırda satışa sunulan makinenin 400 saatlik kullanımda, aynı şartlarda yer alan başka bir dizel motorlu makinelere göre 6000 kg karbondioksit emisyonunda azalma ve 2100 litre kadar yakıt sağladığı ifade edilmektedir.



Şekil 12 Volvo L25 Elektrikli Kompakt Lastikli Yükleyici [Volvo CE, 2021]

Ayrıca yağ, yağ filtreleri ve dizel partikül filtreleri gibi bakım gerektirmeyen elektrikli makinelerin bakım ihtiyaçlarının azaldığı yönünde de olumlu geri dönüşler belirtilmiştir. Dizel egzoz sıvısı (DEF) deposu ihtiyacı da ortadan kalkmıştır. Projenin sonunda kaldırma, yükleme ve boşaltma performansları dahil olmak üzere birçok önemli alanda dizel performansıyla eş değerler elde edilmiştir [Volvo CE, 2021].

3. SONUÇ VE ÖNERİLER

Bu çalışma ile gerçekleştirilen tüm araştırma ve değerlendirmeler sonucunda, iş makinesi tasarımında alternatif yakıt teknolojileri kullanımına ilişkin güncel ve uygulanabilir teknikler derlenmiştir. Yapılan çalışmanın, iş makinesi sektörünün yakın gelecekte alternatif yakıt kullanımında karşılaşması muhtemel tasarım kriterleri adına ışık tutacağı düşünülmektedir.

İş makinesi sektöründe elektrikli ve hibrit araçlara doğru bir evrim söz konusu fakat batarya sürelerinin kısa, şarj sürelerinin uzun olması ve altyapı eksikliği (şarj istasyonları) kullanıcı için dezavantaj yaratmaktadır. Ayrıca elektrik komponentleri yaygınlaşmadığı için maliyet olarak standart tahrik sistemlerinden oldukça maliyetlidir. Belirtilen eksiklikler giderildiğinde sıfır emisyonlu, çevre dostu iş makineleri kullanımının artması beklenmektedir. Elektrik ve hibrite paralel olarak dünya hidrojene odaklanmış durumda ve hidrojene yapılan yatırımlar günden güne artmaktadır. Elektrikli ve hibrit araçların aksine depo dolum süreleri kısa ve çalışma saatlerinin uzun olması kullanıcı için daha iyi bir seçenek olarak görünmektedir fakat yeterli altyapıya sahip değildir. Hidrojenin sıvılaşma sıcaklığının çok düşük, basıncının çok yüksek olmasından dolayı gaz halinde depolanmaktadır. Bu sebeple tank hacminin büyük olması bir dezavantajdır. İş makinesi imalatçılarının en büyük problemlerinden biri de sınırlı alanlar içerisine komponent yerleşimidir. Bu sebeple büyük hidrojen tanklarının makine üzerine yerleşimi üreticileri zorlayacaktır. Gelişen kompozit teknolojisi ile bu problem de çözüldüğünde kullanıcılar için en uygun yakıt haline gelmesi ön görülmektedir. Yenilenebilir kaynak olarak hiç tükenmeyecek bir yakıt olan hidrojen, sıfır emisyon ile çevre dostu iş makineleri üretiminde geleceği şekillendirmesi beklenmektedir.

KAYNAKÇA

1. **Huang, L., Krigsvoll, G., Johansen, F., Liu, Y., Zhang, X., (2018),** "Carbon emission of global construction sector ". Renew. Sustain. Energy Rev. 81, 1906–1916.
2. **IEA (2018).** "Renewable electricity generation by source, world 1990–2018". Ishida, K., Higurashi, M., 2015. Hybrid wheel loaders incorporating power.
3. **İnternet: BNEF (2022).** "Europe's Path to Clean Energy: A $5.3 Trillion Investment Opportunity", Web: https://about.bnef.com/blog/europes-path-to-clean-energy-a-5-3-trillion-investment-opportunity/, Son Erişim Tarihi: 18.06.2022.
4. **European Commission (2021),** "A European Green Deal: Striving to be the First Climate- Neutral Continent by 2050."
5. **KALOCIŃSKI, T., (2022),** Modern trends in development of alternative powertrain systems for non-road machinery. Combustion Engines. 188(1), 42-54
6. **MERKISZ, J., PIELECHA, I., (2015),** Układy mechaniczne pojaz-dów hybrydowych. Wydawnictwo Politechniki Poznańskiej. Poznań.
7. **MEPEG Motorlu Araçlar Teknolojisi Alanı., (2014),** Alternatif Yakıtlı Motorlar, Ankara.
8. **European Commission, (2014),** Procedure 2014/0268/COD, COM(2014) 581 final, Proposal for a regulation of the European parliament and of the council on requirements relating to emission limits and type-approval for internal combustion engines for non-road mobile machinery, 2014.
9. **Ratzinger J.M.,Buchberger S., Eichlseder H., (2021),** '' Electrified powertrains for wheel-driven non-road mobile machinery '' Automotive and Engine Technology 6:1–13
10. **Hosseini S.E., Butler B., (2019),** An overview of development and challenges in hydrogen powered vehicles, International Journal of Green Energy, DOI: 10.1080/15435075.2019.1685999
11. **Subash, G.P., Das, L.M., (2011),** An experimental investigation on the performance and emission characteristics of a hydrogen fueled spark ignition engine. Int. J. Sci. Technol. Manag., 197–208.
12. **İnernet: Pochari Technologies, (2019),** Web: https://pocharitechnologies.com/2019/03/01/closed-cycle-hydrogen-internal-combustion-engine-technology/ , Son Erişim Tarihi:21.06.2022
13. **Dang T. D., Yu Y., (2019),** Design, Modeling and Analysis of a PEM Fuel Cell Excavator with Supercapacitor/Battery Hybrid Power Source Journal of Drive and Control, Vol.16 No.1 pp.45-53.
14. **T. Li, H. Liu, D. Ding, (2018),** "Predictive energy management of fuel cell supercapacitor hybrid construction equipment," Energy, Vol.149, pp.718-729.
15. **T. Li, L. Huang, H. Liu, (2019),** "Energy management and economic analysis for a fuel cell supercapacitor excavator," Energy, Vol.172, pp. 840-851.

16. **Biyodizel Sanayi Derneği**, ‘’BİYODİZEL ENDÜSTRİ RAPORU 1’’
17. **Akyaz, S., (2007),** Benzin–tersiyer bütil alkol ve benzin naftalin karışımlarının buji ateşlemeli motorun performansına ve egzoz emisyonlarına etkisinin deneysel olarak incelenmesi, Yüksek Lisans Tezi, Karadeniz Teknik Üniversitesi Fen Bilimleri Enstitüsü.
18. **Özer ve Özdalyan, (2013),** Dizel yakıtı-alkol karışımlarının doğrudan dizel motorlarında kullanılması (Sayın; Huang ve ark. 2009; Ejder 2008;).
19. **İnternet: Hidromek, (2022),** “%100 Elektrikli Bir Şehir Ekskavatörü!” Web: https://hiconbyhidromek.com/tr/products/7w/ , Son Erişim Tarihi: 20.06.2022
20. **İnternet: Komatsu, (2022),** “Hybrid Crawler Excavators HB365LC/NLC-3 Hybrid”, Web: https://www.komatsu.eu/en/excavators/crawler-excavators/hybrid-crawler-excavators/hb365lcnlc-3-hybrid/, Son Erişim Tarihi: 20.06.2022
21. **İnternet: JCB, (2021),** “SUPER-EFFICIENT JCB HYDROGEN ENGINE GETS £100 MILLION INJECTION”, Web:https://www.jcb.com/en-gb/news/2021/10/jcb-hydrogen-engine-gets-100m-injection/, Son Erişim Tarihi: 20.06.2022.
22. **İnternet: DP, (2021),** “JCB develops hydrogen-fueled engine”, Web: https://www.dieselprogress.com/news/JCB-develops-hydrogen-fuelled-engine/8012602.article/, Son Erişim Tarihi: 20.06.2022.
23. **İnternet: Hyundaı CE, (2021),** “Eco-friendly is the trend in construction sites! ‘Hydrogen Wheel Excavator’ by HCE”, Web:https://www.hyundai-ce.com/en/media/englishNews/506 /, Son Erişim Tarihi: 20.06.2022.
24. **İnternet: CASE, (2022),** “CASE UNVEILS “PROJECT ZEUS” — THE ALL-NEW 580 EV — THE INDUSTRY’S FIRST FULLY ELECTRIC BACKHOE LOADER”, Web: https://www.casece.com/northamerica/en-ca/resources/articles/media-case-unveils-project-zeus-580ev-first-fully-electric-backhoe-loader /, Son Erişim Tarihi: 20.06.2022.
25. **İnternet: HUDDIG, (2021),** “The world's first hybrid backhoe loader HUDDIG TIGON on the market”, Web: https://www.huddig.com/updates/press/the-world-s-first-hybrid-backhoe-loader-huddig-tigon-on-the-market/, Son Erişim Tarihi: 20.06.2022.
26. **İnternet: PM, (2018). “**Backhoe Loader Relies on Hybrid Hydraulic Drive”, Web: https://www.powermotiontech.com/hydraulics/hydraulicpumpsmotors/article/21887634/backhoe-loader-relies-on-hybrid-hydraulic-drive/, Son Erişim Tarihi: 20.06.2022.
27. **Küçük, K., Katmer, M. C., Genç, İ., Varlı, T., Karahan, M., Fıçıcı, F., (2021),** Hibrit Yükleyici Mimari Yapısının Oluşturulup, Gereksinimlerinin Belirlen-mesi ve Tasarımı, INTERNATIONAL SYMPOSIUM ON AUTOMOTIVE SCIENCE AND TECHNOLOGY, Ankara.
28. **İnternet: Volvo Ce, (2021).** “ELECTRIC COMPACT WHEEL LOADER VOLVO L25 ELECTRIC”, Web: https://www.volvoce.com/europe/en/products/electric-machines/l25-electric/#features/ , Son Erişim Tarihi: 21.06.2022

TÜP HİDROŞEKİLLENDİRMEDE YÜKLEME PROFİLLERİNİN BULANIK MANTIK KONTROL ALGORİTMASI İLE BELİRLENMESİ

Yusuf Furkan YAPAN, *yapan@yildiz.edu.tr* Yıldız Teknik Üniversitesi, 34349, İstanbul

Mevlüt TÜRKÖZ, *mturkoz@ktun.edu.tr* Konya Teknik Üniversitesi, 42250, Konya

Murat DİLMEÇ, *muratdilmec@erbakan.edu.tr* Necmettin Erbakan Üniversitesi,42090, Konya

Hüseyin Selçuk HALKACI, *halkaci@ktun.edu.tr* Konya Teknik Üniversitesi, 42250, Konya

ÖZET

Bu çalışmada, dövme yöntemiyle üretilmesi problemli olan otomobil salıncak bağlantı parçasının Tüp Hidroşekillendirme (THŞ) prosesiyle üretilmesi için gerekli basınç ve eksenel besleme yükleme profilleri, sonlu elemanlar analiziyle birlikte Bulanık Mantık Kontrol Algoritması (BMKA) ile elde edilmiştir. 3 mm kalınlıklı St 37 malzeme borudan salıncak parçası üretilecek şekilde THŞ sonlu elemanlar modeli ve bulanık mantık kontrol algoritması oluşturulmuştur. Hasar kriteri olarak; yüzde incelme, kalıp dolum oranı ve yüzde buruşma yüksekliği olmak üzere üç adet giriş değişkeni kullanılmıştır. Çıkış değişkeni basınç artış miktarı olarak belirlenmiştir. BMKA ile elde edilen yükleme profili ile deneme-yanılmayla elde edilen profil karşılaştırılmıştır. BMKA ile elde edilen eğrinin avantajları ve parça kalitesine etkisi ortaya konulmuştur.

Anahtar Kelimeler: Bulanık mantık, tüp hidroşekillendirme, yükleme profili

ABSTRACT

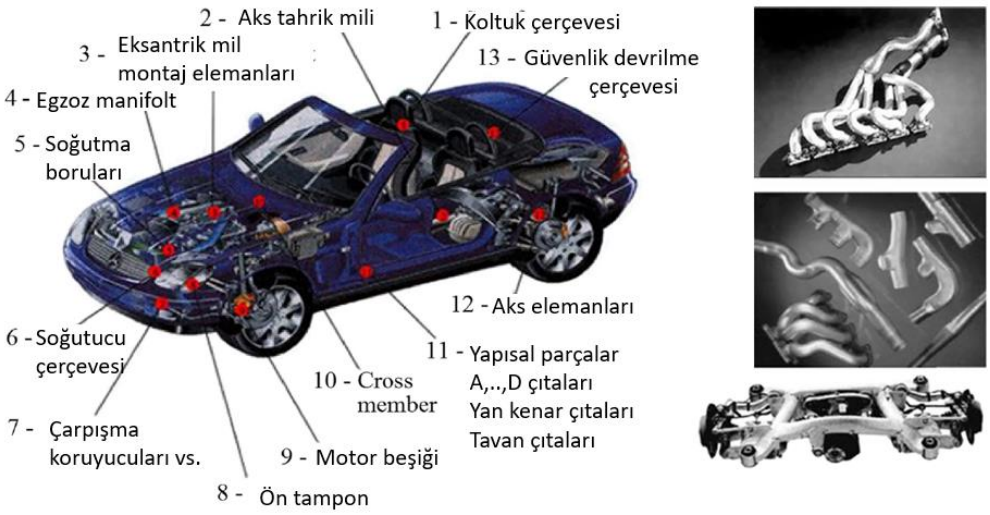
In this study, the pressure and axial feeding loading profiles required for the production of the automobile suspension bushings inner tube part, which is problematic to be produced by the forging method, were obtained with the Fuzzy Logic Control Algorithm (FLCA) together with the FEA by the Tube Hydroforming (TH) process. FEA and FLCA of the TH were created to produce bushing part with 3 mm thick St 37 material pipe. As a damage criterion; three input variables were used: % thinning, die filling ratio and % wrinkling height. The output variable is determined as the amount of pressure increase. The loading profiles obtained by FLCA and the profile obtained by trial and error were compared. The advantages of the curve obtained with FLCA and its effect on the part quality were presented.

Keywords: Fuzzy logic, tube hydroforming, loading profile

1. GİRİŞ

İleri bir imalat yöntemi olan hidroşekillendirme prosesi, sac veya boru şeklindeki malzemelerin sıvı basıncı yardımıyla şekillendirilmesinde kullanılan bir imalat yöntemidir. Bu yöntem, özellikle şekillendirilebilirlikte artış kabiliyeti nedeniyle otomotiv, uzay ve savunma sektörlerinde kullanılmaktadır. Hidroşekillendirme prosesi şekillendirilebilirlikte artışın yanında kalıp maliyetlerinde azalma, ağırlık tasarrufu, daha üniform kalınlıkta ürün elde edilmesi, parça konsolidasyonu, yüzey kalitesinde ve boyutsal doğrulukta artış, karmaşık geometrilerin tek kademede üretilebilmesi gibi avantajları nedeniyle tercih edilmektedir [Koç, 1998; Xu, 2004; Halkacı, 2014]. Üretim prosesinin hızlı olmaması ve hidroşekillendirme preslerinin fiyatlarının yüksek oluşu nedeniyle, bu proses genellikle az sayıda veya teknolojik avantajı yüksek parçaların üretiminde kullanılmaktaydı ancak hidrolik alanındaki gelişmelerle birlikte günümüzde seri üretimde de kullanılmaktadır. Bu avantajlara rağmen prosesin karmaşık oluşu ve uygulama bilgisinin eksikliği nedeniyle ülkemizde yaygın olarak kullanılmamaktadır.

Hidroşekillendirme imalat yöntemlerinden tüp hidroşekillendirme (THŞ), boru şeklindeki malzemelerin akışkan bir ortamın uyguladığı iç basınç ve/veya eksenel kuvvet etkisinde şekillendirilmesidir. Bu proses, son yıllarda otomotiv parçalarının şekillendirilmesi için geliştirilmiş [Schultz, 1999; Carpenter, 2004] ve daha kaliteli ürünlerle beraber parça sayısı azaltılarak daha hafif otomobillerin üretimi mümkün kılınmıştır [Wang, 1994]. THŞ ile üretilen bazı otomotiv bileşenlerinin (manifoldlar, borular, miller, dönen motor bileşenleri, tamponlar, motor beşikleri ve yapısal elemanlar) örnekleri Şekil 1'de verilmiştir [Bell, 2019].



Şekil 1. THŞ çeşitli otomotiv uygulamaları [Bell, 2019]

THŞ proses çıktısına etki eden parametreler çoğunlukla malzeme, geometri, sürtünme ve yükleme profilidir (sıvı basıncı ve eksenel besleme miktarı). Eksenel besleme düşük, iç basınç yüksekse yırtılma meydana gelir. Eksenel besleme yüksek, iç basınç düşükse

buruşma oluşur ve istenilen kalitede ürün elde edilmez. Genellikle müşterilerin isteği doğrultusunda geometri ve malzemede büyük çaplı değişiklikler yapılamaz ancak iç basınca karşılık eksenel besleme miktarında (yükleme profili) değişiklik yapılarak istenen ürün elde edilebilir. THŞ yükleme profilinin belirlenmesi, prosesin en önemli adımıdır. Eksenel besleme düşük, iç basınç yüksekse yırtılma meydana gelir. Eksenel besleme yüksek, iç basınç düşükse buruşma oluşur ve istenilen kalitede ürün elde edilmez. Bu sebepten dolayı başarılı bir şekillendirme için yükleme eğrisinin optimum şekilde ayarlanması gerekmektedir. Literatürde, THŞ prosesi için gerekli uygun yükleme profillerinin belirlenmesi kapsamında çeşitli çalışmalar mevcuttur. Bu çalışmalar genellikle, günümüzde çok yaygın olarak kullanılan Sonlu Elemanlar Analizi (SEA) yazılımlarında yapılan deneme ve yanılma yöntemini içermektedir.

Bu yöntem ile SEA yazılımına farklı yükleme profilleri girilmektedir ve yapılan analizler sonucunda genelde boru malzemede buruşma ve/veya patlama olup olmadığı kontrol edilmektedir. Eğer malzemede buruşma veya patlama gözlemlenirse, daha önceden girilen yükleme profilleri birbirinden bağımsız bir şekilde değiştirilip tekrar yazılıma girilmektedir. Bu işleme başarılı bir THŞ prosesi elde edilene kadar devam edilmektedir. Yani tüp hidroşekillendirme deneylerinin yapılmasının zor olması kadar sonlu elemanlar yazılımlarında kullanılan deneme ve yanılma yöntemi de büyük bir iş gücü, maliyet ve zaman gerektirmektedir. Deneme ve yanılma metodunun bu dezavantajını ortadan kaldırmak için uygun yükleme profilleri, SEA yazılımları ile birlikte çalışan çeşitli kontrol algoritmaları ile belirlenmektedir. Bu kontrol algoritmaları ise buruşma veya yırtılma gibi erken hasar durumlarının belirlenmesi ve bu durumlardan kaçınılması için yapılmaktadır. Aynı zamanda bu algoritmalar, sıvı basıncı ve eksenel besleme miktarı gibi proses parametrelerinin uygun değerlerinin bulunması için kullanılmaktadır. Bu tarz proses simülasyonu, proses parametrelerinin şekillendirme boyunca yeni koşullar altında sürekli olarak güncellendiği için adaptif proses simülasyonu olarak adlandırılmaktadır [Aydemir ve ark., 2005].

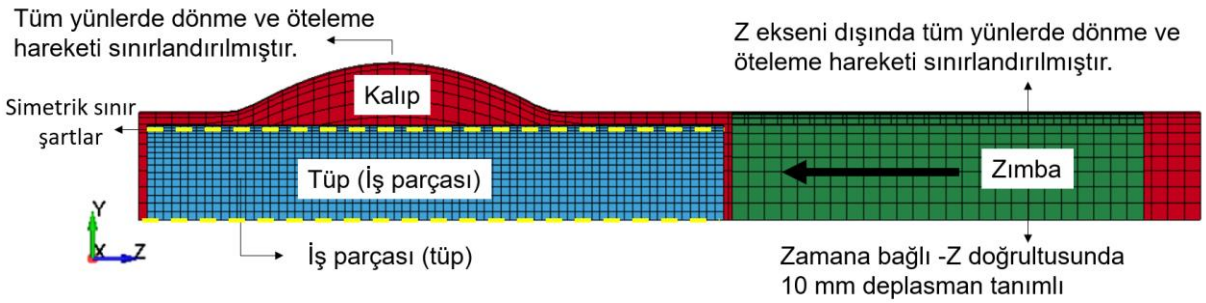
Zhou ve Cheng (2009) çalışmalarında MATLAB bulanık mantık araç kutusu alt program olarak kullanılmıştır. AA3003 Alüminyum boru malzeme kullanılmıştır. Simülasyon işlemi 20 aşamaya bölünmüş ve her simülasyon aşaması bittikten sonra simülasyon sonucuna göre giriş değişkeni elde edilmiştir. Girdi değişkeni bulanık mantıksal kontrol sistemine aktarılmıştır ve çıktı değişkeni elde edilmiştir. Daha sonra çıktı değişkeni simülasyon yazılımına geri yüklenmiştir ve bir sonraki simülasyon adımı buna göre ayarlanmıştır. Son olarak, simülasyon süreci yeniden başlatılmış ve simülasyon sırayla hesaplanmıştır. Bu çalışmada iki giriş değişkeni bir çıkış değişkeni kullanılmıştır. Çıkış değişkeni olarak eksenel besleme seçilmiştir ve iç basınç doğrusal bir şekilde arttırılmıştır.

Lorenzo ve ark. (2004) çalışmalarında 1.5 mm et kalınlığına sahip 40 mm çapında AA6060-T5 alüminyum tüpün, ortasında 56 mm genleşme bölgesi bulunan eksenel simetrik tüpün hidroşekillendirilmesini incelemişlerdir. Bu kapsamda bulanık mantık kontrollü adaptif sonlu elemanlar yazılımında analiz gerçekleştirerek optimum eksenel besleme hızına karşılık basınç profilini belirlemişlerdir. Çalışmalarında bulanık mantık giriş değişenleri olarak patlamanın başlangıcını tespit etmede kullanılan hasar kriterini ve kalıp dolumunu yani boş olmayan kalıp hacminin yüzdesini seçmişlerdir. Hasar kriteri için beş, yüzde kalıp dolum hacmi için üç adet üyelik fonksiyonu kullanmışlardır. Bulanık mantık çıkış değişkenleri iç basınç ve besleme hızı olarak seçilmiştir. İç basınç ve besleme hızı için üçer adet üyelik fonksiyonu kullanılmıştır. Eğer-O halde (if-then) kurallarına dayanan kural tabanı oluşturmuşlardır ve analizi gerçekleştirmişlerdir. Deneyler gerçekleştirilmiştir ve istenilen geometri elde edilerek bulanık mantık tabanlı yaklaşımın doğruluğu kanıtlanmıştır.

2. MATERYAL VE YÖNTEM

2.1. Tüp Hidroşekillendirme Prosesinin Modellenmesi

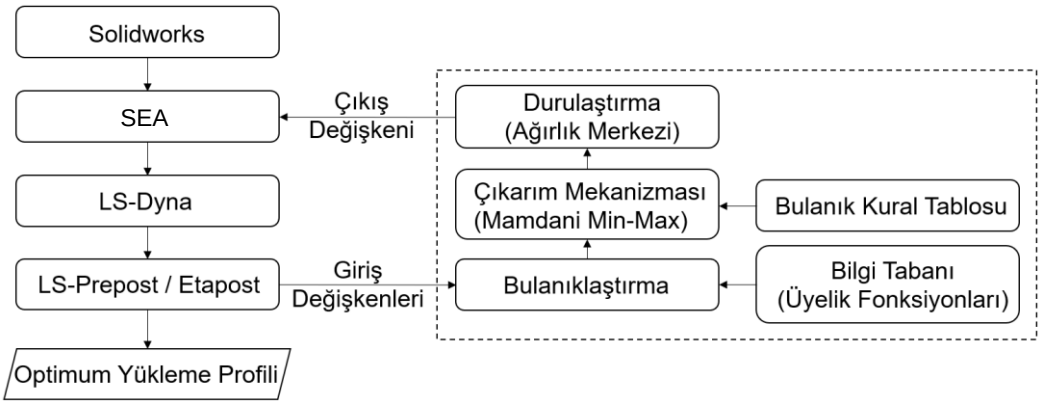
THŞ prosesi ile otomobil salıncak bağlantı parçasının üretimi için gerekli geometrik model; iş parçası (tüp), kalıp ve zımba olmak üzere çeyrek olarak modellenmiştir (Şekil 2). Modeldeki tüm parçalar yüzey olarak modellenmiştir ve iş parçasına 1 mm boyutunda dörtgen kabuk elemanlarla ağ örülmüştür. Kalıp ve zımbaya ise 2 mm boyutunda dörtgen kabuk elemanlarla ağ örülmüştür. Çalışmada 3 mm et kalınlığında ve 27 mm çapında St37 boru malzemesi kullanılmıştır. Parçalar arasındaki sürtünme katsayıları 0.125 olarak ayarlanmıştır. Sınır şartları olarak kalıbın üç eksende hareketi sınırlandırılmıştır. Zımbanın ise sadece eksenel yöndeki hareketine izin verilmiştir ve hareketi zamana bağlı lineer artacak şekilde 10 mm olarak ayarlanmıştır. Analizin çözümlenmesi için zamana bağlı bir başlangıç basınç eğrisi oluşturulmuştur. SEA'lar kapsamında öncelikle deneme-yanılma yöntemi kullanılarak yükleme profili belirlenmiştir ve sonrasında karşılaştırma yapılabilmesi için bulanık mantık kontrol algoritması kullanılmıştır.



Şekil 2. THŞ SE Modeli

2.2. Bulanık Mantık Kontrol Algoritması

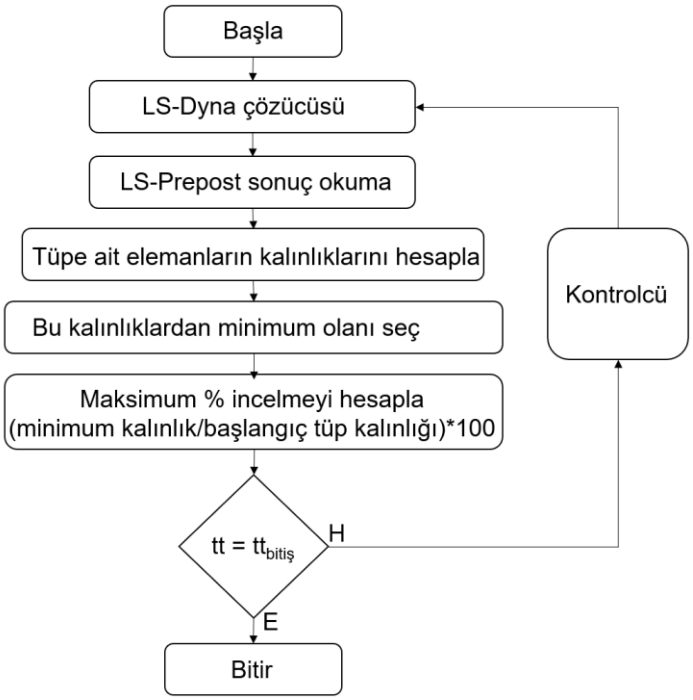
Salıncak bağlantı parçasının THŞ ile üretilmesinde, optimum yükleme profillerinin Bulanık Mantık Kontrol Algoritması (BMKA) ile elde edilmesi için giriş değişkeni olarak maksimum % kalınlık incelmesi, maksimum % buruşma yüksekliği ve maksimum % kalıp doldurma oranı belirlenmiştir. Çıkış değişkeni olarak optimum sıvı basıncı hesaplanmıştır. BMKA'nın akış şeması Şekil 3'te verilmiştir. SEA'nın her bir zaman adımında elde edilen sonuçlar (giriş değişkenleri) MATLAB programında yazılan bulanık mantık kodları (EK-1) yardımıyla kontrol edilip çıkış değişkeni elde edilmiştir. Proseste, oluşturulan üyelik fonksiyonları vasıtasıyla giriş değişkenleri bulanıklaştırılmıştır. Elde edilen bulanık değerler Mamdani çıkarım mekanizması ile dilsel olarak yazılan kurallar çerçevesinde kontrol edilmiştir. Bu aşamadaki veriler halen bulanık değerlerdir. Son olarak ağırlık merkezi yöntemi kullanarak durulaştırma işlemi gerçekleştirilmiştir ve bulanık değerler keskin değere dönüştürülmüştür. Elde edilen değer çıkış değişkeni yani basınç artışı (α)'dır. Arttırılan basınç değeri bir sonraki çözüm adımı için SE programına verilmiştir. 12 Adımın sonunda işlem tamamlanmıştır ve optimum yükleme profili belirlenmiştir.



Şekil 3. Çalışma kapsamında izlenen akış şeması

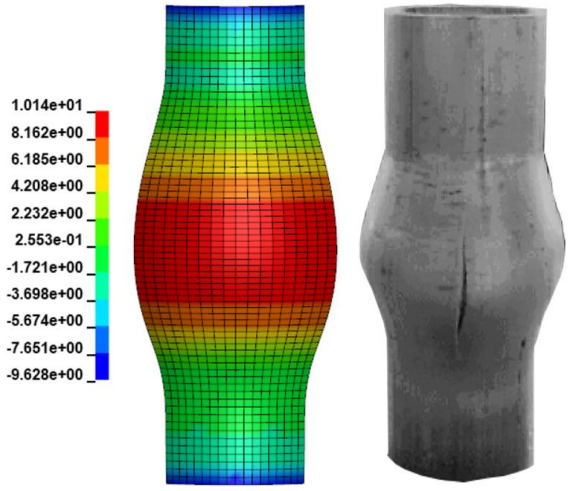
2.2.1. Maksimum yüzde kalınlık incelmesi giriş değişkeni

Maksimum yüzde kalınlık incelmesi giriş değişkeni değeri için her bir zaman adımında tüp malzemedeki bütün kabuk elemanların kalınlıkları hesaplanmıştır. Bu kalınlıklardan minimum olan kalınlık değeri bulanık mantık kontrol algoritmasında kullanılmak üzere seçilmiştir. (Minimum kalınlık/Başlangıç tüp kalınlığı)*100 formülü ile maksimum yüzde incelme belirlenmiştir. Maksimum yüzde kalınlık incelmesi değerinin sonucu SEA yazılımında her çözüm adımında hesaplanmıştır ve elde edilen maksimum yüzde incelme değeri MATLAB programına giriş değişkeni olarak verilmiştir (Şekil 4).



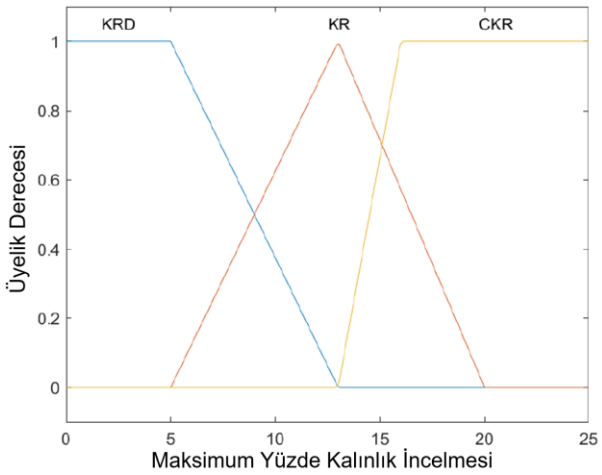
Şekil 4. Maksimum % kalınlık incelme giriş değişkeninin bulunmasına ait akış şeması

Şekil 5'te yüzde maksimum incelmenin nerede oluştuğu ve tarafımızdan hidroşekillendirme presinde üretilen deney parçasında nerede yırtılmanın gerçekleştiği gösterilmiştir. Sonlu elemanlar analizinde maksimum kalınlık incelmesi daima tüpün şişme bölgesinin merkezinde bulunan elemanlarda meydana gelmektedir.



Şekil 5. Maksimum incelmenin oluştuğu bölge

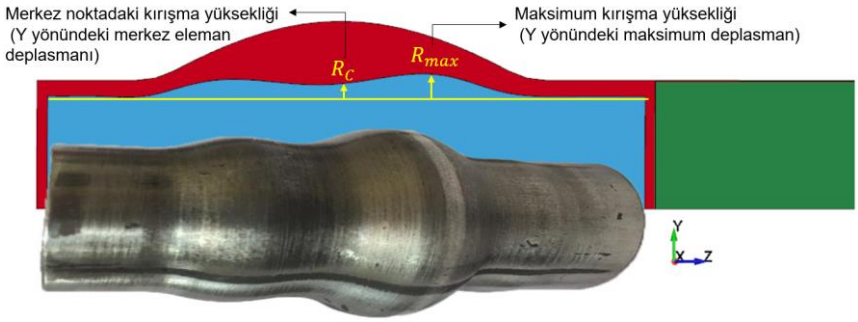
Bu giriş değişkeni için bulanık mantık kontrol algoritmasında kullanılan üyelik fonksiyonları Şekil 6'da verilmiştir. Kritik değil 'KRD', kritik 'KR' ve çok kritik 'CKR' olmak üzere üç adet üyelik fonksiyonu kullanılmıştır ve trapez ve üçgen üyelik fonksiyonlarından oluşturulmuştur. Deneylerden elde edilen verilerde maksimum % incelme değerlerinin %13-16 arasına ulaşmasının sonucunda yırtılmanın meydana geldiği gözlenmiştir. Bu nedenle, maksimum %13 kalınlık incelme kritik, maksimum %16 kalınlık incelmesi çok kritik olarak belirlenmiştir.



Şekil 6. Maksimum yüzde kalınlık incelmesi üyelik fonksiyonu

2.2.2. Maksimum yüzde buruşma yüksekliği giriş değişkeni

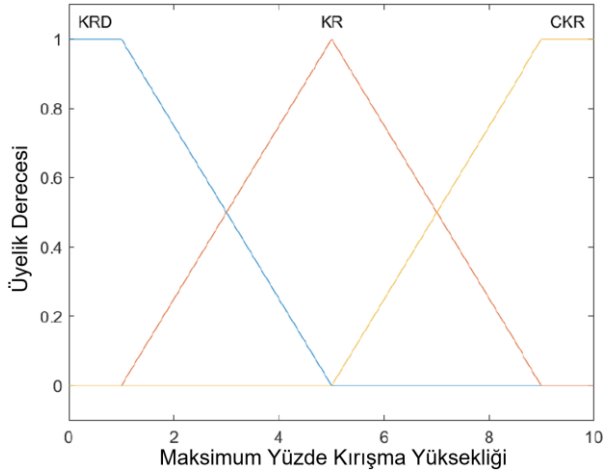
Tüp malzeme eksenel yönde basmaya zorlanıldığından, buruşma ihtimali oldukça yüksektir. Başlangıçta az miktarda buruşmanın şekillendirmeye olumlu yönde etkisi vardır. Boru şiştikçe incelmeye başlar ve arkasından patlama meydana gelir. Patlamanın engellenmesi için eksenel besleme ile şişme bölgesine malzeme akışı sağlanır. Böylece incelen kısımlara sağlanan malzeme akışı ile daha fazla incelmenin önüne geçilir ve yırtılma gerçekleşmez. Ancak eksenel besleme miktarı gereğinden fazla ise düzeltilemez buruşma meydana gelir. Şekil 7'de buruşma meydana gelmiş sonlu elemanlar modeli ile deneyler sonucunda elde edilen parça gösterilmiştir. Buradaki sarı çizgi tüpün şişirilmeden önceki halidir.



Şekil 7. Buruşma meydana gelmiş SE modeli ve deneysel olarak elde edilen parça

Tüpün buruşma kontrolü tüpün maksimum % deplasman miktarı (y yönündeki buruşma yükseklikleri) hesaplanarak kontrol edilir. Maksimum % buruşma yüksekliği giriş değişkeni şişme bölgesinin merkezinde bulunan elemanın y yönündeki deplasmanı (R_c) ile kalan diğer bölgelerdeki elemanlardan maksimum deplasmana sahip olan elemanın y yönündeki deplasmanı (R_{max}) mukayese edilerek elde edilir. Eğer tüpün merkezindeki deplasman diğer bölgelere kıyasla küçükse ($R_c<R_{max}$ ise) buruşma meydana gelir. Buruşmanın bulunmasındaki izlenen akış şeması Şekil 4'teki akış şemasına benzer şekilde oluşturulmuştur. Merkezdeki yükseklik (R_c) ile maksimum oluşan yükseklik (R_{max})

hesaplandığında aralarındaki fark %5 ise geri düzeltilemez buruşukluk meydana geleceği varsayılmıştır ve bundan dolayı %5 buruşma yükseklik farkı değeri kritik olarak alınmıştır (Şekil 8).

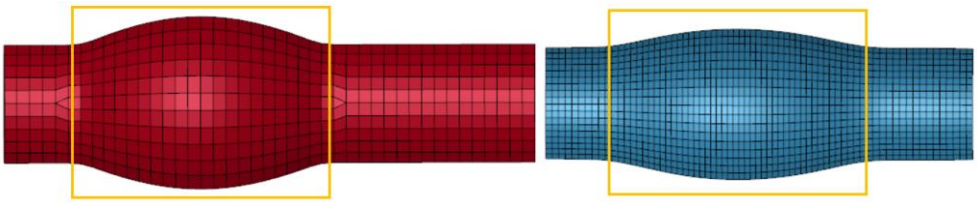


Şekil 8. Maksimum % kırışma yüksekliği üyelik fonksiyonu

2.2.3. Kalıp doldurma oranı giriş değişkeni

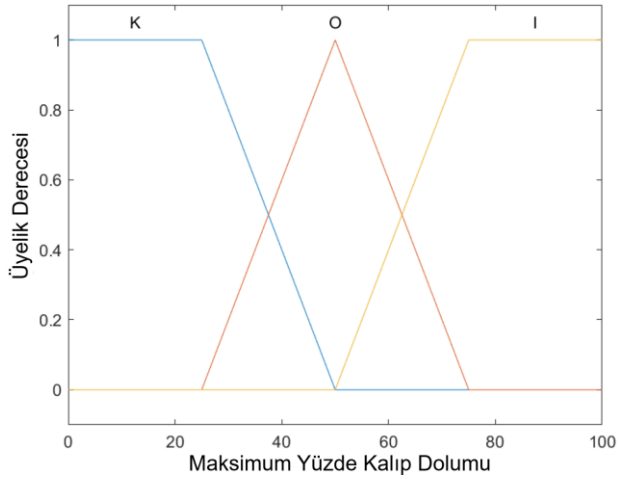
BMKA'da şekillendirmenin üç aşamasında üç farklı kural matrisi kullanılmıştır. Şekillendirmenin hangi seviyede olduğuna BMKA'nın karar vermesi için kalıp doldurma kriterinden yararlanılmıştır. Kalıp doldurma oranını, tüpün şişme bölgesindeki bulunan elemanların toplam yüzey alanının kalıbın şişme bölgesindeki bulunan elemanlarının toplam yüzey alanına oranıyla hesaplanmıştır (Şekil 9).

Kalıp doldurma oranı giriş değişkeninin bulunmasına ait akış şeması da Şekil 4'teki akış şemasına benzer şekilde oluşturulmuştur. Kalıp şişme bölgesindeki elemanların yüzey alanı ve şişmiş tüpün yüzey alanı hesaplanmıştır. Kalıpta şişme bölgesindeki elemanların yüzey alanı 1121,3 mm^2'dir. Tüpün başlangıçtaki şişmemiş yüzey alanı 844,3 mm^2'dir. Bu durumda dolması gereken yüzey alanı (Ak) 1121,3 – 844,3 = 277 mm^2 olarak bulunur. Şişmiş borunun yüzey alanının (A) dolması gereken yüzey alanına oranı kontrol edilmiştir. (A/Ak) sonucu 1 olduğunda kalıp % 100 dolmuş anlamına gelecektir.



Şekil 9. Kalıp ve tüpün yüzey alanının hesaplandığı bölgeler

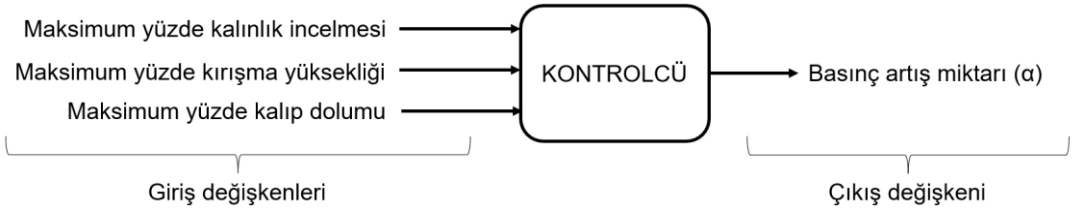
Kötü 'K', orta 'O' ve iyi 'I' olmak üzere üç adet üyelik fonksiyonu kullanılmıştır (Şekil 10). Üyelik fonksiyonları kalıbın dolumuna göre ayarlanmıştır. Buradaki üyelik fonksiyonlarının değer aralıkları yapılan denemeler sonucunda en uygun olacak şekilde seçilmiştir.



Şekil 10. Kalıp doldurma oranı üyelik fonksiyonu

2.2.4. Basınç artış miktarı (α) çıkış değişkeni

Her bir zaman adımında hesaplanan giriş değişkenleri değerleri MATLAB programında hazırlanan bulanık mantık kontrol kodlarına girdi olarak verilmiştir. Bunun neticesinde basınç artış miktarı (α) çıkış değişkeni elde edilmiştir (Şekil 11).

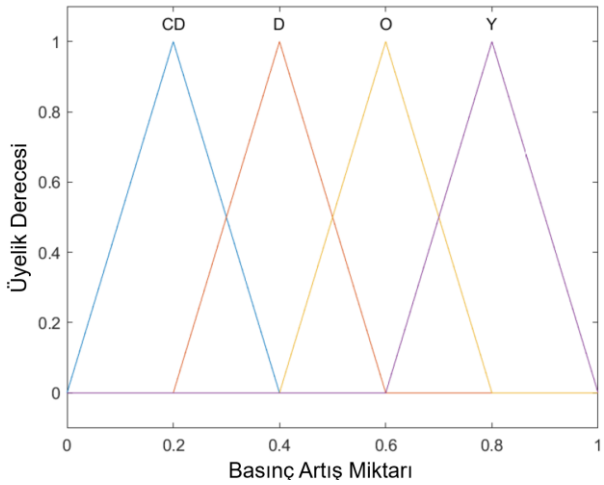


Şekil 11. Giriş değişkenleri ve çıkış değişkeni

Bulanık mantık tabanlı kontrol ile her bir zaman adımında SE modeline bir sonraki adımda yırtılma ve buruşma olmadan ne kadar basınç verilmesi gerektiği belirlenmiştir. Aşağıdaki denklemden her bir zaman adımında uygulanacak olan yeni sıvı basıncı (P_i^{yeni}) değerleri hesaplanmaktadır. Basınç artış miktarı (α) her bir zaman adımında basıncın ne oranda arttırılması gerektiği sonucunu bize verir. Ayrıca denklemde yer alan P_i^{eski} ifadesi bir önceki zaman adımında elde edilen sıvı basıncı, ΔP_i ifadesi ise ön tanımlı sıvı basıncı değerini temsil etmektedir. Ön tanımlı sıvı basıncı değeri ΔP_i=12 MPa olarak belirlenmiştir. Bu değer, bulanık mantık kontrol algoritmasının yeterli yükleme profillerini oluşturacağı şekilde elde edilmiştir.

$$P_i^{yeni} = P_i^{eski} + \alpha * \Delta P_i$$

Çok düşük 'CD', düşük 'D', orta 'O' ve yüksek 'Y' olmak üzere dört adet üyelik fonksiyonu kullanılmıştır (Şekil 12). Buradaki üyelik fonksiyonlarının küme aralıkları yapılan denemeler sonucunda en uygun sonucu verecek şekilde ayarlanmıştır.



Şekil 12. Basınç artış miktarı üyelik fonksiyonu

2.2.5. Bulanık mantık kural tabanı

Her bulanık kontrol sistemi bir kural tabanı matrisine ihtiyaç duymaktadır. Bu matris ise bilgi tabanı ile tecrübenin özel bir tipidir ve prosesin karar verme basamağını oluşturmaktadır. Bu matrisler sıvı basıncının artış miktarının çok düşük, düşük, orta ve yüksek olması gibi kararların belirlenmesi için gerekli kurallardan oluşmaktadır. Bu kural matrislerinin THŞ prosesi için uygun olup olmadığı yapılan analizlerin sonuçlarına göre karar verilmiştir.

THŞ prosesi başlangıç (% kalıp dolumu kötü), orta (% kalıp dolumu orta) ve son (% kalıp dolumu iyi) olarak üç aşamada incelenmiştir. Burada her aşamadaki kurallar birbirinden farklıdır. İşlemin başlangıcında eksenel besleme artışı az olmalı, basınç artışı yüksek olmalıdır. Bunun sebebi buruşmanın veya burkulmanın meydana gelmemesi içindir. İşlemin orta aşamasında eksenel besleme artmalı, basınç artış miktarı azalmalıdır. Tüp et kalınlığı şişmeden dolayı azalır ve patlama riski artar. Bundan dolayı eksenel beslemenin artışı basınç artış miktarından yüksek olmasıyla beraber şişme bölgesine malzeme akışı sağlanır ve kalınlık incelmesinin önüne geçilir. İşlemin son aşamasında tüpün kalıbı tam olarak doldurabilmesi için basınç artış miktarı tekrardan yükseltilmelidir. Bu mantıkla kural tabanı dilsel olarak Çizelge 1'deki gibi hazırlanmıştır. Örnek olarak incelersek; prosesin başlangıcında % kalıp dolumu kötü 'K' iken maksimum % kalınlık incelmesi kritik 'KRD' değilse, maksimum % buruşma yüksekliği çok kritikse 'CKR' basınç artış miktarını yükselt gibi dilsel kurallar oluşturulmuştur. Prosesin başlangıcında ve ortasında 10'ar ve sonunda 13 olmak üzere toplamda 33 adet kural oluşturulmuştur.

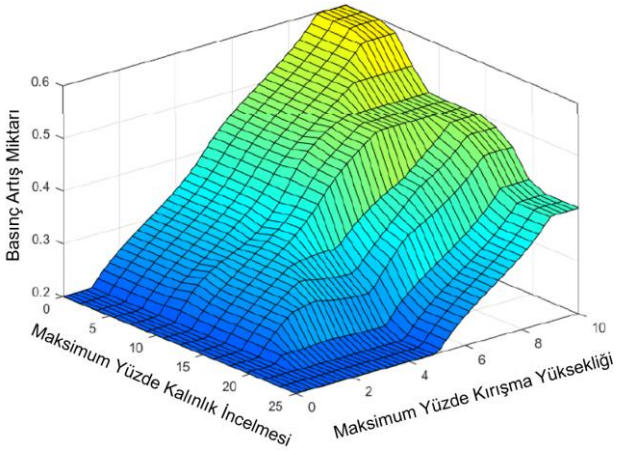
Çizelge 1. Kural Tabanı

Kalıp Dolum Oranı (K)					Kalıp Dolum Oranı (O)					Kalıp Dolum Oranı (I)				
α		Maksimum Yüzde İncelme			α		Maksimum Yüzde İncelme			α		Maksimum Yüzde İncelme		
		KRD	KR	CKR			KRD	KR	CKR			KRD	KR	CKR
Maksimum Yüzde Kırışma Yüksekliği	KRD	Y	Y	O	Maksimum Yüzde Kırışma Yüksekliği	KRD	CD	CD	CD	Maksimum Yüzde Kırışma Yüksekliği	KRD	Y	Y	O
	KR	Y	Y	D		KR	D	D	CD		KR	O/Y	O/Y	O
	CKR	Y	Y/O	D		CKR	O	O/D	D		CKR	Y	O/Y	O/Y

2.2.6. Bulanık mantık kontrol algoritmasının THŞ prosesine uygulanması

EK 1'deki oluşturulan kodlar çalıştırılmıştır ve bulanık mantık kontrol sistemi elde edilmiştir. Adım adım çözdürülen analizlerdeki gerekli sonuçlar okunmuş ve giriş değişkenleri olarak bulanık mantık kontrol sistemine verilmiştir. Bunun sonucunda basınç artış miktarı çok düşük, düşük, orta ve yüksek olarak belirlenmiş ve bir sonraki adımın basınç değeri hesaplanıp SE yazılıma girilmiştir. Bu işlem 12 adımda tamamlanmıştır. Şekil 13'te MATLAB programındaki 'surfview' komutuyla oluşturulan BMKA'nın yüzey modeli gösterilmiştir.

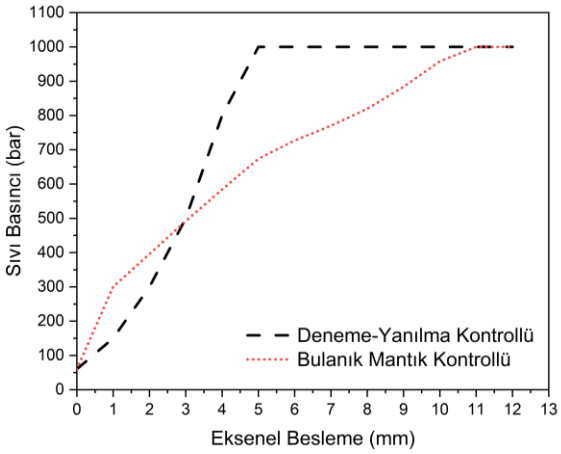
Bulanık mantık tabanlı kontrol sisteminin sayısal olarak sonucu ise 'ruleview' komutuyla okunabilir. Örneğin % kalıp dolumu 35, % kalınlık incelmesi 11 ve % buruşma yüksekliği 3 iken basınç artış miktarı 0,452 olarak elde edilir. Bir önceki adımda SE yazılımına girilen basıncın 700 bar ve ön tanımlı basıcın 120 bar olduğunu varsayarsak yeni basınç değerinin 754,52 bar olması gerektiği belirlenir. 12 adım boyunca bu işlem devam ettirilerek optimum yükleme profili belirlenmiştir. Basınç değeri 1000 bara ulaştıktan sonraki adımlarda 1000 bar basıncı pres kapasitesinden dolayı sabit tutulmuştur.



Şekil 13. Bulanık mantık sistemi yüzey modeli

3. ARAŞTIRMA SONUÇLARI VE TARTIŞMA

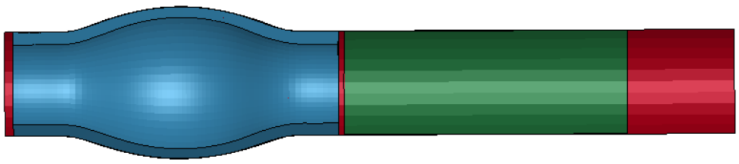
BMKA ile elde edilen yükleme profili ile ilk deneylerde kullanılan deneme yanılma kontrollü yükleme profili Şekil 14'te karşılaştırılmıştır.



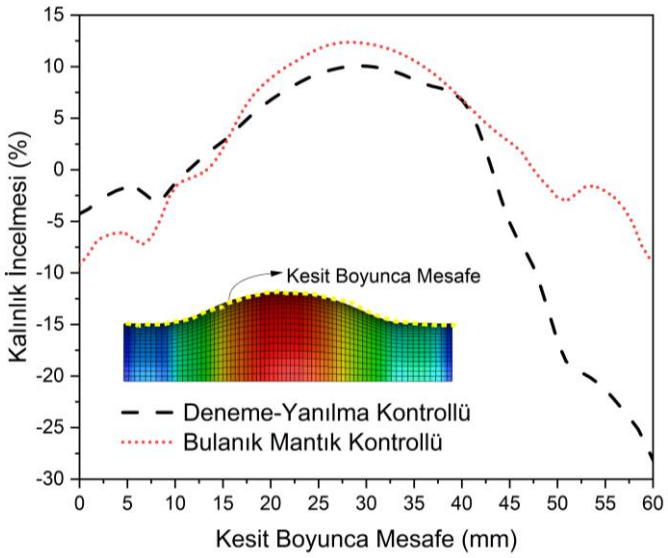
Şekil 14. İlk deneylerdeki deneme-yanılma profili ile bulanık mantıktan elde edilenin karşılaştırması

Şekil 14'ten görüleceği üzere deneme-yanılma yöntemiyle elde edilen yükleme profilinde eksenel besleme miktarı 5 mm iken, iç basınç 1000 bar seviyesine ulaşmıştır ve 7 mm ilerleme boyunca 1000 bar'da sabit kalmıştır. Ancak bulanık mantık kontrollü yükleme profilinde eksenel besleme miktarı 11 mm iken 1000 bar seviyesine ulaşılıp 2 mm boyunca sabit kalmıştır.

Her iki yükleme profili ile elde edilen parça Şekil 15'te görüldüğü gibi kalıbı tam olarak doldurmuştur. Bu noktada parçaların kalitesi kalınlık dağılımları üzerinden karşılaştırılmıştır. Her iki yükleme profili ile elde edilen parçaların kalınlık dağılımı Şekil 16'da görülmektedir. Boru et kalınlık dağılımı parça dayanımı ve kalitesi açısından oldukça önemlidir. BMK yükleme profili ile elde edilen parçanın kalınlık dağılımının deneme-yanılma yöntemiyle elde edilene göre daha homojen olduğu görülmektedir. Deneme-yanılma ile elde edilen parçada %10 incelme oluşurken %28 kalınlaşma olmuştur. Buradan toplam kalınlık farkı %39'dur. BMK elde edilen parçanın kalınlık dağımı incelendiğinde %14 incelme meydana gelirken, %9 kalınlaşma meydana gelmiştir. Dolayısıyla toplam kalınlık farkı %23 olup deneme ve yanılma ile elde edilen kalınlık dağılımına göre %41 oranında daha homojen kalınlık dağılımı elde edilmiştir.

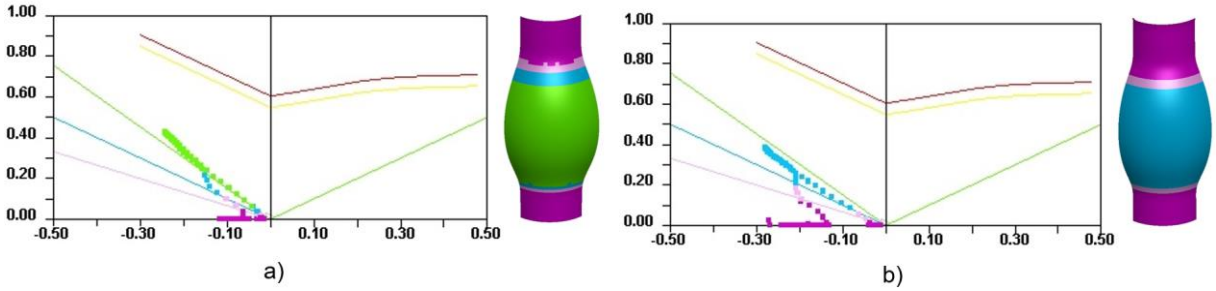


Şekil 15. Kalıbın tam olarak dolduğunu gösteren SEA sonucu



Şekil 16. BMK ve deneme-yanılma kontrollü kalınlık dağılımı karşılaştırması

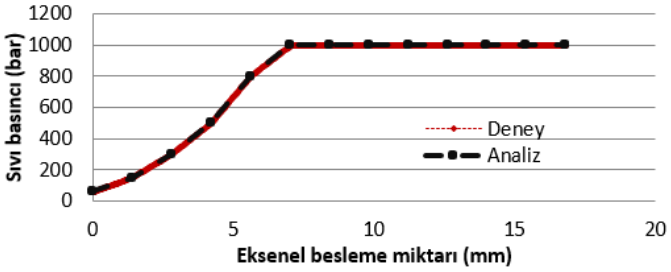
Şekil 17'de St37 malzemenin şekillendirme sınır diyagramı (ŞSD) verilmiştir. Buradaki kırmızı çizgi yırtılma, sarı çizgi yırtılma riski, yeşil çizgi başarılı şekillendirme, mavi çizgi buruşma riski, mor çizgi ise ciddi buruşma anlamına gelmektedir. Şekil 17a'da bulanık mantık kontrollü elde edilen parça için birim şekil değiştirme dağılımı, Şekil 17b'de ise deneme-yanılma kontrollü elde edilen birim şekil değiştirme dağılımı verilmiştir. Bulanık mantık kontrollü deformasyon dağılım incelendiğinde başarılı şekillendirme çizgisi üzerinde ilerlemektedir, ancak deneme-yanılma kontrollü dağılım incelediğinde, başarılı şekillendirmeye yakın ancak buruşma riskinin bulunduğu görülmektedir.



Şekil 17. Birim şekil değiştirme durumunun karşılaştırılması a) BMK b) Deneme-yanılma kontrollü

Elde edilen SEA sonuçlarına göre kalıplar imal edilmiş ve hidroşekillendirme presinde hedeflenen salıncak bağlantı parçası tüp hidroşekillendirme prosesi ile üretilmiştir. Son olarak elde edilen parçanın geometrik ölçümleri yapılmış, boşluk doldurma oranı hesaplanmış ve istenilen toleransları sağlayıp sağlamadığı kontrol edilmiştir.

Deneme-yanılma kontrollü elde edilen yükleme profili Şekil 18'de gösterilmiştir. Şekil incelendiğinde analizde oluşturulan yükleme profili ile presten elde edilen yükleme profili eşleşmiştir. Yani pres istenilen yükleme profiline cevap verebilmektedir.



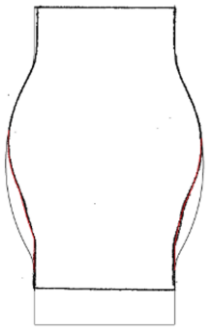
Şekil 18. Deneme-yanılma ile elde edilen yükleme profili

Bu basınç değerleriyle hedef parça Şekil 19'da görüldüğü gibi üretilmiştir. THŞ yöntemiyle dövme yöntemine göre daha düzgün yüzey elde edilmiştir. Şekil 19a'da ise dövme yöntemiyle elde edilen parça görülmektedir.



Şekil 19. a) Dövme yöntemiyle elde edilen parça b) THŞ yöntemiyle elde edilen parça

Şekil 20**Error! Reference source not found.**'de kalıbın şekli ile parçanın aldığı şekil karşılaştırılmıştır. Boşluk doldurma oranı parametreleri hesaplanmış ve Çizelge 2'de görülen değerler elde edilmiştir. Bu parametrelerle yapılan hesaplamada boşluk doldurma oranı %83.6 bulunmuştur.



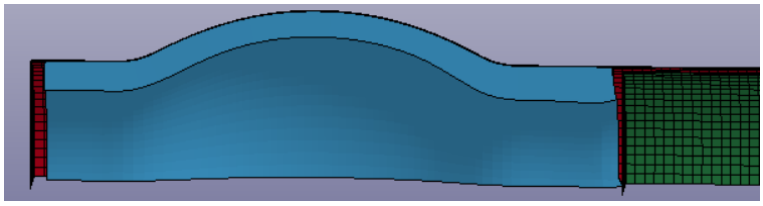
Şekil 20. Boşluk dolum oranının belirlenmesindeki geometri

Şekil 21'de gösterilen analiz sonucuna göre parçanın kalıbın şeklini tam olarak aldığı görülmektedir. Ancak deney sonuçlarına göre kalıbın %83.6'sı dolmuştur. Buradan analizlerin doğruluk oranının %83.6 olduğu değerlendirilmiştir. Uygun olmayan basınç eğrisiyle Şekil 20'de görüldüğü gibi parçalar hedef geometriden çok

uzak olarak elde edilirken, SEA'de deneme yanılma ile elde edilmiş optimum yükleme profilleri ile hedef geometriye %83.6 oranında yaklaşılabilmiştir.

Çizelge 2. Hesaplanmış boşluk doldurma oranı parametreleri

Toplam Kalıp Alanı	2275,44 mm²
Boru Alanı	1998 mm²
Dolması Gereken Alan	277,4 mm²
Dolmayan Alan	45.57 mm²
Boşluk Doldurma Oranı	% 83.6



Şekil 21. Analiz sonucunda tüpün kalıbın şeklini alması

4. SONUÇLAR

Bu çalışmada, otomotiv sanayisinde kullanılan salıncak bağlantı parçasının tüp hidroşekillendirme prosesi için gerekli uygun yükleme profili bulanık mantık kontrol algoritmalı bir adaptif SEA metodu ile belirlenmiştir. Belirlenen bu yükleme profili ile deneysel çalışması yapılan deneme-yanılma kontrollü yükleme profili karşılaştırılmıştır. Bu çalışmadan aşağıdaki sonuçlar çıkarılmıştır:

- Tüp hidroşekillendirme prosesi için gerekli uygun yükleme profili bulanık mantık kontrol algoritmalı adaptif SEA yöntemi sayesinde daha hızlı ve doğru bir şekilde elde edilebilmektedir. Dolayısıyla geleneksel deneme ve yanılma veya hesaplamalı deney yöntemi ile harcanan işgücü, para ve zaman, bulanık mantık kontrol algoritmalı adaptif SEA yöntemi kullanılarak büyük oranda düşürülmektedir.
- Bulanık mantık kontrollü yükleme profili ile elde edilen parçanın kalınlık dağılımı deneme yanılma yöntemiyle elde edilene göre %42 oranında daha homojendir. Bu durum endüstriyel üründe daha büyük boyutsal doğruluk ve dayanımda artış sağlar.

KAYNAKÇA

1. **Aydemir, A., De Vree, J.H.P., Brekelmans, W.A.M., Geers, M.G.D., Sillekens, Werkhoven, R.J. (2005)**, "An adaptive simulation approach designed for tube hydroforming processes", Journal of Materials Processing Technology, Vol. 159, pp 303-310.

2. **Bell, C., Corney, J., Zuelli, N., Savings, D. (2019)**, "A state of the art review of hydroforming technology", International Journal of Material Forming, 12289-019-01507-1.

3. **Carpenter, J.A. (2004),** “The Freedom CAR Challenge and Steel, American Iron and Steel Institute”, Great Designs in Steel Seminar, Livonia, MI, 96-111.

4. **Halkacı, H.S., Türköz, M., Dilmeç, M. (2014),** “Enhancing formability in hydromechanical deep drawing process adding a shallow drawbead to the blank holder”, Journal of Materials Processing Technology, Vol. 214, pp 1638-1646.

5. **Koç M., Altan T. (1998),** “Development of guidelines for part, process and tooling design in the tube hydroforming technology”, Ohio State University, Columbus.

6. **Lorenzo, D., Filice, L., Umbrello D., and Micari, F. (2014)**, “Optimal design of tube hydroforming processes: a fuzzy-logic-based approach”, Proc. Instn Mech. Engrs, Vol. 218 Part B: J. Engineering Manufacture, pp 599-605.

7. **Schultz, R. A. (1999),** “Aluminum for Light Vehicles an Objective Look at the Next Ten to Twenty Years”, 14th International Aluminum Conference, Montreal, Canada, Ducker Research.

8. **Wang, Q. (1994),** “Hydromechanical deep drawing”, New Technol. New Process, pp 23-24.

9. **Zhou L. and Cheng, X. (2009),** “Loading Path Design for Tube Hydroforming Based on Fuzzy Logical Control and CAE Method”, School of Mechanica Engineering Ningbo University of Technology, pp 889-893.

PA12 MALZEMESİNDEN İMAL EDİLMİŞ 3 KATMANLI YAKIT BORUSUNUN SICAKLIK İLE ŞEKİLLENDİRME ANALİZİ VE YAPILAN ANALİZİN DOĞRULANMASI

Metin ALİBAŞOĞLU, metinalibasoglu@gmail.com TI Fluid System, 16160, Bursa

M. Cemal ÇAKIR, cemal@uludag.edu.tr Bursa Uludağ Üniversitesi, 16160, Bursa

ÖZET

Binek araçlarda yakıtın iletimi ve geri beslemesi, yakıt taşıma sisteminin bir parçası olan yakıt boruları ile gerçekleştirilmektedir. Günümüzde plastik ve fluoraplastik yakıt boruları yaygın olarak kullanılmaktadır. Çalışma kapsamında PA12 malzemesi kullanılarak imal edilmiş üç katmanlı yakıt borusunun sıcaklık girdisi ile şekillendirilmesi ile analiz edilmesi ve gerçekleştirilen analizin ürün doğrulaması amaçlanmıştır. Modelleme ve analiz programı olarak Solidworks tercih edilmiştir. Analiz sonrası elde edilen model ile fiziki üretimi yapılıp tersine mühendislik ile taranarak datası elde edilen model çakıştırılarak kıyaslama yapılmıştır. Elde edilen sonuçların, fiziki üretimlerde uygulanması gereken sıcaklık değerini vermesi ile zaman ve maliyet tasarrufu sağlaması amaçlanmıştır.

Anahtar Kelimeler: Yakıt borusu, modelleme, ürün doğrulama, Solidworks

ABSTRACT

In passenger cars, the feeding and feedback of the fuel is carried out by fuel tubes, which are a part of the fuel system. Today, plastic and fluoroplastic fuel tubes are widely used. Within the scope of the study, it is aimed to analyze the three-layer fuel tube manufactured using PA12 material by shaping it with temperature input and to verify the product of the analysis performed. Solidworks was chosen as the modeling and analysis program. The model data which is obtained with analyze is compared by superposed with the model data which is obtained by reverse engineering after physical production. It is aimed that the results obtained will provide time and cost savings by giving the temperature value that should be applied in physical productions.

Keywords: Fuel tube, modelling, product verification, Solidworks

1. GİRİŞ

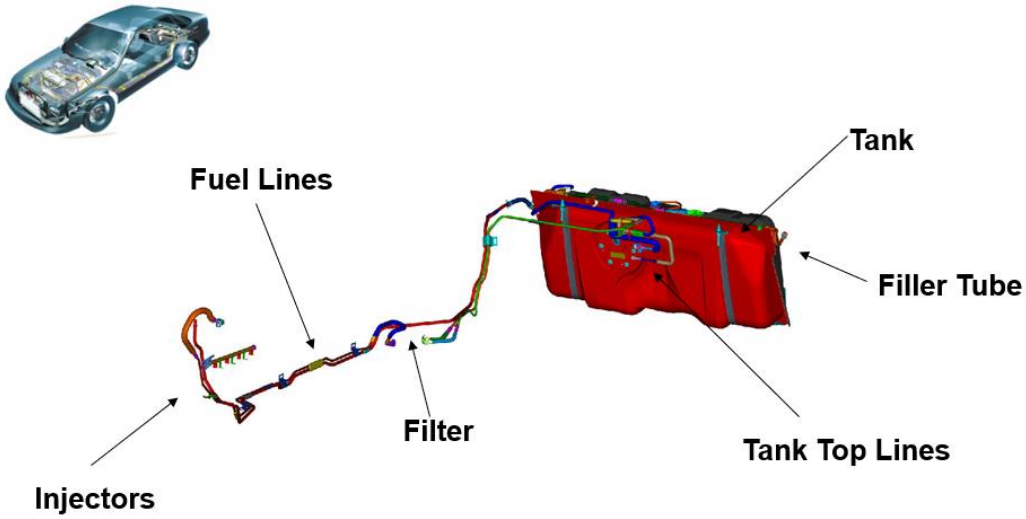
Otomotiv endüstrisindeki plastik uygulamaları olağanüstü bir büyüme kaydetmektedir. Bu uygulamaların en önemli kullanım alanlarından olan yakıt ve havanın taşınması, herhangi bir otomobilin çalışması için kritik öneme sahiptir. Kauçuktan yapılmış borular, bazı durumlarda metal borular da kullanılmış olsa da yakıt veya hava taşımanın başlıca yolu olmuştur. Yakıt olarak alkol kullanımının artması, petrol yakıtlarından kaynaklanan emisyonlara ilişkin katı çevresel düzenlemeler ve yakıtlarda katkı maddesi olarak çeşitli kimyasalların kullanımına ilişkin kısıtlamalar, modern otomobillerde geleneksel kauçuk, plastik veya metal hortumları yakıt veya hava taşımacılığı için uygunsuz hale getirmiştir. Son zamanlardaki eğilim, farklı işlevlere sahip ve gereksinimlere özel hibrit malzemeler kullanan çok katmanlı borular geliştirmek olmuştur. Çok katmanlı kauçuk borulara ek olarak, naylon gibi çok sayıda polimer ve çok katmanlı boruları geliştirmek için türevler kullanılmıştır [Jing ve ark., 2005].

Düzenleyici gereklilikler, otomobil üreticilerinin ve araç yakıt sistemi üreticilerinin bu gereksinimleri karşılayabilecek yakıt sistemleri tasarlamasını giderek daha zor hale getirmiştir. Bu eğilimler, borular ve yakıt hatları için daha iyi geçirgenliğe sahip malzemelerinin, daha iyi ve daha az sayıda bağlantının ve zorunlu dayanıklılık gereksinimini karşılayacak kadar dayanıklı malzemelerin kullanılmasını gerektirmiştir. Bir araç için yakıt borusu evaporatif emisyon ihtiyaçları, borunun yüzey alanına, yapım malzemelerine ve aracın diğer yakıt bileşenlerinin toplam emisyonlarına bağlı olarak değişebilmektedir. Yakıt borusu, çarpmaya dayanıklılık ve montaj kolaylığı gibi performans gereksinimlerini de karşılamalıdır. Bu çeşitli gereksinimleri karşılamak için yeni boru yapılarının geliştirilmesi, genellikle benzer yapılar için malzeme bilgisi ve geçmiş performans verileri kullanılarak yapılmaktadır. Uç etkiler ve mikro sızıntılar daha önemli bir rol oynamaya başladığından, buharlaşma emisyonları gereksinimleri çok düşük olduğunda boru geçirgenliği ve toplam emisyon performansının tahmini daha zordur. Bu nedenle, belirli bir boru yapısının buharlaşma emisyonunun makul bir tahminini sağlayabilecek bir modele sahip olmak faydalıdır. Bu, deneme yanılma sürecini ortadan kaldıracak ve düşük emisyonlu boruların daha hızlı geliştirilmesine olanak sağlayacaktır [Molnar ve ark., 2002].

Bu çalışma kapsamında, PA12 malzemesi kullanılarak imal edilmiş üç katmanlı yakıt borusunun bilgisayar destekli tasarım programlarıyla modellenmesi, analiz edilmesi ve oluşturulan modellerin fiziki olarak doğrulanması amaçlanmaktadır. Bu amaçlar doğrultusunda elde edilen bulgular yakıt borularının şekillendirilmesinde önemli çalışma parametrelerinden olan sıcaklık değerinin tahmin edilmesine olanak sağlayacaktır.

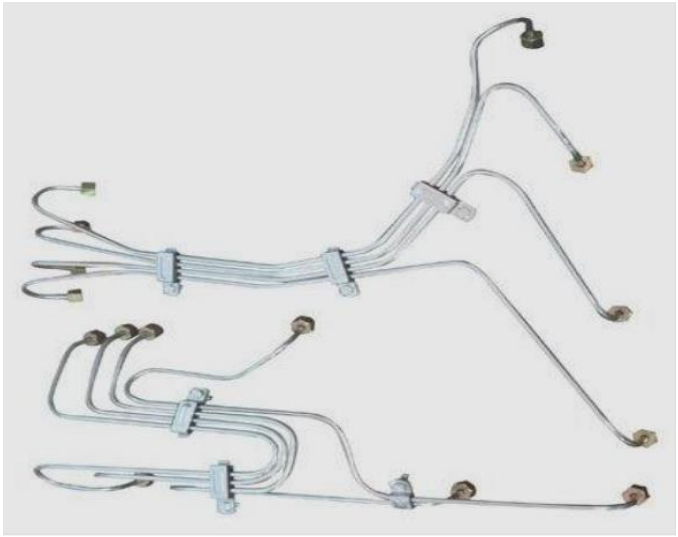
2. KURAMSAL TEMELLER ve KAYNAK ARAŞTIRMASI

Araç yakıt sistemi, motor için gerekli mazotu sıkıştırma zamanı sonunda silindir içerisine püskürterek yanma işlemini sağlamayı ve araç için gerekli gücü üretmeyi sağlar (Şekil 1).



Şekil 1. Araç yakıt sistemi şeması-1

Yakıt iletimini sağlayan borulara yakıt boruları denilmektedir (Şekil 2)



Şekil 2. Yakıt boruları [Anonim1, 2022]

Alçak basınç boruları

Alçak basınç boruları, yakıtın depodan besleme pompası ve filtre vasıtasıyla yakıt pompasına kadar iletilmesine yarayan parçalardır. Bu borulardaki basıncın düşük olması nedeniyle alçak basınç boruları olarak adlandırılmaktadır [Anonim2, 2022].

Yüksek Basınç Boruları

Yüksek basınç boruları yakıt pompasından enjektörlere yüksek basınçlı yakıt iletilmesine yarayan parçalardır. Yüksek basınca mukavemetinin artırılması amacıyla çelik materyalden özel olarak üretilen cidarı kalın borular kullanılmaktadır [Anonim2, 2022].

Geri Dönüş ve Sızıntı Boruları

Geri dönüş ve sızıntı boruları, yakıt sisteminde kullanılmayan yakıtın depoya taşımına yarayan parçalardır. Sistemin bu bölümünde yakıt basınç değeri düşük olduğu için geri dönüş ve sızıntı borularının yüksek basınçlara dayanım özelliğine sahip olmasına gerek yoktur [Anonim1, 2022].

Naylon 12 reçineleri, 25 yılı aşkın bir süredir otomobillerdeki sıvı yakıt hatları için kullanılmaktadır. Yeni yakıtların (çoğunlukla alkol içerenler) geliştirilmesi ve çeşitli devlet kurumları tarafından yeni hidrokarbon emisyon standartlarının oluşturulması bunu değiştirmiştir. Değişen duruma yanıt olarak, başta geçirgenlik direnci olmak üzere naylon 12 borunun özelliklerini iyileştirmek için çok katmanlı boru sistemi geliştirilmiştir. Metal yakıt hatları ile karşılaştırıldığında, Naylon 12 boru sisteminin iki ana avantajı yüksek korozyon direnci ve düşük ağırlıklı olmasıdır. Naylon 12 hatlarının esnekliği de bu tür boruların taşınmasında ve montajı açısından oldukça önemlidir. Bir yakıt sisteminde ortaya çıkabilecek hidrokarbon emisyonları için, metal hatların Naylon 12 boruya göre bir avantajı bulunmaktadır; hidrokarbonların çelik borunun duvarından geçme hızı sıfırdır. Naylon 12 boru duvarından az miktarda geçirgenlik olmakla beraber bu durumun, aynı zamanda bir yakıt sisteminin parçası olarak da kullanılabilen geleneksel elastomer borularda meydana gelebilecek geçirgenlik kayıplarından önemli ölçüde daha az olduğu belirtilmiştir [Hopf ve ark., 1994].

Floropolimerler ise iyi kimyasal ve termal dirençlere sahiptir [Drobny 2007; Hedenqvist ve ark., 2003]. Ek olarak, bu ürünler yakıt için iyi engelleyiciler olup, bu nedenle poliviniliden florür (PVDF) ve polietilen-ko-tetrafloroetilen (ETFE) gibi floropolimerlerin bazı PA bazlı çok katmanlı yakıt borularında bariyer katmanları olarak kullanılmaktadır [Kallio ve Hedeqvist. 2008]. Floropolimerler dizel/biyodizel yakıt boru sistemlerinde iç bariyer tabakaları olarak potansiyel göstermektedir [Wei ve ark., 2018].

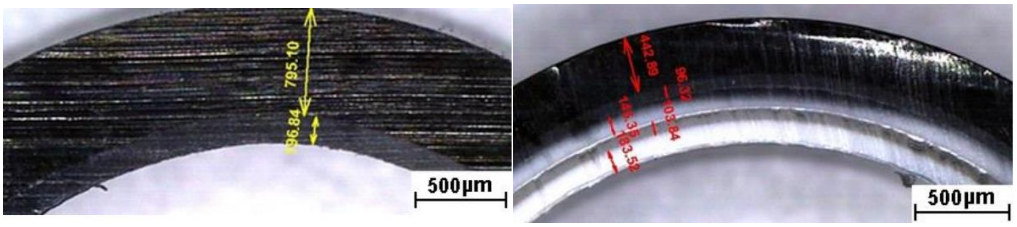
2.1. Yakıt Borularının İmalatı ve Şekillendirilmesi

Yakıt boruları tek katmanlı veya çok katmanlı olarak imal edilebilir. İmalat yöntemi genel olarak ekstrüzyon makinalarıdır. Son yıllarda otomotiv yakıt sistemlerinde PA malzemeleriyle çok katmanlı yakıt boruları tercih edilmektedir. Bu borular yüksek performansları ve emisyon salınımlarındaki verimlilikleri ile uluslararası alanda tercih sebebi olmaktadırlar [Şekil 3]. Çok

katmanlı yakıt boruları 2, 3, 4 veya daha fazlı katmandan oluşabilirler ve boru dış çapı 6 mm, 8 mm, 10 mm veya istenen daha büyük çap değerinde imal edilebilirler. Katmanlar arası yapıştırıcı malzeme olarak PA6 kullanılabilmektedir. Şekil 4 de 2 katmanlı PA12 borunun katman kalınları gösterilmektedir. Alt katmanda 0,2 mm kalınlığa sahip PA9T malzemesi, üst katmanda ise 0,8 mm kalınlığa sahip PA12 malzemesi mevcuttur. Yapılan üretim sonrası malzeme katlarının görüntüsü mikroskop altında incelenmiştir. Diğer bir örnekte, 5 katmanlı yakıt borusunda malzeme olarak 0,2 mm kalınlığında PA612, 0,2 mm yapıştırıcı ara kat PA6, 0,15 mm kalınlığında EVOH, 0,2 mm yapıştırıcı ara kat PA6 ve 0,45 mm kalınlığında PA12 kullanılmıştır. 2 katlı PA boru üretimi sırasında borunun alt katının ekstrüzyon sıcaklığı 300±30°C iken, borunun üst katının ekstrüzyon üretim sıcaklığı ise 200±20°C olacak şekilde uygulanmıştır. 5 katlı PA boru üretimi sırasında ise bütün katlardaki malzemeler için 200±40°C ekstrüzyon üretim sıcaklığı uygulanmıştır [Kurnaz 2019].



Şekil 2. Ekstrüzyon hattı örneği [Anonim4, 2022]



Şekil 3. İki katmanlı ve beş katmanlı yakıt borusu örnekleri

Düz haldeki yakıt boruları kalıcı form verme işlemi için kalıp gözlerine yerleştirilmekte ve ardından sıcak hava fırınına gönderilmektedir. Sıcak hava fırınlarında, rezistanslar yardımıyla ortam havası ısıtılmakta, ısıtma sonrası parçalar duşlama ile şoklanmakta ve form kalıcı hale getirilmektedir. Kullanılan malzemenin türü, boyu, çapı, katman sayısı, formu gibi etkenler, proses parametre ayarlarıyla optimize edilmektedir. Bu parametreler maksimum ve minimum

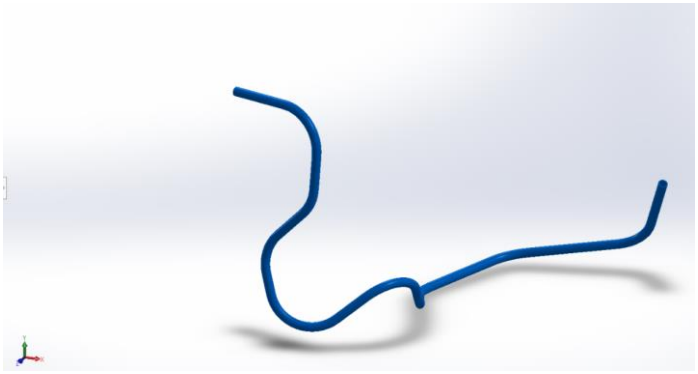
ortam sıcaklığı, ısıtma süresi, duşlama suyu sıcaklığı, duşlama süresi, parça sürme hızı şeklindedir.

3. MATERYAL ve YÖNTEM

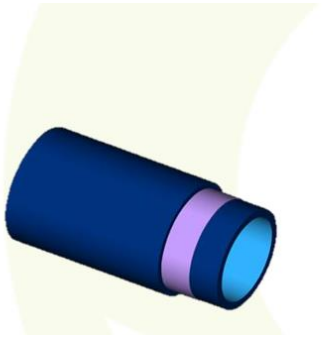
Çalışma kapsamında yakıt boruları için materyal olarak PA12 malzemeleri kullanılmış olup, Solidworks programı kullanılarak müşterinin paylaştığı yüzey datadan üç boyutlu model elde edilmiştir ve sonlu elemanlar yönetimiyle elde edilen modele termal ve statik analizler yapılmıştır. Elde edilen modeller sıcak hava fırınları ile fiziki olarak üretilmiş, proses sonrası ürün tersine mühendislik ile taranmıştır ve elde edilen datalar çakıştırılarak ürün doğrulaması yapılmıştır.

Modeli oluşturulan yakıt borusu PA12 malzemesine sahip olmakla birlikte, her katmanında aynı PA12 malzemesinin bulunduğu farklı kalınlıklardaki 3 katmandan oluşmaktadır. Boru iletken değildir. Dış çapı 8mm ve boru et kalınlığı 1 mm şeklindedir. Teorik boru boy uzunluğu 813 mm'dir.

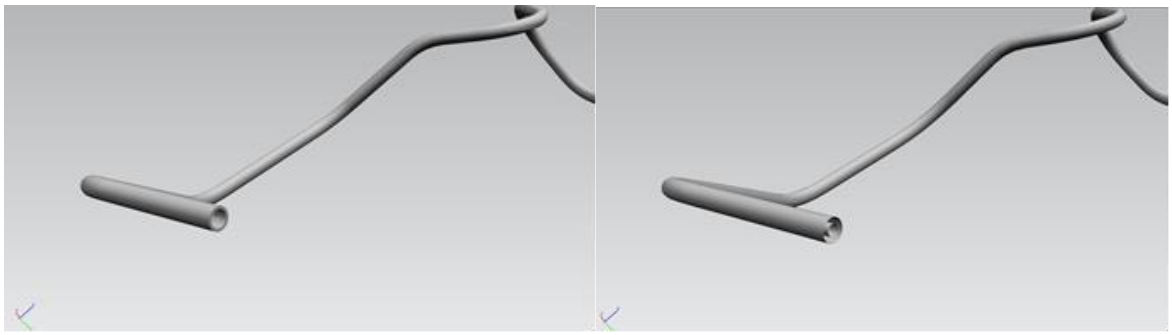
Tez kapsamında kullanılan yakıt borusunun datası iki farklı aşama ile ortaya konmuştur. Birincisi, mevcut OEM müşterisi tarafından dış çapı belli ve yüzey data olacak şekilde paylaşılmıştır. Bu dataya göre, boru et kalınlığı verilerek analizlerin yapıldığı data elde edilmiştir [Şekil 4, Şekil 6]. Diğer data ise, üretimde kullanılan sıcak hava prosesi sonrası yakıt borusu taratılarak 3 boyutlu model datası elde edilmiştir [Şekil 7]. Teorik data sonucu analizlerde kullanılmış data ve tersine mühendislik ile elde edilmiş olan data çakıştırılmıştır. Böylece yapılan analizlerin fiziki olarak doğrulanması hedeflenmiştir.



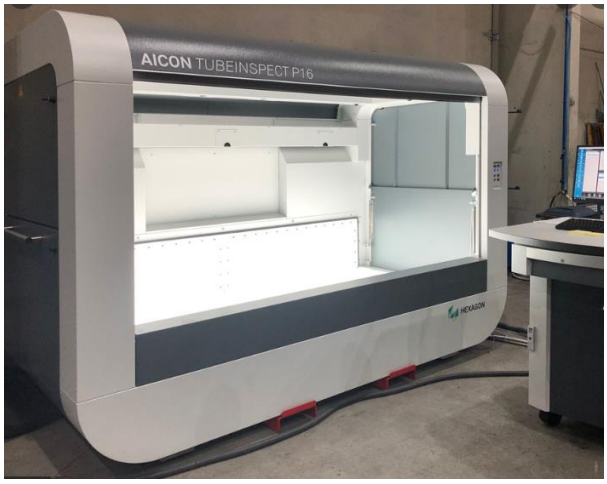
Şekil 4. Yakıt borusu üç boyutlu modeli-1



Şekil 5. Üç katmanlı yakıt borusu



Şekil 6. Boru yüzey datası ve yüzey dataya kalınlık vererekelde edilen 3D boru datası



Şekil 7. Tersine mühendislik ile taramanın yapıldığı AICON makinesi-1 [Anonim3, 2022]

3.1. Oluşturulan Modelin Fiziki Olarak Doğrulanması

Yakıt borularının şekillendirilmesinde kullanılan yöntemlerinden biri sıcak hava fırınlarıdır. Parçaya formu verecek şekilde imal edilen sarım kalıpları ve aynı anda birden fazla parça üretilmesini sağlayan kalıp gözleri prosesin en önemli araçlarıdır. Bununla birlikte minimum ve maksimum ortam hava sıcaklığı, ortalama ortam sıcaklığı, bant sürme hızı, duşlama suyu sıcaklığı ve duşlama süresi de prosesi oluşturulan diğer parametrelerdir.



Şekil 8. Fırın prosesi öncesi düz haldeki yakıt borusu

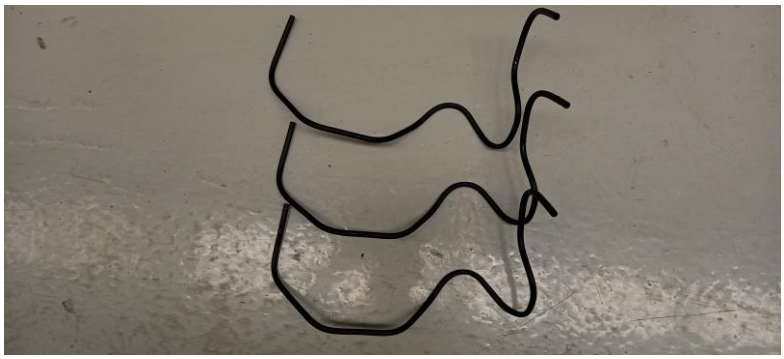
Fırın prosesi öncesinde, düz halde olan yakıt boruları yaklaşık 40ºC'lık ön ısıtma işlemine tabii tutulur [Şekil 8]. Ön ısıtma işleminin uygulanmasındaki amaç, yakıt borularının fırın kalıplarına daha kolay sarılmasını sağlamaktır. Fırın kalıp gözelerine sarılan yakıt borularının her iki tarafından, esnek yaylar geçirilir [Şekil 9]. Yayların amacı büküm bölgelerindeki deformasyonları ve yüzeyde yaşanabilecek bozulmaları engellemektir. Proses esnasında, minimum ve maksimum ortam sıcaklığı, proses hızı ve duşlama süresi ile alakalı deneme çalışmaları gerçekleştirilmiştir. Çalışma kapsamında uygun veya uyguna en yakın sıcaklığın tespit edilebilmesi için, proses hızı ve duşlama süresi sabit tutularak, fırın ortam sıcaklığının parça üzerindeki etkisi değerlendirilmiştir.



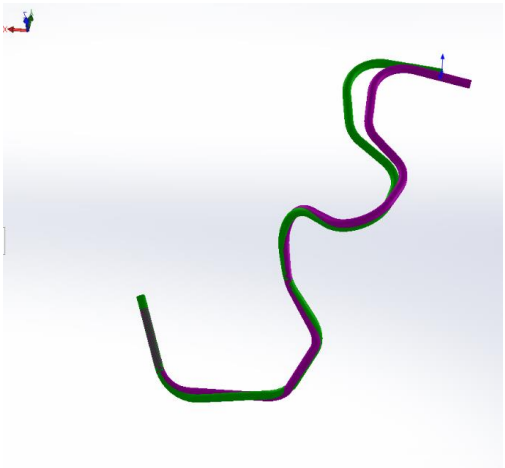
Şekil 9. Fırın prosesine girmek üzere kalıp gözlerine yerleştirilen yakıt boruları

4. BULGULAR ve TARTIŞMA

Çalışma kapsamında yakıt boruları için malzeme olarak PA12 kullanılmış olup, Solidworks programı kullanılarak müşterinin paylaştığı yüzey datadan üç boyutlu model elde edilmiştir ve sonlu elemanlar yönetimiyle elde edilen modele termal ve statik analizler yapılmıştır. Elde edilen modeller sıcak hava fırınları ile fiziki olarak üretilmiştir [Şekil 10]. Analiz sonucuna göre elde edilen datanın fırın prosesi sonrası tersine mühendislik ile taranan data ile çakıştırılması gerçekleştirilerek ürün doğrulaması yapılmıştır [Şekil 11].



Şekil 10. Fırın prosesi tamamlanan ve şekil verilen yakıt boruları



Şekil 11. Analiz sonucuna göre elde edilen data ile fırın sonrası taranan datanın çakıştırılması

Farklı sıcaklıklara ait çalışma sonuçları Çizelge 1.'de sunulmaktadır.

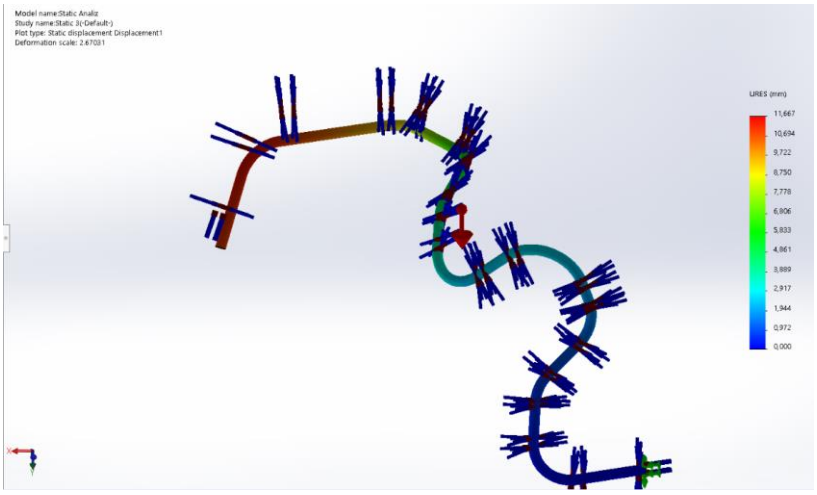
Çizelge 1. Farklı sıcaklıklara ait deneme sonuçları

Deneme Numarası	Boru Ölçüsü	Üst Sıcaklık [°C]	Alt Sıcaklık [°C]	Ortalama Sıcaklık [°C]	Frekans [hz]	Soğutma süresi [sec]	Sonuç
1	8X1	185	175	180	26	150	NOK
2	8X1	185	175	180	26	120	NOK
3	8X1	185	175	180	26	150	NOK
4	8X1	190	180	185	26	150	OK
5	8x1	185	170	175	32	150	NOK
6	8x1	185	170	175	26	150	NOK

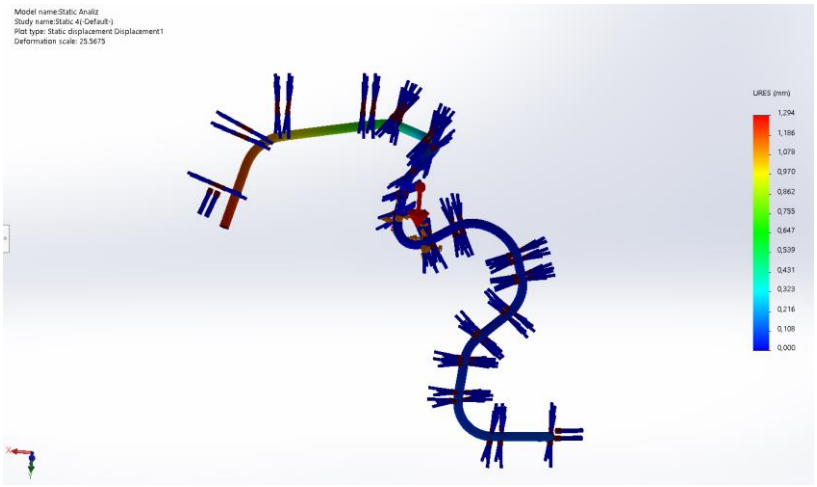
4.1. Yakıt borusunun sabitleme bölgesine göre analiz sonuçları

Çalışma kapsamında kullanılan yakıt borusu, 2 eksenli olmayıp, farklı eksenlerde düz ve kıvrımlı bir yapıya sahiptir. Dolayısıyla iki datanın hangi nokta veya noktalardan çakıştırılarak farklılıkların gözlemlendiği önem arz etmektedir. Parça Şekil 12 de görüldüğü üzere en sol

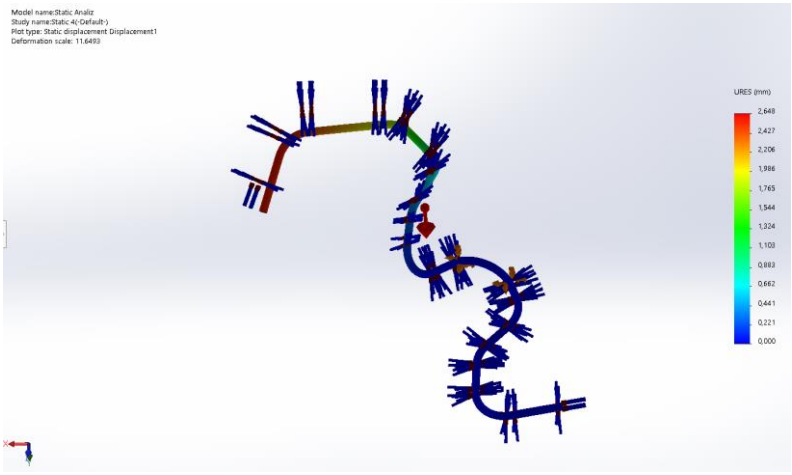
tarafındaki konnektör bağlantısından sabitlendiğinde, şeklin en sağ kısımdaki konnektör bağlantısının bulunduğu bölgenin deplasmanı 10 mm ye çıkmaktadır. Yine aynı şekilde, en sağ kısımdan sabitlenerek, en sol kısımdaki deplasman gözlemlenmeye çalışıldığında bu fark yine 10 mm civarında olmaktadır [Şekil 13]. Fakat 2. ve 3. sabitleme noktaları olarak parçanın orta kısmına daha yakın bükümlerden sabitleme yapıldığında, deplasman farkının 1,5 - 2,5 mm civarında olduğu görülmektedir [Şekil 14]. Parçanın sahip olması beklenen genel konum toleransının ±3 mm olduğu göz önüne alındığında, bu durum kabul edilebilir ve uygun seviyede bir durumdur.



Şekil 12. Yer değiştirme analiz sonuçları-1



Şekil 13. Yer değiştirme analiz sonuçları-2



Şekil 14. Yer değiştirme analiz sonuçları-3

5. SONUÇ

Bu çalışma kapsamında, 3 katmanlı yakıt borusunun modellenmesi, sonlu elemanlar metoduyla analiz edilmesi ve yapılan analiz sonuçlarının, sıcak hava fırınıyla üretildikten sonra tersine mühendislik ile taranarak datası elde edilen fiziki parçalar ile doğrulanması çalışması yapılmıştır. Modelleme ve sonlu elemanlar metodunun uygulanmasında SolidWorks programından yararlanılmıştır. Fiziki olarak üretilen parçanın taranmasında AICON makinesi kullanılmıştır.

Sıcak hava fırınında üretim yapılırken; fırın alt sıcaklığı, fırın üst sıcaklığı, ortalama fırın sıcaklığı, proses frekansı, duşlama süresi, duşlama sıcaklığı gibi farklı parametreler belirlenmiştir. Ortalama fırın sıcaklığının etkisini gözlemleyebilmek adına, diğer parametreler optimum çalışma şartlarında sabitlenmiştir ve değişken olarak ele alınmamıştır.

Fiziki üretimler sırasında optimum şartların belirlenmesinde deneme-yanılma yöntemi ile başlangıç parametreleri seçilmiştir. Çalışma kapsamında belirlenen amaçlardan biri de, deneme-yanılma sayısını mümkün olduğunca en aza indirmek ve ortadan kaldırmaktır. Sıcak hava fırın prosesi sonrası parça kontrolleri için kontrol fikstüründen yararlanılmaktadır. Parçanın sahip olması beklenen genel konum toleransına göre düz ve bükümlü kısımların uygunluğuna karar verilmektedir.

Fırın prosesi sonrası elde edilen data ile analiz sonucu ortaya çıkan nominal data arasında fark görülmektedir. Ancak bu fark, parçanın her iki ucunda yer alacak ve montaj prosesinde kullanılacak konnektör bağlantılarından çakıştırıldığında ortaya çıkmaktadır. Parçanın sahip olduğu üç boyutlu form ve üzerindeki farklı yönlerdeki bükümler düşünüldüğünde, en uçta yaşanan farklılık kabul edilebilir seviyededir. Parçanın orta kısımlarına yakın bölgede yer alan bükümlerden yapılan çakıştırmalarda, aradaki deplasman farkının 1,5 mm-2,5 mm seviyelerinde olması, parçanın sahip olduğu genel konum toleransı göz önüne alındığında,

uygundur. Ortalama fırın sıcaklığı, parçanın görsel uygunluğuna da doğrudan etki etmektedir. Parça üzerinde gözle görülebilecek deformasyonlar veya uygunsuzluklar mevcut ise parametreler değiştirilerek görsel olarak da uygun hale getirilmektedir.

7. KAYNAKÇA

Anonim1, http://www.megep.meb.gov.tr/mte_program_modul/moduller_pdf/Dizel%20Motorlar%C4%B1%20Yak%C4%B1t%20Sistemleri%20(Motorlu%20Ara%C3%A7lar).pdf (Erişim Tarihi: 02.05.2022).

Anonim2, http://web.hitit.edu.tr/dosyalar/materyaller/hicriyavuz@hititedutr100220179U6G8Q9S.pdf (Erişim Tarihi: 01.05.2022)

Anonim3, https://www.leku- ona.com/en/aicon-nueva-maquina-medicion-optica-tubos/ (Erişim Tarihi: 02.05.2022).

Anonim4, http://www.baodie.cn/en/productsh.aspx?Id=31d2b87e-c12c-4547-b550-f894c381c3cc (Erişim tarihi: 19.06.2022)

Hopf, G., Hans, R., Edward, K.G. (1994), Development of Multilayer Thermoplastic Fuel Lines With Improved Barrier Properties, SAE Transactions. *Journal Of Materıals & Manufacturıng*, 103(5):64-80

Jing, N., Fukushi, T., Molnar, A., Bilbrey, D,B., Muggli, M,W., Hine, A,M., Spurgeon, K,M., Christopher, A, H. (2005), *Fluoropolymer blends and multilayer articles.* United States Patent # 6849314.

J.G. Drobny. (2007), Fluoropolymers in automotive applications. *Polymers for Advanced Technologies,* 18(2):117-121. https://doi.org/10.1002/pat.5732

K.J. Kallio, M.S. Hedenqvist, (2008), Ageing properties of polyamide-12 pipes exposed to fuels with and without ethanol. *Polymer Degradation Stabiliy,* 93(10), 1846-1854.

Kurnaz, U. (2019), Çok Katlı Poliamid Kompozit Borunun Extrüzyon İle Üretiminde Alev Uygulamasının Mekanik Özelliklere Etkisinin İncelenmesi. Sakarya Üniversitesi, Fen Bilimleri Enstitüsü, Yüksek Lisans Tezi, Sakarya

M.S. Hedenqvist, J. Ritums, M. Condé-Brana, G. Bergman. (2003), Sorption and desorption of tetrachloroethylene in fluoropolymers: Effects of the chemical structure and crystallinity. *Journal of Applied Polymer Science*, 87(9): 1474-1483.

Molnar, A., Baker, J., Tuckner, P., Bilbrey, D. (2002), Comparison of Fuel Hose SHED Test Results and Predicted Values Using Fundamental Material Barrier Properties. *SAE Transactions, Journal Of Materıals Andmanufacturıng,* 111 (5): 373-385.

Wei, Xin-Feng; Kallio, Kai J.; Bruder, Stefan; Bellander, Martin; Gedde, Ulf W.; Hedenqvist, Mikael S. (2018), Long-term performance of a polyamide-12-based fuel line with a thin poly(ethylene-co-tetrafluoroethylene) (ETFE) inner layer exposed to bio- and petroleum diesel. *Polymer Degradation and Stability,* (), S0141391018302830–. doi:10.1016/j.polymdegradstab.2018.09.003

AUTHORS INDEX

LAST NAME	NAME	Paper Id(page no)
ACAR	B. Serpil	53, 83
AHMED	Kazi Sher	137
AKAR	Samet	241
AKDENİZ	Özgür	447
AKSOY	Cansu	523
AKŞUN	Serhat	523
AKYÜZ	Murat Erkin	613
Al-HUMAIRI	Elaf Riyadh Resen	171
ALİBAŞOĞLU	Metin	721
ALİSİNOĞLU	M. Berkan	557
ALKAN	Ahmet H.	409
ALMUS	F. Ginaz	325, 339
ALPAR	Mert	447
ALTINAY	T. Yasin	689
ALTUN	Barış	259
AMİNBAKHSH	Saman	171
ASLAN	Yusuf	603
ASLANTAŞ	Kubilay	591
ATİK	Hediye	543
AYDOĞAN	Asude	289
BAKKAL	Mustafa	191, 275
BALCI	Mehmet N.	301
BARANOĞLU	Besim	579, 485
BARNES	Jo	73
BARZEGAR	Ramin	423, 447
BAYRAM	Mustafa B.	423
BECERİKLİ	S. Can	423
BEDİZ	Bekir	137
BENGÜR	Suat	241
BEYHAN	Canberk	41
BOUAZZA-MAROUF	Kaddour	381
BROWN	Laurie	73
BUDAK	Erhan	191
ÇAĞLAYAN	Recep	627
ÇAKIR	M. Cemal	457, 673,721
ÇALIŞKAN	Hakan	259
ÇAVDAR	Kadir	557
ÇAVUŞOĞLU	Hasan Safa	579

LAST NAME	NAME	Paper Id(page no)
ÇELİK	Salih	523
CİVELEK	Hasan Ali	557
COŞKUN	Hakan	369
COŞKUNER	Evren	485
COURTY	Léo	111
DALLI	Bilgin	457
DANISH	Mohd	591
DEĞİRMENCİ	Bensu	409
DELBARRE	Samuel	111
DEMİR	Kerem Utku	153
DEMİRCİ	Emre	433
DİLMEÇ	Murat	705
DİZECİ	Şehram	317
DOĞRUSADIK	Ahmet	231
ERDOĞAN	Hatice	423
ERGÜVEN	Ö. Faruk	325
ESAT	Volkan	53
EZME	Enes	567
FIÇICI	Ferhan	689
FİLİZ	Erkin	409
GENÇ	Mehmet Onur	471
GÖKMEN	Onur	557
GÜL	Ceyhun	689
HACALOĞLU	Tuğçe	289
HALKACI	Hüseyin Selçuk	705
HANCOX	Graham	83
HASÇELİK	Ahmet	591
HATİPOĞLU	Ersen	191
HİMMETOĞLU	Selçuk	41, 97
HOROZOĞLU	İsmail U.	447
İBİŞ	Muhammed Mahbub	485
ISIK	Yahya	627
KAFTANOĞLU	Bilgin	289
KARAKAŞ	Oğuzhan	339
KARAMAN	Mustafa	409
KATMER	Şükran	603
KATMER	M. Can	689
KAYA	Arda	325

LAST NAME	NAME	Paper Id(page no)
KAYA	Necmettin	471
KAYNAK	Yusuf	369
KOÇ	Enes	339
KOÇUM	A. Tardu	339
KONUKSEVEN	E. İlhan	409
KOPMAZ	Osman	663
KOYAŞ	Barış	613
KOYUNCU	Eminalp	339
KÜÇÜKGENÇ	Cem	339
KURAL	Sami	369
KURT	Hasan Aytuğ	275
KURTOĞLU	Baturay	339
LOMOV	Stepan V.	27
LOTFİ	Bahram	171
MAYNARD	Sally	83
MORRIS	Andrew	73, 83
MUMCU	L. Furkan	689
NEHRİ	Y. Emre	567
NORY	Hayatullah	523
ÖNAL	Sinan Yalçın	497
ÖNER	Güven	325
ORAL	Ali	209, 567
ORHAN	Tayfun	369
ORHAN	Sadettin	641
ÖZBEY	Mehmet Furkan	125
ÖZCAN	Bülent	339
ÖZDEMİR	Mustafa	497
ÖZŞAHİN	Orkun	259
ÖZTÜRK	Osman	221
PAYGOZAR	Bahman	317
POUR RAHMATİ KHALEJAN	S. H.	511
REİS	Murat	613
SABUNCUOĞLU	Barış	27
ŞEKER	Ulvi	603
ŞEN	Deniz Kavala	663
ŞENER	Batıhan	153
ŞERİFAĞAOĞLU	Emre	613
SEVEN	Seher	485, 579

LAST NAME	NAME	Paper Id(page no)
SOETE	Jeroen	27
SONGÜR	Kaan	241
TANABİ	Hamed	27
TEKİN	Ozan	423, 447
TUNCER	Can	209
TÜREDİ	Derin	409
TURHAN	Cihan	125
TÜRK	M. Ayberk	241
TÜRKÖZ	Sakıp	209
TÜRKÖZ	Mevlüt	705
TÜTÜNCÜ	Furkan	673
ÜNÜVAR	Ali	221
ÜNVER	Hakkı Özgür	153
WILLIAMS	Toby	381
YALÇIN	Fatma	689
YAPAN	Yusuf Furkan	705
YAY	İsmail	433
YETER	Alper	275
YILDIRIM	Ender	325, 339
YILDIZ	Betül Sultan	391, 399
YILMAZ	Okan Deniz	357
YILMAZ	Mahmut	275
YILMAZ	Muhammet Mustafa	641
ZENGİN	Elif Nur	41